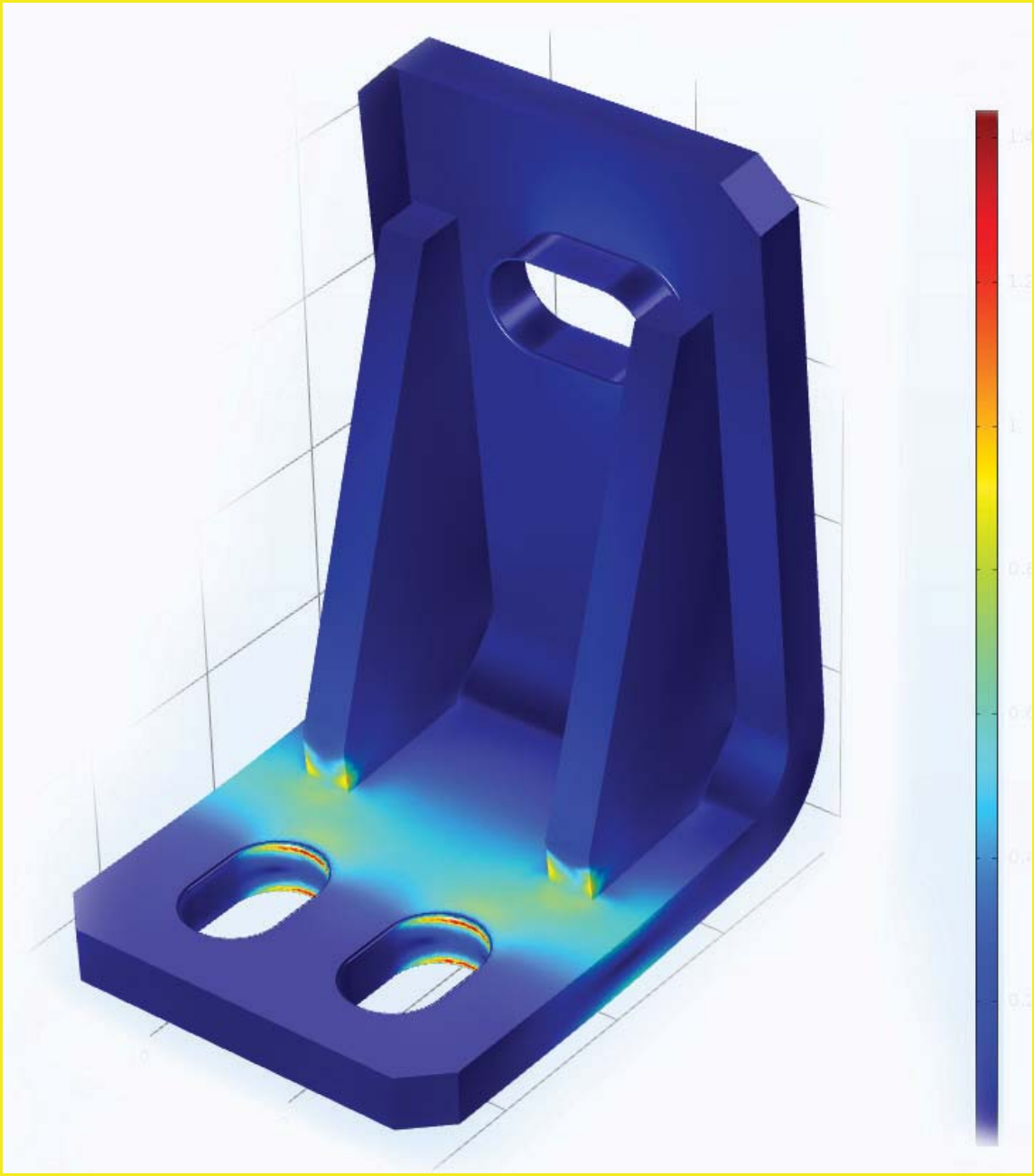
DYNA

Journal of the Facultad de Minas, Universidad Nacional de Colombia - Medellin Campus



DYNA 85 (205), June, 2018 - ISSN 0012-7353
Tarifa Postal Reducida No. 2014-287 4-72
La Red Postal de Colombia, Vence 31 de Dic. 2018.

UNIVERSIDAD
NACIONAL
DE COLOMBIA
SEDE MEDELLÍN
FACULTAD DE MINAS

UNIVERSIDAD NACIONAL DE COLOMBIA
SEDE MEDELLÍN
FACULTAD DE MINAS

DYNA
http://dyna.medellin.unal.edu.co/

DYNA is an international journal published by the Facultad de Minas, Universidad Nacional de Colombia, Medellín Campus since 1933. DYNA publishes peer-reviewed scientific articles covering all aspects of engineering. Our objective is the dissemination of original, useful and relevant research presenting new knowledge about theoretical or practical aspects of methodologies and methods used in engineering or leading to improvements in professional practices. All conclusions presented in the articles must be based on the current state-of-the-art and supported by a rigorous analysis and a balanced appraisal. The journal publishes scientific and technological research articles, review articles and case studies.

DYNA publishes articles in the following areas:

Organizational Engineering
Civil Engineering
Materials and Mines Engineering
Geosciences and the Environment
Systems and Informatics
Chemistry and Petroleum
Mechatronics
Bio-engineering
Other areas related to engineering

Publication Information

DYNA (ISSN 0012-73533, printed; 2346-2183, online) is published by the Facultad de Minas, Universidad Nacional de Colombia, with a bimonthly periodicity (February, April, June, August, October, and December). Circulation License Resolution 000584 de 1976 from the Ministry of the Government.

Contact information
Web page: http://dyna.unalmed.edu.co
E-mail: dyna@unal.edu.co
Mail address: Revista DYNA
Facultad de Minas Universidad Nacional de Colombia - Medellín Campus
Carrera 80 No. 65-223 Bloque M9 - Of.:107
Telephone: (574) 4255068 Fax: (574) 4255343
Medellín - Colombia

© Copyright 2016. Universidad Nacional de Colombia
The complete or partial reproduction of texts with educational ends is permitted, granted that the source is duly cited. Unless indicated otherwise.

Notice
All statements, methods, instructions and ideas are only responsibility of the authors and not necessarily represent the view of the Universidad Nacional de Colombia. The publisher does not accept responsibility for any injury and/or damage for the use of the content of this journal.
The concepts and opinions expressed in the articles are the exclusive responsibility of the authors.

Institutional Exchange Request
DYNA may be requested as an institutional exchange through the e-mail canjebib_med@unal.edu.co or to the postal address:

Biblioteca Central “Efe Gómez”
Universidad Nacional de Colombia, Sede Medellín
Calle 59A No 63-20
Teléfono: (57+4) 430 97 86
Medellín - Colombia

Indexing and Databases

DYNA is admitted in:

The National System of Indexation and Homologation of Specialized Journals CT+I-PUBLINDEX, Category A2

Science Citation Index Expanded
Web of Science - WoS, Thomson Reuters
Journal Citation Reports - JCR
SCImago Journal & Country Rank - SJR
Science Direct
SCOPUS
Chemical Abstract - CAS
Scientific Electronic Library on Line - SciELO
GEOREF
PERIÓDICA Data Base
Latindex
Actualidad Iberoaméricana
RedALyC - Scientific Information System
Directory of Open Acces Journals - DOAJ
PASCAL
CAPES
UN Digital Library - SINAB
CAPES
EBSCO Host Research Databases

Publisher’s Office
Juan David Velásquez Henao, Director
Mónica del Pilar Rada T., Editorial Coordinator
Catalina Cardona A., Editorial Assistant
Amilkar Álvarez C., Diagrammer
Byron Llano V., Editorial Assistant
Landsoft S.A., IT

Reduced Postal Fee
Tarifa Postal Reducida # 2014-287 4-72. *La Red Postal de Colombia,* expires Dec. 31st, 2018

UNIVERSIDAD NACIONAL DE COLOMBIA
SEDE MEDELLÍN
FACULTAD DE MINAS

DYNA

UNIVERSIDAD NACIONAL DE COLOMBIA
SEDE MEDELLÍN
FACULTAD DE MINAS



DYNA
http://dyna.medellin.unal.edu.co/

COUNCIL OF THE FACULTAD DE MINAS

Dean
Pedro Nel Benjumea Hernández PhD

Vice-Dean
Ernesto Pérez González, PhD

Vice-Dean of Research and Extension
Santiago Arango Aramburo, PhD

Director of University Services
Santiago Medina Hurtado, PhD

Academic Secretary
Francisco Javier Díaz Serna, PhD

Representative of the Curricular Area Directors
Wilfredo Montealegre Rubio, PhD

Representative of the Curricular Area Directors
Evelio Andrés Gómez Giraldo, PhD

Representative of the Basic Units of Academic-Administrative Management
Juan David Velásquez Henao, PhD

Representative of the Basic Units of Academic-Administrative Management
Néstor Ricardo Rojas Reyes, PhD

Professor Representative
Luis Hernán Sánchez Arredondo, MSc

Delegate of the University Council
León Restrepo Mejía, PhD

Student representative (alternate) undergraduate at the Faculty Council
Alejandra Jiménez Upegui

FACULTY EDITORIAL BOARD

Dean
Pedro Nel Benjumea Hernández, PhD

Vice-Dean of Research and Extension
Santiago Arango Aramburo, PhD

Members
Oscar Jaime Restrepo Baena, PhD
Juan David Velásquez Henao, PhD
Jaime Aguirre Cardona, PhD
Alfonso Espinosa Parada, PhD
Mónica del Pilar Rada Tobón, MSc

JOURNAL EDITORIAL BOARD

Editor-in-Chief
Juan David Velásquez Henao, PhD
Universidad Nacional de Colombia, Colombia

Editors
George Barbastathis, PhD
Massachusetts Institute of Technology, USA

Tim A. Osswald, PhD
University of Wisconsin, USA

Juan De Pablo, PhD
University of Wisconsin, USA

Hans Christian Öttinger, PhD
Swiss Federal Institute of Technology (ETH), Switzerland

Patrick D. Anderson, PhD
Eindhoven University of Technology, the Netherlands

Igor Emri, PhD
Associate Professor, University of Ljubljana, Slovenia

Dietmar Drummer, PhD
Institute of Polymer Technology University Erlangen-Nürnberg, Germany

Ting-Chung Poon, PhD
Virginia Polytechnic Institute and State University, USA

Pierre Boulanger, PhD
University of Alberta, Canadá

Jordi Payá Bernabeu, Ph.D.
Instituto de Ciencia y Tecnología del Hormigón (ICITECH)
Universitat Politècnica de València, España

Javier Belzunce Varela, Ph.D.
Universidad de Oviedo, España

Luis Gonzaga Santos Sobral, PhD
Centro de Tecnología Mineral - CETEM, Brasil

Agustín Bueno, PhD
Universidad de Alicante, España

Henrique Lorenzo Cimadevila, PhD
Universidad de Vigo, España

Mauricio Trujillo, PhD
Universidad Nacional Autónoma de México, México

Carlos Palacio, PhD
Universidad de Antioquia, Colombia

Jorge Garcia-Sucerquia, PhD
Universidad Nacional de Colombia, Colombia

Juan Pablo Hernández, PhD
Universidad Nacional de Colombia, Colombia

John Willian Branch Bedoya, PhD
Universidad Nacional de Colombia, Colombia

Enrique Posada, Msc
INDISA S.A, Colombia

Oscar Jaime Restrepo Baena, PhD
Universidad Nacional de Colombia, Colombia

Moisés Oswaldo Bustamante Rúa, PhD
Universidad Nacional de Colombia, Colombia

Hernán Darío Álvarez, PhD
Universidad Nacional de Colombia, Colombia

Jaime Aguirre Cardona, PhD
Universidad Nacional de Colombia, Colombia

UNIVERSIDAD
NACIONAL
DE COLOMBIA
SEDE MEDELLÍN
FACULTAD DE MINAS



DYNA
http://dyna.medellin.unal.edu.co/

UNIVERSIDAD NACIONAL DE COLOMBIA
SEDE MEDELLÍN
FACULTAD DE MINAS



DYNA
http://dyna.medellin.unal.edu.co/

DYNA 85 (205), June, 2018. Medellin. ISSN 0012-7353 Printed, ISSN 2346-2183 Online

CONTENTS

Discrimination between the lognormal and Weibull distributions by using multiple linear regression 9
Jesús Francisco Ortiz-Yañez & Manuel Román Piña-Monarrez

Study of agglomeration and magnetic sedimentation of Glutathione@Fe_3O_4 nanoparticles in water medium 19
Wilfredo Marimón-Bolívara & Edgar E. González

Ab-initio analysis of magnetic, structural, electronic and thermodynamic properties of the Ba_2TiMnO_6 manganite 27
Críspulo Enrique Deluque-Toro, David A. Landínez-Téllez & Jairo Roa-Rojas

A geometrical robust design using the Taguchi method: application to a fatigue analysis of a right angle bracket 37
Rafael Barea, Simón Novoa, Francisco Herrera, Beatriz Achiaga, Nuria Candela

Normalized difference vegetation index for rice management in El Espinal, Colombia 47
Mauricio González-Betancourt & Zaira Liceth Mayorga-Ruíz

Effects of cutting parameters on surface roughness and hardness in milling of AISI 304 steel 57
Luis Wilfredo Hernández-González, Roberto Pérez-Rodríguez, Ana María Quesada-Estrada & Luminita Dumitrescu

Verification of the vibrational theoretical assignment of the DADP using isotopic labelling 64
Eduardo Espinosa-Fuentes, Edgardo Meza-Fuentes, Fredy Colpas-Castillo, John R. Castro-Suarez, Gilberto Chiquillo-Correa & Malka Mora

Effect of the tryptone concentration on the calcium carbonate biomineralization mediated by Bacillus cereus 69
Gerardo Andrés Caicedo-Pineda, María Consuelo Prada-Fonseca, Ana Elisa Casas-Botero & Hader Vladimir Martínez-Tejada

Development of a high performance batteries charger with low THD, high power factor, and high efficiency 76
Johan Sebastián Sánchez-Choachi, Miguel Ángel Dávila & Cesar Leonardo Trujillo

Elastic behavior of stiffened curved plates subjected to transverse loading 83
Abel Noguera-Garban, Carlos Graciano & David G. Zapata-Medina

Incorporation of aluminum oxide in the formulation of pastes for building materials 90
Luis Miguel Carrillo-Rodriguez, Leonardo Cely-Illera, Jairo Cely-Niño & Claudia Vanessa Cely-Illera

Risk analysis using meteorological weather factors in solar energy conversion systems 98
David Cardoza, Jorge M. Uribe & Jairo Palacios

Obtaining the electrical impedance phase using Wavelet transform and Fourier transform from transient signals. Part 2: practical assessment and validation 105
Eduardo Gómez-Luna, Juan Sebastián Cuartas-Bermúdez & Eduardo Marlés-Sáenz

Streptomyces clavuligerus strain selection for clavulanic acid biosynthesis: a study based on culture composition effects and statistical analysis 111
Laura Pinilla, León F. Toro, Claudio Avignone-Rossa, Mariana Peñuela & Rigoberto Ríos-Estepa

Hydraulic conductivity in layered saturated soils assessed through a novel physical model 119
Eduardo Dulcey-Leal, Fausto Molina-Gómez & Lenin Alexander Bulla-Cruz

Impact of changing location and power of a PV system in electrical distribution networks, integrating MATLAB and OpenDSS 125
Javier Andrés Ruíz-Garzón, Daniel José González-Tristancho & Francy Catalina Espinosa-González

Crack filling in concrete by addition of Bacillus subtilis spores – Preliminary study 132
Nicole Schwantes-Cezario, Maria Vânia Nogueira do Nascimento Peres, Thomas Kehrwald Fruet, Geovana Souza Ferreira Nogueira, Berenice Martins Toralles & Davi De Souza Cezario

Thermal conductivities estimation in orthotropic materials making use of global optimization algorithms 140
Jefferson Vega-Suarez, Edgar García-Morantes & Rodrigo Correa-Cely

Obtention and characterization of lithium superionic conductors using the glass-ceramic method 148
José Luis Narváez-Semanate, Ana Cândida Martins Rodrigues, Rodrigo Arbey Muñoz-Meneses, José Rodrigo Muñoz-Hoyos & Julián Antonio Villamarín-Muñoz

Hydrogen production in a novel configuration of UASB reactor under different hydraulic retention time 157
Diana Margarita Hernández, Lucía Andrea del Pilar Hurtado & Adela Tatiana Rodríguez-Chaparro

Flash flotation of free coarse gold using dithiophosphate and dithiocarbamate as a replacement for traditional amalgamation 163
Moisés Oswaldo Bustamante-Rúa, Doria Maria Najanjo-Gómez, Alan José Daza-Aragón, Pablo Bustamante-Baena & Julián David Osorio-Botero

Model of nonlinear behavior applied to prediction of settlement in deep foundations 171
Jean Rodrigo Garcia & Paulo José Rocha-de Albuquerque

Evaluation of the lubricating power of sweet almond oil without additives 179
Arnoldo Emilio Delgado-Tobón, William Arnulfo Aperador-Chaparro & Rafael Guillermo García-Cáceres

Application of double filtration with granular activated carbon for Atrazine reduction on water treatment processes 184
Lina Fuentes-López, Claudia Amézquita-Marroquín & Patricia Torres-Lozada

Experimental characterization, modeling and compensation of hysteresis in force sensing resistors 191
Leonel Paredes-Madrid, Arnaldo Matute, Andrés F. Cruz-Pacheco, Carlos A. Parra-Vargas & Elkin I. Gutiérrez-Velásquez

Comparison of three IRP-based models to reduce logistics costs and greenhouse gas emissions 199
Julian Andres Zapata-Cortes, Martín Darío Arango-Serna & Conrado Augusto Serna-Urán

Highway designs: effects of heavy vehicles stability 205
Gonzalo Moreno, Rodrigo Vieira & Daniel Martins

UNIVERSIDAD NACIONAL DE COLOMBIA
SEDE MEDELLÍN
FACULTAD DE MINAS



DYNA
http://dyna.medellin.unal.edu.co/

An analysis of the socioenvironmental problems created by the construction of road tunnels in Colombia: case study 211
Tania Ramírez & Carlos Zárate

Microalgae biorefineries: applications and emerging technologies 219
Néstor David Giraldo-Calderón, Raquel Juliana Romo-Buchelly, Andrés Alonso Arbeláez-Pérez, Danilo Echeverri-Hincapié & Lucia Atehortúa-Garcés

Evaluation of turbidity and dissolved organic matter removal through double filtration technology with activated carbon 234
Torres-Lozada P; Amezquita-Marroquín C. P. Agudelo Martínez K. D. Ortiz Benítez N. Martínez Ducuara D. S.

Construction of a short circuit frequency map to define GMAW-S parameters during WPSs development 240
David Bernardo Hoyos-Arango, Oscar León Mejía-López & Jorge Enrique Giraldo-Barrada

Analysis of the European tourist mines and caves to design a monitoring system 249
Lluís Sanmiquel, Pura Alfonso, Marc Bascompta, Carla Vintró, David Parcerisa & Josep Oliva

Characterization of postures to analyze people's emotions using Kinect technology 256
Julián Alberto Monsalve-Pulido & Carlos Alberto Parra-Rodríguez

Local polynomial approximation and intersection of confidence intervals for removing noise of lightning electric field measurements 264
Herbert Enrique Rojas-Cubides, Camilo Andrés Cortés-Guerrero, María Carolina Forero-Mejía

Methodology to determine the mean and extreme sea level regimes (astronomical and meteorological tide) considering scarce records in microtidal zones: colombian Caribbean case 274
Andrés Fernando Orejarena-Rondón, Luis Jesús Otero-Díaz, Juan Camilo Restrepo L. Isabel María Ramos-De la Hoz & Leonardo Marriaga-Rocha

Development of an information system for teleoperated physical rehab care service via Internet. Pilot case: patients with mild knee injury who live in geographically vulnerable zones 284
José Rafael Tovar-Cuevas, Juan David Díaz-Mutis, Getssy Elizabeth Quiñones-Mora, Anabella Pabón-Romero & José Isidro García-Melo

Design and implementation of a photolithography system to fabricate microdevices from thin films 294
Jhon Jairo Realpe, Gilberto Bolaños-Pantoja & Juan Fernando Florez

Mitigation potential of active transport projects: trip attraction and CO_2 avoidance indicators in colombian cities 302
Mónica Espinosa, José Pacheco & Juan Felipe Franco

Shear modulus of mining tailings from resonant column tests 310
Eliana Martínez-Rojas, Fausto Molina-Gómez & Juan Carlos Ruge

Assessment strategies for the integral management of waste electrical and electronic equipment-WEEE 319
Johan Manuel Redondo, Danny Ibarra-Vega, Liliana Monroy & Jorge Bermúdez

Bioactivity analysis of the AZ31 Mg alloy coated by PEO (Plasma Electrolytic oxidation) 328
Kevin Dorado-Bustamante, Benjamín Zuluaga-Díaz & Hugo Estupiñán-Duran

Manufacture of oxy-acetylene thermally sprayed coatings on refractory substrates from unconventional feedstock material 338
Edwin H. Cadavid-Iglesias, Fabio Vargas-Galvis, María Esperanza López-Gómez, Carlos Mario Mesa, Fabio Alonso Vargas, Guillermo Latorre & Gabriel Peña

Risk assessment in treatment processes for the development of a Water Safety Plan – WSP 348
Claudia Espinosa, Lina Marcela Hoyos-Palacio, Lucelly López-López, Daniel Gallego-González, Andrés David Aranzazu-Ceballos, Juan Sebastián Marín-Cárdenas, Dayana Andrea Quintero-Moreno & Isabel Cristina Ortiz-Trujillo

Freight vehicle condition monitoring through the availability 355
Laksmi Penabad-Sanz, Pedro Antonio Rodríguez-Ramos & Arsenio Miguel Iznaga-Benítez

Integration of tools for decision making in vehicular congestion 363
Nelson Iván Herrera-Herrera, Sergio Luján-Mora & Estevan Ricardo Gómez-Torres

Our cover
Image alluding to Article:
A geometrical robust design using the Taguchi method: application to a fatigue analysis of a right angle bracket

Authors:
Rafael Barea, Simón Novoa, Francisco Herrera, Beatriz Achiaga, & Nuria Candela



UNIVERSIDAD NACIONAL DE COLOMBIA
SEDE MEDELLÍN
FACULTAD DE MINAS



DYNA
http://dyna.medellin.unal.edu.co/

DYNA 85 (205), June, 2018. Medellin. ISSN 0012-7353 Printed, ISSN 2346-2183 Online

CONTENIDO

Discriminación entre la distribución lognormal y la distribución Weibull utilizando regresión lineal múltiple 9
Jesús Francisco Ortiz-Yañez & Manuel Román Piña-Monarrez

Estudio de aglomeración y sedimentación magnética de nanopartículas de Glutatión@Fe_3O_4 en medio acuoso 19
Wilfredo Marimón-Bolívara & Edgar E. González

Análisis ab-initio de las propiedades magnéticas, estructurales, electrónicas y termodinámicas de la manganita Ba_2TiMnO_6 27
Críspulo Enrique Deluque-Toro, David A. Landínez-Téllez & Jairo Roa-Rojas

Un diseño geométrico robusto empleando el Método de Taguchi: aplicación a un análisis de fatiga de una escuadra 37
Rafael Barea, Simón Novoa, Francisco Herrera, Beatriz Achiaga, & Nuria Candela

Índice de vegetación de diferencia normalizada para el manejo del arroz en El Espinal, Colombia 47
Mauricio González-Betancourt & Zaira Liceth Mayorga-Ruíz

Efectos de los parámetros de corte en la rugosidad superficial y la dureza en el fresado del acero AISI 304 57
Luis Wilfredo Hernández-González, Roberto Pérez-Rodríguez, Ana María Quesada-Estrada & Luminita Dumitrescu

Verificación de la asignación vibracional teórica de DADP usando marcaje isotópico 64
Eduardo Espinosa-Fuentes, Edgardo Meza-Fuentes, Fredy Colpas-Castillo, John R. Castro-Suarez, Gilberto Chiquillo-Correa & Malka Mora

Efecto de la concentración de triptona en la biomineralización de carbonato de calcio mediada por Bacillus cereus 69
Gerardo Andrés Caicedo-Pineda, María Consuelo Prada-Fonseca, Ana Elisa Casas-Botero & Hader Vladimir Martínez-Tejada

Desarrollo de un cargador de baterías de alto desempeño con bajo THD, alto factor de potencia y alta eficiencia 76
Johan Sebastián Sánchez-Choachi, Miguel Ángel Dávila & Cesar Leonardo Trujillo

Comportamiento elástico de placas curvas rigidizadas sometidas a cargas transversales 83
Abel Noguera-Garban, Carlos Graciano & David G. Zapata-Medina

Incorporación de óxido de aluminio en la formulación de pastas para materiales de construcción 90
Luis Miguel Carrillo-Rodriguez, Leonardo Cely-Illera, Jairo Cely-Niño & Claudia Vanessa Cely-Illera

Análisis de riesgo usando factores meteorológicos en sistemas de conversión de energía de solar 98
David Cardoza, Jorge M. Uribe & Jairo Palacios

Obtención de la fase de la impedancia eléctrica usando transformada Wavelet y transformada de Fourier de señales transitorias. Parte 2: evaluación práctica y validación 105
Eduardo Gómez-Luna, Juan Sebastián Cuartas-Bermúdez & Eduardo Marlés-Sáenz

Selección de una cepa de Streptomyces clavuligerus para la biosíntesis de ácido clavulánico: un estudio basado en los efectos de la composición del medio de cultivo y análisis estadístico 111
Laura Pinilla, León F. Toro, Claudio Avignone-Rossa, Mariana Peñuela & Rigoberto Ríos-Estepa

Estimación de la conductividad hidráulica en suelos saturados estratificados mediante un nuevo modelo físico 119
Eduardo Dulcey-Leal, Fausto Molina-Gómez & Lenin Alexander Bulla-Cruz

Impacto del cambio de la ubicación y la potencia de un sistema FV en redes de distribución eléctrica, integrando MATLAB y OpenDSS 125
Javier Andrés Ruíz-Garzón, Daniel José González-Tristancho & Francy Catalina Espinosa-González

Relleno de fisuras en concreto por la adición de esporas de Bacilos subtilis - Estudio preliminar 132
Nicole Schwantes-Cezario, Maria Vânia Nogueira do Nascimento Peres, Thomas Kehrwald Fruet, Geovana Souza Ferreira Nogueira, Berenice Martins Toralles & Davi De Souza Cezario

Estimación de conductividades térmicas en materiales ortotrópicos mediante algoritmos de optimización global 140
Jefferson Vega-Suarez, Edgar García-Morantes & Rodrigo Correa-Cely

Obtención y caracterización de conductores superiónicos de litio utilizando la ruta vitrocerámica 148
José Luis Narváez-Semanate, Ana Cândida Martins Rodrigues, Rodrigo Arbey Muñoz-Meneses, José Rodrigo Muñoz-Hoyos & Julián Antonio Villamarín-Muñoz

Producción de hidrogeno utilizando una nueva configuración de reactor anaerobio UASB bajo diferentes tiempos de retención hidráulica 157
Diana Margarita Hernández, Lucía Andrea del Pilar Hurtado & Adela Tatiana Rodríguez-Chaparro

Flotación flash de oro nativo grueso usando ditiofosfato y ditiocarbamato como remplazo de la amalgamación tradicional 163
Moisés Oswaldo Bustamante-Rúa, Doria Maria Najanjo-Gómez, Alan José Daza-Aragón, Pablo Bustamante-Baena & Julián David Osorio-Botero

Modelo de comportamiento no lineal aplicado a la predicción de asentamiento en fundaciones profundas 171
Jean Rodrigo Garcia & Paulo José Rocha-de Albuquerque

Evaluación del poder lubricante de aceite de almendras dulces sin aditivos 179
Arnoldo Emilio Delgado-Tobón, William Arnulfo Aperador-Chaparro & Rafael Guillermo García-Cáceres

Aplicación de la doble filtración con carbón activado granular para la reducción de Atrazina en procesos de tratamiento de agua potable 184
Lina Fuentes-López, Claudia Amézquita-Marroquín & Patricia Torres-Lozada

Caracterización experimental, modelado y compensación de la histéresis en sensores de fuerza resistivos 191
Leonel Paredes-Madrid, Arnaldo Matute, Andrés F. Cruz-Pacheco, Carlos A. Parra-Vargas & Elkin I. Gutiérrez-Velásquez

Comparación de tres modelos basados en el IRP para reducir costos logísticos y emisiones de gases efecto invernadero 199
Julian Andres Zapata-Cortes, Martín Darío Arango-Serna & Conrado Augusto Serna-Urán

UNIVERSIDAD NACIONAL DE COLOMBIA
SEDE MEDELLÍN
FACULTAD DE MINAS



DYNA
http://dyna.medellin.unal.edu.co/

Diseño de autopistas: efectos de la estabilidad de vehículos pesados 205
Gonzalo Moreno, Rodrigo Vieira & Daniel Martins

Análisis de la problemática socioambiental generada por la construcción de túneles viales en Colombia: caso de estudio 211
Tania Ramírez & Carlos Zárate

Biorefinerías de microalgas: aplicaciones actuales y nuevas tecnologías en desarrollo 219
Néstor David Giraldo-Calderón, Raquel Juliana Romo-Buchelly, Andrés Alonso Arbeláez-Pérez, Danilo Echeverri-Hincapié & Lucia Atehortúa-Garcés

Evaluación de la remoción de turbiedad y materia orgánica disuelta mediante la tecnología de doble filtración con carbón activado 234
Torres-Lozada P; Amezquita-Marroquín C. P. Agudelo Martínez K. D. Ortiz Benítez N. Martínez Ducuara D. S.

Construcción de un mapa de frecuencias de corto-circuito para definir parámetros de GMAW-S durante el desarrollo de WPSs 240
David Bernardo Hoyos-Arango, Oscar León Mejía-López & Jorge Enrique Giraldo-Barrada

Análisis de las cuevas y minas turísticas de Europa para diseñar un sistema de monitorización 249
Lluís Sanmiquel, Pura Alfonso, Marc Bascompta, Carla Vintró, David Parcerisa & Josep Oliva

Caracterización de posturas para el análisis de emociones de personas, por medio de la tecnología Kinect. 256
Julián Alberto Monsalve-Pulido & Carlos Alberto Parra-Rodríguez

Aproximación local polinomial e intersección de intervalos de confianza para la remoción de ruido en mediciones de campo eléctrico generado por rayos 264
Herbert Enrique Rojas-Cubides, Camilo Andrés Cortés-Guerrero, María Carolina Forero-Mejía

Metodología para determinar regímenes medios y extremales del nivel del mar (marea astronómica y meteorológica) cuando se cuenta con escasos registros instrumentales en áreas micromareales: caso Caribe colombiano 274
Andrés Fernando Orejarena-Rondón, Luis Jesús Otero-Díaz, Juan Camilo Restrepo L. Isabel María Ramos-De la Hoz &Leonardo Marriaga-Rocha

Desarrollo de un sistema de información para el servicio de atención tele-operado de rehabilitación física, vía Internet. Caso piloto: pacientes con lesiones leves de rodilla que viven en zonas de vulnerabilidad geográfica 284
José Rafael Tovar-Cuevas, Juan David Díaz-Mutis, Getssy Elizabeth Quiñones-Mora, Anabella Pabón-Romero & José Isidro García-Melo

Diseño e implementación de un sistema de fotolitografía para fabricar microdispositivos a partir de películas delgadas 294
Jhon Jairo Realpe, Gilberto Bolaños-Pantoja & Juan Fernando Florez

Potencial de mitigación de proyectos de transporte activo: indicadores de atracción de viajes y emisiones CO_2 en ciudades colombianas 302
Mónica Espinosa, José Pacheco & Juan Felipe Franco

Módulo de corte de relaves mineros a partir de ensayos de columna resonante 310
Eliana Martínez-Rojas, Fausto Molina-Gómez & Juan Carlos Ruge

Evaluación de estrategias para la gestión integral de residuos de aparatos eléctricos y electrónicos 319
Johan Manuel Redondo, Danny Ibarra-Vega, Liliana Monroy & Jorge Bermúdez

Análisis de la bioactividad de Mg AZ31 recubierta por PEO (Plasma Electrolytic Oxidation) 328
Kevin Dorado-Bustamante, Benjamín Zuluaga-Díaz & Hugo Estupiñán-Duran

Elaboración de recubrimientos cerámicos sobre sustratos refractarios utilizando proyección térmica oxiacetilénica a partir de materias primas no convencionales 338
Edwin H. Cadavid-Iglesias, Fabio Vargas-Galvis, María Esperanza López-Gómez, Carlos Mario Mesa, Fabio Alonso Vargas, Guillermo Latorre & Gabriel Peña

Evaluación del riesgo en procesos de tratamiento para el desarrollo de un Plan de Seguridad del Agua – PSA 348
Claudia Espinosa, Lina Marcela Hoyos-Palacio, Lucelly López-López, Daniel Gallego-González, Andrés David Aranzazu-Ceballos, Juan Sebastián Marín-Cárdenas, Dayana Andrea Quintero-Moreno & Isabel Cristina Ortiz-Trujillo

Monitoreo de la degradación de los vehículos de transporte de cargas a través de la disponibilidad 355
Laksmi Penabad-Sanz, Pedro Antonio Rodríguez-Ramos & Arsenio Miguel Iznaga-Benítez

Integración de herramientas para la toma de decisiones en la congestión vehicular 363
Nelson Iván Herrera-Herrera, Sergio Luján-Mora & Estevan Ricardo Gómez-Torres

Nuestra carátula
Imagen alusiva al artículo:
Un diseño geométrico robusto empleando el Método de Taguchi: aplicación a un análisis de fatiga de una escuadra

Autores:
Rafael Barea, Simón Novoa, Francisco Herrera, Beatriz Achiaga, & Nuria Candela



UNIVERSIDAD NACIONAL DE COLOMBIA
SEDE MEDELLÍN
FACULTAD DE MINAS



DYNA
http://dyna.medellin.unal.edu.co/

Discrimination between the lognormal and Weibull distributions by using multiple linear regression

Jesús Francisco Ortiz-Yañez [a] & Manuel Román Piña-Monarrez [b]

[a] *Validation Laboratory, Ted de México SA de CV, Ciudad Juárez, México. Jesus.ortiz@stoneridge.com*
[b] *Industrial and Manufacturing Department at IIT Institute, Universidad Autónoma de Ciudad Juárez, Ciudad Juárez, México. Manuel.pina@uacj.mx*

Received: July 29th, 2017. Received in revised form: January 16th, 2018. Accepted: March 13th, 2018.

Abstract
In reliability analysis, both the Weibull and the lognormal distributions are analyzed by using the observed data logarithms. While the Weibull data logarithm presents skewness, the lognormal data logarithm is symmetrical. This paper presents a method to discriminate between both distributions based on: *1)* the coefficients of variation (CV), *2)* the standard deviation of the data logarithms, *3)* the percentile position of the mean of the data logarithm and *4)* the cumulated logarithm dispersion before and after the mean. The efficiency of the proposed method is based on the fact that the ratio of the lognormal (b_{1ln}) and Weibull (b_{1w}) regression coefficients (slopes) b_{1ln}/b_{1w} efficiently represents the skew behavior. Thus, since the ratio of the lognormal (R_{ln}) and Weibull (R_w) correlation coefficients R_{ln}/R_w (for a fixed sample size) depends only on the b_{1ln}/b_{1w} ratio, then the multiple correlation coefficient R^2 is used as the index to discriminate between both distributions. An application and the impact that a wrong selection has on R(t) are given also.

Keywords: Weibull distribution; lognormal distribution; discrimination process; multiple linear regression; Gumbel distribution.

Discriminación entre la distribución lognormal y la distribución Weibull utilizando regresión lineal múltiple

Resumen
En el análisis de confiabilidad, las distribuciones Weibull y lognormal son ambas analizadas utilizando el logaritmo de los datos observados. Debido a que mientras el logaritmo de datos Weibull presenta sesgo, el logaritmo de datos lognormales es simétrico, entonces en este artículo basados en *1)* los coeficientes de variación (CV), *2)* en la desviación estándar del logaritmo de los datos, *3)* en la posición del percentil de la media del logaritmo de los datos y *4)* en dispersión acumulada del logaritmo antes y después de la media, un método para discriminar entre ambas distribuciones es presentado. La eficiencia del método propuesto está basado en el hecho de que el radio entre los coeficientes de regresión (pendientes) b_{1ln}/b_{1w} de la distribución lognormal (b_{1ln}) y de la distribución Weibull (b_{1w}), eficientemente representa el comportamiento del sesgo. De esta manera, dado que el radio de los coeficientes de correlación de la distribución lognormal (R_{ln}) y de la distribución Weibull (R_w), (para un tamaño de muestra fijo), solo depende del radio b_{1ln}/b_{1w}, entonces el coeficiente de correlación múltiple R^2 es utilizado como un índice para discriminar entre ambas distribuciones. Una aplicación y el impacto que una mala selección tiene sobre R(t) son también dadas.

Palabras clave: distribución Weibull; distribución lognormal; proceso de discriminación, regresión lineal múltiple; distribución Gumbel.

1. Introduction

Because of their flexibility to model several behaviors, the Weibull and the lognormal distributions are two of the most used types of distribution in reliability. However, because the Weibull distribution is based on a non-homogeneous Poisson process, it models additive effect behavior [1]. Similarly, because the lognormal distribution is based on a geometric Brownian motion, then it models multiplicative effect behavior [2]. Therefore, they should not be used interchangeably. Hence, a discrimination process between both distributions is needed. In particular, the negative effect on reliability due to a wrong selection between these distributions is shown by using the stress- strength analysis, where the reliability represents all probabilities that the failure

How to cite: Ortiz-Yañez, J.F. and Piña-Monarrez, M.R., Discrimination between the lognormal and Weibull distributions by using multiple linear regression. DYNA, 85(205), pp. 9-18, June, 2018.

© The author; licensee Universidad Nacional de Colombia.

Table 1
Compression loads

9.6	12.5	13.5	14.4	14.9	15.7	16.6	17.9	20
9.6	12.6	13.8	14.4	15	15.9	16.8	18	20.1
12.3	12.7	14	14.6	15.2	16	16.8	18.1	22.3
12.4	12.7	14.2	14.6	15.3	16.1	16.9	19.1	
12.4	13.2	14.4	14.7	15.3	16.5	17.9	19.7	

Source: Adapted from [4]

Table 2
Strength of the product

21	25	23	31	32
22	26	30	31	33
23	27	30	32	34

Source: Adapted from [4]

Table 3
Stress-strength reliability

Combination	*R*
Lognormal-Lognormal	0.9957
Lognormal-Weibull	0.9860
Weibull-Lognormal	0.9984
Weibull-Weibull	0.9882

Source: The authors

governing strength (S) exceeds the failure governing stress (s) [3]. The stress-strength formulation is given by

$$R = P(S > s) = \int_{-\infty}^{\infty} f(s)\left[\int_{s}^{\infty} f(S)\, dS\right] ds \quad (1)$$

In the stress-strength analysis it is assumed that time is not the cause of failure; instead, failure mechanisms are what cause the part to fail [4]. In addition, as can be seen in eq. (1), the estimated reliability depends entirely on the selected stress and strength distributions. Thus, because a wrong selection will overestimate or underestimate reliability, a wrong selection will largely impact the analysis conclusions. To illustrate the impact of a wrong selection on reliability, following data published in Wessels has been used ([4], sec. 7). Table 1 shows the stress data; and Table 2 the strength data.

Finally, the stress-strength analysis for the four possible combinations between the Weibull and lognormal distributions, is presented in Table 3. The estimation of the stress-strength reliability was performed by using the eq. (40-43) given in section 7.

From Table 3, we conclude that because each combination shows a different reliability index, then the accurate discrimination between the Weibull and the lognormal distributions is an issue that must be solved. To this end, researchers have used several selection procedures. Among the oldest ones are the Chi-square, the Anderson-Darling and the Cramer-Von Mises goodness-of-fit tests [5]. On the other hand, the most widely used methods are those based on the maximum likelihood (ML) function as they are those given in [6-10] and recently in [11-12]. In particular, the methods based on probability plot (PP) tests are in [13-15]. Those based on Kolmogorov-Smirnov (KS) test are in [16] and [17], and those based on Bayes analysis are in [18]. The discrimination process between the Weibull and the lognormal distributions depends *1)* on the relationship between the Coefficient of Variation (CV) of the observed data and their standard deviation (σ_x), *2)* on the mean position of the logarithm of the data (μ_x) and *3)* on the dispersion behavior before and after μ_x. Unfortunately, since none of the above approaches takes into account the skew behavior of the logarithm of the data, then none of them is effective in discriminating between both distributions.

Based on the fact that the Weibull data logarithm (Gumbel behavior) *always presents negatively skewed behavior*, the logarithm of lognormal data *always presents symmetrical dispersion behavior*, the b_{1ln}/b_{1w} ratio of the estimated lognormal and Weibull coefficients effectively discriminates between the negative and symmetrical dispersion behaviors, a method based on R^2 to effectively discriminate between both distributions is offered by this paper in sec. 4. The reason for the method's efficiency is that the R^2 index for a fixed sample size (*n)* depends only on the b_{1ln}/b_{1w} ratio (see sec. 4.3). That is, because the b_{1ln}/b_{1w} ratio effectively discriminates between negative and symmetrical dispersion behaviors, the R^2 index effectively discriminates between both distributions also.

This paper is structured as follows. Section 2 shows that the behavior of the logarithm of a Weibull variable is always negatively skewed and that the logarithm of a lognormal variable is always symmetrical. In section 3, based on the data behavior log, the characteristics that completely define whether data follow a Weibull or a lognormal distribution are given. Also, in section 3, the case where the dispersion (*Sxx*) contribution is not fulfilled is presented also. Section 4 shows the multiple linear regression (*MLR*) analysis for the Weibull and lognormal distributions. Section 5 presents *1)* how via *MLR*, the b_{1ln}/b_{1w} ratio efficiently captures the *Sxx* dispersion behavior, and *2)* that because the R^2 index for a fixed *n* value only depends on the b_{1ln}/b_{1w} ratio, it captures the *Sxx* dispersion behavior also. The application of a stress-strength analysis is given in section 6, while Section 7 shows the effect that a wrong selection has over the reliability index. Finally, the conclusions are presented in section 8.

2. Behavior of log-Weibull and log-lognormal variables

Since the discrimination method is based on the logarithm of the Weibull or lognormal observed data and on its dispersion behavior, then in this section, we show that the Weibull data logarithm follows a Gumbel distribution and that it is always negatively skewed. Similarly, we show that the logarithm of the lognormal data follows a Normal distribution and that it is always symmetrical.

2.1. Weibull and Gumbel relationship

The Weibull distribution is given by

$$f(t) = \frac{\beta}{\eta}\left(\frac{t}{\eta}\right)^{\beta-1} \exp\left\{-\left(\frac{t}{\eta}\right)^{\beta}\right\} \quad (2)$$

In eq. (2), $t > 0$ and β and η are the Weibull shape and scale parameters respectively. On the other hand, the Gumbel distribution is given by

$$f(x) = \frac{1}{\sigma_G}\exp\left\{\left(\frac{x-\mu_G}{\sigma_G}\right) - \exp\left\{\frac{x-\mu_G}{\sigma_G}\right\}\right\} \quad (3)$$

In eq. (3) $-\infty < x < \infty$ with $x=ln(t)$ and μ_G is the location parameter and σ_G is the scale parameter [19]. Thus, based on eq. (2) and eq. (3), the relation between both distributions is as follows.

Theorem: If a random variable t follows a Weibull distribution [$t\sim W(\beta, \eta)$], then its logarithm $x=ln(t)$ follows a Gumbel distribution [$x\sim G(\mu_G,\sigma_G)$] [20].

Proof: Let $F(ln(t)) = P(ln(t) \leq ln(T))$ be the cumulative function of $x = ln(t)$, with T representing the failure time value. Thus, in terms of x, $F(ln(t)) = Pr[ln(t) \leq x]$; $F(x) = Pr[t \leq exp(x)]$. Then by substituting $t = exp(x)$, $F(x)$ is

$$F(x) = 1 - \exp\left\{-\left(\frac{t}{\eta}\right)^{\beta}\right\} = 1 - \exp\left\{-\left(\frac{\exp(x)}{\eta}\right)^{\beta}\right\} \quad (4)$$

Finally, based on the relations between the Weibull and Gumbel parameters given by [20].

$$\mu_G = ln(\eta) \quad (5)$$

$$\sigma_G = \frac{1}{\beta} \quad (6)$$

and by taking $W=((x-\mu_G)/\sigma_G)$, eq. (4) is given by $F(x) = 1-exp\{-exp\{(x-ln(\eta))\cdot\beta\}\}$ which in terms of W is

$$F(x) = 1 - \exp\{-\exp\{w\}\} \quad (7)$$

from eq. (7), the reliability function is

$$R(t) = 1 - F(t) = \exp\{-\exp\{w\}\} \quad (8)$$

and the density function is given by

$$f(x) = -\frac{dR(t)}{dt} = \exp\{w - \exp\{w\}\} \quad (9)$$

clearly, eq. (9) in terms of W is

$$f(x) = \frac{1}{\sigma_G}\exp\left\{\left(\frac{x-\mu_G}{\sigma_G}\right) - \exp\left\{\frac{x-\mu_G}{\sigma_G}\right\}\right\} \quad (10)$$

Since eq. (10) is as in eq. (3), we conclude that the logarithm of Weibull data follows a Gumbel distribution. On the other hand, by using the moment method [21] (sec. 1.3.6.6.16), the parameters of eq. (10) are given by:

$$\mu_{EV} = E(x) = \mu_Y + \gamma\sigma_{EV} \quad (11)$$

$$\sigma_{EV} = \frac{\sqrt{6}}{\pi}\sigma_Y \quad (12)$$

where μ_Y and σ_Y are the mean and the standard deviation of the log data.

2.1.1. Dispersion of the Gumbel distribution

In order to show the dispersion of the log Weibull variable, several Weibull probability density functions (pdf) with fixed scale parameter $\eta=50$ and variable shape parameter β are plotted in Fig. 1. Fig. 2, corresponds to the conversion of the Weibull pdf of Fig. 1 on Gumbel pdf.

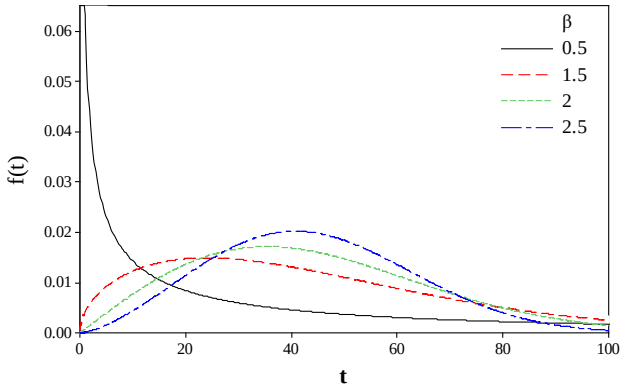


Figure 1 Weibull pdf for $\eta=50$
Source: The authors

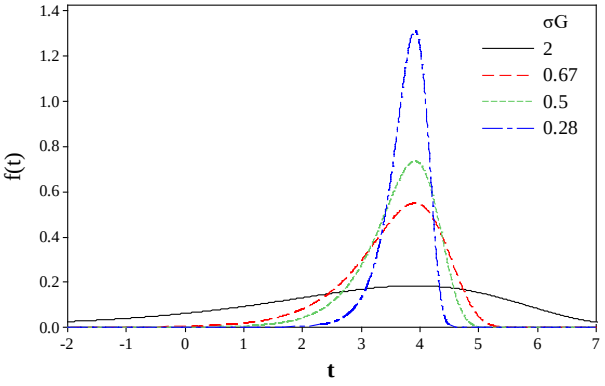


Figure 2 Gumbel pdf for $\mu_G=3.91$
Source: The authors

As can be seen in Fig. 2, the Gumbel distribution is always negatively skewed. Moreover, it is important to highlight that the Gumbel skew is constant at $\gamma_1 = -1.13955$, and as demonstrated by [22], it can be estimated as

$$-2\cdot 6^{3/2}\zeta(3)/\pi^3 \approx -1.13955.$$

On the other hand, as shown in next section, the logarithm of lognormal data follows a Normal distribution.

2.2. Lognormal and normal relationship

As it is well known, the lognormal data logarithm follows a Normal distribution [19]. If $Y\sim N(\mu, \sigma^2)$, then $X=e^Y$ (non-negative) has a lognormal distribution. Thus, because the logarithm of X yields a Normal variable ($Y=ln(X)$) then the lognormal distribution is given by

$$f(t) = \frac{1}{t\sigma_x\sqrt{2\pi}}\exp\left\{-\frac{1}{2}\left(\frac{ln\,t-\mu_x}{\sigma_x}\right)^2\right\} \quad (13)$$

In eq. (13) μ_x and σ_x are the log mean and log standard deviation. Similarly, the Normal distribution is given by

$$f(t) = \frac{1}{\sigma_N\sqrt{2\pi}}\exp\left\{-\frac{1}{2}\left(\frac{t-\mu_N}{\sigma_N}\right)^2\right\} \quad (14)$$

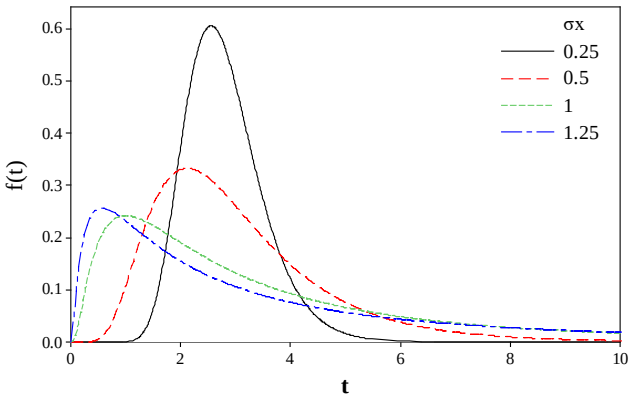


Figure 3 Lognormal pdf for $\mu_x=1$
Source: The authors

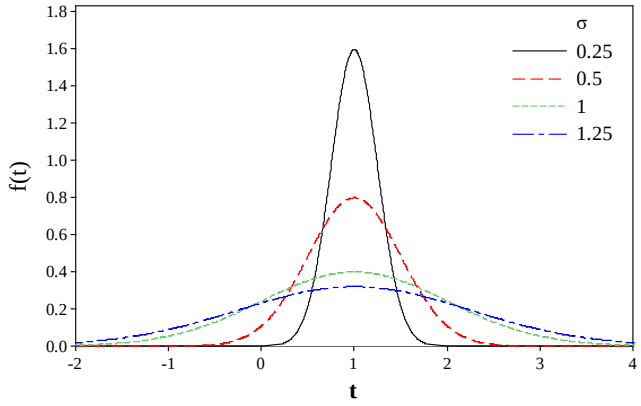


Figure 4 Normal pdf for $\mu=1$
Source: The authors

Note that, although the Normal distribution is the most widely used distribution in statistics, it is rarely used as lifetime distribution. However, in reliability the Normal distribution is used as a model for *ln(t)*, when *t* has a lognormal distribution.

2.2.1. Dispersion of the normal distribution

Fig. 3 represents several lognormal pdf for μ_x=1 and variable σ_x. Plotted Normal pdfs of Fig. 4 correspond to the logarithm of the lognormal pdfs plotted in Fig.3. By comparing Fig.3 and Fig.4, we observe although the lognormal distribution is always positively skewed, its logarithm is always symmetrical.

Therefore, based on the log data behavior, the characteristics that completely define whether data follow a Weibull or lognormal distribution are given in next section.

3. Discrimination properties

This section presents that enough conditions are met in order to show that lognormal data follow a lognormal distribution and that Weibull data follow a Weibull distribution. Additionally, the critical characteristic to discriminate between both distributions when data follow neither a lognormal nor a Weibull distribution is given also.

3.1. Lognormal properties

In order to select the lognormal distribution as the best model to represent the data, the following characteristics have to be met. *First*, the coefficient of variation has to be equal to the log-standard deviation σ_x (σ_x=*CV*). Thus, because based on the mean and on the standard deviation of the observed data defined as

$$\mu = \exp\left\{\mu_x + \frac{\sigma_x^2}{2}\right\} \tag{15}$$

$$\sigma^2 = \exp\{2\mu_x + \sigma_x^2\}\,(\exp\{\sigma_x^2\} - 1) \tag{16}$$

the *CV* index is given by

$$CV = \frac{\sigma}{\mu} = \sqrt{\exp\{\sigma_x^2\} - 1} \tag{17}$$

Then from eq. (17) clearly $\sigma_x \approx CV$. *Second*, the log mean μ_x should be located at the 50th percentile. The reason is that the lognormal data logarithm follows a Normal distribution (see sec. 2.2). *Third*, since the total sum square (*Sxx*) is cumulated by the contribution before (*Sxx*$_-$) and after (*Sxx*$_+$) the mean μ_x is as follow

$$Sxx = Sxx_- + Sxx_+ = \sum(x - \mu_x)^2 \tag{18}$$

Then, due to the symmetrical behavior of the lognormal data logarithm, then in the lognormal case, the contribution before and after the mean must be equal; it is to say for the lognormal case *Sxx*$_-$= *Sxx*$_+$.

Thus, because when $\sigma_x \approx CV$, μ_x is located in the 50th percentile and *Sxx*$_-$= *Sxx*$_+$, we should directly fit the lognormal model. Similarly, the characteristics to be met for the Weibull distribution are as follow:

3.2. Weibull properties

In the Weibull case, because the Weibull data logarithm follows a Gumbel distribution, and because the Gumbel distribution is always negatively skewed (See sec 2.1.1), then the following characteristics have to be met. *First*, the coefficient of variation should be different from the standard deviation of the data logarithm ($\sigma_x \neq CV$). *Second*, the log mean μ_x should be located around the 36.21th percentile. Third, the contribution to *Sxx* before μ_x is always greater than the contribution after μ_x; in other words, due to the negative skewness of the Gumbel distribution, in the Weibull case *Sxx*$_-$>*Sxx*$_+$. Thus, because $\sigma_x \neq CV$, μ_x is located around the 36.21th percentile and *Sxx*$_-$>*Sxx*$_+$, then we should directly fit the Weibull distribution. Nonetheless, the next section will describe what happens when the above statements do not hold at all.

3.3. Weibull or lognormal distribution?

The discrimination process, when data neither completely follow a Weibull distribution nor completely follow a lognormal distribution, is based on the following facts. 1) For a Weibull shape parameter $\beta \geq 2.5$, the Weibull *pdf* is similar to the lognormal *pdf* [23]. 2) For $\beta \geq 2.5$, the log-standard

deviation σ_x tends to be the *CV* ($\sigma_x \approx CV$), and μ_x tends to be located near the 50th percentile. 3) For Weibull data, regardless of the β value, the contribution before and after the mean tends to be different ($Sxx_{--}>Sxx_{+}$). Now for the Normal distribution we always expect that $Sxx_{--}=Sxx_{+}$ and for the Gumbel distribution we always expect that $Sxx_{--}>Sxx_{+}$; thus, because from eq. (18), Sxx_{--} captures the skewness of the Gumbel distribution, then based on the *MLR* analysis, in the proposed method the product of the *y* vector with the Sxx_{--} and Sxx_{+} contribution is used as the critical variable to discriminate between the Weibull and the lognormal distributions. In order to show that, the linear regression analysis on which the proposed method is based must first be introduced.

4. Weibull and lognormal linear regression analysis

This section shows that by using *MLR*, the ratio of the slopes of the lognormal and Weibull distributions (b_{1ln}/b_{1w}) is indeed efficient to discriminate between the negative and symmetrical skew behavior. Before showing that, the *MLR* analysis for the Weibull and lognormal distributions will first be introduced.

4.1. Weibull linear model

The Weibull and lognormal distributions can be analyzed as a regression model of the form

$$y = b_0 + b_1 x \tag{19}$$

The linear form of the Weibull distribution is based on the cumulative density function, given by

$$F(t) = 1 - R(t) = 1 - \exp\left\{-\left(\frac{t}{\eta}\right)^{\beta}\right\} \tag{20}$$

Thus, by applying double logarithm, its linear form is

$$\begin{aligned} y_i &= \ln\left(-\ln\left(1 - F(t_i)\right)\right) \\ &= -\beta \ln(\eta) + \beta \ln(t_i) = b_0 + b_1 x_i \end{aligned} \tag{21}$$

where $F(t_i)$ is estimated by the median rank approach [24] given by

$$F(t_i) = \frac{i-0.3}{n+0.4} \tag{22}$$

From eq. (21), the shape parameter β is directly given by the slope b_1, and the scale parameter η is given by

$$\eta = \exp\left\{\frac{-b_0}{\beta}\right\} = \exp\left\{\mu_x - \frac{\mu_y}{\beta}\right\} \tag{23}$$

Additionally, it is necessary to note that in eq. (21) $y=ln(-ln(1-F(t)))$ represents the behavior of the Gumbel distribution (negative skew), and that once the Weibull parameters β and η are known, the expected data can be estimated as

$$\ln(t_i) = \frac{y_i}{\beta} + \ln(\eta) = \frac{\ln\left(-\ln\left(1-F(t_i)\right)\right)}{\beta} + \ln(\eta) \tag{24}$$

Clearly, from eq. (24), the $ln(t_i)$ value depends only on *y*. And since from the double logarithm the *y* values before $F(t)=1-e^{-1}=0.6321$ *are always* negatively skewed, then in order for that data follows a Weibull distribution, its logarithm has to be negatively skewed as well. This fact implies that in the Weibull case, $Sxx_{--}>Sxx_{+}$ is always true. On the other hand, the analysis for the lognormal distribution is as follows.

4.2. Lognormal linear model

Since for the lognormal distribution the cumulative density function is given by

$$F(t) = 1 - R(t) = \Phi\left(\frac{\ln t - \mu_x}{\sigma_x}\right) \tag{25}$$

Then the lognormal linear relationship is given by

$$\begin{aligned} y_i &= \Phi^{-1}\left(F(t_i)\right) = Z_i \\ &= -\frac{1}{\sigma_x}\mu_x + \frac{1}{\sigma_x} ln(t_i) = b_0 + b_1 x_i \end{aligned} \tag{26}$$

where μ_x is given by $\mu_x=-b_0/b_1$, and σ_x is given by $\sigma_x=1/b_1$ and $F(t_i)$ is estimated as in eq. (22). On the other hand, μ_x and σ_x can respectively be estimated directly from the data as

$$\mu_x = \frac{1}{n}\sum_{i=1}^{n} \ln t_i \tag{27}$$

$$\sigma_x = \sqrt{\frac{\sum_{i=1}^{n}(\ln t_i - \mu_x)^2}{n-1}} \tag{28}$$

From eq. (26) $y=\Phi^{-1}(F(t))$ represents the behavior of the Normal distribution (*symmetrical behavior*). Thus, once the lognormal parameters μ_x and σ_x are known, the expected data can be estimated from eq.(26) as follows:

$$\ln(t_i) = \sigma_x y_i + \mu_x = \sigma_x \Phi^{-1}\left(F(t_i)\right) + \mu_x \tag{29}$$

On the other hand, since $ln(t_i)$ in eq. (29) follows a normal distribution, then its behavior is always symmetrical, and as a consequence of the lognormal case, the contribution to the *Sxx* variable is equivalent before and after μ_x. In other words, in the lognormal case, $Sxx_{--}=Sxx_{+}$. Now that it has been seen that for the Weibull distribution $Sxx_{--}>Sxx_{+}$, and that for the lognormal distribution $Sxx_{--}=Sxx_{+}$, let us describe the linear regression analysis to show that the ratio of the Weibull and lognormal regression coefficients efficiently represents the Sxx_{--} and Sxx_{+} behavior.

4.3. Multiple linear regression analysis

In order to discriminate between the Weibull and lognormal distributions, first, the Weibull parameters of eq. (21) and the lognormal parameters of eq. (26) have to be estimated by using linear regression analysis as follows

$$b_0 = \mu_y - b_1 \mu_x \tag{30}$$

$$b_1 = \frac{\sum_{i=1}^{n} y_i (x_i - \mu_x)}{\sum_{i=i}^{n} (x_i - \mu_x)^2} = \frac{Sxy}{Sxx} \tag{31}$$

The related multiple determination coefficient (R^2), is

$$R^2 = \frac{b_1 \sum_{i=1}^{n} y_i(x_i-\mu_x)}{\sum_{i=1}^{n}(y_i-\mu_y)^2} = \frac{b_1 Sxy}{Syy} \quad (32)$$

Thus, since from eq. (30) and eq. (31), we observe that the estimated coefficients are based on the *key variable Sxx*, then we conclude that the regression coefficients b_0 and b_1 represent the *Sxx* behavior also. Based on these parameters, the proposed method is outlined in the next section.

5. Proposed method

The proposed method is based on the fact that the critical characteristic to discriminate between the Weibull and the lognormal distributions is the *Sxx* contribution to the log standard deviation σ_x. Thus, in order to present the steps of the proposed method to discriminate between the Weibull and lognormal distributions, it is necessary first to show that via *MLR*, the regression coefficients (slopes) b_{1ln}/b_{1w} ratio completely incorporates the negative skew and the symmetrical behavior of the observed data, and that the multiple linear regression coefficient R^2 completely depends on the b_{1ln}/b_{1w} ratio.

5.1. The ratio b_{1ln}/b_{1w} efficiently capture the Sxx behavior

The analysis for the Weibull and lognormal distributions is given below.

5.1.1. Weibull analysis

In order to show that the regression coefficients (slopes) b_{1ln}/b_{1w} ratio completely incorporates the skew behavior of the Weibull distribution represented by *Sxx*, it is necessary to first show that based on the b_{1ln}/b_{1w} ratio given by

$$\frac{b_{1ln}}{b_{1w}} = \frac{\sum_{i=1}^{n} y_{iln}(x_i-\mu_x)}{\sum_{i=1}^{n} y_{iw}(x_i-\mu_x)} = \frac{Sxy_{ln}}{Sxy_w} \quad (33)$$

For the Weibull distribution, $Sxy_w > Sxy_{ln}$. To observe this, it should be remembered that because the Weibull response variable y_w given by $y_w = ln[-ln(1-F(t))]$ is higher weighted in the initial values (lower percentiles), and because for Weibull data, Sxx_- tends to be greater than Sxx_+, then the impact of Sxx_- over Sxy_w given by $Sxy_w = y_w(x-\mu)$ is higher in the initial values. As should be noted, this fact implies that when data follows a Weibull distribution, the difference between Sxy_w and Sxy_{ln} tends to be higher. Likewise, from eq. (33), this fact implies that for Weibull data the b_{1ln}/b_{1w} ratio or Sxy_{ln}/Sxy_w decreases.

5.1.2. Lognormal analysis

In the lognormal case, because the lognormal response variable y_{ln}, given by $y_{ln} = \Phi^{-1}(F(t))$, is symmetrical around the 50th percentile, then for lognormal data Sxx_- it tends to be Sxx_+ (see sec 3.1). As a consequence, the impact of Sxx_- on $Sxy_{ln} = y_{ln}(x-\mu)$ is lower than that of the Weibull distribution. This fact implies that for lognormal data, the difference between Sxy_w and Sxy_{ln} tends to be lower than when data is Weibull. As a result of this lower impact, when data is lognormal in eq. (33), the b_{1ln}/b_{1w} ratio or its equivalent Sxy_{ln}/Sxy_w increases.

Thus, because based on the *Sxx* behavior, for Weibull data the b_{1ln}/b_{1w} ratio decreases, and for lognormal, data it increases, then we conclude that because $Sxy = y(x-\mu)$ clearly captures the behavior of *Sxx*, then the b_{1ln}/b_{1w} ratio efficiently captures the behavior of *Sxx* also.

Now it will be shown that because the R^2 index depends only on the b_{1ln}/b_{1w} ratio, then it also captures the behavior of *Sxx*. Consequently, the R^2 index can also be used to discriminate between the Weibull and the lognormal distributions.

5.2. The R^2 index is completely defined by the b_{1ln}/b_{1w} ratio

In order to show that the R^2 index is completely defined for the b_{1ln}/b_{1w} ratio, it will be first be noted that based on eq. (32), the relationship between b_{1w} parameter and the Weibull R_w index and the relationship between the b_{1ln} parameter and the lognormal R_{ln} index can be formulated by the following relation

$$b_1 = \frac{R^2 Syy}{Sxy} \quad (34)$$

Secondly, in doing this it should be observed that by taking away $Sxy = b_1 Sxx$ from eq. (31), and by replacing it in eq. (34), b_1 is directly related with σ_x, σ_y and R^2, as follows

$$b_1 = \frac{R^2 Syy}{b_1 Sxx} = \frac{R\,\sigma_y}{\sigma_x} \quad (35)$$

where

$$\sigma_y = \sqrt{\frac{\sum_{i=1}^{n}(y_i-\mu_y)^2}{n-1}} \quad (36)$$

$$\sigma_x = \sqrt{\frac{\sum_{i=1}^{n}(x_i-\mu_x)^2}{n-1}} \quad (37)$$

Thus, from eq. (35), the Weibull b_{1w} and R_w values are related with the lognormal b_{1ln} and R_{ln} values as follows

$$b_{1w} = \frac{R_w\,\sigma_{yw}}{\sigma_x} \quad (38)$$

$$b_{1ln} = \frac{R_{ln}\,\sigma_{yln}}{\sigma_x} \quad (39)$$

Next, it will be shown that because the R_{ln}/R_w ratio depends only on the b_{1ln}/b_{1w} ratio, then the R^2 index can be used to efficiently discriminate between the Weibull and the lognormal distributions. Having done this, it should also be noted from eq. (38) and eq. (39) that σ_x is the standard deviation of the data logarithm, and that it is the same for both distributions. This fact ($\sigma_x = \sigma_x$) implies from eq. (38) and eq. (39) that

$$\frac{R_w\,\sigma_{yw}}{b_{1w}} = \frac{R_{ln}\,\sigma_{yln}}{b_{1ln}} \quad (40)$$

Therefore, based in eq. (40), the relationship between the R_{ln} and the R_w indices is given by

$$R_{ln} = R_w \left(\frac{b_{1ln}}{b_{1w}}\right)\left(\frac{\sigma_{y\,w}}{\sigma_{y\,ln}}\right) \quad (41)$$

And because the $\sigma_{y\,w}/\sigma_{y\,ln}$ ratio is constant in the analysis, we conclude that the R_{ln}/R_w ratio depends only on the b_{1ln}/b_{1w} ratio. Consequently, the R^2 index is efficient to discriminate between the Weibull and the lognormal distributions. Additionally, it is important to highlight that the σ_{yw}/σ_{yln} ratio in eq. (41) is constant also, and that this is so because σ_y defined in eq. (36) depends only on the sample size *n*. Thus, once *n* is known (or selected, see [25] eq. (13)), σ_y is constant.

5.3. Steps of the proposed method

Because based on the observed data, the R^2 index efficiently represents the Sxx behavior, then based on the observed data, the steps of the proposed method to discriminate between the Weibull and the lognormal distributions are as follows.

By using the Weibull y vector defined in eq. (21) (or the lognormal y vector defined in eq. (26)) and the observed data logarithm (ln(t)=x), the Weibull (or lognormal) correlation is estimated as $Sxy=\sum y_i(x_i-\mu_x)$.

1) From the logarithm of the observed data, estimate the variance of *x* as $Sxx=\sum(x_i-\mu_x)^2$.
2) By using the Weibull (or lognormal) *Sxy* value from step 1 and the *Sxx* value from step 2 into eq. (31), estimate the Weibull (or lognormal) slope b_1 coefficient.
3) By using the Weibull *y* vector defined in eq. (21) (or the lognormal *y* vector defined in eq. (26)), estimate the Weibull (or lognormal) variance of *y* as $Syy=\sum(y_i-\mu_y)^2$.
4) By using the Weibull (or lognormal) slope b_1 coefficient from step 3, Weibull (or lognormal) *Sxy* value from step 1 and the Weibull (or lognormal) *Syy* value from step 4 into eq. (32), estimate the Weibull (or lognormal) coefficient R^2.
5) Compare the Weibull and the lognormal R^2 indices, select the distribution with higher R^2 value. If $R_w^2>R_{ln}^2$ select Weibull distribution; otherwise select lognormal distribution.

6. An application

The efficiency of the R^2 index to discriminate between the Weibull and the lognormal distribution is shown in a stress-strength analysis by using data in section 1. Table 1 Data corresponds to the stress load in a machine that uses a plunger to press a shaft into a bushing. Table 2 Data corresponds to the strength of the plunger when it is subjected to compression loads [26]. Thus, the selection of the stress distribution by using the proposed method is as follows.

6.1. Stress data analysis

From the stress observed data shown in Table 4, we note that because 1) the $\sigma_x \approx CV$ ($\sigma_x=CV=0.0055$), 2), μ_x is located near the 50th percentile, and 3) $Sxx_{--} = 53\% \approx Sxx_{+} = 47\%$. Then, from section 3.1, it is reasonable to expect that the lognormal distribution represents the data.

The above statement is verified by applying the proposed method to the Table 1 data. The required values *Sxy*, *Sxx* and *Syy* to apply the method are estimated by applying the *MLR* analysis to the stress data. The values for the Weibull and the lognormal distributions are given in Table 4.

Thus, by using data of Table 4, the lognormal analysis is as follows. From **step 1**, $Sxy_{ln}=7.1714$ (column 9). From **step 2**, $Sxx=1.3412$ (column 10). From **step 3**, and eq. (31), $b_{1ln}=5.3471$. From **step 4**, $Syy_{ln}=39.4812$ (column 13). Therefore, from **step 5**, and eq. (32), $R_{ln}^2=0.9712$.

Similarly, by applying the proposed method to the Weibull distribution, we have from **step 1**, $Sxy_w=8.8996$ (column 8). From **step 2**, *Sxx*, as in the lognormal case, is also $Sxx=1.3412$ (column 10). From **step 3**, and eq. (31), $b_{1w}=6.6357$. From **step 4**, $Syy_w=61.9775$ (column 12). Therefore, from **step 5**, and eq. (32), $R_w^2=0.9528$.

Finally, as expected, by comparing the Weibull and lognormal R^2 indices, in **step 6**, we have that $R_{ln}^2=0.9712>R_w^2=0.9528$. Thus, we conclude that the failure governing the stress distribution is the lognormal distribution. On the other hand, the selection of the strength distribution by using the proposed method is as follows.

6.2. Strength data analysis

The strength data is given in Table 5. From this data, we note that while 1) the $\sigma_x \approx CV$ ($\sigma_x=CV=0.0077$) and 2) the μ_x is located near the 50th percentile, 3) the Sxx_{--} contribution is greater than the Sxx_{+} contribution $Sxx_{--}=61\% > Sxx_{+}=39\%$. Thus, because from section 3.3 the characteristics of the lognormal distribution are not completely met, then we conclude that data can be better represented by the Weibull distribution. However, the estimation of the R^2 index is necessary. When doing this, the values of *Sxy*, *Sxx* and *Syy* are estimated by using an *MLR* analysis of the strength data. The *MLR* analyses for the Weibull and the lognormal distributions are summarized in Table 5.

By using Table 5 data and by applying the proposed method for the lognormal distribution, we have that, from **step 1**, $Sxy_{ln}=1.9402$ (column 9). From **step 2**, $Sxx=0.3298$ (column 10). From **step 3**, and eq. (31), $b_{1ln}=5.8820$. And from **step 4**, $Syy_{ln}=12.2451$ (column 13). Therefore, from **step 5**, and eq. (32) $R^2=0.9319$.

Similarly, by applying the proposed method for the Weibull distribution, we have that, from **step 1**, $Sxy_w=2.4320$ (column 8). From **step 2**, *Sxx* as in the lognormal case, is $Sxx=0.3298$ (column 10). From **step 3**, and eq. (31), $b_{1w}=7.3730$. And from **step 4**, $Syy_w=18.5330$ (column 12). Therefore, from **step 5**, and eq. (32), $R_w^2=0.9675$.

Finally, by comparing the R^2 indices as in **step 6**, we have that $R_w^2=0.9675>R_{ln}^2=0.9319$. Thus, the failure governing the strength distribution is the Weibull distribution.

As a summary, because the stress data follows a lognormal distribution and the strength data follows a Weibull distribution, then for the stress-strength analysis the lognormal-Weibull combination has to be used. Therefore, from Table 3, the corresponding lognormal-Weibull reliability is $R(t)=0.9860$. Finally, the effect that a wrong selection of the distribution has over the estimated reliability is given in Table 3. Although the reliability values given in Table 3 were estimated by using the Weibull++ software, the next section provides the formulas to estimate such values.

Table 4
Load data analysis

1	2	3	4	5	6	7	8	9	10	11	12	13
th perc	*i*	*T*	*x=ln(t)*	*F(t)*	y_w	y_{ln}	Sxy_w	Sxy_{ln}	*Sxx*	∑*Sxx*	Syy_w	Syy_{ln}
	1	9.6	2.2618	0.0161	-4.1190	-2.1412	1.8617	0.9678	0.2043		12.6740	4.5847
	2	9.6	2.2618	0.0392	-3.2199	-1.7604	1.4553	0.7956	0.2043		7.0807	3.0990
	3	12.3	2.5096	0.0622	-2.7453	-1.5365	0.5604	0.3136	0.0417		4.7799	2.3607
	4	12.4	2.5177	0.0853	-2.4179	-1.3706	0.4740	0.2687	0.0384		3.4557	1.8785
	5	12.4	2.5177	0.1083	-2.1661	-1.2356	0.4246	0.2422	0.0384		2.5830	1.5268
	6	12.5	2.5257	0.1313	-1.9604	-1.1201	0.3686	0.2106	0.0353		1.9641	1.2546
	7	12.6	2.5337	0.1544	-1.7857	-1.0178	0.3215	0.1832	0.0324		1.5049	1.0360
	8	12.7	2.5416	0.1774	-1.6332	-0.9252	0.2811	0.1593	0.0296		1.1539	0.8561
	9	12.7	2.5416	0.2005	-1.4974	-0.8400	0.2577	0.1446	0.0296		0.8806	0.7056
	10	13.2	2.5802	0.2235	-1.3745	-0.7604	0.1835	0.1015	0.0178		0.6651	0.5782
	11	13.5	2.6027	0.2465	-1.2620	-0.6854	0.1401	0.0761	0.0123		0.4943	0.4698
	12	13.8	2.6247	0.2696	-1.1579	-0.6141	0.1031	0.0547	0.0079		0.3587	0.3771
	13	14	2.6391	0.2926	-1.0607	-0.5457	0.0792	0.0408	0.0056		0.2518	0.2978
	14	14.2	2.6532	0.3157	-0.9694	-0.4798	0.0586	0.0290	0.0037		0.1685	0.2303
	15	14.4	2.6672	0.3387	-0.8829	-0.4160	0.0411	0.0193	0.0022		0.1050	0.1730
	16	14.4	2.6672	0.3618	-0.8007	-0.3538	0.0372	0.0165	0.0022		0.0584	0.1252
	17	14.4	2.6672	0.3848	-0.7220	-0.2929	0.0336	0.0136	0.0022		0.0266	0.0858
	18	14.6	2.6810	0.4078	-0.6463	-0.2331	0.0211	0.0076	0.0011		0.0076	0.0543
	19	14.6	2.6810	0.4309	-0.5733	-0.1741	0.0188	0.0057	0.0011		0.0002	0.0303
	20	14.7	2.6878	0.4539	-0.5026	-0.1158	0.0130	0.0030	0.0007		0.0032	0.0134
	21	14.9	2.7014	0.4770	-0.4337	-0.0578	0.0054	0.0007	0.0002	∑=0.7109	0.0157	0.0033
	22	15	2.7081	0.5000	-0.3665	0.0000	0.0021	0.0000	0.0000	53%	0.0370	0.0000
50	23	15.2	2.7213	0.5230	-0.3007	0.0578	-0.0023	0.0004	0.0001		0.0667	0.0033
	24	15.3	2.7279	0.5461	-0.2359	0.1158	-0.0033	0.0016	0.0002		0.1043	0.0134
	25	15.3	2.7279	0.5691	-0.1721	0.1741	-0.0024	0.0025	0.0002		0.1497	0.0303
	26	15.7	2.7537	0.5922	-0.1088	0.2331	-0.0043	0.0093	0.0016		0.2026	0.0543
63.21	27	15.9	2.7663	0.6152	-0.0460	0.2929	-0.0024	0.0154	0.0028		0.2631	0.0858
	28	16	2.7726	0.6382	0.0167	0.3538	0.0010	0.0208	0.0035		0.3313	0.1252
	29	16.1	2.7788	0.6613	0.0794	0.4160	0.0052	0.0271	0.0042		0.4075	0.1730
	30	16.5	2.8034	0.6843	0.1424	0.4798	0.0128	0.0430	0.0080		0.4919	0.2303
	31	16.6	2.8094	0.7074	0.2061	0.5457	0.0197	0.0522	0.0092		0.5853	0.2978
	32	16.8	2.8214	0.7304	0.2707	0.6141	0.0291	0.0661	0.0116		0.6883	0.3771
	33	16.8	2.8214	0.7535	0.3366	0.6854	0.0362	0.0738	0.0116		0.8021	0.4698
	34	16.9	2.8273	0.7765	0.4044	0.7604	0.0459	0.0864	0.0129		0.9280	0.5782
	35	17.9	2.8848	0.7995	0.4745	0.8400	0.0812	0.1437	0.0293		1.0679	0.7056
	36	17.9	2.8848	0.8226	0.5477	0.9252	0.0937	0.1583	0.0293		1.2246	0.8561
	37	18	2.8904	0.8456	0.6251	1.0178	0.1104	0.1798	0.0312		1.4019	1.0360
	38	18.1	2.8959	0.8687	0.7080	1.1201	0.1290	0.2041	0.0332		1.6053	1.2546
	39	19.1	2.9497	0.8917	0.7988	1.2356	0.1885	0.2916	0.0557		1.8435	1.5268
	40	19.7	2.9806	0.9147	0.9010	1.3706	0.2405	0.3658	0.0712		2.1315	1.8785
	41	20	2.9957	0.9378	1.0214	1.5365	0.2880	0.4333	0.0795		2.4977	2.3607
	42	20.1	3.0007	0.9608	1.1755	1.7604	0.3374	0.5052	0.0824	∑=0.6302	3.0084	3.0990
	43	22.3	3.1046	0.9839	1.4176	2.1412	0.5541	0.8369	0.1528	47%	3.9067	4.5847
	μ	15.319	2.7137		-0.5590	0.0000						
	Σ	2.6934	0.1787									
	CV	0.1758				∑	8.8996	7.1714	1.3412		61.9775	39.4812

Source: The authors

Table 5
Strength data analysis

1	2	3	4	5	6	7	8	9	10	11	12	13
th perc	*I*	*t*	*x=ln(t)*	*F(t)*	y_w	y_{ln}	Sxy_w	Sxy_{ln}	*Sxx*	∑*Sxx*	Syy_w	Syy_{ln}
	1	21	3.0445	0.0455	-3.0679	-1.6906	0.8862	0.4884	0.0834		6.4067	2.8582
	2	22	3.0910	0.1104	-2.1458	-1.2245	0.5200	0.2967	0.0587		2.5892	1.4993
	3	23	3.1355	0.1753	-1.6463	-0.9333	0.3258	0.1847	0.0392		1.2311	0.8711
	4	25	3.2189	0.2403	-1.2918	-0.7055	0.1479	0.0808	0.0131		0.5701	0.4977
	5	26	3.2581	0.3052	-1.0103	-0.5095	0.0761	0.0384	0.0057		0.2242	0.2596
	6	27	3.2958	0.3701	-0.7717	-0.3315	0.0290	0.0124	0.0014	∑=0.2015	0.0552	0.1099
	7	28	3.3322	0.4351	-0.5603	-0.1635	0.0007	0.0002	0.0000	61%	0.0006	0.0267
50	8	30	3.4012	0.5000	-0.3665	0.0000	-0.0249	0.0000	0.0046		0.0290	0.0000
	9	30	3.4012	0.5649	-0.1836	0.1635	-0.0125	0.0111	0.0046		0.1247	0.0267
63.21	10	31	3.4340	0.6299	-0.0061	0.3315	-0.0006	0.0334	0.0101		0.2815	0.1099
	11	31	3.4340	0.6948	0.1713	0.5095	0.0172	0.0513	0.0101		0.5012	0.2596
	12	32	3.4657	0.7597	0.3549	0.7055	0.0470	0.0934	0.0175		0.7950	0.4977
	13	32	3.4657	0.8247	0.5545	0.9333	0.0734	0.1235	0.0175		1.1908	0.8711
	14	33	3.4965	0.8896	0.7902	1.2245	0.1289	0.1997	0.0266	∑=0.1283	1.7606	1.4993
	15	34	3.5264	0.9545	1.1285	1.6906	0.2178	0.3262	0.0372	39%	2.7730	2.8582
	μ	28.3333	3.3334		-0.5367	0.0000						
	Σ	4.1519	**0.1535**									
	CV	**0.1465**				∑	2.4320	1.9402	0.3298		18.5330	12.2451

Source: The authors

7. Stress-Strength reliability

The stress-strength reliability values of Table 3 were estimated as follow. For the lognormal-lognormal stress-strength, the formulation given in eq. (42) was used

$$R = \phi\left(\frac{\mu_{xS}-\mu_{xs}}{\sqrt{\sigma_S^2+\sigma_s^2}}\right) \quad (42)$$

For the lognormal-Weibull stress-strength, the formulation given in eq. (43) was used

$$R = \int_0^{\infty} \frac{1}{s\sigma_x\sqrt{2\pi}} \exp\left\{-\left[\frac{1}{2}\left(\frac{\ln s-\mu_x}{\sigma_x}\right)^2 + \left(\frac{s}{\eta_S}\right)^{\beta_S}\right]\right\} ds \quad (43)$$

For the Weibull-lognormal stress-strength, the formulation given in eq. (44) was used

$$R = 1 - \int_0^{\infty} \frac{1}{S\sigma_{xS}\sqrt{2\pi}} \exp\left\{-\left[\frac{1}{2}\left(\frac{\ln S-\mu_{xS}}{\sigma_{xS}}\right)^2 + \left(\frac{S}{\eta_s}\right)^{\beta_s}\right]\right\} dS \quad (44)$$

Finally, for the Weibull-Weibull stress-strength, the formulation given in eq. (45) was used

$$R = 1 - \int_0^{\infty} \exp\left\{-\left[w + \left(\frac{\eta_S w^{1/\beta_S}}{\eta_s}\right)^{\beta_s}\right]\right\} dw \quad (45)$$

Where

$$w = \left(\frac{s}{\eta_S}\right)^{\beta S} \quad (46)$$

8. Conclusions

The reliability analysis for the Weibull and the lognormal distributions is performed by using the data logarithm. For the Weibull distribution, the logarithm data is negatively skewed. For the lognormal distribution, the logarithm data is symmetrical. Because for the Weibull distribution, the contribution to the variance before the mean is always greater than the contribution after the mean [Sxx_{-}>Sxx_{+}], then this behavior is used to discriminate between the Weibull and the lognormal distributions. Since the b_{1ln}/b_{1w} ratio efficiently represents the contribution behavior, and since the R^2 index depends only on this ratio, then the R^2 index is indeed efficient to discriminate between the Weibull and the lognormal distributions. Finally, it is important to highlight that when in the observed data, σ_x=CV, μ_x tends to the 50th percentile and Sxx_{-}=Sxx_{+}, then the lognormal distribution can be directly fitted. And when for the observed data, $\sigma_x \neq CV$, μ_x tends to the 36.21th percentile and Sxx_{-}>Sxx_{+}, then the Weibull distribution can be directly fitted.

References

[1] Rinne, H., The Weibull distribution, a handbook. Boca Raton, FL: CRC Press, 2008.

[2] Marathe, R.R. and Ryan, S.M., On the validity of the geometric Brownian motion assumption. The Engineering Economist, 50(2), pp. 159-192, 2005. DOI: /10.1080/00137910590949904

[3] Kececioglu, D., Robust engineering design-by-reliability with emphasis on mechanical components & structural reliability. Lancaster, PA: DEStech Publications, 2003.

[4] Wessels, W.R., Practical reliability engineering and analysis for system design and life-cyce sustainment. Boca Raton, FL: CRC Press, 2010.

[5] Kececioglu, D., Reliability & life testing handbook, volume 1. Lancaster, PA: DEStech Publications, 2002.

[6] Kim, J.S. and Yum, B.J., Selection between Weibull and lognormal distributions: A comparative simulation study. Computational Statistics & Data Analysis, 53(2), pp. 477-485, 2008. DOI: 10.1016/j.csda.2008.08.012

[7] Dey, A.K. and Kundu, D., Discriminating among the log-normal, Weibull, and generalized exponential distributions. IEEE Transactions on Reliability. 58(3), pp. 416-424, 2009. DOI: 10.1109/TR.2009.2019494

[8] Mitosek, H.T. Strupczewski, W.G. and Singh, V.P., Three procedures for selection of annual flood peak distribution. Journal of Hydrology. 323(1–4), pp. 57-73, 2006. DOI: 10.1016/j.jhydrol.2005.08.016

[9] Pasha, G.R. Khan, M.S. and Pasha, A.H., Discrimination between Weibull and lognormal distributions for lifetime data. Journal of Research (science) [Online]. 17(2), pp. 103-114, 2006. [date of reference March 15th of 2017]. Available at: https://www.bzu.edu.pk/jrscience/vol17no2/

[10] Fan, J. Yung, K.C. and Pecht, M., Comparison of statistical models for the lumen lifetime distribution of high power white LEDs, Proceedings of IEEE Prognostics and Systems Health Management Conference (PHM), 2012. pp. 1-7. DOI: 10.1109/PHM.2012.6228801

[11] Bagdonavičius, V.B. Levuliene, R.J. and Nikulin, M.S., Exact goodness-of-fit tests for shape-scale families and type II censoring. Lifetime Data Analysis. 19(3), pp. 413-435, 2013. DOI:10.1007/s10985-013-9252-x

[12] Wilson, S.R., Leonard, R.D., Edwards, D.J., Swieringa, K.A. and Murdoch, J.L., Model specification and confidence intervals for voice communication. Quality Engineering. 27(4), pp. 402-415, 2015. DOI: 10.1080/08982112.2015.1023313

[13] Cain, S., Distinguishing between lognormal and Weibull distributions. IEEE Transactions on Reliability. 51(1), pp. 32-38, 2002. DOI: 10.1109/24.994903

[14] Whitman, C. and Meeder, M., Determining constant voltage lifetimes for silicon nitride capacitors in a GaAs IC process by a step stress method. Microelectronics Reliability. 45(12), pp. 1882-1893, 2005. DOI: 10.1016/j.microrel.2005.01.016

[15] Prendergast, J., O'Driscoll, E. and Mullen, E., Investigation into the correct statistical distribution for oxide breakdown over oxide thickness range. Microelectronics Reliability. 45(5–6), pp. 973-977, 2005. DOI: 10.1016/j.microrel.2004.11.013

[16] Marshall, I., Meza, A.W. and Olkin, J.C., Can data recognize its parent distribution?. Journal of Computational and Graphical Statistics [Online]. 10(3), pp. 555-580, 2001. [dae of reference April 24th 2017]. Available at: https://www.jstor.org/stable/1391104?seq=1#page_scan_tab_contents

[17] Yu, H.-F.. The effect of mis-specification between the lognormal and Weibull distributions on the interval estimation of a quantile for complete data. Communications in Statistics - Theory and Methods. 41(9), pp. 1617-1635, 2012. DOI: 10.1080/03610926.2010.546548

[18] Upadhyay, S.K. and Peshwani, M., Choice between Weibull and lognormal models: a simulation based bayesian study. Communications in Statistics - Theory and Methods. 32(2), pp. 381-405, 2003. DOI: 10.1081/STA-120018191

[19] Crowder, M.J., Kimber, A.C., Smith, R.L. and Sweeting, T.J., Statistical analysis of reliability data. CRC Press, 1994.

[20] Genschel, U. and Meeker, W.Q., A comparison of maximum likelihood and median-rank regression for Weibull estimation. Quality Engineering. 22(4), pp. 236-255, 2010. DOI: 10.1080/08982112.2010.503447

[21] NIST/SEMATECH. Extreme value distributions. e-Handbook of Statistical Methods [Online]. [date of reference January 9th 2017]. Available at: http://www.itl.nist.gov/div898/handbook/.
[22] Kahle, J. and Collani, F., Advances in stochastic models for reliability, quality and safety. Boston, MA: Springer Science & Business Media, 2012.
[23] Dodson, B., The Weibull analysis handbook. Milwaukee, WI: ASQ Quality Press, 2006.
[24] Mischke, C.R.. A distribution-independent plotting rule for ordered failures. Journal of Mechanical Design. 104(3), pp. 5, 1982. DOI: 10.1115/1.3256391
[25] Piña-Monarrez, M.R., Ramos-Lopez, M.L., Alvarado-Iniesta, A. and Molina-Arredondo, R.D., Robust sample size for Weibull demonstration test plan. DYNA Colombia. 83(197), pp. 52-57, 2016. DOI: 10.15446/dyna.v83n197.44917
[26] Wessels, W.R., Practical reliability engineering and analysis for system design and life-cycle sustainment. Boca Raton, FL: CRC Press, 2010.

J.F Ortiz-Yañez, received the BSc. Eng in Industrial Engineering in 2009, the MSc. degree in Industrial Engineering, Sp. in Quality in 2012, and the PhD degree in Science in Engineering in 2016, all of them from the Universidad Autónoma de Ciudad Juárez, México. His PhD research was on reliability with focus on the Weibull and lognormal comparisons. Currently, he is the Reliability Engineer in the electrical and mechanical Validation Laboratory at Ted de México SA de CV in Ciudad Juárez, México.
ORCID: 0000-0002-4807-432X

M.R. Piña-Monarrez, is a researcher-professor in the Industrial and Manufacturing Department at the Autonomous University of Ciudad Juárez, México. He completed his PhD. in Science in Industrial Engineering in 2006 at the Instituto Tecnológico de Ciudad Juárez, México. He had conducted research on system design methods including robust design, reliability and multivariate process control. He is member of the National Research System (SNI), of the National Council of Science and Technology (CONACYT) in México.
ORCID: 0000-0002-2243-3400.

UNIVERSIDAD NACIONAL DE COLOMBIA
SEDE MEDELLÍN
FACULTAD DE MINAS

Área Curricular de Ingeniería Administrativa e Ingeniería Industrial

Oferta de Posgrados

Especialización en Gestión Empresarial
Especialización en Ingeniería Financiera
Maestría en Ingeniería Administrativa
Maestría en Ingeniería Industrial
Doctorado en Ingeniería - Industria y Organizaciones

Mayor información:

E-mail: acia_med@unal.edu.co
Teléfono: (57-4) 425 52 02

UNIVERSIDAD NACIONAL DE COLOMBIA
SEDE MEDELLÍN
FACULTAD DE MINAS



DYNA
http://dyna.medellin.unal.edu.co/

Study of agglomeration and magnetic sedimentation of Glutathione@Fe_3O_4 nanoparticles in water medium

Wilfredo Marimón-Bolívar [a,b] & Edgar E. González [a]

[a] *Geophysical Institute. Faculty of Engineering, Pontificia Universidad Javeriana, Bogotá, Colombia. egonzale@javeriana.edu.co*
[b] *Research Group DSGAA, Research Center of Science and Agro-Environmental Resources – CENIGAA, Huila, Colombia. w.marimon@javeriana.edu.co*

Received: October 10th, 2017. Received in revised form: March 2nd, 2018. Accepted: March 21th, 2018

Abstract
The study of the efficiency of the magnetic separation of nanoparticles in environment is important for its implementation in the remediation of water bodies. In this work the sedimentation dynamics of *Glutathione@MNPs* were evaluated for water systems with addition of calcium, zinc and sodium ions in a concentration range of 0-40 mg/L in the presence and absence of a vertical magnetic field of 0.2 T. Also, critical coagulation concentrations (CCC) were determined based on the DLVO theory. Particles stability in the absence of metal ions higher than 8 weeks could be observed, whereas in the presence of these ions the stability was reduced to 8 weeks. Separation of the material from the aqueous phase higher than 90% was obtained both for the presence of ions and for the material after the addition of heavy metals such as Hg and Cr.

Keywords: Glutathione; magnetic nanoparticles; aggregation kinetics; magnetic sedimentation.

Estudio de aglomeración y sedimentación magnética de nanopartículas de Glutatión@Fe_3O_4 en medio acuoso

Resumen
El estudio de la eficiencia de la separación magnética de nanopartículas del medio ambiente es importante para su implementación en la remediación de cuerpos de agua. En este trabajo se evaluó la dinámica de sedimentación de los Glutatión@MNPs en sistemas de agua con adición de iones de calcio, zinc y sodio en un rango de concentración de 0-40 mg/L en presencia y ausencia de un campo magnético vertical de 0,2 T. Las concentraciones críticas de coagulación (CCC) se determinaron basándose en la teoría de DLVO. Se observó estabilidad de la partícula mayor de 8 semanas en ausencia de iones metálicos, mientras que con la presencia de estos iones la estabilidad se redujo a 8 semanas. La separación del material de la fase acuosa superior al 90% se obtuvo tanto para la presencia de iones como para el material después de la adición de metales pesados tales como Hg y Cr.

Palabras clave: Glutatión; nanopartículas magnéticas; cinética de agregación; sedimentación magnética.

1. Introduction

The large-scale application of nanomaterials in the field of remediation has been limited by different factors ranging from economic to difficulties in implementation and scaling. One of these factors - in the context of using and reusing management - is the separation of the nanomaterials from the aqueous medium after performing their function, since conventional techniques such as precipitation, centrifugation or filtration are in some cases inefficient or costly [1–3].

For this reason, the implementation of magnetic nanoparticles (MNPs) has been seen as one of the most promising alternatives, since apart from its potential as a remediation agent is added the fact that their separation of the aqueous medium is simpler and more efficient [4–6].

The process of separating MNPs from the aqueous solution is based on cooperative phenomena of magnetophoresis, is a reorientation of the magnetic moment that holds particles under the action of non-uniform external magnetic fields towards the highest field gradient. The magnetic force involved can be expressed as [7]:

How to cite: Marimón-Bolívar, W. and González, E.E. Study of agglomeration and magnetic sedimentation of Glutathione@Fe3O4 nanoparticles in water medium. DYNA, 85(205), pp. 19-26, June, 2018.

© The author; licensee Universidad Nacional de Colombia.

$$F_m = \mu_0 V_p M_p \Delta H \quad (1)$$

where μ_0 is the permeability constant in vacuum, V_p is the particle volume, M_p is the magnetization of the particle and ΔH is the gradient of the magnetic field strength at the particle position. Also, the magnetization of the particle is given as a function of the volumetric magnetic susceptibility (χ) and the field strength applied [8]:

$$M_p = \chi H \quad (2)$$

Also, it is important consider the gravitational force F_g and the hydrodynamic drag force F_d [7,9,10]. For the gravitational force is fulfilled:

$$F_g = (\rho_p - \rho_g) V_p g \quad (3)$$

And for the drag force:

$$F_d = 6\pi\eta b(v_f - v_p) \quad (4)$$

where ρ_p is the density of the particle, b is a constant that depends on the properties of the fluid and the dimensions of the particle, ρ_g the density of the fluid, g the gravity, η the viscosity of the fluid and v_f and v_p are the velocities of the fluid and the particle respectively.

As seen in the equations 3 and 4, the volume - and hence the size - of particles plays a fundamental role in the recovery process. However, the increase in particle size leads to a decrease in the reactivity and removal capacity of the contaminant as it reduces the surface area/volume ratio [11,12]. For this reason, the study of the dynamics of aggregation of particles in water takes relevance.

Nanoparticles with a high free surface energy tend to aggregate, in trend toward stability. The smaller particles have a greater aggregation tendency due to lower energy barriers [13,14]. Aggregate formation decreases the surface area of magnetic nanoparticles. This reduces the reactivity, thus limiting the performance in catching pollutants. Aggregation also reduces the effectiveness of magnetic nanoparticles during remediation due to loss of Brownian mobility [15].

The most appropriate way to study this phenomenon is the DVLO model. The traditional DLVO (Fig. 1) theory describes colloidal stability by considering the total energy of the interaction in a particle with another particle. The main interaction energy can be estimated and calculated as the sum of Van der Waals and the double layer of electrical interactions [2,16,17].

2. Methodology

2.1. Materials

Iron (III) chloride hexahydrate ($FeCl_3 \cdot 6H_2O$) and Sodium hydroxide (NaOH) were purchased from Merck Colombia. Reduced L-Glutathione ($C_{10}H_{17}N_3O_6S$) was purchased from Sigma-Aldrich. All reactive were analytically pure and used as received without further purification, and all solutions were prepared with double-distilled water.

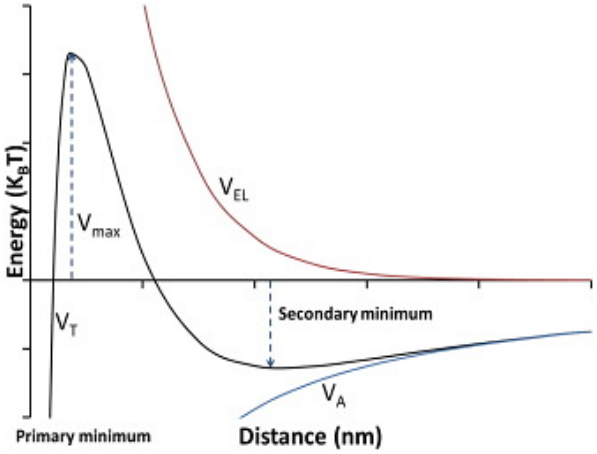


Figure 1. DLVO theory diagram.
Source: [18]

2.2. Samples preparation

The Fe_3O_4 NPs obtained through the green method (Glutathione@MNPs) were synthesized using an improved method described by [19] . Briefly, we added 10 mL of a $FeCl_3$ (0,1 mol/L) solution to a 100-mL beaker under mechanical stirring (140 rpm) at 75°C. On reaching this temperature, 20 mL of an aqueous solution of L-Glutathione (0,214mol/L) were added dropwise into the beaker with the pH value of the mixed solution adjusted to 10. The mixture was brought to a temperature of 85°C and this solution was stirred (120 rpm) for another hour. At the end of this period, the nanoparticles were separated by magnetic field application and then washed several times with deionized water and alcohol, and then vacuum dried at 40°C for 12 hours.

2.3. Characterization

The particle size and morphology of all the synthesized nanoparticles were characterized using transmission electron microscopy (CARL ZEISS MODEL EVO HD MA 15). The magnetic properties of the nanoparticles were studied through vibrating sample magnetometer (VSM Lakeshore, Model 665) measurements. The particle size was measured through the SEM and dynamic light scattering (DLS) methods, the size distribution of the particles and Zeta Potential were determined using a Malvern Zetasizer Nano (ZS90).

2.4. Agglomeration kinetics studies

In order to establish the aggregation rates of Glutathione@MNPs, suspensions of this material were prepared in deionized water at a concentration of 20 mg / L and sonicated for 10 minutes at 250 W. Thereafter, temporal changes in hydrodynamic radius as a function of ionic strength were measured by Dynamic Light Scattering (DLS) using a Zetasizer Nano ZS instrument (Malvern Instruments, UK). It has a 633nm laser as the light source and the intensity of the light scattered by the particles is measured as the photon count rate by a detector at 173°. Particle size is determined by the analysis of the fluctuation of light intensity diffused by particles subjected to Brownian motion.

With the measurement of these changes in the hydrodynamic radius from an initial value R_h0 to 1,25R_{h0}, the initial rate of aggregation of the nanoparticles (k) is determined [20,21]:

$$k = \frac{1}{N_0}\left(\frac{dR_h(t)}{dt}\right)_{t\to 0} \quad (5)$$

where *N* is the concentration of the particles. With this value, it was possible to determine the fixation efficiency and easily obtained from the relation of the initial aggregation rate to a given chemical condition of the solution with the aggregation rate constant measured under conditions bound by diffusion (rapid) [20–22]:

$$\alpha = \frac{k}{k_{fast}} = \frac{\left(\frac{dR_h(t)}{dt}\right)_{t\to 0}}{\left(\frac{dR_h(t)}{dt}\right)_{t\to 0,fast}} \quad (6)$$

In order to establish the concentration that decreases the potential barrier causing the flocculation of the nanoparticles and which ions normally found in surface water like rivers (Na^{1+}, Zn^{1+}, Ca^{2+}), concentration is tabulated 5 to 30 mg/L) of electrolyte at the intersection of the reaction-limited stability curve (extrapolated from the linear section of the real stability curve) and the diffusion-limited stability curve (constant α value) and Thus finding the critical concentration of CCC coagulation [22-24].

2.5. Studies of magnetic sedimentation

Looking forward to studying the feasibility of the separation of the nanoparticles after being implemented in a treatment process, the study of the sedimentation of the nanomaterial was carried out as a function of time and the applied magnetic field. The magnetic system that was implemented produced a magnetic field gradient from a neodymium magnet cylinder with a diameter of 40mm and a height of 5mm that produced a field of 0,2 T. The suspension of nanoparticles in water was carried out in a volume of 250 ml where the influence of the magnetic field was measured in absence and presence of it by measuring the turbidity of the solution with a turbidimeter at different pH values (4, 7 and 9). Similarly, the influence of ionic strength (Na^{1+}, Zn^{1+}, Ca^{2+}) at different concentrations (10, 20 and 30 mg/L) as a function of time. On the other hand, the sedimentation of the magnetic nanoparticles after the adsorption of heavy metals (Hg and Cr) was also evaluated as a function of time.

With this, the percentage separation of the magnetic nanoparticles from the aqueous phase over a period was calculated as follows:

$$\% = \frac{Initial\ Turbidity - Final\ Turbidity}{Initial\ Turbidity} \times 100\% \quad (7)$$

3. Results and discussion

Characterization of Magnetic nanoparticles synthesized by the green methodology using glutathione with reducing agent and stabilizer can be observed in Fig. 2. TEM image (Fig. 2a) shows an average size of 60 nm. Saturation magnetization curve of the nanomaterial at room temperature (Fig. 2b.) was 85.4 emu/g, which is a close to theoretical value and a little larger to conventional synthesis which are 90 and 82.4 emu/g respectively. The surface charge of the material was determined by measuring the zeta potential (Fig. 2c.). A surface charge of -35.5 mV was obtained. This value represents the repulsion force of groups on the structure of glutathione (carbonyl and the very weak acid behavior of 1° and 2° amines), in order to stabilize the colloidal solution [25].

3.1. Kinetic aggregation studies

The evolution of the hydrodynamic radio profile of the magnetic nanoparticles modified with Glutathione over time in relation to the concentration of the ions in solution can be observed in Figs. 3 to 5. The Z-average can be expressed as the intensity based harmonic mean and is shown by the equation below [26]:

$$Z_{average} = \frac{\Sigma S_i}{\Sigma\left(S_i/D_i\right)} \quad (8)$$

Here, S_i is the scattered intensity from particle *i* and D_i is the diameter of particle *i*. Note that the result is in the form of a harmonic mean.

Taking into account the behavior of the nanoparticles in these media it can be observed that the increase in the ionic strength in the solutions decreases the steric repulsion force between the particles given by the charges of the amino, carboxyl and thiol groups on the surface of the material. This is because interactions between the charges of the ions and the loads of these functional groups are presented [27–31]. The conditions under which the rapid initial aggregation occurs in a specific system may be related to its CCC, which is discussed below. Likewise, the agglomeration phenomenon in the solution that does not have ions in solution also takes place although they are low or despicable, processes of oxidation of the particle and electrostatic interactions between the positive and negative charges of the different functional groups occur [14,32–35].

This decrease in charges could be evaluated in the Zeta potential analysis, where the relationship between the surface charge of the particle and the concentration of the electrolytes in the aqueous solution can be seen in Fig 6. Since the pH of the solutions after the addition of the nanoparticles was approximately 7, we can establish the decrease in the stability of the material since the long absolute value was higher under conditions of absence of electrolytes regarding to the addition of these.

The efficiency of binding or agglomeration of Glutathione@MNPs as a function of the concentration of the medium and the concentration of the electrolytes can be seen in Fig 7.

The binding efficiency profile shows typical DLVO behavior with two distinct regions. The former is known as limited reaction agglomeration (RLA), where binding efficiency gradually increases with increased concentrations of media and electrolytes due to the decreased surface charge of the nanoparticles. The second is known as diffusion-limited agglomeration (DLA), where the binding efficiency reaches a constant value in certain media and known electrolyte concentrations (CCC). The CCC values found are presented in Table 1.

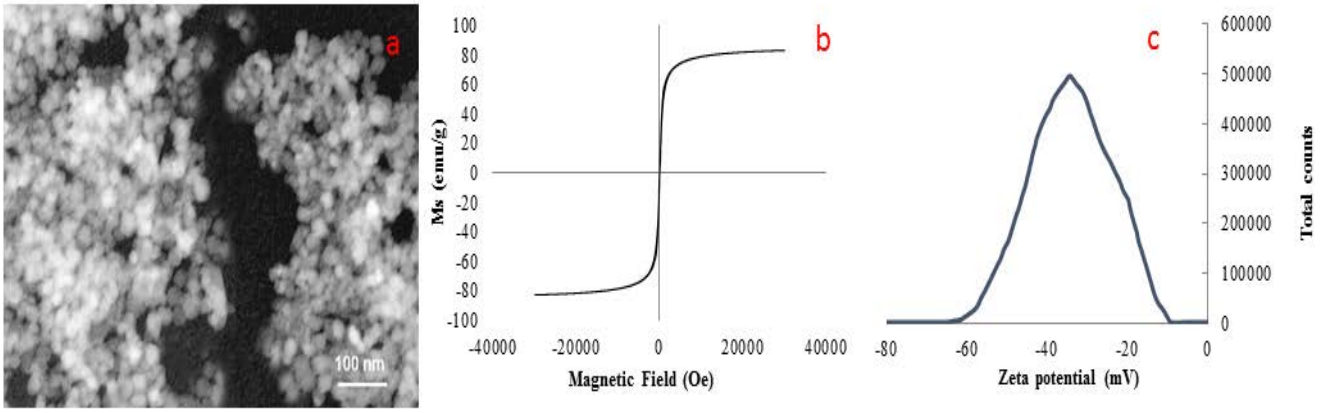


Figure 2. Characterization of Glutathione@Fe_3O_4 NPs. a) TEM image, b) Room temperature magnetization and c) Zeta potential of Glutathione@MNPs.
Source: The authors

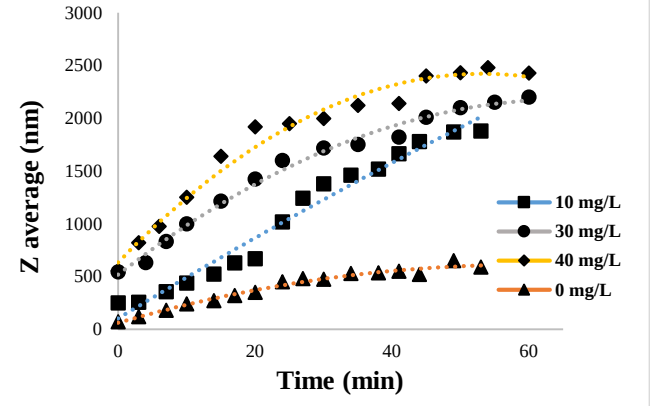


Figure 3 Evolution of $Z_{average}$ of Glutathione@MNPs in water with Na.
Source: The authors

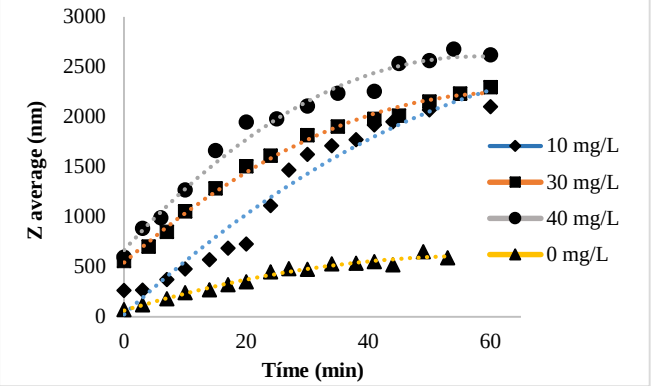


Figure 5. Evolution of $Z_{average}$ of Glutathione@MNPs in water with Zn.
Source: The authors

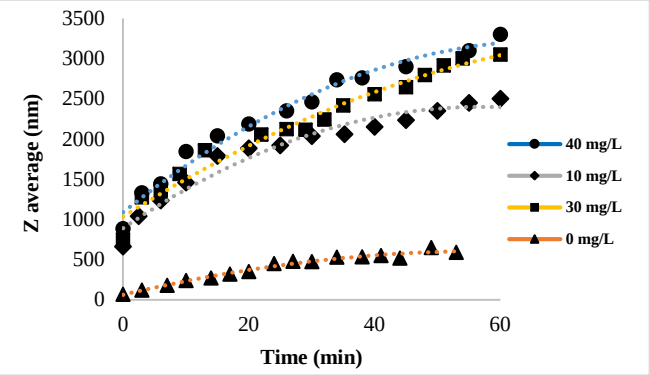


Figure 4. Evolution of $Z_{average}$ of Glutathione@MNPs in water with Ca.
Source: The authors

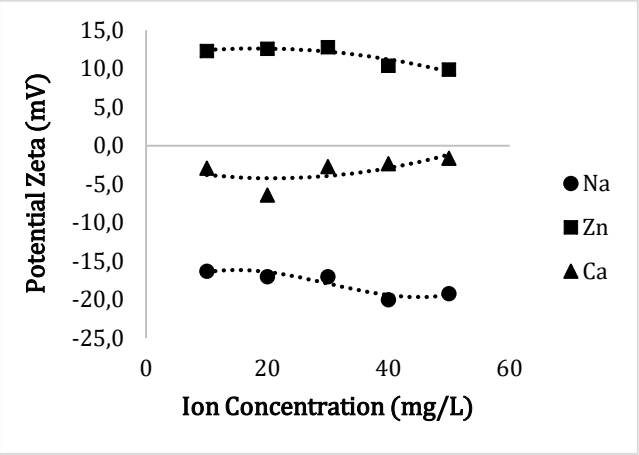


Figure 6. Behavior of the surface charge of Glutathione@MNPs as a function of the concentration of Na, Zn and Ca ions.
Source: The authors

Other reported values of critical coagulation concentrations have been reported for materials of similar chemical structure. In [36,37] a CCC value for Hematite nanoparticles of about 65Mm (1495 mg Na/L) was reported at near neutral pH when NaCl was used as the sodium precursor salt. Compared with the obtained value of 30 mg/L, the required amount of the salt would be lower to promote the precipitation and separation of the magnetic material from the aqueous solution.

Table 1.
Critical Coagulation Concentration of Glutathione@MNPs with different salts in aqueous medium.

Ion	CCC (mg/L)
Sodium	30
Calcium	20
Zinc	25

Source: The Authors

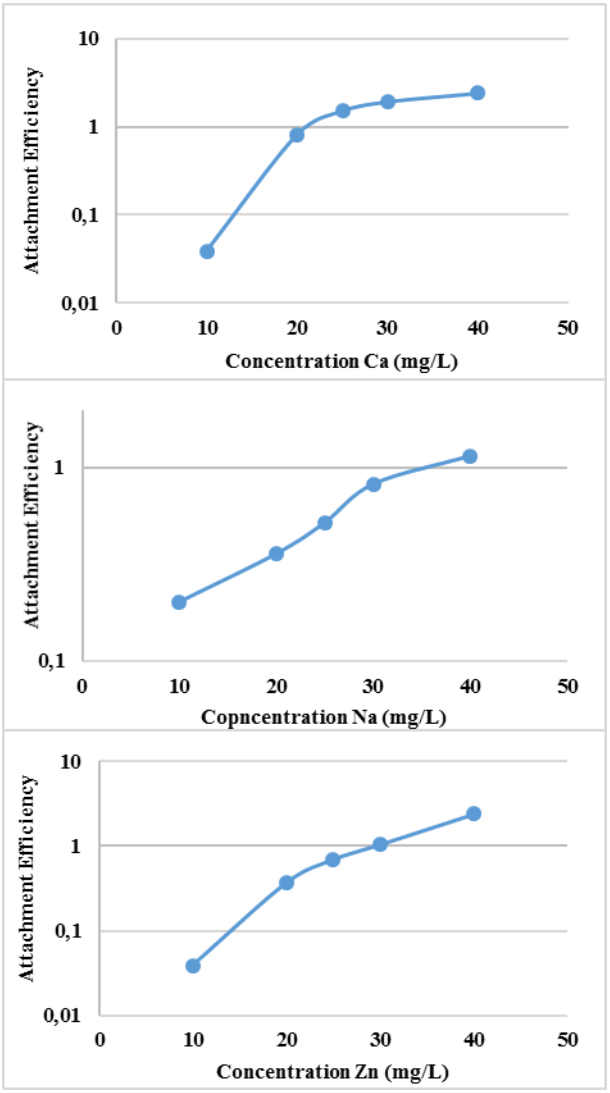


Figure 7. Agglomeration efficiency of Glutathione@MNPs in aqueous systems with ion salts at different concentration.
Source: The authors

3.2. Studies of magnetic sedimentation

Fig. 8 shows the sedimentation dynamics of Glutathione@MNPs in aqueous solution in the absence and presence of a magnetic field at different pH values. Suspensions of particles in the absence of magnetic field and affected only by the gravitational one remains stable for several weeks (approximately 8) which shows greater stability regarding to unmodified MNPs which normally show agglomeration and precipitation after 2 weeks. This could have important implications for the transport behavior of pollutants in the natural environment because, due to the high reactivity of the nanoparticles, the contaminants could be incorporated into the nanoparticles through adsorption, co-precipitation and other geochemical processes [37,38]. Therefore, stable suspended MNPs could improve transport of contaminants.

In contrast, the particles in the presence of the applied field suffer an acceleration in sedimentation velocity since in a period of 2 hours more than 80% of these are attracted by the magnetic field. The remaining 20% of the particles in that period have not yet undergone processes of agglomeration and/or attraction due to their size or the strength of the steric forces of the functional groups belonging to Glutathione, in addition, a steric interaction due to the formation of a layer of water around the material could also be important, however so far there is no adequate model to quantitatively estimate such contribution [39].

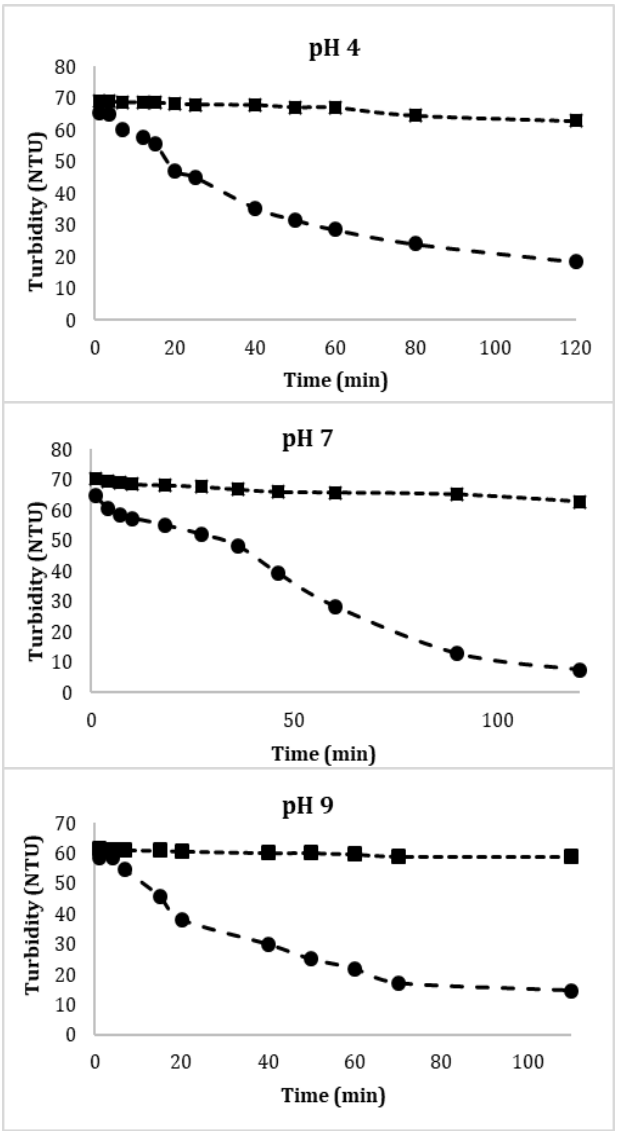


Figure 8. Effect of the magnetic gradient on the sedimentation dynamics of Glutathione@MNPs in aqueous systems at different pH values. ●With magnetic field, ■ without magnetic field.
Source: The authors

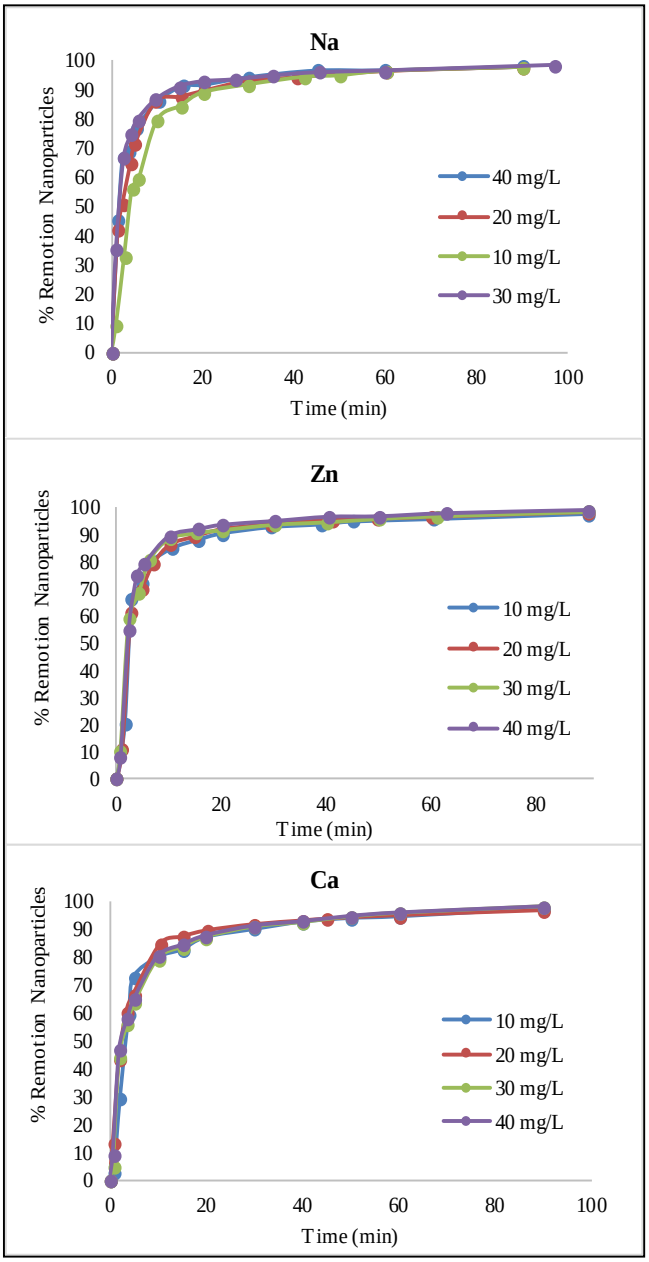


Figure 9. Sedimentation dynamics of Glutathione@MNPs in aqueous suspension in a magnetic gradient in the presence of ions at different concentrations.
Source: The authors

Aqueous suspensions of Glutathione@MNPs with small additions of salts in the absence of a magnetic field remain stable for a long time (2 weeks) but less time than in the absence of the salts. The difference in stability based on the nature of salt was expressed in greater stability with Zn > Na > Ca. Despite this difference, when the nanoparticle suspensions are exposed to the magnetic field, the separation of the aqueous phase is almost complete (> 90%) for solutions with Zn, Na and Ca (Fig 9).

The increase of sedimentation velocity in the presence of salts with charge 1+ and 2+ in the presence of magnetic field, especially in the initial period, is evidently related to the strengthening of aggregate formation processes. The dependence of the sedimentation rate on the concentration of salts in the suspensions gives evidence of the change in the electrostatic surface charge of the particles, which is confirmed by the change in the zeta potential of the particles in the presence of the salt additives. The fact that calcium ions promote a greater increase in sedimentation rate is due to its higher ionic charge (2+ compared to Zn and Na which is 1+), as well as the possibility of creating additional bonds (since it is of the bridge group type) between the particles of Glutathione@MNPs, accelerating the aggregation process [34].

With this result, there is the possibility that triply charged cations further strengthen the aggregation of particles in the suspension, which would be an open study area for future work.

These results are quite encouraging given that, for an implementation of the magnetic material in water treatment operations, some of these salts can be added to obtain a more efficient separation and to remove the nanoparticles from the effluent and thus not have a release to the environment that can Affect ecosystems or human health.

The separation rates of Glutathione@MNPs after performing the heavy metal (Hg and Cr) adsorption processes for 120 min was evaluated. It can be seen from Fig. 10 that the separation of the heavy Nanomaterial-Metal assembly is effective since more than 90% is withdrawn from the aqueous phase. This is because the active adsorption sites such as thiols, amines and carboxyl groups react with the metal ions of Hg and Cr reducing the effective surface charge and consequently the steric forces that provide the stability leading to an increase in the ease of separation by means of the magnetic field [40– 42].

The above results provide the possibility of creating water treatment systems for heavy metal remediation with MNPs, as it gives control of non-release of nanomaterial or heavy metal into the body of water.

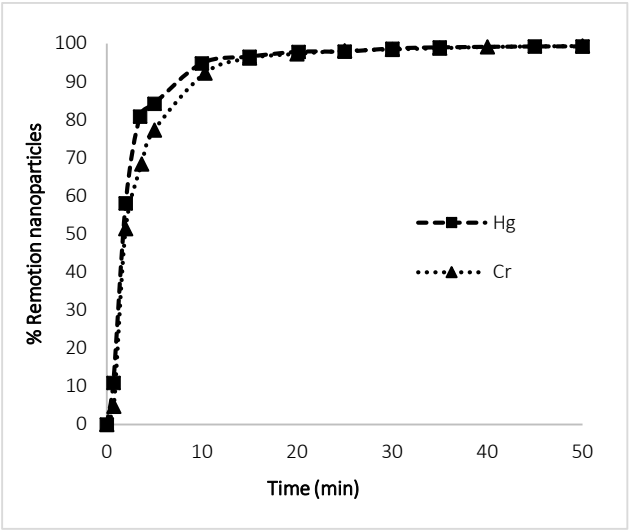


Figure 10. Sedimentation dynamics of Glutathione@MNPs in aqueous suspension after adsorption of Hg and Cr.
Source: The authors

4. Conclusions

Glutathione@MNPs show a stability in aqueous medium with no presence of ion metals over 8 weeks. This stability is due to the steric repulsions of the carboxyl, amine and thiol groups on the surface of the material.

This stability was reduced by the presence of valves in calcium, zinc and sodium, where an increase of more than 500% in the average hydrodynamic radius of the nanoparticles was found.

If the critical concentrations of coagulation come from the application of the DLVO theory, where calcium sales consume the lowest concentration to promote the agglomeration of the particles and that the charge of these emulsions is mayor in comparison of air of zinc and sodium.

The application of magnetic field for the separation of the particles of the aqueous medium is effective, since with the fields of 0.2T a separation greater than 90% of the material was reached. Also, for nanoparticles bound to heavy metals such as the Hg and Cr son, they do not inhibit the separation of material from the aquatic medium, which gives indications for the use of this material for environmental remediation.

The above results provide the possibility of creating water treatment systems for heavy metal remediation with MNPs, as it gives control of non-release of nanomaterial or heavy metal into the body of water.

References

[1] Bagbi, Y., Sarswat, A., Mohan, D., Pandey, A. and Solanki, P.R., Lead (Pb^{2+}) adsorption by monodispersed magnetite nanoparticles: Surface analysis and effects of solution chemistry, J. Environ. Chem. Eng., 4(4), pp. 4237-4247, 2016. DOI: 10.1016/j.jece.2016.09.026

[2] Pratt, A., Nanomagnetism: Fundamentals and Applications, vol. 6. Elsevier, 2014.

[3] Bystrzejewska-Piotrowska, G., Golimowski, J. and. Urban, P.L., Nanoparticles: their potential toxicity, waste and environmental management., Waste Manag., 29(9), pp. 2587-2595, Sep. 2009. DOI: 10.1016/j.wasman.2009.04.001

[4] Zhao, J. et al., Highly efficient removal of bivalent heavy metals from aqueous systems by magnetic porous Fe3O4-MnO2: Adsorption behavior and process study, Chem. Eng. J., 304, pp. 737-746, 2016. DOI: 10.1016/j.cej.2016.07.003

[5] Rajput, S., Pittman, C.U. and Mohan, D., Magnetic magnetite (Fe_3O_4) nanoparticle synthesis and applications for lead (Pb^{2+}) and chromium (Cr^{6+}) removal from water, J. Colloid Interface Sci., 468, pp. 334-346, 2016. DOI: 10.1016/j.jcis.2015.12.008

[6] Shen, W., Mu, Y., Xiao, T. and Ai, Z., Magnetic Fe_3O_4-FeB nanocomposites with promoted Cr(VI) removal performance, Chem. Eng. J., 285, pp. 57-68, 2016. DOI: 10.1016/j.cej.2015.09.053

[7] Tang, S.C.N., and Lo, I.M.C., Magnetic nanoparticles: essential factors for sustainable environmental applications., Water Res., 47(8), pp. 2613-2632, May 2013. DOI: 10.1016/j.watres.2013.02.039

[8] Bland, J.A., Nanomagnetism: Ultrathin films, multilayers and nanostructures, vol. 1. Elsevier, 2006.

[9] Luo, L. and Nguyen, A.V., A review of principles and applications of magnetic flocculation to separate ultrafine magnetic particles, Sep. Purif. Technol., 172, pp. 85-99, 2017. DOI: 10.1016/j.seppur.2016.07.021

[10] Petosa, A.R., Jaisi, D.P., Quevedo, I.R., Elimelech, M. and Tufenkji, N., Aggregation and deposition of engineered nanomaterials in aquatic environments: role of physicochemical interactions., Environ. Sci. Technol., 44(17), pp. 6532-6549, Sep. 2010. DOI: 10.1021/es100598h

[11] Reddy, D.H.K. and Yun, Y.-S., Spinel ferrite magnetic adsorbents: alternative future materials for water purification?, Coord. Chem. Rev., 315, pp. 90-111, Feb. 2016. DOI: 10.1016/j.ccr.2016.01.012

[12] Wei, X., and Viadero, R.C., Synthesis of magnetite nanoparticles with ferric iron recovered from acid mine drainage: Implications for environmental engineering, Colloids Surfaces A Physicochem. Eng. Asp., 294(1–3), pp. 280-286, Feb. 2007. DOI: 10.1016/j.colsurfa.2006.07.060

[13] Gambinossi, F., Mylon, S.E. and Ferri, J.K., Aggregation kinetics and colloidal stability of functionalized nanoparticles., Adv. Colloid Interface Sci., 222, pp. 332-349, Aug. 2015. DOI: 10.1016/j.cis.2014.07.015

[14] Topuz, E., Traber, J., Sigg, L. and Talinli, I., Agglomeration of Ag and TiO_2 nanoparticles in surface and wastewater: Role of calcium ions and of organic carbon fractions., Environ. Pollut., 204, pp. 313-323, Sep. 2015. DOI: 10.1016/j.envpol.2015.05.034

[15] Bakhteeva, I. et al., Magnetic field-enhanced sedimentation of nanopowder magnetite in water flow, Environ. Technol., 36(14), pp. 1828-1836, Jul. 2015. DOI: 10.1080/09593330.2015.1013570

[16] Nur, Y., Lead, J.R. and Baalousha, M., Evaluation of charge and agglomeration behavior of TiO<inf>2</inf> nanoparticles in ecotoxicological media, Sci. Total Environ., 535, pp. 45-53, 2015. DOI: 10.1016/j.scitotenv.2014.11.057

[17] Binns, C., Medical Applications of Magnetic Nanoparticles, Nanomagnetism Fundam. Appl., 6(2), pp. 217-258, 2014. DOI: 10.1263/jbb.100.1

[18] Baalousha, M., Effect of nanomaterial and media physicochemical properties on nanomaterial aggregation kinetics, NanoImpact, 6. pp. 55-68, Apr-2017. DOI: 10.1016/j.impact.2016.10.005

[19] Cao, H., Li, J., Shen, Y., Li, S., Huang, F. and Xie, A., Green synthesis and surface properties of Fe_3O_4@SA core–shell nanocomposites, Appl. Surf. Sci., 301, pp. 244-249, May 2014. DOI: 10.1016/j.apsusc.2014.02.054

[20] Zhang, H., Sun, J. and Guo, L.-H., UV irradiation mediated aggregation of TiO_2 nanoparticles in simulated aquatic system, NanoImpact, 2016. DOI: 10.1016/j.impact.2016.08.004

[21] Saleh, N.B., Pfefferle, L.D. and Elimelech, M., Influence of biomacromolecules and humic acid on the aggregation kinetics of single-walled carbon nanotubes, Environ. Sci. Technol., 44(7), pp. 2412-2418, Apr. 2010. DOI: 10.1021/es903059t

[22] Gallego-Urrea, J.A., Hammes, J., Cornelis, G. and Hassellöv, M., Coagulation and sedimentation of gold nanoparticles and illite in model natural waters: Influence of initial particle concentration, NanoImpact, 3, pp. 67-74, 2016. DOI: 10.1016/j.impact.2016.10.004

[23] Wang, M., Gao, B. and Tang, D., Review of key factors controlling engineered nanoparticle transport in porous media, J. Hazard. Mater., 318, pp. 233-246, 2016. DOI: 10.1016/j.jhazmat.2016.06.065

[24] Pu, S., et al., Narrowing size distribution widths of small α-Al2O3 nanoparticles by addition of large nanoparticles in coagulation separation, Ceram. Int., 2016. DOI: 10.1016/j.ceramint.2016.12.065

[25] Koppel, D.E., Analysis of macromolecular polydispersity in intensity correlation spectroscopy: the method of cumulants, J. Chem. Phys., 57(11), pp. 4814-4820, Dec. 1972. DOI: 10.1063/1.1678153

[26] Kharissova, O.V., Dias, H.V.R., Kharisov, B.I., Pérez, B.O. and Pérez, V.M.J., The greener synthesis of nanoparticles., Trends Biotechnol., 31(4), pp. 240-248, Apr. 2013. DOI: 10.1016/j.tibtech.2013.01.003

[27] Shen, X., Wang, Q., Chen, W. and Pang, Y., One-step synthesis of water-dispersible cysteine functionalized magnetic Fe_3O_4 nanoparticles for mercury(II) removal from aqueous solutions, Appl. Surf. Sci., 317, pp. 1028-1034, Oct. 2014. DOI: 10.1016/j.apsusc.2014.09.033

[28] Andrade, Â.L., Fabris, J.D., Ardisson, J.D., Valente, M.A. and Ferreira, J.M.F., Effect of tetramethylammonium hydroxide on nucleation, surface modification and growth of magnetic nanoparticles, J. Nanomater., 2012, pp. 1-10, 2012. DOI: 10.1155/2012/454759

[29] Atarod, M., Nasrollahzadeh, M. and Mohammad Sajadi, S., Green synthesis of Pd/RGO/Fe_3O_4 nanocomposite using Withania coagulans leaf extract and its application as magnetically separable and reusable catalyst for the reduction of 4-nitrophenol., J. Colloid Interface Sci., 465, pp. 249-258, Mar. 2016. DOI: 10.1016/j.jcis.2015.11.060

[30] Pei, W., Kumada, H., Natusme, T., Saito, H. and Ishio, S., Study on magnetite nanoparticles synthesized by chemical method, J. Magn. Magn. Mater., 310(2), pp. 2375-2377, Mar. 2007. DOI: 10.1016/j.jmmm.2006.10.837
[31] Oriekhova, O., and Stoll, S., Stability of uncoated and fulvic acids coated manufactured CeO_2 nanoparticles in various conditions: From ultrapure to natural Lake Geneva waters, Sci. Total Environ., 562, pp. 327-334, 2016. DOI: 10.1016/j.scitotenv.2016.03.184
[32] Mohd-Omar, F., Abdul-Aziz, H. and Stoll, S., Aggregation and disaggregation of ZnO nanoparticles: Influence of pH and adsorption of Suwannee River humic acid, Sci. Total Environ., 468, pp. 195-201, 2014. DOI: 10.1016/j.scitotenv.2013.08.044
[33] Romanello, M.B. and Fidalgo-de Cortalezzi, M.M., An experimental study on the aggregation of TiO2 nanoparticles under environmentally relevant conditions, Water Res., 47(12), pp. 3887-3898, 2013. DOI: 10.1016/j.watres.2012.11.061
[34] Tirado-Miranda, M., Schmitt, A., Callejas-Fernández, J. and Fernández-Barbero, A., The aggregation behaviour of protein-coated particles: a light scattering study., Eur. Biophys. J., 32(2), pp. 128-136, May 2003. DOI: 10.1007/s00249-002-0275-6
[35] Chen, X.G., Li, J.P., Li, Z., De Chen, J.B. and Han, Y.J., Vegetation change in Yanchi of Ningxia and its relationship with climate change in recent years, Acta Ecol. Sin., 26(5), pp. 1516-1522, 2006.
[36] He, Y.T., Wan, J. and Tokunaga, T., Kinetic stability of hematite nanoparticles: the effect of particle sizes, J. Nanoparticle Res., 10(2), pp. 321-332, Feb. 2008. DOI: 10.1007/s11051-007-9255-1
[37] Yeap, S.P., Lim, J.K., Ooi, B.S. and Ahmad, A.L., Agglomeration, colloidal stability, and magnetic separation of magnetic nanoparticles: collective influences on environmental engineering applications, J. Nanoparticle Res., 19(11), 368 P., Nov. 2017. DOI: 10.1007/s11051-017-4065-6
[38] Bakhteeva, I.A. et al., Magnetic sedimentation and aggregation of Fe_3O_4@SiO_2 nanoparticles in water medium, Sep. Purif. Technol., 159, pp. 35-42, 2016. DOI: 10.1016/j.seppur.2015.12.043
[39] Bagbi, Y., Sarswat, A., Mohan, D., Pandey, A. and Solanki, P.R., Lead and chromium adsorption from water using L-Cysteine functionalized magnetite (Fe3O4) Nanoparticles, Sci. Rep., 7(1), p. 7672, Dec. 2017. DOI: 10.1038/s41598-017-03380-x
[40] Fan,, H.L., Li, L., Zhou, S.F. and Liu, Y.Z., Continuous preparation of Fe3O4 nanoparticles combined with surface modification by L-cysteine and their application in heavy metal adsorption, Ceram. Int., 42(3), pp. 4228-4237, 2016. DOI: 10.1016/j.ceramint.2015.11.098
[41] Sheikhmohammadi, A., et al., Application of graphene oxide modified with 8-hydroxyquinoline for the adsorption of Cr (VI) from wastewater: Optimization, kinetic, thermodynamic and equilibrium studies, J. Mol. Liq., 233, pp. 75-88, May 2017. DOI: 10.1016/j.molliq.2017.02.101

W. Marimón-Bolívar, received the BSc. Eng in Chemical Engineering in 2011 at University of Cartagena, and the PhD degree in Engineering (Nanotechnology for water treatment) in 2018 at the Javeriana University Bogotá, Colombia. From 2012 to 2014, he worked as a Young researcher at the Cartagena University on remediation for wastewater treatment. Currently, he is a researcher in CENIGAA from 2015 making projects about environmental chemistry. In addition, he is a part time teacher in Sergio Arboleda University teaching environmental chemistry and water treatment. His research interests include Nanotechnology for environmental application; water quality modelling, environmental chemistry.
ORCID: 0000-0002-6947-2220

E.E. González, received his BSc. degrees in Physics from the Universidad Nacional de Colombia, his MSc. in Physics from Universidad del Valle, Colombia, and his PhD. degree in Physics from Universidad Autónoma de Barcelona, España. He is a full professor in the Instituto Geofísico, Facultad de Ingeniería, Pontificia Universidad Javeriana, Bogotá, Colombia. Research Leader Group of Nanoscience and Nanotechnology. He is a member of the Academia Colombiana de Ciencias Exactas Físicas y Naturales. He is a COLCIENCIAS Senior Researcher. He has had director of Nanoscale Science and Technology Center, Editor of Journal Nano Science and Technology, General Coordinator of NanoColombia Network, and Bio-Nano Convergence Network. His research interests include: quantum phenomenology and quantum computing, nanomaterials, specifically production of nanostructures, characterization, study and modeling of physicochemical properties and their implementation in systems and processes for the production of clean energy, environmental remediation, diagnosis and treatment in the area of health.
ORCID: 0000-0003-3103-3959



UNIVERSIDAD NACIONAL DE COLOMBIA
SEDE MEDELLÍN
FACULTAD DE MINAS

Área Curricular de Ingeniería
Química e Ingeniería de Petróleos

Oferta de Posgrados

Maestría en Ingeniería - Ingeniería Química
Maestría en Ingeniería - Ingeniería de Petróleos
Doctorado en Ingeniería - Sistemas Energéticos

Mayor información:

E-mail: qcaypet_med@unal.edu.co
Teléfono: (57-4) 425 5317

UNIVERSIDAD NACIONAL DE COLOMBIA
SEDE MEDELLÍN
FACULTAD DE MINAS



DYNA
http://dyna.medellin.unal.edu.co/

Ab-initio analysis of magnetic, structural, electronic and thermodynamic properties of the Ba_2TiMnO_6 manganite

Críspulo Enrique Deluque-Toro [a], David A. Landínez-Téllez [b] & Jairo Roa-Rojas [b]

[a] *Grupo de Nuevos Materiales, Facultad de Ingeniería, Universidad del Magdalena, Santa Marta, Colombia, deluquetoro@gmail.com*
[b] *Grupo de Física de Nuevos Materiales, Departamento de Física, Universidad Nacional de Colombia, Bogotá, Colombia, dalandinezt@unal.edu.co, jroar@unal.edu.co*

Received: October 26th, 2017. Received in revised form: March 2nd, 2018. Accepted: March 14th, 2018

Abstract
Perovskite-like materials, which include magnetic elements, have relevance because their technological perspectives of applications in the spintronics industry. In this work, the magnetic, structural, electronic and thermodynamic properties of the Ba_2TiMnO_6 of the perovskite-like manganite are investigated. Calculations are carried out through the Full-Potential Linear Augmented Plane Wave method (FP-LAPW) within the framework of the Density Functional Theory (DFT) with exchange and correlation effects in the Generalized Gradient (GGA) and Local Density (LDA) approximations, including spin polarization. From the minimization of energy as a function of volume using the Murnaghan's state equation the equilibrium lattice parameter and cohesive properties of this compound were obtained. The study of the electronic structure was based in the analysis of the electronic density of states (DOS), and the band structure, showing that this compound evidences an effective magnetic moment of 3.0 μ_B. The pressure and temperature dependence of specific heat, entropy, thermal expansion coefficient, Debye temperature and Grüneisen parameter were calculated by DFT from the state equation using the quasi-harmonic model of Debye. A specific heat behavior $C_V \approx C_P$ was found at temperatures below $T = 400\ K$, with Dulong-Petit limit values, which are quite higher than those, reported for simple perovskites.

Keywords: perovskite material; electronic structure; thermodynamic properties; DFT.

Análisis *ab-initio* de las propiedades magnéticas, estructurales, electrónicas y termodinámicas de la manganita Ba_2TiMnO_6

Resumen
Los materiales de tipo perovskita que incluyen elementos magnéticos son relevantes debido a sus perspectivas de aplicabilidad tecnológica en la industria de la espintrónica. En este trabajo fueron investigadas las propiedades magnéticas, estructurales, electrónicas y termodinámicas de la manganita de tipo perovskita Ba_2TiMnO_6. Los cálculos fueron realizados a través del método del potencial de ondas planas aumentadas y linealizadas (FP-LAPW), en el marco de la Teoría del Funcional Densidad (DFT), con efectos de intercambio y correlación en las aproximaciones de gradiente generalizado (GGA) y de densidad local (LDA), incluyendo polarización de espín. A partir de la minimización de la energía en función del volumen, usando la ecuación de estado de Murnaghan se obtuvieron los parámetros de equilibrio de la red las propiedades de cohesión de este compuesto. El estudio de la estructura electrónica se basó en el análisis de la densidad de estados (DOS) y la estructura de bandas, mostrando que este compuesto evidencia un momento magnético efectivo de 3.0 μ_B. la dependencia con la temperatura y la presión del calor específico, la entropía, el coeficiente de expansión térmica, la temperatura de Debye y el parámetro de Grüneisen fueron calculados mediante DFT a partir de la ecuación de estado, usando el modelo cuasi-armónico de Debye. Se encontró que el calor específico $C_V \approx C_P$ para temperaturas por debajo de $T = 400\ K$, con un límite de Dulong-Petit relativamente mayor que el reportado para perovskitas simples.

Palabras clave: material tipo perovskita; estructura electrónica; propiedades termodinámicas; DFT.

1. Introduction

Physical properties of perovskite-like ceramics are particularly sensible to inhomogeneities like distortions from the ideal cubic structure of the ABO_3 formula, vacancies and chemical substitutions [1]. One of these anomalies, which

How to cite: Deluque-Toro, C. E., Landínez-Téllez, D. A. and Roa-Rojas, J., Ab-initio analysis of magnetic, structural, electronic and thermodynamic properties of the Ba2TiMnO6 manganite. DYNA, 85(205), pp. 27-36, June, 2018.

© The author; licensee Universidad Nacional de Colombia.

raises the complex perovskite with $A_2BB'O_6$ formula, results from the ordering of B and B' cations on the octahedral site of the primitive perovskite unit cell [2]. The importance of complex perovskites is in the possibility of creating new magnetic materials $A_2BB'O_6$, with A being alkaline earth or rare earth cations and B, B' transition metal or rare earth ions. Recently, study of these materials has increased due to the possibility to apply them in the design and technology of magnetic memories, tunnel junctions and other magnetic devices in the novel spintronics area [3]. In previous work, we have analyzed the magnetic properties of the Sr_2TiMnO_6 and Ca_2TiMnO_6 compounds, finding that these perovskite type ceramics show antiferromagnetic characteristics at temperatures below *44.8 K* and *15.5 K*, respectively [4-5]. Recently the density functional theory (DFT) has constituted in a strong tool to study electronic properties in perovskite-like material [6-7] and, with the aim of theoretically determine the physical effects in the chemical composition of the material as a result of the inclusion of magnetic elements, in this work we developed an *ab initio* exhaustive study of a double perovskite with A=Ba, B=Ti and B'=Mn. In particular, we focus on the cohesive properties, electronics of the Bi_2TiMnO_6 double perovskite, and calculate their single crystal elastic constants to analyze their mechanical stability, and predict polycrystalline mechanical properties. On the other hand, calculations of thermodynamic properties have been performed in order to study their dependence on temperature, correlating these results with the structural and electronic properties of the material.

2. Theoretical details

2.1. Ab-*initio* calculations

The spin polarized Full-Potential Linear Augmented Plane Wave method (SP-FP-LAPW) within the framework of the Kohn-Sham Density Functional Theory (DFT) [8] was applied by adopting the Generalized Gradient (GGA) approximation for the exchange-correlation energy by Perdew, Burke and Ernzerhof (PBE) [9], and also the Local Density (LDA) approximation with the exchange-correlation potentials of Perdew and Wang [10]. The numeric package Wien*2k* [11] was used to calculate self-consistently the total energy for the constituent elements and alloys. Taking the experimental unit cell data as input, all the structures studied in this work were fully relaxed with respect to their lattice parameters and the internal degrees of freedom compatible with the space group symmetry of the crystal structure. The resulting energies versus volume functions have been fitted to the Murnaghan´s equation of state [12] in order to obtain the minimum energy value, the bulk modulus, its pressure derivative, and the equilibrium lattice parameters and associated volume. The muffin-tin radius of the elements were 2.5, 1.93, 1.85 and 1.6 (in au) Ba, Ti, Mn and O respectfully, angular momentum up to l =10 inside the muffin-tin sphere, a maximum vector in the reciprocal space of G_{max} *=12.0* and $R_{MT}K_{max}$*= 7.0*. A mesh of *1500 k*-points in the first Brillouin zone was considered, equivalent to a maximum of 56 k points in the irreducible Brillouin zone depending on the considered structure. Finally, the convergence criterion for the self-consistent calculation was 0.0001 Ry for the total energies, 0.0005 a.u. in the charge and 1.0 mRy/a.u. in the internal forces. The elastic constants here reported for the Ba_2TiMnO_6, cubic phase were calculated using the Wien*2k* Cubic-elastic package [13] by considering the second-order derivative ($E(\delta)$) of a polynomial fit ($E=E(\delta)$) of energy vs. strains (δ) at zero strain ($\delta=0$).

2.2. Theoretical model

The vibrational density of states *g(w)* of a crystal can be used to determine some of its thermodynamic properties, because this function provides the number of normal modes of vibration in an infinitesimal range of frequencies between *w* and *w+dw*. This concept is applied in the Debye model, considering that the crystal can be modeled as a continuous medium so with normal vibrations like elastic stationary waves. Thus, through the density of states, the wave number can be calculated in that infinitesimal frequency range. In the Debye model, a harmonic consideration of the potential energy is made to evaluate the force constants, whereby the temperature of Debye (Θ_D) is constant and must be obtained from the elastic constants. Meanwhile, this harmonic model lacks the thermal expansion, which is one of the most important experimental properties that can be measured in the crystals. Since the temperature only influences the function of Helmholtz through the vibrational term, and this in turn depends on the elastic constants, in principle there would be no relation between the temperature and the geometry of the system. For this reason, it is necessary to introduce into the model the interdependence between temperature and volume. This circumstance suggests the application of the quasi-harmonic approximation, in which harmonic vibrations are assumed in positions that are no equilibrium. In this way, the vibration frequencies become dependent on the volume and can be evaluated from the second derivatives of the potential energy surface at those off-balance positions. We must note that under static conditions, the second derivative produces vibration frequencies that occur around a minimum. On the other hand, in the presence of generalized forces such as pressure, the equilibrium geometry is displaced in such a way that the external forces tend to override the gradient of the static potential energy surface. Thus, the quasi-harmonic model of Debye has harmonic behavior, but anharmonic effects are introduced through the dependence of the frequencies in the configuration. It is then possible to predict the thermal expansion of the crystal by the dependence of volume and temperature on equilibrium.

From the above, it can be established that a non-static equilibrium configuration can be achieved through external links. Because the stringent treatment of these bonds is quite complex, the way to simplify it is by resorting to thermodynamic equilibrium conditions. Then, assuming that the system is at a given temperature and pressure, the system can be thermodynamically described by the non-equilibrium Gibbs function, which, in its general form, can be written as

$$G^*(T,P,\vec{a}) = E_e(\vec{a}) + PV(\vec{a}) + A_{vib}[T, w_j(\vec{a})], \quad (1)$$

which is a function of temperature *T*, pressure *P* and the lattice parameters $\vec{a}$. In equation (1), E_e is the total energy of the crystal and A_{vib} represents the vibrational Helmholtz free energy. The equilibrium situation of the system corresponds to the lowest Gibbs energy at a given set of temperature and pressure. The dependence of the E_e on the lattice parameters $\vec{a}$ is explicit, while A_{vib} depends implicitly on $\vec{a}$ through the vibration frequencies of the solid. The equilibrium configuration of the system will be the minimum of this Gibbs function that depends on *T* and *P*. Since the volume is also dependent on $\vec{a}$, this gives the desired interdependence between temperature and volume. Once the system equilibrates the external bonds are eliminated, because their strength cancels terms associated with the first derivatives of E_e at each point of the potential energy, as this is an equilibrium point. Under certain conditions of *T* and *P*, the equilibrium configuration of the system corresponds to the lowest Gibbs energy. Within this scheme, it is possible to consider the geometries of quasi-harmonic crystalline equilibrium and all the thermodynamic properties of the crystal as functions of temperature and pressure. The difference between this model and the Debye model is that A_{vib} depends on the geometry through Θ_D, which in turn can be calculated from the elastic constants of the crystal, and these are the second derivatives of energy with respect to displacements of the lattice parameters.

A good simplification of the problem to obtain the Θ_D can be made by the isotropic solid approximation, but it is necessary to further reduce the number of properties required for the Θ_D of the system in any configuration. One-way to do this is by assuming that the solid acts as a fluid, which does not exhibit resistance to shear deformations ($c_{44}=0$). For this reason, transverse elastic waves are no taken into account. For the purposes of the approximation, the average speed for the longitudinal velocity of the solid calculated as done in a fluid is considered. Thus, the expression $\bar{c} = c_l = \sqrt{c_{11}/\rho}$ is obtained, which is associated with the static compression module of the crystal through $B_{static} = V\left(\frac{\partial^2 E_e}{\partial V^2}\right) = \left(\lambda + 2\mu/3\right)$, which takes the λ value as in a fluid, with μ the chemical potential. This gives the average speed $\bar{c} \approx \sqrt{B_{static}/\rho}$, which in turn gives rise to the Debye temperature

$$\Theta_D = \frac{h\bar{c}}{k_B}\left(\frac{3n_r}{4\pi V_r}\right)^{\frac{1}{3}} \approx \frac{h}{k_B}\left(\frac{3n_r}{4\pi V_r}\right)^{\frac{1}{3}}\sqrt{B_{static}/\rho}\,, \tag{2}$$

where $\rho=M_r/V_r$, with M_r the molecular mass and $\hbar = \frac{h}{2\pi}$. Then, the Debye temperature in an isotropic fluid model can be written as [14]

$$\Theta_D = \frac{\hbar}{k_B}\left(6\pi^2 n_r V_r^{1/2}\right)^{\frac{1}{3}}\sqrt{B_{static}/M_r}\,. \tag{3}$$

A second approach to reduce the elastic constants consists in the consideration of the Poisson ratio value, which is defined as the ratio between the transverse deformation and the longitudinal deformation for an isotropic crystal under axial tension. This coefficient that can be written as $\nu = \lambda/2(\lambda+\mu)$ usually has a value between *0.2* and *0.5*, and depends of the particular material [15]. Thus, it is possible to determine a parameter that can be chosen between λ, γ, and B_{static}. When choosing the parameter B_{static}, the equations for the velocity of transverse and longitudinal sound are as follows

$$c_t = \sqrt{\frac{3B_{static}}{2\rho}\frac{(1-2\nu)}{(1+\nu)}}\,, \tag{4}$$

$$c_l = \sqrt{\frac{3B_{static}}{\rho}\frac{(1-\nu)}{(1+\nu)}}\,, \tag{5}$$

such that the average velocity can be expressed in the form

$$\bar{c} = \sqrt{\frac{B_{static}}{\rho}f(\nu)}\,, \tag{6}$$

where

$$f(\nu) = \left\{3\left[2\left(\frac{2(1+\nu)}{3(1-2\nu)}\right)^{3/2} + \left(\frac{1+\nu}{3(1-\nu)}\right)^{3/2}\right]^{-1}\right\}^{1/3} \tag{7}$$

then equation (3) changes and the temperature of Debye becomes

$$\Theta_D = \frac{\hbar}{k_B}f(\nu)\left(6\pi^2 n_r V_r^{1/2}\right)^{\frac{1}{3}}\sqrt{B_{static}/M_r} \tag{8}$$

This expression is analogous to the fluid model, except for the function $f(\nu)$, where the bulk modulus and the Poisson coefficient are still present. Considering the ions in centrosymmetrical positions, the potential energy surface could be described as a sum of the potential for central interaction. Thus, it is possible to apply the Cauchy relation, for which $\nu=1/4$ [16]. Then the function $f(\nu)=0.85995$, and the Debye temperature for the considered isotropic Cauchy solid is

$$\Theta_D = 0.85995\frac{\hbar}{k_B}\left(6\pi^2 n_r V_r^{1/2}\right)^{\frac{1}{3}}\sqrt{B_{static}/M_r}\,. \tag{9}$$

With this approach, the Gibbs function of equation (1) can now be written as

$$G^*(T,P,\vec{a}) = E_e(\vec{a}) + PV(\vec{a}) + A_{vib}[T,\Theta_D(V(\vec{a}))] \tag{10}$$

This expression has the advantage that the dependencies of the internal parameters $\vec{a}$ are contained in E_e and *V*, so that in obtaining the internal parameters $\vec{a}$ that minimize E_e in a certain *V*, the Gibbs function will also be minimal in that volume. Therefore, assuming that the minimum energies with respect to internal parameters at different volumes are known, i.e., $E_e(V)$ is known, the Gibbs non-equilibrium function is then

$$G^*(T,P,V) = E_e(V) + PV + A_{vib}[T,\Theta_D(V)]\ . \quad (11)$$

As can be seen, internal parameters are a function of volume, but this is a function of temperature and pressure, *a[V(T,P)]*. That is, the internal parameters change with the temperature in an isotropic form, such that an increase in *T* equals a decrease in *P*. This isotropic approximation is quite reasonable, although it has not been considered that the vibrational frequencies depend on all coordinates. With the above approximations, equation (11) allows to obtain the Gibbs function of the crystal as a function of *T*, *P* and *V*. this function must be minimum with respect to any geometric parameter, and in particular with respect to the volume. Thus, by minimizing this function for values other than *T* and *P*, the system state equation is obtained and, from this, any thermodynamic property can be determined.

The bulk module is related to the electronic energy by means of the expression

$$B_{static}(V_r) = V_r\left(\frac{\partial^2 E_e(V_r)}{\partial V_r^2}\right) \quad (12)$$

which allows to rewrite the temperature of Debye as well

$$\Theta_D = 0.85995\frac{\hbar}{k_B}\left(6\pi^2 n_r V_r^{1/2}\right)^{\frac{1}{3}}\sqrt{\left(\frac{\partial^2 E_e(V_r)}{\partial V_r^2}\right)/_{M_r}} \quad (13)$$

Then, $\Theta_D(V_r)$ can be obtained through the second derivative of the curve $E_e(V_r)$. In order to determine the vibration function of Helmholtz at different temperatures and volumes, it can be inferred that [17]

$$\bar{A}_{vib}(T,V_r) = \bar{U}_{vib} - T\bar{S}_{vib} = \frac{9}{8}n_r k_B\Theta_D(V_r) + 3n_r k_B T Ln\left(1-e^{-\Theta_D(V_r)/T}\right) - n_r k_B T D[\Theta_D(V_r)/T], \quad (14)$$

where

$$\bar{U}_{vib} = \frac{9}{8}n_r R\Theta_D(V_r) + 3n_r RTD[\Theta_D(V_r)/T]\ , \quad (15)$$

$$\bar{S}_{vib} = 4n_r RTD[\Theta_D(V_r)/T] - 3n_r RLn\left(1-e^{-\Theta_D(V_r)/T}\right), \quad (16)$$

where it is known that

$$D(x) = \frac{3}{x^3}\int\frac{x^3 dx}{e^{x-1}}\ , \quad (17)$$

with

$$x = \frac{h\nu_D}{k_B T} = \frac{hw_D}{k_B T} = \frac{\Theta_D}{T}\ , \quad (18)$$

for which it is necessary to evaluate the function of Debye *D(x)* at arbitrary points. In equation (14) U_{vib} represents vibrational energy and S_{vib} is the entropy.

To determine the equilibrium situation of the system it is necessary to minimize the expression

$$\bar{G}^*(T,P,V_r) = E_e(V_r) + PV_r + \bar{A}_{vib}(T,V_r)\ , \quad (19)$$

with respect to V_r; i.e.,

$$\left(\frac{\partial\bar{G}^*}{\partial V_r}\right)_{T,P} = 0\ . \quad (20)$$

The asterisk symbolizes that the function has been evaluated in non-equilibrium states, so that the function has three variables, not two as in equilibrium thermodynamics.

Through the above-described model it is clear that the thermodynamic properties can be obtained from the state equation. First, the Gibbs equilibrium function is obtained by minimizing equation (19) for given values of *P* and *T*,

$$\bar{G}(T,P,) = \bar{G}^*\left(T,P;V_r(T,P)\right)\ . \quad (21)$$

Also, an evaluation of the second derivative of the Gibbs function allows checking that it is positive for all points and the stationary point is minimum. Thus, from the second derivative it is possible to obtain the isothermal volume modulus of the system. It is important to remember that

$$\left(\frac{\partial\bar{G}^*}{\partial V_r}\right)_{T,P} = f(T,P,V_r) = 0\ . \quad (22)$$

so that, at equilibrium, one of the three variables can be defined as a function of the other two. By implicitly deriving the functions,

$$\left(\frac{\partial P}{\partial V_r}\right)_T = -\frac{\left(\frac{\partial f}{\partial V_r}\right)_{T,P}}{\left(\frac{\partial f}{\partial P}\right)_{T,V_r}}\ . \quad (23)$$

Replacing the function *f* by equation (22)

$$\left(\frac{\partial P}{\partial V_r}\right)_T = -\frac{\left(\frac{\partial f}{\partial V_r}\right)_{T,P}}{\left(\frac{\partial f}{\partial P}\right)_{T,V_r}} = -\frac{\left(\frac{\partial^2\bar{G}^*}{\partial V_r^2}\right)_{T,P}}{\left(\frac{\partial^2\bar{G}^*}{\partial P\partial V_r}\right)_{T,[V_r,P]}}\ . \quad (24)$$

According to equation (19), $\left(\frac{\partial\bar{G}^*}{\partial P}\right)_{T,V_r} = V_r$, and the second derivative of the denominator is equal to unity, such that

$$B_T = -V_r\left(\frac{\partial P}{\partial V_r}\right)_T = -V_r\left(\frac{\partial^2\bar{G}^*}{\partial V_r^2}\right)_{T,P}. \quad (25)$$

Deriving equation (25) with respect to the pressure, we obtain

$$B'_T = \left(\frac{\partial B_T}{\partial P}\right)_T = \left(\frac{\partial B_T}{\partial V_r}\right)_T\left(\frac{\partial V_r}{\partial P}\right)_T. \quad (25)$$

The heat capacity at constant volume can be obtained as

$$\bar{C}_v = 3n_r R\left(4D[\Theta_D/T] - \frac{3\Theta_D/T}{e^{\Theta_D/T}-1}\right). \quad (26)$$

The Grüneisen parameter, which depends explicitly on the volume and implicitly on *T* and *P*, is defined as

$$\gamma = -\frac{dLn[\Theta_D(V_r)]}{dLn(V_r)}\,. \tag{27}$$

On the other hand, it is more accurate to evaluate the parameter of Grüneisen from the equation of state of Mie-Grüneisen, because that is a more general equation than the Debye model, since it ensures that all vibrational frequencies change in the same way in the volume of the crystal.

$$P - P_{static} = \gamma \frac{\bar{U}_{vib}}{V_r}, \tag{28}$$

where

$$P = -\left(\frac{\partial \bar{A}}{\partial V_r}\right)_T, \tag{29}$$

and $P_{static} = -\frac{dE_e(V_r)}{dV_r}$ is the pressure that the crystal volume V_r would have on the static model, and therefore represents the thermal vibrational contribution to the pressure.

The coefficient of thermal expansion at constant pressure can be found through the expression

$$\alpha = \frac{1}{V_r}\left(\frac{\partial V_r}{\partial T}\right)_P = \frac{1}{B_T}\left(\frac{\partial P}{\partial T}\right)_{V_r}. \tag{30}$$

α can be derived from State Equation-$V_r(T,P)$, but it is preferable to get α from γ because the quasi-harmonic Debye model necessarily satisfies the Mie-Grüneisen equation. Thus, from equations (29) and (30), we obtain

$$\left(\frac{\partial P}{\partial T}\right)_{V_r} = \gamma \frac{\bar{C}_v}{V_r}, \tag{31}$$

thus

$$\alpha = \gamma \frac{\bar{C}_v}{B_T V_r}. \tag{32}$$

The isobaric heat capacity is given by

$$\bar{C}_p = \bar{C}_v + TV_r\alpha^2 B_T = \bar{C}_v(1 + \alpha\gamma T), \tag{33}$$

and, from the adiabatic bulk modulus

$$B_S = B_T \frac{\bar{C}_p}{\bar{C}_v} = B_T(1 + \alpha\gamma T), \tag{34}$$

because $B_S = -V_r\left(\frac{\partial P}{\partial V_r}\right)_S$.

3. Results and discussion

3.1. Crystal structure

In order to establish the ideal structure of the material we have used the Structure Prediction Diagnostic Software SPuDs [18], which is a special program designed for perovskite-like materials. From the SPuDs prediction for the *Fm-3m* (#125) space group, we have obtained the lattice parameter *a=7.8121 Å* for the respective Wyckoff positions shown in Table 1.

Once we know the atomic positions and lattice parameter expected for the *Fm-3m* (#125) space group, we have used the PowderCell (PCW) code [19] to simulate the respective diffraction pattern of the material, as presented in Fig. 1.

As predicted for Glazer [20], in this ideal cubic perovskite the formation of a superstructure with Co-Mo-Co cations ordered along the crystallographic axis is expected. This effect can be described as shown in Fig. 2.

Fig. 3 shows the energy as a function of volume. Each one of the circle points constitutes an individual calculation and the line corresponds to a fitting with the Murnaghan state equation, which was carried out by using the concept of the least-square fitting method [12].

From minimization of energy as a function of volume shown in the picture we calculate the lattice parameter from the GGA approximation *a=15.3370 Bohr* (*8.1160 Å*), which is *3.9%* above the value predicted by the SPuDs, and from the LDA approximation *a=14.667 Bohr* (*7.7614 Å*), which is *0.6%* below the value predicted by the SPuDs. The bond lengths Ti(4a)-O is *1.9650 Å*, Mn(4b)-O is *1.9030 Å* and Ba(8c)-O is *2.7353 Å*, which reveals that O is closer to the Mn cation.

In these ceramic materials the explanation of distortion from the ideal cubic perovskite structure is clear because the double perovskite have the generic formula $A_2BB'O_6$, and for this type of material the tolerance factor *τ*, is calculated by the ratio $\tau = \frac{r_A + r_0}{\sqrt{2}\left(\frac{r_B + r_{B'}}{2} + r_0\right)}$, where r_A, r_B, $r_{B'}$ and r_o are the ionic radii of the *A*, *B*, *B'*, and O ions, respectively. If *τ* is

Table 1.
Atomic positions for the Bi_2TiMnO_6 double perovskite in the *Fm-3m* (#225) space group as predicted by the SPuDs software [18].

Atom	Wyckoff	x	y	z
Ba	*8c*	*0.2500*	*0.2500*	*0.2500*
Ti	*4a*	*0.0000*	*0.0000*	*0.0000*
Mn	*4b*	*0.5000*	*0.0000*	*0.0000*
O	*24e*	*0.2540*	*0.0000*	*0.0000*

Source: The authors.

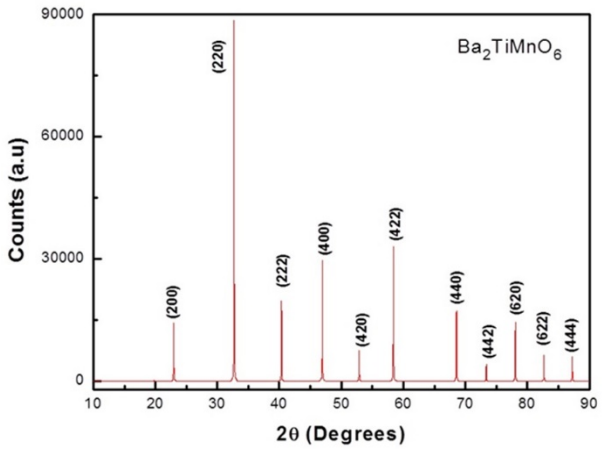


Figure 1. XRD simulated pattern for the Ba_2TiMnO_6 double cubic perovskite obtained from the theoretical lattice parameters.
Source: The authors.

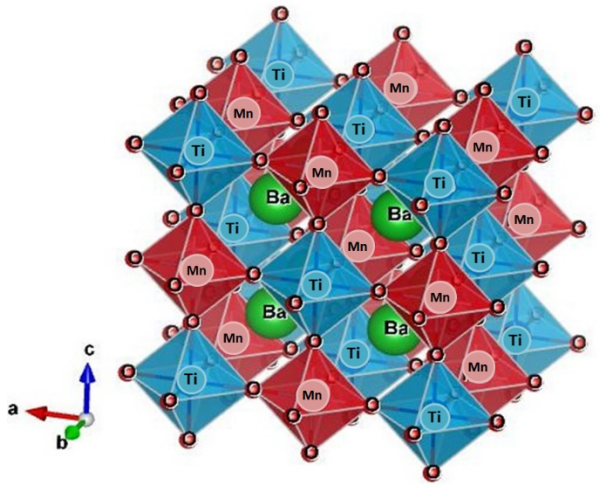


Figure 2. Crystal structure of the Ba_2TiMnO_6 material for the *Fm-3m* (#125) space group.
Source: The authors.

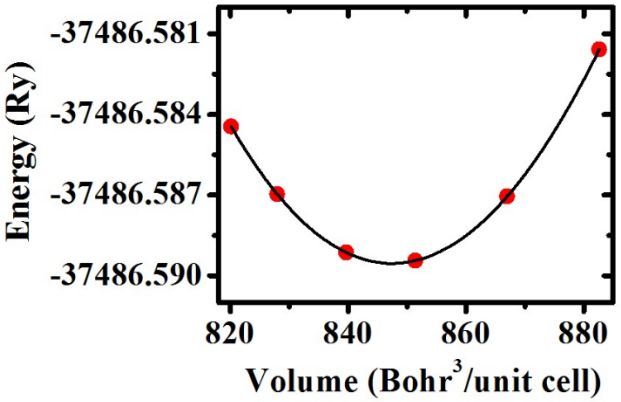


Figure 3. Points represent the calculated data of energy as a function of volume for the primitive cell of Ba_2TiMnO_6. Line corresponds to the fitting with the Murnaghan's state equation by the least-square method.
Source: The authors.

equal to unity, there is ideal cubic perovskite structure, and if $\tau \neq 1$ the structure is distorted from the cubic symmetry. The value of tolerance factor obtained for the Ba_2TiMnO_6 complex perovskite was *1.0778*, which surely is a consequence of the difference between the ionic radii of the Ti and Mn cations, which prevent a perfect packing of ions in a compact structure. In Table 2 a comparison between the atomic positions for the GGA and LDA approximations and the SPuDs prediction is showed.

Table 2.
Ba_2TiMnO_6 unit cell internal coordinates obtained from the *ab-initio* calculations. SPuDs data are included for comparison.

Atom	GGA (*x,y,z*)	LDA (*x,y,z*)	SPuDs (*x,y,z*)
Ba	0.250, 0.250, 0.250	0.250, 0.250, 0.250	0.250, 0.250, 0.250
Ti	0.000, 0.000, 0.000	0.000, 0.000, 0.000	0.000, 0.000, 0.000
Mn	0.500, 0.000, 0.000	0.500, 0.000, 0.000	0.500, 0.000, 0.000
O	0.253, 0.000, 0.000	0.253, 0.000, 0.000	0.253, 0.000, 0.000

Source: The authors.

3.2. Elastic properties

The elastic constants for this compound have not been previously reported in the literature; knowledge of these properties is important since they might be correlated with the equation of state (EOS) and thermo physical properties such as the specific heat, thermal expansion, Debye temperature, melting point, etc. Also, from the elastic constants, valuable information about the binding and mechanical stability of the solid can be obtained.

By considering the generalized Hook´s law: $\sigma_{ij}=c_{ij}\varepsilon_j$, we calculated the elastic constants for the Ba_2TiMnO_6 compound in the cubic structure. There are three independent elastic constants for the cubic structure, called C_{11}, C_{12}, C_{44}. The requirement of mechanical stability of the crystalline systems for any homogeneous lattice deformation places restrictions for the elastic constants [21]. The necessary conditions for mechanical stability in the cubic crystal are: $C_{11} > 0$ and $C_{11}-C_{12} > 0$.

From the elastic constants of single crystals we calculate the elastic moduli, which are of more interest for the development of technological materials [22]. The Reuss (R), Voigt (V), and Hill (H) polycrystalline average values of the Young modulus (E), the shear modulus (G), and the Poisson ratio (ν) for the cubic Ba_2TiMnO_6 calculated by means of the expressions given in Ref. [13] are given in Table 3. Also indicated in Table 3 is the Zener´s anisotropy factor $A = 2C_{44}/(C_{11}-C_{12})$. Since a departure from unity of this factor is a measure of anisotropy, the results in Table 3 indicate that the Ba_2NiMoO_6 compound is less anisotropic than pure Ti.

Table 3.
Calculated elastic constants (in GPa) for single-crystal and polycrystalline elastic modulii for Ba_2TiMnO_6. The corresponding experimental data for the elastic constants for pure Ti [23] is also included for comparison; the polycrystalline elastic moduli are calculated from these values.

	Ti *Exp.*	Ba_2TiMnO_6
C_{11}	160.0	281.6
C_{12}	90.0	104.9
C_{13}	66.0	
C_{33}	181.0	
C_{44}	46.5	121.6
B	128.1	163.8
A	1.5	1.4
G_v	40.1	108.3
G_R	25.8	105.7
G	33.0	107.0
Y_v	106.7	266.2
Y_R	73.3	281.8
Y	90.0	274.0
υ_V	0.42	0.23
υ_R	0.33	0.33
υ	0.37	0.28

Source: The authors.

Materials with high B and G are likely to be hard materials. The Young modulus on the other side determines the stiffness of the material. From the results shown in Table 3, we note that the elastic moduli of the Ba_2TiMnO_6 compound are close but lower than those of Ti pure. The present results predict that the stiffness and hardness of the compound are big than of Ti pure [23].

The brittle/ductile behavior can be predicted through the ratio of B/G as an index of the plastic characteristic of materials [24]. The critical threshold value for differentiating the physical properties of materials is about *1.75*. If the B/G ratio is larger than this value, it is predicted that the polycrystal behaves like a ductile material; otherwise, it would act as a brittle material. The present value of B/G is *1.53* for the Ba_2TiMnO_6 compound, indicating that this compound will behave as a brittle material. The Poisson's ratio provides more information about the characteristics of the bonding forces than any of the other elastic constants. The calculated Poisson's ratio for the studied Ba_2TiMnO_6 compound is *~0.3*, which falls within the expected range for materials of double perovskite type [25].

3.3. Electronic structure

Fig. 4 exemplifies the band structure and total Density of States (DOS) calculated for the Ba_2TiMnO_6 in the *Fm-3m* (#125) space group. The Fermi level is the reference for energy. The first observation is that the material exhibits semiconductor-like behavior with gap energy *1.0 eV*.

Fig. 5 shows the partial DOS calculated for the Ti, Mn, Ba and O individual cations. The non-symmetry observed for both up and down spin contributions close to the Fermi level suggests the occurrence of an effective magnetic moment, which was calculated to be *3.0* μ_B and attributed to the contribution of the Mn-d-t_{2g} orbitals. In the energy range from *-2.0 eV* to *0 eV* it is observed that the density of states due to Mn-d-t_{2g} orbitals for spin up orientation is the dominant.

About the conductivity is important to note that the material behaves as a semiconductor (E_g*=1.0 eV*) for the spin up channel and insulator (E_g*=3.9 eV*) for the other. Above the Fermi level, in the conduction band, spin up and down contributions of the Mn-d-e_g

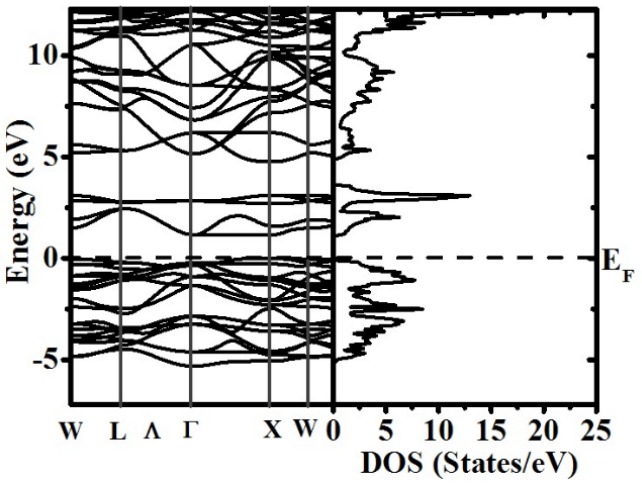


Figure 4. Band structure and total DOS calculated for the Ba_2TiMnO_6 complex perovskite.
Source: The authors.

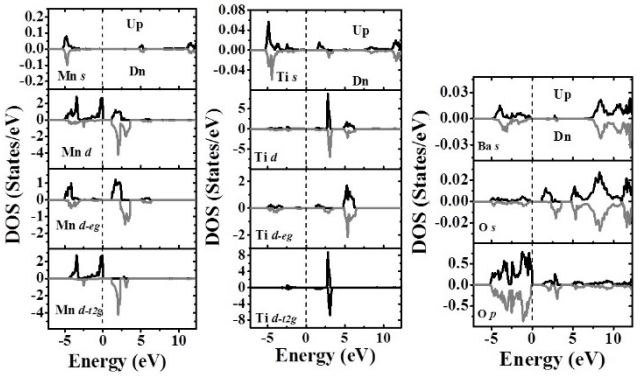


Figure 5. Spin polarized partial DOS of the Mn, Ti, Ba and O separated cations.
Source: The authors.

and spin down Mn-d-t_{2g} levels are observed. On the other hand, it we notice that the comparison of spin up and down contributions for both Mn-d-e_g and Mn-d-t_{2g} evidence split characteristics. Spin up and down contributions of the Ti-d-e_g and Ti-d-t_{2g} are no relevant close to the Fermi level. Those appear superposed between *2.8 eV* and *3.2 eV* in the conduction band.

3.4. Thermodynamic properties

The effects of temperature and pressure on the thermodynamic properties of the Ba_2TiMnO_6 material from the state equation, under the considerations of the quasi-harmonic approximation of the Debye model described in section 2.2, were analyzed as presented below. Fig. 6 shows the results of specific heat at constant volume, C_V (a), and at constant pressures, C_P (b), as functions of temperature. As can be seen in the figures, the temperature was varied between *0 K* and *1500 K* for eight applied pressure values, from 0 to *20 GPa*. It is observed in Fig. 6 that below *T=400 K*, for all applied pressure values, $C_V \approx C_P$. This result occurs because $\alpha^2 B_T V_r$ is a very small number in equation (33).

Fig. 6(a) shows more clearly than in 6(b) the trend of specific heat towards the Dulong-Petit limit, which is the specific heat value independent of temperature. From this limit value of Dulong-Petit, as the temperature increases, each of the atoms in the material absorbs the same amount of energy proportional to this temperature increase. In the case of C_V, this value corresponds to *241.11 J/mol.K* for all applied pressure values, while for C_P this limit is between *226.13 J/mol.K* and *239.06 J/mol.K* for pressures between *10* and *20 GPa*. These values of the Dulong-Petit specific heat limit are high, since they practically duplicate other results reported for simple perovskites [26]. At high temperatures (*T>700 K*) a specific heat divergence is observed, which can be due to that for very high temperatures the model is not reliable. At very low temperatures it should be possible to determine a behavior dominated by the purely electronic response, while at medium and high temperatures the predominance of the phononic response should be expected. When the material is heated, contributions to specific heat are mostly results of the movement of the atoms and ions around their equilibrium positions as a result of the absorption of heat. In the real

Ba_2TiMnO_6 this result may vary because this material is polycrystalline and the specific heat depends on the porosity, since the thermal energy needed to increase the temperature of the material is lower in the less porous materials and higher in the denser ones. However, it is important to note that *Mn-d-$_{t2g}$* orbitals for the spin-up polarization, in the state density and in the band structure there are enough electronic states close to the Fermi level to give a reasonable electronic contribution to specific heat. In addition, there is a small contribution of up and down electrons corresponding to the p orbitals of oxygen. Fig. 6(c) exemplifies the temperature dependence of the entropy calculated from equations (14) and (16). As expected, the increase in temperature creates an increase in the randomness of some physical properties of the system, allowing inferring effects of intra and intermolecular vibrations, structural distortions, structural transitions and thermal expansion (as we shall see below), and adopting a rapid growth character in the regime of temperature studied and with an asymptotic tendency to very high temperatures, according to the predicted by the equation (16).

In Fig. 7 results of calculations of the Debye temperature (a), thermal expansion (b) coefficient and Grüneisen coefficient (c) as functions of temperature are presented. We have calculated the dependence of $\Theta_D(T)$ (as a function of temperature), plotting isobar curves as shown in Fig. 7a. The result of Fig. 7a shows that the temperature of Debye is increased substantially with increasing pressure, from *550.28 K* for *P = 0 GPa* to *677.12 K* for *P=20 GPa* (at *T=0 K*). This occurs because as the pressure increases, all the velocities of the elastic waves increase gradually and their increase directly affects the temperature of Debye. Likewise, a mild nonlinear decreasing behavior of $\Theta_D(T)$ can be observed with increasing temperature for applied pressures. This decrease in temperature of Debye as a function of temperature is characteristic of perovskite type materials [27]. Interpreting the Debye temperature as the highest temperature that can be achieved as a result of a single normal vibration, it can be argued that the effect of pressure is the increase of cation-anion vibration frequencies while the effect of temperature is the expansive distortion of the structure, increasing the wavelength of the vibrations, decreasing the frequency and, consequently, the temperature of Debye.

Fig. 7(b) shows the dependence of thermal expansion coefficient, α, with temperature and pressure. It can be established from the figure that $\alpha(T)$ decreases drastically with increasing pressure. On the other hand, it can be seen that at low temperatures (between *0 K* and *300 K*), $\alpha(T)$ grows rapidly with temperature, and above 300 K it grows smoothly, following an approximately linear behavior. In spite of considering that the Ba_2TiMnO_6 has a cubic structure, its character of perovskite type confers an anisometric structure to it and, therefore, very great differences of the thermal expansion must be presented along the different crystallographic directions. This behavior can be associated to the structural distortions to which the perovskite-type materials are sensitive, because both temperature and pressure can give rise to inclinations and/or rotations of the TiO_6 and MnO_6 octahedrons, elongation of the structure in certain crystallographic directions and eventual contractions in other directions. Thus, the type of response in $\alpha(T)$ is associated with the type of distortion or transition that is occurring because of the application of temperature and pressure to the material. This circumstance could slightly divert any experimental results with respect to the theoretical result of Fig. 9(b). On the other hand, the relatively low value of $\alpha(T)$ is characteristic of ceramic materials [28]. One aspect not considered in the calculations that we have made is that as the temperature increases, structural phase transitions can occur and the material could no longer have a cubic structure. Finally, the Grüneisen parameter, shown in Fig. 7(c), shows a gradual decrease with the increase in applied pressure (for example, from 2.23 for *P=0 GPa* to *2.00* for *P=20 GPa*, at *T=0 K*). This behavior is observed for all the temperatures considered in the calculations. On the other hand, the Grüneisen coefficient presents a smooth and non-linear increase with the increase in temperature. These characteristics observed in the Grüneisen parameter as a function of pressure and temperature are related to the alteration in the vibration frequency of a crystalline lattice, according to the discussion presented above in relation to the coefficient of thermal expansion [29].

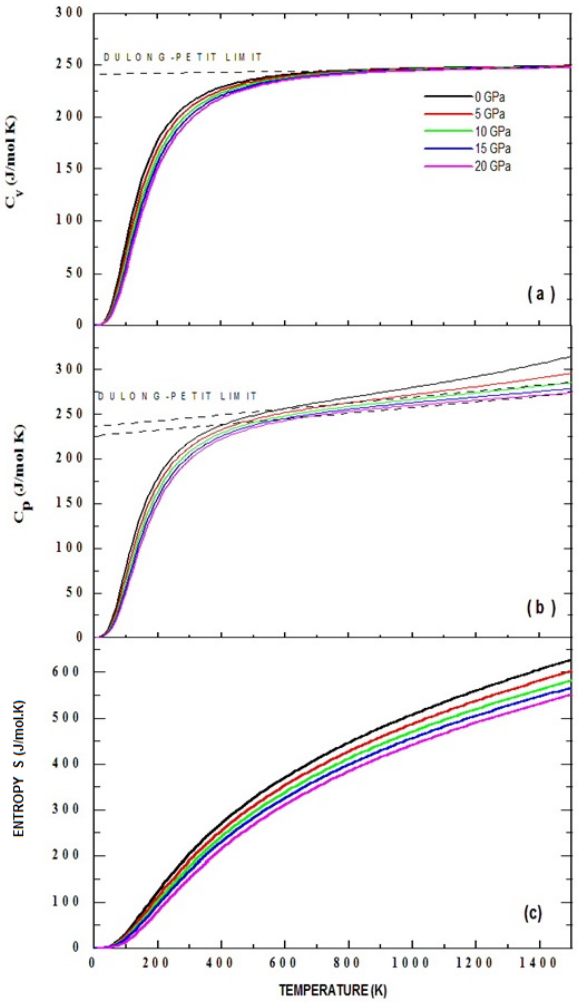


Figure 6. Specific heat C_v (a), C_p (b) and entropy (c) calculated through the quasi-harmonic Debye model for the Ba_2TiMnO_6 material from the Murnaghan state equation.
Source: The authors.

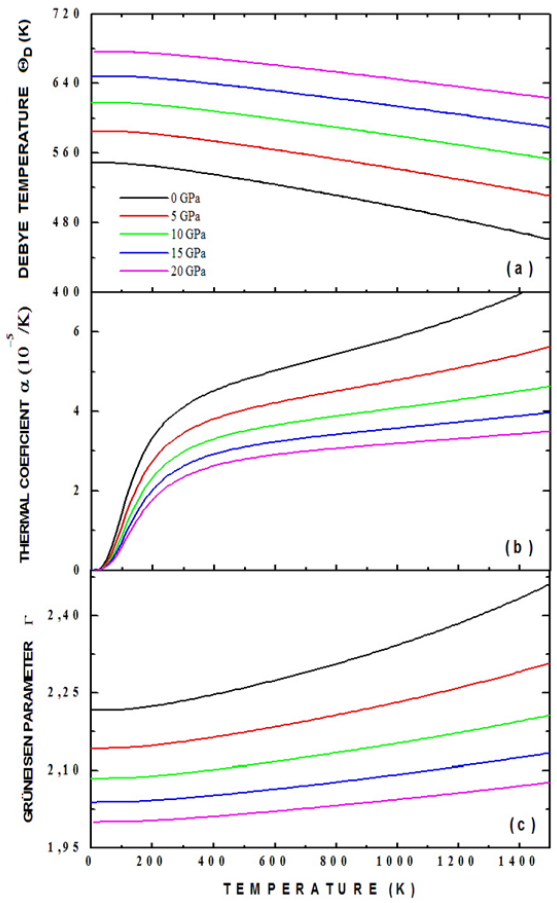


Figure 7. Debye temperature (a), thermal expansion coefficient (b) and Grüneisen coefficient (c) for the Ba_2TiMnO_6 calculated by the application of the quasi-harmonic Debye model.
Source: The authors.

4. Conclusions

We have performed several *ab initio* calculations over the Ba_2TiMnO_6 double perovskite. Our results show that it has a semiconductor behavior for the spin up orientation and insulator for the other one. Analysis of electronic structure of the material by means calculations of density of states for both spin orientations, based on the DFT-LAPW method permitted to infer that the t_{2g} spin up states are responsible by the conductivity feature for the Mn-*3d* states. On the other hand, the insulate behavior of the spin down configuration can be attributed to the Mn-d-e_g states in the valence band and to the Mn-d-t_{2g} in the conduction band. The effective magnetic moment determined from the asymmetry of the spin up and down contributions close to the Fermi level is *3.0* μ_B. We also have calculated the cell dimensions that minimize the total energy for each configuration using the Murnaghan equation state. The calculated zero-temperature elastic constants satisfy the criteria for mechanical stability, indicating that the bulk form of this phase is experimentally accessible. From the calculated polycrystalline average values of the Young modulus, shear modulus, the Poisson ratio and the Zener´s anisotropic factor for the cubic Ba_2TiMnO_6, it is predicted that the stiffness and hardness of the compound are big than of Ti pure. Moreover, the compound is expected to be anisotropic and brittle. The calculations of the thermodynamic properties from the state equation, by means of the quasi-harmonic approximation of the Debye model, show that the effects of the interatomic vibrations give rise to a specific heat that decreases with the applied pressure and evidences a Dulong-Petit limit relatively high (*241.11 J/mol.K*), compared to other results reported for simple perovskite type materials. Likewise, we conclude that $C_V \approx C_P$ as a consequence of the low value of the coefficient of thermal expansion. As expected, entropy increased dramatically with increasing temperature, as a result of molecular vibrations and structural distortions. The Debye temperature shows an increasing dependence on the pressure and decreasing with the temperature. By contrast, both the coefficient of thermal expansion and the Grüneisen parameter decrease with the pressure and increase slightly as a function of temperature. In general, except for the high specific heat value of Dulong-Petit, the behavior observed in the thermodynamic properties is characteristic of the perovskite-like ceramic materials. We emphasize that the thermodynamic properties depend fundamentally on the value of the parameter Grüneisen. Since the γ is derived from a third derivative of the E_e function, it is very sensitive both to the numerical errors in the derivation and to the smoothness of the $E_e(V_r)$ curves. For this reason, it would be highly advisable to obtain experimental results of the thermodynamic properties in order to more objectively establish the microscopic mechanisms that originate them.

Acknowledgments

This work was partially supported by División de Investigaciones Sede Bogotá (DIB) of Universidad Nacional de Colombia and FONCIENCIAS of Universidad del Magdalena.

References

[1] Triana, C.A., Corredor, L.T., Landínez-Téllez, D.A. and Roa-Rojas, J., High temperature-induced phase transitions in Sr_2GdRuO_6 complex perovskite, Materials Research Bulletin, 46, pp. 2478-2483, 2011, DOI: 10.1016/j.materresbull.2011.08.024.

[2] Howard, C.H., Kennedy, B.J. and Woodward, P.M., Ordered double perovskites – a group-theoretical analysis, Acta Crystallographica B 59, pp. 463-471, 2003, DOI: 10.1107/S0108768103010073.

[3] Jin, S., Teifel, T.H., McCormack, M., Fastacht, R.A., Ramesh, R. and Chen, L.H., Thousandfold change in resistivity in magnetoresistive la-ca-mn-o films, Science 254, pp. 413-415, 1994, DOI: 10.1126/science.264.5157.413.

[4] Roa-Rojas, J. Salazar Mejía, C., Llamosa Pérez, D., León-Vanegas, A.A., Landínez Téllez, D.A., Pureur, P., Dias, F.T. and Vieira, V.N., Magnetoelectric response of new Sr2TiMnO6 manganite-like material, Journal of Magnetism and Magnetic Materials 320, pp. e104-e106, 2008, DOI: 10.1016/j.jmmm.2008.02.023.

[5] Ochoa-Burgos, R., Martínez, D., Parra-Vargas, C.A., Landínez-Téllez, D.A., Vera-López, E., Sarmiento, A. and Roa-Rojas, J., Magnetic and ferroelectric response of Ca_2TiMnO_6 manganite-like perovskite, Revista Mexicana de Física [online]. S58, pp. 45-47, 2012. Available at: https://rmf.smf.mx/pdf/rmf-s/58/2/58_2_44.pdf.

[6] Moreno, L.C., Valencia, J.S., Landínez-Téllez, D.A., Martínez, M.L. and Roa-Rojas, J., Preparation and structural study of LaMnO3 magnetic material, Journal of Magnetism and Magnetic Materials 320, pp. e19-e21, 2008, DOI: 10.1016/j.jmmm.2008.02.052.

[7] Landínez-Téllez, D.A., Llamosa-Pérez, D., Deluque-Toro, C.E., Gil-Rebaza, A.V. and Roa-Rojas, J., Structural, magnetic, multiferroic and electronic properties of Sr_2ZrMnO_6 double perovskite, Journal of Molecular Structure, 1034, pp. 233-237, 2013, DOI: 10.1016/j.molstruc.2012.10.023.

[8] Hohenberg, P. and Kohn, W., Inhomogeneous electron gas, Physical Review, 136, pp. B864-B871, 1964, DOI: 10.1103/PhysRev.136.B864.

[9] Perdew, J.P., Burke S. and Ernzerhof, M., Generalized gradient approximation made simple, Physical Review Letters, 77, pp. 3865-3868, 1996, DOI: 10.1103/PhysRevLett.77.3865.

[10] Bonilla, M., Landínez-Téllez, D.A., Rodríguez, J.A., Aguiar, J.A. and Roa-Rojas, J., Study of half-metallic behavior in Sr2CoWO6 perovskite by ab initio DFT calculations, Journal of Magnetism and Magnetic Materials, 320, pp. e397-e399, 2008, DOI: 10.1016/j.jmmm.2008.02.179.

[11] Blaha, P., Schwarz, K., Madsen, G.K.H., Kvasnicka, D. and Luitz J., WIEN2k, An Aug-mented plane wave + local orbitals program for calculating crystal properties, Karlheinz Schwarz, Techn. UniversitÄat Wien, Austria, 2001, ISBN 3-9501031-1-2.

[12] Murnaghan, F.D., The compressibility of media under extreme pressures, Proceedings of National Academy of Sciences, USA. [online]. 30, pp. 244-247, 1944. Available at: http://www.pnas.org/content/30/9/244.

[13] Jamal, M., Jalali-Asadabadi, S., Ahmad, I. and Rahnamaye-Aliabad, H.A., Elastic constants of cubic crystals, Computational Materials Science, 95, pp. 592-599, 2014, DOI: 10.1016/j.commatsci.2014.08.027.

[14] Marzari, N., Vanderbilt, D., de Vita, A. and Payne, M.C., Thermal contraction and disordering of the Al(110) surface, Physical Review Letters 82, pp. 3296-3299, 1999, DOI: 10.1103/PhysRevLett.82.3296.

[15] Brillouin, L., Tensors in mechanics and elasticity. Academic, New York, 1964.

[16] Maradudin, A.A., Montroll, E.W., Weiss, G.H. and Ipatova, I.P., Theory of lattice dynamics in the harmonic approximation. Academic Press, New York, 2nd edition, 1971.

[17] Blanco, M.A., Francisco, E. and Luaña, V., GIBBS: isothermal-isobaric thermodynamics of solids from energy curves using a quasi-harmonic Debye model, Computer Physics Communications, 158, pp. 57-72, 2004, DOI: 10.1016/j.comphy.2003.12.001.

[18] Cuervo-Farfán, J.A., Arbey-Rodríguez, J., Fajardo, F., Vera-López, E., Landínez-Téllez, D.A. and Roa-Rojas, J., Structural properties, electric response and electronic feature of $BaSnO_3$ perovskite, Physica, B 404, pp. 2720-2722, 2009, DOI: 10.1016/j.physb.2009.06.126.

[19] Kraus, W. and Nolze, G., POWDER CELL - A program for the representation and manipulation of crystal structures and calculation of the resulting X-ray powder patterns, Journal of Applied Crystallographic, 29, pp. 301-303, 1996, DOI: 10.1107/S0021889895014920.

[20] Glazer, A.M., Simple ways of determining perovskite structures, Acta Crystallographica A 31, pp. 756-762, 1975, DOI: 10.1107/S0567739475001635.

[21] Press, W.H., Teukolsky, S.A., Vetterling, W.T. and Flannery, B.P., Numerical Recipes in Fortran, 2nd. Ed., Cambridge University Press, 1992.

[22] Born, M. and Huang, K., Dynamical theory of crystal lattices, Clarendon, Oxford, 1954.

[23] Tromans, D., Elastic anisotropy of hcp metal crystals and polycrystals, International Journal of Recent Research and Applied Studies, [online]. 6, pp. 462-483, 2011. Available at: www.arpapress.com/Volumes/Vol-6Issue4/IJRRAS_6_4_14.pdf.

[24] Pugh, S.F., XCII. Relations between the elastic moduli and the plastic properties of polycrystalline pure metals, The London, Edinburgh, and Dublin Philosophical Magazine and Journal of Science 45, pp. 823-843, 1954, DOI: 10.1080/14786440808520496.

[25] Faizan, M., Murtaza, G., Khan, S.H. Khan, A., Mehmood, A., Khenata, R. and Hussain, S., First-principles study of the double perovskites Sr2XOsO6 (X = Li, Na, Ca) for spintronics applications, Bulletin of Materials Science, [online]. 39(6), pp. 1419-1425, 2016. Available at: http://www.ias.ac.in/article/fulltext/boms/039/06/-1419-1425.

[26] Li, X., Zhang, W. and Du, J., Effect of composition and microstructure of Pd-Cu-Si metallic glassy alloy thin films on hydrogen absorbing properties, Materials Transactions 52, pp. 1717-1806, 2011, DOI: 10.2320/matertrans.M2011105.

[27] Tsuchiya, J., Tsuchiya, T. and Wentzcovitch, R.M., Vibrational and thermodynamic properties of MgSiO3 postperovskite, Journal of Geophysical Research, 110, B02204, 2005, DOI: 10.1029/2004JB003409.

[28] Dedova, E.S., Shadrin, V.S., Petrushina, M.Y. and Kulkov, S.N., The study on thermal expansion of ceramic composites with addition of ZrW_2O_8, IOP Conf. Series: Materials Science and Engineering, 116, 012030, 2016, DOI: 10.1088/1757-899X/116/1/012030.

[29] Qiang, L., Duo-Hui, H., Qi-Long, C. and Fan-Hou, W., Phase transition and thermodynamic properties of $BiFeO_3$ from first-principles calculations, Chinese Physics, B 22, 037101, 2013, DOI: 10.1088/1674-1056/22/3/037101.

C.E. Deluque-Toro, received the BSc.as Physicist (2004) from University of Magdalena, Santa Marta (Colombia), MSc degree in physics (2007) from Universidad Nacional de Colombia, Bogotá (Colombia) and PhD degree in physics (2015) from the Instituto Jorge Sabato (Argentina). Is associated professor in the Faculty of Engineering, University of Magdalena, Santa Marta, Colombia. Research issues: electronic structure, perovskite materials, semiconductors, superconductors.
ORCID: 0000-0002-4003-9116.

D.A. Landínez-Téllez, received the BSc. as Physicist in 1991 (Universidad Industrial de Santander, Bucaramanga, Colombia, MSc. degree in physics in 1994 (Universidade de Brasília, Brasília, Brasil), PhD degree in physics in 1999 (Universidade Federal de Pernambuco, Recife, Brasil). Is titular professor in Physics Department, Universidad Nacional de Colombia, Bogotá. Research issues: electronic structure, perovskite materials, crystallography, superconductivity, magnetism, synthesis of ceramic materials, ferroelectricity, multiferroics materials and devices.
ORCID: 0000-0001-7108-617X.

J. Roa-Rojas, received the BSc. as Physicist in 1991 (Universidad Industrial de Santander, Bucaramanga, Colombia, MSc. degree in physics in 1994 (Universidade de Brasília, Brasília, Brasil), PhD degree in physics in 1999 (Universidade Federal do Rio Grande do Sul, Brasil). Is titular professor in Physics Department, Universidad Nacional de Colombia, Bogotá. Research issues: electronic structure, perovskite materials, crystallography, superconductivity, magnetism, synthesis of ceramic materials, ferroelectricity, multiferroics materials and devices.
ORCID: 0000-0002-5080-8492.

UNIVERSIDAD NACIONAL DE COLOMBIA
SEDE MEDELLÍN
FACULTAD DE MINAS



DYNA
http://dyna.medellin.unal.edu.co/

A geometrical robust design using the Taguchi method: application to a fatigue analysis of a right angle bracket

Rafael Barea [a], Simón Novoa [a], Francisco Herrera [b], Beatriz Achiaga [c] & Nuria Candela [d]

[a] *Department of Industrial Engineering, Nebrija University, Madrid, Spain. rbarea@nebrija.es*
[b] *Consultant Robust Engineering, Madrid, Spain. fco.herrera@mac.com*
[c] *Department of industrial technologies, Faculty of Engineering. Deusto University. Bilbao, Spain. beatriz.achiaga@deusto.es*
[d] *ESNE, University School of Design, Innovation and Technology, Madrid, Spain. nuria.candela@esne.es*

Received: September 7th, 2017. Received in revised form: February 12th, 2018. Accepted: March 15th, 2018.

Abstract
The majority of components used in aeronautic, automotive or transport industries are subjected to fatigue loads. Those elements should be designed considering the fatigue life. In this paper the geometrical design of a right angle bracket has been simulated by FEM, considering the type of material, the applied load and the geometry of the pieces. The geometry of the right angle bracket has been optimized using the Taguchi's robust optimization method. As far as the authors know, there are no publications dealing with the use of the Taguchi's robust optimization method applied to the geometric design of industrial pieces having as output variable the Findley fatigue coefficient. This paper presents a method for determining the critical design parameters to extend the product life of components subject to fatigue loading. This pioneer idea is applicable to any other design or physical or mechanical application so it can be widely used as new methodology to fatigue robust design of mechanical parts and components.

Keywords: robust design; Taguchi method; fatigue; Findley critical plane; geometrical design; right angle bracket.

Un diseño geométrico robusto empleando el Método de Taguchi: aplicación a un análisis de fatiga de una escuadra

Resumen
La gran parte de los componentes usados en la industria aeronáutica, automovilista o del transporte están sometidos a cargas de fatiga. Esos componentes deberían ser diseñados considerando la vida a fatiga. En este artículo el diseño de una escuadra ha sido simulad por MEF teniendo en cuenta el tipo de material, cargas aplicadas y la geometría. La geometría de la escuadra se ha optimizado usando el método de optimización robusta de Taguchi. Hasta donde los autores han comprobado no hay ninguna publicación que emplee el método de optimización robusta de Taguchi aplicándolo al diseño geométrico de elementos industriales tomando como variable de salida el coeficiente de fatiga de Findley. Este artículo presenta un método para determinar los parámetros críticos en el diseño que afectan a la vida a fatiga del componente. Esta idea es pionera y aplicable a otros diseños o aplicaciones mecánicas que pueden emplear esta metodología para el diseño robusto a la fatiga de partes y componentes mecánicos.

Palabras clave: diseño robusto; método de Taguchi; plano crítico de Findley; diseño geométrico; escuadra.

1. Introduction

Product design is an iterative and complex decision-making engineering process. It starts identifying a necessity, applying a sequences of steps to provide an optimal solution to a particular problem, and that ends with a detailed description of the product.

In conceptual design, optimization techniques have been used to derive an optimal trade-off between conflicting objectives and criteria [1]. Thus the design goal can be expressed as an objective function. This objective function is a scalar for a single criterion optimization and a vector of functions for a multi-objective optimization. Some technique assume that the multiple responses are independent of each

How to cite: Barea, R., Novoa, S., Herrera, F., Achiaga, B. and Candela, N., A geometrical robust design using the Taguchi method: application to a fatigue analysis of a right angle bracket. DYNA, 85(205), pp. 37-46, June, 2018.

© The author; licensee Universidad Nacional de Colombia.

other while other techniques exploit the correlation in the responses for obtaining optimal design using statistics [2]. Many techniques have been proposed to solve optimization problems [3]. However, apart from these techniques, it is necessary to develop a robust design in order to optimize the reliability of the project.

A robust design is considered a design that works properly even when it is subjected to several variable manufacturing processes, variations in the environment, variability of the used materials, and by the behavior of the final user and by the characteristics of parts that have been provided by outside suppliers [4]. The impact of such factors has a direct effect on product quality. The first proposal of robust design can be traced to [5,6] when he presented the "Two-stage Design" method. This design method is based on two assumptions: firstly, a good design should be associated to variable settings that produce the best low variability of the response and secondly, it must be on the target value. Based on these assumptions, Taguchi introduced a univariate response using function of the product o process with emphasis on the two-step strategies. The Taguchi method consists of planned experiments, with the objective of acquiring data in a controlled way, executing these experiments and analyzing data, in order to obtain information about the behavior of the design process. Numerous studies[7–16] endorse Taguchi's method for the optimization of parameters for many applications such as erosion studies, thermal applications, process optimization, microstructures, etc. However, it is still to be developed in the field of structural mechanical components design.

It is estimated that about 80% of the engineering failures of structures are caused by fatigue [17]. Fatigue life varies due to random factors, load history and environment variables. Engineering structures fail when the service life of the structure is below than the expected design life. Therefore, robust optimization should be applied in structure design to minimize the sensitivity of service life caused by these factors. The development of modern computer technology has created favorable conditions, for robust design, giving the possibility to simulate many experiments, impacting in a spectacular way in the development cost (less parts for testing and iterative modifications looking for the acceptable specification).

Although the application of robust optimization to design purposes have been already applied in previous papers [17,18] the present paper combines a finite element method with a robust optimization of a parametrical model for geometrical design of a right angle bracket. Geometric optimization represents an effective tool that systematically pursue for an optimum design. This will help engineers to attain the optimal structure for the bracket. The effect on fatigue life due to accumulative damage was taken into consideration, and the applied methodology has allowed a robust design, aside from material selection, to optimize the design.

2. Geometric modeling

2.1. Model parametrization and materials

In this paper, the geometric design of a right angle bracket was selected due to its extensive use in the industry. Brackets

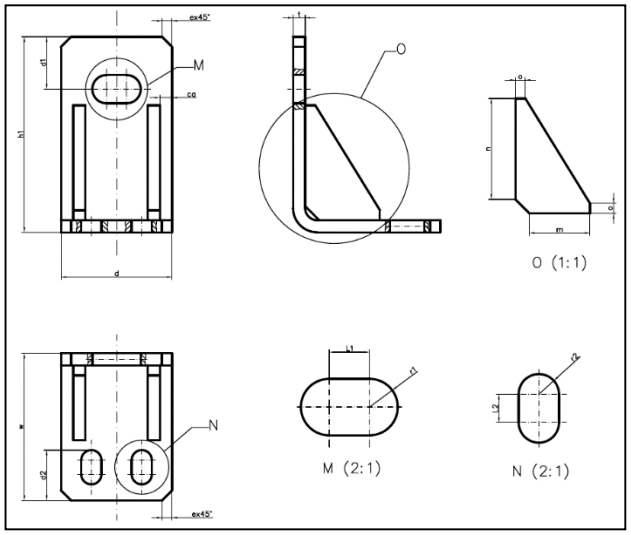


Figure 1. Parameters used to design optimization
Source: The authors

Table 1.
Parameters used in the geometrical design of right angle bracket that have been used in Taguchi M. as control factors for the orthogonal internal array.

Parameter	Description
h1	Bracket height
d	Bracket depth
d1	Upper hole border distance
w	Bracket width
d2	Lower holes border distance
t	Thickness
L1	Upper hole length
r1	Upper hole radius
L2	Lower holes length
r2	Lower holes radius
m	Triangle gussets length
n	Triangle gussets height
o	Triangle gussets thickness
ca	Gussets border distance

Source: The authors

are normally used to assemble different parts in a particular structure. A right angle bracket usually supports a weight in a right angle, in this context, if the weight is mounted over a structure subjected to vibrations, the bracket can fall by fatigue. The model geometry of a parametrized right angle bracket is shown in Fig. 1.

The parameters proposed are shown in Table 1 and they will be considered as the factors used in the Taguchi Method.

In this paper, two different materials were used for the design optimization: carbon steel and Ti-6Al-4V. The use of two different materials is appropriate in order to obtain a design that must be independent from the used material and a way of achieving a robust design, the two different materials will allocated in an external array. Parameters determination for multiaxial fatigue is based on experimental curves of uniaxial cyclic test, for different values of the cycle asymmetry parameter $R=\sigma_min/\sigma_max$ where σmin and σmax are the minimum and maximum stresses respectively in the cycle.

Carbon steel used in this study had a fatigue limit of 700 MPa in the case of R=-1 and a fatigue limit of 560 MPa in the case of R=0, both of them testing in torsion mode [19].

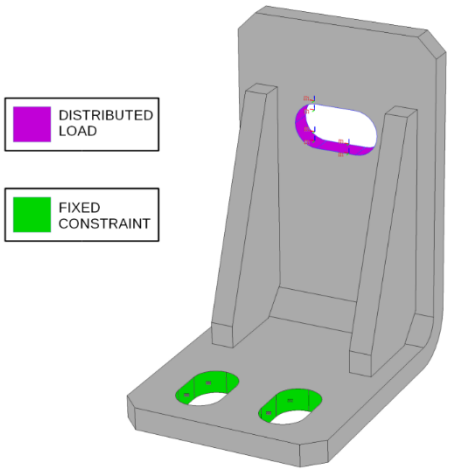


Figure 2. Parameters used to design optimization
Source: The authors

The smooth high cycle fatigue (HCF) life of the titanium alloy Ti-6Al-4V was predicted correctly by Findley parameter over a range of fatigue tests and stress ratio by Kallmeyer [20]. The fatigue data for Ti-6Al-4V in a torsion mode are a stress limit for R=0 and R=-1 of 350MPa and 450MPa, respectively.

Finite element simulations were performed with COMSOL Multiphysics® 3.5 solver and the software used for post processing was MATLAB®. Both programs can communicate with each other through a server-client connection. This allows MATLAB® to make use of COMSOL Multiphysics capabilities.

The model was subjected to a cyclic load that consists of a distributed load applied in the upper drill while the lower ones are fully constrained. Load was distributed on the inner face of the upper hole as shown in the Fig. 2. According to Fig. 2 the load is applied in the Y axis and it fully reversible.

3. Methods

3.1. Finite element method

Several multiaxial fatigue criteria have been considered based on previous papers [21–24] and results of simulated durability were compared with service data. This criterion in relation to the crack initiation phenomenon assumes that the fatigue failure of the material is due to some stress and strain components acting on the critical plane. Uniaxial tests are one of the tests used for experimental data that usually are parametrized with the stress amplitude ($\sigma_a=(\sigma_{max}-\sigma_{min})/2$) and the stress range ($\Delta\sigma=\sigma_{max}-\sigma_{min.}$), and the results are described by Wöhler curves, which can analytically be represented by the Baskin relation, eq. 1.

$$\sigma = \sigma_{limit} + \sigma_s N^{\beta} \quad (1)$$

where σ_{limit} is the fatigue limit, σ_s is the fatigue strength coefficient, β is the fatigue strength exponent and N is the number of cycles before fracture.

In order to generalize the results obtained by uniaxial tests with Baskin, in relation with the case of multiaxial stresses the Findley model is used [24]. It consists on a "critical-plane" model defined in terms of maximum shear stress amplitude on a given plane and the maximum normal stress on that plane multiplied by an adjustable factor, k.

The critical plane method is based on experimental evidences that cracks usually initiate in preferential material planes associated with high shear stresses. The influence of mean normal stresses is also considered because these tensile stresses are expected to keep the crack faces opened, favoring the crack growth.

Findley's critical-plane criterion has been commonly used to describe fatigue failure under multiaxial stress [25]. This criterion is exposed in Eq. 2.

$$\left(\frac{\Delta\tau(\theta)}{2} + k\sigma_{max}(\theta)\right)_{max} = f_F \quad (2)$$

where $\Delta\tau(\theta)$ is the shear stress amplitude on the θ plane and σ_{max} is the maximum normal stress on that plane during a load cycle. The plane where this expression is maximized is considered to be the critical plane. Findley criterion has two independent material parameters f_F and k, and it is assumed that they are constant over the considered life range. It is necessary to determine two fatigue limits with different loading conditions to obtain these data. In such a way, test with two different R values can be used to determine k and f_F. In this case the fatigue limits according to the curves for R=-1 and R=0 has been used to obtain k according to eq. 3 [19]

$$\frac{\sigma_{a,R=0}}{\sigma_{a,R=-1}} = \frac{k+\sqrt{1+k^2}}{2k+\sqrt{1+(2k)^2}} \quad (3)$$

Based on the results of earlier studies [19,20] the calculated parameters for carbon steel (f_{crit} =442.6 MPa and k=0.237) and Ti6Al4V (f_{crit} =294.3 k=0.271) were obtained.

The flow diagram in Fig. 3 describes the procedure used for fatigue assessment in the simulation.

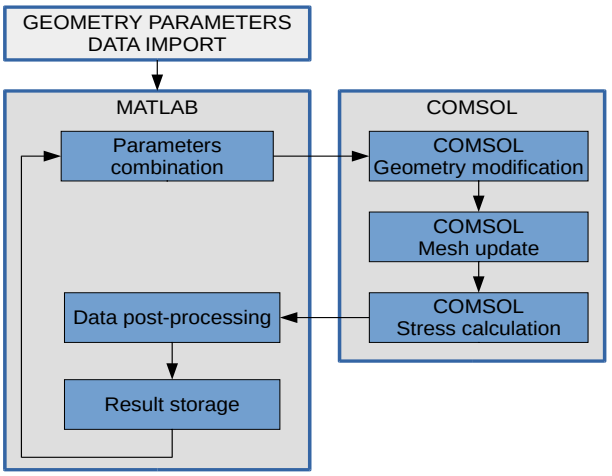


Figure 3. Flow diagram of a method used to calculate the fatigue usage factor.
Source: The authors

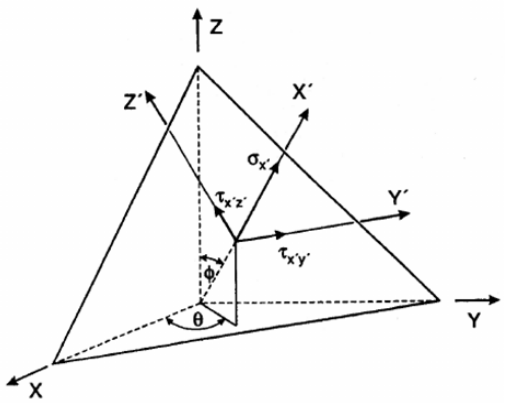


Figure 4. Calculated projections stresses in every plane depend on θ and ∅.
Source: The authors

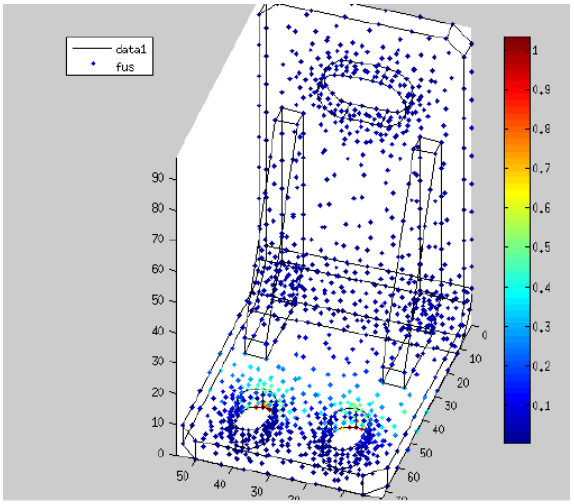


Figure 5. Graphical representation of fatigue results for one geometry variables set. It can be observed the node in the bottom (in red, this is fus=1) where a possible fatigue crack can start.
Source: The authors

The different combinations of geometrical factors are specified through the parameters already defined in the Table 1. These combinations have to be imported in MATLAB® to further use. Computation of shear stress history is stored for each plane in every material mesh nodes. It is necessary the computation of shear stress vector history at each plane passing through a material point.

Fatigue failure assessment is carried out automatically by the communication from both sides. MATLAB® parses a combination to COMSOL® in order to modify the geometry of the model. A new mesh is then produced and the solver resolves for the load combination case. At this point, data sets which contains the stresses is exported to MATLAB® for continuing with the analysis.

Stress data sets from the simulation are used to assess the critical plane on every node of the mesh by performing a loop for a discrete number of planes. On each iteration a f_F value is obtained for a plane which is defined by the angles with the Z axis (θ) and the X axis (∅) according to Fig. 4.

Stresses for the X'-Y'-Z' coordinate system are computed and a fatigue failure result is produced for every plane. The critical plane is determined by the plane with the maximum f_F value.

After calculation of the critical plane set of values, they are compared to the fatigue limit of the material obtained from the experiments. For this purpose a factor that relates these two values is defined as the fatigue usage factor (fus), eq. 4.

$$fus = \frac{f_F}{f_{crit}} \tag{4}$$

This expression implies that the nodes with a fus equal or greater than 1 are susceptible to fatigue failure.

Fatigue usage factors are stored in a data set as a result of every iteration. This process is repeated for all parameters combination so that a set of fatigue results is produced (see Fig. 5).

3.2 Taguchi method

While the ideal univariate response is a minimal variation of the output variable being on-target to have a design that should be compensated between performance and variability. Taguchi uses an ideal function with two-step strategies [26]. This measure can be modeled as a transfer function of the fixed control variables (e.g. the geometry in this paper) and the random noise variables (e.g. the material in this paper) as shown in eq. 5

$$Response = f(\boldsymbol{M}, \boldsymbol{x}, \boldsymbol{N}) \tag{5}$$

where **M** is the of signal factor vector that, in this research, has been the load applied to the right angle bracket, **x**=(x1,x2,x3,…) is the vector of control factors that are in this case the geometry parameters and **N**=(N1,N2,…) is the vector of noise factors, that in this paper represent two different materials, and f is the transfer function. The aim of the optimization design is to know a combination of control factors that minimize the influence of noise factors. Due to the material noise factors, the optimal bracket design only depends on the geometrical features.

Taguchi (Taguchi. 1987) introduces the concept of ideal function as a relationship that provides an output which is proportional to the input or signal. The linear nature of the relationship between the output response (fus) and the input signal factor (M) is adjusted to produce the desired output. It also combines the dynamic characteristics considering the different outputs which can be obtained by submitting the system to different input signals, on a progressive scale within logical range of functioning of this system. This allows, in a single design, to know the system role as a whole, facilitating future developments and thus innovation.

A dynamic characteristic study involves a two-step optimization procedure, in which initially the variation around a linear function is minimized, and secondly the sensitivity of the linear function is adjusted to an objective value by changing control factors levels, looking for the optimal combination.

Considering the dynamic relationships, the zero-point proportional equation provides a useful tool to adjust the output changing the input signal factor. This equation expresses a simple linear relationship between the response, Y , the signal factor, M, and the error, ε. This combination

will be adjusted to have the appropriate slope of the linear function between the output response and the signal factor that can be adjusted (eq. 6)

$$Y_{ijk} = \beta_i M_j + \varepsilon_{ijk} \quad (6)$$

where the control factors is i=1,2,… I , the signal factor is j=1,2,… J and the noise factor k=1,2. In this case when the load is zero (M=0) the output Y will be zero and bracket will not break by fatigue. As we are speaking about an ideal function the ε_{ijk} has to be zero, and the ideal function of the brackets is expressed in eq. 7.

$$Y_{ijk} = \beta_i M_j \quad (7)$$

Where Y_{ijk} is the output, in this study the Fatigue Usage Factor –fus-, M is the signal that is the oscillatory load and β represents the slope of the function depending on the sensitivity of the system to the combination of controlling factors. In this case for every oscillatory load and every combination of geometrical parameters there is a directly related fus coefficient.

Changing the geometrical parameters (control factors) different results (fus) will be obtained for every load (M) and every noise factor (steel or titanium). The results can be analyzed with respect to the control factor like a $\frac{\text{Signal (S)}}{\text{Noise (N)}}$ ratio (η) as shown in eq. 8:

$$\eta_i = 10log\left(\frac{\beta_i^2}{\sigma_i^2}\right) \quad (8)$$

Where β_i, (slope in Eq. 1) is determined by the least squares method and σ_i^2 is the mean square error for the ith factor (Taguchi 1986) and is given by eq. 9:

$$\sigma_i^2 = \frac{1}{r_o J - 1}\sum_{j=1}^{J}\sum_{k=1}^{r0}(Y_{ij} - \beta_i M_k)^2 \quad (9)$$

The beta (β_i) will be adjusted (optimized) to ensure that the fus coefficient does not exceed the maximum admitted value (if fus ≥1 the bracket will collapse).

Therefore, with a small amount of experiments these engineering optimization tools can provide compelling results employing some standard tables of experiments, called orthogonal arrays [27]. These orthogonal arrays provides specific arrangement of fractional experiments with regard to the influencing factor and their levels. In the Table 2 the factors and levels are listed for every factor that will be used in this paper. In the current work L36 (Table 3) orthogonal array was used, which implied carrying out 36 tests with 3 factor of 2 levels and 12 factors of 3 levels as listed in Table 2.

Therefore, the present robust design case is defined as a dynamic characteristic arrangement and the main objective of the design activity is to optimize the S/N ratio defined in Eq. 8. In a parameter design experiment, the control factors are assigned to an inner array, while the signal factor and noise factors are configured in an outer array. The signal factor (M_j) will be the vibration weight supported by the bracket (50 kg, 60 kg or 70 kg). Noise will have two levels: Ti6Al4V and carbon steel materials (Table 3)

Table 2.
Factors and level for the Taguchi design.

Factors			Level 1	Level 2	Level 3	Unit
Factors	**Drawing Parameter**	**Definition**				
A	m	rib segment	20	25		mm
B	n	rib segment	45	55		mm
C	o	rib segment	3	6		mm
D	h1	height	87	97	107	mm
E	w	width	65	73	80	mm
F	d	depth	50	55	60	mm
G	c	radius hole	0	0.5	1	mm
H	t	thickness	5	6	7	mm
I	r1	radius hole1	5	6	7	mm
J	L1	length hole1	9	10	11	mm
K	d1	distance hole 2	23	26	28	mm
L	r2	radius hole 2	4	5	6	mm
O	L2	length hole 2	6	7	8	mm
P	d2	distance hole	22	25	27	mm
Q	ca	distance border	5	6	7	mm

Source: The Authors.

4. Robust design, with dynamic characteristic, of the geometry of a right angle bracket

Finite element simulations were performed for each of the 36 experimental test of the Table 3. Fig. 6 shows the stress produced in a vibration cycle in one of the runs. It is clearly shown that the area close to the holes is more affected by the fatigue damage.

Having completed the finite element simulations, the S/N ratio and β values for each test run were obtained. Results are presented in Table 4.

4.1. Predicting the optimal combination for controlling factors

In the two-step optimization process the bracket geometry is firstly optimized identifying the controlling factors which influence the S/N ratio and the sensitivity in every level. This study is carried out starting from S/N ratio (η) and β response graphs presented in the Fig. 5. According to that, the value of controlling factor with higher value for S/N better, lower variation, and higher values for each factor level are chosen and added together.

The second step, which consists in the adjustment of the slope it is carried out after the optimal combination chosen in the first step.

Graphics enable to identify the best level of each control factor. Results clearly show that control factors such as E, H, I, K, L, O, P or Q have a significant influence in S/N ratio while factors such as A, D, H or L exerts a clear influence in the slope.

Table 3.
Taguchi L36 Array to test 12 factors with 3 levels and 3 factors with 2 levels

L36	rib segment	rib segment	rib segment	height	wid th	dep th	chamfer hole	thicknes s	radius hole1	length hole1	distance hole 2	radius hole 2	lenght hole 2	distance hole	distance border
	1	**2**	**3**	**4**	**5**	**6**	**7**	**8**	**9**	**10**	**11**	**12**	**13**	**14**	**15**
Group 1	**m**	**n**	**o**	**h1**	**w**	**d**	**c**	**t**	**r1**	**L1**	**d1**	**r2**	**L2**	**d2**	**ca**
1	1	1	1	1	1	1	1	1	1	1	1	1	1	1	1
2	1	1	1	1	2	2	2	2	2	2	2	2	2	2	2
3	1	1	1	1	3	3	3	3	3	3	3	3	3	3	3
4	1	2	2	1	1	1	1	1	2	2	2	2	3	3	3
5	1	2	2	1	2	2	2	2	3	3	3	3	1	1	1
6	1	2	2	1	3	3	3	3	1	1	1	1	2	2	2
7	2	1	2	1	1	1	2	3	1	2	3	3	1	2	2
8	2	1	2	1	2	2	3	1	2	3	1	1	2	3	3
9	2	1	2	1	3	3	1	2	3	1	2	2	3	1	1
10	2	2	1	1	1	1	3	2	1	3	2	3	2	1	3
11	2	2	1	1	2	2	1	3	2	1	3	1	3	2	1
12	2	2	1	1	3	3	2	1	3	2	1	2	1	3	2
13	1	1	1	2	1	2	3	1	3	2	1	3	3	2	1
14	1	1	1	2	2	3	1	2	1	3	2	1	1	3	2
15	1	1	1	2	3	1	2	3	2	1	3	2	2	1	3
16	1	2	2	2	1	2	3	2	1	1	3	2	3	3	2
17	1	2	2	2	2	3	1	3	2	2	1	3	1	1	3
18	1	2	2	2	3	1	2	1	3	3	2	1	2	2	1
19	2	1	2	2	1	2	1	3	3	3	1	2	2	1	2
20	2	1	2	2	2	3	2	1	1	1	2	3	3	2	3
21	2	1	2	2	3	1	3	2	2	2	3	1	1	3	1
22	2	2	1	2	1	2	2	3	3	1	2	1	1	3	3
23	2	2	1	2	2	3	3	1	1	2	3	2	2	1	1
24	2	2	1	2	3	1	1	2	2	3	1	3	3	2	2
25	1	1	1	3	1	3	2	1	2	3	3	1	3	1	2
26	1	1	1	3	2	1	3	2	3	1	1	2	1	2	3
27	1	1	1	3	3	2	1	3	1	2	2	3	2	3	1
28	1	2	2	3	1	3	2	2	2	1	1	3	2	3	1
29	1	2	2	3	2	1	3	3	3	2	2	1	3	1	2
30	1	2	2	3	3	2	1	1	1	3	3	2	1	2	3
31	2	1	2	3	1	3	3	3	2	3	2	2	1	2	1
32	2	1	2	3	2	1	1	1	3	1	3	3	2	3	2
33	2	1	2	3	3	2	2	2	1	2	1	1	3	1	3
34	2	2	1	3	1	3	1	2	3	2	3	1	2	2	3
35	2	2	1	3	2	1	2	3	1	3	1	2	3	3	1
36	2	2	1	3	3	2	3	1	2	1	2	3	1	1	2

Source: The Authors.

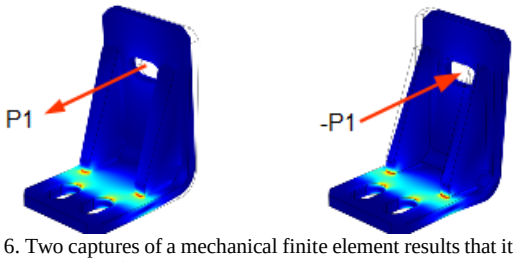


Figure 6. Two captures of a mechanical finite element results that it has been used to estimate the fus. It can be observed that high stress are in the bottom surface where the ribs are connected.
Source: The authors.

4.2. Prediction and verification

The optimum control factor combination will be established selecting the parameters with higher S/N ratio and lower β. In those cases in which a conflict between these two variables existed, the parameters which values are closer to the mean values have been selected. The optimum factor levels for the robust design are:

A1 because it has a little influence in S/N ratio and the value of β is lower.

B2 and C2 in the mean point because they have no influence.

D1 because it has not influence in S/N ratio and the value of β is lower.

E2 because it has a higher influence in S/N ratio, but it is not lineal. In this aspect it has been selected the mean value

F2 and G2 because as B and C has a less influence.

H3 has the higher S/N ratio with lower β.

I2 due to the weak effect in the S/N ratio and with I3 increases the slope.

J2 and K2 because they increase S/N ratio with a bad influence in the slope.

L3 is obviously that is better because have a higher S/N ratio and lower β slope.

O2 is a compromise solution in the mean value.

P3 has a good S/N ratio and a small influence in the slope.

Q3 because it improves S/N ratio with a little influence in slope.

Table 4.
Results (fatigue use factor) for two levels of noise (materials) and three signal factors. If fatigue user factor (fus) is higher than 1 then the bracket will break at service

	M1		M2		M3	
	50		60		70	
	N1	N2	N1	N2	N1	N2
	Steel	Titanium	Steel	Titanium	Steel	Titanium
1	0.569	0.930	0.683	1.115	0.797	1.301
2	0.301	0.482	0.362	0.579	0.421	0.675
3	0.197	0.310	0.237	0.372	0.276	0.434
4	0.426	0.675	0.511	0.810	0.596	0.945
5	0.274	0.437	0.329	0.524	0.383	0.612
6	0.262	0.439	0.315	0.527	0.367	0.615
7	0.250	0.385	0.300	0.462	0.350	0.539
8	0.505	0.824	0.606	0.989	0.707	1.153
9	0.287	0.470	0.344	0.564	0.401	0.658
10	0.273	0.426	0.328	0.511	0.382	0.596
11	0.247	0.415	0.297	0.498	0.346	0.581
12	0.433	0.700	0.520	0.840	0.606	0.980
13	0.455	0.732	0.547	0.878	0.637	1.024
14	0.392	0.650	0.471	0.780	0.550	0.910
15	0.263	0.426	0.316	0.511	0.368	0.596
16	0.326	0.533	0.392	0.640	0.457	0.747
17	0.227	0.360	0.273	0.432	0.318	0.505
18	0.603	0.994	0.725	1.192	0.845	1.391
19	0.261	0.427	0.313	0.512	0.365	0.598
20	0.412	0.669	0.495	0.802	0.577	0.936
21	0.407	0.656	0.489	0.787	0.570	0.918
22	0.599	0.900	0.720	1.080	0.839	1.260
23	0.506	0.821	0.608	0.986	0.709	1.150
24	0.362	0.580	0.435	0.696	0.507	0.812
25	0.676	1.116	0.812	1.339	0.947	1.562
26	0.427	0.709	0.513	0.851	0.598	0.993
27	0.293	0.453	0.352	0.544	0.410	0.635
28	0.350	0.562	0.421	0.675	0.491	0.787
29	0.355	0.586	0.426	0.704	0.497	0.821
30	0.550	0.900	0.661	1.080	0.770	1.260
31	0.337	0.521	0.405	0.626	0.472	0.730
32	0.510	0.800	0.612	0.960	0.714	1.120
33	0.472	0.764	0.567	0.917	0.661	1.070
34	0.602	0.940	0.722	1.128	0.842	1.316
35	0.319	0.525	0.383	0.630	0.446	0.734
36	0.527	0.840	0.633	1.008	0.738	1.176

Source: The Authors

The comparisons of S/N ratio between original design and robust design, in accordance with Taguchi methods, are shown in Table 6. It can be seen that robust design slightly improves the S/N ratio and a significant effect in the slope that ensures a smaller influence on material resistance at vibration of the º.

The results shown in Fig. 8 demonstrate that the Taguchi dynamic characteristic design process successfully improves the fatigue resistance of the bracket. The optimum geometry improves the life fatigue of the component and it is independent of the material used in the manufacturing process.

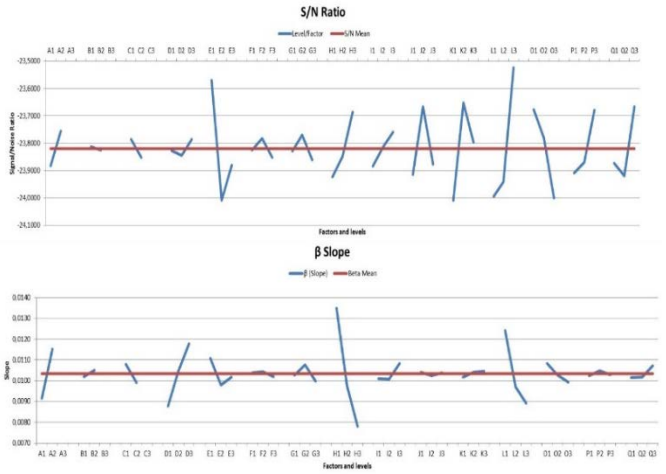


Figure 7. The magnitudes of the average response of the control factors for the S/N ratio and for the slope β, respectively.
Source: The authors.

Table 5
Optimum factors level.

Optimum Factor Level														
A	B	C	D	E	F	G	H	I	J	K	L	O	P	Q
1	2	2	1	2	2	2	3	2	2	2	3	2	3	3

Source: The Authors

Table 6.
Comparisons of the SN Ratio and beta between Original design and robust design.

	Original geometry	Taguchi Optimum	Improvement
S/N Ratio	-24.187264	-23.325328	-0.861937
β slope	0.013828	0.002872	0.010956

Source: The Authors

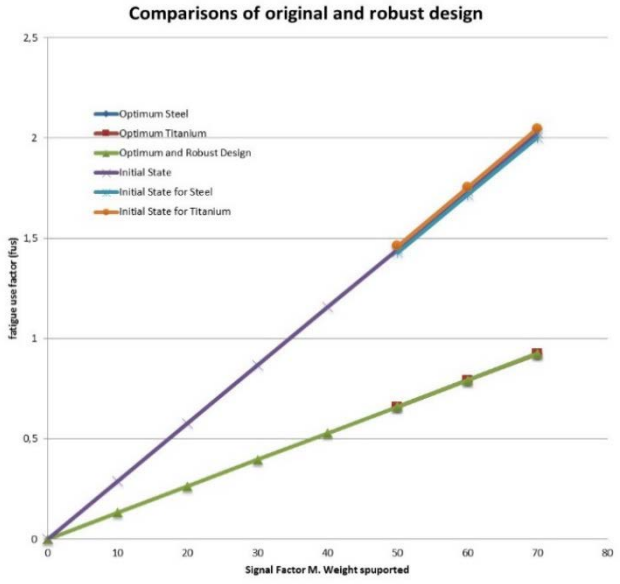


Figure 8. Visual comparisons between original fatigue and optimal design behavior.
Source: The authors.

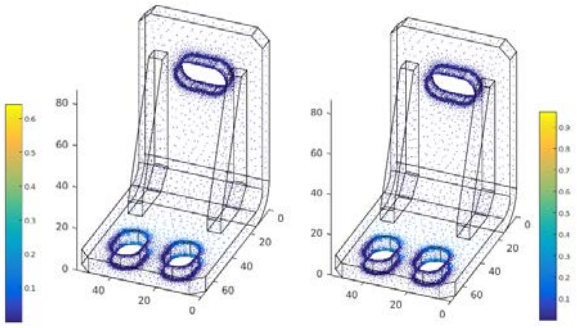


Figure 9. Final results for M=70 kg. a) Steel bracket and b) Titanium bracket. It can be see that the fus is less than one in all surface.
Source: The authors

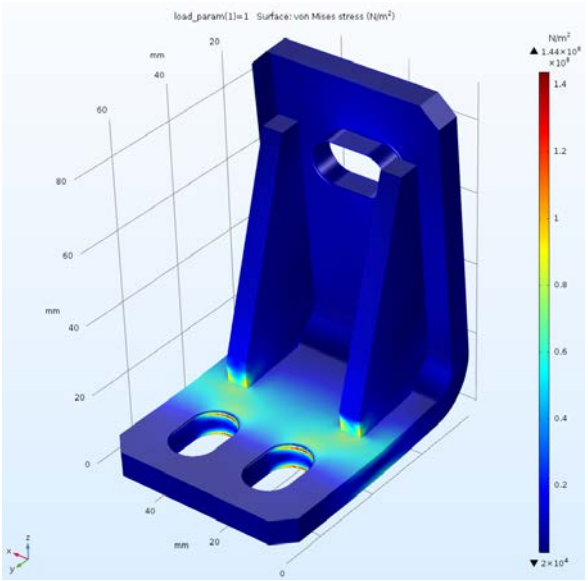


Figure 10. Final results for Von-Misses stress in steel bracket. It can be seen that maximum stresses (144 MPa) on the holes are

The optimized bracket geometry obtained by this method is shown in Fig. 9 where It can be see that fus is less than one in al surface and that the Von-Misses stress in Fig.10 is below of fatigue limit of this steel.

The optimized bracket geometry obtained by this method has been compared with the results of applying the Eurocode 3.

From the industrial point of view, the calculation of the fatigue resistance of a right angle is not contemplated in the regulations in a specific way. Normally the rules of fatigue tests (EN 61373: "Railway applications, Rolling stock equipment, Shock and vibration tests"; SAE J 1455: "Environmental Practices for Electronic Equipment Design in Heavy-Duty Vehicle Applications"; MIL-STD 810F Method 514.5 "Random mechanical vibration", ...) require that the test be done on the entire structure to be validated and not on the components, because the resonance frequencies depend on the complete set. Eurocode 3 "Design of steel structures - Part 1 -9: Fatigue ", like the rest of Eurocodes, provides common rules of structural design for the design of complete structures and component products. In this sense the calculation of the fatigue, strength of a right angle, according to the Eurocode, should be made based on the detail of the stiffening ribs in table 8.5 of Eurocode 3: 1-9. In this table, a detail category of 80 MPa is specified.

Fatigue assessment should be undertaken using the tolerant method to compare it with the results of this paper. The effective stress range may be calculated by adding the tensile portion of the stress range and 60% of the magnitude of the compressive portion of the stress range, this is 230.4 MPa in this case. This value is below of fatigue limit of these materials.

Table 7.
Cost

Phase	Time (hours)
Study of the system and the limits of its application	2
Ideal function and noise factors determination	2
Control factors, usage levels, orthogonal matrix determination	3
Experiment planning. Spreadsheet arrangement	5
Parametric Design and variables selection	6
Run simulations and produce fatigue results	18
Fatigue results analysis. Estimation of best relation between S/N ratio and slope	4
Run simulation of optimum design	1
Validate results. Conclusions	4
TOTAL	**45**

5. Cost

In this paper all parameters used for applying Taguchi's method are automatically changed in order to simulate final stress and therefore assess fatigue life.

Thus, fatigue assessment can be looped through all desired parameter combinations by setting their values in a database.

In this study 36 simulations have been produced for applying the Taguchi method.

The cost of the complete study is shown in the following Table 7.

To obtain an optimum design using the Taguchi method it would be necessary to perform fatigue failure tests of all combinations which would lead to high cost in terms of time and money.

Thanks to the approach used in this study a few work hours can be used to achieve a better design by optimizing the final geometry of the component.

Therefore the number of specimens to be manufactured and tested can be greatly reduced by using the methodology described in this paper.

In addition, final design of the specimen would be more efficient which also impacts cost since it directly reduces the material required to produce the component.

6. Conclusion

This study allows combining Taguchi dynamic design method with FEM simulation in order to optimize geometrical design of a mechanical component under fatigue. The results indicate that the adopted methodology improves fatigue resistance and reduces the influence of the material used, enabling a cheaper construction, beside a short

development time with no experimental testing, producing a significant cost reduction.

With the Taguchi method, the final optimal design depends mainly on the geometrical characteristics and it is possible to design straight angles tolerant to fatigue with a geometry that will behave optimally independently of the material chosen for its manufacture. This geometry is the one that best distributes the accumulated damage that will occur in the piece

A small number of experiments (36) provide the necessary data for an engineering optimization tool to improve the geometric design to optimally use the material. In this sense it is observed that the union of the stiffeners to the base of the right angle is an area of tension that must not be aligned with the area of fastening (holes) in order to avoid that the fatigue damage produced in these elements accumulates in the same region.

The present robust design has confirmed that good design components can improve its fatigue life in all types of applications independently of materials used to manufacturing

References

[1] Hsu, W. and Woon, I.M.Y., Current research in the conceptual design of mechanical products, 30, pp. 377-389, 1998.

[2] Murphy, T.E., Tsui, K.-L. and Allen, J.K., A review of robust design methods for multiple responses, Res. Eng. Des. 16, pp. 118-132, 2005. DOI: 10.1007/s00163-005-0004-0.

[3] Koski, J., Optimization of large structural systems, NATO ASI S, Springer Netherlands, Dordrecht, 1993. DOI: 10.1007/978-94-010-9577-8.

[4] Downey, K., Parkinson, A. and Chase, K., An introduction to smart assemblies for robust design, Res. Eng. Des. 14, pp. 236-246, 2003. DOI: 10.1007/s00163-003-0041-5.

[5] Taguchi, G., E. Elsaed, and Hsiang, T., Quality engineering in production systems, McGraw Hill, Emeryville CA, 1989.

[6] Taguchi, G., Performance analysis design, Int. J. Prod. Res. 16, pp. 521-530, 1987. DOI: 10.1080/00207547808930043.

[7] Kotcioglu, I., Cansiz, A. and Nasiri-Khalaji, M., Experimental investigation for optimization of design parameters in a rectangular duct with plate-fins heat exchanger by Taguchi method, Appl. Therm. Eng. 50, pp. 604-613. 2013. DOI: 10.1016/j.applthermaleng.2012.05.036.

[8] Arias-Nava, E.H., Ríos-Lira, A.J., Vázquez-López, J.A. y Pérez-González, R., Estudio comparativo entre los enfoques de diseño experimental robusto de Taguchi y tradicional en presencia de interacciones de control por control, Ing. Investig. y Tecnol. 16(1), pp. 131-142, 2015. DOI: 10.1016/S1405-7743(15)72114-1.

[9] Zhang, F.B., Wang, Z.L. and Yang, M.Y., Assessing the applicability of the Taguchi design method to an interrill erosion study, J. Hydrol. 521, pp. 65-73, 2015. DOI: 10.1016/j.jhydrol.2014.11.059.

[10] Hong, Y.Y., Beltran, A.A. and Paglinawan, A.C., A robust design of maximum power point tracking using Taguchi method for stand-alone PV system, Appl. Energy. 211, pp. 50-63, 2018. DOI: 10.1016/j.apenergy.2017.11.041.

[11] Balak, Z., Azizieh, M., Kafashan, H., Asl, M.S. and Ahmadi, Z., Optimization of effective parameters on thermal shock resistance of ZrB2-SiC-based composites prepared by SPS: using Taguchi design, Mater. Chem. Phys. 196, pp. 333-340, 2017. DOI: 10.1016/j.matchemphys.2017.04.062.

[12] Sayeed-Ahmed, G.M., Quadri, S.S.H. and Mohiuddin, M.S., Optimization of feed and radial force in turning process by using Taguchi design approach, Mater. Today Proc. 2, pp. 3277-3285, 2015. DOI: 10.1016/j.matpr.2015.07.141.

[13] Mitra, A.C., Jawarkar, M., Soni, T. and Kiranchand, G.R., Implementation of Taguchi method for robust suspension design, Procedia Eng. 144, pp. 77-84, 2016. DOI: 10.1016/j.proeng.2016.05.009.

[14] Deepak-Kumar, S., Karthik, D., Mandal, A. and Pavan-Kumar, J.S.R., Optimization of thixoforging process parameters of A356 alloy using Taguchi's experimental design and DEFORM Simulation, Mater. Today Proc. 4, pp. 9987-9991. 2017. DOI: 10.1016/j.matpr.2017.06.307.

[15] Sangkharat, T. and Dechjarern, S., Spinning process design using finite element analysis and Taguchi method, Procedia Eng. 207, pp. 1713-1718, 2017. DOI: 10.1016/j.proeng.2017.10.927.

[16] Sun, G., Fang, J., Tian, X., Li, G. and Li, Q., Discrete robust optimization algorithm based on Taguchi method for structural crashworthiness design, Expert Syst. Appl. 42, pp. 4482-4492, 2015. DOI: 10.1016/j.eswa.2014.12.054

[17] Li, F., Meng, G., Sha, L. and Zhou, L., Robust optimization design for fatigue life, Finite Elem. Anal. Des. 47, pp. 1186-1190, 2011. DOI: 10.1016/j.finel.2011.05.009.

[18] Sun, G., Fang, J., Tian, X., Li, G. and Li, Q., Discrete robust optimization algorithm based on Taguchi method for structural crashworthiness design, Expert Syst. Appl. 42, pp. 4482-4492, 2015. DOI: 10.1016/j.eswa.2014.12.054.

[19] Socie, D. and Marquis, G., Multiaxial fatigue, Warrendale, PA 15096-0001 USA, 2000.

[20] Kallmeyer, A.R., Krgo, A. and| Kurath, P., Evaluation of multiaxial fatigue life prediction methodologies for Ti-6Al-4V, J. Eng. Mater. Technol. 124, pp. 229-237, 2002. DOI: 10.1115/1.1446075.

[21] Karolczuk, A. and Macha, E., Selection of the critical plane orientation in two-parameter multiaxial fatigue failure criterion under combined bending and torsion, Eng. Fract. Mech. 75, pp. 389-403, 2008. DOI: 10.1016/j.engfracmech.2007.01.021.

[22] Marquis, D. and Socie, D.F., Long-life torsion fatigue with normal mean stresses, Fatigue Fract. Eng. Mater. Struct. Fract. Eng. Mater. Struct. 23, pp. 293-300, 2000. DOI: 10.1046/j.1460-2695.2000.00291.x

[23] Banvillet, A., Łagoda, T., Macha, E., Niesłony, A., Palin-Luc, T. and Vittori, J.F., Fatigue life under non-Gaussian random loading from various models, Int. J. Fatigue. 26, pp. 349-363, 2004. DOI: 10.1016/j.ijfatigue.2003.08.017.

[24] Findley, W.N., A theory for the effect of mean stress on fatigue of metals under combined torsion and axial load or bending, J. Eng. Ind. [online]. 39, pp. 301-306, 1958. Available at: http://hdl.handle.net/2027/coo.31924004583708.

[25] Findley, W.N., Fatigue of metals under combinations of stresses, Trans. ASME. 79, pp. 1337-1348, 1957.

[26] Taguchi, G., Introduction to quality engineering: designing quality into products and processes, American Supplier Institute, 1990. Dearborn (Mich.), [online]. 1986. [accessed on: March 18th of 2015]. Available at: http://trid.trb.org/view.aspx?id=1179550

[27] Taguchi, G. and Konishi, S., Orthogonal arrays and linear graphs: tools for quality engineering, American Supplier Institute, Dearborn (Mich.), 1987.

R. Barea, received the PhD degree in 2009 from Universidad Autónoma de Madrid, Spain. He is working on thermal properties of porous ceramics obtained by powder compaction since 2000. He is working as a researcher and senior lecturer since 2007 at industrial engineering department, Nebrija University, where is the principal research (IP) of Nebrija's Materials Group. He was working as researcher in the Spanish Research Council (CSIC) for 8 years.
ORCID ID: 0000-0002-6784-6110
ResearcherID: A-7594-2011
Scopus Author ID: 56406676700

S.J. Novoa, received the BSc. in Mechanical Engineering specialized in Aerospace Industry from the Universidad de Vigo, Spain and he did his MSc. in Mechanical Engineering at 'Universidad Nebrija' Madrid, Spain. Afterwards, he studied a post Master degree in Aerospace Design at 'CFO Leganés' in Madrid, Spain. Currently he is working at Airbus D&S in Getafe, Spain as an engineer at the innovation area of the Manufacturing Engineering department Additionally, he is studying a Materials Science and

Engineering PhD at 'Universidad Nebrija' about graded materials in technical ceramics. .
ORCID ID: 0000-0003-3627-0566

F. Herrera, obtained his degree of Technical Industrial Engineering from the University of Malaga, Spain in the year 1964. Later made MSc. of Production Management by Madrid School of Industrial Organization (EOI) and the MSc. of High Management by the Madrid and Paris Chamber of Commerce. He has developed his working life in different companies in the industry of transportation, consulting and manufacturing of components for the automotive industry. Its functions have been related to mechanical engineering, manufacturing and quality management. In the field of consultant, he has specialized in business strategic design, quality improvement and variability reduction through robust design, in accordance with the method of Dr. Genichi Taguchi.
ORCID ID 0000-0001-9722-2678

B. Achiaga, received PhD degree in 2015 fromr Universidad Nebrija, Spain. Started her research in powder technology in 2011 focussing on powder compaction, in her monograph "A novel method to estimate Drucker-Prager parameters and the compaction pressure influence on SPS process applied on powder technology". She is working as research teaching associate at Deusto University, in the department of industrial engineering. She was working in material die powder compaction characterization at the University of Leicester (UK).
ORCID ID: 0000-0002-5184-7944

N. Candela received the PhD degree in 1997. She is working on powder metallurgy since 1996. She was involved in a number of research projects in one of the most important research department in Spain of powder metallurgy (GTP-Carlos III), under the supervision of Prof. Jose Manuel Torralba. She was working as a researcher and head at Industrial Engineering Department of Nebrija University until 2016. Now she is working as a head of postgraduate education at ESNE University School of Design, Innovation and Technology. As a researcher he was involved in research projects related with powder metallurgy and materials.
ORCID ID: 0000-0002-0568-753X

UNIVERSIDAD NACIONAL DE COLOMBIA
SEDE MEDELLÍN
FACULTAD DE MINAS

Área Curricular de Ingeniería
Geológica e Ingeniería de Minas y Metalurgia

Oferta de Posgrados

Especialización en Materiales y Procesos
Maestría en Ingeniería - Materiales y Procesos
Maestría en Ingeniería - Recursos Minerales
Doctorado en Ingeniería - Ciencia y Tecnología de Materiales

Mayor información:

E-mail: acgeomin_med@unal.edu.co
Teléfono: (57-4) 425 53 68

UNIVERSIDAD NACIONAL DE COLOMBIA
SEDE MEDELLÍN
FACULTAD DE MINAS



DYNA
http://dyna.medellin.unal.edu.co/

Normalized difference vegetation index for rice management in El Espinal, Colombia

Mauricio González-Betancourt [a] & Zaira Liceth Mayorga-Ruíz [b]

[a] *Agreement between COLCIENCIAS- SENA. Tecnológico de Antioquia, Medellín, Colombia. mao275@yahoo.com*
[b] *Centro Agropecuario "La Granja", Servicio Nacional de Aprendizaje (SENA), El Espinal, Colombia. zlmayorgar@ut.edu.co*

Received: December 19th, 2017. Received in revised form: April 3rd, 2018. Accepted: April 11th, 2018.

Abstract
Aerial images and the Normalized Difference Vegetation Index (NDVI) of the stage after panicle initiation were evaluated as tools that help large-scale rice monitoring and decision-making that favors crop profitability. NDVI was used to identify problems in the development and growth of FEDEARROZ-2000. FEDEARROZ-2000 is a variety of rice, which is resistant to the "hoja blanca" virus and direct "sogata" damage that affect fields in tropical America. The temporal dynamics of the NDVI for FEDEARROZ-2000 were estimated. An NDVI lower than 0.8 in the Stage of Rice Panicle Development (SRPD) was related to areas with levelling problems, differences in the vegetative stage, water stress, and spacing between plants. The NDVI for the SRPD had a significant positive correlation with yield, 1,000 grain weight and the number of panicles (Pearson's R≥0.86; probability value P ≤0.04). NDVI mapping at milky stage helped to identify production environments and to schedule the harvest areas.

Keywords: NDVI; rice; unmanned aerial vehicle

Índice de vegetación de diferencia normalizada para el manejo del arroz en El Espinal, Colombia

Resumen
Se evaluaron las imágenes aéreas y el NDVI como herramientas para la supervisión del arroz a gran escala. El índice de vegetación de diferencia normalizada (NDVI) se utilizó para identificar problemas en el desarrollo de la variedad de arroz FEDEARROZ-2000, la cual es resistente al virus de la hoja blanca y al daño directo de la "sogata". Se estimó la dinámica temporal del NDVI para FEDEARROZ-2000. En la Etapa de Desarrollo de la Panícula del Arroz (EDPA), el NDVI inferior a 0,8 se relacionó con áreas con problemas de nivelación, estrés hídrico y diferencias en el estado de las plantas. El NDVI de la EDPA tuvo una correlación positiva significativa con las panículas/m^2, el peso de los 1000 granos, y con el rendimiento (Coeficiente de correlación de Pearson R≥0.86; Probabilidad≤0.04). El NDVI en la etapa lechosa ayudó a identificar ambientes de producción y a programar áreas para la cosecha.

Palabras clave: NDVI; arroz; vehículo aéreo no tripulado

1. Introduction

Yield trends are insufficient for satisfying consumer demand and for duplicating crop pEroduction by 2050 [1], especially in a context where variability and climate change cause between 32 and 60 percent of yield variability [2,3]. Central American agriculture-dependent countries, the big island nations in the Caribbean, Venezuela, Colombia and Ecuador have a higher risk of climate change [4]. As such, major efforts have been made to obtain varieties that can grow in low fertility soils and are resistant to water stress, disease and increased temperatures, and to avoid improper agronomic management, which limits varietal potential and the possibility of competing on the international market [3,5]. It is highlighted that the Free Trade Agreement (FTA) between Colombia and the United States is gradually reducing rice import tariffs which will disappear altogether by 2030 [6].

How to cite: González-Betancourt, M. and Mayorga-Ruíz L., Normalized difference vegetation index for rice management in El Espinal, Colombia. DYNA, 85(205), pp. 47-56, June, 2018.

© The author; licensee Universidad Nacional de Colombia.
Revista DYNA, 85(205), pp. 47-56, June, 2018, ISSN 0012-7353
DOI: http://doi.org/10.15446/dyna.v85n205.69516

The challenge of rice *vis-à-vis* the FTA in Latin America establishes: a) the protection of the current yield and increase the yield in the context of climate change; b) the reduction of the production costs and a difference made in terms of rice quality [5,7]; and c) the adoption of a production system with a low environmental footprint and increased water productivity [7,8]. Given that rice crops require the greatest water demand at global level, more crops must be produced per volume of water used. Irrigated rice receives between 34 and 43 percent of the total of irrigation water in the world [9]. Therefore, Latin America requires rice producers and researchers to apply agronomic management with an eco-efficient approach [10].

The Colombian rice sector is a heterogeneous one, in which modernized and efficient agribusinesses coexist with others which have a relative technological catch-up, and inefficient and unsustainable farming practices [5]. Both types of agribusiness feel the pressure on the water resources and the need to take advantage of the environmental offer (solar radiation, precipitations and water allocation by the irrigation district) [11]. As such, farmers have needed to make agricultural work more efficient to comply with sowing dates. Thus, farmers have been working faster in terms of plot design, soil preparation labors and sowing both during daylight and night-time. This has increased the deficiencies in seed distribution, unduly levelled areas and vulnerability to water stress. Nocturnal sowings without precision equipment leads to unsown areas, which are corrected days later through broadcast sowing. The lag in germination generates differences in physiological maturity, and the untimely harvests of the rice crop generate great money losses [12,13]. As many of the mechanized labors in Colombia are contracted to third parties, it is common to make operative decisions in field, which are difficult to detect by the professionals in big areas in order to apply a differentiated agronomic management. Site-specific agriculture helps to decrease the impact on grain production and quality [10].

The aforementioned highlights that being a rice farmer is a risky business in Colombia. As such, tools are necessary to help to close the yield gap and assure quality rice through timely decision-making. Effective agronomic management is crucial to closing the yield gap, as it allows some of the factors that may limit the expression of the varietal potential to be controlled [7].

Normalized Difference Vegetation Index (NDVI) is a reflectance indicator for different wavelengths of plant cover, soil, water and other materials. It is characterized by having a linear measurement scale, with a range of values between 0 and 1. The vegetation generates positive values and the soil or other objects (not vegetation), are recognized by values of less than 0.1 [14]. Healthy plant cover is characterized by the leaves absorbing most of the light in the red region (Wavelengths between 0.6 and 0.7 μm) and reflecting the near infrared (Wavelengths between 0.7 and 1.1 μm). This vegetation property allows an assessment of the condition of the rice. The NDVI is sensitive to the amount of humidity, biomass, chlorophyll concentration, leaf area index (LAI) [15], vegetation density, phenological stages, panicle stage [16], nitrogen in the plant [17], weed detection [18], etc. As such, the NDVI may have multiple applications in rice, which should be developed and validated locally to facilitate technological adoption and adjustment of the production processes. The adoption and transfer of technology is decisive in closing the yield gap in Latin and Central American countries [7,19].

This work was developed using the FEDEARROZ-2000 variety in Espinal, Tolima, Colombia, in a semi-commercial field, and with NDVI calculated from multispectral photographs taken from an Unmanned Aerial Vehicle (UAV). FEDEARROZ-2000 is farmers' preferred variety due to its yield and resistance to the rice "hoja blanca" (white leaf) virus (RHB) and the mechanical damage caused by the "sogata" insect (*Tagosodes orizicolus* Muir). FEDEARROZ 2000 presents two quantitative trait loci: one located on chromosome 4 for resistance to RHB and the other located on chromosome 5 for resistance to mechanical damage produced by "sogata" [20]. Rice hoja blanca (RHB; white leaf) devastated rice crops in Cuba, Venezuela, Panama, Colombia, Brazil, Belize, Costa Rica, Dominican Republic, El Salvador, Ecuador, Guatemala, Guyana, Honduras, Mexico, Nicaragua, Peru, Puerto Rico, Surinam and the USA [21]. On the other hand, the photographs taken from the UAV allow a resolution of 5.5 cm per pixel and isolate the atmospheric noise that may be present in satellite images.

This work was aimed at assessing the potential of high resolution aerial images and the NDVI as an indicator to detect problems in the development and growth of rice in El Espinal, Tolima, Colombia

2. Methodology

Adopting cultural practices under pressure to comply with sowing dates, rice crops were established in the "La Granja" experimental plot in the Agricultural Center, National Apprenticeship Service (Servicio Nacional de Aprendizaje - SENA), at El Espinal, Tolima, Colombia. In recent years, the 4.9 ha plot of land has been managed through crop rotation alternating between rice and cotton or maize. The soils had a sandy loam texture in the upper and medium parts of the plot of land, and a loamy sand texture in its lower part. The organic matter contents are low across the plot of land. Fig. 1 shows a summary of the methodology used.

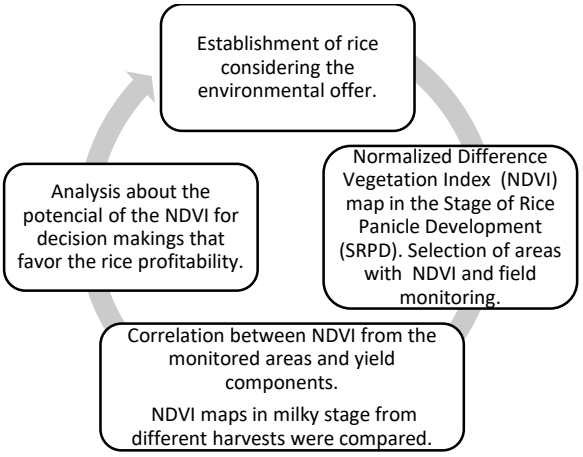


Figure 1. Methodological scheme
Source: The authors.

Soil preparation consisted in scything, plant waste management, two disc harrow passes, and a LandPlane pass, implemented in daytime. Contour levee and sowing were carried out with two highly experienced technicians for two consecutive nights. The technicians provide such services in Tolima. The rice was sown using a SEMEATO PD 17 sowing machine (17 lines x 17 cm) without fertilizer. Sowing density was 104.5 ± 3.3 kg of seed/ha. The tice cultivar FEDEARROZ-2000 was used and its seed germination test obtained 91 percent of germination. After the sowing, a strip of unsown soil and areas with germination problems were identified. The pre-germinated seed broadcast sowing was carried out 16 Days After Emergency (DAE) in areas which were not sown or where the seed did not emerge. As such, different rice development stages were expected in some areas.

Controls for broadleaf (*Cucumis melo*), Cyperaceas (*Cyperus rotundus*) and *Echinochloa colona* in post-early and applications focusing on post-late were undertaken. Fungicide was applied three times in the reproductive stage to control *Pyricularia* given that this variety has a higher susceptibility to disease in relative moisture greater than 80 percent [3]. The maximum moisture during crop development was 83 percent. Insecticide was not applied.

Considering the chemical analysis of the soil and the nutritional requirements of FEDEARROZ-2000 calculated with the SIFA Program ("Sistema de Fertilización Arrocera" in Spanish; [22]), it was determined to perform a fractioned fertilization with 160 kg/ha of N, 33 kg/ha P_2O_5 and 119 kg K_2O. The application of the nitrogen fertilizer (NH_4) to rice was carried out when the average readings in the field using the SPAD 502 chlorophyll meter were between 34 ± 1 SPAD. The field with the chlorophyll meter was monitored according to the guidelines established by Garcés and Castilla [23]. The third fertilization (41 DAE) application was carried out using the differentiation of floral primordium in several tillers analyzed in the field.

Rice was developed with intermittent irrigation in the dry season from May to October 2016, where the maximum solar radiation coincided with the rice's reproductive and ripening stages, in which average solar radiation was 215.5 Cal/cm^2/day. The applied depth of irrigation was 921 mm of water, and the precipitation contributed a depth of 350 mm of water. The first irrigation was carried out 12 DAE. The distribution of the monthly precipitation in the area occurs due to a bimodal regime, with abundant rainfall from March to May and from October to November, 2016. The temperature in which the crop was developed in the vegetative stage ranged between 21 and 36 °C, and in the reproductive phase between 20 and 38 °C. The sown variety, FEDEARROZ-2000, tolerates daytime temperatures of between 29 and 37 °C and does not tolerate nighttime temperatures outside a range of 21 to 25 °C [3]. In the panicle emergence in the reproductive stage (66 DAE - 78 DAE), limitations in water availability in the irrigation district channels were presented, which caused stress in rice. So a set of cultivation areas with water stress were presented.

The aerial photographs were taken during the Stage of Rice Panicle Development (SRPD; 58 DAE) and the Milky Stage (MS; 106 DAE) with a multispectral camera, and an UAV. The UAV was the PHANTOM FX-61, weighing 1.05 kg, measuring 1550 mm in width and 683 mm in length and made from EPO material (expanded polyolefin). The UAV has a KV900 brushless motor, helix, 2 servomotors (one for each aileron) and an Ardupilot Mega control system (APM 2.5). The MicaSense multispectral camera weighs 150 g. It has a resolution of 8 cm per pixel/band at 120 m high and allows to take the spectral bands in red, green, blue, "red edge" and near infrared. Image capture was carried out at 80 meters high.

The flights were carried out from 9:30 am to 12:00 pm, when the incident solar radiation is at its highest and wind speeds are at their lowest. For the flights, the following were identified: allowed heights, obstacles, winds, launching, and landing points. The height, speed, coordinates, and software for definition of the polygon of the study area were programmed. In the processing, the images were grouped with the "Pix4Dmapper pro Educational" and then, the NDVI was calculated according to Eq. 1.

$$NDVI = \frac{NIR - R}{NIR + R} \quad (1)$$

Where NIR is the datum in the near infrared and R is in the red area. The maps were represented using color scale, where the lowest NDVI were associated with black, gradually changing to gray and white, the latter with values closer to 1.

The NDVI changes with the physiological condition of the rice plant. Therefore, the temporal dynamics of the NDVI for FEDEARROZ-2000 were estimated from the temporal dynamics of the NDVI for the subspecies indica reported by Lin et al. [24]. NDVI temporal dynamics were calibrated with the NDVI for the SRPD and the MS associated with an area with good rice growth and development (Area 1). Furthermore, the in-field physiological stages detected were checked against the physiological stages forecast by NDVI temporal dynamics and the physiological stages reported by Degiovanni et al. [25].

Area 1 or the reference area presented the highest NDVI (greater than 0.8 in SRPD). The curve of NDVI temporal dynamics is a reference through which to interpret the NDVI as a function of rice stage.

Areas in the NDVI map of the SRPD with NDVI lesser than 0.8 were identified. Each area was approximately 26 m long and 7 m wide. The NDVI of each area was the weighted average of the NDVI, considering the area as the weight. The polygon with the NDVI values from the Pix4Dmapper pro Educational software were used for calculating the area and the respective weights. In the loamy sand soil, four areas with the lowest NDVI were chosen (Areas 2-5); and one in loamy sand soil (Area 6). Area 6 was in the lowest part of the plot of land with the thickest soil texture, where the effects of water stress should be higher.

Field monitoring was carried out during the SRPD (64 DAE), the MS (101- 103 DAE), and grain and plant maturity (127-129 DAE). In the SRPD (64 DAE) and with three replications, the Plant Length (PL) and the number of Tillers per m^2 (T/m^2) were measured in a frame of 0.25 m^2. During flowering and water stress of the crop, samplings of the areas were taken with a frame of 0.25 m^2. Fresh Plant Weight (FPW), Dry Plant Weight (DPW), percentages of Dry Matter (% DM) and Plant Moisture (%PM; eq. 2) were determined in laboratory. The drying temperature was 60 °C. The T/m^2 and the number of Panicles per m^2 (#Pa/m^2) were also determined.

$$\%PM = (1 - \frac{DPW}{FPW})*100 \quad (2)$$

During the maturity stage, 25 panicles were randomly collected within each plot. The number of filled spikelets by panicle, number of Grains per Panicle (#G/Pa), 1000 Grain Weight (1000 GW), percentage of Sterile Spikelet (% SS) and Panicle Weight (PaW) were characterized. In each plot and with two frames of 0.25 m^2, the rice was harvested manually with 20.6% of average moisture, and the paddy yield (Y (Ton/ha)) was estimated. The procedures for measuring yield components were set according to the guidelines established by Dobermann and Fairhurst [26].

The NDVI was correlated with the yield components. Statistical analysis of the information collected in the software "Excel" was performed, using regression data analysis tool with 5% significance. The linear regression analysis using the "least squares" method was performed to fit a line through a set of observations. Regression statistics and variance analyses were interpreted using the Pearson Correlation Coefficient (R), Coefficient of Determination (R2) and the significance associated P-Value (P).

Two NDVI maps in Milky Stage (MS) from different harvests were compared to identify production environments (Fig. 2). The second NDVI map was constructed from the satellite image taken on December 16th 2013 in MS (108 DAE approximately; Fig. 2d). The polygons of NDVI map were reconstructed in AutoCAD (Fig. 2d).

3. Results and discussion

Fig. 2a-c shows the NDVI maps associated with the SRPD and the MS. The areas with agronomic management problems (Table 1) were associated with the NDVI in the SRPD lower than 0.8, the lowest yields and deficiencies in the grain quality (Table 2).

Areas 1, 2, 3, 4 and 5 were located in a sandy loam soil, while area 6 was located in a loamy sand soil (Fig. 2b).

Area 1 presented a good crop development, an acceptable plant height, the highest number of viable tillerings, the highest number of grains per panicle, and a good weight for the one thousand grains. This means that there was a good relationship between the gained biomass and the tillerings, from which the panicles were originated and consequently, the rice harvested. The NDVI was 0.89 and 0.84 in the SRPD and the MS, respectively (Table 1).

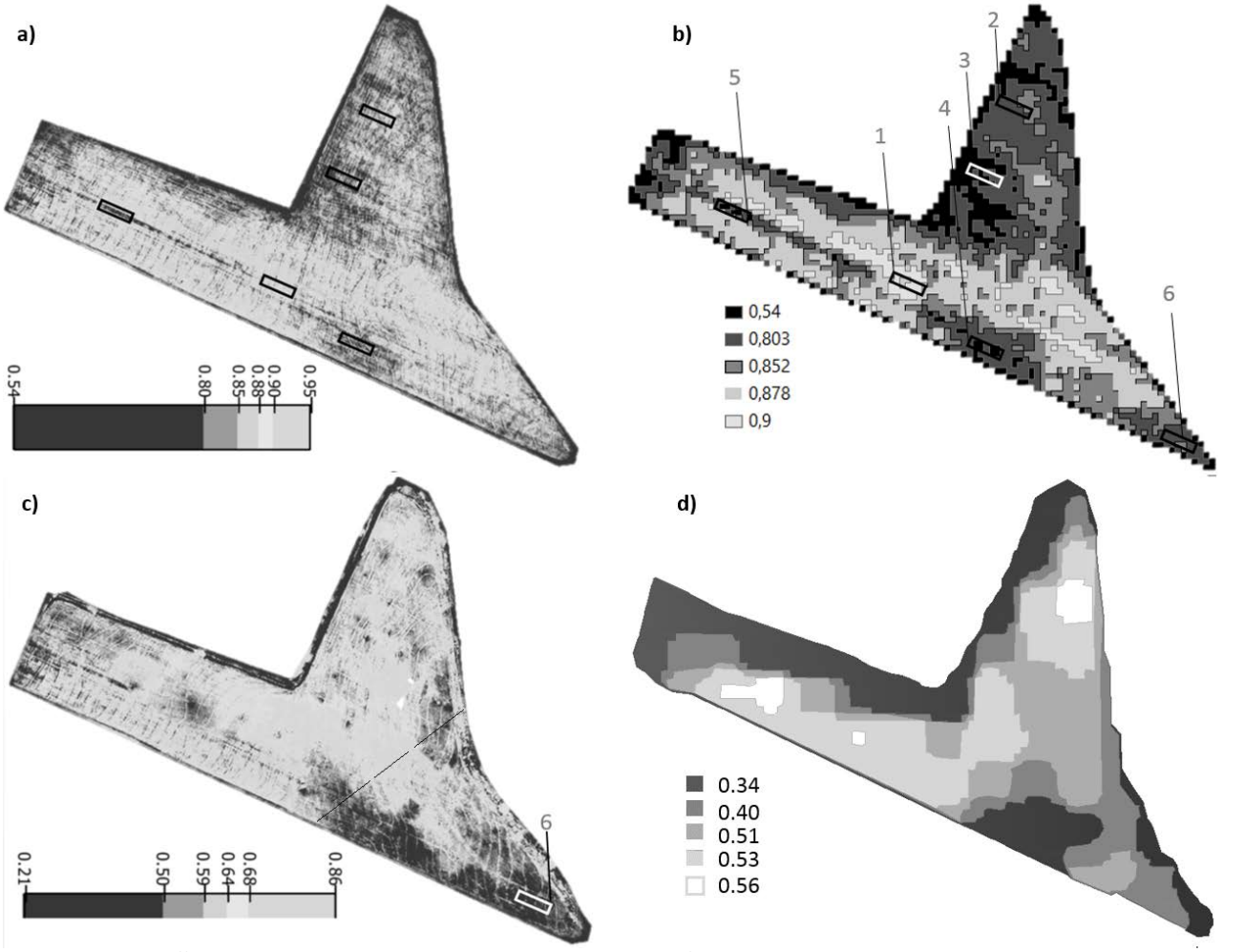


Figure 2. Normalized difference vegetation index (NDVI) maps. a) Map in the Stage of Rice Panicle Development (SRPD). b) NDVI polygons map in the SRPD. c) Map in the Milky Stage (MS). d) Map elaborated from a satellite image taken in the MS.
Source: a)-c) Barrero O. and the authors. d) Adapted from GEOAGRIS

Table 1.
Normalized difference vegetation index (NDVI) and qualitative monitoring parameters for the study areas of rice crop.

A	58 DAE NDVI (SRPD)	106 DAE NDVI (MS)	Problem of the area	Cause	Effect
1	0.89	≤ 0.84	Minor problems.	Good development.	Reference yield in the plot of land.
2	0.83	≤ 0.8	Non-uniform germination. Slight decrease in the plant population density.	Micro-Levelling. Death of the seed by anoxia.	Spacing between plants that minimizes competition between them and maximized yield.
3	0.75	≤ 0.7	Non-uniform germination. Low population density. Temporal water stress.	Soils and seed erosion.	Water stress and excessive spacing between plants that decreases the yield.
4	0.59	≤ 0.5	Water stress throughout the development.	Lack of levelling. Irrigation management.	Very low yield and very low grain quality.
5	0.67	≤ 0.6	Differences in the vegetative stage.	Non-effective sowing (Non-uniform).	Decrease in yield and grain quality. Higher percentage of straighthead disease.
6	0.81	≤ 0.5	Non-uniform germination. Delay in the rice development. Water stress.	Soil preparation. Irrigation management. Type of soil.	Low yield.

SRPD: Stage of Rice Panicle Development. MS: Milky Stage.
Source: The authors.

Table 2.
Monitoring parameter for the study areas of rice crop

	Reproductive			Ripening											
	SRPD			MS		Maturity									
						1000 grains		25 panicles			Yield	Rice Quality			
A	T/m²	PL (cm)	PM (%)	T/m²	Pa/m²	1000 GW(g)	SS (%)	PaW	G/Pa	SS (%)	Y (Ton/ha)	Imp. (%)	Ch. (%)	HR (%)	BG (%)
1	544	63	66	607	580	23,9	14	2,7	113,6	15,9	7,3	7	2	55	14
2	331	67	67	427	403	24,7	8,2	2,3	93,8	21,1	7,8	4	3	53	17
3	343	64	60	476	456	19,8	25,9	2,1	84,4	11,2	6,2	9	2	61	9
4	539	46	53	360	139	17	33,1	1,9	81,3	19,5	3,3	16	7	56	12
5	445	56	72	377	77	15,6	27	1,6	91,6	54,7	6.1	2	16	35	28
6	368	47	63	388	159	22,5	10,5	2	88	17,9	5.4	2	5	54	15

Source: The authors.

Fig. 3 presents the NDVI temporal dynamics for FEDEARROZ-2000. The period between 0 to 10 days corresponds from the germination until its seedling stage, where the NDVI is influenced mostly by soil and water.

The DAE corresponding to maximum tillering (30 DAE), flowering (85 DAE) and rice maturity (123 DAE) were predicted by NDVI temporal dynamics (Fig. 3). The largest spike in the curve of the NDVI slope indicated the duration of tillering stage.

After the panicle initiation, the NDVI should be above 0.8 in a plant with a good development and above 0.85 between the panicle development and flowering. NDVI increase with rice growing and tillering. The second spike corresponded to panicle development [24]. The heading and flowering stage is characterized by the maximum NDVI, and at the maturity stage, NDVI decreased continuously (the change of the NDVI slope began at 123 DAE, Fig. 3).

Harvesting was carried out with 20.6% of grain moisture content in the reference area and 127 DAE. The grain moisture content indicates that the harvest was delayed. Hence, the intersection between NDVI temporal dynamics and line corresponding to DAE to harvest was coherent.

NDVI allowed to corroborate water stress and differences in the population density, *i.e.*, abnormal spacing between plants despite a good biomass.

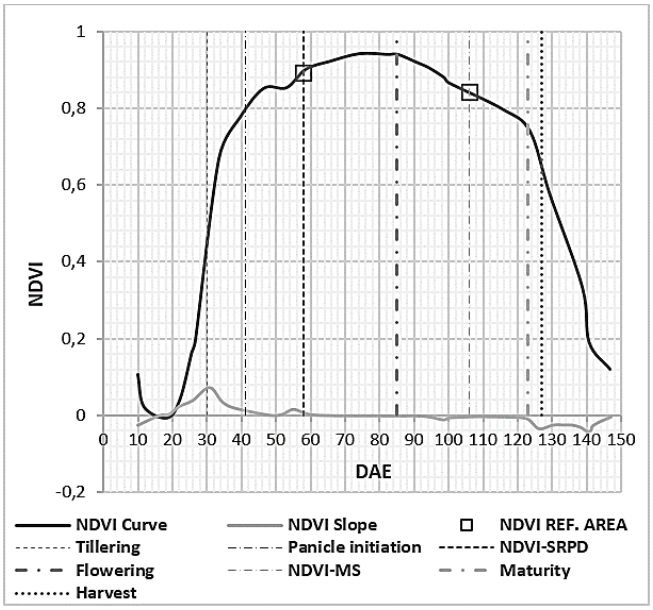


Figure 3. Estimation of the temporal dynamics of normalized difference vegetation index for rice cv. FEDEARROZ-2000.
Source: The authors. Information reported by [24] was used.

NDVI for the SRPD were lesser than 0.83 and 0.75 in areas 2 and 3, respectively. The population density in areas 2 and 3 decreased (Fig. 4a), as reflected in the T/m^2 (Table 2). The reduction was of between 27 and 18% in the T/m^2 in areas 2 and 3 compared with Area 1, whereas the plants were between 2 and 6% higher in areas 2 and 3. The emergence of the plants was inhibited by anoxia in Area 2 and, there was seed erosion by water flow and deficiencies in the leveling in Area 3.

In the NDVI map for the MS, areas 2 and 3 showed values below 0.84 and 0.7 respectively. According to the yield components (Table 2), Area 2 showed the highest yield and the highest 1000 grain weight, as competition between plants for nutrients, water and light was minimized.

Area 3 showed a large percentage of spikelet sterility (SS = 25.9%) probably caused by water stress. In Area 3, NDVI was associated with both water stress and population density.

Water stress also had a great impact in Area 4, which was reflected in the NDVI map of the SRPD with values below 0.59. Plant height was 27% less than the reference area (Table 2). In terms of rice field work, deficiencies were detected for the micro-leveler (Land plane). The lack of soil moisture affected weed and disease control, favoring a reduction in the tillers population due to senescence processes (competition among the tillers). The T/m^2 decreased by 33% between the SRPD and the MS. Therefore, despite the good number of tillers, many of them were not effective. The delay in irrigation during the emergence of the panicle was clearly evidenced in the NDVI map corresponding to the MS (Fig. 2c), and in the necrotic plant tissue (Fig. 4c). Area 4 had the highest percentage of sterility in spikelet (SS = 33.0%), the lowest number of grains per panicle and lowest yield. The rice plant is very sensitive to drought from the panicle initiation stage until the spikelet, which may reduce the yield when increasing spikelet sterility [27].



Figure 4. Monitoring in Field. Area 3 (a) and Area 5 (b) during the Stage of Rice Panicle Development (SRPD). Area 4 (c) and Area 6 (d) during the Milky Stage (MS).
Source: The authors.

Area 5 in the SRPD showed a NDVI of 0.67, 445 T/m^2, and a plant height of 56 cm which, with respect to the

reference area, corresponds on average to differences of 25, 82 and 84 percent, respectively.

The sowing machine did not pass over Area 5 and the pre-germinated broadcast seed was distributed. An NDVI lower than 0.8 reflect differences in the development of rice with respect to the rest of the crop (Fig. 4b). In this area the plants had not reached the maximum tillers elongation. In the second MS overflight, NDVI lower than those from the Area 1 were observed. Given that the whole plot of land was harvested on a same day, limitations in the grain quality and yield for this area were presented (Table 2). For the FEDEARROZ variety, head rice percentage for normal rice should be above 55%, and the percentage of broken grain should be between 8 and 20% (BG (%)) [12, 13]. The grain harvested in Area 5 was not within this range (HR = 35%; BG = 28%). When rice is harvested very early, chalkiness increases leading to a significant increase of broken grains in the milling process [12]. This causes economic loss for the farmer as their product is damaged in the mill, as white rice in these conditions is considered to be of poor quality and appearance.

Area 6 was located at the entrance and exit of the machinery, and is also the lowest part of the plot where water drains. This area showed NDVI below 0.81 in the SRPD and the MS, a very low number of productive tillerings, number of grains per panicle and the second lowest yield. Particularly, Area 6 had a thicker soil consistency (Loamy sand, Fig. 2c), which is why it was sensitive to the delay in the irrigation. The competition between close plants for water and nutrients decreased the amount of productive tillerings [28,29].

The NDVI in the SRPD for areas 1, 2, 3, 4 and 5, areas with the same type of soil, showed a high positive correlation with the T/m2 ($R=0.869$; $p\leq0.056$), #Pa/m2 ($R=0.895$; $p\leq0.040$), PaW ($R=0.858$; $p\leq0.063$), 1000 grain weight ($R=0.898$; $p\leq0.039$) and yield ($R=0.898$; $p\leq0.043$). Given that the p value is less than 0.05 in the relationship between NDVI and #Pa/m2, 1000 grain weight and yield, the results are statistically significant. The results of the relationship between NDVI and PaW and T/m2 are marginally significant. This highlights the potential of the NDVI to estimate the rice yield. Fig. 5 and 6 showed the coefficient of determination, R2.

Fig. 2d shows the NDVI map constructed from the satellite image. The maximum, minimum and median NDVI, and its variance were 0.56, 0.34 and 0.51, 0.004, respectively. The NDVI values were within the range for identifying rice crops with satellite images ($0.36\leq NDVI\leq0.71$; [30]); although they were lower with respect to NDVI from UAV images. NDVI is sensitive to atmospheric noise (presence of clouds) and height between the multispectral camera and the crop. Furthermore, NDVI is affected by the seasons and date, as there are changes in the solar radiation intensity [18, 30]. Despite differences in magnitude between NDVI maps from different harvests (Fig. 2c-d), the lowest NDVI is common around areas 4 and 6, while Area 1 is associated with higher NDVI. Considering that areas 4 and 6 in the plot of land show a thicker soil, lower yield and lower NDVI, the presence of a low production environment has been identified. Area 1 has a sandy-loam soil, a higher yield and NDVI, thus this may be associated with a production environment with high potential.

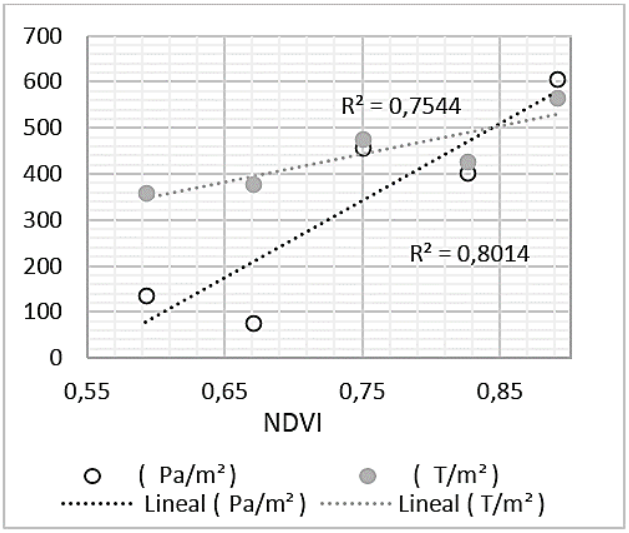


Figure 5. Normalized difference vegetation index (NDVI) during Stage of Rice Panicle Development (SRPD) *vs* #T/m^2 and #Pa/m^2 in the Milky Stage
Source: The authors.

The commercial harvest of the experimental lot was carried out in two zones. One of them included areas 4 and 6 (Dotted line, Fig. 2c; low production environment), which tend to lose price in the rice harvested due to impurities and quality. To make a difference in the quality of rice, the commercial harvest of Area 5 must be differentiated from Area 1, 2 and 3 with precision harvester. Thus, the NDVI helps to identify environments in rice [31] and harvest areas.

It is highlighted that the NDVI from satellite images possesses a resolution lower (5 to 25 cm/pixel) than the UAV images (5 cm/pixel), which is why satellite images have greater limitations to focus agronomic management problems.

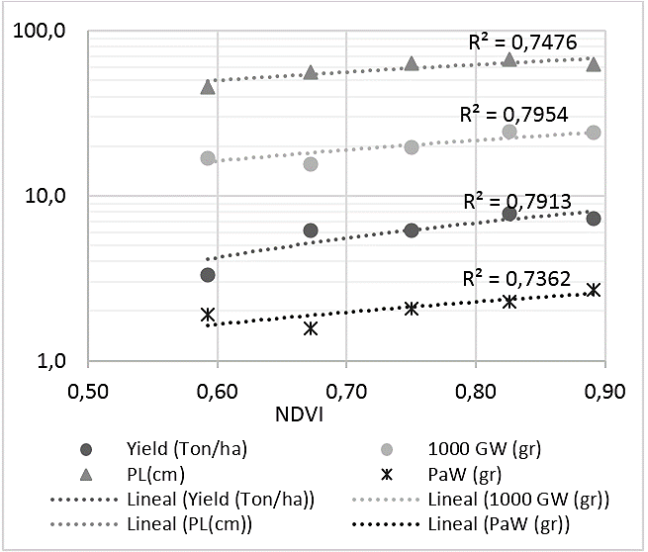


Figure 6. Normalized difference vegetation index (NDVI) *vs.* Yield, Panicle Weight (PaW), 1000 Grain Weight and Length Plant (LP)
Source: The authors.

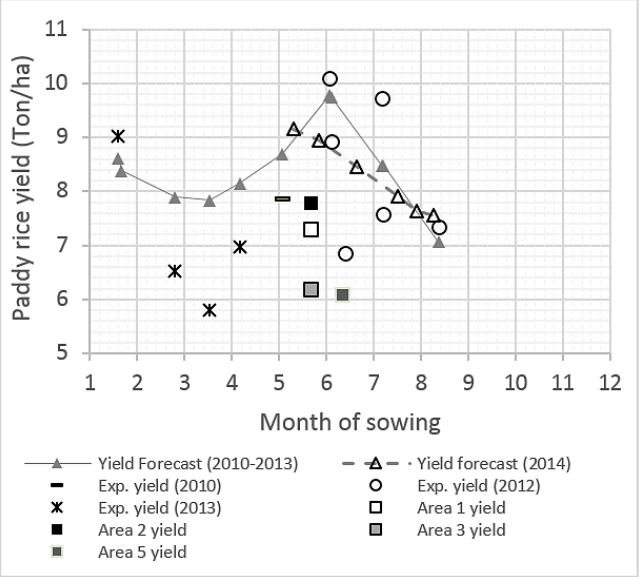


Figure 7. Paddy rice yield (Ton/ha) of FEDEARROZ-2000 in Tolima. Source: The authors. Information reported by [32] was used.

Areas 2, 3, 4, 5 and 6 showed deficiencies in leveling and sowing, which affected water distribution in the plot of land, and had consequences on crop development. In Area 2, moderate spacing between plants favored the development of strong plants which was reflected in the highest yield. The plants located in areas 3, 4 and 6 were developed with water stress during the whole cycle, limiting the yield potential. The yield from Area 5 showed how the delay in sowing affected yield by differences in rice development and changes in the environmental offer (Fig. 7). If farmers in El Espinal decide to sow after May, all cultivars would likely have lower yields ([32]; Fig. 7).

After the initiation of the reproductive stages, the NDVI map is a tool with which to diagnose rice in large scales. Rice in these stages should have reached maximum tillering, making the NDVI reach a threshold and a minimum change with respect to time (Fig. 3). The above facilitate the standardization of the method and the interpretation of information. Moreover, the rice biomass minimizes the effect of water and soil in the NDVI map [33], which is why areas with a low NDVI can be associated with abnormal spacing between plants or with rice development problems.

The NDVI accompanied by field monitoring allows the detection of rice areas with the following: Deficiency of phosphorus (delays in growth) and nitrogen, differences in the physiological stages, water stress, plant diseases, insect infestation, problems of sowing date and optimal sowing density. Nitrogen in rice is significantly correlated with NDVI in panicle initiation [17]. An NDVI taken between the panicle development and heading may predict the rice yield [17] and production environments [30].

Once the problems have been identified using the NDVI map, corrective measures should be taken to obtain a good panicle size and a good number of grains during the reproductive stage. To decrease the impact on the production due to differences in the vegetative stage of the plants, a specific agronomic management by area can be carried out with fertilizers. In the healthy crop, there can be a late application of nitrogen in the flowering stage to delay the senescence of tillers and improve the grain filling. Of 68% of the carbohydrates stored until flowering stage, 26% are invested in grain filling [34]. Thus, the reserves in the flowering stage may increase the yields from 1 to 2 ton/ha [34]. Given the case, phosphorus can also be applied to the most delayed plants to advance flowering and maturing. Methods for delaying and advancing flowering are presented in Verma et al. [35].

NDVI is a conservative indicator of water stress [36]. It may help to assess the effectiveness of the intermittent irrigation, plan differentiated irrigations [37] and, in this sense, it contributes to water productivity. Between the flowering stage and the waxy stage, corrective measures should be taken to avoid water stress and protect the grains filling and their weight.

Harvesting immature rice with moistures greater than 28% should be avoided, as this causes an increase in harvest loss of up to 8%, and impurity content of up to 10% [12,13]. Therefore, the harvest areas can be defined with an NDVI map in Milky Stage (Fig. 2c) and the NDVI temporal dynamics, since they are indicators of the stage of the rice [37,38]. This can make a difference in rice quality.

Fig. 8 shows the methodology proposed to introduce the NDVI as a tool for decision making in the productive sector.

According to Berrío et al. [39], the area of coverage by a UAV flight may be of around 9 km^2 (900ha) (depending on the resolution). This is why the tool is useful for large-scale monitoring.

The NDVI map is a tool for decision making that contributes to the effectiveness in the agronomic management [37,38,40]. The effectiveness tries to find a balance between efficiency and efficacy to achieve the greatest profitability. An NDVI map helps to apply a differentiated agronomic management for results achievement (efficacy: good plant population/m^2, good number of panicles/m^2 and a good yield). Hence, NDVI maps can help to close the rice yield gap. Fig. 7 showed the yield gap for FEDEARROZ 2000 in Espinal, Tolima. The yield gap was the difference between experimental yield (□) and

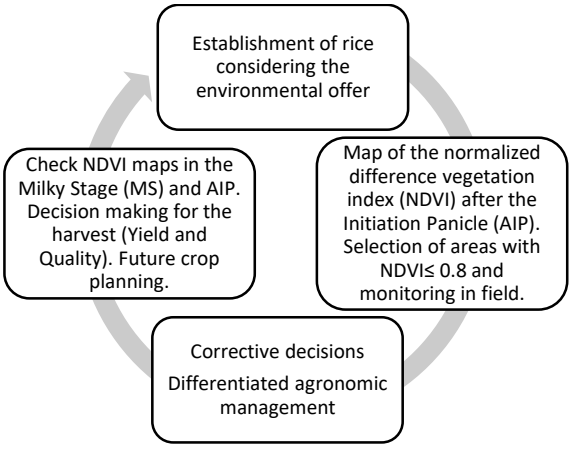


Figure 8. Methodology proposed to introduce the NDVI as a tool for decision making (Based on the Deming Cycle)
Source: The authors.

yield forecast (Δ) as reported by FEDEARROZ and CIAT [3] and Cock and Yoshida, [34].

The efficiency seeks to optimize the relationship between the resources used and the results obtained. Hence, the economic viability of NDVI maps should be supported with local economic research. The reduction of inputs, rice quality and yield increase must compensate the costs of NDVI maps.

The costs of an NDVI map in Colombia ranges between 8 and 20 dollars per hectare, and association among small-scale users is essential to reduce costs. Assuming the price of 290 US/T of paddy rice in Colombia (estimated from FEDEARROZ [41]), the investment in the NDVI map would be recovered with an increase in production of 0.07 t/ha (closing the rice yield gap; Fig. 7).

According to Preciado [13], a harvest moisture content of 18% generates losses of approximately 203 US/ha in Colombia; while with a harvest moisture content of 28% approximately 192 US/ha is lost. Hence, to schedule the harvest areas with NDVI maps helps to recover their costs.

Some multispectral cameras have begun to incorporate the high quality RGB image as a complement. This new tool of the camera will obtain the following in one single overflight with UAV: multispectral image and images to the Digital Surface Model (DSM) and the Digital Terrain Model (DTM). DSM represents the Earth's surface and includes all objects on it. DTM represents the bare ground surface without any objects [42]. The DTM information with elevation accuracies of up to 6 cm allows the design of draining, irrigation and rainwater harvesting. This would help return their costs too.

4. Conclusions

Areas with agronomic management problems were associated with an NDVI of lower than 0.8 in the stage of rice panicle development. NDVI allowed to focus areas with levelling problems, differences in the vegetative stage, water stress and abnormal spacing between plants. In addition, NDVI in the SRPD had a significant positive correlation with the 1000 grain weight, number of panicles per square meter, and the rice yield ($0.86 \leq R \leq 0.90$; $P \leq 0.043$).

The use of NDVI in the reproductive stages is an input with a great potential for the decision making to favor the grain production and quality. It can be used to make corrective agronomic management decisions or as a planning tool for future harvests (Estimating rice yield). The NDVI map in Milky Stage helped to identify production environments and to spatially and temporally plan the harvest.

The NDVI focuses on areas with limitations in the terms of rice development and growth, which is why the tool can be very useful for large-scale monitoring.

Adjusted the temporal dynamics of the NDVI for FEDEARROZ-2000, this work establishes bases to plan, monitor and control agronomic management problems with Unmanned Aerial Vehicle, multispectral camera and NDVI maps.

Acknowledgments

This project was partially funded by SENNOVA, Universidad de Ibague and COLCIENCIAS. The authors would like to give a special thanks to Oscar Barrero Mendoza (Universidad de Ibague), Nilson Alfonso Ibarra (FEDEARROZ EL Espinal), Marlon Stivel Cruz Ladino (Apprentice), Rodrigo Mendoza Cárdenas (ICA-El Espinal), Ana Milena Alonso (SENA) and apprentices of Technology in Agrobiotechnology, Technology in Agricultural Mechanization, and Technology in Agricultural Production. The experiments necessary for the development of this research were undertaken at "La Granja" Agricultural Center, “Servicio Nacional de Aprendizaje (SENA)” [National Apprenticeship Service], El Espinal, Tolima.

References

[1] Ray, D.K., Mueller, N.D., West, P.C. and Foley, J.A., Yield trends are insufficient to double global crop production by 2050. PloS one, 8(6), e66428, 2013. DOI: 10.1371/journal.pone.0066428

[2] Ray, D.K., Gerber, J.S., MacDonald, G.K., and West, P.C., Climate variation explains a third of global crop yield variability. Nature communications, 6, pp. 1-9, 2015. DOI: 10.1038/ncomms6989.

[3] FEDEARROZ and CIAT (2014). Adopción masiva de tecnología (AMTEC). Validación de modelos y parametrización de la variedad FEDEARROZ. [en línea]. 2000. [Consultado: Julio 25 de 2017]. Disponible en: https://es.slideshare.net/cgiarclimate/fe-39197270

[4] Mapplecroft. Índice de vulnerabilidad y adaptación al cambio climático en la región de América Latina y el Caribe. Corporación Andina de Fomento (CAF), 2014.

[5] Graterol E. y Torres E.A., Mejorando la competitividad del arroz en América Latina mediante el cierre de brechas de rendimiento. FLAR, CIAT, CGIAR, [en línea]. 2013. [Consultado: Nov. 21th of 2017]. Disponible en: http://flar.org/wp-content/uploads/2015/06/Taller-GRiSP-Cierre-de-brechas-ESP2.pdf

[6] Chica, J., Tirado, O. and Barreto, J.M., Indicadores de competitividad del cultivo del arroz en Colombia y Estados Unidos. Revista de Ciencias Agrícolas, 33(2), pp. 16-31, 2016.

[7] Sanint, L.R., Nuevos retos y grandes oportunidades tecnológicas para los sistemas arroceros: producción, seguridad alimentaria y disminución de la pobreza en América Latina y el Caribe, en: Degiovanni, B., Víctor, M., Martínez, R., César, P. and Motta, O., Producción eco-eficiente del arroz en América Latina. CIAT, 2010.

[8] World Water Assessment Programme -WWAP. Informe de las Naciones Unidas sobre el desarrollo de los recursos hídricos en el mundo 2016, París, UNESCO, [en líena]. 2016. [Consultado en: Julio 25 de 2017]. Disponible en: http://unesdoc.unesco.org/images/0024/002441/244103s.pdf

[9] Bouman, B.A.M., Humphreys, E., Tuong, T.P. and Barker, R. Rice and water. Advances in Agronomy 92, pp. 187-237, 2006. DOI: 10.1016/S0065-2113(04)92004-4

[10] Degiovanni, B., Víctor, M., Martínez, R., César, P. and Motta, O., Producción eco-eficiente del arroz en América Latina. CIAT, 2010.

[11] González, M. y Alonso, A.M., Tecnologías para ahorrar agua en el cultivo de arroz. Nova, 14(26), pp. 67-82, 2016. DOI: 10.22490/24629448.1757

[12] Preciado-Pérez L.G., Época oportuna de cosecha y calibración de cosechadoras para el cultivo del arroz. Memorias del curso internacional sobre el manejo del cultivo de arroz. Ibagué, [en líena]. 2014. [Consultado: enero 21 de 2017]. Disponible en: http://flar.org/ii-curso-internacional/memorias-curso-internacional/

[13] Preciado-Pérez L.G., Pérdidas al cosechar en el momento no oportuno. Boletín de la Federación Nacional de Arroceros. [en línea]. 243, pp. 1, 2011. [Consultado: enero 21 de 2017]. Disponible en: http://www.fedearroz.com.co/revistanew/correo_243.pdf

[14] López-Pérez, A., Martínez-Menes, M.R. and Fernández-Reynoso, D.S., Priorización de áreas de intervención mediante análisis morfométrico e índice de vegetación. Tecnología y Ciencias del Agua, 6(1), 121-137, 2015.

[15] Chen, R.K. and Yang, C.M., Determining the optimal timing for using LAI and NDVI to predict rice yield. J. Photogramm. Remote Sens, 10(3), pp. 239-254, 2005.

[16] Li, L., Zhang, Q. and Huang, D., A review of imaging techniques for plant phenotyping. Sensors, 14(11), pp. 20078-20111, 2014. DOI: 10.3390/s141120078
[17] Naito, H., Ogawa, S., Valencia, M.O., Mohri, H., Urano, Y., Hosoi, F. and Omasa, K., Estimating rice yield related traits and quantitative trait loci analysis under different nitrogen treatments using a simple tower-based field phenotyping system with modified single-lens reflex cameras. ISPRS Journal of Photogrammetry and Remote Sensing, 125, pp. 50-62, 2017. DOI: 10.1016/j.isprsjprs.2017.01.010
[18] Barrero, O., Rojas, D., Gonzalez, C. and Perdomo, S., Weed detection in rice fields using aerial images and neural networks. In: Signal Processing, images and artificial vision, XXI Symposium on IEEE, pp.1-4, 2016. DOI: 10.1109/STSIVA.2016.7743317
[19] Pulver, E., Manejo estratégico y producción competitiva del arroz con riego en América Latina. En: DeGiovanni, V., Martínez, C.P. y Motta, F., eds. Producción ecoeficiente del arroz en América Latina. CIAT, Colombia, 2010.
[20] Romero, L.E., Lozano, I., Garavito, A., Carabali, S.J., Triana, M., Villareal, N. and Lorieux, M., Major QTLs control resistance to rice hoja blanca virus and its vector Tagosodes orizicolus. G3: Genes, Genomes, Genetics, 4(1), pp. 133-142, 2014. DOI: 10.1534/g3.113.009373
[21] Morales, F.J. and Jennings, P.R., Rice hoja blanca: a complex plant–virus–vector pathosystem. Plant Sciences Reviews, 5(043), pp 1-16, 2010. DOI: 10.1079/PAVSNNR20105043
[22] Castilla L.y Florez E., SIFA: Sistema de fertilización en el cultivo de arroz a través de la web. Arroz, 62 (509), pp. 4-15, 2014.
[23] Garcés, G. y Castilla L., Uso del clorofilometro (indice de verdor) como estrategia en la fertilización nitrogenada en el cultivo. Arroz, 63(517), pp. 34 - 43, 2015.
[24] Lin, W., Zhang, F.C., Jing, Y.S., Jiang, X.D., Yang, S.B. and Han, X.M., Multi-temporal detection of rice phenological stages using canopy spectrum. Rice Science, 21(2), pp. 108-115, 2014. DOI: 10.1016/S1672-6308(13)60170-5
[25] Degiovanni, V.M., Gómez, J.A. y Sierra, J.M., Análisis de crecimiento y etapas de desarrollo de tres variedades de arroz (Oryza sativa L.) en Montería, Córdoba. Temas Agrarios, 9(1), 2004, pp 21-29.
[26] Dobermann, A. and Fairhurst T., Rice: Nutrient disorders and nutrient management (Vol. 1). Int. Rice Res. Inst. 2000.
[27] Chaudhary R.C., Nanda J.S. y Tran. D.V. Guía para identificar las limitaciones de campo en la producción de arroz. FAO, Rome, 2003.
[28] Yoshida, H., Bhattacharjee, D. and Cabuslay, G.S., Relationship between plant type and root growth in rice. Soil Science and Plant Nutrition, 28, pp. 473-482, 1982. DOI: 10.1080/00380768.1982.10432387
[29] Nuruzzaman, M., Yamamoto, Y., Nitta, Y., Yoshida, T and Miyazaki, A., Varietal differences in tillering ability of fourteen japonica and indica rice varieties. Soil Science and Plant Nutrition, 46, pp. 381-391, 2000. DOI: 10.1080/00380768.2000.10408792
[30] García, J., Andres, S., Martínez, M. y Joel, L., Método para identificación de cultivos de arroz (Oryza sativa L.) con base en imágenes de satélite. Agronomía Colombiana, [en línea]. 28(2), pp. 281-290, 2010. Disponible en: http://www.redalyc.org/articulo.oa?id=180315602018
[31] Castilla A., Morales F., Ramirez O. y Mayorga Z., Manejo agronómico por ambiente rumbo a una agricultura de precisión en el cultivo de arroz. Arroz, 63(519), pp. 38-43, 2015.
[32] Barrios, P.C., Giraldo, D., Llanos, L., Obando, D., Espinoza, J. and Gourdji, S., Agro-climatic risk management for better agricultural decision making in Latin America. Conference: ASABE 1st Climate Change Symposium, Illinois, 2015. DOI: 10.13031/cc.20152122545
[33] Beget, M.E. and Di Bella, C.M., Flooding: the effect of water depth on the spectral response of grass canopies. J Hydrol, 335, pp. 285-294, 2007. DOI: 10.1016/j.jhydrol.2006.11.018
[34] Cock, J.H. and Yoshida, S., Accumulation of 14 C-labelled carbohydrate before flowering and its subsequent redistribution and respiration in the rice plant. Japanese Journal of Crop Science, 41(2), pp. 226-234, 1972. DOI: 10.1626/jcs.41.226
[35] Verma, R., Katara, J.L., Samantaray, S., Patra, B.C., Sahu, R.K., Patnaik, S. and Mohapatra, T., A practical guide for successful hybrid seed production in rice-A Profitable Venture, Research Gate, pp. 1-21, 2016. DOI: 10.13140/RG.2.1.2333.5443
[36] Galiano, S.G., Assessment of vegetation indexes from remote sensing: Theoretical basis. Options Méditerranéennes, 67, pp. 65-75, 2012.
[37] Zheng, H., Cheng, T., Yao, X., Deng, X., Tian, Y., Cao, W. and Zhu, Y., Detection of rice phenology through time series analysis of ground-based spectral index data. Field Crops Research, 198, pp. 131-139, 2016. DOI: 10.1016/j.fcr.2016.08.027
[38] Wang, H., Lin, H., Munroe, D.K., Zhang, X. and Liu, P., Reconstructing rice phenology curves with frequency-based analysis and multi-temporal NDVI in double-cropping area in Jiangsu, China. Frontiers of Earth Science, 10(2), pp. 292-302, 2016. DOI: 10.1007/s11707-016-0552-9
[39] Berrio, V.A.M., Téllez, J.M. y Velasquez, D.F.A., Uso de drones para el análisis de imágenes multiespectrales en agricultura de precisión. @limentech, Ciencia y Tecnología Alimentaria, 13(1), pp. 28-40, 2015.
[40] Ajith, K., Geethalakshmi, V., Ragunath, K.P., Pazhanivelan, S. and Dheebakaran, G., Rice yield prediction using MODIS-NDVI (MOD13Q1) and land based observations. Int. J. Curr. Microbiol. App. Sci, 6(12), pp. 2277-2293, 2017. DOI: 10.20546/ijcmas.2017.612.263
[41] FEDEARROZ (2017, Nov. 10). Precio promedio mensual arroz paddy verde en Colombia Pesos / Tonelada 2009 – 2017. [en línea]. [Consultado: Nov 01, 2017]. Disponible en: http://www.fedearroz.com.co/new/precios.php
[42] Li, Z., Zhu, Q. and Gold, C., Digital terrain modeling: principles and methodology. CRC Press. Boca Raton, 2005.

M. Gonzalez-Betancourt, was awarded his BSc. in Agricultural Engineering jointly from the Universidad Nacional de Colombia (Palmira campus) and the Universidad del Valle, Cali, Colombia in 2008. He received his PhD in Engineering with an emphasis on Hydraulic Resources in 2014 from the Universidad Nacional de Colombia, Medellin, Colombia. Between 2008 and 2010, he worked at the Hydraulics Laboratory at the Universidad del Valle. Since 2009 he has been associated with the Posgrado en Aprovechamiento de Recursos Hidráulicos, research group [Postgraduate program in the use of Hydraulic Resources] at the Universidad Nacional de Colombia. From 2014 to 2017, he has worked as a Colombia-based researcher subject to the terms of the joint agreement between the "Organización de Estados Iberoamericanos" [Organization of Ibero-American States], the "Servicio Nacional de Aprendizaje" [National Apprenticeship Service] and "COLCIENCIAS" [Administrative Department of Science, Technology and Innovation]. Currently, he is a professor in Tecnológico de Antioquia, Medellín, Colombia.
ORCID: 0000-0001-5485-8043

Z.L. Mayorga-Ruíz, was awarded her BSc. in Agronomic Engineering from the Universidad del Tolima, Ibague, Colombia. Between 2014 and 2016, she worked at FEDEARROZ [National Rice Growers Federation] as technical assistant in Ibague, Colombia. Since 2016, she has worked as a researcher at the Servicio Nacional de Aprendizaje (SENA) and has an association with the SENAGROTIC research group.
ORCID: 0000-0003-0403-0082

UNIVERSIDAD NACIONAL DE COLOMBIA
SEDE MEDELLÍN
FACULTAD DE MINAS



DYNA
http://dyna.medellin.unal.edu.co/

Effects of cutting parameters on surface roughness and hardness in milling of AISI 304 steel

Luis Wilfredo Hernández-González [a], Roberto Pérez-Rodríguez [a], Ana María Quesada-Estrada [b] & Luminita Dumitrescu [b]

[a] *Centro de Estudios CAD/CAM, Universidad de Holguín, Holguín, Cuba. wilfredo@uho.edu.cu, roberto.perez@uho.edu.cu*
[b] *Departamento de Ingeniería Mecánica. Universidad de Holguín, Holguín, Cuba. aquesada@uho.edu.cu, dumitrescul@uho.edu.cu*

Received: May 11th, 2017. Received in revised form: January 23th, 2018. Accepted: March 25th, 2018.

Abstract
This paper presents an experimental study in dry milling of austenitic AISI 304 stainless steel with hard alloy milling cutters, related to the influence of feed rate and cutting speed on surface roughness and hardness. The results show that machining caused a decrease in hardness of the workpiece with respect to the initial hardness, however, the feed rate and the cutting speed did not show any statistically significant effects on the established level of confidence. The lower surface roughness values were obtained for higher cutting speeds and for smaller feed rates, being the cutting speed the factor of greater contribution. The multiple regression model was computed and the requirements were tested to state that the variables are correlated. Finally, the most appropriate cutting parameters were determined using the contour plot.

Keywords: surface roughness; hardness; milling; AISI 304 steel; analysis of variance and regression.

Efectos de los parámetros de corte en la rugosidad superficial y la dureza en el fresado del acero AISI 304

Resumen
Este trabajo presenta un estudio experimental, en el fresado en seco del acero inoxidable austenítico AISI 304 con fresas de aleación dura, relacionado con la influencia del avance y de la velocidad de corte sobre la rugosidad superficial y la dureza. Los resultados muestran que, el maquinado provocó una disminución de la dureza de la pieza con relación a la pieza inicial, no obstante, el avance y la velocidad de corte no representaron efectos estadísticamente significativos para el nivel de confianza establecido. Los menores valores de rugosidad superficial se obtuvieron para las mayores velocidades de corte y para los menores avances, siendo la velocidad de corte el factor de mayor contribución. El modelo de regresión múltiple fue calculado y se comprobaron los requisitos para plantear que las variables están correlacionadas. Finalmente, se determinaron los parámetros de corte más adecuados utilizando el gráfico de contorno.

Palabras clave: rugosidad superficial; dureza; fresado; acero AISI 304; análisis de varianza y regresión.

1. Introduction

Austenitic stainless steel materials play an important role in many fields, such as modern power and chemical industries. However, austenitic stainless steel is difficult to machine [1]. Its poor machinability is usually due to low heat conductivity, high tensile strength, high ductility, high fracture toughness and high work-hardening rate [1,2].

A number of difficulties occur when machining austenitic stainless steel, such as intensive vibration, poor surface finish, built-up edge on the tool flank face, and cutting edge breakage [3].

In recent years, research has generally been focused on the role of cutting fluids and machining variables, surface roughness and cutting forces, and milling of stainless steel.

The effects of cryogenic cooling on cutting forces in the milling process of AISI 304 stainless steel, using different cutting speeds, were investigated by Nalbant and Yildiz [1].

How to cite: Hernández-González, L.W., Pérez-Rodríguez, R., Quesada-Estrada, A.M. and Dumitrescu, L., Effects of cutting parameters on surface roughness and hardness in milling of AISI 304 steel. DYNA, 85(205), pp. 57-63, June, 2018.

© The author; licensee Universidad Nacional de Colombia.

Influence of radial depth on vibration, chip formation and surface roughness during face milling of AISI304 stainless steel with cemented carbide milling cutters, were studied by Shen and collaborators [3]. They found that high radial depth increases the vibration, and the machining quality deteriorates.

Results of dry and wet milling of AISI 316 stainless steel were compared by Ozcelik et al. [4], in terms of tool wear, surface roughness and force components. The authors established that tools used in wet milling failed catastrophically before reaching the fixed machining length, although cutting fluid application was efficient at low-cutting speeds, and in some cutting conditions, dry milling gave lower surface roughness.

Hamdan et al. presented an optimization method of machining parameters in high-speed milling of stainless steel with coated carbide tool using different types of lubrication modes. This study showed feed rate as the most prominent factor influencing cutting force and surface roughness, moreover, lower values of feed rate and depth of cut were recommended to achieve minimum machining forces and better surface roughness [5].

The research paper by Thangarasu et al. [6], made a study on optimization of milling parameters using Multi Objective Genetic Algorithm. They found that feed rate and depth of cut were the most significant parameters affecting surface roughness.

Nurul and colleagues [7], revealed that surface roughness was reduced when milling was done under the influence of magnetic field, and feed per tooth had the most significant effect on Ra, followed by cutting speed. Authors recommended a combination of higher cutting speed, lower feed rate, and small depth of cut to produce a good surface roughness in machined stainless steel specimens.

A study of machining of AISI 304L steel in dry milling was performed by Maurotto et al. [8], with the aim of characterizing its surface quality and microstructure. They found that high feed per tooth with less depths of cut and cutting speed rate, improved the surface roughness, besides cutting speed was the variable with the largest influence on it.

Muñoz-Escalona et al. [9] showed that dry cutting environment was the best option in terms of power consumption, surface roughness and materials microhardness values in milling of AISI 303 steel. The authors emphasized that high cutting speed with less feed rate improved these results.

Influence of undeformed chip thickness on cutting forces and temperature was studied by San-Juan et al. [10]. In their research, a comparison between up-milling and down-milling was performed, over the AISI 316L steel.

Influence of milling on the development of stress corrosion cracks in austenitic stainless steel was examined by Lyon et al. [11]. They found that machined samples have a biaxial tensile surface stress with a higher stress in the direction of milling.

Taner et al. [12] examined the effect of minimal quantity lubrication on surface integrity in robotic milling of AISI 316L steel. Their experiments showed that surface roughness is not affected by the MQL settings. However, the surface residual stresses can be decreased by well controlled MQL oil flow.

Table 1.
Chemical composition of AISI 304 stainless steel workpiece (mass fraction, %).

C	Si	Mn	P	S	Cr	Mo	Ni	Al
0,03	0,46	1,85	0,03	0,004	18,55	0,66	8,94	0,00
Co	Ti	V	W	Sn	Pb	As	B	Fe
0,27	0,00	0,05	0,08	0,02	0,00	0,01	0,00	68,57

Source: The authors.

Maurel-Pantel et al. analyzed the effect of milling cutter angular position on cutting force, using the numerical simulation and the experimental study, in milling of AISI 304L steel [13].

Kumbhar et al. performed the optimization of milling parameters of stainless steel 304, using surface roughness and material removal rate as target variables [14].

A geometric approach for the milling cutter tool wear prediction was developed by Liu et al., in machining of AISI 304 steel with the high vanadium high-speed steel tool [15].

Based on this review, studies focused on searching for an optimum combination of cutting parameters to obtain a better value of surface roughness such as: high speed machining by Thangarasu et al. [6]; articles on medium speed machining by Nurul et al. [7], Maurotto et al. [8], Muñoz-Escalona et al. [9], as well as Kumbhar et al. [14]. However, there is not much research on low cutting speed, and the effect of feed rate and cutting speed on workpiece hardness has not been considered; therefore, these are the aims of this work.

2. Experimental procedure

The experiments are designed to investigate the effects of cutting speed and feed rate on surface roughness and hardness in dry milling of AISI 304 austenitic stainless steel.

AISI 304 steel in the hot rolled condition was the material chosen for the present study. It was provided in the form of plate with dimensions 800 mm x 20 mm x 20 mm. Its chemical composition was determined using a spectrometer of spark emission, and is presented in Table 1.

Machining trials were carried out on a X5032 universal milling machine, equipped with a maximum spindle speed of 1 500 r/min and a 7,5 kW drive motor.

Five workpieces for milling tests were used, with dimensions of 75 mm × 20 mm × 20 mm. Samples were identified with letters (A, B, C, D and E), and its lateral side with numbers (1, 2, 3 and 4).

The cutting tools used in this study were two end mill with three helicoidal flutes and a diameter of 16 mm. Chemical composition of the cemented carbide milling cutter was: 5 % of carbide of titanium, 10 % of cobalt and 85 % of carbide of tungsten.

Three cutting speed and three feed rate, as well as a constant depth of cut (0,5 mm), and two replicates were included, leading to 18 experimental runs. Tests were randomized to minimize influences of the cutting tool wear and operator on the results. The machining experiment was stopped every pass to record the surface roughness (R_a) and hardness (HRB) of workpiece. The matrix of experiment is presented in Table 2.

Table 2.
Matrix of experiment.

Nr.	Order	V (m/min)	f (mm/min)	Tool	Sample	Replica
1	6	1,884	23,5	1	A1	1
2	7	1,884	23,5	2	A2	2
3	1	1,884	37,5	1	A3	1
4	11	1,884	37,5	2	A4	2
5	17	1,884	60	1	B1	1
6	12	1,884	60	2	B2	2
7	13	5,931	23,5	1	B3	1
8	16	5,931	23,5	2	B4	2
9	3	5,931	37,5	1	C1	1
10	8	5,931	37,5	2	C2	2
11	18	5,931	60	1	C3	1
12	4	5,931	60	2	C4	2
13	9	11,812	23,5	1	D1	1
14	14	11,812	23,5	2	D2	2
15	5	11,812	37,5	1	D3	1
16	15	11,812	37,5	2	D4	2
17	2	11,812	60	1	E1	1
18	10	11,812	60	2	E2	2

Source: The authors.

In order to analyze possible changes in hardness of machined surface, ten hardness tests were conducted in each sample surface using a HRS - 150 hardness equipment. Hardness of the initial workpiece was measured in two specimens, with dimensions of 25 mm × 20 mm × 20 mm.

When a number of measurements of a same parameter is repeated, it could be obtained atypical or suspicious values, because it presents a notable difference with respect to other ones. Generally, applying normal distribution curve's properties, suspicious values can be detected and eliminated.

For numerous measurements of a magnitude, the average ($\bar{x}$) and standard deviation (S) are calculated. Then, the interval is set up (eq. 1) for a given confidence level, and all the values that are left out of the aforementioned range are eliminated, because they are considered unusual. So, necessary calculations to express the final result are made again, without the uncommon values [16].

$$\bar{x} \pm t\, S \quad (1)$$

where t is interval that contain to μ. For 95 % of confidence level t = 1,96 [16].

In the Territorial Office of Standardization of Holguín, the surface roughness was determined using standard samples of comparison. It is a method in which touch, vision and experience are used to compare the roughness of a pattern plate with the surface to be evaluated. Grades are assigned to this surface according to the standards of the pattern used.

3. Discussion of results

The results obtained in the present investigation, as well as their discussion, are shown below.

The surface roughness was measured two times, while ten hardness measure were conducted, for each surface of the samples.

The mean, median, standardized bias, standardized kurtosis, first quartile and third quartile, for the hardness and surface roughness of machined samples, are shown in Table 3.

Table 3.
Mean, median, standardized bias, standardized kurtosis, first quartile and third quartile, for the hardness and surface roughness of machined samples.

Variab.	Mean	Median	Stand. bias	Stand. kurtosis	First quartile	Third quartile
HB_{A1}	145,0	144,0	0,4486	- 0,7003	142,0	150,0
HB_{A2}	139,3	140,5	- 0,236	- 1,0857	128,0	147,0
HB_{A3}	136,1	137,0	- 0,651	- 1,0882	132,0	139,0
HB_{A4}	139,2	143,0	- 1,327	0,4927	135,0	144,0
HB_{B1}	147,0	131,5	0,7521	- 0,9582	118,0	174,0
HB_{B2}	136,5	137,0	- 0,560	- 0,6919	132,0	139,0
HB_{B3}	140,6	140,5	0,7546	- 0,2545	137,0	142,0
HB_{B4}	139,5	139,0	0,9545	- 0,2935	137,0	142,0
HB_{C1}	135,0	137,0	- 0,870	- 0,4728	130,0	139,0
HB_{C2}	141,8	142,0	- 0,843	0,1555	142,0	142,0
HB_{C3}	141,7	142,0	- 0,461	- 0,8874	139,0	144,0
HB_{C4}	141,8	142,0	- 0,843	0,1555	142,0	142,0
HB_{D1}	136,4	137,0	0,5598	- 0,1826	135,0	137,0
HB_{D2}	135,3	135,0	- 1,147	1,2578	135,0	137,0
HB_{D3}	137,0	137,0	0,0	0,0518	137,0	137,0
HB_{D4}	138,4	139,0	- 1,336	- 0,7904	137,0	139,0
HB_{E1}	138,7	139,0	1,1475	1,2578	137,0	139,0
HB_{E2}	136,3	137,0	- 0,864	0,4471	135,0	137,0
R_a	3,305	2,4	0,3641	- 1,6285	0,8	6,3

Source: The authors.

Generally, if the data are symmetric the mean and median coincide (HB_{D3}). Usually, we find that median < mean if the distribution is skewed to the right (HB_{A1}, HB_{B1}, HB_{B3}, HB_{B4}, HB_{D2} and R_a), whereas median > mean if the distribution is skewed to the left (the rest).

When an ordered set of data is divided into four equal parts, the division points are called quartiles. The first or lower quartile, is a value that has approximately 25 % of the observations below it and approximately 75 % of the observations above. The second quartile, has approximately 50 % of the observations below its value. The second quartile is exactly equal to the median. The third or upper quartile, has approximately 75 % of the observations below its value.

The lowest first quartile (HB_{B1} = 118) and the highest third quartile (HB_{B1} = 174), coincide with the extreme values of cutting parameters (f = 60 mm/min and V = 1,884 m/min). Consequently, it coincides with the highest interquartile range (56), which indicates the maximum hardness variability. So, the difference between the Mean (147) and the Medium (131,5) is the highest (15.5) also.

The milling process is very difficult in these conditions (f = 60 mm/min and V = 1,884 m/min), because the distance in meters traveled by a point in the periphery of the milling cutter in one minute (v) is very low, and on the other hand, the linear distance traveled by the cutting tool at a constant feed speed with respect to the workpiece in one minute (f) is high. The vibrations increase during the cutting process.

Another high interquartile range were registered for HB_{A2} (19), HB_{A4} (9), HB_{C1} (9) and HB_{A1} (8).

The standardized bias and the standardized kurtosis can be used to determine if the sample comes from a normal distribution. Values of these statistical ones outside the rank from -2 to 2 indicate significant deviations of normality. In this case, the value of the standardized bias and standardized kurtosis are within the rank of data a normal distribution.

Atypical values of hardness were not found, then the average was determined, and converted from HRB to HB

according to [17]. The hardness of the first sample was 181 HB and for the second 171 HB, therefore, the average hardness for this steel in supply state was 176 HB, a value that is within the theoretical parameters of original hardness of the material.

The hardness of the machined workpiece was 139 HB, that is, it decreased by 21 % with respect to the original hardness of the specimen (176 HB), which could be related to the heating of workpiece during the cutting process, this fact could be beneficial to a roughing pass, not so for a finishing pass.

Fig. 1, shows the effect of feed rate (a) and cutting speed (b) on the hardness of the machined workpiece. The increase of feed rate caused an initial decrease and then an increase in hardness for the lower cutting speeds, while for V = 11,81 m/min, hardness first grew and then tended to remain constant.

Fig. 2 shows the effect of feed rate (a) and cutting speed (b) on the surface roughness of the machined workpiece. The average surface roughness recorded was 3,3 μm, close to the recommended value for this type of operation (R_a = 3,2 μm), and ranged from 0,4 μm to 6,3 μm.

The increase of feed rate (Fig. 2a) caused an increase in the surface roughness value, while the increase of cutting speed induced the reduction of roughness (Fig. 2b).

As for feed rate, it is usually assumed that surface roughness increases with the increase of feed rate, but not in linear proportion [18]. In the present study, a lower value of surface roughness was obtained at a lower feed rate, coinciding with the investigations of Hamdan et al. [5], Nurul et al. [7], Muñoz-Escalona et al. [9].

By decreasing feed rate and depth of cut, less material has to be cut per tooth per revolution, thus energy required is lower. Consequently, this would reduce the cutting forces, thus, preserve material properties against residual stress, the change in micro hardness at the subsurface, and leading to better surface roughness [4].

The result of cutting speed agrees with what is generally accepted, and with studies by Ozcelik et al. [4], Hamdan et al. [5], Thangarasu et al. [6], Muñoz-Escalona et al. [9], Kumar and Venkateswara [19].

The multifactorial analysis of variance (Table 4) shows that the values of P are lower than 0,05; so the feed rate and cutting speed have a statistically significant effect on the surface roughness, at 95,0 % confidence level. However, the interaction of these two factors does not have a significant effect on the dependent variable, since the value of p is greater than 0,05.

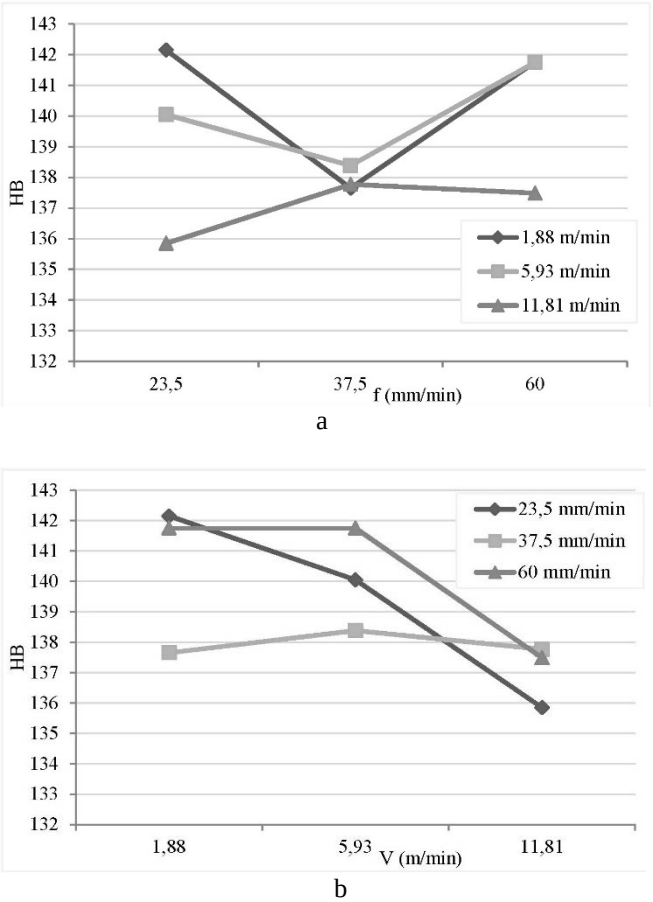


Figure 1. Effect of feed rate (a) and cutting speed (b) on the hardness of the workpiece.
Source: The authors.

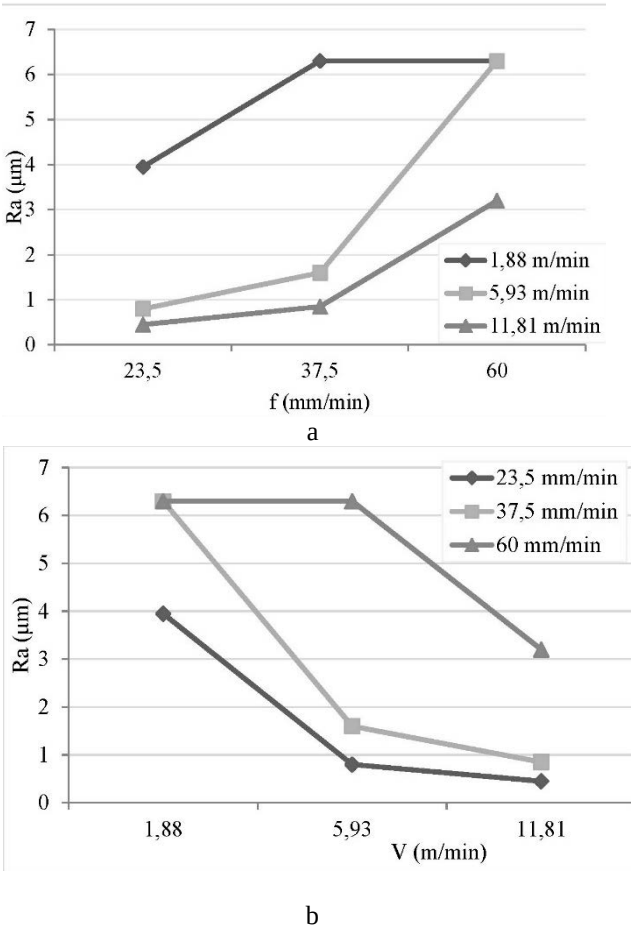


Figure 2. Effect of feed rate (a) and cutting speed (b) on the surface roughness of the workpiece.
Source: The authors.

Table 4.
Multifactor variance analysis of surface roughness.

Source	Sum of Square	Degrees of Freedom	Mean Square	F	P
f	38,814	2	19,407	14,07	0,001
V	49,881	2	24,940	18,08	0,000
fV	12,698	4	3,174	2,30	0,137
Error	12,41	9	1,379		
Total	113,809	17			

Source: The authors.

3. Evaluation of results using the correlation among feed rate, cutting speed and surface roughness.

Below, the results obtained when using the feed rate, cutting speed and surface roughness in the regression study are shown.

To determine whether the variables (f, V, and R_a) are related, the following conditions must be met:

- The coefficient of determination (R2) must be at least greater than 50%.
- The F-value of the analysis of variance of the model is less than 0,05 (there is a statistically significant relationship between the variables with a confidence level at 95,0 %).
- The P-value (the probability of t) of the independent variables should be less than 0,05 (statistically significant with a confidence level at 95,0 %).
- The basic assumptions of regression analysis [20].

To determine the fitting model, multiple regression analysis is performed using the STATGRAPHICS software, equation obtained is as follows:

$$R_a = 0{,}129661\ f - 0{,}321637\ V \quad (2)$$

The R^2 statistic indicates that the fitting model accounts for 88,62 % of the variability in R_a, sufficient value.

Table 5 shows that the value of P (probability of F) is less than 0,05; so there is a statistically significant relationship between the surface roughness and the independent variables for a confidence level at 95,0 %.

In Table 6, the P (probability of t) values of the coefficients are shown, they are less than 0,05; so they are statistically significant for a 95% confidence level.

Table 5.
Analysis of variance of the multiple regression model for surface roughness.

Source	Sum of Square	Degrees of Freedom	Mean Square	F	P
Model	275,175	2	137,587	62,34	0,000
Residual error	35,315	16	2,207		
Total	310,49	18			

Source: The authors.

Table 6.
Analysis of variance of the coefficients of the multiple regression model.

Coefficients	Estimating	Standard error	t	P
f	0,1296	0,01341	9,6623	0,000
V	-0,3216	0,07493	-4,292	0,000

Source: The authors.

In order to validate the model, it was verified that the basic assumptions were fulfilled, according to the classical Astakhov [21], it is sufficient that they fulfill the homoscedasticity and non-autocorrelation assumptions of the residues, and that coefficients of variables are statistically significant. In the present investigation, the assumptions of normality and zero mean were also checked. EVIEWS software was used for this purpose.

From the obtained histogram, the assumptions of normality and null mean were verified.

The critical region is: Probability (Jarque-Bera) < α (0,05 % significance level).

Decision: 0,71 > 0,05; therefore, the normality assumption is fulfilled.

The mean is equal to $5{,}34\ 10^{-16}$ and the assumption of zero mean is fulfilled.

The Breusch-Godfrey test was used to verify the non-autocorrelation assumption. The critical region is: Probability ($n\ R^2$) <α.

For non-first-order serial autocorrelation: 0,307 > 0,05. Therefore, the assumption is fulfilled.

For non-order serial autocorrelation: 0,590 > 0,05. Consequently, the assumption is also fulfilled.

To verify compliance with the homoscedasticity assumption, the assumption will be verified with the non-crossover regression terms.

Critical Region: Probability ($n\ R^2$) <α.

Decision: 0,055 > 0,05. Therefore, the assumption is fulfilled.

Consequently, the conditions are fulfilled to state that, the variables feed rate, cutting speed and surface roughness are related.

Figure 3 shows the contour plot to determine the lowest surface roughness values and their corresponding cutting speed and feed rate values. The best surface roughness values (Ra ≤ 2 μm) were obtained for the feed rates of f ≤ 43 mm/min, and for cutting speeds of V ≥ 6 m/min.

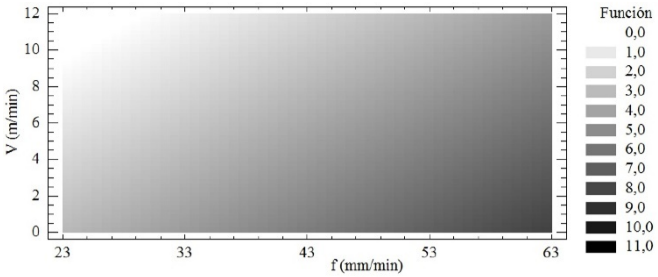


Figure 3. Contour plot for surface roughness.
Source: The authors.

4. Conclusions

- When analyzing the results of dry milling of austenitic stainless steel AISI 304, with a milling cutter of uncoated carbide inserts, they show that it is possible to obtain an adequate surface roughness for low values of feed rate and cutting speed. The grinding operation could be discarded.
- The hardness of the machined workpiece decreased by 21 % with respect to the original hardness, which could be

related to the heating of the workpiece during the cutting process. However, no significant change in hardness was observed with increasing feed rate and cutting speed. This was confirmed by the analysis of variance, since these variables did not present a statistically significant effect for a 95 % confidence level.

- The highest interquartile ranges of hardness of the machined workpiece were observed for the lower values of cutting speed and the higher feeding speed, that is, a greater dispersion in the results, which is related to an increase in the vibrations of the cutting process, and therefore, the surface roughness worsens.
- The statistical importance of cutting speed and feed rate in the surface roughness of the milled workpiece was verified. Being the cutting speed, the factor that most contributed to the variation of roughness.
- The correlation equation between feed rate, cutting speed and surface roughness was determined. In addition, the model was verified by means of: the calculation of the coefficient of determination, the analysis of variance of the model, the statistical importance of the independent variables and the fulfillment of the basic assumptions of the regression analysis.
- The contour plot of the model allowed to determine the best values of surface roughness ($Ra \leq 2$ μm), which were obtained for feed rates of $f \leq 43$ mm/min, and for cutting speeds of $V \geq 6$ m/min.

Acknowledgements

The authors would like to thank Professors Alberto Lewis Rodríguez, David Verdecia Fruto, Raúl Reyes Camareno, Romilio Montero Sarmiento, as well as Professor Irma Lerma Gómez, for the support provided to carry out this research.

References

[1] Nalbant, M. and Yildiz, Y., Effect of cryogenic cooling in milling process of AISI 304 stainless steel. Transactions of Nonferrous Metals Society of China, 21(1), pp. 72-79, 2011. DOI: 10.1016/S1003-6326(11)60680-8

[2] Ciftci, I., Machining of austenitic stainless steels using CVD multi-layer coated cemented carbide tools. Tribology International, 39(6), pp. 565-569, 2006. DOI: 10.1016/j.triboint.2005.05.005

[3] Shen, Y., Chen, Y., Zhang, L., Fang, H., Pang, J., Liu, M., Wang, S., Ma, X., Zhang, J. and Liu, Z., Effect of radial depth on vibration and surface roughness during face milling of austenitic stainless steel. Transactions of Tianjin University, 17(5), pp. 336-339, 2011. DOI: 10.1007/s12209-011-1604-6

[4] Ozcelik, B., Kuram, E. and Simsek, B.T., Comparison of dry and wet end milling of AISI 316 stainless steel, Materials and Manufacturing Processes, 26(8), pp. 1041-1049, 2011. DOI: 10.1080/10426914.2010.515645

[5] Hamdan, A., Sarhan, A. and Hamdi, M., An optimization method of the machining parameters in high-speed machining of stainless steel using coated carbide tool for best surface finish. International Journal of Advanced Manufacturing Technology, 58(1), pp. 81-91, 2012. DOI: 10.1007/s00170-011-3392-5

[6] Thangarasu, V.S., Devaraj, G. and Sivasubramanian, R., High speed CNC machining of AISI 304 stainless steel; optimization of process parameters by MOGA. International Journal of Engineering, Science and Technology [Online]. 4(3), 2012. [date of reference May 25th of 2016]. Available at: http://www.oalib.com/paper/1333002#.WKMqvnvcq7w

[7] Nurul, A.K., Akma, S., Izzati, S.N. and Arif, M.D., Surface roughness optimization in end milling of stainless steel AISI 304 with uncoated WC-Co insert under magnetic field, Advanced Materials Research, 576, pp. 119-122, 2012. DOI: 10.4028/www.scientific.net/AMR.576.119

[8] Maurotto, A., Tsivoulas, D. and Burke, M.G., Surface integrity in dry milling of 304L steel: a parametric study, Procedia CIRP, 13, pp. 156-162, 2014. DOI: 10.1016/j.procir.2014.04.027

[9] Muñoz-Escalona, P., Shokrani, A. and Newman, S.T., Influence of cutting environments on surface integrity and power consumption of austenitic stainless steel, Robotics and Computer-Integrated Manufacturing, 36, pp. 60-69, 2015. DOI: 10.1016/j.rcim.2014.12.013

[10] San-Juan, M., Martín, Ó., de Tiedra, M.P., Santos F.J., López, R. and Cebrián, J.A., Study of cutting forces and temperatures in milling of AISI 316L, Procedia Engineering, 132, pp. 500-506, 2015. DOI: 10.1016/j.proeng.2015.12.525

[11] Lyon, K.N., Marrow, T.J. and Lyon, S.B., Influence of milling on the development of stress corrosion cracks in austenitic stainless steel, Journal of Materials Processing Technology, 218, pp. 32-37, 2015. DOI: 10.1016/j.jmatprotec.2014.11.038

[12] Taner, L., Gu, Y. and Grace, M., Effects of minimal quantity lubrication (MQL) on surface integrity in robotic milling of austenitic stainless steel, Procedia CIRP, 45, pp. 215-218, 2016. DOI: 10.1016/j.procir.2016.02.337

[13] Maurel-Pantel, A., Fontaine, M., Thibaud S. and Gelin, J.C., 3D FEM simulations of shoulder milling operations on a 304L stainless steel, Simulation Modelling Practice and Theory, 22, pp. 13-27, 2012. DOI: 10.1016/j.simpat.2011.10.009

[14] Kumbhar, A., Bhosale, R., Modi, A., Jadhav, S. Nipanikar, S., and Kulkarni, A., Multi-objective optimization of machining parameters in CNC end milling of stainless steel 304, International Journal of Innovative Research in Science, Engineering and Technology, 4(9), pp. 8419-8426, 2015. DOI: 10.15680/IJIRSET.2015.0409061

[15] Liu, H-B., Wang, Y-Q., Wu, D. and Hou B., Mesh node rigid moving algorithm for the uncoated milling cutter tool wear prediction considering periodic process variables, Proceedings of the Institution of Mechanical Engineers Part C Journal of Mechanical Engineering Science, (203-210), pp. 1989-1996, 2016. DOI: 10.1177/0954406216646602

[16] Ostle, B., Estadística Aplicada. La Habana: Científico Técnico, 1981.

[17] ASM. Metals Handbook Desk Edition. New York: ASM International, 1998.

[18] Chang, C.K. and Lu, H.S., Study on the prediction model of surface roughness for side milling operations, International Journal of Advanced Manufacturing Technology, 29, pp. 867-878, 2006. DOI: 10.1007/s00170-005-2604-2

[19] Kumar, N.S. and Venkateswara, P., Selection of optimum tool geometry and cutting conditions using a surface roughness prediction model for end milling. International Journal of Advanced Manufacturing Technology, 26(11), pp. 1202-1210,2005. DOI: 10.1007/s00170-004-2110-y

[20] Pupo, J., González, E., Neníngер, D. y Gómez, R., Análisis de regresión y series cronológicas, La Habana: Félix Varela, 2004.

[21] Astakhov, V.P., Design of experiments in metal cutting tests, in Briscoe B.J. Tribology of Metal Cutting, 1a ed., London, Elsevier Ltd., 2006. pp. 276-324.

L.W. Hernández-González, is a professor in the CAD/CAM Study Center at the University of Holguín, Cuba. He is BSc. in Mechanical Engineer, MSc. of Science in CAD/CAM (2007), and PhD (2012) at the University of Holguín, Cuba too. He has more than 25 publications and more than 40 communications in Congress. He was a visiting professor at Universidad Autónoma de Nuevo León, México and at Tecnológico de Monterrey, Campus Monterrey, México. His research interests include Concurrent Engineering, Micro Machining, HSM, and CAD/CAM systems for manufacturing industry.
ORCID: 0000-0002-6122-4935

R. Pérez-Rodríguez, is the Director of the CAD/CAM Study Center at the University of Holguín, Cuba. He is BSc. in Mechanical Engineer at the

University of Holguín too. He received his PhD in Mechanical Engineering by the Polytechnic University of Catalonia (Barcelona Tech), Spain (2002). He was a visiting professor at Integrated Manufacturing System Center (2004); Research Chair of Rapid Products Development for Emergent Markets (2009); Mechatronic Department (2012); and National Research Department (2016) at Tecnológico de Monterrey, Mexico. His research interests include Concurrent Engineering, Design Theory and Methodology, HSM, RmMT, Micro Machining and CAD/CAM systems for manufacturing industry.
ORCID: 0000-0001-5741-5168

A.M. Quesada-Estrada, is a professor in the Mechanical Engineering Department at the University of Holguın in Cuba. She is BSc. in Mechanical Engineer at the University of Holguin too. She received her PhD degree in Mechanical Engineering at 'Jose Antonio Echeverria' Higher Technical University (La Habana, Cuba, 1991). She has more than 20 publications and more than 35 communications in Congress. She was a visiting professor at Don State Technical University (Rostov-on-Don, Russia). Her research interests include Cutting Tools, Machine Tools, Manufacturing Process, and CAD/CAM systems.
ORCID: 0000-0002-6131-6928

L. Dumitrescu, is a professor in the Mechanical Engineering Department at the University of Holguın in Cuba. She is BSc. in Mechanical Engineer at the University of Holguin too. She received her MSc degree in Agricultural Machinery at Holguin University (2007). She has more than 15 publications and more than 20 communications in Congress. Her research interests include Material Science, Cutting Tools, Machine Tools and Manufacturing Process.
ORCID: 0000-0001-7350-9922



UNIVERSIDAD NACIONAL DE COLOMBIA
SEDE MEDELLÍN
FACULTAD DE MINAS

Área Curricular de Ingeniería Mecánica

Oferta de Posgrados

Maestría en Ingeniería - Ingeniería Mecánica

Mayor información:

E-mail: acmecanica_med@unal.edu.co
Teléfono: (57-4) 4259262

UNIVERSIDAD NACIONAL DE COLOMBIA
SEDE MEDELLÍN
FACULTAD DE MINAS



DYNA
http://dyna.medellin.unal.edu.co/

Verification of the vibrational theoretical assignment of the DADP using isotopic labelling

Eduardo Espinosa-Fuentes [ab], Edgardo Meza-Fuentes [c], Fredy Colpas-Castillo [d], John R. Castro-Suarez [e], Gilberto Chiquillo-Correa [d] & Malka Mora [f]

[a] *Grupo GESSA, Departamento de Ingeniera Civil y Ambiental, Corporación Universidad de la Costa, Barranquilla, Colombia.*
[b] *Grupo de investigación GIDE Universidad Libre, Barranquilla, Colombia. eduardo.espinosa.fuentes@gmail.com*
[c] *Grupo de Carboquímica, Universidad de Cartagena, Cartagena, Colombia. emezaf@unicartagena.edu.co*
[d] *Grupo de Estudios en Materiales y Combustibles, Universidad de Cartagena, Cartagena, Colombia. fcolpasc1@unicartagena.edu.co*
[e] *Grupo KUAGRO, Fundación Universitaria Colombo Internacional-UNICOLOMBO, Cartagena, Colombia. jhoncs54@yahoo.com.mx*
[f] *Departamento de Ciencias Exactas y Naturales, Corporación Universidad de la Costa, Barranquilla, Colombia. mmora10@cuc.edu.co*

Received: September 20th, de 2016. Received in revised form: June 15th, 2017. Accepted: October 5th, 2017

Abstract
This work deals with the comparison of the theoretical assignment of the DADP vibrational spectrum with the experimental displacements by isotopic labeling. For this, the DADP-C_4 and DADP-C_2 isotopomers were synthesized from acetone labeled isotopically in the methyl and the carbonyl carbon atoms, respectively. The acetone and DADP-isotopomer compounds were characterized using Raman and infrared spectroscopy. Theoretical assignments were taken from previous studies on the potential energy distribution of a vibrational mode, which provide an approach to the internal coordinates related to each band. The selective isotopic labeling allowed us to approach to the dependence of each band, because the energy of a molecular vibration also depends on the reciprocal mass of the atoms involved. In general, the results showed that some bands assigned experimentally do not coincide with the theoretical assignments by quantum mechanical simulations.

Keywords: diacetone diperoxide; isotopomer; Raman and infrared spectroscopy; molecular vibration.

Verificación de la asignación vibracional teórica de DADP usando marcaje isotópico

Resumen
Este trabajo trata sobre la comparación de la asignación teórica del espectro vibracional de DADP con los desplazamientos experimentales por marcación isotópica. Para ello, se sintetizaron los isotopómeros DADP-C_4 y DADP-C_2, los cuales son isotopómeros parcialmente marcados. DADP-C_4 y DADP-C_2 fueron sintetizados a partir de acetona marcada isotópicamente en los átomos de carbonos del grupo metilo y carbonilo, respectivamente. La acetona y los compuestos isotopómeros de DADP fueron caracterizados usando espectroscopia Raman e Infrarroja. Las asignaciones teóricas fueron tomadas de estudios previos sobre la distribución de energía potencial de un modo vibracional, el cual proporciona una aproximación a las coordenadas internas relacionadas con cada banda vibracional. La marcación isotópica selectiva nos permitió acercarnos a la dependencia de cada banda, debido a que, la energía de una vibración molecular depende también de la masa recíproca de los átomos involucrados. En general, los resultados mostraron que algunas bandas asignadas experimentalmente no coinciden con las asignaciones teóricas mediante simulaciones mecánicas cuánticas.

Palabras clave: diacetona diperóxido; isotopómero; espectroscopia Raman e infrarroja; vibración molecular.

1. Introduction

Although, the organic peroxides are widely used as bleaching agents, antibacterial and polymeric initiators, the current interest on these substances lies in the application of these derivatives as explosive initiators [1]. Particularly, the compounds diacetone diperoxide (DADP) and triacetone triperoxide (TATP), are the most common acetone peroxides for the synthesis of homemade explosives (HME), and for this reason they are of interest for defense and national

How to cite: Espinosa-Fuentes, E., Meza-Fuentes, E., Colpas-Castillo, F., Castro-Suarez, J.R., Chiquillo-Correa, G. and Mora M., Verification of the vibrational theoretical assignment of the DADP using isotopic labelling. DYNA, 85(205), pp. 64-68, June, 2018.

© The author; licensee Universidad Nacional de Colombia.

security applications. Their easy synthesis from the reaction of hydrogen peroxide with acetone catalyzed by acid, together with the high availability of the basic products make them attractive precursors for the preparation of homemade explosive materials [1-6].

Due to the great instability presented by these materials they are not normally used for military purpose, but rather for criminal purposes, therefore their identification and proper detection becomes of great importance [7]. Although there are many studies on the TATP molecule, the DADP molecule has a feature that makes it more attractive for the design of energetic materials; this fact is because the oxygen atoms in the molecule are more accessible than in the TATP, which enables them to be easily functionalized [8].

For many years, the infrared and Raman spectra have been used for the identification and structural elucidation of organic molecules due to its potential to provide vibrational information on what type of atoms are involved in a particular bond, these techniques prevail as one of the most commonly used for the characterization of DADP and others compounds of interest. In most of the studies described, the band assignment is done theoretically, or by isotopic labeling of hydrogen atoms with deuterium atoms. With this type of isotopic labeling is not achieved the strategic labeling of the carbon atoms involved in the different vibrational modes [3,9-12].

This research deals with the assessment of the theoretical assignment of the different bands in the vibrational spectrum of the DADP molecule. This verification was made through partial isotopic labeling of the different carbon atoms in the molecule, thus achieving, the corresponding displacement in the bands involved. Use Time New Roman font with size of 10 points for normal text paragraphs. The first line of each paragraph is indented 0.5 cm.

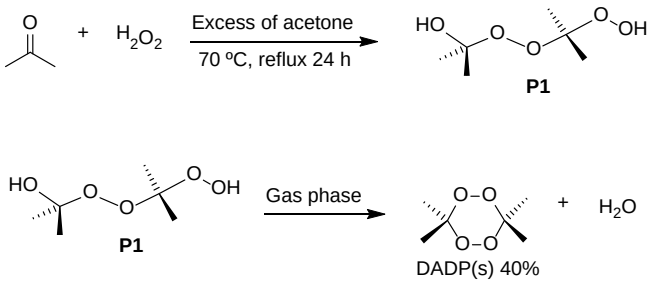
2. Experimental setup

2.1. Reagents

The reagents used in the synthesis of the DADP isotopomers were: acetone-^{13}C, acetone-$^{13}C_2$, and neat acetone at 99.7%, hydrogen peroxide stabilized at 50%, ultra-pure water, m-sulphonic and toluene-sulphonic acids. Dichloromethane at 99.8% stabilized HPLC grade. All the reagents listed above were purchased in Fisher Scientific and used without further purification.

2.2. Synthesis of DADP

DADP and its isotopomers was prepare using a modified procedure of the reported by Espinosa-Fuentes et al, which consists in the oxidation of acetone with hydrogen peroxide catalyzed by m-sulphonic or toluene-sulphonic acids [6]. The acetone labeled on the carbonyl carbon and the methyl carbons atoms were used for the synthesis of the DADP-C_2 and DADP-C_4 isotopomers respectively. The white crystals of DADP were washed with deionized water and recrystallized in dichloromethane. Immediately shows a reaction scheme.



Scheme 1. Synthesis route of DADP Source: Own elaboration
Source: The authors.

2.3. Instrumental analysis

The infrared spectra were recorded in an infrared spectrophotometer with Fourier transformed, Bruker Optics brand, model IFS 66v/S, equipped with a DTGS detector, in the spectral region of 400 to 4000 cm^{-1}, 10 scans per spectrum and a resolution of 4 cm^{-1} were used. The Raman spectra were recorded using a Raman spectrophotometer, EZ-Raman, equipped with an excitation line of 785 nm, in the spectral region of 400 to 3200 cm^{-1}, 10 accumulations per spectrum and a resolution of 1 cm^{-1}.

3. Results and discussion

To verify the assignment of each band in the vibrational spectra of the DADP molecule, it was taken as a basis the theoretical distribution reported by Coronel et al [10]. For DADP, a nonlinear molecule, the 3N-6 modes correspond to 50 vibrations. Before checking the theoretical assignment of each vibrational band, we will explain the relationship between the atoms in the molecule (see Fig. 1) with the internal coordinates and the distribution of the potential energy of a particular band. For this, was chosen the vibrational mode 44 (ν44), which has the following distribution of potential energy 50S2+44S1, this means that, the internal coordinates S1 and S2 contribute to the vibration energy in a percentage of 50 and 44 respectively. According to supplementary Table 1 and the molecular numbering of Fig. 1, the atoms involved in this vibration are H(14), H(13), H(12) and C-methyl(11) for S1 and S2: H(18), H(16), H(17) and C-methyl(15). For this particular band, is possible to corroborate experimentally its assignment, by labeling the methyl atoms. The isotopic labeling of a carbon atom different to the previous ones should not displace the band corresponding to Mode 44 (Table 1-2 of the supplemental material); if this happens, then the theoretical contribution is wrong.

The theoretical energy distribution of the DADP spectrum presented several differences, regarding the experimental displacements of the isotopomers spectra (DADP-$^{13}C_4$ and DADP-$^{13}C_2$); among others, which agreed with the theoretical assignment. The bands at 3034, 3033, 2958, 3008, 1466, 1477, 1377, 1010, 943, 860, 687, 525, 476 cm^{-1} showed concordance with potential energy distribution (PED). These spectral bands correspond to the vibrational modes 20, 32, 2, 19, 45, 31, 3, 46, 45, 5, 48, 54, 37, 57, 58, 39 according to reported by Coronel et al [10]. These modes are related only with movements of the methyl group (C and H atoms) (Fig. 2-6).

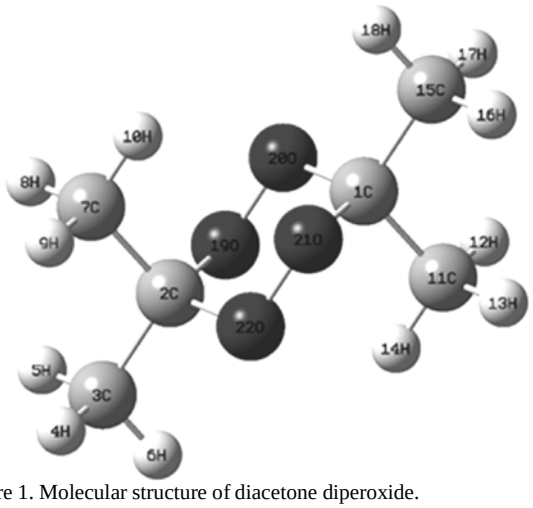


Figure 1. Molecular structure of diacetone diperoxide.
Source: Gausview® and the authors.

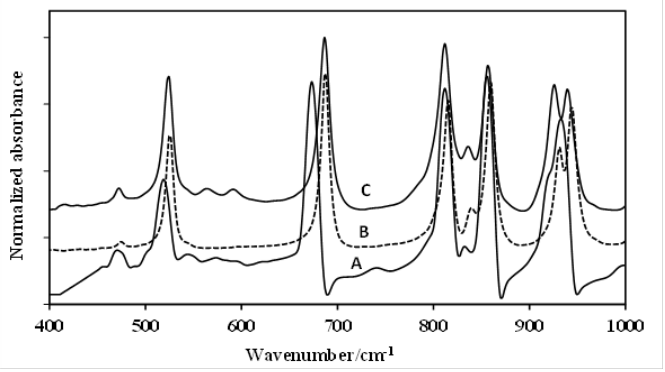


Figure 2. First portion of the FT-IR spectra of: A-DADP-C4, B-DADP and C-DADP-C2.
Source: The authors.

In contrast with the bands above, some differences were observed in the others assignments. For example, the band at 1439 cm^{-1}, despite the fact that its theoretical contribution is only for methyl groups, when other atoms were isotopically labeled (specifically annular peroxyl carbons), the band showed a displacement of 7 cm^{-1} by change in its reduced mass. The above analysis demonstrates that the theoretical assignment is wrong and the peroxyl carbon atoms also contribute to vibrational mode.

The band at 1273 cm^{-1} (ν52), despite that its theoretical contribution includes methyl group and carbon atoms of the DADP ring, it only presented displacement, when carbon atoms of the ring were labeled isotopically. This result suggests that the methyl groups do not contribute to the mode ν52. The bands at 1205 cm^{-1}, 1141 cm^{-1} and 951 cm^{-1} (ν35, ν23 and ν11) showed concordance in the response by mass variation of their correspondent groups. But the largest displacement was observed when the peroxyl carbon atoms of the ring were labeled isotopically, despite the methyl groups have greater contribution to the band.

The following difference was found in the assignment of the band at 931 cm-1 (ν55), which is entirely due to the methyl groups motions, however this mode presented displacement by mass change of the non-methylic atoms. The opposite happened with the bands at 841 cm^{-1}, 833 cm^{-1}, 761 cm^{-1}, 687 cm^{-1}, 525 cm^{-1}, 496 cm^{-1}, 337 cm^{-1}, 312 cm^{-1} and 280 cm^{-1} (ν56, ν25, ν14, ν57, ν58, ν26, ν17, ν28 and ν18), which presented displacement only when methyl carbon atoms (DADP-C_4) were labeled.

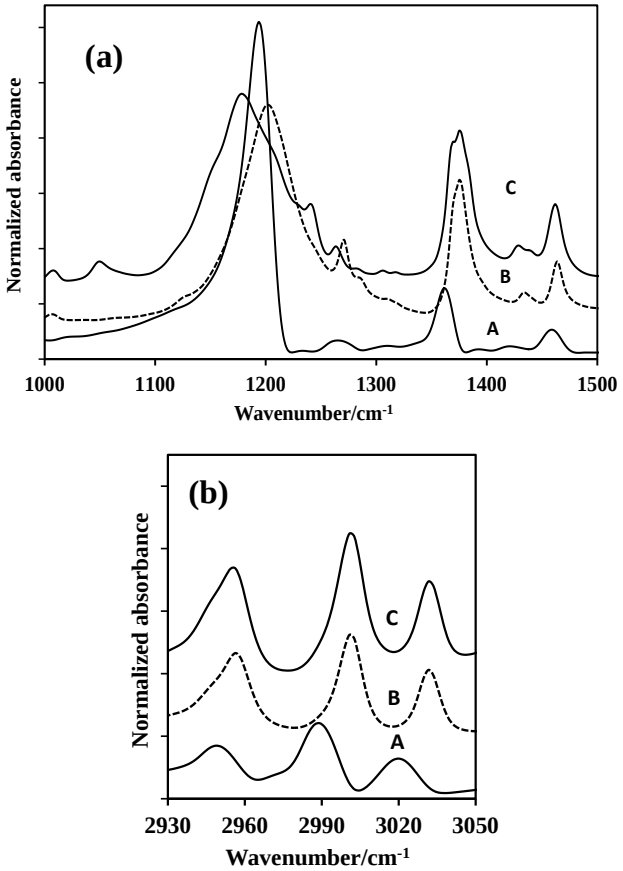


Figure 3. FT-IR spectra of: A-DADP-C_4, B-DADP and C-DADP-C_2. (a) at 1000-1500 cm^{-1} (b) at 2900-3050 cm^{-1} spectral range.
Source: The authors.

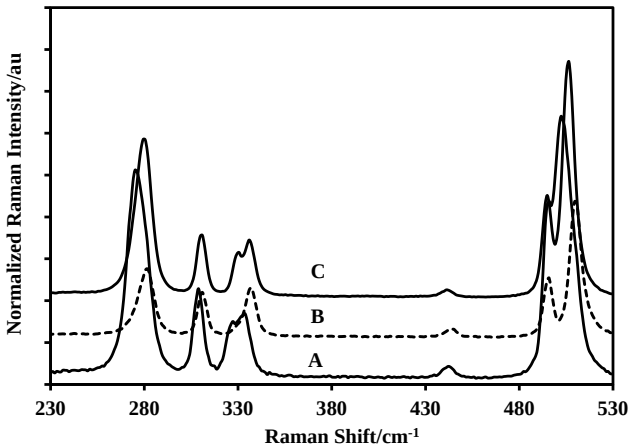


Figure 4. First portion of the Raman spectra of: A-DADP-C_4, B-DADP and C-DADP-C_2.
Source: The authors.

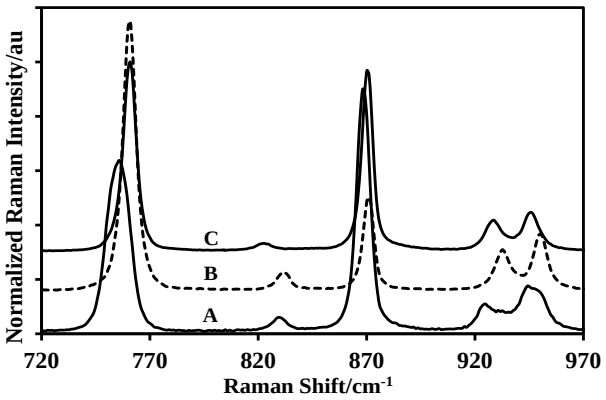


Figure 5. Second portion of the Raman spectra of: A-DADP-C_4, B-DADP and C-DADP-C_2.
Source: The authors.

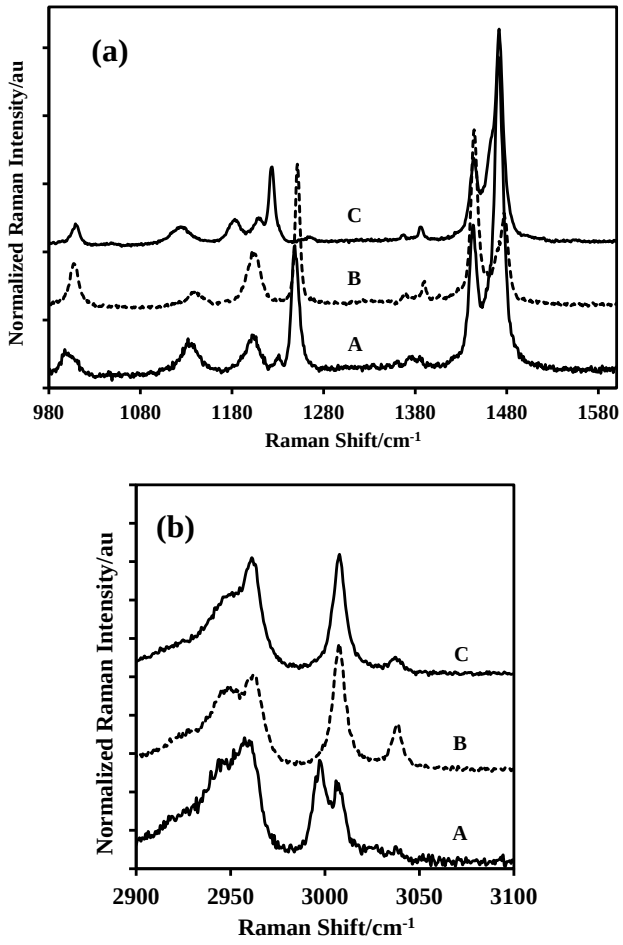


Figure 6. Last portion of the Raman spectra of: A-DADP-C_4, B-DADP and C-DADP-C_2 (a) at 2900-3100 cm^{-1} spectral range. (b) at 1000.1600 cm^{-1} spectral range.
Source: The authors.

Finally, according to the theoretical PED, the band at 873 cm^{-1} is due to vibration of the O-O bond, therefore this band should not present any mass-shift in the spectra of the DADP isotopomers, however, the spectrum of both isotopomers showed vibrational displacement, specifically with the methyl and peroxyl carbon atoms. The band at 860 cm^{-1} also showed dependence with the methyl group, despite that the theoretical distribution does not consider it.

Over the years have been shown that the theoretical methods are a useful tool for understanding certain complex problems. However, in this report was observed that, the theoretical method is fairly efficient for movements of pure groups. For vibrational movements involving various functional groups, the method does not work well. For example, fairly predicts mappings between methyl atoms, nor it predicts vibrations between methyl atoms and peroxyl carbon atoms in the molecule studied.

4. Conclusions

In general, the theoretical method for the assignment of vibrational bands is fairly efficient for pure group's movements. For vibrational movements involving various functional groups, the method works with some difficulty. For example, barely predicts combined assignment between methyl atoms, but does not predict vibration between methyl atoms and peroxyl carbon atoms in the molecule studied. For peroxyl displacements, which are not totally pure, the theoretical PED was unable to predict its contribution. Finally, it is important that the vibrational assignment is based on strategic isotopic marking and not in theoretical assignments, for the unequivocal acceptance in applied research.

References

[1] Landenberger, K.B., Bolton, O. and Matzger, A.J., Energetic–energetic cocrystals of diacetone diperoxide (DADP): dramatic and divergent sensitivity modifications via cocrystallization, Journal of the American Chemical Society, 137(15), pp. 5074-5079, 2015. DOI: 10.1021/jacs.5b00661.

[2] Pena, A.J., Pacheco-Londono, L., Figueroa, J., Rivera-Montalvo, L.A., Roman-Velazquez, F.R. and Hernandez-Rivera, S.P., Characterization and differentiation of high energy cyclic organic peroxides by GC/FT-IR, GC-MS, FT-IR, and Raman microscopy, Proc. SPIE, 5778, pp. 347-358, 2005. DOI: 10.1117/12.604194.

[3] Oxley, J., Smith, J., Brady, J., Dubnikova, F., Kosloff, R., Zeiri, L. and Zeiri, Y., Raman and infrared fingerprint spectroscopy of peroxide-based explosives, Applied Spectroscopy, 62(8), pp. 906-915, 2008.

[4] Jensen, L., Mortensen, P.M., Trane, R., Harris, P. and Berg, R.W., Reaction kinetics of acetone peroxide formation and structure investigations using Raman spectroscopy and X-ray diffraction, Applied spectroscopy, 63(1), pp. 92-97, 2009.

[5] Matyáš, R. and Pachman, J., Study of TATP: influence of reaction conditions on product composition. Propellants, Explosives, Pyrotechnics, 35 (1), pp. 31-37, 2010. DOI: 10.1002/prep.200800044

[6] Espinosa-Fuentes, E.A., Pacheco-Londoño, L.C., Barreto-Cabán, M.A. and Hernández-Rivera, S.P., Novel Uncatalyzed Synthesis and Characterization of Diacetone Diperoxide, Propellants, Explosives, Pyrotechnics, 37(4), pp. 413-421, 2012. DOI: 10.1002/prep.201000130

[7] Bellamy, A.J., Triacetone triperoxide: its chemical destruction, Journal of Forensic Science, 44(3), pp. 603-608, 1999. DOI: 10.1520/JFS14517J

[8] Wappel, J., Grudzień, K., Barbasiewicz, M., Michalak, M., Grela, K. and Slugovc, C., Initiation efficacy of halo-chelated cis-dichloro-configured ruthenium-based second-generation benzylidene complexes in ring-opening metathesis polymerization, Monatshefte

für Chemie-Chemical Monthly, 146(7), pp. 1153-1160, 2015. DOI: 10.1007/s00706-015-1494-8.
[9] Jubert, A.H., Diez, R. and Cafferata, L.F.R., Experimental and theoretical studies of the vibrational spectra of 3, 3, 6, 6-tetramethyl-1, 2, 4, 5-tetroxane, Journal of Raman spectroscopy, 30(6), pp. 479-484, 1999. DOI: 10.1002/(SICI)1097-4555(199906)30:6<479::AID-JRS400>3.0.CO;2-L
[10] Coronel, A.C., Agüera, M.B., Torres, A.C., Fernández, L.E. and Varetti, E.L., A vibrational study of 3, 3, 6, 6-tetramethyl-1, 2, 4, 5-tetroxane: The spectra of the deuterated substance and the scaled quantum mechanics force field, Vibrational Spectroscopy, 58, pp. 67-73, 2012. DOI: 10.1016/j.vibspec.2011.10.004.
[11] Keresztury, G., Holly, S., Besenyei, G., Varga, J., Wang, A. and Durig, J.R., Vibrational spectra of monothiocarbamates-II. IR and Raman spectra, vibrational assignment, conformational analysis and ab initio calculations of S-methyl-N, N-dimethylthiocarbamate, Spectrochimica Acta Part A: Molecular Spectroscopy, 49(13-14), pp. 2007-2026, 1993. DOI: 10.1016/S0584-8539(09)91012-1.
[12] Evans, J.C., The vibrational assignments and configuration of aniline, aniline-NHD and aniline-ND2, Spectrochimica Acta, 16(4), pp. 428-442, 1960. DOI: 10.1016/0371-1951(60)80037-9.

E. Espinosa-Fuentes received the BSc. in Chemistry in 2003 from University of Cartagena, Colombia, the MSc. degree in Chemistry in 2009, and the PhD degree in 2013, both in Applied Chemistry from University of Puerto Rico- Mayaguez, Puerto Rico. His research interests include: synthesis and physicochemical characterization of bio-adsorbents material. vibrational studies of explosives material.
ORCID: 0000-0003-1653-5408.

E. Meza-Fuentes, received the BSc. in Chemistry in 2001 from university of Cartagena, the MSc. degree in Chemistry in Universidade Federal de Bahía, Brazil en 2006, and the PhD degree in Universidade Federal de Bahía, Brazil en 2009. Actually, he is professor at Universidad de Cartagena, Colombia in the exact sciences department.
ORCID: 0000-0003-3725-8112.

F. Colpas-Castillo received the BSc. Eng in Chemical Engineering in 1989, MSc. degree in Chemical Sciences; she worked in programs and projects of the mining area, with emphasis on environmental management and since 1998 for the Universidad de Cartagena, Colombia. He is currently full professor of the Universidad de Cartagena, Colombia.
ORCID: 0000-0001-7203-6983

J.R. Castro-Suarez, received the BSc. in Chemistry in 2006 from University of Cartagena, the MSc. degree in Chemistry in 2010, and the PhD degree in 2016, both in Applied Chemistry from University of Puerto Rico-Mayaguez, Puerto Rico, with emphasis in synthesis, characterization and detection of highly dangerous materials. His research interests include: use of software of chemometrics (multivariate analysis) as PLS toolbox under the Matlab and pirouette platform, for the elaboration of multivariate models like PCA, PLS, DA-PLS, etc., with spectroscopic data infrared and Raman, which allow the design of sensors for the early, rapid and accurate detection of dangerous substances of industrial and academic interest, in real world samples with little or no sample pretreatment.
ORCID: 0000-0003-4900-7097

G. Chiquillo-Correa, received the BSc. Eng in Chemical Engineering in 1999; actually, he is student of MSc. in Chemistry, all of them from the Universidad Cartagena. Cartagena, Colombia. From 1999 to present, he had worked for Regional Corporation of the Canal del Dique.
ORCID: 0000-0003-3210-1167

M. Mora, received her BSc. in Chemistry in 2008 from University of Cartagena, Colombia. She obtained her PhD degree in Inorganic Chemistry in 2015 from University of Zaragoza, Spain. She is currently associate professor at the Universidad de la Costa, Colombia. Her research interests are mainly focus on the design, synthesis and characterization of new materials with application in catalytic dehydrogenation of amineboranes, construction of luminescent and anticorrosive materials.
ORCID: 0000-0003-0907-1772



UNIVERSIDAD NACIONAL DE COLOMBIA
SEDE MEDELLÍN
FACULTAD DE MINAS

Área Curricular de Ingeniería Química e Ingeniería de Petróleos

Oferta de Posgrados

Maestría en Ingeniería - Ingeniería Química
Maestría en Ingeniería - Ingeniería de Petróleos
Doctorado en Ingeniería - Sistemas Energéticos

Mayor información:

E-mail: qcaypet_med@unal.edu.co
Teléfono: (57-4) 425 5317

UNIVERSIDAD NACIONAL DE COLOMBIA
SEDE MEDELLÍN
FACULTAD DE MINAS



DYNA
http://dyna.medellin.unal.edu.co/

Effect of the tryptone concentration on the calcium carbonate biomineralization mediated by *Bacillus cereus*

Gerardo Andrés Caicedo-Pineda [a], María Consuelo Prada-Fonseca [b], Ana Elisa Casas-Botero [c] & Hader Vladimir Martínez-Tejada [d]

[a] *Escuela de Ciencias Químicas, Universidad Pedagógica y Tecnológica de Colombia, Tunja, Colombia. gerardo.caicedo@uptc.edu.co*
[b] *Área Ingeniería de Procesos, Biofenix S.A.S, Medellín, Colombia. mcpradafonseca@gmail.com*
[c] *Escuela de Ingenierías, Universidad Pontificia Bolivariana, Medellín, Colombia. ana.casas@upb.edu.co*
[d] *GINUMA, Universidad Pontificia Bolivariana, Medellín, Colombia. hader.martinez@upb.edu.co*

Received: October 21th, 2016. Received in revised form: November 13th, 2017. Accepted: January 25th, 2018.

Abstract
Five tryptone concentrations (0.2%, 0.4%, 0.6%, 0.8% and 1.0%) were evaluated on calcium carbonate biomineralization processes, using 0.5% of calcium acetate. A culture of *Bacillus cereus*, isolated from the gardens of The Universidad Pontificia Bolivariana (Medellin, Antioquia, Colombia) was used in all the assays. The experiments were monitored by pH measurements and mineralogical analyses of X-ray diffraction (XRD), Fourier transform infrared spectroscopy (FTIR) and Scanning electronic microscopy (SEM). Vaterite was the predominant polymorph in the precipitates after 6 days of the process. However, a considerable proportion of calcite appeared (above 30%) when the tryptone concentration was 0.4% or below. Additionally, the other experiments had a similar precipitate formation (between 3.2-3.6 g/L) except the assay using 0.2% of tryptone, which presented a low calcium carbonate production (1.79 g/L). A tryptone concentration below 0.4% would limit the bacterial metabolism and CO_2 formation, necessary for calcium carbonate production.

Keywords: *Bacillus cereus*; biomineralization; calcium carbonate; tryptone; calcite; vaterite.

Efecto de la concentración de triptona en la biomineralización de carbonato de calcio mediada por *Bacillus cereus*

Resumen
Se evaluaron cinco concentraciones de triptona (0.2%, 0.4%, 0.6%, 0.8% y 1.0%) en procesos de biomineralización de carbonato de calcio, utilizando acetato de calcio al 0.5%. Todos los ensayos se hicieron con una cepa de *Bacillus cereus*, aislada de los jardines de la Universidad Pontificia Bolivariana (Medellín, Antioquia, Colombia). Los experimentos fueron monitoreados con mediciones de pH y análisis mineralógicos de difracción de rayos X (XRD), espectroscopía de infrarrojo con transformada de Fourier (FTIR) y microscopía electrónica de barrido (SEM). La vaterita fue el polimorfo predominante en los precipitados después de 6 días de proceso. Sin embargo, una proporción considerable de calcita (por encima de 30%) apareció cuando la concentración de triptona fue de 0.4% y menor. Adicionalmente, los experimentos tuvieron una formación de precipitados similar (entre 3.2 y 3.6 g/L), menos el ensayo con 0.2% de triptona, que presentó una baja producción de carbonato de calcio (1.79 g/L), indicando que una concentración de triptona menor a 0.4% limitaría el metabolismo bacteriano y la formación de CO_2, necesaria para la producción de carbonato de calcio.

Palabras clave: *Bacillus cereus*; biomineralización; carbonato de calcio; triptona; calcita; vaterita.

1. Introduction

The biomineralization of calcium carbonate is a process associated with eukaryotic and prokaryotic physiologies. In the bacterial world, many microorganisms are capable of precipitating calcium carbonate crystals in the form of calcite or vaterite [1]. The bacteria of the genus *Bacillus spp.* (mainly *Bacillus subtilis, Bacillus pasteurii, Bacillus amyloliquefaciens, Bacillus cereus*) are ones of the most widely known. This microorganism require CO_2 dissolved in

How to cite: Caicedo-Pineda, G.A., Prada-Fonseca, M.C., Casas-Botero, A.E. and Martínez-Tejada, H.V., Effect of the tryptone concentration on the calcium carbonate biomineralization mediated by Bacillus cereus. DYNA, 85(205), pp. 69-75, June, 2018.

© The author; licensee Universidad Nacional de Colombia.

the medium (in the form of HCO_3^{2-} and CO_3^{2-}) and a defined source of calcium (generally as a salt) to carry out the biocrystallization of calcium carbonate [2]. It is believed that the microorganisms produce an induced biomineralization (activated), where the bacteria regulate the calcium entry and exit through of a protein-non protein channel. The Ca^{2+} ions expelled by the bacterium in presence of CO_3^{2-} facilitate the formation of calcium carbonate [3,4].

The ability to precipitate calcium carbonate crystals is continuously studied, because of its multiple applications in the industries of construction, bioremediation, medicine, cosmetics and others [5,6]. It is noteworthy that the formation of calcium carbonate is a complex process that can be manipulated in several ways. The control of the morphology and the size of the crystals are very important, considering its final application. The kind of the obtained mineral depends on several conditions of the medium, including temperature, saturation, pH as well as the presence of additives and impurities [7].

In general, the culture media employed in the induced biomineralization processes of calcium carbonate require a calcium salt (usually calcium acetate) and a nutritious broth, composed of various components (glucose, yeast extract, tryptone, etc.) [8-10]. In preliminary trials for this work, it was found that a strain of *Bacillus cereus* was capable of producing calcium carbonate from a medium that only contained 1.0% of tryptone and 0.5% of calcium acetate (data not shown).

This work evaluated the effects of reducing the tryptone concentration on the carbonate bioproduction to determine a minimum concentration of the compound that can allow an adequate carbonate precipitate index, considering a scalable process at a commercial level with a lower reactive consumption. All the obtained precipitates were mineralogically analyzed to observe if there were morphologic and or polymorphic variations.

2. Experimental procedure

2.1. Microorganism

A pure culture of *Bacillus cereus* was selected for the experiments. It was isolated from soil material from the gardens of the Universidad Pontificia Bolivariana (Medellin, Colombia). The strain was adapted prior to the calcium carbonate biomineralization process. The adaptation consisted in several subcultures in a modified M3 medium (0.5% calcium acetate and 1.0% tryptone) up to observe no variations on pH and the quantity of precipitate generated between the replicas.

The inocula were prepared in a 250 mL erlenmeyer, using different concentrations of tryptone for each bacterial assay (from 0.2% to 1.0%). The working volume was 100 mL and the culture composition had a ratio of 1 mL of inoculum per 9 mL of M3 modified medium (evaluating the respective tryptone concentration) [9]. The strains were incubated for 6 days in an orbital agitator at a temperature of 30°C ± 1°C and an agitation velocity of 180 rpm ± 2 rpm.

2.2. Biomineralization of calcium carbonate

Each assay was prepared in a 250 mL erlenmeyer (working volume of 100 mL), using a ratio of 1 mL bacteria inoculum per 9 mL or modified M3 modified medium. The variable evaluated was the tryptone concentration (%w): 0.2, 0.4, 0.6, 0.8 and 1.0.

All assays were incubated for 6 days under temperature and agitation conditions like the used in the preparation of the inocula. The experiments also had their respective replica and abiotic control (without presence of microorganisms). Additionally, the pH was periodically monitored for each sample, using an HACH HQ 30d pH meter.

At the end of each assay, 80 mL were extracted from each erlenmeyer and centrifuged at 3500 rpm for 10 minutes. After this time, the supernatant was discarded and the precipitate was washed 4 times with distilled water and other 4 times with ethylic alcohol (90 %v), agitating in a vortex for 1 minute and then centrifuging at 3500 rpm for 10 minutes. Afterwards, the samples were dried at room temperature. The final product was used to determine the amount of formed precipitate per liter of medium, dividing the obtained weight over the sample volume.

2.3. Mineralogical analyses

The mineralogical composition of the samples was established with X-ray diffraction (XRD), Fourier transform infrared analysis (FTIR) and scanning electronic microscopy (SEM). For all the analyses, the original sample was used, without particle size transformations.

The XRD analyses were made in a Rigaku Miniflex II diffractometer, using the step by step method, with 5° start angle, 70° stop angle, 0.05° step angle, and counting time of 50 s. The minerals present in the precipitate were quantified using a Rietveld refinement in the X'Pert HighScore Plus© software with the PDF-4-2012 database and the American Mineralogist Crystal Structure Database [11].

The FTIR analyses were carried out in a Thermo Scientific Nicolet spectrometer, using the ATR method with the pure sample, using an interval of 400-4000 cm^{-1}, 32 scans and a spectral resolution of 4 cm^{-1}.

For the SEM analyses, the sample was coated with a fine silver layer. The "sputtering" (cathodic pulverization) coating technique was performed with a DENTON VACCUM DESK IV. The analysis was carried in a JEOL JSM-6490LV sweep electron microscope. Additionally, an Oxford Instruments INCA PentaFETx3 X-ray-EDX analyzer was employed to carry out the microchemical sample analyses.

3. Results and discussion

3.1. Biomineralization of calcium carbonate

Fig. 1 illustrates the pH behavior, where all the assays had a continuous increase of the value. Probably, the bacterial growth could have affected this parameter, because *Bacillus cereus* is heterotrophic and it is able to carry out the aerobic ammonification process of amino acids in presence of dissolved oxygen, organic matter and calcium [6].

According to Periasiami et al. (2016), the microorganisms might be able to produce carbonate compounds (CO_3^{2-}) during its cellular growth and metabolism activation. This

compounds might have reacted with Ca^{2+} ions (from calcium acetate), affecting the acid-base environment in the culture medium [12].

Although the assays using a tryptone concentration ≥ 0.4% tended to stabilize at day 6 of the process, the assay using 0.2% of tryptone decreased its raising from the second day. The final pH for all assays were around 9 and the highest values were achieved by the assays using tryptone concentrations of 0.6% (9.19) and 0.8% (9.18), followed by the 0.4% (9.08), 1.0% (8.98) and 0.2% (8.92) tests.

The differences among pH tendency can be explained by the availability of energy source. A high tryptone concentration might imply a higher access to proteins necessaries to bacterial multiplication, giving as result a higher carbonate compounds and therefore alkalization of the medium [13,14].

Fig. 2 presents the quantity of precipitate obtained in each assay. The assays with tryptone concentration higher than 0.4% obtained values above 3.2 grams of precipitate per liter of solution. The highest precipitate quantity was obtained in the assays with 0.8% (3.56 g/L) and 1.0% (3.58 g/L). In contrast, the assay using 0.2% tryptone obtained the lowest precipitation, 44.5% lower than the experiment with the subsequent precipitate concentration (3.23 g/L).

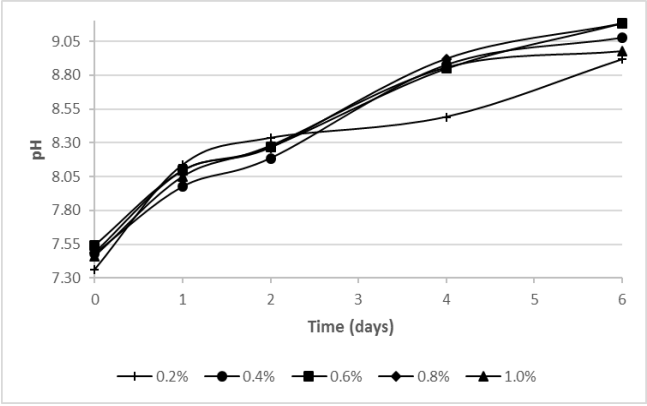


Figure 1. pH vs. time during the calcium bioprecipitation process at different tryptone concentrations.
Source: The authors.

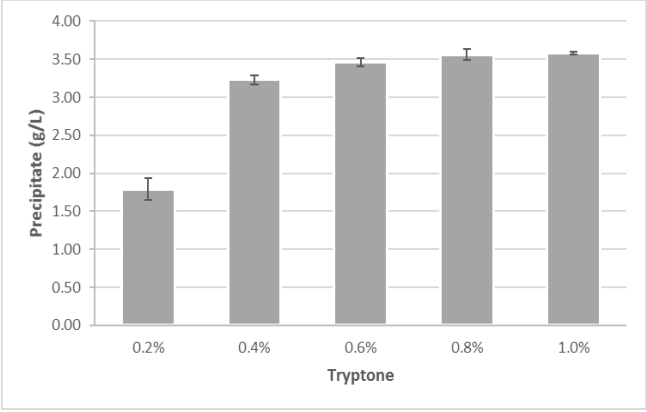


Figure 2. Obtained precipitate during the calcium bioprecipitation process at different tryptone concentrations.
Source: The authors.

The precipitation of calcium carbonate observed in the assays using the highest concentrations tryptone (Fig. 2) might be related with the propagation and metabolism of the microorganism which promote the mineral synthesis, either segregating metabolites which accelerating CO_2 hydration, regulating CO_2 y HCO_3^- concentrations and modifying pH of the medium, as shown in eq. (1) and eq. (2) [15,16]. For the last reason, calcium carbonate biomineralization is product of the quantity of CO_3^{2-} and Ca^{2+} ions in the medium.

$$CO_2 + H_2O \rightarrow H_2CO_3 \leftrightarrow HCO_3^- + H^+ \leftrightarrow CO_3^{2-} + 2H^+ \quad (1)$$

$$CO_3^{2-} + Ca^{2+} \rightarrow CaCO_3 \quad (2)$$

3.2. Mineralogical analyses

Fig. 3 shows the diffractograms of the precipitates for all the assays using different tryptone concentrations. The presence of calcium carbonate was identified in two crystalline phases: vaterite and calcite, where vaterite was the predominant polymorph. Notwithstanding, the assays using 0.2% and 0.4% of tryptone presented a greater intensity in the calcite peaks in comparison to the other experiments. On the other hand, none of the assays presented formations of other minerals.

From Rietveld refinement of the XRD patterns (Fig. 1), Table 1 presents the semi-quantitative ratios of the crystalline phases of both vaterite and calcite for all the precipitates. The weighted residual profile of the refinements (R_{wp}) was below 10% which did not vary more than 20% with respect to the residual expected (R_{exp}). These parameters determined that the refinement models were good to accept the values obtained [17-19]. The assays with the three highest tryptone concentrations had a greater vaterite formation (above 97%), while the percentage of calcite was increased considerably when concentrations below 0.4% tryptone were used.

Wei et al. (2015), explain that the polymorphism of carbonate biomineralization to calcite, vaterite or aragonite depends of the environmental conditions and the culture medium. Additionally, different types of bacteria can precipitate calcium carbonate with diverse crystalline structure (spherical or polyhedral) or even amorphous forms [20].

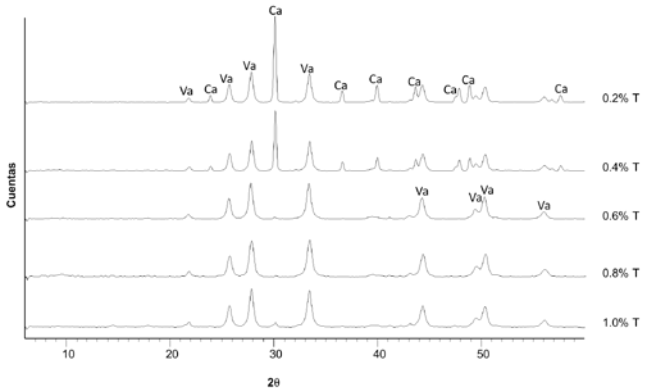


Figure 3. Diffractograms of the precipitates for each trial at different tryptone (T) concentrations. Va: vaterite, Ca: calcite
Source: The authors.

Table 1.
Percentage of calcite and vaterite in crystalline phase of the obtained precipitates in the tests at different tryptone concentrations.

Assay	Calcite	Vaterite
0.2% T	41.0%	59.0%
0.4% T	32.4%	67.6%
0.6% T	2.2%	97.8%
0.8% T	2.0%	98.0%
1.0% T	7.0%	93.0%

Source: The authors.

Bacillus cereus is an ureolytic bacterium which promotes the production of calcium carbonate when the culture medium is enriched with a protein source, as tryptone. For this purpose, the microorganism activates the biochemical metabolism of the enzyme urease [1]. Although vaterite is the less stable among the three polymorphs of anhydrous calcium carbonate at environmental conditions and it tends to transform into calcite, several research have found stability of bio-vaterite by biomolecules from the cellular wall of the bacteria, where compounds with phosphorus ions, carboxylic groups or polysaccharides play an important key role to coordinate calcium and carbonate orientation [1].

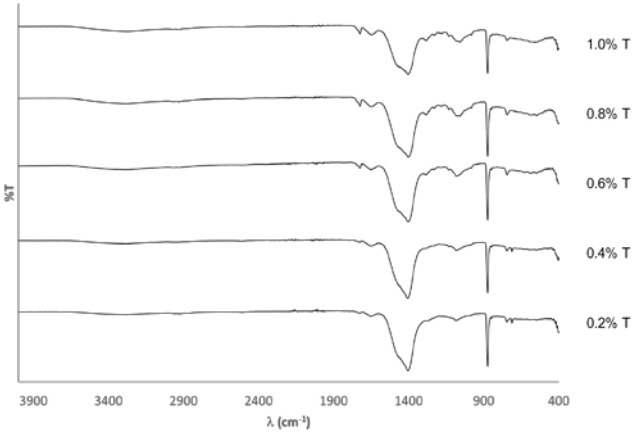


Figure 4. FTIR spectra of the precipitates for each test at different tryptone (T) concentrations.
Source: The authors.

Table 2.
Bands of the FTIR spectra for the obtained precipitates at different tryptone concentrations.

Band	Assignation	Assays
713	CO_3^{2-} associated to the calcite	0.2% T y 0.4% T
745	CO_3^{2-} associated to the vaterite	All
874-875*	CO_3^{2-} of carbonates	All
1058	CO_3^{2-} of carbonates	0.8% T y 1.0% T
1075	CO_3^{2-} associated to the vaterite	0.6% T
1087	CO_3^{2-} associated to the vaterite	0.2% T y 0.4%T
1280	C-O (organic)	0.8% T y 1.0% T
1400-1404*	CO_3^{2-} associated to the calcite	All
1430-1437*	CO_3^{2-} associated to the vaterite	All
1648-1653*	H-OH	All
1707-1725*	C=O (organic)	All
3282-3300*	O-H (alcohol)	All

*The tests only have one band between the values, which represent the same label.
Source: [1,21-32]

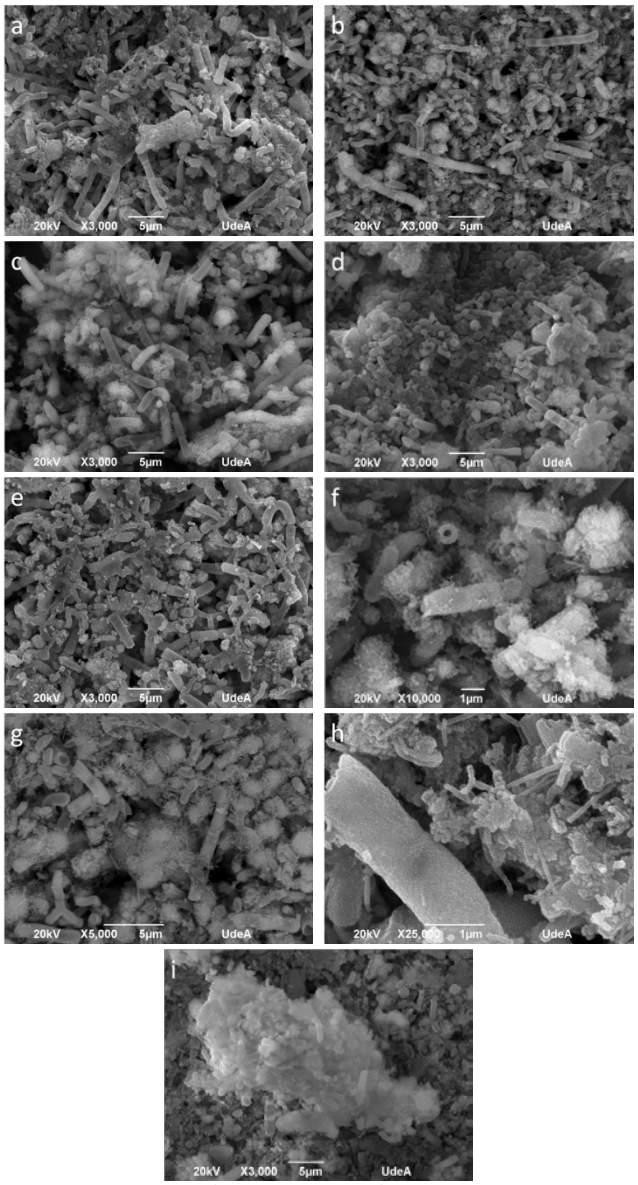


Figure 5. SEM images of the precipitates of the tests at varying tryptone concentrations. Formation of bacillary structures from the biomineralized microorganisms of the tests 0.2% T (a), 0.4% T (b), 0.6% T (c) and 1.0% T (e). Accumulation of vaterite spheres in the 0.8% T (d) test. Magnification of the precipitates of test 0.4% T which indicates that the cylindrical structures are hollow (f). Coating of the shells with stem shaped mineral growths (g and h) and accumulation of agglomerate particles (i).
Source: The authors.

Based on the results of this work, the reduction of the main nutrient source below 0.4% probably reduce the synthesis of the biomolecules that maintain the stability of vaterite, thus it might have allowed a transformation of a part of calcium carbonate into calcite.

Fig. 4 shows the FTIR spectra for all the precipitates and Table 2 presents the bands identification with their respective assignations. The presence of calcite and vaterite was validated for all assays. The band at 713 cm^{-1}, corresponding to calcite, indicated the greatest presence of this mineral in the assays with 0.2% and 0.4% of tryptone. The bands at 1280

cm^{-1} and 1707-1725 cm^{-1} indicated that the precipitates had traces of organic matter after the washing phase, probably originating from one of the compounds of the cultivation medium. The band at 1648-1653 cm^{-1} signaled the presence of natural humidity of the sample and the band at 3282-3300 cm^{-1} indicates interactions of O-H, possibly corresponding to the to the residual alcohol from the washing phase of the precipitates [21,22].

Fig. 5 illustrates SEM images. All the precipitates presented a cylindrical, hollow structure formation pattern with an external diameter of approximately 1 µm and variable lengths between 5 µm and 15 µm, possibly originated from the biomineralization of calcium carbonate nanoparticles over the microorganisms. Probably, the bacteria had a surface with charged nucleation sites where the mineral could initialize its generation [23]. The samples of the assays with the highest tryptone concentrations (Fig. 5d) also presented other typical structures, including spherical particles which correspond to the formation of vaterite [29]. Other formations founded were ramified carbonate less than 1 micron (Fig. 5h), product of particles that did not probably tend to form the shells of microorganisms. The accumulation of some particles (Fig. 5i) could be attributed to the washing phase of the precipitates.

From the SEM and EDS analyses, microchemical analyses were carried out to some of the structures found in the precipitates (Fig. 5). Fig. 6 and Table 3 illustrates the particles that covered the biomineralized shells of the microorganisms (assay 0.4% T), where a low calcium concentration and a high carbon concentration was identified. Comparing with the ideal atomic relations of calcium carbonate (1 Ca:1 C:3 O), it indicates that the particles or their surroundings presented components of organic matter possibly from precipitated organic compounds, product of the reaction mechanisms of the microorganisms or traces of the bacteria that were within the structures.

Fig. 7 and Table 4 shows the microchemical analysis of the surface of a shell (assay 0.4% T). The highest calcium peak indicates a higher purity in the structure. Notwithstanding, the high carbon content indicates the presence of residual organic matter in the surroundings.

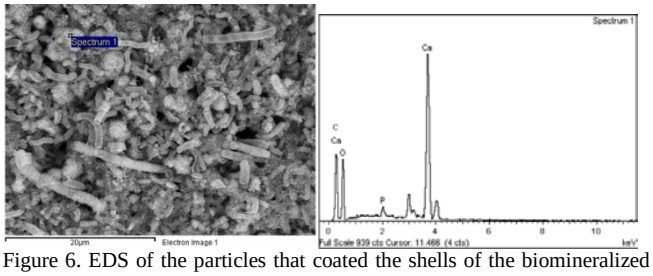


Figure 6. EDS of the particles that coated the shells of the biomineralized microorganisms (test 0.4% T)
Source: The authors.

Table 3.
Microchemical analysis of particles that coated the shells of the biomineralized microorganisms (Fig. 6).

Element	Weight%	Atomic%
C	25.23	36.27
O	48.41	52.25
P	0.99	0.55
Ca	25.36	10.93
Total	100.00	100.00

Source: The authors.

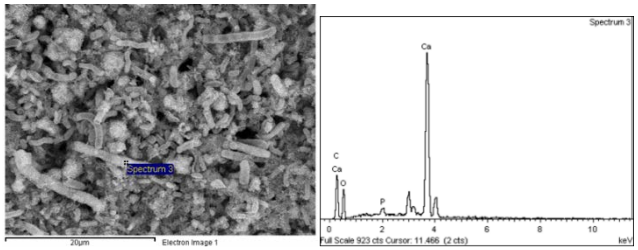


Figure 7. EDS of the shell of the biomineralized microorganisms (test 0.4% T).
Source: The authors.

Table 4.
Microchemical analysis of the biomineralized microorganisms (Fig. 7).

Element	Weight%	Atomic%
C	21.47	33.96
O	40.19	47.72
P	1.09	0.67
Ca	37.24	17.65
Total	100.00	100.00

Source: The authors.

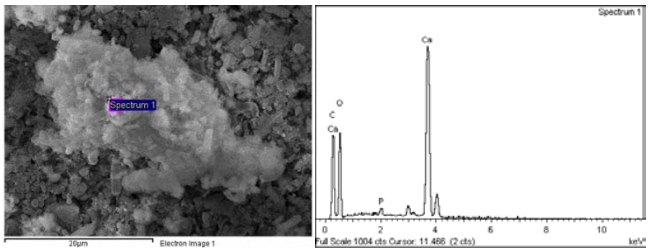


Figure 8. EDS of shell accumulations of the biomineralized microorganisms (test 0.4% T).
Source: The authors.

Fig. 8 and Table 5 shows the microchemical analysis of an accumulation of particles (assay 0.4% T). As was observed in Fig. 6 and Fig. 7, the high amount of carbon indicates the presence of residual organic matter in the surroundings.

The mineral formation over the bacterial surface could have presented in two stages:

Table 5.
Microchemical analysis of shell accumulations of the biomineralized microorganisms (Fig. 8).

Element	Weight%	Atomic%
C	25.13	35.53
O	51.20	54.35
P	0.67	0.37
Ca	22.99	9.74
Total	100.00	100.00

Source: The authors.

The possible reaction in the nucleation sites mediated by Ca^{2+} ions by the mechanism showed in the eq. (3) to eq. (5) [33]. In first place, the metallic ions from the medium might have stoichiometrically interacted with the charges groups of the bacterial surface structures, allowing the mineral deposition and generating bacillary walls, as observed in Fig. 5 to Fig. 7 [34].

$$Ca^{2+}{}_{(l)} + cell \longrightarrow cell - Ca^{2+}{}_{(l)} \quad (3)$$

$$HCO_{3\,(l)}^{-} \Longleftrightarrow H^{+}_{(l)} + CO_{2\,(l)}^{3-} \quad (4)$$

$$cell - Ca^{2+}_{(l)} + CO_{2\,(l)}^{3-} \longrightarrow cell - CaCO_{3(s)} \quad (5)$$

After precipitation, the second stage implies the increasing of the calcium carbonate concentration and saturation of the cell surface, generating an agglomeration and precipitation outside the cell, as shown Fig. 8. This precipitation is not controlled by the microorganism, but by the physic-chemical environment of the surface around each bacterium.

On the other hand, the traces of phosphorous identified in the microchemical analyses (Table 3 to Table 5) can have their origin in some of the components present in the Tryptone of the cultivation medium.

4. Conclusions

The microorganisms used in the project had a greater tendency to produce calcium carbonate nanoparticles as vaterite. The ratio of vaterite-calcite and its degree of purity can be affected by the tryptone concentration. However, a tryptone concentration below 0.4% would limit the metabolism of the bacteria and therefore the CO_2 formation, which could cause a deficit in the production of the precipitate. Notwithstanding, a 0.4% concentration produced a good precipitate rate, which is comparable to the results obtained at higher concentrations.

The processes carried out allowed the formation of shell shaped structures, which are composed of calcium carbonate nanoparticles (vaterite-calcite) with a bacillary morphology and hollow core, which could be considered as “microbricks”. Because the shells do not collapse after the washing phases of the precipitate, these could have potential applications in the manufacture of osseous structures for the microencapsulation of medications due to their hollow and almost uniform distribution.

Acknowledges

To Biofenix S.A.S. and the Universidad Pontificia Bolivariana, where the investigation was carried out and RutaN (Medellin) who finances the project.

References

[1] Daskalakis, M.I., Rigas, F., Bakolas, A., Magoulas, A., Kotoulas, G., Katsikis, I., Karageorgis, A.P. and Mavridou, A., Vaterite bio-precipitation induced by *Bacillus pumilus* isolated from a solutional cave in Paiania, Athens, Greece, International Biodeterioration and Biodegradation, 99, pp. 73-84, 2015. DOI: 10.1016/J.Ibiod.2014.12.005

[2] Stocks-Fischer, S., Galinat, J.K. and Bang, S.S., Microbiological precipitation of $CaCO_3$. Soil Biology and Biochemistry, 31(11), pp. 1563-1571, 1999. DOI: 10.1016/S0038-0717(99)00082-6

[3] Cacchio, P., Ercole, C., Cappuccio, G. and Lepidi, A., Calcium carbonate precipitation by bacterial strains isolated from a limestone cave and from a loamy soil. Geomicrobiology Journal, 20(2), pp. 85-98, 2003. DOI: 10.1080/01490450303883

[4] De Muynck, W., De Belie, N. and Verstraete, W., Microbial carbonate precipitation in construction materials: a review. Ecological Engineering, 36, pp. 118-136, 2010. DOI: 10.1016/J.Ecoleng.2009.02.006

[5] Tiano, P., Biagiotti, L. and Mastromei, G., Bacterial bio-mediated calcite precipitation for monumental stones conservation: methods of evaluation. Journal of Microbiological Methods, 36, pp. 139-145, 1999. DOI: 10.1016/S0167-7012(99)00019-6

[6] Castanier, S., Le Metayer-Levrel, G., Orial, G., Loubiere, J.F. and Perthuisot, J.P., Bacterial carbonatogenesis and applications to preservation and restoration of historic property, en Ciferri, O. Of Microbes and Art: The role of microbial communities in the degradation and protection of cultural heritage [online], Springer Sicence+Business Media, 2000, pp. 203-218. [consulted, October 20th of 2016]. Available at: https://goo.gl/ffsuIw

[7] Wada, N., Yamashita, K. and Umegaki, T., Effects of carboxylic acids on calcite formation in the presence of Mg^{2+} ions. Journal of Colloid and Interface Science, 212, pp. 357-364, 1999. DOI: 10.1006/Jcis.1998.6067

[8] Boquet, E., Boronat, A. and Ramos-Cormenzana, A., Production of calcite (calcium carbonate) crystals by soil bacteria is a general phenomenon. Nature, 246, pp. 527-529, 1973. DOI: 10.1038/246527a0

[9] Rodriguez-Navarro, C., Rodriguez-Gallego, M., Chekroun, K.B. and Gonzalez-Muñoz, M.T., Conservation of ornamental stone by *Myxococcus xanthus* - induced carbonate biomineralization. Applied and Environmental Microbiology, 69(4), pp. 2182-2193, 2003. DOI: 10.1128/Aem.69.4.2182

[10] Jimenez-Lopez, C., Jroundi, F., Pascolini, C., Rodriguez-Navarro, C., Piñar-Larrubia, G., Rodriguez-Gallego, M. and González-Muñoz, M.T., Consolidation of quarry calcarenite by calcium carbonate precipitation induced by bacteria activated among the microbiota inhabiting the stone. International Biodeterioration and Biodegradation, 62(4), pp. 352-363, 2008. DOI: 10.1016/J.Ibiod.2008.03.002

[11] Downs, R.T. and Hall-Wallace, M., The American mineralogist crystal structure database. American Mineralogist [online], 88(1), 2003. [date of reference October 20th of 2016]. Available at: https://goo.gl/LwfD48

[12] Anbu, P., Kang, C.-H., Shin, Y.-J. and So, J.-S., Formations of calcium carbonate minerals by bacteria and its multiple applications. Springerplus, 5(250), pp. 1-26 DOI: 10.1186/S40064-016-1869-2

[13] Baskar, S., Baskar, R., Mauclaire, L. and Mckenzie, J.A., Microbially induced calcite precipitation in culture experiments: possible origin for stalactites in Sahastradhara caves, Dehradun, India. Current Science [online], 90(1), 2006. [date of reference October 20th of 2016]. Available at: https://goo.gl/j3axfc

[14] Rusznyák, A., Akob, D.M., Nietzsche, S., Eusterhues, K., Totsche, K.U., Neu, T.R., Torsten, F., Popp, J., Keiner, R., Geletneky, J., Katzschmann, L., Schulze, E.D. and Küsel, K., Calcite biomineralization by bacterial isolates from the recently discovered Pristine Karstic Herrenberg cave. Applied and Environmental Microbiology, 78(4), pp. 1157-1167, 2012. DOI:10.1128/Aem.06568-11

[15] Chahal, N.K., Rajor, A. and Siddique, R. Calcium carbonate precipitation by different bacterial strains. African Journal of Biotechnology, 10(42), pp. 8359-8372, 2011. DOI: 10.5897/Ajb11.345

[16] Weiner, S. and Dove, P.M., An overview of biomineralization processes and the problem of the vital effect. Reviews in Mineralogy and Geochemistry, 54(1), pp. 1-29, 2003. DOI: 10.2113/0540001

[17] Mccusker, L.B., Von Dreele, R.B., Cox, D.E., Loue, D. and Scardi, P., Rietveld refinement guidelines. Journal of Applied Crystallography, 32, pp. 36-50, 1999. DOI: 10.1107/S0021889898009856

[18] Simanjuntak, W. and Sembiring, S., The use of the Rietveld method to study the phase composition of cordierite ($Mg_2Al_4Si_5O_{18}$) ceramics prepared from rice husk silica. Makara, Sains [online], 15, 2011. [date of reference October 20th of 2016]. Available at: https://goo.gl/8RrF3w

[19] Kniess C.T., Cardoso-de Lima, J. and Prates, P.B., The quantification of crystalline phases in materials: applications of Rietveld method, en Shatokha, V. Sintering - Methods and Products [en línea], Intech,

2012, pp. 293-316. [consulta, 20 de octubre de 2016]. Available at: http://goo.gl/NWoIs4
[20] Wei, S., Cui, H., Jiang, Z., Liu, H., He, H. and Fang, N., Biomineralization processes of calcite induced by bacteria isolated from marine sediments. Brazilian Journal of Microbiology, 46(2), pp. 455-464, 2015. DOI: 10.1590/S1517-838246220140533
[21] Wang, F., Xu, Z., Zhang, Y., Li, J., Nian, S. and Zhou, N., Green synthesis and bioactivity of vaterite-doped beta-dicalcium silicate bone cement. Ceramics International, 42(1), pp. 1856-1861, 2016. DOI: 10.1016/J.Ceramint.2015.09.150
[22] Silverstein, R.M., Webster, F.X., Kiemle, D.J. and Bryce, D.L., Spectrometric identification of organic compounds [online], 8th Edition, Wiley Online Library, 2014 [consulted: October 20th of 2016]. Available at: https://goo.gl/gt91UY
[23] Zhou, G.-T., Guan, Y.-B., Yao, Q.-Z. and Fu, S.-Q., Biomimetic mineralization of prismatic calcite mesocrystals: relevance to biomineralization. Chemical Geology, 279, pp. 63-72, 2010. DOI: 10.1016/J.Chemgeo.2010.08.020
[24] Montoya, C., Márquez, M.A., López, J. y Cuervo, C., Caracterización de cristales de calcita bioprecipitada por un aislamiento nativo de *Bacillus subtilis*. Revista Colombiana de Biotecnología [en línea], 7(2), 2005. [Consultado: Octubre 20 de 2016]. Disponible en: https://goo.gl/GV5C0I
[25] Patil, V.J., Patil, U.D., Bhoge, Y.E. and Kulkarni, R.D., Facile synthesis of calcium carbonate nanoparticles using solution spray reactor system. International Journal of Applied Engineering Research [online], 9(10), 2014. [date of reference October 20th of 2016]. Available at: Http://Www.Ripublication.Com/Ijaer.Htm
[26] Wang, Y.-Y., Yao, Q.-Z., Zhou, G.-T. and Fu, S.-Q., Formation of elongated calcite mesocrystals and implication for biomineralization. Chemical Geology, 360-361, pp. 126-133, 2013. DOI: 10.1016/J.Chemgeo.2013.10.013
[27] Singh, M., Kumar, V.S., Waghmare, S.A. and Sabale, P.D., Aragonite-vaterite-calcite: polymorphs of $CaCO_3$ in 7th century CE lime plasters of Alampur group of temples, India. Construction and Building Materials, 112, pp. 386-397, 2016. DOI: 10.1016/J.Conbuildmat.2016.02.191
[28] Sevcík, R., Pérez-Estébanez, M., Viani, A., Sasek, P. and Mácová, P., Characterization of vaterite synthesized at various temperatures and stirring velocities without use of additives. Powder Technology, 284, pp. 265-271, 2015. DOI: 10.1016/J.Powtec.2015.06.064
[29] Liu, J., Liu, Y., Kong, Y., Yao, J. and Cai, Y., Formation of vaterite regulated by silk sericin and its transformation towards hydroxyapatite microsphere. Materials Letters, 110, pp. 221-224, 2013. DOI: 10.1016/J.Matlet.2013.08.021
[30] Trushina, D.B., Bukreeva, T.V., Kovalchuk, M.V. and Antipina, M.N., $CaCO_3$ vaterite microparticles for biomedical and personal care applications. Materials Science and Engineering C, 45, pp. 644-658, 2015. DOI: 10.1016/J.Msec.2014.04.050
[31] Saikia, J. and Das, G., Framboidal vaterite for selective adsorption of anionic dyes. Journal of Environmental Chemical Engineering, 2(2), pp. 1165-1173, 2014. DOI: 10.1016/J.JECE.2014.04.016
[32] dePaula, S.M., Huila, M.F.G., Araki, K. and Toma, H.E., Confocal raman and electronic microscopy studies on the topotactic conversion of calcium carbonate from *Pomacea lineate* shells into hydroxyapatite bioceramic materials in phosphate media. Micron, 41(8), pp. 983-989, 2010. DOI: 10.1016/J.Micron.2010.06.014
[33] Li, W., Liu, L.-P., Zhou, P.-P., Cao, L., Yu, L.-J. and Jiang, S.-Y., Calcite precipitation induced by bacteria and bacterially produced carbonic anhydrase. Current Science [online], 100(4), 2011. [date of reference October 20th of 2016]. Available at: https://goo.gl/qp8RrA
[34] Douglas, S. and Beveridge, T.J., Mineral formation by bacteria in natural microbial communities. FEMS Microbiology Ecology [online], 26, pp. 79-88, 1998. DOI: 10.1016/S0168-6496(98)00027-0

G.A. Caicedo-Pineda, received the BSc. Eng. in Chemical Engineering in 2005, the MSc. degree in Biotechnology in 2008, and the PhD. degree in Engineering - Science and Technology of the Materials in 2015, all of them from the Universidad Nacional de Colombia, Manizales (Bs. Eng.) and Medellin (MSc. and PhD. degrees). From 2006 to 2010, he worked as researcher in the Universidad Nacional de Colombia, Medellin. From 2011 to 2015, he worked as process engineering researcher in Biofenix S.A.S. and Inverdesarrollo S.A.S. From 2015 to 2017, he worked as researcher in the Universidad Pontificia Bolivariana. Currently, he is a full professor in Escuela de Ciencias Químicas, Universidad Pedagógica y Tecnológica de Colombia. His research interest includes biomining, bioleaching, nanobiotechnology, bioremediation, biological wastewater treatment, green technology and raw materials bioimprovement.
ORCID: 0000-0003-2320-0980

M.C. Prada-Fonseca, received the BSc. Eng. in Biological Engineering in 2010 and the MSc. degree in Materials Engineering in 2016, all of them from the Universidad Nacional de Colombia, Medellin. From 2010 to 2014, she worked as researcher in the Universidad Nacional de Colombia, Medellin. From 2015 to 2017, she worked as researcher in the Universidad Pontificia Bolivariana, Medellín, Colombia. His research interest includes biomining, bioleaching, nanobiotechnology, bioremediation, biological wastewater treatment, green technology and raw materials bioimprovement.
ORCID: 0000-0003-2472-6191

A.E. Casas-Botero, received the BSc. Eng. in Chemical Engineering in 1998 from the Universidad Pontificia Bolivariana, Colombia the MSc. degree in Biotechnology in 2003 from the Universidad Nacional de Colombia, Medellin and the PhD. degree in Metallurgic Engineering in 2007 from Pontifícia Universidade Católica Do Rio De Janeiro, Brazil. From 1998 to the present, she mainly worked as full professor in the Universidad Pontificia Bolivariana. His research interest includes biomining, bioleaching, nanobiotechnology, bioremediation, biological wastewater treatment and green technology.
ORCID: 0000-0003-3194-4429

H.V. Martínez-Tejada, received the BSc. Eng. in Mechanical Engineering in 1998, the MSc. degree in Materials Science and Engineering in 2005 and the PhD. degree in Mechanical Engineering in 2005, all of them from the Universidad Pontificia Bolivariana (UPB), Medellín, Colombia. From 1999 to the present, he mainly worked as full professor in the UPB. He has participated in the creation of reference documents for science and technology programs at Colciencias National Program of Industry, Technology, Development and Innovation and he has been a member of the evaluation committee for the system of quality assurance in higher education, belonging to the National Ministry of Education in Colombia. He was Scientific Director of the EPM's Nanotechnology Center. He is currently managing the knowledge Research Agenda in Energy at the RDI Department at the UPB. His research interest includes nanotechnology, materials science and engineering, materials for energy, defense and materials for transport.
ORCID: 0000-0002-4693-2466

UNIVERSIDAD NACIONAL DE COLOMBIA
SEDE MEDELLÍN
FACULTAD DE MINAS



DYNA
http://dyna.medellin.unal.edu.co/

Development of a high performance batteries charger with low THD, high power factor, and high efficiency

Johan Sebastián Sánchez-Choachi, Miguel Ángel Dávila & Cesar Leonardo Trujillo

Facultad de Ingeniería, Universidad Distrital Francisco José de Caldas, Bogotá, Colombia. jossanchezc@correo.udistrital.edu.co, miadavilar@correo.udistrital.edu.co, cltrujillo@udistrital.edu.co

Received: October 23th, 2016. Received in revised form: June 14th, 2017. Accepted: December 15th, 2017

Abstract
This paper presents the design, simulation, and implementation of an off-board charger of medium and low capacity batteries that incorporates a power factor corrector, reaches a low THD current with the advantage of providing higher robustness against network frequency variations, and allows the implementation of three different charging strategies. On the one hand, this charger consists of a galvanic isolation stage, followed by a bridge rectifier connected to a Boost converter, which regulates the power factor and THD. On the other hand, a Buck converter cascaded with the Boost serves as a current or voltage source, depending on the operating charging strategy. Subsequently, results obtained in the testing phase are presented, placing great emphasis on obtaining a power factor of 0.978 and a THD of 5.7%, which are compared to standard IEC 61000-3-2. Finally, the efficiency of the prototype, which reaches a maximum of 91.1%, is evaluated; conclusions are therefore presented.

Keywords: battery charger; DC-DC converter; electromagnetic compatibility; power factor corrector; total harmonic distortion.

Desarrollo de un cargador de baterías de alto desempeño con bajo THD, alto factor de potencia y alta eficiencia

Resumen
Este articulo presenta el diseño, simulación e implementación de un cargador off-board de baterías de mediana y baja capacidad que incorpora un corrector de factor de potencia, alcanza una baja distorsión armónica (THD) en corriente y permite la implementación de tres diferentes estrategias de carga. Este cargador está compuesto de una etapa de aislamiento galvánico, seguida por un puente rectificador el cual es conectado a un convertidor Boost quien regula el factor de potencia y el THD. Por otro lado, un convertidor Buck es conectado a la salida del convertidor Boost, actuando como una fuente de corriente o tensión, dependiendo de la estrategia de carga que se implemente. Posteriormente, se presentan los resultados haciendo énfasis en el valor de 0.978 para el factor de potencia y el de 5.7% para el THD, el cual es comparado con el estándar IEC 61000-3-2. Finalmente, se evalúa la eficiencia del prototipo encontrando un valor máximo de 91.1% y luego se presentan las conclusiones.

Palabras clave: cargador de baterías; convertidor DC-DC; compatibilidad electromagnética; corrector de factor de potencia; distorsión armónica total.

1. Introduction

Considering the large number of batteries currently in existence and their potential exploitation for second activities that may make them have a greater presence in the energy sector [1], their chargers have become a device of great importance. On the other hand, electric vehicles are seen as an important alternative to face problems caused by pollution [2]; they also help alleviate the current oil crisis. However, such technology still poses some difficulties, especially in the energy storage system [3], this being the main reason why chargers are once again an essential part in the use of batteries.

How to cite: Sánchez-Choachi, J.S., Dávila, M.A. and Trujillo, C.L., Development of a high performance batteries charger with low THD, high power factor, and high efficiency. DYNA, 85(205), pp. 76-82, June, 2018.

© The author; licensee Universidad Nacional de Colombia.

Currently, a large number of chargers can be found in the market, but many of them do not include features of great importance for the consumer. Four of these characteristics can be efficiency, power factor (PF), total harmonic distortion (THD) of current, and implemented charging strategies. The first of such features requires a good use of energy drawn from the grid, something that has a strong impact on both the consumer and the environment. The second and third features are related to the first one, but in addition to this, they are required to meet the present need to improve the quality of energy taken from the grid as well as the electromagnetic compatibility [4]. This is because the quality of power supply emerges as an important factor in its distribution, since the performance of devices connected to the grid largely depends on this; as shown in [5], the increase of temperature in the low voltage cables, due to stationary disturbance, can reduce the lifetime and the isolation of conductor, an increases of nearly 5 ºC can reduce its lifetime in 50%. Moreover, the connection of different loads to the grid, such as electric vehicles in order to recharge their batteries, can cause voltage drops and injection of harmonic currents to the grid, if the control strategies are not adequate [6].

Considering that the current harmonics also depend on the magnitude of the grid voltage harmonics and its angles, and in most cases these relations are nonlinear [7], another drawbacks would be mentioned, such as problems related to synchronization, energy meter setbacks, malfunctioning of protection systems, interference with communication lines, and deterioration in the service life of a transformer [8].

This paper presents the design, simulation, and implementation of a battery charger with different capacities that also incorporates the four aforementioned features. Section 2 shows the design of a Buck and a Boost converter, whereas the third section presents the modelling of such converters using state variables. In section 4, a strategy control and its corresponding controllers are developed, taking into consideration the modelling produced in section 3. Section 5 shows the charger simulation with the aim of validating the power stage and controller design, which also includes a simple battery model. Finally, experiment results performed on the prototype, such as efficiency, load profile, PF, THD, and its comparison with standard IEC 61000-3-2 are shown.

2. DC-DC Converter design

As mentioned above, such charger consists of a stage of galvanic isolation, a rectifier, a PFC (Power Factor Corrector), and a buck converter, as shown in Fig. 1. This section presents the design of the Buck-Boost PFC converter using the small ripple approximation, in which the value of every element is determined according to the operating characteristics given in each converter.

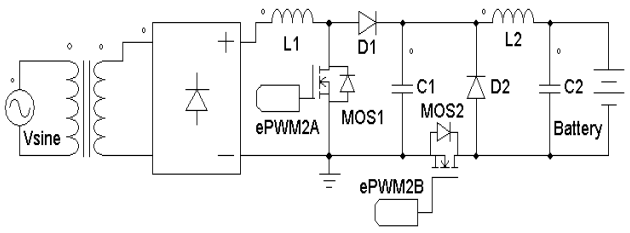


Figure 1 Schematic of battery charger
Source: The authors

2.1. Boost converter

The topology chosen for the PFC is Boost-type as it has a coil in its input; this makes it much easier to control the line current. Once the operating values of the converter have been established, it is necessary to begin with the input voltage, which is calculated as the nominal peak value of grid 170 V, divided by the transformation ratio, being 6 in this particular case; this results in 28.33 V. The next parameter to define is the Boost output voltage which, according to previous studies of efficiency conducted, is set at 50 V so as to obtain a duty cycle close to 0.43 and operate at maximum efficiency. Considering this output voltage, equation (1) is applied to solve for the duty cycle value, which yields a result of $D = 0.4848$.

$$V_o = \frac{V_i}{1 - D} \tag{1}$$

On the other hand, it is established that the device will handle a maximum power of about 150 W that, when conduction losses are ignored, represents a load resistance equal to 20.16 Ω, which in turn yields a load current equal to 5.29 A. Inductance value, as noted in Table 1, is determined by using equation (2) and establishing a ripple of 5 % for the output current of the PFC, along with the above parameters.

$$L_{min} = \frac{D(1 - D)^2 R}{2f} \tag{2}$$

To find the output capacitance, a 5% ripple is set at the output voltage (ΔVo) and replaced in equation (3); its result is shown in Table 1.

$$C = \frac{DTVo}{R\Delta Vo} \tag{3}$$

2.2. Buck converter

With the aim of regulating the current or voltage delivered to the battery, and taking into consideration the operating charging strategy, a Buck-type converter is connected. For its design, the range of duty cycle in which it will operate using equation (4) is defined, starting with minimum and maximum voltage values given at the Boost converter output.

$$Vo = DVi \tag{4}$$

By performing a similar procedure of the Boost design, the Buck converter is designed. The inductance (L) and capacitance (C) values are found and set forth in Table 1, together with the element values found for the boost and parameters such as duty cycle (D) and switching frequency (fs).

Table 1
Values of converter elements

	C[µF]	*L*[µH]	*D*	S[kHz]
Boost	2,200	865	0.48	30
Buck	467	370	0.28	30

Source: The authors

3. Converter modelling

The AC modelling of the converters is performed in this section. In order to do this, the procedure described in [9] is carried out, in which voltages across the coils and capacitor currents are disturbed and linearized, ignoring second order terms.

3.1. Boost converter

For this converter, the modelling was done taking into account coil losses (R_l), switch losses (Ron) and the diode forward voltage (V_D), obtaining equation (5). In this equation, $\hat{V}_{out}$ and $\hat{I}_L$ are the linear terms of *C1* voltage and *L1* current, respectively.

$$\begin{pmatrix} C1 & 0 \\ 0 & L1 \end{pmatrix} \begin{pmatrix} \frac{d\hat{V}_{out}}{dt} \\ \frac{dI_L}{dt} \end{pmatrix} = \begin{pmatrix} -\frac{1}{R} & 1 \\ -1 & -R_L - R_{on}D_1 \end{pmatrix} \begin{pmatrix} \hat{V}_{out}(t) \\ \hat{I}_L(t) \end{pmatrix} + \begin{pmatrix} 0 & 0 \\ V & V_D - R_{on}I_L \end{pmatrix} + \begin{pmatrix} 0 & 0 \\ D_1 & D_1 - 1 \end{pmatrix} \begin{pmatrix} \hat{V} \\ \hat{V}_D \end{pmatrix} \quad (5)$$

3.2. Buck converter

For this analysis, conduction loss in the coil *L2* and in the switch, denoted as R_l and R_{on}, respectively, are also included. The result of such analysis is equation (6). In this equation, *D* is the stationary value of the duty cycle and $\hat{d}$ is the duty cycle variation around the equilibrium point.

$$\begin{pmatrix} C2 & 0 \\ 0 & L2 \end{pmatrix} \begin{pmatrix} \frac{d\hat{V}}{dt} \\ \frac{d\hat{I}}{dt} \end{pmatrix} = \begin{pmatrix} \frac{-1}{R} & 1 - D_2 \\ D_2 - 1 & -R_L - R_{on}D_2 \end{pmatrix} \begin{pmatrix} \hat{V}(t) \\ \hat{I}(t) \end{pmatrix} + \begin{pmatrix} 0 \\ 1 \end{pmatrix} \hat{V}_s + \begin{pmatrix} 0 & -I \\ V & -R_{on}I \end{pmatrix} \hat{d} \quad (6)$$

4. Control loop design

This section presents the corresponding block diagrams for each of the converters. Transfer functions of the specific blocks are obtained by means of the modelling performed in the previous section; in this way, the resultant controllers are therefore designed.

4.1. Boost circuit controller

In the design of the Boost circuit controller that serves as PFC, the block diagram in Fig. 2 is presented, showing the input current loop (internal), which is responsible for maintaining the sinusoidal input current in phase with the line voltage waveform.

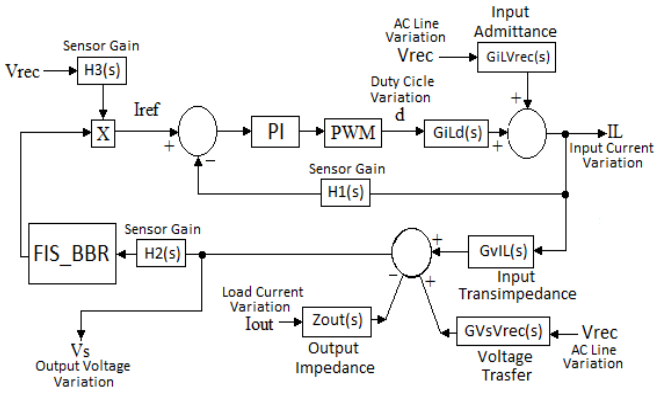


Figure 2 Block diagram of PFC
Source: The authors

On the other hand, the voltage loop (external), which regulates voltage output of the PFC, is built under the control scheme of average current [10]. The two previous loops consist of GiLVrec, Gild, GvIL, and GVsVrec, which are the current transfer functions in the current depended voltage source, duty cycle dependent current source, output voltage-dependent current source, and output voltage-dependent line voltage source, respectively. H1, H2, and H3 are the transfer functions of the corresponding filters. The compensator of current loop is PI type, whereas a fuzzy controller based on Boolean relations (FIS BBR) [11] was implemented due to the complexity of the voltage loop and the temporal variations of some of its parameters.

To facilitate the control task, the gains of direct path are intended to be significantly greater than the loop, so that disturbances can be ignored, as shown in Fig. 2. Bearing in mind the above, a frequency-based PI compensator is designed, whose necessary parameters for its implementation are described in Table 2.

The fuzzy voltage control loop takes that losses in the Boost can be ignored, making the PFC power input (P_{in}) and output equal, which allows it to solve for the constant of proportionality *K* between the voltage (V_{rms}) and line current, therefore obtaining equation (7), where Ss and Sr are the voltage and current sensors, respectively.

$$K = \frac{P_{in}}{{V_{rms}}^2} \frac{S_s}{S_r} \quad (7)$$

Taking into account the range of variation of P_{in} (from 0 W to 180 W), an operating range of *K* between 0 and 0.58 is presented. On the other hand, equation (8), in which V_{C1}, K_{ADC}, and K_C represent the rated voltage on the capacitor, amplification of ADC (gain) and sensor gain, respectively, is obtained; this equation yields a result of 3,078.8 for the antecedent variable (V_{XD}).

$$V_{XD} = V_{C1}K_{ADC}K_c \quad (8)$$

Therefore, for the sake of simplicity, three membership functions for the antecedent variable as well as three virtual actuators are set; equation (9) is obtained as the output controller.

$$\sum_{m=1}^{3} Y_m V_m = 0.1Y_1 + 0.3Y_2 + 0.5Y_3 \quad (9)$$

4.2. Buck circuit controller

Since at this stage the charger will act as a source of current or voltage, depending on the charging strategy adopted, it is necessary to develop two control loops which can operate independently and regulate the output voltage and current of the charger. The block diagram in Fig. 3 (top) shows the Buck converter operating in the constant current mode, while Fig. 3 (bottom) presents the block diagram when operating in constant voltage mode. Once again, this seeks to ensure that the gains of direct path are large enough to ignore disturbances coming from external agents.

Finally, using the modelling performed in section 3, transfer functions for current and voltage of the Boost converter are obtained and shown in equations (10, 11).

$$G_{vd} = \frac{V-V_g}{D\prime} \frac{1-\frac{LI}{D\prime(V_g-V)}s}{1+s\frac{L}{D\prime^2 R}+s^2\frac{LC}{D\prime^2}} \quad (10)$$

$$G_{ig} = -\frac{D}{D\prime} \frac{1}{1+s\frac{L}{D\prime^2 R}+s^2\frac{LC}{D\prime^2}} \quad (11)$$

The transfer current and voltage transfer functions of the Buck converter are shown in equations (12, 13).

$$G_{vd} = \frac{\frac{D'(V_g-V)}{LI}-s}{1+s\frac{L}{D\prime^2 R}+s^2\frac{LC}{D\prime^2}} \quad (12)$$

$$G_{ig} = \frac{1}{\frac{L}{D\prime^2 R}+\frac{LC}{D\prime^2}s+s^2} \quad (13)$$

Additionally, an analysis in frequency is conducted. The result is PI controllers, whose gains (P and I) for a discrete implementation are described in Table 2, which includes the corresponding bandwidths (B), phase margin (PM), and gain margin (GM).

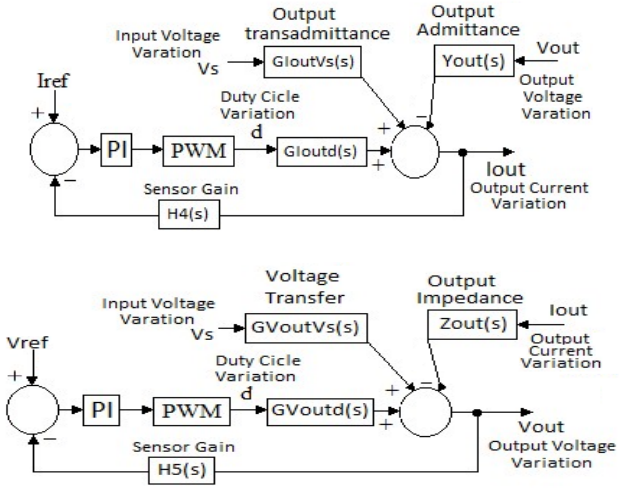


Figure 3 Block diagram of Buck converter when operating in constant current mode (top). Block diagram of Buck converter when operating in constant voltage mode (bottom)
Source: The authors

Table 2
Parameters of discrete time PI controllers

Controller	P	I	MF	MG(dB)	B(kHz)
I loop-Boost	0.89	1,054	57º	25	3
I loop-Buck	0.134	50.11	60º	37	5
V loop-Buck	1.8742	3,280	60º	44	3.5

Source: The authors

5. Simulations

To check the task of converters and controllers design, this section presents the simulation of the charger. However, it is first of all necessary to choose a reliable detection method for the state of charge (SOC). To this end, models are based on neural networks [12,13], fuzzy logic [14], and Adaptive Unscented Kalman Filter and support vector machine [15].

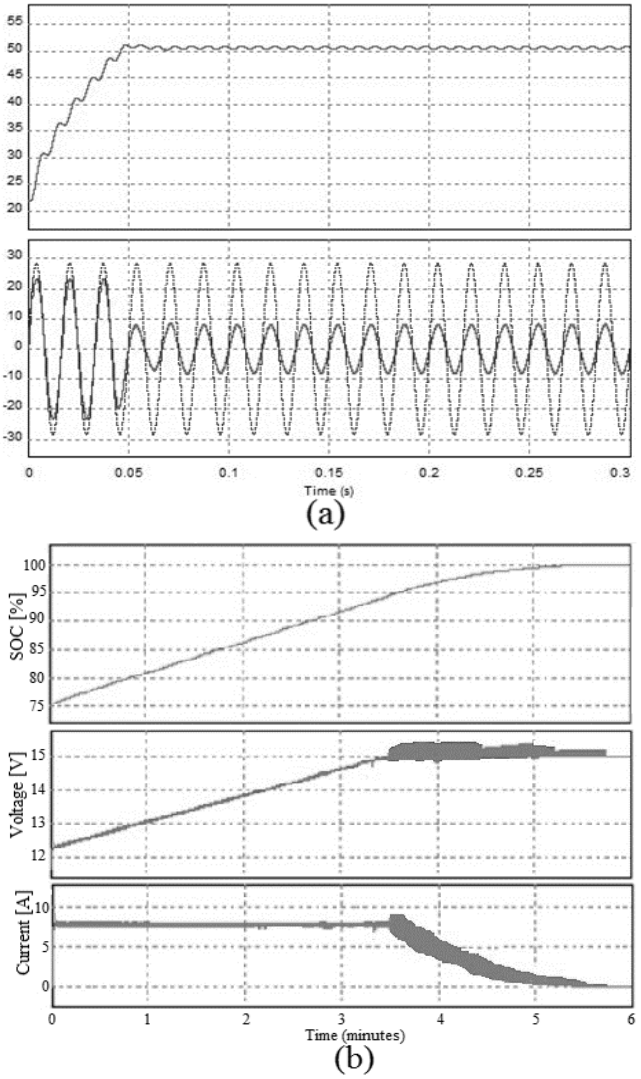


Figure 4(a) PFC output voltage (top), voltage (dashed line), and current (continuous line) line (down); (b) SOC (top), battery voltage (middle), and battery current (down)
Source: The authors

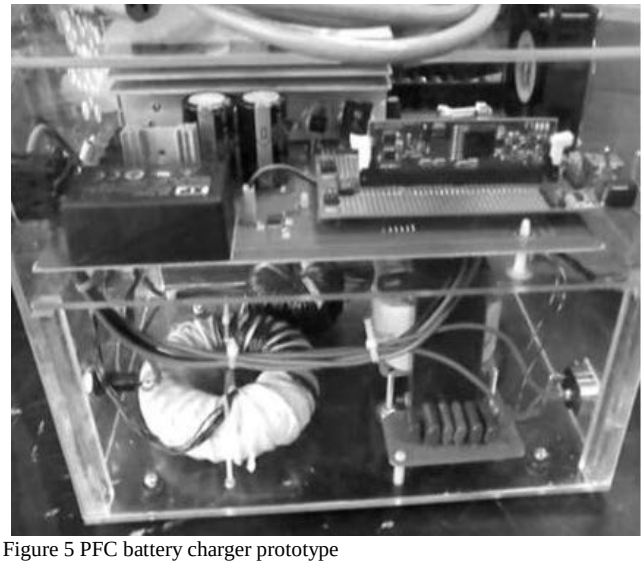


Figure 5 PFC battery charger prototype
Source: The authors

When analyzing these different methods, the one suggested in [16] is chosen because of simplicity and effectiveness. The upper part of Fig. 4(a) shows the PFC output, indicating a stable behavior close to the value at which it was designed (50 V). On the other hand, the lower part of Fig. 4(a) shows the line voltage (dashed line) and current (grid), in which the sinusoidal behavior as well as its input voltage phase can be seen, implying a THD equal to 4.3 % and a PF of 0.998.

The operation of charger is now simulated, intended to recharge a battery of 12 V in the constant current-voltage mode. In order to do this, constant current is used until the battery reaches 15 V, time at which it is necessary to make the transition to constant voltage, ending the process completely until a state of charge (SOC) equal to 95 % is reached. Fig. 4(b) shows the result of this operation

6. Experiment results

The prototype shown in Fig. 5 was obtained as a result of the proposed charger implementation, along with tests performed when recharging a battery of 12 V and 26 AH so as to obtain the SOC. Voltage and current in the ba tery during the entire charging process are shown and presented in Fig. 6. In this latter figure, it is important to highlight the good behavior of these variables during the process and the smooth transition between the two operating modes.

To evaluate the THD and the PF, current waveforms and line voltage in Fig. 7 are firstly shown, which indicates a sinusoidal current behavior; it implies a low THD. However, it also demonstrates that it is approximately proportional to the phase voltage, which means a PF close to the unit.

Fig. 8 compares the amplitude of each harmonic regarding standard IEC 61000-3-2 with the line current waveform of the charger. In addition, the measurement of THD of voltage and line current during the charging process is presented in zoom-in waveforms of the same figure, made with a properly calibrated 824 PQA. The figure highlights an

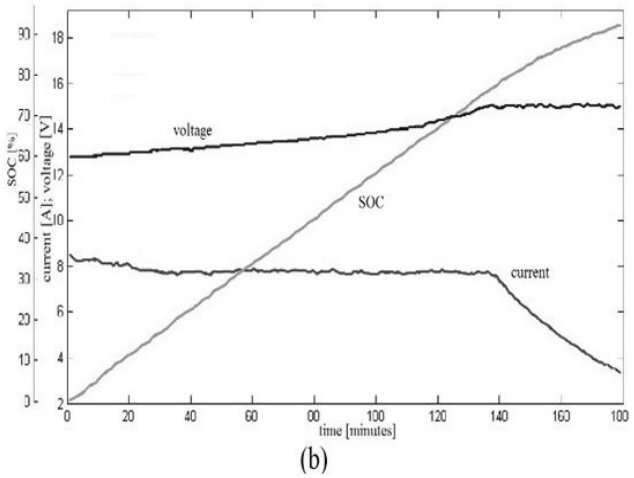


Figure 6. SOC, voltage, and current battery during charging process
Source: The authors

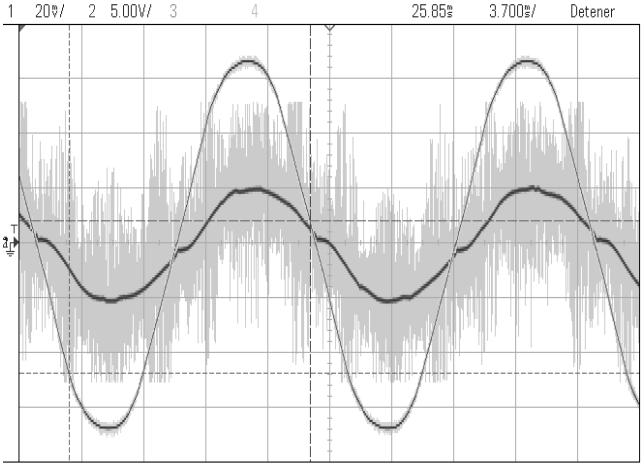


Figure 7 Voltage and current line waveforms of the prototype
Source: The authors

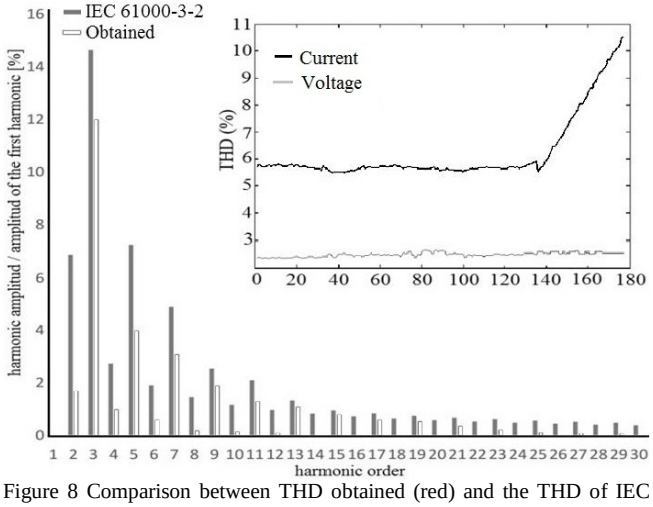


Figure 8 Comparison between THD obtained (red) and the THD of IEC 61000-3-2 (blue) and a zoom of temporal behavior of current (blue) and voltage (red) line THD
Source: The authors

average value of THD of 5.7% in current during the constant current mode, which increases to a maximum of 10.3% for the end of the process. However, it is worth noting that the grid voltage also presents an inherent THD of 2.3% on average, affecting the input current behavior. As discussed in the design, the PFC is synchronized with the grid; this is an advantage over other strategies, such as resonant and repetitive control that have been proposed in recent works and where their performance is affected by changes in grid frequency. Other works such as [17] proposes odd-harmonic high order repetitive control, which yields better results; its drawback, however, is that only removes the odd harmonic.

In addition to the good quality of sinusoidal input current, this also presents a very small gap with respect to the line voltage, which implies a PF close to the unit as can be seen in Fig.9 (top); it shows the cosine of the phase angle between line voltage and current as well as the PF of the charger, each reaching an average value for the constant current mode of 0.977 and 0.976, respectively. However, these values decrease to a minimum of 0.912 and 0.892 at the end of the charging process. Similarly, the low value of THD and the PF close to the unit make the losses in the various elements of the charger diminish, thereby contributing significantly to the efficiency of the device. According to Fig. 9(b), it reaches a maximum value of 91.1 % for the constant current mode until reaching a value of 60% at the end of the loading process. At this stage, the power consumption is 18 W, which can be compared to the inherent losses in the charger.

As can be seen in many of the results presented above, the benefits of the charger decrease in the constant voltage mode since, at this stage, the power consumption considerably decreases, distancing the charger from the operating nominal conditions for which it was designed.

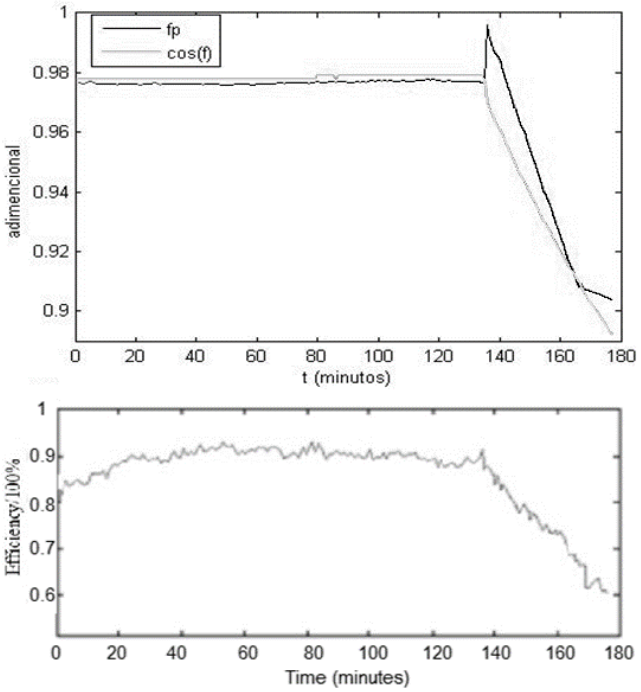


Figure.9 (a). FP and cosine of the phase angle between current and voltage line; (b) charger's efficiency during recharging process
Source: The authors

Conclusions

A battery charger with dual power converter topology was designed and implemented, capable of operating three separate loading strategies: constant voltage, constant current, and constant current-voltage. Unlike chargers currently found in the market, the developed prototype includes a power factor corrector which establishes a PF unit and a control strategy that allows it to generate a semi-sinusoidal input current and in turn makes it attain THD values in current close to 5.7 %, this in compliance with the standard IEC 61000-3-2. In addition to that, it also reduces losses in the device. Another important feature of the developed prototype is that it can be programmed for charging batteries for a wide range of capacities. Nevertheless, it is recommended that this should be between 10 AH and 80 AH, so that the THD and PF can be kept in satisfactory values.

Acknowledge

This work is supported by project entitled "Low and Medium capacity battery charger with low current THD, high power factor and high efficiency for electric vehicles" sponsored by COLCIENCIAS aims to support initiatives for the developing of novel technologies in the field of energy storage.

References

[1] Sathre, R., Scown, C., Kavvada, O. and Hendrickson, T., Energy and climate effects of second-life use of electric vehicle batteries in California through 2050. Journal of Power Sources, 288, pp. 82-91, 2015. DOI: 10.1016/j.jpowsour.2015.04.097.

[2] Liu, H., Huang, X., Tan, L., Gou. J. and Wang, W., Switchig control optimisation strategy segmented transmitting coils for on-road charging of electrical vehicles. IET Power electronics, 9(11) ,pp. 2282-2288, 2016. DOI: 10.1049/iet-pel.2015.0778.

[3] Arco, D., Piegari, L. and Tricoli, P., A Modular converter with embedded battery cell balancing for electric vehicles, electrical systems for aircraft, Railway and Ship Propulsion (ESARS), 2012. pp. 1-6.

[4] Koshy, S., Ballal, M. and Suryawanshi, H., Power quality analysis and its effects on energy meter readings and life expectancy, International Conference on Circuit, Power and Computing Technologies [ICCPCT], 2014, pp. 674- 679.

[5] Duran-Tovar, I., Pavas-Martinez, F. and Duarte-Velasco, O., Effects of lifetime of low voltage conductors due to stationary power quality disturbance, DYNA, 82(192), pp. 44-51, 2015. DOI: DOI: 10.15446/dyna.v82n192.48568

[6] Mendoza, C., Quintero, A., Santamaria, F. and Alarcon, A. Cordinated recharge of electrical vehicles in real time, DYNA, 83 (197), pp. 222-231, 2016. DOI: 10.15446/dyna.v83n197.55342

[7] Blanco, A., Yanchenko, S., Meyer, J. and Schegner, P., The impact of supply voltage distortion on the harmonic current emission of non-linear loads, DYNA, 82(192), pp. 150-159, 2015. DOI: 10.15446/dyna.v82n192.48591

[8] Liu, J., Xiao, F., Chen, W. and Yang, G., A Novel control scheme for three-level full-bridge converter achieving low THD output voltage. The 2014 International Power Electronics Conference 18-21, 2014, pp. 66-71.

[9] Alassi, A. and Massoud, A., Modeling of DC-DC converters with continuous input current for high power PV aplications. IEEE Symposium on Computer Applications & Industrial Electronics (ISCAIE), 2016. pp. 171-176.

[10] Moldaschl, J., Broulím, J. and Paločko, L., Boost power factor correction topology with average current control, International conference Applied Electronics, 2014, pp. 213-216.
[11] Gantiva, J., Soriano, J. and Salazar, O., Fuzzy control of spacecraft attitude by Fuzzy Inference System Based on Boolean Relations (FISBBR). Norbert Wiener in the 21st Century (21CW), 2014 IEEE Conference on, 2014, pp. 1-7.
[12] Liu, F., Liu, T. and Fu, Y., An improved SoC estimation algorithm based on artifitial neural network. 8th International Symposium on Computational Intelligence and Design (ISCID), 2015. pp. 152-155.
[13] Wang, Z. and Yang, D., State-of-charge stimation of lithium iron phosphate battery using extreme learning machine. 6th International Conference on Power Electronics Systems and Applications (PESA), 2015. pp. 1-5.
[14] Du. J., Liu, Z., Wang, Y. and Wen, C., A fuzzy logic-based model for Li-ion battery with SOC and temperature effect. 11th IEEE International Conference on Control & Automation (ICCA), 2014. pp. 1333-1338.
[15] Meng, J., Luo, G. and Gao, F., Lithium polymer battery state-of-charge estimation based on adaptive unscented Kalman filter and support vector machine. IEEE Transactions on Power Electronics, 31(3), pp. 2226-2238, 2016. DOI: 10.1109/TPEL.2015.2439578.
[16] Araujo, J., Hartmann, L.V., Correa, M.B.R. and Lima, A.M.N., lead-acid battery modeling and state of charge monitoring. Applied Power Electronics Conference and Exposition (APEC), 2010 Twenty-Fifth Annual IEEE, 2010, pp. 239-243. DOI: 10.1109/APEC.2010.5433666.
[17] Ramos, G., Melo-Lagos, I. and Cifuentes, J., High performance control of a three-phase PWM rectifier using odd harmonic high order repetitive control, DYNA, 83(198), pp. 27-36, 2016. DOI: 10.15446/dyna.v83n198.53276

J.S. Sanchez-Choachi, received the BSc. Eng in Electronic Engineering from the Universidad Distrital Francisco José de Caldas, Bogotá, Colombia in 2015. Graduated of Physics at the Universidad Nacional de Colombia in 2015. From 2015 to 2017 he worked as asistant profesor at Universidad Nacional de Colombia. Currently, he is a master student and a researcher at the Universidad Distrital Francisco Jose de Caldas, Bogotá, Colombia. His research interest include: power quality, power converters and control technics.
ORCID: 0000-0002-1945-5975

M.A. Dávila Rojas, received the BSc. Eng in Electronic Engineering from the Universidad Distrital Francisco José de Caldas, Bogotá, Colombia in 2015. Currently, he is a student of Electronic Engineering master. His topics of interest are: power converters, power quality and battery chargers.
ORCID: 0000-0003-4215-8116.

C.L. Trujillo-Rodríguez, received the BSc. degree in Electronics Engineering from the Universidad Distrital Francisco José de Caldas, Bogotá, Colombia, the MSc. degree in Electrical Engineering from the Universidad Nacional de Colombia, Bogotá, Colombia, and the PhD. degree in Electronics Engineering from the Universidad Politécnica de Valencia, Valencia, Spain. He is a full professor in the Department of Electrical Engineering, Universidad Distrital Francisco José de Caldas, where he currently teaches courses on analog circuits and power electronics. His main research interests include: modeling and control of power converters applied to the distributed generation and microgrids.
ORCID: 0000-0002-0985-1472



UNIVERSIDAD NACIONAL DE COLOMBIA
SEDE MEDELLÍN
FACULTAD DE MINAS

Área Curricular de Ingeniería
Eléctrica e Ingeniería de Control

Oferta de Posgrados

Maestría en Ingeniería - Ingeniería Eléctrica

Mayor información:

E-mail: ingelcontro_med@unal.edu.co
Teléfono: (57-4) 425 52 64

UNIVERSIDAD NACIONAL DE COLOMBIA
SEDE MEDELLÍN
FACULTAD DE MINAS



DYNA
http://dyna.medellin.unal.edu.co/

Elastic behavior of stiffened curved plates subjected to transverse loading

Abel Noguera-Garban [a], Carlos Graciano [b] & David G. Zapata-Medina [b]

[a] *División de Ciencias Físicas y Matemáticas, Universidad Simón Bolívar, Venezuela. abel_noguera@yahoo.es*
[b] *Facultad de Minas, Universidad Nacional de Colombia, Medellín, Colombia. cagracianog@unal.edu.co, dgzapata@unal.edu.co*

Received: February 02nd, 2017. Received in revised form: November 1rd, 2018. Accepted: February 15th, 2018.

Abstract
This paper presents a numerical study on the elastic behavior of stiffened curved plates subjected to transverse loading. The analyses are performed by means of linear static analysis using finite element modelling. Firstly, flat plates under transverse loading (uniform and non-uniform-trapezoidal) are modelled to validate the computational model against analytical solutions available in the literature. Secondly, the behavior of unstiffened curves plates under transverse loading is analyzed. Then, the influence of both, transversal and longitudinal stiffening in controlling the out-of-plane displacements and stresses distribution of the curve plates is demonstrated. Finally, a case-study concerning the response of a hydroelectric power plant intake gates subjected to a hydrostatic head is further investigated. The results show that the increase in gate stiffness is reflected in smaller deformations implying a better performance and system integrity.

Keywords: curved plates; stiffeners; finite elements; intake gates; hydrostatic head; deformations.

Comportamiento elástico de placas curvas rigidizadas sometidas a cargas transversales

Resumen
Este trabajo presenta un estudio numérico del comportamiento elástico de placas curvas rigidizadas sometidas a carga transversal. Los análisis se realizaron mediante análisis estático lineal utilizando modelación por elementos finitos. Inicialmente, placas planas bajo carga transversal (uniforme y no uniforme-trapezoidal) se modelan para validar el modelo computacional frente a soluciones analíticas disponibles en la literatura. En segundo lugar, se analiza el comportamiento de las placas curvas no rigidizadas bajo carga transversal. Luego, se demuestra la influencia de la rigidez longitudinal y transversal en el control de la distribución de desplazamientos y tensiones fuera de plano de las placas curvas. Finalmente, la respuesta de una compuerta radial de una planta hidroeléctrica sometida a una cabeza hidrostática es investigada. Los resultados muestran que el aumento en la rigidez a la puerta se refleja en las deformaciones más pequeñas lo que implica un mejor rendimiento y la integridad del sistema.

Palabras clave: placas curvas; rigidizadores; elementos finitos; compuertas; carga hidrostática; deformaciones.

1. Introduction

Curved plate elements have traditionally been used in mechanical, aeronautical and marine/off-shore engineering. These structural elements are found in the fuselage of aircrafts, oil and gas storage structures, cooling towers and ship hulls. Their applications in civil engineering are relatively recent and mainly focus on the construction of steel bridges. Typical examples of curved panels in bridge engineering are orthotropic decks in box-girder bridges and webs of in-plane curved I-girders.

Stiffened curved plates are also becoming more and more popular as recent developments of the curving process allow for a faster and more economic manufacturing. Nevertheless, their design is complex and difficult due to the lack of standard building code specifications [1], few studies related to their stability are available in the literature [2-4]. Consequently, curved plate analysis and design rely

How to cite: Noguera-Garban, A., Graciano, C. and Zapata-Medina, D.G., Elastic behavior of stiffened curved plates subjected to transverse loading. DYNA, 85(205), pp. 83-89, June, 2018.

© The author; licensee Universidad Nacional de Colombia.

significantly on expensive and time-consuming finite element modeling [2,3].

Recently, the influence of longitudinal stiffening on both, critical and ultimate strength of plate girders has been investigated [5-7]. The primary function of the stiffeners is to control out-of-plane displacements of the thin-walled webs and increase bending resistance.

This paper presents a numerical investigation on the elastic behavior of stiffened curved plates subjected to transversal loading. A parametric study is performed through finite element analysis to evaluate the beneficial effects of including longitudinal and transverse stiffeners on the performance of curved plates. Firstly, the numerical model is validated against theoretical formulae available in the literature. Then, a case study is further analyzed to evaluate the response of a hydroelectric power plant intake radial gate subjected to a hydrostatic head. At the end, the results show that stiffeners are a practical way to retrofit existing structural elements as they increase the system stiffness and reduce transversal deformations, which is directly reflected in an improvement of system reliability.

2. Numerical modeling

This section presents a numerical study conducted to investigate the influence of transversal and longitudinal stiffening on the out-of-plane displacements of stiffened curved plates subjected to transverse loading.

Various computational models for plates under transversal loading are elaborated using the finite element software ANSYS [8]. A detailed description of the employed numerical models can be found in [9]. These models are validated using a procedure that considers the influence of the plate geometry (flat and curved), boundary and loading conditions and finally considering the presence of transverse and longitudinal stiffening. Thereafter, a more complex numerical model is elaborated to investigate the influence of the stiffening on the out-of-plane displacements and stress distribution of a curved plate.

The material used in all analyses is an ASTM A516 Gr 70 steel, with Young's modulus, E= 206 GPa; Poisson ratio, υ= 0.3; density, γ= 7.85×10^{-6} kg/m^3; yield strength, f_y= 260 MPa and ultimate strength f_u= 485 MPa.

2.1. Flat plates under transverse loading

As mentioned above, the first step into the validation procedure of the numerical methodology is to investigate the influence of boundary and loading conditions on the structural response of flat plates subjected to transverse loading. In this regard, Table 1 shows a schematic view of boundary and loading conditions for the three numerical models developed for flat plates herein: Model *N1* with the upper and lower ends free to move and the lateral ends simply supported, under uniform transverse loading (p = 0.001 MPa); Model *N2* with the upper and lower ends free to move and the lateral ends simply supported, under non-uniform (trapezoidal) transverse loading (p = 0.01667 MPa); and Model *N3* clamped at four ends, under uniform transverse loading (p = 0.001 MPa).

Table 1.
Flat plate models.

Model	Schematic of boundary and loading conditions	Eqs. for σ_{max} (MPa) and δ_{max} (mm) [10]
N1	Free end; Uniform loading; Simply supported; Free end	$\sigma_{max} = \frac{0.75\omega b^2}{t^2(1+1.61\alpha^3)}$ $\delta_{max} = \frac{0.1422\omega b^4}{Et^3(1+2.21\alpha^3)}$
N2	Free end; Trapezoidal loading; Simply supported; Free end	$\sigma_{max} = \beta\frac{\omega b^2}{t^2}$ $\delta_{max} = \alpha\frac{\omega b^4}{Et^3}$
N3	Clamped end; Uniform loading; Clamped; Clamped end	$\sigma_{max} = \frac{0.75\omega b^2}{t^2(3+4\alpha^3)}$ $\delta_{max} = \frac{0.0284\omega b^4}{Et^3(1+1.056\alpha^5)}$

Source: The authors.

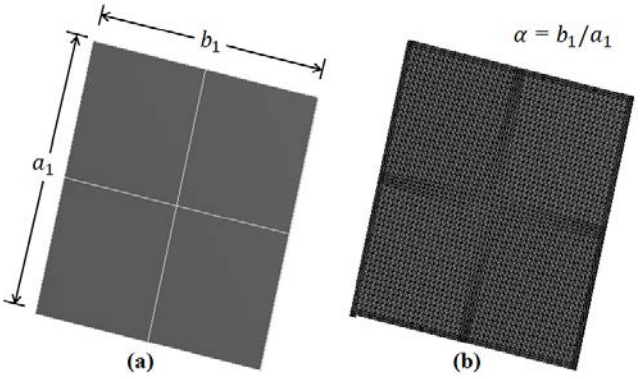


Figure 1. (a) Dimensions for Models *N1*, *N2* and *N3*, and (b) Mesh for flat plates.
Source: The authors.

Table 1 also shows formulas for the calculation of maximum stresses σ_{max} and displacements δ_{max} [10]. Shell181 elements from the ANSYS element library [8] were used to model the plates. The dimensions of the plates were: width, b_1= 10000 mm; height, a_1= 10000 mm; and thickness, t_p= 20 mm (see Fig. 1a). An additional parametric study was conducted regarding the panel aspect ratio, α= b_1/a_1= 1.5, 2 and 2.5, maintaining constant the height, a_1= 10000 mm. Fig. 1b shows a representative mesh of the flat plates, while Figs. 2a and 2b show the out-of-plane displacements plots obtained numerically for Models *N1* and *N2*, respectively.

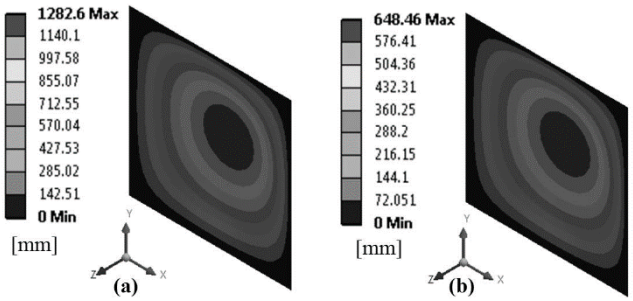


Figure 2. Radial displacement with p = 0.001 MPa and α=1: (a) Model *N1* and (b) Model *N2*.
Source: The authors.

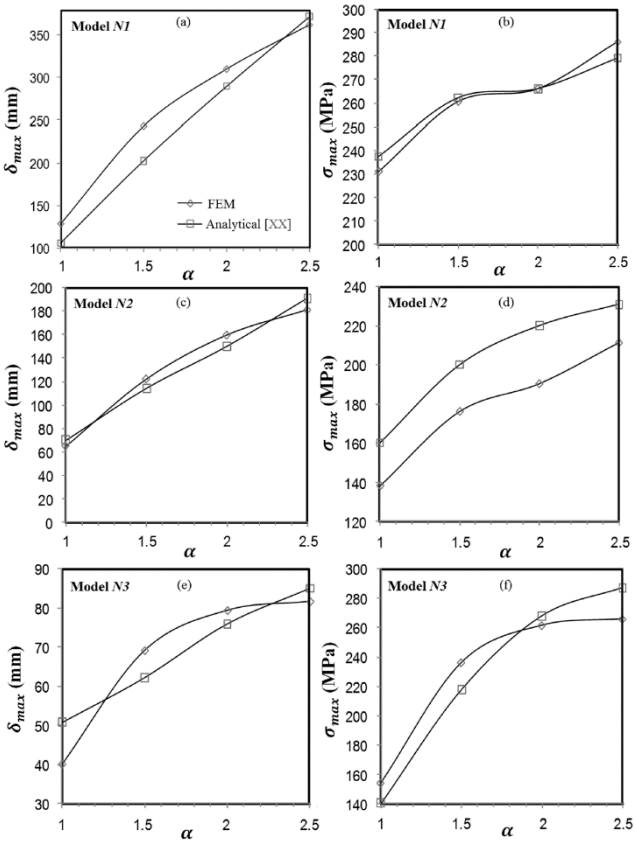


Figure 3. Maximum radial displacement at the center of the plate and maximum von Mises stress intensity for Models *N1*, *N2* and *N3*.
Source: The authors.

Fig. 3 shows a comparison for maximum displacements and stresses, between computed values and those obtained analytically with the equations proposed by [10] and summarized in Table 1. A good agreement between numerical and analytical results is achieved with a maximum difference of approximately 10%. It is worth noticing that the available formulas were obtained for stresses and displacements in the elastic range. Even though, the stresses are slightly higher than the corresponding yield strength of the material (f_y = 260 MPa). The figure shows that for Model *N1* the maximum radial displacement increases with the panel aspect ratio, α. For Model *N2*, with the same boundary conditions as Model *N1* but different load distribution, the maximum radial displacement reduces about 30% compared to Model *N1*. For Model *N3*, clamped in all ends and uniformly loaded, the maximum displacement is reduced around 50% with regards to Model *N1*. These results demonstrate the impact of boundary and loading conditions on both, maximum displacements and maximum stress when modeling flat plates subjected to transverse loading. The results also show that both, the maximum displacement and the maximum stress increases with the panel aspect ratio for the three Models (*N1*, *N2* and *N3*).

2.2. Curved plates under transverse loading

Continuing the methodology applied for flat plates, this section aims at investigating the influence of boundary and loading conditions on the structural response of curved plates subjected to transverse loading. Four additional models were developed as shown in Fig. 4, hence: Model *N4* with the upper and lower ends free to move and the lateral ends simply supported, under uniform transverse loading (p= 0.1 MPa); Model *N5* with the upper and lower ends free to move and the lateral ends simply supported, under non-uniform (trapezoidal) transverse loading (p = 0.1 MPa); Model *N6* clamped at four ends, under uniform transverse loading (p= 0.1 MPa); and Model *N7* clamped at four ends, under non-uniform (trapezoidal) transverse loading (p = 0.1 MPa).

Fig. 4 shows a schematic view of boundary and loading conditions of the four models. Shell 181 elements from the ANSYS element library [8] were also used to model the plates. The dimensions of the plates were: width, b_2= 10000 mm; height, a_2= 10000 mm; plate radius, r= 9500 mm; and thickness, t_p= 10 mm. The panel aspect ratio, $\alpha = b_2/a_2$ (see Fig. 5a), was varied as α= 1, 1.5, 2 and 2.5 maintaining constant the height, a_2= 10000 mm. Fig. 5b shows a representative mesh of the modeled curved plates.

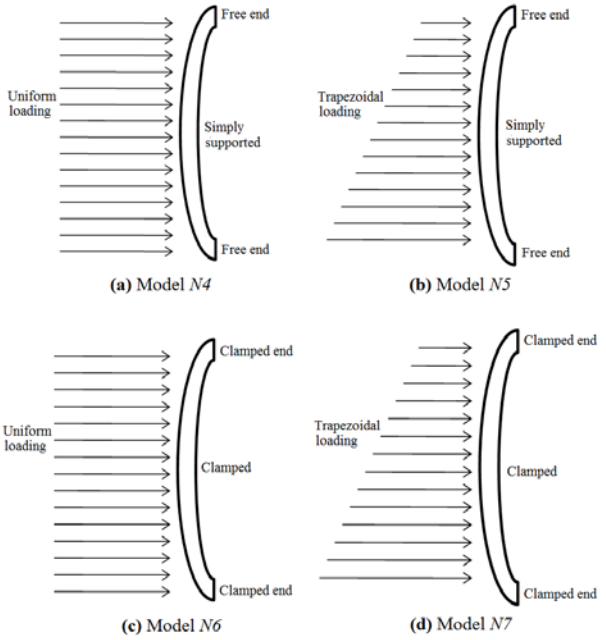


Figure 4. Curve plate models.
Source: The authors.

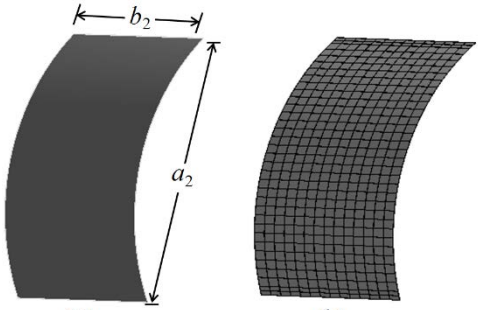


Figure 5. (a) Dimensions for Models *N4*, *N5*, *N6* and *N7*; and (b) Meshing for the curved plates.
Source: The authors.

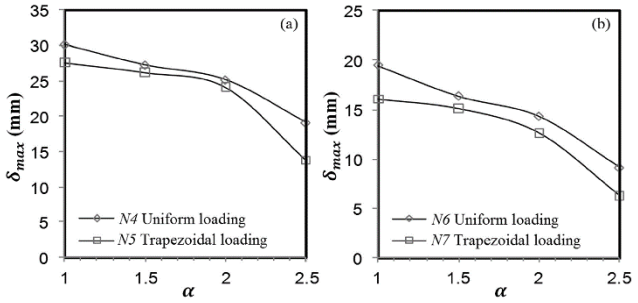


Figure 6. Maximum radial displacement, δ_{max}, with p = 0.1 MPa.
(a) Models *N4* and *N5* (b) Models *N6* and *N7*.
Source: The authors.

Regarding the influence of the loading conditions, Fig. 6 shows a comparison between numerical results of the out-of-plane displacements for Models *N4*, *N5*, *N6* and *N7*. In these cases, the radial displacement decreases when the panel aspect ratio increases, for both conditions, simply supported (Fig. 6a) and fully clamped (Fig. 6b). The reduction in the magnitude of the displacement between the former and the latter is close to 30%. When comparing the displacements for the two loading types with same boundary conditions the obtained difference is abou10%.

2.3. Stiffened curved plates under transverse loading

In this section, a third parametric study is conducted to investigate the influence of transversal and longitudinal stiffening on the maximum out-of-plane displacement of curved plates. At this stage, it is important to quote that simply supported and trapezoidal loadings are the corresponding boundary and loading conditions for curved plates. Hence, the current analysis is performed taking into account these conditions. Hot-rolled profiles are currently used in the steel industry to stiffen plated structures.

The geometry parameters of four (4) IPN steel profiles, namely IPN100, IPN180, IPN240 and IPN300 used in this study, are listed in Table 2. Fig. 7 shows the corresponding numerical models for different number of transversal stiffeners and Fig. 8 presents the results for the maximum radial displacements in the plane of symmetry of the curved plate considering the different profiles. As expected, the stiffener with the largest second moment of area (IPN300) gives the largest reduction in out-of-plane displacements of the curved plate.

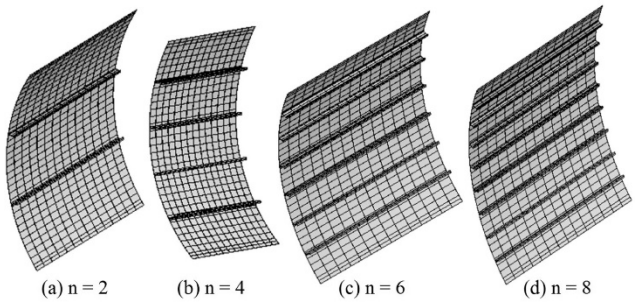


Figure 7. Models considering transversal stiffening (n = 2, 4, 6 and 8 stiffeners).
Source: The authors.

Table 2.
Geometry of the IPN steel profiles.

Profile ***IPN***	b_f **(mm)**	t_w **(mm)**	t_f **(mm)**	h_w **(mm)**	I_{st} **(cm^4)**	γ_s **(-)**
100	50	4.5	6.8	75	171	1471.21
180	82	6.9	10.4	142	1450	1827.72
240	106	8.7	13.1	192	4250	1898.08
300	125	10.8	16.2	241	9800	1976.55

Source: The authors.

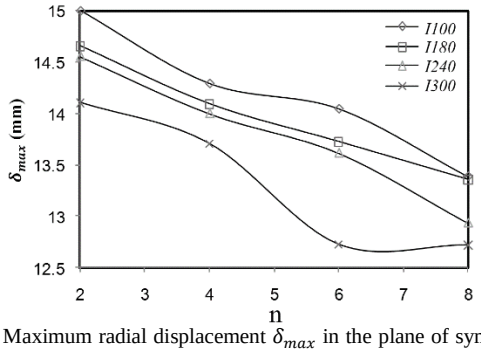


Figure 8. Maximum radial displacement δ_{max} in the plane of symmetry of the curved plate (n = 2, 4, 6 y 8 transversal stiffeners).
Source: The authors.

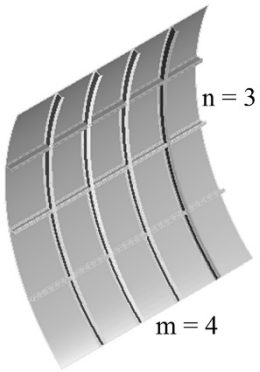


Figure 9. Model considering combined stiffening (longitudinal m = 4 and transversal n = 3).
Source: The authors.

To complete the study regarding the effect of stiffening on the deflection of curved plates, it is necessary to investigate the combined case with transversal and longitudinal stiffening.

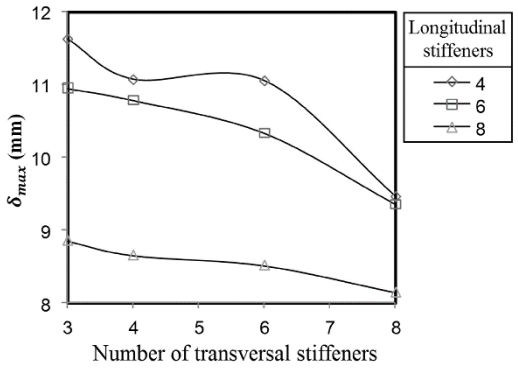


Figure 10. Maximum radial displacement for the combined stiffening model.
Source: The authors.

In this analysis, only one stiffener IPN100 was considered in the study. The number of the stiffeners in both directions was varied in both, the transverse direction (n= 3, 4, 6 and 8) and longitudinal direction (m= 4, 6 and 8). Fig. 9 shows a model with seven stiffeners, four in the longitudinal and three in the transversal direction. Boundary and loading conditions are the same as in the previous case.

Fig. 10 shows the results for the maximum radial displacement achieved with the stiffener's combinations investigated. It is observed that the radial displacements are reduced significantly for 8 longitudinal stiffeners. A reduction of 20% in the radial displacement is observed in Fig. 10, when compared to the corresponding displacements for only transversal stiffeners. Obviously, a larger displacement reduction may be achieved by using larger stiffeners.

3. Applications

Intake gates are among the main elements regarding dam safety in a hydroelectric power plant as they control water levels in the reservoir. When the water level rises, the pressure on the gates increases and excessive deformations can take place compromising the safety of the reservoir [11-13]. In many cases, intake gate systems have surpassed the service life for which they were designed for the original operating conditions, such as hydrostatic load, opening and closing frequency, among others, have been significantly modified to meet new energy generation requirements. All this is reflected on structural changes of intake gates and their possible failure, which can yield the electric plant unserviceable and in some cases the collapse of the reservoir. That is precisely why intake gate systems require rehabilitation works to improve their operation and adapt to current operating requirements.

In this section, the performance of the intake radial gates of the *Antonio José de Sucre - Macagua I Hydroelectric Power Plant* [14] is investigated. For this particular case, the intake radial gates were originally designed to withstand a hydrostatic head at an elevation of 48.0 m.s.n.m. In recent years, the water level of the reservoir was raised to 54.5 m.s.n.m. to accommodate for the increase in energy demand [15]. This increase in the level of the reservoir resulted in large gate deformations causing excessive water loss.

Fig. 11 shows a picture of the radial gate of the *Antonio José de Sucre - Macagua I Hydroelectric Power Plant* and its main structural components. Table 3 lists the geometry and dimensions of the radial gate. Due to symmetry in load and boundary conditions only one-half of the gate is modeled as shown in Fig. 12. The longitudinal and vertical stiffeners were modeled using BEAM44 elements from the ANSYS element library [8]. Accordingly, the plate in the gate was modeled using SHELL 181 elements, the remaining parts were modeled with SOLID 187 elements. Also included in the figure are the boundary conditions used in the numerical model for the radial gate. In the middle, a symmetry line was established, the other ends of the gate were simply supported. In the horizontal beam, clamped conditions were used to consider the support provided by three stiff arms that maintain the gate in place.

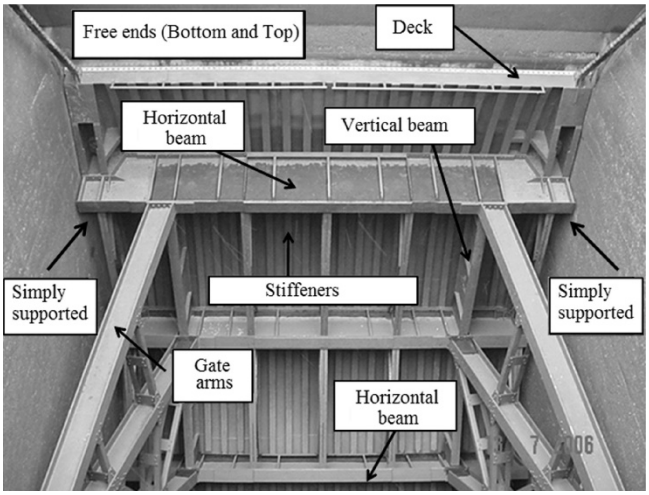


Figure 11. Radial gate of the Antonio José de Sucre - Macagua I Hydroelectric Power Plant.
Source: [9].

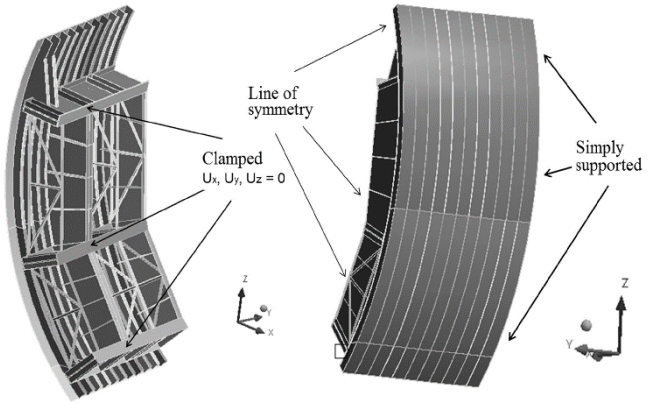


Figure 12. Model geometry and boundary conditions considering symmetry.
Source: The authors.

After conducting a convergence analysis, a mesh with 142.593 elements was chosen. Fig. 13 shows the meshing used in the main supporting elements and the radial panel.

Table 3.
Radial gate actual geometry and dimensions.

Element	Amount	Profile	L (mm)	Width (mm)	t_s (mm)	h_w (mm)	t_w (mm)	b_f (mm)	t_f (mm)
Deck	3	Rectangular	11000	10000	10, 11, 12	-	-	-	-
Stiffeners	21	T	11000	-	-	284	16	125	16
Vertical beam	3	Box	1190	3800	16	-	-	-	-
Lateral beam	2	Open Box	6000	-	-	300	16	125	16
Truss elements	6	L	4500	-	-	65	10	65	10
Horizontal beam	3	Double T	10000	-	-	1250	12	350	12

Source: The authors.

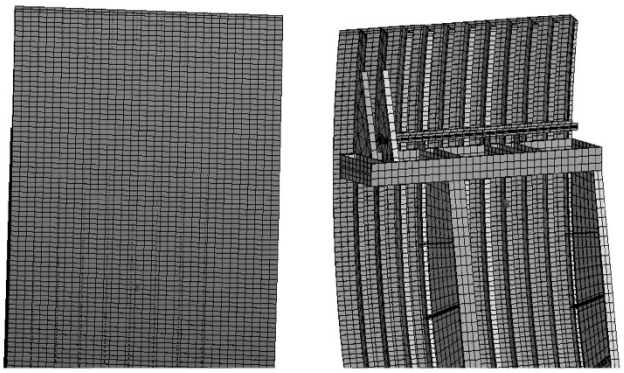


Figure 13. Meshing used in the gate.
Source: The authors.

In practice, radial gates sustain high transversal loadings due to the hydrostatic pressure gradient. Its determination is precisely the first step to adequately size a radial gate [16]. An upper bound for the hydrostatic pressure gradient acting on the gate can be defined using the maximum expected water level of the reservoir as shown in Fig. 14.

The magnitude of the resultant hydrostatic load, W, can be found as:

$$W = \sqrt{W_H^2 + W_V^2} \tag{1}$$

$$W_H = \gamma_w BH(H - h/2) \tag{2}$$

$$W_V = \gamma_w BR\left[D_m(cos\alpha_s - cos\alpha_i) + \frac{R}{2}(\alpha_i - \alpha_s) + \frac{R}{2}(sin\alpha_s \cdot cos\alpha_s - sin\alpha_i \cdot cos\alpha_i)\right] \tag{3}$$

where $\alpha_s = sin^{-1}(D_s/R)$, $\alpha_i = sin^{-1}(D_i/R)$, H is the maximum expected water level of the reservoir, h_1 is the depth to the radial gate, h is the height of the gate, B is the width of the gate, R is the radius of the gate, γ_w is the specific weight of water and D_m is depth to the point of curvature of the gate. The line of action of the resultant hydrostatic load on radial gates is assumed to pass through the point of curvature of the gate [16] at an orientation:

$$\beta = sin^{-1}(W_V/W_H) \tag{4}$$

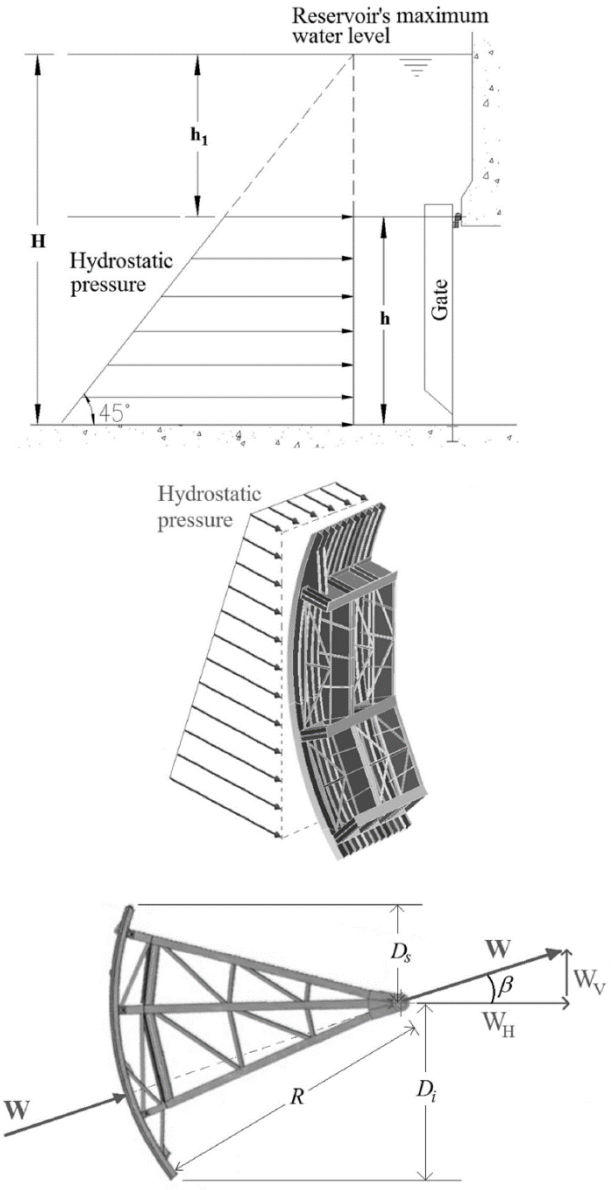


Figure 14. Hydrostatic pressure distribution assumed for the gate.
Source: Adapted from [12].

Based on the above loading conditions, two design conditions arise: large displacements at the supported ends and high stress levels. As mentioned earlier, the situation may be solved by stiffening the gate by adding either transverse,

longitudinal of both types of stiffeners.

The maximum stress in a radial gate [17] can be estimated as:

$$\sigma = \pm \frac{k}{100} p \frac{a^2}{t^2} \quad (5)$$

where k is a dimensionless parameter that depends on the ratio b/a and on the boundary conditions ($k = 25$ [18]), p is the hydrostatic pressure at the middle of the gate, t is the plate thickness and a and b are the minimum and maximum spacing between stiffeners, respectively.

The maximum deflection of the radial gate can be determined as:

$$\delta_{max} = \frac{\xi\, p\, a^4}{E\, t^3} \quad (6)$$

where E is the Young's modulus and ξ is a dimensionless parameter that depends on the dimensions of the gate (see Table 4). For this specific case, ξ was assumed equal to 0.0284.

Eqs. (5) and (6) provide the maximum values for stresses and displacements, respectively. After substituting the corresponding values into these formulas, a maximum stress of σ_{max} =200 MPa and a maximum deflection $\delta_{max} = 5.5$ mm are obtained for the considered gate. It must be mentioned that these values represent operational conditions.

Fig. 15 shows the displacement profile at the upper end of the gate. Note that a good agreement is obtained between the numerical results and the actual measurements [20]. From a practical point of view a maximum displacement of 22 mm means that the gate is leaking as such displacement goes beyond the allowable value of 5.5 mm.

Taking into account that the maximum stress and the maximum displacement control the integrity of the gate and keeping in mind that the current design allows greater values for these parameters, it is necessary to solve this situation by adding stiffeners. Then, a parametric analysis using a simplified finite element model is conducted in order to reduce the maximum stress and the maximum displacement in the gate. In the simplified model, the arms are correspondingly substituted by a fixed boundary condition.

In general, the flexural rigidity of the stiffener, γ_s, is used to describe the capacity of a stiffener to resist buckling and control lateral deflection. Usually, this rigidity is expressed relative to the plate stiffness, D, as follows:

$$\gamma_s = \frac{EI_{st}}{h_w D} \quad (7)$$

where $D = Et_w^3/12(1-\nu^2)$ is the flexural rigidity of a unit width of the web plate. The flexural stiffness for the IPN profiles is also listed in Table 2.

Fig. 16 shows the maximum displacements and stresses attained for the radial gate with stiffeners in both directions. These results are presented for the gate stiffened with IPN100 (Figs. 16a and 16b) and IPN300 (Figs. 16c and 16d). The distribution of the stiffeners was even in both directions. There is a reduction in the out-of-plane displacements of the gate after increasing the number of stiffeners, as well as after increasing the size of the stiffener. Similar results are observed for the maximum stresses. All the structural elements (plate and stiffeners) are subjected to bending, therefore an increase in the second moment of area of the stiffener leads to redistribution of the stresses in the gate, attaining a significant reduction.

Fig. 17 shows the maximum displacements for the gate with 8 longitudinal and 8 transversal stiffeners. It is observed that an increasing flexural rigidity reduces the out-of-plate displacements. Comparing these results with the maximum allowable displacement found from Eq. (6) (δ_{max}= 5.5 mm) it is seen that the IPN300 stiffener is the only one capable of reducing the displacements below this limit.

Table 4.
Dimensionless parameter ξ

b/a	1	1.2	1.4	1.6	1.8	2	∞
ξ (×10^{-2})	1.38	1.88	2.26	2.51	2.67	2.77	2.84

Source: Adapted from [19].

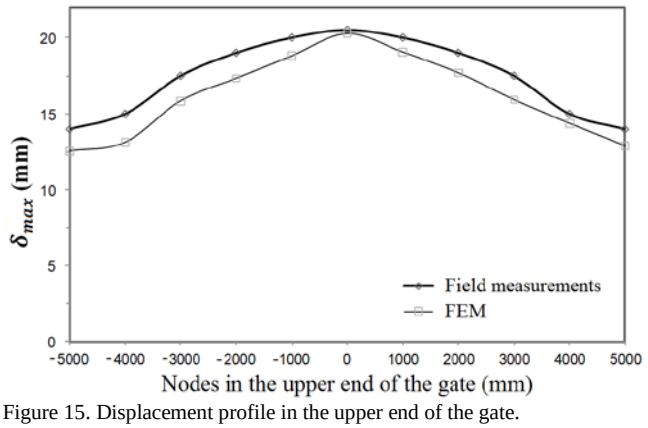


Figure 15. Displacement profile in the upper end of the gate.
Source: The authors.

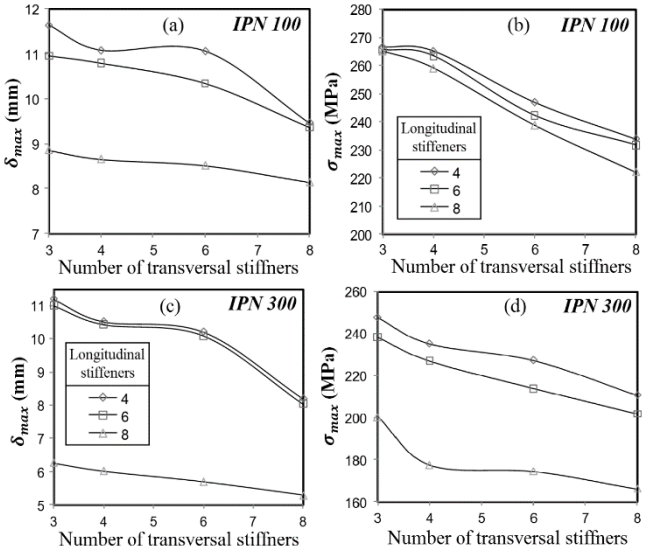


Figure 16. Maximum von Mises stress and maximum displacement at the supported ends from numerical simulations for profiles *IPN 100* and *300*.
Source: The authors.

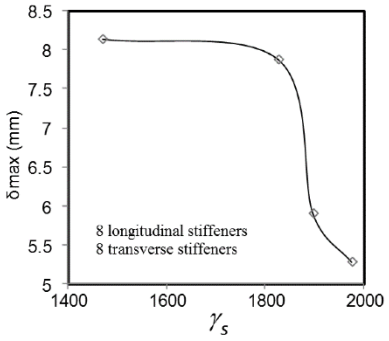


Figure 17. Maximum displacement in the gate with 8 longitudinal and 8 transverse stiffeners. Source: The authors.

4. Summary and conclusions

This paper has presented a numerical study on the elastic behavior of stiffened curved plates subjected to transverse loading; a parametric analysis to evaluate the beneficial effects of including longitudinal and transverse stiffeners; and the application of the proposed methodology to the specific case of radial intake gates in a hydroelectric power plant. The computational model was validated with analytical solutions available in the literature for flat and curved plates and by comparing it with a case history concerning the response of a hydroelectric power plant intake radial gate subjected to a hydrostatic head. It is shown that the static behavior of a curved plate subjected to hydrostatic head is a suitable way to size intake gates and define the maximum reservoir water level; and that stiffeners are a practical way to retrofit existing elements as they increase system stiffness and reduce transversal deformations, which are directly reflected in an improvement of system reliability and capacity to meet new power generation requirements.

References

[1] Tran, K.L., Davaine, L., Douthe, C. and Sab, K., Stability of curved panels under uniform axial compression. Journal of Constructional Steel Research, 69(1), pp. 30-38, 2012. DOI: 10.1016/j.jcsr.2011.07.015.

[2] Tran, K.L., Douthe, C., Sab, K., Dallot, J. and Davaine, L. A preliminary design formula for the strength of stiffened curved panels by design of experiment method. Thin-Walled Structures, 79, pp. 129-137, 2014. DOI: 10.1016/j.tws.2014.02.012.

[3] Tran, K.L., Douthe, C., Sab, K., Dallot, J. and Davaine, L., Buckling of stiffened curved panels under uniform axial compression. Journal of Constructional Steel Research, 103, pp. 140-147, 2014. DOI: 10.1016/j.tws.2016.05.003.

[4] Seo, J.K., Song, C.H., Park, J.S. and Paik, J.K., Nonlinear structural behaviour and design formulae for calculating the ultimate strength of stiffened curved plates under axial compression. Thin-Walled Structures, 107, pp. 1-17, 2016. OI: 10.1016/j.tws.2016.05.003.

[5] Graciano, C.A., Mendez, J. and Zapata-Medina, D.G., Influence of the boundary conditions on FE- modeling of longitudinally stiffened I-girders subjected to concentrated loads. Revista Facultad de Ingeniería Universidad de Antioquia, [online]. 71, pp. 221-229, 2014. Available at: http://www.scielo.org.co/pdf/rfiua/n71/n71a20.pdf.

[6] Graciano, C.A. and Zapata-Medina, D.G., Effect of longitudinal stiffening on bridge girder webs at incremental launching stage. Ingeniería e Investigación, 35(1), pp. 24-30, 2015. DOI: 10.15446/ing.investig.v35n1.42220.

[7] Graciano, C.A., Casanova, E. and Zapata-Medina, D.G., Elastoplastic behavior of longitudinally stiffened girder webs subjected to patch loading and bending. DYNA, 82(189), pp. 103-109, 2015. DOI: 10.15446/dyna.v82n189.42222.

[8] ANSYS, Inc. ANSYS Release 12.1 Elements Reference, U.S.A. 2009.

[9] Noguera, A., Estudio de deformaciones transversales sobre la estructura de una compuerta radial, MSc. Thesis, Coordinación de postgrado en Ingeniería Civil y Mecánica, Universidad Simón Bolívar, Caracas, Venezuela, 2011.

[10] Young, W.C. and Budynas, R.G., Roark's formulas for stress and strain. 7th Edition, New York, NY: McGraw-Hill, 2002.

[11] USSD Committee on Hydraulics of Dams. Improving Reliability of Spillway Gates. Denver, CO: U.S. Society on Dams, 2002.

[12] ICOLD (International Commission on Large Dams). Dam Safety Guidelines, Bulletin 59. Paris: Commission Internationale des Grands Barrages, 1987.

[13] ICOLD (International Commission on Large Dams). Risk Assessment in Dam Safety Management: A Reconnaissance of Benefits, Methods and Current Applications, Bulletin 130. Paris: Commission Internationale des Grands Barrage, 2005.

[14] Ministerio de Fomento. Criterios de Diseño y Especificaciones Técnicas Central Hidroeléctrica Macagua, Puerto Ordaz, Venezuela, 1959.

[15] OPSIS. Cifras 1997 EDELCA. Síntesis informativa de gestión, Caracas, Venezuela, 1997.

[16] Erbisti, P.C., Design of hydraulic gates. 2nd Edition, The Netherlands: CRC Press/Balkema, 2014.

[17] NBR 8883. Cálculos de compuertas hidráulicas. Brasil: Asociación Brasilera de Normas Técnicas (ABNT), 2002. (In Portuguese).

[18] DIN 19704 (1976-09). Hydraulic steel structures - criteria for design and calculation. Berlin, Germany: Deutsches Institut für Normung, 1976.

[19] Timoshenko, S.P. and Gere, J.M., Theory of elastic stability. 2nd Ed., New York: McGraw-Hill, 1982.

[20] EDELCA, Informe de inspección de las compuertas de toma de la central hidroeléctrica Antonio José de Sucre Macagua I. Reporte Interno, Venezuela, 2007, 24 P.

A. Noguera-Garban, received a BSc. in Mechanical Engineering (2002) Major in Process Plants (2006) and MSc. (2011) in Mechanical Engineering from the Simon Bolivar University, Venezuela. Currently, he is a Mechanical Equipment Head of Department at Thyssenkrupp. His research interests include the study of the influence of uncertainties (i.e., material properties, geometry, boundary conditions, etc.) on the numerical modeling of different mechanical systems.
ORCID: 0000-0002-1990-6318

C. Graciano, received both BSc. (1992) and MSc. (1995) in Mechanical Engineering from the Simon Bolivar University, Venezuela. He later moved to Sweden where he obtained a Licentiate of Engineering (2001) and a PhD. (2002) in Structural Engineering from Chalmers University of Technology and Luleå University of Technology, respectively. From 1997 to 2013, he served as assistant, associate and full professor in the Mechanical Engineering Department at the Simon Bolivar University. Currently, he is an associate professor in the Civil Engineering Department at the Universidad Nacional de Colombia, Medellin, Colombia. His research interests include: finite element modeling, structural stability, piping stress analysis and crashworthiness among others.
ORCID: 0000-0003-0659-7963

D.G. Zapata-Medina, received a BSc. (2004) in Civil Engineering from the Universidad Nacional de Colombia, Medellin, Colombia, a MSc. (2007) in Geotechnical Engineering from the University of Kentucky, USA and a PhD. (2012) in Geotechnics from Northwestern University, USA. Currently, he is an associate professor in the Civil Engineering Department at the Universidad Nacional de Colombia, Medellin, Colombia. His research interests include: soil characterization and constitutive soil modeling for geotechnical earthquake engineering applications; field instrumentation, numerical simulation and performance evaluation of earth retaining structures; and analytical and numerical solutions to calculate the static and dynamic stability of soil-structure interaction problems.
ORCID: /0000-0001-8868-8740

UNIVERSIDAD NACIONAL DE COLOMBIA
SEDE MEDELLÍN
FACULTAD DE MINAS



DYNA
http://dyna.medellin.unal.edu.co/

Incorporation of aluminum oxide in the formulation of pastes for building materials

Luis Miguel Carrillo-Rodriguez [a], Leonardo Cely-Illera [a], Jairo Cely-Niño [a] & Claudia Vanessa Cely-Illera [b]

[a] *Faculty of Engineering, University Francisco de Paula Santander, Cúcuta, Colombia. luismcarrillor@ufps.edu.co, leonardocely@ufps.edu.co, jairowilgbertocn@ufps.edu.co*
[b] *BT LATAM Bogota, Colombia (British Telecommunications), London, United Kingdom, claudiacelyillera@gmail.com*

Received: February 15th, 2017. Received in revised form: November 16th, 2017. Accepted: January 25th, 2018.

Abstract
This work analyzes the influence of aluminum oxide with a particle size of less than 75 µm on the behavior in a clay, when it is mixed with this material at 10% by weight. It is observed how it influences the different stages of the manufacturing process and its effect on structural, mechanical and tribological properties. In previous works it has been used in different percentages increasing the mechanical resistance. For this work a composition was formulated using clay of high plasticity and making the conforming by the extrusion method. The results show the efficacy and efficiency of this material and its mechanism of action, showing increases in mechanical properties and a decrease in porosity. In addition to improving its tribological properties, granting to the products added value and the possibility to be suitable manufacture materials to be used in environments of intense pedestrian traffic or in industrial environments.

Keywords: aluminum oxide; extruded; structural; mechanical; tribological.

Incorporación de óxido de aluminio en la formulación de pastas para materiales de construcción

Resumen
En este trabajo se analiza, la influencia que ejerce el óxido de aluminio con una granulometría menor a 75 µm sobre el comportamiento en una arcilla, al ser mezclada con este material al 10% en peso. Se observa cómo influye en las distintas etapas del proceso de fabricación, y su efecto en propiedades estructurales, mecánicas y tribológicas. En trabajos anteriores se ha utilizado en diferentes porcentajes incrementando la resistencia mecánica. Para este trabajo se formuló una composición utilizando una arcilla de elevada plasticidad y realizando el conformado por el método de extrusión. Los resultados muestran la eficacia y eficiencia de este material y su mecanismo de actuación, observándose incrementos en las propiedades mecánicas y una disminución de su porosidad, además de mejorar propiedades tribológicas, otorgándole a los productos valor agregado y la posibilidad fabricar materiales idóneos a ser usados en ambientes de intenso tráfico peatonal o en entornos industriales.

Palabras claves: oxido de aluminio; extruido; estructurales; mecánicas; tribológicas.

1. Introduction

Norte de Santander is known for being a clay region par excellence and one of the regions with the best clays in the world, it is for this reason that 70% of its economy revolves around companies that are engaged in the transformation of this material in coating products but above all in masonry products (bricks, tiles and blocks), being the extrusion formed the type of ceramic process most used in this region, this is why only one of 60 companies legally constituted currently is dedicated to the manufacture of pressed ceramic tiles [1,2].

It is for this reason that it was necessary to study an alternative to improve the pulps used in these extrusion processes as the manufacturing companies have begun to detect an increase in the percentage of breaks and defects in

How to cite: Carrillo-Rodriguez, L.M., Cely-Illera, L., Cely-Niño, J. and Cely-Illera, C.V., Incorporation of aluminum oxide in the formulation of pastes for building materials. DYNA, 85(205), pp. 90-97, June, 2018.

© The author; licensee Universidad Nacional de Colombia.

their final products, which is why today there is more interest in the search of materials that increase the mechanical strength of the ceramic pieces and thus increase their productivity and decrease the maximum manufacturing costs [3]. One feasible solution that has been investigated is the incorporation of industrial waste in clay bodies. In particular, the use of these is investigated through their addition to natural raw materials used to manufacture ceramic products [4-7].

In works and articles published previously, it was found that aluminum oxide shows in pastes of ceramic products for pressing an excellent behavior serving as an effective substitute for any existing degreaser. To date it has not been studied the mechanisms of action of this material used in furnaces of ceramic companies, nor have studies been found in the literature on the use in this type of compositions in extrusion processes [8]. For this reason and in view of the need to increase the mechanical strength of the products this research has been proposed in order to verify the efficiency of the aluminum oxide in pastes used in the extrusion forming process and to analyze the effects of the change in the formula and the possible modifications in the behavior of the composition in the different stages of the process, as well as in the properties of the tile.

2. Materials and methods

The materials used in this research were a clay from the Guayabo formation of the Norte de Santander region (Colombia) usually used in the manufacture of blocks, bricks and tiles; aluminum oxide (corundum) powder of ASTM 200 mesh (75 μm) of white color at 99% purity from the enterprise Cerámicos Asociados.

Both natural materials were initially dried at 110 °C before obtaining the representative samples by quartet. The clay was then analyzed by X-ray fluorescence (FRX), particle size distribution and plasticity index. The particle size distribution of the clay was determined by sieving and sedimentation according to ASTM D422-63, where it calculates the equivalent spherical diameter of the materials using Stoke's law.

The chemical composition was obtained by X-ray fluorescence in an equipment brand Panalytica, model Axios Max. The plasticity (IP) of the clay material was determined by the Pferfferkorn method, which determines the consistency value of a material to be formed by the extrusion method, exerted by the compression of the clay material when hit with a pylon hammer which runs a fixed path.

For the research, pure clay was used as the standard reference; the mixture was prepared with an amount of 10% by weight of aluminum oxide added to the clay, these were referenced as P0 and P10 respectively throughout the investigation. Prism specimens of $13\ \text{cm} \times 8\ \text{cm} \times 1\ \text{cm}$ were molded with a percentage of extrusion water of 37.5% for pure clay (P0) and 28.6% for the mixture (P10) using a laboratory extruder with vacuum New Wave model with rectangular mold and a gauge pressure of 35 mmHg. From each composition, a specimen was taken and subjected to a dilatometric analysis (DIL) which was developed in a Dil 402 C dilatometer, where the coefficient of thermal expansion and the characteristic temperatures of glass transition and softening were determined (Tm and Tg), the equipment was operated with a heating rate of 10 °C/min to a maximum temperature of 1000 °C using a $25\ \text{mm} \times 6\ \text{mm}$ probe. The other specimens were dried at room temperature (±30 °C) for 96 h and then subjected to convection drying at 110 °C for 24 h in a drying oven.

The cooking process was carried out in a laboratory electric muffle with final temperatures of 900 ºC, 1000 ºC, 1100 ºC, 1150 ºC and 1200 ºC, the first four temperatures are normally used in the manufacture of clay tiles and bricks in the region. The heating rate for cooking was 3 °C/min without heating table at maximum temperatures. The cooling was performed by natural convection inside the oven after it was turned off. Technological properties were evaluated using four specimens per composition, properties such as bulk density, linear shrinkage, water absorption, flexural strength and deep abrasion were calculated using the mean values in each analysis. The bulk density was measured by dividing the mass by the external volume of each specimen. Linear shrinkage was obtained by varying the length of the samples using a calibrator $(\text{precision} \pm 0.01\ \text{mm})$. Water absorption was determined according to the standard procedures of standard NTC 4321-3. The flexural strength was obtained using the standard procedures of standard NTC 4321-4. Finally, the tribological property or wear resistance of ceramic tiles was determined according to norm NTC 4321-6. This property was determined by the wear resistance by calculating the length left by the constant pressure of a rotating disk of a 200 mm diameter and an abrasive material (alumina F80) on the surface of the specimen at a rotation speed of 75 rpm (the development of testing is performed by wearing the specimens during 150 turns).

3. Results and discussion

3.1. Physicochemical characterization of clay

Table 1 shows the chemical composition of the clay material in which it can be observed that it presents SiO_2 and Al_2O_3, as the most predominant oxides [9,10]. These oxides are mainly associated with the kaolinite structure. The contained silica is associated with the quartz particles and the high percentage of alumina is associated with gibsite. The value of 3.81 molar ratio (SiO_2/Al_2O_3) in the clay indicates a high presence of kaolinite [11]. Fe_2O_3 is the main oxidant that gives the clay a red hue and according to the data in Table 1, the clay presents a high percentage of this oxide, which will give it after cooking an intense red hue, this is an important technological aspect because with this material, products cannot be made with clear shades [12].

Another important aspect to consider in clay is its high percentage of K_2O which will generate a material with a low cooking range, since this oxide is considered the main flux in the clay materials [13,14]. In the same way it can be detailed that the value of LoI is high, this indicates a loss of mass in enormous cooking due mainly to the dehydroxylation of clay minerals, to the oxidation of the organic matter but especially to the decomposition of carbonates, hydroxides and sulfates, the latter associated with the high value of SO_3 which during



Figure 1. Specimens used in research.
Source. Authors.

Table 1.
Chemical composition of the clay (% by weight).

Oxides	P0 (%)
SiO_2	52,90
Al_2O_3	23,57
Fe_2O_3	7,09
K_2O	2,70
NaO_2	0,73
MgO	1,28
CaO	0,90
SO_3	1,40
LIO	1,40

Source. CEMEX Laboratory.

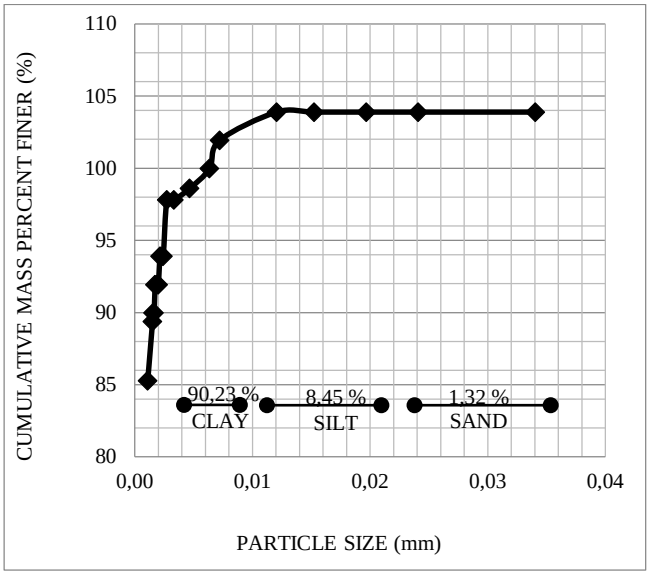


Figure 2. Grain size distribution of the clay. Clay.
Source. Authors

cooking can generate not only contamination in the furnace atmosphere but also contamination in the material causing aesthetic problems such as veils, blooms or stains in its structure or changing the color of the product darkening even more its hue as seen in Fig. 1 [15-18].

Fig. 2 shows the distribution of the particle size of the clay made by the method of the 152H hydrometer, within the graph it is shown the fraction of clay, silt and sand [19]. The clay fraction is associated with fine minerals (<2 μm) which are responsible for the plasticity of the material, as described, the material has a high percentage of clay fraction of 90.23% and a low fraction of silt and sand of 8.45% and 1.32% respectively, this is the reason for the high plasticity index (40.3%) and the large amount of extrusion water used to make clay molding as can be seen in Table 2 [20].

This is an important aspect to take into account as the addition of corundum affects in a tangible way the decrease of this high amount of extrusion water reducing it by 23.7%, generating not only a control in the percentage of water of tempering or of rehydration, the main cause of breakage and deterioration of the material in the drying but also the decrease in the formation of defects during molding, in addition to a lower economic cost in the process window during the wetting stage of the material, all directly influenced by a progressive increase of the concentration of clay minerals in the structure of the clay.

3.2. Process parameters in wet and dry conditions

As seen in Table 2, the addition of the aluminum oxide to the clay significantly improves the working parameters and properties of the material under wet and dry conditions. As mentioned, the amount of extruded water is significantly reduced, helping to reduce differences in the drying of the parts, controlling serious problems such as cracks and deformations, speeding the drying process (decreasing time and costs), etc., all this without affecting other properties such as density, which is directly related to the molding conditions and the volume of water added [21,22].

It is detailed that the density of P10 increases in 11.0% and in 4.9% in wet and dry respectively, in comparison with clay, generating that the material is more resistant, controlling its dry shrinkage and increasing its mechanical resistance, typical behavior when the density is improved. The reduction in linear shrinkage results in a lower percentage of breakages in the products by cracking, especially those that appear in the last phase of the drying cycle and the increase in mechanical resistance guarantees the manufacture of parts for coating or parts of large masonry because as it is shown, it gives values of 45.5 kgf/cm², when required for dry products at international level for this type of products values are between 25 kgf/cm^2 and 30 kgf/cm² with the aim of avoiding breaks of the pieces at this stage of the process [23,24].

It is important to note that with the reduction in shrinkage and the increase in dry strength by the addition of aluminum oxide it will provide the possibility of using only this type of residue in pastes formulations for construction products since it will not be necessary to add high percentages (between 20% and 30%) of degreasing materials, which is what is normally used to increase porosity and reduce drying shrinkage especially in plastic materials with fine granulometry and with large specific surfaces such as the material investigated; This is an important contribution to the process because it reduces time in the preparation of these degreasers and reduces the final costs for the acquisition of non-plastic raw materials [25].

Table 2.
Parameters working in wet and dry condition.

MATERIAL	Plasticity Index	Extrusion Water	WORKING PARAMETERS			
			Apparent Density (Wet)	Linear Shrinkage (Dry)	Apparent Density (Dry)	Rupture Module (Dry)
	%	%	g/cm^3	%	g/cm^3	kg/cm^2
P0	40,3	37,5	1,437	8,6	1,667	24,0
P10	NA	28,6	1,632	8,0	1,749	45,5

Source. Authors

3.3. Thermal and dilatometric behavior of the clay by the addition of corundum

Regarding the thermal behavior, the sample P0 has a glass transition temperature (Tg) of 621 °C and softening (Tm) of 691 °C. The sample P10 presents Tg of 637.8 °C and a Tm of 710.4 °C, with these results it is observed that the material to add the residue has a better performance in the resistance to high temperatures since its softening point increases by 2.81% by improving in the cooking step the time of appearance of the liquid phase and controlling the sintering which decreases the viscosity of the material and the deformation thereof [26,27].

Fig. 3 shows the dilatometric curves of P0 and P10 while Table 3 shows the values corresponding to the linear coefficients of thermal expansion. As shown, the two curves have a similar behavior with the difference that the coefficient of expansion is lower in P10 indicating that the corundum will generate a control in the dimensions developed by the high plasticity in the clay which gives us the idea of a reduction in the stress differences that produce cracks in the heating stage [13,28].

It is observed initially a rectilinear section which is interrupted in the peak I when arriving approximately to the 200 ºC, possibly it is in this point where the water of constitution completely evaporates of the structure of the specimens; It is explained that the coefficient of expansion ($\alpha_{50\text{-}300}$) is higher in P10, possibly because the corundum generates an increase between the reticular spaces of the clay material causing the water to evaporate rapidly and generating an increase in its dilation from the starting point up to 200 ºC, it is recommended that around this temperature a decrease in the cooking time is exerted to avoid high tensions differences that occurs in this phase of the process, especially in materials as clayey as the one studied.

From point I another straight section with a progressive increase in the slope up to 600 °C (Point II) is initiated, it is in this area where the allotropic change of quartz develops, the most problematic turning point in the whole cycle of cooking of any ceramic material, at this point the values of the coefficient of thermal expansion of P10 decreases up to 6.9% with respect to P0, generating a greater control in the formation of microcracks, characteristic defect in this phase.

Finally, the curve reaches a horizontal section, which reaches point III, it is here where the slope begins to decrease and the softening of the material is indicated beginning the contraction. It is important to note that the low coefficients of

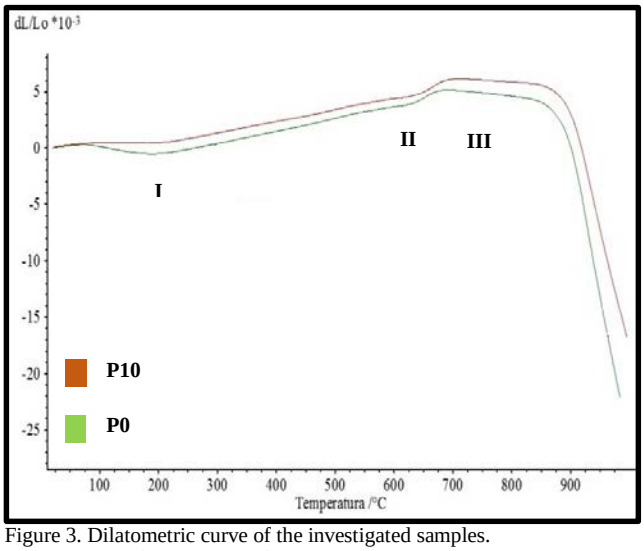


Figure 3. Dilatometric curve of the investigated samples.
Source. Center for Research of Ceramic Materials - CIMAC.

Table 3.
Coefficient of thermal expansion of the samples.

SAMPLES	$\alpha_{(50\text{-}300)}$ x 10^{-7}°C^{-1}	$\alpha_{(50\text{-}500)}$ x 10^{-7}°C^{-1}	$\alpha_{(500\text{-}600)}$ x 10^{-7}°C^{-1}
P0	7,42	111,62	101,89
P10	41,45	103,92	98,68

Source. Center for Research of Ceramic Materials - CIMAC.

expansion generated by the addition of corundum will generate the possibility of sintering the material at high temperatures, as this will control the increase in the liquid phase content of the specimen and improves the densification thereof, which will be reflected in the improvement of mechanical properties due to the decrease in porosity [29].

3.4. Technological behavior as a function of temperature and addition of corundum

Figs. 4 to 8 show, respectively, bulk density, linear shrinkage, water absorption, flexural strength and deep abrasion in the baked condition of P0 and P10. It is observed in Fig. 4 that the apparent density for P10 decreases between 900 °C and 1100 °C with respect to P0, which indicates that the mechanisms of consolidation of the particles at the cooking temperatures typical for ceramic processes in the region are not efficient to increase this property but that are improved when corundum is added to the material, as an increase is observed above 1100 ºC, this is probably a consequence of the refractoriness of the corundum, developing this behavior in the clay material at elevated temperatures being a significant contribution as it contributes to control the porosity at elevated temperatures, increasing mechanical and tribological properties as detailed later [30,31].

The linear contraction in cooking is detailed in Fig. 5; this is influenced by the cooking temperature. These results indicate moderate changes between 900 °C and 1000 °C. However, above 1100 °C significant changes can be observed in P10 since linear shrinkage decreases in comparison with

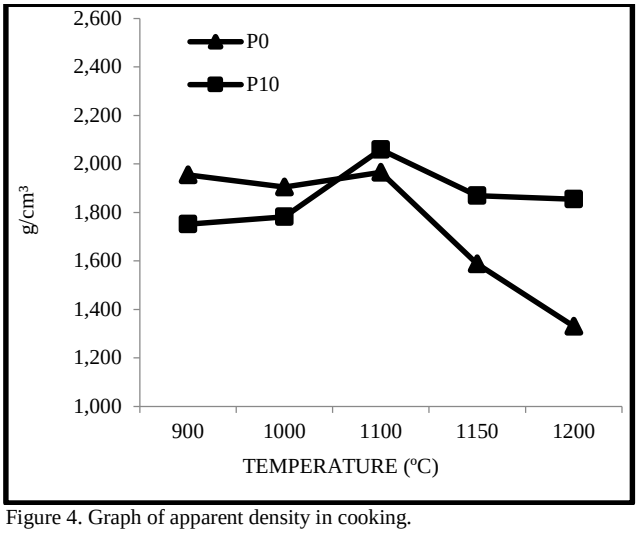


Figure 4. Graph of apparent density in cooking.
Source. Authors.

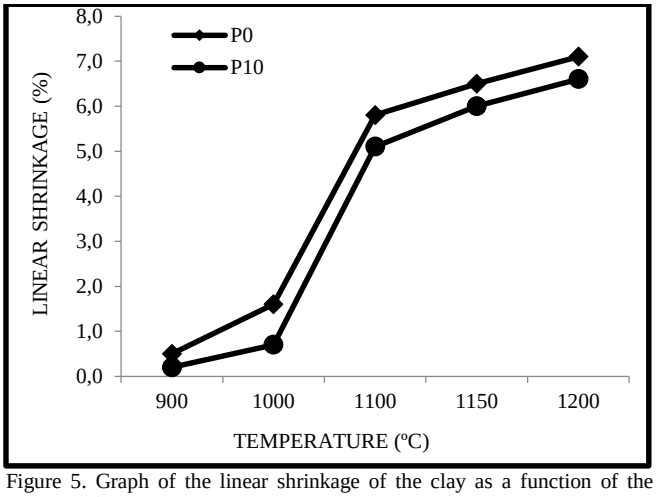


Figure 5. Graph of the linear shrinkage of the clay as a function of the addition of corundum and the cooking temperature.
Source. Authors.

P0, this is associated to the sintering mechanisms and is generated by the densification of the samples as observed in Fig. 4, the importance is that as the temperature increases the control in the contraction does not change since it continues to decrease, this indicates a good behavior in any temperature range [32].

In Fig. 6, it is observed that the water absorption is elevated between 900 °C and 1000 °C in P0 and P10 but decreases markedly above 1100 °C. The obtained values of water absorption at low temperatures indicate that the mechanisms of particle consolidation were not effective, as it has been mentioned during the investigation and can also be attributed to the high percentage of alumina in the clay that generates a refractory behavior as well as aluminum oxide [32,31]. It should be noted that P10 shows a significant decrease, this is associated with the increase of dry mass density. In general, the samples show a decrease in the water absorption above 1100 °C which generates the manufacture of products with a higher added value, in addition to complying with Colombian standards for the manufacture of masonry products and coating without the need to reformulate the pulp with other materials that would increase the cost of the final product [30].

In ceramic processes the sintering contributes to improve the flexural strength considering that optimizing the cooking temperature it is possible to densify the material better and decrease the porosity which in turn reduces the formation of cracks, defects that generate the reduction of the mechanical resistance of the products. As shown in Fig. 7, this property increases as the temperature increases generating more resistant materials and improving the final use of the products. Thus the presence of aluminum oxide helps to increase the modulus of rupture in the pulp at temperatures between 900 °C and 1200 °C in 25.4%, 34.1%, 50.3%, 52.2% and 58.7% respectively, being progressive and controlled increases of P10 with respect to P0 [33].

The tribological characterization was carried out by means of the deep abrasion test, the results obtained for P0 and P10 are shown in Fig. 8, comparing the wear resistance

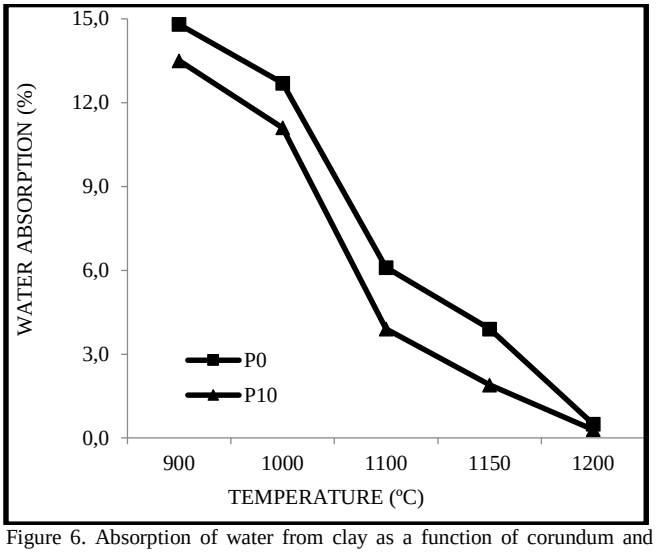


Figure 6. Absorption of water from clay as a function of corundum and cooking temperature.
Source. Authors.

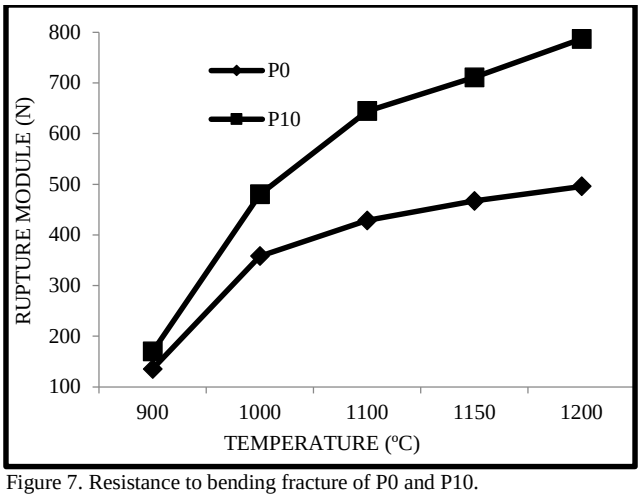


Figure 7. Resistance to bending fracture of P0 and P10.
Source. Authors.

(volume removed of material) exerted by the abrasive agent on the surface of the specimens; In both cases the reduction of the volume removed is observed as the temperature increases, this can be attributed to the increase in the densification and the reduction in the porosity, as this property is related to the open porosity of the material [34-36]. Thus the addition of aluminum oxide minimizes wear resulting in an improvement in the protection of construction products and increasing its use especially in coating products where abrasive agents attack with greater force.

Finally, it can be said that the mixture of natural clay materials with residues such as aluminum oxide is effective and promising helping not only to the increase in the technical characteristics of the products but also to the reduction in the pollution of the planet, as well as minimizing cost of production that will ultimately be reflected in the final value of the product and generating a trend product with technical and decorative characteristics superior to the ceramic, with higher added value, which in many cases can greatly exceed the price of the traditional pottery [22,37,38].

4. Conclusions

The pure clay is composed of 90.23% of materials with a particle size of less than 2 microns, being this the reason why it has an extrusion behavior that is not acceptable for the processing of the clay body. The problem is solved with the addition of oxide of aluminum to the paste generating not only the reduction of cracks and deformations but also the addition of this residue to improve its workability.

Aluminum oxide effectively controls the liquid phase content and the viscosity of the paste in the cooking step above 1000 °C, since a more compact and more dense product is observed, as evidenced by the minimal alterations in the linear contraction and the water absorption.

The addition of aluminum oxide to the clay produces a very compact and resistant material, essential for building materials, as it has a low porosity, which gives it excellent mechanical and chemical properties, which makes it useful for use as a pavement or external cladding in cold areas.

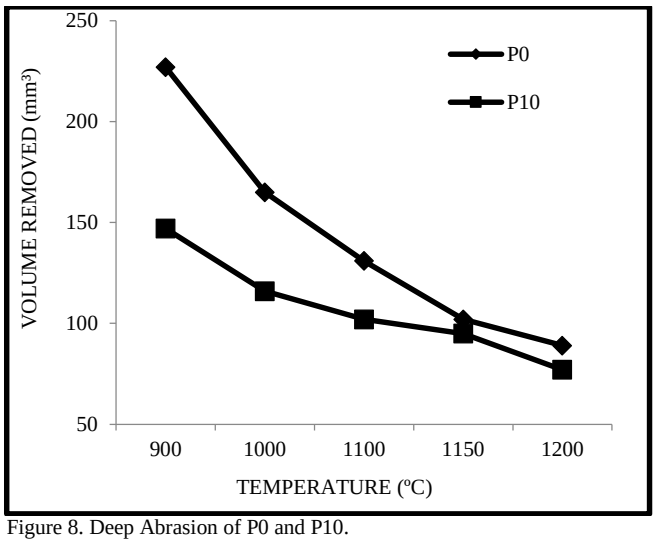


Figure 8. Deep Abrasion of P0 and P10.
Source. Authors.

The results show a high resistance against wear exerted by the abrasive agent during the development of the abrasion resistance test, which facilitates its use in environments of intense pedestrian traffic or in industrial environments, making this paste essential to manufacture materials suitable for the paving of high-traffic spaces and environments such as schools, commercial centers, airports, industries, etc. In addition to having low open porosity, manufactured products are effective for placement in open (exterior) environments such as facades being more resistant to the inclemencies of the environment (humidity,

Ttemperature and resistance to wear). An environmentally important aspect is that aluminum oxide begins to generate excellent structural, mechanical and tribological properties at temperatures above 1000 °C, which makes feasible to manufacture masonry products (products of higher consumption in the region) without requiring too high temperatures, helping to reduce the energy consumption during the cooking stage, generating in turn less consumption in fuel and greater profitability in the processes.

Acknowledgments

The authors thank the CIMAC Ceramic Materials Research Center and the Ceramic Training Laboratory of the Francisco de Paula Santander University of Cúcuta-Colombia for the support provided to carry out the tests.

References

[1] Sánchez-Molina, J. y Ramírez-Delgado, R.P., El cluster de la cerámica del área metropilitana de Cúcuta, 1ra ed., Unversidad Francisco de Paula Santander, 2013, pp. 112-120.

[2] Asociación de Industriales de la Arcilla de Norte de Santander - INDUARCILLA-, Estudio de empresas cerámica de la región de Norte de Santander, Colombia, 2015, 100 P.

[3] Benveniste, G., Gazulla, C., Fullana, P., Celades, I., Ros, T., Zaera, V. y Godes, B., Análisis de ciclo de vida y reglas de categoría de producto en la construcción. El caso de las baldosas cerámicas, Informes de la Construcción, 63, pp. 71-81, 2011. DOI: 10.3989/ic.10.034

[4] Monteiro, S.N., Alexandre, J., Margem, J.I., Sánchez, R. and Vieira, C.M., Incorporation of sludge waste from water treatment plant into red ceramic, Construction and Building Materials, 22, pp. 1281-1287, 2008. DOI: 10.1016/j.conbuildmat.2007.01.013.

[5] Reig, L., Tashima, M.M., Borrachero, M.V., Monzó, J., Cheeseman, C.R. and Payá, J., Properties and microstructure of alkali-activated red clay brick waste, Construction and Building Materials, 43, pp. 98-106, 2013. DOI: 10.1016/j.conbuildmat.2013.01.031

[6] Cely-Illera, L., Cely-Illera, C.V. and Anteliz-Contreras, K., Evaluation of the technological characteristics of clay when adding building materials to manufacture structural products without implementing a sintering process, Ciencia e Ingeniería Neogranadina, 26(2), pp. 5-20, 2016. DOI: 10.18359/rcin.1811

[7] Debueno-Pradillas, P., Tomás-Catalán. A-E., Reig-Cerdà, L., Pitarch-Roig, Á. y Palencia-Guillén, J.J., Una alternativa sostenible para los residuos procedentes de baldosas cerámicas. Congreso mundial de la calidad del azulejo y del pavimento cerámico (QUALICER), pp. 1-12, 2016.

[8] Cely Illera, L., Cely-Illera, C. and Anteliz-Contreras, K., Raw material for the ceramic industry in Norte de Santander. III. Assessment of the technological properties when the residue test of deep abrasion is added, Bol. Soc. Esp. Cerám. Vidrio, 54(2), pp. 77-83, 2015. DOI: 10.1016/j.bsecv.2015.03.005

[9] Alcântara, A.C., Beltrão, M.S., Oliveira, H.A., Gimenez, I.F. and Barreto, L.S., Characterization of ceramic tiles prepared from two

clays from Sergipe – Brazil, Applied Clay Science, 39, pp. 160-165, 2008. DOI: 10.1016/j.clay.2007.05.004
[10] Aramide, F.O., Alaneme, K.K., Olubambi, P.A. and Borode, J.O., Characterization of some clay deposits in South West Nigeria, Leonardo Electronic Journal of Practices and Technologies, 25, pp. 46-57, 2014. DOI: 10.13140/2.1.4890.5920
[11] Vieira, C.M., Sánchez, R. and Monteiro, S.N., Characteristics of clays and properties of building ceramics in the state of Rio de Janeiro, Brazil, Construction and Building Materials, 22, pp. 781-787, 2008. DOI: 10.1016/j.conbuildmat.2007.01.006
[12] Cely-Illera, L., Raw materials for the ceramics industry from Norte de Santander. I. Mineralogical, chemical and physical characterization, Revista Facultad de Ingeniería, Universidad de Antioquia, 80, pp. 31-37, 2016. DOI: 10.17533/udea.redin.n80a04
[13] Bresciani, A. Y Spinelli, B., Deformación piroplástica durante la cocción y variaciones de planaridad después de la cocción en el gres porcelánico, Congreso mundial de la calidad del azulejo y del pavimento cerámico (QUALICER), pp. 1-13, 2012.
[14] Melchiades, F.-G, Dos Santos L.-R, Suelen, N. y Boschi, A.-O., Agentes fundentes para las piezas de gres porcelánico producidas por vía seca, Congreso mundial de la calidad del azulejo y del pavimento cerámico (QUALICER), 2012, pp. 1-12.
[15] Colin-Cass, B.-Ed., Prevención de la eflorescencia en el recubrimiento cerámico exterior a través de los principios de diseño y construcción, Congreso mundial de la calidad del azulejo y del pavimento cerámico (QUALICER), pp. 155-165, 2008.
[16] Cultrone, G. and Sebastián Pardo, E., Deterioro en muros de edificios ocasionado por eflorescencias Salinas, Revista de la sociedad española de mineralogía, 9, pp. 75-76, 2008.
[17] Rincón, J. M., and Romero, M. Fundamentos y clasificación de las eflorescencias en ladrillos de construcción, Materiales de Construcción, 50 (260), pp. 63-69, 2000.
[18] Rincón, J.M. y Romero, M., Prevención y eliminación de eflorescencias en la restauración de ladrillos de construcción, Materiales de Construcción, 51(261), pp. 73-78, 2001.
[19] Karkanis, P.G., Au, K. and Schaalje, G.B., Comparison of four measurement schedules for determination of soil particle-size distribution by the hydrometer method, Canadian Agricultural Engineering, 4, pp. 211-215, 1991.
[20] Medina-González, H., García-Coronado, J. and Núñez-Acosta, D., El método del hidrómetro: base teórica para su empleo en la determinación de la distribución del tamaño de partículas de suelo, Revista Ciencias Técnicas Agropecuarias, 16(3), pp. 19-24, 2007.
[21] Afanador-García, N., Guerrero-Gómez, G. y Monroy-Sepúlveda, R., Propiedades físicas y mecánicas de ladrillos macizos cerámicos para mampostería, Ciencia e Ingeniería Neogranadina, 22(1), pp. 43-58, 2012. DOI: 10.18359/rcin.248
[22] Amorós-Albero, J.L., Beltán-Porcar, V., Blasco-Fuentes, A., Enrique-Navarro, J.E., Escardino-Benlloch, A. y Negre-Medall, F., Defectos de fabricacion de pavimentos y revestimientos ceramicos, 1a ed., IMPIVA. Instituto de la mediana y pequeña industria valenciana – Ministerio de Industria, Comercio y Turismo, 1991, pp. 102-105.
[23] Amorós, J.-L., Felíu, C., Ginés, E. y Agramunt, J.-V., Resistencia mecánica y microestructura de soportes cerámicos en crudo, Congreso mundial de la calidad del azulejo y del pavimento cerámico (QUALICER), 1996, pp. 340-356.
[24] Amorós, J.-L., Sánchez, E., Cantavella, V. y Monzó, M., Propiedades mecánicas de los soportes cerámicos crudos, Congreso mundial de la calidad del azulejo y del pavimento cerámico (QUALICER), pp. 59-75, 2000.
[25] De Pablos, A., Miranzo, P., Osendi, M.I., Romero, J.C., Crespo, P., Gargallo, L. y Bengoechea, M.A., Estudio de las propiedades mecánicas de pavimentos cerámicos en crudo, Bol. Soc. Esp. Cerám. Vidrio, 39(5), pp. 631-634, 2000.
[26] Amorós, J.L., Blasco, A., Caeceller, J.V. y Sanz, V.. Acuerdo esmalte-soporte (III). Expansión térmica de soportes y esmaltes cerámicos, Técnica Cerámica, 179, pp. 644-657, 1989.
[27] Belda, A., Blasco, A., Montiel, E. y Orts, M.-J., El acoplamiento vidriado-soporte factores de los que depende y su control industrial, Congreso mundial de la calidad del azulejo y del pavimento cerámico (QUALICER), pp. 209-230, 1990.
[28] Hoffmann, C., Urano-de Carvalho, E.-F., Gracher-Riella, H. y Bernardin, A.-M., Acuerdo dilatométrico en gres porcelánico de doble compactación, Congreso mundial de la calidad del azulejo y del pavimento cerámico (QUALICER), 2008, pp. 149-154.
[29] Alayón-Sauma, M.V., Efecto del ajuste dilatometrico esmalte-bizcocho en la planitud de baldosas esmaltadas, Tesis, Departamento de Materiales, Universidad Simon Bolivar, Sartenejas Venezuela, 2004.
[30] Araque-Pabón, M., Peña-Rodríguez, G. y Vargas-Galvis, F. Desempeño mecánico y tribológico de baldosas cerámicas de arcilla roja recubiertas por proyección térmica a partir de alumina, Tecno Lógicas, 18(35), pp. 125-135, 2015. DOI: 10.22430/22565337.194
[31] Jordan-Vida, M.M., Sanfeliu-Montolio, T. y de la Fuente-Cullell, C., Resistencia mecánica y porosidad de soportes para pavimentos y revestimientos cerámicos obtenidos con arcillas de Castellón, Materiales de Construcción, 51(261), pp. 5-20, 2001.
[32] Bou, E., García-Ten, J., Pérez, R., Arrufat, S. and Atichian, G., Influence of alumina characteristics on glaze properties, Bol. Soc. Esp. Cerám. Vidrio, 49(4), pp. 271-278, 2010.
[33] Bagán, V., Enrique, J.E., Mallo, G. y Sanchez, E., Gres porcelanico. Influencia de las variables de proceso sobre la calidad del producto acabado, Congreso mundial de la calidad del azulejo y del pavimento cerámico (QUALICER), pp. 357-389, 1990.
[34] Abitante, A.L., Bergmann, C.P. y Ribeiro, J.L., Abrasión en baldosas cerámicas esmaltadas: Consideraciones sobre la vida útil y evaluación de su desempeño, Engenharia Civil • UM, 29, pp. 71-79, 2007.
[35] Esposito, L. y Tucci, A., Abrasión de superficies de azulejos cerámicos esmaltados. Bol. Soc. Esp. Cerám. Vidrio, 39(1), pp. 165-171, 2000.
[36] Felíu, C., Ibáñez, M.-J., Moreno, A. y Carceller., J.-V., Analisis de algunos factores relacionados con la degradacion por abrasion de baldosas ceramicas esmaltadas, Congreso mundial de la calidad del azulejo y del pavimento cerámico (QUALICER), pp. 345-356, 1990.
[37] Estrada, D.A. y Espinosa-de los Monteros, J., Ahorro de energía por el empleo de nuevas composiciones cerámicas, Bol. Soc. Esp. Cerám. Vidrio, 19(1), pp. 17-23, 1980.
[38] Gilabert, J., Zumaquero, E., Machí, C., Toledo, J. and Gómez-Tena, M.P., Caracterización mecánica y tribológica de recubrimientos diamond-like carbon aplicados por la técnica deposición química de vapor sobre baldosas cerámicas, Bol. Soc. Esp. Cerám. Vidrio, 54(5), pp. 209-218, 2015. DOI10.1016/j.bsecv.2015.09.002.

L.M. Carrillo-Rodriguez, currently, is pregrade student of the Technician in Manufacture of Ceramic Products from Universidad Francisco de Paula Santander, Colombia. citizenship: Cúcuta, Norte de Santander, Colombia.
ORCID: 0000-0003-3595-7657

L. Cely-Illera, is BSc. Eng in Environmental Engineering, MSc. in Science and Technology of Materials and Sp. in Senior Management, Foreign Trade; Currently, professor in the Departamento de Ingeniería Industrial, Universidad Francisco de Paula Santander (Cúcuta, Colombia), Active member of the Grupo de Investigación en Arquitectura y Materiales Alternativos – GRAMA. The research lines of interest: ceramic building materials, advanced materials, recycling and renovation of sustainable and renewable resources in the manufacture of construction materials. He is currently director of theses aimed at recycling reusable materials for the formulation of new ceramic pastes that improve the properties of the products. Citizenship: Cúcuta, Norte de Santander, Colombia.
ORCID: 0000-0002-9476-7100

J.W. Cely-Niño, is BSc. in Mechanical Engineer, he is currently an associate professor in the Departamento de Ingeniería de Sistemas, Universidad Francisco de Paula Santander, Cúcuta, Colombia. He served as president of the teachers' association of the Universidad Francisco de Paula Santander for 7 years. Citizenship: Cúcuta, Norte de Santander, Colombia.
Orcid: 0000-0001-6469-0280

C.V. Cely-Illera, received the BSc. in Biotechnology Engineer from the Universidad Francisco de Paula Santander in 2009, and the MSc. degree in Engineering Project Management from Bournemouth University, United Kingdom, with meritorious degree in 2013, obtained an MBA in Business

Administration and Management from Eude Business Management School in 2017, developed as a team leader in JD Wetherspoon, from Bournemouth, United Kingdom (March 17, 2009 to January 25, 2014), worked as Engineering Project Manager at VERGAS Ltd. in Poole, United Kingdom, worked as Project Manager in SAAF S.A.S., worked as a Project Leader in KAPPA 10 Ltda, curremtly working as Project Manager in BT (British Telecommunication). Citizenship: Cúcuta, Norte de Santander, Colombia.
ORCID: 0000-0002-3092-2685

UNIVERSIDAD NACIONAL DE COLOMBIA
SEDE MEDELLÍN
FACULTAD DE MINAS

Área Curricular de Ingeniería Civil

Oferta de Posgrados

Especialización en Vías y Transportes
Especialización en Estructuras
Maestría en Ingeniería - Infraestructura y Sistemas de Transporte
Maestría en Ingeniería – Geotecnia
Doctorado en Ingeniería - Ingeniería Civil

Mayor información:

E-mail: asisacic_med@unal.edu.co
Teléfono: (57-4) 425 5172

UNIVERSIDAD NACIONAL DE COLOMBIA
SEDE MEDELLÍN
FACULTAD DE MINAS



DYNA
http://dyna.medellin.unal.edu.co/

Risk analysis using meteorological weather factors in solar energy conversion systems

David Cardoza [a], Jorge M. Uribe [b] & Jairo Palacios [a]

[a] *Department of Electrical Engineering, Universidad del Valle, Cali, Colombia. david.cardoza@correounivalle.edu.co, jairo.palacios@correounivalle.edu.co*
[b] *Department of Economics, Universidad del Valle, Cali, Colombia. jorge.uribe@correounivalle.edu.co*

Received: February 27th, 2017. Received in revised form: November 16th, 2017. Accepted: January 25th, 2018

Abstract
We propose a methodology for conducting simulations of operational scenarios for energy projects based on photovoltaic generation systems. It considers several documented facts about time series of weather, such as strong seasonality and structural breaks, which the previous literature has not explored in depth. Our proposal uses public weather time series, which are usually recorded by meteorological observatories. This makes our approach a suitable strategy for any firm interested in applying it to its own data and projects. This approach also allows the user to set an appropriate level of confidence for the scenarios depending on her interests.

Keywords: photovoltaic systems; horizontal solar radiation; structural breakpoints; renewable energy sources; risk measurement.

Análisis de riesgo usando factores meteorológicos en sistemas de conversión de energía de solar

Resumen
Se propone una metodología para realizar simulaciones de escenarios de operación de sistemas solares fotovoltaicos. Esta aproximación tiene en cuenta características documentadas de las variables climáticas, como su estacionalidad y la presencia de quiebres estructurales, las cuales no han sido exploradas anteriormente con profundidad. La propuesta usa series de tiempo de datos de diferentes variables climáticas, las cuales son normalmente recolectadas por estaciones meteorológicas; esto le da utilidad a nuestra propuesta, ya que cualquier firma interesada pueda aplicar nuestro planteamiento a sus propios datos y proyectos. Este enfoque también les permite a los usuarios establecer un nivel de confianza adecuado para los escenarios de operación en los cuales se tenga interés.

Palabras clave: sistemas fotovoltaicos; radiación solar horizontal; quiebres estructurales; energías renovables; evaluación del riesgo.

1. Introduction

Forecasting and construction of operational scenarios is a key component of the appropriate functioning of any firm in the energy sector; it is crucial to project management and thus to decisions about the operational and financial viability of a given project. This is also true for companies with a business unit focused on exploiting renewable energy sources, such as photovoltaic energy conversion systems. Indeed, a correct assessment of operational risks, in terms of the energy that a firm could expect to offer to the market in a given day, is a crucial input when constructing cash flow scenarios and estimating returns on assets, liquidity ratios, present values, and other financial indicators. One can even make the argument that the execution of an entire energy conversion project depends on the accuracy of this exercise, and hence, it warrants considerable research efforts.

For the above reasons, the literature has explored several alternatives to forecasting the level of radiation a user can expect to be recovered by a photovoltaic system in a given period. These alternatives generally take into account the crucial relationship that exists between weather conditions and collected radiation, including the stochastic nature of the weather variables. For instance, [1] aim at forecasting

How to cite: Cardoza, D., Uribe, J.M. and Palacios J., Risk analysis using meteorological weather factors in solar energy conversion systems. DYNA, 85(205), pp. 98-104, June, 2018.

© The author; licensee Universidad Nacional de Colombia.

radiation using *k*-th neighbor and interpolation methods, level of persistency, artificial neural networks, support vector regressions and time series analysis. These authors focus on the explanation of horizontal global radiation and use measures of radiation in a given location, alongside measures of weather variables in sparse locations around the radiation recording devices. [2] estimate an artificial neural network by genetic algorithms, aiming at forecasting daily radiation. They consider seven variables as inputs when training their network: average air temperature, minimum and maximum temperatures, relative humidity, atmospheric pressure, wind velocity and ground temperature. Using similar variables, [3] report that between three and four meteorological variables suffice to explain radiation, at least at the highest frequencies of their analysis. These authors base their conclusions on calculations of adjusted- R squared statistics, square residuals and forecasting errors. In contrast [4], employing similar methods and variables, finds that the best model includes all the available variables (seven in his case).

[5] estimate Multivariate GARCH models (time series models with autoregressive patterns in the conditional variance process), which include climatological variables such as solar brightness, precipitation, average minimum and maximum air temperatures, relative humidity and saturation deficit. [6] emphasize the importance of the range between the maximum and minimum temperatures when forecasting radiation, and they also highlight the changing nature of the relationship between radiation and weather variables, very likely driven by the strong seasonal patterns that characterize the latter.

In this study we do not focus on the point-forecast of radiation in a given period, instead we emphasize the construction of operational scenarios for an energy project in terms of the radiation that a photovoltaic unit can expect to collect, under certain weather conditions, in a given period, with an appropriate level of confidence. This enriches the tools available for energy project administrators and allows the unit in charge to make more accurate decisions, based on richer information, about a project's realization or continuation.

Our methodology aims at providing thresholds of minimum radiation that one may expect to observe given certain weather parameters and for a desired confidence level. That is, we focus on the estimation of a specific quantile of the distribution of radiation conditional on weather variables, which increases the accuracy of our estimates. We explore several weather indicators in our empirical exercise and work with daily averages of those, as has been done previously (for instance in [7]). Given the impaired evidence regarding the number of variables required to explain radiation [3,4], we performed an automatic search algorithm to determine how many and which variables should be included in an optimal model. Importantly, our methodology takes into account the dynamic relationship that exists between weather and radiation. The changing nature of the relation between weather and radiation has been mainly ignored so far. That is, strong evolving weather conditions may change the way

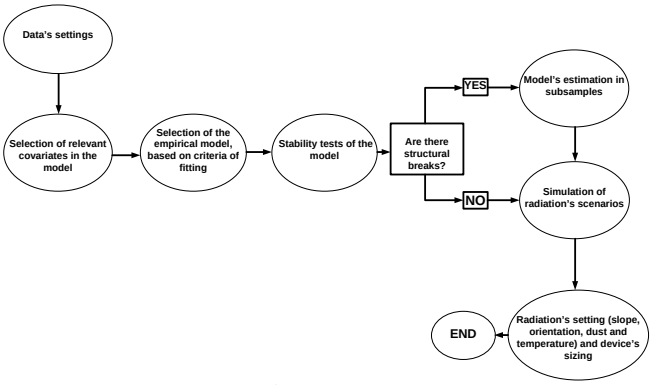


Figure 1. Graphical summary of the proposed methodology.
Source: The authors.

in which radiation interacts with temperature, wind, precipitation and other variables. Therefore, any model that is estimated under the assumption of a stable relationship among these variables may display spurious patterns, which may be avoided only by explicitly considering this possibility. Endogenous structural tests in time series analysis, such as the ones employed herein, are specially designed to address this challenge.

In what follows we present the proposed methodology, and we illustrate it using data from a company that manages photovoltaic energy conversion systems, located in Colombia. We present our empirical results in section 3, and we discuss the results and conclude in sections 4 and 5, respectively.

2. Materials and methods

Our methodology focuses on the problem of estimating the expected global radiation on a horizontal surface, given a set of weather-related covariates. The proposal consists of five steps: i) selection of relevant variables to be included in the model, ii) selection of a parsimonious empirical model, iii) stability tests of the model's parameters, iv) simulation of operation-scenarios, conditional on weather parameters and v) generation of the output variable to be included in traditional project management designs (see Fig. 1).

2.1. Selection of relevant covariates in the model

We assume a linear relationship[1] between the total amount of radiation y_t, and a set of weather-related covariates $x_{i,t}$ i=1,2,…k, . In our empirical implementation, we imposed a maximum possible number of covariates k^{max}=7, following data availability from regular records of a meteorological observatory. Working explanatory variables were: temperature, humidity, dew point, wind velocity, precipitation level, atmospheric pressure, and an indicator of cloudiness (the highest minus the lowest temperature within a day). In all cases, except for the last one, the recorded frequency of each variable was half an hour, and therefore we needed to transform the original series to daily averages to obtain standardized frequencies among all the covariates and

[1] Perhaps non-constant in time, as will be explained in step 2.3.

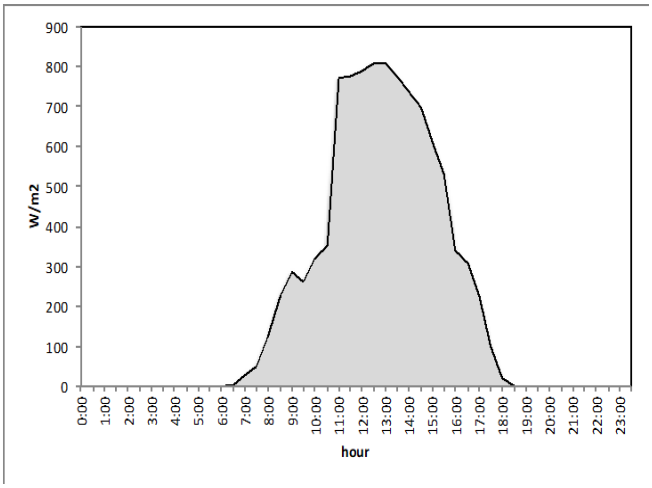


Figure 2. Radiation recorded on January 1st 2015
Source: The authors.
Note: the Figure shows the level of radiation collected by a solar panel during each half- hour on a given day. The area below the curve corresponds to the total level of radiation collected by the solar panel. The data shown in the Figure was selected just for illustration purposes.

the dependent variable[2]. This dependent variable was constructed as the cumulated level of radiation collected by the panel during the course of a day. We had measures of the level of radiation collected at half hourly intervals. These measures were aggregated by integrating out the area below the curve in Fig. 2 for each day within the sample.

In this case, the population model that describes the relation between the collected radiation and the weather regressors can be written as follows:

$$y_t = \beta_1 x_{1,t} + \beta_2 x_{2,t} + \cdots + \beta_k x_{k,t} + \varepsilon_t, \qquad (1)$$

In practice, we do not know coefficients β_i, nor do we know the value of k. That is, we must estimate the marginal effects of each covariate on the total amount of collected radiation, and, at the same time, we must decide how many and which variables may appear in eq. (1). Once this is done we end up with a sample-counterpart of eq. (1):

$$y_t = \hat{\beta}_1 x_{1,t} + \hat{\beta}_2 x_{2,t} + \cdots + \hat{\beta}_{\hat{k}} x_{\hat{k},t} + e_t, \qquad (2)$$

In eq.(2), marks over each of the coefficients indicate that those coefficients are related to the sample, instead of the population, and therefore they can be obtained from the data.

In the process of deciding which variables to include in eq. (2), we consider that redundant variables will conduce to inefficient estimations of the model's parameters, while omitted (and relevant) variables will likely conduce to biased and non-consistent estimations. Hence, lacking a generally accepted theory regarding the shape and composition of eq. (2) led us to undertake a data-driven model selection process using ordinary least squares (OLS) and subsets of regressions. We conduced our exhaustive search for relevant covariates among subsets of variables typically recorded by meteorological observatories, many of which have been previously explored in the empirical literature.

Formally, given a maximum number of variables recorded by the meteorological observatory, k^{max}, we estimated different models fitted on subsets of variables, each of cardinality $\bar{k} \leq k^{max}$. For each value of $\bar{k}$, which must be chosen a *priori* by the researcher, it was necessary to evaluate all possible combinations of covariates. Then, for each $\bar{k}$, we selected the model that minimized the sum of squared residuals, $SSR = \sum_{t=1}^{T} e_t^2$ [3]. This strategy is equivalent to selecting the subset of variables for a given $\bar{k}$, that maximize the coefficient of determination, R^2, of the linear projection of y_t onto $x_{1,t}, x_{2,t}$, ..., defined as $R^2 = 1 - SSR/STS$, where $STS = \sum_{t=1}^{T} y_t^2$. There are several alternative approaches that may be used to accomplish this task. One that is widely accepted in the statistical literature, which, moreover, is available in the statistical software R, consists of conducing an exhaustive (forward or backward) search for the best subsets as explained in [8]. In practical terms, this can be done using the function 'regsubsets()', from the package 'leaps'. In our implementation, we set $\bar{k} = 1 \ldots 7$ because our maximum number of variables was constrained by the number of variables available from the original observatory data.

2.2. *Selection of the empirical model, based on criteria of fitting and parsimony*

Notice that the preceding step gives us the best linear model for each value $\bar{k}$. Nevertheless, in practice, the researcher also needs to estimate the optimum value of $\bar{k}$. That is, we must select the best model among those available, taking into account model's parsimony considerations, by penalizing the inclusion of redundant variables in the estimations. That is, if a variable is to be included in a model, it must add to the model in terms of explanatory power more than it takes from it in terms of efficiency. To this end, we used two different criteria: Akaike's Information Criterion (AIC) and a Bayesian Information Criterion (BIC)[9], defined as:

$$AIC = 2\bar{k} - ln(L), \qquad (3)$$

$$BIC = ln(T)\bar{k} - ln(L), \qquad (4)$$

where L is the likelihood of the model, $ln()$ stands for the natural logarithm, and T is the number of time series observations in the sample. The best model minimizes either of these two criteria.

[2] In our empirical implementation, other alternatives to averages were explored. Specifically, we conducted some preliminary exercises using principal components instead of averages, with no significant gains in terms of model fitting.

[3] Since our algorithm returns a best model of each $\bar{k}$ the results do not depend on a penalty model for model size such as AIC or BIC.

2.3. Stability tests of the model's estimates due to weather conditions

With the best model determined, after steps 1 and 2 we test for parameters' stability. In the case of photovoltaic energy conversion systems, this is a crucial step of the methodology because weather-related variables are known to exhibit strong seasonality patterns, which in principle may have a significant effect on the relationship between the covariates in the model and the collected radiation during the year. This is even more important when modeling weather variables for energy companies located in countries characterized by higher latitudes and markedly contrasting seasons.

To this end, we used endogenous structural break tests following [10,11]. These procedures offer a reliable strategy to identify changes in the relationship between the covariates and the explained variable. The multiple-breaks statistic is intuitively a set of Chow's statistics [12], calculated using recursive regressions over subsamples of increasing lengths. Several candidates for breaks are selected using the biggest F-statistics for which the null hypothesis in the Chow tests (i.e., parameters stability) is rejected. Then, asymptotic (corrected) critical values are used to contrast the null of no-breaks.

If we define $\hat{\theta} = \{\hat{\beta}_1, \hat{\beta}_2, \dots, \hat{\beta}_{\hat{k}}\}$ and $X_t = \{x_{1,t}, x_{2,t} \dots x_{\hat{k},t}\}$ eq.(2) can be rewritten as:

$$y_t = X_t'\theta_j + e_t, \tag{5}$$

where $j = 1, \dots, m+1$ represent a given model regime. That is, if we have m structural breaks in the model's parameters, it allows us to estimate $m+1$ regimes (or 'seasons'). To identify and estimate the model in eq. (5), it is necessary first to estimate the number and location of breaks. The general idea underlying Bai and Perron's [10] algorithm consists of the following steps:

i. First, we estimate a model through recursive regressions, increasing the sample from $h * T$ to $T * (1-h)$, where $h \in (0,1)$. The sample is divided into two sub-samples, in the period where R^2 of the global regression is maximized. We set $h = 0.05$.
ii. Once this break point is determined, the same searching procedure is applied to each of the two sub-samples. The process continues to the point where either it reaches a maximum number of breaks determined a priori ($m^{max} = 5$ in our case) or to the point at which new break candidates are no longer statistically significant.
iii. To conduct hypothesis testing about the significance of each break point, critical values provided by Andrews [13] and Hanssen [14] must be used to avoid the identification of spurious break estimates.

Once the numbers and locations of the endogenous breaks are known, it is possible to estimate eq.(6):

$$y_t = X_t'\hat{\theta}_j + e_t. \tag{6}$$

Notice that the model has different coefficients for each regime or season. Such coefficients are determined endogenously, provided $j > 1$. Estimations like those described above are performed using the package 'strucchange' in the statistical software R.

2.4. Simulation of scenarios

The simulation exercises in our methodology take into account, by construction, the most relevant variables explaining radiation, such as structural changes associated with different weather regimes. Eq.(6) for each regime can be rewritten as:

$$y_t = \hat{y}_t + e_t, \tag{7}$$

where $\hat{y}_t = X_t'\hat{\theta}$ for a given j, which has been supressed to simplify notation. The sources of uncertainty in this case are $\hat{y}_t$ and e_t. In the former case, we may observe different arrangements of the meteorological variables relevant to the model, which may conduce to distinct scenarios of operation. In the latter case, uncertainty may arise from other variables not included in the model, which may potentially affect the operation. To take into account both sources of uncertainty, we generated different scenarios of operation S, conducting re-sampling with replacement in the series of $\hat{y}_t$ and in the series of e_t. Then, we aggregated the two generated series into a single series to formulate comprehensive scenarios of operation for y. This procedure is justified as long as $\hat{y}_t$ is orthogonal to e_t, which holds by construction in our case.

The final idea consists of estimating some order statistics of the simulated scenarios for y_i, $\{y_i\}_{i=1}^{S}$. These are percentiles of interest for the administrator in charge of the project decisions. For example, percentiles $\alpha \in (0,1)$ close to 0 ($\alpha = 0.01, 0.05, 0.10$) may be interpreted as conservative scenarios for decision making.

2.5. Data

We use data from February 4th 2014 to October 26th 2015. The variable of main interest is radiation, which was constructed as explained in section 2.1 and in Fig. 2. As explanatory variables we used average daily temperature, humidity, dew-point temperature, wind velocity, precipitation level, atmospheric pressure, and the difference between maximum and minimum temperatures each day. All variables were collected at half-hour intervals, and all but the last one were averaged to work with a daily version of each. All data were taken from a meteorological observatory located in Colombia, latitude 3.4383 and longitude -76.5161. After transforming each variable, according to our requirements we ended up with a total of 580 days of observations. Fig. 3 depicts our variables, and in Table 1 we show the summary statistics of our sample. Fig. 3 also highlights two regimes in the sample, which were detected using structural breaks tests as explained above.

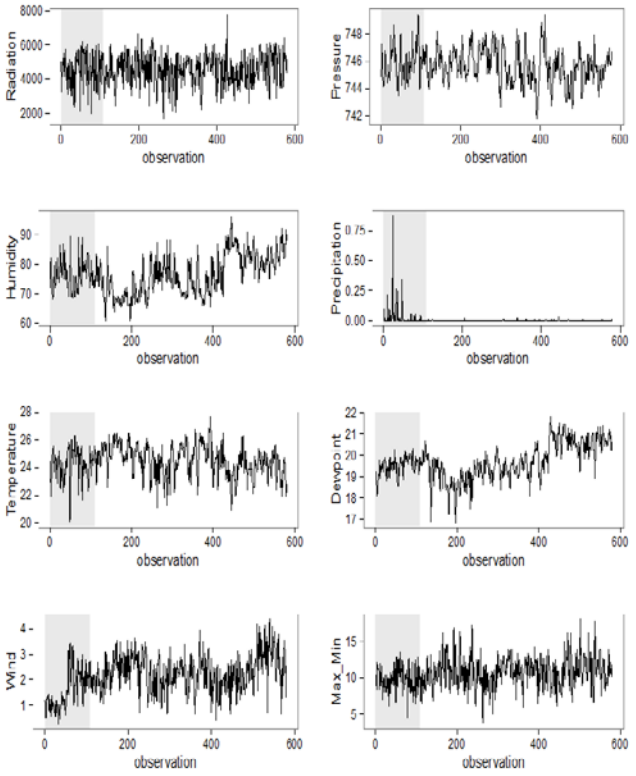


Figure 2. Radiation and Explanatory Variables Used in The Analysis.
Source: The authors.
Note: The Figure shows the daily averages of the variables employed in our estimations. Radiation is measured in kWh/m2, temperature is measured in °C, humidity is measured in %, dew-point temperature is measured in °C, wind velocity is measured in m/s, precipitation is measured in mm, atmospheric pressure is measured in Bar. Max-Min corresponds to the difference between the highest and the lowest temperatures registered each day. The shadowed area corresponds to the first regime in our sample, detected by using structural breaks tests.

Table 1.
Summary statistics of the variables used in the estimations.

	Radiation	Temperature	Humidity	Dew Point
Min.	1646	20.03	60.81	16.86
1st Quartile	3938	23.78	71.21	19.17
Median	4569	24.51	76.30	19.67
Mean	4559	24.44	76.49	19.70
3rd Quartile	5274	25.24	81.40	20.24
Max.	7812	27.64	96.54	21.81
	Wind Velocity	**Precipitation**	**Atmospheric Pressure**	**Max-Min Temperature**
Min.	0.275	0.0000000	741.7	3.667
1st Quartile	1.621	0.0000000	744.8	9.278
Median	2.229	0.0000000	745.7	10.667
Mean	2.167	0.0066074	745.7	10.703
3rd Quartile	2.688	0.0002083	746.4	12.111
Max.	4.396	0.8750000	749.5	18.167

Source: The authors.
Note: Minimum, 1st and 3rd quartiles, median, mean and maximum for each variable.

Table 2.
Selected variables given k, from k=2 to k=7.

k	Temp.	Dew Point	Humidity	Wind Velocity	Precip.	Atmosp. Pressure	Max-Min Temp.
1							*
2	*						*
3	*			*			*
4	*			*		*	*
5	*	*		*		*	*
6	*	*		*	*	*	*
7	*	*	*	*	*	*	*

Source: The authors.
Note: An asterisk indicates that a given variable is included in the model with the number of variables indicated in the first column. The variables were selected using exhaustive (forward or backward) searches for the best subsets.

Before conducting our estimations, we had to stabilize the mean of the atmospheric pressure variable using a dummy variable regression. We detected two changes in the scale of the series on March 31st 2014 and on October 5th 2015. These changes were unrelated to weather, but they were caused by settings in the measurement device.

2.6. Target

The procedure described above aims at sizing a photovoltaic system in an accurate fashion. We seek a suitable radiation value that could be used for sizing solar photovoltaic and photo-thermal panels, batteries, battery chargers and inverters. Applying the proposed methodology, we provide an option for performing sizing of these devices, which uses statistical tools for the selection of the level of radiation to be employed.

3. Results and discussion

Here we present the main results of our empirical implementation. First, we set the relevant variables to be included in our model. Given an optimal number of variables, the selected combinations are presented in Table 2. As can be seen, the difference between maximum and minimum temperatures appears in all selected models, using one to seven variables. The second most recurring variable is average temperature and the third is wind velocity. The least relevant variables, in terms of their significance in the models, are humidity and level of precipitation.

We estimated six models using the indications provided in Table 2. The models included between two and seven variables (we omitted the model with only one variable). Following the AIC criterion, the optimal model should include five variables, namely, average temperature, dew point temperature, wind velocity, atmospheric pressure and the differences between the max and min temperatures. According to BIC criteria, the optimal model should include only four variables, namely the same as those listed above except for dew-point temperature. In the interest of parsimony we followed BIC in the final specification (Table 3).

Table 3.
Criteria for model selection.

k	2	3	4	5
AIC	8,987.542	8,959.928	8,952.471	8,951.929
BIC	9,004.994	8,981.743	8,978.649	8,982.471
k	**6**		**7**	
AIC	8,953.383		8,955.363	
BIC	8,988.288		8,994.630	

Source: The authors.
Note: Two criteria were used to determine the optimal number of variables in the model, the Bayesian Information Criterion (BIC) and the Akaike's Information Criterion (AIC). The best models are those with lower values and are highlighted using bold type in each case.

Having selected the best model, we test for the stability of its parameters. We detected one statistically significant structural break in the sample that minimizes the BIC criterion (8914.26) when including partitions. The break is located on May 25th 2014 (day 110) with an associated 95% confidence interval between May 16th 2014 and June 1st 2014. Thus, we documented two different regimes in our sample, the first one from February 4th 2014 to May 25th of the same year, and the second one from May 26th until the end of the sample (see Fig. 1).

We present the estimated coefficients corresponding to the two detected regimes in Table 4. In the first regime, only two variables - temperature and the highest minus the lowest temperatures in a day - were statistically significant. Both of them exhibited positive signs in the regressions, meaning that an increase of one degree in the average temperature recorded in a given day increases the radiation collected by 342.44 kWh/m2. In the same line, an increase in the difference between the max and the min temperatures (i.e., indicating a less cloudy day) increases the supply of radiation by 364.68 kWh/m2, all other variables remaining constant. Although only two variables were significantly different from zero during this regime, the model is highly significant on a joint basis, as shown by an associated F statistic of 85.81, which is also significant at a 99% confidence level. The coefficient of determination, which is usually interpreted as a measure of a model's goodness of fit, is relatively high, indicating that the estimated model accounted for 76.57% of the total variation in the collected radiation series.

In the second regime, all the variables were statistically significant. Although, the two variables (temperature and max-min) continued to explain radiation in a significant fashion, their average effect on radiation was considerably less pronounced compared to the first regime. That is, with an increase of one degree in the average temperature, collected radiation increases by 139.15 kWh/m2 during the second regime (in contrast with 342.44 w/m2 in the first regime). The same holds true for the level of cloudiness. This means that during the second period of the sample, other variables, such as wind velocity and atmospheric pressure, were also highly relevant to explain the total level of radiation collected by a panel. Both variables have positive signs. These changes in the model were only possible to detect by testing the model's stability by means of structural break statistics. This is a key point when modeling energy generation devices that depend on weather variables, especially when modeling renewable energies, which are characterized by strong seasonality patterns and are, therefore, very sensitive to structural instabilities associated with weather.

In Table 5 we report the expected operational scenarios at different levels of confidence from 5% to 90%. This information is valuable for project managers who seek to determine how much of their energy supply can be compromised for future delivery depending on the weather conditions. For example, during regime 2, the 5th percentile of the generated scenarios corresponds to 3,058.46 kWh/m2, this means that on only 5% of the days during a year (approximately 18 days) will the collected level of radiation be lower than 3,058.46 kWh/m2. Analogously, the 90th percentile is 5,685.84 kWh/m2, which tells us that on only 10% of the days will the collected radiation be higher than this level. Those scenarios can be interpreted as corresponding to 'optimistic' or 'pessimistic' expectations. The lowest quantiles are associated with very conservative scenarios of operation, and they can be used as forecasts of the worst scenarios a firm might face, during a particular weather regime, in terms of energy supply.

Notice that the percentiles vary considerably from one regime to another. Specifically, they are almost always higher for the second regime than for the first regime. This seems quite natural because, during the first period of the sample, the observatory recorded more precipitation, lower dew-point temperatures, fewer differences between the highest and the lowest temperatures in a day (cloudier days) and a lower wind velocity (see Fig. 1). Nevertheless, when

Table 4.
Coefficient estimates that relate each explanatory variable to radiation in each regime of the sample.

First Regime		
Dependent Variable: Radiation		
Degrees of Freedom 105		
	Estimate	Robust S.E.
Intercept	-64684.2	43926.6
Temperature	342.4***	84.4
Wind Velocity	32.7	69.5
Max-Min Temp.	364.7***	31.2
Atmospheric Pre.	76.8	56.9
R-squared	0.77	F-statistic 85.8***
Adjusted R-squared	0.76	(4 and 105 DF)
Second Regime		
Degrees of Freedom 465		
	Estimate	Robust S.E.
Intercept	-68581.1***	16099.6
Temperature	139.2***	28.4
Wind Velocity	338.4***	37.9
Max-Min Temp.	274.0***	13.9
Atmospheric Pre.	88.5	21.2
R-squared	0.70	F-statistic 272.9***
Adjusted R-squared	0.70	(4 and 465 DF)

Source: The authors.
Note: * significant at 90% of confidence, ** significant at 95% of confidence, *** significant at 99% of confidence.

Table 5.
Operation's Scenarios

	5%	10%	15%
Regime 1	2969.396	3342.907	3579.546
Regime 2	3058.455	3401.363	3627.674
	20%	**50%**	**90%**
Regime 1	3768.835	4570.654	5774.753
Regime 2	3808.448	4572.227	5685.841

Source: The authors.
Note: The Table shows how much radiation we can expect the panel to collect, on a given day, during each regime in the sample, under certain levels of confidence. For example, in the second regime, we can expect that the collected level of radiation will surpass 5,685.841 w/m2 in a day only 10% of the time, while we can expect it to be lower than 3,401.363 w/m2 only 10% of the time.

we focus on the 90th percentile during the first regime, the average level of collected radiation was lower compared to the second regime, but it was also more volatile. Therefore, we can conclude that the first regime of operation is also more risky in terms of the level of radiation that one may expect to receive in photovoltaic panels.

5. Conclusions

We propose a methodology for conducting simulations of operational scenarios for energy projects based on photovoltaic generation systems. It considers several documented facts about time series of weather, such as strong seasonality and structural breaks. Our proposal uses public weather time series, which are usually recorded by meteorological observatories. This makes our approach a suitable strategy for any firm interested in applying it to its own data and projects. We illustrate our methodology using data for a Colombian energy firm and we document that the difference between maximum and minimum temperatures appears in all selected models, using one to seven variables. The second most recurring variable is average temperature and the third is wind velocity. The least relevant variables, in terms of their significance in the models, are humidity and level of precipitation.

Bibliography

[1] Lazzaroni, M., Ferrari, S., Piuri, V., Salman, A., Cristaldi, L. and Faifer, M., Models for solar radiation prediction based on different measurement sites, Measurement, 63, pp. 346-363, 2015. DOI: 10.1016/j.measurement.2014.11.037

[2] Mousavi, S.M., Mostafavi, E.S., Jaafari, A., Jaafari, A. and Hosseinpour, F., Using measured daily meteorological parameters to predict daily solar radiation, Measurement, 76, pp. 148-155, 2015. DOI: 10.1016/j.measurement.2015.08.004

[3] Ododo, J. and Usman, A., Correlation of total solar radiation with common meteorological parameters for Yola and Calabar, Nigeria, Energy Conversion and Management, 37(5), pp. 521-530, 1996. DOI: 10.1016/0196-8904(95)00217-0

[4] Skeiker, K., Correlation of global solar radiation with common geographical and meteorological parameters for Damascus province, Syria, Energy Conversion and Management, 47(4), pp. 331-345, 2006. DOI: 10.1016/j.enconman.2005.04.012

[5] Sun, H., Zhao, N. Zeng, X. and Yan, D., Study of solar radiation prediction and modeling of relationships between solar radiation and meteorological variables, Energy Conversion and Management,105, pp. 880-890, 2015. DOI: 10.1016/j.enconman.2015.08.045

[6] Shamshirband, S., Mohammadi, K., Chen, H., Narayana-Samy, G., Petković, D. and Ma, C., Daily global solar radiation prediction from air temperatures using kernel extreme learning machine: A case study for Iran, Journal of Atmospheric and Solar-Terrestrial Physics, 134, pp. 109-117, 2015. DOI: 10.1016/j.jastp.2015.09.014

[7] Ouali, K. and Alkama, R., A new model of global solar radiation based on meteorological data in Bejaia City (Algeria), Energy Procedia, 50, pp. 670-676, 2014. DOI: 10.1016/j.egypro.2014.06.082

[8] Wooldridge, J.M., Introductory econometrics a modern approach, 5th ed. Michigan: Cengage Learning, 2013.

[9] Bai, J. and Perron, P., Computation and analysis of multiple structural change models, Journal of Applied Econometrics, 18(1), pp. 1-22, 2003. DOI: 10.1002/jae.659

[10] Perron, P., Dealing with structural breaks, in Hassani, H. et al. Palgrave Handbook of Econometrics Vol. 1: Econometric Theory, UK, Palgrave Macmillan, 2006, pp. 278-352.

[11] Chow, G,. Tests of equality between sets of coefficients in two linear regressions, Econometrica, 28, pp. 591-605, 1960. . DOI: 10.2307/2288492

[12] Andrews, W.K.D., Test for parameter instability and structural change with unknown change point, Econometrica, 61(4), pp. 821-856, 1993. DOI: 10.2307/2951764

[13] Hansen, B.E., Approximate asymptotic P values for structural change tests, Journal of Business & Economic Statistics, 15(1), pp. 60-67, 1997. DOI: 10.1080/07350015.1997.10524687

D. Cardoza-Montalvo, has a MSc.in Engineering with Sp. in Electric Engineering from Universidad del Valle, Cali, Colombia, and a BSc. in Electric Engineer from the same institution. Currently he works as a professional in regulatory analysis at the division of Regulatory Analysis of EPSA E.S.P. S.A. David belongs to the research group in Energy Conversion (Convergía) attached to the School of Electric and Electronic Engineering at Universidad del Valle, Colombia. His research areas include the study of renewable energies, efficient energy usage, electric sector regulation and power systems analysis.
ORCID: 0000-0003-2319-981X

J.M. Uribe, has a Ph.D. in Economics, Universitat de Barcelona, Spain, a MSc. of Research in Economics, European University Institute, and a MSc. in Economics, Universidad de los Andes, Colombia. He is an Economist from Universidad del Valle, Colombia and a BSc. in Finance from Santiago de Cali University. Currently he is an associate professor in the Economics Department at Universidad del Valle and director of the research group in Applied Macroeconomics and Finance. He is author of several publications in energy and finance fields in international peer-review academic journals and has participated with contributed papers and presentations in many international congresses and conferences about energy markets, finance, and risk. His research has focused on the econometrics of risk and uncertainty, so as on asset pricing in energy and stock markets.
ORCID: 0000-0002-5844-2771

J.A. Palacios-Peñaranda, has a PhD. in Energy Generations Systems and is a Specialist in Rational Use of Energy, both from Universidad Politécnica de Madrid, Spain. He is also an BSc. Electrical Engineer from Universidad del Valle, Colombia. Currently he is full professor at Universidad del Valle, and he belongs to the Group in Energy Conversion at the School of Electric and Electronic Engineering at Universidad del Valle. He has been part of Universidad del Valle since 1984 and has been in charge of numerous courses both at undergraduate and graduate levels. He also has served as director and committee member at numerous master and PhD thesis, in the research lines of: alternative sources of energy, rational use of energy, electric power generation and electric machines. He has participated as speaker in numerous national and international professional and academic meetings.
ORCID: 0000-0002-9742-5608

UNIVERSIDAD NACIONAL DE COLOMBIA
SEDE MEDELLÍN
FACULTAD DE MINAS



DYNA
http://dyna.medellin.unal.edu.co/

Obtaining the electrical impedance phase using Wavelet transform and Fourier transform from transient signals. Part 2: practical assessment and validation

Eduardo Gómez-Luna [a], Juan Sebastián Cuartas-Bermúdez [b] & Eduardo Marlés-Sáenz [c]

[a] *Grupo GITICAP, Potencia y Tecnologías Incorporadas S.A, Cali, Colombia. eduardo.gomez@pti-sa.com.co*
[b] *Universidad del Valle, Cali, Colombia. Juan.cuartas.bermudez@correounivalle.edu.co*
[c] *Grupo GRALTA, Universidad del Valle, Cali, Colombia. eduardo.marles@correounivalle.edu.co*

Received: October 24th, 2017. Received in revised form: March 8th, 2018. Accepted: April 9th, 2018.

Abstract
This article presents a practical assessment and validation of the new proposed approach based on the continuous wavelet transform (CWT) to obtain the electrical impedance phase from online transient signals for a real transformer. Besides the mathematical procedure presented in a previous paper, an electronic system was also designed and implemented, in order to inject superimposed controlled pulses to the power system (50/60 Hz) wave. The results show improved performance of the wavelet transform compared to that of the Fourier Transform, for transient signal analysis to be applied on a nonintrusive transformer monitoring approach. Particularly, this new approach proves useful in overcoming problems related to signal filtering and signal processing in an online frequency-response analysis of a transformer diagnosis.

Keywords: continuous wavelet transform (CWT); frequency response; online supervision and control; power system transients and transformers.

Obtención de la fase de la impedancia eléctrica usando transformada Wavelet y transformada de Fourier de señales transitorias. Parte 2: evaluación práctica y validación

Resumen
Este artículo presenta la validación y evaluación práctica para la nueva propuesta presentada, basada en la Transformada Wavelet Contínua (CWT) para obtener la fase de la impedancia eléctrica de señales transitorias en línea de un transformador real. A parte del procedimiento matemático presentado en la parte 1, también se diseñó e implementó un sistema electrónico para inyectar pulsos controlados en la onda del sistema de potencia (50/60 Hz). Los resultados muestran un mejor rendimiento de la Transformada Wavelet en comparación con la transformada de Fourier, para el análisis de señales transitorias para ser aplicado en un enfoque de monitoreo de transformadores no intrusivo. En particular, este nuevo enfoque permite superar algunos problemas de filtrado y procesamiento de señales en el análisis de respuesta en frecuencia de un transformador en servicio.

Palabras clave: transformada Wavelet continua (CWT); respuesta en frecuencia; supervisión y control en línea; transitorios del sistema eléctrico y transformadores.

1. Introduction

A new theoretical method to obtain the frequency response from the online transient signals measurement (with the transformer in service) was presented in a previous paper [1-6].

This new method is based on the continuous wavelet transform (CWT), which enables improved performance compared to the traditional Fourier transform. The transient

How to cite: Gómez-Luna, E., Cuartas-Bermúdez, J.S. and Marlés-Sáenz, E., Obtaining the electrical impedance phase using Wavelet transform and Fourier transform from transient signals. Part 2: practical assessment and validation. DYNA, 85(205), pp. 105-110, June, 2018

© The author; licensee Universidad Nacional de Colombia.

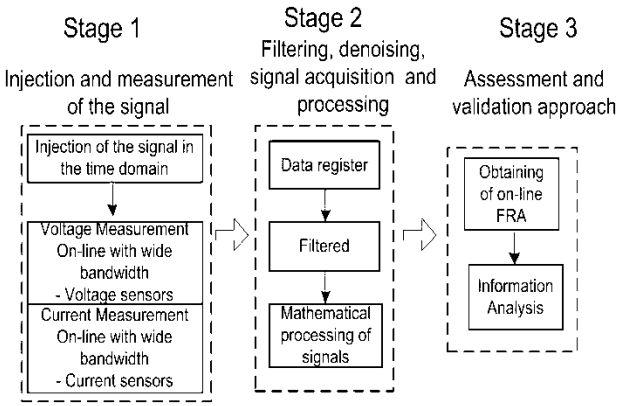


Figure 1. Schema of the proposed method for the *measurement of the online FRA* in transformers.
Source: [5].

signals presented as examples in that paper came from simulations within the Alternative Transients Program (ATP). In recent years, there has been a growing interest in frequency-response analysis (FRA) with the transformer in service, since no transformer disconnection is required to conduct the test.

Testing under these conditions allows for the monitoring of the transformer and the detection of any abnormalities before they cause catastrophic failures in power grids [2,3]. Although there have been efforts and contributions to carry out the frequency response test with the transformer in service, state of the art is not mature and there is still much research to be done [4].

This paper presents the assessment and validation of the proposed method in real transformers, using the continuous wavelet transform (CWT) [1] as a powerful tool for the filtering, denoising, and processing of transient signals. As will be shown, improvement is achieved when using this new method, including non-repeatability effects and noise content in the measurements, as well as in non-periodical waveforms processing constraints.

2. Experimental set in the pilot transformer

Fig. 2 shows the experimental set in the pilot transformer carried out in the high-voltage laboratory of the Universidad del Valle [6] and Fig. 3 shows the pilot transformer. An OFF-

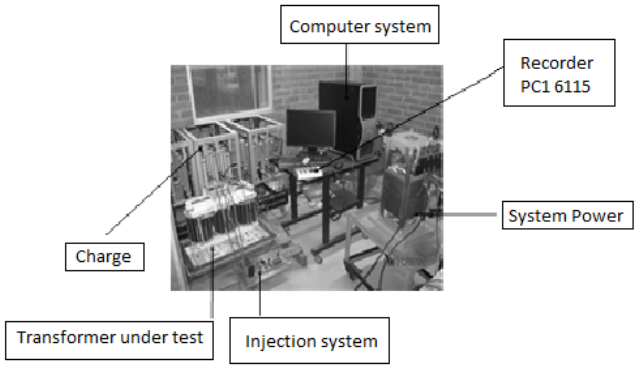


Figure 2. Experimental set in the pilot transformer.
Source: [6].

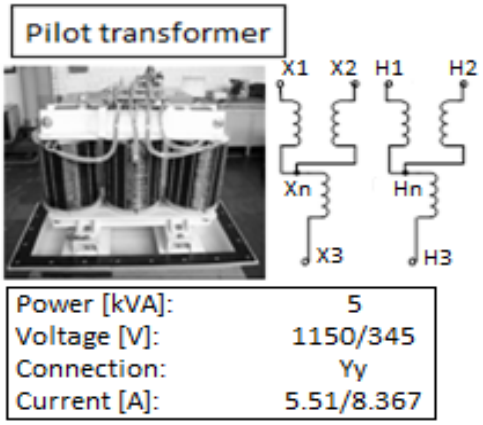


Figure 3. Pilot transformer.
Source: [6].

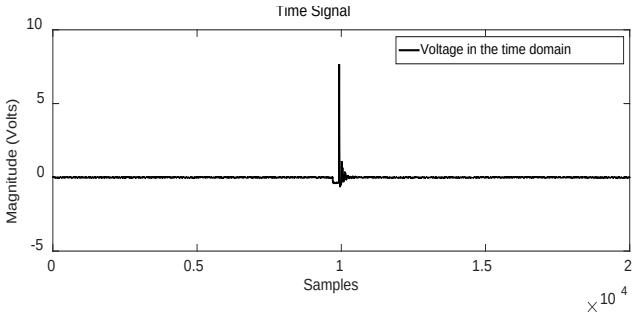


Figure 4. Time domain voltage signal, with a 2ms window of 20.000 samples at 10M samples/s.
Source: The authors.

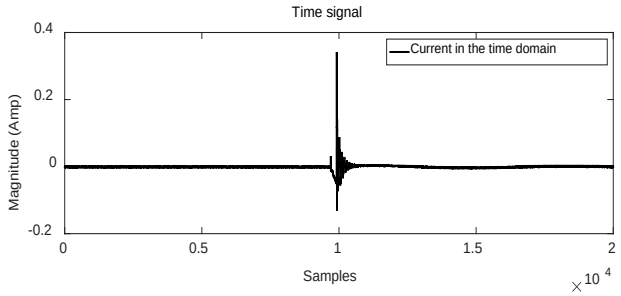


Figure 5. Time domain current signal, with a 2ms window of 20.000 samples at 10M samples/s.
Source: The authors.

LINE test was performed in a transformer, with high voltage winding short circuited and low winding open to obtain the transient signals. Results of voltage and current signal measurements are shown in Fig. 4 and Fig. 5, respectively

3. Practical proposed method for carrying out the online FRA test

The proposed method to obtain the frequency response with the transformer in service (online) involves the three stages presented in the block diagram shown in Fig. 1.

3.1. Stage 1. Injection and signal measurements

An electronic circuit was designed and implemented for the injection system to inject microsecond-width controlled voltage pulses on the power wave of 60 Hz [4]. The injection system enables setting the amplitude, width, and phase of the generated pulses, by means of the circuit shown in Fig. 6, with Fig. 7 showing an example of controlled pulses on the (60 Hz) voltage signal.

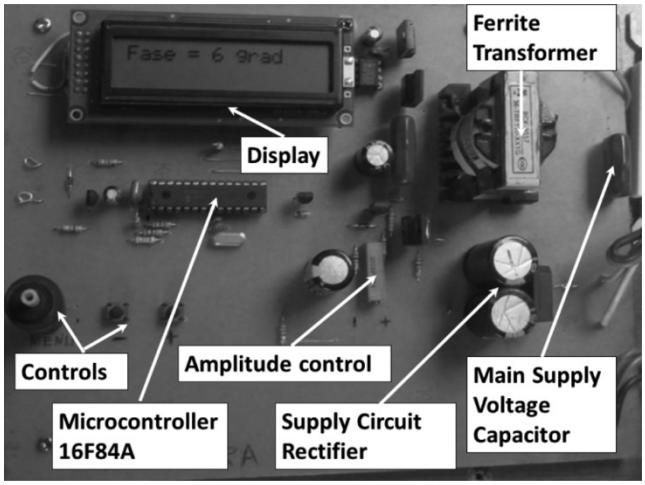


Figure 6. Actual assembly of the injection system for online IFRA.
Source: [3].

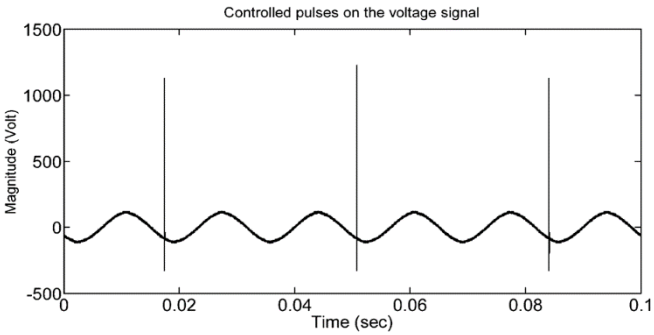


Figure 7. Controlled pulses on the (60 Hz) voltage signal used for the online IFRA method.
Source: The authors.

3.2. Stage 2. Filtering, denoising, signal acquisition, and processing

The voltage and current signals were modeled according to $S(t)$ presented in Eq. (1), which is composed of three terms. The first one represents the nature of the transformer's condition itself and constitutes the main information we want to extract from the measurement. It is mathematically defined as a summation of N terms, where B_k are the residues and P_k the modes or poles determining the shape of the transient signal. This main information is contaminated by the background noise $n(t)$, and the harmonic distortion $h(t)$ coming from the fundamental power 50/60-Hz frequency component.

$$S(t) = \sum_{k=1}^{N} B_k e^{P_k t} + h(t) + n(t) \quad (1)$$

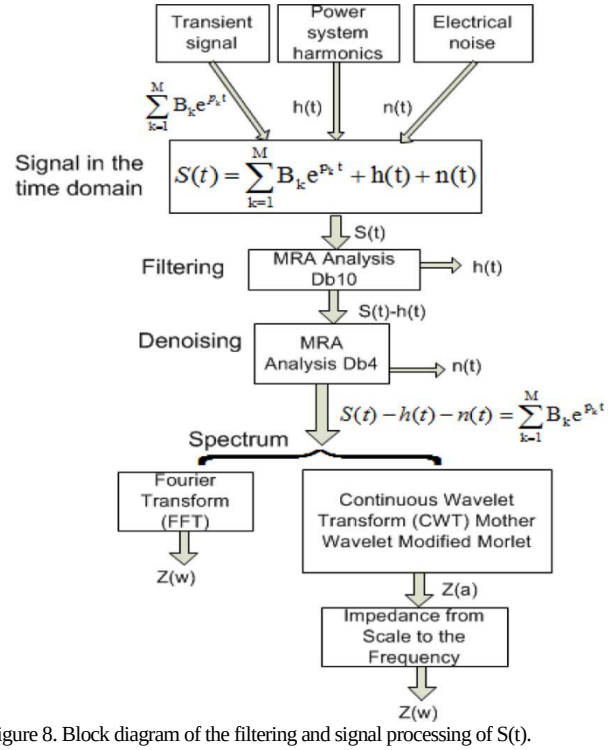


Figure 8. Block diagram of the filtering and signal processing of S(t).
Source: [3].

Once made filtering applies the CWT, it is defined as Eq. (2) [5].

$$CWT = \frac{1}{\sqrt{a}} \int_{-\infty}^{\infty} f(t)\psi^*\left(\frac{t-\tau}{a}\right)dt \quad (2)$$

Where the asterisk represents the conjugate of the complex function, $f(t)$ is the transient signal itself, $\psi(t)$ is the wavelet function which defines the mother wavelet in use, in which "τ" conducts the translation and factor, and "a" provides the dilation (or scaling) factor.

In part 1, it was demonstrated that using the mother wavelet Complex Morlet yields excellent results [1]. The complex Morlet wavelet transform is defined in Eq. (3) [5-16].

$$\psi(t) = \pi^{-\frac{1}{4}}\left(e^{jw_o t} - e^{-\frac{1}{2}w_0^2}\right)e^{-0.02r^2} \quad (3)$$

Applying the wavelet transform to the transient signals of both current and voltage [10-15] in its discrete form. Eq. (4) and Eq. (5), since a measured transient is not a continuous function but a matrix of points [16-20].

$$C_V(\tau, a) = \frac{1}{\sqrt{a}} \sum_{N} V(n)\psi^*_{a,\tau}\left(\frac{n-\tau}{a}\right) \quad (4)$$

$$C_I(\tau, a) = \frac{1}{\sqrt{a}} \sum_{N} I(n)\psi^*_{a,\tau}\left(\frac{n-\tau}{a}\right) \quad (5)$$

With the information of the data we can get the ratio between the coefficients C_V y C_I as shown in Eq. (6) obtaining the coefficients C_Z.

$$C_Z(\tau, a) = \frac{C_V(\tau, a)}{C_I(\tau, a)} \quad (6)$$

The impedance phase at the scale defined by "a" can be obtained from the integration of Eq. (6) along the whole window time of the transient. Due to its complex nature, the integration is performed under a vector approach. The phase can be obtained by means of Eq. (7).

$$\theta(a) = \tan^{-1}\{\frac{\sum_\tau Im[C_z(\tau, a)]}{\sum_\tau Re[C_z(\tau, a)]}\} \quad (7)$$

Where the operators "Re" and "Im" are the real part and imaginary part of the complex coefficients, respectively.

3.2. Stage 3. Assessment and validation approach

The transformer impedance, computed from online time-domain records was measured while the transformer was energized and compared with the corresponding sweep frequency- response analysis (SFRA) offline response, obtained by using frequency-response analysis equipment.

4. Experimental results

With a commercial instrument (MEGGER FRAX-101), the transformer SFRA was obtained and taken as reference, as shown in Fig. 9.

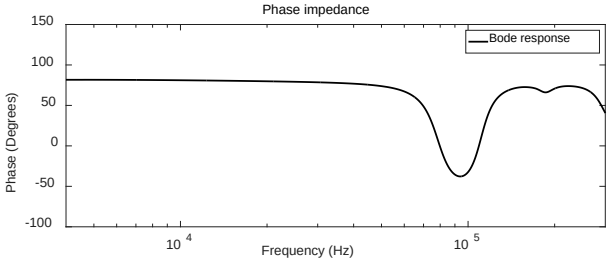


Figure 9. Transformer frequency response SFRA (reference signal).
Source: The authors.

The result with Fourier transform was obtained as shown in Fig. 10 and with Wavelet transform as shown in Fig. 11.

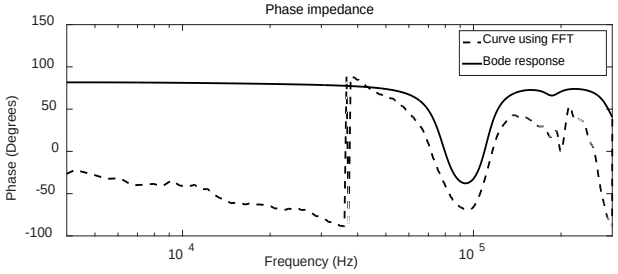


Figure 10. FFT assessments using a 2ms time window: phase frequency response.
Source: The authors.

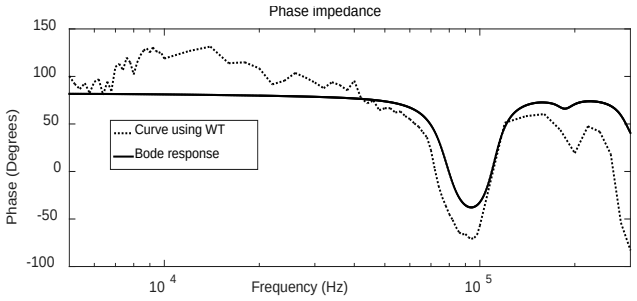


Figure 11. WT assessments using a 2ms time window: phase frequency response.
Source: The authors.

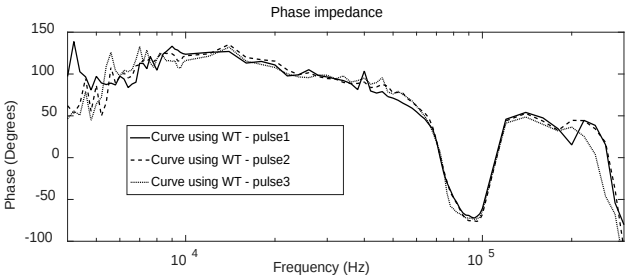


Figure 12. WT assessments using a 2ms time window: phase frequency response for three pulses.
Source: The authors.

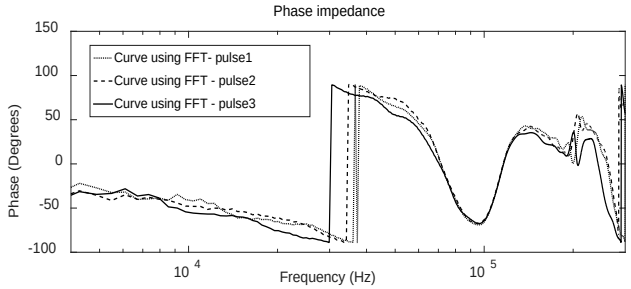


Figure 13. FFT assessments using a 2ms time window: phase frequency response for three pulses.
Source: The authors.

Table 1.
Quantitative analysis of the curves.

Analyzed parameter	Analysis based on CWT	Analysis based on FFT	Frequency ranges [kHz]- Figure 12 and Figure 13.
Repeatability: Average Relative error (ERM) between the answers obtained.	17.29%	64.89%	4 to 300
	38.61%	141.87%	
	10.14%	20.53%	4 to 40
	14.67%	49.36%	
	23.36%	7.07%	40 to 100
	59.84%	22.25%	
	29.10%	89.94%	100 to 300
	73.09%	193.75%	

Source: The authors.

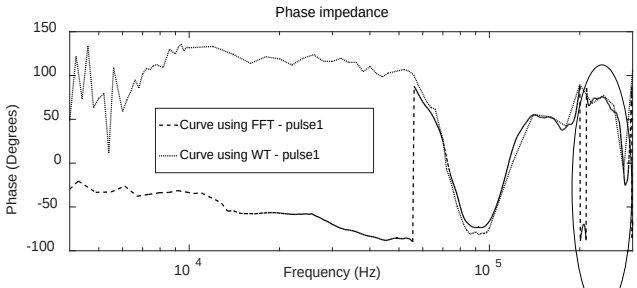


Figure 14. FT and WT assessments using a 1,5ms window of 15,000 samples at 2.5 M samples/s.: phase frequency response.
Source: The authors.

As observed in Fig. 11, WT offers a better approximation to reference, in a frequency range 4kHz to 40kHz, compared to FFT; After this, a repeatability analysis was performed, obtaining the response for the first three pulses of the time signal for WT and FFT methods, as shown in Fig. 13 and Fig. 14, respectively.

Table 1 shows the quantitative analysis, of the results obtained when using-both methods.

A qualitative analysis, using the average Relative error (TERM), was made to compare the two methods, in which best results were obtained for the CWT method [19-22].

To confirm the advantage in using WT, the same experimental example was used with a time window of 1,5ms and 15.000 samples, but with a sampling frequency of 2,5M samples / s.

Unlike the FFT, the WT is not altered by the changes generated shown in the part enclosed in Fig. 14, which demonstrates that the proposed method is a suitable one.

5. Conclusions

This article proposes an improved method for processing signals from time to frequency for the impedance phase. It allows overcoming the traditional Fourier Transform performance, since no periodical signals are required at all. This feature can be much more useful for engineering design and analysis because it allows working with non-periodical transient responses.

A simple example showed that, when the measurement conditions are tightened, the proposed WT based procedure performs better than the FT.

The key points in the procedure are a suitable election of the mother wavelet (Complex Morlet, in this case) and of the proposed frequency response values calculation (frequency domain) from the wavelets coefficients (time-scale domain). Thus, a correct analysis of the phase of the impedance, leads to better results for the wavelet transform, in comparison with those of the Fourier transform under both simulated and experimental conditions, which adds to the potential of WT as a suitable for the processing of transient signals.

Acknowledgments

The authors express their heartfelt thanks to the PTI S.A. Company for its support in the elaboration of this paper. They also thank COLCIENCIAS for its support for Project 54558, 2016, an approved project to access tax benefits and The Universidad del Valle for all it provided us with.

References

[1] Gómez-Luna, E., Cuartas-bermúdez, J. S. and Marlés-sáenz, E., Obtaining the electrical impedance phase using Wavelet transform and Fourier transform from transient signals. Part 1 : Theoretical analysis Wavelet y transformada de Fourier de señales transitorias. Parte 1: Análisis teórico DYNA vol. 84, no. 201, pp. 138–144, 2017. DOI: https://doi.org/10.15446/dyna.v84n201.58694

[2] Krieg, T. and Napolitano, M., Techniques and experience in on-line transformer condition monitoring and fault diagnosis in ElectraNet SA. in Proc. IEEE Int. Conf. Power Syst. Technol. PowerCon Substation Maint.e Dept., 2000, vol. 2, pp. 1019–1024. DOI: 10.1109/ICPST.2000.897160

[3] Mackenzie, E. A., Crossey, J., DePablo, A. and Ferguson, W., On-line monitoring and diagnostics for power transformers, in Proc. IEEE Int. Symp. Elect. Insul. Conf., 2010, pp. 1–5. DOI: 10.1109/ELINSL.2010.5549734

[4] Gómez-Luna, E., Aponte, G., Gonzalez-Garcia, C. and Pleite, J., Current status and future trends in the Frequency Response Analysis (FRA) with the transformer in service, IEEE Trans. Power Del., vol. 28, no. 2, pp. 1024–1031, Apr. 2013. Research Group Gralta, Desarrollo. DOI: 10.1109/TPWRD.2012.2234141

[5] Gómez-Luna, E., Silva, D., Aponte, G., Pleite, J. and Hinestroza, D., Obtaining the electrical impedance using wavelet transform from the time response, IEEE Transactions on Power Delivery, Vol. 28, No. 2, pp. 1242-1244, April 2013. DOI: 10.1109/TPWRD.2012.2234942

[6] Krieg, T., and Napolitano, M., Techniques and experience in on-line transformer condition monitoring and fault diagnosis in ElectraNet SA, in Proc. IEEE Int. Conf. Power Syst. Technol. PowerCon Substation Maint.e Dept., 2000, vol. 2, pp. 1019–1024. DOI: 10.1109/ICPST.2000.897160

[7] Gómez-Luna, E., Aponte, G. and Pleite, J., Application of Wavelet Transform to obtain the Frequency Response of a Transformer from Transient Signals – Part 2: Practical assessment and validation. IEEE Transactions on Power Delivery, Vol. 29, No. 5, pp. 2231 - 2238, October 2014. DOI: 10.1109/TPWRD.2013.2295377

[8] Gomez-Luna, E., Obtención De La Respuesta En Frecuencia De Transformadores En Servicio a Partir De La Medida De Señales Transitorias. Tesis de Doctorado, Universidad del Valle. p. 95, 2013.

[9] Research Group Gralta, Desarrollo de una prueba piloto para obtener la respuesta en frecuencia de un transformador en servicio, Universidad del Valle, Valle, Spain, Tech. Rep. 2653, Aug. 2012.

[10] Yunhui, S. and Qiuqi, R., Continuous wavelet transforms, Proc. 7th Int. Conf. Signal Process. 2004. Proceedings. ICSP '04. 2004., vol. 1, pp. 207–210, 2004. DOI: 10.1109/ICOSP.2004.1452618

[11] Li, H., Complex Morlet Wavelet Amplitude and Phase Map Based Bearing Fault Diagnosis no. 50775219, pp. 6923–6926, 2010. DOI: 10.1109/WCICA.2010.5554232

[12] Nieto, N. and Orozco, D., El uso de la transformada wavelet discreta en la reconstrucción de señales senosoidales, no. 38, pp. 381–386, 2008. DOI: http://dx.doi.org/10.22517/23447214.3809

[13] Butler, K. L., Bagriyanik. M., Characterization of transients in transformers using discrete Wavelet Transformer. IEEE Transactions on Power Systems, Vol. 18, No. 2, pp. 648-656, Mayo 2003. DOI: 10.1109/TPWRS.2003.810979

[14] Mallat, S., A Wavelet Tour of Signal Processing. A Wavelet Tour Signal Process. Third Edition. pp. 20–41, 1999.

[15] Leigh, G. M. Fast FIR Algorithms for the Continuous Wavelet Transform From Constrained Least Squares. IEEE Transactions on Signal Processing, Vol. 61, No. 1, January 1, 2013. DOI: 10.1109/TSP.2012.2222376

[16] Robertson, D. C., Camps, O. I., Mayer, J. S., Gish, W. B., Wavelets and electromagnetic power system transients. IEEE Transactions on Power Delivery, Vol, 11. Abril de 1996. DOI: 10.1109/61.489367

[17] Dwivedi, U. D. and Singh, S. N., Denoising techniques with change-point approach for wavelet-based power-quality monitoring. IEEE Trans. Power Deliv., vol. 24, no. 3, pp. 1719–1727, 2009. DOI: 10.1109/TPWRD.2009.2022665

[18] Gomez-Luna, E., Aponte Mayor, G., Pleite Guerra, J., Silva Salcedo, D. F. and Hinestroza Gutierrez, D., Application of wavelet transform to obtain the frequency response of a transformer from transient signals-part 1: Theoretical analysis. IEEE Trans. Power Deliv., vol. 28, no. 3, pp. 1709–1714, 2013. DOI: 10.1109/TPWRD.2013.2262058

[19] Pleite, J., Olias, E., Barrado, a., Lazaro, a. and Vazquez, J., Transformer modeling for FRA techniques. IEEE/PES Transm. Distrib. Conf. Exhib., vol. 1, pp. 317–321, 2002. DOI: 10.1109/TDC.2002.1178342

[20] Cortés, J. A., Cano-Garzón, H. B. and Chaves, J. A., Del análisis de Fourier a las Wavelets - Transformada continua wavelet (CWT). Sci. Tech., vol. XIII, no. 37, pp. 133–138, 2007. DOI: http://dx.doi.org/10.22517/23447214.4017

[21] Montoya, F. G., Manzano-Agugliaro, F., López, J. G. and ALGUACIL, P. S., Técnicas De Investigación En Calidad Eléctrica: Ventajas E Inconvenientes. Dyna, vol. 79, no. 173, pp. 66–74, 2012.

[22] Gómez-Luna, E., Aponte, G. and Pleite, J., Sistema de obtención de la respuesta en frecuencia de máquinas eléctricas, Madrid España Patente ES-2534954_B1, February 09, 2016.

E. Gómez-Luna, (M'11) was born Pradera, Colombia, 1982, he graduated the BSc. as Technologist in Electronics, Electrical Engineering and PhD. in Electrical Eng. at the Universidad del Valle, Cali, Colombia in 1982, 2009 and 2014 respectively. He worked as a researcher and assistant professor at the Universidad del Valle. He currently leads the R&D department of the company power technologies incorporated PTI S.A. His areas of interest are transformers, applied mathematics, power electronics, signal processing, power systems and real-time simulation. He is currently an active member of the IEEE.
ORCID: 0000-0003-2263-6758.

J.S. Cuartas, was born Cali, Colombia in 1994. He graduated the BSc. in Electrical Engineering at the Universidad del Valle, Cali, Colombia, in 2016. His areas of interest are transformers, applied mathematics, power electronics, signal processing and power systems.
ORCID: 0000-0002-7064-6072.

E. Marlés-Sáenz, was born Cali, Colombia, in, 1970, he graduated the BSc. as Electrical Eng. and MSc. on power generation of the Universidad del Valle in 1997 and 2001 respectively. He currently works as an assistant professor at the School of Electrical and Electronic Engineering from the Universidad del Valle and he is part of the Research Group on High Voltage GRALTA.
ORCID: 0000-0001-8792-4190.



UNIVERSIDAD NACIONAL DE COLOMBIA
SEDE MEDELLÍN
FACULTAD DE MINAS

Área Curricular de Ingeniería
Eléctrica e Ingeniería de Control

Oferta de Posgrados

Maestría en Ingeniería - Ingeniería Eléctrica

Mayor información:

E-mail: ingelcontro_med@unal.edu.co
Teléfono: (57-4) 425 52 64

UNIVERSIDAD NACIONAL DE COLOMBIA
SEDE MEDELLÍN
FACULTAD DE MINAS



DYNA
http://dyna.medellin.unal.edu.co/

Streptomyces clavuligerus strain selection for clavulanic acid biosynthesis: a study based on culture composition effects and statistical analysis

Laura Pinilla [a], León F. Toro [a], Claudio Avignone-Rossa [b], Mariana Peñuela [c] & Rigoberto Ríos-Estepa [c]

[a] *Grupo de Bioprocesos, Instituto de Biología, Universidad de Antioquia, Medellín, Colombia. laura.pinilla@udea.edu.co, lfelipe.toro@udea.edu.co*
[b] *Department of Microbial Sciences, University of Surrey, Guildford, Surrey, United Kingdom. c.avignone-rossa@surrey.ac.uk*
[c] *Grupo de Bioprocesos, Departamento de Ingeniería Química, Universidad de Antioquia, Medellín, Colombia. mariana.penuela@udea.edu.co, rigoberto.rios@udea.edu.co*

Received: December 12th, 2017. Received in revised form: March 16th, 2017. Accepted: April 18th, 2017.

Abstract
The clinical and industrial importance of clavulanic acid (CA) promotes the search for novel strategies to boost productivity at lower costs. In this contribution, the production of CA was evaluated in two reference strains of *Streptomyces clavuligerus (Sc)*, ATCC27064 and DSM41826; the strains were tested in different culture media, using product yields and culture media costs as selection criteria. On average, Sc_{ATCC} reached a concentration of CA 1.6-fold higher than Sc_{DSM}, using the isolated soybean protein (ISP) culture medium. A central composite experimental design was used to optimize the medium, by studying the influence of ISP and K_2HPO_4 concentration on the production of CA. The maximum CA concentration obtained in this optimized medium was 56 $mg \cdot L^{-1}$, close to the theoretical optimum. Our results confirm that a culture medium containing a rich carbon source such as glycerol and/or starch provides the best conditions for CA production.

Keywords: clavulanic acid; culture media design; strain selection; *Streptomyces clavuligerus*; antibiotics.

Selección de una cepa de *Streptomyces clavuligerus* para la biosíntesis de ácido clavulánico: un estudio basado en los efectos de la composición del medio de cultivo y análisis estadístico

Resumen
La importancia clínica e industrial del ácido clavulánico (AC) promueve la búsqueda de nuevas estrategias para aumentar su productividad a un menor costo. En esta contribución, se evaluó la producción de AC en dos cepas de referencia de *Streptomyces clavuligerus (Sc)*, ATCC27064 y DSM41826; éstas se probaron en diferentes medios de cultivo; los rendimientos de producto y costo de los medios se usaron como criterios de selección. En promedio, Sc_{ATCC} alcanzó una concentración de AC 1.6-veces mayor que Sc_{DSM}, en el medio de proteína de soya (ISP). Se optimizó el medio con un diseño experimental central compuesto, estudiando la influencia del ISP y K_2HPO_4 sobre la producción de AC. La concentración máxima de AC obtenida en el medio optimizado ($56 mg \cdot L^{-1}$) estuvo cerca del óptimo teórico. Nuestros resultados confirman que medios de cultivo con fuentes de carbono como glicerol y/o almidón proporcionan las mejores condiciones para la producción de AC.

Palabras clave: ácido clavulánico; diseño de medios de cultivo; selección de cepa; *Streptomyces clavuligerus*; antibióticos.

1. Introduction

Clavulanic acid (CA) is a potent inhibitor of β-lactamases, enzymes synthesized by some gram-positive and gram-negative bacteria, which provide them a defense mechanism against β-lactam antibiotics. CA is commonly used along with β-lactam antibiotics, resulting in a more efficient antibiotic with a broader spectrum of antimicrobial activity. CA is synthesized by *Streptomyces clavuligerus*, and is produced at large scale by conventional submerged culture

How to cite: Pinilla, L., Toro, L.F., Avignone-Rossa, C., Peñuela, M. and Ríos-Estepa, R., Streptomyces clavuligerus strain selection for clavulanic acid biosynthesis: a study based on culture composition effects and statistical analysis. DYNA, 85(205), pp. 111-118, June, 2018

© The author; licensee Universidad Nacional de Colombia.

processes. Besides CA, *S. clavuligerus* also produces secondary metabolites such as cephamycin C and various clavam structure compounds, with antifungal and antitumoral activities [1].

Due to its clinical and industrial importance, attempts to improve CA titers and productivity have focused on assessing the effect of nutrient concentration, environmental conditions and the species metabolic capabilities for CA biosynthesis. The composition of the culture medium is a very important issue; *S. clavuligerus* is able to metabolize diverse carbon sources, including oils and carbohydrates, but the primary carbon substrate for CA biosynthesis is glycerol. Culture media composed by cereal flours and digested proteins supply the amino acids required in the biosynthesis of clavam-related metabolites [2].

Selection strategies for different *S. clavuligerus* strains have been designed by the analysis of their metabolic capabilities and their ability to produce CA at high levels, under nutrient stress conditions and/or media supplementation. In some cases, interest has been focused into identifying CA overproducer strains able to metabolize low-cost substrates. However, issues such as genetic variability and overproduction of unwanted metabolites (such as clavams) have suggested the rational manipulation of metabolic pathways as a promising alternative for overproducer strains [3].

In this work, we performed a comparative study of the metabolic capabilities of two standard reference strains of *S. clavuligerus* to metabolize diverse media components and produce CA; the strains used were *S. clavuligerus* DSM 41826 (Sc_{DSM}) and *S. clavuligerus* ATCC 27064 (Sc_{ATCC}). Various synthetic, semi-synthetic and complex culture media were tested for their suitability to induce and/or improve CA biosynthesis. Furthermore, the effect of the nitrogen and phosphorous source on CA biosynthesis was evaluated for the selected strain (Sc_{ATCC}). The selection procedure was supported by an economic analysis.

2. Materials and methods

2.1. Microorganism and culture conditions

S. clavuligerus ATCC 27064 (Sc_{ATCC}) and *S. clavuligerus* DSM 41826 (Sc_{DSM}) were used throughout this study. Mycelium was obtained following the standard protocol for *Streptomyces* [4], and was stored in 1.5 mL Eppendorf tubes with a 20 % glycerol sterile solution at -80 °C. The seed medium consisted of 50 mL TSB medium (30 $g \cdot L^{-1}$; pH 7.0) in 250 mL baffled Erlenmeyer flasks inoculated with mycelium stock and incubated at 28 ºC for 36h at 220 rpm. The following culture media were used:

Synthetic media (SM): A basal synthetic medium was composed of [g/L]: glycerol, 15; sucrose, 20; NaCl, 5.0; L-proline, 2.5; K_2HPO_4, 2.0; $MgSO_4 \cdot 7H_2O$, 1.0; $CaCl_2$, 0.4; $MnCl_2 \cdot 4H_2O$, 0.1; $FeCl3 \cdot 6H_2O$, 0.1; $ZnCl_2$, 0.05; MOPS, 20.9. The N-source was either 1.5 g/L glutamic acid (medium GSPG) or 1.5 g/L L-asparagine (medium GSPA) [5].

Semi-synthetic media (SSM): Two semi-synthetic media were used: SA (Starch-Asparagine) was composed of (g/L): soluble starch, 10.0; asparagine, 2.0; $MgSO_4$, 0.60; K_2HPO_4, 4.40; MOPS, 20.0; $MgSO4 \cdot 7H_2O$, 0.75; $MnCl_2 \cdot 4H_2O$, 0.001; $FeSO4 \cdot 7H_2O$, 0.001 and $ZnSO_4 \cdot 7H_2O$, 0.001, pH was adjusted at 6.8 using NaOH [6]. NZ-Amine medium was composed of (g/L): NZ-Amine (casein hydrolyzate) 15.0; glycerol 15; NaCl 5.0; K_2HPO_4, 2.0; $MgSO_4 \cdot 7H_2O$; MOPS, 21.0, and 1 ml/L of a trace elements solution containing (g/L): $MnCl_2 \cdot 4H_2O$, 0.1; $FeSO_4 \cdot 7H_2O$, 0.1; $ZnCl_2$, 0.05; $CaCl \cdot 2H_2O$, 0.4.

Complex media (CM): Four different soy-based media were used: Tryptic Soy Broth (TSB) composed of (g/L): TSB, 30.0; glycerol, 15.0; MOPS, 21.0. Soy protein isolate (ISP) composed of (g/L): glycerol, 15.0; soy protein isolate, 10.0; malt extract, 10.0; yeast extract, 1.0; K_2HPO_4, 2.5; $MgSO_4 \cdot 7H_2O$, 0.75; $MnCl_2 \cdot {}_4H_2O$, 0.001; $FeSO_4 \cdot 7H_2O$, 0.001; $ZnSO_4 \cdot 7H_2O$, 0.001; MOPS, 21.0 [7].

Soybean flour based medium (SF): composed of: glycerol, 15.0; soybean flour, 10.0; malt extract, 10.0; yeast extract, 1.0; K_2HPO_4, 2.5; $MgSO_4 \cdot 7H_2O$, 0.75; $MnCl_2 \cdot 4H_2O$, 0.001; $FeSO_4 \cdot 7H_2O$, 0.001; $ZnSO_4 \cdot 7H_2O$, 0.001; MOPS, 21.0.11 Soybean flour with casamino acids (SF-CSS), same composition as SF with addition of 5 g/L casamino acids [8].

All cultures were performed in 250-baffled Erlenmeyer flasks containing 50 mL of medium. Flasks were inoculated with seed medium (10% v/v) as described above, at an average initial biomass concentration of 0.09 ± 0.015 $g \cdot L^{-1}$. Cultures were incubated for 120 h, at 220 rpm and 28 ºC.

2.2. Analytical techniques

Clavulanic acid was determined by HPLC using an Agilent 1200 Series equipped with a Diode Array Detector, using a reverse phase column ZORBAX Eclipse XDB-C_{18} (4.6 x 150 mm, 18 µm). The mobile phase was a 96% v/v KH_2PO_4 (50 mM, pH 3.2) and 6% v/v methanol solution at a flow rate of 1mL/min. Culture samples were centrifuged at 14000 g for 10 min at 4°C and filtered through a 0.22 µm membrane. The filtered sample (300 µL) was mixed with 100 µL of imidazole reagent (99.0%) and allowed to stand for 15 min at 30 °C. After incubation, 20 µL were injected into the HPLC unit. The CA derivative was detected at 311 nm [9].

For amino acid determination, an analytical column ZORBAX Eclipse AAA-C_{18} (5 µm, 4.6 x 150 mm) was used a mobile phase gradient elution composed by water, methanol, acetonitrile and NaH_2PO_4 buffer (40mM and pH 7.8) at conditions 2.0 $mL \cdot min^{-1}$ and 40 °C. Each sample was derivatized online using o-phthalaldehyde (OPA) for primary amino acids and 9-fluorenyl-methyl-chloroformate (FMOC) for secondary amino acids. The primary and secondary AAs were detected at 338 nm and 262 nm respectively [10].

Phosphate was quantified using a colorimetric method, as described elsewhere [11]. Glycerol was quantified spectrophotometrically [12]. Biomass was determined by calculating the dry cell mass of culture samples [13].

2.3. Analysis of clavulanic acid production

The soy-based culture media that were used for strain selection included ISP, SF and TSB, all containing 15 $g \cdot L^{-1}$ glycerol. Flask cultures, inoculated with 10% seed medium, were carried out at 28 ºC, pH 6.80 + 0.20 and 250 rpm for

120h. Production rates of biomass and CA, and consumption rates of phosphate and glycerol were calculated in TSB medium supplemented with glycerol. For the remaining soy-based medium studies, only CA was measured. Experiments were performed in biological triplicates.

2.4. Experimental design

A central composite experimental design was carried out with two variables at two levels each (soy protein isolate: 10 and 20 $g \cdot L^{-1}$; K_2HPO_4: 0.50 and 2 $g \cdot L^{-1}$), using CA production ($mg \cdot L^{-1}$) as the response variable. Assays were run in triplicates. Experimental results were statistically analyzed by using Statgraphics® software (version 6.0).

2.5. Cost analysis

The Net Income associated with the maximum yield of clavulanic acid was calculated based on culture media cost using eq. (1) as follows:

$$NI = USD_{CA} \times C_{CA} - \sum Co_{comp} \times C_{comp} \qquad (1)$$

3. Results and discussion

3.1. Analysis of clavulanic acid production

The dynamics of biomass, substrate and product biosynthesis for the strains Sc_{ATCC} and Sc_{DSM} grown in TSB-glycerol are shown in Fig. 1a and 1b. In contrast to the biosynthesis of most secondary metabolites, CA was detectable at very early stages of growth, rather than at the onset of the stationary growth phase. On average, the glycerol uptake rate was 1.80.30 $mmol \cdot gDW^{-1} \cdot h^{-1}$ and 0.6±0.20 $mmol \cdot gDW^{-1} \cdot h^{-1}$, for the Sc_{ATCC} and Sc_{DSM} strains, respectively. Sc_{ATCC} seems to be catabolically more active and due to the lower biomass concentration, it might be more appropriate for CA production. For the Sc_{ATCC} culture conditions, carbon flux distribution seems to favor product biosynthesis rather than biomass growth.

The strains showed different substrate uptake rate profiles. In Sc_{ATCC} (Fig. 1a), substrate concentration decreased fast up to 30 h of cultivation, when the biomass production slowed down and CA production accelerated. A peak in biomass concentration was observed at approximately 35h, while maximum CA concentration was observed at 42h. After this, the substrate uptake rate increased and glycerol was completely depleted at 70h. For Sc_{DSM} (Fig. 1b), maximum substrate uptake rate was sustained up to 30h, decreasing thereafter until complete depletion of glycerol at 120h. While the highest CA concentrations in both strains were detected when substrate uptake rate decreased, product degradation was observed in both strains (see Fig. 1a). Sc_{ATCC} presented a higher CA production per gram of biomass than Sc_{DSM} (2.90 and 1.10 $mg \cdot g^{-1}$, respectively); this might suggest that the strain ScA_{TCC} is more efficient than Sc_{DSM} for redirecting metabolic fluxes towards secondary metabolism rather than growth, an important feature in the selection of a CA-producer microorganism.

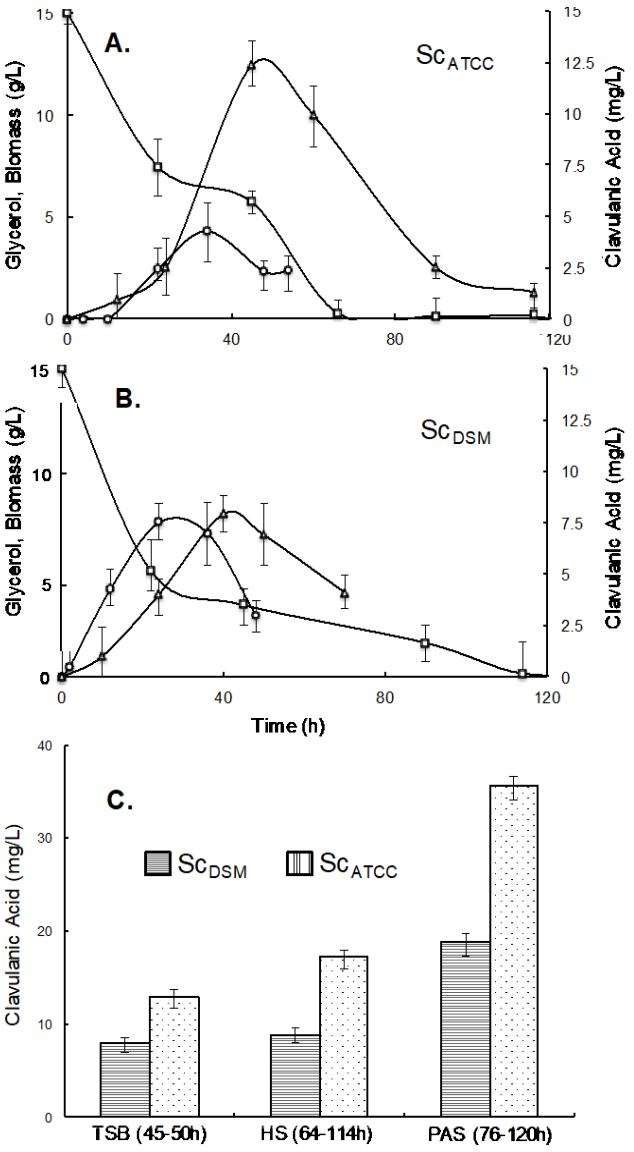


Figure 1. Clavulanic acid production during *Streptomyces clavuligerus* batch cultures **a.** Strain Sc_{ATCC} grown in TSB supplemented with glycerol. **b**. Strain Sc_{DSM} grown in TSB supplemented with glycerol, (Δ) clavulanic acid, (□) glycerol, (o) biomass. **c.** Clavulanic acid production using the strains Sc_{ATCC} and Sc_{DSM} growing in different culture media.
Source: The authors

Strains were also assessed in three soy-based culture media, Tryptic Soy Broth (TSB), Soybean Flour based medium (SF) and Soy Protein Isolate (ISP), to identify the best strain for CA production (Fig. 1c). The highest CA concentration (45.70 $mg \cdot L^{-1}$) was observed in the strain Sc_{ATCC} grown in ISP medium. This titer was almost double than that observed for the Sc_{DSM} strain in the same medium.

3.2. Culture media for clavulanic acid production by the strain Sc_{ATCC}

Culture media formulations included complex nitrogen sources that provide significant concentrations of amino acids (AAs). Fig. 2 shows the characterization of the amino acid content of complex and semi-synthetic NZ-Amine media, compared

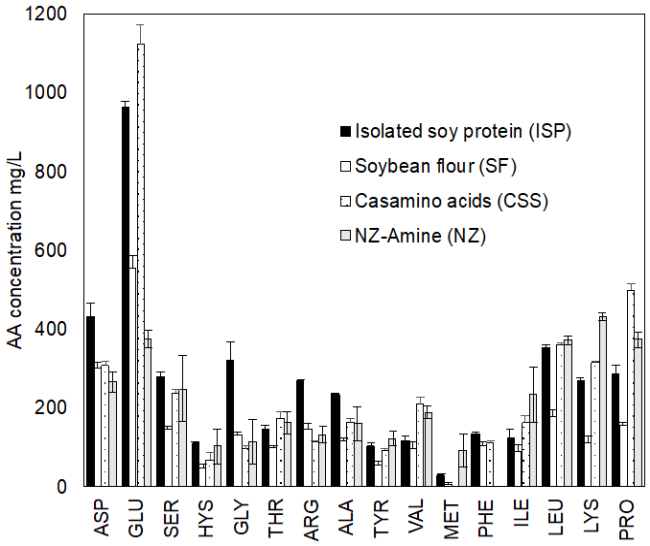


Figure 2. Free Amino acid characterization for the complex media used.
Source: The authors

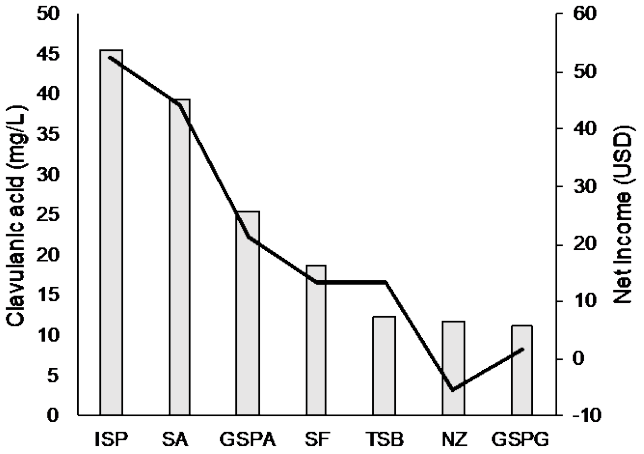


Figure 3. Culture media and economic analysis for clavulanic acid production in *Streptomyces clavuligerus* Sc_{ATCC}.
Source: The authors

with the widely used casamino acids (CSS). As expected, the total AA content was higher in the complex media, particularly in hydrolysed products i.e., ISP (4.20 $g \cdot L^{-1}$) and NZ-Amine (3.38 $g \cdot L^{-1}$). In contrast to SF (2.34 $g \cdot L^{-1}$), containing no hydrolyzed component, CSS provided 4.04 $g \cdot L^{-1}$ of total amino acids. TSB does not contribute significant amounts of amino acids.

When a complex nitrogen source is employed, the combination of AAs results in a positive effect on CA synthesis, a fact not fully elucidated [14,15]. In the presence of glycerol, AAs derived from aspartate (asparagine and threonine) and alpha-ketoglutarate (glutamine and glutamate), which are present in high concentrations in the ISP, SF and CSS media, have proved to favor CA production [16,17]. The ISP, SF and CSS media are good sources of lysine, which is known to stimulate the production of Cephamycin C rather than CA in Streptomyces clavuligerus.

The production of CA by strain Sc_{ATCC} was studied in different media (Fig. 3). Overall, complex media showed low CA titers, with the highest production and lowest cost observed in ISP (45.70 $mg \cdot L^{-1}$). This is a nutrient-rich medium, with a high protein content, which, after hydrolysis, provides the medium with important anabolic precursors for CA biosynthesis, such as amino acids from the aspartate and glutamate families.

A low CA concentration (18.80 $mg \cdot L^{-1}$) was observed in the SF medium, despite its nutrient-rich composition (carbohydrates, lipids, proteins and free amino acids such as lysine, valine, tyrosine, leucine and threonine) [18]. SF is composed of non-hydrolyzed soy flour, which does not provide any additional easy-to-uptake substrates.

The TSB medium rendered a lower CA concentration (12.50 $mg \cdot L^{-1}$), probably due to its low amino acid content (Fig. 2). TSB has a weak buffering capacity, and the accumulation of CA might have caused the decrease of the pH outside of the favorable range (6.80 - 7.20), affecting *S. clavuligerus* metabolism and physiology.

In the semi-synthetic medium SA, with starch as the main carbon source, *S. clavuligerus* cultures showed the second highest CA concentration of all media tested (39.50 mg $CA \cdot L^{-1}$). *Streptomyces* species slowly hydrolyze soluble starch releasing maltotriose as the primary product of hydrolysis. This eventually prevents repression and/ or inhibition in β-lactam antibiotic biosynthesis, which is normally triggered by C-sources easily metabolized [19]. Using the NZ-Amine medium a CA production of 11.80 $mg \cdot L^{-1}$ was achieved. Likewise, the NZ- amine has lysine as the main amino acid source with a high concentration (430 $mg \cdot L^{-1}$), which favors cephamycin C biosynthesis [20].

S. clavuligerus grown in the chemically defined medium GSPA produced 25.50 mg $CA \cdot L^{-1}$; this medium contains proline and asparagine which facilitate microbial anabolic activity conducing to increased CA biosynthesis. Besides, maintenance and growth are well supported by two carbon sources, saccharose and glycerol, hence ensuring availability of the C3 precursor, GAP. Conversely, despite having a similar composition to GSPA, the medium GSPG produced the lowest CA concentration of all media tested (11.30 $mg \cdot L^{-1}$). This concentration represents half of that observed in media containing asparagine, which confirms, once again, the importance of this amino acid, rather than the direct CA precursor arginine, in CA biosynthesis.

In order to test whether CA production is affected by the availability of free amino acids, *S. clavuligerus* was grown in a medium containing a complex nitrogen source, SF-CSS (non-hydrolysed soybean flour), supplemented with free amino acids (casamino acids-casein hydrolysate). The maximum CA concentration reached was 195 $mg \cdot L^{-1}$ at 120 h, and the maximum yield was $Y_{P/X}$=18.60 $mg \cdot g^{-1}$. The difference between yields achieved using the medium non-supplemented and supplemented with free amino acid might be attributed to the presence of extracellular proteases. *Streptomyces* are heterotrophic microorganisms that can use both complex and simple molecules as nutrients by means of extracellular enzymes induced by complex sources, also related with aerial mycelium formation and sporulation [21].

Table 1.
Yield coefficient and productivities attained for clavulanic acid biosynthesis in cultures of *Streptomyces clavuligerus*, Sc_{ATCC}

Culture media	$Y_{P/S}$ ($mg \cdot g^{-1}$)	$Y_{P/X}$ ($mg \cdot g^{-1}$)	Q_P ($mg \cdot L^{-1} \cdot h^{-1}$)
GSPG	0,760	1,142	0,094
GSPA	1,708	2,290	0,212
NZ-Amine	-	0,724	0,160
SA	-	5,580	0,280
TSB	1,418	1,795	0,284
SF	1,802	2,721	0,165
ISP	3,080	5,187	0,439

$Y_{P/S}$: substrate to product yield; $Y_{P/X}$: biomass to product yield; Q_p: volumetric productivity
Source: The authors

Table 2.
Effect of the phosphate and nitrogen source on clavulanic acid biosynthesis.

ISP ($g \cdot L^{-1}$)	Phosphate ($g \cdot L^{-1}$)	CA ($mg \cdot L^{-1}$)
22.07	1.25	24.51
10.00	2.00	47.01
20.00	0.50	23.45
15.00	2.31	57.02
15.00	1.25	36.56
15.00	1.25	36.04
15.00	1.25	40.22
10.00	0.50	23.80
7.93	1.25	22.90
15.00	0.19	27.14
20.00	2.00	48.48

Source: The authors

Table 1 shows the yield coefficients and productivities attained for Sc_{ATCC} growing in different media. ISP was the most favorable medium for CA biosynthesis (Qp = 0.44 $mg \cdot L^{-1} \cdot h^{-1}$; $Y_{P/X}$ = 5.20 $mg \cdot g^{-1}$; $Y_{P/S}$ = 3,08 $mg \cdot g^{-1}$), while medium GSPG showed the lowest yield and productivity (Qp = 0.09 $mg \cdot L^{-1} \cdot h^{-1}$; $Y_{P/X}$ = 1.14 $mg \cdot g^{-1}$; $Y_{P/S}$ = 0.76 $mg \cdot g^{-1}$). These values confirm the different response observed between complex and synthetic media [8,22]. The synthetic media GSPG and GSPA showed production levels similar to published results [5]. In these media, glycerol is the main carbon source and the amino acids glutamate or asparagine and proline are used as nitrogen source. Nonetheless, some reports have shown that the most important amino acids for CA production are ornithine or arginine, rather than glutamate or proline [5].

The production of CA or cephamycin C may be enhanced not only by nutrients in the culture medium but also by intermediates produced along the biosynthetic route [23,24]. Cephamycin C and CA are synthesized by different pathways, which are controlled by intra and extracellular factors through complex regulatory mechanisms. These factors include components of the culture medium and/or intermediate compounds of primary metabolism, which in turn participate directly or indirectly in product biosynthesis [25]. Glycerol, for example, is preferentially used as carbon source forCAproduction [5,26], whereas starch is more suitable for the production of cephamycin C [2,25,27]. The regulation of cephamycin C and CA production are interconnected by the pathway specific regulatory gene *Ccar* [28].

3.3. Economic analysis

In large-scale production of antibiotics, the composition of the culture medium has the highest impact on process costs [29]. Therefore, any detailed analysis should include an economic evaluation to establish the feasibility of the process. In this work, the net income associated with the maximum yield of CA was calculated based on culture media costs. Fig. 3 shows the net income calculated for all of the media tested. Among the complex media, the use of ISP results in an economically feasible process, with a total gain of 50.5 $USD \cdot L^{-1}$. SF and TSB exhibited an average total gain of 12 $USD \cdot L^{-1}$ for the production of CA.

Regarding the semi-synthetic media, SA (Starch-Asparagine medium) proved to be economically feasible, with a total gain of 41 $USD \cdot L^{-1}$, while NZ-amine showed a net loss of 5 $USD \cdot L^{-1}$. The chemically defined media GSPA showed an acceptable product concentration, with a very low total gain (18.1 $USD \cdot L^{-1}$), mainly due to the high cost of its components. Medium GSPG showed a very low gain.

Clavulanic acid production and the net profit were highly favored when complex nitrogen sources were used. In contrast, in the second-best CA production medium, glycerol, the conventional carbon source, was replaced by starch. For the other media, the high cost of individual components such as free amino acids and casein hydrolysate showed to be expensive and unpromising alternatives.

3.4. Effect of the P-source and N-source on clavulanic acid production

The effect of phosphate and nitrogen sources on CA biosynthesis was tested using ISP, the medium showing the highest CA production; for this, a surface response analysis was used, (see Table 2).

The results show that the highest concentration of CA (57 $mg \cdot L^{-1}$) is obtained when the levels of isolated soy protein and phosphate (KH_2PO_4) were 15 $g \cdot L^{-1}$ and 2.30 $g \cdot L^{-1}$, respectively. Decreasing concentrations of P- and N-sources showed a decrease in CA titters, which suggests the role of these components in driving the cell metabolic activities towards CA biosynthesis. The analysis of the effect of phosphate on secondary metabolism shows that the activity of the enzymes, CA synthetase and cephamycin C synthetase, is higher at low concentrations of phosphate, as previously reported [30,31].

Table 3.
Variance Analysis for clavulanic acid biosynthesis in *Streptomyces clavuligerus cultures*

Source	Sum of squares	Mean square	P-value
A: ISP	1.44247	1.44247	0.6479
B: Phosphate	1023,71	1023,71	**0.0034**
AA	220.78	220.78	**0.0018**
AB	0.8281	0.8281	0.7281
BB	48.6378	48.6378	**0.0372**
Total error	30.6175	6.12351	-

R^2=97,8412%; R^2(adjusted)=95,6824%; Durbin-Watson Statistic = 1,95556 (P=0,3048).
Source: The authors

The analysis of variance indicates the existence of three statistically significant effects ($p<0.05$) on CA biosynthesis: the effect of phosphate is highly significant, followed by the interaction ISP-ISP, and the phosphate-phosphate interaction, with an R-squared coefficient of 0.978412. The complete variance analysis is presented in Table 3.

In the Pareto chart (Fig. 4a), the left vertical axis represents the significant effect with a 95% confidence interval (phosphate, ISP-ISP and phosphate-phosphate interaction), as indicated by the anova analysis. Phosphate positively affects CA production while the ISP-ISP interaction presents a negative effect. However, high phosphate concentrations (>100 mM) induce biomass growth but somehow inhibit cephamycin C and CA biosynthesis [23,31].

The combination of variables and their levels, predicted by the surface methodology analysis, to yield the highest CA biosynthesis (phosphate 2.30 $g \cdot L^{-1}$ and ISP 15.40 $g \cdot L^{-1}$) is presented in Fig. 4b. These values were experimentally tested, obtaining 56 $mg \cdot L^{-1}$ of CA at 118h with no residual glycerol (Fig. 4c). Concerning biomass growth, the stationary phase in this culture was achieved at the same time as CA starts to be detectable (75h), following the typical pattern of secondary metabolite biosynthesis. Fig. 4c also shows the kinetic parameters obtained after exploring the predicted values from the surface methodology approach. Both performance and productivity increased after the adjustment of the culture medium, though the final CA concentration is not comparable with values from literature. Besides, it was observed that the nitrogen source greatly influences the final product concentration, while phosphate is limiting for secondary metabolism in *S. clavuligerus* [3].

Overall, it is clear that the soybean-based media favors CA biosynthesis due to the high content of amino acids known to be precursors of CA biosynthesis [22]. Our results also suggest that the ISP culture medium components induce the formation of extracellular hydrolases and proteases in *S. clavuligerus*, forcing the bacterium to further degrade the protein during growth, thus ensuring a constant supply of nutrients, essential for primary and secondary metabolism. The use of a non-hydrolyzed nitrogen complex source (soybean flour), supplemented with free amino acids, suggests that proteolytic activity might have been insufficient to release the required nitrogen precursors from the components of flour, resulting in CA titers lower than those achieved in media containing free amino acids.

4. Conclusions

Our results clearly show that the strain exhibiting the best metabolic capabilities was Sc_{ATCC}. This strain has been widely used in medium optimization studies. Medium optimization is an essential part of process development for microbial fermentation products, as it enables cost reduction by developing culture media with increased productivity and confers ability to use inexpensive raw materials.

Our results showed that the complex culture media providing the most favorable conditions for CA production was ISP, a soybean protein-based media, possibly due to its high free amino acid content. In that medium, the maximum concentration observed was 45.70 mg/L. Medium SF was not effective for CA production (18.8 mg/L). The evaluation of chemically defined media showed that the carbon source, along with appropriate amino acid sources, favors the production of CA. In the case of media GSPG and GSPA, replacing glutamate by asparagine enhanced product concentration by 2.1-fold, suggesting that amino acids of the

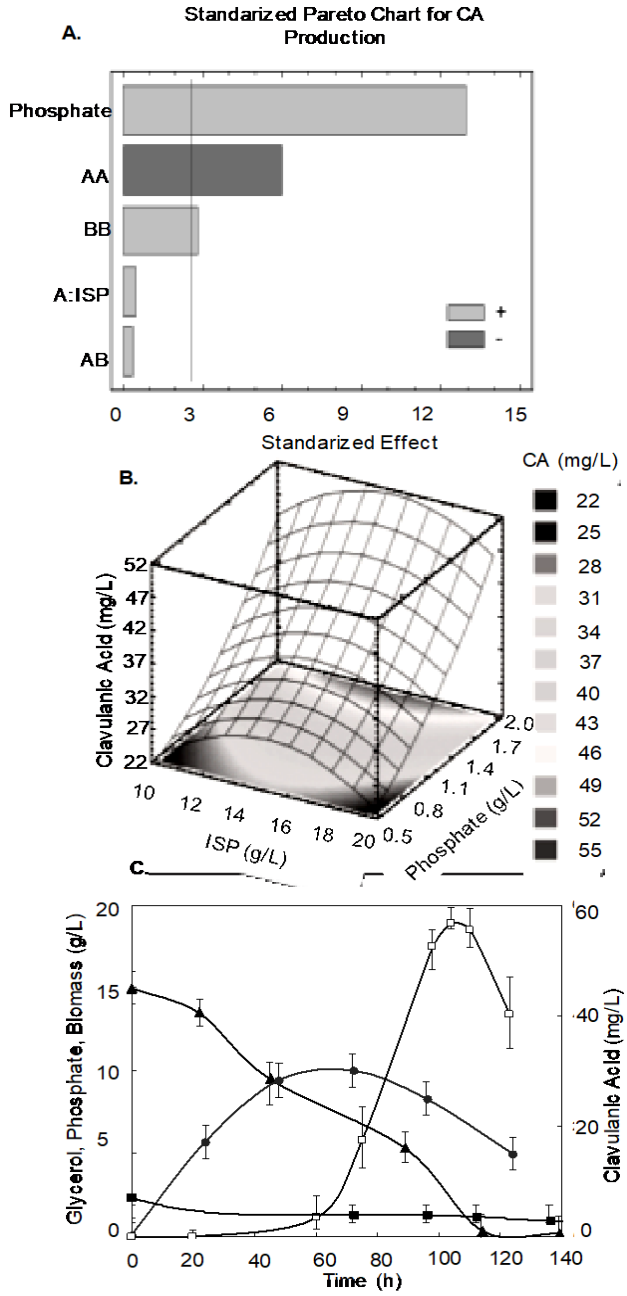


Figure 4. Effect of phosphate- and nitrogen- sources on CA biosynthesis using the ISP medium by a surface response analysis. a. Standardized Pareto chart for clavulanic acid biosynthesis. b. Response surface diagram for the experimental design aim at studying the effect of isolated soy protein and phosphate concentration on clavulanic acid biosynthesis. c. Experimental validation of the predicted values by the surface methodology approach ([A: ISP] [B: Phosphate]), and their effect on clavulanic acid biosynthesis by Sc_{ATCC}: (□) Clavulanic acid, (▲) glycerol; phosphate (■) and (•) biomass, $Y_{X/S}$ ($g \cdot g^{-1}$) =0.74, $Y_{P/S}$ ($mg \cdot g^{-1}$)=4.32, $Y_{P/X}$($g \cdot g^{-1}$)=5.82, Q_P($mg \cdot L^{-1} \cdot h^{-1}$)=0.54, q_p(h^{-1}) =0.06, μ (h^{-1}) =0.097.
Source: The authors

aspartate family such as asparagine, improve the availability of the C5 CA precursor. The semisynthetic medium SA, using starch as the carbon source, favored product biosynthesis; the production of CA is limited mainly by the availability of the C5 precursor rather than the C3. It seems that starch might have favored the accumulation of GAP.

On the other hand, the use of a non-hydrolyzed nitrogen complex source (soybean flour), supplemented with free amino acids, suggests that the protease activity might have been insufficient to degrade the components of flour, thus rendering lower CA titers compared to those achieved when free amino acids were present.

In the optimization studies, ISP medium showed an increase of CA production by 11 mg/L. The presence of phosphate, in the end, remained in the margins of restrictive concentration thus favoring antibiotic biosynthesis.

Acknowledgments

L. Pinilla and L. Toro thank COLCIENCIAS – Colombia for scholarships. The authors thank the Committee for Research Development (CODI) at the University of Antioquia. Projects ID: Sustainability 2013 and PRG 2014-1058. C. Avignone Rossa was supported by grant BB/L02683X/1 from the Biotechnology and Biological Sciences Research Council (BBSRC, United Kingdom).

References

[1] Liras, P., Gomez-Escribano, J.P. and Santamarta, I. Regulatory mechanisms controlling antibiotic production in *Streptomyces clavuligerus*. Journal of Industrial Microbiology & Biotechnology, 35(7), pp. 667, 2008. DOI: 10.1007/s10295-008-0351-8

[2] Ozcengiz, G. and Demain, A.L., Recent advances in the biosynthesis of penicillins, cephalosporins and clavams and its regulation. Biotechnology Advances, 31(2), pp. 287-311, 2013. DOI: 10.1016/j.biotechadv.2012.12.001

[3] Ser, H.L., Law, J.W.F., Chaiyakunapruk, N., Jacob, S.A., Palanisamy, U.D., Chan, K.G., Goh, B.H. and Lee, L.H., Fermentation conditions that affect clavulanic acid production in *Streptomyces clavuligerus*: a systematic review. Frontiers in Microbiology, 7, 2016. DOI: 10.3389/fmicb.2016.00522

[4] Kieser T. Practical *Streptomyces* genetics. John Innes Foundation, UK. Academic Press, 2000.

[5] Romero, J., Liras, P. and Martin, J., Dissociation of cephamycin and clavulanic acid biosynthesis in *Streptomyces clavuligerus*. Appl Microbiol Biotechnol., 20(5), pp. 318-325, 1994. DOI: 10.1093/femsle/fnv215

[6] Paradkar, A. and Jensen, S., Functional analysis of the gene encoding the clavaminate synthase 2 isoenzyme involved in clavulanic acid biosynthesis in *Streptomyces clavuligerus*. J. Bacteriol., 177(5), pp. 1307-1314, 1995.

[7] Rosa, J.C., Baptista-Neto, A., Hokka, C. and Badino, A., Influence of dissolved oxygen and shear conditions on clavulanic acid production by *Streptomyces clavuligerus*. Bioprocess Biosyst Eng., 27, pp. 99-104, 2005. DOI:10.1007/s00449-004-0386-9

[8] Jnawali, H.N., Liou, K. and Sohng, J.K., Role of σ-factor (orf21) in clavulanic acid production in *Streptomyces clavuligerus* NRRL3585. Microbiological Research, 166(5), pp. 369-379, 2011. DOI: 10.1016/j.micres.2010.07.005

[9] Foulstone, M. and Reading, C., Assay of amoxicillin and clavulanic acid, the components of Augmentin, in biological fluids with high-performance liquid chromatography. Antimicrob Agents and Chemother, 22(5), pp. 753-762, 1982.

[10] Henderson, J.W., Ricker, R.D., Bidlingmeyer, B.A. and Woodward, C., Rapid, accurate, sensitive, and reproducible HPLC analysis of amino acids. Amino acid analysis using Zorbax Eclipse-AAA columns and the Agilent, 1100, pp.1-10. 2000.

[11] Chen, P.S., Toribara, T.Y. and Warner, H., Microdetermination of phosphorus, Anal Chem 28(11), pp. 1756-1758, 1956. DOI: 10.1021/ac60119a033

[12] Bok, S. and Demain, A., An improved colorimetric assay for polyols. Anal Biochem 81(1), pp. 18-20, 1977. DOI: 10.1016/0003-2697(77)90593-0

[13] O'Toole, D.K., Weighing technique for determining bacterial dry mass based on rate of moisture uptake. Appl Environ Microbiol., 46(2), pp. 506-508, 1983.

[14] Bushell, M.E., Kirk, S., Zhao, H.J. and Avignone-Rossa, C.A., Manipulation of the physiology of clavulanic acid biosynthesis with the aid of metabolic flux analysis. Enzyme and Microbial Technology, 39(1). pp. 149-157, 2006. DOI: 1016/j.enzmictec.2006.01.017

[15] Hood, D.W., Heidstra, R., Swoboda, U.K. and Hodgson, D.A., Molecular genetic analysis of proline and tryptophan biosynthesis in *Streptomyces coelicolor* A3 (2): Interaction between primary and secondary metabolism—a review. Gene., 115(1), pp. 5-12, 1992. DOI: 10.1016/0378-1119(92)90533-U

[16] Lynch, H.C. and Yang, Y., Degradation products of clavulanic acid promote clavulanic acid production in cultures of *Streptomyces clavuligerus.* Enzyme Microb. Technol. 34(1), pp. 48-54, 2004. DOI: 10.1016/j.enzmictec.2003.08.003

[17] Miñambres, B., Olivera, E.R., Jensen, R.A. and Luengo, J.M., A new class of glutamate dehydrogenases (GDH) biochemical and genetic characterization of the first member, the AMP-requiring nad-specific GDH of *Streptomyces clavuligerus*. J. Biol. Chem., 275(50), pp. 39529-39542, 2000. DOI: 10.1074/jbc.M005136200

[18] Luna, A., Composicion y procesamiento de la harina de soya para consumo humano. Investig Cienc 37, pp. 35-44, 2007.

[19] Kashiwagi, N., Miyake, M., Hirose, S., Sota, M., Ogino, C. and Kondo, A., Cloning and starch degradation profile of maltotriose-producing amylases from *Streptomyces* species. Biotechnol Lett., 36(11), pp. 2311-2317, 2014. DOI: 10.1007/s10529-014-1611-5

[20] Leite, C.A., Cavallieri, A.P. and Araujo, M.L., Enhancing effect of lysine combined with other compounds on cephamycin C production in *Streptomyces clavuligerus*. BMC Microbiol. 13, pp. 296-307, 2013. DOI: 10.1186/1471-2180-13-296

[21] Jayasree, D.S., Kumara, T.D., Kavi-Kishor, P.B., Vijaya-Lakshmi, M. and Lakshmi-Narasu, M., Optimization of production protocol of alkaline protease by *Streptomyces pulvereceus*. Inter JRI Sci Technol. 1, pp. 79-82, 2009. DOI: arXiv:1002.0048

[22] Gouveia, E.R., Baptista-Neto, A., Azevedo, A.G. et al., Improvement of clavulanic acid production by *Streptomyces clavuligerus* in medium containing soybean derivatives. World Journal of Microbiology and Biotechnology, 15, pp. 623, 1999. DOI: 10.1023/A:1008942405378

[23] Bibb, M.J., Regulation of secondary metabolism in *Streptomycetes*. Curr Opin Microbiol., 8(2), pp. 208-215, 2005. DOI: 10.1016/j.mib.2005.02.016

[24] Lebrihi, A., Lefebvre, G. and Germain, P., A study on the regulation of cephamycin C and expandase biosynthesis by *Streptomyces clavuligerus* in continuous and batch culture. Appl Microbiol Biotechnol., 28, pp. 39-43, 1988. DOI: 10.1007/BF00250495

[25] Oliveira, L.M., Cruz, G. and Hokka, C., Effect of different carbon and nitrogen sources on *Streptomyces clavuligerus* metabolism for clavulanic acid and cephamycin C production. New Biotechnol., 25, pp. S217-S217, 2009. DOI: 10.1016/j.nbt.2009.06.175

[26] Chen, K.C., Lin, Y.H., Tsai, C.M., Hsieh, C.H. and Houng, J.Y., Optimization of glycerol feeding for clavulanic acid production by *Streptomyces clavuligerus* with glycerol feeding. Biotechnol. Lett., 24, pp. 455-458, 2002. DOI: 10.1023/A:1014553109425

[27] Fang, A. and| Demain, A.L., The substrate specificity of deacetoxycephalosporin C synthase (expandase) of *Streptomyces clavuligerus* is extremely narrow. Enzyme Microb. Technol., 17(3), pp. 231-234, 1995. DOI: 10.1016/0141-0229(94)00001-8

[28] Pérez-Llarena, F.J., Liras, P., Rodríguez-García, A. and Martín, J.F., A regulatory gene (ccaR) required for cephamycin and clavulanic acid production in *Streptomyces clavuligerus*: amplification results in overproduction of both beta-lactam compounds. J. Bacteriol., 179, pp. 2053-2059, 1997. DOI: 10.1128/jb.179.6.2053-2059.1997

[29] Elander, R.P., Industrial production of b-lactam antibiotics. Appl.

Microbiol. and Biotechnol., 61(5), pp. 385-392, 2003. DOI: 10.1007/s00253-003-1274-y
[30] Lebrihi, A., Germain, P. and Lefebvre, P., Phosphate repression of cephamycin and clavulanic acid production by *Streptomyces clavuligerus*. Appl Microbiol and Biotechnol., 26, pp. 130-135, 1987. DOI: 10.1007/BF00253896
[31] Saudagar, P., Singhal, R., Optimization of nutritional requirements and feeding strategies for clavulanic acid production by *Streptomyces clavuligerus.* Bioresour. Technol., 98, pp. 2010-2017, 2007. DOI: 10.1016/j.biortech.2006.08.003.

L. Pinilla, received the BSc. in Biology in 2010 from Universidad Industrial de Santander, Colombia and PhD. degree in Biotechnology in 2018, from Universidad de Antioquia, Colombia. Researcher at Bioprocess research group in Universidad de Antioquia. Her research interests include: biotechnology; antibiotics production; transcriptomic analysis; and molecular biology.
ORCID: 0000-0002-8753-0017

L.F. Toro, is BSc. in Eng. in Chemical Engineering in 2010, from the Universidad Nacional de Colombia, Manizales, Colombia. PhD. degree in Biotechnology in 2018, from Universidad de Antioquia, Colombia. Researcher at Bioprocess research group in Universidad de Antioquia. His research interests include: biotechnology; antibiotics production; metabolic flux analysis; and metabolic engineering.
ORCID: 0000-0002-3074-396X

C. Avignone-Rossa, obtained his BSc. degree in Chemistry (1987), followed by a Licentiate degree in Biochemical Sciences (1989) and a PhD in Biochemical Sciences (1994) from the University of La Plata (Argentina). He was appointed associate professor of biotechnology at the University of Quilmes, Argentina, in 1994, and moved to the University of Amsterdam, where he joined the Microbial Physiology Group as a research fellow from 1995 to 1999. He joined the University of Surrey as a research associate in 1999, and was appointed as lecturer in Microbial Physiology in 2000, promoted to senior lecturer in Microbial Systems Biology in 2006 and became a Reader in 2012.
ORCID: 0000-0002-1625-6487

M. Peñuela, is BSc. Eng. in Chemical Engineering in 2001, from the Universidad de Antioquia, Colombia. MSc. and PhD. degrees in Tecnologia de Processos Químicos e Bioquímicos in 2005 and 2008 respectively, from Universidade Federal do Rio de Janeiro, Brazil. Professor at Universidad de Antioquia, Colombia. Her research interests include: biotechnology; biofuels; microalgae; and use of Lignocellulosic materials - Biorefinery.
ORCID: 0000-0002-5453-2171

R. Ríos-Estepa, has a BSc. degree in Chemical Engineering (1993) and is professor at Universidad de Antioquia, Colombia. His MSc. degree is in Chemical Engineering from Universidad Nacional de Colombia, Bogotá, Colombia, (1997) and PhD in Chemical Engineering from the Washington State University, USA (2008). He has experience in metabolic engineering focuses on antibiotic production and systems biology.
ORCID: 0000-0002-3287-7056

UNIVERSIDAD NACIONAL DE COLOMBIA
SEDE MEDELLÍN
FACULTAD DE MINAS

Área Curricular de Ingeniería Química e Ingeniería de Petróleos

Oferta de Posgrados

Maestría en Ingeniería - Ingeniería Química
Maestría en Ingeniería - Ingeniería de Petróleos
Doctorado en Ingeniería - Sistemas Energéticos

Mayor información:

E-mail: qcaypet_med@unal.edu.co
Teléfono: (57-4) 425 5317

UNIVERSIDAD NACIONAL DE COLOMBIA
SEDE MEDELLÍN
FACULTAD DE MINAS



DYNA
http://dyna.medellin.unal.edu.co/

Hydraulic conductivity in layered saturated soils assessed through a novel physical model

Eduardo Dulcey-Leal [a], Fausto Molina-Gómez [b] & Lenin Alexander Bulla-Cruz [c]

[a] *Facultad de Estudios a Distancia, Universidad Militar Nueva Granada, Colombia. eduardo.dulcey@unimilitar.edu.co*
[b] *Facultad de Ingeniería, Universidad Militar Nueva Granada, Colombia. fausto.molina@unimilitar.edu.co*
[c] *Facultad de Ingeniería, Universidad Nacional de Colombia, Colombia. labullac@unal.edu.co*

Received: April 27th, 2017. Received in revised form: November 1rd, 2017. Accepted: February15th, 2018.

Abstract
This paper introduces a novel physical model for measuring the hydraulic conductivity of granular materials in saturated conditions. An innovation in the location of the device's piezometers allows the device to be used to assess the permeability of layered soils for both parallel and perpendicular flows. The model's square section construction makes soil compaction easy. Design methodology took issues of construction, calibration and implementation into account. Permeability coefficients in directions parallel and perpendicular to soil stratification were measured, and Student's *t*-test was performed for the relation of experimental results and existing numerical correlations. Analysis of the results shows that the physical model can replicate seepage in layered soils with parallel and perpendicular flows as occurs in field. Furthermore, it was found that it is possible to validate the experimental calibration data by use of statistical techniques.

Keywords: equivalent permeability coefficient; seepage; statistical analysis; *t*-test.

Estimación de la conductividad hidráulica en suelos saturados estratificados mediante un nuevo modelo físico

Resumen
Este documento presenta un modelo físico novedoso que permite medir la conductividad hidráulica en materiales granulares saturados. Una innovación en la ubicación de los piezómetros del dispositivo permite que este se use para evaluar la permeabilidad de los suelos estratificados tanto para flujos paralelos como perpendiculares. La construcción de la sección cuadrada del modelo facilita la compactación del suelo. La metodología de diseño tuvo en cuenta aspectos de construcción, calibración e implementación. Se midieron los coeficientes de permeabilidad en direcciones paralelas y perpendiculares a la estratificación del suelo. Además, se realizó la prueba-*t* de Student para la relación de los resultados experimentales y correlaciones numéricas existentes. El análisis de resultados muestra que el modelo físico puede replicar el fenómeno de filtración de agua a través de suelos granulares estratificados como sucede en campo. Por otra parte, se encontró que es posible validar el procedimiento de calibración experimental mediante técnicas estadísticas.

Palabras clave: análisis estadístico; coeficiente de permeabilidad equivalente; filtración, prueba-*t*.

1. Introduction

Hydraulic conductivity is one of the most important properties of soils [1]. Seepage through the soils may affect the stability of geotechnical structures such as pavement, tunnels, walls, slopes and excavations. For Nagaraj et al., Ozgurel & Vipulanandan and Mokwa & Trimble [2-4] the parameter which controls the permeability of soils is grain size while Lambe & Whitman [5] affirm that a soil's hydraulic conductivity depends on connectivity of pores within the material, and Haigh et al. [6] have established that tortuosity, void ratios and relative density are the parameters

How to cite: Dulcey-Leal, E., Molina-Gómez, F. and Bulla-Cruz, L.A., Hydraulic conductivity in layered saturated soils assessed through a novel physical model. DYNA, 85(205), pp. 119-124, June, 2018.

© The author; licensee Universidad Nacional de Colombia.

which permit seepage through granular soils. Nevertheless, soil permeability also depends on several additional factors including temperature, atmospheric pressure and absorption [7].

Seepage in soils is established by Darcy's Law according to which flow through a soil is laminar while flow velocity depends on the hydraulic gradient (*i*) [8]. The law is expressed by an equation for flow velocity that can be used to estimate the permeability coefficient (*k*) [9]. Flows only occur when an energy differential exists which is another way of saying when *i* exists. Hence, differences of energy or potential between two points must exist into the soil.

On the other hand, the soil is a non-homogenous, anisotropic and non-continuous material [10]. In nature, and at the majority of building sites, soil is layered. This means that soil properties may change from one stratum to another [1]. Because of processes of material formation and soil stratification, it is necessary to assess the hydraulic conductivity of each layer of soil in order to calculate the equivalent permeability coefficient (*k'*) which is a weighted average that takes the number of soil layers and their thicknesses into account. It can be used to monitor the hydraulic conductivity of a layered soil mass as well as flow direction within that mass [11].

Numerous methods have been developed to measure hydraulic conductivity of soils either in the field or through laboratory procedures [12,13]. In the field, permeability is evaluated by instrumentation of boreholes [12], but in the laboratory, the most popular procedure for evaluating hydraulic conductivity of granular soils is constant head testing which is described in ASTM standard D2434 [14]. The falling head test method is equally popular for fine-grained soils [13,15].

Various groups have developed new methods and insights in this area. Ghanizadeh et al. [16] estimated *k* in various types of fractured rocks in the field, using three different methods: *i*) profile probe, *ii*) pulse-decay, and *iii*) the crushed-rock permeability technique. They presented laboratory results for gas permeability measurements for the low matrix permeability Duvernay shale formation of Alberta, Canada. Estabragh et al. have done numerical simulations of seepage in porous media through which they obtained a numerical simulator that is useful for interpreting tests in which permeability changes affect flows within geomaterials [17]. Ai & Hu [18] have used the finite element method (FEM) to assess hydraulic conductivity in layered soils through which they established a method, based on the application of stiffness matrix in a multilayered soil model, to compute shear deformation and rotary inertia in soil-structure interaction problems. Others have made new developments in the laboratory. Goh et al. [19] modified a triaxial cell to estimate permeability in unsaturated soils, Anderson et al. [20] used a geotechnical centrifuge to estimate permeability in fine-grained soils, and Israr et al. [21] used a modified filtration apparatus to directly evaluated soil hydraulic conductivity under static and dynamic conditions. Meanwhile, Ilek & Kucza [22] have presented a novel apparatus for measuring infiltration properties of undisturbed soil samples.

This paper describes the construction, calibration and implementation of a novel physical model for measuring hydraulic conductivity in layered soils. It describes our experimental program which included the development of a method for assessing *k* and *k'* in two different types of sandy soils, Guamo sand and Ottawa sand. These parameters were obtained from tests performed in perpendicular and parallel flow directions using our new physical model for permeability testing. Finally, Student's t-test is used to compare experimental results and results obtained by using equations reported in the literature.

2. Experimental program

2.1. Materials

The study was carried out with Ottawa sand and Guamo sand which are both well-known materials in Colombia. Ottawa sand is obtained from Ottawa, Illinois in the United States and has uniform size distribution and is composed of quartz minerals [23]. Guamo sand comes from deposits from the Machín volcano and is acquired in the Luisa River in Tolima, Colombia [24]. Grain size grain distribution was obtained according to ASTM standard procedure D422 [25]. Fig. 1 shows the granulometric curves of both materials. Moreover, Table 1 presents the physical properties and classifications parameters of the sands.

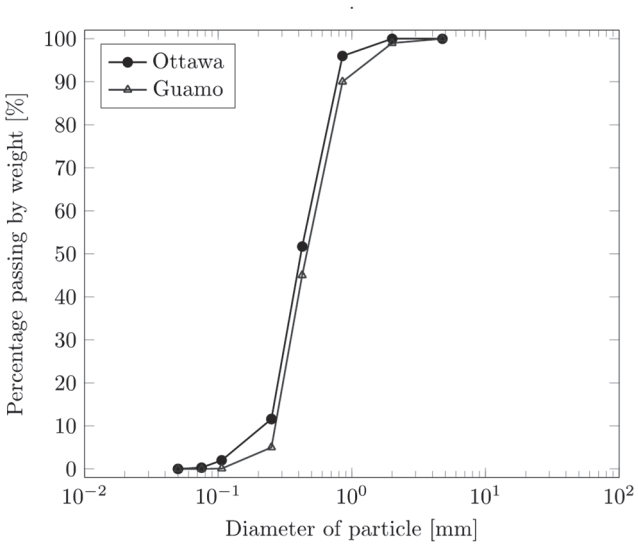


Figure 1. Grain size curve of sandy soils.
Source: The authors.

Table 1.
Physical properties of sandy soils

Parameter	Ottawa sand	Guamo sand
Gs	2.67	2.70
γ_{max} (kN/m^3)	17.61	16.25
γ_{min} (kN/m^3)	14.62	13.94
$e_{máx}$	0.79	0.90
$e_{mín}$	0.49	0.63
D_{10} (mm)	0.25	0.29
D_{60} (mm)	0.46	0.51
USCS	SP	SP

Source: The authors.

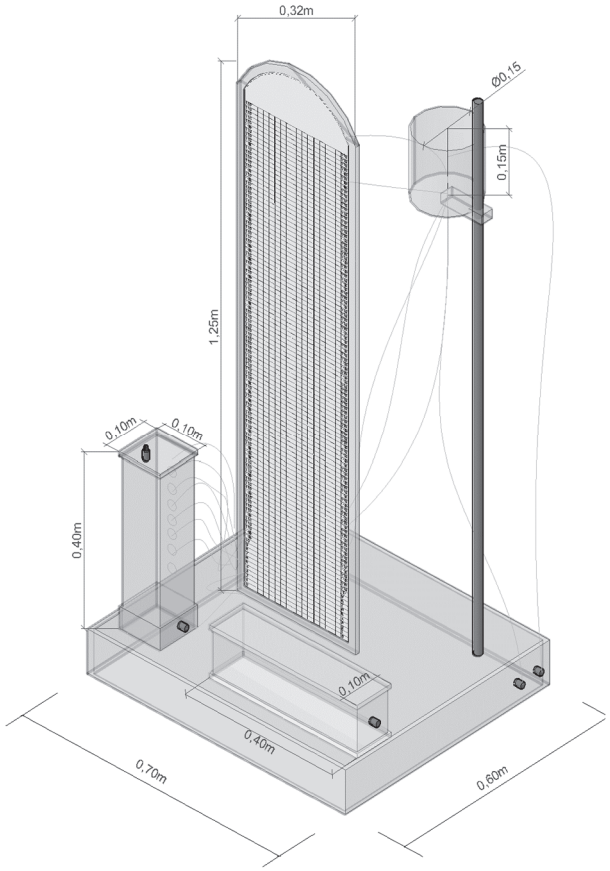


Figure 2. Physical model.
Source: The authors.

2.2. Equipment

A constant head apparatus was designed and developed on the basis of the apparatus suggested in ASTM standard procedure D2434 [14]. This device is capable of measure hydraulic conductivity of soils for both perpendicular and parallel flow directions of granular soils. In addition, the apparatus was built with two square acrylic permeameters as described in Dulcey et al. [26].

The geometry of the elements was selected in accordance with the sample preparation method. The device's tubes are 40 cm long, 10 cm high, and 10 cm wide. Each permeameter has seven piezometers with parallel configurations. For each permeameter, piezometer number 1 is connected to the porous stone, piezometers 2 to 4 are connected to the first soil layer and piezometers 5 to 7 are connected to the second soil layer. Fig. 2 presents a schematic view of the physical model.

2.3. Test procedure

Several soil specimens using Ottawa and Guamo sands were prepared in order to test measurement of hydraulic conductivity by the physical new model. Ottawa and Guamo sands were compacted into two distinct layers with a relative density of 70% in accordance with the procedure proposed by Camacho-Tauta et al. [27]. Each layer had a thickness of 19 cm for perpendicular flows and a thickness of 4 cm for parallel flows.

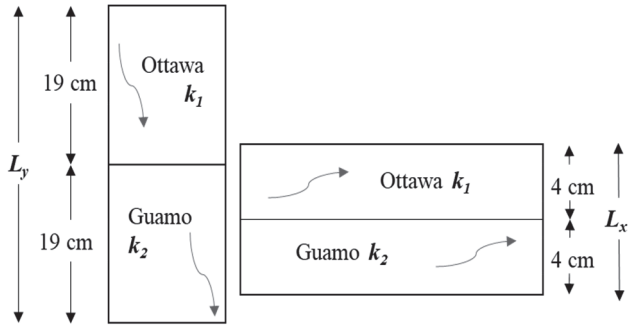


Figure 3. Schematic view of layered soils.
Source: The authors.

In addition, *k'* was simultaneously evaluated for perpendicular and parallel flow directions. Twenty different specimens, each composed of layers of the two, were compacted inside of each permeameter. The layers were prepared to reach a thickness of 19 cm for the perpendicular direction flow tests and 4 cm for the parallel direction flow test (Fig. 3). Similarly, conventional constant head tests were developed in the model to estimate *k* values for sandy soils.

3. Results and discussion

3.1. Hydraulic conductivity

Values of *k* were measured in the laboratory using the physical model, and computation was done according to the method described in ASTM D2434 [14]. Eq. (1) shows the calculation procedure.

$$k = \frac{QL}{At\Delta h} \tag{1}$$

where, *k* is the permeability coefficient (cm/s), *Q* is the flow rate (cm^3/s), *L* is the infiltration length (cm), *A* is the cross-sectional area (cm^2), *t* is the measurement time (s), and *Δh* is the difference in head pressure (cm).

Values of *k* were also estimated through numerical models based on granulometric results and relative density parameters. Eq. (2) proposed by Hazen [28], and eq. (3) proposed by Chapuis [29] were used to compare the experimental results.

$$k = 100D_{10}^2 \tag{2}$$

$$k = 2.4622\left(D_{10}\frac{e^3}{1+e}\right)^{0.7825} \tag{3}$$

where, D_{10} is the grain diameter (mm) of particles corresponding to 10% by weight (or mass) of particles passing through a certain sieve opening and *e* is the void ratio of the material. Table 2 presents the mean values of *k* obtained by means of tests performed with the apparatus for each sand independently plus the numerical correlations presented previously.

Table 2.
Hydraulic conductivity of sandy soils

Method	*k* (cm/s)	
	Ottawa sand	Guamo sand
Experimental	0.19	0.31
Hazen	0.06	0.08
Chapuis	0.16	0.33

Source: The authors.

Table 3.
Equivalent permeability coefficients

Method	Perpendicular flow, k'_y (cm/s)	Parallel flow, k'_x (cm/s)
Experimental correlation	0.24	0.25
Hazen	0.07	0.07
Chapuis	0.22	0.25

Source: The authors.

Results indicate that the *k* values obtained experimentally are within the range of soils classified as SP, according to authors including Bowles [11], Cedergren [12], Warrick [7] and Budhu [13]. However, the values obtained through Hazen's method are notably different from our experimental results. This is due to the fact that eq. (2) only incorporates one parameter of soil, D_{10}. Conversely, the outcomes found with the method proposed by Chapuis were very close to our experimental results. This is accounted for by the fact that this method includes a parameter, relative density, which is related to the state of the soil and depends on the void ratio. Ren et al. [30] mention the relationship between hydraulic conductivity and briefly review void ratio in a way that validates the outcomes obtained from the equations proposed by Hazen and Chapuis.

3.2. Equivalent permeability coefficient

Twenty different two-layered samples of Ottawa sand in the upper layer and Guamo sand in the lower layer were compacted in each permeameter for a total of ten permeability tests. Equivalent values of *k'* were measured in perpendicular and parallel flow directions simultaneously. Eq. (4) indicates the computation of the equivalent permeability coefficient in the perpendicular direction (k'_y), while eq. (5) indicates the equivalent permeability coefficient in the parallel direction (k'_x). These equations were obtained after taking energy losses of the soil mass in each layer into account [13]. Table 3 shows the mean results of all *k'* experimental values and the results obtained from correlations.

$$k'_y = \frac{L_y}{\frac{z_1}{k_1}+\frac{z_2}{k_2}} \quad (4)$$

$$k'_x = \frac{z_1 k_1 + z_2 k_2}{L_x} \quad (5)$$

Direct measurements were made by determining the differences in hydraulic potentials measured by the piezometers located in distinct layers in both permeameters. Fifty measurements were made in each permeameter. Findings show that the equivalent permeability coefficients differ according to flow direction. This is the result of the sample preparation process in which soil compaction produces a non-isotropic condition that induces modifications of hydraulic conductivity. According to Juárez Badillo & Rico Rodríguez [31], k'_x is never equal to k'_y in anisotropic soils because of natural processes of stratification plus compacting techniques in horizontal layers.

3.3. Statistical analysis

Nevertheless, the results of the twenty tests performed in the physical model presented no relevant variations, and the values of *k'* were statistically stable. Computation of the mean and median, both measures of spread, show them to be equal indicating an insignificant amount of variation. Figs. 4-5 illustrates the box plots of the data sets. Table 4 presents the findings from our statistical analysis.

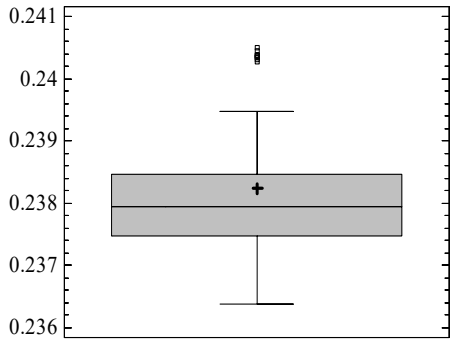


Figure 4. Box plot of k'_y (cm/s) test results.
Source: The authors.

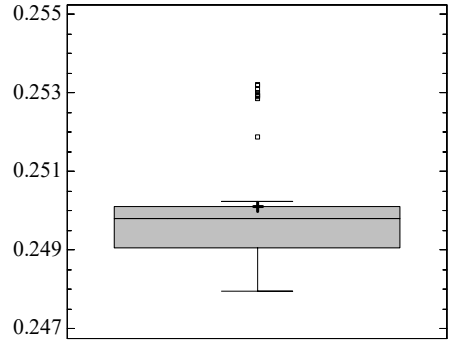


Figure 5. Box plot of k'_x (cm/s) tests results.
Source: The authors.

Table 4.
Descriptive statistics for k'

Statistic	Perpendicular flow, k'_y	Parallel flow, k'_x
Mean (cm/s)	0.2382	0.2501
Median (cm/s)	0.2379	0.2498
Standard deviation (cm/s)	0.0011	0.0015
Variation (%)	0.4772	0.5994

Source: The authors.

A comparison of the values obtained from Equations (4) and (5) with tests results shows that the relative errors between them are 0.73% for k'_y and 0.05% for k'_x, assuming that the values obtained from the equations are true.

To verify the behavior of the results, a *t*-test using the null hypothesis in which the experimental coefficient mean values are equal to the mean obtained from eqs. (4)-(5) was performed. Table 5 shows the normality test statistics: skewness presented slightly high values, but kurtosis is acceptable as can be seen in Fig. 6-7.

According to [32,33], the *t*-test is robust to non-normality when sample sizes have more than 30 observations. Due to the previous results and a sample size of 50, normality was assumed. With a 95% confidence level (α=0.05), the *t*-test could be used to show that experimental correlation results (Eq. 4-5) are close to the mean of the empirical data, particularly for the parallel flow (*p*-value = 0.58), as shown in Table 6. In the case of perpendicular flow, the null hypothesis is rejected because the empirical value (0.24) is not close to the experimental value of 0.2382 within the range evaluated. However, the relative error between these two values of 0.73% is negligible.

Table 5.
Normality test

Statistic	Perpendicular flow	Parallel flow
Skewness	2.73	3.29
Kurtosis	-0.29	0.08

Source: The authors.

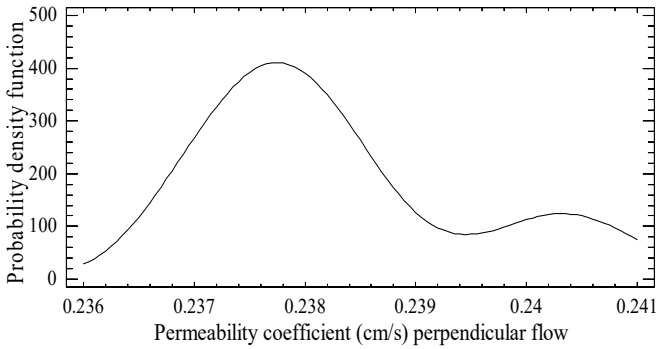


Figure 6. Density plot of k'_y.
Source: The authors.

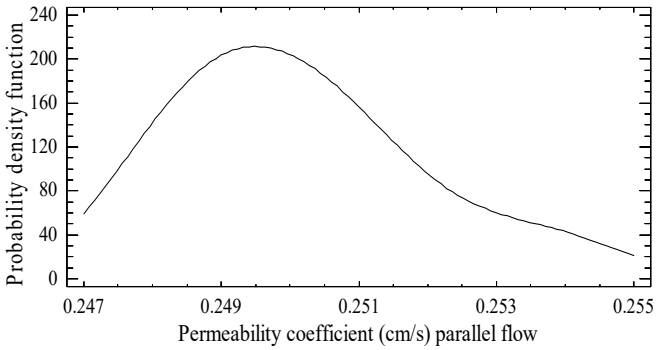


Figure 7. Density plot of k'_x.
Source: The authors.

Table 6.
T-test outcomes

Flow	T-statistic	P-value
Perpendicular	-10.95	0.00
Parallel	0.55	0.58

Source: The authors.

In the same sense, the 95% confidence intervals found for the mean are

- k'_y: 0.2382 +/- 0.00032312 [0.2379, 0.2385]
- k'_x: 0.2501 +/- 0.00042607 [0.2497, 0.2505]

which indicates the accuracy of the experimental procedures.

Based on the results, it is possible to affirm that experimental and empirical values are close and that variation is small. Moreover, the outcomes of the physical model show that the differences between k'_y and k'_x remain constant throughout the experimental replicas. For all the above reasons, the physical model is capable of replicating seepage in layered granular soils.

4. Conclusions

This paper proposes an alternative physical model for evaluating the hydraulic conductivity of granular materials. This can be used to measure hydraulic conductivity directly and to establish the equivalent permeability coefficient in layered soils, and is therefore capable of replicating seepage as it occurs in the field. The technique has proven to be efficient and relatively easy to apply.

Importantly, this physical model is highly reliable for testing permeability since it generates statistically stable results as evidenced by equality between mean and median values. In addition, the variability of all permeability coefficients (*k* and *k'*) was less than 1%. In a physical context, such relative errors do not represent important changes for practical designs, even if the hypothesis of the equal means of the *t*-test was rejected.

The *t*-test is a powerful tool for comparing variation in experiments with sample sizes of less than 30 observations. Since this technique also allows evaluation of dispersion of data obtained from experimental procedures, it can contribute to the calibration and implementation of laboratory apparatuses.

Our results show that the equivalent permeability coefficient varies according to flow direction. Data presented higher values for perpendicular flows than for parallel flows due to the sample preparation method. The compaction process induces an anisotropic condition within the granular soil that is reflected in the void distribution, which in turn produces an increase of the flow velocity.

The comparison of numerical methods with experimental techniques demonstrated a clear relationship between experimental correlations (weighted average) and direct measurements. This establishes that the assessment performed with the physical model was adjusted to the postulate of eq. (4)-(5). Nevertheless, the numerical models in this study did present differences with respect to the direct

measurements indicating that the parameters of each numerical model must be computed and adjusted according to the soil type.

References

[1] Gupta, P., Alam, J. and Muzzammil, M. Influence of thickness and position of the individual layer on the permeability of the stratified soil. Perspectives in Science, 8, pp. 757-759. 2016. DOI: 10.1016/j.pisc.2016.06.080

[2] Nagaraj, T.S., Pandian, N.S. and Narashimha Raju, P.S.R., Stress state-permeability relationships for fine-grained soils. Géotechnique, 43(2), pp. 333-336. 1993. DOI: 10.1680/geot.1993.43.2.333

[3] Ozgurel, H.G. and Vipulanandan, C., Effect of grain size and distribution on permeability and mechanical behavior of acrylamide grouted sand. Journal of Geotechnical and Geoenvironmental Engineering, 131(12), pp. 1457-1465. 2005. DOI: 10.1061/(ASCE)1090-0241(2005)131:12(1457)

[4] Mokwa, R.L. and Trimble, N.R., Permeability of Coarse-Grain Soil from Void Space and Pore Distribution. In GeoCongress 2008. Reston, VA: American Society of Civil Engineers, 2008, pp. 428-435DOI: 10.1061/40972(311)54

[5] Lambe, T.W. y Whitman, R.V., Mecánica de Suelos. Limusa. 1991.

[6] Haigh, S.K., Eadington, J. and Madabhushi, S.P.G., Permeability and stiffness of sands at very low effective stresses. Géotechnique, 62(1), pp. 69-75. 2012. DOI: 10.1680/geot.10.P.035

[7] Warrick, A.W., Soil Water Dynamics (1st ed.). New York: Oxford University Press. 2003.

[8] Darcy, H., Les fontaines publiques de la Ville de Dijon. Dalmont. Dalmont. Paris: Dalmont. 1856.

[9] Mitchell, J.K. and Soga, K., Fundamentals of Soil Behavior. John Wiley & Sons. 2005.

[10] Ramos-Cañón, A.M., Influence of the void ratio and the confining on the static liquefaction in slopes in changi sand. Revista Tecnura, 19(43), pp. 63, 2015. DOI: 10.14483/udistrital.jour.tecnura.2015.1.a04

[11] Bowles, J.E., Physical and Geotechnical Properties of Soils (2nd ed.). New York: McGraw-Hill. 1979.

[12] Cedergren, H.R., Seepage, drainage and flow nets. (3rd ed.). New York: Wiley. 1998.

[13] Budhu, M., Soil Mechanics and Foundations (3rd ed.). New York: Wiley. 2010.

[14] ASTM International., D2434 - Standard Test Method for Permeability of Granular Soils (Constant Head) (2006).

[15] Bowles, J., Manual de laboratorio de suelos en ingeniería civil. McGraw-Hill. 1980.

[16] Ghanizadeh, A., Bhowmik, S., Haeri-Ardakani, O., Sanei, H. and Clarkson, C.R., A comparison of shale permeability coefficients derived using multiple non-steady-state measurement techniques: Examples from the Duvernay Formation, Alberta (Canada). Fuel, 140, pp. 371-387. 2015. DOI: 10.1016/j.fuel.2014.09.073

[17] Estabragh, A.R., Soltani, A. and Javadi, A.A., Models for predicting the seepage velocity and seepage force in a fiber reinforced silty soil. Computers and Geotechnics, 75, pp. 174-181. 2016. DOI: 10.1016/j.compgeo.2016.02.002

[18] Ai, Z.Y. and Hu, Y.D., The analysis of beams on layered poroelastic soils with anisotropic permeability and compressible pore fluid. Applied Mathematical Modelling, 40(11), pp. 5876-5890. 2016. DOI: 10.1016/j.apm.2016.01.032

[19] Goh, S.G., Rahardjo, H. and Leong, E.C., Modification of triaxial apparatus for permeability measurement of unsaturated soils. Soils and Foundations, 55(1), pp. 63-73. 2015. DOI: 10.1016/j.sandf.2014.12.005

[20] Anderson, C., Sivakumar, V. and Black, J.A., Measurement of permeability using a bench-top centrifuge. Géotechnique, 65(1), pp. 12-22, 2015. DOI: 10.1680/geot.13.P.112

[21] Israr, J., Indraratna, B. and Rujikiatkamjorn, C., Laboratory investigation of the seepage induced response of granular soils under static and cyclic loading. Geotechnical Testing Journal, 39(5), pp. 795-812, 2016. DOI: 10.1520/GTJ20150288

[22] Ilek, A. and Kucza, J., A laboratory method to determine the hydraulic conductivity of mountain forest soils using undisturbed soil samples. Journal of Hydrology, 519, pp. 1649-1659. 2014. DOI: 10.1016/j.jhydrol.2014.09.045

[23] Robertson, P.K., Sasitharan, S., Cunning, J.C. and Sego, D.C., Shear-Wave Velocity to Evaluate In-Situ State of Ottawa Sand. Journal of Geotechnical Engineering, 121(3), pp. 262-273. 1995. DOI: 10.1061/(ASCE)0733-9410(1995)121:3(262)

[24] Molina-Gómez, F.A., Thesis, Physical modelling of liquefiable soils in shaking table. Universidad de los Andes, Colombia. 2016.

[25] ASTM International., D422 - Standard Test Method for Particle-Size Analysis of Soils (2007).

[26] Dulcey, E., Molina-Gómez, F.A. y Bulla-Cruz, L.A., Modelo físico del equipo de carga constante para el ensayo de permeabilidad. In C. Rodríguez (Ed.), XV Congreso Colombiano de Geotecnia (p. 7). Cartagena: Sociedad Colombiana de Geotecnia. 2016.

[27] Camacho-Tauta, J., Molina-Gómez, F.A. y Reyes-Ortiz, Ó.J. Preparación de especímenes de arena para ensayos triaxiales mediante un método controlado de compactación. Revista Científica General José María Córdova, 12, pp. 185-196. 2014. DOI: 10.21830/19006586.63

[28] Hazen, A., Price, W.G., Potter, A., Thomson, T.K., Smith, G.E.P. and Beardsley, R.C., Discussion of dams on sand foundations: some principles involved in their design, and the law governing the depth of penetration required for sheet-piling by Arnold C. Koenig. Transactions of the American Society of Civil Engineers, LXXIII(3), pp. 190-207, 1911.

[29] Chapuis, R.P., Predicting the saturated hydraulic conductivity of sand and gravel using effective diameter and void ratio. Canadian Geotechnical Journal, 41(5), pp. 787-795. 2004. DOI: 10.1139/t04-022

[30] Ren, X., Zhao, Y., Deng, Q., Kang, J., Li, D. and Wang, D., A relation of hydraulic conductivity — void ratio for soils based on Kozeny-Carman equation. Engineering Geology, 213, pp. 89-97. 2016. DOI: 10.1016/j.enggeo.2016.08.017

[31] Juárez-Badillo, E. y Rico-Rodríguez, A., Mecánica de suelos - Tomo 3: flujo de agua en suelos. Limusa. 1974.

[32] Wackerly, D.D., Mendenhall, W. and Scheaffer, R.L., Mathematical statistics with applications. Thomson Brooks/Cole. 2008.

[33] Ramachandran, K.M. and Tsokos, C.P., Mathematical statistics with applications. Elsevier/Academic Press. 2009.

E. Dulcey-Leal, received the BSc. of Civil Engineer in 2017 at Universidad Militar Nueva Granada, Colombia.
ORCID**:** 0000-0003-4657-4184

F.A. Molina-Gómez, received the BSc. of Civil Engineer in 2014 at Universidad Militar Nueva Granada, Colombia, the Sp. degree in Applied Statistics in 2017 at the Fundación Universitaria Los Libertadores, and the MSc. degree in Civil Engineering with emphasis in Geotechnics in 2016 at the Universidad de los Andes, Colombia. He worked as a young researcher and academic director of the graduate programs at the engineering faculty of the Universidad Militar Nueva Granada.
ORCID: 0000-0002-8831-0315

L.A. Bulla-Cruz, received the BSc. of Civil Engineer in 2000 at Universidad Militar Nueva Granada, Colombia, the Sp. degree in Soil Mechanics and Foundations in 2001 at the Universidad Politécnica de Madrid, Spain, the Sp. degree in Traffic, Design and Road Safety in 2009 at the Universidad Nacional de Colombia, the MSc. degree in Civil Engineering - Road Infrastructure in 2004 at the Universidad de los Andes, Colombia, the MSc. degree in Engineering - Transport in 2011 at the Universidad Nacional de Colombia.
ORCID: 0000-0002- 3476-9067

UNIVERSIDAD NACIONAL DE COLOMBIA
SEDE MEDELLÍN
FACULTAD DE MINAS



DYNA
http://dyna.medellin.unal.edu.co/

Impact of changing location and power of a PV system in electrical distribution networks, integrating MATLAB and OpenDSS

Javier Andrés Ruíz-Garzón, Daniel José González-Tristancho & Francy Catalina Espinosa-González

Programa de Ingeniería Eléctrica, Escuela Colombiana de Ingeniería Julio Garavito, Colombia. javier.ruiz@escuelaing.edu.co, daniel.gonzalez@escuelaing.edu.co, francy.espinosa@mail.escuelaing.edu.co

Received: November 15th, 2017. Received in revised form: March 16th, 2018. Accepted: April 3rd, 2018.

Abstract
This paper presents the electrical impact of connecting a photovoltaic (PV) system without storage to the electric distribution network 13-bus IEEE test case, integrating MATLAB and OpenDSS using a fluctuated vector of irradiance as an input for the PV system. The capacity of the primary source is reduced to a value where the system requires to add PV modules to provide a reliable source of power. PV modules are placed in both source bus and buses affected by voltage drops. Then, PV source is progressively increased to evaluate the voltage variations when combining PV and conventional sources. The results showed how a reduction in the generation affects the voltage levels of the system and how the inclusion of PV modules located in specific nodes tend to recover the system.

Keywords: solar power generation; power system simulation; OpenDSS; photovoltaic modules; IEEE test cases; irradiance.

Impacto del cambio de la ubicación y la potencia de un sistema FV en redes de distribución eléctrica, integrando MATLAB y OpenDSS

Resumen
Este artículo presenta el impacto eléctrico de conectar un sistema fotovoltaico (FV) sin almacenamiento a la red de distribución IEEE de 13 nodos, mediante la integración de MATLAB y OpenDSS utilizando un vector de irradiancia fluctuante como entrada para el sistema fotovoltaico. La capacidad de la fuente primaria se reduce a un valor en el que el sistema requiere agregar módulos fotovoltaicos para proporcionar una fuente confiable de electricidad. Los módulos fotovoltaicos se colocan tanto en el nodo fuente como en los nodos afectados por caídas de tensión. Luego, la fuente fotovoltaica se incrementa progresivamente para evaluar las variaciones de tensión al combinar fuentes fotovoltaicas y convencionales. Los resultados mostraron cómo una reducción en la generación afecta los niveles de tensión del sistema y cómo la inclusión de módulos fotovoltaicos ubicados en nodos específicos tiende a recuperar el sistema.

Palabras clave: generación de energía solar; simulación de sistemas de potencia; OpenDSS; módulos fotovoltaicos; caso de prueba IEEE; irradiancia.

1. Introduction

Solar radiation is defined as the energy coming from the sun as electromagnetic waves; incident solar power over a surface is known as solar irradiance, measured in [W/m^2] and the solar energy corresponds to incident solar power over a surface on a period of time in [Wh/m^2] [1].

The generation of electricity from solar radiation, namely photovoltaics, is directly proportional to the incident radiation on the photovoltaic panels and depends on the geographical area where they are located, the season of the year, cloudiness, among other climatic and environmental factors, in addition to the technical and constructive characteristics of the panels [2].

Solar irradiance fluctuates throughout the day and its impact on the distribution grid is an important issue regarding the effect of variable irradiance on large-scale application of photovoltaic systems [3]. The growth of the energy demand leads to the use of photovoltaic (PV) modules as an alternative to conventional sources. The use of this non-

How to cite: Ruíz-Garzón, J.A., González-Tristancho, D.J. and Espinosa-González, F.C., Impact of changing location and power of a PV system in electrical distribution networks, integrating MATLAB and Open DSS. DYNA, 85(205), pp. 125-131, June, 2018.

© The author; licensee Universidad Nacional de Colombia.

conventional type of renewable energy must fulfill the requirements established by the Colombian Mining and Energy Planning Unit (UPME for its acronym in Spanish) in law 1715 of 2014 [4], regarding the rational use of energy and renewable resources.

Under Resolution 121 of 2017 from the Energy and Gas Regulatory Commission (CREG for its acronym in Spanish) [5], the activities concerned to small scale self-generation (up to 1 MW) and large-scale distributed generation (up to 5 MW) are regulated. It was established that the installed power capacity must be equal or below 5 % of the distribution circuit nominal capacity. With CREG's Resolution 030 of 2018 [6], the capacity of the distributed generators was increased up to 15%, promoting the use of renewable energies.

However, the use of photovoltaic systems to supply the growing demand may create some electrical issues because it is a DC source; it is converted to an AC signal; it needs to be synchronized to the grid; and, even most importantly, it does not provide a steady energy source. Therefore, the technical issues of replacing generators in the IEEE 13 node test system with a photovoltaic system are analyzed, working with a variable irradiance provided by the Institute of Hydrology, Meteorology, and Environmental Studies of Colombia (IDEAM for its acronym in Spanish) [7]. The power from both sources, renewable and conventional energy, are gradually changed to supply the system loads, in accordance to the power quality requirements regarding voltage sags and swells for PV systems included in standards IEEE STD 1547-1,2003 [8], ANSI C84.1-2006 [9], and CREG 024-2005 [10], for voltage variations allowed in Colombia. This study has been done using the EPRI open source software OpenDSS through a MATLAB interface that allows working with time-variable irradiance which is processed by OpenDSS to provide the required outputs.

This paper is organized as follows: the second section presents the integration of MATLAB and OpenDSS tools for modeling of distribution networks with PV systems. The third section shows the results of simulating an IEEE 13-bus test case system, including a PV generation embedded in the OpenDSS model. In the fourth section, obtained results and their analyses are presented. Finally, the conclusions are shown.

2. Modelling PV systems under variable irradiance

Earlier studies [11,12] have shown the influence of variable irradiance and temperature on the Maximum Power Point Tracking (MPPT) on PV systems, leading to a change, usually a decrease of the energy output, which impacts the operation of the entire grid.

2.1. Modelling PV systems

A PV array consists of PV cells connected in either series or parallel and its mathematical model can be expressed as follows [13,14]:

$$P_{cc,inv} = P_{cc,fov}(1 - L_{cab}) \quad (1)$$

$$P_{cc,fov} = P_o R_{to,var}[1 - g(T_c - 25)]\frac{E}{1000} \quad (2)$$

$$T_c = T_{amb} + (TONC - 20)\frac{E}{800} \quad (3)$$

Where $P_{cc,fov}$ is the DC power output from the PV panels; L_{cab} is the power losses at the DC wiring between the PV panels and the inverter input (including fuse losses, switches, wirings, antiparallel diodes if any, etc.); E is the solar irradiance; g is the temperature coefficient of power in 1/°C; T_c is the temperature of solar cells; T_{amb} is the room temperature in the shade; *TONC* is the nominal operating temperature of the module, P_o is the nominal power of the generator; and $R_{to,var}$ is the performance which includes the percentages of losses due to the photovoltaic modules operating at normal condition.

PV modules can be mathematically modeled as follows [13]:

$$I_o = n_p I_{ph} - n_p I_{rs}\left(exp\left(k_o \frac{V}{n_s}\right)\right) \quad (4)$$

Where, I_o is the PV array output current; V is the PV output voltage; I_{ph} is the cell photocurrent, proportional to solar irradiation; I_{rs} is the cell reverse saturation current that depends on the temperature; k_o is related to Boltzmann constant; n_p is the numbers of parallel strings in the PV array and n_s is the numbers of series strings in the PV array.

Using Equations (1) - (4), the output power versus output voltage curve can be obtained (Fig. 1) [11].

2.2. PV Systems under Variable Irradiance

Previous works, based on the fluctuation of irradiance and temperature, have shown that such variability modifies the maximum power point (MPP) making the flux of energy unstable [15].

Solar irradiance depends on several meteorological parameters such as air temperature (T), relative humidity (RH), wind speed (Ws), wind direction (Wd), cloudiness (Cl), sunshine duration (S), clearness index (Kt), pressure (P), etc., and geographical coordinates such as latitude and longitude. Another study [16] illustrates that irradiance can be predicted; but its results comes from measured data in a specific weather station located at El Dorado International Airport in Bogotá, Colombia [7].

One of the main issues of PV systems without stable irradiance is the reliability of the data, considering that this kind of analysis requires a minimum amount of data for a 24-hour period as previous work shows [15].

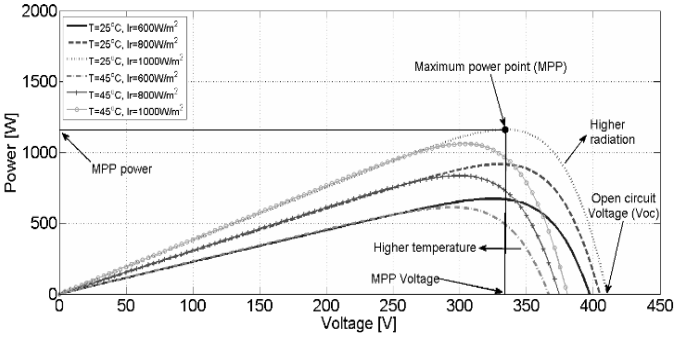


Figure 1. Power vs voltage curve of a photovoltaic system
Source: Adapted from [11].

The exponential growth of renewable resources has created the requirement of more accurate PV system models. There are several studies proposing and validating MPPT techniques such as *perturb and observe*, *incremental conductance*, *current sweep*, and *constant voltage* [11]. Since this paper does not focus on the MPPT, MPP placement is not considered, even though irradiance will be a variable.

According to standards IEEE STD 1547-2003 [8] and ANSI C84.1-2006 [9], which establish parameters for distribution systems working under a 60Hz frequency, this study considered the fact that irradiance and temperature lead to changes in voltage levels. Such changes are within the acceptable voltage variations found in the abovementioned standards.

2.3. Modelling variable irradiance using OpenDSS

OpenDSS can simulate power systems with the key advantage of modeling different types of variable conditions such as irradiance and loads. The frequency of the input data determines the time range of the simulation; for instance, if the input data is acquired every half an hour, the results shall be displayed as a function of this interval. Considering the active power, either supplied or absorbed by a specific bus bar, the results will be shown using the same rate of the input data. It is important to mention that all the data could be acquired from physical metering devices such as a pyrometer for irradiance. These data are normally obtained and displayed as a vector, which contains the required information that allows the software to run the simulations. To guarantee power flow convergence, there must be consistency among the quantity of data used and vector size.

OpenDSS models variable irradiance by working with vectors that can be introduced directly as a variable (vector type) or called from an Excel file, saved as a comma-separated values (CSV) file.

Once the requirements for vectors are fulfilled, the vector is called to OpenDSS using a simple line code which has five parts: the irradiance vector with any desirable name (*MyIrrad* for example); the number of points used and the time frame between each point specified; the command to call the vector with the actual name found in the CSV; and finally, the *useActual* command which represents the data entered as a per unit value.

To run the simulation, the user must ensure that all CVS files used and the OpenDSS script are in the same folder with the data vector either introduced as a line vector code or written as numbers separated by a single space.

3. Modelling distribution networks in OpenDSS

In this study, the 13-bus IEEE test case included in OpenDSS is used, the code was developed by students from Tennessee Technological University [17].

The general single-line diagram is shown in Fig. 2, and it is given by the IEEE-PES, divided in voltages nodes [18] to represent the general system. Initially, bus 632 is connected to a voltage regulator and from this to the source or node 650 which OpenDSS adopts it as a slack node.

According to the official test case from IEEE [19], a validation was required to ensure that power flow results in terms of voltage and currents evaluated in the nodes of the system were accurate. This revision led to a correction on the library code in element 603 which represents a line that connects nodes 632-645 and 645-646, as shown below.

Figs. 3 to 5 show that such correction has a relevant effect in the line impedances. Fig. 3 indicates the initial code for line 603 and Fig. 4 shows the information given by IEEE regarding the same power line. Comparing those two figures, a typographical error is observed due to the first and last value from both resistance and reactance are shifted. The correction is shown in Fig. 5.

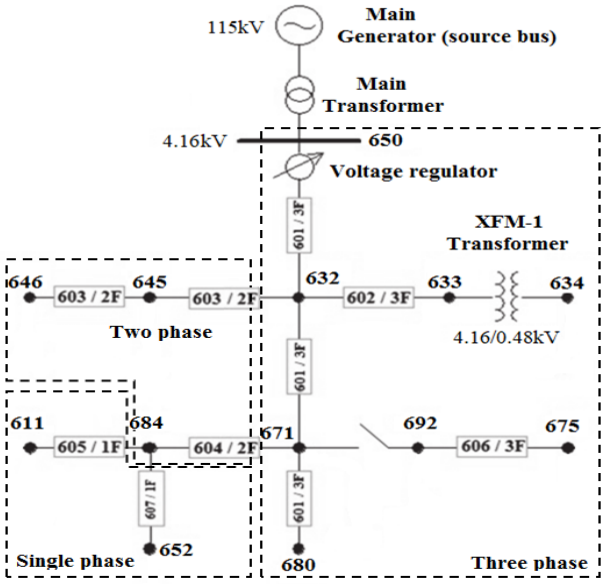


Figure 2. Modified IEEE 13 Node test feeder
Source: Adapted from [19]

```
New linecode.mtx603 nphases=2
~ rmatrix = (1.3238 | 0.2066 1.3294 )
    ~ xmatrix = (1.3569 | 0.4591 1.3471 )
        ~ units=mi
```

Figure 3. Original code line at the Tennessee Tech students' script
Source: [17]

```
Configuration 603:
        Z (R +jX) in ohms per mile
0.0000  0.0000  0.0000  0.0000  0.0000  0.0000
                1.3294  1.3471  0.2066  0.4591
                                1.3238  1.3569
```

Figure 4. Impedance matrix configuration for line 603 given by IEEE
Source: The authors

```
New linecode.mtx603 nphases=2
~ rmatrix = (1.3294 | 0.2066 1.3238)
    ~ xmatrix = (1.3471 | 0.4591 1.3569)
        ~ units=mi
```

Figure 5. Corrected line code used for the original script
Source: The authors

4. Integration of MATLAB and OpenDSS for the modelling

4.1. Linking together MATLAB and OpenDSS

To improve the results' user-friendliness obtained by OpenDSS, it is possible to establish a link between OpenDSS and MATLAB following the flowchart shown in Fig. 6. It is important to clarify that all power flows are carried out by OpenDSS calling Excel files. These files contain the environmental resources such as irradiance or temperature while MATLAB displays the results and gives the users the opportunity to modify those parameters in real time.

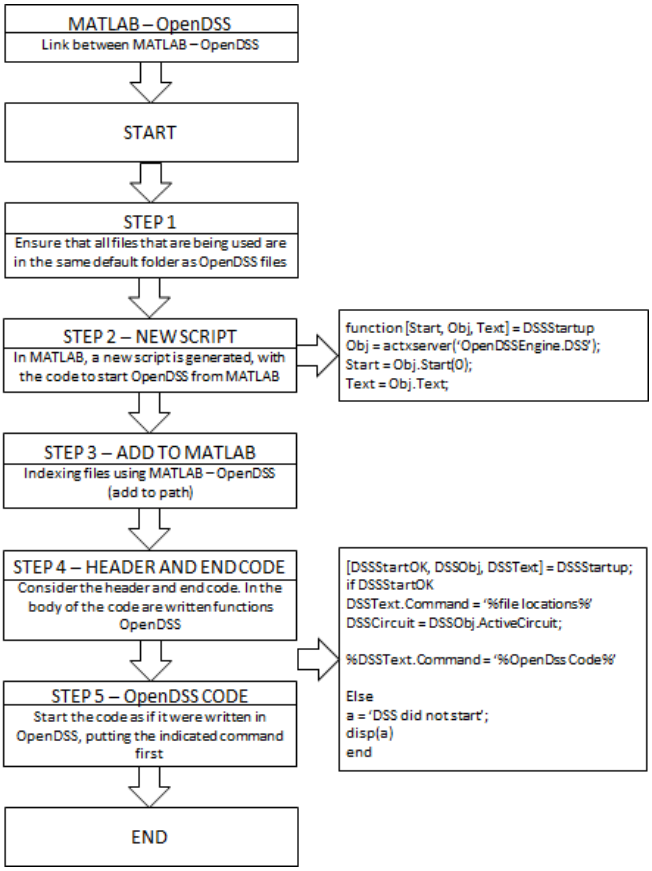


Figure 6. Flowchart to connect OpenDSS with MATLAB
Source: The authors

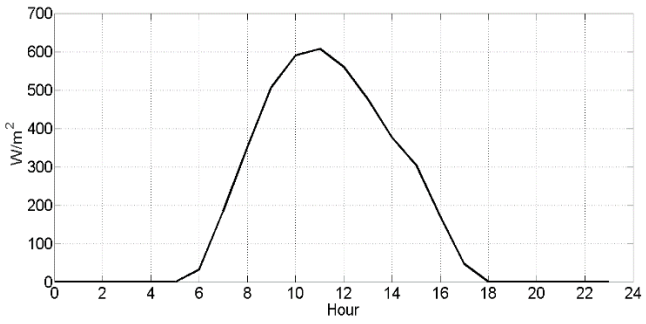


Figure 7. Irradiance using MATLAB and OpenDSS
Source: The authors

Table 1.
Utilization voltage limits according to ANSI C84.1-1 of 2006

	Utilization voltage limits	
	Optimal voltage range	**Acceptable voltage range**
Minimum	90%	86.7%
Maximum	105%	105.8%

Source: [9]

Following the previous flowchart, OpenDSS can be linked using any C-based programming language software such as Python or LabVIEW.

4.2. Evaluating OpenDSS results using MATLAB

According to the data provided by IDEAM [7], an Excel file was called to OpenDSS as explained in section *Modelling variable irradiance using OpenDSS*. The raw data were used as input for the model and the information is presented in this study as a daily irradiance curve generated by MATLAB, as shown in Fig. 7.

There are other advantages for using a connection between OpenDSS and MATLAB, mainly the visualization of results, since MATLAB allows to display the charts with a range variety of options.

5. Case study

The study is divided into four stages. In the first one, the total power from the source bus is gradually decreased to assess the effect of voltage drops in different buses according to the power flow. A reduction of 16.68% in the total power system led to voltage levels in several nodes to drop below the acceptable voltage range (0.867 pu, according to Table 1).

In the second stage, a PV array is added in the source bus to compensate the changes in the system using 680 kVA. Then, in the third stage of the study, the response of the system adding a greater PV capacity of 1360 kVA in the source bus is analyzed. A fourth stage of the study is considered shifting the location from source bus to a distant node of the network to assess the effect in voltage levels.

Since a PV system is added, the information used must be real and accurate; therefore, a KC85TS High Efficiency Multicrystal Photovoltaic Module has been selected [20] and the array has been calculated using Eqs. (1) - (4) to fit the needs of the different stages of the study. Considering that the irradiance of January 2014 is the highest and most unwavering registered in [7], it is used as an input to evaluate the behavior of the system.

All stages for this study are done with a variable measured irradiance, therefore the variation in voltage levels of the system is affected.

Originally, the critical buses were found while decreasing the power generated by the main source; the IEEE 13 node test feeder is connected to the grid, which virtually acts as an "infinite source". This source needs to be changed to a regular generator or a synchronous machine to be able to control its power capacity. To make this happen, both generator and grid must be modeled under the same conditions. Same initial results are guaranteed.

With the synchronous machine installed in the model a power flow was conducted and a selection of the altered

Table 2.
Service voltage limits according to ANSI C84.1-1 of 2006

	Service voltage limits	
	Optimal voltage range	**Acceptable voltage range**
Minimum	97.5%	95%
Maximum	105%	105.8%

Source: [9]

Table 3.
Bus voltages for 16.68% of total power reduction

Bus/Node	Phase	VLN [kV]	Angle [degrees]	VLN [pu]	Base [kV]
675	1	2.0216	15	0.8417	4.16
	2	2.3144	-101.1	0.96361	4.16
	3	1.9761	136.5	0.82278	4.16
611	3	1.9711	136.2	0.82068	4.16
684	1	2.0319	15.2	0.84602	4.16
	3	1.9756	136.4	0.82254	4.16

Source: The authors

buses is made based on those that were below 90% of its nominal value or over 110% as CREG 024-2005 [10] stablishes, and those that go under the values allowed by ANSI C84.1-2006 for service and utilization voltage levels, as shown in Table 1 and Table 2 [9].

6. Results and analysis

An analysis of the power flows considering the stages of the study were carried out for the different scenarios previously described. Results of the power flows lead to determine that the most critical outputs were obtained in the nodes 611 (single-phase), 684 (two-phase) and 675 (three-phase). The evaluation of the impact of installing PV arrays on certain buses shows that the voltage in the system is compensated.

Table 3 shows the results of voltage level in the most critical nodes with a reduction of 16.68% in the total power system. Voltage drops below 86.7% in the buses are highlighted following the criteria allowed by ANSI C84.1-2006 [9].

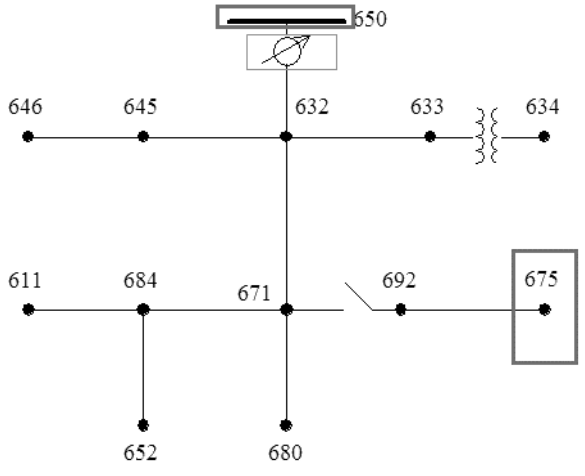


Figure 8. Modified IEEE 13 Node test feeder
Source: The authors

Table 4.
Bus voltages with a PV array of 680 kVA in the source bus

Bus/Node	Phase	VLN [kV]	Angle [degrees]	VLN [pu]	Base [kV]
675	1	2.0831	14.1	0.86731	4.16
	2	2.407	-101.6	1.0022	4.16
	3	2.0326	135.8	0.84629	4.16
611	3	2.0274	135.5	0.84411	4.16
684	1	2.0939	14.3	0.87183	4.16
	3	2.032	135.7	0.84602	4.16

Source: The authors

Table 5.
Bus voltages with a PV array of 1360 kVA in the source bus

Bus/Node	Phase	VLN [kV]	Angle [degrees]	VLN [pu]	Base [kV]
675	1	2.0831	14.1	0.86731	4.16
	2	2.407	-101.6	1.0022	4.16
	3	2.0326	135.8	0.84629	4.16
611	3	2.0274	135.5	0.84411	4.16
684	1	2.0939	14.3	0.87183	4.16
	3	2.032	135.7	0.84602	4.16

Source: The authors

In the first case, when the total power of the system is reduced, all nodes have voltage drops below 86.7%. The most critical case between three-phase nodes is at bus 675 as showed in Fig. 8, in which the third phase drops to 0.82278 pu, as seen in Table 3, despite the largest drop in the voltage occurring in the single-phase bus 611 with a value of 0.82068 pu.

Table 4 presents the results when a PV array is added in the source bus trying to compensate the changes in the system using 680 kVA. Under these conditions, the inclusion of the PV array in the source bus shows an increase in the voltage levels of the system, however these levels are still below the allowed limits.

A greater PV array capacity of 1360 kVA installed in the source bus led to results showed in Table 5, which shows how the system recovers acceptable voltage levels by duplicating the PV array capacity installed in the source bus.

During the last stage of the analysis, the PV array of 1360kVA is shifted from source bus to a distant three-phase node of the network (675). Results are showed in Table 6.

Finally, a greater impact is observed when a power PV capacity of 1360 kVA is installed in the most critical three-phase node. The difference between installing this PV capacity in the 675 node, rather than the source bus, represents an increase from 0.8728 pu to 0.9021 pu for the voltage in the third phase.

Table 6.
Bus voltages with a PV array of 1360 kVA in bus 675

Bus	Phase	VLN [kV]	Angle [degrees]	VLN [pu]	Base [kV]
675	1	2.213	19.7	0.92138	4.16
	2	2.516	-95.4	1.0476	4.16
	3	2.1667	141.8	0.90213	4.16
611	3	2.1499	141.3	0.89515	4.16
684	1	2.2119	19.8	0.92094	4.16
	3	2.1549	141.5	0.8972	4.16

Source: The authors

It is important to highlight that in the second, third and fourth stages of the study the behavior analyzed in the 611, 684 and 675 nodes can be seen in the rest of the nodes.

As expected, installing more PV capacity in the most critical node can generate a positive impact, trying to recover the system as shown in Table 6.

The previous results open the possibility of performing other simulations in different tools for load flows, to carry out verifications of the veracity of the simulations of distribution networks with PV systems in OpenDSS and MATLAB.

7. Conclusions

The electrical impact of connecting a photovoltaic (PV) system without storage to an existing electric distribution network has been described. Modeling power systems in OpenDSS allows to modify the capacity of generation in parallel with PV penetration considering variable inputs in a time basis interval transforming the standard distribution network into a distributed generation network.

As expected, the synchronous machine installed in the system affected the voltage levels in the nodes when the power capacity is reduced. Overexciting occurs when the power in the generator decreases, because of a higher load requisition, leading to a voltage decrease in the nodes, which can be compensated installing PV arrays as seen in Tables 4, 5 and 6.

Prior to the installation of PV arrays, it is important to determine the nodes of the system where a larger impact in the voltage level is evidenced. As shown in Table 6, installing PV arrays in the critical node allows to mitigate the voltage drops increasing from 0.8228 pu to 0.9021 pu for the voltage in the third phase of node 675.

Historic data regarding irradiance or variable loads can be used as vector inputs without any hardware in the loop configuration to run time-varying conditions in power systems. The integration of OpenDSS and MATLAB allows not only to visualize results but also to modify and iterate them under new conditions in the system.

References

[1] National Renewable Energy Laboratory [NREL]. Concentrating solar power- best practices handbook for the collection and use of solar resource data, 2010, [Online] Available at: https://www.nrel.gov/docs/fy10osti/47465.pdf

[2] Boyle, G., Renewable energy power for a sustainable future. Third edition. Amersham, UK: Oxford University Press, 2012.

[3] Woyte, A., Van Thong, V., Belmans, R. and Nijs, J.,Voltage fluctuations on distribution level introduced by photovoltaic systems, IEEE Transactions on Energy Conversion, 21 (1), pp. 202-209, 2006, DOI: 10.1109/TEC.2005.845454

[4] Unidad de Planificación Minero Energética [UPME]. Ley 1715 DE 2014, "Por medio del cual se regula la integración de las energías renovables no convencionales al sistema energético nacional", 2014, [Online]. Available at: http://www.upme.gov.co/Normatividad/Nacional/2014/LEY_1715_2014.pdf

[5] Comisión de Regulación de Energía y Gas [CREG]. Resolución 121 de 2017 por la cual se ordena hacer público el proyecto de resolución "Por la cual se regulan las actividades de autogeneración a pequeña escala y de generación distribuida en el sistema interconectado nacional", 2017 [Online]. Available at: http://apolo.creg.gov.co/Publicac.nsf/1c09d18d2d5ffb5b05256eee00709c02/b5341fbcfab96db80525819b006d42fa?OpenDocument

[6] Comisión de Regulación de Energía y Gas [CREG]. Resolución 030 de 2018 "Por la cual se regulan las actividades de autogeneración a pequeña escala y de generación distribuida en el sistema interconectado nacional", 2018 [Online]. Available at: http://apolo.creg.gov.co/Publicac.nsf/1c09d18d2d5ffb5b05256eee00709c02/83b41035c2c4474f05258243005a1191/$FILE/Creg030-2018.pdf

[7] Instituto de Hidrología, Meteorología y Estudios Ambientales de Colombia [IDEAM]. Atlas de radiación solar, ultravioleta y ozono de Colombia, 2016. [Online]. Available at: http://atlas.ideam.gov.co/visorAtlasRadiacion.html

[8] Institute of Electrical and Electronics Engineers [IEEE]. Standard for Interconnecting Distributed Resources with Electric Power Systems. (Std 1547-2003), 2003. [Online]. Available at http://ieeexplore.ieee.org/document/1225051/

[9] American National Standards Institute, Inc. [ANSI]. American national standard for electric power systems and equipment — voltage ratings (60 Hertz). (C84.1-2006), 2006. [Online]. Available at: https://www.nema.org/Standards/ComplimentaryDocuments/Contents-and-Scope-ANSI-C84-1-2011.pdf

[10] Comisión de Regulación de Energía y Gas [CREG]. Resolución 024-2005, "Por la cual se modifican las normas de calidad de la potencia eléctrica aplicables a los servicios de Distribución de Energía Eléctrica", 2005. [Online]. Available at: http://apolo.creg.gov.co/Publicac.nsf/2b8fb06f012cc9c245256b7b00789b0c/7ef77a545ceb66680525785a007a6b88/$FILE/Creg024-2005.pdf

[11] González, D., Prototipo de energía eléctrica fotovoltaica, para el laboratorio de energía de la Escuela Colombiana de Ingeniería. MSc. thesis, Escuela Colombiana de Ingeniería Julio Garavito, Bogotá, Colombia, 2016.

[12] Bialasiewicz, J., Renewable energy systems with photovoltaic power generators: operation and modeling. IEEE Transactions on Industrial Electronics, 55, 7, 2752-2758, 2008. DOI: 10.1109/TIE.2008.920583

[13] Liu, F., Duan, S., Liu, F., Liu, B. and Kang, Y., A variable step size INC MPPT method for PV systems. IEEE Transactions on Industrial Electronics, 55(10074567), pp. 2622-2628, 2008. DOI: 10.1109/TIE.2008.920550

[14] Instituto para la Diversificación y Ahorro de la Energía [IDAE]. Pliego de condiciones técnicas de instalaciones conectadas a Red, 2011. [Online]. Available at: http://www.idae.es/uploads/documentos/documentos_5654_FV_pliego_condiciones_tecnicas_instalaciones_conectadas_a_red_C20_Julio_2011_3498eaaf.pdf

[15] Maranda, W. and Piotrowicz, M., Efficiency of maximum power point tracking in photovoltaic system under variable solar irradiance. Bulletin of the Polish Academy of Sciences, Technical Sciences, 62(4), pp. 713-721, 2014. DOI: 10.2478/bpasts-2014-0077

[16] Mellit, A. and Pavan, A.M., A 24-h forecast of solar irradiance using artificial neural network: Application for performance prediction of a grid-connected PV plant at Trieste, Italy. Solar Energy, 84(5), pp. 807-821, 2010. DOI: 10.1016/j.solener.2010.02.006

[17] Electric Power Research Institute [EPRI]. Discussion forum for the 13 bus IEEE test case EPRI Distribution System Simulator (OpenDSS) script, 2009. [Online]. Available at: https://sourceforge.net/p/electricdss/discussion/861977/thread/79ed9387/

[18] Nyangoma, J. and Awodele, K., Comparison of different reactive power compensation methods in a power distribution system. Paper presented at the 22nd Southern African Power Universities Engineering Conference, 2014.

[19] Institute of Electrical and Electronics Engineer [IEEE]. Distribution test feeders, 1992. [Online]. Available at: http://ewh.ieee.org/soc/pes/dsacom/testfeeders/index.html

[20] Kyocera Corporation. KC85TS high efficiency multicrystal photovoltaic module, 2016. [Online]. Available at: https://www.kyocerasolar.com/dealers/product-center/archives/spec-sheets/KC85TS.pdf

J.A. Ruíz-Garzón, received the BSc. Eng in Electrical Engineering in 2012 from the Universidad de la Salle, Bogotá, Colombia, and the MSc degree in

Renewable Energy and Environmental Modelling in 2014 from the University of Dundee, Dundee, Scotland. Currently, he is a full time professor in the Electrical Program at Escuela Colombiana de Ingeniería Julio Garavito, Colombia.
ORCID: 0000-0003-1551-2554

D.J. González-Tristancho, received the BSc. Eng in Electrical Engineering in 2002 and the MSc. degree in Electronic Engineering in 2016, both of them from Escuela Colombiana de Ingeniería Julio Garavito, Bogotá, Colombia. Currently he is a full time professor in the Electrical Program, Escuela Colombiana de Ingeniería Julio Garavito, Colombia.
ORCID: 0000-0003-0905-5019

F.C. Espinosa-González, received the BSc. Eng in Electrical Engineering in 2017 from Escuela Colombiana de Ingeniería Julio Garavito, Colombia.
ORCID: 0000-0001-7823-4788

UNIVERSIDAD NACIONAL DE COLOMBIA
SEDE MEDELLÍN
FACULTAD DE MINAS

Área Curricular de Ingeniería
Eléctrica e Ingeniería de Control

Oferta de Posgrados

Maestría en Ingeniería - Ingeniería Eléctrica

Mayor información:

E-mail: ingelcontro_med@unal.edu.co
Teléfono: (57-4) 425 52 64

UNIVERSIDAD NACIONAL DE COLOMBIA
SEDE MEDELLÍN
FACULTAD DE MINAS



DYNA
http://dyna.medellin.unal.edu.co/

Crack filling in concrete by addition of *Bacillus subtilis* spores – Preliminary study

Nicole Schwantes-Cezario [a], Maria Vânia Nogueira do Nascimento Peres [b], Thomas Kehrwald Fruet [b], Geovana Souza Ferreira Nogueira [a], Berenice Martins Toralles [a] & Davi De Souza Cezario [c]

[a] *State University of Londrina, Londrina, Brazil. nicoleschwantes@hotmail.com; geovanasouzanogueira@gmail.com, betoralles@gmail.com*
[b] *FAG University, Cascavel, Brazil. vaniaperes@gmail.com; thomas@fag.edu.br*
[c] *State University of São Paulo, Ilha Solteira, Brazil. davi.scezario@gmail.com*

Received: October 30th, 2017. Received in revised form: March 16th, 2018. Accepted: April 4rd, 2018.

Abstract
This study aimed to analyze the performance of two concrete mixtures with the addition of *B. subtilis* spores regarding their capacity of filling cracks during the curing time, evaluating whether the addition can influence the compressive strength of the concrete. For so, six concrete mixtures were studied divided in two mix compositions: 1:1:2 and 1:2:3 (cement: sand: gravel) with w/c of 0.33 and 0.45, respectively. For each composition were added concentrations of 0, $0.3x10^8$ or $1.2x10^8$ of *B. subtilis* spores/mL. The results showed that all the samples with spores addition presented crystals precipitation, possibly calcium carbonate, that visually filled the cracks. However, more studies of microstructural analysis should be conducted to prove that the cracks were closed. The compressive strength presented satisfactory results, because the addition of $1.2x10^8$ spores/mL did not present significant differences in compressive strength at probability level of 5%, when compared to the reference concrete.

Keywords: bioconcrete; concrete with addition of spores; *Bacillus subtilis*; crack filling; cracks.

Relleno de fisuras en concreto por la adición de esporas de *Bacilos subtilis* - Estudio preliminar

Resumen
Este estudio tiene como objetivo analizar el desempeño de dos composiciones de hormigón con adición de esporas de *B. sutilis* con relación a su capacidad de relleno de fisuras durante el periodo de cura, evaluando la influencia de la adición en la resistencia a compresión. Para ello han sido estudiadas seis composiciones de hormigón, divididas en dos dosificaciones: 1:1:2 y 1:2:3 (cemento: árido fino: grava) en peso, con relación a/c de 0,33 y 0,45. Para cada una de las mezclas se utilizaran concentraciones de 0, $0.3x10^8$ or $1.2x10^8$ de esporas de *B. sutilis*/mL. Los resultados obtenidos han demostrado que todas las muestras con adición de esporas presentaron precipitación de cristales, posiblemente carbonato de calcio, que fue visualizado en las fisuras. Más estudios microestructurales deberán ser realizados para comprobar que de hecho ocurrió el relleno de las fisuras. La resistencia a compresión presentó resultados satisfactorios, pues no hubo diferencias significativas en relación al hormigón de referencia, a nivel de 5% de probabilidad.

Palabras clave: biohormigón; hormigón con adición de esporas; *Bacilos subtilis;* relleno de fisuras*;* fisuras.

1. Introduction

Concrete is the main material used in construction, as other materials are limited compared to it, by either cost, ease of execution, durability or flexibility to adapt to various geometric shapes [1]. However, concrete is subject to pathological manifestations, which compromise its integrity and durability [2]. Among these manifestations, cracking is a frequent problem, which in addition to an aesthetic damage, can cause leakage and may compromise the entire structure [3].

Moreover, in environmental terms, the production of concrete is unsustainable [4], for the manufacture of the main

How to cite: Schwantes-Cezario, N., Peres, M.V.N.doN., Fruet, T.K., Nogueira, G.S.F., Toralles, B.M: and Cezario, D.deS., Crack filling in concrete by addition of Bacillus subtilis spores – Preliminary study. DYNA, 85(205), pp. 132-139, June, 2018.

© The author; licensee Universidad Nacional de Colombia.

component, Portland cement, is a major global carbon dioxide emitter [5]. The emission of CO_2 from the calcination process of limestone and from the combustion in the furnace of the cement industry accounts for about 7% of global CO_2 emissions, making it an important sector for mitigation strategies concerning this pollutant gas [6].

In view of these problems and the need to make concrete a more durable and sustainable material, researches are being conducted on the addition of different materials that provide healing of concrete cracks [7].

In this context, there arises a technological innovation that seeks to minimize the problem of cracks in concrete structures, the bioconcrete. The incorporation of bacteria to the concrete matrix has been used from the bio-precipitation of minerals, with the goal of closing pores and cracks. Thus, the bacteria are considered a self-healing agent of concrete cracks, because they have the ability to precipitate minerals that close the cracks autonomously [8].

However, obtaining a greater understanding of the basic mechanisms and principles of materials that are able to close concrete cracks is still a challenging goal. If this goal is achieved, it will undoubtedly lead to the development of a new generation of self-healing materials [7].

The mineral precipitated by the bacteria in cement materials is from calcium carbonate ($CaCO_3$), which can be precipitated by microorganisms from several mechanisms. The precipitation of $CaCO_3$ promoted by bacteria is classified as a Biologically Induced Mineralization (BIM) [9]. This process will result in minerals formed from three possible ways: enzymatic hydrolysis of urea, dissimilation of nitrates and aerobic metabolic conversion of calcium salts [10]. This last one results in minerals that are formed from an involuntary metabolic activity [11].

After investigation about equations that could summarize possible ways for $CaCO_3$ bioprecipitations, researchers found three main results (Eqs. 1-3) for these biochemical reactions in which the cell surface works as a nucleation site [12].

$$Ca^{2+} + CO_3^{2-} \leftrightarrow CaCO_3 \quad (1)$$

$$HCO_3^- \leftrightarrow CO_3^{2-} + H^+ \quad (2)$$

$$HCO_3^- + OH^- \leftrightarrow CO_3^{2-} + H_2O \quad (3)$$

This bioprecipitations happen as the bacteria finds a calcium source such as limestone rocks or cements. This source, due its negativity, tends to approach the cell wall of the bacteria forming a complex. This complex precipitates calcium carbonate due to the reaction with ion CO_3 (Eq. 1). The carbonate and biocarbonate ions dissolved in solutions are formed mainly from the CO_2 produced during the microbial respiration (Eq. 2 and 3) [12].

Some bacteria that produce minerals by BIM have been used to repair limestone monuments [13-16] and to fill pores and cracks in concrete and other cementitious materials [17-22].

The success of the use of bacteria to close pores in cement materials is directly related to their ability to form spores [8]. The pH of the concrete is highly alkaline, has no nutrients and there is oxygen only in its open pores and on its surface, tending to restrict bacterial growth [19].

Thus, this research aims at evaluating the crack filling and the compressive strength of two concrete mixtures with addition of B. *subtilis* spores isolated in Brazil [23] at different concentrations.

2. Microrganisms and growth conditions

2.1. Materials

This study was conducted with *B. subtilis* AP91, isolated in Brazil from leaves of long grain rice. This bacterium has the potential to bioprecipitate $CaCO_3$ according previous researches [23]. Initially the bacteria was reproduced from two culture medium: Mueller Hinton (MH) (Sigma-Aldrich, USA) and Trypton Soy Broth (TS) (Sigma-Aldrich, USA). These two culture medium were tested to verify in which one the bacteria have the more effectively reproduction ability. From the analysis of this tests, it was select the best culture medium, which provided the highest bacterial growth, enabling to obtain the experiment.

The culture media (MH and TS) were formulated to 500 mL and autoclaved for 15 minutes at 121°C and 1 atm. After sterilization, the bacteria were inoculated in the culture medium and samples were placed in shaker TE 400 (Tecnal) for 66 hours at an average temperature of 29.1ºC to induce bacterial growth.

After the stir period, the solution with the bacteria was washed in order to remove the culture medium and to obtain a more concentrated solution of bacteria. For this, the culture media was centrifuged in Falcon tubes for 20 minutes at 3600 rpm spin, the supernatant was removed and replaced with 0.85% saline solution [1177]. The experiment was repeated twice (n = 2).

Then, the solution containing bacteria was stored for two days at the temperature of 8ºC to induce spore formation. It is important to mention that spores formation are fundamental for the survival of the bacteria in the cementitious materials.

2.2. Quantification of bacteria

Quantification of the bacteria grown in MH and TS were performed with the spectrophotometer UV340GX (Gehaka), with reading at 600 nm. For this test, three samples were used: the control with 0.85% of saline solution, the bacteria grown in MH dissolved in 0.85% saline solution and the bacteria grown in ST dissolved in 0.85% saline solution. To calculate the concentration of bacteria in the medium through the absorbance, Equation 4 was applied [17].

$$Y = 8.59 * 10^7 * X^{1.3627} \quad (4)$$

Where:

- X = absorbance (A);
- Y = Spore concentration per mL.

After complete this stage, the culture medium that resulted in the highest cell growth was identified and then the procedure was repeated with this medium to obtain the required concentrations in the experiment, which are $0.3x10^8$

and $1.2x10^8$ spores/mL according to previous experiment with the bacteria *B. pasteurii* and *Pseudomonas aeruginosa* [17].

2.3. Concrete mixture proportions

For the production of concrete mix, the following materials were used: Portland cement, high early strength (CPV ARI, Brazilian denomination); fine aggregate: medium quartz sand; coarse aggregate: gravel 19 mm of basalt, water and *B. subtilis* spores dissolved in 0.85% of saline solution. The aggregates were characterized according to Brazilian standard [24].

The cement specifications and the requirements of NBR 5733 (Brazilian standard) [25] are presented in Table 1.

Mixture proportions are presented in Table 2. The mix proportions used were 1:1:2 and 1:2:3 (cement: sand: gravel), in mass, with water to cement ratio of 0.33 and 0.45, respectively. For each composition used, two treatments were made with the addition of *B. subtilis* spores to the mixing water in the concentration of $0.3x10^8$ and $1.2x10^8$ spores/mL. Besides, in the mixing water it was added 0.85% saline solution to maintain the medium isotonic for the bacteria.

The concrete mixture was performed in a vertical shaft mixer and bacteria concentrations were added to the mixing water.

For each treatment, six cylindrical specimens (100x200 mm) were made, being three for visual analysis of crack filling (n=3) over the curing time and the other three for the compressive strength test at 28 days (n=3). It should be noted that, for each mix compositions, reference specimens were made without bacterial spores, with 0.85% sodium chloride to ensure the same conditions as the specimens with spores.

Specimens were molded in 100x200 mm cylindrical samples according to NBR 5738/2015 (Brazilian standard) [26]. The specimens were demolded after 24 hours and stored in a dripping wet chamber at 20ºC ± 2ºC and relative humidity

Table 1.
Characteristics of cement CPV ARI (Brazilian denomination) and the requirements of NBR 5733 (1991).

Ages	Compressive strength (MPa)				Blaine(cm^2/g)	Cement setting	
	24 hours	3 days	7 days	28 days		Start (min)	End (min)
NBR 5733*	≥ 14	≥ 24	≥ 34	-	≥ 3000	≥ 60	≥600
CPV ARI	27	37	42	48	5330	160	265

Source: Brazilian standard [25].

Table 2.
Mixture proportions.

Mix proportions	w/c	Cement (g)	Sand (g)	Gravel (g)	Water (g)	NaCl (g)	Treatment (spores/mL)
1:1:2	0.33	5.750	5.750	11.500	1.900	16.15	0 $0.3x10^8$ $1.2x10^8$
1:2:3	0.45	3.860	7.710	11.560	1.740	14.79	0 $0.3x10^8$ $1.2x10^8$

Source: The authors.

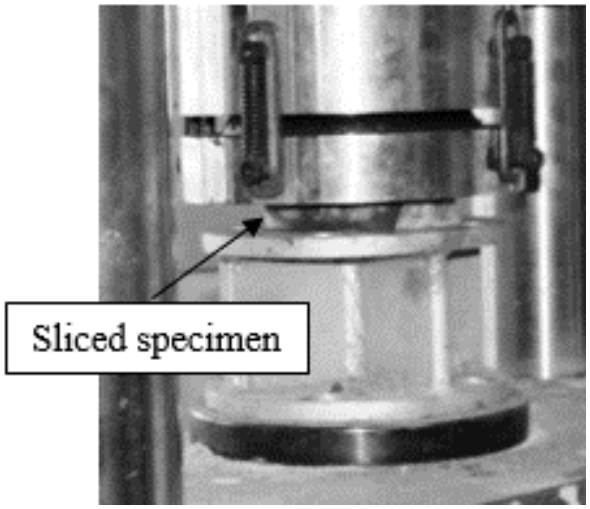


Figure 1. Cracking simulation.
Source: The authors.

greater than 95% until the test ages, which was 7 days for cracking, 8, 15, 22, 29, 36 and 43 days for the monitoring visual of crack filling, and 28 days for the compressive strength test.

2.4. Simulation and analysis of cracks

In order to evaluate the cracks filling by spores addition compared to reference, a 2 centimeters slice was extracted from each concrete (n=3). These slices were sent to the hydraulic press on the seventh day of healing to apply a strength to simulate a crack, as shown in Fig. 1.

The visual monitoring of cracks during the curing period, at 8, 15, 22, 29, 36 and 43 days, was conducted by images taken from an optical microscope with an attached camera (Olympus), with magnification of 100x. To ensure that the analysis was always held in the same position of the crack, it was demarcated. It is worth mentioning that from this method of cracking simulation it was not possible control it's thickness.

2.5. Compressive strength

The compressive strength test was performed with non cracked specimens of 100x200mm at the age of 28 days (n = 3) according to a NBR 5739/2007 (Brazilian denomination) [27].

2.6. Statistical design

A statistical analysis was performed only for the evaluation of compressive strength, from a completely randomized design experiment (CRD), in a 2x3 factorial scheme, consisting of two concrete mixtures (1:1:2 and 1:2:3) and three bacteria content (0, $0.3x10^8$ and $1.2x10^8$). In this statistical scheme, the two concrete mixtures were evaluated with all bacterial contents, with three replications.

For the statistical analysis, the software Sisvar was used to perform an analysis of variance [28].

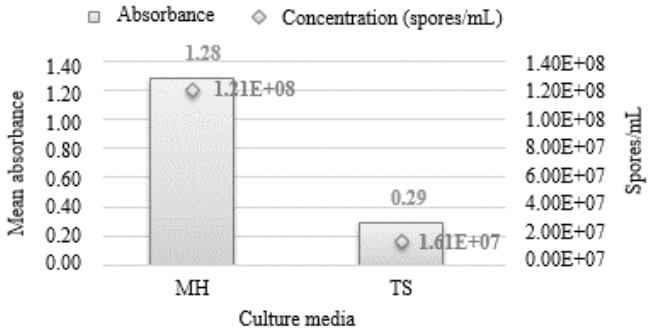


Figure 2. Mean absorbance and concentration of bacteria in each culture medium.
Source: The authors.

3. Results and discussion

3.1. Quantification of spores

From the two culture medium used in the experiment, the spores quantification of each medium was performed in accordance with Eq. 1., Fig. 2 shows the results of absorbance and concentration of spores/mL of culture media MH and TS.

Through the analysis of Fig. 3, it was observed a higher absorbance values and concentration of spores in the medium MH, of 1.28 and $1.21x10^8$ spores/mL, respectively, while under the same conditions, the medium TS presented, respectively, 0.29 and $1.61x10^7$ spores/mL. From this result, only the culture medium MH was selected for this experiment.

The reproduction procedure was repeated only with the medium MH, which presented the highest concentration of spores/mL, until it reached the concentrations of $1.2x10^8$ and $0.3x10^8$ spores/mL, which was quantified by spectrophotometer.

3.2. Characterization of aggregates

Sand was performed by Particle size analysis [24]. The results of these test were presented in Fig. 3.

The fine aggregate used was a medium sand. The particle size analysis is shown in Fig. 3. It was found that the grading curve is inside the limits established by NBR 7211/2009 (Brazilian standard) [29]. Analyzing the grading curve it should be noted that it has a continuous particle size, with desirable characteristic for use in cementitious materials due to the better packaging of the grains in the structure of the material. For the grading curve, it were calculated the maximum size, specific mass and unit mass. The values found were 2.36 mm, 2.62 g/cm³ and 1.57 g/cm³, respectively. Besides that, the gravel has maximum size of 19 mm.

3.3. Crack filling visual analysis

The visual analysis of crack filling was performed with one crack per specimen until 43 days of curing, being that three specimens of each concrete were analyzed (n=3). The images obtained from an optical microscope with attached camera are shown in Figs. 3 and 4.

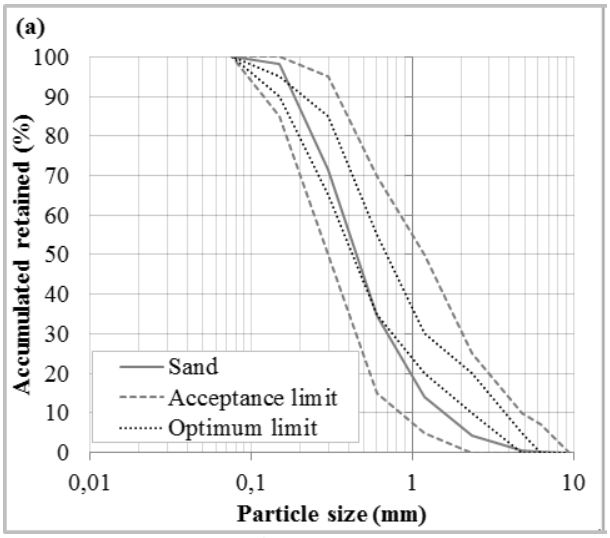


Figure 3. Particle size analysis of sand.
Source: The authors.

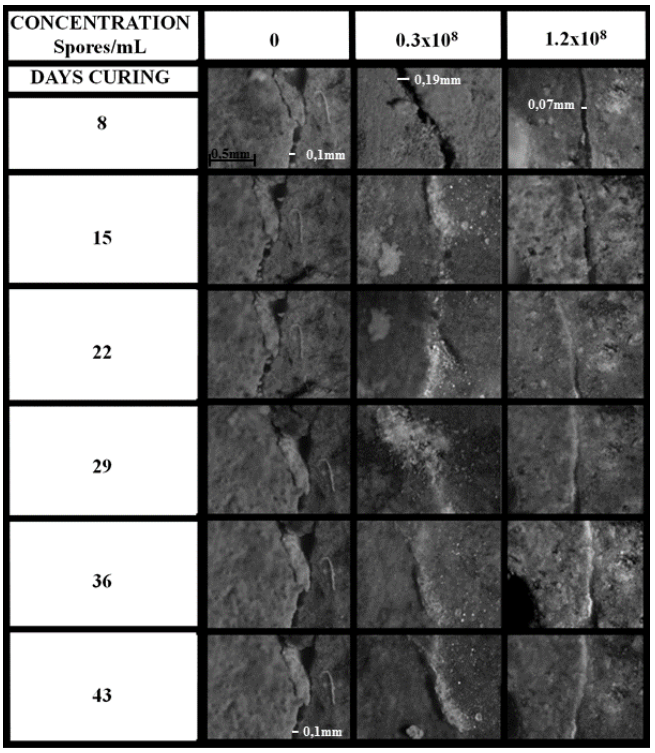


Figure 4. Visual monitoring of crack filling in the specimens of composition 1:1:2.
Source: The authors.

It can be seen that in all the compositions in which bacteria were added, there was a crystal precipitation from the 15th day on, possibly calcium carbonate ($CaCO_3$) according to literature [20,22,30-35]. Besides that, the same strain was used in another study [23] that performed an analysis in vitro of the bioprecipitation of calcium carbonate by pH change during biofilm formation. The authors found that the *B. subtilis* AP91 were able to precipitate crystals of $CaCO_3$ with the same morphology as other researches [11,36-40].

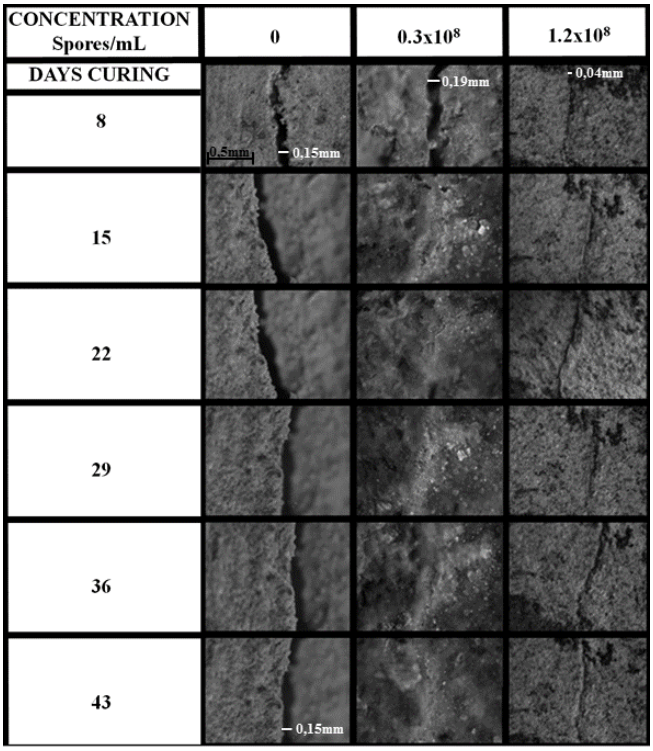


Figure 5. Monitoring the crack filling in the specimens of composition 1:2:3.
Source: The authors.

Other investigators conducted the studies in the same way, first studying whether the bacterium has the ability to precipitate $CaCO_3$ and in the sequence analyzing how that addition would behave in the cement matrix [9,41].

The filling of cracks up to 0.19 mm were visible in concretes with addition of spores of *B. subtilis*. However, in the samples without spores addition, precipitated material was not visible and the crack remained with the same feature throughout the curing period analyzed.

Although the cracks have different thickness sizes, it was visually found that in the concretes with addition of *B. subtilis* spores there was filling of the cracks by precipitation of crystals, even if the crack were of greater thickness compared to the reference concrete, without spores. Besides, in the reference concretes this filling was not visualized in this analysis. It is noteworthy that this analysis was just visual. To a better detailing a microstructural analysis would be necessary.

Fig. 6 shows the crystals formed by calcium carbonate precipitation promoted by the bacterium *B. alkalinitrilicus* added with a nutrient source and curing totally submerged under water for the healing regime [3]. It was observed that there was closure of the cracks from 0.13 to 0.40 mm thickness after 100 days of curing. Similar results were found in this research. Besides the above referenced authors, similar results using the bacterium B. sphaericus have been presented [18].

Thus, it was observed that the crystals precipitation promoted by the addition of *B. subtilis* spores under the conditions analyzed was visually satisfactory in crack filling. However, for more specific studies a microstructural analysis would be required.

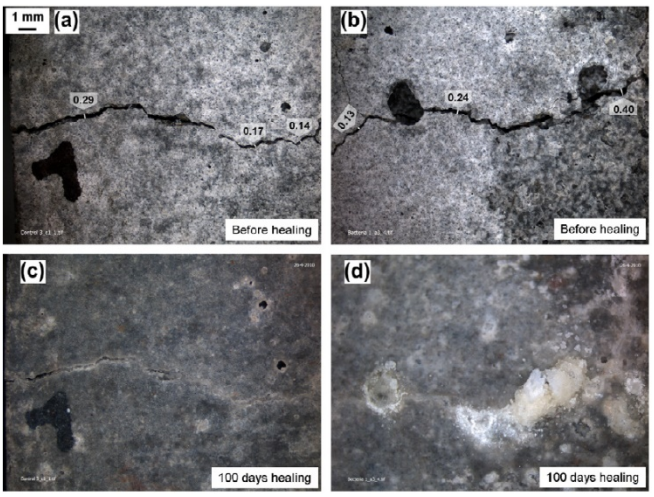


Figure 6. Stereomicroscopic images of crack-healing process in control mortar specimen before (a) and after 100 days healing (c), in bio-chemical agent-based specimen before (b) and after 100 days healing (d).
Source: [3].

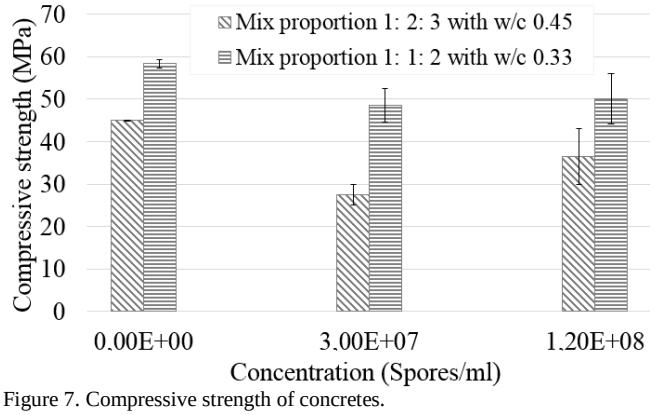


Figure 7. Compressive strength of concretes.
Source: The authors.

3.4. Compressive strength

The compressive strength test was performed on the 28th day of curing and the results are shown in Fig. 7. There was a difference in resistance between the compositions due to the proportions of materials used and the water/cement ratio (w/c), with higher resistance for the mix proportion 1:1:2 compared to w/c of 0.33 and without addition of bacteria, and the lowest resistance for the mix proportion 1:2:3 with w/c of 0.45.

Through the analysis of the results, it was noted that there was a decrease in the mean resistance of samples with added spores when compared to the reference. This decrease in the mix proportion 1:1:2 was of 20.06 and 16.58% for the treatments $0.3x10^8$ and $1.2x10^8$ spores/mL, respectively. For the mix proportion 1:2:3, the difference was greater, corresponding to 63.63 and 23.28% for the treatments $0.3x10^8$ and $1.2x10^8$ spores/mL.

There was an increase in the resistance of the samples with $1.2x10^8$ spores/mL compared to the ones with $3.0\ x10^7$ spores/mL in both mix proportions, demonstrating that the

amount of bacteria added to concrete influences the compression strength. However, it is necessary to test a larger number of bacteria concentrations for a better understanding. According to the literature [31], calcium hydroxide ($Ca(OH)_2$) is the most important source of calcium for concrete, but it does not alter mechanical resistance. On the other hand, calcium carbonate ($CaCO_3$) contributes to increase this resistance, which makes the bioprecipitation a positive contribution [31]. It should be noted that the crystals precipitated by bacteria in cementitious materials, calcium carbonate stand out [12, 20, 22-23, 30-35]. But, to confirm that the crystal precipitated by *B. subtilis* was calcium carbonate more studies need to be conducted, since this research is a preliminary test.

3.4.1. Statistical analysis

The statistical analysis was performed in Sisvar [28] and the results of analysis of variance are shown in Table 3. The sources of variation were the mix proportions of concrete and concentration of added spores, as well as the interaction of these two sources of variation.

There was a significant difference ($P < 0.05$) at 5% probability, for the parameter compressive strength in the variation of Mix proportion (M) and Spores Concentration (C), indicating that there are variations to compressive strength according to the concentration of spores added and to the mix proportion analyzed.

Table 4 presents the tests of means performed for the parameter compressive strength with variation of Mix proportion (M) and Table 5 present the test of means for the parameter Spores Concentration (C).

Table 3.
Mean squares and summary of the Analysis of Variance (ANOVA).

Sources of variation	Mean squares
Spores Concentration (C)	189.00 *
Mix proportion (M)	768.00 *
Interation (C x M)	19.51 ns
Residue	33.84

* Significant at 5% probability by the Fisher test; ns: non-significant
Source: The authors.

Table 4.
Tukey test for compressive strength with variation in mix proportion.

Mix proportion	Mean Square
1:2:3	38.050 a
1:1:2	43.275 b
DMS	8.218
CV (%)	13.120

Source: The authors.

Table 5.
Tukey test for compressive strength with the addition of *B. subtilis* spores

Spores concentration (spores/mL)	Mean Square
$0.3x10^8$	38.050 a
$1.2x10^8$	43.275 ab
0	51.675 b
DMS	12.617
CV (%)	13.120

Source: The authors.

It was noted that there were significant differences in compressive strength by varying both the concentration of spores added and the mix proportion. A significant difference between the compressive strengths of the two mix compositions were expected, since the w/c ratio is a factor directly related to it [6].

Regarding the addition of bacterial spores, it was observed that the lowest concentration of spores resulted in a minor compressive strength, significantly differing from the reference (without addition of spores). The concentration of $1.2x10^8$ spores/mL presented minor compressive strength than the reference; however, there was no significant difference between them.

Based on this analysis (Tukey test), it's possible that the addition of spores of *B. subtilis* could be used in concretes with these specific mix proportions without significant influences in compressive strength, nevertheless it is necessary more investigations about the use of this kind of material, since this study is a preliminary analysis.

4. Conclusion

From the experimental results, it was verified that there was a visual crack filling when the *B. subtilis* spores were added in two studied concentrations ($0.3x10^8$ and $1.2x10^8$ spores/mL). However the analysis by microscope with attached camera is just a visual analysis. To confirm that there was a closure of cracks a microstructural analysis would be necessary.

The addition of $0.3x10^8$ spores/mL resulted in a statistically significant decrease (at 5% probability) of the compressive strength of the specimens, while the addition of $1.2x10^8$ spores/mL did not present statistically significant differences when compared to the reference concrete. It possible happened because the highest concentration of spores was capable to produce more crystals that could increase the strength. Although further analysis need to be performed to confirm this theory.

Thus, these preliminary study has shown that the addition of *B. subtilis* spores isolated in Brazil to unarmored concrete could be beneficial and this practice should be developed in order to obtain a material capable of self-healing and consequently increase its lifetime. For this, further studies on the concentration of addition of these spores are required, as well as on the adding procedure, curing process and microstructural analysis.

Acknowledgements

The authors are grateful to Assis Gurgacz College, State University of Londrina and CNPQ for all financial support.

References

[1] Carmona Filho, A. and Carmona, T.G., Fissuração nas estruturas de concreto. Asociación Latinoamericana de Control de Calidad, Patología y Recuperación de la Construcción, Boletim Técnico. Revista ALCONPAT, 3, 2013.

[2] Koch, G.H., Brongers, M.P., Thompson, N.G., Virmani, Y.P. and Payer, J.H., Corrosion cost and preventive strategies in the United States (No. FHWA-RD-01-156), 2002.

[3] Wiktor, V. and Jonkers, H.M., Quantification of crack-healing in novel bacteria-based self-healing concrete. Cement & Concrete Composites, 33, pp. 763-770, 2011. DOI: 10.1016/j.cemconcomp.2011.03.012
[4] Gerilla, G.P., Teknomo, K. and Hokao, K., An environmental assessment of wood and steel reinforced concrete housing construction. Building and Environment, 42(7), pp. 2778-2784, 2007. DOI: 10.1016/j.buildenv.2006.07.021
[5] Worrell, E., Price, L., Martin, N., Hendriks, C. and Meida, L.O., Carbon dioxide emissions from the global cement industry. Energy Environ, 26(1), pp. 303-329. DOI: 10.1146/annurev.energy.26.1.303
[6] Mehta, P.K. and Monteiro, P.J.M., Concrete: microstructure, properties and materials. 2nd ed. Ibracon, São Paulo; 2014.
[7] Van Tittelboom, K., Gruyaert, E., Rahier, H. and De Belie, N., Influence of mix composition on the extent of autogenous crack healing by continued hydration or calcium carbonate formation. Construction and Building Materials, 37, pp. 349-359, 2012. DOI: 10.1016/j.conbuildmat.2012.07.026
[8] Jonkers, H.M., Thijssen, A., Muyzer, G., Copuroglu, O. and Schlangen, E., Application of bacteria as self-healing agent for the development of sustainable concrete. Ecological Engineering, 36(2), pp. 230-235, 2010. DOI: 10.1016/j.ecoleng.2008.12.036
[9] Barabesi, C., Galizzi, A., Mastromei, G., Rossi, M., Tamburini, E. and Perito, B., Bacillus subtilis gene cluster involved in calcium carbonate biomineralization. Journal of bacteriology, 189, pp. 228-235, 2007. DOI: 10.1128/JB.01450-06
[10] Alazhari, M., Sharma, T., Heath, A., Cooper, R. and Paine, K., Application of expanded perlite encapsulated bacteria and growth media for self-healing concrete. Construction and Building Materials, 160, pp. 610-619, 2018. DOI: 10.1016/j.conbuildmat.2017.11.086
[11] Park, S.J., Park, J.M., Kim, W.J. and Ghim, S.Y., Application of Bacillus subtilis 168 as a multifunctional agent for improvement of the durability of cement mortar. Journal of Microbiology and Biotechnology, 22, pp. 1568-1574, 2012.
[12] Stocks-Fischer, S., Galinat, J.K. and Bang, S.S., Microbiological precipitation of $CaCO_3$. Soil Biol. Biochem. 31(11), pp. 1563-1571, 1999. DOI: 10.1016/S0038-0717(99)00082-6.
[13] Bang, S.S., Galinat, J.K. and Ramakrishnan, V., Calcite precipitation induced by polyurethane-immobilized Bacillus pasteurii. Enzyme and microbial technology, 28(4), pp. 404-409, 2001. DOI: 10.1016/S0141-0229(00)00348-3
[14] Bachmeier, K.L., Williams, A.E., Warmington, J.R. and Bang, S.S. Urease activity in microbiologically-induced calcite precipitation. Journal of Biotechnology, 93(2), pp. 171-181, 2002. DOI: 10.1016/S0168-1656(01)00393-5
[15] Dick, J., De Windt, W., De Graef, B., Saveyn, H., Van Der Meeren, P., De Belie, N. and Verstraete, W., Bio-deposition of a calcium carbonate layer on degraded limestone by Bacillus species. Biodegradation, 17(4), pp. 357-367, 2006. DOI: 10.1007/s10532-005-9006-x
[16] Rodriguez-Navarro, C., Rodriguez-Gallego, M., Benchekroun, K. and Gonzalez-Munoz, M.T., Conservation of ornamental stone by Myxococcus xanthus-induced carbonate biomineralization. Applied and Environmental Microbiology, 69(4), pp. 2182-2193, 2003. DOI: 10.1128/AEM.69.4.2182-2193.2003
[17] Ramachandran, S.K., Ramakrishnan, V. and Bang, S.S., Remediation of concrete using microorganisms. ACI Materials Journal-American Concrete Institute, 98(1), pp. 3-9, 2001. DOI: 10.14359/10154
[18] De Muynck, W., Debrouwer, D., De Belie, N. and Verstraete, W., Bacterial carbonate precipitation improves the durability of cementitious materials. Cement and Concrete Research, 38(7), pp. 1005-1014, 2008. DOI: 10.1016/j.cemconres.2008.03.005
[19] Van Tittelboom, K., De Belie, N., De Muynck, W. and Verstraete, W., Use of bacteria to repair cracks in concrete. Cement and Concrete Research, 40, pp. 157-166, 2010. DOI: 10.1016/j.cemconres.2009.08.025
[20] Xu, J. and Yao, W., Multiscale mechanical quantification of self-healing concrete incorporating non-ureolytic bacteria-based healing agent. Cement and Concrete Research, 64, pp. 1-10, 2014. DOI: 10.1016/j.cemconres.2014.06.003
[21] De Koster, S.A.L., Mors, R.M., Nugteren, H.W., Jonkers, H.M., Meesters, G.M.H. and Van Ommen, J.R., Geopolymer coating of bacteria-containing granules for use in self-healing concrete. Procedia Engineering, 102, pp. 475-484, 2015. DOI: 10.1016/j.proeng.2015.01.193
[22] Luo, M., Qian, C.X. and Li, R.Y., Factors affecting crack repairing capacity of bacteria-based self-healing concrete. Construction and Building Materials, 87, pp. 1-7, 2015. DOI: 10.1016/j.conbuildmat.2015.03.117
[23] Schwantes-Cezario, N., Meideiros, L.P., De Oliveira Jr. A.G., Nakazato, G., Kobayashi, R.K.T. and Toralles, B.M., Bioprecipitation of calcium carbonate induced by Bacillus subtilis isolated in Brazil. International Biodeterioration & Biodegradation, 123, pp. 200-205, 2017. DOI: 10.1016/j.ibiod.2017.06.021
[24] Brazilian Standards NBR NM 248 – Agregados: determinação da composição granulométrica. ABNT, 2003.
[25] _____. NBR 5733 – Cimento Portland de alta resistência inicial. Rio de Janeiro: ABNT, 1991.
[26] _____. NBR 5738 – Concreto: procedimento para moldagem e cura de corpos de prova. ABNT, 2015.
[27] _____. NBR 5739 – Concreto: ensaio de compressão de corpos de prova cilíndricos. São Paulo: ABNT, 2007.
[28] Ferreira, D.F., Programa de análises estatísticas (Statistical analysis software) e planejamento de experimentos. Universidade Federal de Lavras, Brasil, 2003.
[29] Brazilian Standards NBR 7211 – Agregados para concreto – Especificação. Rio de Janeiro: ABNT, 2009.
[30] Abo-El-Enein, S.A., Ali, A.H., Talkhan, F.N. and Abdel-Gawwad, H.A., Application of microbial biocementation to improve the physico-mechanical properties of cement mortar. HBRC Journal, 9, pp. 36-40, 2013. DOI: 10.1016/j.hbrcj.2012.10.004
[31] Pei, R., Liu, J., Wang, S. and Yang, M., Use of bacterial cell walls to improve the mechanical performance of concrete. Cement and Concrete Composites, 39, pp. 122-130, 2013. DOI: 10.1016/j.cemconcomp.2013.03.024
[32] Schlangen, E. and Sangadji, S., Addressing infrastructure durability and sustainability by self healing mechanisms-Recent advances in self healing concrete and asphalt. Procedia Engineering, 54, pp. 39-57, 2013. DOI: 10.1016/j.proeng.2013.03.005
[33] Achal, V., Mukerjee, A. and Reddy, M.S., Biogenic treatment improves the durability and remediates the cracks of concrete structures. Construction and Building Materials, 48, pp. 1-5, 2013. DOI: 10.1016/j.conbuildmat.2013.06.061
[34] Chahal, N. and Siddique, R., Permeation properties of concrete made with fly ash and silica fume: influence of Ureolytic bacteria. Construction and Building Materials, 49, pp. 161-174, 2013. DOI: 10.1016/j.conbuildmat.2013.08.023
[35] Krishnapriya, S., Venkatesh-Babu, D.L. and Prince-Arulraj, G., Isolation and identification of bacteria to improve the strength of concrete. Microbiological Research, 174, pp. 48-55, 2015. DOI: 10.1016/j.micres.2015.03.009
[36] Schwantes-Cezario, N., Nogueira, G.S.F. and Toralles, B.M., Biocimentação de compósitos cimentícios mediante adição de esporos de B. subtilis AP91, 2017. Revista de Engenharia Civil IMED, 4(2), pp. 142-158. DOI: 10.18256/2358-6508.2017.v4i2.2072
[37] Hammes, F., Boon, N., De Villiers, J., Verstraete, W. and Siciliano, S.D., Strainspecific ureolytic microbial calcium carbonate precipitation. Appl. Environ. Microbiol, 69(8), pp. 4901-4909, 2003. DOI: 10.1128/AEM.69.8.4901-4909.2003.
[38] Braissant, O., Cailleau, G., Dupraz, C. and Verrecchia, E.P., Bacterially induced mineralization of calcium carbonate in terrestrial environments: the role of exopolysaccharides and amino acids. Journal of Sedimentary Research, 73(3), pp. 485-490, 2003. DOI: 10.1306/111302730485.
[39] Dupraz, S., Parmentier, M., Ménez, B. and Guyot, F., Experimental and numerical modeling of bacterially induced pH increase and calcite precipitation in saline aquifers. Chemical Geology, 265(1), pp. 44-53, 2009. DOI: 10.1016/j.chemgeo.2009. 05.003.
[40] Daskalakis, M.I., Rigas, F., Bakolas, A., Magoulas, A., Kotoulas, G., Katsikis, I. and Mavridou, A., Vaterite bio-precipitation induced by Bacillus pumilus isolated from a solutional cave in Paiania, Athens, Greece. International Biodeterioration & Biodegradation, 99, pp. 73-84, 2015. DOI: 10.1016/j.ibiod.2014.12.005.
[41] Perito, B., Marvasi, M., Barabesi, C., Mastromei, G., Bracci, S.,

Vendrell, M. and Tiano, P., A Bacillus subtilis cell fraction (BCF) inducing calcium carbonate precipitation: biotechnological perspectives for monumental stone reinforcement. Journal of Cultural Heritage, 15(4), pp. 345-351, 2014. DOI: 10.1016/j.culher.2013.10.001

N. Schwantes-Cezario, received the BSc. in Civil Engineering in 2015, the MSc. degree in Building Engineering and Sanitation in State University of Londrina, Brazil in 2016, and is a PhD student in Civil Engineering at State University of Londrina, Brazil.
ORCID: 0000-0002-3254-6396

M.V.N.N. Peres, received the BSc. in Civil Engineering in 2004, the MSc. degree in Structures in Federal University of Rio Grande do Sul, Brazil in 2008, and is a PhD. student in Structures by Federal University at Rio Grande do Sul, Brazil. Currently is a professor at Centro Universitário Fundação Assis Gurgacz (FAG), Brazil.
ORCID: 0000-0002-3986-3503

T.K. Fruet, received the degree in Biological Sciences in 2010, the MSc. degree in Conservation and management of natural resources in State University of Western Paraná in 2013 and is a PhD student in Biology at State University of Maringá, Brazil. Currently is a professor at Centro Universitário Fundação Assis Gurgacz (FAG), Brazil.
ORCID: 0000-0002-3521-600X

G.S.F. Nogueira, graduated in Civil Engineering in 2016 at the State University of Londrina, and is a MSc. degree student in Civil Engineering at State University of Londrina, Brazil.
ORCID: 0000-0002-7059-257X

B.M. Toralles, received the BSc. in Civil Engineering in 1982, the MSc. degree in Civil Engineering in Federal University of Rio Grande do Sul, Brazil in 1986, and the PhD degree in Enginyeria de Camins Canals i Ports - Universitat Politècnica de Catalunya - Barcelona Tech, Spain, in 1996 and PhD. in Universitat Politècnica de Catalunya, Spain, in 2013. Currently is an associate professor at the State University of Londrina, Brazil.
ORCID: 0000-0001-8828-7250

D.S. Cezario, received the BSc. in Mechanical Engineering in 2014 at the State University of São Paulo and post graduated in Labor Safety at the State University of Maringá, Brazil in 2017.
ORCID: 0000-0001-6137-731X

UNIVERSIDAD NACIONAL DE COLOMBIA
SEDE MEDELLÍN
FACULTAD DE MINAS

Área Curricular de Ingeniería Civil

Oferta de Posgrados

Especialización en Vías y Transportes
Especialización en Estructuras
Maestría en Ingeniería - Infraestructura y Sistemas de Transporte
Maestría en Ingeniería – Geotecnia
Doctorado en Ingeniería - Ingeniería Civil

Mayor información:

E-mail: asisacic_med@unal.edu.co
Teléfono: (57-4) 425 5172

UNIVERSIDAD NACIONAL DE COLOMBIA
SEDE MEDELLÍN
FACULTAD DE MINAS



DYNA
http://dyna.medellin.unal.edu.co/

Thermal conductivities estimation in orthotropic materials making use of global optimization algorithms

Jefferson Vega-Suarez, Edgar García-Morantes & Rodrigo Correa-Cely

Facultad de Fisicomecánicas, Universidad Industrial de Santander, Bucaramanga, Colombia. jefferson.vega@correo.uis.edu.co, edgar.garcia1@correo.uis.edu.co, crcorrea@uis.edu.co

Received: September 29th, 2017. Received in revised form: April 10th, 2018. Accepted: April 19th, 2018

Abstract
There are situations where the knowledge of thermodynamic properties such as thermal conductivity for the present case is required. In some of them an additional requirement appears, as the measurement has to be made along the three perpendicular space axes. In the present article, three thermal conductivities that appear in orthotropic materials were predicted by solving an inverse heat transfer problem. This inverse problem was solved using the Cuckoo algorithm, the deterministic Levenberg-Marquardt, and with the new hybrid of these two. It was found that these three strategies produce excellent results when compared to each other. Nevertheless, the hybrid algorithm proved to be more efficient than its precursors in solving the present problem. The hybrid algorithm consumed in average less computing time compared to the metaheuristic algorithm and extended the search range in comparison to the deterministic one, always maintaining precision in its results.

Keywords: inverse problem; optimization; Levenberg-Marquardt; cuckoo algorithm; thermal conductivity.

Estimación de conductividades térmicas en materiales ortotrópicos mediante algoritmos de optimización global

Resumen
Existen situaciones en donde se requiere el conocimiento de propiedades termodinámicas como la conductividad térmica para el presente caso. En algunas de ellas aparece una exigencia adicional, al tener que hacerse la medición a lo largo de los tres ejes espaciales perpendiculares. En el presente artículo, se propone predecir estas tres conductividades térmicas que aparecen en materiales ortotrópicos, mediante la solución de un problema inverso de transferencia de calor. El problema inverso se resolvió mediante el algoritmo Cuckoo, el determinístico de Levenberg-Marquardt, y con el nuevo híbrido entre estos dos. Se encontró que estas tres estrategias producen excelentes resultados al compararse entre ellas. Sin embargo, el algoritmo híbrido resultó ser más eficiente que sus precursores al resolver el presente problema. El algoritmo híbrido consumió en promedio menos tiempo de cómputo en comparación con el algoritmo metaheurístico y amplió el rango de búsqueda en comparación con el determinístico, manteniendo siempre precisión en sus resultados.

Palabras clave: problema inverso; optimización; Levenberg-Marquardt; algoritmo cuckoo; conductividad térmica.

1. Introduction

Despite the incredible development of electronics that in turn drives the creation of new analytical instrumentation for measurement purposes, it still turns out to be not only costly to perform certain measurements, but in some cases, an arduous task such as, for example, in the characterization of orthotropic materials, [1]. By definition, an orthotropic material is known as one in which its properties, whether for example mechanical or thermal, are unique and independent in their three perpendicular unitary spatial axes$(\hat{\imath};\hat{\jmath};\hat{k})$. That is, the magnitude of its properties or some of them depends on the direction in which it is measured. This characteristic imparts certain properties to the material that make it unique and is reserved for very specific applications. Examples of these are polycrystalline metals,

How to cite: Vega-Suarez, J., García-Morantes, E. and Correa-Cely, R., Thermal conductivities estimation in orthotropic materials making use of global optimization algorithms. DYNA, 85(205), pp. 140-147, June, 2018.

© The author; licensee Universidad Nacional de Colombia.

composite polymeric materials, graphite fibers, wood, among others. Given this property, it is very difficult in some situations to experimentally measure the variation of, for example, its electrical or thermal conductivity in those three coordinate axes. Therefore, there are some proposals in the literature to solve this difficulty, one of them being the approach and solution of an inverse problem that proved to be very effective in this situation, [2-5]. Regarding the approach and solution of the inverse problems, it is worth mentioning that its versatility and usefulness are well known in situations where experimentation is limited by obstacles such as high costs of the required instrumentation, and complexity in the realization and direct interpretation of its results, mainly. For the case presented in this article, the problem of heat transfer in a solid is a cause and effect relationship. The causes are determined by the initial conditions, the boundary conditions, the thermodynamic properties, the sources of internal generation and the geometry of the body. On the other hand, the effects are related to the profile of temperature and heat flow in the solid. Therefore, the inverse problem is a powerful conceptual tool that allows linking the mathematical model (cause) with the experimental data (effect). Moreover, this has allowed to address problems and propose solutions that were previously virtually impossible to obtain as, for example: the study of the interior of the earth without the need for expensive drilling, estimating heat transfer coefficients in highly aggressive processes for conventional instrumentation, such as the presence of high intensity electromagnetic fields, measure temperatures in inaccessible places even for the modern instrumentation that is available today, process complex images in astronomy, in computerized tomography for medical analysis, and in many others that it is impossible to number, [6-26]. In all these cases, the strategy used is to solve the problem directly analytically or numerically and solve the inverse problem associated with it. From an analysis of the literature on the subject, it can be seen that conventional methods of local optimization were initially used, such as, for example, the Levenberg-Marquardt method that requires knowing the derivatives of the objective situation function that requires the continuity of the function and stocks of these derivatives. Over time, global optimization strategies appeared that allow obtaining optimal values through a heuristic approach. Again, recent literature is abundant in examples of its use in the solution of inverse problems.

In the present article, the Cuckoo Search Algorithm (*ABC*) and the Levenberg-Marquardt (*LM*) Search Algorithm, as well as its hybrid (*HCLM*), are used to solve the inverse problem that concerns us. The main objective of this work is to estimate the thermal conductivity in an orthotropic material. A couple of numerical solutions are presented as an illustrative example of this strategy. This article summarizes below some relevant concepts about the mathematical model and its solution, together with the description of the optimization algorithms *ABC*, *LM* and *HCLM*. Then, the approach of the direct and inverse problem is presented. It is followed later, compiling the results of the simulations and finalized, with some of the most relevant conclusions.

2. Fundamentals

In this section the optimization algorithms are described very succinctly. In the same way, the objective of the direct problem is established. Then the mathematical model of the conduction heat transfer process that happens inside the solid and its analytical solution is stated. Then, the objective of the inverse problem is established. And in the final part, the objective function to be solved is defined.

2.1. Optimization algorithms

Global optimization is a part of mathematics aimed at finding the extremes of a function in its domain. Within this global optimization there is a generic classification related to the structure of the algorithms, which arbitrarily calls them deterministic and stochastic. In the first are those algorithms that for the same input necessarily produce the same output. In the second, it is characterized because its algorithms depend on randomness, that is, variables or stochastic (random) parameters are present within its components. The deterministic method (*LM*), the metaheuristic (*ABC*), and the hybrid of these two (*HCLM*), which were used, are described below.

2.1.1. Levenberg-Marquardt Method (*LM*)

The *LM* is a traditional deterministic algorithm, widely used to solve problems of non-linear characteristics. This method results from the combination of the gradient descent minimization and the Gauss-Newton methods [27]. In this algorithm, when the parameters are far from their optimal value, it acts more like the gradient minimization method. But when they are close to their optimal value, it acts more like the Gauss-Newton method, which makes it easier to determine the desired parameters. Given its wide dissemination in the literature [3], we will not go into greater detail here.

2.1.2. Cuckoo search algorithm (*ABC*)

This global optimization algorithm was proposed in 2009 by Xin-She Yang and Suash Deb [28], who relied on the behavior of the bird species, the cuckoos and their aggressive breeding strategy. This is related to the way in which these birds deposit their eggs in nests of other species. Such eggs will have a probability P_a of being discovered by the "host" birds and not survive. To increase this probability, some species of female cuckoos have managed to perfect the mimetization and posture of their eggs with those of the host species. For the selection of these nests, the cuckoos explore their surroundings using Lévy flights, that is, a small part of the new nests are generated around the best nest found so far. While the other part are generated far enough away from this to avoid being in a non-optimal nest. This algorithm is based on the following rules: The first one says that each cuckoo places one egg at a time and selects a random host nest where it will deposit it. The second says that the nests with the eggs in better quality, will pass to the next generation. And the third part of the assumption that the number of available host

Table 1.
ABC algorithm pseudocode.

Entrada	The objective function $f(x)$. Here $x = (x_1, \dots, x_d)^T$, and d is the dimension of the problem. The value of tolerance Tol; the probability of abandoning the worst nests P_a; and the number of nests n.
1:	Generate a population of host nests x_i, where $i = 1,2, \dots, n$.
2:	while ($F_i > Tol$)
3:	Get a cuckoo i randomly through the realization of the flights of Lévy.
4:	Evaluate the objective function of the nest F_i.
5:	Choose randomly a nest j (among the n nests)
6:	if ($F_i < F_j$)
7:	Replace j by the new solution.
8:	end if
9:	Leave a fraction (P_a) of the worst nests and build new nests to replace them in other locations through the flights of Lévy
10:	Keep the best nests
11:	Sort the nests and find the best.
12:	Move the best nest to the next generation.
13:	end while
14:	Establish the best nests and the best current F_i.

Source: The authors.

nests is fixed and that the host bird can discover the egg left by a cuckoo with a probability P_a (in the interval between [0, 1]). In this case, the host bird can throw the egg at a great distance or leave the nest in order to build a new one in another place. These abandoned nests are replaced by new nests (with new solutions in new random locations). Based on these three rules, the *ABC* steps are summarized in Table 1. From this table it can be seen that the algorithm requires few input parameters for its execution. These are, the objective function, the initial population n, the probability P_a and the search limits.

2.1.3. Hybrid algorithm (*HCLM*)

The proposed hybrid algorithm combines the main characteristic of *LM* (better precision) with that of *ABC* (greater search space), in order to design a global algorithm that adopts the qualities of its two individual components. This is because the *LM* is deterministic by nature and if it is provided with initial values sufficiently close to the optimum, it will always find it. On the other hand, *ABC* is random in nature and finds the optimum in a short time (repetitions), but there is a different success to failure relationship for each run. Thus, the *ABC* improves efficiency, as well as, accuracy and precision. Fig. 1 shows the behavior of the *HCLM*. It is emphasized that its topology (serial) is such that the best *ABC* results become the initial conditions of search for the *LM*.

2.2. Objective of the direct problem

Determine the transient internal temperature profile in the solid orthotropic material with a defined geometry (rectangular parallelepiped), which is initially at a uniform temperature $T_0 = 0$. A uniform heat flux is applied to the material in each of the surfaces for $x = a$, $y = b$ and $z = c$, in such a way that there is heat transfer by conduction to the interior of the latter. In addition, it is established that the other three surfaces are thermally insulated. The dimensionless mathematical model is presented in equation , (1) where, K_x, K_y and K_z are the respective components of the thermal conductivity in the directions of the unit Cartesian axes, [3]. T is the absolute temperature, t is the time and q_x, q_y and q_z are the uniform flows of heat of entry in each direction.

$$\begin{aligned}
K_x\frac{\partial^2 T}{\partial x^2}+K_y\frac{\partial^2 T}{\partial y^2}+K_z\frac{\partial^2 T}{\partial z^2}&=\frac{\partial T}{\partial t} && 0<x<a,\ 0<y<b,\ 0<z<c,\ t>0\\
-K_x\frac{\partial T(0,y,z,t)}{\partial x}&=q_x && 0<y<a,\ 0<z<c,\ t>0\\
\frac{\partial T(a,y,z,t)}{\partial x}&=0\\
-K_y\frac{\partial T(x,0,z,t)}{\partial x}&=q_y && 0<x<a,\ 0<z<c,\ t>0\\
\frac{\partial T(x,b,z,t)}{\partial x}&=0\\
-K_z\frac{\partial T(x,y,0,t)}{\partial x}&=q_z && 0<x<a,\ 0<y<b,\ t>0\\
\frac{\partial T(x,y,c,t)}{\partial x}&=0\\
T(x,y,z,0)&=0 && 0<x<a,\ 0<y<b,\ 0<z<c
\end{aligned} \tag{1}$$

To solve the direct problem, the three components of the thermal conductivity, the geometry of the solid and the initial and border conditions were assumed as known and with sufficient precision in their measurement. The solution of the direct problem, that is, of the mathematical model of the process, is shown in equation (2), [3].

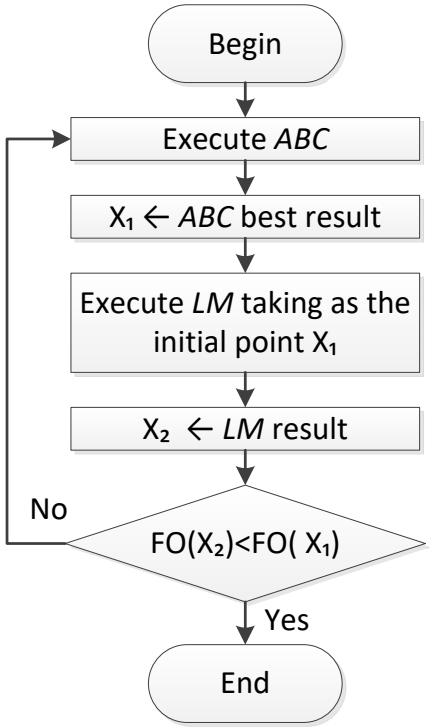


Figure 1. *HCLM* flowchart.
Source: The authors.

$$\mathrm{T}(x,y,z,t) = a\frac{q_x}{K_x}\gamma_x + b\frac{q_y}{K_y}\gamma_y + c\frac{q_z}{K_z}\gamma_z$$

Where,

$$\gamma_x = -\frac{1}{6} + \frac{x^2}{2a^2} + \frac{K_x t}{a^2} + \frac{2}{\pi^2}\sum_{i=1}^{\infty}\frac{(-1)^{i+1}}{i^2}\cos\left(\frac{i\pi x}{a}\right)e^{-\pi^2\frac{K_x t}{a^2}i^2}$$

$$\gamma_y = -\frac{1}{6} + \frac{y^2}{2b^2} + \frac{K_y t}{b^2} + \frac{2}{\pi^2}\sum_{i=1}^{\infty}\frac{(-1)^{i+1}}{i^2}\cos\left(\frac{i\pi y}{b}\right)e^{-\pi^2\frac{K_y t}{b^2}i^2} \quad (2)$$

$$\gamma_z = -\frac{1}{6} + \frac{z^2}{2c^2} + \frac{K_z t}{c^2} + \frac{2}{\pi^2}\sum_{i=1}^{\infty}\frac{(-1)^{i+1}}{i^2}\cos\left(\frac{i\pi z}{c}\right)e^{-\pi^2\frac{K_z t}{c^2}i^2}$$

2.3. Objective of the inverse problem

To determine the coefficients of the three thermal conductivities K_x, K_y and K_z, in an orthotropic material with defined geometry (rectangular parallelepiped), assuming known the measured temperature profile within the solid, together with the other parameters of the model, all of them with sufficient precision. To estimate these coefficients, the aforementioned global optimization algorithms were used.

2.4. Objective function

The objective function is the standard L2 squared which is shown in equation (3), where Y are the measured temperatures, and T is the temperature estimated by the model of equation (2). In this work two options were taken as measured temperatures. The first was simply to take the theoretical temperature profile which is obtained by solving the direct problem. On the other hand, the second option was to add Gaussian noise to the theoretical temperature profile to emulate possible sensor errors in the measurement.

$$OF(K_x,K_y,K_z) = \left(Y - T(K_x,K_y,K_z)\right)'\left(Y - T(K_x,K_y,K_z)\right)$$
$$K_x^*, K_y^*, K_z^* = \underset{K_x,K_y,K_z}{\operatorname{argmin}}\, OF(K_x,K_y,K_z) \quad (3)$$

Restricted to

$$K_x, K_y, K_z > 0$$

3. Results and analysis

In this section, some of the results are first shown using the *ABC* algorithm in preliminary tests, then, the conductivities of an orthotropic material are found using the *LM*, *ABC* and *HCLM* algorithms and finally an analysis of the obtained results is made.

3.1. Preliminary tests with the ABC algorithm

In this part, two tests were performed on the *ABC* algorithm. In the first, classic global optimization functions were used in order to verify the correct functioning of the algorithm and in the second, the objective function defined in equation (3) was used to see how it behaves before a spectrum of values of the thermal conductivity.

Table 2.
Hardware specifications.

Manufacturer	Toshiba
Model	Satellite L45-B
Processor	Intel® Core TM i5-5200U
RAM	6 [GB]
Operative system	Microsoft® Windows TM10 64- bit

Source: The authors.

Table 3.
Results obtained by applying the *ABC* algorithm to the test functions.

D	FO	n	Best	Worst	Std. Dev.	Mean FO_{min}	Mean Iter.	Mean time. [s]
2	a)	5	0.000	1.989	0.597	0.139	6988	0.124
		25	0.000	0.000	0.000	0.000	31954	0.365
		50	0.000	0.000	0.000	0.000	62836	0.658
	b)	5	0.000	0.000	0.000	0.000	5535	0.095
		25	0.000	0.000	0.000	0.000	26792	0.293
		50	0.000	0.000	0.000	0.000	53070	0.541
	c)	5	0.000	-4.440	0.002	0.001	6720	0.130
		25	0.000	0.000	0.000	0.000	29486	0.397
		50	0.000	0.000	0.000	0.000	57294	0.675
3	a)	5	0.000	1.989	0.729	0.318	8486	0.150
		25	0.000	0.000	0.000	0.000	40359	0.453
		50	0.000	0.000	0.000	0.000	80156	0.856
	b)	5	0.000	0.000	0.000	0.000	5864	0.102
		25	0.000	0.000	0.000	0.000	28208	0.337
		50	0.000	0.000	0.000	0.000	56246	0.576
	c)	5	0.000	-5.440	0.003	0.003	8094	0.166
		25	0.000	0.004	0.000	0.000	34794	0.462
		50	0.000	0.001	0.000	0.000	67972	0.831

Source: The authors.

3.1.1. Test functions

This section shows the verification of the *ABC* algorithm through the solution of classic optimization functions (FO) such as a) Rastrigin, b) De Jong and c) Griewank. To do this, an algorithm analysis was performed with different population sizes (i.e., n = 5, 25 y 50) in two and three dimensions (D). Each configuration was executed 50 times. The specifications of the computer used to perform the tests are shown in Table 2.

The results obtained such as the best solution, the worst, the standard deviation of the solutions, the average value of the objective function, the average iterations used by the algorithm and the computational time of execution, are shown in Table 3. From this, it can be seen that increasing the population improves the search results. However, the use of computational resources also increases.

3.1.2. Objective function

In this section, preliminary tests of the algorithm with the objective function were performed. For this, the temperature profiles were found by varying the components (K_x, K_y, K_z) (the other parameters of equation (2) are shown below in Table 5). Then, the algorithm *ABC* was executed by varying the population of cuckoos (n = 5 y n = 10). These results are summarized in Table 4, which includes parameters such as

Table 4.
Results of the algorithm varying the population of cuckoos and the conductivities.

K (K_x, K_y, K_z)	Search Lim. [L_{inf}, L_{sup}]	n	FO_{min}	Std. Dev.	Hits/ Misses	Mean Iter.	Mean time [s]
(1500, 1700, 2000)	[0.1, 3000]	5	0.000	0.000	30/20	5125	26.7
		10	0.000	0.000	28/22	10165	55.3
(500, 600, 700)	[0.1, 1000]	5	0.000	0.000	31/19	5174	26.2
		10	0.000	0.000	36/14	10217	59.7
(50, 60, 70)	[0.1, 100]	5	0.001	0.001	30/20	7037	38.3
		10	0.000	0.000	42/8	10896	82.4
(0.1, 0.2, 0.3)	[0.01, 100]	5	0.000	0.000	50/0	6776	43.1
		10	0.000	0.000	50/0	14964	111.7
(0.01, 0.02, 0.03)	[0.001, 100]	5	0.000	0.000	42/8	6593	40.7
		10	0.000	0.000	41/9	14507	89.8

Source: The authors.

the search limits, the minimum value of the objective function, its standard deviation, the number of hits and misses, the average of iterations and the average execution time of the *ABC* algorithm. The criterion for selecting the correct and incorrect results was directly related to the search range used to find the thermal conductivities and therefore was not fixed during all the tests.

This table shows a hit rate of more than 82% for values of thermal conductivity less than 50. On the contrary, when increasing this conductivity value the hit rate starts to deteriorate up to 56%. A slight improvement in the results is also observed when increasing the population of cuckoos in the algorithm. These results demonstrate the need to combine stochastic and deterministic algorithms, generating *hybrids* that highlight the positive characteristics of each of their predecessors, as discussed below.

3.2. Estimation of thermal conductivities

Next, the behavior of the three algorithms for different situations will be analyzed. For this, the results obtained by finding the thermal conductivities are compared by solving the inverse problem, using *ABC*, *HCLM* and the *LM* method. In the first case the values of the thermal conductivities proposed in [3] (K_x = 1, K_y = 2 y K_z = 3). Moreover, in the second case, the thermal conductivities for crystalline silicon proposed in [30] (K_x = 1.3, K_y = 1.46, y K_z = 1.78) will be taken. This element was chosen since it is widely used in the development of elements in electronic engineering such as transistors and solar cells. The other parameters of equation (2) are shown in Table 5.

Fig. 2 shows the theoretical temperature profile of the sensor located in (0.004,0.004,0.004) for the case 1 as well as the temperature profile for different signal-to-noise ratios (SNR) (i.e., 30, 40 y 50 [dB]). The graph of the other case was omitted because it is very similar to the one shown. On the other hand, white Gaussian noise was added to the theoretical temperature profile in order to simulate real temperature profiles for cases 1 and 2. According to preliminary results, a SNR of 30 [dB] was defined as the amount of noise minimum allowed to simulate because values below this distort the signal too much.

Table 5.
Parameter values to simulate the equation (2).

Parameter	Name	Value
$\begin{pmatrix} q_x, \\ q_y, \\ q_z \end{pmatrix}$	Heat flux	$\begin{pmatrix} 1, \\ 1, \\ 1 \end{pmatrix}$
$\begin{pmatrix} a, \\ b, \\ c \end{pmatrix}$	Dimensions of the parallelepiped	$\begin{pmatrix} 0.01, \\ 0.01, \\ 0.01 \end{pmatrix}$
$\begin{pmatrix} x, \\ y, \\ z \end{pmatrix}$	Location of the sensors	$\begin{pmatrix} 0.004, \\ 0.004, \\ 0.004 \end{pmatrix}$

Source: The authors.

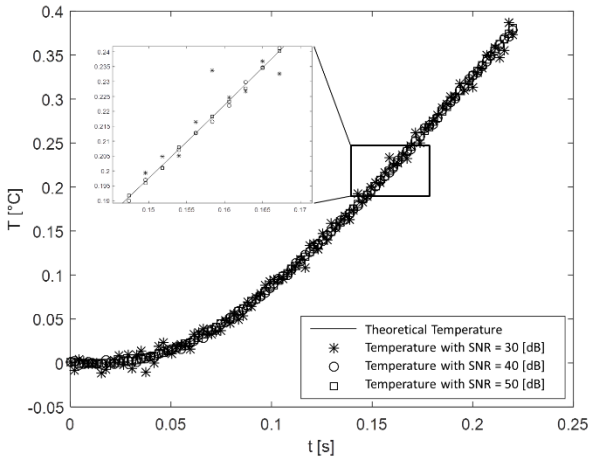


Figure 2. Theoretical and measured temperature profile with SNR = 30, 40 y 50 [dB].
Source: The authors.

3.2.1. Results of the Levenberg-Marquardt method (*LM*)

To apply the *LM* method, preliminary tests were done to find the limits of the initial conditions where it converged and then proceeded to perform the particular tests in each case. As mentioned above, the *LM* is deterministic so it converges to the same point, as long as the initial conditions are the same. Due to this property, the algorithm was executed once.
Case 1

Table 6 shows results such as the estimated parameters and the percentage of error obtained by the *LM* method, as well as the initial search points, the number of iterations and the execution time used. On the other hand, from this table you can see the limited search range to find the thermal conductivities. This evidences a great disadvantage of the *LM* if some information of the required parameters is not known.
Case 2

Table 7 shows results such as the estimated parameters and the percentage of error obtained by the *LM* method, as well as the initial search points, the number of iterations and the execution time used. Now, from the results it can be seen that by increasing the noise level (decreasing the SNR), errors increase. This is due to the low quality of the data at small SNR. On the other hand, it is important to note that just as in case 1, there is a limited search range to find the thermal conductivities and that, in addition, this range suffers a reduction compared to case 1 because the thermal conductivities to be found have a greater proximity between them.

Table 6.
Results obtained by applying the *LM* method to the *case 1*.

SNR	Initial search point	Estimated parameters	Error %	Iter.	Time [s]
∞	[0.3, 1.3, 2.6]	[0.989, 2.064, 2.924]	[1.10, 3.20, 2.53]	68	2.02
	[1.8, 2.6, 3.6]	[1.001, 1.920, 3.119]	[0.10, 4.00, 3.97]	130	3.67
50	[0.2, 1.0, 2.7]	[0.981, 2.092, 2.906]	[1.90, 4.60, 3.13]	88	2.45
	[1.5, 2.3, 3.3]	[1.008, 1.949, 3.078]	[0.80, 2.55, 2.60]	99	2.81
40	[0.4, 1.5, 2.6]	[0.961, 2.130, 2.904]	[3.90, 6.50, 3.20]	110	3.08
	[1.6, 2.3, 3.3]	[1.023, 1.919, 3.071]	[2.30, 4.05, 2.37]	45	1.39
30	[0.8, 1.8, 2.8]	[0.992, 2.059, 2.978]	[0.08, 2.95, 0.73]	52	1.59
	[1.6, 2.2, 3.3]	[1.014, 1.957, 3.071]	[1.40, 2.15, 2.37]	80	2.38

Source: The authors.

Table 7.
Results obtained by applying the *LM* method to the *case 2*.

SNR	Initial search point	Estimated parameters	Error %	Iter.	Time [s]
∞	[1.27, 1.41, 1.72]	[1.308, 1.456, 1.774]	[0.62, 0.27, 0.34]	131	3.46
	[1.33, 1.48, 1.80]	[1.303, 1.456, 1.781]	[0.23, 0.27, 0.06]	119	3.19
50	[1.25, 1.40, 1.70]	[1.318, 1.463, 1.754]	[1.39, 0.21, 1.46]	18	0.69
	[1.34, 1.49, 1.80]	[1.306, 1.459, 1.774]	[0.46, 0.07, 0.34]	12	0.53
40	[1.20, 1.40, 1.70]	[1.291, 1.482, 1.769]	[0.69, 1.51, 0.62]	11	0.51
	[1.40, 1.50, 1.80]	[1.339, 1.442, 1.751]	[3.00, 1.23, 1.63]	17	0.65
30	[1.20, 1.40, 1.70]	[1.288, 1.480, 1.768]	[0.92, 1.37, 0.67]	14	0.60
	[1.40, 1.50, 1.80]	[1.341, 1.437, 1.751]	[3.15, 1.58, 1.63]	14	0.61

Source: The authors.

3.2.2. Results with the cuckoo search algorithm

As indicated in section 3.1, the *ABC* presents a good performance with a population of cuckoos equal to or greater than five ($n \geq 5$). Therefore, that population size of cuckoos was chosen to implement the algorithm. To verify the reliability of the results, the tests were repeated 50 times.

Case 1

Table 8 shows the results such as the minimum value of the objective function, its standard deviation, the number of hits and misses, the average of iterations and the average execution time of the *ABC* algorithm. On the other hand, an acceptable performance can be observed in the rate of successes and failures for the four tests carried out. As expected, when the perturbations increase (decrease the SNR) in the temperature profile, the *ABC* begins to lose precision in the results. It is important to note that those estimated values that differed with the expected values in 0.5 were considered correct and that the search range for each variable is in the range of 0.1 to 100.

Case 2

Table 9 shows the results such as the minimum value of the function objective, its standard deviation, the number of hits and misses, the average of iterations and the average execution time of the *ABC* algorithm. As in the previous case, when the perturbations increase, the algorithm deteriorates in the results. It is important to highlight that those estimated values that differed with the expected values in 0.2 were considered correct and that the search range for each variable is in the range of 0.1 to 100.

3.2.3. Results with the hybrid method (*HCLM*)

For the hybrid method, the same parameters were used of the *ABC* and the first two cases were analyzed.

Case 1

Table 10 shows the results such as the minimum value of the objective function, its standard deviation, the number of hits and misses, the average iterations and the average execution time of the algorithm *HCLM*. It is important to note that those estimated values that differed with the expected values in 0.5 were considered to be correct. On the other hand, the search range was performed in the range of 0.1 to 100 of each variable. Now, from this table it can be seen that the success rate improves compared to the *ABC* by 12% if the worst results are compared, which indicates a greater precision of the method to find the required variables. Finally, there is a slight decrease in the execution time, as well as the iterations used if compared with the ABC.

Table 8.
Results of the *ABC* algorithm for the *case 1*.

SNR	FO_{min}	Std. Dev.	Hits/ Misses	Mean Iter.	Mean Time[s]
∞	0.004	0.007	43/7	14644	81.0
50	0.047	0.002	41/9	11353	63.0
40	0.123	0.001	39/11	9106	51.3
30	0.501	0.001	34/16	8707	64.0

Source: The authors.

Table 9.
Results of the *ABC* algorithm for the *case 2*.

SNR	FO_{min}	Std. Dev.	Hits/ Misses	Mean Iter.	Mean Time[s]
∞	0.000	0.000	44/6	9373	53.5
50	0.038	0.000	40/10	9022	51.2
40	0.125	0.000	36/14	8627	48.9
30	0.343	0.000	29/21	8171	46.3

Source: The authors.

Table 10.
Results of the hybrid algorithm for the *case 1*.

SNR	FO_{min}	Std. Dev.	Hits/ Misses	Mean Iter.	Mean Time[s]
∞	0.000	0.000	50/0	11725	65.8
50	0.047	0.006	46/4	9800	54.1
40	0.124	0.004	42/8	10298	58.0
30	0.501	0.003	40/10	8860	49.7

Source: The authors.

Table 11.
Results of the hybrid algorithm for the *case 2*.

SNR	FO_{min}	Std. Dev.	Hits/ Misses	Mean Iter.	Mean Time[s]
∞	0.000	0.000	50/0	9401	52.5
50	0.038	0.000	40/10	8881	49.0
40	0.125	0.000	32/18	7423	42.9
30	0.412	0.000	28/22	10049	57.7

Source: The authors.

Case 2

Table 11 shows the results such as the minimum value of the objective function, its standard deviation, the number of hits and misses, the average of iterations and the average execution time of the *HCLM* algorithm. In this, it can be seen that the success rate improves slightly with respect to the results obtained in case 2 with ABC. We consider that this is due to the noise level of the data used to solve the inverse problem, which does not allow the desired parameters to be reached. Finally, a similar behavior is observed both in the time of convergence and in the number of iterations, in the previous case.

Finally, from the simulations carried out, it can be seen from Tables 6, 8 and 10, that the time of convergence of *LM* was lower compared to the other two algorithms (*ABC* and *HCLM*). One of the factors that influenced this was the search range, since being higher for *ABC* and *HCLM* (between 0.1 to 100) compared to *LM* (0.2 to 3.6), it required more iterations and therefore more computation time. On the other hand, it is observed that the *HCLM* presents in general a lower number of iterations in comparison with the *ABC*. This is mainly due to the nature of the hybrid algorithm that takes advantage of the fact that *ABC* provides *LM* (as seen in Fig. 1) an optimal starting point, so it does not require many additional iterations to find the optimal global. Similarly, it stands out from Tables 7, 9 and 11, as in the first case, the time of convergence of *LM* was lower compared to the other two algorithms (*ABC* and *HCLM*). This was mainly due to the search range, since being higher for *ABC* and *HCLM* (between 0.1 to 100) compared to *LM* (1.2 to 1.8), it required more iterations and therefore more computational time.

4. Conclusions

This article describes an alternative way of estimating properties such as thermal conductivity in orthotropic materials. For this, the mathematical model that defines the internal temperature profile was used, when the material is subjected to a conduction heat transfer process. Next, the respective inverse problem was defined, which was solved by the cuckoo search algorithm, the Levenberg-Marquardt method and a new hybrid of the latter two. When contrasting the results of the simulations with these three algorithms, it was found that all were able to find the solution, that is, the thermal conductivities for the three orthogonal directions. However, the hybrid has a lower number of iterations and in some cases better execution time when compared to the *ABC*. We believe that this is due to the presence of the *LM*. On the other hand, when compared with both, the hybrid algorithm presented a better performance in terms of execution time and number of iterations in most cases. In addition, the solutions turned out to be more precise, even though the search rank was equal to the *ABC*. Similarly, it was observed that the consumption of computational resources is lower in the *LM* algorithm. Remember that this traditional deterministic method has the limitation of having to know in advance a region close to the optimal solution, or the probability of not finding it will increase markedly. Thus, we can conclude that for the problem addressed in this work, it is very advantageous to use the new hybrid *HCLM* algorithm. It is important to highlight that the *HCLM* can be applied in other fields of engineering as long as the objective function is defined. Readers who wish to follow this methodology, should perform preliminary tests to choose the internal parameters of the algorithm according to each particular application, to obtain better results.

References

[1] Abad, B.D., Borca-Tasciuc, A. and Martin-Gonzalez, M.S., Non-contact methods for thermal properties measurement, Renew. Sustain. Energy Rev., 76, pp. 1348-1370, 2017. DOI: /10.1016/j.rser.2017.03.027

[2] Adamczyk, W., Białecki, R. and Kruczek, T., Retrieving thermal conductivities of isotropic and orthotropic materials, Appl. Math. Model., 40(4), pp. 3410-3421, 2016. DOI: /10.1016/j.apm.2015.10.028

[3] Ozisik, M.N., Inverse heat transfer, Illustrate. CRC Press, 2000, 2000.

[4] Aslak-Tveito, H.P., Langtangen, B.F., Nielsen and Cai, X., Elements of scientific computing. Springer-Verlag Berlin, 2010.

[5] Alifanov, O.M., Inverse heat transfer problems, 1st ed. Springer-Verlag Berlin Heidelberg, 1994.

[6] Berntsson, F., Lin, C., Xu, T. and Wokiyi, D., An efficient regularization method for a large scale ill-posed geothermal problem, Comput. Geosci., 105, pp. 1-9, 2017. DOI: /10.1016/j.cageo.2017.04.010

[7] Zhuo, S., Yi, L. and Meng, F., An inverse method for the estimation of a long-duration surface heat flux on a finite solid, Int. J. Heat Mass Transf., 106, pp. 1087-1096, 2017. DOI: /10.1016/j.ijheatmasstransfer.2016.10.085

[8] Ramallo-González, A.P., Brown, M., Gabe-Thomas, E., Lovett, T. and Coley, D.A., The reliability of inverse modelling for the wide scale characterization of the thermal properties of buildings, J. Build. Perform. Simul., pp. 1-19, 2017. DOI: /10.1080/19401493.2016.1273390

[9] Nenarokomov, A.V., Dombrovsky, L.A., Krainova, I.V., Alifanov, O.M. and Budnik, S.A., Identification of radiative heat transfer parameters in multilayer thermal insulation of spacecraft, Int. J. Numer. Methods Heat Fluid Flow, 27(3), pp. 598-614, 2017. DOI: /10.1108/HFF-03-2016-0136

[10] Belayachi, N., Do, D.-P. and Hoxha, D., Transverse thermal conductivity estimation of vegetable fibers from inverse identification, Poromechanics 2017 - Proc. 6th Biot Conf. Poromechanics, pp. 1258-1265, 2017. DOI: /10.1061/9780784480779.156

[11] Chanda, G.R., Balaji, S., Venkateshan, C. and Yenni, S.P., Estimation of principal thermal conductivities of layered honeycomb composites

using ANN-GA based inverse technique, Int. J. Therm. Sci.(111), pp. 423-436, 2017. DOI: 10.1016/j.ijthermalsci.2016.09.011
[12] Reddy, S. and Somasundharam, K.S., An inverse method for simultaneous estimation of thermal properties of orthotropic materials using Gaussian process regression, J. Phys. Conf. Ser., 745(3), 2016. DOI: 10.1088/1742-6596/745/3/032090
[13] Czajkowski, Ł., Olek, W., Weres, J. and Guzenda, R., Thermal properties of wood-based panels: thermal conductivity identification with inverse modeling, Eur. J. Wood Wood Prod., 74(4), pp. 577-584, 2016. DOI: 10.1007/s00107-016-1021-6
[14] Adili, A., Lachheb, M., Brayek, A., Guizani, A. and Ben Nasrallah, S., Estimation of thermophysical properties of lightweight mortars made of wood shavings and expanded polystyrene beads using a hybrid algorithm, Energy Build., 118, pp. 133-141, 2016. DOI: 10.1016/j.enbuild.2016.02.039
[15] Cascone, Y. and Perino, M., Estimation of the thermal properties of PCMs through inverse modelling, Energy Procedia, 78, pp. 1714-1719, 2015. DOI: 10.1016/j.egypro.2015.11.275
[16] Cui, M., Zhao, Y., Xu, B., Wang, S. and Gao, X., Inverse analysis for simultaneously estimating multi-parameters of temperature-dependent thermal conductivities of an Inconel in a reusable metallic thermal protection system, Appl. Therm. Eng., 2017. DOI: 10.1016/j.applthermaleng.2017.06.113
[17] Mohebbi, T., Sellier, F. and Rabczuk, M., Estimation of linearly temperature-dependent thermal conductivity using an inverse analysis, Int. J. Therm. Sci. (117), pp. 68-76, 2017. DOI: 10.1016/j.ijthermalsci.2017.03.016
[18] Liu, H., Xia, X., Xie, X., Ai, Q. and Li, D., Experiment and identification of thermal conductivity and extinction coefficient of silica aerogel composite, Int. J. Therm. Sci. (121), pp. 192-203, 2017. DOI: 10.1016/j.ijthermalsci.2017.07.014
[19] Hafid, M. and Lacroix, M., Fast inverse prediction of the freezing front in cryosurgery, J. Therm. Biol. (69), pp. 13-22, 2017. DOI: 10.1016/j.jtherbio.2017.05.008
[20] Mayeli, P., Nili-Ahmadabadi, M., Pirzadeh, M. and Rahmani, P., Determination of desired geometry by a novel extension of ball spine algorithm inverse method to conjugate heat transfer problems, Comput. Fluids. (154), pp. 390-406, 2017. DOI: 10.1016/j.compfluid.2016.05.022
[21] Huntul, M.J. and Lesnic, D., An inverse problem of finding the time-dependent thermal conductivity from boundary data, Int. Commun. Heat Mass Transf. (85), pp. 147-154, 2017. DOI: 10.1016/j.icheatmasstransfer.2017.05.009
[22] Reddy, S.R., Dulikravich, G.S. and Zeidi, S.M.J., Non-destructive estimation of spatially varying thermal conductivity in 3D objects using boundary thermal measurements, Int. J. Therm. Sci. (118), pp. 488-496, 2017. DOI: 10.1016/j.ijthermalsci.2017.05.011
[23] Su, J., Chen, X., Li, Y., Pons, M. and Blanquet, E., A niching genetic algorithm applied to optimize a SiC-bulk crystal growth system, J. Cryst. Growth. (468), pp. 914-918, 2017. DOI: 10.1016/j.jcrysgro.2016.10.061
[24] Cheng, L., Yue, K., Wang, J. and Zhang, X., A small-plane heat source method for measuring the thermal conductivities of anisotropic materials, Meas. Sci. Technol., 28(7), 2017. DOI: 10.1088/1361-6501/aa6e81
[25] Ohmichi, M., Noda, N. and Sumi, N., Plane heat conduction problems in functionally graded orthotropic materials, J. Therm. Stress., 40(6), pp. 747-764, 2017. DOI: 10.1080/01495739.2016.1249989
[26] Mohebbi, F., Sellier, M. and Rabczuk, T., Inverse problem of simultaneously estimating the thermal conductivity and boundary shape, Int. J. Comput. Methods Eng. Sci. Mech., 18(2-3), pp. 166-181, 2017. DOI: 10.1080/15502287.2017.1303006
[27] Marquardt, D., An algorithm for least-squares estimation of nonlinear parameters, J. Soc. Ind. Appl. Math., 11(2), pp. 431-441, 1963. DOI: 10.1137/0111030
[28] Yang, X.-S. and Deb, S., Cuckoo search via Lévy flights, Proc. World Congr. Nat. \& Biol. Inspired Comput. (NaBIC 2009), pp. 210-21, 2009. DOI: 10.1109/NABIC.2009.5393690
[29] Sanz, S.S., Modern meta-heuristics based on nonlinear physics processes: A review of models and design procedures, Phys. Rep., 655, pp. 1-70, 2016. DOI: 10.1016/j.physrep.2016.08.001
[30] J.X. y Wingert, R.C.M.C., Kwon, S., Hu, M. and Poulikakos, D., Sub-amorphous Thermal Conductivity in Ultrathin Crystalline Silicon, Nano Lett., 15(4), pp. 2605-2611, 2015. DOI: 10.1021/acs.nanolett.5b00167

J. Vega-Suarez, received the BSc. on Electronic Engineering in 2016 from the Universidad Industrial de Santander, Colombia. His fields of interests include metaheuristic optimization and dynamic systems modeling.
ORCID: 0000-0003-2838-9399

E. García-Morantes, received the BSc. and MSc. on Electronic Engineering from the Universidad Industrial de Santander, Colombia. His fields of interests include metaheuristic optimization and dynamic systems modeling.
ORCID: 0000-0002-5866-3136

R. Correa-Cely, received the BSc. on Chemical Engineering from the Universidad Nacional de Colombia (Bogotá) and PhD. from the Lehigh University, USA. His fields of interests include global optimization methods and the modeling of dynamic systems applied to process control. Currently, he is a laureate professor at the Universidad Industrial de Santander, Colombia and a senior researcher.
ORCID: 0000-0002-6507-1809

UNIVERSIDAD NACIONAL DE COLOMBIA
SEDE MEDELLÍN
FACULTAD DE MINAS

Área Curricular de Ingeniería Eléctrica e Ingeniería de Control

Oferta de Posgrados

Maestría en Ingeniería - Ingeniería Eléctrica

Mayor información:

E-mail: ingelcontro_med@unal.edu.co
Teléfono: (57-4) 425 52 64

UNIVERSIDAD NACIONAL DE COLOMBIA
SEDE MEDELLÍN
FACULTAD DE MINAS



DYNA
http://dyna.medellin.unal.edu.co/

Obtention and characterization of lithium superionic conductors using the glass-ceramic method

José Luis Narváez-Semanate [a], Ana Cândida Martins Rodrigues [b], Rodrigo Arbey Muñoz-Meneses [c], José Rodrigo Muñoz-Hoyos [d] & Julián Antonio Villamarín-Muñoz [a]

[a] *Grupo de Investigación en Bioingeniería, Universidad Antonio Nariño, Popayán, Colombia. jose.narvaez@uan.edu.co, jvilla22@uan.edu.co*
[b] *Departamento de Ingeniería de Materiales, Universidad Federal de Sao Carlos, Sao Carlos, Brasil. acmr@ufscar.br*
[c] *Facultad GAMA, Universidad de Brasilia, Brasilia, Brasil. ramunoz@unb.br*
[d] *Servicio Nacional de Aprendizaje SENA, Neiva, Colombia. jomunozh@sena.edu.co*

Received: February 7th, 2018. Received in revised form: April 4th, 2018. Accepted: April 23th, 2018.

Abstract
This paper proposes the glass-ceramics method for obtaining lithium ion (Li^+) solid electrolytes. This technique provides high chemical and microstructural homogeneity as well as low porosity. Glass samples were subjected to either single or double heat treatments, between 700 °C and 1000 °C, in order to obtain the glass-ceramics. Differential Scanning Calorimetry – *DSC* – results evidenced the possibility of fabricating these ceramics from glass in the system $Li_2O{\cdot}Al_2O_3{\cdot}TiO_2{\cdot}P_2O_5$. Samples observed by Scanning Electron Microscopy – *SEM* – showed a finely grained microstructure which was homogeneously distributed and non-porous. X-ray Diffraction – *XRD* – patterns showed the formation of the high conducting phase $LiTi_2(PO_4)_3$. A high ionic conductivity, in the order of 10^{-3} S/cm at 1000 °C, was measured by Impedance Spectroscopy – *IS*. It suggests that the synthesis method used in this research is useful for fabricating lithium ion glass-ceramics and opens up a new alternative for manufacturing different electrical ceramics.

Keywords: glass-ceramics; lithium ion batteries; impedance spectroscopy; superionic conductors; $Li_2O{\cdot}Al_2O_3{\cdot}TiO_2{\cdot}P_2O_5$ system.

Obtención y caracterización de conductores superiónicos de litio utilizando la ruta vitrocerámica

Resumen
Este artículo propone la ruta vitrocerámica para obtener electrolitos sólidos por ion litio (Li^+). Esta técnica provee alta homogeneidad química y microestructural, así como baja porosidad. Muestras vítreas fueron sometidas a tratamientos térmicos, simples y dobles, entre 700 °C y 1000 °C, para obtener las vitrocerámicas. Resultados de calorimetría diferencial de barrido – *DSC* – evidenciaron la posibilidad de fabricar estas cerámicas a partir de vidrios del sistema $Li_2O{\cdot}Al_2O_3{\cdot}TiO_2{\cdot}P_2O_5$. Muestras observadas por microscopía electrónica de barrido – *SEM* – mostraron una microestructura de granos finos, homogéneamente distribuidos y sin porosidad. Patrones de difracción de rayos-x – *XRD* – permitieron verificar la formación de la fase altamente conductora $LiTi_2(PO_4)_3$. Una conductividad iónica alta, del orden de 10^{-3} S/cm a 1000 °C, fue medida utilizando espectroscopía de impedancia – *IS*. Lo anterior sugiere que el método de síntesis, utilizado en este trabajo, es útil para fabricar vitrocerámicas de ion litio y abre una nueva alternativa para fabricar diferentes cerámicas eléctricas.

Palabras clave: vitrocerámicas; baterías de ion litio; espectroscopía de impedancia; conductores superiónicos; sistema $Li_2O{\cdot}Al_2O_3{\cdot}TiO_2{\cdot}P_2O_5$.

1. Introduction

Conduction of electricity in metallic materials is achieved by means of the movement of a large number of electrons, which easily migrate from one side to another within the material. In ceramic materials, such ease of movement does not exist, as they lack free electrons [1]. However, a current can also be achieved through the displacement of charged carriers like positive ions, negative ions or both [1,2]. In liquid electrolytes both types of ions can move easily. In solid

How to cite: Narváez-Semanate, J.L., Rodrigues, A.C.M., Muñoz-Meneses, R.A., Muñoz-Hoyos, J.R. and Villamarín-Muñoz, J.A., Obtention and characterization of lithium superionic conductors using the glass-ceramic method. DYNA, 85(205), pp. 148-156, June, 2018.

© The author; licensee Universidad Nacional de Colombia.

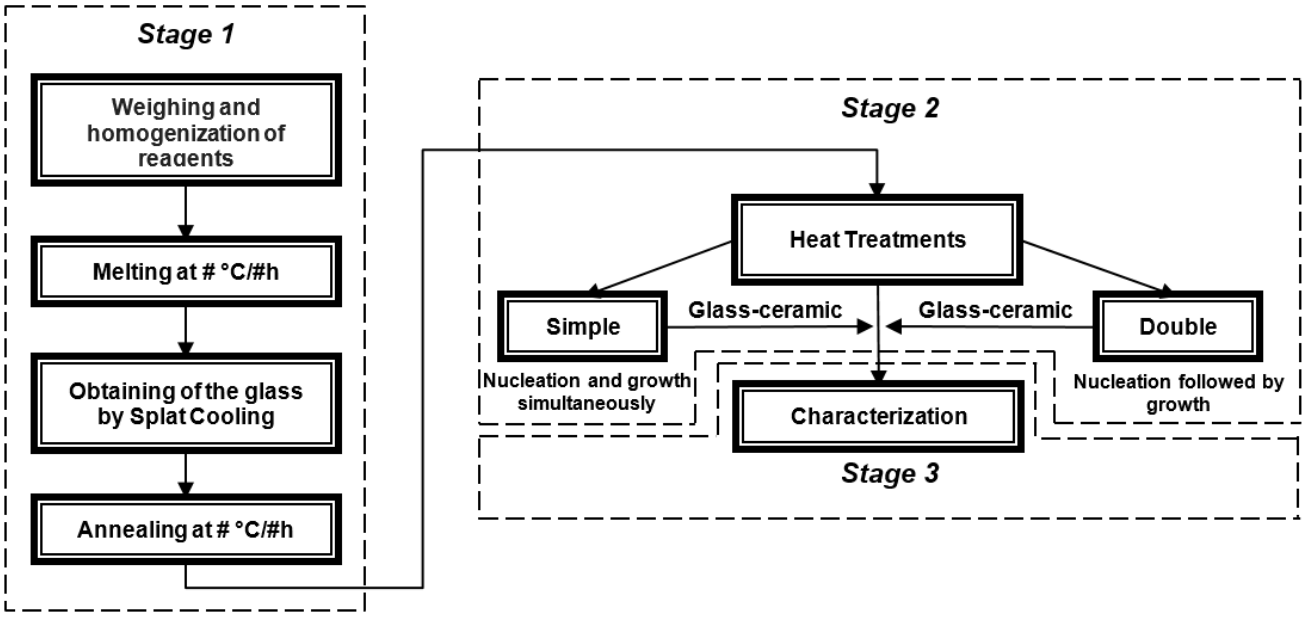


Figure 1. General flowchart for obtaining glass-ceramic materials [6].
Source: The authors.

electrolytes, only one type can move while the other maintains the mechanical stability of the material [3,4]. Such materials have very good ionic conduction properties, as well as being safe to work with (low flammability), which is one of the reasons why they have been studied for several decades. Ceramic superionic conductors have been synthesized using well-known techniques such as solid-state reaction, controlled co-precipitation and the polymeric precursor method. A relatively new method of obtention, compared to those mentioned above, is the glass-ceramic technique. This process has several advantages over conventional methods, such as the possibility of maintaining greater control over the microstructure and obtaining materials with low porosity, among others [5]. For the reasons stated above, the main objective of this paper is to show that is possible to obtain lithium ionic conductors using the glass-ceramic method and that their electrical response makes them attractive for applications in secondary batteries.

1.1. Theoretical background

Glass-ceramics are crystalline materials obtained from the controlled crystallization of precursor glasses. The process regularly used to obtain these materials, from the obtention of the amorphous solid to the glass-ceramic, is shown in Fig. 1.

It is possible to observe three stages in Fig. 1. The first corresponds to the obtention of the precursor glass. After the reagents have been weighed and homogenized, they are brought to melting temperature (generally between 1200 °C and 1450 °C), depending on their composition. The mixture is kept at this temperature for about 30 minutes in order to guarantee the complete transformation from the solid phase into the liquid phase. Then the melt is cooled as fast as possible in between two metallic plates (a technique known as *Splat Cooling*), to avoid the organization of the atoms and, consequently, the crystallization of the material. Subsequently, an annealing heat treatment must be carried out at a heat close to the glass transition temperature (T_g), which allows for the release of residual stresses derived from the difference in cooling rates of the surface and the interior of the glass. This heat treatment makes it possible to handle the glass and cut it into small pieces (5 mm x 5 mm). The second stage shows glass-ceramic fabrication, where annealed glasses are subjected to heat treatments which can be single (nucleation and crystal growth occur at the same time) or double (nucleation is accomplished in the first heat treatment and crystal growth in a second one, at a higher temperature). Double heat treatment allows for a better microstructural control over the physical and chemical properties of the glass. Finally, the last stage shown in the flowchart consists of the different techniques used to characterize the glass-ceramics in order to study the microstructure-properties relationship.

The crystallization of glass occurs through a combination of the processes of nucleation and crystal growth. This process can be described by Equation 1, which represents the crystallized volumetric fraction, as follows:

$$x(t) = 1 - exp[-(Kt)^n] \quad (1)$$

Equation 1 is known as the *JMAK* equation, named for its developers, *Johnson, Mehl, Avrami and Kolmogorov* [7]. Where *x* is the fraction of glass transformed into crystals at a given temperature and time (*t*), *n* is *Avrami's* coefficient that is associated with both the dimension of the crystal and the

nucleation mechanism. Finally, *K* is a constant of reaction, which has an Arrhenius-type expression, whose activation energy corresponds to the crystallization process. It is worth noting that *Avrami's* coefficient may vary between 1 and 4 depending on the crystallization mechanism and morphology of the crystals. A value of 3 may indicate volume crystallization, essential when microstructural control is required. As a consequence, for this last case, a double heat treatment could provide the best results for producing a determined microstructure. Further information can be found in *Rodrigues'* paper [7].

The most suitable thermal treatment temperatures for obtaining the glass-ceramic material can be determined through *DSC*. By means of this technique, endothermic and exothermic peaks are obtained which give a generalized indication of the glass transition (T_g) and melting temperatures (T_m), and the crystallization temperature (T_x) respectively. For example, nucleation is carried out at temperatures below but near to T_g. By varying the time in which the heat treatment is applied, it is possible to control the number of nuclei formed. Crystal growth occurs near T_x, where the time it is heated for plays an important role for crystal size.

2. Materials and methods

2.1. Preparation of the precursor glass

Using a digital scale (*Chyo JEX-200*) the necessary quantities were weighed to obtain glass of molar composition $16.2Li_2O{\cdot}3.8Al_2O_3{\cdot}42.5TiO_2{\cdot}37.5P_2O_5$ or $Li_{1.3}Al_{0.3}Ti_{1.7}(PO_4)_3$. High purity reagents, Li_2CO_3 (*Synth-C1006.01.AE 99%*), Al_2O_3 (*Pc Alcoa A16 >99.5%*), TiO_2 (*Aldrich-CAS 1317-80-2 >99.9%*) and $NH_4H_2PO_4$ (*Aldrich-7722-76-1 >98%*), were disaggregated in a mortar and then mixed. The mixture was placed into an alumina crucible and heated in a *Bloomfield N.J., CM Inc* furnace using different programs. The first ramp, at 10 °C/min, was at a temperature of 700 °C for 60 min to allow the decomposition of Li_2CO_3 and $NH_4H_2PO_4$. The next ramp, heated at the same rate, was at 1400 °C for 30 min to allow the complete melting of the mixture. The molten liquid was rapidly cooled using the *Splat Cooling* method and immediately subjected to thermal annealing treatment at 550 °C (approximately 70 °C below T_g) for 2 hours and, subsequently, cooled in the furnace at its normal cooling rate. To perform the corresponding analysis, 3 mm cubes were cut using a fine diamond saw. Both a solid and a powder sample were subjected to a *DSC* (*DSC 404 NETZSCH*) scan at a rate of 10 °C/min in order to determine firstly, the obtention of the amorphous material, secondly, to ascertain the characteristic temperatures of the glass and thirdly, to demonstrate crystallization, specifically the volumetric crystallization of the materials.

2.2. Preparation of the glass-ceramics

Two types of thermal treatments were used, one simple and one double, in order to determine their influence on the microstructure and, consequently, the electrical properties of the glass-ceramics. Simple treatments were performed above T_x, that is, at 700 °C, 800 °C, 900 °C and 1000 °C for 20 min. For double heat treatments a nucleation treatment was performed at 606 °C (T_g – 10 °C) for 10 min, 30 min, 120 min and 480 min, followed by a treatment for crystal growth at 900 °C for 20 min. These treatments were carried out in tubular furnaces which were previously stabilized at the set temperatures. After this process, the samples were sanded (from sandpaper grit size 100 up to 1200) and then polished with cerium oxide to obtain smooth and level surfaces.

2.3. Characterization of the glass-ceramics

XRD was carried out in order to verify that the *NASICON*-type phase (***Na-S****uper****I****onic* ***CON****ductor*) of the lithium-based super-ionic glass-ceramics had been obtained. A *Siemens* diffractometer with *CuKα* radiation was used. The data was taken from samples in powder form in a glass sample holder at room temperature, with 2θ varying from 5 to 80°, using an angular step size of 0.02° and counting time of 1 s. Peaks were indexed using the software *Search Match*®. The microstructural characteristics, morphology and grain size were analyzed by *SEM*, using a *Philips XL 30* Scanning Electron Microscope with a field emission gun (*FEG – Field Emission Gun*). For the *SEM* study, the fractured surface was coated with gold, using a *sputtering* technique. The *DeHoff* methodology was used to perform the calculations of average grain size [8]. The electrical response was studied using *IS*, using a *Solartron 1260 Impedance/Gain Phase Analyzer* in a frequency range from 10 Hz to 10 MHz, with a voltage of 1000 mV, from 18 °C (room temperature) up to 64 °C. The surfaces of these samples were also gold coated by *sputtering* so that they acted as contact electrodes. Results were analyzed by calculating the total impedance of the system. Five impedance spectra were taken for each sample at 10 °C intervals in the aforementioned temperature range. The total resistance was taken at Z'' = 0 and the conductivity was calculated ($\sigma = 1/\rho$), where ρ is the resistivity. Finally, the logarithm of the conductivity as a function of the inverse of the temperature was plotted, resulting in a straight line whose slope provides information about the activation energy for lithium ion conduction and, therefore, about the mechanisms of ionic conduction. It should be noted that the plotted data was multiplied by the geometrical parameter of the samples.

3. Results and discussion

3.1. Precursor glass

The prepared glass showed a strong tendency to crystallize, so it became necessary to pour smaller amounts of the molten liquid to improve heat dissipation and avoid crystallization. Curves obtained by calorimeter are shown in Fig. 2.

Fig. 2 shows the obtained curve for the bulk sample (circles). It is possible to see a slight deviation of the baseline around 620 °C (897 K), attributed to the glass transition temperature, T_g. An exothermic peak can be observed at about 660 °C (933 K) which corresponds to the crystallization temperature (T_x) of the material and, finally, close to 1250 °C (1521 K) an endothermic peak shows the

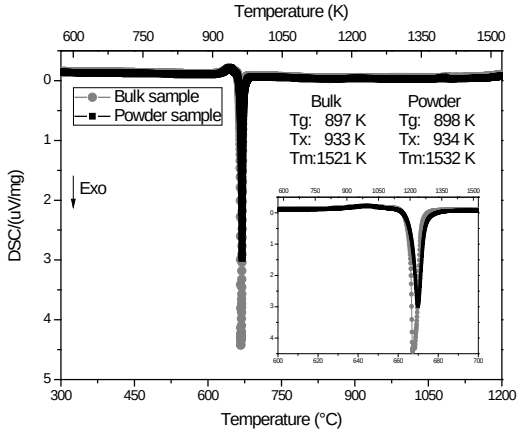


Figure 2. Curves obtained by *DSC* at 10 °C/min for vitreous samples, solid and powder, of composition $Li_{1.3}Al_{0.3}Ti_{1.7}(PO_4)_3$.
Source: The authors.

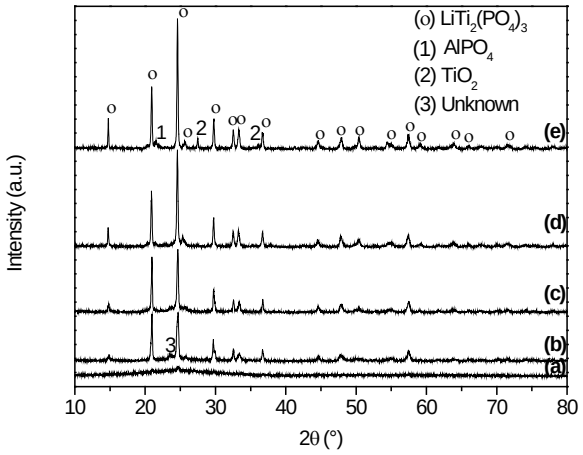


Figure 3. X-ray diffractograms of samples of composition $Li_{1.3}Al_{0.3}Ti_{1.7}(PO_4)_3$, (a) precursor glass, and glass-ceramics obtained by simple heat treatment at (b) 700 °C, (c) 800 °C, (d) 900 °C and (e) 1000 °C, for 20 min.
Source: The authors.

beginning of the melting temperature (T_m). The curve of the powder material (squares), behaves quite similarly to that described above. The fact that these two curves are similar (see inset) is a clear indication that the crystallization of the material is taking place volumetrically [9,10]. If the crystallization was predominantly superficial, the crystallization peak of the powder sample (which has a greater surface area) would occur earlier than that shown by the bulk sample. This behavior has been observed in another system [11] and it may be explained by considering that during the milling process the powder surface is hydrated and this inhibits crystallization [11]. It should be noted that volumetric crystallization is important because it allows greater control of the microstructure through double heat treatments [12]. Other conclusions that can be established from the analysis of these curves are those related to thermal stability parameters [13]. It is evident that the difference between the crystallization temperature and the glass transition temperature is small (36 °C), which indicates a high tendency to crystallize [7,9,10]. This coincides with what was observed during the experimental stage, since the molten liquid tended to crystallize rapidly when it was poured. On the other hand, the reduced glass transition temperature (T_{gr}), which is the ratio between T_g and T_m, is an indication of volumetric nucleation, as long as it is less than or equal to 0.6 [9,14,15], in this case T_{gr} = 0.589. This parameter is important to be able to have microstructural control.

3.2. Glass-ceramics obtained by simple heat treatment

The X-ray diffractograms of the samples obtained by simple heat treatment are shown in the Fig.3.

In Fig. 3 (a) the diffraction pattern of the bulk sample, obtained after the annealing process, can be observed. It is a pattern that does not have any diffraction peak and presents a deviation in the baseline between $20° \leq 2\theta \leq 30°$ which is known as an amorphous halo, which is distinctive to glass [16]. This coincides with the *DSC* results that showed satisfactory obtention of the precursor glass. Fig. 3 (b) shows a diffraction pattern, whose principal and most intense peaks correspond to the highly conductive phase with *NASICON*-type structure - $LiTi_2P_3O_{12}$ (*JCPDS 35-754*) [17-21], in which aluminum is in solid solution in the unit cell, however, a trace of an unidentified phase is also observed, which was also reported by Fu [19,22]. Figs. 3 (c) and (d) also show the presence of the *NASICON* phase, with an increase in the intensity of the peaks, in addition, in Fig. 3 (c) it is still possible to see traces of the unidentified phase that disappear in Fig. 3 (d). Finally, Fig. 3 (e) shows, besides the *NASICON* phase, spurious phases such as TiO_2 and $AlPO_4$, as well as a more intense peak corresponding to the phase of interest. Taking into account that both the conditions of the equipment and sample conditions were maintained throughout, it is reasonable to conclude that the higher the heat treatment temperature, the more intense the peaks of the main phase are and the narrower the width of the peaks at half height (quantitative data provided by the analysis software Origin®, not shown in this paper). It suggests a better crystallinity (major structural order) of the unit cells and therefore of the glass-ceramics. Other authors have also reported impurities as those found in this study [23,24]. These spurious phases are dielectric and may block the movement of the charge carriers, although they could also provide low energy paths for charge transport [24]. Subsequent to the X-ray diffraction analysis, the samples were visualized by scanning electron microscopy, the micrographs are presented in Fig. 4.

Although it was mentioned before that the glass-ceramic method allows the obtention of non-porous materials, in the micrograph shown in Fig. 4 (a) pores are visible in the microstructure, possibly due to differences in density between the vitreous matrix and crystals. In Figs. 4 (b) and (c) microstructures consisting of fine and uniform grains are observed and no porosity is evident. Finally, in Fig. 4 (d) grain growth is observed as the temperature is raised. It can be understood from a thermodynamic perspective, since at high temperatures diffusive processes accelerate. The characteristics observed in the micrographs are consistent

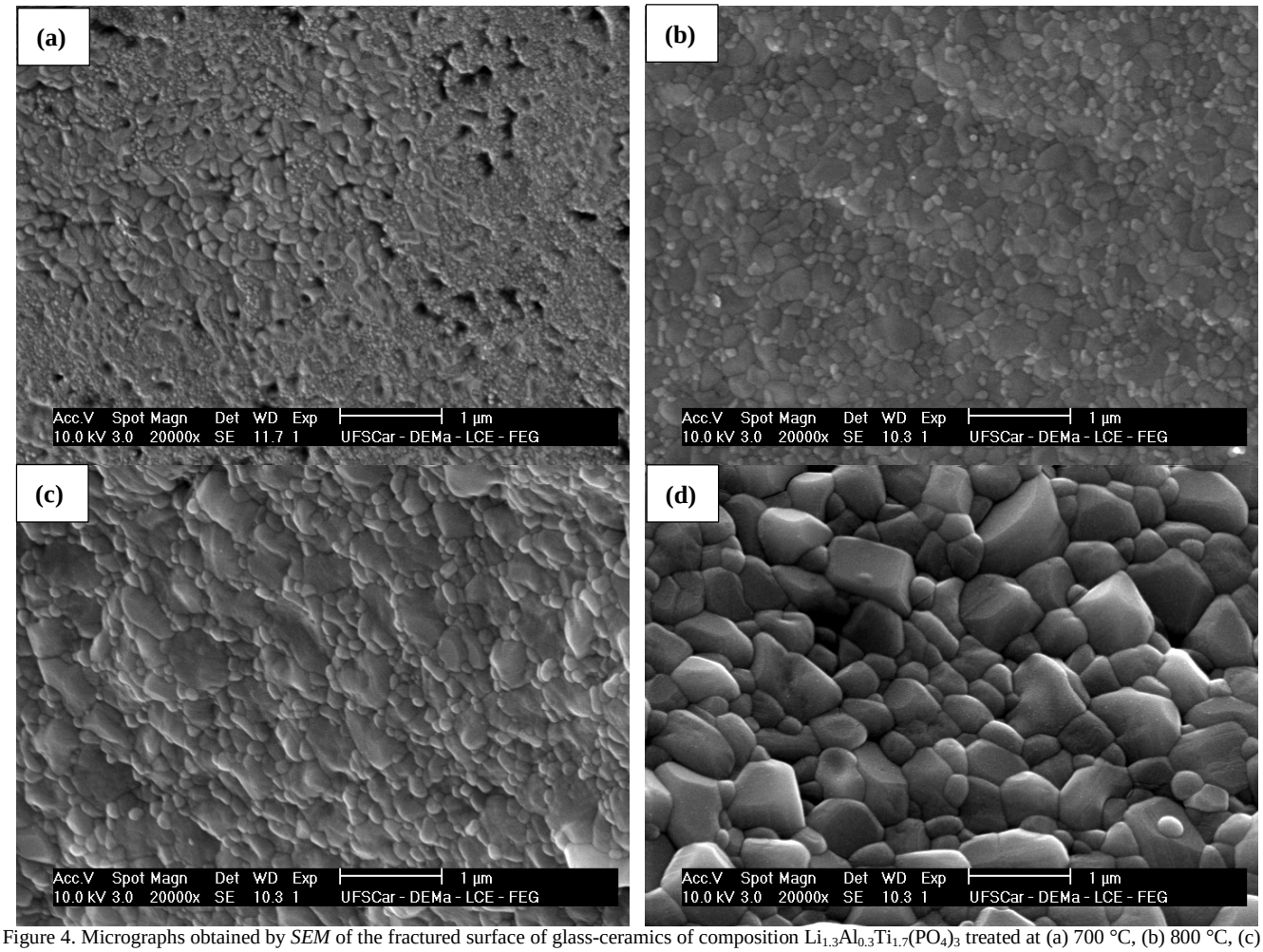


Figure 4. Micrographs obtained by *SEM* of the fractured surface of glass-ceramics of composition $Li_{1.3}Al_{0.3}Ti_{1.7}(PO_4)_3$ treated at (a) 700 °C, (b) 800 °C, (c) 900 °C y (d) 1000 °C, for 20 min.
Source: The authors.

with the X-ray results, showing that when heat treatment temperature is increased, a more ordered and homogeneous microstructure is observed, which is directly tied to both the increase in the intensity of the peaks and their decrease in width at half height. It is worth mentioning that microstructural aspects such as grain size, porosity, morphology and grain boundaries, among other aspects, directly influence the properties of materials [25], in this case the electrical properties. The average grain size, measured as suggested by *DeHoff* [8], ranges between 100 nm and 400 nm when the heat treatment temperature is increased from 700 °C to 1000 °C.

Electrical characterization by impedance spectroscopy allowed the drafting of Arrhenius plots, taking the total electrical resistance of each sample. The behavior of conductivity as a function of inverse of temperature is shown in Fig. 5.

Fig. 5 shows a plot of the logarithm of the conductivity as a function of the inverse of temperature. In the temperature range used for measuring (18 °C – 64 °C), it is possible to see that the slope of the straight lines does not change, which suggests that the conduction mechanism is the same [26]. It is also evident that the greater the heat treatment temperature,

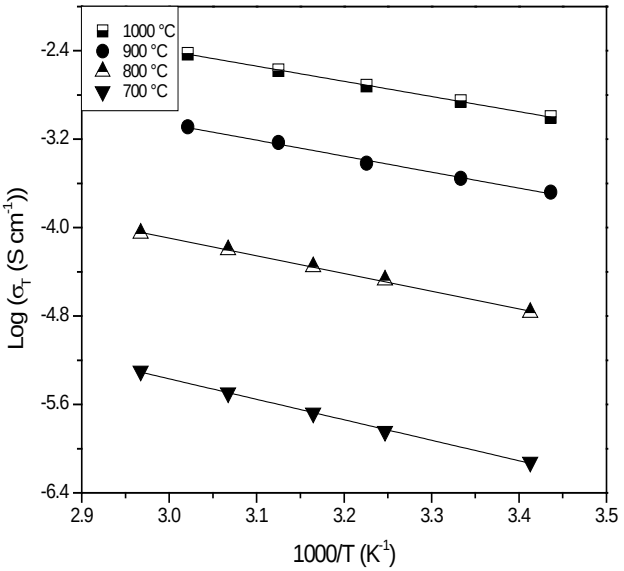


Figure 5. Characteristic Arrhenius plots of glass-ceramics of composition $Li_{1.3}Al_{0.3}Ti_{1.7}(PO_4)_3$ obtained by simple heat treatment.
Source: The authors.

Table 1.
Electrical properties of glass-ceramics of composition $Li_{1.3}Al_{0.3}Ti_{1.7}(PO_4)_3$ obtained by simple heat treatment, where E_{aT} is the total activation energy and $\sigma_{T25°C}$ is the total conductivity at room temperature.

Heat Treatment (°C)	E_{aT} (eV)	$\sigma_{T25°C}$ (S·cm^{-1})
700	0.37	$9.6x10^{-7}$
800	0.32	$2.2x10^{-5}$
900	0.29	$2.7x10^{-4}$
1000	0.27	$1.3x10^{-3}$

Source: The authors.

the greater the conductivity at a given temperature, which means that the thermal treatment influences the glass-ceramics' conductivity positively [22,27]. This observation is in agreement with the *XRD* results, indicating that a sample's crystallinity (structural order) is favored by a high heat treatment temperature which improves its electrical properties. In fact, the increase in crystallinity can be understood as an alignment of the conduction channels through the highly conductive structure [22,27]. The electrical properties of the glass-ceramics are summarized in Table 1.

A decrease in activation energy while the temperature of the thermal heat treatment increased is evidenced in Table 1. This statement can also be explained by the idea of higher-order structure. Sample heat treated at 700 °C presents a very low conductivity (10^{-7} S/cm), even when at this temperature the *NASICON*-type structure has already been formed, see Fig. 3 (b). This fact could be closely related to the porosity seen in the sample, see Fig. 4 (a), therefore it can be concluded that porosity has a direct and negative effect on electrical conductivity [28,29]. The sample with the highest electrical conductivity (10^{-3} S/cm) was treated at 1000 °C for 20 min, this behavior is attributed to microstructure's homogeneity, better crystallinity and lower porosity when compared with the other samples with naked eye.

3.3. Glass-ceramics obtained by double heat treatment

These glass-ceramics were obtained by performing a nucleation heat treatment at 606 °C (T_g – 10 °C) for 10 min, 30 min, 120 min and 480 min, followed by a heat treatment for crystal growth at 900 °C for 20 min.

Samples obtained by double heat treatments were also characterized by x-ray diffraction. The results are shown in Fig. 6.

X-ray diffraction patterns presented in Fig. 6 show, in all cases, peaks corresponding to the highly conductive phase that has a *NASICON*-type structure. It is important to add that in all glass-ceramics, small impurities of the compound $AlPO_4$ can be found [30,31]. If we compare the diffraction patterns of the double heat-treated samples with the patterns obtained at the same temperature using the simple heat treatment in Fig. 3 (d), it can be seen that in both cases well defined diffraction peaks are obtained.

After determining the different phases present in these double heat-treated glass-ceramics, their fractured surfaces were analyzed using scanning electron microscopy. Images can be seen in Fig. 7.

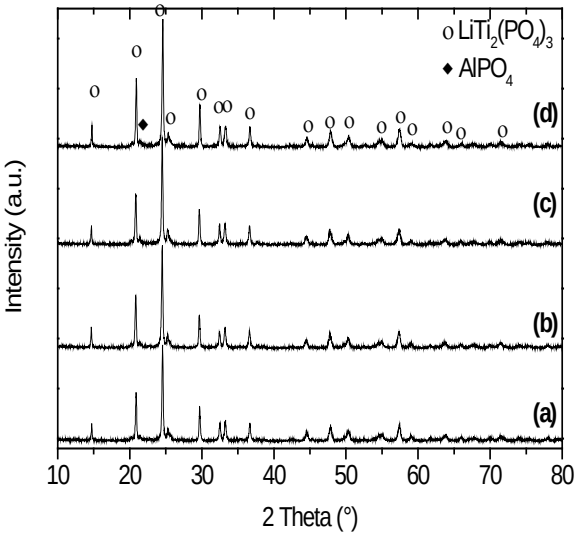


Figure 6. X-ray diffraction patterns of samples of composition $Li_{1.3}Al_{0.3}Ti_{1.7}(PO_4)_3$ obtained by double heat treatment. Nucleation at 606 °C (T_g – 10 °C) during (a) 10, (b) 30, (c) 120 and (d) 480 min, with subsequent thermal treatment for crystal growth at 900 °C for 20 min.
Source: The authors.

Fig. 7 presents the microstructure of the glass-ceramics obtained by double heat treatment. The examination of the micrographs allows to see that the morphology is, in general, composed of spherical grains. There is no evidence of porosity and the average grain size, measured using the procedure proposed by *DeHoff* [8], increases from 100 nm to 180 nm, when nucleation time decreases from 480 min to 10 min respectively. This behavior is expected if it is taken into account that the higher the nucleation time (for example 480 min) the higher the number of formed nuclei and, therefore, the less space they have to grow, resulting in a microstructure composed of small grains (for example 100 nm).

As a summary of the effects on the microstructure, in Fig. 8 (a) and (b) is possible to see the variation of grain size as a function of the simple and double heat treatments more clearly.

By comparing Figs. 8 (a) and (b), it is possible to observe that a wider range of grain sizes (80 nm – 400 nm) were obtained using the simple heat treatment than the double heat treatment (110 nm – 190 nm), with increased grain size strongly linked to heat treatment temperature, see Fig. 8 (a). This behavior can be explained from a thermodynamic perspective because at higher temperatures, diffusional processes become more effective and, consequently, crystal growth takes place more rapidly. This fact is more evident in the samples exposed to the simple heat treatment in which athermic nuclei grew while the liquid cooled [10,15]. In Fig. 8 (b) there is a clear trend that can be observed showing that grain size decreases as nucleation time increases.

Finally, glass-ceramics were analyzed using impedance spectroscopy method. Arrhenius-type plots are shown in Fig. 9.

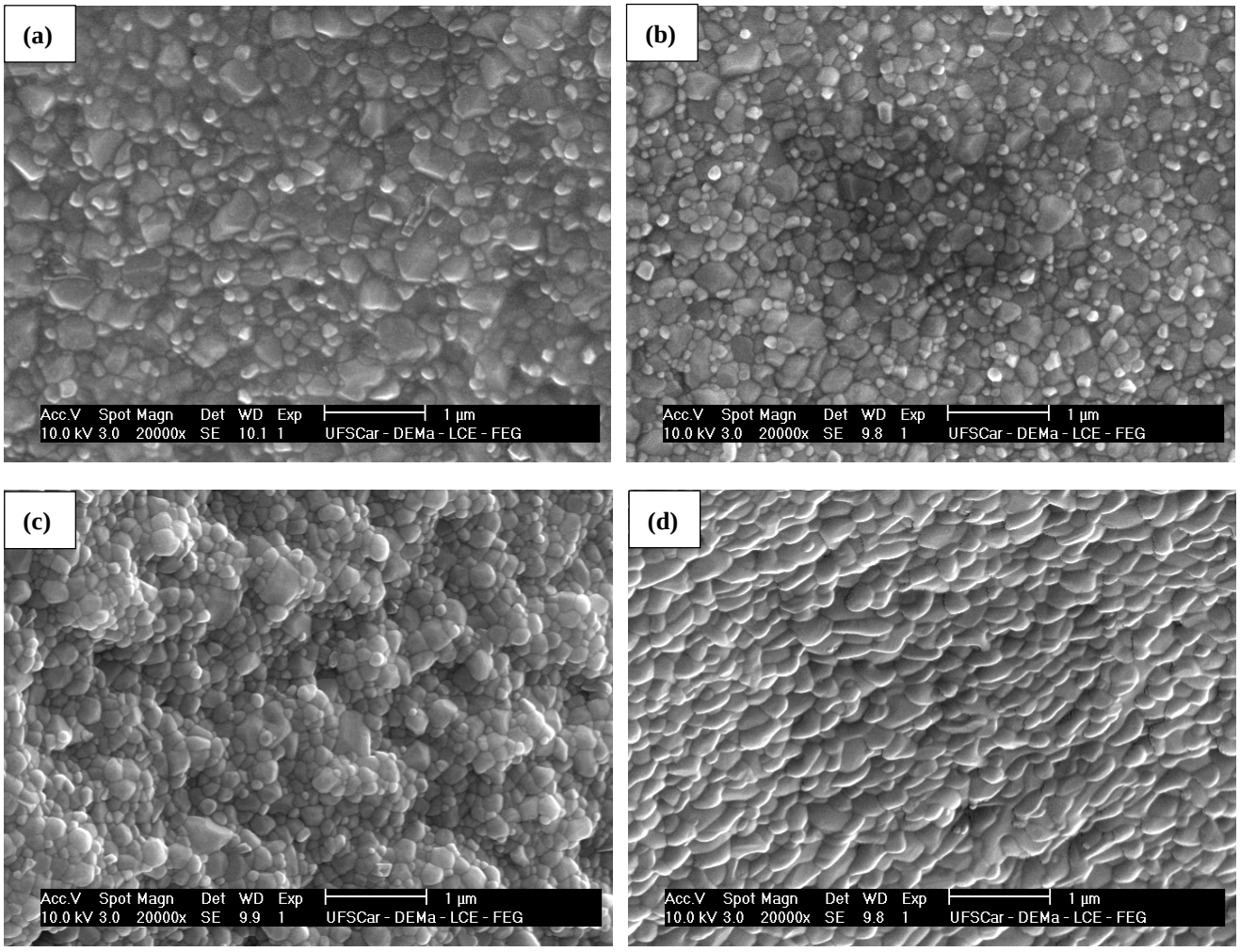


Figure 7. Micrographs obtained by *SEM* of the fractured surface of glass-ceramics of composition $Li_{1.3}Al_{0.3}Ti_{1.7}(PO_4)_3$ treated at 606 °C (T_g – 10 °C) during (a) 10, (b) 30, (c) 120 and (d) 480 min, followed by crystal growth heat treatment at 900 °C for 20 min.
Source: The authors.

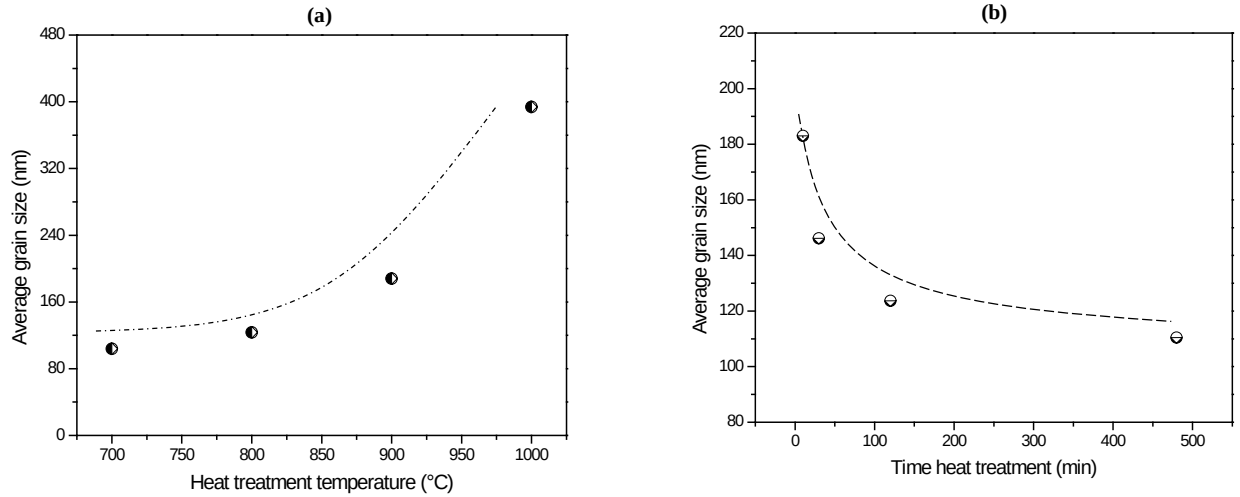


Figure 8. Variation of average grain size of glass-ceramics of composition $Li_{1.3}Al_{0.3}Ti_{1.7}(PO_4)_3$ as a function of thermal heat treatment (a) simple and (b) double. Dotted lines do not correspond to a curve-fitting of the data but it serves as a visual guide for readers to follow.
Source: The authors.

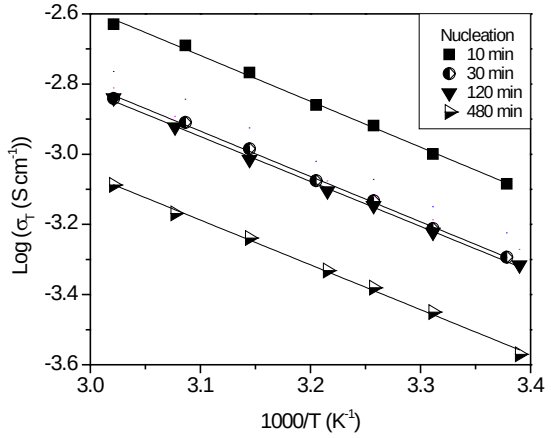


Figure 9. Arrhenius plots corresponding to glass-ceramics of composition $Li_{1.3}Al_{0.3}Ti_{1.7}(PO_4)_3$ obtained by double heat treatment. Nucleation at 606 °C (T_g – 10 °C) during 10, 30, 120 and 480 min, followed by crystal growth heat treatment at 900 °C for 20 min.
Source: The authors.

Table 2.
Electrical properties of glass-ceramics of composition $Li_{1.3}Al_{0.3}Ti_{1.7}(PO_4)_3$ obtained by double heat treatment, where E_{aT} is the total activation energy and $\sigma_{T25°C}$ is the total conductivity at room temperature.

Nucleation at T_g – 10 °C (min)	**E_{aT} (eV)**	**$\sigma_{T25°C}$ (S·cm^{-1})**
10	0.26	8.9x10^{-4}
30	0.26	5.5x10^{-4}
120	0.25	5.2x10^{-4}
480	0.25	3.1x10^{-4}

Source: The authors.

As shown in Fig. 9, the behavior corresponds to an Arrhenius type whose slope does not change in the measured range. As mentioned before, when analyzing glass-ceramics obtained through simple heat treatment, it is apparent that the conduction mechanisms do not change in the studied range [26]. In Table 2, it is shown that activation energy values and total conductivity at room temperature for these glass-ceramics are resumed.

It is noticeable in Table 2 that activation energy is essentially constant, while electrical conductivity shows a tendency to decrease while increasing nucleation time. As already mentioned, the higher the nucleation time the higher the number of formed nuclei, subsequently, these nuclei will have less space to grow, which leads to a small grain microstructure. In fact, Fig. 8 (b) shows that grain size decreases from 190 nm down to 110 nm as the nucleation time increases, thus, it results in a greater number of grain boundaries (disordered region) that negatively affect the total conductivity of the glass-ceramics. However, if these samples are compared with the sample obtained at 900 °C by simple heat treatment, is clear that the latter presents a higher activation energy and lower conductivity, which suggests that the double heat treatment favors the electrical properties somehow. One way of understanding this is to think of the grains in tighter contact, which favors the conductivity of the material, as suggested by Fu [32].

4. Conclusions

The glass-ceramic method proved to be a useful and versatile alternative for obtaining lithium ion conductors. The composition of the glass-ceramic used revealed a strong tendency to crystallize, which was proved by means of thermal stability parameters, since the difference between the crystallization temperature and the glass transition temperature was small (36 °C). However, it was possible to obtain glass-ceramics using two types of heat treatment, one simple and one double, which had an influence on the microstructure of the glass-ceramics, as well as on their electrical response. The calculation of the reduced glass transition temperature (T_{gr}) showed that the glass tended to crystallize volumetrically, a fact that allowed for a better control of the microstructure of the samples obtained using the double heat treatment. The highest value of conductivity was obtained for the glass-ceramics treated at 1000 °C/20 min, of the order of 10^{-3} S·cm^{-1}, while the lowest value was of the order of 10^{-7} S·cm^{-1}, for the glass-ceramic obtained at 700 °C/20 min. Taking into account the previous values of conductivity and that in both cases the *NASICON*-type structure was obtained (evidenced by *XRD*), it was concluded that the microstructure of glass-ceramics plays a very important role in its electrical properties. In fact, high values of conductivity were related to non-porous and highly homogeneous microstructures, while low values of conductivity are related to porosity (see Fig. 4 (a)) and poorly aligned microstructures. In the case of glass-ceramics obtained by double heat treatment it was observed that where there was a longer nucleation time, there was also a smaller grain size and in turn lower electrical conductivity. This behavior can be understood as follows: smaller grain size implies greater number of grain boundaries (regions of microstructural disorder), which negatively affect the conductivity of the samples.

Acknowledgment

The authors express their gratitude to the Department of Materials of the Federal University of São Carlos, SP, Brazil, for the assistance in the characterization of the glass-ceramics.

References

[1] Moulson, A.J. and Herbert, J.M., Electroceramics: materials, properties, applications. John Wiley & Sons, Inc., 2003.
[2] West, A.R., The activation d.p. almond entropy for transport in ionic conductors, 23, pp. 27-35, 1987. DOI: 10.1016/0167-2738(87)90078-6
[3] Macdonald, J.R., Impedance spectroscopy: theory, experiment and applications. USA: John Wiley & Sons, Inc., 2005.
[4] West, A.R. Solid state chemistry and its applications, 2nd ed. John Wiley & Sons, Inc., 2014.
[5] Zanotto, E.D., A bright future for glass-ceramics, Am. Ceram. Soc. Bull., vol. 89, 2010.
[6] Narváez-Semanate, J.L., Obtenção e condutividade elétrica de vitrocerâmica Li1+xAlxTi2-x(PO4)3 com diferentes microestruturas, M.Sc. Thesis, Departamento de Engenharia de Materiais, Universidade Federal de São Carlos, São Carlos, Brasil, 2009.

[7] Rodrigues A.M., Narváez-Semanate J.L., Cabral A.A. and Rodrigues A.C.M., Determination of crystallization kinetics parameters of a Li1.5Al0.5Ge1.5(PO4)3 (LAGP) glass by differential scanning calorimetry, Mater. Res., 16(4), pp. 811-816, 2013. DOI: 10.1590/S1516-14392013005000055

[8] DeHoff, R.T., Quantitative microscopy. McGraw-Hill Book Company, 1968.

[9] Nascimento, M.L.F., Souza, L.A., Ferreira, E.B. and Zanotto, E.D., Can glass stability parameters infer glass forming ability?, J. Non. Cryst. Solids, 351(40-42), pp. 3296-3308, 2005. DOI: 10.1016/j.jnoncrysol.2005.08.013

[10] Fokin, V.M., Cabral, A.A., Reis, R.M.C.V., Nascimento, M.L.F. and Zanotto, E.D., Critical assessment of DTA–DSC methods for the study of nucleation kinetics in glasses, J. Non. Cryst. Solids, 356(6-8), pp. 358-367, 2010. DOI: 10.1016/j.jnoncrysol.2009.11.038

[11] Nuernberg, R.B. and Rodrigues, A.C.M., A new NASICON lithium ion-conducting glass-ceramic of the Li1+xCrx(GeyTi1-y)2-x(PO4)3 system, Solid State Ionics, 301, pp. 1-9, 2017. DOI: 10.1016/j.ssi.2017.01.004

[12] Cruz, A.M., Ferreira E.B. and Rodrigues A.C.M., Controlled crystallization and ionic conductivity of a nanostructured LiAlGePO4 glass–ceramic, J. Non. Cryst. Solids, 355(45-47), pp. 2295-2301, 2009. DOI: 10.1016/j.jnoncrysol.2009.07.012

[13] Hrubý, A., Evaluation of glass-forming tendency by means of DTA, Czech. J. Phys. B, 22, pp. 1187-1193, 1972. DOI: 10.1007/BF01690134

[14] Zhang, L., Ghussn, L., Schmitt, M.L., Zanotto, E.D., Brow R.K. and Schlesinger, M.E., Thermal stability of glasses from the Fe4(P2O7)3–Fe(PO3)3 system, J. Non. Cryst. Solids, 356(52-54), pp. 2965-2968, 2010. DOI: 10.1016/j.jnoncrysol.2010.03.044

[15] Fokin, V.M., Nascimento, M.L.F. and Zanotto, E.D., Correlation between maximum crystal growth rate and glass transition temperature of silicate glasses, J. Non. Cryst. Solids, 351(10-11), pp. 789-794, 2005. DOI: 10.1016/j.jnoncrysol.2005.02.005

[16] Romero, M., Rincón, J.M., Mûsik S. y Kozhukharov, W., Caracterización estructural de vidrios con altos contenidos de óxidos de hierro obtenidos a partir de un residuo de la hidrometalurgia del zinc, Rev. Metal., 33(5), pp. 317-323, 2010. DOI: 10.3989/revmetalm.1997.v33.i5.844

[17] Joint Commission on Powder Diffraction Standards (JCPDS) PDF#: 35-754, International Center for Diffraction Data, Newton Square, PA USA.

[18] Hagman, L. and Kierkegaard, P., The crystal structure of NaMe2(PO4)3; Me = Ge, Ti, Zr, Acta Chem. Scand., 22, pp. 1822-1832, 1968. DOI: 10.3891/acta.chem.scand.22-1822

[19] Fu, J., Superionic conductivity of glass-ceramics in the system Li2O—Al2O3—TiO2—P2O5, Solid State Ionics, 96(3-4), pp. 195-200, 1997. DOI: 10.1016/S0167-2738(97)00018-0

[20] Fu, J., Fast Li+ ion conduction in Li2O-Al2O3-TiO2-SiO2-P2O2 Glass-Ceramics, J. Am. Ceram. Soc., 80(7), pp. 1901-1903, 1997. DOI: 10.1111/j.1151-2916.1997.tb03070.x

[21] Mariappan, C.R., Galven C., Crosnier-Lopez M.-P., Le Berre F. and Bohnke O., Synthesis of nanostructured LiTi2(PO4)3 powder by a Pechini-type polymerizable complex method, J. Solid State Chem., 179(2), pp. 450-456, 2006. DOI: 10.1016/j.jssc.2005.11.005

[22] Aono, H., Sugimoto, E., Sadaoka, Y., Imanaka, N. and Adachi, G., Ionic conductivity of the lithium titanium phosphate (Li1+xMxTi2-x(PO4)3, M = Al, Sc, Y, and La) systems, J. Electrochem. Soc., 136, pp. 590-591, 1989. DOI: 10.1002/chin.198929007

[23] Maldonado-Manso, P. et al., High lithium ionic conductivity in the Li1+xAlxGeyTi2-x-y(PO4)3 NASICON Series, Chem. Mater., 15(9), pp. 1879-1885, 2003. DOI: 10.1021/cm021717j

[24] Kosova, N.V., Devyatkina E.T., Stepanov A.P. and Buzlukov A.L., Lithium conductivity and lithium diffusion in NASICON-type Li1+xTi2–xAlx(PO4)3 (x= 0; 0.3) prepared by mechanical activation, Ionics (Kiel)., 14(4), pp. 303-311, 2008. DOI: 10.1007/s11581-007-0197-5

[25] Badwal, S.P.S. and Rajendran, S., Effect of micro- and nano-structures on the properties of ionic conductors, Solid State Ionics, 70-71, pp. 83-95, 1994. DOI: 10.1016/0167-2738(94)90291-7

[26] Thokchom, J. and Kumar, B., Composite effect in superionically conducting lithium aluminium germanium phosphate based glass-ceramic, J. Power Sources, 185(1), pp. 480-485, 2008. DOI: 10.1016/j.jpowsour.2008.07.009

[27] Aono, H., Sugimoto, E., Sadaoka Y. and Imanaka, N., Electrical properties and crystal structure of solid electrolyte based on lithium hafnium phosphate LiHf2(PO4)3, Solid state ionics, 62, pp. 309-316, 1993. DOI: 10.1016/0167-2738(93)90387-I

[28] Best, A., Stoichiometric changes in lithium conducting materials based on Li1+xAlxTi2−x(PO4)3: impedance, X-ray and NMR studies, Solid State Ionics, 136-137(1-2), pp. 339-344, 2000. DOI: 10.1016/S0167-2738(00)00493-8

[29] Yoshio, M., Brodd, R.J. and Kozawa, A., Lithium-ion batteries. New York, NY: Springer New York, 2009.

[30] Arbi, K., Mandal, S., Rojo, J.M. and Sanz, J., Dependence of ionic conductivity on composition of fast ionic conductors Li1+xTi2-xAlx(PO4)3, $0 \leq x \leq 0.7$. A parallel NMR and electric impedance study, Chem. Mater., 14(3), pp. 1091-1097, 2002. DOI: 10.1021/cm010528i

[31] Forsyth, M., NMR studies of modified nasicon-like, lithium conducting solid electrolytes, Solid State Ionics, 124(3-4), pp. 213-219, 1999. DOI: 10.1016/S0167-2738(99)00213-1

[32] Fu, J., Fast Li+ ion conducting glass-ceramics in the system Li2O–Al2O3–GeO2–P2O5, Solid State Ionics, 104(3-4), pp. 191-194, 1997. DOI: 10.1016/S0167-2738(97)00434-7

J.L. Narváez-Semanate, received his BSc. degree in Physics Engineering in 2006 from the University of Cauca, Popayán, Colombia, and his MSc. and PhD. in Materials Science and Engineering in 2009 and 2013 respectively, from the Federal University of Sao Carlos, Sao Carlos, Brazil. Currently, he is a full-time professor for the Biomedical Program at Antonio Nariño University, Popayán, Colombia. His research interests include: glass-ceramics, biomaterials, biosensors and materials characterization.
ORCID: 0000-0002-4937-1414

A.C.M. Rodrigues, holds a BSc. degree in Chemistry from São Paulo University (1982), both a MSc. (1984) and PhD. (1988) in Solid State Electrochemistry from the Higher National College of Electrochemistry and Electrometallurgy in Grenoble, a Postdoctorate from the Federal Institute for Materials Research and Testing (BAM), Germany (2000) and a Postdoctorate from Friedrich Schiller University – Jena, Germany (1997). Currently, she works at the Federal University of Sao Carlos, Brazil. She is experienced in the area of Materials and Metallurgical Engineering, with emphasis on Non-metallic Materials. Her research focusses mainly on glasses, electrochemistry and solid electrolytes.
ORCID: 0000-0003-1689-796X

R.A. Muñoz-Meneses, received his BSc. degree in Physics Engineering in 2007 from the University of Cauca, Popayán, Colombia, and his MSc. and PhD., both in Mechatronic Systems in 2010 and 2013 respectively, from Brasilia University, Brasilia, Brazil. Currently he is a full-time professor at the University of Brasilia. His research interests include: oxygen sensors, fuel cells and composite materials.
ORCID: 0000-0003-4634-8910

J.R. Muñoz-Hoyos, received his BSc. degree in Physics Engineering in 2009 from the University of Cauca, Popayán, Colombia, and his MSc. and PhD. both in Materials Science and Engineering in 2012 and 2016 respectively, from the Federal University of Sao Carlos, Sao Carlos, Brazil. Currently, he is a full-time professor at Santo Tomás University, Bucaramanga, Colombia. His research interests include: ceramics, synthesis methods and structural refinements by the Rietveld method.
ORCID: 0000-0001-8974-0379

J.A. Villamarín, received his BSc. degree in Biomedical Engineering in 2005 from Manuela Beltrán University, Bogotá, Colombia, his MSc. in Bioengineering in 2007 and PhD. degree in Electrical Engineering in 2012 both from Sao Paulo University, Sao Carlos, Brazil. Currently, he is a full-time professor in the Biomedical Program at Antonio Nariño University, Popayán, Colombia. His research interests include: ultrasound digital signal processing, acoustic characterization of biological tissue and statistical processing of signals.
ORCID: 0000-0001-8383-8340

UNIVERSIDAD NACIONAL DE COLOMBIA
SEDE MEDELLÍN
FACULTAD DE MINAS



DYNA
http://dyna.medellin.unal.edu.co/

Hydrogen production in a novel configuration of UASB reactor under different hydraulic retention time

Diana Margarita Hernández, Lucia Andrea del Pilar Hurtado & Adela Tatiana Rodríguez-Chaparro

Laboratorio de Saneamiento Ambiental, Programa de Ingeniería Civil, Universidad Militar Nueva Granada, Bogotá, Colombia.
u1100846@unimilitar.edu.co, andrehuruiz@gmail.com, adela.rodriguez@unimilitar.edu.co

Received: February 16th, 2018. Received in revised form: April 3rd, 2018. Accepted: April 26th, 2018.

Abstract
The aim of this work was to evaluate the production of hydrogen in a conventional and hybrid Upflow Anaerobic Sludge Blanket (UASB) reactors by modifying the hydraulic retention time (HRT). Both reactors operated continuously close to 135 days, with organic loading rate (OLR) of 11.26 $kgCOD.m^{-3}.d^{-1}$ at 12, 8 and 4 h. In the hybrid reactor, Biopack® rings with polyurethane foam at its center were used. The results showed that the UASB hybrid reactor achieved a stable and continuous production of over 60% of hydrogen gas at each HRT, related to carbon dioxide reduction until the end of the operation. The ANOVA and TUKEY tests, with a 95% reliability level, showed that there was a significant difference between the HRT evaluated, observing that the highest hydrogen production was obtained with 4 h of HRT. In the conventional UASB reactor, there was no stability during the operation time.

Keywords: Biopack® rings; total volatile acids; UASB reactors

Producción de hidrogeno utilizando una nueva configuración de reactor anaerobio UASB bajo diferentes tiempos de retención hidráulica

Resumen
El objetivo de este estudio fue evaluar la producción de hidrógeno en un reactor anaerobio de manto de lodos y flujo ascendente (UASB) convencional y otro híbrido, modificando el tiempo de retención hidráulica (TRH). Los dos reactores operaron cerca de 135 días continuamente, con una carga orgánica volumétrica de 11.26 $kgDQO.m^{-3}.d^{-1}$ y valores TRH de 12, 8 y 4 h. En el reactor híbrido se utilizaron anillos de marca Biopack, adicionando espuma de poliuretano en su centro. Los resultados mostraron que la producción de hidrógeno en el reactor UASB híbrido fue estable y superior al 60% en cada uno de los TRH, relacionada con la reducción de dióxido de carbono hasta el final de la operación. Las pruebas de ANOVA y TUKEY mostraron que existen diferencias significativas entre los TRH evaluados, con un nivel de confiabilidad del 95%, observando que la mayor producción de hidrógeno fue obtenida con un TRH de 4 h. En el reactor UASB convencional no se detectó estabilidad en la producción de hidrógeno durante el tiempo de operación.

Palabras clave: anillos de Biopack; ácidos totales volátiles; reactor UASB.

1. Introduction

Depending on fossil fuels as our main energy source will cause in the mid-term an energy crisis and several environmental contamination problems. Hydrogen gas is one of the most promising alternatives to fossil fuels. The H_2 gas is considered renewable, clean, and produces only water during its combustion. Among the different ways to produce hydrogen, biological production seems to be the most attractive alternative due to different products can be used as raw material, most of which are cost efficient and easy to find. Moreover, if the process is optimized, we can obtain byproducts with added value, for instance, organic acids and biopolymers [1]. Nevertheless, on the hydrogen production through dark fermentation, there are several

How to cite: Hernández, D.M., Hurtado, L.A.del P. and Rodríguez-Chaparro, A.T., Hydrogen production in a novel configuration of UASB reactor under different hydraulic retention time. DYNA, 85(205), pp. 157-162, June, 2018.

© The author; licensee Universidad Nacional de Colombia.

factors that influence and limit the process, among which there are: pH value, temperature, C/N relation, carbon source, S/X relation, configuration of the reactor, fermentation route, the dominant microbial community, etc. [2,3].

The UASB reactor is the most widely used reactor in the world for treating domestic and industrial wastewaters. Ever since its creation by Gatze Lettinga in the 1980s, it has been an economically viable technology, easily used with promising results. The feasibility of UASB reactors for the production of hydrogen was initially studied by [4], who found values of 0.16 L. $L^{-1}.h^{-1}$ of Hydrogen Production Rate (HPR) operating at 2 h of HRT without presence of methane in the biogas, using an inoculum of mixed cultures and wastewater from the rice processing as substrate. [5] carried out similar experiments and observed that the granule formation was formed on the 173rd day of operation, and from that moment, the hydrogen production was stable for an 8-month period. [6] Studied the feasibility of producing hydrogen by treating cheese whey in UASB reactors and noted that the H_2 production was of 112 mLH_2. $L^{-1}.d^{-1}$ for an organic load of 20 g COD. $L^{-1}.d^{-1}$ and 2.5 g COD. $VSS^{-1}.d^{-1}$. These authors state that, although these values are low, the possibility of using UASB reactors fed with industrial wastewaters for the production of hydrogen was proven. [7] evaluated the production of hydrogen after the production of methane in UASB reactors by treating wastewaters from the cassava industry. They used as inoculum active sludge from an anaerobic lagoon previously treated with thermal shocks for inhibiting methanogenic organism and optimizing the production of hydrogen on its first stage. The results were promising not only because of the reactor used but also because was used real industrial wastewater. The maximum hydrogen production reached 37% with a volumetric organic load of 25 $KgCOD.m^{-3}$ d^{-1}. At a high load, the system collapsed and the hydrogen production was reduced mainly due to the accumulation of fatty organic acids.

Despite the already known advantages of UASB reactors, the practical application of these systems for producing hydrogen is still limited, mainly due to long initial times, the type of inoculum capable of minimising the biomass drag, proper handling of hydraulic detention times, etc. [8] mentioned that, by placing supporting structures at the suspension, the process could be accelerated; this is known as hybrid UASB. [9] used a hybrid UASB reactor to treat wastewaters with phenolic compounds. The reactor consisted of an acrylic cylinder at a bench scale in which approximately 54 rings were placed in a 30.48 cm in the middle of the reactor. Hence, a larger biomass concentration would be retained at shorter hydraulic retention time. The results showed that the anaerobic hybrid reactor tolerates 2.5 times more the phenolic organic load increase than the conventional UASB reactor. [10] also demonstrated that having an area with a filtering medium in suspended biomass anaerobic reactors improves the contact between the substrate and the sludge, minimizing the sludge loss and reducing the hydraulic retention time.

The Hydraulic Retention Time (HRT) is one of the operational variables that can be easily manipulated to optimize the hydrogen production. [11] compared the hydrogen production using glucose as a carbon source in a CSTR and UASB reactor with different HRT values (12-2 h). They discovered that there was more stability in UASB reactors and larger volumetric production values of H_2, 19.05 $mmolH_2$. $L^{-1}.h^{-1}$ for a 2 h of HRT. Research conducted by [12] treating wastewater with starch as a carbon source and activated carbon as support in an expanded bed anaerobic reactor concluded that the HRT with the highest volumetric production values was 4 h. These authors modified the HRT to a 24-4 h rate. Recently conducted research by [13] shows that unlike what was previously thought, at low HRTs in both conventional UASB reactors and packed bed reactors, the hydrogen production considerably decreases, being more noticeable at UASB reactors than at packed bed reactors.

In this sense, this research evaluated the effects of three different HRT on H_2 production at conventional and hybrid UASB reactors, using on the top of the reactor a layer of polyethylene rings with foam of polyurethane in its center. This work could contribute to practical knowledge for the hydrogen production at UASB reactors.

2. Material and methods

2.1. Experimental design

Two Upflow Anaerobic Sludge Blanket Reactors (UASB) were used, a hybrid one (R_1) and a conventional one (R_2) with an internal diameter of 74 mm and a useful volume of 2.94 L and 3.0 L, respectively (Fig. 1). The Setting of the R_1 reactor is characterized by the addition of a suspended bed of 100 mm in height composed of high-density polyethylene rings (Ø =19 mm and 10 mm in height) that contains a polyurethane foam core, with the purpose of avoiding sudden biomass washing and improving the biogas production stability [14,15].The specific surface area of each ring is 950 $m^2 \cdot m^{-3}$.

The reactors operated with a constant flow for 134 and 104 days, respectively. The operation time for R_1 was 12 h for 39 days and the second stage with an 8h for 48 days; and the third stage with a 4 h for 45 days. On the other hand, the R_2 reactor was operated with a 12 h, 8 h and 4 h HRT for 45, 40 and 12 days, respectively. The reactors were placed in a thermocontolled chamber at a constant temperature of 35 ºC

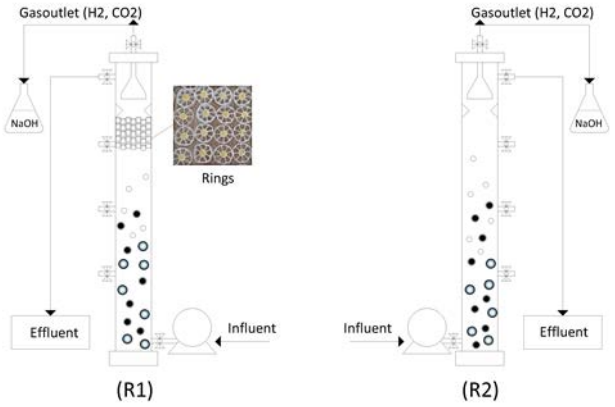


Figure 1. Schematic diagram of the UASB hybrid (R_1) and conventional (R_2) reactors.
Source: The authors.

The reactors were fed with synthetic wastewater using the sucrose as a carbon source. Additionally, an inorganic nutritional source used by [1] was added that contains CH_4N_2O (20 mg.L^{-1}), $NiSO_4 \cdot 6H_2O$ (0.5 mg. L^{-1}), $FeSO_4 \cdot 7H_2O$ (2.5 mg. L^{-1}), $FeCl_3 \cdot 6H_2O$ (0.25 mg. L^{-1}), $CaCl_2 \cdot 2H_2O$ (2.06 mg.L^{-1}), $CoCl_2 \cdot 2H_2O$ (0.04 mg. L^{-1}), SeO_2 (0.036 mg. L^{-1}), KH_2PO_4 (1.3 mg. L^{-1}), $KHPO_4$ (5.36 mg. L^{-1}) and $Na_2HPO_4 \cdot 2H_2O$ (2.76 mg. L^{-1}). The volumetric organic load for the three operation stages was kept at 11.26 Kg COD m^{-3} .d^{-1}, which improve a stable hydrogen production at fixed biomass reactors using recycled pneumatic as support [16] (Mendez et al. 2017). The initial pH of the synthetic wastewater was adjusted at 5.5, adding HCL (10 M).

For both reactors, the inoculum was obtained using the natural fermentation mechanism. Some authors like [17-19] demonstrated that this fermentation that is caused by the combination between the microorganism present in the atmosphere and in the tap water is beneficial to maintain the acidogenic conditions.

2.2. Analytical methods

Percentage concentrations of H_2, CO_2 and CH_4 were simultaneously measured using the gas chromatography equipment Agilent 7890A GC with a thermal conductivity detector (TCD) and a capillary column Carboxen 1010 plot, with a length of 30 m, 0.32 mm internal diameter and 25 µm of the internal stationary layer. The carrier gas was Argon and the injection volume was of 0.6 mL. The average values were the result of three measurements per sample.

The physical-chemical parameters of the influent and effluent samples were monitored three times per week. The organic content (COD), the total volatile acid amount (TVA), volatile suspended solids (VSS), and pH were assessed following the standard methods guideline [20]. The concentration of total carbohydrates on the influent and effluent of the reactor were analyzed using the phenol method [21].

2.3. Statistical analysis

The OriginPro (Version 8.0) software was used to conduct the statistical analysis of variance (ANOVA) of only one path to determine the statistically significant differences (p<0.05) between the measured and calculated parameter for each reactor at the different HRT. In addition, the Tukey test was conducted to do multiple comparisons between the parameter averages studied with 95% reliability. For each parameter, a statistical description was applied.

3. Results

From Figs. 2 and 3, it is evident that the suspended bed in the R_1 reactor improves the system performance regarding stability in the hydrogen production. Not only the production is stable throughout the entire operation process, but the percentage value of the hydrogen gas also remains over 50%. This is not the case of the total volatile acid behavior, which despite a percentage production over 90%, there is no visible difference related to the type of reactor, indicating that its production is probably affected by the biomass inside the biological reactors. These results are confirmed with the ANOVA test, *p=0.8203* for R_1 and *p=0.2194* for R_2, and it shows that there was no significant difference on the TVA production for both reactors at the different studied HRT values. These observations contradict the stated by authors such as [22] Kim et al., (2013) who, from several experiments varying the HRT from 0.5 to 2.5 days determined that this parameter has a direct influence on the TVA production.

[23] on a deep revision about the anaerobic digestion emphasise that this technology is not only designed to treat wastewater with high organic loads and to produce methane, but it must also be planned to produce hydrogen separately or simultaneously with methane and other byproducts with high added value such as volatile fatty acids (VFA). It is important to mention that VFAs are considered to be probable precursors of the biopolymer production and other products such as biofuels, alcohols, aldehyde and ketones.

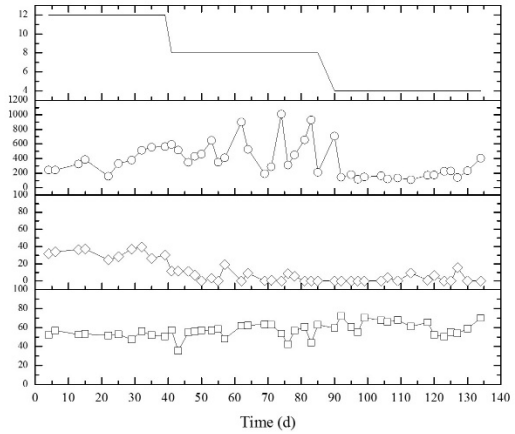


Figure 2. Performance of UASB Hybrid reactor (R_1). (−○−, Total volatile acids in the effluent as mgHAc/L, − ◊ − , production of CO_2 in %,− □ −, production of H_2 in %, - Hydraulic retention time).
Source: The authors.

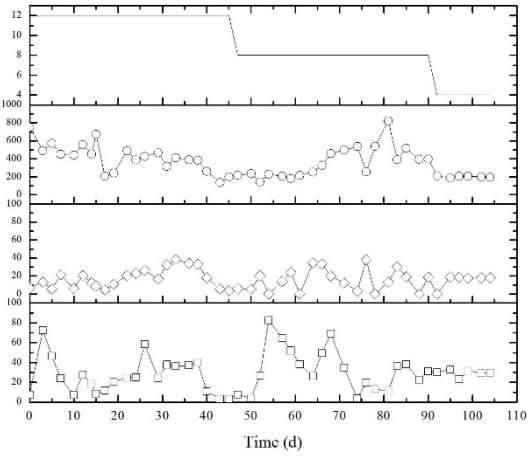


Figure 3. Performance of UASB Conventional reactor (R_2). (−○−, Total volatile acids in the effluent as mgHAc/L, − ◊ − , production of CO_2 in %,− □ −, production of H_2 in %,- Hydraulic retention time).
Source: The authors.

Although the purpose of this research was evaluating the influence of HRT on biohydrogen production in two different high rate anaerobic reactors, it was noted that the TVA results showed methanogenesis inhibition and very low pH values at the effluent, on average 3.4±0.2 and 3.3±0.2 for the R_1 and R_2 reactors respectively. This behavior was already mentioned by [24,25], who state that, when there is an accumulation of volatile organic acids in the system, there is also a pH reduction, causing destabilisation in the anaerobic process represented by inhibition in the methane production.

[6,26] show that there is both a minimum value of volatile acid where the inhibition of methanogenesis is produced and a maximum value where hydrogen-producing organisms are inhibited at 400 mgHAc. L^{-1} for the first and 10,000 mgHAc.L^{-1} for the second. On this research in particular, the minimum value for R_1 was 101.95 mgHAc. L^{-1} (113th day of operation) and the maximum value was 1008.48 mgHAc. L^{-1} (74th day of operation). For R_2, the values were 138.67 mgHAc. L^{-1} (43st day of operation) and 822.42 mgHAc. L^{-1} (81st day of operation). With these results, we can observe that the minimum values in which there is inhibition of methanogenesis are lower than the ones found in the literature.

At reactor R_1, in which the hydrogen production was more stable, there was no accumulation of organic acids that would increase toxicity at hydrogen producers. A possible explanation to this observation can be that the pH value in the system was always kept at 3.5 units, which creates an extremely acid environment that permits that there are not associated this contributes to a reduction of toxicity amongst microorganisms.

On the other hand, [27] state that the organic loading rate (OLR) does have an influence on the variation and accumulation of organic volatile acids, unlike other parameters. Amongst the results presented by these authors, it is important to highlight the proportional increase in the total volatile acid concentration when they vary the organic load at molasses synthetic wastewater. The TVAs increased their concentration from 2.000 mg. L^{-1} to 7.000 mg.L^{-1} with values from 5 to 12 Kg COD. m^{-3}.L^{-1}, respectively. Furthermore, it is important to highlight that butyric acid shows the highest percentage at the total value.

Particularly, the organic loading rate (OLR) value was taken from previous results in reactors similar to ours, whose purpose was finding the load that would permit a good stability when producing hydrogen. These results can be consulted at Show and Tay, (1999) who found that, with load values above 11.26 Kg COD. m^{-3}.d^{-1}, not only was the system unstable when producing hydrogen, but there was also a percentage reduction of total volatile acids from 90% to 60%. The latter one indicates that there is a limit in the organic load value that optimises the production of organic acids and that it also guarantees stable and concomitant hydrogen production.

The results from ANOVA and the TUKEY test for reliability levels of 95% showed that there was a significant difference on the hydrogen production value for the R_1 reactor (p=0.0033) during the 12 and 4 h; and the 8 and 4 h. As for R_2, (p =0.4333), the result was different due to its high instability during the process. The average hydrogen production at reactor R_1 was 53±3, 55±8, and 62±7 % for 12.8 and 4h, respectively. While the hydrogen production value for R_2 did not exceed the average value of 35±21 % presented at the 8 h, previous results indicated that the hydrogen production especially depends on the reactor setting and on the operation using low HRT values. The latter is similar to the stated by authors such as [29-30], who showed that the H_2 content in biogas is lower when the HRT value increases. This behavior is also detailed by [31,12], who mentioned that high HRTs allow the consumption of H_2 through methanogenesis and homoacetogenesis at high rate continuous stirred tank reactors (CSTR), packed bed reactors (PBR), and UASB. Moreover, authors such as [32] indicate that low HRT values affect the ability to hydrolyse substrate and, therefore, affect the possibility of reaching high H_2 production rates.

It is evident that the R_2 reactor setting is less appropriate for the production of hydrogen. [7,33] mention that a biomass loss significantly affects both H_2 production and the process stability. For instance, authors such as [3,34], who used hybrid UASB reactors with carbon nanotubes and plastic pall rings, respective, obtained H_2 production values of 50%, similar to our R_1 reactor, using a 12h . Whereas [5] obtained a H_2 production of 42% using a conventional UASB reactor with an 8h HRT.

According to [25], the H_2 content in the produced gas increases when the organic load reaches an optimal value of 68 Kg .m^{-3}.d^{-1}. Then, from that value despite the load increase of up to 79 Kg .m^{-3}.d^{-1}, the hydrogen percentage decreases about 30% whereas the CO_2 content in the gas notably increases up to 80%. On our research, a larger concentration of hydrogen gas than carbon dioxide was observed. R_1 showed CO_2 values close to 0% especially after the 40th day of operation, which was the end of the 12 h. In the R_2 reactor, the behavior was different; not only was it oscillating like hydrogen gas, but also 40% values were reached (Figs. 2 and 3). [35] mentions that low H_2 productions are caused by non-H_2 producing bacteria that produce, instead, excessive amounts of CO_2 from the sucrose conversion.

Table 1.
Comparison of optimal values for the production of hydrogen at different bioreactor settings.

Parameters	**[26]**	***Apud* by [26]**	**[36]**	**This study - Hybrid UASB**
Organic load (Kg m^{-3}.d^{-1})	68.0	30.0	75.0	11.3
% H_2 in the Biogas	43.0±0.3	38±0.5	35.0	62.0±7.0
VSS Concentration in the reactor (mg L^{-1})	3200±0.2	13000±0.2	20000	7525.0
VSS Concentration in the effluent (mg L^{-1})	4500±0.42	4000±0.3	30000	60.0±43.0
TVA (mgHAc L^{-1})	13300±0.3	12600±0.4	6200	1008±229.0
Removal of COD (%)	32.0±0.3	20.0±0.3	40.0	13.0±9.0
HRT (h)	---	----	5 day	4.0

Source: The authors.

The latter validates the already explained regarding the optimisation of a H_2 producing system in the sense that HRT variations do not have an influence on the system's stability, which particularly depends on the organic load value, the reactor's setting and the inoculation methodology that, as it was observed, have improved the reactor's performance thus allowing it to appropriately maintain the acidogenesis stage.

From Table 1, there is a comparison amongst the different types of reactors and the optimal conditions observed for the production of hydrogen. These results were more remarkable regarding percentage productions, which were higher than the previously mentioned, thus contradicting the stated by authors such as [25,36], who claim that thermophilic bacteria are more efficient for this kind of process.

4. Conclusions

This research verifies that placing Biopack® rings with polyurethane foam in its core, in UASB-reactors, allows its use for producing hydrogen. The maximum reached gas percentage was 62±7%, obtained at 4 h of HRT, thus showing that the process is favored by low hydraulic retention time. Furthermore, it is important to highlight that the support media not only allowed minimizing the loss of biomass, but also contributes to the stability of the hydrogen production if compared with a conventional UASB reactor. Lastly, it was observed that the 90% increase of total volatile acids in both conventional and hybrid UASB reactors had no effect on the hydrogen production.

Acknowledgement

The authors wish to acknowledge to Military University for financial support by the project INV- ING 2104 and to the Sanitation Laboratory for technical support.

References

[1] Peixoto, G., Saavedra, N.K., Varesche, M.B.A. and. Zaiat, M., Hydrogen production from soft-drink wastewater in an upflow anaerobic packed-bed reactor, Int. J. Hydrogen Energy, 36(15), pp. 8953-8966, 2011. DOI: 10.1016/j.ijhydene.2011.05.014.

[2] Li, W.W. and Yu, H.Q., Biohydrogen production with high-rate bioreactors, 1st ed. Elsevier Inc., 2011. DOI: 10.1016/B978-0-12-385099-7.00025-5.

[3] Kahyaoğlu, M., Şahin, Ö. and Saka, Ö., Biohydrogen production from waste substrates as a clean energy energy sources, Part A recover. Util. Environ. Eff., 34(12), pp. 1084-1103, 2012. DOI: 10.1080/15567031003753546.

[4] Yu, H., Zhu, Z., Hu, W. and Zhang, H., Hydrogen production from rice winery wastewater in an upflow anaerobic reactor by using mixed anaerobic cultures, Int. J. Hydrogen Energy, 27(11-12), pp. 1359-1365, 2002. DOI:10.1016/S0360-3199(02)00073-3.

[5] Chang, C. and Feng-Yuan, L., Biohydrogen production using an up-flow anaerobic sludge blanket reactor, Int. J. Hydrogen Energy, 29(1), pp. 33-39, 2004. DOI: 10.1016/S0360-3199(03)00082-X.

[6] Castelló, E, García y Santos, C., Iglesias, T, Paolino,W., Wenzel, W., Borzacconi, J.L. and Etchebehere, C., Feasibility of biohydrogen production from cheese whey using a UASB reactor: Links between microbial community and reactor performance, Int. J. Hydrogen Energy, 34(14), pp. 5674-5682, 2009. DOI: 10.1016/j.ijhydene.2009.05.060.

[7] Intanoo, P., Chaimongkol, P. and Chavadej, S., Hydrogen and methane production from cassava wastewater using two-stage upflow anaerobic sludge blanket reactors (UASB) with an emphasis on maximum hydrogen production, Int. J. Hydrogen Energy, 41(14), pp. 6107-6114, 2016. DOI: 10.1016/j.ijhydene.2015.1.125

[8] Lew, B., Tarre, S., Belavski, M. and Green, M., UASB reactor for domestic wastewater treatment at low temperatures: A comparison between a classical UASB and hybrid UASB-filter reactor, Water Sci. Technol., 49(11-12), pp. 295-301, 2004.

[9] Ramakrishnan, A. and Surampalli, R.Y., Comparative performance of UASB and anaerobic hybrid reactors for the treatment of complex phenolic wastewater, Bioresour. Technol., 123, pp. 352-359, 2012. DOI: 10.1016/j.biortech.2012.07.072.

[10] Zhang, Y., Ma, Y., Quan, X,, Jing, Y. and Dai, S., Rapid startup of a hybrid UASB-AFF reactor using bi-circulation, Chem. Eng. J., 155(1-2), pp. 266-271, 2009. DOI: 10.1016/j.cej.2009.08.005.

[11] Gavala, H.N., Skiadas, I.V. and Ahring, B.K., Biological hydrogen production in suspended and attached growth anaerobic reactor systems, Int. J. Hydrogen Energy, 31(9), pp. 1164-1175, 2006. DOI: 10.1016/j.ijhydene.2005.09.009.

[12] Guo, W.Q., Ren, N.Q., Chen, Z.B., Liu, B.F., Wang, X.J., Xiang, W.S. and Ding, J., Simultaneous biohydrogen production and starch wastewater treatment in an acidogenic expanded granular sludge bed reactor by mixed culture for long-term operation, Int. J. Hydrogen Energy, 33(24), pp. 7397-7404, 2008. DOI: 10.1016/j.ijhydene.2008.09.039.

[13] Si, B., Liu, Z., Zhang,Y., Li, J., Shen, R., Zhu, Z. and Xing, X., Towards biohythane production from biomass: Influence of operational stage on anaerobic fermentation and microbial community, Int. J. Hydrogen Energy, 41(7), pp. 4429-4438, 2016. DOI: 10.1016/j.ijhydene.2015.06.045.

[14] Karadag, D., Köroılu, O.E., Ozkaya, B. and Cakmakci, M., A review on anaerobic biofilm reactors for the treatment of dairy industry wastewater, Process Biochem., 50(2), pp. 262-271, 2015. DOI: 10.1016/j.procbio.2014.11.005.

[15] Choi, W.-H., Shin,C.-H., Son,S-M., Ghorpade, P.A., Kim, J-J. and Park, J-Y., Anaerobic treatment of palm oil mill effluent using combined high-rate anaerobic reactors., Bioresour. Technol., 141, pp. 138-44, 2013. DOI: 10.1016/j.biortech.2013.02.055.

[16] Mendez, A., Torres, Y. and Chaparro, R.T., Effect of organic loading rate in hydrogen production with different support materials in anaerobic fixed-bed reactors., Rev. Ing. Investig. y Tecnol., XVIII(2), pp. 223-232, 2017.

[17] Chen, W., Tseng, Z., Lee, K. and Chang, J., Fermentative hydrogen production with CGS5 isolated from anaerobic sewage sludge, Int. J. Hydrogen Energy, 30(10), pp. 1063-1070, 2005. DOI: 10.1016/j.ijhydene.2004.09.008.

[18] Fernandes, B.S, Saavedra, N.K., Maintinguer, S.I., Sette, L.D., Oliveira, V.M., Varesche, M.B. and Zaiat, M., The effect of biomass immobilization support material and bed porosity on hydrogen production in an upflow anaerobic packed-bed bioreactor., Appl. Biochem. Biotechnol., 170(6), pp. 1348-66, 2013. DOI: 10.1007/s12010-013-0262-7.

[19] Fontes-Lima, D.M., Moreira, W.K. and Zaiat, M., Comparison of the use of sucrose and glucose as a substrate for hydrogen production in an upflow anaerobic fixed-bed reactor, Int. J. Hydrogen Energy, 38(35), pp. 15074-15083, 2013. DOI: 10.1016/j.ijhydene.2013.09.003.

[20] APHA, Standard methods for examination of water and wastewater, 21th ed. Washington, 2005.

[21] Herbert, D., Phipps, P.J. and Strange, R.E., Chemical analysis of microbial cells, Chem. Anal. Microb. Cells, pp. 209-344, 1971. DOI: 10.1016/S0580-9517(08)70641-X.

[22] Kim, W., Shin, S.G., Lim, J. and Hwang, S., Effect of temperature and hydraulic retention time on volatile fatty acid production based on bacterial community structure in anaerobic acidogenesis using swine wastewater, Bioprocess Biosyst. Eng., 36(6), pp. 791-798, 2013. DOI: 10.1007/s00449-013-0905-7.

[23] Khan, M.A., Ngo, H.H., Guo, W.S., Liu, Y., Nghiem, L.D, Hai, F.I., Deng, L.J., Wang, J. and Wu, Y., Optimization of process parameters for production of volatile fatty acid, biohydrogen and methane from anaerobic digestion, Bioresour. Technol., 219, pp. 738-748, 2016. DOI: 10.1016/j.biortech.2016.08.073.

[24] Fezzani, B. and Cheikh, R.B., Two-phase anaerobic co-digestion of olive mill wastes in semi-continuous digesters at mesophilic temperature, Bioresour. Technol., 101(6), pp. 1628-1634, 2010. DOI: 10.1016/j.biortech.2009.09.067.
[25] Cysneiros, D., Banks, C.J., Heaven, S. and Karatzas, K.A.G.. The effect of pH control and 'hydraulic flush' on hydrolysis and Volatile Fatty Acids (VFA) production and profile in anaerobic leach bed reactors digesting a high solids content substrate, Bioresour. Technol., 123, pp. 263-271, 2012. DOI: 10.1016/j.biortech.2012.06.060.
[26] Intanoo, P., Rangsunvigit, P., Namprohm, W., Thamprajamchit, B., Chavadej, J. and Chavadej, S., Hydrogen production from alcohol wastewater by an anaerobic sequencing batch reactor under thermophilic operation: Nitrogen and phosphorous uptakes and transformation, Int. J. Hydrogen Energy, 37(15), pp. 11104-11112, 2012. DOI: 10.1016/j.ijhydene.2012.04.129.
[27] Wijekoon, K.C., Visvanathan, C. and Abeynayaka, A., Effect of organic loading rate on VFA production, organic matter removal and microbial activity of a two-stage thermophilic anaerobic membrane bioreactor, Bioresour. Technol., 102(9), pp. 5353-5360, 2011. DOI: 10.1016/j.biortech.2010.12.081.
[28] Show, K.Y. and Tay, J.H., Influence of support media on biomass growth and retention in anaerobic filters, Water Res., 33(6), pp. 1471-1481, 1999. DOI: 10.1016/S0043-1354(98)00352-2.
[29] Mu, Y., Wang, G. and Yu, H.Q., Response surface methodological analysis on biohydrogen production by enriched anaerobic cultures, Enzyme Microb. Technol., 38(7), pp. 905-913, 2006. DOI: 10.1016/j.enzmictec.2005.08.016.
[30] Chang, F. and Lin, C., Fermentative hydrogen production using granulated sewage sludge microflora, J. Environ. Eng. Manag., 17(1), pp. 57-62, 2007.
[31] Yun, J.H. and Cho, K.S., Effect of hydraulic retention time on suppression of methanogens during a continuous biohydrogen production process using molasses wastewater, J. Environ. Sci. Heal. Part A, 0(0), pp. 1-8, 2016. DOI: 10.1080/10934529.2016.1221221.
[32] Nualsri, C., Reungsang, A. and Plangklang, P., Biochemical hydrogen and methane potential of sugarcane syrup using a two-stage anaerobic fermentation process, Ind. Crops Prod., 82, pp. 88-99, 2016. DOI: 10.1016/j.indcrop.2015.12.002.
[33] Liu, Z., Lv, F., Zheng, H., Zhang, C., Wei, F. and Xing, X.H., Enhanced hydrogen production in a UASB reactor by retaining microbial consortium onto carbon nanotubes (CNTs), Int. J. Hydrogen Energy, 37(14), pp. 10619-10626, 2012. DOI: 10.1016/j.ijhydene.2012.04.057.
[34] Mohammadi, P., Ibrahim, S. and Mohamad-Annuar, M.S., High-rate fermentative hydrogen production from palm oil mill effluent in an up-flow anaerobic sludge blanket-fixed film reactor, Chem. Eng. Res. Des., 92(10), pp. 1811-1817, 2014. DOI: 10.1016/j.cherd.2014.04.023.
[35] Chang, J., Lee, K. and Lin, P., Biohydrogen production with fixed-bed bioreactors, Int. J. Hydrogen Energy, 27, pp. 1167-1174, 2002.
[36] Krishnan, S., Singh, L., Sakinah, M., Thakur, S., Wahid, Z.A. and Sohaili, J., Effect of organic loading rate on hydrogen (H2) and methane (CH4) production in two-stage fermentation under thermophilic conditions using palm oil mill effluent (POME), Energy Sustain. Dev., 34, pp. 130-138, 2016. DOI: 10.1016/j.esd.2016.07.002.

D.M. Hernández, received the BSc. Eng in Civil Engineering in 2012 from the Universidad Militar Nueva Granada and the Sp. degree in hydraulic resources and environment in 2017 from the Escuela Colombiana de Ingeniería Julio Garavito, Colombia. From 2014, she has been worked in scientific research projects related to the production of renewable energies and water treatment. She is currently Professor in the Civil Engineering Department at Universidad Militar Nueva Granada, Bogotá, Colombia.
ORCID: 0000-0002-1505-7478.

L.A. del P. Hurtado, received the BSc. Eng in Mechatronics Engineering (2014) from Military University Nueva Granada, Bogotá, Colombia. From 2012 to 2015, she worked in heating, ventilation, and air conditioning projects for pharmaceutical and alimentary industry, with emphasis on automation and control development. In 2016 she began her research career in the Water Treatment group of Military University. Currently she is research assistant and has been involved in projects under the guidance of PhD. Tatiana Rodriguez in energy recovery from wastewater treatment and applications on conversion devices such as fuel cells. In addition, she has worked in the implementation of instrumentation and real time monitoring of laboratory scale anaerobic reactors in environmental sanitation Laboratory, Military University.
ORCID: 0000-0002-9362-882X.

A.T. Rodriguez-Chaparro, received the BSc. in Civil Engineering from Universidad Militar Nueva Granada, Colombia (1999), MSc. degree in Civil Engineering from Universidad de Los Andes, Colombia (2002) and Dr. in Hydraulic and Sanitation from Universidad de Sao Paulo (Brazil). Associated professor at Civil Department in the Military University and head of the Sanitation Laboratory .With experience in wastewater treatment in particular in anaerobic processes and advanced oxidation processes for the treatment of recalcitrant and toxic compounds.
ORCID: 0000-0002-0600-5414

UNIVERSIDAD NACIONAL DE COLOMBIA
SEDE MEDELLÍN
FACULTAD DE MINAS

Área Curricular de Medio Ambiente

Oferta de Posgrados

Especialización en Aprovechamiento de Recursos Hidráulicos
Especialización en Gestión Ambiental
Maestría en Ingeniería Recursos Hidráulicos
Maestría en Medio Ambiente y Desarrollo
Doctorado en Ingeniería - Recursos Hidráulicos
Doctorado Interinstitucional en Ciencias del Mar

Mayor información:

E-mail: acma_med@unal.edu.co
Teléfono: (57-4) 425 5105

UNIVERSIDAD NACIONAL DE COLOMBIA
SEDE MEDELLÍN
FACULTAD DE MINAS



DYNA
http://dyna.medellin.unal.edu.co/

Flash flotation of free coarse gold using dithiophosphate and dithiocarbamate as a replacement for traditional amalgamation

Moisés Oswaldo Bustamante-Rúa[a], Doria Maria Naranjo-Gómez[b], Alan José Daza-Aragón[a], Pablo Bustamante-Baena[a] & Julián David Osorio-Botero[a]

[a] *Facultad de Minas, Universidad Nacional de Colombia, Medellín, Colombia. mobustam@unal.edu.co, ajdazaa@unal.edu.co, pabustamanteba@unal.edu.co, judosoriobo@unal.edu.co*
[b] *Distribuidora de Quimicosindustriales S.A, Medellín, Colombia. dmnaranjog@unal.edu.co*

Received: January 19th, 2018. Received in revised form: April 4th, 2018. Accepted: April 27th, 2018.

Abstract
This article develops the flash flotation as an alternative method to gravitational separation and amalgamation in order to achieve a greater recovery of coarse native gold through selective hydrophobicity. This method is directly applicated in the discharge of the mills and / or classifiers to recover free and coarse gold; which size is superior than approximately 150 micrometers. Physicochemical characterization of the free gold surfaces was carried out by the measurements of contact angle, Z potential (ZPC) and atomic force microscopy (AFM). The reagent was determined by specific conditions (basic pH, no requirements of an activator and a flotation time of the order of 2 minutes) achieving a superior recovery than 90%. In this case, the isoamyl dialkyl dithiophosphate collector (AERO 3501®) was the reagent which basically got the best results.

Keywords: flash flotation; free coarse gold; dithiophosphate; ditiocarbamato; amalgamation.

Flotación flash de oro nativo grueso usando ditiofosfato y ditiocarbamato como remplazo de la amalgamación tradicional

Resumen
En el presente trabajo se desarrolla la flotación flash como un método alternativo a la separación gravitacional y la amalgamación con el fin de alcanzar una mayor recuperación de oro nativo grueso a través de la hidrofobicidad selectiva. Esta puede ser usada directamente en la descarga de los molinos y/o clasificadores para recuperar oro libre y grueso, cuyo tamaño sea mayor a 150 micrómetros aproximadamente. Se realizó una caracterización fisicoquímica de las superficies de oro libre a partir de las mediciones de ángulo de contacto, potencial Z (ZPC) y microscopia de fuerza atómica (AFM), y se determinó el reactivo que bajo ciertas condiciones (pH básico, sin requerimientos de un activador y un tiempo de flotación del orden de 2 minutos) logró una recuperación mayor al 90%. En este caso, el colector dialquil ditiofosfato isoamilico (AERO 3501®) fue el reactivo que presentó los mejores resultados.

Palabras clave: flotación flash; oro nativo grueso; ditiofosfato; ditiocarbamato; amalgamación.

1. Introduction

The minerals concentration is the operation about the tenor or concentration rise (in percentage) of an ore or mineral rises, through the use of solid-solid separation equipment which allows the segregation of two or more mineralogical species, generating an enrichment of the aforementioned mineral in the stream [1]. The flash flotation is a method that uses the minerals concentration by means of the physical-chemical mineral properties such as hydrophobicity and hydrophilicity [1-3]. This process is one of the most important for the recovery of gold and other valuable metals [4]. Its main restriction is to recover particles of thick material (range of 400-250 μm) by gravitational effects that interrupt the mechanism of the froth [5]. Flotation is a complex process which involve studies of hydrodynamic

How to cite: Bustamante-Rúa, M.O., Najanjo-Gómez, D.M., Daza-Aragón, A.J., Bustamante-Baena, P. and Osorio-Botero, J.D., Flash flotation of free coarse gold using dithiophosphate and dithiocarbamate as a replacement for traditional amalgamation. DYNA, 85(205), pp. 163-170, June, 2018.

© The author; licensee Universidad Nacional de Colombia.

phenomenals and physicochemical surfaces [6], In addition, the process considere the interaction between several factors, such as: the chemical nature of flotation reagents, equipment components and operation components [5].

The native gold ores which are susceptible to flotation treatment has different mineralogical compositions ranging from free gold ore to metal ore, where the gold constitutes a secondary component recovered as a by-product [7]. The geological shapes of occurrences includes pleasure deposits, hydrothermal and epithermal deposits, volcanic material, sedimentary rocks, metamorphic rocks, rusted and weathered material [8].

The recovering of relatively thick native gold (up to 250 μm) by mean of froth flotation, has inaccuracies respecting to hydrophobic behavior of native gold and its relationship with the aspect ratio of some auriferous particles, their malleability have the tendency to be flattened (flakes), which provides the particles with enough large areas, to reach mechanical buoyancy in the recovery equipments [3,9]. Native gold is an alloy of non-specific composition and natural occurrence that contains around 80-99 % gold, 1-15 % silver and between 0-5 % copper [10]. In a non-complexed aqueous medium, gold is not reactive, since gold ions and oxides are thermodynamically unstable, requiring strongly oxidizing conditions for their formation, Eq. (1)

$$Au_2O_3 + 6H^+ + 6e^- \leftarrow \rightarrow 2Au_2 + 3H_2O \quad (1)$$

The oxygen chemisorption upon the gold surface starts at a potential above 1.4 Volts with coating monolayers reached at 2.0 Volts. This is attributed to the growth of an oxide layer (Au_2O_3) in acid solutions and to the layer of hydroxide (Au (OH) 3) in basic solutions with high potentials. According to volttertry, it has been determined that this reactions happen in ranges, depending the orientation of the gold crystals and the presence of impurities [11].

Gold surfaces without patinas are naturally hydrophilic, however, if a monolayer of carbonaceous contaminants is adsorbed from the air or solution, those may be sufficient to produce a hydrophobic surface. As a result, gold can present natural hydrophobicity basically associated with its patinas [12]. The chemical composition of gold particles and their associations with other minerals affects flotation [13] when gold is associated with sulfides, its hydrophobicity is enhanced by the addition of flotation collectors such as xanthates, dithiophosphates and mercaptobenzothiolates [14]. The lack of a good release is a problem in the comminution circuits since it is a key element in the gold extraction operation [15]. Factors that probably affect the buoyancy of free gold are: particle size, absence of scale form, composition, surface contaminants, collector types and cell type [16].

1.1. Effect of particle size

The particle size has a great effect on the recovery of gold by flotation due to its high density. The flotation is effective for gold particles in the range of 20-200 μm. For finer sizes, the selectivity of the gold decrease because of the floating of ore gangue. For thicker particle sizes, flotation must be done at high densities of the mixture (35 % solids) since this reduces the particle size of sedimentation [8].

There is a range of particle size that presents a greater metallurgical recovery, generally the decrease of this could be observed for thicker and finer sizes of the ore [17]. Recovery decreases for small sizes, which is related to the difficulty of particle/bubble adhesion, because they do not acquire enough kinetic energy to produce a stable particle/bubble aggregate. On the other hand, in the optimum size range the particles are more easily dragged into the foam, since the drainage of the pulp is favored with the increase of the sedimentation rate [18]. It is important to note that, in the primary flotation stage ("rougher" stage) the flotation is carried out with an ore granulometry in which the total release of the gold particles is not necessary, however, in the cleaning stage where the selectivity of the particles is necessary, it is essential to carry out a regrind of the concentrate of the ¨rougher¨ stage for the release of the useful species of the ore [1,8].

1.2. Collector selection and dosage.

The function of the collector is to hydrophobize the surface of the desired mineral, the is the reason why it is the most important chemical reagent used in flotation [19]. The extensive experience in the flotation of minerals allows efficient use of certain types of collectors depending on the types of minerals and the mineralogical associations present where the collectors for the flotation of native gold usually prefer xantats and dithiophosphates, or mixtures of them [11,20,21]. The xanthates used to oscillate from ethyl xanthate to amyl xanthate, In addition, with sodium dithiophosphate, in amounts from 50 g/t to 200 g/t, respectively [2,9]. In applications in which native gold is presented along with submicrometer gold and unreleased gold included in mineral sulfides, the combination of these reagents has been shown to be efficient for the recovery of sulfides and at same way for the native gold; so later, cyanidation can be applied to the concentrates to obtain the gold.

The free gold particles can be recovered very selectively, specially against pyrite, keeping the gold surfaces clean from sludge and organic species, without the use of pH regulators, although with the use of small or zero doses of apolar collectors [20]. It should be taken into account that the flotation reagents require a certain conditioning time to be in contact with the pulp, so this way them could react efficiently on the interesting species of the ore [22]. zxThus, the conditioning stage acquires great importance, since some reagents must be added in the grinding stage to have greater contact with the ore, while others are added directly to the discharge box of the ball mills or to the conditioner [14].

1.3. Activators

For the flotation of native gold with clean surfaces it is not necessary to add activators, however activation may be required if there are coatings in the gold or if there are gold particles associated with coated pyrite. In such cases, copper

sulphate, sodium carbonate (which precipitates calcium and heavy metal ions) sodium sulphide (carefully dosesed) and sulfur dioxide are implemented [7,10].The activators include salts of base metals whose metallic ions are adsorbed on the surface of the mineral particles, modifying their superficial chemical properties; as a consequence, the pH range for mineral flotation can be extended, and the rate of flotation, recovery and selectivity are increased.

2. Methodology

2.1. Ore sample

The mineral used in the tests belongs to the San Nicolás mine in the municipality of Segovia-Antioquia-Colombia. We worked with a sulfide mineral that contained free gold, whose sample was taken at the discharge of the primary mill. The San Nicolás Mine corresponds to the mining district of Segovia - Remedios, an important mining district of vetiform gold and silver deposits inside of an intrusive granodiorotic monolithic (Batolito de Segovia). Wich is dated from Jurassic-Triassic [23]. The mineral moisture is 3.2 %, with an apparent density (measured with Burette) of 2.7 g/ml and a real density (measured with a Picnometer) of 2.6 g/ml. The granulometric analysis for the sampls to be floated are described in the Fig. 1.

2.2. Chemical analysis

The chemical analysis for the sample studied can be seen in the Table 1.

Table 1.
Chemical analysis of floated samples

Specie	(%)
FeS_2	77.017
PbS	0.777
ZnS	0.418
$CuFeS_2$	0.067
Insolubles	19.633
Total	97.012

Source: The authors.

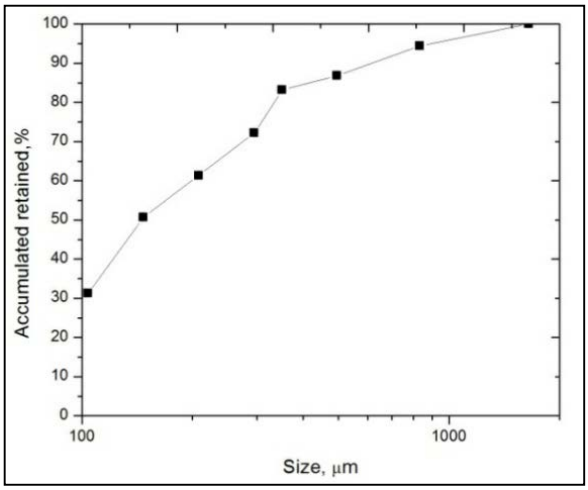


Figure 1. granulometric analysis for the sample.
Source: The authors.

Ignition losses are close to 41.39 % associated with sulfur, obtaining a higher percentage of pyrite, and in the case of galena, sphalerite and calcopitira as less contributors to the floated sample.

2.3. Determination of native gold susceptible to floating in a flash cell

The native gold that is susceptible to flotation is determined by means of an unconventional fire proof, which consists in avoid the generation of the famous "nugget effect", using the Colombian patent generated in the research group CIMEX of the National University of Colombia [24] This method consists in the incorporation of the gravimetric concentration to the conventional tests, allowing to estimate with an accuracy between 1 % and 5%, a precision of 90%, even higher. The gold and silver levels in minerals of an alluvial or vein deposits, are discriminated if the concentration present, in the example, comes from the native element or the element associated with sulfides.

2.3. Flotation cell

To perform the flotation tests in the laboratory, it was required to manufacture a prototype flash flotation cell (Fig. 3 and Table 3). To arrive at the design of the optimal prototype, some variables are already established in the designs suggested by the industry were we are taken into account [25].

Based on the parameters previously established and knowing that a special condition is required in the internal geometry of the cell, an internal cone was designed inside the tank, in order to achieve the rises of the particles, therefore reducing the cells area and favoring the ascent of the heavier particles towards the mineralized foam.

(Bernoulli's Principle) The actual volume of the cell is 20 l and its design is shown in Fig. 2.

2.4. Reagents

The microflotation tests carried out in the Hallimond cell were previosly determinated in order the behavior in the selective gold flotation of the different preselected collectors (tionocarbamate and dithiophosphates).

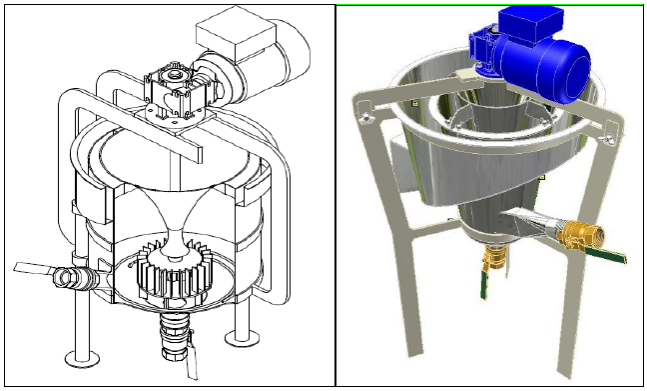


Figure 2. Flotation cell for the test in 3D.
Source: [26,25]

Table 2.
Gold in samples of native gold susceptible to floating in flash cell.

ID	Total Au (g)			Total Au (%)		
	Sample	Concentrate	Tails	Sample	Concentrate	Tails
+48	0.0378	0.0081	0.0297	100	21.4	78.6
+48	0.0352	0.0081	0.0271	100	23	77
+48'	0.0206	0.0123	0.0083	100	59.8	40.2
+48'	0.0393	0.0123	0.0270	100	31.4	68.6
-48 / +100	0.0108	0.0069	0.0039	100	63.8	36.2
-48 / +100	0.0116	0.0069	0.0048	100	59.2	40.8
-48 / +100'	0.0151	0.0099	0.0052	100	65.8	34.2
-48 / +100'	0.0147	0.0099	0.0048	100	67.2	32.8

Source: The authors.

Table 3.
Collectors used for mineral flotation.

	Tank volume [m^3]	A	B	C	D	E	Weight [kg]
SkimAir® -2400	120	9600	7200	4900	3800	6600	30600
SkimAir® -2400	49	8400	5700	4000	2800	4960	23000
SkimAir® -2400	23	6270	5000	3650		4040	8900
SkimAir® -2400	8	4520	3120	2280		2760	3800
SkimAir® -2400	2.2	3390	2400	1740		1900	1800
SkimAir® -2400	1.3	2920	2175	1575		1640	1260
SkimAir® -2400	0.3	1970	800	800		1290	350

Source: [25]

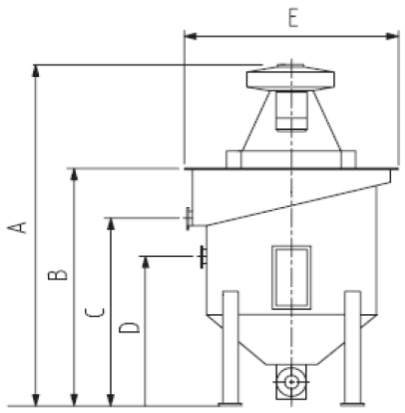


Figure 3. Flotation cell for the test.
Source: [25]

Among the used reagents were: monoalkyl dithioncarbamate (8474), isoamyl dialkyl dithiophosphate (Aero 3501), dithiophosphinate (AEROPHINE 3418 A), dithionocarbamate (S-9411), allyl thionocarbamates allyl thionocarbamates alkyls (5100), isoamyl dialkyldithiophosphate plus amyl xanthate. (PAX) and allyl, a type dithionocarbamate alkyls plus dithionocarbamate, emphasizing the highest recovery of the first two (88-100%). The flotation conditions were as follows: collector conditioning time 10, 20 or 30 minutes, pH of the solution varying between 4 and 11, water volume of 30 ml, and a glycols type foaming agent.

The Thiol collector-type reagents were selected to favor the chemisorption on metal-type bonds, frequently used in the flotation of metal sulfides.

In Table 4, are present the general characteristics of the used collectors, whose were selected through the microflotation tests of free gold. Both collectors were used for the quantification of gold hydrophobicity by measuring the contact angle, and at the same way to carrying out the flotation tests.

3. Results and discussion

3.1. Contact angle

According to the results obtained from these measurements, could seen that the reagents induce greater hydrophobicity to the gold particles and a better conditioning time for the reagent. Additionally, it was possible to identify the variables to be taken into account in the design of experiments for the flash flotation tests.

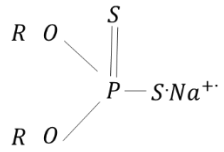
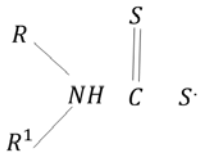
Fig. 4 shows the results obtained in the contact angle measurements with the gold particle trough the collector AERO 3501®, selected for the flotation at different conditioning times.

The greater value obtained for the contact angle indicates that the collector induces greater selective hydrophobicity to the gold surface when there is a longer conditioning time and the pH is 11. On the other hand, the reagent S-8474®, provides selective hydrophobicity to the gold surface with a natural pH and a conditioning time of 10 min.

3.2. Potential z and surface free energy

In Fig. 5 the measurement of the zeta potential for gold, pyrite and galena at different basic pH, are shown. A region of zeta potential is observed (between -25 and -50 mV), of which can be said that the gold particle, pyrite and galena are unstable and susceptible to be collected by a surfactant in the flotation process. When it is taken in place at a pH between 8-11. At pH 11, the zeta potential for gold, pyrite and galena, is close to -50 mV, meaning that at a pH of 11, there will be no separation of gold from its accompanying minerals. This result confirms that activators and depressants should be used.

Table 4.
Collectors used for mineral flotation.

Chemical struture	Comercial reference	Name	Description
	AERO 3501®	Isoamyl dialkyl dithiophosphate	Dosages of 5-25 gpt. Solutions of 5-20% or undiluted. Flotation of ZN, Cu and precious metals to float thick particles.
	S-8474®	Dithiocarbamate (monoalkyl and dialkyl dithiocarbamates)	Dosages of 5-100 gpt. Solution at 5-20% or undiluted. Flotaminerals of Pb, Zn, Cu, Fe and precious metals. For the flotation of most sulfides and precious metals in neutral circuits and pH..

Source: The authors.

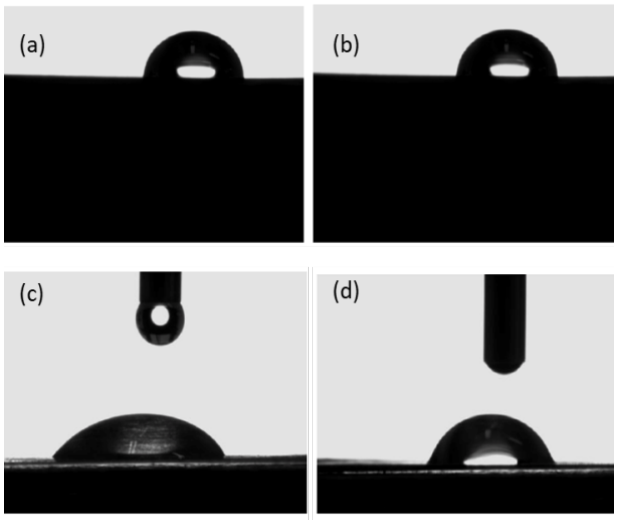


Figure 4. Contact angle for gold samples with 3501 collector (a) 30 minutes (b) 30 minutes and pH. (c) 10 minutes (d) 20 minutes.
Source: The authors.

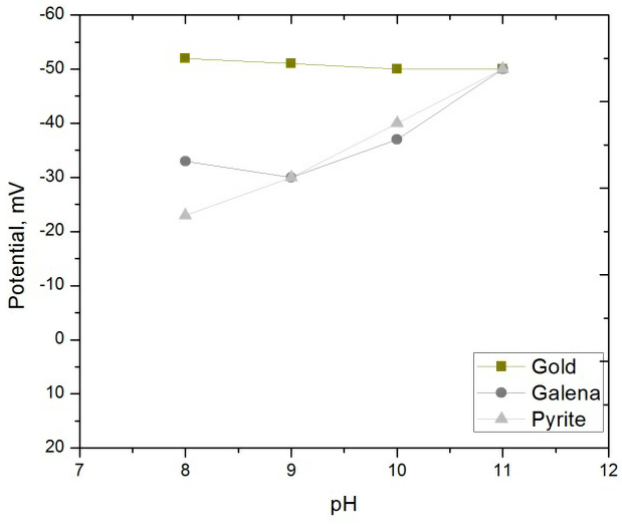


Figure 5. Z potential for gold, pyrite and galena at basic pH.
Source: The authors.

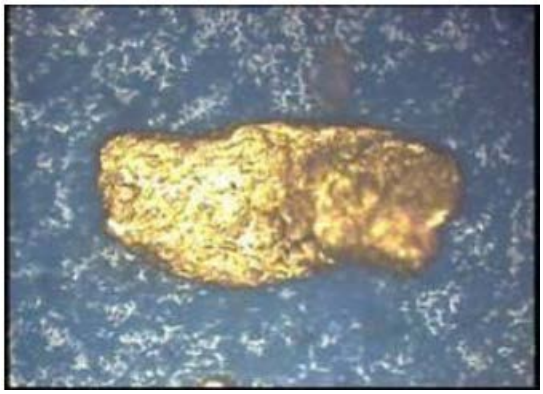


Figure 6. Gold particle.
Source: The authors.

For the measurement of surface free energy, Atomic Force Microscopy (AFM), we made some measurements to a gold particle without a collector and to a gold particle with a collector (Fig. 6).

With the AFM measurements, it is sought to establish if the surfactants are decreasing the superficial tension in the surface of the gold particle.

The results obtained from the first measurements are shown in Fig. 7.

Comparing both graphs, it can be determined that the energy of the surface with the presence of the collector decreased substantially, which indicates a process of adsorption of the surfactant in the gold-water interface.

With the measurements in the AFM, it is not quantitatively determined which collector induces greater hydrophobicity to the gold surface, but at the same, the effect of different collectors on the surface free energy, as well can be determined.

3.4. Operational aspects

The flash cell can be used in the discharge of primary mill, in a small mining and/or in the discharge of classifiers in the return, when grinding circuits are closed (see Fig. 8.). This process competes with the use of mercury and the use of jig and centrifugal gravimetric concentrations, whose are currently used.

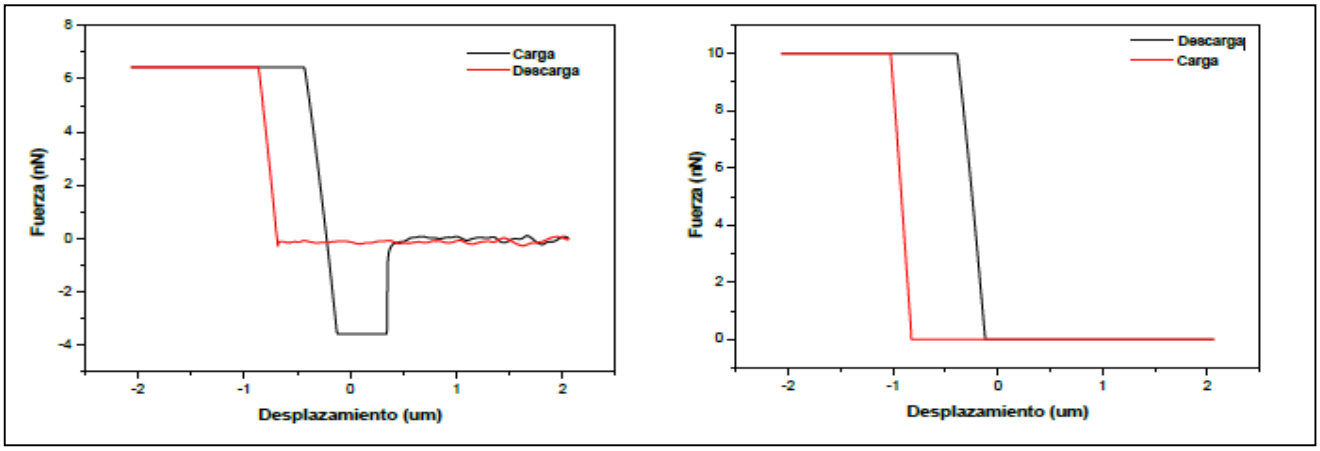


Figure 7. AFM measurements to a gold particle without a collector (left) and to a gold particle with a collector (rigth).
Source: The authors.

Table 5.
Results of the flotations with the collectors AERO 3501® and S-8474®

Collector	Collector Dosage (g/t)	pH	collector conditioning time (min)	Flotation time (min)	Recovery (%)
3501	50	10.5	10	5	84.56
8474	50	10.5	10	5	97.22
8474	50	10.5	10	2	95.58
3501	50	10.5	10	2	99.28
8474	50	10.5	10	2	95.55
3501	50	10.5	10	2	94.92
3501	50	10.5	10	2	79.10
3501	50	11	10	2	52.20
3501	50	11	10	1	98.21

Source: The authors.

3.3. Flotation tests

After the results described above, the best upshots of the tests in Flash flotation are shown in Table 5.

Analyzing the recovery of free gold from the flotation tests carried out with the AERO 3501® and S-8474® collectors, it is observed that the best results were achieved by implementing a 10-min conditioning time and 2-min flotation times, with recoveries of free gold particles of 99.28 % and a conditioning time of 10 min and a flotation times of 5 min., with recoveries of free gold particles of 97.22 %, respectively.

Because of the characteristics of the stream in which a Flash cell is installed, the float gold is thick (greater than 150 μm), therefore this technique is frequently used for the rapid concentration of minerals that have reached their releases in the discharges of the classifiers, allowing to increase the global recovery of the plants, whose main objectives are to avoid the overmoulding of released minerals and at the same way in the recirculation of the stream in the mill.

The main benefits with the use of flash flotation Cells are:

- Lower stock market
- Increase in typical recovery
- Better humidity of concentrates "
- High grade final concentrates are recovered only in a single stage
- Minor volumes in conventional cells.
-

3.4. Environmental impact of the project

The use of mercury in Colombian mining has generated serious environmental and technological impacts, which historically make a detrimental association between gold mining and the soil contamination, the surface water and other actors in the environments around the mines [27].

There is a good correlation between artisanal mining and the increase of mercury losses in th the enrichment processes of gold-bearing minerals. While the large-scale mining reports orders of 0.001 g of mercury per gram of gold produced, small-scale mining reports losses of up to 14.5 g of mercury per gram of produced gold on average, whose can amount to 66.5 g of mercury per gram of gold with the minimum values of 7.5 g of mercury per gram of the produced gold [28], which implies global losses of Mercury around 55.1 t/year just in 5 municipalities of Northeast Antioquia: (Segovia, remedies, Nechí, El Bagre, Zaragoza).

It is estimated from the 100 % of the lost, 34 % is emitted to the atmosphere and 66 % goes to the water streams [28]. The technology, traditionally used by miners in these regions, consists of the use of amalgamating coconuts, in which it is estimated that around 50% of the mercury is lost in the process. This project is basically aimed at the elimination of a historical problem, which has been the use of mercury in gold mining, to search the developing of the least environmental impact and to generate conditions that allow improving the relations between mining and the environment in pro of the sustainability of the exploitation of gold.

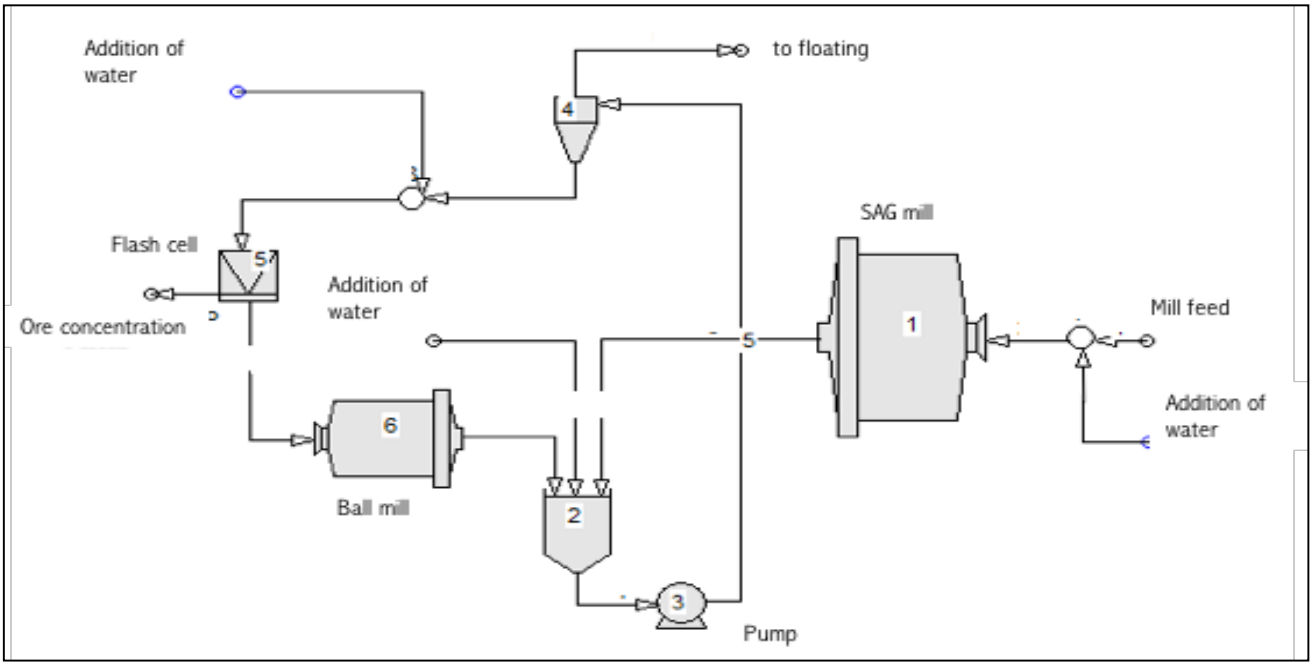


Figure 8. Scheme flash flotation in grinding circuit.
Source: The authors.

4. Conclusion

The surfactant substances adhered to the surface of the particle modify the ZPC, a condition that can favor the adherence or non-adherence of the particles to the air bubbles to guarantee a selective foaming flotation, also an important measure for the flotation of minerals is the contact angle that according to the experimental data of the average value of the contact angle measured on a gold surface, without applying collector is 43.70º and the contact angle for gold can be favorably modified, by means of the addition of different manifolds and collector mixtures, as is the case for mixtures with isoamyl dialkyl dithiophosphate (AERO 3501®), which reached values of up to 96. The reagent used allows to obtain selective hydrophobicity of gold in auriferous ores accompanied by sulphides, such as: pyrites, chalcopyrites, galena and sphalerite, since at no time did the native gold present natural drofobicity. The grain size of the gold particles obtained in the flotation using flash cell is relatively thick, greater than 100 mesh (Tyler, approximately 150 microns). The residence time in the flash flotation as its name indicates is suggested to be short of the order of up to 2 min to 5 min of flotation in the flash cell, depending on which type of collector is used. Times greater than this compromise the selectivity of the flotation and generate a decrease in the gold content in the concentrates that come out in the flotation foam. A prototype of the Flash cell was designed and manufactured, considering hydrodynamic parameters to avoid the sedimentation of too thick gold particles, since the tendency of this type of particles (coarse gold) is to sediment quickly and avoid being collected in mineralized foams and having relatively thick native gold buoyancy in a flash cell designed by this research and that can be an alternative for the direct elimination of mercury.

References

[1] Bustamante-Rúa, M.O., Gaviria-Cartagena, A.C. y Restrepo-Baena, O.J., Notas de la asignatura concentración de minerales. Medellín, Colombia, pp. 1-100, 2008.

[2] Chryssoulis, S.L., Venter, D. and Dimov, S., On the floatability of gold grains, 35th Annu. Meet. Can. Miner. Process., pp. 455-472, 2003. DOI: 10.1016/j.apsusc.2004.03.058

[3] Fuerstenau, M.C., Jameson, G.J. and Yoon, R.H., Froth flotation: A century of Innovation. Society for Mining Metallurgy and Exploration, 2007.

[4] Tayebi-Khorami, M., Manlapig, E., Forbes, E., Bradshaw, D. and Edraki, M., Selective flotation of enargite from copper sulphides in Tampakan deposit, Miner. Eng., 112(June), pp. 1-10, 2017. DOI: 10.1016/j.mineng.2017.06.021

[5] Fuerstenau, M.C., The froth flotation century, in Advances in Flotation Technology, Parekh, B.K. and Miller, J.D., Littelton: Society for Mining, Metallurgy and Exploration, 1999.

[6] Laplante, A. and Dunne, R.C., The gravity recoverable gold test and flash flotation, Proceedings of the 34th Annual Meeting of the Canadian Mineral Processors. 19 P, 2002.

[7] Allan, G.C. and Woodcock, J.T., A review of the flotation of native gold and electrum, Miner. Eng., 14(9), pag. 765-784, 2000. DOI: 10.1016/S0892-6875(01)00103-0

[8] Castro, S. y Garcia, J.A., Flotación, fundamentos y aplicaciones, Universidad de Concepción, Chile, 2003.

[9] O'Connor, C.T. and Dunne, R.C., The flotation of gold bearing ores - A review, Miner. Eng., 7(7), pp. 839-849, 1994. DOI: 10.1016/0892-6875(94)90128-7

[10] Allan, G.C. and Woodcock, J.T., A review of the flotation of native gold and electrum, Miner. Eng., 14(9), pp. 931-962, 2001. DOI: 10.1016/S0892-6875(01)00103-0

[11] Lin, Y.C., Yu, B.Y., Lin, W.C., Lee, S.H., Kuo, C.H. and Shyue, J.J., Tailoring the surface potential of gold nanoparticles with self-assembled monolayers with mixed functional groups, J. Colloid Interface Sci., 340(1), pp. 126-130, 2009. DOI: 10.1016/j.jcis.2009.08.014

[12] Chryssoulis, S., Venter, D. and Dimov, S., On the floatability of gold grains. 35th Annual Meeting of the Canadian Mineral Processors. Canada, pp. 455-472, 2003.

[13] Bulatovic, S.M., Flotation behaviour of gold during processing of porphyry copper-gold ores and refractory gold-bearing sulphides, Miner. Eng., 10(9), pp. 895-908, 1997. DOI: 10.1016/S0892-6875(97)00072-1
[14] CYTEC, Manual de productos quimicos para minería. 2008, P 347.
[15] Aksoy, B.S. and Yarar, B., Natural hydrophobicity of native gold flakes and their flotation under different conditions, in International symposium on Processing of complex ores, Halifax, 1989, pp. 19-27.
[16] Teague, A.J., Van Devente, J.S.J. and Swaminthan, C., A conceptual model for gold flotation, Miner. Eng., 12(9), pp.1001-1019, 1999. DOI: 10.1016/S0892-6875(99)00087-4
[17] King, R.P., Principles of flotation. 1982.
[18] Klimpel, R.R., Dhasen, R. and Free, B.S., Flotation reagents for improved sulphide mineral flotation, in Design and Installation of Concentrating and Dewatering Circuits, 1986, pp. 384-404.
[19] Moncayo-Riascos, I. and Hoyos, B.A., Effect of collector molecular structure on the wettability of gold for froth flotation, Appl. Surf. Sci., 420, pp. 691-699, 2017. DOI: 10.1016/j.apsusc.2017.05.197
[20] Klimpel, R.R., Industrial experiences in the evaluation of various flotation reagent schemes for the recovery of gold, Miner. Metall. Process., 16(1), p. pag. 1-11, 1999.
[21] Pavez, O., Apuntes sobre concentración de minerales. Facultad de Ingenieria, Universidad de Atacama, Chile, 2005.
[22] Cruz, N., Peng, Y., Wightman, E. and Xu, N., The interaction of pH modifiers with kaolinite in copper-gold flotation, Miner. Eng., 84, pp. 27-33, 2015. DOI: 10.1016/j.mineng.2015.09.019
[23] Ortiz, F., Geologia de los depósitos Minerales Metálicos. Medellín: Universidad Nacional de Colombia, 1992.
[24] Bustamante-Rúa, M.O., Restrepo-Baena, O.J. and Gaviria, A.C., Cartagena, Procedimiento para la determinación de metales preciosos, 13-102498--00000-0000, 2011.
[25] OUTOKUMPU Technology, SkimAir® For Flash Flotation and Flash RoughingTM., 2004.
[26] Nicol, M.J., Fleming, C.A. and Paul, R.L., The chemistry of the extraction of gold, Extr. Metall. Gold, pp. 831-905, 1992.
[27] Marrugo-Negrete, J.L. et al., Estudio de la cadena del mercurio en Colombia con énfasis en la actividad minera de oro, Mesa diálogo Perm., 252 P, 2014.
[28] Díaz-Arriaga, F.A., Mercurio en la minería del oro: impacto en las fuentes hídricas destinadas para consumo humano Mercury in ASGM and its impact on water resources used for domestic water supply, Rev. salud pública, 16(6), pp. 947-957, 2014. DOI: 10.15446/rsap.v16n6.45406

M.O. Bustamante-Rúa, is BSc. in Mining and Metallurgy Eng. at the Universidad Nacional de Colombia, MSc. in Sciences of Engineering with a Mention in Extractive Metallurgy - Mention - Mineralurgy of the University of Concepción -Chile, DSc. in Engineering Sciences with a Mention Extractive Metallurgy - Mining of the Universidad de Concepción - Chile. Is full professor of the Universidad Nacional de Colombia, Medellín, director and researcher of the Mineral Institute CIMEX.
ORCID: 0000-0002-1692-991X

D.M. Naranjo-Gómez, is BSc. in Mining and Metallurgy Eng. with a MSc. degree in Materials and Processes. Currently he works in the company Distribuidora de Quimicos Industriales S.A. which provides flotation reagents for the mining industry.
ORCID: 0000-0002-9052-5788

P. Bustamante-Baena, is BSc. in Mining and Metallurgy Eng. at the Universidad Nacional de Colombia. MSc. in Mineral Resources of the same university. Has winner for best undergraduate work and Otto de Greiff National Contest. Belongs to the research group CIMEX Institute of minerals. He is currently the winner of the "Joven Investigador" for Colciencias. Has worked in the industry in the underground coal sector, open pit coal, mineral processing and transformation.
ORCID: 0000-0002-8409-5531

A.J. Daza-Aragón, is BSc. in Mining and Metallurgy Eng.r of the Universidad Nacional de Colombia, finished his studies in 2015, MSc. in Mineral Resources of the Universidad Nacional de Colombia,. He was an auxiliary student of the CIMEX Mineral Institute, where he participated in two seedbeds in association with the National Program of Seeds of Research, Creation and Innovation of the Universidad Nacional de Colombia, 2013-2015.
ORCID: 0000-0001-7596-9666

J.D. Osorio-Botero, is BSc. in Mining and Metallurgy Eng. from the Universidad Nacional de Colombia, completed his studies in 2015. He is currently a student of the MSc. in Engineering - Mineral Resources of the Universidad Nacional de Colombia. He works as a support engineer in the project flotation and separation of magnetic minerals that realized between the Universidad Nacional de Colombia and the company Anglogold Ashanti.
ORCID: 0000-0002-2845-937X



UNIVERSIDAD NACIONAL DE COLOMBIA
SEDE MEDELLÍN
FACULTAD DE MINAS

Área Curricular de Ingeniería
Geológica e Ingeniería de Minas y Metalurgia

Oferta de Posgrados

Especialización en Materiales y Procesos
Maestría en Ingeniería - Materiales y Procesos
Maestría en Ingeniería - Recursos Minerales
Doctorado en Ingeniería - Ciencia y Tecnología de Materiales

Mayor información:

E-mail: acgeomin_med@unal.edu.co
Teléfono: (57-4) 425 53 68

UNIVERSIDAD NACIONAL DE COLOMBIA
SEDE MEDELLÍN
FACULTAD DE MINAS



DYNA
http://dyna.medellin.unal.edu.co/

Model of nonlinear behavior applied to prediction of settlement in deep foundations

Jean Rodrigo Garcia [a] & Paulo José Rocha-de Albuquerque [b]

[a] *Federal University of Uberlândia, Uberlândia, Brazil. jean.garcia@ufu.br*
[b] *University of Campinas, Campinas, Brazil. pjra@fec.unicamp.br*

Received: October 26th, 2017. Received in revised form: April 27th, 2018. Accepted: May 2nd, 2018.

Abstract
Prediction of pile settlement is considered as a highly complex task by geotechnical engineering researchers and professionals, owing to the diversity of prediction methods and also to the difficulty to use predictive models that represent the nonlinear behavior of the soil. In this sense, this work assesses two methods for nonlinear prediction of the settlement of a 23-m long, 31-cm diameter instrumented root pile tested via slow maintained load (SML) test. The local subsoil is composed of colluvional silty-sandy, lateritic clay with a collapsible surface layer (6.5 m), followed by silty clayey sandy soil (diabase residue) down to 20 m. The results showed that the models of nonlinear behavior were in appropriate agreement with the experimentally obtained results. It was also noted that, for small displacements of the top (5.1 mm), the tip load increased continuously from its reaction to the final stage of the test.

Keywords: settlement; root pile; load test; nonlinear model.

Modelo de comportamiento no lineal aplicado a la predicción de asentamiento en fundaciones profundas

Resumen
La predicción de los asentamientos de pilotes es considerada una tarea compleja para los investigadores y profesionales de la ingeniería geotécnica, lo anterior, teniendo en cuenta la diversidad de métodos de previsión y la dificultad de emplear modelos de previsión que representen el comportamiento no lineal del suelo. De esta manera, en este trabajo se evalúan dos métodos de previsión no lineal del asentamiento de un pilote raíz instrumentado, de 23 m largo y 31 cm de diámetro, a través de una prueba de carga estática lenta (SML). El subsuelo del área de estudio está compuesto por arcilla limo-arenosa coluvial, laterítica y colapsable en el estrato superficial (6,5 m), seguido por un estrato de limo arcillo-arenoso (residual) hasta una profundidad de 20 m. Los resultados mostraron que los modelos de comportamiento no lineal concuerdan correctamente con los resultados experimentales. También se verificó que fueron necesarios pequeños desplazamientos de la parte superior del pilote (5,1 mm), para la saturación de la fricción lateral, y que la reacción de la punta presentó un aumento continuo hasta la etapa final del ensayo.

Palabras clave: asentamiento; pilote raíz; prueba de carga; modelo no lineal.

1. Introduction

Root-type piles were created in the 1950's when Fernando Lizzi, an Italian engineer, developed an innovative process to manufacture grouted piles named root piles (Pile Radice). Because of their differentiated execution process, this type of piles has advantages over other existing excavation processes, depending on the local conditions and on the peculiarities of the soil where the piles are to be executed.

Several authors have reported improved performance of deep foundations via tip grouting in comparison to conventional means of perforation installed in similar conditions [1-4].

Laboratory tests have shown that the stress vs. strain behavior of sands is highly nonlinear, even at stresses well below the maximum strength of sand. On the other hand, at

How to cite: Garcia, J.R. and Rocha-de Albuquerque P.J., Model of nonlinear behavior applied to prediction of settlement in deep foundations. DYNA, 85(205), pp. 171-178, June, 2018.

© The author; licensee Universidad Nacional de Colombia.

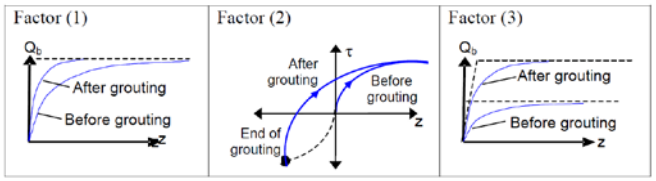


Figure 1. Effect on the t-z and Q_{b-z} load transfer.
Source: [9].

the start of loadings, rigidity is characterized by the shear modulus of 'little strain' (G_0), characterizing an apparent linear behavior. [5].

According to [6,7], the pre-rupture behavior of sand can be represented by a hyperbolic model, with prevalence of nonlinear behavior and the following parameters: strain modulus (E) and shear modulus (G).

Outside the region with elastic behavior, as shear stress builds up to rupture, rigidity is a function of the level of shear stress. Therefore, it cannot be characterized by one single value of modulus of elastic shear, although in many cases a reasonable stress modulus can be obtained by selecting a value of appropriate secant shear modulus [5].

This way, the predictive methods used in this article are based on the hyperbolic stress / strain ratio of [8].

According to [9], due to the executive process of the root pile, the effects that grouting produces on the soil, around and under the drilled bore are still under research; however, three factors are considered to control the soil - foundation interaction, as follows:

- Compression of the soil beneath the pile;
- Redistribution of residual stresses along the shaft due to the ascending mobilization during grouting; and
- Increase in the area of the tip of the stack due to formation of the grout bulb. These effects are summarized in Fig. 1.

Based on the complexity of the model to predict settlements in deep foundations, as well as the effects of the executive process of root-type piles, this work has been developed to assess two nonlinear methods to predict the load vs. displacement curve of a 23-m long, 0.31-m diameter root pile, compression loaded and instrumented in depth with strain gages.

2. Prediction of Settlement

It is common practice to use a wide range of methods to predict the behavior of the admissible pile settlement, since sometimes no experimental results of load tests are available to make this critical task easier. Therefore, two methods of prediction are described, which take into account the effect of nonlinearity of the stress vs. strain behavior of foundation elements of piles.

2.1. Verbrugge's method (1986)

The Verbrugge's Method shows that the load vs. settlement behavior of a pile foundation depends primarily on the load transfer mechanism at the contact between the soil and the pile shaft and also on the propagation of these loads to the soil surrounding the pile. It is necessary to estimate the rupture load in order to apply this method. To do so, [10] suggests using the method of [11].

As set by [12,13], the ratio between stress and settlement at a spot of the pile can be successfully obtained by means of Equation (1).

$$w_0 = R \cdot \lambda \frac{D_b}{E_0} \cdot \sigma_0 \quad (1)$$

Where:

w_0 = settlement at the spot;

E_0 = soil strain modulus beneath the spot in consideration;

λ = axis coefficient (circular pile = 1, and square pile = 1.12);

R is spot coefficient (round pile = 0.32, and pile with broad base = 0.25);

σ_0 = stress in the soil / pile interface.

[10] proposes Equation (2) to calculate the strain modulus of the soil from the values of the cone test (CPT).

$$E=2.2 \cdot q_c + 3.6 \ (MPa) \quad (2)$$

The shear stress, τ_i, is calculated via Equation (3). In this equation, the values found must respect the criterion set in Equation (4), as proposed by [10].

$$\tau_i = B \cdot \frac{E_i}{\lambda \cdot D} \cdot w_i \quad (3)$$

$$\tau_i \leq f_{si} \leq f_{máx} \quad (4)$$

Where:

τ_i – Mobilization of the soil - axis friction;

E_i - Strain modulus of the soil around element i;

D – Pile diameter;

$w_{i=1}$ - Vertical displacement to the lowest face of element i;

B - Axis coefficient obtained by [14].

In order to estimate f_{si} , the proposal of [11] is used per Equation (5).

$$f_{si} = \alpha_f \cdot \frac{q_{ci}}{\alpha_s} \quad (5)$$

Where:

α_f - Philipponnat factor, which depends on the type of pile;

q_{ci} – Value of q_c for layer i;

α_s – Depends on the type of soil;

2.2. t-z Curve

This method models soil resistance through surface friction using a nonlinear spring (t-z of the spring), and the pile tip resistance using a nonlinear spring (Q_{b-z} of the spring) as shown in Fig. 2. The appropriate load transfer curves (t-z and Q_{b-z} curves) are critical in this method to get appropriate estimates of settlements and load transfer to individual axially loaded piles.

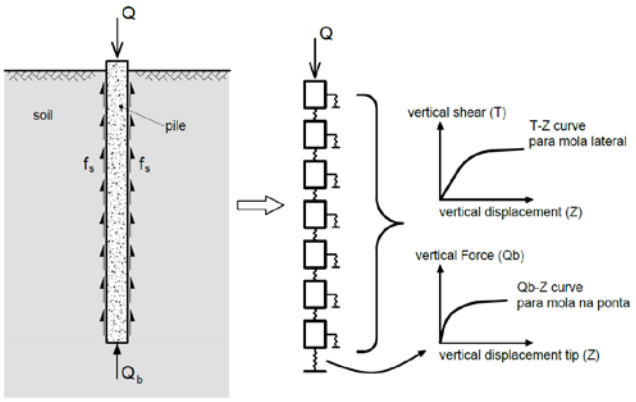


Figure 2. Model proposed for analysis
Source: [16].

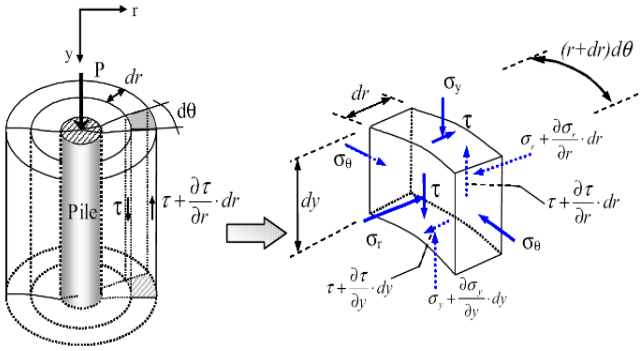


Figure 3. Model of concentric cylinder for analysis of pile settlement.
Source: [16].

Such load transfer curves can be obtained either empirically or theoretically by using initial shear rigidity (resistance) of low effort of the soil around the pile. [15].

According to [15], the asymptotic values required to determine the load transfer curves can be calculated via CPT tests using the LCPC method. The proposed methodology includes soil nonlinearity using a modified hyperbolic model of the type proposed by [5]. The model adopted for analysis is similar to the one proposed by [16] (Fig. 3).

According to [15], using this hyperbolic model is required to be incorporated to the quick reduction of the secant shear modulus, when very low values of effort of G_0 of measurements of seismic CPT are used as initial reference. The predictions of pile settlements employing this method are then compared to the results of the load test. Still according to the authors, the prediction of pile settlement using the proposed theoretical approach and the data from the seismic CPT are in conformance with the static load tests.

The authors make two considerations to calculate settlement: the first one is an approach to soils of elastic-linear behavior; the second one considers soil nonlinearity, which is closer to the actual behavior.

Case 1: Load transfer curves for elastic-linear behavior soils.

The load transfer curve for the pile tip can be approximated using Boussinesq's solution, Equation (6), for a rigid base which is supported in an elastic medium [18]:

$$Z_{base} = \frac{Q_{base} \cdot (1-\nu)}{4 \cdot G \cdot r_0} \quad (6)$$

Where:
Q_{base} = load applied to the pile tip;
G = Soil shear strength modulus;
r_0 = pile radius;
ν = Poisson's ratio of the soil.

The pile shaft settlement, Z, as originally proposed by [16], is obtained by supposing an elastic linear soil with no radial variation of G, as per Equation (7).

$$Z = \frac{\tau_0 \cdot r_0}{G} \cdot ln\left(\frac{r_m}{r_0}\right) \quad (7)$$

Where:
r_m = radial distance in which the shearing in the soil around the pile shaft becomes insignificant;
τ_0 = initial shear stress of the soil. [16] propose to estimate r_m using Equation (8).

$$r_m = 2.5 \cdot l_p \cdot r \cdot (1 - \nu) \quad (8)$$

Where:
r = factor of homogeneity of the soil shear stress;
l_p = pile embedding depth;
ν = Poisson's ratio of the soil.

Case 2: Load transfer curves for soils with nonlinear behavior.

According to the authors, it is of great importance to get parameters to be used in the formulations correctly. The initial shear modulus (G_0) can be obtained in situ by means of Equation (9).

$$G_0 = \rho \cdot {V_s}^2 \quad (9)$$

Where:
ρ = specific soil mass;
V_s = speed of the shear wave obtained from seismic refraction tests.

It must be pointed out that the values of the modulus of neighboring piles will be affected by the process of installation of a pile, and such effects are hard to be quantified. However, they are considered less important than the nonlinear ones and generally smaller when compared to the uncertainties involved in the estimation of soil properties [18,19].

Soil nonlinearity is an important factor to be analyzed to correctly predict the behavior of the load transfer curve.

The hyperbolic models of stress vs. strain shear are used to suitably represent the nonlinear behavior of soils [8, 20, 21], according to Equation (10).

$$\tau = \frac{\gamma}{\frac{1}{G_0} + \frac{\gamma}{\tau_{ult}}} \quad (10)$$

Where:
γ = strain by the shearing agent;
G_0 = tangent initial shear modulus;
τ_{ult} = ultimate shear stress, i.e., the stress in which strains

tends to infinite.

[22] report the ratio between the asymptotic value of τ_{ult} and the maximum shear stress, τ_{max}, as per Equation (11).

$$\tau_{max} = R_f \cdot \tau_{ult} \tag{11}$$

Where:

R_f = rupture ratio ($\leq$1).

By replacing Equation 11 in 10, we get Equation (12) for secant shear modulus:

$$G_{sec} = G_0 \cdot \left(1 - \frac{\tau \cdot R_f}{\tau_{max}}\right) \tag{12}$$

Same as the procedure in case 1, Equation (13) can be used to calculate the settlement of the pile axis.

$$Z = \frac{\tau_0 \cdot r_0}{G_0} \cdot \ln\left(\frac{\frac{r_m}{r_0} - \frac{\tau_0 \cdot R_f}{\tau_{máx}}}{1 - \frac{\tau_0 \cdot R_f}{\tau_{max}}}\right) \tag{13}$$

The initial rigidity (G_0) of Equation (13) comes from the elastic linear behavior of the t-z curve when $R_f = 0$, resulting in Equation (14).

$$\frac{G_{sec}}{G_0} = 1 - f \cdot \left(\frac{\tau}{\tau_{max}}\right)^g \tag{14}$$

Where:

f and g = empirical parameters (f = 0.98 and g = 0.3).

The methodology proposed by [15] to assess the supporting capacity is based on an approach of load transfer that models the quick nonlinear degradation of soil rigidity in small strains using a modified hyperbolic model such as the one proposed by [5], resulting in Equation (15).

$$Z = \frac{\tau_0 \cdot r_0}{G_0 \cdot g} \cdot \ln\left[\frac{\left(\frac{r_m}{r_0}\right)^g - f \cdot \left(\frac{\tau_0}{\tau_{máx}}\right)^g}{1 - f \cdot \left(\frac{\tau_0}{\tau_{máx}}\right)^g}\right] \tag{15}$$

First of all, the value of K_0 must be calculated from Equation (16) for the behavior of the base.

$$K_0 = \frac{4 \cdot G_0 \cdot r_0}{(1 - \nu)} \tag{16}$$

When the rigidity coefficient of the spring (representing the soil) is degraded at the pile tip, it can be corrected by Equation (17) as reported by [23].

$$K_{sec} = K_0 \cdot \left[1 - f \cdot \left(\frac{Q_b}{Q_{b,max}}\right)^g\right] \tag{17}$$

After getting the parameters and variables, the following step is the calculation of the settlement of the pile tip as expressed in Equation (18).



Figure 4. Location of the experimental field
Source: [24]

$$Z_{base} = \frac{Q_b}{K_0 \cdot \left[1 - f \cdot \left(\frac{Q_b}{Q_{b,max}}\right)^g\right]} \tag{18}$$

The key contribution of this method is that it improves the perception of soil nonlinearity when the initial shear modulus with very low strength is used as the initial reference. Another advantage of this method is the use of the CPT data, which is a common test in geotechnics, and this expands the applicability of this method.

3. Material and methods

The research was developed at the Experimental Field of Mechanics of Soils and Foundations of the State University of Campinas (Unicamp), located at Zeferino Vaz University City in Barão Geraldo district, Northwest region of Campinas, as shown in Fig. 4.

The profile of the Experimental Field is composed of diabase soil with a 6.5-m thick surface layer consisting of highly porous silty-sandy clay (colluvial) followed by a layer of clayey-sandy silt (diabase residue) down to 20m. The water level is found only at 17-m depth depending on the season of the year.

Several field tests have already been conducted at the site, such as: Standard Penetration Test SPT and SPT-T, CPT, Crosshole, DMT, PMT, refraction seismic, vertical electrical probing and laboratory tests.

The first layer is composed by mature soil (lateritic and collapsible), which has undergone intense weathering and lixiviation processes. These processes caused an increase in porosity due to fines being carried to the deeper horizon, thus providing the emergence of a soil with void indexes of approximately 1.8. This layer has values of indexes of resistance to penetration $N_{SPT} \leq 5$. The second layer is composed of recent residual soil that preserves characteristics from its origin rock, with values of indexes of void equal to 1.5. Some of the characteristics of resistance obtained for this layer are $N_{SPT} \leq 35$.

The values for lateral friction (f_s) and tip resistance (q_c) collected in the Cone Penetration Test (CPT) are shown in

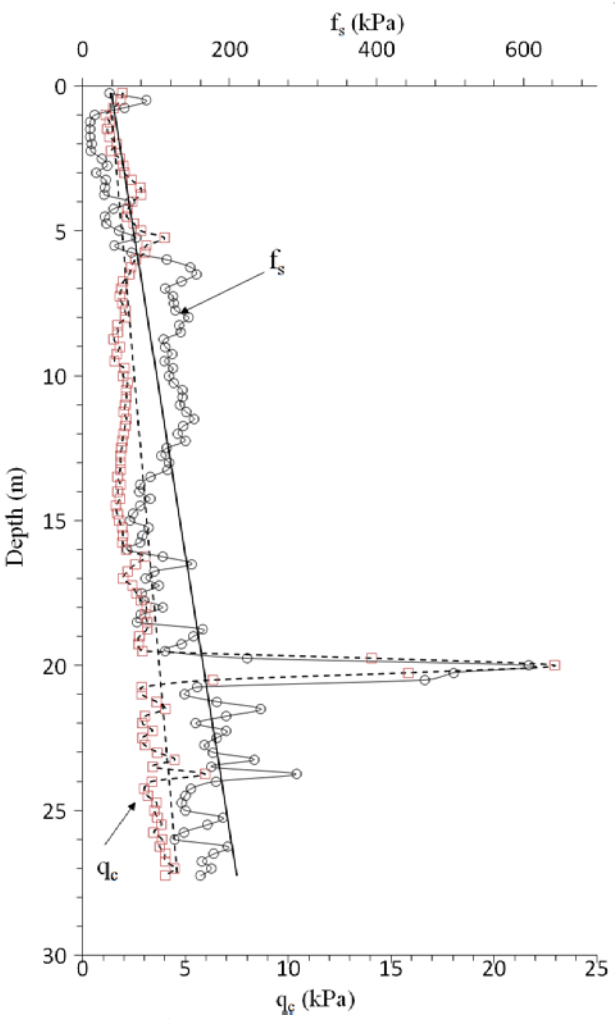


Figure 5. Results of the CPT test
Source: The authors.

the graph of Fig. 5. The massif was prospected down to the depth of 27 m.

In means terms of lateral friction (f_s) and tip resistance (q_c), Equation (19) and Equation (20), respectively, were obtained. The values obtained with these equations are expressed in kPa.

$$q_c = 100 \cdot z + 1200 \text{ (kPa)} \quad (19)$$

$$f_s = 6.33 \cdot z + 10 \text{ (kPa)} \quad (20)$$

The values of the moduli of strain (E), shear (G) and initial shear (G_0) were obtained from former studies conducted by [25], as shown in Table 1.

The pile tested was of the root type with a 0.31-cm diameter and 23 meters long. It was instrumented along the shaft so as to obtain the load transfer curve between soil layers.

The load test was taken to the limit of the reaction system (2000 kN). The load increments and respective vertical displacements produced the load vs. displacement curve for the tested pile, as shown in Fig. 6.

Table 1.
Strain and shear parameters

Depth (m)	E (MPa)	G (MPa)	G_0* (MPa)
2.0	3.11	1.17	-
4.0	10.10	3.80	-
7.0	-	-	90
8.0	11.65	4.38	78
9.0	-	-	60
10.0	13.03	4.90	-
12.0	13.06	4.91	-
14.0	10.49	3.94	-
16.0	6.98	2.62	-

* obtained from the crosshole test.
Source: Adapted from [25]

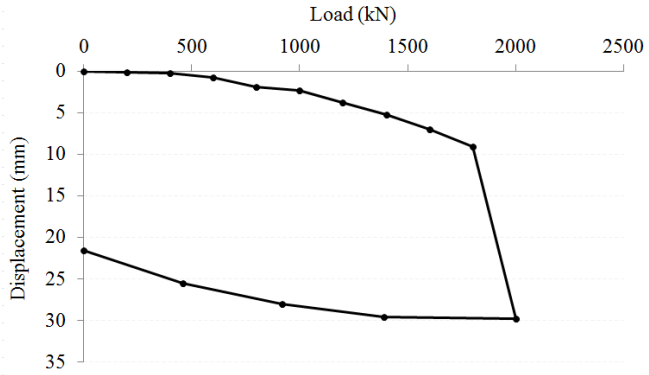


Figure 6. Load vs. displacement curve.
Source: [24].

The maximum displacement observed was 30 mm for the maximum test load of 2,000 kN. It must be pointed out that this is not the rupture load, since no geotechnical or structural rupture of the foundation element was observed. When the method of [26] modified by [27] is applied, the pile rupture load is approximately 2,010 kN, whereas the rigidity method proposed by [28,29] provides a load of 2,140 kN. Based on the results obtained with the methodologies, the conclusion is that the load test was taken to displacements that characterize values close to the geotechnical rupture load of the pile.

The stress vs. strain behavior for the respective instrumentation levels was obtained from the instrumentation readings, as shown in Fig. 7.

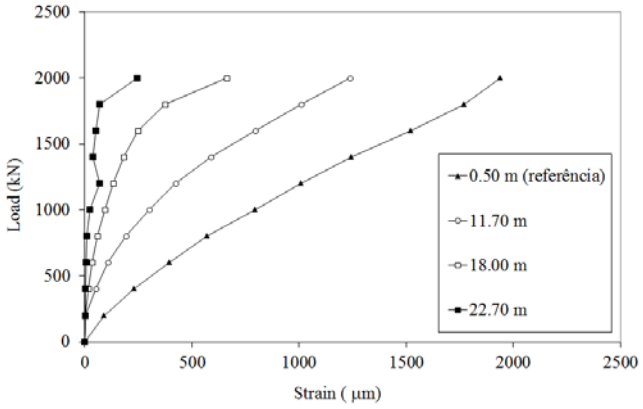


Figure 7. Stress vs. strain graph.
Source: [24].

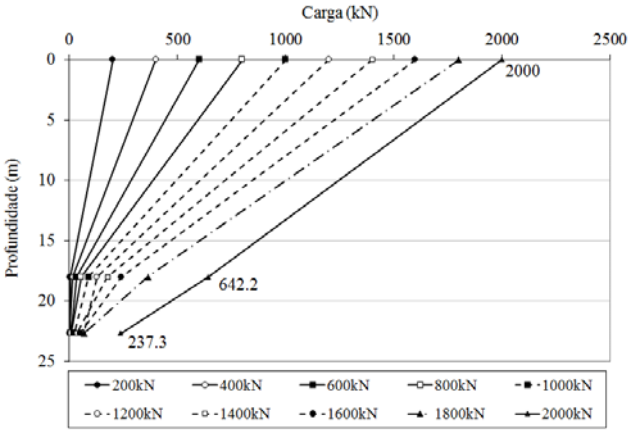


Figure 8. In-depth load transfer
Source: The authors.

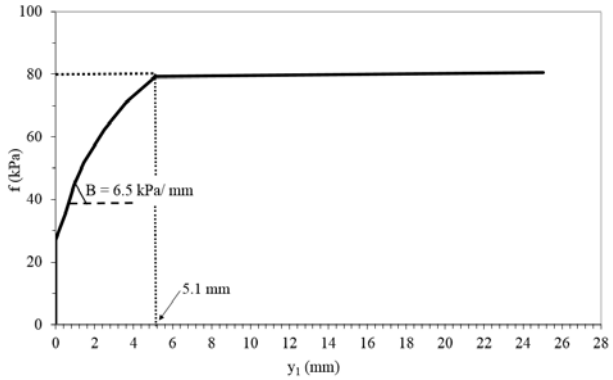


Figure 9. Mean unit lateral friction as a function of mean displacement
Source: The authors.

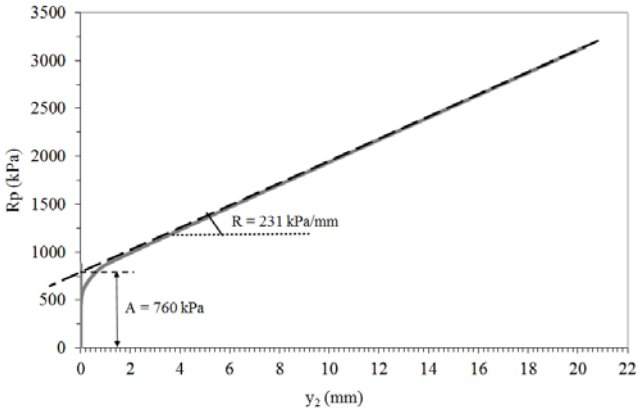


Figure 10. Tip resistance per the Second Law of Cambefort
Source: The authors.

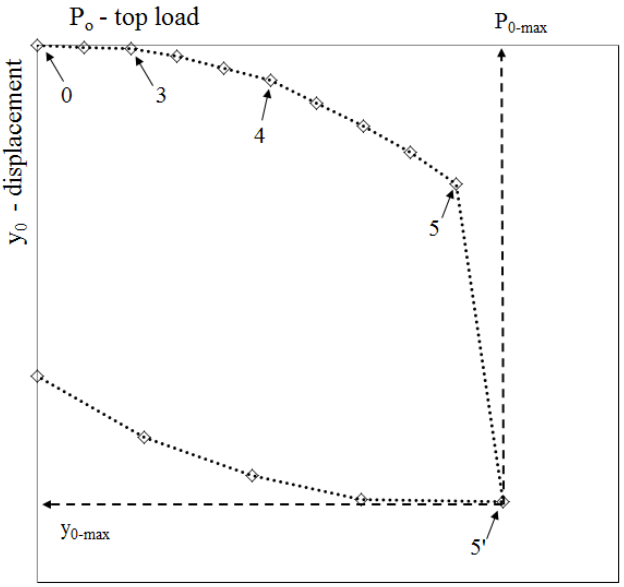


Figure 11. Behavior of the load vs. displacement curve
Source: The authors.

An analysis of the instrumentation data of the reference section produced a pile strain modulus of 33.4 GPa, which showed that the instrumentation behaved appropriately, i.e., the strains were coherent with the depth of the installation.

The data obtained from the instrumentation produced the load transfer curves in depth (Fig. 8). In the figure, the values of the portion relating to tip resistance are 237 kN (11.9%) and 19 kN (1.9%) for the maximum load (Q_{max}), and work load (Q_{trab}), respectively. The observation is that the tip portion, under the action of the maximum load, is 12.4 larger in comparison to the tip mobilization upon action of the work load, whereas the work load is half the maximum load.

As to the First Law of Cambefort, as shown in Fig. 9, the saturation of lateral friction was found to be 80 kPa. The shaft had a displacement in the order of 5.1 mm (y_1), which means 1.6 % of the pile diameter, to show that small displacements were required for full mobilization of friction. The Cambefort Parameter (B) referring to the inclination of the straight line of the model was approximately 6.5 kPa/mm, which produced the rigidity of the pile (K_r= 109 kN/mm) and relative rigidity between the pile - soil (friction) of the order of 0.13 (k). It must be noted that, as this is the first load, there is no residual load P_h=0 and μ=1

An analysis of Fig. 10 referring to the pile tip reaction showed that there is a linear increase in reaction as the tests advances. The analysis also showed that parameter A is approximately 760 kPa; the pile tip rigidity is 231 kPa/mm. This indicates a rigid elastoplastic behavior for the soil of the pile tip, which means that the tip reacts significantly with small displacements [30].

Particularly by means of application of Cambefort's Laws and the shape of the load transfer, the lateral friction was completely saturated along the pile length. Part of the tip resistance is mobilized as a function of the load increments.

Based on Cambefort's analyses and on the parameters obtained, it was possible to analyze the load vs. displacement curve of the load test, as shown in Fig. 11.

Based on an analysis of the graph in Fig. 11 obtained by means of the load test, the noticeable points of the load vs. settlement curve can be observed. Sections 0 and 3 represent the pseudoelastic interval; 3 and 4 (progressive mobilization

Table 2.
Settlements values for work load

Methods	Settlement (mm)		ME / PC
	ME	PC	
Verbrugge (1986)	1.15	2.31	0.50
t-z curve	2.15		0.93

Source: The authors.

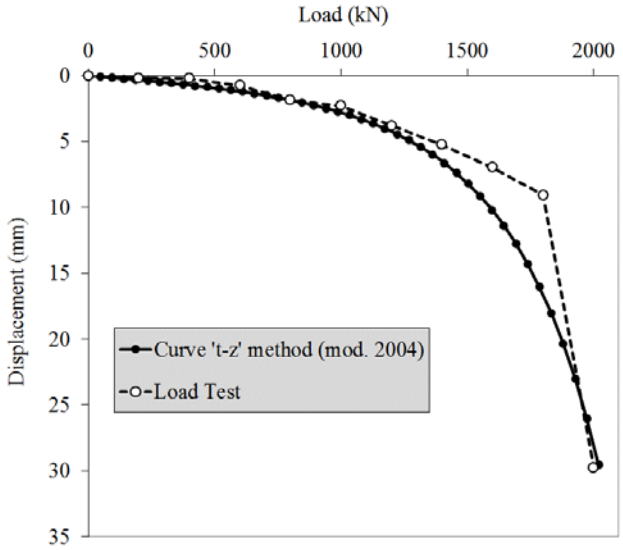


Figure 12. t-z curve method - modified by Pando *et. al* (2004)
Source: The authors.

of lateral friction of the top to the tip); 4 and 5 (development of the tip reaction) and points 5 and 5' (associated to maximum load). These points are not necessarily the rupture load.

4. Prediction of Load vs. Settlement

The methods that were analyzed, [10,15], provided good approximation between the prediction and the experimental result, as shown in Figs. 12 and 13.

An assessment in terms of displacement of work load concluded that the work load is equal to 50% of the maximum test load. In this sense, the values of settlement obtained are shown in Table 2, which evaluates the assertiveness of each method as to the values of the load test.

The t-z curve method was the one that was closest to the settlement value obtained in the load test for the work load, with 93% accuracy percentage. On the other hand, the performance of the Verbrugge method scored 50% accuracy in this same comparison, as shown in Table 2.

The curves obtained by the methods agree appropriately to the curve obtained with the load test, particularly in the initial elastic section of the curve in which the t-z curve method agrees better with the actual curve (Fig. 12).

The method proposed by Verbrugge demonstrates the complexity of predicting the load vs. settlement behavior in a simplified way with the equations applied; however it proved to be appropriate to predict settlement. The key mechanism taken into consideration involved the basic concept of load dissipation via lateral resistance provided to the foundation element by the surrounding soil.

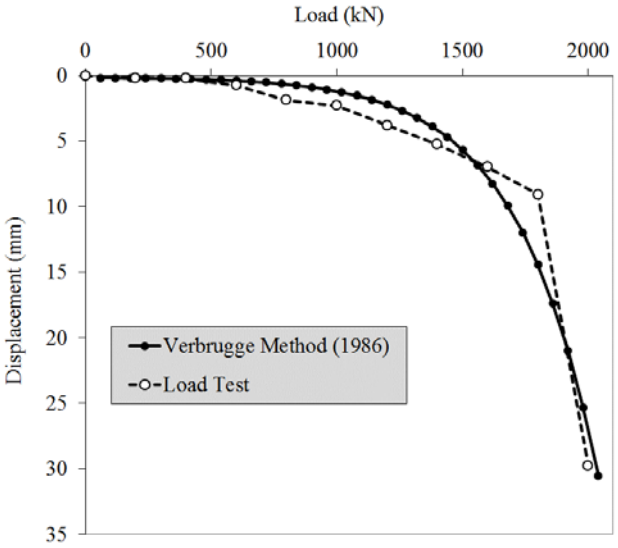


Figure 13. Verbrugge Method (1986)
Source: The authors.

In the section with elastoplastic behavior where the soil enters a yield condition, the methods tend to follow the same behavior, but the load test curve is more 'rigid', i.e., the loss of pile/soil contact resistance takes place abruptly.

5. Conclusions

The considerations adopted by these methods deal with the nonlinearity of the soil stress vs. strain behavior, particularly as to use of the initial shear modulus of the soil (G_0) and its respective degradation when loads are applied. Such inference becomes more evident when checking the results found through methods that use this key parameter of the soil.

It is known that two of the key parameters that govern the nonlinear behavior of the soil-pile element are: strain modulus and shear modulus of the soil. However, publications on settlement of separate piles that use the t-z curve method modified by [16] lead to the conclusion that the shear modulus for small strains or the initial shear modulus (G_0) represent a critical soil parameter to be used in the formulations that are developed. This modulus provides quick reduction when the first efforts produced by the initial load take place, coherently together with quick reduction of soil resistance.

The methods proposed by [16,11] include making complex calculations since the process is iterative and includes 'n' repetitions. Therefore, it is critical to develop a plan of the methods, in this case, with the use of the Visual Basic software program in interface with MS Excel.

The adequacy of the methods to predict the load vs. displacement curve is required to calibrate the variable coefficients that each method uses, and to adjust them to the conditions of the local subsoil. On the other hand, the greater the number of comparative tests of these methods with results of actual load tests, the better their performance to predict settlement.

The methods of the t-z curve [16,11] did not take

slenderness (L / D) into consideration, nor the type of pile or the executive process employed. On the other hand, these methods were influenced by the initial shear modulus (G_0) and also by the strain modulus (E), which can be estimated via in situ tests.

For a better understanding and checking of the efficacy of the prediction obtained by the methods of the t-z curve [10,15], it is recommended to carry out a greater number of analyses of actual and predicted results for several types of piles manufactured by different executive processes.

Acknowledgments

The authors wish to thank the Coordination for the Improvement of Higher Education Personnel (CAPES), University of Campinas (Unicamp), São Paulo Research Foudation (FAPESP) and the National Council for Scientific and Technologic Development (CNPq).

References

[1] Bolognesi, A.J.L. and Moretto, O., Stage grouting preloading of large piles on sand. Proceedings of 8th ICSMFE, Moscow, pp. 19-25, 2011.

[2] Stocker, M.F., The influence of post grouting on the load bearing capacity of bored piles. Proceedings of 8th European Conference on Soil Mechanics and Foundation Engineering, Helsinki, pp. 167-170, 1983.

[3] Silwinski, Z.J. and Fleming, W.G.K., The integrity and performance of bored piles. Proceedings of the International Conference on Advances in Piling and Ground Treatment for Foundations, Institution of Civil Engineers, London, 2004.

[4] Mullins, G. and Winters, D., Post grouting drilled shaft tips - Phase II, Final Report to the Florida Department of Transportation, 2004.

[5] Fahey, M. and Carter, J.P., A finite element study of the pressuremeter test in sand using a nonlinear elastic plastic model. Canadian Geotechnical Journal, 30(2), pp. 348-362, 1993. DOI: 10.1139/t93-029.

[6] Hardin, B.O. and Drnevich, V.P., Shear modulus and damping in soils: measurement and parameter effects. Journal of the Soil Mechanics and Foundations Division (ASCE), 98(6), pp. 603-624, 1972a.

[7] Hardin, B.O. and Drnevich, V.P. Shear modulus and damping in soils: design equations and curves. Journal of the Soil Mechanics and Foundations Division (ASCE), 98(7), pp. 667-692, 1972b.

[8] Kondner, R.L., Hyperbolic stress-strain response: Cohesive soils. Journal of the Soil Mechanics and Foundations Division (ASCE), 89(1), pp. 115-144, 1963.

[9] Fernandez, A.L., Pando, M.A. and King, P.G., Load test program to validate model for post grouted drilled shafts, Contemporary Issues in Deep Foundations, Geotechnical Special Publication (ASCE). 158(1), 2007.

[10] Verbrugge, J.C., Pile foundations design using C.P.T. results. Structural Engineering Practice, Belgium, 3(2), pp. 93-112, 1986.

[11] Philipponnat, G., Méthode pratique de calcul d'un pieu isolé a l'aide du pénétromètre statique. Revue Française de Géotechnique, 10(1), pp. 55-64, 1980.

[12] Cambefort, M., Essai sur le comportement en terrain homogène des pieux isolés et des groupes de pieux. Proceedings of l'Institut du Bâtiment et des Travaux Public, 204, 1964.

[13] Cassan, M., Les essais in situ en mécanique des sols. Paris: Editora Eyrolles, v.2, 1978.

[14] Verbrugge, J.C., Evaluation du tassement des pieux, à partir de l'essai de pénétration statique. Revue Française de Géotechnique, 15(1), pp. 75-82, 1981.

[15] Pando, M.A., Fernandez, A.L. and Filz, G.M., Pile settlement predictions using theoretical load transfer curves and seismic CPT data. Proceedings of the ISC-2 Symposium on Geotechnical and Geophysical Site Characterization, Porto, Portugal, 2004, Vol. II. pp. 1525-1531.

[16] Randolph, M.F. and Wroth, C.P., Analysis of deformation of vertically loaded piles. Journal of the Geotechnical Engineering Division, 104(12), pp.1465-1487, 1978.

[17] Poulos, H.G. and Davis, E.H., Pile foundation analysis and design. Sidney: Rainbom-Bridge Book Co., 1980.

[18] Kraft L.M., Ray, R.P. and Kagawa T., Theoretical t-z curves. Journal of the Geotechnical Engineering Division (ASCE), 107(11), pp. 1543-1561, 1981.

[19] Randolph, M.F. Design methods for piles groups and piles rafts. State-of-the-art report, Proceedings of XIII ICSMFE, New Delhi, 5, 1994, pp. 61-82.

[20] Kondner, R.L. and Zelasko, J.S., A hyperbolic stress-strain formulation for sands. Proceedings of 2nd Pan-American Conference on Soil Mechanics and Foundations Engineering, São Paulo, Vol. I, 1963, pp. 289-324.

[21] Duncan J.M. and Chang C.Y., Nonlinear analysis of stress and strain in soils. Journal of the Soil Mechanics and Foundations Division (ASCE), 96(5), pp. 1629-1653, 1970.

[22] Chang, C.Y. and Duncan, J.M., Analysis of soil movement around a deep excavation. Journal of the Soil Mechanics and Foundations Division (ASCE), 96(5), pp. 1655-1681, 1970.

[23] Chow, Y.K., Analysis of vertically loaded pile groups. International Journal for Numerical and Analytical Methods in Geomechanics, 10, pp. 59-72, 1986.

[24] Garcia, J.R., Estudo do comportamento carga vs recalque de estacas raiz carregadas à compressão, MSc. dissertation, Faculty of Civil Engineering, Architecture and Urbanism, Unicamp, Campinas, 2006.

[25] Fontaine, E.B., Utilização de ensaios geotécnicos especiais de campo (cone elétrico e pressiométrico) em solos do interior do estado de São Paulo, PhD Thesis. Faculty of Agricultural Engineering, Unicamp, Campinas, Brazil, 2004.

[26] Van Der Veen, C., The bearing capacity of a pile. Proceedings of International Conference on Soil Mechanics and Foundation Engineering (III ICSMFE), Switzerland, 1953, V.2, pp. 84-90.

[27] Aoki, N., Considerações sobre a capacidade de carga de estacas isoladas. Curso de extensão universitária em engenharia de fundações. Universidade Gama Folho, Rio de Janeiro, Brazil, 44 P, 1976.

[28] Décourt, L., Ruptura de fundações e coeficientes de segurança a luz do Conceito de Rigidez. Proceedings of XI COBRAMSEG, Brasília, V.3, 1998, pp. 1599-1606.

[29] Décourt, L., Provas de carga em estacas podem dizer muito mais do que têm dito. Proceedings of VI SEFE, São Paulo, V.1, pp. 221-245, 2008.

[30] Viana da Fonseca, A., Santos, J.A., Esteves, E.C. and Massad, F., Analysis of piles in residual soil from granite considering residual soils. Soils & Rocks, 30(1), pp. 63-80, 2007.

J.R. Garcia, is graduated the BSc. from Civil Engineering at the Engineering School of Ilha Solteira FEIS/Unesp (2003), got his MSc. Degree (2006) and Dr. (2015) in Civil Engineering from the State University of Campinas (UNICAMP). He is currently a Civil Engineering professor at the Federal University of Uberlândia (UFU) and a Collaborating Researcher at UNICAMP. He operates in the area of analysis of geotechnical structures, containment and excavation works, foundations and earthworks, soil investigation tests and numerical analyses of geotechnical problems via finite elements. Member of technical commissions of foundations (CTF) and of field investigation (CTIC), and also a member of the Brazilian Association of Soil Mechanics and Geotechnical Engineering (ABMS)
ORCID: 0000-0002-8645-2555

P.J.R. Albuquerque, received the BSc. in Civil Engineering in 1993, MSc. in Engineering in 1996, PhD. in Soil and Foundation Engineering in 2001 and postdoctoral in 2010 at the Polytechnic University of Catalonia in Barcelona/Spain. He has been an associate professor at University of Campinas, Brazil since 2001, teaching and researching, with emphasis in in-Situ tests, laboratory tests and foundations. He was the secretary of the Technical Commission of In-Situ Tests of the Brazilian Association of Soil Mechanics (ABMS) between 2007 and 2010 and the president for the Biennium 2011/2012. He is the secretary of the Technical Commission of Foundation of the Brazilian Association of Soil Mechanics for the Biennium 2013-2016. In biennia 2013-2016 he will act as Vice-President of the Regional Center of São Paulo (ABMS). Since 2015 he has been a Brazilian representative of ABMS on TC102 Technical Commission of Foundations of ISSMGE.
ORCID: 0000-0003-0726-7165

UNIVERSIDAD NACIONAL DE COLOMBIA
SEDE MEDELLÍN
FACULTAD DE MINAS



DYNA
http://dyna.medellin.unal.edu.co/

Evaluation of the lubricating power of sweet almond oil without additives

Arnoldo Emilio Delgado-Tobón[a], William Arnulfo Aperador-Chaparro[a] & Rafael Guillermo García-Cáceres [b]

[a] *Programa de Ingeniería Mecatrónica, Universidad Militar Nueva Granada. Bogotá- Colombia. arnoldo.delgado@unimilitar.edu.co, william.aperador@unimilitar.edu.co*
[b] *Escuela de Ingeniería Industrial, Universidad Pedagógica y Tecnológica de Colombia - UPTC, Sogamoso - Colombia. rafael.garcia01@uptc.edu.co*

Received: September 29th, 2017. Received in revised form: April 3rd, 2018. Accepted: May 2nd, 2018.

Abstract
The lubricity of sweet almond oil (*Prunus amygdalus var. Dulcis*) was evaluated through Anti Wear (AW) properties and Extreme Pressure (EP) performance in a four-ball tribometer. The results were compared to those obtained with two mineral oils of contrasting viscosity, namely technical white mineral oil and delta 360 plasticizer, neither of them containing additives. Sweet almond oil was found to have greater lubricity than the mineral oils, as the spheres it lubricated had lower average wear track diameter and friction coefficient. In addition, sweet almond oil showed better performance under extreme pressure conditions and a greater weld point than mineral oils. Finally, an FT-IR spectroscopic analysis allowed determining that under the conditions of the current assays almond oil does not oxidize.

Keywords: oil; wear preventive; lubricant; extreme pressure; tribology.

Evaluación del poder lubricante de aceite de almendras dulces sin aditivos

Resumen
En esta investigación se evaluó el poder lubricante del aceite de almendras dulces *(Prunus amygdalus var. dulcis)* mediante ensayos de desgaste preventivo (AW) y presión extrema (EP) en un tribómetro cuatro bolas. Los resultados obtenidos, se compararon con el comportamiento de dos aceites minerales de diferente viscosidad, blanco técnico y plastificante delta 360, sin aditivos. Se determinó que el aceite de almendras dulces posee mayor poder lubricante con respecto a los aceites minerales. Las esferas lubricadas con aceite de almendras presentaron menor diámetro promedio de la huella de desgaste y menor coeficiente de fricción. Además, el aceite de almendras dulces presentó mejor desempeño en condiciones de extrema presión, mostrando un punto de soldadura mayor que los aceites minerales. Finalmente, mediante el análisis por espectroscopia FT-IR, se determinó que en las condiciones en las que se realizaron los ensayos el aceite de almendras no se oxida.

Palabras clave: aceite; desgaste preventivo; lubricante; presión extrema; tribología.

1. Introduction

In time, fossil fuels (petrol, gas and carbon) will necessarily and progressively have to be replaced by renewable raw materials for fuel and the manufacture of chemical industry products. Currently, mineral oil-based lubricants are gradually being replaced by green lubricants made using renewable raw materials. In general, bio lubricants are made using vegetable oils, which have excellent properties for application such as high viscosity index, high lubricity, low volatility and, in particular, low toxicity and high biodegradability [1-5]. Aspects that have stimulated the research into and development of lubricants based on harvestable resources in many parts of the world, to promote their generalized use for some types of application. However, vegetable oils have some limitations, which have to be technologically improved, in particular, those related to their thermo-oxidative stability, crystallization at relatively

How to cite: Delgado-Tobón, A.E., Aperador-Chaparro, W.A. and García-Cáceres, R.G., Evaluation of the lubricating power of sweet almond oil without additives DYNA, 85(205), pp. 179-183, June, 2018.

© The author; licensee Universidad Nacional de Colombia.

Table 1.
Composition of sweet almond oil fatty acids.

Fatty acid name		Fraction (%)
Palmitic acid	C 16:0	4.0 - 9.0
Palmitoleic acid	C 16:1	< 2.0
Stearic acid	C 18:0	0.5 - 3.0
Oleic acid	C 18:1	62.0 - 86.0
Linoleic acid	C 18:2	20.0 - 30.0

Source: adapted from [11].

high temperatures, and the limited range of viscosity values available [6-8].

In general, vegetable oils consist of a mixture of triglycerides, glycerol molecules long-chain fatty acids joined to hydroxyl groups with ester linkage. Their structure offers desirable qualities in a lubricant, their long-chain fatty acids and polar properties provide a highly resistant lubricant film which interact strongly with metallic surfaces, reducing friction and wear. In addition, the strong intramolecular interactions are resistant to temperature changes providing a more stable viscosity or a high viscosity coefficient [6,9,10].

In recent years, a great variety of oleaginous plants have been studied in order to determine their characteristics and potential of every species for use as a possible lubricant. In particular, almond oil, extracted from sweet almond seed meal (*Prunus amygdalus* var. *dulcis*), with 52 % fatty acids, of which most are unsaturated: Oleic acid and Linoleic acid (see Table 1), is a raw material of interest for the manufacture of green lubricants, for its positive behavior at low temperatures. It was found that, with respect to other vegetable and mineral oils, almond oil is more fluid at lower temperatures due to its high concentration of olefinic double bonds [12,13].

The main purpose of this study was to determine the lubricant power of sweet almond oil, in order to assess its possible use as a base for green lubricants. The potential of almond oil as a lubricant was assessed using antiwear testing and extreme pressure in a four-ball tribometer. In order to establish differences between the lubricant properties of vegetable and mineral oils, the power of sweet almond oil with no additives was compared to the behavior of two mineral oils with different levels of viscosity, used under the same conditions in tribometer tests.

2. Materials and methods

2.1. Materials

Unrefined sweet almond oil was acquired in a local market and it presented the following characteristics: density: 0.916 g/mL, peroxide value: 1.3 meq/kg a 20 °C, kinematic viscosity: 34.2 cSt a 37.8 °C. Technical grade white mineral oil and delta 360 plasticizer were used as they were received, without additional purification or additives. Their characteristics are described below: Technical grade white mineral oil: density: 0.867 g/mL, kinematic viscosity: 24.42 cSt a 40 °C; 4.94 cSt a 100 °C, viscosity index: 125, flash point: 210 °C. Mineral oil delta 360 plasticizer: density: 0.865 g/mL, kinematic viscosity: 56.50 cSt a 40 °C; 7.86 cSt a 100 °C, viscosity index: 98, flash point: 240 °C.

2.2. Tribometer tests

2.2.1. Antiwear testing

The lubricant power of sweet almond oil and the mineral oils was determined using a four-ball tribometer. AISI 52100 chrome alloy steel balls were used, with diameters of 12.7 mm and hardness Rockwell C (HRC) of 60–66. Antiwear testing was carried out using the ASTM D 4172-94 method, with the following conditions: 75 °C, 1200 rpm, a load of 147 N, test time of 60 minutes. The parameters through which to evaluate the lubricity of the oils considered were the average wear track diameter (WTD) and the friction coefficient. The WTD was measured in mm using a digital microscope.

2.2.2. Properties of extreme pressure

The properties of extreme pressure, load before visible wear and weld point, sweet almond oil and the mineral oils were determined using the ASTM D 2783-03 method, with the following conditions: room temperature, 1760 rpm, variable loads: 59, 78, 98, 127, 157, 196, 235, 314 N, time for each test: 10 seconds.

2.2.3. FT-IR spectroscopy

Analysis using FT-lR was carried out using a Nicolet iS10 spectrometer (Thermo Fisher Scientific) equipped with a deuterated triglycine sulphate detector (DTGS) and KBr beamsplitter. The equipment was subjected to an automatic dehumidifier to reduce interference from the water vapor. Using the Horizontal Attenuated Total Reflectance (HATR) sample technique, the samples were placed in direct contact with the zinc selenide crystal in the Smart ARK™ multi-bounce accessory at 23 °C. The FT-IR spectra had a resolution of 4 cm^{-1}, the number of sweeps was 32 and the spectral range 4000–650 cm^{-1}. The spectra were analyzed using OMNIC 9.1.27 software (Thermo Fisher Scientific Inc.).

3. Results and Discussion

3.1. Antiwear testing (AW)

The WTD and friction coefficient presented for each of the oils studied are shown in Fig. 1 and Table 2, respectively.

It was found that the balls lubricated with almond oils presented a smaller wear track (WTD= 1.63mm) when compared to the balls lubricated with plasticizer mineral oil 360 (WTD= 2.45mm) and white mineral oil (WTD= 4.96mm).

Also, the friction coefficient observed when using almond oil is lower than that observed with mineral oils. When we compare the results for the different mineral oils, we can see that the wear track and the friction coefficient are lower with the 360 plasticizer oil.

Fig. 2 shows images of the wear track, observed in a digital microscope, after the antiwear testing. Greater wear is observed on the metal surface of the balls lubricated with mineral oils, whereas the sweet almond oil exhibits a greater

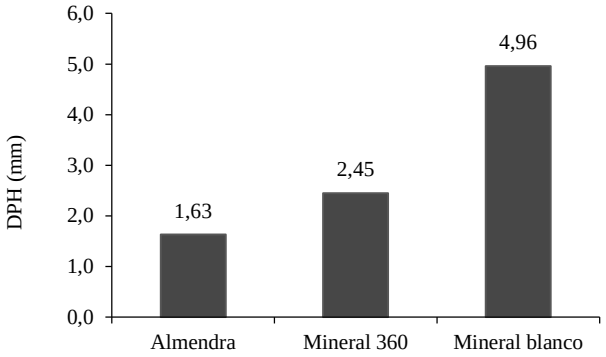


Figure 1. Average track diameter. Antiwear testing.
Source: Authors.

Table 2.
Friction coefficient obtained with the antiwear testing.

Oil	Friction coefficient
Almond	7.4
Mineral 360	8.2
White mineral	8.9

Source: Authors.

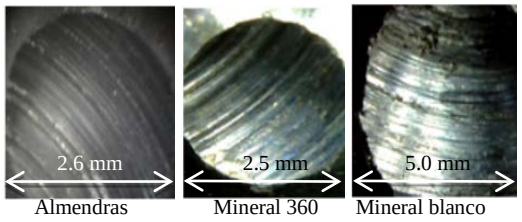


Figure 2. Surface tracks on balls subjected to antiwear testing.
Source: Authors.

lubrication capacity. This difference may be explained by the structure and chemical nature of the oils. Almond oil consists of a mixture of triglycerides formed by fatty acids (See Table 1), whereas the mineral oils are made up by blends of hydrocarbons. The polar nature of sweet almond oil, makes it more suited to metal surfaces and consequently greater lubricity with respect to non-polar mineral oils, made up by aliphatic hydrocarbons [10,14].

During the process, the polar heads of the fatty acid chains in vegetable oils join the metal surfaces through an adsorption process, which allows the formation of a monolayer film with the non-polar extreme of the fatty acids, protruding away from the metal surface. As such, the hydrocarbonaceous fatty acids chains offer a sliding surface that avoids direct metal-to-metal contact, reducing the friction coefficient between the two surfaces [6].

On the other hand, when comparing only the mineral oils, the more viscous one (mineral oil 360) has the greatest lubricating power.

3.1.1. Extreme pressure (EP) properties

The performance of the oil under extreme pressure was evaluated in terms of load before visible wear and the weld point. Fig. 3 shows the behavior of the average wear track

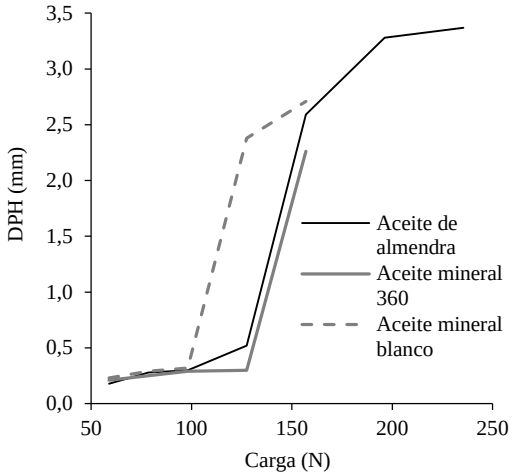


Figure 3. Average wear track diameter based on the load applied to the oils. Extreme pressure testing.
Source: Authors.

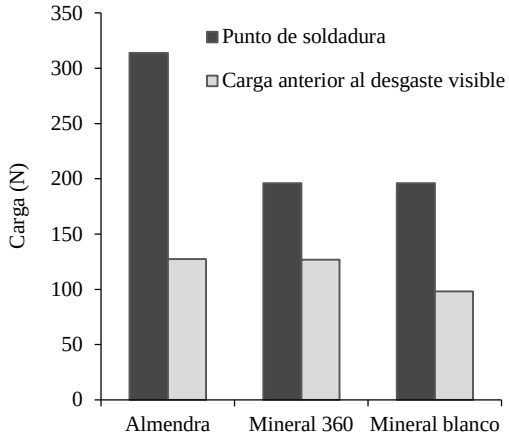


Figure 4. Extreme pressure properties of the oils.
Source: Authors.

diameter based on the applied load. The chart shows a change of incline based on the load before visible wear. This load is 127 N for sweet almond oil, and 127 and 98 N for mineral oils 360 and white, respectively.

Almond oil presents a weld point at 314 N, whereas the mineral oils have the same weld point at 196 N (see Fig. 4). These results indicate that almond oil performs better under extreme pressure than technical grade white mineral oil and plasticizer 360.

This behavior is explained by the fact that the vegetable oil is made up of highly polar molecules that allow it stronger interactions with the lubricated surfaces, inhibiting contact between the metal surfaces and allowing the oil to withstand greater loads [6,14-16].

3.1.2. FT-lR spectrum: sweet almond oil

Bearing in mind that among the oils studied, sweet almond oil presented the greatest lubricant power. The oil was tested before and after the antiwear and extreme pressure

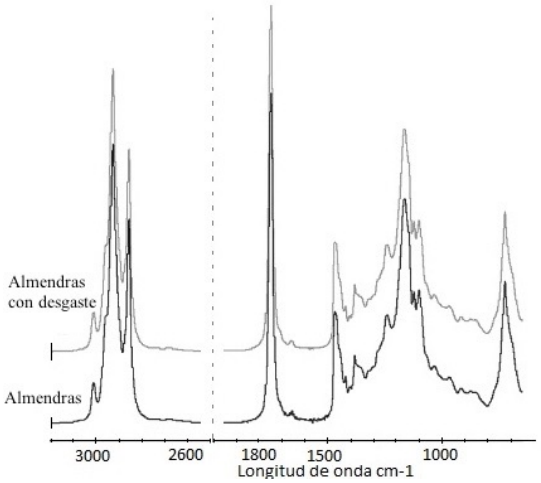


Figure 5. FT-IR spectrum: almond oil before and after antiwear testing. Source: Authors.

testing, using FT-IR spectroscopy in order to establish variations in the chemical composition of the oil when subjected to the abovementioned processes in order to determine whether the technique presents any sign of degradation and loss of lubricant properties.

Fig. 5 shows the FT-IR spectra of sweet almond oil before and after antiwear testing.

It is possible to observe characteristic bands of olefinic double bonds (3007 cm^{-1}), methylene group (2922, 2853, 1464 and 722 cm^{-1}), methyl group (1464 and 1377 cm^{-1}) and triglyceride ester group (1743, 1237, 1159 and 1097 cm^{-1}). No changes are perceived between the spectra of fresh and used oil; there are no new absorptions originating due to oxidation products or any displacements in the bands' frequency values [17]. The IR spectra for the oil samples used in the extreme pressure tests do not present any differences with respect to the spectrum for fresh oil. These results indicate that almond oil does not suffer any changes in its functional groups in the conditions in which the tribometer tests were carried out. The results coincide with those obtained in previous studies whereby thermal analysis by DSC showed that for sweet almond oil thermal decomposition under an atmosphere of inert N_2 begins at 181.48 °C and at a 174.00 °C in air atmosphere [13], so that the conditions in which the tests are carried out are not sufficient to degrade the vegetable oil.

4. Conclusions

The results of antiwear and extreme pressure testing carried out using a four-ball tribometer revealed that sweet almond oil has greater lubricant power than technical grade white mineral oil and delta 360 plasticizer. The balls lubricated with almond oil presented a smaller average wear track diameter and lower friction coefficient. In addition, almond oil performs better in conditions of extreme pressure, presenting a greater weld point when compared to the mineral oils. FT-IR Spectroscopy analysis of fresh and used almond oil allowed us to establish that in the conditions in which the tribometer tests were carried out, the oil does not oxidize. The results of this work suggest that sweet almond oil is a raw material of interest for the formulation of green lubricants. These results are a starting point subsequent studies that seek to improve the lubricant properties of sweet almond oil, by incorporating antiwear additives. The work follows a line of research that also relates the work of [18] for sesame oil.

Acknowledgements

The authors wish to thank the Vice-Rector of Research at Universidad Militar Nueva Granada (UMNG) for the financial support granted. They would also like to thank MSc. Nelson Nuñez-Dallos for his contribution to the research and elaboration of this manuscript.

References

[1] Adhvaryu, A., Erhan, S. and Perez, J., Tribological studies of thermally and chemically modified vegetable oils for use as environmentally friendly lubricants. Wear, 257(3–4), pp. 359-67, 2004. DOI: 10.1016/J.WEAR.2004.01.005

[2] Alves, S., Barros, B., Trajano, M., Ribeiro, K. and Moura, E., Tribological behavior of vegetable oil-based lubricants with nanoparticles of oxides in boundary lubrication conditions. Tribology International, 65, pp. 28-36, 2013. DOI: 10.1016/J.TRIBOINT.2013.03.027

[3] Bart, J.C., Cavallaro, S. and Gucciardi, E., Biolubricants: Science and Technology, cambridge, Woodhead Publishing Series, 2013, cap 3, Lubricants: properties and characteristics. [online]. Available at: https://www.sciencedirect.com/science/article/pii/B9780857092632500033

[4] Mannekote, J.K. and Kailas, S.V., The effect of oxidation on the tribological performance of few vegetable oils. Journal Materials Research and Technology, 1(2), pp. 91-95, 2012. DOI: 10.1016/S2238-7854(12)70017-0

[5] Delgado, A.E. y Aperador, W., Estudio comparativo del poder lubricante y estabilidad oxidativa entre el aceite de ajonjolí y aceite mineral 360. Información Tecnológica, 25(4), pp. 79-90, 2014. DOI: 10.4067/S0718-07642014000400011

[6] Bart, J.C., Cavallaro, S. and Gucciardi, E., Biolubricants: science and technology, Cambridge, Woodhead Publishing Series, 2013, cap 1, Renewable lubricants. [ONLINE] Available at: https://www.sciencedirect.com/science/article/pii/B978085709263250001X

[7] Campanella, A., Rustoy, E., Baldessari, A. and Baltanás, M.A., Lubricants from chemically modified vegetable oils. Bioresources Technology, 101(1), pp. 245-54, 2010. DOI: 10.1016/J.BIORTECH.2009.08.035

[8] Jayadas, N.H. and Nair, K.P., Coconut oil as base oil for industrial lubricants-evaluation and modification of thermal, oxidative and low temperature properties. Tribology International, 39(9), pp. 873-878, 2006. DOI: 10.1016/J.TRIBOINT. 2005.06.006

[9] Fox, N.J. and Stachowiak G.W., Vegetable oil-based lubricants—A review of oxidation. Tribology International, 40(7), pp. 1035-1046, 2007. DOI: 10.1016/J.TRIBOINT.2006.10.001

[10] Syahrullail, S., Kamitani, S. and Shakirin, A., Performance of vegetable oil as lubricant in extreme pressure condition. Procedia Engineering, 68, pp. 172-177, 2013. DOI: 10.1016/J.PROENG.2013.12.164

[11] Hernández, S.A. and Zacconi, F., Sweet almond oil: extraction, characterization and application. Química Nova, 32(5), pp. 1342-1345, 2009. [online]. Available at: https://quimicanova.sbq.org.br/detalhe_artigo.asp?id=438

[12] Naveed A., Qazi, A., Mehmood, A., Ahmad, M. and Kalsoom, F., Rheological Studies and Characterization of Different Oils. Journal of the chemical society of Pakistan, 31(2), pp. 201-206, 2009. Disponible en https://www.jcsp.org.pk/ViewByVolume.aspx?v=17&i=VOLUME%2031,%20NO2,%20APR%202009

[13] Delgado, E., Buitrago, O. and Palacio, O., Characterization of sweet almond oil by FT-IR spectroscopy and differential scanning calorimetry, 2015. Submitted.
[14] Chatra, K., Jayadas, N.H. and Kailas, S.V., Green tribology, Springer Berlín Heidelberg, 2012, cap, Natural Oil-Based Lubricants, [online]. pp. 287-328. Disponible eAvailable at: n https://link.springer.com/chapter/10.1007/978-3-642-23681-5_11
[15] Kabuya, A. and Bozet, J.L., Comparative analysis of the lubricating power between a pure mineral oil and biodegradable oils of the same mean iso grade. Tribology Series, Elsevier, 1995, pp. 25-30. DOI: 10.1016/S0167-8922(08)70613-8
[16] Mendoza, G., Igartua, A., Fernandez-Diaz, B., Urquiola, F., Vivanco, S. and Arguizoniz, R., Vegetable oils as hydraulic fluids for agricultural applications. Grasas y Aceites. 62(1), pp. 29-38, 2011. DOI: 10.3989/gya.056210
[17] Guillén, M.D. and Cabo, N., Usefulness of the frequency data of the fourier transform infrared spectra to evaluate the degree of oxidation of edible oils. Journal of Agricultural and Food Chemistry, 47(2), pp. 709-719, 1999. DOI: 10.1021/jf9808123
[18] Delgado, A.E., García, R. y Aperador, W., Estudio del poder lubricante del aceite de ajonjolí aditivado con nanopartículas de cobre. Información Tecnológica. 27(6), pp. 175-184, 2016. DOI: 10.4067/S0718-07642016000600018

A.E. Delgado-Tobón, has a BSc. degree in Mechanical Engineering, an MSc. in Mechanical Engineering, and is associate professor on the Mechatronic Engineering Program at Universidad Militar Nueva Granada, Bogotá, Colombia. ORCID: 0000-0002-8743-8958.

W.A. Aperador-Chaparro, has a PhD. in Materials Engineering, a MSc. in Mechatronic Engineering and is associate professor on the Mechatronic Engineering Program at Universidad Militar Nueva Granada, Bogotá, Colombia. ORCID: 0000-0003-1778-0851

R.G. García-Cáceres, has a PhD., in Engineering, a MSc. Industrial Engineering and is associate professor at the School of Industrial Engineering at Universidad Pedagógica y Tecnológica de Colombia (UPTC), Sogamoso, Colombia. ORCID: 0000-0003-0902-1038

UNIVERSIDAD NACIONAL DE COLOMBIA
SEDE MEDELLÍN
FACULTAD DE MINAS

Área Curricular de Ingeniería Administrativa e Ingeniería Industrial

Oferta de Posgrados

Especialización en Gestión Empresarial
Especialización en Ingeniería Financiera
Maestría en Ingeniería Administrativa
Maestría en Ingeniería Industrial
Doctorado en Ingeniería - Industria y Organizaciones

Mayor información:

E-mail: acia_med@unal.edu.co
Teléfono: (57-4) 425 52 02

UNIVERSIDAD NACIONAL DE COLOMBIA
SEDE MEDELLÍN
FACULTAD DE MINAS



DYNA
http://dyna.medellin.unal.edu.co/

Application of double filtration with granular activated carbon for Atrazine reduction on water treatment processes

Lina Fuentes-López, Claudia Amézquita-Marroquín & Patricia Torres-Lozada

Study and Control of Environmental Pollution Research Group - ECCA, Faculty of Engineering, Universidad del Valle, Cali, Colombia.
lina.fuentes@correounivalle.edu.co, claudia.amezquita@correounivalle.edu.co, patricia.torres@correounivalle.edu.co

Received: October 25th, 2017. Received in revised form: March 21th, 2018. Accepted: May 4rd, 2018

Abstract
Atrazine is one of the most often used herbicides in the world. It reaches the surface water body by runoff, direct application or airborne dispersal. Conventional water treatment methods do not efficiently remove these types of pollutants, whereas granular activated carbon (GAC) adsorption is an adequate technique for the removal of organic compounds from water. In this work, the Atrazine reduction of water doped with two concentrations of Atrazine, was evaluated during the conventional treatment process (coagulation, flocculation, sedimentation and sand and anthracite filtration), followed by double filtration with two adsorbent granular media (vegetal and mineral GAC), which resulted in an efficient reduction of UV_{254} (86%) and Atrazine (99%).

Keywords: adsorption; drinking water; Atrazine; granular activated carbon.

Aplicación de la doble filtración con carbón activado granular para la reducción de Atrazina en procesos de tratamiento de agua potable

Resumen
La Atrazina es uno de los herbicidas de mayor aplicación en el mundo, ingresa a los cuerpos de agua superficial por escorrentía, aplicación directa o dispersión aérea. Los métodos de tratamiento convencional de agua no remueven eficientemente este tipo de contaminantes, mientras que la adsorción con Carbón Activado Granular (CAG), es una técnica apropiada para la remoción de compuestos orgánicos del agua. En este trabajo, se evaluó la reducción de Atrazina de un agua dopada con dos concentraciones Atrazina, durante el proceso de tratamiento convencional (coagulación, floculación, sedimentación y filtración con arena y antracita) seguido de una doble filtración con dos medios adsorbentes granulares (CAG de origen Vegetal y Mineral), la cual permitió obtener una eficiente reducción de UV_{254} (86%) y Atrazina (99%).

Palabras clave: adsorción; agua potable; Atrazina; carbón activado granular.

1. Introduction

Atrazine is an organochlorine herbicide from the triazine family and is used as a selective pre- and post-emergent herbicide to control weeds and as a non-selective herbicide in non-cultivated regions [1]. Being one of the most widely used herbicides in the world, particularly for energetic biomass crops such as maize and sugar cane [2], its annual global production is between 70,000 and 90,000 tons [3-5].

Due to its high water solubility, extensive use and persistence in soil, atrazine presents a high risk of leaching, resulting in the pollution of soils and underground and surface water sources [6], which presents a potential threat to human health due to its association with endocrine disruption and possible teratogenic and carcinogenic effects [4, 7, 8]. Authors such as Graymore 2001 [9] indicate that atrazine has been found in concentrations of up to 1000 µg/L in waters adjacent to treated fields and up to 80 µg/L in drinking water (DW).

In the production of DW, the conventional or complete treatment technology (coagulation, flocculation, sedimentation and conventional filtration), is most often used; however, most of these processes were not designed to remove organic compounds

How to cite: Fuentes-López, L., Amézquita-Marroquín, C. and Torres-Lozada, P., Application of double filtration with granular activated carbon for Atrazine reduction on water treatment processes. DYNA, 85(205), pp. 184-190, June, 2018.

© The author; licensee Universidad Nacional de Colombia.

such as pesticides, which due to their heterogeneity are difficult to reduce [10,11]. In contrast, one of the most used and efficient techniques for the removal of organic compounds in water is adsorption [12]. Given that production and regeneration costs are its main limitation, different adsorbent media have been implemented, derived from low-cost materials such as tires, wood, bone, fruit peels and agricultural waste, with low inorganic content and high carbon content [12,13].

In this sense, the effectiveness of the conventional treatment comprised of clarification (coagulation, flocculation and sedimentation) and conventional filtration, followed by a second stage of filtration with two adsorbent media of mineral granular activated carbon (MAC) from bituminous coal, as well as vegetal granular activated carbon (VAC) made from coconut shell, was evaluated. Raw water from the Cauca River, doped with atrazine to reach concentrations close to 0.50 and 1.00 mg/L, was used.

2. Methodology

2.1. Preparation and characterization of atrazine-doped water

Raw Cauca River Water, coming from the intake of the Puerto Mallarino drinking water treatment plant (DWTP), was doped with 0.44 and 0.86 mg/L atrazine. Turbidity (NTU), UV_{254} (cm^{-1}: due to its use for the qualitative estimation of the presence of organic substances [14]) and atrazine (mg/L) were measured.

2.2. Clarification

The clarification tests (coagulation - flocculation - sedimentation) were performed in jar test devices according to the recommendations of [15] and [16] (Table 1); the experimental unit corresponded to a two-liter acrylic jar. Ferric chloride ($FeCl_3$) was used as coagulant due to its high use in DWTPs [17,18]; a constant coagulant dose (22 mg/L) was determined from previous jar tests.

2.2. Conventional filtration

As the experimental unit for the conventional filtration and GAC filtration, transparent glass filters of 19 mm in inner diameter, 25 mm in nominal diameter and 40 cm in length were used; the filter bed thickness was 15 cm, with a metal mesh as support to avoid plugging the filter outlet with the filter medium [19-21]. The outlet consisted of a silicone hose with one end attached to the bottom part of the filter and the other end placed above the upper part of the filter bed to promote an available hydraulic load so that the bed would not run out of water (Figure 1). The experiments were performed in triplicate with a total of six experimental units.

Table 1.
Clarification test conditions

Process	Stirring speed (rpm)	Time (min)
Fast mixture (coagulation)	300	1
Slow mixture (flocculation)	40	20
Sedimentation	0	20

Source: The authors

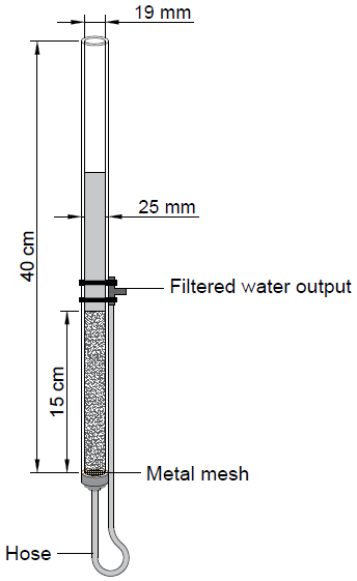


Figure 1. Filtration experimental unit scheme.
Source: The authors

For the conventional filtration, sand and anthracite were used with the configuration defined by [22]: sand (30%) with an effective size (d10) of 0.61 mm and anthracite (70%) with an effective size (d10) of 1.16 mm, with a flow rate of 12 ml/min. The filtration was performed for seven hours; the effluent water was subjected to the next phase of the treatment. Turbidity (NTU) (2130B) and UV_{254} (cm^{-1}) (2510B) were measured every 15 minutes, and the atrazine (mg/L) (EPA 523) was measured at the beginning and end of the experiment [23].

2.3. GAC filtration

The water obtained from the conventional filtration was stored for the second filtration stage, which lasted four hours. The filtration columns consisted entirely of the selected adsorbent media: mineral granular activated carbon (MAC) and vegetal granular activated carbon (VAC) [24-26]. According to authors such as Mukherjee et al., 2007; Giraldo & Moreno 2008; Giraldo & Moreno 2012; and Vukčević et al., 2015 [27-30], the GAC adsorbent media must be washed several times to remove impurities and residual chemical substances from the GAC activation process; in this case, the media were washed seven times with distilled water. The same was performed for sand and anthracite.

The experiments were performed in triplicate using three experimental units for each adsorbent medium (MAC and VAC) and atrazine concentration, resulting in a total of 12 experimental units. A flow distribution system and a constant load tank were used for the dosing of the conventional filtered water. Figure 2 shows the experimental configuration for one concentration.

The filtration was performed for four hours, and the samples collected during the filtration test for the two concentrations were measured for turbidity (NTU) and UV_{254} (cm^{-1}) every 15 minutes during filtration; the atrazine (mg/L) was measured at the beginning and end of the process.

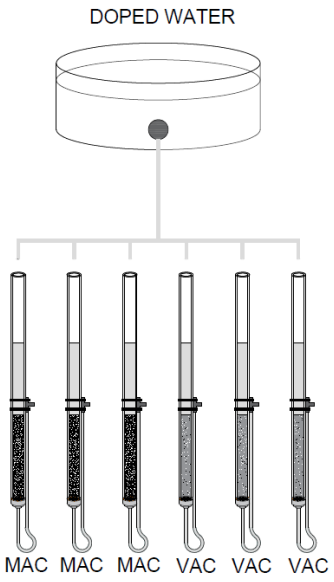


Figure 2. Flow distribution system and filter configurations for each evaluated atrazine concentration.
Source: The authors

2.4. Statistical analysis

An analysis of variance (ANOVA), using the statistical program Minitab 17 [31], was performed to determine if there were statistically significant differences between the evaluated filter media configurations.

3. Results and discussion

3.1. Clarification

Table 2 presents the turbidity, UV_{254} and atrazine concentration of raw water, atrazine-doped water and clarified water.

Table 2 shows that the addition of atrazine to the doped water did not alter the turbidity level because it is primarily related to colloidal and suspended matter [32]. In contrast, the UV_{254} absorbance increased with the addition of atrazine due to its relationship with the dissolved material and the organic matter content [33,34].

After the clarification process (coagulation, flocculation and sedimentation), the turbidity decreased by 98 and 99% for concentrations 1 and 2, respectively. In contrast, the low performance was confirmed based on organic compound reduction in terms of UV_{254} and the atrazine concentration; the UV_{254} efficiency reductions were 38 and 39% for concentrations 1 and 2, respectively.

Table 2.
Characterization of raw, doped and clarified water.

Parameter	Raw Water	DW 1	DW 2	CW 1	CW 2
Turbidity (NTU)	106	105	103	1.70	0.72
UV_{254} (cm^{-1})	0.13	0.15	0.15	0.09	0.09
Atrazine (mg/L)	1.92×10^{-3}	0.44	0.86	-	0.69

DW: doped water, CW: clarified water
Source: The authors

Table 3.
Characteristics of the filter media and adsorbents

Characteristic	Sand	Anthracite	VAC		MAC	
			Min	Max	Min	Max
Particle effective size (mm)	0.61	0.60-1.80	0.80	1.20	0.55	0.75
Uniformity coefficient	<1.70	<1.70	-	2.10	-	1.90

Source: Supplier information

Regarding atrazine reduction, a reduction efficiency of 20% was obtained for concentration 2. Notably, atrazine is characterized by its high solubility (28 mg/L) and partition coefficient (2.30) [35]. According to [36], compounds with partition coefficients above 3.20 are more easily reduced by this type of process; therefore, it is likely that conventional processes are not very effective for the reduction of atrazine.

3.2. Evaluation of conventional filtration and GAC filtration

3.2.1. Characteristics of filter media and adsorbents

Table 3 shows the characteristics of the filter media and absorbents used.

Sand and anthracite, which have a smaller effective particle size and uniformity coefficient than GAC, which in turn favors the entrapment of particles that cause turbidity, were used for the conventional filtration. Thus, the conventional media are expected to have a higher turbidity reduction efficiency than that of GAC [37,38].

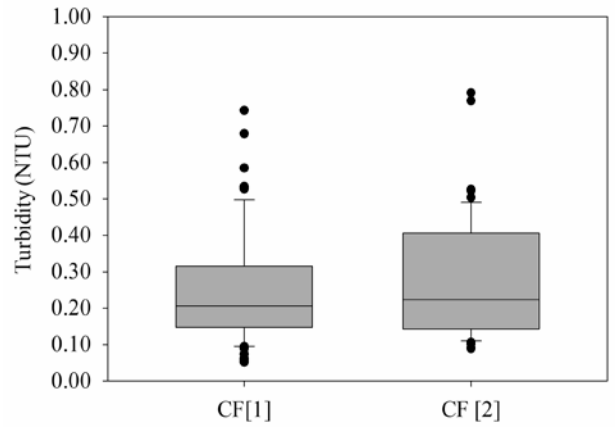
The GAC media used differ in the precursor and the effective particle size. In this study, MAC presented lower values; in its manufacture, there is a tendency to form a wide range of pores, and therefore, it is more often used for applications in which the compounds to be retained are of different molecular sizes, such as the substances in water, whereas the VAC manufactured from coconut shell tends to present small pores [12]. According to these characteristics, it could be expected that MAC would present a greater decrease in organic compounds.

3.2.2. Turbidity

Figure 3 shows a box-plot of the turbidity results of the conventional and GAC filtrations for the two concentrations used.

In Colombia, the maximum permissible level of turbidity in drinking water is 2 NTU [39], whereas the Pan American Health Organization (PAHO) [40] recommends a turbidity below 1.00 NTU for achieving an effective disinfection, and the World Health Organization (WHO) [14] recommends that the turbidity median must be lower than 0.10 NTU. The Environmental Protection Agency (EPA) [41] establishes 1.00 NTU as the maximum limit for treated water and a 95th percentile of 0.15 NTU and a maximum of 0.30 NTU for the control of the microbiological risk due to cryptosporidium.

a Conventional filtration (CF)



b GAC filtration (MAC and VAC)

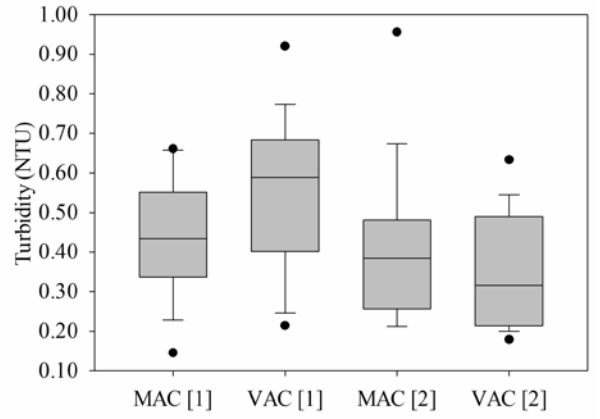
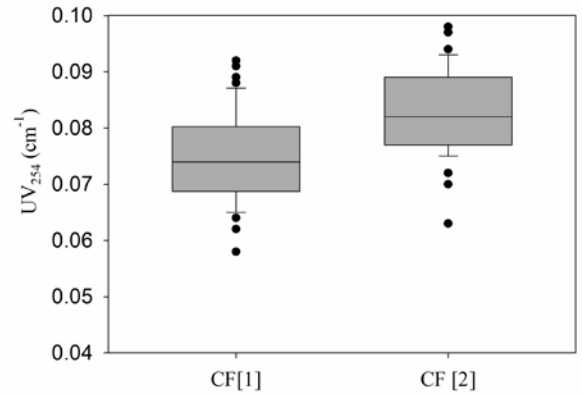


Figure 3. Turbidity box-plot for: (a) Conventional filtration and (b) GAC filtration for the two evaluated concentrations.
Source: The authors

a Conventional filtration (CF)



b GAC filtration (MAC and VAC)

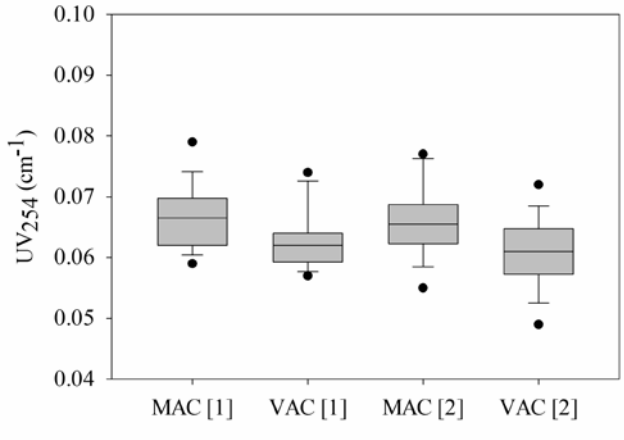


Figure 4 UV_{254} box-plot for: (a) Conventional filtration and (b) GAC filtration, for the two evaluated concentrations.
Source: The authors

With the conventional sand and anthracite filtration, minimum values between 0.05 and 0.09 NTU were achieved for concentrations 1 and 2, respectively; in the second filtration with GAC, the minimum values obtained were higher (between 0.15 and 0.21 NTU); in this sense, authors such as Feng et al., 2012 [42], indicate that filters that use GAC are more susceptible to turbidity infiltration. Another important aspect that could affect the turbidity of the GAC filtration effluent is the washing of the adsorbent medium [27-30].

The statistical analysis by the ANOVA test shows that for the conventional filtration, there are no significant differences between the two evaluated pesticide concentrations. Likewise, no significant differences were found between the two adsorbent media used (MAC and VAC) with each evaluated pesticide concentration; notably, in all cases, the data were below 2.00 NTU, the upper limit of the Colombian standard for drinking water [39].

3.2.3. UV_{254} absorbance

Figure 4 shows a box-plot of the UV_{254} results of the conventional filtration and GAC filtration for the two concentrations used.

The conventional filtration effluent varied between 0.065 and 0.092 cm^{-1} for concentration 1 and between 0.075 and 0.098 cm^{-1} for concentration 2. The ANOVA tests indicate that there are statistically significant differences between the two pesticide concentrations, being lower under the lowest concentration condition (CF1). According to [43], when using a conventional treatment with sand filters, the UV_{254} values of the filtered water decrease slightly.

Regarding the second filtration with GAC, lower values were obtained compared to conventional filtration (between 0.049 and 0.079 cm^{-1}), which confirms the higher organic compounds removal capacity (represented in terms of UV_{254}) of the GAC filter media. The application of the ANOVA tests showed that there are significant differences between the media used only for concentration 2, because this concentration corresponds to the highest doped concentration (0.86 mg/L). Previous studies have shown that GAC filters are more efficient than sand filters and dual media composed of sand and GAC or other media in the removal of organic matter (UV_{254}) [44, 45, 42, 21], which is in accordance with this study.

3.2.4. Atrazine

To determine the reduction of atrazine, its concentration was

measured in raw water (1.92×10^{-3} mg/L), in water doped with the two pesticide concentrations, and at the end of each of the following processes: clarification (coagulation - flocculation - sedimentation), conventional filtration and GAC filtration (MAC and VAC). Table 4 presents the concentrations and the reduction percentages in the different processes.

Although the pesticide concentration was reduced in each stage of the treatment, the GAC filtration (MAC and CAV) stage is what obtained a sufficient reduction (99.73 and 99.80% for MAC with concentrations 1 and 2, respectively, and 99.74 and 93.26% for VAC with concentrations 1 and 2, respectively), with MAC being more efficient.

Factors such as the contact time and the presence of dissolved organic matter (DOM) in water influenced the absorption efficiency of the media used [46, 47], perhaps because the contact time may have been insufficient for adsorption of the pesticide, and the presence of DOM reduces the GAC effectiveness; these conditions can be explained because most of the results are within the limit established by the WHO [48] (0.002 mg/L), and the efficiencies with concentration 2 are lower.

Adsorption with different materials has been demonstrated to effectively reduce pesticides, such as in [49], where GAC filters were used for the removal of chlorpyrifos, diazinon and carbofuran, attaining removal efficiencies on the order of 80%, subsequent to the conventional treatment, which had a maximum removal efficiency of approximately 20%. For atrazine, wood charcoal has been used with a maximum efficiency of 95.50% [50], coconut charcoal with reduction efficiencies between 85.90 and 86.30% [3], and sawdust with efficiencies of approximately 74.70 - 80.50% [3]; notably, these studies were performed with distilled water or drinking water doped with the pesticide.

Regarding the regulation for drinking water, the EPA [41] establishes a concentration of 0.003 mg/L as the permissible limit of atrazine; the WHO [48] establishes a limit of 0.002 mg/L; and in Colombia, according to [39], the sum of the pesticide concentrations cannot exceed 0.010 mg/L. The concentrations evaluated in this study (0.44 and 0.86 mg/L) are concentrations that are found in surface water in the local and international context [51]. The atrazine concentrations at the end of the treatment process varied between 1.16×10^{-3} and 1.75×10^{-3} mg/L. Thus, they complied with the regulation in all cases other than concentration 2 filtered with VAC, which presented a concentration of 0.06 mg/L.

Table 4.
Atrazine concentrations and reduction percentages throughout the treatment process

Sample	Atrazine (mg/L)		Reduction with respect to doped water (%)	
	[1]	[2]	[1]	[2]
Doped Water	0.44	0.86	-	-
Clarified Water	0.17	0.69	-	19.77
Conventional Filtered Water	0.07	0.42	83.64	51.16
MAC Filtered Water	1.21×10^{-3}	1.75×10^{-3}	99.73	99.80
VAC Filtered Water	1.16×10^{-3}	0.06	99.74	93.26

Source: The authors

4. Conclusions

The clarification processes, in addition to conventional sand and anthracite filtration, reduced turbidity by 97%, with turbidity values below 0.80 NTU; however, these treatments are inefficient in the reduction of organic compounds, represented in this study in terms of UV_{254} absorbance and atrazine.

In general, the second filtration with both types of evaluated GAC (MAC and VAC) showed a favorable effect on the reduction of UV_{254} and atrazine, obtaining atrazine values within the international and national standards for drinking water.

Acknowledgments

The authors thank the Universidad del Valle and Pontificia Universidad Javieriana - Cali, for the financing of research project CI 2869, and the Universidad del Valle and COLCIENCIAS for the financing of research project CI 2937; the authors are also thankful for the financing of student Claudia Patricia Amézquita Marroquín - fellow of the National Doctorate support program [programa de apoyo a Doctorados Nacionales] - Call 567-2012 of COLCIENCIAS.

References

[1] Mendas, G., Vuletic, M., Galic, N. and Drevenkar, V., Urinary metabolites as biomarkers of human exposure to atrazine: Atrazine mercapturate in agricultural workers. Toxicol Letters, 210(2), pp. 174-181, 2012. DOI: 10.1016/j.toxlet.2011.11.023

[2] Jablonowski, N., Hamacher, G., Martinazzo, R., Langen, U., Köppchen, S., Hofmann, D. and Burauel, P., Metabolism and persistence of atrazine in several field soils with different atrazine application histories. Journal of Agricultural and Food Chemistry, 58(24), pp. 12869-12877, 2010. DOI: 10.1021/jf103577j

[3] Sharma, R., Kumar, A. and Joseph, P., Removal of atrazine from water by low cost adsorbents derived from agricultural and industrial wastes. Bulletin of Environmental Contamination and Toxicology, 80(5), pp. 461-464, 2008.DOI: 10.1007/s00128-008-9389-6

[4] Udikoviç, N., Scott, C. and Martin, F., Evolution of atrazine-degrading capabilities in the environment. Applied Microbiology and Biotechnology, 96(5), pp 1175-1189, 2012. DOI: 10.1007/s00253-012-4495-0

[5] Hou, X., Huang, X., Ai, Z., Zhao, J. and Zhang, L., Ascorbic acid induced atrazine degradation. Journal of Hazardous Materials, 327, pp. 71-78, 2017.DOI: 10.1016/j.jhazmat.2016.12.048

[6] Papadakis, E., Tsaboula, A., Kotopoulou, A., Kintzikoglou, K., Vryzas, Z. and Papadopoulou, E., Pesticides in the surface waters of Lake Vistonis Basin, Greece: Occurrence and environmental risk assessment. The Science of the Total Environment, 536, pp. 793-802, 2015.DOI: 10.1016/j.scitotenv.2015.07.099.

[7] Copeland, C., Pesticide use and water quality: are the laws complementary or in conflict. Congressional Research Service [online]. 2012 [Reference date 15 June of 2017]. Available at: https://www.fas.org/sgp/crs/misc/RL32884.pdf

[8] Lesmes, C. and Binder, C., Pesticide flow analysis to assess human exposure in greenhouse flower production in Colombia. International Journal of Environmental Research and Public Health, 10(4), pp. 1168-1185, 2013. DOI: 10.3390/ijerph10041168

[9] Graymore, M, Stagnitti, F. and Allinson, G., Impacts of atrazine in aquatic ecosystems. Environment International, 26(7-8), pp. 483-495, 2001. DOI: 10.1016/S0160-4120(01)00031-9

[10] Sarkar, B., Venkateswralu, N., Rao, R., Bhattacharjee, C. and Kale, V., Treatment of pesticide contaminated surface water for production of potable water by a coagulation-adsorption-nanofiltration approach. Desalination, 212(1-3), pp. 129-140, 2007. DOI:

10.1016/j.desal.2006.09.021
[11] Jardim, W., Montagner, C., Pescara, I., Umbuzeiro, G., Di Dea Bergamasco, A., Eldridge, M. and Sodré, F., An integrated approach to evaluate emerging contaminants in drinking water. Separation and Purification Technology, 84, pp. 3-8, 2012. DOI: 10.1016/j.seppur.2011.06.020
[12] Gupta, V. and Ali, I., Environmental water: water treatment for inorganic pollutants by adsorption technology, Elsevier, 2013
[13] Peláez, A. and Teutli, M., Lignocellulosic precursors used in the synthesis of activated carbon - characterization techniques and applications in the wastewater treatment: lignocellulosic precursors used in the elaboration of activated carbon, México, InTech, 2012.
[14] World Health Organization (WHO). Drinking water guidelines, Volumen 1, 3ra. Edición 2006
[15] Di Bernardo, L. and Di Bernardo, A., Métodos e técnicas de tratamento de água. Brasil, Rima, Editor. 2005.
[16] Di Bernardo, L. and Sabogal, L., Seleção de tecnologias de tratamento de água, Brasil, LDiBe, editor, 2008.
[17] Arboleda, J., Teoría y práctica de la purificación del agua, Colombia, McGraw-Hill, editor. 2000.
[18] Freese, S., Nozaic, D., Pryor, M., Rajogopaul, R., Trollip, D. and Smith, R., Enhanced coagulation: a viable option to advance treatment technologies in the South African context. Water Science and Technology [online], 1(1), pp. 33-41, 2001. [Reference date 17 July of 2017]. Available at: http://elaguapotable.com/Mejora de la coagulacion.pdf.
[19] Ho, L. and Newcombe, G., Granular activated carbon adsorption of 2-methylisoborneol (MIB): pilot- and laboratory-scale evaluations. Journal of Environmental Engineering, 136(9), pp. 965-974, 2010. DOI: 10.1061/(ASCE)EE.1943-7870.0000231.
[20] Di Bernardo, L., Di Bernardo, A. y Nogueira, P., Tratabilidad del agua y residuos generados en estaciones de tratamiento de agua: procedimientos para realización de ensayos de tratabilidad de agua, Brasil, LDiBe, 2011.
[21] Rigobello, E., Di Bernardo, A., Di Bernardo, L. and Vieira, E., Removal of diclofenac by conventional drinking water treatment processes and granular activated carbon filtration. Chemosphere, 92(2), pp. 184-191, 2013. DOI: 10.1016/j.chemosphere.2013.03.010.
[22] Perea, L., Torres, P., Cruz, C. y Escobar, J., Influencia de la configuración del medio filtrante sobre el proceso de filtración a tasa constante del agua clarificada del río Cauca. Revista de Ingeniería [en línea], (38), pp. 38-44, 2013 [Referencia: Mayo 12 de 2017]. Disponible en: http://www.redalyc.org/articulo.oa?id=121028408006.
[23] Environmental Protection Agency (EPA). Method 523: Determination of triazine pesticides and their degradates in drinking water by Gas Chromatography/Mass Spectrometry (GC/MS) Version 1.0. 2012.
[24] Huang, J., Wang, X., Jina, Q., Liua, Y. and Wang, Y., Removal of phenol from aqueous solution by adsorption onto OTMAC-modified attapulgite. Journal of Environmental Management, 84, pp. 229-236, 2007. DOI: 10.1016/j.jenvman.2006.05.007.
[25] Kim, J. and Kang, B., DBPs removal in GAC filter-adsorber. Water Research, 42(1-2), pp. 145-152, 2008. DOI: 10.1016/j.watres.2007.07.040
[26] Gibert, O., Lefèvre, B., Fernández, M., Bernat, X., Paraira, M. and Pons, M., Fractionation and removal of dissolved organic carbon in a full-scale granular activated carbon filter used for drinking water production. Water Research, 47(8), pp. 2821-2829, 2013. DOI: 10.1016/j.watres.2013.02.028
[27] Mukherjee, S., Kumar, S., Misra, A. and Fan, M., Removal of phenols from water environment by activated carbon, bagasse ash and wood charcoal. Chemical Engineering Journal, 129(1), pp. 133-42, 2007. DOI: 10.1016/j.cej.2006.10.030
[28] Giraldo, L. and Moreno, J., Pb^{2+} adsorption from aqueous solutions on activated carbons obtained from lignocellulosic residues. Brazilian Journal of Chemical Engineering, 25(1), pp. 143-151. 2008. DOI: 10.1590/S0104-66322008000100015
[29] Giraldo, L. and Moreno, J., Synthesis of activated carbon mesoporous from coffee waste and its application in adsorption zinc and mercury ions from aqueous solution. E-Journal of Chemistry, 9(2), pp. 938-948, 2012. DOI: 10.1155/2012/120763
[30] Vukčević, M., Kalijadis, A., Vasiljević, T., Babić, B., Laušević, Z. and Laušević, M., Production of activated carbon derived from waste hemp (Cannabis sativa) fibers and its performance in pesticide adsorption. Microporous Mesoporous Mater, 214, pp. 156-165, 2015. DOI: 10.1016/j.micromeso.2015.05.012
[31] Montgomery, D. y Runger, G., Probabilidad y estadística aplicadas a la ingeniería, McGraw-Hill, 2012.
[32] Marcó, L., Azario, R., Metzler, C. y Garcia, M., La turbidez como indicador básico de calidad de agua potabilizada a partir de fuentes superficiales. Propuesta a propósito del estudio del sistema de potabilización y distribución en la ciudad de Concepción del Uruguay, higiene, sanidad y ambiente [en línea], pp. 72-82, 2004. [Referencia agosto 10 de 2017]. Disponible en: http://salud-publica.es/secciones/revista/revistaspdf/bc 510156890491c_Hig.Sanid.Ambient.4.72-82(2004).pdf
[33] Aráuz, M. y Castillo, V., Determinación de la concentración de trihalometanos producidos por reacción del cloro con la materia orgánica nitrogenada en muestras del río Fonseca, Departamento de Boaco, BSc. Tesis, Facultad de Ciencia, Tecnología y Ambiente, Universidad Centroamericana, Managua, Nicaragua, 2008.
[34] Leiva, A., Caracterización de calidad de agua en el ciclo de consumo del municipio de Guaimaca, Franciso Morazán, Honduras. Escuela Agrícola Panamericana, San Antonio de Oriente, Honduras, 2010.
[35] Fray, M., Occurrence of herbicides/pesticides in drinking water, United States, American Water Works Association, editors, 2000.
[36] Tadkaew, N., Hai, F., McDonald, J., Khan, S. and Nghiem, L., Removal of trace organics by MBR treatment: The role of molecular properties. Water Research, 45(8), pp. 2439-2451, 2011. DOI: 10.1016/j.watres.2011.01.023
[37] Friedler, E. and Alfiya, Y., Physicochemical treatment of office and public buildings greywater. Water Science and Technology, 62(10), pp. 2357-2363, 2010. DOI: 10.2166/wst.2010.499.
[38] Christopher, D., The effect of granular activated carbon pretreatment and sand pretreatment on microfiltration of greywater, MSc Thesis, Civil Engineering, Clemson University, South Carolina, United States, 2012.
[39] Ministerio de Ambiente Vivienda y Desarrollo Territorial (MAVDT). Resolución 2115, Colombia, 2007.
[40] Organización Panamericana de Salud (OPS). Guías para la calidad del agua potable, Número 481, Volumen 3, Org PAH, editor. 1987.
[41] United States Environmental Protection Agency (USEPA). EPA 816-F-09-004, National Primary Drinking Water Regulations. 2009.
[42] Feng, S., Xie, S., Zhang, X., Yang, Z., Ding, W., Liao, X., Liu, Y. and Chen, Ch., Ammonium removal and microbial community in GAC-sand dual media filter in drinking water treatment. Journal of Environmental Sciences, 24(9), pp. 1587-1593, 2012. DOI: 10.1016/S1001-0742(11)60965-0.
[43] Serrano, M., Montesinos, I., Cardador, M., Silva, M. and Gallego, M., Seasonal evaluation of the presence of 46 disinfection by-products throughout a drinking water treatment plant. The Science of the Total Environment, 56(13), pp 246-58, 2015. DOI: 10.1016/j.scitotenv.2015.02.070.
[44] Babi, K., Koumenides, K., Nikolaou, A., Makri, C., Tzoumerkas, F. and Lekkas, T., Pilot stufy of the removal of THMs, HAAs and DOC from drinking water by GAC adsorption. Desalination, 210(1-3), pp. 215-224, 2007. DOI: 10.1016/j.desal.2006.05.046.
[45] Lu, Y., Wang, D., Ma, C. and Yang, H., The effect of activated carbon adsorption on the photocatalytic removal of formaldehyde. Building and Environment, 45(3), pp 615-621, 2010. DOI: 10.1016/j.buildenv.2009.07.019.
[46] Zadaka, D., Nir, S., Radian, A. and Mishael, Y., Atrazine removal from water by polycation - clay composites : Effect of dissolved organic matter and comparison to activated carbon. Water Research, 43(3), pp. 677-683, 2009. DOI: 10.1016/j.watres.2008.10.050
[47] Tejada, C., Villabona, Á. y Núñez, J., Uso de biomasas para la adsorción de plomo, níquel, mercurio y cromo. Universidad de Cartagena Colombia, Ingenium, 9, pp 41-51, 2015. DOI: 10.21774/ingenium.v9i24.520
[48] World Health Organization (WHO). Atrazine in drinking-water background document for development of WHO guidelines for drinking-water quality, Geneva, 2003.
[49] Pham, T., Nguyen, V. and Van der Bruggen, B., Pilot-scale evaluation of GAC adsorption using low-cost, high-performance materials for removal of pesticides and organic matter in drinking water production.

Journal of Environmental Engineering, 139(7), pp. 958-965, 2013. DOI: 10.1061/(ASCE)EE.1943-7870.0000704.
[50] Alam, J., Dikshit, A. and Bandyopadhyay, M., Efficacy of adsorbents for 2, 4-D and atrazine removal from water environment. Global Nest: The Int. J. [online], 2(2), pp. 139-48, 2000 [Reference date: 6 July of 2017]. Available at: https://journal.gnest.org/sites/default/files/Journal Papers/02_dikshit.pdf.
[51] Perez-Vidal, A., Torres-Lozada, P. and Escobar-Rivera, J., Hazard identification in watersheds based on water safety plan approach: case study of Cali-Colombia. Environmental Engineering and Management [online]. 15(4), pp. 861-872, 2016. [Reference date: 18 may of 2017]. Available at: https://www.researchgate.net/publication/312210775_Hazard_identification_in_watersheds_based_on_water_safety_plan_approach_case_study_of_Cali-Colombia.

L.M. Fuentes-López, is BSc. in Sanitary and Environmental Engineer, graduated in 2015 from the University of Valle (Colombia). Presently, she is a MSc. in Engineering student with an emphasis on Sanitary and Environmental Engineering from the same university, where she has worked on projects related to drinking water treatment. She belongs to the ECCA Research Group - Faculty of Engineering - University of Valle, Colombia.
ORCID: 0000-0001-8213-5491

C.P. Amezquita-Marroquin, is BSc. in Sanitary Engineer, graduated in 2009 from University of Valle (Colombia), MSc. in Engineering with an emphasis on Sanitary and Environmental Engineering (2013). Presently, she is a PhD student in Sanitary and Environmental Engineering at the same university, where she has worked on research projects related to drinking water treatment. She belongs to the ECCA Research Group - Faculty of Engineering - University of Valle, Colombia.
ORCID: 0000-0002-0094-2204

P. Torres-Lozada, is BSc. in Sanitary Engineer, graduated in 1988 from the University of Valle (Colombia), MSc (1993) and PhD (2001) in Civil Engineering: Hydraulics and Sanitation from the Universidad de São Paulo (Brazil). Since 1995, she has been associated with the University of Valle, Colombia as a full professor, categorized by Colciencias as a senior researcher and leader of Study and Control of Environmental Pollution Research Group - ECCA - Category A1- Faculty of Engineering - University of Valle, Colombia. Her research areas are water quality, drinking water treatment, wastewater and solid waste treatment.
ORCID: 0000-0001-9323-6677

UNIVERSIDAD NACIONAL DE COLOMBIA
SEDE MEDELLÍN
FACULTAD DE MINAS

Área Curricular de Medio Ambiente

Oferta de Posgrados

Especialización en Aprovechamiento de Recursos Hidráulicos
Especialización en Gestión Ambiental
Maestría en Ingeniería Recursos Hidráulicos
Maestría en Medio Ambiente y Desarrollo
Doctorado en Ingeniería - Recursos Hidráulicos
Doctorado Interinstitucional en Ciencias del Mar

Mayor información:

E-mail: acma_med@unal.edu.co
Teléfono: (57-4) 425 5105

UNIVERSIDAD NACIONAL DE COLOMBIA
SEDE MEDELLÍN
FACULTAD DE MINAS



DYNA
http://dyna.medellin.unal.edu.co/

Experimental characterization, modeling and compensation of hysteresis in force sensing resistors

Leonel Paredes-Madrid [a] Arnaldo Matute [a], Andrés F. Cruz-Pacheco [b], Carlos A. Parra-Vargas [b] & Elkin I. Gutiérrez-Velásquez [a]

[a] *Facultad de Ingeniería Mecánica, Electrónica y Biomédica Universidad Antonio Nariño, Tunja, Colombia. paredes.leonel@uan.edu.co, arnaldo.matute@uan.edu.co, elkin.gutierrez@uan.edu.co*
[b] *Grupo de Física de Materiales (GFM), Universidad Pedagógica y Tecnológica de Colombia, Tunja, Colombia. andresfelipe.cruz@uptc.edu.co, carlos.parra@uptc.edu.co*

Received: July 18th, 2017. Received in revised form: April 11th, 2018. Accepted: May 5th, 2018.

Abstract
Force Sensing Resistors (FSRs) exhibit considerable amounts of hysteresis and repeatability error inhibiting their usage in applications that require high-accurate force readings. This paper presents the hysteresis characterization and modeling of the Tekscan A201-1 FSR employing the Preisach Operator (PO) function. In order to compensate for hysteresis during sensor operation, the inverse PO was numerically found on the basis of the Closest Match Algorithm (CMA). A test bench, capable of handling sixteen sensors simultaneously, was built, which allowed the characterization and later testing of the CMA. Grip force profiles were applied to the sensors during testing and the experimental results showed a considerable reduction in the force estimation error compared with the linear regression method proposed by the manufacturer. These results enable a wider use of FSRs in applications with tight accuracy requirements. Finally, a generalized sensor model for hysteresis compensation that simplifies the obtaining of PO parameters is presented.

Keywords: hysteresis; force sensing resistors; Preisach operator; closest match algorithm.

Caracterización experimental, modelado y compensación de la histéresis en sensores de fuerza resistivos

Resumen
Los Sensores de Fuerza Resistivos (FSRs) despliegan cantidades considerables de histéresis y de error de repetitividad que inhiben su uso en aplicaciones que requieren lecturas de fuerza de alta precisión. En este trabajo se presenta la caracterización y modelado de histéresis del sensor de presión Tekscan A201-1 empleando la función Operador de Preisach (OP). Con el fin de compensar la histéresis durante el funcionamiento del sensor, el OP inverso se halló numéricamente sobre la base del algoritmo de coincidencia más cercana (CMA). Se construyó un banco de pruebas, capaz de manejar dieciséis sensores simultáneamente, lo que permitió la caracterización y posterior prueba del CMA. Los perfiles de fuerza de agarre se aplicaron a los sensores durante la prueba y los resultados experimentales mostraron una reducción considerable del error de estimación de la fuerza en comparación con el método de regresión lineal propuesto por el fabricante. Estos resultados abren el camino para un uso más amplio de los FSRs en aplicaciones con exigentes requisitos de precisión. Finalmente, un modelo de sensor generalizado para compensación de histéresis que simplifica la obtención de los parámetros PO, es presentado.

Palabras clave: sensores de fuerza resistivos; operador de Preisach; algoritmo de coincidencia más cercana.

1. Introduction

Biomechanical researches strongly rely on accurate force measurements to provide reliable studies and outstanding developments: ground reaction forces occurring during gait analysis and gripping forces occurring during object manipulation are only some applications that demand non-invasive and accurate force measurements.

How to cite: Paredes-Madrid, L., Matute, A., Cruz-Pacheco, A.F., Parra-Vargas. C.A. and Gutiérrez-Velásquez, E.I., Experimental characterization, modeling and compensation of hysteresis in force sensing resistors. DYNA, 85(205), pp. 191-198, June, 2018.

© The author; licensee Universidad Nacional de Colombia.

Inertia and position readings are also demanded in biomechanical studies; with the added complexity that the employed transducers must be installed with minimal interference on the human or animal under study in order to avoid discomfort during motion, consequently, the sensors in Biomechanical studies must be either low profile or such variables must be remotely tracked when possible [1,2].

Performing accurate position and inertia readings has been practically resolved through the usage of encoders, resolvers and Inertial Measuring Units (*IMUs*). However, if such sensors result too bulky, high-speed cameras can be used instead [3]. However, performing accurate force readings has always been a difficult task in biomechanical studies because force, unlike position, cannot be remotely tracked.

Force Sensing Resistors (*FSRs*) are cost-affordable force sensors that can be easily integrated into multiple Biomechanical applications [4-6]. Nonetheless, the main reasons for its widespread usage are their low profile and low weight, which are highly desirable characteristics when attempting to perform non-invasive force measurements [6]. Another reason for their wide acceptance is the simple interface circuit required to read sensor's output, e.g.: voltage dividers or inverting amplifiers. When using an inverting amplifier, see Fig. 1a, an estimation of sensor's conductance ($1/R_s$) is obtained through output voltage (V_{o1}). Conversely, when using a voltage divider, see Fig. 1b, sensor's resistance (R_s) is measured through V_{o2}.

Commercially available *FSRs* can be found on different shapes and nominal ranges: round (FSR400 and FSR402) and squared (FSR406 and FSR408) *FSRs* are manufactured by Interlink Electronics, Camarillo, CA [7]. Tekscan Inc. from South Boston, MA, offers round (A201-1, A201-25 and A201-100) and several customizable *FSRs* in his product catalog [8], see Fig. 1c and Fig. 1d. Unfortunately, the overall performance of *FSRs* is poor compared to well-established force sensing solutions such as load cells and strain gauges. Previous works from Lebosse [9], Hollinger [10] and Komi [11] present a comprehensive review on *FSR* limitations. Hysteresis and drift are typically one or two orders of magnitude greater in *FSR*s than in load cells. These conditions are the main drawbacks for the extensive usage of *FSRs* in industrial and research applications, but a great effort is currently placed on improving their performance.

One trend, within *FSR* research, is to model sensors' response with the aim of compensating hysteresis and drift. Relevant works on this scope have been developed by Lebosse [9], Schofield [5], Dabling [12], Vecchi [13] and Urban [14]. Likewise, authors' previous work has demonstrated that the A201 sensors, working on the piezoresistive principle, are also capable of exhibiting a piezocapacitive response. Different methods were proposed and evaluated by the authors to combine Capacitance (C_s) and Conductance (V_{o1}) readings with the aim of increasing *FSR* accuracy under static loading [15, 16]. It must be noted that DC/AC voltages were alternately applied to the *FSRs* to read V_{o1} and C_s respectively, followed by a feedforward neural network to optimally combine V_{o1} and C_s readings. When compared to the purely conductance model of Fig. 1e [8], a 64% reduction in the force Mean Squared Error (*MSE*) was obtained. The reduction in the *MSE* was done at the price of increasing the complexity of the driving circuit which may result prohibitive for certain applications with power or space constraints.

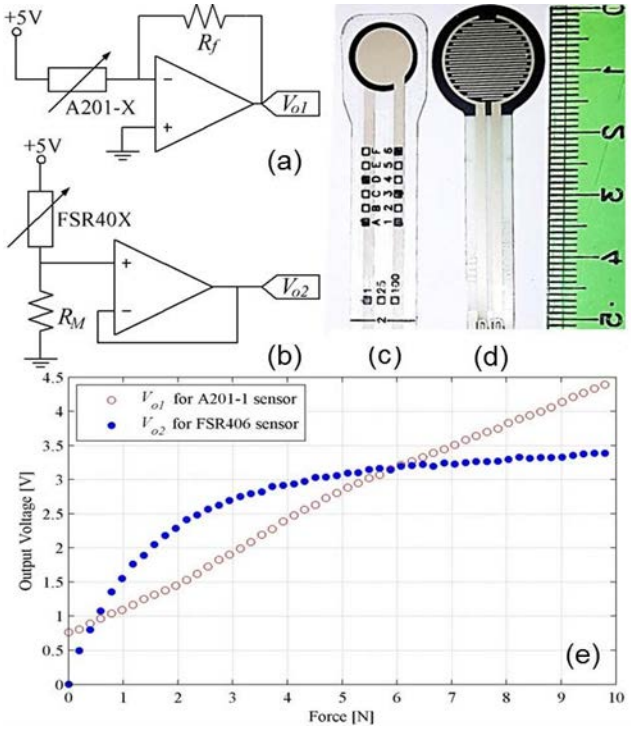


Figure 1. Driving circuits for: (a) FlexiForce A201-X, (b) Interlink FSR40X. Pictures of: (c) A201-1 and (d) FSR402 next to a ruler in centimeters. (e) Typical sensors' response: A201-1 (circle red) and FSR406 (solid blue). Source: The authors.

By modeling *FSR's* hysteresis through the Preisach operator [17], an improved algorithm for estimating applied forces is here presented. The algorithm only requires conductance readings form the sensor, and thus, the simple driving circuit of Fig. 1a is needed, or Fig. 1b when using Interlink sensors. A considerably computational effort is required to run the inverse Preisach algorithm, but such an effort is justified when the force *MSE* is dramatically reduced. In order to obtain a valid generalization of results, a total of sixteen A201-1 FlexiForce sensors are used; this sensor matches the required force range (*4.5N*) of biomechanical applications involving grip and grasp operations. Nonetheless, the methods henceforth discussed are applicable to other models of *FSRs*.

This paper is organized as follows: Section II describes the experimental setup for gathering sensor data. Later in Section III, experimental data from the sixteen A201-1 sensors are presented with statistics regarding hysteresis. A brief description of the Preisach Operator and its inverse are also available on Section III. Later in Section IV, grip force profiles are exerted on the A201-1 sensors and the inverse Preisach algorithm is tested and compared with the traditional conductance model. In Section V, a generalized sensor model based on the Preisach Operator is presented, followed by conclusions and future work on Section VI.

2. Experimental Set-Up

Previous work demonstrated that the A201-X sensors can be electrically modeled as a parallel R_s-C_s device as shown in Fig. 2a [15,16], with R_s exhibiting a hyperbolical dependence on the applied force (F). Since this paper focusses on reducing the force *MSE* through conductance readings only, capacitance measurements are not henceforth considered. For linearization purposes, conductance variations – measured through V_{o1} – have been preferably used in several studies to estimate F [8, 9, 12, 15]; this is possible by inverting the model of Fig. 1e, which yields:

$$F = mV_o + b \tag{1}$$

Where m and b are obtained from a least-squares minimization process; the whole procedure is known in literature as sensor characterization and may comprise only increasing or increasing/decreasing forces. It must be noted that the application of either pattern produces a significant effect in m and b values given the hysteresis in the device; this is later exemplified on Section IV. The test bench for sensor characterization and testing comprises electrical and mechanical sensors/actuators as described next.

2.1. Mechanical setup

In order to get a trade-off between nominal force and resolution, a linear stepper motor was accommodated with a spring to exert forces over the bunch of sensors depicted in Fig. 2b. The mechanical compliance of the test bench was modified through the stiff constant of the spring; and the force control loop was closed using data from a high accuracy LCHD-5 load cell with 22N capacity. The set-up could arrange up to sixteen sensors simultaneously with a resolution of 1.4mN and a maximum dF/dt of 22.6N/s. These characteristics were more than enough to emulate force profiles exerted during grip and grasp operations such as those reported by Stolt [18] and Melnyk [19].

The sensors were arranged in a sandwich configuration and then placed inside a temperature chamber that held operating temperature at 25ºC±1ºC to avoid undesired effects caused by thermal drift, see Fig 2c. Considering that the main scope of this article is to reduce the force *MSE* through hysteresis modeling and compensation, it was not embraced the inclusion of changing temperatures as an additional variable. Finally, it must be noted that the sandwich configuration depicted in Fig. 2b added extra weight to the sensors located at the bottom; this condition was taken into account for the linear regression method (1) and the Preisach Operator later described on Sections III, IV.

2.2. Electrical setup

A modified version of the circuit from Fig. 1a was implemented to perform voltage readings in the sixteen sensors, see Fig. 3. A time-multiplexed scheme comprising four analog multiplexers (ADG444) was implemented to readout V_o. The feedback Resistor (R_f) was set to 10KΩ and the supply Voltage (V_s) was set to -1V.

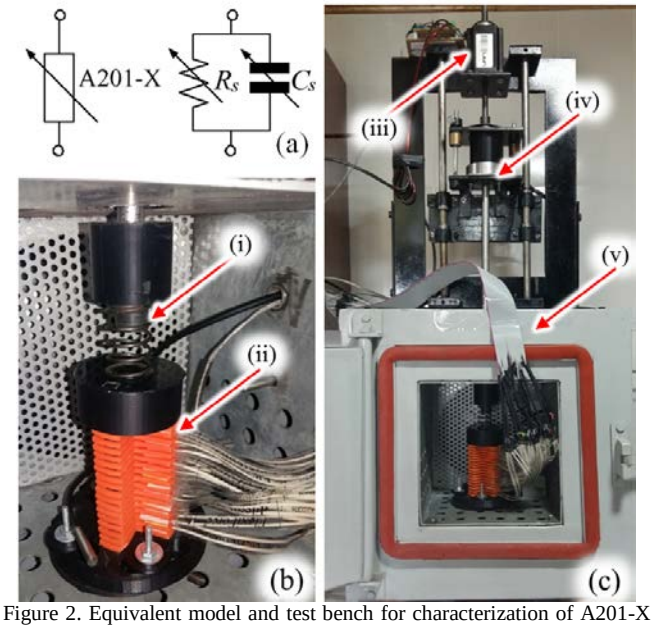


Figure 2. Equivalent model and test bench for characterization of A201-X sensors. (a) Black box model and equivalent circuit for an A201-X *FSR*. (b) Zoom-in picture depicting the spring (i) for mechanical compliance of the test bench and the bunch of sixteen A201-1 sensors (ii) arranged in a sandwich configuration. (c) Picture of the test bench showing the stepper motor (iii), the LCHD-5 load cell (iv) and the temperature chamber (v). Source: The authors.

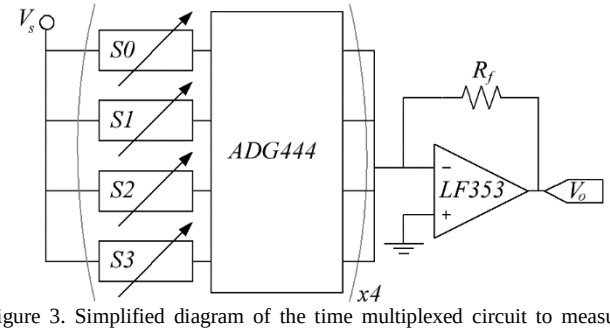


Figure 3. Simplified diagram of the time multiplexed circuit to measure conductance (V_o) in sixteen A201-1 sensors, S0 through S15. Source: The authors.

It must be remarked that the FlexiForce sensors exhibit a subtle saturation effect in the form of hyperbolic tangent in regard to V_s variations; this avoids that m and b can be recalculated when V_s is changed given that k in (2) changes from one sensor to another [16]. In practice, this implies that (1) is valid only for a constant V_s during sensor operation:

$$V_o = -(mF + b)\,atanh\,(V_s / k) \tag{2}$$

3. Hysteresis characterization, modeling and compensation based on the Preisach operator

3.1. Characterization of hysteresis in FSRs

Triangle force profiles of 4.5N were exerted over the sensors to observe V_o during loading and unloading events.

Equation (3) was employed to assess the Hysteresis Error (*HE*) based on the metrics shown on Fig. 4a. Results from the sixteen sensors are represented by data points on Fig. 4b.

$$HE = 100\% \cdot (V_o^u - V_o^l)/V_o^M \tag{3}$$

Note that hysteresis ranges from 7.6% to 17%, with the maximum V_o^u–V_o^l occurring typically at half of the nominal sensor range, such values notably differ from what the sensor manufacturer reports at [8] with *HE*<4.5%. However, the manufacturer estimates the *HE* at 80% of the nominal sensor range. Dabling reports in [12] a 7.4% hysteresis for the Tekscan A401-25 sensor, which is consistent with the results from Fig 4b.

3.2. Modeling hysteresis through the Preisach operator

In order to compensate for hysteresis, it needs first to be modeled. The Preisach Operator (*PO*) is a common approach to model hysteresis; it has been successfully employed in nanopositioning applications with piezoelectric and magnetostrictive actuators [17, 20]. An in-depth explanation of the *PO* theory has not been provided here, but readers may refer to Tan [21] and Visone [17] for such a purpose.

The ability of the Preisach Operator to model hysteresis is next described with an example focused on the A201-1 sensor, where $R_{\alpha,\beta}[F,H(t\text{-}1)]$ is the delayed relay output represented in Fig. 5a as *H* and as *H(t)* in (4). The applied force, *F*, is the time-varying input.

$$H(t) = R_{\alpha,\beta}[F, H(t-1)] = \begin{cases} 1 & for \;\; F \geq \alpha \\ H(t-1) & for \;\; \beta < F < \alpha \\ -1 & for \; F \leq \beta \end{cases} \tag{4}$$

The function $R_{\alpha,\beta}[F,H(t\text{-}1)]$ is known in literature as the Preisach Operator or Hysteron, where parameters α and β come from the discretization of *F* into n_h levels, summing a total of n_q Hysterons:

$$n_q = n_h(n_h+1)/2 \tag{5}$$

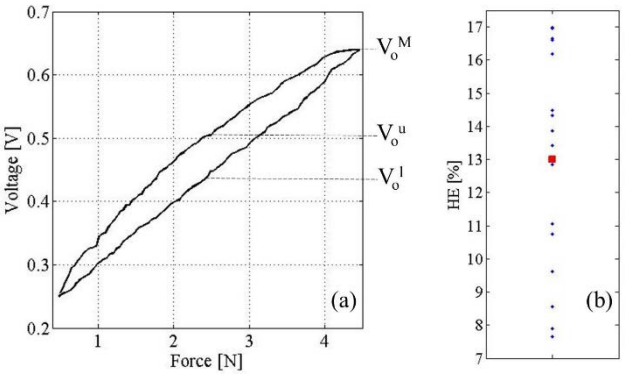


Figure 4. Hysteresis in the A201-1 sensor. (a) Plot representing the maximum voltage difference between loading (V_o^l) and unloading (V_o^u) events, occurring at the same *F*. (b) Scatter plot of the *HE* for sixteen A201-1 sensors. The average *HE* is shown with a squared red marker.
Source: The authors.

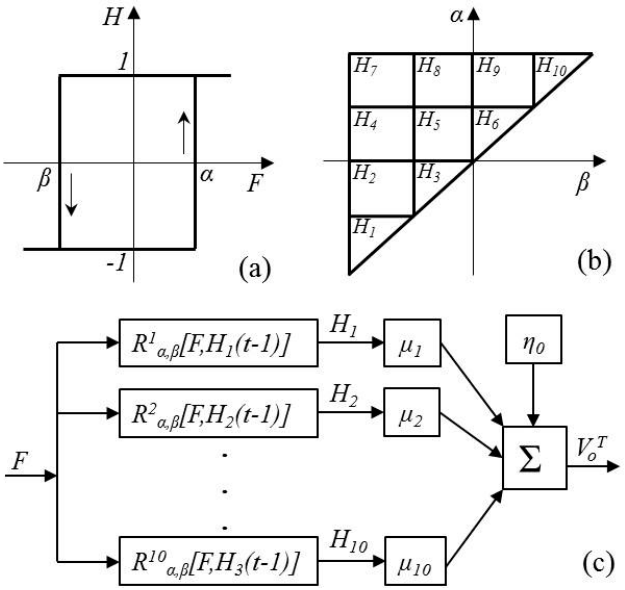


Figure 5. Preisach Operator and elements. (a) Plot of the delayed relay output representing the mathematical function of a Hysteron. (b) Preisach plane with n_h=*4* and 10 Hysterons. (c) Block diagram representing the totaling function for modeling hysteresis in the A201-1 FSR.
Source: The authors.

As in Fig. 5b with n_h=*4*, there is a total of 10 Hysterons (H_1~H_{10}). The totaling function ($V_o^T(t)$) is a discrete function that embraces the contribution from each delayed relay output (H_1~H_{10}) weighted by (μ_1~μ_{10}) plus an offset (η_0); this process is performed on each sampling interval to obtain a discrete model of the sensor hysteresis. A graphical representation of the totaling process is depicted on Fig. 5c.

At the beginning of a trial, all of the Hysterons are deactivated, i.e., initialized at *y(t-1)=-1*, see Fig. 6a; this implies that $F(t_1) \leq \alpha_1$. As $F(t_2)$ increases beyond α_3, Hysterons H_1 to H_6, are activated and their relay outputs change from *-1* to *1*. Active relay outputs are gray colored in Fig. 6a and ahead. Later, the applied force decreases up to $F(t_3)$ where $F(t_3) \leq \beta_2$, and thus, Hysterons H_3, H_5 and H_6 are deactivated as shown on Fig. 6c. Finally, in Fig. 6d, force is increased again up to $F(t_4)$ and the only Hysteron that changed is H_3 since $\alpha_2 < F(t_4) < \alpha_3$.

The ability of the Preisach Operator to model hysteresis is exemplified as follows: let's say that in a new trail represented in Fig. 6e, the applied force is straight incremented from $F(t_1) \leq \alpha_1$ up to $F(t_5)$, with $F(t_5)=F(t_4)$. Note that in Fig. 6e the Hysterons H_1 to H_3 are activated, which differs from the previous memory curve of Fig 6d. Such a difference yields different values on the output totaling function, $V_o^T(t)$, because of the different trajectories employed to reach $F(t_4)$ and $F(t_5)$ on each case.

The weight values of each Hysteron, μ_1~μ_{10}, and the offset, η_0, are estimated on an empirical basis, following a characterization process somewhat similar to that recommended by the sensor manufacturer [8]. In a general case with n_h levels of discretization, there is a total of n_q Hysterons that are grouped in the so-called memory curve (Ψ). The Preisach density function ($\mu_{(\alpha,\beta)}$) is defined as the collection of weights representing the contribution of each

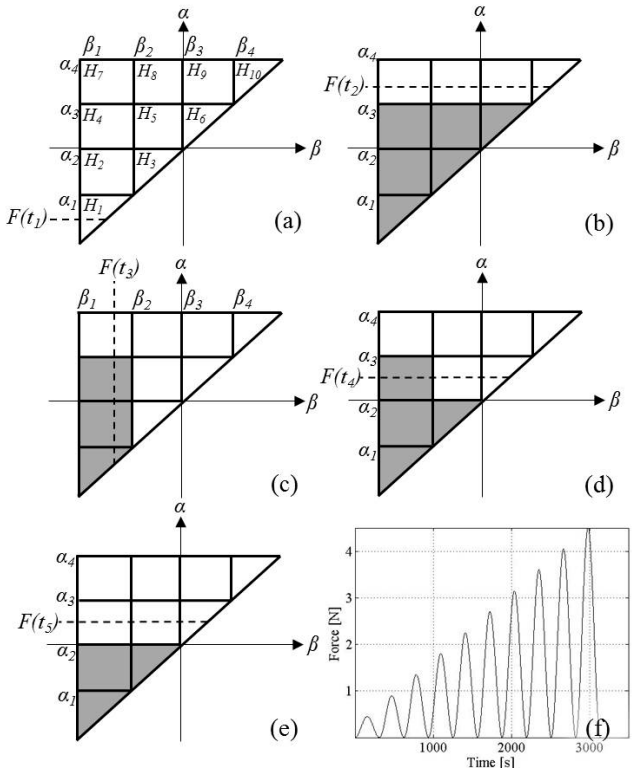


Figure 6. Preisach plane and input signal for hysteresis characterization, active hysterons are gray colored. (a through d) Evolution of the Preisach plane under increasing and decreasing forces with initial condition $\Psi_0=(H_1\sim H_{10})=-1$ at Fig. 6a. (e) Final Preisach plane for an input force $F(t_5)$ with initial condition $\Psi_0=(H_1\sim H_{10})=-1$.(f) General form of the required input signal for hysteresis characterization.
Source: The authors.

Hysteron to the totaling function, $V_o^T(t)$. The function $\mu_{(\alpha,\beta)}$ is nonnegative with a total of n_q elements. It must be noted that in order to model hysteresis, a total of n_q+1 parameters – $\mu_{(\alpha,\beta)}$ plus η_0 – must be estimated through a least-squares minimization process that ensures the nonnegative constraint of the Preisach density function. During characterization, it is important that the input force profile ensures the activation and deactivation of all the Hysterons; by doing this, an appropriate estimation of $\mu_{(\alpha,\beta)}$ and η_0 is obtained.

Stakvik presented in [20] a guideline for creating an adequate input signal intended for hysteresis characterization; the signal consists of incremental-amplitude sine waveforms as shown on Fig. 6f. It must be remarked that the hysteresis is a rate independent phenomenon, and thus, the frequency of the input-sine profile does not affect the identification process.

Finally, the identification of $\mu_{(\alpha,\beta)}$ and η_0 was carried out by applying a modified version of Fig. 6f. Triangle force profiles were used instead of sines with forty evenly spaced amplitudes starting from 0N up to 4.5N. Likewise, the discretization level was set to $n_h=40$ during the data fitting process that estimated $\mu_{(\alpha,\beta)}$ and η_0. The resulting $\mu_{(\alpha,\beta)}$ is plotted on Fig. 7 for one of the sixteen sensors previously shown on Fig. 2b, similar density functions were obtained for the rest of sensors.

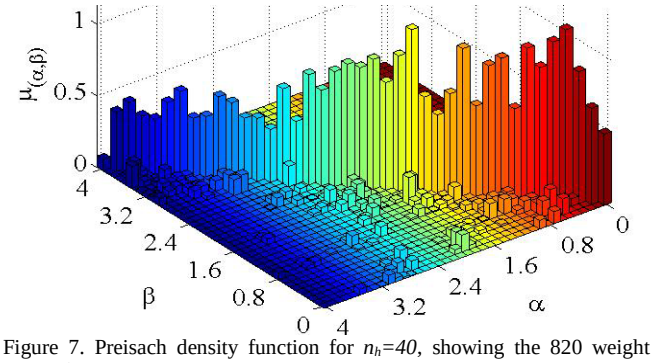


Figure 7. Preisach density function for $n_h=40$, showing the 820 weight values for an A201-1 FlexiForce sensor.
Source: The authors.

In practice, the maximum value of n_h is limited by the Repeatability Error (*RE*) of the device; typically *RE=2.5%* for the A201-1 sensor [8]. This implies that the uncertainty in sensor output, V_o, for a given applied force is of 2.5% and thus, the sensor can resolve a maximum of 100/2.5 force intervals without overlapping.

3.3. *Compensating hysteresis in FSRs through the inversion of the Preisach operator*

When estimating *F* based on V_o readings, the *PO* model must be inverted in order to compensate for hysteresis. Unfortunately, an analytical expression for the delayed relay operator cannot be formulated; and thus, an approximate numerical solution must be found instead.

Given the initial conditions: Ψ_0 curve with all Hysterons deactivated, $(H_1\sim H_{10})=-1$, and the applied force $F_0=0N$. At the next sampling interval with $F_1>F_0$, the numerical inversion algorithm activates the Hysterons following the same order depicted in Fig. 6, i.e. H_1, H_2-H_3, H_4-H_5-H_6, and so on. The process is repeated until $V_o^T(t)$ reaches the closest match to the measured voltage V_1 at the *FSR*. The required force to activate the above-cited Hysterons is the approximate numerical solution of the inverse *PO* model. The procedure is conveniently known in literature as the Closet Match Algorithm (*CMA*) [21]. The output of the *CMA* is discrete (*F*), just as the *PO* model is. However, a continuous implementation of the *CMA* has been already developed in [20], but for space constraints, it has not been discussed or implemented here.

4. Experimental results and analysis

Grip force profiles, based on grip data issued from Stolt [18] and Melnyk [19], were exerted on the A201-1 sensors using the experimental set-up previously described on Section II. The performance of the *CMA* to estimate *F* was comparatively evaluated with the linear regression model (1), which is the manufacturer recommended method. It must be noted that the linear regression model is the preferred method in research applications [4,5,9-13]. Two sets of *m* and *b* constants were calculated using the triangle force profiles of Section III.B. The first set of *m* and *b* constants used only the increasing data points, whereas the second fit employed the whole data.

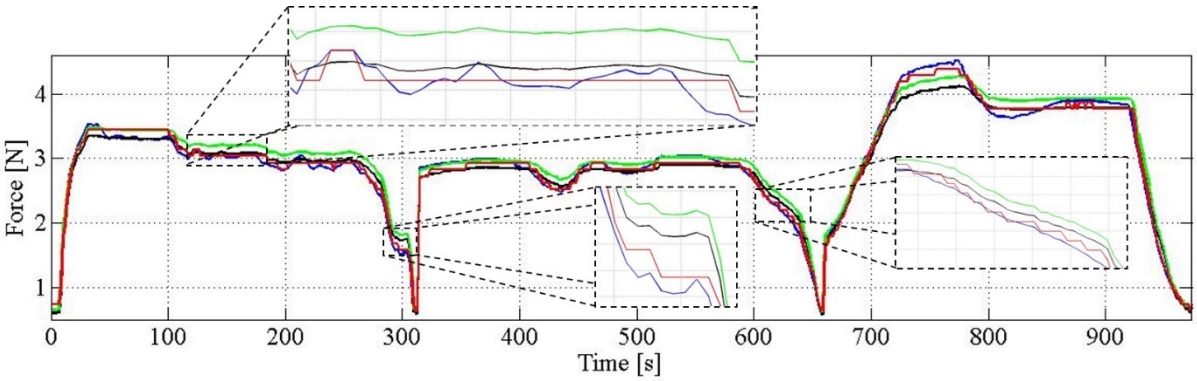


Figure 8. Force estimation through different methods: (red) *CMA* using a sensor-tuned Preisach density function and η_0, linear regressions using increasing data points only (green) and the entire dataset (black). Real force profile based on grip data from Stolt [18] and Melnyk [19] (blue).
Source: The authors.

Experimental results for a given sensor are graphed on Fig. 8, together with an error bar plot on Fig. 9 representing the force *MSE* for the sixteen sensors and the three models, i.e.: the *CMA* and the two aforesaid linear regressions. In average, the *CMA* yields a considerable reduction in the *MSE* compared to the models based on (1), 54% and 76% respectively. The reduction in the force *MSE* is paid by a larger computation time, which may limit the usability of the *CMA* in some real-time applications, but if time is not a constraint; the *CMA* can run off-line and get the best of a *FSR*. This is the case of most biomechanics researches in which data are collected and later analyzed [4, 5]. However, a fast implementation of the *CMA* is possible if dedicated hardware is used, i.e., employing FPGA technology [22].

Note that the dispersion of the *MSE* is narrowed when force estimation is done on the *CMA* (red bars on Fig. 9), this occurs because the remaining *MSE* is only produced by: the Repeatability Error, *RE*, and the quantization error derived from the discrete *CMA*. The contribution of the *HE* to the *MSE* is suppressed thanks to the *PO* modeling and compensation via the *CMA*. Further reduction of the *MSE* is possible if a continuous implementation of the *CMA* is performed, just as Stakvik demonstrated in [20]. This statement can be illustrated from the zoom-in plot at the top of Fig. 8. Note that both linear regressions exhibit a subtle swinging due to V_o variations, nonetheless, such variations are not great enough to change the memory curve Ψ, and consequently, the *CMA* yields a constant output. The implementation of a continuous *CMA* can better adapt to subtle V_o variations amid a constant memory curve Ψ, and thus, the force *MSE* would be further reduced.

5. Generalized sensor model for hysteresis compensation: an approach

Obtaining $\mu_{(\alpha,\beta)}$ and η_0 is not a straightforward procedure; specialized hardware is required and a time consuming characterization must be performed followed by non-trivial programing. Fortunately, it is possible to simplify the characterization process if the parametrization is performed as follows: Given b_0, the output voltage of a *FSR* at null force, and V_{nom}, the maximum output voltage at the nominal sensor range; then, the following linear transformation can be applied

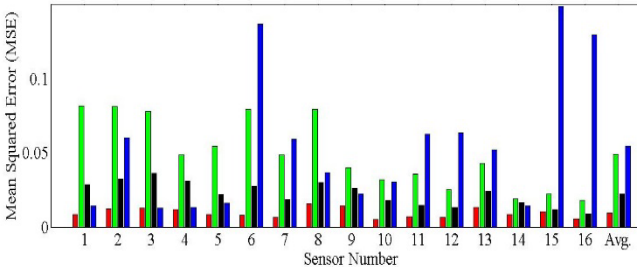


Figure 9. Error bar plot depicting the force *MSE* for the sixteen A201-1 sensors operating on the following estimation methods: (red) *CMA* using a sensor-tuned Preisach density function and η_0, linear regressions using increasing data points only (green) and the entire dataset (black), *CMA* using the Preisach-scaled parameters, $\mu^s_{(\alpha,\beta)}$ and η^s_0 (blue).
Source: The authors.

to any V_o reading during both: the estimation of $\mu_{(\alpha,\beta)}$ and η_0, and later, during sensor operation.

$$V_o{}^s = (V_o - b_0)/(V_{nom} - b_0) \tag{6}$$

The scaled output voltage (V_o^s) is normalized, just as the resulting Preisach-scaled parameters are, $\mu^s_{(\alpha,\beta)}$ and η^s_0; this implies that they can be used to estimate F with hysteresis compensation for any sensor, requiring only the experimental measuring of b_0 and V_{nom} on each new device.

However, it must be pointed out that during sensor operation, the *CMA* running on the basis of $\mu^s_{(\alpha,\beta)}$ and η^s_0 can compensate for a specific amount of *HE*, see Fig 4, this implies that if a given sensor exhibits a larger *HE* than that modeled by $\mu^s_{(\alpha,\beta)}$ and η^s_0, the resulting F will still exhibit some hysteresis (underfitting case). Conversely, if a given sensor has a lower *HE*, the resulting F will reflect hysteresis overfitting; both cases are presented on Fig. 10. Hysteresis overfitting is characterized by a time-ahead output during sensor unloading (green data on Fig. 10), especially noticeable around the maximum $V_o{}^u$–$V_o{}^l$ which occurs at half of the nominal sensor range, see Fig. 4. Conversely, if hysteresis is under-fitted, the *CMA* produces a lagged sensor output during the unloading stage (red line on Fig. 10).

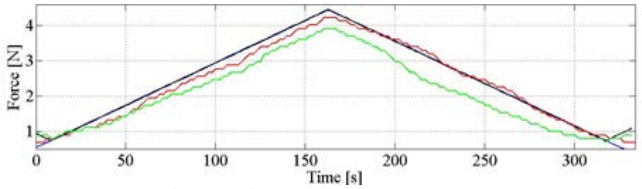


Figure 10. Triangle force profile (blue) and sensors output response showing hysteresis underfitting (red) and overfitting (green).
Source: The authors.

The Preisach-scaled parameters were obtained by applying the linear transformation (6) to the data gathered for the sixteen sensors. The resulting $\mu^s_{(\alpha,\beta)}$ and η^s_0 were later used to estimate *F* using the *CMA*. The blue error bars of Fig. 9 shows the resulting *MSE* when using the Preisach-scaled parameters during force estimation. Note that the *MSE* is higher than that reported on Section IV (individual Preisach parameters tuned for each sensor); this is a logical consequence of hysteresis-overfitting and underfitting. Likewise, mixed results were obtained when comparing to the linear regression methods, indicating that additional work is required on this subject.

6. Conclusion and future work

The Preisach Operator and the Closest Match Algorithm (*CMA*) have been successfully implemented on sixteen A201-1 sensors to both: model hysteresis and compensate for hysteresis effects during sensor operation. In the latter case, a considerably reduction of 54% was obtained in the force *MSE* compared with the manufacturer-recommended method based on linear regression. This is an important contribution that narrows the gap between the highly accurate load cells and the low-profile low-cost FSRs. Further *MSE* reduction is possible by implementing a continuous *CMA*, this is left as a pending task for future work. It must be remarked that hysteresis modeling and compensation required no-additional hardware during sensor operation, which is a highly desirable characteristic in applications with power or space constraints.

Considering that hysteresis modeling is not a straightforward procedure, a generalized model for hysteresis compensation has been proposed for the A201-1 sensor. However, mixed results were obtained because of hysteresis overfitting and underfitting. Future work is required on the subject in order to develop several Preisach density function focused on compensating for a specific amount of Hysteresis Error. This task can be carried out for sensors exhibiting a linear output, such as the Tekscan A201-X, and for sensors with a nonlinear response, e.g. Interlink FSR40X and Peratech QTC sensors.

Acknowledgment

This study was supported by Colciencias through Francisco José de Caldas Fund (FP44842-335-2015) and by grant PI/UAN-2017-603GIBIO

References

[1] Overduin, S., Zaheer, F., Bizzi, E. and D'avella, A., An instrumented glove for small primates, Journal of Neuroscience Methods, 187(1), pp. 100-104, 2010. DOI: 10.1016/j.jneumeth.2009.12.007

[2] Fong, D. and Chan, Y.-Y., The use of wearable inertial motion sensors in human lower limb biomechanics studies: A systematic review, Sensors, 10(12), pp. 11556-11565, 2010. DOI: 10.3390/s101211556

[3] Fosty, B., Ben-Sadoun, G., Sacco, G., Konig, A., Manera, V., Foulon, P., Brisswalter, J., Robert, P.H. and Bremond., F., Accuracy and reliability of the rgb-d camera for measuring walking speed on a treadmill, Gait and Posture, 48, pp. 113-119, 2016. DOI: 10.1016/j.gaitpost.2016.04.011

[4] Faraz, M., Salcic, Z. and Wang, K., Analysis and selection of the force sensitive resistors for gait characterization, in Int. Conf. on Automation, Robotics and Applications, Feb 2015, pp. 370-375, Queenstown, New Zealand.

[5] Schofield, J., Evans, K., Hebert, J., Marasco, P. and Carey, J., The effect of biomechanical variables on force sensitive resistor error: Implications for calibration and improved accuracy, Journal of Biomechanics, 49(5), pp. 786-792, 2016. DOI: 10.1016/j.jbiomech.2016.01.022

[6] Tiwana, M., Redmond, S. and Lovell, N., A review of tactile sensing technologies with applications in biomedical engineering, Sensors and Actuators A: Physical, 179, pp. 17-31, 2012. DOI: 10.1016/j.sna.2012.02.051

[7] Interlink Electronics, FSR400 Series Datasheet, [online]. Available at: http://www.interlinkelectronics.com/datasheets/Datasheet_FSR.pdf.

[8] Tekscan Inc, FlexiForce, Standard Force & Load Sensors Model A201. Datasheet, [online]. Available at: https://www.tekscan.com /sites/default/files/resources/FLX-A201-A.pdf.

[9] Lebosse, C., Renaud, P., Bayle, B. and Mathelin, M., Modeling and evaluation of low-cost force sensors, IEEE Transactions on Robotics, 27(4), pp. 815-822, 2011. DOI: 10.1109/TRO.2011.2119850

[10] Hollinger, A. and Wanderley, M., Evaluation of commercial force-sensing resistors, in Int. Conf. on new interfaces for musical expression NIME06, 2006, Paris, France.

[11] Komi, E., Roberts, J., and Rothberg, S., Evaluation of thin, flexible sensors for time-resolved grip force measurement, Proc. Institution of Mechanical Engineers, Part C: Journal of Mechanical Engineering Science, 221(12), pp. 1687-1699, 2007. DOI: 10.1243/09544062JMES700

[12] Dabling, J., Filatov, A. and Wheeler, J., Static and cyclic performance evaluation of sensors for human interface pressure measurement, in Annual Int. Conf. of the IEEE Engineering in Medicine and Biology Society, Aug 2012, pp. 162-165, San Diego, CA.

[13] Vecchi, F., Freschi, C., Micera, S., Sabatini, A.M, Dario, P. and Sacchetti, R., Experimental evaluation of two commercial force sensors for applications in biomechanics and motor control, in Annual Conf. of the Int. Functional Electrical Stimulation Society, 2000, pp. 45-54, Aalborg, Denmark.

[14] Urban, S., Ludersdorfer, M. and Van der Smagt, P., Sensor calibration and hysteresis compensation with heteroscedastic gaussian processes, IEEE Sensors Journal, 15(11), pp. 6498-6506, 2015. DOI: 10.1109/JSEN.2015.2455814

[15] Paredes-Madrid, L., Torruella, P., Solaeche, P., Galiana, I. and Gonzalez-de Santos, P., Accurate modeling of low-cost piezoresistive force sensors for haptic interfaces, in Proc. IEEE Int. Conf. Robotics and Automation, 2010, pp. 1828-1833, Anchorage, AK. DOI: 10.1109/ROBOT.2010.5509436

[16] Paredes-Madrid, L., Emmi, L., Garcia, E. and Gonzalez-de Santos, P., Detailed study of amplitude nonlinearity in piezoresistive force sensors, Sensors, 11(9), pp. 8836-8854, 2011. DOI: 10.3390/s110908836

[17] Visone, C., Hysteresis modelling and compensation for smart sensors and actuators, Journal of Physics: Conference Series, 138(1), p. 012028, 2008. DOI: 10.1088/1742-6596/138/1/012028

[18] Stolt, A., Linderoth, M., Robertsson, A. and Johansson, R., Force controlled robotic assembly without a force sensor, in Proc. IEEE. Int. Conf. Robotics and Automation, May 2012, pp. 1538-1543, St. Paul, MN.

[19] Melnyk, A., Henaff, P., Khomenko, V. and Borysenko, V., Sensor network architecture to measure characteristics of a handshake

between humans, in Proc. IEEE Int. Conf. Electronics and Nanotechnology, April 2014, pp. 264-268, Kiev, Ukraine. DOI: 10.1109/ELNANO.2014.6873983
[20] Stakvik, J., Ragazzon, M., Eielsen, A. and Gravdahl, J., On implementation of the Preisach model identification and inversion for hysteresis compensation, Modeling, Identification and Control, 36(3), pp. 133-142, 2015. DOI: 10.4173/mic.2015.3.1
[21] Tan, X., Venkataraman, R. and Krishnaprasad, P., Control of hysteresis: Theory and experimental results, in SPIE's 8th Annual International Symposium on Smart Structures and Materials, 2001, pp. 101-112, Newport Beach, CA.
[22] Tan, X. and Bennani, O., Fast inverse compensation of Preisach-type hysteresis operators using field-programmable gate arrays, in 2008 American Control Conference, June 2008, pp. 2365-2370, Seattle, WA. DOI: 10.1109/ACC.2008.4586845

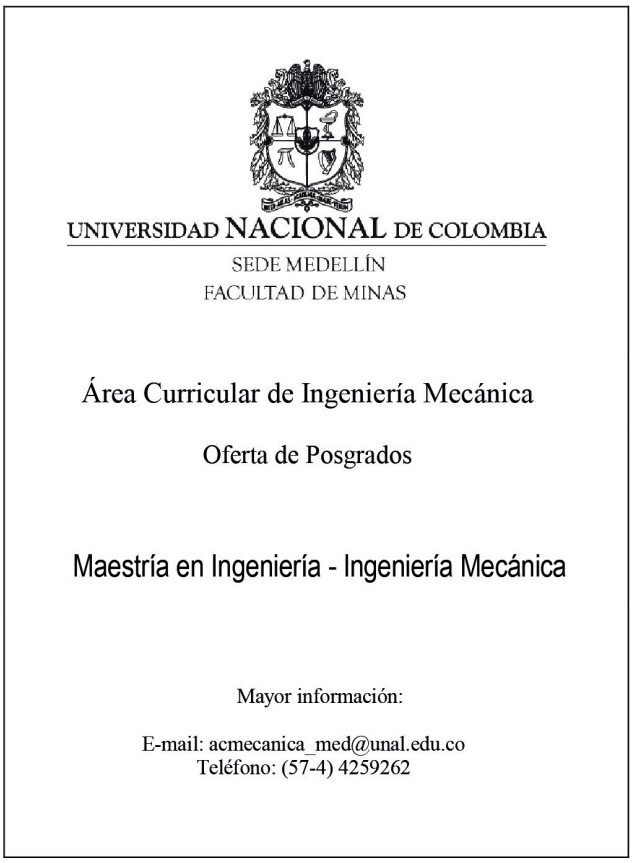
L. Paredes-Madrid, was born in Caracas, Venezuela in 1985. He received his BSc. degree in Electronic Engineering from Simon Bolivar University, Caracas, Venezuela, in 2007 and the PhD. degree in system engineering and automation from Complutense University of Madrid, Spain, in 2014. He has been a research assistant in the Centre for Automation and Robotics CSIC, Madrid, Spain and in Northwestern University, Evanston, IL. He is currently a full-time professor at Antonio Nariño University in Tunja, Colombia, since 2014. His research interests are the instrumentation and control of autonomous systems.
ORCID: 0000-0001-8609-0681

A. Matute, was born in Valencia, Venezuela in 1984. He received his BSc. and MSc. degree in 2008 and 2014 respectively, both in Electronic Engineering from Simon Bolivar University in Caracas, Venezuela. He has conducted research in the implementation of soft computing techniques for modelling of nonlinear systems and recently piezoresistive sensors. In addition, he worked at industry for eight years in managerial positions. Currently he continues research in piezoresistive sensors characterization at Antonio Nariño University in Tunja, Colombia.
ORCID: 0000-0002-6746-2168

A.F. Cruz-Pacheco, received his BSc. and MSc. degree in 2011 and 2015 respectively, both in Pedagogical and Technological University of Colombia –UPTC– in Tunja, Colombia. He has conducted research in Synthesis, characterization and evaluation of ceramics and materials in general. He is currently conducting research on characterization of piezoresistive materials in Pedagogical and technological University of Colombia.
ORCID: 0000-0003-3562-246X

C.A. Parra-Vargas, received his BSc. degree in physical and mathematics education from Pedagogical and Technological University of Colombia - UPTC, Tunja, Colombia, in 1990, In addition he is MSc. and Dr. in Physical Sciences from Universidad Nacional de Colombia, Bogotá, in 2005. He has conducted studies in research on characterization of materials in Pedagogical and Technological University of Colombia. He is currently a full-time professor at Pedagogical and technological University of Colombia in Tunja, Colombia.
ORCID: 0000-0001-8968-8654

E.I. Gutiérrez-Velásquez, received his BSc. degree in mechanical engineering and MSc. degree in engineering in 2001 and 2008 respectively, both from University of Antioquia in Medellín, Colombia and the PhD. degree in Mechanical Engineering from Federal University of Itajubá, Brazil, in 2013. He has conducted research in optimization and modelling of thermal systems. He is currently a full-time professor at Antonio Nariño University in Medellín, Colombia since 2014.
ORCID: 0000-0002-4326-946X



UNIVERSIDAD NACIONAL DE COLOMBIA
SEDE MEDELLÍN
FACULTAD DE MINAS



DYNA
http://dyna.medellin.unal.edu.co/

Comparison of three IRP-based models to reduce logistics costs and greenhouse gas emissions

Julian Andres Zapata-Cortes [a], Martín Darío Arango-Serna [b] & Conrado Augusto Serna-Urán [c]

[a] Escuela de Posgrados, Institución Universitaria CEIPA, Sabaneta, Colombia. julian.zapata@ceipa.edu.co
[b] Facultad de Minas, Universidad Nacional de Colombia, Medellín, Colombia. mdarango@unal.edu.co
[c] Facultad de Ingeniería, Universidad de San Buenaventura, Medellín, Colombia. Conrado.serna@usbmed.edu.co

Received: October 13th, 2017. Received in revised form: March 11th, 2018. Accepted: May 11th, 2018.

Abstract
Goods distribution processes must reconcile the economic interests of the companies, which seek higher levels of profitability through costs reduction and service level improvements, with the negative impacts to society and environment, such as chemical pollution and the generation of vehicular congestion and accidents. This paper presents the comparison of three models that analyze the logistics costs associated with the distribution of goods and the greenhouse gas emissions generated by such processes. These models use the Vehicle Routing Problem (IRP) as the basis for optimizing the logistics activities, from which, through multi-objective approaches the CO_2 emissions are analyzed. As the main result of the article, it can be observed that the multiobjective models allow finding an adequate combination between logistics costs and emissions, which is attractive to companies and society.

Keywords: goods distribution; multiobjective model; collaborative inventory; greenhouse gases.

Comparación de tres modelos basados en el IRP para reducir costos logísticos y emisiones de gases efecto invernadero

Resumen
Los procesos de distribución de mercancías deben conciliar los intereses económicos de las empresas, que buscan mayores niveles de rentabilidad a través de disminución de los costos y mejoras del nivel de servicio, con los impactos negativos que se producen a la sociedad y al medio ambiente, como es el caso de la contaminación química y problemas de calidad de vida, como la generación de congestión vehicular y accidentes. En este artículo se presenta la comparación de tres modelos que analizan los costos logísticos asociados a la distribución de mercancías y las emisiones de gases efecto invernado que generan dichos procesos. Estos modelos utilizan el Problema de Ruteo de Vehículos (IRP) como base para optimizar las actividades logísticas, a partir del cual, mediante enfoques multiobjetivo, es posible analizar también las emisiones de gases contaminantes como el CO_2. Como principal resultado de la investigación que deriva este artículo, se observa que los modelos multiobjetivo permiten encontrar una combinación adecuada entre los costos logísticos y las emisiones de CO_2, que sea atractivo para empresas y la sociedad.

Palabras clave: distribución de mercancías; modelo multiobjetivo; inventario colaborativo; gases de efecto invernadero.

1. Introduction

Transport processes in cities, regions and countries have increased due to new marketing processes generated by globalization and changes in consumers habits. These highly dynamic transportation processes generate high costs in organizations, which have been studied for many years and have usually sought for their optimization through models such as the Travelling Salesman Problem (TSP) or the vehicle routing problem (VRP). However, these transport processes not only generate economic impacts for companies, but also for society and cities, as it generates congestion and physical and chemical pollution. For that reason, practitioners in charge of these professional areas

How to cite: Zapata-Cortes, J.A., Arango-Serna, M.D. and Serna-Urán, A., Comparison of three IRP-based models to reduce logistics costs and greenhouse gas emissions. DYNA, 85(205), pp. 199-204, June, 2018.

© The author; licensee Universidad Nacional de Colombia.

within companies and also academics must to continue with search processes looking for models that will improve both the economic and social/environmental conditions for companies and society.

Many authors have argued that collaboration among supply chain is one of the main strategies to reduce the cost of goods distribution, highlighting the Vendor Managed Inventory model -VMI as one of the more important ways companies can collaborate. Through VMI the inventory quantity can be optimized for multiple companies and from there to configure more efficient distribution systems, which effectively reduces the costs and the intensity of transport activities, as a result of a better allocation of inventory. This is the concept behind the Inventory Routing Problem -IRP optimization model, which, based on the collaborative inventory, allows transportation and inventory costs to be reduced simultaneously.

This paper analyzes the effect of the IRP model on the inventory and transportation costs of goods distribution, but also considering the effect of CO_2 emissions, seeking to reduce the greenhouse gas emissions produced by the logistics activities. The impact on these variables was studied using three optimization processes: the IRP Model, a multiobjective model of IRP vs. CO_2 emissions and finally a multiobjective model that contemplates the IRP background, but optimizing separately the inventory and transportation costs and also including CO_2 emissions as a third objective function.

2. Inventory collaboration and optimization processes

Collaboration in logistics and supply chain is understood as the joint effort of several organizations seeking to obtain superior benefits to those that can be found separately. For this the companies cooperate in processes such as transportation, inventory management, storage, facility design, information exchange and other logistics activities [1-3]. Since many years supply chain collaboration has been developed through approaches such as Quick Response (QR), Efficient Customer Response (ECR), Continuous product Replenishment (CPR), Vendor Managed Inventory (VMI), Planning, Collaborative Forecasting and Replenishment (CPRF) and Centralized Inventory Management, among others [3-5].

According to Díaz-Batista and Pérez-Armayor [6], inventory collaboration in supply chains produces a lower total annual cost than when companies work individually, generating performance improvements in the entire supply chain [7-9]. The main problem lies in the allocation of inventory and transportation, which has been studied by multiple authors [10-12], for what the most used techniques are the VMI [13] and the IRP [14]. Through the IRP it is possible to simultaneously assign the inventory quantity and the routes to supply a set of customers that collaborate with one or several suppliers [14-17].

In the IRP model, the inventory is assigned to the customers in the planning periods and from there the routes are assigned to its supply [18-20]. For this, it is required that the supplier, who makes the supply decisions, know the information about customer demands, inventory levels and other parameters for the stock management and also the transportation process information, from which generates the routes are generated [21]. Campbell and Savelsbergh [22] studied the IRP model for long-term decision-making approaches, using a decomposition scheme of two-step decisions: in the first one the inventory is assigned and in the second the routes are generated. Other authors have performed schemes for the simultaneously allocation of inventory and routes generation [1,15,21].

The joint assignment of inventory and transportation can be performed using multiobjective optimization approaches, as it is made in the works of Pechlivanos [23], Chen and Lee [24], Liang [25], Liao et al. [26], Afshari et al., [27], Shankar et al. [28], Nekooghadirli et al [29], Andriolo et al., [30], Pasandideh et al., [31] and Pasandideh et al ., [32].

Both for the IRP or multiobjective solutions there are require heuristic and metaheuristic techniques. The most used heuristic and metaheuristic for solving these optimization problems are Simulated annealing, Genetic algorithms, Evolution algorithms, Evolutionary programming, Artificial immune system algorithm, Particle swarm optimization and tabu search [33,34].

Particularly, to solve multiobjective optimization models, the main methods are: MOGA (Multi- Objective Genetic Algorithm), NSGA y NSGA-II (Nondominated Sorting Genetic Algorithm), SPEA y SPEA2 (Strength Pareto Evolutionary Algorithm), PAES (Pareto Archived Evolution Strategy) y PESA (Pareto Envelope-based Selection Algorithm), MO-VNS (Multiobjective Variable Neighborhood Search), DEPT (Differential Evolution with Pareto Tournaments), MO-TLBO (Multiobjective Teaching-Learning-Based Optimization), MOABC (Multiobjective Artificial Bee Colony), among others [33,34-37].

3 Methodology

In order to analyze the impact of the distribution processes on greenhouse gas emissions, different distribution processes were designed from three mathematical optimization processes:

- IRP Model.
- Multiobjective analysis using as objective functions the IRP and the CO_2 emissions.
- Multiobjective model using the IRP background, but optimizing as separate objective function the inventory and transportation costs and also including CO_2 emissions as a third objective function.

For the three optimization processes, the same parameters were used and two genetic algorithms were used for its development. The first is a genetic algorithm specially configured for the solution of the IRP model, which evaluates the jointly allocation of inventory and transport routes, as is presented in Arango et al. [21]. For the multiobjective analysis an algorithm based on the NSGA2 is used, similar to what is presented in [14,37,38].

The emission factor of a typical vehicle used for the urban goods distribution was used to analyze the effect of the CO_2 emission. The vehicle corresponds to a VAN with an average city emission of e = 190 g of CO_2 / km [39]. This parameter is multiplied by the number of kilometers traveled, in order

to calculate the amount of CO_2 gases emitted.

The objective function for the IRP model is presented in equation 1, subject to a set of constraints as formulated in [14,15,21,38].

$$minimizing \quad \sum_{i\in v'}\sum_{t\in\tau} h_i I_i^t + \sum_{t\in\tau} h_0 I_0^t + \sum_{t\in\tau}\sum_{i\in v}\sum_{i\in v}\sum_{k\in K} c_{ij}x_{ij}^{kt} \tag{1}$$

The first term is the sum of the inventory costs, which is obtained by multiplying the holding cost h_i by the amount of product I_i^t hold in every time *t* for every customer *i*. The second term is the inventory costs at the supplier facility represented with the sub index *0*. Transport costs are calculated by multiplying the transport costs c_{ij} of traveling from node *i* to *j* by the binary variable x_{ij}^{kt} which is equal to 1 if the vehicle k travel from I to j in the period t and zero otherwise. The set v includes all the nodes of the problem and v' only includes the customers' nodes.

In the case of the multiobjective models, the formulation of the first model, in which the IRP costs and the CO_2 are evaluated is presented in equation 2. In equation 5, the formulation for the multiobjective model separating transport costs, inventory and the CO_2 emission is presented.

$$minimizing\ F(f_1, f_2) \tag{2}$$

$$f_1 = \sum_{i\in v'}\sum_{t\in\tau} h_i I_i^t + \sum_{t\in\tau} h_0 I_0^t + \sum_{t\in\tau}\sum_{i\in v}\sum_{i\in v}\sum_{k\in K} c_{ij}x_{ij}^{kt} \tag{3}$$

$$f2 = \sum_{t\in\tau}\sum_{i\in v}\sum_{i\in v}\sum_{k\in K} e\cdot c_{ij}x_{ij}^{kt} \tag{4}$$

The Multiobjective model formulation separating transport costs, inventory and CO_2 emission is:

$$minimizing\ G(g_1, g_2, g_3) \tag{5}$$

$$g_1 = \sum_{t\in\tau}\sum_{i\in v}\sum_{i\in v}\sum_{k\in K} c_{ij}x_{ij}^{kt} \tag{6}$$

$$g_2 = \sum_{i\in v'}\sum_{t\in\tau} h_i I_i^t + \sum_{t\in\tau} h_0 I_0^t \tag{7}$$

$$g3 = \sum_{t\in\tau}\sum_{i\in v}\sum_{i\in v}\sum_{k\in K} e\cdot c_{ij}x_{ij}^{kt} \tag{8}$$

Those objective functions are restricted to the following equations that assure the correct distribution process and correspond to the IRP Model constraints, according to Arango et al. [15] and Archetti et al., [16].

$$minimizing\ G(g_1, g_2, g_3) \tag{9}$$

$$I_0^t = I_0^{t-1} + r_0^{t-1} - \sum_{k\in K}\sum_{i\in v} q_i^{kt-1} \tag{10}$$

$$I_0^t \geq \sum_{k\in K}\sum_{i\in v} q_i^{kt}\, Y_i^{kt} \tag{11}$$

$$I_i^t = I_i^{t-1} + \sum_{k\in K}\sum_{i\in v} q_i^{kt} - d_i^t \tag{12}$$

$$I_i^t \geq 0 \tag{13}$$

$$I_i^t \leq C_i \tag{14}$$

$$q_i^{kt} \leq C_i - I_i^t \tag{15}$$

$$q_i^{kt} \leq C_i Y_i^{kt} \tag{16}$$

$$\sum_{i\in v} q_i^{kt} \leq Q_k \tag{17}$$

$$\sum_{i\in v} q_i^{kt} \leq Q_k Y_0^{kt} \tag{18}$$

$$\sum_{i\in v, i<j} X_{ij}^{kt} + \sum_{i\in v, j<i} X_{ji}^{kt} = 2y_i^{kt} \tag{19}$$

$$\sum_{i\in S}\sum_{j\in S} X_{ij}^{kt} \leq \sum_{i\in S} y_i^{kt} - y_m^{kt} \quad \forall\, subset \;\; S\subseteq V \tag{20}$$

$$q_i^{kt} \geq 0; Q_k \geq 0; I_i^t \geq 0; d_i^t \geq 0; C_i \geq 0; \tag{21}$$

For an explanation of the restrictions, readers may refer to [15-16] and [18].

The input parameters are obtained from the instance of 15 customers and one supplier proposed by Archetti [16], increasing the amount of inventory that can be stored in each of the customers, as a strategy to produce better distribution costs and decrease the CO_2 Emission. These parameters are presented in Table 1.

4. Results

The IRP model, in which transport and inventory costs are added, generates a distribution process in which is not necessary to supply all the customers in all the periods. This produces a decrease in transport costs generated by an increase in inventory costs. The distribution plan that is generated from the best individual of the genetic algorithm used to solve the model is presented in figure 1. In the gray part is shown the inventory quantity that must be delivery to each of the customers, while in the unlabeled part the distribution sequence is presented.

This way, for period 1 only customers 1, 14, 10, 12, 13, 15, 6 and 9 should be served in that sequence. The quantities to be delivery are 128, 260, 108, 184, 220, 219, 30 and 88, respectively.

This distribution process generates a total cost of $ 2839.7, of which $ 468.2 correspond to inventory costs and produces a CO_2 amount of 454.39 g.

Table 1.
Input parameters

Customer	1	2	3	4	5	6	7	8	9	10	11	12	13	14	15
Demand each Period	32	36	91	52	76	10	85	79	22	36	68	46	55	65	73
Inventory Cost ($)/100	2	3	3	2	2	3	4	4	2	4	2	2	2	3	2
Initial Inventory	32	72	182	52	152	20	85	79	22	72	136	46	55	65	146
X position	237	180	141	163	282	455	326	235	412	113	266	257	363	158	423
Y position	182	332	388	188	374	296	332	432	488	46	302	23	22	81	95

Source: The authors.

In the multiobjective model in which both the IRP costs and the CO_2 emission are simultaneously optimized. A single optimal individual is produced, which is presented in figure 2. This result generates a cost of $ 2851.5, of which $ 463.9 are inventory cost and a CO_2 emission of 453.6 g that is virtually identical to the solution generated by the IRP model. However, this solutions corresponds to a distribution system that assigns inventory and routes to customers in a different way than the IRP model does. For this reason, a slight decrease in CO_2 emissions is generated, as a consequence of an increase in the distribution costs.

The multiobjective model, in which the transport, inventory and CO_2 emission costs are analyzed separately, generates a set of individuals similar to those presented in figures 1 and 2. The set of individuals are produced by the non-dominance of the solutions, so it is not possible to argue that one solution is better than another and for that reason the decision maker, depending on his preference, can take any of the individuals solutions produced by the model. Table 2 presents the results for the 3 optimized objective functions, and includes a column adding the inventory and transport cost.

Inventory															
Customer	1	2	3	4	5	6	7	8	9	10	11	12	13	14	15
Period 1	128	0	0	0	0	30	0	0	88	108	0	184	220	260	219
Period 2	0	36	91	208	228	0	340	316	0	0	0	0	0	0	0
Period 3	0	72	182	0	0	0	0	0	0	0	204	0	0	0	0
Period 4	0	0	0	0	0	0	0	0	0	0	0	0	0	0	0
Period 5	0	0	0	0	0	0	0	0	0	0	0	0	0	0	0

Routes sequence															
Routes starts on Depot (0) and ends on it.															
Period 1	0	1	14	10	12	13	15	6	9	0	0	0	0	0	0
Period 2	0	5	8	3	2	4	7	0	0	0	0	0	0	0	0
Period 3	0	3	2	11	0	0	0	0	0	0	0	0	0	0	0
Period 4	0	0	0	0	0	0	0	0	0	0	0	0	0	0	0
Period 5	0	0	0	0	0	0	0	0	0	0	0	0	0	0	0

Figure 1. IRP Result -individual solution.
Source: The authors.

Inventory															
Customer	1	2	3	4	5	6	7	8	9	10	11	12	13	14	15
Period 1	160	0	0	219	0	0	0	0	0	110	0	223	225	271	0
Period 2	0	0	0	0	0	30	353	338	106	0	0	0	0	0	242
Period 3	0	139	276	0	288	0	0	0	0	0	245	0	0	0	0
Period 4	0	0	0	0	0	0	0	0	0	0	0	0	0	0	0
Period 5	0	0	0	0	0	0	0	0	0	0	0	0	0	0	0

Routes sequence															
Routes starts on Depot (0) and ends on it.															
Period 1	0	1	4	14	10	12	13	0	0	0	0	0	0	0	0
Period 2	0	8	9	6	15	7	0	0	0	0	0	0	0	0	0
Period 3	0	11	5	3	2	0	0	0	0	0	0	0	0	0	0
Period 4	0	0	0	0	0	0	0	0	0	0	0	0	0	0	0
Period 5	0	0	0	0	0	0	0	0	0	0	0	0	0	0	0

Figure 2. Multiobjective Model Solution (IRP vs. CO_2 emission).
Source: The authors.

Table 2.
Results of the three objective functions multi-objective model.

Individual Solutions	Transport cost	CO_2 Emissions	Inventory cost	Total cost
1	3288.4	624.8	445.0	3733.3
2	4982.8	946.7	404.3	5387.1
3	5111.9	971.3	403.7	5515.6
4	3502.8	665.5	413.1	3915.9
5	5427.4	1031.2	403.7	5831.0
6	3902.6	741.5	406.9	4309.5
7	3642.3	692.0	407.5	4049.9
8	4156.1	789.7	404.9	4561.0
9	3304.3	627.8	421.3	3725.5
10	5012.8	952.4	404.2	5417.0
11	4831.7	918.0	404.8	5236.4
12	5692.9	1081.7	403.4	6096.3
13	3580.2	680.2	411.3	3991.5

Source: The authors.

Table 2 shows that the values of total cost and CO_2 emissions for each individual are higher than those reported in the solutions for the single IRP model and for the multiobjective IRP vs. CO_2 emissions. However, inventory values in each solution are lower, with a behavior that the lower the inventory level the higher the transport cost and the CO_2 emission, as a consequence of an increase in the transportation intensity in order to minimize inventory.

The behavior of the three-functions multiobjective model differs in its results to the previous models, since in the first the transport and inventory costs are added up, so in the optimization process the costs are compensated, while in the three-functions multiobjective model the algorithm must also look for which is the best solution that generates the minimum inventory costs without an excessively increase in transport costs. In order to compare these solutions, the problem was solved supplying all customers in each of the periods, what minimizes the inventory costs. For that, the Vehicle Routing Problem - VRP was used and solved with a genetic algorithm, for that the transport cost is $ 1722.5 for each period, which corresponds a total cost of $ 8612.5 for the 5 periods. This single VRP cost is higher than the transport cost for all individuals produced by the three-functions multiobjective model and becomes a non-optimal solution for the distribution process

Table 3 presents the results of the three models. The individual solution one is selected for the three-function multiobjective model (presented in figure 3), which is the individual that generates the lowest CO_2 emissions for that model.

Table 3.
Comparison of the three models.

Model	Total Cost	Inventory Cost	CO_2 Emissions
IRP.	2839.7	468.2	454.4
MO-IRP vs. CO_2.	2851.5	463.9	453.6
MO-Three functions	3733.3	445.0	624.8

Source: The authors.

Inventory																
Customer	1	2	3	4	5	6	7	8	9	10	11	12	13	14	15	
Period 1	0	167	0	0	0	45	0	0	109	0	0	215	275	0	427	
Period 2	158	0	0	253	0	0	183	316	0	128	317	0	0	386	0	
Period 3	0	0	288	0	329	0	271	0	0	0	0	0	0	0	0	
Period 4	0	0	0	0	0	0	0	0	0	0	0	0	0	0	0	
Period 5	0	0	0	0	0	0	0	0	0	0	0	0	0	0	0	

Routes sequence																		
Routes starts on Depot (0) and ends on it.																		
Period 1	0	6	9	15	12	13	2	0	0	0	0	0	0	0	0	0	0	
Period 2	0	4	14	10	1	11	7	8	0	0	0	0	0	0	0	0	0	
Period 3	0	5	3	7	0	0	0	0	0	0	0	0	0	0	0	0	0	
Period 4	0	0	0	0	0	0	0	0	0	0	0	0	0	0	0	0	0	
Period 5	0	0	0	0	0	0	0	0	0	0	0	0	0	0	0	0	0	

Figure 3. Individual 1 of the three-function multiobjective model.
Source: The authors.

From the results presented in Table 3, it is possible to observe that the total cost, inventory and CO_2 emissions for the IRP and multiobjective IRP vs. CO_2 are very similar, but differ with the solution that produced the fewer emissions in the three-function multiobjective model. This is caused by the reduction of the inventory costs, due to the three-function multiobjective algorithm generates solutions that somehow represent the best conditions for each of the objective functions, this way producing solutions with smaller inventory quantities but generating higher transport costs and CO_2 emissions.

From this result, it is possible to infer that companies must make efforts in collaborative processes that allow to simultaneously reduce inventory, transportation and CO_2 emissions, since a local optimum, as is the case of individual 1 of the three-functions multiobjective model, which generates the smallest inventory with a cost of 403.7, what is equivalent to a 13% reduction compared to the inventory for the IRP vs. CO_2 emissions model, is also generating a 138% increase in CO_2 emissions and a 114% higher distribution costs, which is not beneficial for both, companies or the environment.

5. Conclusions

Through inventory collaboration it is possible to reduce goods distribution cost for companies, but also to minimize the CO_2 emission for these logistics activity, which contributes to the reduction of pollution problems in cities. Based on the results found in this paper, the search for the reduction of inventory costs in companies generates large increases in logistical costs as well as greenhouse gas emissions, which is not beneficial for Company nor the environment.

In this paper, the collaborative process through inventory and its effect on the pollutant gases emission are analyzed from different models, finding that it is better to use the IRP, which combines inventory and transport costs, than the three-function multiobjective model. This is because the multiobjective model, which seeks to simultaneously minimize transport, inventory and CO_2 emissions, within its optimization process, must look for solutions that generate adequate relations between these three variables. This leads to the production of distribution plans that increase CO_2 emissions and total costs, as a consequence of finding lower inventory cost, what is a local optimum that is not good for integral logistics.

As future research lines, it is recommended to use more objectives that are important for companies and customers, as it can be the service level. Other routing conditions are also important to be included in the presented models, as several suppliers, backhauls, dynamic conditions and multiple distribution levels. Finally it is interesting to include other logistics activities in the optimization process, as it can be warehousing and purchasing processes. These research lines allow to model more realistic situations and improve decision making in logistics activities.

References

[1] Chan, F.T.S. and Prakash, A., Inventory management in a lateral collaborative manufacturing supply chain: a simulation study. International Journal of production Research, 50(16), pp. 4670-4685, 2012.

[2] Simatupang, T. and Sridharan, R., An integrative framework for supply chain collaboration. International Journal of Logistics Management, 16, pp. 257-274, 2005.

[3] Arango-Serna, M.D., Adarme-Jaimes, W. y Zapata-Cortes, J.A., Inventarios colaborativos en la optimización de la cadena de suministros. DYNA, 80(181), pp. 71-80, 2013.

[4] Holweg, M., Disney, S., Holmström, J. and Smaros, J., Supply chain collaboration: making sense of the strategy continuum. European Management Journal, 23(2), pp. 170-181, 2005.

[5] Derroiche, R., Neubert, G. and Bouras, A., Supply chain management: a framework to characterize the collaborative strategies. International Journal of Computer Integrated Manufacturing, 21(4), pp. 426-439, 2008.

[6] Díaz-Batista, J. and Pérez-Armayor, D., Optimización de los niveles de inventario en una cadena de suministro. Ingeniería Industrial, 33(2), pp. 126-132, 2012.

[7] Won-Cho, D., Hae-Lee, Y., Youn-Lee, T. and Gen, M., An adaptive genetic algorithm for the time dependent inventory routing problem. Journal of Intelligent Manufacturing, 25(5), pp 1025-1042, 2014.

[8] Bertazzi, L. and Esperanza, M.G., Inventory routing problems with multiple customers. EURO J Transp Logist 2. pp 255-275, 2013.

[9] Moin, N.H., Salhi, S. and Aziz, N.A.B., An efficient hybrid genetic algorithm for the multi-product multi-period inventory routing problem. Int. J. Production Economics, 133 pp. 334-343, 2011.

[10] Rushton, P. Croucher, P. and Baker, P., The handbook of logistics and distribution management, 3rd edition. London, Ed. Kogan Page Limited, 2010.

[11] Estrada, M.A., Análisis de estrategias eficientes en la logística de distribución de paquetería. PhD. Thesis, Programa de Doctorado de Ingeniería Civil, E.T.S. de Ingenieros de Caminos, Canales y Puertos de Barcelona, Universitat Politècnica de Catalunya, España, 2007.

[12] Arango, M.D., Zapata, J.A. y Adarme, W., Aplicación del modelo de inventario manejado por el vendedor en una empresa del sector alimentario colombiano, Revista EIA, 15, pp. 21-32, 2011.

[13] Gonzalez-Feliu, J., Peris-Pla, C. and Rakotonarivo, D., Simulation and optimization methods for logistics pooling in the outbound supply chain. Third International Conference on Value Chain Sustainability, Towards a Sustainable Development and Corporate Social Responsibility Strategies in the 21st Century Global Market, Nov 2010, Spain, pp. 394-401, 2010.

[14] Arango, M.D. and Zapata, J.A., Multiobjective model for the simultaneous optimization of transportation costs, inventory costs and service level in goods distribution, IEEE Latin America Transactions,. 15(1), Jan. 2017 pp. 129-136, 2017.

[15] Arango, M.D., Zapata, J.A. and Gutierrez, D., Modeling the inventory routing problem (IRP) with multiple depots with genetic algorithms, IEEE Latin American Transactions., 13(12), pp.3959-3965, 2015.
[16] Archetti, C., Bertazzi, L., Laporte, G. and Speranza, M.G., A branch-and- cut algorithm for a vendor-managed inventory-routing problem, Transportation Science, 41(3), pp. 382-391, 2007.
[17] Coelho, L.C., Cordeau, J-F. and Laporte, G., Thirty years of inventory-routing, Transportation Science, 48, pp. 1-19, 2013.
[18] Coelho, L.C. and Laporte, G., The exact solution of several classes of inventory-routing problems, Computers & Operations Research, 40(2013), pp. 558-565, 2013.
[19] Archetti, C., Bianchessi, N., Irnich, S. and Speranza, M.G., Formulations for an inventory routing problem, Intl. Trans. in Op. Res. 21, pp. 353-374, 2014.
[20] Zeng, Z. and Zhao, J., Study of stochastic demand inventory routing problem with soft time windows based on MDP. In: Zeng, Z., Wang, J., (eds), Advances in neural network research and applications. Lecture Notes in Electrical Engineering, 67. Springer, Berlin, Heidelberg, pp. 193-200, 2010.
[21] Arango-Serna, M.D, Andrés-Romano, C. and Zapata-Cortés, J.A., Collaborative goods distribution using the IRP model, DYNA, 83(196), pp. 204-2012, 2016.
[22] Campbell, A. and Savelsbergh, M.A., Decomposition approach for the inventory-routing problem. Transportation Science 38(4), pp. 488-502, 2004.
[23] Seferlis, P. and Pechlivanos, L., Optimal inventory and pricing policies for supply chain networks. European Symposiumon Computer-Aided Process Engineering- 14, 2004.
[24] Chen, C.L. and Lee, W.C., Multi-objective optimization of multi-echelon supply chain networks with uncertain product demands and prices, Computers and Chemical Engineering 28, pp. 1131-1144, 2004.
[25] Liang, T.F., Fuzzy multi-objective production/distribution planning decisions with multi-product and multi-time period in a supply chain, Computers & Industrial Engineering, 55, pp. 676-694, 2008.
[26] Liao, H-S., Hsieh, C-H. and Lai, P-G., An evolutionary approach for multi-objective optimization of the integrated location-inventory distribution network problem in vendor-managed inventory, Expert Systems with Applications 38, pp. 6768-6776, 2011.
[27] Afshari, M., Sharafi, T., ElMekkawy, T. and Peng, Q., Optimizing multi- objective dynamic facility location decisions within green distribution network design. Procedia CIRP 17, pp. 675-679, 2014.
[28] Shankar, B.L., Basavarajappa, S., Kadadevaramath, R.S. and Chen, J.C.H., A bi-objective optimization of supply chain design and distribution operations using non-dominated sorting algorithm: A case study, Expert Systems with Applications, 40, pp. 5730-5739, 2013.
[29] Nekooghadirli, N., Tavakkoli-Moghaddam, R., Ghezavati, V.R. and Javanmard, S., Solving a new bi-objective location-routing-inventory problem in a distribution network by meta-heuristics, Computers & Industrial Engineering, 76, pp. 204-221, 2014.
[30] Andriolo, A., Battini, D., Persona, A. and Sgarbossa, F., Haulage sharing approach to achieve sustainability in material purchasing: new method and numerical applications, Int. J. Production Economics, 164, pp. 308-318, 2015.
[31] Pasandideh, S.H.R., Niaki, S.T.A. and Asadi, K., Optimizing a bi-objective multi-product multi-period three echelon supply chain network with warehouse reliability, Expert Systems with Applications, 42, pp. 2615-2623, 2015.
[32] Pasandideh, S.H.R., Niaki, S.T.A. and Asadi, K., Bi-objective optimization of a multi-product multi-period three-echelon supply chain problem under uncertain environments: NSGA-II and NRGA, Information Sciences, 292, pp. 57-74, 2015.
[33] Arango, M.D., Zapata, J.A. and Andres, C., Metaheuristics for goods distribution. Proceedings of 2015 International Conference on Industrial Engineering and Systems Management (IESM), IEEE Publications, pp. 99-107, 2015. DOI. 10.1109/IESM.2015.7380143, 2015.
[34] Villalobos, M.A., Análisis de heurísticas de optimización para problemas multiobjetivo. PhD. Thesis, Departamento de Matemáticas. Centro de investigación y de estudios avanzados del Instituto Politécnico Nacional, Mexico, 2005.
[35] López, J., Zapotecas, S. and Coello, C.A., An introduction to multiobjective optimization techniques. In: Ajith, A., Lakhmi, J. and Goldberg, R. (eds)., Evolutionary multiobjective optimization: theoretical advances and applications, London, Springer-Verlag, pp. 7-32, 2009.
[36] González-Álvarez, D., Optimización multiobjetivo y paralelismo para descubrir Motifs en secuencias de ADN, PhD. Thesis, Universidad de Extremadura, Extremadura, España, 2013.
[37] Zapata-Cortes, J.A., Optimización de la distribución de mercancías utilizando un modelo genético multiobjetivo de inventario colaborativo de m proveedores con n clientes, PhD. Thesis, Universidad Nacional de Colombia, Medellín, [en línea]. 2016. Disponible en: www.bdigital.unal.edu.co/53703/1/71366786. 2016.pdf, 2016
[38] Arango-Serna, M.D., Zapata-Cortes, J.A. and Serna-Uran, C.A., Collaborative multiobjective model for urban goods distribution optimization, in: García-Alcaraz, J., Alor-Hernández, G., Maldonado-Macías, A., Sánchez-Ramírez, C. (eds), New perspectives on applied industrial tools and techniques. Management and Industrial Engineering. Springer, Cham, 2018.
[39] Ford Motor Company. Ford Transit, [online]. [Date of reference: April of 2016]. 2016. Available at: http://es.ford.com/trucks/transitvanwagon/specifications/

J.A. Zapata-Cortes, is graduated as BSC in Chemical Eng. in 2006, MSc. in Administrative Engineering in 2011 and PhD in Engineering in 2017 at the Universidad Nacional de Colombia, Medellín Campus. Currently he is full time professor at the Institución Universitaria CEIPA, Medellín, Colombia. The topics of interest of professor Zapata-Cortes are: transport networks and inventory optimization, supply chain management, information and communication technologies applied to the supply chain, business process management, among others.
ORCID: 0000-0002-1270-3577

M.D. Arango-Serna, is graduated BSc. as Industrial Eng. in 1991 at the Universidad Autónoma Latinoamericana, Colombia. Graduated as Sp. in finance and project formulation and evaluation in 1993 at the University of Antioquia, Colombia. He is also Sp. in university teaching in 2007 at the Universidad Politécnica de Valencia, Spain, professor Arango has an MSc. in Systems Engineering in 1997 by the Universidad Nacional de Colombia, Medellín campus and a PhD. in Industrial Engineer in 2001 by the Polytechnic University of Valencia, Spain. He is a full-time profesor at Departamento de Ingeniería de la Organización, Facultad de Minas, Universidad Nacional de Colombia, Medellín Campus. The topics in which professor Arango-Serna work are: logistics processes in the supply chain, operations research, plant designs, industrial optimization techniques, among other.
ORCID: 0000-0001-8448-8231

C.A. Serna-Urán, is graduated BSc. as Industrial Eng. in 2002, MSc. in Administrative Engineering in 2009 and PhD in Engineering in 2017 at the Universidad Nacional de Colombia, Medellín Campus. Currently he is full time professor at the Universidad de San Buenaventura, Colombia. The topics of interest of professor Serna-Urán are: transport networks optimization, supply chain management, operations research, among others.
ORCID: 0000-0002-1620-8290

UNIVERSIDAD NACIONAL DE COLOMBIA
SEDE MEDELLÍN
FACULTAD DE MINAS



DYNA
http://dyna.medellin.unal.edu.co/

Highway designs: effects of heavy vehicles stability

Gonzalo Moreno [a], Rodrigo Vieira [b] & Daniel Martins [b]

[a] *Grupo de Investigación en Ingeniería Mecánica - GIMUP, Department of Mechanical Engineering, University of Pamplona, Pamplona. Colombia. gmoren@hotmail.com, gmoren@unipamplona.edu.co*
[b] *Laboratory of Robotic Raul Guenther – UFSC, Department of Mechanical Engineering, Federal University of Santa Catarina. Florianopolis, SC. Brazil.*

Received: January 5th, de 2018. Received in revised form: April 27th, 2018. Accepted: May 15th, 2018

Abstract
From the perspective of heavy vehicles stability, some criteria of stability should be adhered to highway designs. In particular, the relationship between minimum radius, superelevation, slope angle, side friction, and design speed should be re-evaluated. In this regard, the static rollover threshold (*SRT*) is one of the most important factors used to define the stability of vehicles. This factor is highly dependent on the maximum lateral acceleration (a_y) of a vehicle until it reaches the rollover threshold. This acceleration in turn is dependent on the vehicle speed and the radius of curvature. Taking into account the stability of vehicles, in this study the highways design is evaluated and compared with the classic design criterion. This study also suggests that in order to ensure driving safety, the State Highway Agencies should make a reevaluation of existing speed limits and the design of highway curves.

Keywords: highway design; static rollover threshold (*SRT*); heavy vehicle; road safety; rollover; slide out.

Diseño de autopistas: efectos de la estabilidad de vehículos pesados

Resumen
Desde la perspectiva de estabilidad de los vehículos pesados, se deben adherir algunos criterios de estabilidad al diseño de carreteras. En particular, la relación entre el radio mínimo, el peralte, el ángulo de pendiente longitudinal, la fricción lateral y la velocidad de diseño deberían reevaluarse. En este sentido, el umbral de vuelco estático (*SRT*) es uno de los factores más importantes utilizados para definir la estabilidad de los vehículos. Este factor depende en gran medida de la aceleración lateral máxima (a_y) cuando un vehículo alcanza el umbral de vuelco, esta aceleración a su vez depende de la velocidad del vehículo y del radio de curvatura. Teniendo en cuenta la estabilidad de los vehículos, en este estudio el diseño de carreteras se evalúa y se compara con el criterio de diseño clásico de vías. Este estudio también sugiere que para garantizar la seguridad de conducción, las agencias de carreteras estatales deberían hacer una revaluación de los límites de velocidad existentes y el diseño de curvas de carretera.

Palabras claves: diseño de vías; umbral de vuelco estático (*SRT*); vehículos pesados; seguridad vial; vuelco; salida de la vía.

1. Introduction

According to Hancock & Write [1], NYSDOT [2], and Chang [3]: "The minimum radius is a limiting value of curvature for a given design speed, and is determined from the maximum rate of superelevation (bank angle in percentage – e_{max}) and the maximum side friction factor selected for design (f_{max}). Use of sharper curvature for that design speed would call for superelevation beyond the limit is considered comfortable by many drivers, or both. Although based on a threshold of driver comfort, rather than safety, the minimum radius of curvature is also an important control value to determine superelevation rates for flatter curves. The minimum radius of curvature, R_{min} (m), can be calculated directly by the next simplified curve formula":

$$R_{min} = \frac{V^2}{127(0.01e_{max} + f_{max})} \quad (1)$$

where V is the vehicle speed (km/h).

However, this method is based on using the limiting values of the superelevation (e) and the friction factor (f); yet, this is a problem because the vehicles in general have two accident possibilities when taking a curve: slide out and rollover, as shown in Fig. 1.

How to cite: Moreno, G., Vieira, R. and Martins, D., Highway designs: effects of heavy vehicles stability, DYNA, 85(205), pp. 205-210, June, 2018.
© The author; licensee Universidad Nacional de Colombia.
Revista DYNA, 85(205), pp. 205-210, June, 2018, ISSN 0012-7353
DOI: https://doi.org/10.15446/dyna.v85n205.69676

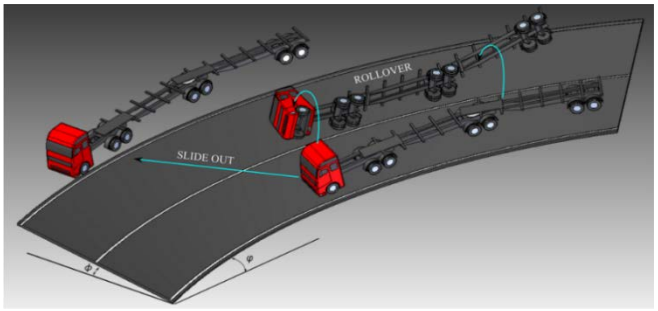


Figure 1. Accident possibilities of heavy vehicles.
Source: The authors.

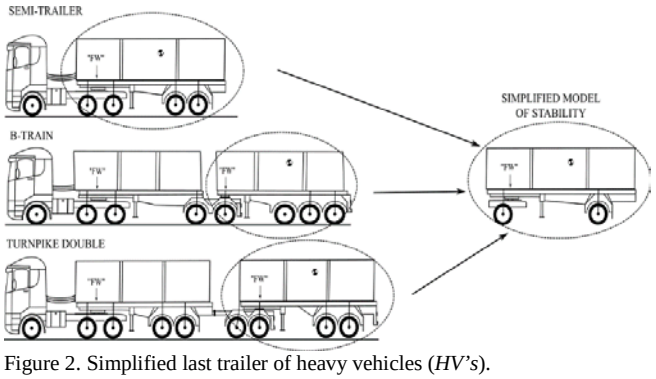


Figure 2. Simplified last trailer of heavy vehicles (*HV*'s).
Source: The authors.

Taking into account the second possibility; the stability of heavy vehicles (*HV's*) has been the focus of research efforts in recent decades. A variety of measurements have been defined to parameterize the stability of *HV's*. The static rollover threshold (*SRT*) is one of the most important parameters used to define the stability of vehicles. This factor is highly dependent on the location of the vehicle's center of gravity (*CG*), and it represents the maximum lateral acceleration - a_y (expressed in terms of gravity acceleration - g) in a quasi-static situation immediately before one tire loses contact with the ground [4-6].

This aspect is very important, since the lateral acceleration (a_y) can also be expressed in terms of the speed of the vehicle and the radius of the curve that is making.

In relation to calculating the *SRT* factor of heavy vehicles, in our previous research [7-10], we developed a three-dimensional simplified mechanism model that represents the last trailer of a *HV*. This model considers the main characteristics of trailer and the road such as: suspension, tires, fifth-wheel, chassis, bank angle, longitudinal slope angle and the trailer/trailer angle.

In this regard, the fifth-wheel is a coupling device. Its purpose is to connect a tractive unit to a towed unit. The tractive unit is normally a tractor, but in the case of a multiple trailer train, the fifth-wheel also can be located on a lead trailer. The fifth-wheel allows an articulation between the tractive and the towed units, and consists of a wheel-shaped deck plate usually designed to tilt or oscillate on mounting pins. The assembly is bolted to the frame of the tractive unit. A sector is cut away from the fifth-wheel plate (sometimes called a throat), allowing a trailer kingpin to engage with locking jaws in the center of the fifth-wheel. The trailer kingpin is mounted on the trailer's upper coupler assembly. The upper coupler consists of the kingpin and the bolster plate [11,12].

The paper is organized as follows. Section 2 introduces the mechanism of the three-dimensional trailer model with the characteristics mentioned above. Section 3 presents the static analysis of the proposed model; the result presented in Section 3 is analyzed and discussed within a case study in Section 4; and finally, conclusions are drawn in Section 5.

2. Mechanism trailer model

Some researchers have described that the last unit (trailer) of a *HV* is subjected to high lateral acceleration in comparison to the tractor unit. This acceleration is caused by the phenomenon known as rearward amplification (*RA*), impacting the rollover threshold of the last unit and the vehicle [13-15]. Thus, the last trailer of the *HV* is the critical unit and it is prone to rollover; taking into consideration this aspect, a simplified trailer model (Fig. 2) is modeled and analyzed to calculate the *SRT* factor.

During cornering or evasive maneuvers, the weight and the lateral inertial forces acting on the center of gravity cause its displacement, which can lead to vehicle rollover.

Mechanical systems can be represented by kinematic chains composed of links and joints, which facilitates their modeling and analysis [16-18]. Using mechanism theory, a three-dimensional model that represents the last trailer of *HV's* is proposed (Fig. 3) [10].

The model of the Fig. 3 is composed of three mechanisms:

- the first mechanism is located at the front of the trailer, and it is composed of sub-mechanisms that represent the tires (tire system), the suspension (rigid suspension system), and the fifth wheel (fifth-wheel system),
- the second mechanism is located at the rear of the trailer, and it is composed of sub-mechanisms that represent the tires (tire system), and the suspension (rigid suspension system); and
- the third mechanism represents the trailer body (chassis), and it links front and rear trailer mechanisms.
- The kinematic chain of the three-dimensional trailer model (Fig. 3) is composed of thirty joints ($j = 30$; 16 - revolute joints "*R*", 12 - prismatic joints "*P*", and 2 spherical joints "*S*"), in addition to twenty-five links ($n = 23$). However, making the expansion of the spherical joint the kinematic chain is composed of thirty-four joints ($j = 34$) and twenty-nine links ($n = 29$), making the workspace planar ($\lambda = 3$) and according to mobility equation Eq. (2) the system has 16-DoF ($M = 16$) [16-18].

$$M = \lambda(n - j - 1) + j \tag{2}$$

Making the simplification of the model, the revolute joint and the prismatic joint of the tires 2 and 3 can be changed by a spherical slider joint (S_d), with constraint in the *z*-axis, which does not modify the operation of the mechanism; the kinematic chain of the trailer model (Figure 4) is composed of twenty-eight joints ($j = 28$; 14 - revolute joints "*R*", 10 - prismatic joints "*P*", 2 spherical joints "*S*", and 2 spherical slider joints "S_d"), and twenty-three links ($n = 23$).

3. Static analysis of the mechanism

Several methods allow us to obtain a complete static analysis of a mechanism. In this study, the formalism presented by Davies [19] was used as the primary mathematical tool to analyze the mechanisms statically.

The Davies method appears in many publications in literature [10,20-22], and was selected due to the fact that it allows the static model of the mechanism to be obtained in a straight forward manner and it is also easily adapted using this approach.

Applying this theory to the vehicle stability, and considering all characteristics of the trailer and the road, the static rollover threshold (*SRT*) of the three-dimensional model of the last trailer is represented by the Eq. (3) [10].

$$SRT_{3D_{\psi\phi\varphi}} = \frac{a_y}{g} = \frac{h_1 \cos\varphi + h_2 e \cos\varphi}{h_2 - (h_1 + P_1)e} \left(1 - \frac{t_1 F_{z3} \cos\psi + P_1 (F_{z17} - W \cos\phi \cos\varphi)}{W \cos\phi \, (h_1 \cos\varphi + h_2 e \cos\varphi)}\right) \quad (3)$$

Where $SRT_{3D_{\psi\phi\varphi}}$ is the three-dimensional static rollover threshold for a trailer model with trailer/trailer angle (ψ), bank angle (ϕ) and grade angle (φ), h_1 is the instantaneous lateral distance between the zero-reference frame and the center of gravity, e is the bank angle in percentage, h_2 is the instantaneous CG height, t_1 is the front track width of the trailer model, W is the weight of the trailer, F_{z3} is the normal force on the front inner tire, F_{z17} is the normal force on the rear outer tire, P_1 is a system variable ($P_1 = (2l_{13}\sin\psi + t_2(\cos\psi - 1)/2)$, l_{13} is the distance between the fifth-wheel and the front axle, and t_2 is the front axle width.

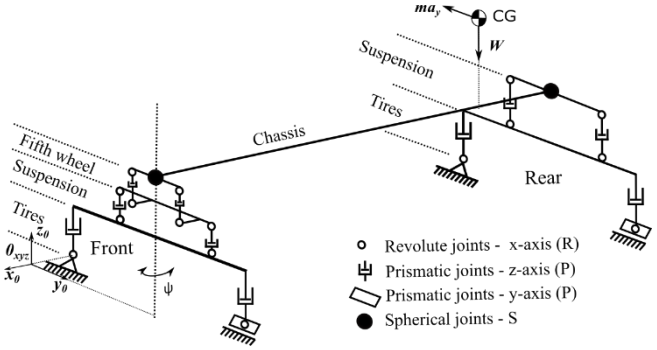


Figure 3. Three-dimensional trailer model.
Source: The authors.

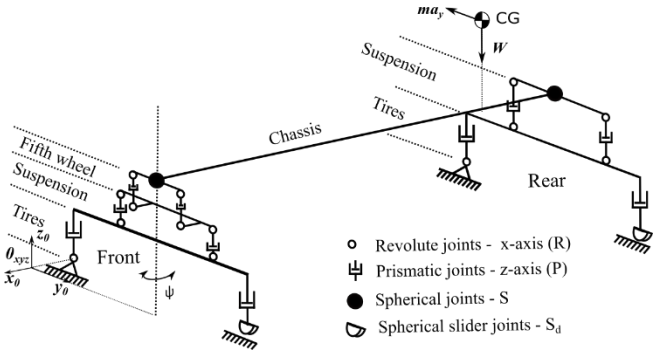


Figure 4. Trailer simplified model.
Source: The authors.

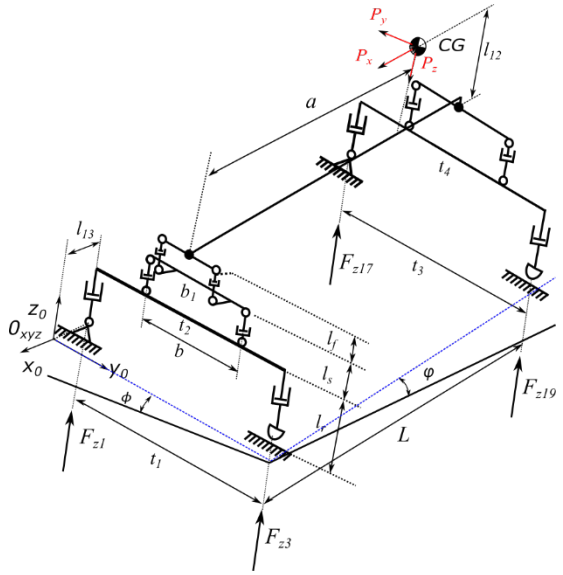


Figure 5. Three-dimensional trailer model.
Source: The authors.

Table 1.
Parameters of the trailer

Parameter of the trailer	Value	Unit.
Trailer weight (W)	355.22	kN
Front and rear track widths ($t_{1,3,3}$)	1.86	m
Front and rear axle widths ($t_{2,4,4}$)	1.86	m
Stiffness of the suspension per axle (k_{Ls}) [24]	1800	kN.m^{-1}
Number of axles at the front (4 tires per axle)	2	
Number of axles at the rear (4 tires per axle)	3	
Vertical stiffness per tire (k_T) [24]	840	kN.m^{-1}
Initial suspension height (l_s)	0.205	m
Initial dynamic rolling radius (l_r) [25]	0.499	m
Initial height of the fifth wheel (l_f)	0.1	m
Lateral separation between the springs (b)	0.95	m
Fifth-wheel width (b_1)	0.6	m
CG height above the chassis (l_{12})	1.346	m
Distance between the fifth wheel and the front axle (l_{13})	0.15	m
Wheelbase of the trailer (L)	4.26	m
Distance between the front axle and the trailer *CG* (a)	3	m

Source: Adapted from [23-25]

4. Case study

In this research study, the last trailer of a B-train with two front axles and three rear axles is analyzed. In this model a suspension system with tandem axle is used. Table 1 and Fig. 5 show the parameters of the trailer used in this analysis [23].

The *SRT* factor calculation was obtained using the steady state circular test [26] and the load condition is a load laterally centered.

The simulation model was applied using MATLAB® [27]. To calculate the *SRT* factor, the inertial force was increased until the lateral load transfer in the rear axle become complete (the normal force in the rear inner tire F_{Z19} reaches zero).

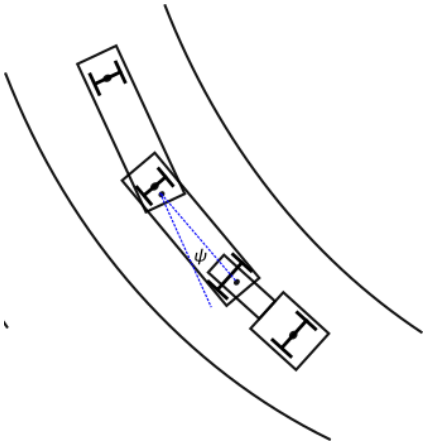


Figure 6. Three-dimensional trailer model on a downhill corner.
Source: The authors.

Table 2.
Static rollover threshold (*SRT*) of the trailer model on downhill corners.

Trailer/trailer angle (ψ)-(^{0})	Bank angle (e)-(%)	Downhill corners - Slope angle (φ)-(%)				
		0	2	4	6	8
0	0	0.202	0.198	0.194	0.190	0.186
0	4	0.244	0.239	0.234	0.230	0.226
0	8	0.285	0.281	0.276	0.272	0.268
0	12	0.328	0.324	0.319	0.315	0.311
10	0	0.202	0.197	0.193	0.189	0.185
10	4	0.243	0.239	0.233	0.229	0.225
10	8	0.285	0.280	0.276	0.271	0.267
10	12	0.328	0.323	0.318	0.314	0.310
20	0	0.200	0.195	0.191	0.187	0.182
20	4	0.242	0.236	0.232	0.227	0.224
20	8	0.283	0.278	0.274	0.270	0.265
20	12	0.326	0.321	0.316	0.312	0.308

Source: The authors.

Additionally and taking into account the flexibility of the chassis and the fifth wheel for the stability analysis, it is considered that when a heavy vehicle makes a spiral maneuver, the lateral load transfer on the front axle (LLR_f) is approximately 70% of the LLT_r coefficient on the rear axle [28]; and that the recommended maximum lateral load transfer for the rear axle (LLT_r) is 60% [29, 30] and also the recommended bank angle and longitudinal slope of the road must be included [1,2], taking into account all these characteristics, the *SRT* factor was calculated for a trailer model on downhill corners, when the vehicle is more prone to rollover, as shown in Fig. 6.

Table 2 shows the influence of the bank angle, longitudinal slope angle, and the trailer/trailer angle on the *SRT* factor calculation on downhill corners.

In the worst-case scenario, the *SRT* factor for the trailer model on a downhill corner with 0 % of bank angle (e), 8 % of longitudinal slope of the road (φ), and 20 degrees of trailer/trailer angle (ψ), is 0.182.

4.1. Road design minimum radius of curvature

Taking into account the Eq. (1), the radius minimum can be calculated replacing the bank angle of the road (e), and the side friction (demand) factor (f_{max}). Table 3 shows the recommended friction factors in relation to speed limits on roads:

Table 3.
Speed limits and friction factors.

Speed limit – (V) (km/h)	Friction factor (f)
30	0.17 – 0.28
40	0.17 – 0.23
50	0.16 – 0.19
60	0.15 – 0.17
70	0.14 – 0.15
80	0.14
90	0.13 – 0.14
100	0.12 – 0.13
110	0.11 – 0.12
120	0.09 – 0.11

Source: Adapted from [1, 2]

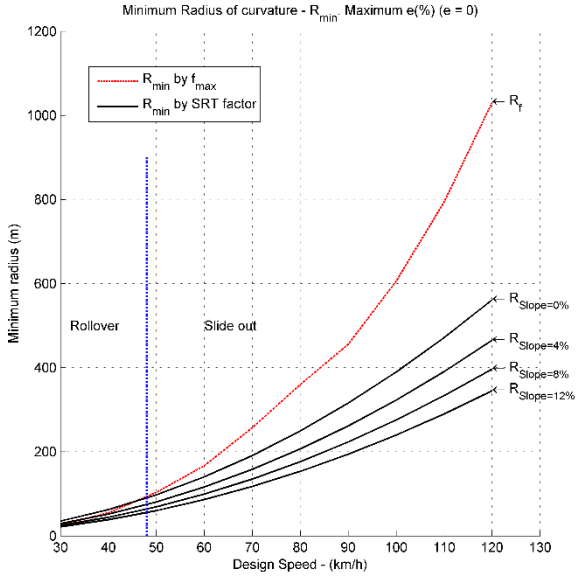


Figure 7. Minimum radius of curvature (R_{min}) – Bank angle (e = 0 %).
Source: The authors.

On the other hand, as previously mentioned, the *SRT* factor is dependent on lateral acceleration (a_y). Rearranging the Eq. (2) and replacing the lateral acceleration, the minimum radius of curvature, R_{min} (m) can be expressed in terms of the *SRT* factor and the vehicle speed (V - km/h), as shown in Eq. (3)

$$SRT_{3D_{\psi\phi\varphi}} = \frac{a_y}{g} = \frac{V^2}{R\,g}$$
$$R_{min} = \frac{V^2}{127\,SRT_{3D_{\psi\phi\varphi}}} \quad (3)$$

Using the data from the Tables 2 and 3, Figs. 7 to 11 compared the minimum radius given by the Eq. (1) and the minimum radius given by the Eq. (3); in these figures the bank angle (e) is fixed and the slope angle (ψ) is varied.

Figs. 7 to 11 show that in certain situations and using the classical minimum radius given by the Eq. (1), the trailer is prone to rollover. This shows that the *SRT* factor plays an important role in road design and the speed limits of vehicles, which contributes to road safety and decreases accidents related to vehicle stability, which are very high nowadays.

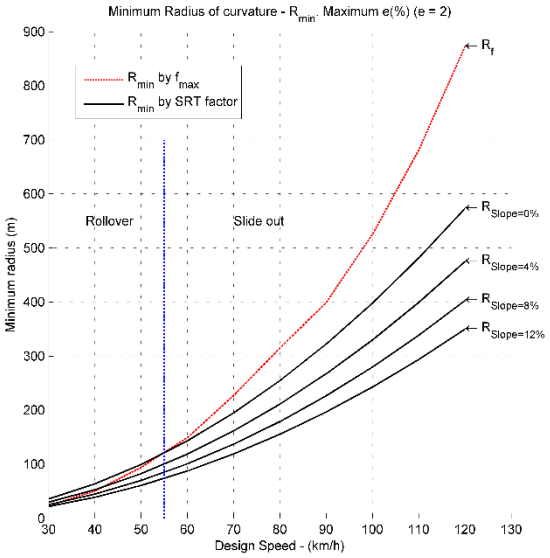


Figure 8. Minimum radius of curvature (R_{min}) – Bank angle ($e = 2$ %). Source: The authors.

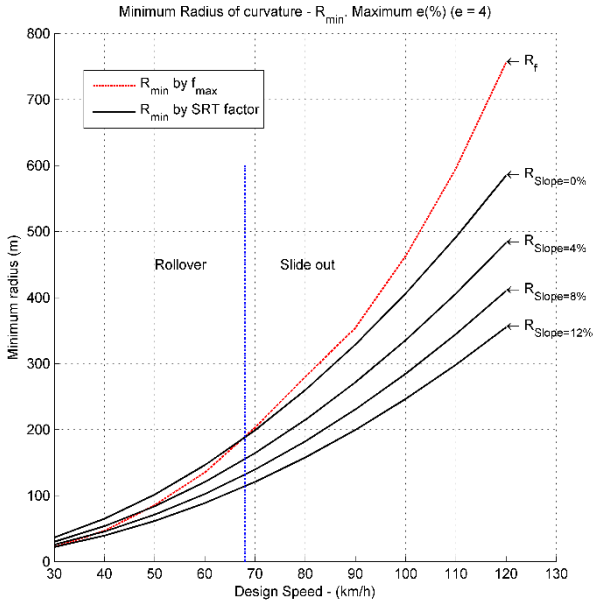


Figure 9. Minimum radius of curvature (R_{min}) – Bank angle ($e = 4$ %). Source: The authors.

Figs. 7 to 11 also show that it is important to re-evaluate the speed limits in certain situations, when the vehicles do not slide out, but instead they are prone to rollover.

5. Conclusions

The analysis showed that, the last trailer of the *HV* is the critical unit and it is prone to rollover when taking a curve, then it is important to re-evaluate the speed limits and the design of roads, which can guarantee greater road safety.

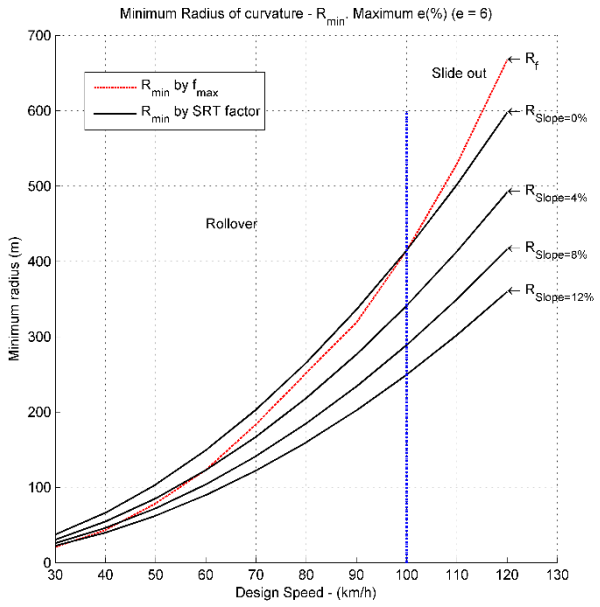


Figure 10. Minimum radius of curvature (R_{min}) – Bank angle ($e = 6$ %). Source: The authors.

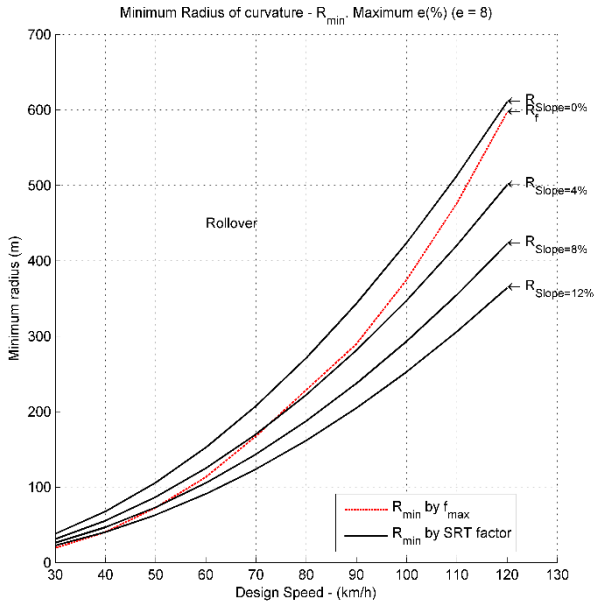


Figure 11. Minimum radius of curvature (R_{min}) – Bank angle ($e = 8$ %). Source: The authors.

Therefore, when road design studies are made, it is important to take into account that the vehicle has two accident possibilities: slide out and rollover.

This research study shows that the *SRT* factor plays an important role in road design and the speed limits of vehicles. We also found that the parameters of the road, such as the bank angle and the longitudinal slope angle, can affect a vehicle's stability. This situation is closer to the actual problem: when the road is not flat, the lateral and the

longitudinal load transfer play an important role in reducing the stability. On the other hand, this provides a very important warning, because some simplifications carried out when estimating the *SRT* factor can lead to a considerably higher stability value. This is a point of concern, leading to the perception that our roads are safer than they really are.

This study also suggests that in order to ensure driving safety, the State Highway Agencies should make a revaluation of existing speed limits and the design of highway curves.

Acknowledgement

This research study was supported by the University of Pamplona – Colombia and the Brazilian governmental agencies Coordenação de Aperfeiçoamento de Pessoal de Nível Superior (CAPES) and Conselho Nacional de Desenvolvimento Científico e Tecnológico (CNPq). The authors declare that there is no conflict of interest regarding the publication of this paper.

References

[1] Hancock, M.W. and Wright, B., A policy on geometric design of highways and streets, 6th ed. Washington, D.C., ISBN 1-56051-156-7. 2011.

[2] Nysdot, D.Q.A.B., Recommendations for AASHTO super-elevation design. Design Quality Assurance Bureau, NYSDOT, Washington, D.C. 2003.

[3] Chang, T., Effect of vehicles suspension on highway horizontal curve design. Journal of Transportation Engineering, 127(1), pp. 89-91. 2001.

[4] Winkler, C., Experimental determination of the rollover threshold of four tractor- semitrailer combination vehicles, Final report to Sandia Labs, Contract 33-8665 Report No. UMTRI-87-43, July, [online]. 1987, 79 P. Available at: http://hdl.handle.net/2027.42/49,1987

[5] Gillespie, T.D., Fundamentals of vehicle dynamics. SAE International, 7th ed., Warrendale, PA, ISBN 1560911999. 1992.

[6] Hac, A., Rollover stability index including effects of suspension design. SAE International - SAE 2002 World Congress, Detroit, March 4–7, 2002.

[7] Moreno, G.G., Nicolazzi, L., Vieira, R.S. and Martins, D., Three-dimensional analysis of the rollover risk of heavy vehicles using davies method. 14th World Congress in Mechanical and Machine Science (IFToMM2015), Taipei, Taiwan, DOI: 10.6567/IFToMM.14TH.WC.PS4.006. 2015.

[8] Moreno, G.G., Flórez, E. and Peña, C., Stability study of heavy vehicles Revista Colombiana de Tecnologías de Avanzada, 2(30), pp. 1-6, 2017. DOI: 10.24054/16927257.v30.n30.2017.2756.

[9] Moreno, G., Nicolazzi, L., Vieira, R.S. and Martins, D., Suspension and tyres: the stability of heavy vehicles, International Journal of Heavy Vehicle Systems, 24(4), pp. 305-326, 2017.

[10] Moreno, G., Nicolazzi, L., Vieira, R.S. and Martins, D., Stability of long combination vehicles, International Journal of Heavy Vehicle Systems, 25(1), pp. 113-131, 2018. DOI: 10.1504/IJHVS.2018.10011111

[11] Bennett, S., Heavy duty systems. 5th. ed. Clifton Park, New York: Cengage Learning. 2011. ISBN 13:9781435483828.

[12] SAF-HOLLAND. About fifth wheels. SAF-HOLLAND Group. Germany. 2006.

[13] Jindra, F., Handling characteristic of tractor-trailer combinations. SAE International, SAE Paper No. 650720. 1966.

[14] Rempel, M.R., Improving the dynamic performance of multiply-articulated vehicles. MSc. Thesis - The University of British Columbia, Vancouver - Canada. 2001.

[15] Melo, R.P., Avaliação da estabilidade lateral de CVCs. MSc. Thesis, Pontifícia Universidade Católica do Paraná - Brazil. 2004.

[16] Kutzbach, K., Mechanische leitungsverzweigung, ihre gesetze und anwendungen, Maschinenbau. Betrieb, 8(8), pp. 710-716, 1929.

[17] Crossley, F.R.E., A contribution to Grübler's theory in number synthesis of plane mechanisms., ASME Journal of Engineering Industry, Serie B, 86(2), pp. 1-8, 1964.

[18] Tsai, L.-W., Mechanism design: enumeration of kinematic structures according to function. CRC Press, ISBN 0849309018, Boca Raton, Florida. 2001.

[19] Davies, T.H., Mechanical networks-III wrenches on circuit screws. Mechanism and Machine Theory, 18(2), pp. 107-112, 1983.

[20] Davies, T.H., The 1887 committee meets again. Subject: freedom and constraint, Ball 2000 Conference, Cambridge University Press, Trinity College, Cambridge, UK, 56 P, 2000.

[21] Tsai, L.-W., Robot analysis - The mechanics of serial and parallel manipulators. John Wiley and Sons, Ltd., ISBN 0-471-32593-7, New York. 1999.

[22] Cazangi, H.R., Aplicação do método de Davies para análise cinemática e estática de mecanismos com múltiplos graus de liberdade. MSc. Thesis, Federal University of Santa Catarina, Florianópolis, Brazil, 2008.

[23] Ervin, R.D. and Guy, Y., The influence of weights and dimensions on the stability and control of heavy duty trucks in Canada. UMTRI - The University of Michigan Transportation Research Institute, Final Report UMTRI-86-35/III, 1986.

[24] Harwood, D.W., Torbic, D.J. and Richard, K.R., Review of truck characteristics as factors in roadway design. National Cooperative Highway Research Program, ISBN 0-309-08779-1, 2003.

[25] Michelin Lta. Michelin XZA Tire, Michelin North America, INc, Greenville, SC 29615, 2013.

[26] ISO-14792, Heavy commercial vehicles and buses - Steady state circular tests International Organization for Starndardization. Geneva, Switzerland, 2011.

[27] MATLAB®. Version R2013a. MathWorks, São Paulo, Brazil, 2013.

[28] Kamnik, R., Boettiger, F. and Hunt, K., Roll dynamics and lateral load transfer estimation in articulated heavy freight vehicles. Proceedings of the Institution of Mechanical Engineers, Part D: Journal of Automobile Engineering, Sage Publications Sage UK: London, England, 217(11), pp. 985-997, 2003.

[29] Woodrooffe, J., Sweatman, P., Arbor, A., Middleton, D., James, R. and Billing, J.R., National cooperative highway research program – NCHRP. Report 671. Review of canadian experience with the regulation of large commercial motor vehicles. Ed. National Academy of Sciences, Washington, D.C., ISBN 978-0-309-15518-2, 2010.

[30] Walker, H.K. and Pearson, J.R., Recommended regulatory principles for interprovincial heavy vehicle weights and dimensions. Tech. rep., CCMTA/RTAC Vehicle Weights and Dimensions Study Implementation Committee Report, 1987.

G. Moreno, is BSc. in Mechanical Eng. degree from the Francisco de Paula Santander University, Colombia (1999), MSc. in Mechanical Engineering from the University of the Andes, Colombia (2004) and Dr. in Mechanical Engineering from the Federal University of Santa Catarina, Brazil (2017). Currently professor of the mechanical engineering department at University of Pamplona, Colombia. Experience in mechanical engineering, focusing on machine design, acting in the following areas: statics and dynamics of mechanical systems with emphasis on mechanical design.
ORCID: 0000-0003-3617-1381

R. de Souza Vieira, is BSc. degree (1991), MSc. (1999) and Dr. (2006) in Mechanical Engineering, all from the Federal University of Santa Catarina, Brazil. Experience in mechanical engineering with emphasis on stress analysis, acting in the following areas: machine design, vehicle dynamics and kinematics.
ORCID: 0000-0001-9137-5024

D.Martins, is BSc. degree (1992), MSc. (1993) and Dr. (2002) in Mechanical Engineering, all from the Federal University of Santa Catarina (UFSC), Brazil. Visiting professor at the University Eduardo Mondlane in Maputo, Mozambique (1994–1995). Honorary Scholar at the University of Melbourne (1999–2000) and visiting professor at King's College London (2011–2012). Currently professor of the mechanical engineering department at UFSC and supervisor of the robotics laboratory. Works in the areas of mechanism design, automotive systems and robotics with emphasis on mechanical design.
ORCID: 0000-0003-1053-9686

UNIVERSIDAD NACIONAL DE COLOMBIA
SEDE MEDELLÍN
FACULTAD DE MINAS



DYNA
http://dyna.medellin.unal.edu.co/

An analysis of the socioenvironmental problems created by the construction of road tunnels in Colombia: case study

Tania Ramírez & Carlos Zárate

Policy, Legislation and Environmental Management Research Group – POLYGESTA, Faculty of Mines, Universidad Nacional de Colombia, Medellín, Colombia., Medellín, Colombia. tcramirezs@unal.edu.co, cazarate@unal.edu.co

Received: October 11th, 2017. Received in revised form: March 9th, 2018. Accepted: May 16th, 2018.

Abstract
One of the most important challenges facing road engineering in Colombia is overcoming the geographical configuration of the central region of Antioquia. Its very nature has made the construction of road tunnels the primary option for improving transport infrastructure, despite the fact that communities located in the scope of the projects have reported being negatively affected by them. The main objective was to carry out a critical analysis of the management implemented during the execution of the Fernando Gómez Martínez Tunnel project. This was achieved using ex-post evaluation methodology-based models, whereby the main results are based on deficiencies in management from the planning and execution stages of the project, together with weaknesses in the process of licensing, monitoring and control by the environmental authority.

Keywords: tunnel; socioenvironmental conflict; environmental impact assessment; environmental management plan; environmental license; ex-post evaluation.

Análisis de la problemática socioambiental generada por la construcción de túneles viales en Colombia: caso de estudio

Resumen
Dentro de los desafíos más importantes que enfrenta la ingeniería de vías en Colombia, se tiene el de sortear la configuración geográfica de la región central de Antioquia, lo que ha convertido a la construcción de túneles viales, en la principal opción para mejorar la infraestructura de transporte, a pesar de traer asociadas denuncias de afectación por parte de las comunidades asentadas en el área de influencia de los proyectos que incluyen obras subterráneas. El objetivo principal fue realizar un análisis crítico de la gestión realizada durante la ejecución del proyecto Túnel Fernando Gómez Martínez, basado en matrices diseñadas bajo la metodología de evaluación Ex post, cuyo resultado principal se basa en deficiencias en la gestión desde las etapas de planeación y ejecución del proyecto, sumadas a debilidades en el proceso de licenciamiento, seguimiento y control por parte de la autoridad ambiental.

Palabras clave: túnel; conflicto socioambiental; evaluación de impacto ambiental; plan de manejo ambiental; licencia ambiental; evaluación ex-post.

1. Introduction

Colombia has complex geomorphological and topographical conditions which create difficulties when constructing and maintaining the road network. The range of altitudes also generates inconveniences when extending or modifying the network. Since the second decade of the 20th century, the construction of road tunnels has become an opportunity for innovation and improvement of the national road infrastructure, representing an important element for boosting the country's growth [1].

Thus, by 2002, Colombia had 33 completed and in operation vehicle tunnels, equivalent to 18,540 linear meters; by 2010, the figure had increased to 90 tunnels, equivalent to 77,929 linear meters. These projects do not take into account the second wave of Fourth Generation Concessions recently

How to cite: Ramírez, T. and Zárate, C., An analysis of the socioenvironmental problems created by the construction of road tunnels in Colombia: case study DYNA, 85(205), pp. 211-218, June, 2018.

© The author; licensee Universidad Nacional de Colombia.

awarded, in which the estimated number of tunnels is 110, and which is expected to make Antioquia the region with the largest number of kilometers of tunnels in Colombia over the coming years [2]. Among these projects, the Fernando Gómez Martínez Tunnel (*Conexión Vial Aburrá - Río Cauca*) stands out, which is 4.6 km long and located on the Medellín - Turbo Road. However, an initial review of the country's main road tunnel projects may lead to the preliminary conclusion that there are socioenvironmental conflicts[1] associated with them due to complaints of alleged environmental impacts.

In light of these circumstances, the importance of investigating the causes of the environmental impacts caused by the construction of tunnels in Colombia was demonstrated using the proposed ex-post evaluation methodology[2] for this case study. Using this method allowed us to analyze whether the environmental studies carried out considered possible impacts on the environment generated by the construction of these works with due depth and importance, revealing in this case a lack of environmental planning; or if, on the contrary, the reality faced is mainly due to the existence of gaps in the applicable environmental regulations, and if this is related to the absence of an adequate monitoring and control process by the environmental authorities.

The *Conexión Vial Aburrá - Río Cauca* project was chosen, which began construction in 1997 and was operating by 2006. This project represented a special interest due to the fact that the construction of a second pipeline is being planned - currently in the study and design stage by the *Agencia Nacional de Infraestructura*[3] (ANI, National Infrastructure Agency). An analysis of environmental management in the pre-construction, construction and operation phases of the first stage of the project was then carried out through the design and application of a model based on the ex-post evaluation methodology [3]. This made it possible to identify relevant aspects in the execution of the project by the different actors involved in its environmental management, as well as to establish conclusions and recommendations that can be considered in road tunnel construction projects in general.

2. Background information

2.1. Importance of ex-post evaluation as a tool for environmental management

A review of existing research on the subject found that Colombia has historically lacked a culture of implementing ex-post evaluations, a situation that is also a problem in several countries around the world. The only evidence found of having developed an ex-post evaluation was for the pilot tunnel 'La Línea'. In this evaluation, the impacts caused by the project and the fulfillment of the objectives and goals were presented, with negative results due to the apparent irreversible nature of the impacts caused.

In 2007, the Institute of Regional Studies of the University of Antioquia (INER) prepared the "Study of the Social, Economic, Political and Cultural Impacts of the Aburrá - Río Cauca Road Connection" for the Fernando Gómez Martínez Tunnel [4], in which the positive and negative impacts caused on the territorial development in western Antioquia were identified, and strategic guidelines were formulated for their management by the different municipalities. There is also the "Master Plan for the Territorial Planning of the Scope of the Project for the Valle de Aburrá - Río Cauca Road Connection in the Western Antioquia Region" [5], in which basic concepts, principles and prospects were defined, as well as a methodological synthesis, strategic lines, diagnosis and description of the scenarios and contingency actions that, in the opinion of the School of Urban & Regional Planning, should be executed immediately and within a maximum period of one year.

As for other road tunnel projects developed in Colombia, such as the Sumapaz Tunnel and the pilot tunnel 'La Línea', the Ministry of the Environment, Housing and Territorial Development contracted Colombia's National University, Water Resources Engineering Research Group, to prepare the "Evaluation of the Impact of Construction on the Neighboring Ecosystems." This study evaluated the impact of the construction of tunnels on the surface and underground water resources of the surrounding areas, determining that the tunnel effectively depressurized the system, causing the drainage of water bodies such as La Gata Creek and the reduction of others such as La Cristalina Creek [6].

In 2010, the Inter-American Development Bank prepared the "Ex-post Impact Evaluation of Environmental Mitigation Measures for the Porce II Hydroelectric Project" [7], and in 2008 it prepared the ex-post evaluation of mitigation measures in the Samalayuca II and Monterrey III thermal generation projects [8].

Upon doing a background review for projects involving the construction of tunnels in different parts of the world, it was found that for Asia, within the studies carried out to assess the environmental impact for the "Tseng Wen Reservoir Diversion Project" in Taiwan [9], timely identification of environmental impacts on water resources was of great importance for the planning, design and construction of tunnel projects, as accidents and delays in the project during construction could be minimized. In this research, software was used to determine the impact of tunnel excavation on the hydrogeological environment in a regional area around the tunnel and in a hot spring area.

With regard to ex-post evaluations implemented in large projects in Europe and which could serve as a guide for the present investigation, we found one carried out on the Øresund Bridge in Copenhagen [10], which provides a socioeconomic analysis and compares it with the evaluation for the Eurotunnel project or the Channel Tunnel [11], in which the errors committed during the planning and

[1] Definition of environmental conflict: Where the controversy of information, interests or values refers to aspects related to access, availability and quality of natural resources and environmental conditions that affect the quality of life of people. CIPMA 1995

[2] Ex-post evaluation: reflective and analytical activity that is applied throughout the decision-making process for the purpose of examining, as systematically and objectively as possible, past actions in relation to well-defined objectives, resources employed and achievements, and to derive relevant lessons to guide decision-makers and improve future activities.

[3] *Agencia Nacional Estatal de Naturaleza Especial* is part of the decentralized sector of Colombia's Executive Branch of the National Order, with legal status, its own patrimony and administrative, financial and technical autonomy, attached to the Ministry of Transport, according to decree 4165 of November 03, 2011.

construction of the aforementioned are analyzed, but mainly in terms of methodological, social and political aspects.

For its part, it is important to take into account the article "Influence of Reference Points in Ex-post Evaluations of Rail Infrastructure Projects" [12], in which the author analyzes the ex-post evaluation of four railway projects in Norway, finding that the choice of study parameters usually influences the results of the evaluation by presenting them as failed or successful projects, depending on the year chosen to carry out the study and the indicators to be evaluated, and therefore recommending that more than one ex-post evaluation method be applied for more reliable results.

Another alternative is to apply the proposed methodology to similar projects, with the possibility of comparing the results and identifying similarities in the execution, operation and settlement stages of projects. This allows us to define how many of the a project's objectives have been achieved or how much capacity a similar project has in order to attain them, for which Zapata Puerta and Tovar Olano, Colombian authors, in their master's thesis [13], present their methodological considerations applied to projects at an international level.

With regard to ex-post Environmental Impact Assessments, the Chinese author, QG Wang [14], states that "Once the projects are completed, the actual environmental impact caused can be determined by implementing an Environmental Impact Post-Assessment (EIPA), and can be compared with the impacts predicted in the Environmental Impact Assessment (EIA)[4], the differences found can be used to predict the effectiveness of the EIA in protecting the environment, replicating the results to similar projects to maximize the positive impacts".

It can be concluded then, that the implementation of ex-post evaluation is clearly important in the monitoring and control of projects, given the advantages it represents in terms of identifying the effectiveness, efficiency and compliance of the proposed measures from the pre-feasibility stage of the projects, in order to design strategies that are considered useful not only for project executors, but also for state entities and environmental authorities in establishing improvement measures.

In general, for large projects, it was found that although the different entities have carried out studies to provide solutions to problems subsequent to the construction of the project, an ex-post evaluation methodology has not been implemented which transcends the reality that the territory has to contend with during the operational stage of the project and which is aimed at determining the effectiveness of the Environmental Impact Assessment (EIA) and Environmental Management Plan (EMP), facilitating its environmental closure and generating management recommendations for future projects.

3. Methodology

The Aburrá - Río Cauca Road Connection project was chosen, which includes the construction of a 4.6 kilometer tunnel, beginning construction in 1997 and operation in 2006. This project represented a special interest due to the fact that the construction of a second pipeline is currently planned - a stage that is currently being studied and designed by the ANI - but which has already generated some opposition in the neighboring community, who report having suffered the environmental impacts of the first stage of the project, which according to the community have not been fully compensated.

In order to establish the methodology to be followed for the application of the proposed evaluation, a review of the existing bibliography related to the ex-post evaluation was carried out. We found that there is no defined procedure for standard projects, nor is there any norm in this regard, so proceeded to design a model, based on the ex-post evaluation methodology, which was applied to the project in its different phases, studies, designs and construction. Fig. 1 shows the description of the methodology.

In order to evaluate the road project during the environmental studies stage, a model was designed containing the main requirements and obligations included in the terms of reference issued by the environmental authority for the preparation of the EIA for road infrastructure projects contained in Auto 234 of 1996. We applied the evaluation model to the study carried out in 1996 and obtained as a result a comparative analysis of the information supplied to the environmental authority and the possible gaps in it.

For the construction stage, file number 0678 was reviewed (which was consulted directly in the National Environmental Licensing Authority's file). The compilation and analysis of the environmental management measures implemented in the construction and operation stages, reported in the Environmental Compliance Reports submitted to the authority, and the main actions of the national and regional environmental authority were carried out. During the review, the sanctioning measures imposed on the road project and the interventions of the different actors, mechanisms for citizen participation and the main judicial processes involved, degree of satisfaction of the benefited community, results, effects and residual impacts were identified.

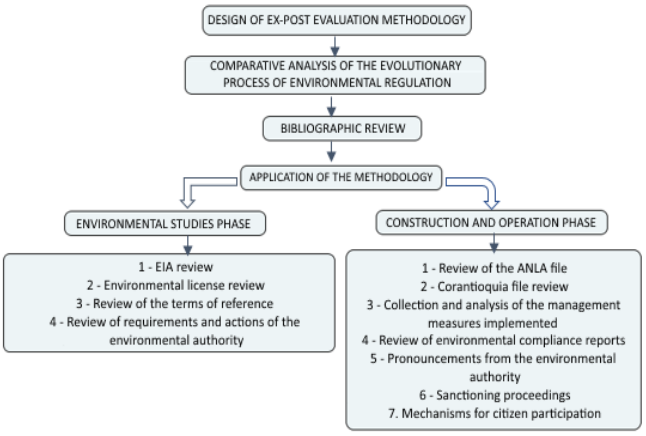


Figure 1. Flowchart research methodology
Source: Authors' elaboration.

[4] An Environmental Impact Assessment is the basic instrument for making decisions on projects, works or activities that require an environmental license and are compulsory in Colombia in all cases in which an environmental license is required. Law 99 of 1993.

Table 1.
Technical Datasheet of the Aburrá - Río Cauca Road Connection Project

Contributing Entities	INVÍAS, Department of Antioquia, Municipality of Medellín and Metropolitan Area of Valle de Aburrá
Design	Integral S.A. Contract No. FO-1047-1901 FONADE (1994-1995) U.T. Impregilo S.p.A - Topco S.A. (Tunnel and bridges in the western sector) U.T. Siemens S.A. – Eléctricas de Medellín S.A. (Design, supply, installation and commissioning of the Electromechanical Tunnel Equipment)
Builder	Initially - U.T. IMPREGILO S.p.A. – TOPCO S.A., Finally - U.T. Mincivil S.A: - Estyma S.A.
Comptroller's Office	INTEGRAL S.A., Consorcio Integral S.A. – Solingral Ltda.
Commencement	November, 1997
Completion	January, 2006

Source: Final audit report of the project. Integral, 2007.

Likewise, the models broken down by component of the subsequent standards related to the licensing of tunnel construction works were also presented. These models served as input for the analysis of the expected impacts with the construction of phase 2 of the project and guided the conclusions and recommendations of the research.

We focused on identifying the impacts generated by the construction of the Fernando Gómez Martínez Tunnel project based on the existing information in the different files of the project from the environmental authority, evaluating their relationship with possible causes of the socioenvironmental conflicts that arose, so that, based on the results of the application of the designed ex-post evaluation model, environmental management recommendations applicable to the second stage of the project can be identified and, in general, can be fed back as lessons learned in other similar projects.

4. Project description. Case study

4.1. General characteristics

The construction of the Aburrá - Río Cauca Road Connection project was carried out under an inter-administrative agreement signed by the National Roads Institute, the Department of Antioquia, the Municipality of Medellín and the Metropolitan Area of the Valle de Aburrá. **¡Error! No se encuentra el origen de la referencia.**1 below presents the technical specifications of the project [15]:

4.2. Project location

The project is located in the Department of Antioquia, specifically in the municipalities of Medellín, (districts of San Cristóbal and San Sebastián de Palmitas), Ebéjico and San Jerónimo. Within the direct scope of the project, which includes the 4.6 kilometers of construction of the western tunnel, the following municipal districts were identified in the field verification trips: Naranjal, La Cuchilla, La Frisola and La Volcana. This section divides the road corridor into three sectors that are described below:

Eastern sector - Between Road 80 and the eastern entrance of the tunnel in the district of San Cristóbal. The road in this sector is designed with a double roadway and central separator, and its layout runs parallel to La Iguaná Creek.

Tunnel - With a length of 4.6 kilometers, 76 m2 of cross section and a slope of 2.25%, it crosses the water divide between La Iguaná Creek, a tributary of the Medellín River, and the La Frisola Creek, a tributary of the Cauca River basin.

Western sector - With a length of 24 kilometers, between the western entrance of the tunnel and the final junction of the project with the current road to the sea at its intersection with the Aurrá River, in the municipality of San Jerónimo.

For the purposes of this investigation, the tunnel section is of particular interest.

4.3. Description of the scope of the project

The section corresponding to the tunnel is located in the district of San Cristóbal, which borders on the north with the municipality of Bello, on the east with the urban perimeter of Medellín, on the south with the districts of Altavista and San Antonio de Prado and on the west with the district of Palmitas. The center of the district is located 11 kilometers from downtown Medellín and has a total area of 49.54 km2 and a population of 34,877 inhabitants, according to the 2005 Statistical Annual of Medellín.

This area has a rugged terrain of mountainous canyons that form a system of small longitudinal valleys, with heights between 1800 and 3000 meters above sea level. The main hydrographic basin of the district is the La Iguaná Creek that crosses the entire territory in a west-east direction and has numerous tributaries that reach the mountains.

The main economic activity is agricultural production; a variety of products are created via intensive use and rotation of the land. Small crops are divided into areas that, according to a report from the Secretary of Community Development, mainly oscillate between 1.5 by 15.5 meters. The principle products grown in the region are vegetables, flowers and, to a lesser extent, fruits and herbs.

The San Cristóbal District is located within the category of suburban land, subcategory of rural population centers, made up of the areas that have the adoption of the necessary provisions to regulate the occupation of their land and the adequate provision of basic public services infrastructure and equipment.

One of the modifications brought about by the construction of the road project is that both districts adopt the category of suburban land, according to which certain areas are constituted into areas or polygons in which rural land uses and rural and urban lifestyles coexist, with housing densities lower than those permitted in rural population centers.

As a result, for the San Cristóbal District, there is a 5.8 hectare polygon defined as a conservation zone. In general, in accordance with the 33/5000 Plan of Territorial Ordinance [16], these areas are part of the protected zones defined for the territory - included in the main ecological structure – and are areas of high threat and non-mitigable risk, which are considered as soils in need of environmental protection in the light of the present regulations.

This approach aims to ensure ecological connectivity, soil

stability and regulation of the hydrological system. In general, these polygons are part of the sustainable production areas of the Valle de Aburrá - Río Cauca Integrated Management District and the Nare River Protected Forest Reserve and include part of the ecological connectivity network of the main and complementary ecological structure.

5. Environmental planning of the project

The company Integral was contracted to carry out the Environmental Impact Assessment in 1996. This study identified the impacts caused by the construction and execution activities of the project on the different environmental elements. The impacts were graded and prioritized in order to establish the elements, components and systems that would be most affected by the construction of the project. Finally, for each of the environmental systems - abiotic, biotic and anthropogenic - the document describes the effects generated by the project, the mitigation, prevention and control measures, and some recommendations.

For the preparation of the EIA, the multifactorial evaluation methodology was used, for which an analysis was conducted of the *environmental supply* with the characteristics of the area at the time of the study, and of the *environmental demand* defined by the characteristics and processes for the execution and operation of the project. Subsequently, the project was broken down into activities and the environment into systems, components and elements. With this information the identification model was constructed which established which project activities/processes are more likely to generate a greater number of impacts on the environmental elements and which of these are more sensitive to said activities.

The study describes parameters measured by water quality, air quality, analysis of land use, land use conflicts, biotic aspects, urban aspects, landscape, social infrastructure, and socioeconomic, sociocultural and archaeological aspects. As a result of the identification model, the environmental effects data sheets corresponding to each stage of the project and the impact rating table for each of the interactions described in the effects data sheets are presented.

Along with the main conclusions resulting from the review of the environmental planning phase of the project, it should be noted that although the methodology applied constitutes a procedure that allows the identification of the cause and effect of the different activities to be carried out in the different stages of the project and the possible impacts to be generated, it can be said that the impact identification model completed for the project does not consider in depth all the interactions between the activities to be developed and the elements and components proposed, leaving aside the possible important impacts associated with the construction of road tunnels. This consideration is justified throughout this document as a conclusion of the analysis of the different impacts identified in the study.

Specifically for the case study, the Environmental Management Plan[5] includes plans for operational, physical and social management, in which the measures to be implemented to prevent, control, mitigate or compensate for the impacts identified as relevant within the impact assessment model were established.

Among the main results obtained for the environmental planning stage of the project, the impacts mentioned in the EIA, section 5.3.1.2, Water Component, presents the possible affectation to fluvial dynamics: alteration of the state of geomorphological equilibrium of the currents due to flow deviations, changes in the slope of the riverbed, cuts, construction of sewers, bridges, etc., modifications in the flow regime, in the water table and in the capacity of sediment transport. Table 5.1 shows the relationship between surface and underground excavations and the effect on river dynamics, referred to as a noticeable effect on the entire corridor to be built.

However, when analyzing the impact ratings presented in Table 5.2., Environmental Qualifications Construction Stage, we can see that the value for the implications of the underground excavation activity on the river dynamics is 0.03 and for surface excavations, 0.07. In addition, the weight assigned to both activities is 0.25, which leads to a score of 'mild' as stated in chapter 5.6, Analysis of Results. The vast majority of interactions in the construction phase are in the 'very mild' category: 41 in total, equivalent to 60%. Of these, 46% can be considered negligible as they have a rating of less than 0.05.

This is without including in the study the description and supporting documentation of complementary studies that allow the reasons for the assigned values to be determined.

The environmental license[6] for the project was granted by the then Ministry of the Environment through Resolution No. 0762 of August 15, 1995 and corresponds to a Standard Environmental License. It establishes the requirements, conditions and obligations that the beneficiary must comply with to prevent, mitigate, correct, compensate and manage the environmental impacts of the project, work or activity authorized, without providing for the granting of permits, authorizations or concessions for the use, exploitation or mobilization of renewable natural resources.

6. Description of the socioenvironmental problem associated with the case study

When reviewing the information contained in the *Autoridad Nacional de Licencias Ambientales's* (National Authority of Environmental Licences, ANLA) file 0678, it was found that, during the month of December 1999, residents of the municipal district of Naranjal in the district of San Cristóbal denounced the depletion of water sources that were used for irrigation of crops. According to the internal communication of the Government of Antioquia, number 168, April 13, 2000, corresponding to the report of

[5] Detailed set of measures and activities that, as a result of an environmental assessment, are aimed at preventing, mitigating, correcting or compensating the duly identified environmental impacts and effects caused by the development of a project, work or activity.

[6] Authorization granted by the competent environmental authority, by means of an administrative act, to a person or company for the execution of a project, work or activity that according to the law and also to the regulations can produce serious deterioration to the renewable natural resources or the environment or introduce considerable or notorious modifications to the landscape.

the municipal district Naranjal, several visits were made to 11 reported points, revealing the collapse of 3 water sources located in the area of the eastern entrance of the tunnel.

Subsequently, the aforementioned report describes: *"The municipal district of Naranjal corresponds to a sector of rural characteristics and dispersed rural dwellings with a predominance of vegetable and flower crops. Particularly in the affected area there are a total of 42 dwellings and approximately 208,000 m2 of cultivated land, as described in the report, with changes in the hydrological regime being evident. Specifically, at the time, 17 families relied on the 3 springs reported as deteriorated"*.

According to Comptroller's Memorandum 1324-E-1147, of the 3 water sources reported as disappeared, only water source number 1 was gauged, since the others were not known to exist when the census was conducted with the local inhabitants.

Reviewing the file of the Corantioquia project, the Technical Report AB 00 00216 of February 23, 2000 was found, which corresponds to the visit carried out to address the complaint about the alleged effects that the construction of the tunnel brought to the municipal district of Naranjal. The objective of the visit was to evaluate the situation, make a diagnosis, identify the factors that caused the situation, determine whether or not the road project is responsible and propose technical alternatives for solutions.

One of the main conclusions of the Corantioquia report is: *"According to field observations, there is only one factor that can cause the infiltration of the waters of these springs: the presence of the tunnel under construction for the Valle de Aburrá-Rio Cauca road interconnection. With the presence of the tunnel work, an empty space has been created inside the earth that generates the infiltration of surface water by gravity and the lowering of the water table"*. A conclusion based on field observations and not on verification studies.

Corantioquia makes the following recommendation: *"Due to the importance of water for the inhabitants of the municipal districts adjacent to the western tunnel projection line, it is necessary to propose a measure to guarantee water supply to the inhabitants of the area. According to the high population, the agricultural tradition (vegetable crops) and livestock sector, it is essential to have a supply of water, both for domestic and agricultural use"*.

The file contains "Design of the System for Water Collection for Irrigation in the Municipal District Naranjal", prepared by the company Integral in 2003. However, during the investigation for the damage, it was found in file number 0678 of 1997, that the Ministry of Environment, Housing and Territorial Development, through Resolution 0358 of 2006, opened an investigation and issued a statement of objections to the National Roads Institute as the holder of the environmental license, among other reasons, requiring the presentation of the schedule of water supply works for the houses in the Naranjal municipal district, and for not having initiated works [17].

The Governor's Office of Antioquia presented its Technical Report on Waivers on April 21, 2006, according to which it stated that: *"The compensation had not been executed to date due to the refusal of the owners to allow the transfer of the piping and the non-acceptance of the appraisals presented.....The community was willing to have the restitution of the water changed, compensating them with the improvement of the road that leads to the municipal district of Naranjal or the construction of a football field. One can see that the community has the precious liquid and can cultivate and exploit their lands agriculturally, without losing the vocation they had"* [18].

It can be observed that, although a consensus was reached between the project and the community, as a result of a working group set up by the Agrarian and Environmental Attorney General's Office, compliance with the commitments to restore the irrigation system did not materialize. The community's comments do not compensate for the fact that the water availability was changed by the paving of a local road, despite the fact that this activity is the result of an agreement between the parties.

7. Results

As the main results of the implementation of the **ex-post evaluation model for the environmental studies stage**, when reviewing the content of the project's EIA and comparing it with the terms of reference contained in Auto 234 of 1996, it can be concluded that there is a lack of depth and detail in the following areas: blasting, description of necessary materials, requirements for channel occupations, transfer of electrical networks, maintenance program, scope of the project, and analysis units.

In addition, it presents little depth and analysis in relation to the identification of the possible impacts that the excavation of the tunnel could generate on the surface and/or underground springs. Furthermore, taking into account that no information was found that was requested in the terms of reference contained in Auto 234 of 1996, applicable at the time, specifically with respect to groundwater hydrology, analysis of land vulnerability as a function of the permeability of materials and their relationship with aquifers, inventory of water points, sources, springs and outcrops, and information on risks of contamination and recharge of aquifers, the temporal evolution of groundwater levels or information on the direction of underground flow lines. Similarly, no evidence was found that the environmental authority had requested information on the matter.

For its part, the **Evaluation Model for the Construction and Operation Stage** made it possible to identify that for section 6.2, Physical Management Plans, in relation to the activities proposed in 6.2.1 Material Management, the status of the main sites authorized by the environmental license and its modifications for excavation material deposit zones is analyzed, based on Auto 4204 of 2015 [19], through which the environmental authority presents an updated consolidated report for these sites. As the main result of the analysis, the file does not include the closure of the obligation for any of the authorized sites, despite the fact that the project has been in operation since 2006.

According to Auto 4204 of 2015, ANLA reiterates the request to present a concept issued by Corantioquia on the non-existence of environmental impacts in the different Debris Management and Excavation Material Area used for the construction of the road project, which was initially

requested by Auto 2937 of 2013. In this regard, it is found that the material management areas located in the jurisdiction of the Territorial Hevéxicos of Corantioquia, have the concept issued by the regional level environmental authority through Technical Report 130HX-1407-122669 of July 16, 2014. However, as of the closing date of this investigation, there is no evidence of the closure of these obligations by ANLA, despite repeated requests.

In the respective Environmental Compliance Reports, the progress of the reforestation activities has been included, which were carried out to partially comply with the EMP. As was the case for the document requesting the closure of commitments sent to ANLA in 2013. However, there are no ANLA pronouncements regarding the closure of this obligation, although follow-up visits are reported.

In general, within the monitoring and control process, the different actions of the environmental authority concentrate on repeatedly requiring, year after year, the same information related to activities such as slope treatment schedules, plans and receipt certificates from the owners of the deposit sites, signage for environmental awareness (installed since 2010), public lighting (which can be seen with the naked eye), reforestation measures, among others, ignoring the evidence of compliance provided in the different Environmental Compliance Reports, and without making a substantive statement on aspects of greater importance that are pending environmental closure, such as the complaint of alleged damages caused by the construction of the tunnel to the water sources in the Naranjal area, the closure of Debris Management and Excavation Material Area and the presentation and execution of the 1% Investment Plan[7].

Additionally, it is found that the visits by the environmental authority are carried out approximately every year and producing the corresponding technical report can even reach a similar time period. This lack of agility makes it difficult to request and implement timely corrective actions, and turns the control process into an endless process, instead of achieving its monitoring function with the expected results.

As for the capacity of the environmental authority, Correal[8], considers that it does not have sufficient personnel available to meet current licensing and project monitoring needs. However, he believes that recently, efforts have been made to incorporate specialists in the hydrogeological field, taking into account the conflicts that have arisen over the construction of tunnels in Colombia. Nonetheless, the general scheme of monitoring and evaluation that the environmental authority has is not very adequate for the country's development projects, through which temporary associations[9] of a team of professionals from the social, biotic and abiotic areas are formed, creating a high variability in the personnel assigned to the projects, making the monitoring and control process difficult.

The above results are validated with the considerations issued by the Office of the Comptroller General of the Republic for the year 1998, indicating that the main shortcomings in the environmental licensing process are mainly due to the lack of technical capacity to evaluate EIAs, the difficulty of objectively defining the cases in which an environmental license is required, and finally, mention is made of deficient monitoring and control [20].

8. Conclusions and recommendations

The environmental license is conceived as a tool for formulating impact management strategies aimed at preventing, controlling, mitigating or compensating impacts; hence the rigor required for its development and implementation from the Colombian regulations that allow the creation of such projects under the principle of sustainability set forth in Article 3 of Law 99 of 1993. In order for environmental licensing to achieve this objective, there must be a comprehensive environmental assessment covering all dimensions so that the project is compatible with the concept of sustainable development and not just focused on economic development.

For its part, environmental impact analysis requires an interdisciplinary perspective, for which it is necessary to create a reference of the context that provides an integrated environmental understanding with the methodological analysis of the stages of execution and operation of the development project, including not only the identification of the impacts that can be attributed to the project, but also those caused by the dynamics of development of the region in which it is located [21].

In the particular case of road tunnel construction projects, the possible impacts of tunnel excavation on the hydrogeological system and on the environment should be taken into account, identifying in advance the impacts that their construction may have on groundwater and surface water in the scope of the project, the alteration of the initial local or regional groundwater flow, reduction of the flow and the impact on existing sources or accumulations of water.

In this sense, identification of the hydrogeological characteristics of the area of intervention, the estimation of the infiltration flows, the location of said filtrations and water pressures, need to be a priority within the environmental studies so they can be considered in the design and construction of the project [22].

In relation to the construction stage, it is important to monitor surface water and ground effects related to groundwater depletion. Instrumentation should be installed to monitor the variation of the water table on a regular basis and the infiltration flows, which will make it possible to verify the relevance of the estimates contemplated in the studies and the need for them to be re-evaluated.

Finally, as recommendations for the operation stage, control over the inventory of water points prepared as input

7 All projects that involve the use of water taken directly from natural sources and that are subject to obtaining an environmental license must allocate 1% of the total investment for the recovery, conservation, preservation and monitoring of the river basin that feeds the respective water source, in accordance with Article 43 of Law 99 of 1993.

8 Carlos Antonio Correal Ramos: Civil Engineer from the National University of Colombia, specialist in Integrated Environmental Management, Specialist in Geotechnics and Numerical Methods for Engineering Calculation, with experience in environmental consulting for road infrastructure projects.

9 Agreement by virtue of which two or more persons jointly submit a proposal for the award, conclusion and execution of a contract, jointly and severally liable for the full performance of the proposal and the contract.

for the baseline of the pre-construction stage must be maintained and instrumentation of the area for monitoring the variation in the piezometric levels must continue, as well as periodic monitoring of the infiltration flows of the tunnel and the composition of the water.

In order to improve environmental management in our country and guarantee the environmental planning of sustainable projects, it is necessary to improve the procedure in relation to the terms of the licenses, the thoroughness of the study of the documentation associated with the licensing process, the control and monitoring of the projects, institutional capacity, improve communication with the environmental authorities and response times, as well as the issuance of monitoring and control reports and access to information, so that they can respond to the challenges that environmental issues demand from them.

Furthermore, it is important to prioritize and emphasize the importance of the implementation of citizen participation mechanisms that enrich the planning process of a development project, and which make it possible to achieve social viability through information, consultation and agreement, through the generation of knowledge that involves communities in the identification and evaluation of environmental impacts and in the design of the respective Environmental Management Plan.

It is necessary to work on the coordination of the entities and institutions related to the development project, including environmental entities, so that joint efforts can be made in favor of the environment. Public or private actors must also work on the optimal organizational design adjusted to the environmental problems associated with their economic activity. Consulting companies need to focus on environmental issues, developing work models applied to the project for which they are hired instead of using generic formats that do not reflect the real situation of the site. And environmental authorities, for their part, must fully execute their roles of authorization, monitoring and control, systematization of existing information and generation of new useful information.

Finally, and perhaps the most important recommendation made throughout the research, is the mandatory implementation of ex-post evaluation methodologies for projects, with the advantages that this practice entails not only in the identification of the level of compliance with the obligations arising from environmental licensing, applicable regulations and various unforeseen events that arise during the different stages of the project, but also in the environmental closure, providing a general overview of management and lessons learned to implement in future operations subject to the much sought-after economic development of the territory.

References

[1] Grupo de Comunicaciones y Relaciones Públicas. Departamento Nacional de Planeación, Plan Nacional de Desarrollo, 2014.

[2] Gil-Chavarria, J.E. y Yarce-Zapata, A.M., Los túneles carreteros en colombia, 2010.

[3] Guerrero, P., Recent experiencies in evaluation systems development in selected developing member countries, 1991.

[4] INER., Estudio de impactos sociales, económicos, políticos y culturales de la conexión vial Aburrá – río Cauca, 2006.

[5] Gobernación de Antioquia, Universidad Nacional, Plan director para la ordenación territorial del área de influencia de la conexión vial, Valle de Aburrá-río Cauca en la región del Occidente Antioqueño, 2006.

[6] ANLA, Resolución 0507 de 26 de junio de 2012, 2012.

[7] BID., Evaluación expost del impacto de las medidas de mitigación ambiental en el proyecto hidroelectrico Porce II, 2010.

[8] BID., Evaluación expost de las medidas de mitigación en los proyectos de generación térmica de Samalayuca II y Monterrey III, 2008.

[9] Feng-Rong, Y., Cheng-Haw, L., Wen-Jui K. and Hsin-Fu, Y., The impact of Tunneling construction on the hidrogeological enviroment of Tseng-Wen reservoir trabnsbasin diversion project, Engineering Geology, 103, pp. 39-58, 2009. DOI: 10.1016/j.enggeo.2008.07.012

[10] Knudsen, M.A. and Rich, J., Expost socio-economic assessment of the Oresund bridge, Transport Policy, 27, pp. 53-65, 2013. DOI: 10.1016/j.tranpol.2012.12.002

[11] Anguera, R., The Channel tunnel- An expost economic evaluation, Transportation Research, 40, pp. 291-315, 2006.

[12] Olsson, O.N., Krane, P.H., Rolstad, A. and Veiseth, M., Influence of reference points in expost evaluations of rail infraestructure projects, Transport Policy, 17, pp. 251-258, 2010. DOI: 10.1016/j.tranpol.2010.01.008

[13] Zapata and Tovar, Elaboración de la evaluación expost para proyectos de consultoría e interventoría técnica, administrativa, contable y ambiental, 2012.

[14] Wang, Q., Enviromental impact post evaluation of dams and recervoirs projects: review, Procedia Enviromental Science, 13, pp. 1439-1443, 2012. DOI: 10.1016/j.proenv.2012.01.135

[15] Integral S.A, Informe final de interventoría del proyecto, 2007.

[16] Alcaldía de Medellín, Acuerdo 048 de 2014, 2014.

[17] Gobernación de Antioquia, Informe Técnico Gobernación de Antioquia, Respuesta a descargos formulados mediante Resolución 0358 del 24 de febrero de 2006 del Ministerio de Ambiente, Vivienda y desarrollo Territorial, 2006.

[18] MAVDT., Comunicación 4120-E1-37446 del 28 de abril de 2006. Expediente 678. Construcción de la conexión vial entre los valles de Aburrá y rio Cauca. Resolución 0358 de 24 de febrero de 2006, 2006.

A. N. d. L. A. ANLA, Auto No. 4204, 2015.

[19] Contraloría General de la República, Estado de los recursos naturales y del medio ambiente, 1998.

[20] Espinosa, M.D., Gestión social en megaproyectos: un enfoque integrador. Codesarrollo Gestión Social y Ambiental., 2010.

[21] Typsa-CRA., C., Estudios técnicos adicionales de las autopistas para la prosperidad, Grupo 3. Obra pública. Tramo: Santa Fé – Cañasgordas. Anexo Nº 13: Estudio Hidrogeológico de los Túneles., 2014.

T.C. Ramírez-Sánchez, is BSc. degree in Environmental Eng. from the Universidad de Medellín, Colombia in 2005, a Sp. degree in Project Management from the Universidad Minuto de Dios, Colombia in 2010, and a MSc. in Environment and Development from the Universidad Nacional de Colombia in 2017. From 2009 to the present, she has been dedicated to the planning and construction of projects that include road tunnels.
ORCID: 0000-0002-6104-3122

C.A. Zárate-Yepes, is BSc. degree in Agricultural Economist from the Universidad Nacional de Colombia in 1990, Lawyer from the Universidad de Antioquia, Colombia in 1995, Sp. in Economics and International Business from the Universidad de Medellín, Colombia in 2000, MSc. in Procedural Environmental Law in 2012, candidate for the degree of Dr. of Law from the Universidad de Antioquia, Colombia. Associate professor at the Faculty of Mines of the Universidad Nacional de Colombia, professorship in Environmental and Mining Legislation and Administrative Law. Zárate-Yepes has been environmental director of Isagen and Northwest Territorial Director in National Natural Parks of Colombia, and currently serves as Secretary of the Universidad Nacional de Colombia Medellín. He also currently directs the Research Group 'Policy, Legislation and Environmental Management' (POLYGESTA).
ORCID: 0000-0002-6476-7193

UNIVERSIDAD NACIONAL DE COLOMBIA
SEDE MEDELLÍN
FACULTAD DE MINAS



DYNA
http://dyna.medellin.unal.edu.co/

Microalgae biorefineries: applications and emerging technologies

Néstor David Giraldo-Calderón, Raquel Juliana Romo-Buchelly, Andrés Alonso Arbeláez-Pérez, Danilo Echeverri-Hincapié & Lucia Atehortúa-Garcés

Grupo de investigación de Biotecnología, Sede de Investigación Universitaria, Universidad de Antioquia, Medellín, Colombia.
ndavid.giraldo@udea.edu.co, jromobuchelly@hotmail.com, andresalonsoap@hotmail.com, decheveh@hotmail.com, latehor@gmail.com

Received: November 10th, de 2017. Received in revised form: April 27th, 2018. Accepted: May 23th, 2018

Abstract
Microalgae transform CO_2 into a broad portfolio of biomolecules, and thus should be considered as a valuable biotechnological platform. Despite several research programs and global efforts to establish a sustainable microalgae-based industry, most applications have not transcended academic boundaries. This limitation raises from the high transformation costs when target products are biofuels or fertilizers. Microalgae biorefinery emerges as an alternative to improve economic competitiveness, as Under such a model scope, the process inputs come from industrial waste, while biomass exploitation prioritizes the highest value molecules followed by extraction of less valuable compounds. This review describes a wide range of microalgae exploitation schemes focused on new uses of its constituents, while discussing emerging technologies designed to improve production and efficiencies as well.

Keywords: microalgae; biorefinery; biofuels; fertilizers; active biomolecules.

Biorefinerías de microalgas: aplicaciones actuales y nuevas tecnologías en desarrollo

Resumen
Las microalgas transforman el CO_2 en un amplio portafolio de biomoléculas, por lo cual, son consideradas una valiosa plataforma biotecnológica. A pesar de múltiples programas de investigación y esfuerzos globales para establecer una industria sostenible basada en microalgas, la mayoría de las aplicaciones potenciales no han trascendido las fronteras académicas. Esta limitación se debe a los altos costos en la transformación del producto principalmente cuando se obtiene compuestos económicos como biocombustibles y fertilizantes. La biorefinería de microalgas surge como alternativa para incrementar la competitividad económica. En este modelo, los insumos del proceso provienen de residuos industriales, mientras que la explotación de la biomasa inicia con las moléculas de alto valor y finaliza con los compuestos menos valiosos. En esta revisión se describe un amplio abanico de esquemas de explotación de microalgas enfocado en nuevos usos de sus constituyentes. Además, se exploran las tecnologías emergentes destinadas a aprovechar esta biomasa de una manera más versátil y eficiente.

Palabras clave: microalgas; biorefinería; biocombustibles; fertilizantes; biomoléculas activas.

1. Introduction

Due to the rapid increase in world population during the recent years, industrial and technological development in many different areas such as agriculture, health, transportation and engineering has accelerated. However, the growing need for food, materials and energy has not made many considerations for sustainability, since a large part of the supplies come from non-renewable sources [1]. In particular, the use of fossil fuels has had an environmental impact on a global scale due to the production of greenhouse gases. [2]. From 1850 to present, the atmospheric concentration of CO_2 has increased from 270 ppm to almost 400 ppm and it is expected that by the end of this century it will increase up to 700 ppm [3]. This represents a global concern with respect to ecological, geopolitical and social impacts.

How to cite: Giraldo-Calderón, N.D., Romo-Buchelly,R.J., Arbeláez-Pérez, A.A., Echeverri-Hincapié, D. and Atehortúa-Garcés, L.A., Microalgae biorefineries: applications and emerging technologies DYNA, 85(205), pp. 219-233, June, 2018.

© The author; licensee Universidad Nacional de Colombia.

Biotechnological processes offer the opportunity to redesign traditional industrial practices through implementation of new and more sustainable approaches [4-7]. For instance, fermentation technology was key to the development of first and second generation biofuels (i.e. bioethanol), which are view worldwide as possible renewable energy sources [8]. Despite the obvious advantages associated with biotechnological processes, some of the fundamental global challenges still require additional efforts. One of the most representative and influential research lines developed during the last decades is microalgae biotechnology. These photosynthetic microorganisms are able to transform sunlight, CO_2, inorganic nutrients and water into ingredients to produce food, feed, fertilizers, biofuels, as well as other products. [9]. In these ways, microalgae can help to reduce the atmospheric concentration of greenhouse gases, without compromising food and energy security. Although many technically feasible bioenergy processes can be developed from microalgae today, much work must be done before this approach becomes an economically viable and competitive with an oil-based economy [10].

In that sense, the application of the concept of biorefinery as a platform for the production of microalgal biomolecules has recently been proposed. This process involves different serial operations designed to produce biomass rich in products that can then be extracted, including high-value molecules such as nutraceuticals, biomaterials, and lower value / large market compounds such as ethanol, biodiesel or methanol. [11,12]. Fig. 1 illustrates the ideal biorefinery process based on microalgae.

The biorefinery concept is relatively new, as it was first mentioned as a "green biorefinery" in Germany in 1977 [13]. Basically, this concept is homologous to the well-known oil refinery in which crude oil is fractionated and transformed into a wide spectrum of products [14]. The biorefining process uses similar operations to those used in oil refineries, such as distillation, thermochemical conversion and separation of products, through an integrated process of fractionation and conversion of its components. In addition, similar products are generated in terms of chemical properties and final applications [15]. However, a biorefinery also offers the opportunity to deploy sustainable processes considering biomass as a renewable raw material, since it comes directly or indirectly from photosynthetic products or industrial waste rich in organic matter. [16].

With this review, we aim to highlight some of the most promising alternatives to take advantage of the photo-biochemical reactions carried out by microalgae, from the simplest molecules to more complex and valuable molecules. It also explores some of the emerging and developing technologies that are being applied to overcome the current technical and economic barriers of this industry.

2. Low complexity products derived from microalgae

2.1. Biofuels

The increase in energy demand and advances in biofuel production have drawn increased interest into studies on the use of microalgae as potential sources of third generation biofuels [20].

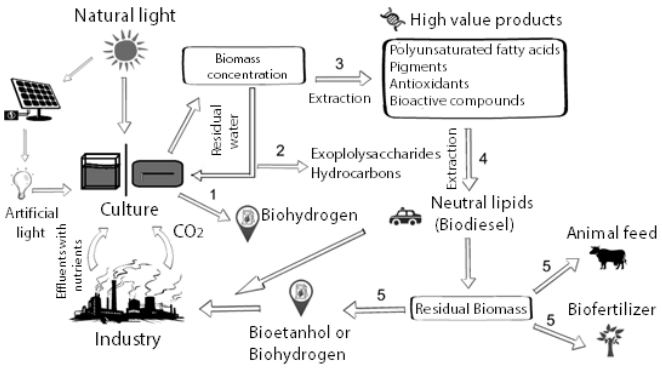


Figure 1. Proposed microalgae cultivation and utilization process including a number of products that could be obtained under the concept of biorefinery. Source: Adapted from [17-19]

Considering the state of the art of microalgae technology and today oil prices, algae cannot currently be a considered representative alternative for fossil fuels in the near future [21]. One of the most relevant bottlenecks is the high cost of infrastructure investment and downstream operations such as concentration, dehydration, transformation and purification. The cost of production for the oil and biodiesel from microalgae is estimated to be USD 3.46 / L and USD 3.69 / L respectively. [22]. By contrast, biodiesel obtained from other crops is less expensive such as soybean biodiesel (USD 0.57 / L - USD 0.67 / L), Fischer-Tropsch biofuels from corn fiber (USD 1.13 / L - USD 1.28 / L) and rapid pyrolysis biodiesel from wood chips (USD 0.58 / L) [22,23].

As a result, several efforts have been made to develop faster and cheaper transformation processes. These technologies are mainly focused on optimization of energy and nutrient utilization efficiency, as well as modification of the cellular characteristics and growth conditions to simplify downstream operations. Although some traditional technologies are well known today, we will briefly describe some of the new approaches that are currently under development.

2.1.1. Biodiesel

Biodiesel is traditionally produced by the transesterification of triglycerides, from a renewable raw material, which react with a short-chain alcohol in the presence of a basic or acid catalyst, yielding alkyl esters of fatty acids biodiesel [17]. Currently, lipids from soy, rapeseed and African palm are the main source for their production. However, biodiesel from these raw materials has had many ethical objections due to its competition with food production, which causes fluctuations in food prices and jeopardizes food security [24].

Microalgae species such as *Desmodesmus* sp., *Monoraphidium* sp., *Chlorella* sp., *Nannochloropsis* sp. show lipid accumulation capacities of 20-40%, exhibiting rapid growth and high biomass production, which implies higher lipid productivity, and thus considered promising candidate strains for industrial biodiesel production. It is estimated that with microalgae capable of accumulating 30% of lipids, 53 t / ha of lipids could be obtained annually, which

higher than obtained from palm oil (3.62 t / ha) or soy (0.4 t/ ha) [24].

Conventional biodiesel production from microalgae consists of concentrating the biomass in suspension, followed by drying, cell wall disruption and lipid extraction. Subsequently, the lipids are transformed into biodiesel by trans-esterification [25]. However, the most energy intensive operation is biomass dehydration [26], and for this reason, some authors have proposed methods for direct transformation of intracellular lipids to biodiesel through processing of wet biomass [27-29]. Another common issue related to microalgal biodiesel is the presence of free fatty acids. These molecules are converted into soaps when they react with alcohols and alkaline catalysts such as potassium hydroxide during transesterification, so the use of acid catalysts such as sulfuric acid has been proposed. [30-32].

This problem is also being addressed by the use of new heterogeneous catalysts that lead to the direct conversion of free fatty acids into biodiesel [33]. Gulde et al. (2017) evaluated a tungsten / zirconium heterogeneous acid catalyst (WO_3 / ZrO_2) to transform lipids from *Scenedesmus obliquus* into biodiesel. The catalytic efficiency of (WO_3/ZrO_2) was compared with a homogeneous acid catalyst and an enzymatic catalyst in terms of conversion efficiency, reaction parameters, energy consumption and reuse. In their experiments, the zirconium catalyst showed a maximum conversion to biodiesel of 94.58%, comparable with the conversion of biodiesel from a homogeneous catalyst and a higher conversion than the enzymatic catalyst. The time required for the heterogeneous catalyst was shorter, while the energy consumption was higher among the selected catalysts [34]. In other studies, Cheng et al. (2016) used graphene oxide (GO) as a solid acid catalyst to transform lipids extracted from wet microalgae into fatty acid methyl esters (FAMEs), through acid-catalyzed transesterification (groups SO_3H) in GO catalysts. The efficiency of lipid conversion to FAME was 95.1% in microwave-assisted transesterification reactions with GO catalyst at 5% by weight at 90 ° C for 40 min [35].

In situ trans-esterification is another alternative to produce biodiesel starting from wet biomass [36]. It has been demonstrated that the average energy consumption for drying and transesterification is 5.42 MJ / L of biodiesel, but being a process based on hydrolysis and esterification of wet biomass, it has a theoretical energy consumption of 1.81 MJ / L [37]. On the other hand, the enzymatic conversion has also been evaluated as an efficient method of biodiesel production. Tian et al. (2016) evaluated a combination of lipase (NS81006 and Novozym435) in a two-stage process, finding a yield of FAMEs of 95% [38]. Kim et al. (2016) used *Aurantiochytrium* sp. KRS101 for enzymatic trans-esterification due to the simplicity of cell disruption associated with its thin cell wall, but this case is an exception because most microalgae present a very resistant cell wall [39].

Normally, microalgae store the lipids intracellularly, and thus it is necessary to both disrupt the cell walls and lyse protoplasts release these molecules. However, such a process is destructive, which implies an irreversible loss of the biological catalyst. Some authors have investigated a novel methodology known as "Milkin*g*" [40-43]. With this method, cells are exposed to biocompatible solvents that can leach intracellular lipids without compromising cell viability [44]. Atta et al. (2016) evaluated an integrated process of production and extraction of lipids of *Chlorella vulgaris* using dodecane and tetradecane as biocompatible solvents in a biphasic system. They found that *C. vulgaris* survives up to four cycles of *in situ* extraction. The highest amount of lipids (1175 mg / l) in the solvent phase was achieved with a maximum lipid recovery ratio of 47 ± 5% during the first cycle when a concentration of 20% dodecane was used as a solvent [45]. They also concluded that the lipids extracted with this system are suitable for the production of biodiesel. Griehl et al. (2014) proposed a continuous extraction system for *Botryococcus braunii SAG 807-1*. The authors developed a method to cultivate the cells and extract hydrocarbons simultaneously, avoiding the operations of high energy demand for filtration, dehydration and cell breakdown [41].

2.1.2. Hydrocarbons

Hydrocarbons are very stable compounds and a substantial source of energy in the world, most of these are naturally found as petroleum [46,47]. However, some studies have shown that cyanobacteria, red algae and dinoflagellates produce noticeable level of hydrocarbons, finding quantities close to 6% of their dry weight. [48-52]. Of particular note, green algae have been shown to have potential for the production of hydrocarbons [50], especially the microalga *Botryococcus braunii*, which can contain up to 86% of hydrocarbons in dry weight basis [53]. *B braunii* has the capacity to produce bio-hydrocarbons similar to petroleum, capable of being transformed into high octane gasoline through hydrocracking processes [54,55]. This strain is classified into three different races according to the type of hydrocarbon it produces. Race *A* produces odd carbon chains (C_{23}-C_{33}) n-alkadienes (mainly diene and triene hydrocarbons); race *B* produces triterpenoid hydrocarbons, such as botryococenes (C_{30}-C_{37}) and methylated squalene (C_{31}-C_{34}), while race L produces licopadiene which is a C_{40} tetraterpene [56].

Diesel, gasoline and jet fuel are mainly composed of C_4-C_{23} alkanes due to their high energy content and hydrophobicity. One of the approaches to producing useful hydrocarbons from microalgae is based on the isoprene molecule. This short-chain volatile hydrocarbon is derived from the first products of the Calvin cycle of photosynthesis, and is produced at substantial rates under certain conditions of environmental stress [57]. The heterologous expression of isoprene synthase in combination with the enzymes of the mevalonic acid pathway has improved the isoprene yield of approximately 2.5 times, compared to that measured in the cyanobacteria transformed only with the isoprene synthase gene. [58].

Another way analyzed by some authors to increase hydrocarbon production is to induce microalgae to produce ethylene. Sakai et al. (1997) studied the conversion of CO_2 to ethylene using *Synechococcus* PCC7942 expressing the ethylene-forming enzyme (EFE) of *Pseudomonas Syringae phaseolicola* PK2. This work showed that this recombinant

cyanobacterium was capable of producing ethylene and 5% of the total carbon incorporated by the cell was transformed into this hydrocarbon.

Regarding the practical evaluations of the fuel obtained from microalgae, there are limited examples that can be mentioned. The company Solazyme has successfully tested the fuel derived from microalgae in real flights. Continental Airlines flew a plane using a fuel mixture with 40% bio-jet microalgae. In addition, the United States Navy tested a mixture with 50% microalgal fuel in a helicopter [59].

2.1.3. Ethanol

Biofuel production from microalgae has been focused on biodiesel, but increasing interest exists for approaches involving bioethanol and biohydrogen as well [20]. This is a feasible technological development because microalgae can reach up to 50% of their dry weight in carbohydrates (glycogen, cellulose and starch), which can then be transformed to ethanol by fermentation [60]. The production of bioethanol is determined by the biochemical composition of the biomass and the biodegradability of the cell wall. Unlike plants, these microorganisms do not produce lignin, which is a recalcitrant aromatic polymer that residue utilization difficult, thus better conversion performance is expected with lignin-free algal biomass [12,61].

Conventional ethanol production is an energy-demanding process due to the multiple steps required, including pretreatment, the cost of enzymes for hydrolysis and bacteria or yeasts for fermentation, in addition to the costs associated with separation and purification [62]. The improvements related to this route are mainly focused on biomass production, hydrolysis and fermentation efficiency. Some authors have reached efficiencies of saccharification from 80% to 98% and a transformation to ethanol of up to 80% [63-65].

Although the transformation of biomass from microalgae to ethanol is usually done by hydrolysis and fermentation, there are new processes in development such as dark fermentation and photofermentation using transgenic strains. Dark fermentation is an alternative method proposed to produce ethanol using microalgae. Basically, the cells are autotrophically grown to accumulate reserve compounds and fermentative metabolism is subsequently redirected to ethanol production by degradation of the intracellular carbohydrate and lipid reserves in the absence of light. This process is still under development with the aim of improving its efficiency [66].

Recently, photofermentation has received special attention because it involves genetically modified organisms and seems to be a promising alternative in terms of efficiency [20]. The cyanobacteria are genetically modified to express the metabolic pathways necessary to convert the photosynthetically-produced compounds into ethanol. In general, microalgae can ferment efficiently, with the additional benefit of using CO_2 as a carbon source [67]. *Synechocystis* sp. PCC 6803 and *Synechococcus elongatus* sp. PCC 7992 were successfully used to produce ethanol [68], and photofermentation processes have been implemented industrially by Algenol Biotech (USA) [69].

Currently, in addition to advances in fermentation technologies for the production of bioethanol and the accumulation capacity of fermentable molecules such as starch, special efforts have been made to reduce production costs. Some such strategies involve the modification or improvement of cellular processes at the metabolic level to increase the efficiency of the transformation or reduce the cost of the raw material [70].

2.1.4. Hydrogen

Hydrogen is considered an attractive future energy source because of its high energy content per unit mass or energy density [71] and its clean combustion that produces only water as byproduct. The ability of certain microalgae to produce molecular hydrogen was discovered more than 70 years ago [72]. Some studies show the potential biohydrogen production of some microalgae for the, due to the high theoretical efficiency they have for the conversion of light, both in aerobic and anaerobic environments [71,73,74].

There are three types of processes used in the production of biohydrogen: direct biophotolysis, photofermetation (indirect biophotolysis) and dark fermentation; however, only the first two can be used by microalgae, which require a light source to produce hydrogen [75]. Current levels of hydrogen production obtained from wild-type microalgae at laboratory scale vary from 0,04 $mLH_2\ L^{-1}\ h^{-1}$ [76] to 7,2 $mLH_2\ L^{-1}\ h^{-1}$ [77]. A known method to increase the hydrogen production capacity is to limit the amount of sulfur. Given this condition the activity of photosystem II gradually decreases and subsequently oxygen release is reduced. Anoxic conditions are favorable for facilitating electron transport with respect to hydrogenase, which gives H_2 as a product [78]. The limitation or starvation of other nutrients such as nitrogen and phosphorus can also favor the production of H_2, however, the limitation of sulfur seems to be the most influential condition [79]. Although this method can be easily implemented on a laboratory scale, it is not easy to scale if industrial production volumes are considered. Some attempts to carry out this process in tubular reactors have been described but always at working volumes lower than 100 L [80]. To improve the efficiency of this process, alternative approaches have been proposed, such as photobioreactors designed to increase cellular efficiency, integrate the production of microalgae with wastewater treatment, and even genetic engineering. [79]. A parallel transformation scheme is based on the production of microalgae biomass by traditional methods to be subsequently used as a substrate in dark fermentation by other hydrogen-producing microorganisms. (*Clostridium, Bacillus, Escherichia, Enterobacter*).

Genetic engineering and “omics” are probably the most promising tools to overcome the current bottlenecks of the microalgae energy industry [81]. *Chlamydomonas reinhardtii*, *Botryococcus braunii* and *Synechococcus elongatus* genomes have been completely sequenced, and there are several genetic transformation and analytic tools that convert them into model organisms for hydrogen production [82-85]. In this direction, some work has been done to seek improved photosynthetic efficiency by

truncation of photoreceptor antennas. This route leads to a reduction in the activity of photosystem II, decreasing the production of oxygen and thus favoring the activity of the hydrogenase. Parallel to this, the effect of light self-attenuation also decreases [84-86]. To carry out the process on a large scale, some authors have proposed to limit the entry of sulphate to the chloroplast by creating mutant strains with altered activity of the sulphate permease at the chloroplast envelope. [86,87].

2.1.5. Syngas

Among the main thermochemical technologies, biomass gasification is considered another promising process and has the best cost / efficiency ratio for the conversion of biomass into bioenergy, including lignocellulosic biomass [90]. Gasification is a technology that converts carbon-based solid material, such as biomass, into syngas for energy purposes through a thermochemical conversion composed of H_2, CO, CO_2 and CH_4 [91-92]. In the gasification process, the algal biomass is normally heated in deficient quantities under low O_2, air or a mixture of both, where the product of the process is an incomplete combustion of the biomass generating synthesis gas, which can improve its yield depending of combustion conditions [93].

In 2014 Duman et al. used residues of *Nannochloropsis oculata* for gasification in fixed bed reactor at temperatures of 600-850ºC with water steam [94]. The results showed a conversion of carbon of 70% and a syngas composed mainly of H_2 (50%) and CO_2 (35%), while CH_4 and CO were also found in proportions of 10 and 6%, respectively. In 2015 Watanabe et al. performed a catalytic gasification with Ni-Fe/Mg/Al to *Botryococcus braunii* biomass residues after extracting their lipid material at a temperature of 750 ºC [95]. The results showed a conversion of 91% of the tar formed in the pyrolysis phase into CO, CO_2 and CH_4 monocarbon gases. The synthesis gas was composed mainly of CO and H_2 in a H_2 / CO ratio of 2.4. The maximum hydrogen yield obtained in this work was 74.7 mmol g-biomass^{-1}, in which they conclude that it is the highest result up to that moment of those reported in the literature.

2.2. Fertilizers

The use of microalgae for agricultural applications is focused on the *in vivo* use of cyanobacteria, which have a high ability to fix atmospheric nitrogen (N_2) and dispose it in the form of NH_3 for the direct assimilation of plants. Although few microalgae have the capacity to fix this nitrogen, their biomass can be used as an ecological input for agricultural crops. In addition, microalgae release growth promoting substances such as auxins and cytokinins, while also solubilizing phosphates, and the inactive biomass provides nutritious organic matter that improves soil fertility and crop quality. The biomass of microalgae can be applied directly, although the previous hydrolysis allows to improve the positive effects of these products on the plants [96]. In flooded crops, especially rice, the positive effect on production attributed to the presence of the freshwater fern *Azolla* and the cyanobacteria *Anabaena azollae* that develop a symbiotic relationship is well known. The annual fixation capacity of atmospheric nitrogen of this system is 350 - 670 kg N fixed / ha, about 12 to 20 times higher than the fixing capacity presented by *A. azollae* isolated [89,90].

Wuang et al. (2016) used the biomass of *Spirulina platensis* as an agricultural biofertilizer in different types of crops. In this work it was observed that the application of *Spirulina* biomass caused an increase in the growth (in dry weight) of the plants *A. rugula* and red spinach in 21.1% and 155.8% respectively, but for Chinese cabbage did not show differences compared to the control [99]. Overall the quality for use as fertilizer depends on the properties of the microalgal biomass and the nutritional requirements of the plant. In order to meet this specific requirement for each plant, the mixture of biomass from different microalga strains has been proposed. This strategy has been useful and effective in achieving the increase in plant growth. In other studies, González et al. (2016) took advantage of the residual water of the microalgae culture, and the cellular extracts obtained after cell disruption and the microalgal biomass was shown to increase germination rates, as well as growth and production of flowers of the tomato plant (*Solanum lycopersicum*) [100].

3. More valuable molecules obtained from microalgae

3.1. Biomass with nutritional value

Algae and human nutrition have been related for centuries, the first record found in South America dates from 13,000 years ago in Chile, where algae were used as food, and their medicinal use was known [101]. Table 1 illustrates the biochemical characterization of some foods and biomass of different microalgae species. The protein content, carbohydrates and lipids in microalgae depend on each species and the culture conditions. Its comparison with the nutritional value of daily food is favorable in terms of quality, quantity and protein intake. Likewise, the profile of fatty acids present in the microalgal biomass is similar to that found in higher plants, which are essential fatty acids for human consumption [102]

Due to its high protein content, which can exceed 70% in dry weight, vitamin B12, minerals and a high content of ɤ linoleic acid, *Arthrospira platensis (Spirulina)* is the most commercialized microalgae species cultivated for use as a dietary supplement [103]. The annual production of *Spirulina* is greater than 5,000 t and the main producers are Japan, USA, India and China [95,96]. In the group of *Chloropyceae*, *Chlorella vulgaris* is the most exploited strain due to its high content of protein (50%), vitamins, carotenoids and β-glucan (immunostimulant). The biomass consumption of these microalgae has gained great interest worldwide as food to treat malnutrition. For its therapeutic properties, *Spirulina* is used for the treatment of cardiovascular diseases, arthritis, anemia and cancer, whereas *Chlorella* is used to treat problems such as gastric ulcers and neurosis [106].

Currently, there is an emerging market of functional foods from microalgae where a biomass or extracted active substance is added to a food matrix to confer additional nutritional characteristics [107].

Table 1.
Biochemical composition of food for daily consumption and biomass of different strains of microalgae

Daily consumption food vs microalgae	Protein (%)	Carbohydrates (%)	Lipids (%)
Meat	43 -74	1	12-34
Milk	22 - 26	35-38	28
Rice	8	77-80	0,6-2
Soya	37	39	20
Arthrospira platensis	63	15	11
Chlorella pyrenoidosa	57 -61	26	2-22
Anabaena cylindrical	43-56	25-30	4-7
Dunaliella salina	57	32	6-9
Isochrysis galbana	29 -35	11-19	4-34

Adapted from [98,101]

Batista et al. carried out various studies on the incorporation of microalgal biomass in different foods such as cookies, pasta and mayonnaise. For example, in one of their investigations, it was observed that the addition *Chlorella vulgaris* and *Haematococcus pluvialis* biomass with high carotenoid content increases the oxidative resistance of the mayonnaise lipids and has an emulsifying effect [99,100].

The use of the different microalgal strains as nutritional products is limited by the legal regulations that must be met so that they can be commercialized. Currently, *A. platensis* and *Chlorella* sp. are currently the only strains globally allowed to be used as food. However, *H. pluvialis* and *Dunalliella* sp. pigments are also produced for use as functional foods. It is expected that in the near future a wide range of strains of microalgae with different nutritional characteristics will be available to expand their use in this field [111].

In animal feed market, especially in aquaculture, the most commonly used strains are *Chlorella, Tetraselmis, Isochrysis, Pavlova, Phaeodactylum, Chaetoceros, Nannochloropsis, Skeletonema* y *Thalassiosira* [103,104].

3.2. Pigments

The main role of pigments in microalgae is the light absorption, which is useful for photosynthesis, in addition they can also provide photoprotection against high light intensity. Among the carotenoids produced by microalgae we can find astaxanthin, β-carotene and xanthophylls such as lutein and fucoxanthin. The most common application of natural pigments relies on food industry due to the benefits for human health related to their antioxidant and pro vitamin A properties, and in lesser amounts are used in the pharmaceutical, textile and cosmetic industries [104]. The global market of carotenoid is covered about 50% by astaxanthin and β-carotene.

Haematococcus pluvialis and *Dunaliella salina* are a worldwide primary source of pigments [107]. *H. pluvialis* is cultivated in two stages, first under ideal conditions for growth and the second under stressful environmental conditions to induce secondary pigments accumulation [114]. It has been reported that this microalga can produce up to 50 mg / g of astaxanthin under light stress, yielding between 0.5% up to 5% of its dry weight [98,106]. Some authors proposed a single stage process with controlled conditions of nutrient supply, especially nitrogen. However, this process has not yet been carried out on a commercial scale. [107,108]. The price of natural astaxanthin for human consumption exceeds the USD 6.000/kg [17,109].

Similarly, *Dunaliella* species accumulate high amounts of β carotene, about 10-14% of their dry weight, and have been shown to increase production in response to high salinity and light intensity [105]. Most of *Dunaliella* cultures are grown in open tanks, taking advantage of their high tolerance to high salt concentrations, which reduces the risks of contamination, and Israel, Australia and the EE. UU are the leading countries in large-scale biotechnological production of β-carotene from microalgae [119].

In relation to lutein, its global market in 2010 was USD 233 million and is likely to increase to USD 308 million by 2018 [120]. Green microalgae produce considerable amounts of this pigment. Chiu et al. (2016) determined that 180 kg of lutein can be obtained annually from 33 tons of biomass / ha of the thermotolerant strains *Desmodesmus sp*. and *Coelastrella sp*. grown in open systems [121]. *Scenedesmus almeriensis* showed a fast growth and high content of lutein for food use and can be produced in closed systems [122], although production in open systems has also been demonstrated [123].

Phycobiloproteins are proteins linked to phycobilins, an accessory photosynthetic pigment, forming a fluorescent active compound present in cyanobacteria and red algae with high potential for application in pharmaceuticals and cosmetics due to its anti-carcinogenic, anti-inflammatory and neuronal protective properties. Phycocyanin (blue) is the main pigment found in *Spirulina* and phycoerythrin is generally found in rhodophyta *Porphyridium*. The accumulation of phycobiliproteins in microalgae occurs due to cellular stress generated mainly by light and carbon source availability, in *Spirulina platensis* the content of phycocyanin varies between 0.11 to 12.7% of the dry weight [124]. These proteins are industrially used as fluorescent marker and in other medical applications [124, 125].

3.3. Polyunsaturated fatty acids

Polyunsaturated fatty acids (PUFAs), especially long-chain fatty acids such as eicosapentaenoic acid (EPA C20:5) and docosahexaenoic acid (DHA C22: 6) are considered essential for humans for being key molecules in health. Due to the low conversion efficiency of the long chains of the omega-3 family, which is about 5% for EPA and less than 0.5% for DHA, whose efficiency decreases even more with age, these fatty acids must be supplemented in the diet [115,116]. Marine microalgae are the primary producers of omega-3 polyunsaturated acids, which are transferred to other organisms through marine food chains. Compared to fish oil, microalgae oil has similar amounts of omega-3, with the advantage of having three times less cholesterol content, has no problems of contamination with heavy metals and toxins, its cultivation is simple and there are some strains that can produce and accumulate a single type of PUFA in a large

percentage, facilitating its extraction and purification [117,118]. For example, *Crypthecodinium cohnii* grows rapidly under heterotrophic conditions, especially when glucose is used as a carbon source and accumulating between 30-50% of DHA dry weight [130].

So far the use *Crypthecodinium cohnii* and *Schizochytrium sp*. are the primary sources of commercial DHA which is sold as a supplement in infant formulas [95,120]. *Phaeodactylum tricornutum* ans *Nannochloropsis* sp. accumulate EPA, but their commercial production is still not very consolidated. The global market for PUFAs, especially DHA and EPA, is growing exponentially [132]. The consumption of DHA / EPA functional products, especially in regions such as North America, Europe and Asia, represented USD 25.4 billion in 2011 and USD 34.7 billion in 2016 [133]. The price per kg of DHA varies between USD 2,000-3,000, offsetting the high processing costs for the production of microalgal DHA [17].

3.4. Functional polysaccharides

The polysaccharides obtained from microalgae have a strong potential for use in biodegradable polymeric materials or natural bioactive products that have shown benefits for human health such as anticoagulants, antithrombotic, antitumor and immunomodulatory agents [134]. Microalgae can produce a large amount of polysaccharides during their life cycle and secrete them into extracellular medium, and in combination with other biomolecules such as proteins, lipids and nucleic acids, providing the backbone for protective biofilms. These exopolysaccharides (EPS) can be recovered from supernatants after concentration of biomass, without generating any additional waste, constituting another byproduct that can be obtained under the concept of biorefinery [123,124]. The structure, physical and chemical characteristic of said polysaccharides determine their biological activity and final application. In the majority of microalgae species, depending on the culture conditions, the synthesized polysaccharides are heteropolymers composed mainly of a combination of sugars such as glucose, xylose and galactose, among others. [132]. For this reason, there is a broad spectrum of bioactive compounds with different molecular weights, ionic charges and properties that can have a high value application in various industries such as mechanical engineering, food or biomedicine.

Additionally, *Chlorella vulgaris* and *Gyrodinium impudicum* have been reported for their ability to generate homopolysaccharides composed of glucose as part of their cell wall and galactose exopolysaccharides, respectively.

4. Sources of microalga biorefinery supplies

The price and availability of the raw materials for the microalgae biomass production represents a significant factor for commercial process, considering that fundamental inputs for its production are carbon, nitrogen, phosphorus and microelements. However, the energy required during incubation, recovery and biomass transformation should also be considered. [125,126].

Bearing in mind the characteristics of the aquatic production system of algae systems coupled to treatment and production to transform industrial wastes into microalgae biomass has raised with the dual purpose of reducing production costs and environmental pollution. The most widely studied alternatives are the capture of CO_2 released in combustion processes and the purification of industrial and domestic wastewater. [61,127,128]. Accordingly, we will describe some of the alternatives that are currently under study to provide some of the process inputs in a more cost-effective manner.

4.1. Carbon

Under autotrophic conditions, microalgae use light and inorganic carbon as sources of energy and carbon, respectively. However, some species can grow mixotropically, assimilating organic carbon sources as well, resulting in higher biomass [129,130]. In spite of this last advantage, traditional organic sources (sugars, organic acids, glycerol etc.) turn out to be costly alternatives if they are used in their pure form and could compromise the quality of the open systems due to the proliferation of contaminants [141]. In that sense, the use of inorganic carbon salts, the use of combustion gases and the implementation of systems coupled with nutrient-rich wastewater treatments have been proposed [131,132].

Some authors have evaluated wastewater from pig farms, as low-cost raw materials, as well as effluents from breweries, and by-products and wastes from the food and agroindustrial industry such as cane molasses, silage juice, serum permeate, among others [129,130,133]. These waste streams have been satisfactorily evaluated and are emerging as low-cost raw materials in the preparation of culture media for microalgae [134,135].

4.2. Nitrogen

Nitrogen is the second most important nutrient for microalgae biomass proliferation, its cellular content can vary from 1% to 14% on a dry weight basis [147]. Algae can assimilate inorganic nitrogen molecules such as NO_3^-, NO_2^-, NO, NH_4^+ and some cyanobacteria, like *Oscillatoria* sp., *Nostoc* sp., *Anabaena* sp., and some diatoms like *Rhizosolenia* sp. and *Hemiaulusare* sp. can fix N_2. They can also assimilate N in organic forms, such as urea, peptone, yeast extract, amino acids and purines [136,137]. In urban wastewater, urine provides 70% nitrogen, 40% phosphorus and 60% potassium of the total load and represents approximately 1% of the volume of water [138,139]. This nitrogen/phosphorous rich residue has been used for cultivation of *Arthrospira platensis* and *Chlorella sorokiniana*.

Markou et al. (2014) proposed a novel alternative ammonium nitrogen recovery using zeolites as an adsorbent material in wastewater with a high content of nitrogen, dissolved solids, dyes and recalcitrant compounds that hinder the passage of light, which inhibit the growth of microalgae [142]. In a subsequent study, Markou et al. (2015)

determined that the microalgae *A. platensis* and *C. vulgaris* can grow with the nutrients provided by the ashes of hatchery residues of birds with high content of phosphorus, potassium, and ammonium recovered from the process of drying this residue. Simultaneously, they proposed the use of these microalgae biomass as feed for birds, creating a closed production system [151].

4.3. Phosphorous

Phosphorus is an essential element for different cellular processes like energy storage and transfer in the form of ATP, as well as biosynthesis of nucleic acids, phospholipids, among many other [148]. The content of this element in the algal biomass is generally from 1.0 to 3.3% by dry weight. The traditional sources of phosphorus at the laboratory level are mainly inorganic salts such as K_2HPO_4, KH_2PO_4, K_3PO_4, $(NH_4)_3PO_4$. Although phosphorus is a minor component of the biomass of microalgae, it is still necessary to identify and evaluate new alternatives for recovery and use of this element, taking into account that for this particular nutrient, there is no a biogeochemical mechanism that recirculate it at the level of the biosphere, in contrast of what happens with carbon and nitrogen [57].

Mukherjee et al. (2015) developed a method of recovering and recycling phosphorus from wastewater generated during rice parboiling using microalgae. They isolated *Cyanobacterium* sp., *Lyngbya* sp., *Anabaena* sp. and *Chlorella* sp. in eutrophic environments and used them as bioremediation agents. After harvesting the biomass, they used them as a biofertilizer to plant rice seedlings and observed that the release of phosphorus by the action of solubilizing organisms is similar between biofertilizer and chemical fertilizer. [152].

Moed et al. (2015) investigated the use of struvite ($MgNH_4PO_4$) as a source of nitrogen, phosphorus and magnesium for the cultivation of *C. vulgaris*. In the tests they used 721 mg / L of struvite for the Bold Basal Medium (BBM). This modified medium can produce 2.85 g / L of lipids suitable for the production of biodiesel, comparable to the use of BBM without struvite [153].

4.4. Micronutrients

These are elements that appear in very small quantities, on the on the micro-level (μg/L), or parts per billion (ppb). These trace elements act as enzymatic cofactors and are important for the biosynthesis of many cellular compounds. The essential micronutrients for microalgae are mainly Mg, S, Ca, Na, Cl, Fe, Zn, Cu, Mo, Mn, B and Co. Many wastewater and industrial by-products all or a large number of these micronutrients and for this reason they are explored as raw material for the cultivation of microalgae. [131,137].

4.5. Energy requirements for biomass production

Considering the processes of obtaining biofuels derived from microalgae, part of the sustainability of the process lies on the favorable nature of the energy balance [154]. Throughout the process of biomass production and byproducts, a series of operations are involved related to incubation, harvesting, processing and purification [155]. The highest proportion of energy consumption is associated with aeration, pumping, centrifugation, harvesting and drying [156].

Shimako et al. (2016) investigated two bioenergy production systems involving biodiesel and biogas, where electricity and heat are generated. These authors found that the net energy balance was negative for the biodiesel production process. However, the energy balance in the biogas production process was positive, which suggests that this could represent an alternative to establish the process to a greater scale [157]. Doušková et al. (2010), proposed a novel process for the use of organic liquid waste in order to simultaneously produce energy and microalgae. They used vinasse as a substrate for the production of biogas in an anaerobic fermentor and later the biogas was fed to photobioreactors as a source of CO_2 for the cultivation of microalgae. Once the biogas is produced, the wastewater from the anaerobic fermentor is processed to obtain an ammonium-based fertilizer that can be used directly as a nitrogen source in the culture medium of the microalgae or for the production of ammonia liquor [158]. Shimako et al. (2016) investigated two bioenergy production systems involving biodiesel and biogas, where electricity and heat are generated. These authors found that the net energy balance was negative for the biodiesel production process, however, the energy balance in the biogas production process was positive, which suggests that this could be the alternative to establish the process to a greater scale [157]. Doušková et al. (2010), proposed a novel process for the use of organic liquid waste in order to simultaneously produce energy and microalgae. They used vinasse as a substrate for the production of biogas in an anaerobic fermentor and later the biogas was fed to photobioreactors as a source of CO_2 for the cultivation of microalgae. Once the biogas is produced, the wastewater from the anaerobic fermentor is processed to obtain an ammonia-based fertilizer that can be used directly as a nitrogen source in the culture medium of the microalgae or for the production of ammonia liquor [158].

Sevigné Itoiz et al. (2012), analyzed the life cycle and energy balance in the production of marine microalgae biomass, finding that in closed systems, the total energy requirement was 923 MJ kg^{-1}, whereas for outdoor cultures it was 139 MJ kg^{-1}. Additionally, these authors affirm that during cultivation, the highest energy consumption occurs in the growth stage. Although the energy balance was negative for both systems under the conditions studied, the authors suggest that outdoor cultivation could be optimized to obtain a positive balance considering the use of raceway or flat panel reactors [159].

In addition to the energy required for the operations described above, light energy can also be considered as a critical input concerning the energy balance. The primary source of PAR (Photosynthetic Active Radiation) photons is sunlight, which is free and available throughout the year in some regions. However, sudden variations in irradiation and change in weather and seasonal conditions can be detrimental

for production. In contrast, the use of artificial sources such as fluorescent tubes, high intensity discharge lamps (HID) and LED lights, offer continuity and stability in the energy supply but can represent prohibitive costs in terms of investment and operation in massive cultures [154]. Under conditions of artificial lighting, Blanken et al. (2013) found that the energy demand during the process can be compared with the enthalpy of combustion of algae biomass (0.477 MJ C-mol^{-1}). They concluded that a PAR light efficiency of 2 μE s^{-1} W^{-1} and a biomass/light yield of 1,0 a 1,5 g-DW E^{-1}, only 4% to 6% of the electric energy supplied initially is conserved in the biomass, so that a large amount of energy is lost in cultures with artificial light and the use of this should be avoided. However, the electrical energy required for the cultivation with artificial light could be generated as 'green' energy by photovoltaic, wind or geothermal [154].

The light quality influences cell growth and biochemistry, so artificial lighting allows manipulation of the final biomass for specific uses. The use of artificial light ensures a better regulation of the flow density of photosynthetic photons, of the photoperiod and the light spectrum in the production of microalgae. LED light can also be used to adjust the biochemical composition of microalgae biomass through individual wavelengths at different intensities or frequencies of light pulses [160]. However, the implementation of artificial lighting feasibility to produce microalgae will be subject to the improvement of the energy efficiency of the sources and their cost of production, as well as the biological improvement of the photosynthetic efficiency.

5. Microalgae biorefinery as an integral system

A biorefinery is defined as a facility which integrates the process of conversion of biomass and suitable equipment to simultaneously produce different products such as fuels, energy and added value chemicals with a minimum of waste and emissions [150,151]. A microalgae platform can easily fit this concept since each species produces a certain amount of lipids, carbohydrates, proteins, among other by-products, so that biomass can be used for different purposes [152,153]. To date, microalgal biorefinery processes in general have concentrated in carrying out the cultivation of microalgae in wastewater for simultaneous water treatment coupled with biomass generation from the microalga-bacteria consortium, which in turn can be allocated to the production of biofuels [165].

With respect to the complete utilization of microalgal biomass, few studies at laboratory scale have been found where different techniques for separating biomass components are evaluated to obtain two or more products in parallel. In general, these investigations point to the use of microalga biomass for lipid extraction and biodiesel production, with the generated residual biomass applied to anaerobic fermentation processes to generate biogas or bioethanol [18]. So far, the number of products obtained under the concept of microalgae biorefinery is up to three to four metabolites, as can be seen in Table 2, which shows a summary of some experimental works that have developed the microalgal biorefinery concept.

Table 2.
Examples of experimental works on microalgae-based biorefinery.

Microalgae	Products	Reference
Chlorella protothecoides	Biodiesel; Pigments	[166]
Chlorella vulgaris	Biodiesel; Biogas	[167]
Chlorella vulgaris	Pigments; Bioelectricity	[168]
Chlorella sp.	Biodiesel; Biogas	[169]
Nanochloropsis sp.	Biodiesel; Biogas; Pigments	[170]
Dunaliella tertiolecta	Biodiesel; Bioethanol	[171]
Dunaliella salina	Biodiesel; Biogas	[172]
Chlamydomonas reinhardtii	Biohydrogen; Biogas	[12]
Spirogyra sp.	Biohydrogen; Pigments	[173]
Phaeodactylum tricornutum	Pigments; Fatty acids	[174]
Scenedesmus obliquus	Biodiesel; Biogas; Fattyacids; Pigments	[175]
Isochrysis galbana	Pigments; fatty acids	[176]
Tetraselmmis suecica	Pigments; fatty acids	[156]

Source: Compilation made by authors and cited in each row

Ferreira et al. (2013) proposed an economic, energy and CO_2 emission analysis comparing two microalgal biorefinery processes. In the first case, supercritical CO_2 was applied for the extraction and fragmentation of lipids and pigments, whereas, in the second case a Soxhlet method is used to obtain lipids. Additionally, residual biomass generated from both extraction process was used for the production of biohydrogen, and these two methodologies were compared with a simple cultivation process for *Nannochloropsis* sp. biomass generation destined for the generation of H_2 [177]. The authors determined that while the extraction by Soxhlet (245 MJ/MJ$_{lip\ prod}$ - 15357 g CO_2/MJ $_{lip\ prod}$) consumed less energy and produced less CO_2 that lipid recovery by supercritical fluids (291 MJ/MJ$_{lip\ prod}$ - 18258 g CO_2/MJ $_{lip\ prod}$), supercritical CO2 allowed fractionation and obtaining of pigments of high added value that do not contribute to an additional expenditure on energy and bring a higher economic benefit. The coupling of the extraction of lipids and the use of residual biomass for an anaerobic process allows the reduction of energy consumption (214-218 MJ/MJ$_{prod}$) and CO_2 emissions (13,982-16,800 g/MJ $_{prod}$) compared to direct use of complete biomass in the production of biogas (9058 MJ/MJ$_{prod}$ - 591,112 g/MJ$_{prod}$). Furthermore, the biorefinery process via supercritical fluid and anaerobic fermentation of the residual biomass has a low production cost of about USD 0.2 / g biomass, which represents approximately half of the cost generated by the biorefinery process via Soxhlet and substantially more economical than the cost of biomass production used only for the production of biogas. Therefore, it is believed that the biorefinery is the only scenario in which the biofuel from microalgae could become economically competitive.

The total, neutral (used for biofuel) and membrane (polyunsaturated fatty acids) lipids were also successfully obtained in the above case studies. Long-chain polyunsaturated fatty acids have a higher price in the pharmaceutical or food market and need to be free of hazardous solvents for such markets, and the extraction of lipids can be done by supercritical fluid with CO_2 and subsequently each type of fatty acid can be concentrated

using the urea complex method. This method entails trapping the the linear chains of saturated fatty acids inside the urea leaving the PUFAs in either solution or centrifuged with a temperature gradient, taking advantage of the differential property at the freezing points of different fatty acids [178].

Currently, most pilot scale publications evaluate biomass production for a single purpose. This is the case of the pilot plant located in Tarragona (Spain), which consists of six photobioreactors operating in batch mode for cultivation of *Nannochloropsis gaditana* for the extraction of lipids [179]. In Brazil, the Petrobras research center launched a pilot plant in 2009 to produce biodiesel from microalgae. Currently, it has the capacity to operate open ponds with a total area of 100 m^2, producing 6,000L of algae culture [180]. The biodiesel factory Grand Valle Bio Energy Ltda., Located in the state of Rio de Janeiro, made some investments in technological development for the cultivation and use of microalgae as an alternative raw material in the production of biodiesel. This company developed the cultivation of the microalga *Monoraphidium* sp. in pilot-scale photobioreactors [181].

Sevrin (1998) carried out experiments in a pilot plant for simultaneous production of microalgae, zooplankton and fish. The main objective of the project was to develop a biological treatment *in situ* for pig manure, which would imply a minimum treatment by the pig farmer, as well as the generation of microalgal biomass. For this, an experimental system of lagoons was established consisting of two algae ponds, two zooplankton ponds and a fish culture pond working in series and in closed circuit. Pollutants like ammonia and the phosphates contained in pig manure are used by the *Chlorococcales* microalgae, which in turn are consumed by the zooplankton *Daphnia magna*, the latter being food for the fish. The operation of this system was analyzed during one year, finding better removals of nitrogen and phosphorus [182]. A promising biorefinery strategy was developed in Almeria (Spain), where an agricultural biofertilizer "Algafert" was created through the cultivation of microalgae in wastewater. The microalga biomass obtained is subjected to enzymatic hydrolysis to release the content of essential amino acids, phytohormones and peptides that can be used more quickly by plants (personal communication from scientists at Almeria).

6. Conclusions

The transformation of light into chemical energy and stable biomolecules through photosynthesis carried out by microalgae is one of the processes with the greatest potential to contribute in solving the global challenges facing humanity today. Although these microorganisms offer a broad portfolio of compounds with diverse applications, only a few of them have transcended the frontiers of research towards commercial production and exploitation. The greatest scientific interest derived from recent academic work with microalgae lies in its exploitation as a source of bioenergy, however, multidisciplinary efforts are still required to make this process sustainable and the application of the biorefinery model provides a plausible outlet. Furthermore, it is necessary to join efforts for the development and innovation in these platforms that allow reductions in production costs, but also the incursion in new markets and the development of new products from the same input.

Acknowledgments

This work was supported by Departamento Administrativo de Ciencia, Tecnología e Innovación - COLCIENCIAS, Universidad de Antioquia - Fondo de Internacionalización and Cervecería Union, under the frame of the project "*Processing of brewery wastes with microalgae for producing valuable compounds*, ELAC2014/BEE-0357".

References

[1] Global CCS Institute. The global status of ccs: 2011; ISBN 9780987186300.

[2] Houghton, J., Global warming, Reports Prog. Phys., 8, pp. 1343-1403, 2005, DOI: 10.1088/0034-4885/68/6/R02.

[3] Collins, M., Knutti, R., Arblaster, J., Dufresne, J.-L., Fichefet, T., Friedlingstein, P., Gao, X., Gutowski, W. J., Johns, T., Krinner, G., Shongwe, M., Tebaldi, C., Weaver, A.J. and Wehner, M., Long-term Climate Change: projections, commitments and irreversibility, Clim. Chang. 2013 Phys. Sci. Basis. Contrib. Work. Gr. I to Fifth Assess. Rep. Intergov. Panel Clim. Chang., pp. 1029-1136, 2013, DOI: 10.1017/CBO9781107415324.024.

[4] Heux, S., Meynial-Salles, I., O'Donohue, M.J. and Dumon, C., White biotechnology: state of the art strategies for the development of biocatalysts for biorefining, Biotechnol. Adv., 33, pp. 1653-1670, 2015, DOI: 10.1016/j.biotechadv.2015.08.004.

[5] Estrela, R. and Cate, J.H.D., Energy biotechnology in the CRISPR-Casera, Curr. Opin. Biotechnol., 38, pp. 79-84, 2016, DOI: 10.1016/j.copbio.2016.01.005.

[6] Malyska, A., Bolla, R. and Twardowski, T., The role of public opinion in shaping trajectories of agricultural biotechnology, Trends Biotechnol., 34, pp. 530-534, 2016, DOI: 10.1016/j.tibtech.2016.03.005.

[7] Corlett, R.T., A bigger toolbox: biotechnology in biodiversity conservation, Trends Biotechnol., 2016, DOI: 10.1016/j.tibtech.2016.06.009.

[8] Naik, S.N., Goud, V.V., Rout, P.K. and Dalai, A.K., Production of first and second generation biofuels: A comprehensive review. Renew. Sustain. Energy Rev. 14, pp. 578-597.

[9] Hlavova, M., Turoczy, Z. and Bisova, K., Improving microalgae for biotechnology — From genetics to synthetic biology, Biotechnol. Adv., 33, pp. 1194-1203, 2015, DOI: 10.1016/j.biotechadv.2015.01.009.

[10] Zhang, T.-Y., Hu, H.-Y., Wu, Y.-H., Zhuang, L.-L., Xu, X.-Q., Wang, X.-X. and Dao, G.-H., Promising solutions to solve the bottlenecks in the large-scale cultivation of microalgae for biomass/bioenergy production, Renew. Sustain. Energy Rev., 60, pp. 1602-1614, 2016, DOI: 10.1016/j.rser.2016.02.008.

[11] Pires, J.C.M., Alvim-Ferraz, M.C.M., Martins, F.G. and Simões, M., Carbon dioxide capture from flue gases using microalgae: engineering aspects and biorefinery concept, Renew. Sustain. Energy Rev., 16, pp. 3043-3053, 2012, DOI: 10.1016/j.rser.2012.02.055.

[12] Mussgnug, J.H., Klassen, V., Schlüter, A. and Kruse, O., Microalgae as substrates for fermentative biogas production in a combined biorefinery concept, J. Biotechnol., 150, pp. 51-56, 2010. DOI: 10.1016/j.jbiotec.2010.07.030.

[13] Schieb, P.-A., Lescieux-Katir, H., Thénot, M. and Clément-Larosière, B., Biorefinery 2030; Springer Berlin Heidelberg: Berlin, Heidelberg; ISBN 978-3-662-47373-3.

[14] Gerardo, M.L., Van Den Hende, S., Vervaeren, H., Coward, T. and

Skill, S.C., Harvesting of microalgae within a biorefinery approach: a review of the developments and case studies from pilot-plants, Algal Res., 11, pp. 248-262, 2015. DOI: 10.1016/j.algal.2015.06.019.
[15] Suganya, T., Varman, M., Masjuki, H.H. and Renganathan, S., Macroalgae and microalgae as a potential source for commercial applications along with biofuels production: A biorefinery approach, Renew. Sustain. Energy Rev., 55, pp. 909-941, 2016. DOI: 10.1016/j.rser.2015.11.026.
[16] Abinandan, S. and Shanthakumar, S., Challenges and opportunities in application of microalgae (Chlorophyta) for wastewater treatment: a review, Renew. Sustain. Energy Rev., 52, pp. 123-132, 2015. DOI: 10.1016/j.rser.2015.07.086.
[17] Li, J., Liu, Y., Cheng, J. J., Mos, M. and Daroch, M., Biological potential of microalgae in China for biorefinery-based production of biofuels and high value compounds, N. Biotechnol., 32, pp. 588-596, 2015. DOI: 10.1016/j.nbt.2015.02.001.
[18] Da Silva, T.L., Gouveia, L. and Reis, A., Integrated microbial processes for biofuels and high value-added products: the way to improve the cost effectiveness of biofuel production, Appl. Microbiol. Biotechnol., 98, pp. 1043-1053, 2014. DOI: 10.1007/s00253-013-5389-5.
[19] Zhu, L.D. and Hiltunen, E., Application of livestock waste compost to cultivate microalgae for bioproducts production: a feasible framework, Renew. Sustain. Energy Rev., 54, pp. 1285-1290, 2016. DOI: 10.1016/j.rser.2015.10.093.
[20] Farias-Silva, C.E. and Bertucco, A., Bioethanol from microalgae and cyanobacteria: a review and technological outlook, Process Biochem., 2015. DOI: 10.1016/j.procbio.2016.02.016.
[21] Valverde, F., Romero-Campero, F.J., León, R., Guerrero, M.G. and Serrano, A., New challenges in microalgae biotechnology, Eur. J. Protistol., 55, pp. 95-101, 2016. DOI: 10.1016/j.ejop.2016.03.002.
[22] Batan, L.Y., Graff, G.D. and Bradley, T.H. Techno-economic and Monte Carlo probabilistic analysis of microalgae biofuel production system, Bioresour. Technol., 219, pp. 45-52, 2016. DOI: 10.1016/j.biortech.2016.07.085.
[23] Swanson, R.M., Platon, A., Satrio, J.A. and Brown, R.C., Techno-economic analysis of biomass-to-liquids production based on gasification, Fuel, 89, 2010. DOI: 10.1016/j.fuel.2010.07.027.
[24] Lam, M.K. and Lee, K.T., Catalytic transesterification of high viscosity crude microalgae lipid to biodiesel : Effect of co-solvent, Fuel Process. Technol., 110, pp. 242-248, 2013. DOI: 10.1016/j.fuproc.2012.12.021.
[25] Rawat, I., Ranjith-Kumar, R., Mutanda, T. and Bux, F., Biodiesel from microalgae: a critical evaluation from laboratory to large scale production. Appl. Energy 103, pp. 444-467, 2013. DOI: 10.1016/j.apenergy.2012.10.004
[26] Liu, J., Lin, R., Nan, Y. and Tavlarides, L.L., Production of biodiesel from microalgae oil (Chlorella protothecoides) by non-catalytic transesterification: Evaluation of reaction kinetic models and phase behavior, J. Supercrit. Fluids, 99, pp. 38-50, 2015. DOI: 10.1016/j.supflu.2015.01.010.
[27] Nan, Y., Liu, J., Lin, R. and Tavlarides, L.L., Production of biodiesel from microalgae oil (Chlorella protothecoides) by non-catalytic transesterification in supercritical methanol and ethanol: process optimization, J. Supercrit. Fluids, 97, pp. 174-182, 2015. DOI: 10.1016/j.supflu.2014.08.025.
[28] Sánchez, E., Ojeda, K., El-Halwagi, M. and Kafarov, V., Biodiesel from microalgae oil production in two sequential esterification/transesterification reactors: pinch analysis of heat integration, Chem. Eng. J., 176-177, pp. 211-216, 2011. DOI: 10.1016/j.cej.2011.07.001.
[29] Kim, J., Yoo, G., Lee, H., Lim, J., Kim, K., Kim, C.W., Park, M.S. and Yang, J.W., Methods of downstream processing for the production of biodiesel from microalgae. Biotechnol. Adv. 3186), pp. 862-876, 2013. DOI: 10.1016/j.biotechadv.2013.04.006
[30] Stacy, C.J., Melick, C.A. and Cairncross, R.A., Esterification of free fatty acids to fatty acid alkyl esters in a bubble column reactor for use as biodiesel, Fuel Process. Technol., 124, pp. 70-77, 2014. DOI: 10.1016/j.fuproc.2014.02.003.
[31] Fu, J., Chen, L., Lv, P., Yang, L. and Yuan, Z., Free fatty acids esterification for biodiesel production using self-synthesized macroporous cation exchange resin as solid acid catalyst, Fuel, 154, pp. 1-8, 2015. DOI: 10.1016/j.fuel.2015.03.048.
[32] Wang, L., Dong, X., Jiang, H., Li, G. and Zhang, M., Ordered mesoporous carbon supported ferric sulfate: a novel catalyst for the esterification of free fatty acids in waste cooking oil, Fuel Process. Technol., 128, pp. 10-16, 2014. DOI: 10.1016/j.fuproc.2014.06.023.
[33] Veillette, M., Giroir-Fendler, A., Faucheux, N. and Heitz, M., Esterification of free fatty acids with methanol to biodiesel using heterogeneous catalysts: from model acid oil to microalgae lipids, Chem. Eng. J., 308, pp. 101-109, 2017. DOI: 10.1016/j.cej.2016.07.061.
[34] Guldhe, A., Singh, P., Ansari, F.A., Singh, B. and Bux, F., Biodiesel synthesis from microalgal lipids using tungstated zirconia as a heterogeneous acid catalyst and its comparison with homogeneous acid and enzyme catalysts, Fuel, 187, pp. 180-188, 2017. DOI: 10.1016/j.fuel.2016.09.053.
[35] Cheng, J., Qiu, Y., Huang, R., Yang, W., Zhou, J. and Cen, K., Biodiesel production from wet microalgae by using graphene oxide as solid acid catalyst, Bioresour. Technol., 221, pp. 344-349, 2016. DOI: 10.1016/j.biortech.2016.09.064.
[36] Salam, K.A., Velasquez-Orta, S.B. and Harvey, A.P., A sustainable integrated in situ transesterification of microalgae for biodiesel production and associated co-product-a review, Renew. Sustain. Energy Rev., 65, pp. 1179-1198, 2016. DOI: 10.1016/j.rser.2016.07.068.
[37] Song, C., Liu, Q., Ji, N., Deng, S., Zhao, J., Li, S. and Kitamura, Y., Evaluation of hydrolysis-esterification biodiesel production from wet microalgae, Bioresour. Technol., 214, pp. 747-754, 2016. DOI: 10.1016/j.biortech.2016.05.024.
[38] Tian, X., Dai, L., Liu, M., Liu, D., Du, W. and Wu, H., Lipase-catalyzed methanolysis of microalgae oil for biodiesel production and PUFAs concentration, Catalysis Communications, 84, pp. 44-47, 2016. DOI: 10.1016/j.catcom.2016.05.026
[39] Kim, K.H., Lee, O.K., Kim, C.H., Seo, J.-W., Oh, B.-R. and Lee, E.Y., Lipase-catalyzed in-situ biosynthesis of glycerol-free biodiesel from heterotrophic microalgae, Aurantiochytrium sp. KRS101 biomass, Bioresour. Technol., 211, pp. 472-477, 2016. DOI: 10.1016/j.biortech.2016.03.092.
[40] Zhang, F., Cheng, L.H., Xu, X.H., Zhang, L. and Chen, H.L., Application of memberane dispersion for enhanced lipid milking from Botryococcus braunii FACHB 357, J. Biotechnol., 165, pp. 22-29, 2013. DOI: 10.1016/j.jbiotec.2013.02.010.
[41] Griehl, C., Kleinert, C., Griehl, C. and Bieler, S., Design of a continuous milking bioreactor for non-destructive hydrocarbon extraction from Botryococcus braunii, J. Appl. Phycol., 27, pp. 1833-1843, 2014. DOI: 10.1007/s10811-014-0472-6.
[42] Hejazi, M.A. and Wijffels, R.H., Milking of microalgae, Trends Biotechnol., 22, pp. 189-194, 2004. DOI: 10.1016/j.tibtech.2004.02.009.
[43] Moheimani, N.R., Matsuura, H., Watanabe, M.M. and Borowitzka, M.A., Non-destructive hydrocarbon extraction from Botryococcus braunii BOT-22 (race B), J. Appl. Phycol., 26, pp. 1453-1463, 2014. DOI: 10.1007/s10811-013-0179-0.
[44] Chaudry, S., Bahri, P.A. and Moheimani, N.R., Proposal of a new pathway for microalgal oil production and its comparison with conventional method. In 12th International Symposium on Process Systems Engineering and 25th European Symposium on Computer Aided Process Engineering; Krist, V., Gernaey, J.K.H. and R.G.B.T.-C.A.C.E., Ed.; Elsevier; 37, pp. 377-382, ISBN 1570-7946.
[45] Atta, M., Bukhari, A. and Idris, A., Enhanced lipid selective extraction from Chlorella vulgaris without cell sacrifice, Algal Res., 20, pp. 7-15, 2016. DOI: 10.1016/j.algal.2016.09.014.
[46] Eroglu, E. and Melis, A., Extracellular terpenoid hydrocarbon extraction and quantitation from the green microalgae Botryococcus braunii var. Showa., Bioresour. Technol., 101, pp. 2359-66, 2010. DOI: 10.1016/j.biortech.2009.11.043.
[47] Hirose, M., Mukaida, F., Okada, S. and Noguchi, T., Active hydrocarbon biosynthesis and accumulation in a green alga, Botryococcus braunii (race A), Eukaryot. Cell, 12, pp. 1132-1141, 2013. DOI: 10.1128/EC.00088-13.
[48] Rezanka, T., Zahradnik, M. and Podojil, M., Hydrocarbons in green and blue-green algae, Folia Microbiol. (Praha)., 27, pp. 450-454, 1982.
[49] Smith, R. and Robley, J.L., Biosynthesis of hydrocarbon in anabaena

variabilis in vivo incorporation of [18-14c] stearate, Biochim. Biophys. Acta - Lipids Lipid Metab., 711, pp. 261-265, 1982.
[50] Nevenzel, J., Biogenic hydrocarbon of marine organism. In Marine Biogenic Lipids, Fats and Oils; 1989, pp. 308-319.
[51] Blummer, M., Guillard, R. and Chase, T., Hydrocarbons of marine phytoplankton, Mar. Biol., 8, pp. 183-189, 1971.
[52] Blummer, M., Mullin, M. and Guillard, R., A polyunsaturated hydrocarbon (3, 6, 9, 12, 15, 18-heneicosahexaene) in the marine food web, Mar. Biol., 6, pp. 226-235, 1970.
[53] Brown, A.C. and Knights, B.A., Hydrocarbon conentent and its relationship to physiological state in the gree alga: botryococcus braunii, Phytochemistry, 8, pp. 543-547, 1969.
[54] Sang, O.Y., Biofuel production from catalytic cracking of palm oil, Energy Sources, 25, pp. 859-869, 2003.
[55] Prado, C.M.R. and Antoniosi-Filho, N.R., Production and characterization of the biofuels obtained by thermal cracking and thermal catalytic cracking of vegetable oils, J. Anal. Appl. Pyrolysis, 86, pp. 338-347, 2009. DOI: 10.1016/j.jaap.2009.08.005.
[56] Metzger, P. and Largeau, C., Botryococcus braunii: a rich source for hydrocarbons and related ether lipids. Appl. Microbiol. Biotechnol. 66, pp. 486-496, 2005.
[57] Venkata-Mohan, S., Nikhil, G.N., Chiranjeevi, P., Nagendranatha Reddy, C., Rohit, M.V., Kumar, A.N. and Sarkar, O., Waste biorefinery models towards sustainable circular bioeconomy: critical review and future perspectives, Bioresour. Technol., 215, pp. 2-12, 2016. DOI: 10.1016/j.biortech.2016.03.130.
[58] Bentley, F.K., Zurbriggen, A. and Melis, A., Heterologous expression of the mevalonic acid pathway in cyanobacteria enhances endogenous carbon partitioning to isoprene, Mol. Plant, 7, pp. 71-86, 2014. DOI: 10.1093/mp/sst134.
[59] Biofuels Digest, United Airlines to operate first US commercial flight on (Solazyme) aviation biofuels. 2011. [online]. Available at: http://www.biofuelsdigest.com/bdigest/2011/11/05/united-airlines-to-operate-first-us-commercial-flight-on-solazyme-aviation-biofuels/.
[60] Ramos, E.A., Domenicali, G. and Bertucco, A., Autotrophic production of biodiesel from microalgae: an updated process and economic analysis, Energy, 76, pp. 807-815, 2014. DOI: 10.1016/j.energy.2014.08.077.
[61] Molinuevo-Salces, B., Mahdy, A., Ballesteros, M. and González-Fernández, C., From piggery wastewater nutrients to biogas: Microalgae biomass revalorization through anaerobic digestion, Renew. Energy, 96, pp. 1103-1110, 2016. DOI: 10.1016/j.renene.2016.01.090.
[62] Ashokkumar, V., Salam, Z., Tiwari, O.N., Chinnasamy, S., Mohammed, S. and Ani, F.N., An integrated approach for biodiesel and bioethanol production from Scenedesmus bijugatus cultivated in a vertical tubular photobioreactor, Energy Convers. Manag., 101, pp. 778-786, 2015. DOI: 10.1016/j.enconman.2015.06.006.
[63] Naveena, B., Armshaw, P., Pembroke, J.T., Gopinath, K.P. Kinetic and optimisation studies on ultrasonic intensified photo-autotrophic ethanol production from Synechocystis sp., Renew. Energy, 95, pp. 522-530, 2016. DOI: 10.1016/j.renene.2016.04.061.
[64] Hwang, J.H., Kabra, A.N., Ji, M.K., Choi, J., El-Dalatony, M.M. and Jeon, B.H., Enhancement of continuous fermentative bioethanol production using combined treatment of mixed microalgal biomass, Algal Res., 17, pp. 14-20, 2016. DOI: 10.1016/j.algal.2016.03.029.
[65] Asada, C., Doi, K., Sasaki, C. and Nakamura, Y., Efficient extraction of starch from microalgae using ultrasonic homogenizer and its conversion into ethanol by simultaneous saccharification and fermentation, Nat. Resour., 3, pp. 175-179, 2012. DOI: 10.4236/nr.2012.34023.
[66] Abo-Hashesh, M., Wang, R. and Hallenbeck, P.C., Metabolic engineering in dark fermentative hydrogen production; theory and practice, Bioresour. Technol., 102, pp. 8414-8422, 2011. DOI: 10.1016/j.biortech.2011.03.016.
[67] Hellingwerf, K.J. and Teixeira de Mattos, M.J., Alternative routes to biofuels: light-driven biofuel formation from CO_2 and water based on the “photanol” approach., J. Biotechnol., 142, pp. 87-90, 2009. DOI: 10.1016/j.jbiotec.2009.02.002.
[68] Savakis, P. and Hellingwerf, K.J., Engineering cyanobacteria for direct biofuel production from CO_2, Curr. Opin. Biotechnol., 33, pp. 8-14, 2015. DOI: 10.1016/j.copbio.2014.09.007.
[69] de Farias-Silva, C.E. and Bertucco, A., Bioethanol from microalgae and cyanobacteria: A review and technological outlook, Process Biochem., 51, pp. 1833-1842, 2015. DOI: 10.1016/j.procbio.2016.02.016.
[70] Gimpel, J.A., Specht, E.A., Georgianna, D.R. and Mayfield, S.P., Advances in microalgae engineering and synthetic biology applications for biofuel production. Curr. Opin. Chem. Biol. 17, pp. 489-495, 2013.
[71] He, M., Li, L. and Liu, J., Isolation of wild microalgae from natural water bodies for high hydrogen producing strains, Int. J. Hydrogen Energy, 37, pp. 4046-4056, 2012. DOI: 10.1016/j.ijhydene.2011.11.089.
[72] Gaffron, H. and Rubin, J., Fermentative and photochemical production of hydrogen in algae, J. Gen. Physiol., pp. 219-240, 1942.
[73] Tamburic, B., Zemichael, F.W., Maitland, G.C. and Hellgardt, K., Parameters affecting the growth and hydrogen production of the green alga Chlamydomonas reinhardtii, Int. J. Hydrogen Energy, 36, pp. 7872-7876, 2011. DOI: 10.1016/j.ijhydene.2010.11.074.
[74] Rashid, N., Rehman, M.S.U., Memon, S., Ur Rahman, Z., Lee, K. and Han, J.I., Current status, barriers and developments in biohydrogen production by microalgae. Renew. Sustain. Energy Rev. 22, pp. 571-579, 2013.
[75] Rahman, S.N.A., Masdar, M.S., Rosli, M.I., Majlan, E.H., Husaini, T., Kamarudin, S.K. and Daud, W.R.W., Overview biohydrogen technologies and application in fuel cell technology, Renew. Sustain. Energy Rev., 66, pp. 137-162, 2016. DOI: 10.1016/j.rser.2016.07.047.
[76] Guan, Y., Deng, M., Yu, X. and Zhang, W., Two-stage photo-biological production of hydrogen by marine green alga Platymonas subcordiformis, Biochem. Eng. J., 19, pp. 69-73, 2004. DOI: 10.1016/j.bej.2003.10.006.
[77] Hacene, H. and Agathos, S.N., Study of hydrogen production by three strains of Chlorella isolated from the soil in the Algerian Sahara, Int. J. Hydrogen Energy, 34, pp. 4941-4946, 2009. DOI: 10.1016/j.ijhydene.2008.10.058.
[78] Burgess, S.J., Tamburic, B., Zemichael, F., Hellgardt, K. and Nixon, P.J., Chapter 3 - Solar-Driven Hydrogen Production in Green Algae; Vol. 75, 2011. ISBN 0065-2164.
[79] Eroglu, E. and Melis, A., Microalgal hydrogen production research, Int. J. Hydrogen Energy, 41, pp. 12772-12798, 2016. DOI: 10.1016/j.ijhydene.2016.05.115.
[80] Touloupakis, E., Benavides, A.M.S., Cicchi, B. and Torzillo, G., Growth and hydrogen production of outdoor cultures of Synechocystis PCC 6803, 18, pp. 78-85, 2016. DOI: 10.1016/j.algal.2016.06.010.
[81] Oncel, S.S., Kose, A., Faraloni, C., Chapter 25 - Genetic optimization of microalgae for biohydrogen production. In; Kim, S.-K.B.T.-H. of M.M., Ed.; Academic Press: Boston; pp. 383-404, ISBN 978-0-12-800776-1.
[82] Banerjee, C., Dubey, K.K. and Shukla, P., Metabolic engineering of microalgal based biofuel production: Prospects and challenges. Front. Microbiol. 7, 2016. DOI: 10.3389/fmicb.2016.00432. eCollection 2016.
[83] De Bhowmick, G., Koduru, L. and Sen, R., Metabolic pathway engineering towards enhancing microalgal lipid biosynthesis for biofuel application - A review. Renew. Sustain. Energy Rev. 50, pp. 1239-1253, 2015.
[84] Brown, D., Jenkins, J., Schmutz, J., Shu, S., Barry, K., Grimwood, J., Chiniquy, J., Sharma, A., Niehaus, T., Weiss, T., Koppisch, A., Fox, D., Dhungana, S., Okada, S., Chappell, J. and Devarenne, T., Draft nuclear genome sequence of the liquid hydrocarbon accumulating green microalga Botryococcus braunii, Race B (Showa), Genome Announc., 5, pp. 1-2, 2017. DOI: 10.1128/genomeA.00215-17.
[85] Blifernez-Klassen, O., Wibberg, D., Winkler, A., Blom, J., Goesmann, A., Kalinowski, J. and Kruse, O., Complete chloroplast and mitochondrial genome sequences of the hydrocarbon oil-producing green microalga Botryococcus braunii Race B (Showa), Genome Announc., 4, pp. e00524-16, 2016. DOI: 10.1128/genomeA.00524-16.
[86] Shin, W.-S., Lee, B., Jeong, B., Chang, Y.K. and Kwon, J.-H., Truncated light-harvesting chlorophyll antenna size in Chlorella vulgaris improves biomass productivity, J. Appl. Phycol., 28, pp. 3193-3202, 2016. DOI: 10.1007/s10811-016-0874-8.
[87] Kirst, H., Garcia-Cerdan, J.G., Zurbriggen, A., Ruehle, T. and Melis, A., Truncated photosystem chlorophyll antenna size in the green

microalga Chlamydomonas reinhardtii upon deletion of the TLA3-CpSRP43 gene., Plant Physiol., 160, pp. 2251-60, 2012. DOI: 10.1104/pp.112.206672.
[88] Melis, A. and Chen, H.C., Chloroplast sulfate transport in green algae - Genes, proteins and effects. Photosynth. Res. 86, pp. 299-307, 2005.
[89] Chen, H.C., Newton, A.J. and Melis, A., Role of SulP, a nuclear-encoded chloroplast sulfate permease, in sulfate transport and H2 evolution in Chlamydomonas reinhardtii. In Photosynthesis Research; 84, pp. 289-296, 2005.
[90] de Lasa, H., Salaices, E., Mazumder, J. and Lucky, R., Catalytic steam gasification of biomass: catalysts, thermodymanics and kinetics, Chem. Rev., 111, pp. 5404-5433, 2011. DOI: 10.1021/cr200024w.
[91] Balat, M., Balat, M., Kirtay, E. and Balat, H., Main routes for the thermo-conversion of biomass into fuels and chemicals. Part 2: gasification systems, Energy Convers. Manag., 50, pp. 3158-3168, 2009. DOI: 10.1016/j.enconman.2009.08.013.
[92] Tiong, L., Komiyama, M., Uemura, Y. and Nguyen, T.T., Catalytic supercritical water gasification of microalgae: Comparison of Chlorella vulgaris and Scenedesmus quadricauda, J. Supercrit. Fluids, 107, pp. 408-413, 2016. DOI: 10.1016/j.supflu.2015.10.009.
[93] Sikarwar, V.S., ZHao, M., Fennell, P.S., Shah, N. and Anthony, E.J., Progress in biofuel production from gasi fi cation Shah d, Prog. Energy Combust. Sci., 61, pp. 189-248, 2017. DOI: 10.1016/j.pecs.2017.04.001.
[94] Duman, G., Uddin, M.A., Yanik, J., Hydrogen production from algal biomass via steam gasification, Bioresour. Technol., 166, pp. 24-30, 2014. DOI: 10.1016/j.biortech.2014.04.096.
[95] Watanabe, H., Li, D., Nakagawa, Y., Tomishige, K. and Watanabe, M.M., Catalytic gasification of oil-extracted residue biomass of Botryococcus braunii., Bioresour. Technol., 191, pp. 452-9, 2015. DOI: 10.1016/j.biortech.2015.03.034.
[96] Romero-García, J.M., Acién-Fernández, F.G. and Fernández-Sevilla, J.M., Development of a process for the production of l-amino-acids concentrates from microalgae by enzymatic hydrolysis, Bioresour. Technol., 112, pp. 164-170, 2012. DOI: 10.1016/j.biortech.2012.02.094.
[97] Wang, R., Peng, B. and Huang, K., The research progress of CO_2 sequestration by algal bio-fertilizer in China, J. CO2 Util., 11, pp. 67-70, 2015. DOI: 10.1016/j.jcou.2015.01.007.
[98] Sevillano, F., Subramaniam, P. y Rodríguez, C., La asociación simbiótica fijadora de nitrógeno atmosférico Azolla- Anabaena. Anuario 1984, Centro de Edafología y Biología Aplicada del CSIC, 11, pp. 233-252, 1986.
[99] Wuang, S.C., Khin, M.C., Chua, P.Q.D. and Luo, Y.D., Use of Spirulina biomass produced from treatment of aquaculture wastewater as agricultural fertilizers, Algal Res., 15, pp. 59-64, 2016. DOI: 10.1016/j.algal.2016.02.009.
[100] Garcia-Gonzalez, J. and Sommerfeld, M., Biofertilizer and biostimulant properties of the microalga Acutodesmus dimorphus, J. Appl. Phycol., 28, pp. 1051-1061, 2016. DOI: 10.1007/s10811-015-0625-2.
[101] Dillehay, T.D., Ramírez, C., Pino, M., Collins, M.B. and Rossen, J., SCIENCE. 2008, pp. 784-786.
[102] Barba, F.J., Food Research International. 2017, pp. 969-970.
[103] Santos, T.D., Freitas, B.C.B. de, Moreira, J.B., Zanfonato, K. and Costa, J.A.V., Development of powdered food with the addition of Spirulina for food supplementation of the elderly population, Innov. Food Sci. Emerg. Technol., 37, pp. 216-220, 2015. DOI: 10.1016/j.ifset.2016.07.016.
[104] Wan-loy, C., Biotechnological applications of microalgae, IeJSME, 20, pp. 243-256, 2012.
[105] Vanthoor-Koopmans, M., Cordoba-Matson, M., Arredondo-Vega, B., Lozano-Ramírez, C., García-Trejo, J. and Rodriguez-Palacio, M., Chapter 8. Microalgae and cyanobacteria production for feed and food supplements. In Biosystems engineering: biofactories for food production in the century XXI, 2014, pp. 253-275, ISBN 9783319038803.
[106] Fradique, Ḿ., Batista, A.P., Nunes, M.C., Gouveia, L., Bandarra, N.M. and Raymundo, A., Incorporation of Chlorella vulgaris and Spirulina maxima biomass in pasta products. Part 1: preparation and evaluation, J. Sci. Food Agric., 90, pp. 1656-1664, 2010. DOI: 10.1002/jsfa.3999.
[107] Gouveia, L., Batista, A.P., Sousa, I., Raymundo, A. and Bandarra, N.M., Microalgae in novel food product, 2008. ISBN 9781604562620.
[108] Mesquita, C., Aplicação de tecnologia enzimática para a obtenção de hidrolisados protéicos de microalgas, Thesis, Universidade Federal do Rio de Janeiro, Brasil, 2013.
[109] Gouveia, L., Raymundo, A., Batista, A.P., Sousa, I. and Empis, J., Chlorella vulgaris and Haematococcus pluvialis biomass as colouring and antioxidant in food emulsions, Eur. Food Res. Technol., 222, pp. 362-367, 2006. DOI: 10.1007/s00217-005-0105-z.
[110] Batista, A.P., Gouveia, L., Bandarra, N.M., Franco, J.M. and Raymundo, A., Comparison of microalgal biomass profiles as novel functional ingredient for food products, Algal Res., 2, pp. 164-173, 2013. DOI: 10.1016/j.algal.2013.01.004.
[111] Aqualgae, Las microalgas como fuente de alimento. [online]. Available at: http://aqualgae.com/es/actualidad/microalgas_fuente_alimento/.
[112] Spolaore, P., Joannis-Cassan, C., Duran, E. and Isambert, A., Commercial applications of microalgae, Bioeng, 101, pp. 87-96, 2006.
[113] Brown, M.R., Barrett, S.M., Volkman, J.K., Nearhos, S.P., Nell, J.A. and Allan, G.L., Biochemical composition of new yeasts and bacteria evaluated as food for bivalve aquaculture, Aquaculture, 143, pp. 341-360, 1996. DOI: 10.1016/0044-8486(96)01286-0.
[114] Gao, X., Wang, X., Li, H., Roje, S., Sablani, S.S. and Chen, S., Parameterization of a light distribution model for green cell growth of microalgae: Haematococcus pluvialis cultured under red LED lights, Algal Res., 23, pp. 20-27, 2017. DOI: 10.1016/j.algal.2016.12.018.
[115] Potvin, G. and Zhang, Z., Strategies for high-level recombinant protein expression in transgenic microalgae: A review, Biotechnol. Adv., 28, pp. 910-918, 2010. DOI: 10.1016/j.biotechadv.2010.08.006.
[116] García-Malea, M.C., Acién, F.G., Del-Río, E., Fernández, J.M., Cerón, M.C., Guerrero, M.G. and Molina-Grima, E., Production of astaxanthin by haematococcus Pluvialis: taking the one-step system outdoors, Biotechnol. Bioeng., 102, pp. 651-657, 2009. DOI: 10.1002/bit.22076.
[117] Del Río, E., Acién, F.G.G., García-Malea, M.C.C., Rivas, J., Molina-Grima, E., Guerrero, M.G., Efficient one-step production of astaxanthin by the microalga Haematococcus pluvialis in continuous culture, Biotechnol. Bioeng., 91, pp. 808-815, 2005. DOI: 10.1002/bit.20547.
[118] Vigani, M., Parisi, C., Rodríguez-Cerezo, E., Barbosa, M.J., Sijtsma, L., Ploeg, M., Enzing, C., Food and feed products from micro-algae: Market opportunities and challenges for the EU, Trends Food Sci. Technol., 42, pp. 81-92, 2015. DOI: 10.1016/j.tifs.2014.12.004.
[119] Andex-Biotechnology DUNALIELLA SALINA. [online] Available at: /www.andexs.org.
[120] Lin, J.H., Lee, D.J. and Chang, J.S., Lutein production from biomass: Marigold flowers versus microalgae, Bioresour. Technol., 184, pp. 421-428, 2015. DOI: 10.1016/j.biortech.2014.09.099.
[121] Chiu, P.H., Soong, K., Chen, C.N.N., Cultivation of two thermotolerant microalgae under tropical conditions: influences of carbon sources and light duration on biomass and lutein productivity in four seasons, Bioresour. Technol., 212, pp. 190-198, 2016. DOI: 10.1016/j.biortech.2016.04.045.
[122] Fernández-Sevilla, J.M., Acién Fernández, F.G. and Molina-Grima, E., Biotechnological production of lutein and its applications, Appl. Microbiol. Biotechnol., 86, pp. 27-40, 2010. DOI: 10.1007/s00253-009-2420-y.
[123] Blanco, A.M., Moreno, J., Campo, J.A. Del, Rivas, J. and Guerrero, M.G., Outdoor cultivation of lutein-rich cells of Muriellopsis sp. in open ponds, Appl. Microbiol. Biotechnol., 73, pp. 1259-1266, 2007.
[124] Manirafasha, E., Murwanashyaka, T., Ndikubwimana, T., Rashid Ahmed, N., Liu, J., Lu, Y., Zeng, X., Ling, X. and Jing, K., Enhancement of cell growth and phycocyanin production in Arthrospira (Spirulina) platensis by metabolic stress and nitrate fed-batch, Bioresour. Technol., 255, pp. 293-301, 2018. DOI: 10.1016/j.biortech.2017.12.068.
[125] Setyaningsih, I., Bintang, M. and Madina, N., Potentially antihyperglycemic from biomass and phycocyanin of Spirulina fusiformis voronikhin by in vivo test, Procedia Chem., 14, pp. 211-215, 2015. DOI: 10.1016/j.proche.2015.03.030.
[126] Gong, Y., Wan, X., Jiang, M., Hu, C., Hu, H. and Huang, F., Metabolic engineering of microorganisms to produce omega-3 very long-chain polyunsaturated fatty acids, Prog. Lipid Res., 56, pp. 19-35, 2014.

[127] Citadin, C., Clonagem e caracterização do gene da enzima Δ 6-dessaturase de ácido graxo e análise de parte do genoma funcional de Thalassiosira fluviatilis, Tesis, Departamento de Biologia Celuelar, Universidade de Brasília, Brasil, 2007.
[128] Conchillo, A., Valencia, I. y Puente, A., Componentes funcionales en aceites de pescado y de alga, Mundo Aliment., pp. 5-10, 2012.
[129] Bianchini, R., Silvana, D. and Maurício, O., Microalgas, produtos e aplicações, Cienc. Rural, pp. 1959-1967, 2006.
[130] Mendes, A., Lopes, T. and Reis, A., DHA Concentration and Purification from the marine heterotrophic microalga Crypthecodinium cohnii CCMP 316 by Winterization and Urea Complexation, Food Technol Biotech, 9862, pp. 38-44, 2007.
[131] Milledge, J.J., Commercial application of microalgae other than as biofuels: a brief review, Rev. Environ. Sci. Bio/Technology, 10, pp. 31-41, 2011. DOI: 10.1007/s11157-010-9214-7.
[132] De Jesus-Raposo, M.F., De Morais, R.M.S.C., De Morais, A.M.M.B., Bioactivity and applications of sulphated polysaccharides from marine microalgae, Mar. Drugs, 11, pp. 233-252, 2013. DOI: 10.3390/md11010233.
[133] Facts, P., Global market for EPA / DHA Omega-3 Products; Rockville, Maryland, 2012, 53 P.
[134] Delattre, C., Pierre, G., Laroche, C. and Michaud, P., Production, extraction and characterization of microalgal and cyanobacterial exopolysaccharides, Biotechnol. Adv., 34, pp. 1159-1179, 2016. DOI: 10.1016/j.biotechadv.2016.08.001.
[135] Soanen, N., Silva, E. Da, Gardarin, C., Michaud, P. and Laroche, C., Bioresource technology improvement of exopolysaccharide production by Porphyridium marinum, Bioresour. Technol., 213, pp. 231-238, 2016. DOI: 10.1016/j.biortech.2016.02.075.
[136] Cheah, W.Y., Show, P.L., Chang, J.-S., Ling, T.C., Juan, J.C., Biosequestration of atmospheric CO_2 and flue gas-containing CO_2 by microalgae., Bioresour. Technol., 184, pp. 190-201, 2014. DOI: 10.1016/j.biortech.2014.11.026.
[137] Acién, F.G., Fernández, J.M., Magán, J.J. and Molina, E., Production cost of a real microalgae production plant and strategies to reduce it, Biotechnol. Adv., 30, pp. 1344-1353, 2012.
[138] Morales-Amaral, M. del M., Gomez-Serrano, C., Acien, F.G., Fernandez-Sevilla, J.M. and Molina-Grima, E., Production of microalgae using centrate from anaerobic digestion as the nutrient source, Algal Res., 9, pp. 297-305, 2015. DOI: 10.1016/j.algal.2015.03.018.
[139] López, C.V.G., Fernández, J.F.S., Fernández, F.G.A., Sevilla, J.M.F. and Grima, E.M., Utilization of the cyanobacteria Anabaena sp. in CO2 removal processes, J. Biotechnol., 100(23), pp. 5904-5910, 2009. DOI: 10.1016/j.biortech.2009.04.070.
[140] Mata, T.M., Melo, A.C., Simões, M. and Caetano, N.S., Parametric study of a brewery effluent treatment by microalgae Scenedesmus obliquus, Bioresour. Technol., 107, pp. 151-158, 2012. DOI: 10.1016/j.biortech.2011.12.109.
[141] Prokop, A., Bajpai, R.K. and Zappi, M.E., Algal biorefineries: volume 2: products and refinery design, 2015, ISBN 9783319202006.
[142] Markou, G., Vandamme, D., Muylaert, K. Using natural zeolite for ammonia sorption from wastewater and as nitrogen releaser for the cultivation of Arthrospira platensis, Bioresour. Technol., 155, pp. 373-378, 2014, DOI: 10.1016/j.biortech.2013.12.122.
[143] Tabernero, A., Martín del Valle, E.M. and Galán, M.A., Evaluating the industrial potential of biodiesel from a microalgae heterotrophic culture: Scale-up and economics, Biochem. Eng. J., 63, pp. 104-115, 2012. DOI: 10.1016/j.bej.2011.11.006.
[144] Olguín, E.J., Dual purpose microalgae-bacteria-based systems that treat wastewater and produce biodiesel and chemical products within a Biorefinery, Biotechnol. Adv., 30, pp. 1031-1046, 2012. DOI: 10.1016/j.biotechadv.2012.05.001.
[145] Gélinas, M., Pham, T.T.H., Boëns, B., Adjallé, K. and Barnabé, S., Residual corn crop hydrolysate and silage juice as alternative carbon sources in microalgae production, Algal Res., 12, pp. 33-42, 2015. DOI: 10.1016/j.algal.2015.08.001.
[146] Espinosa-Gonzalez, I., Parashar, A. and Bressler, D.C., Heterotrophic growth and lipid accumulation of Chlorella protothecoides in whey permeate, a dairy by-product stream, for biofuel production, Bioresour. Technol., 155, pp. 170-176, 2014. DOI: 10.1016/j.biortech.2013.12.028.
[147] Markou, G., Vandamme, D. and Muylaert, K., Microalgal and cyanobacterial cultivation: the supply of nutrients, Water Res., 65, pp. 186-202, 2014. DOI: 10.1016/j.watres.2014.07.025.
[148] Richmond, A., Handbook of microalgal culture: biotechnology and applied phycology/edited by Amos Richmond., Orton.Catie.Ac.Cr, pp. 472, 2004. DOI: 10.1002/9780470995280.
[149] Coppens, J., Lindeboom, R., Muys, M., Coessens, W., Alloul, A., Meerbergen, K., Lievens, B., Clauwaert, P., Boon, N. and Vlaeminck, S.E., Nitrification and microalgae cultivation for two-stage biological nutrient valorization from source separated urine, Bioresour. Technol., 211, pp. 41-50, 2016. DOI: 10.1016/j.biortech.2016.03.001.
[150] Zhang, S., Lim, C.Y., Chen, C.L., Liu, H. and Wang, J.Y., Urban nutrient recovery from fresh human urine through cultivation of Chlorella sorokiniana, J. Environ. Manage., 145, pp. 129-136, 2014. DOI: 10.1016/j.jenvman.2014.06.013.
[151] Markou, G., Depraetere, O., Vandamme, D., Muylaert, K., Cultivation of Chlorella vulgaris and Arthrospira platensis with recovered phosphorus from wastewater by means of zeolite sorption, Int. J. Mol. Sci., 16, pp. 4250-4264, 2015. DOI: 10.3390/ijms16024250.
[152] Mukherjee, C., Chowdhury, R. and Ray, K., Phosphorus recycling from an unexplored source by polyphosphate accumulating microalgae and cyanobacteria-a step to phosphorus security in agriculture, Front. Microbiol., 6, pp. 1-7, 2015. DOI: 10.3389/fmicb.2015.01421.
[153] Moed, N.M., Lee, D.J. and Chang, J.S., Struvite as alternative nutrient source for cultivation of microalgae Chlorella vulgaris, J. Taiwan Inst. Chem. Eng., 56, pp. 73-76, 2015. DOI: 10.1016/j.jtice.2015.04.027.
[154] Blanken, W., Cuaresma, M., Wijffels, R.H. and Janssen, M., Cultivation of microalgae on artificial light comes at a cost. Algal Res. 2, pp. 333-340, 2013.
[155] Yang, J., Xu, M., Zhang, X., Hu, Q., Sommerfeld, M. and Chen, Y., Life-cycle analysis on biodiesel production from microalgae: Water footprint and nutrients balance, Bioresour. Technol., 102, pp. 159-165, 2011. DOI: 10.1016/j.biortech.2010.07.017.
[156] Pérez-López, P., González-García, S., Ulloa, R.G., Sineiro, J., Feijoo, G. and Moreira, M.T., Life cycle assessment of the production of bioactive compounds from Tetraselmis suecica at pilot scale, J. Clean. Prod., 64, pp. 323-331, 2014. DOI: 10.1016/j.jclepro.2013.07.028.
[157] Shimako, A.H., Tiruta-Barna, L., Pigné, Y., Benetto, E., Gutiérrez, T.N., Guiraud, P. and Ahmadi, A., Environmental assessment of bioenergy production from microalgae based systems, J. Clean. Prod., 139, pp. 51-60, 2016. DOI: 10.1016/j.jclepro.2016.08.003.
[158] Doušková, I., Kaštánek, F., Maléterová, Y., Kaštánek, P., Doucha, J. and Zachleder, V., Utilization of distillery stillage for energy generation and concurrent production of valuable microalgal biomass in the sequence: Biogas-cogeneration-microalgae-products, Energy Convers. Manag., 51, pp. 606-611, 2010. DOI: 10.1016/j.enconman.2009.11.008.
[159] Sevigné-Itoiz, E., Fuentes-Grünewald, C., Gasol, C.M., Garcés, E., Alacid, E., Rossi, S. and Rieradevall, J., Energy balance and environmental impact analysis of marine microalgal biomass production for biodiesel generation in a photobioreactor pilot plant, Biomass and Bioenergy, 39, pp. 324-335, 2012. DOI: 10.1016/j.biombioe.2012.01.026.
[160] Schulze, P.S.C., Barreira, L.A., Pereira, H.G.C., Perales, J.A. and Varela, J.C.S., Light emitting diodes (LEDs) applied to microalgal production, Trends Biotechnol., 32, pp. 422-430, 2014. DOI: 10.1016/j.tibtech.2014.06.001.
[161] Yen, H.W., Hu, I.C., Chen, C.Y., Ho, S.H., Lee, D.J., Chang, J.S., Microalgae-based biorefinery - From biofuels to natural products, Bioresour. Technol., 135, pp. 166-174, 2013. DOI: 10.1016/j.biortech.2012.10.099.
[162] Vanthoor-Koopmans, M., Wijffels, R.H., Barbosa, M.J., Eppink, M.H.M., Biorefinery of microalgae for food and fuel, Bioresour. Technol., 135, pp. 142-149, 2013. DOI: 10.1016/j.biortech.2012.10.135.
[163] Cuellar-Bermudez, S.P., Romero-Ogawa, M.A., Rittmann, B.E. and Parra-Saldivar, R., Algae biofuels production processes, carbon dioxide fixation and biorefinery concept, J. Pet. Environ. Biotechnol., 5, 2014. DOI: 10.4172/2157-7463.1000185.
[164] Berntsson, T., Sanden, B., Olsson, L. and Asblad, A., What is a biorefinery? In systems perspectives on biorefineries; Sandén, B., Pettersson, K., Eds.; Chalmers University of Technology: Göteborg;

2014, pp. 16-25. ISBN 978-91-980973-8-2.
[165] Olguín, E.J., Dual purpose microalgae-bacteria-based systems that treat wastewater and produce biodiesel and chemical products within a Biorefinery, Biotechnol. Adv., 30, pp. 1031-1046, 2012. DOI: 10.1016/j.biotechadv.2012.05.001.
[166] Campenni, L., Nobre, B.P. and Santos, C.A., Carotenoid and lipid production by the autotrophic microalga Chlorella protothecoides under nutritional, salinity, and luminosity stress conditions, Bioenergy and biofuels, 97, pp. 1383-1393, 2013. DOI: 10.1007/s00253-012-4570-6.
[167] Collet, P., Hélias-Arnaud, A., Lardon, L., Ras, M., Goy, R.A. and Steyer, J.P., Life-cycle assessment of microalgae culture coupled to biogas production, Bioresour. Technol., 102, pp. 207-214, 2011. DOI: 10.1016/j.biortech.2010.06.154.
[168] Gouveia, L., Neves, C., Sebastião, D., Nobre, B.P., Matos, C.T., Effect of light on the production of bioelectricity and added-value microalgae biomass in a Photosynthetic Alga Microbial Fuel Cell, Bioresour. Technol., 154, pp. 171-177, 2014. DOI: 10.1016/j.biortech.2013.12.049.
[169] Ehimen, E.A., Sun, Z.F., Carrington, C.G., Birch, E.J. and Eaton-Rye, J.J., Anaerobic digestion of microalgae residues resulting from the biodiesel production process, Appl. Energy, 88, pp. 3454-3463, 2011. DOI: 10.1016/j.apenergy.2010.10.020.
[170] Nobre, B.P., Villalobos, F., Barragán, B.E., Oliveira, A.C., Batista, A.P., Marques, P.A.S.S., Mendes, R.L., Sovová, H., Palavra, A.F. and Gouveia, L., A biorefinery from Nannochloropsis sp. microalga - Extraction of oils and pigments. Production of biohydrogen from the leftover biomass, Bioresour. Technol., 135, pp. 128-136, 2013. DOI: 10.1016/j.biortech.2012.11.084.
[171] Lee, O.K., Kim, A.L., Seong, D.H., Lee, C.G., Jung, Y.T., Lee, J.W. and Lee, E.Y., Chemo-enzymatic saccharification and bioethanol fermentation of lipid-extracted residual biomass of the microalga, Dunaliella tertiolecta, Bioresour. Technol., 132, pp. 197-201, 2013. DOI: 10.1016/j.biortech.2013.01.007.
[172] Sialve, B., Bernet, N. and Bernard, O., Anaerobic digestion of microalgae as a necesary step to make microalgae biodiesel sustainable, Biotechnol. Adv., 27, pp. 409-416, 2009. DOI: 10.1016/j.biotechadv.2009.03.001.
[173] Pacheco, R., Ferreira, A.F., Pinto, T., Nobre, B.P., Loureiro, D., Moura, P., Gouveia, L. and Silva, C.M., The production of pigments & hydrogen through a Spirogyra sp. biorefinery, Energy Convers. Manag., 89, pp. 789-797, 2015. DOI: 10.1016/j.enconman.2014.10.040.
[174] Gilbert-López, B., Barranco, A., Herrero, M., Cifuentes, A. and Ibáñez, E., Development of new green processes for the recovery of bioactives from Phaeodactylum tricornutum, Food Res. Int., 99, pp. 1056-1065, 2017. DOI: 10.1016/j.foodres.2016.04.022.
[175] Patnaik, R. and Mallick, N., Utilization of Scenedesmus obliquus biomass as feedstock for biodiesel and other industrially important co-products: an integrated paradigm for microalgal biorefinery, Algal Res., 12, pp. 328-336, 2015. DOI: 10.1016/j.algal.2015.09.009.
[176] Gilbert-López, B., Mendiola, J.A. and Fontecha, J., Downstream processing of Isochrysis galbana : a step towards microalgal biorefinery, Green Chem., 17, pp. 4599-4609, 2015. DOI: 10.1039/c5gc01256b.
[177] Ferreira, A.F., Ribeiro, L.A., Batista, A.P., Marques, P.A.S.S., Nobre, B.P., Palavra, A.M.F., da Silva, P.P., Gouveia, L. and Silva, C., A biorefinery from Nannochloropsis sp. microalga - Energy and CO_2 emission and economic analyses, Bioresour. Technol., 138, pp. 235-244, 2013. DOI: 10.1016/j.biortech.2013.03.168.
[178] Tang, S., Qin, C., Wang, H., Li, S. and Tian, S., Study on supercritical extraction of lipids and enrichment of DHA from oil-rich microalgae, J. Supercrit. Fluids, 57, pp. 44-49, 2011. DOI: 10.1016/j.supflu.2011.01.010.
[179] Nurra, C., Torras, C., Clavero, E., Ríos, S., Rey, M., Lorente, E., Farriol, X. and Salvadó, J., Biorefinery concept in a microalgae pilot plant. Culturing, dynamic filtration and steam explosion fractionation, Bioresour. Technol., 163, pp. 136-142, 2014. DOI: 10.1016/j.biortech.2014.04.009.
[180] Bacellar-Mendes, L.B., Vermelho, A.B., Allelopathy as a potential strategy to improve microalgae cultivation, Biotechnol. Biofuels, 6, pp. 152-153, 2013. DOI: 10.1186/1754-6834-6-152.
[181] Díaz, G.C., Cruz, Y.R., Carliz, R.G., Paula, R.C.V. De, Aranda, D.A.G., Dario, M.A.G., Marassi, G.S. and Furtado, N.C., Cultivation of microalgae Monoraphidium sp., in the plant pilot the Grand Valle bio energy, for biodiesel production, Nat. Sci., 7, pp. 370-378, 2015.
[182] Sevrin-Reyssac, J., Biotreatment of swine manure by production of aquatic valuable biomasses, Agric. Ecosyst. Environ., 68, pp. 177-186, 1998. DOI: 10.1016/S0167-8809(97)00070-4.

N.D. Giraldo-Calderón, received the BSc. Eng Biological Engineering in 2011 from the Universidad Nacional de Colombia, Medellín. He has worked in public and private funded projects on microalgae biotechnology as a research associate and currently is working on his PhD. in Biotechnology at the Universidad de Antioquia, Medellín, Colombia, being photobiology applied to microalgal systems his main focus of study.
ORCID: 0000-0001-9017-1265.

R.J. Romo-Buchelly, received a BSc. Eng. Biological Engineering in 2011, a Sp. degree in Biotechnology in 2013, and a MSc. degree in Technology in chemistry and biochemistry process in 2016. She works focuses on biotechnology with emphasis on microalgae culture and the use of microalgae biomass. She is currently a researcher in the biotechnology group of Universidad de Antioquia, Colombia.
ORCID: 0000-0002-1681-8670

A.A. Arbeláez-Pérez, works at the Biotechnology Group since 2012, after having THE BSc. graduated in food engineering in 2014. He made a student internship as a “Joven Investigador Colciencias” in 2015. Currently works as a research associate in the microalgae line. He is currently a master student in the biotechnology group of Universidad de Antioquia, Colombia.
ORCID: 0000-0002-2922-8055

D. Echeverri-Hincapié, received the BSc. Eng Biological Engineering in 2016 from the Universidad Nacional de Colombia, Medellín, Colombia. He has worked in microalgal biotechnology with emphasis in microalgae culture and biorefinery and is currently a researcher at the Universidad de Antioquia, Colombia.
ORCID: 0000-0001-7522-9289

L. Atehortúa-Garcés, founded the Biotechnology Group in 2000, she is BSc. in Biologist from Universidad de Antioquia, Colombia and received her PhD. in Biology in City University of New York, USA, in 1981. She is currently the coordinator of Biotechnology Group and professor at the Universidad de Antioquia, Colombia. Lucía has been involved in applied biotechnology and bioeconomy programs during her entire career.
ORCID: 0000-0001-5502-1288

UNIVERSIDAD NACIONAL DE COLOMBIA
SEDE MEDELLÍN
FACULTAD DE MINAS



DYNA
http://dyna.medellin.unal.edu.co/

Evaluation of turbidity and dissolved organic matter removal through double filtration technology with activated carbon

Patricia Torres-Lozada, Claudia Patricia Amezquita-Marroquín, Karen Daniela Agudelo-Martínez, Natalia Ortiz-Benítez & David Santiago Martínez-Ducuara

Study and Control of Environmental Pollution (ECCA) Research Group, Engineering Faculty, Universidad del Valle, Cali, Colombia.
patricia.torres@correounivalle.edu.co, claudia.amezquita@correounivalle.edu.co, karen.agudelo@correounivalle.edu.co,
natalia.ortiz.benitez@correounivalle.edu.co, david.martinez.ducuara@correounivalle.edu.co

Received: June 06th, 2017. Received in revised form: February 12th, 2018. Accepted: March 15th, 2018.

Abstract
The decrease of physicochemical and microbiological quality of surface supply source for human consumption, requires specific complementary treatments to ensure the supply of safe drinking water. This study evaluated the double filtration technology with two types of Granular Activated Carbon (GAC: vegetable-coconut and mineral-bituminous shells, respectively), to determine its influence in reducing turbidity and mainly dissolved organic matter (UV_{254}). We used filtered water from a Conventional Water Treatment Plant (WTP) and the second filtration stage were made using continuous flow gravity columns at laboratory-scale with different percentages of GAC:sand (100:0, 80:20, 50:50, 30:70, and 0:100). While the sand filter presented the best turbidity removal efficiency, the CAG filters were more efficient at UV_{254} removal, being most efficient the filters with greater percentage of GAC. The results demonstrate that the use of double filtration technology with GAC can be an efficient alternative for the removal of organic matter to obtain safe drinking water.

Keywords: drinking water; granular activated carbon; double filtration; organic material; filter medium; turbidity.

Evaluación de la remoción de turbiedad y materia orgánica disuelta mediante la tecnología de doble filtración con carbón activado

Resumen
La reducción de la calidad fisicoquímica y microbiológica de las fuentes superficiales de suministro para consumo humano, requiere utilizar tratamientos complementarios para garantizar el suministro de agua segura. En este estudio se evaluó la doble filtración con carbón activado granular (CAG: vegetal- cáscara de coco y mineral-bituminoso), para evaluar la reducción de turbiedad y materia orgánica disuelta (UV_{254}). Se empleó agua filtrada de una Planta de Tratamiento Convencional–PTAP; la segunda filtración se realizó en columnas de laboratorio de flujo continuo a gravedad, con porcentajes CAG:arena 100:0, 80:20, 50:50, 30:70, 0:100. Mientras el filtro de arena fue más eficiente en remoción de turbiedad, las configuraciones con CAG lo fueron en la remoción de $UV_{254,}$ siendo más eficientes los filtros con mayor porcentaje de CAG. Los resultados demuestran que la doble filtración empleando CAG, puede ser una alternativa eficiente para la remoción de materia orgánica y la producción de un agua potable segura.

Palabras clave: agua potable; carbón activado granular; doble filtración; materia orgánica; medio filtrante; Turbiedad.

1. Introduction

In developing countries, the majority of sources for drinking water supply systems are affected by natural phenomena and anthropogenic effects that deteriorate their quality [1]. Limitations on the efficiencies of the production processes result in drinking water that complies with established quality standards [2-4]. Various treatment technologies, which use several combinations of processes, are available for the purification of surface water, including coagulation/flocculation, sedimentation, filtration, disinfection and pH stabilization [2,5,6].

Filtration is a process that is always used in water treatment technology. It consists of the separation or removal of particles

How to cite: Torres-Lozada, P., Amezquita-Marroquín, C.P., Agudelo-Martínez K.D., Ortiz-Benítez N. and Martínez-Ducuara, D.S., Evaluation of turbidity and dissolved organic matter removal through double filtration technology with activated carbon. DYNA, 85(205), pp. 234-239, June, 2018.

© The author; licensee Universidad Nacional de Colombia.

in a liquid by flowing through a porous bed [2,5]. Conventional treatment technology with sand or sand and anthracite rapid filters has allowed compliance with Colombian Resolution 2115 of 2007, which established a maximum permissible turbidity in drinking water of 2 NTU [7]. However, several authors recommend that to ensure the minimum risk of drinking water, the turbidity of the filtered water should be in the range of 0.1 to 0.5 NTU to eliminate or deactivate pathogenic microorganisms [3,8,9].

Several typical filtration systems do not have the ability to effectively remove turbidity and dissolved organic matter, and it is necessary to evaluate other treatments to improve the quality of drinking water [3]. Double filtration is a treatment technology that consists of a first stage of filtration in which the water flows through a granular medium with a high capacity of solids removal. This process reduces the turbidity and is followed by a second stage of filtration for polishing [10]. In the last stage, mineral or vegetal GAC has been used as a filtration medium for water purification due to its characteristics, which allow it to remove turbidity and dissolved organic matter and increase the treatment efficiency [11-14].

Turbidity is a key parameter for evaluating the efficiency of filtration because it is simple and rapid to quantify, and it is indirectly related to the particles in the water, which in turn are associated with bacteria, protozoa and viruses [15,16]. Organic matter is associated with aesthetic impacts on water quality, with the formation of disinfection byproducts that may become carcinogenic and/or with synthetic organic compounds (e.g., pesticides, personal care products, pharmaceuticals) that are difficult to remove with conventional drinking water treatments [6,17].

GAC is one of the most widely used adsorbents in water treatment [18]. According to Wiecheteck et al. [19] and Silva et al. [20] double filtration has several favorable characteristics, such as greater solids retention and a more effective response in the removal of organic matter. Authors such as Bundy et al. [21] have used conventional sand and anthracite filtration and secondary filtration with GAC and achieved a turbidity reduction to less than 1 NTU and a removal efficiency of pharmaceutical compounds on the order of 95%. Silva et al. [20] also used GAC to eliminate cyanobacteria, color, organic matter and halogenated organic by-products. Pham et al. [22] used coconut husk GAC and obtained removal efficiencies of turbidity (97%) and organic matter (COD:68%) and a pesticide adsorption capacity greater than 50%. Thiel et al. [17] concluded that sand:GAC filters are effective at removing precursor organic matter from disinfection products and generate effluents with turbidities less than 0.3 NTU.

Based on these investigations, this study evaluates at laboratory scale, the secondary filtration with different proportions of mineral and vegetal activated carbon using filtered water from a conventional water treatment plant in the city of Cali. The second filtration was evaluated to determine its effect on the removal of turbidity and dissolved organic matter, which were measured as UV_{254}.

2. Matherials and methods

2.1. Experimental unit

Twenty-four laboratory glass filters with a nominal diameter of 25 mm, an internal diameter of 19 mm and a length of 40 cm were used. The lower part of the filter was supported by a metal mesh to prevent clogging of the filter outlet and loss of the filter medium, which was 15 cm high [5,23,24]. To provide a hydraulic load to ensure that water was present throughout the filter medium, the effluent was collected through a silicone hose attached to the bottom of the filter. The other end of the hose was located above the upper part of the filter medium [5]. The filtration columns were placed in a support structure, which allowed proper operation of the filters (Fig. 1).

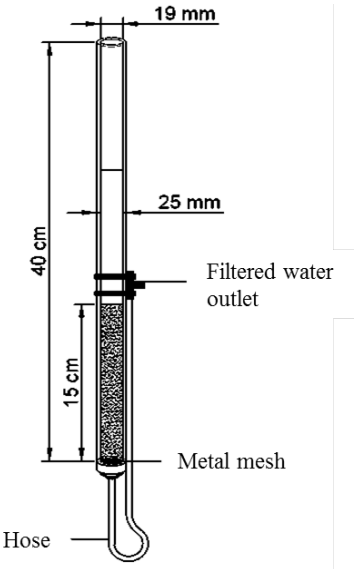


Figure 1. Experimental unit
Source:

Table 1.
Quality characteristics of the filtered water used for the study.

PM filtered	pH (units)	Color (UPC)	Conductivity (µs/cm)	Turbidity (NTU)	UV_{254} (cm^{-1})
WTP water	5.87	3	156.3	0.44	0.034

Source:

The experimental unit was fed by a multi-partition distribution system. Gravity flow was distributed to each laboratory filter through silicone hoses, which had flow control valves at their ends to allow the flow to be distributed through constant dripping to the filters. This distribution system was supplied from a temporary storage tank in which the water level was kept constant to avoid variations in the inlet flows to the filters.

2.2. Water used in the study

The laboratory-scale study used filtered water from the Puerto Mallarino WTP, which had undergone coagulation, flocculation, clarification and downstream sand and anthracite filtration [25,26]. Table 1 shows the characteristics of the filtered water.

2.3. Filter media

The characteristics of the GAC and sand filter media used in the test are given in Table 2.

Table 2.
Characteristics of the filter media used in the test.

Characteristics	GAC Media		Sand Medium
Raw material	Coconut shell	Bituminous coal	Silica
Amount of iodine (mg/g)	900	850	--
Ash (% by weight)	5	8	--
Bulk Density (g/cc)	0.48	0.58	1.5
Effective Size (mm)	0.8-1.2	0.55-0.75	0.61
Coefficient of Uniformity	2.1	1.9	1.5

Source:

Table 3.
Configurations of GACVEG, GACMIN and sand filter media used in the study.

Configuration	GACVEG	Sand
100VEG	100% (15 cm)	0%
80VEG	80% (12 cm)	20% (3 cm)
50VEG	50% (7.5 cm)	50% (7.5 cm)
30VEG	30% (3 cm)	70% (12 cm)
Configuration	**GACMIN**	**Sand**
100MIN	100% (15 cm)	0%
80 MIN	80% (12 cm)	20% (3 cm)
50 MIN	50% (7.5 cm)	50% (7.5 cm)
30 MIN	30% (3 cm)	70% (12 cm)
Configuration	**CORE**	**Sand**
SAND	0%	100% (15 cm)

Source:

Table 4.
Variables and methods used to characterize water during the test.

Variables	Units	Method
pH	Units	4500-H+-B
Conductivity	µs/cm	2510-B
Turbidity	NTU	2130-B
UV_{254}	cm-1	5310-B

Source:

The configurations correspond to the height proportions of the filter media that consist of GACVEG and sand, GACMIN and sand and only sand. These configurations are presented in Table 3 and were analyzed in triplicate.

2.4. Operation of the experimental units and process monitoring

Filtered water from the WTP, was distributed to each laboratory filters at a constant filtration rate of 61 m^3/m^2d for a flow rate of 12 ml/min and a filtration time of six hours [5, 24]. The follow-up variables are shown in Table 4 and were measured every 5 minutes during the first half hour of filtration. Subsequently, they were measured at 10 minute intervals for the remainder of the first three hours and every 15 minutes in the last three hours of the test. The physical and chemical variables were measured according to the guidelines established in the standard method [27].

3. Results and discussion

3.1. Influence on turbidity removal

Turbidity is an indirect parameter that indicates the potential of microbiological risk in drinking water. Low values of turbidity

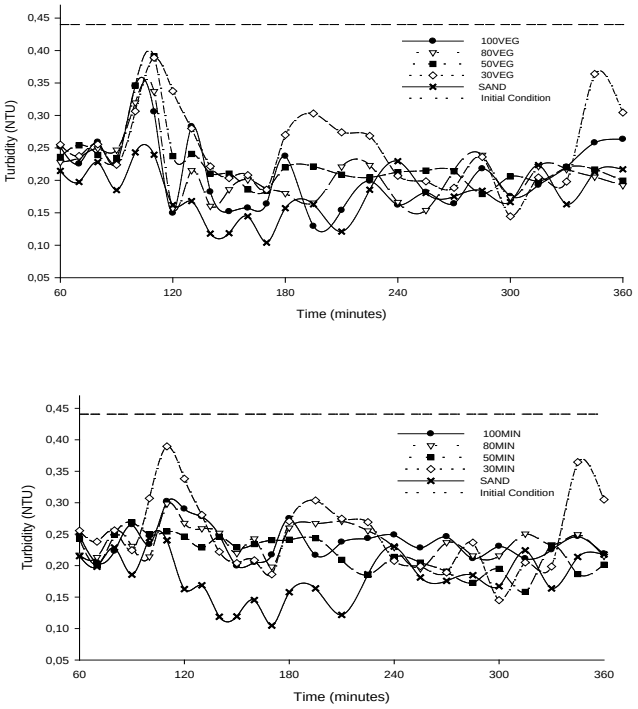


Figure 2. Behavior of the turbidity over time for the two types of activated carbon and sand with their respective configurations.
Source:

in filtered water (<0.30 NTU) indicate greater efficiencies in the removal of protozoa (Giardia and Cryptosporidium) during filtration and favor the elimination of bacteria and viruses during disinfection [15]. Fig. 2 shows the behavior of the turbidity during the test for the two types of carbon (vegetable/mineral) and sand with their respective filter media configurations.

Fig. 2 shows that all of the media configurations resulted in similar turbidity behavior as a function of time. The turbidity values are below the initial turbidity value obtained in the first filtration stage. As indicated by Wiecheteck et al. [19] and Silva et al. [20], double filtration provides greater turbidity removal than conventional filtration.

Ninety-seven percent of the data for all configurations resulted in turbidity values less than 0.3 NTU, which is the threshold value of the WHO [2] and the EPA [15] before disinfection to eliminate chlorine-resistant pathogens and ensure the effective elimination of Giardia, Cryptosporidium, and other material. All of the turbidity values measured for each configuration in this study complied with the national regulations for drinking water (<2 NTU) [7].

Graese et al. [28] founded turbidity <0.2 NTU in the effluent with GAC filtration, which is consistent with this study. The median values for the filters with the GACVEG configurations were between 0.199 and 0.238 NTU, those for the GACMIN filters were between 0.206 and 0.236 NTU, and those with sand had the lowest value of 0.181 NTU.

The median values obtained for each configuration show that the configuration with the sand filter resulted in the best reduction of turbidity; however, all configurations with GAC provided effective turbidity removal.

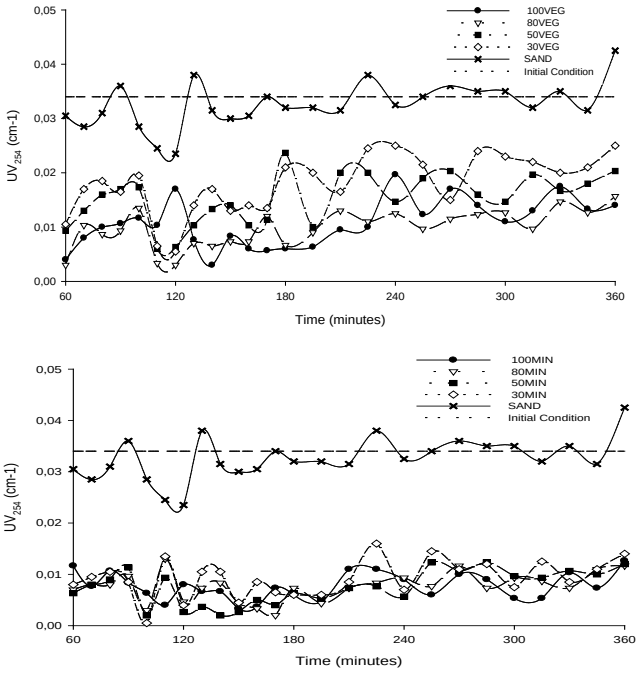


Figure 3. Behavior of UV_{254} over time for the two types of activated carbon and their respective configurations.
Source:

Although the GAC configurations showed lower turbidity removal than the sand filter, these results demonstrate that the implementation of activated carbon ensured the quality of the final effluent.

3.2. Influence on the removal of organic matter measured as UV_{254}

Organic matter is an important constituent of water that affects the performance of treatments in drinking water processes and the quality of drinking water. As a result, it requires the extensive use of coagulants, oxidants and disinfectants in addition to being a precursor to the formation of disinfection byproducts [29]. Several studies have used the UV_{254} absorbance test as a parameter to evaluate the efficiency of the GAC filtration process for the removal of dissolved organic matter, which is capable of absorbing UV light [6, 20, 29]. Figure 3 shows the behavior of UV_{254} during the tests for the two types of carbon (vegetable/mineral) and sand with their respective filter medium configurations.

Fig. 3 shows that the configurations with GACMIN and GACVEG were below the UV_{254} absorbance value reported in the first filtration stage, whereas the sand filter remained very similar to the initial UV_{254} value. Similar results were obtained by other studies, which concluded that sand does not effectively remove compounds associated with organic matter [30,31].

Median values of UV_{254} between 0.010 and 0.019 cm^{-1} were obtained with the GACVEG configurations, median values between 0.007 and 0.008 cm^{-1} were obtained with the GACMIN configurations, and a median of 0.032 cm^{-1} was obtained with the sand. The results indicate that the sand did not significantly affect the reduction of organic matter because its values oscillated near the initial absorbance of 0.034 cm-1, and the configurations with GACMIN had a greater effect. The GAC filters clearly yielded a reduction of organic compounds as measured by UV_{254}. Therefore, the use of granular activated carbon as a filter media is recommended not only for reducing odor and flavor but also in the adsorption of organic compounds [9].

Silva et al. [20] demonstrated the removal of UV_{254} using GAC in double filtration, and Pham et al. [22] achieved removal efficiencies of organic matter greater than 68%. These results were similar to those found in this study; the removal percentages for the GACVEG configurations ranged from 46% to 72%. The GACMIN configurations resulted in the highest removal percentages, between 75% and 78%, whereas the sand configuration only removed 6% of the organic matter.

The results indicate that filters with GAC in double filtration technology can remove organic substances, which reduces the possible risk associated with the formation of disinfection byproducts [17,32].

Additionally, Kim and Kang [33] found that replacing sand filters with dual-medium GAC-sand filters represents an ideal choice for the removal of organic matter compared to turbidity removal. This was confirmed by the results of this study, which showed small differences in the turbidity decrease between the GAC and sand configurations, whereas the configurations of the GAC filters eliminated organic matter more effectively than the sand filter alone.

4. Conclusions

Although the sand filter achieved a higher turbidity removal efficiency, all configurations with GAC provided effective removal that complied with the limit of 0.3 NTU recommended by the WHO and EPA to mitigate microbiological risk and with the limit of <2 NTU provided by Colombian Resolution 2115 of 2007.

For organic matter, which was measured as UV_{254}, all configurations containing GAC were more efficient than the sand, which removed only 6% of the organic matter. A greater proportion of GACVEG resulted in a greater percentage of reduction of UV_{254} in the effluent (100VEG: 70%, 80VEG: 70%, 50 VEG: 53%, 30VEG: 46%), and GACMIN obtained similar and higher efficiencies than GACVEG (100MIN: 78%, 80MIN: 77%, 50MIN: 77%, 30MIN: 75%).

Although Resolution 2115 of 2007 does not provide a maximum allowable amount of organic matter in drinking water in terms of UV_{254}, the removal efficiencies for organic matter of the configurations with GAC were greater, which confirmed that GAC is suitable as a filter medium not only for the reduction of odor and flavor but also in the adsorption of organic compounds.

Double filtration has several favorable characteristics, including a greater retention of solids and a more effective removal of organic matter, which make it an efficient technology to ensure the quality of the final effluent, minimize risk and reduce the limitations in the treatment of water for human consumption.

Acknowledgements

The authors thank the Universidad del Valle and to the Department of Science, Technology and Research (COLCIENCIAS) for financing the research project "Evaluation of enhanced coagulation for the removal of pesticides in water as a strategy for mitigating environmental factors with incidence in health - CI 2937" and the doctoral formation to Eng. Claudia Patricia Amézquita Marroquín (National Doctorate Convocation 567).

References

[1] Perez-Vidal, A., Torres-Lozada, P. and Escobar-Rivera, J.C., Hazard identification in watersheds based on water safety plan approach: case study of Cali-Colombia. Environmental Engineering and Management Journal [Online]. 15(4), pp. 861-872, 2016. [date of reference June of 2016]. Available at: http://eemj.eu/index.php/EEMJ/article/view/2903

[2] World Health Organization (WHO). Guidelines for drinking-water quality. Genéva: WHO, 2011.

[3] World Health Organization (WHO). Guidelines for drinking water quality. Genéva: WHO, 2006.

[4] Jimenez, B. and Rose, J., Urban water security: managing risks. Boca Raton: Taylor & Francis, UNESCO-IHP, 2009.

[5] Di Bernardo, L., Di Bernardo, A. and Nogueira, P., Tratabilidade de agua e dos residuos gerados em estacoes de tratamiento de agua. Sao Carlos: LDiBe editora, 2011.

[6] Crittenden, J.C., Trussell, R.R., Hand, D.W., Howe, K.J. and Tchobanoglous, G. Granular filtration. In Crittenden, et al. MWH's Water Treatment: Principles and Design, 3rd Edition, USA, 2012. pp. 727-818.

[7] Minambiente (Ministerio de Ambiente, Vivienda y Desarrollo Territorial). Resolución 2115 del 22 de junio de 2007. Por medio de la cual se señalan características, instrumentos básicos y frecuencias del sistema de control y vigilancia para la calidad del agua para consumo humano. Minambiente, Bogotá. 2007.

[8] Environmental Protection Agency (EPA). Estándares del reglamento nacional primario de agua potable [on line]. EPA, USA, 2000. [date of reference June of 2016]. Available at: http://water.epa.gov/drink/agua/estandares.cfm

[9] American Water Works Asociation (AWWA). Water quality & treatment. A Handbook on Drinking Water. USA: McGraw-Hill, 2011.

[10] Sandobal-Paz, L., Marques, E., Butti, F. and Akiko, J., Avaliação técnico-econômica da tecnologia de tratamento de água de dupla filtração. Eng. Sanit. Ambient., 20(4), pp. 525-532, 2015. DOI: 110.1590/S1413-41522015020040129909.

[11] Gupta, V.K., and Ali, I., Water treatment for organic pollutants by adsorption technology. In. Gupta, V.K. and Ali, I., Environmental water: advances in treatment, remediation and recycling, Elsevier, 2013, pp. 29-91. DOI:10.1016/B978-0-444-59399-3.00002-7.

[12] Karanfil, T., Activated carbon adsorption in drinking water treatment. In Bandosz, T.J., Activated Carbon Surfaces in Environmental Remediation, Elsevier, 2006, pp. 345-373. DOI: 10.1016/S1573-4285(06)80016-5

[13] Przepiórski, J., Activated carbon filters and their industrial applications. In Bandosz, T.J., Activated Carbon Surfaces in Environmental Remediation, Elsevier, 2006, pp.421-474. DOI: 10.1016/S1573-4285(06)80018-9.

[14] Ratnayaka, D.D., Brandt, M.J. and Johnson, K.M., Specialized and advanced water treatment processes. In Ratnayaka, D.D., Brandt, M.J., Johnson, K M., Water Supply, Elsevier, 2009, pp. 365-423. DOI: 10.1016/B978-0-7506-6843-9.00018-4.

[15] Environmental Protection Agency (EPA). National primary drinking water regulations. EPA 816-F-09-004 [on line]. EPA, USA, 2009. [date of reference June of 2016]. Available at: http://pbadupws.nrc.gov/docs/ML1307/ML13078A040.pdf

[16] CEPIS and OPS. Tratamiento de agua para consumo humano: plantas de filtración rápida [en líena]. CEPIS, OPS, Perú, 2004. [dato de consulta: June of 2016]. Disponible en: http://bibliotecavirtual.minam.gob.pe/biam/bitstream/id/5657/BIV00012.pdf

[17] Thiel, P., Zappia, L., Franzmann, P., Warton, B., Alessandrino, M., Heitz, A., Nolan, P., Scott, D., Hiller, B. and Masters, D., Activated carbon VS anthracite as primary dual media filters - a pilot plant study. 69th Annual Water Industry Engineers and Operators' Conference, Bendigo, 2006. [online]. Available at: http://www.wioa.org.au/conference_papers/06_vic/documents/PetaThiel1.pdf

[18] Bhatnagar, A., Hogland, W., Marques, M. and Sillanpääc, M., An overview of the modification methods of activated carbon for its water treatment applications. Chemical Engineering Journal, 219, pp. 499-511, 2013. DOI: 10.1016/j.cej.2012.12.038

[19] Wiecheteck, G., Da silva, B. and Di bernardo, L., Remoção de substâncias húmicas utilizando dupla Filtração com filtro ascendente de areia grossa Ou de pedregulho. Engenharia Sanitaria e Ambiental, 9(2), pp. 156-203, 2004.

[20] Silva, G.G., Naval, L.P., Di Bernardo, L. and Dantas, A.D.B., Tratamento de água de reservatórios por dupla filtração, oxidação e adsorção em carvão ativado granular. Engenharia Sanitaria e Ambiental, 17(1), pp. 71-80, 2012. DOI: 10.1590/S1413-41522012000100011.

[21] Bundy, M., Doucette, W., McNeill, L. and Ericson, J.F., Removal of pharmaceuticals and related compounds by a bench-scale drinking water treatment system. Journal of Water Supply: Research and Technology—AQUA, 56(2), pp. 105-115, 2007. DOI: 10.2166/aqua.2007.091

[22] Pham, T., Nguyen, V. and Van der Bruggen, B., Pilot-scale evaluation of GAC adsorption using low-cost, high-performance materials for removal of pesticides and organic matter in drinking water production. Journal of Environmental Engineering, [online]. 139(7), pp. 958-965, 2013. Available at: http://ascelibrary.org/doi/abs/10.1061/%28ASCE%29EE.1943-7870.0000704#sthash.voYLqbDx.dpuf

[23] Ho, L. and Newcombe, G., Granular activated carbon adsorption of 2-Methylisoborneol MIB Pilot- and laboratory-scale evaluations. Journal of environmental engineering, 136(9), pp. 965-974, 2010. DOI: 10.1061/(ASCE)EE.1943-7870.0000231#sthash.JdMlljtE.dpuf

[24] Rigobello-Sloboda, E., Di Bernardo-Dantas, A., Di Bernardo, L. and Vieira, E.M., Removal of diclofenac by conventional drinking water treatment processes and granular activated carbon filtration. Chemosphere, 92(2), pp. 184-191, 2013. DOI: 10.1016/j.chemosphere.2013.03.010

[25] Montoya, C., Loaiza, D., Torres, P. y Cruz, C., Efecto del incremento en la turbiedad del agua cruda sobre la eficiencia de procesos convencionales de potabilización. Revista EIA [online]. 8(16), pp. 137-148, 2011. [date of reference June of 2016]. Available at: http://repository.eia.edu.co/handle/11190/148

[26] Perea, L.M., Torres, P., Cruz-Velez, C.H. y Escobar-Rivera, J.C., Influencia de la configuración del medio filtrnate sobre el proceso de filtración a tasa constante del agua clarificada del Rio Cauca. Revista de Ingeniería [Online]. 38, pp. 38-44, 2013. [date of reference June of 2016]. Available at: http://www.scielo.org.co/scielo.php?pid=S0121-49932013000100007&script=sci_abstract&tlng=es

[27] APHA, AWWA, WEF. Standard methods for water and wastewater examination. USA: American Public Health Association, 2012.

[28] Graese, S., Snoeyink, V. and Lee, R., Granular activated carbon filter-adsorber systems. Journal American Water Works Association [Online]. 79(12), pp. 64-74, 1987. [date of reference June of 2016]. Available at: https://www.awwa.org/publications/journal-awwa/abstract/articleid/11937.aspx. DOI: 10.1002/j.1551-8833.1987.tb02961.x

[29] Zouboulisa, A., Traskasa, G. and Samarasb, P., Comparison of single and dual media filtration in a full-scale drinking water treatment plant, Desalination, 213(1–3), pp. 334-342, 2007. DOI: 10.1016/j.desal.2006.02.102

[30] Lopes, M.P., Matos, C.T., Pereira, V.J., Benoliel, M.J., Valério, M.E., Bucha, L.B., Rodrigues, A., Penetra, A., Ferreira, E., Cardoso, V., Reis, M. and Crespo, J., Production of drinking water using a multi-

barrier approach integrating nanofiltration: a pilot scale study, Separation and Purification Technology, 119, pp. 112-122, 2013. DOI: 10.1016/j.seppur.2013.09.002
[31] Grace, M.A., Healy, M.G. and Clifford, E., Use of industrial by-products and natural media to adsorb nutrients, metals and organic carbon from drinking water, The Science of the Total Environment, 518-519, pp. 491–497, 2015. doi:10.1016/j.scitotenv.2015.02.075
[32] Rosero, M., Latorre, J., Torres, W. y Delgado, L. Presencia de materia orgánica y subproductos de la desinfección con cloro. Caso sistema de tratamiento de agua para consumo humano, Puerto Mallarino, Cali-Colombia, MSc. Thesis, Maestría en Ingeniería Sanitaria y Ambiental - Escuela de Ingeniería de Recursos Naturales y del Ambiente, Universidad del Valle, Colombia, 2005.
[33] Kim, J. and Kang, B., DBPs removal in GAC filter-adsorber, Journal Water Research, 42(1-2), pp. 145-152, 2008. DOI: 10.1016/j.watres.2007.07.040

P. Torres-Lozada, received the BSc. of Sanitary Engineer in 1982 from the Universidad del Valle, Cali, Colombia, MSc. (1993) and PhD (2001) in Civil Engineering: Hydraulics and Sanitation from the Universidade de São Paulo, Brazil. From 1995 to date, she is linked to the Universidad del Valle as full professor. She is categorized by Colciencias as a senior researcher and is a Leader of the Environmental Pollution Study and Control - ECCA Research Group with category A1. The research areas are water quality, water treatment for human consumption, wastewater treatment and solid waste.
ORCID: 0000-0001-9323-6677

C.P. Amezquita-Marroquín, received the BSc. of Sanitary Engineer in 2009, the MSc. degree in sanitary and environmental engineering in 2013 all of them from the Universidad del Valle, Cali, Colombia. She has worked on water treatment projects, currently a PhD student in engineering of the Universidad del Valle and she belongs to ECCA Research Group - Universidad del Valle, Engineering Faculty.
ORCID: 0000-0002-0094-2204

K.D. Agudelo-Martínez, received the BSc. of Sanitary and Environmental Engineer in 2016 from the Universidad del Valle, Cali, Colombia.
ORCID: 0000-0002-2728-2998

N. Ortiz-Benítez, received the BSc. of Sanitary and Environmental Engineer in 2016 from the Universidad del Valle, Cali, Colombia.
ORCID: 0000-0003-1614-1396

D.S. Martínez-Ducuara, received the BSc. of Sanitary and Environmental Engineer in 2016 from the Universidad del Valle, Cali, Colombia.
ORCID: 0000-0002-8803-3864

UNIVERSIDAD NACIONAL DE COLOMBIA
SEDE MEDELLÍN
FACULTAD DE MINAS

Área Curricular de Medio Ambiente

Oferta de Posgrados

Especialización en Aprovechamiento de Recursos Hidráulicos
Especialización en Gestión Ambiental
Maestría en Ingeniería Recursos Hidráulicos
Maestría en Medio Ambiente y Desarrollo
Doctorado en Ingeniería - Recursos Hidráulicos
Doctorado Interinstitucional en Ciencias del Mar

Mayor información:

E-mail: acma_med@unal.edu.co
Teléfono: (57-4) 425 5105

UNIVERSIDAD NACIONAL DE COLOMBIA
SEDE MEDELLÍN
FACULTAD DE MINAS



DYNA
http://dyna.medellin.unal.edu.co/

Construction of a short circuit frequency map to define GMAW-S parameters during WPSs development

David Bernardo Hoyos-Arango [a], Oscar León Mejía-López [b] & Jorge Enrique Giraldo-Barrada [c]

[a] *Universidad Nacional de Colombia, Medellín, Colombia. dbhoyosa@unal.edu.co*
[b] *Laboratory of Manufacturing Processes, Faculty of Mines, Universidad Nacional de Colombia, Medellín, Colombia. olmejia@unal.edu.co*
[c] *Welding group, Faculty of Mines, Universidad Nacional de Colombia, Medellín, Colombia. jegirald@unal.edu.co*

Received: December 5th, 2017. Received in revised form: May 10th, 2018. Accepted: May 28th, 2018.

Abstract
A short circuit frequency map was constructed for GMAW-S using a carbon steel filler metal class AWS ER70S-6 and 75%Ar-25%CO_2 shielding gas. This kind of map is proposed as a tool for selecting GMAW-S currents and voltages that enable welds with higher stability and quality. The map was constructed by analyzing current and voltage signals recorded during welding applications at 5000 samples/second. Adequate operation regions were defined over the map based on visual inspection results of bead-on-plate welds and the establishment of instability boundaries. Some examples were analyzed by locating two common parameters for industrial welding qualification (current and voltage) and drawing the limits established by AWS D1.1:2015 code for these essential variables (±7% PQR voltage and ±10% PQR amperage) on the frequency map. The results show that sometimes these limits may contain regions with poor stability related to electrode stubbing against the base metal and lack of arc re-ignition.

Keywords: metal transfer mode (MTM); MTM map; short circuit frequency map; stubbing; WPS.

Construcción de un mapa de frecuencias de corto-circuito para definir parámetros de GMAW-S durante el desarrollo de WPSs

Resumen
Se construyó un mapa de frecuencias para GMAW-S usando un aporte clase AWS ER70S-6 y gas de protección 75%Ar-25%CO2. Este tipo de mapa es una herramienta para seleccionar corrientes y voltajes de soldeo con proceso GMAW-S con mayor estabilidad. El mapa se construyó analizando señales de voltaje y amperaje registradas durante la aplicación de soldaduras a 5000 muestras por segundo. Se definieron regiones de operación sobre los mapas basados en resultados de inspección visual de soldaduras sobre platina y ubicando los límites de inestabilidad. Se analizaron dos ejemplos de parámetros de calificación de soldaduras usados industrialmente (corriente y voltaje) dibujando los límites establecidos por el código AWS D1.1:2015 para estas variables esenciales (±7% en voltaje y ±10% en amperaje del PQR) en el mapa de frecuencias. Se mostró como estos límites pueden contener regiones de baja estabilidad asociada al "stubbing" contra el metal base y al no reinicio del arco.

Palabras clave: modo de transferencia de metal (MTM); mapa de MTM; mapa de frecuencia de cortocircuito; "Stubbing"; WPS.

1. Introduction

Gas Metal Arc Welding (GMAW) is a widely-used process in the welding industry because of its technical and economic advantages over other joining processes like SMAW or GTAW. Its main features include: high deposition rate, it enables to make welds in all positions and long welds without interruption, it can be operated in mechanized or automatic manufacturing systems and it offers the possibility to weld most commercially available alloys [1]. Nevertheless, one of the main problems in said industry is poor arc stability in GMAW caused, most times, by the wrong selection of welding parameters. This is the result of limited available technical information, the broad range of

How to cite: Hoyos-Arango, D.B., Mejía-López, O.L. and Giraldo-Barrada, J.E., Construction of a short circuit frequency map to define GMAW-S parameters during WPSs development. DYNA, 85(205), pp. 240-248, June, 2018.

© The author; licensee Universidad Nacional de Colombia.

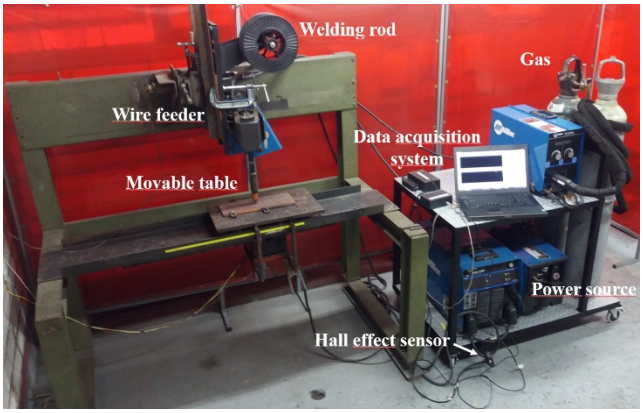
welding parameters (wire feed speed and voltage) provided by consumables or shielding gases manufacturers and setting welding parameters according to iterative (trial and error) or subjective criteria.

The metal transfer mode (MTM) in GMAW depends on several process variables such as polarity, current, electrode extension, wire composition, wire diameter and shielding gas [1]. Welds made with a given MTM have particular conditions of bead penetration, heat input, deposition rate, arc stability, surface condition, and spatter; thereby, a weld made with some MTM has specific performance characteristics, properties and applications. Therefore, MTM is considered an essential variable in many welding codes (AWS, ASME, API, among others) because it might impact the quality and performance of weldments, particularly, their mechanical properties.

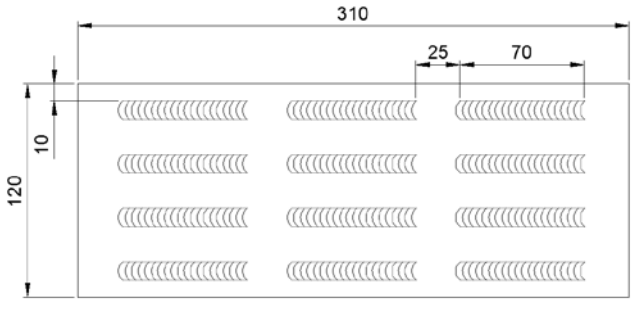
Short circuit metal transfer mode in GMAW is a MTM characterized by the lowest range of currents and voltages of GMAW which produce small and fast-freezing weld pools by means of periodic contacts (short circuits) between the electrode tip and the weld pool. A metal droplet is detached on the weld during each short circuit. This MTM produces low heat input that enables to weld thin plates and work in all welding positions. GMAW used in this MTM is sometimes called GMAW-S and such procedures must be qualified by testing according to AWS D1.1 Code (Clauses 3.2.2 and 4.14.1) because of their tendency to produce a lack of fusion [2].

Stable metal transfer in GMAW-S requires uniform and periodic detachment. In this regard, Liu and Siewert [3] studied the change in short circuit frequency in GMAW-S caused by the variation of current and voltage. They found that the stability of the process can be described by the statistical variation of droplet-transfer period and droplet rate. Among all the statistical parameters that were examined, average and standard deviation of the transfer period were the best for characterizing the stability of the process. When maximum stability is achieved, there is a minimum average short circuit period (maximum short circuit frequency) and the standard deviation of the short circuit period is also a minimum. This indicates that, during welding, the population of short circuit periods in a stable metal transfer has a close distribution and the process is less erratic. To show the effect of welding current and voltage, Liu and Siewert plotted maps with droplet-rate (transfer frequency) isopleths in order to identify regions of maximum stability. Hermans and Den Ouden [4] also found that, when the droplet frequency is maximum, the standard deviation is minimum and the process has maximum stability. Furthermore, maximum short circuit frequency was correlated with weld pool oscillation frequency. They found that, when these frequencies are the same, the greatest stability of the process is achieved. Besides, weld pool frequency was estimated through a model developed by Sorensen and Eagar [5].

Both AWS D1.1:2015 [2] (Table 4.5(14)) and Section IX of ASME B&PVC [6] (Table QW-255 paragraph QW-409.2) consider the change in transfer mode in GMAW like an essential variable. Other codes and specifications (such as AWS D1.5:2015, AWS D1.6:2017, and AWS B2.1:2014) have identical approaches to the transfer mode in GMAW. Some of them are more specific and state that a change from short circuit transfer to globular, spray or pulsed, or vice versa, requires requalification. The GMAW-S process is not allowed in prequalified procedures and it must always be qualified by mechanical testing. However, sometimes it is very difficult to establish the actual metal transfer mode obtained with a particular set of welding parameters. There have been several studies about the simulation or prediction of MTMs in GMAW. For instance, Zhao and Zung [7] simulated the transition of metal transfer between globular and spray. In turn, Rudas et al. [8] tried to predict the MTM in GMAW through modeling. Both studies are mathematically complex and difficult to extrapolate to industrial situations. US Patent 9,808,879 B2, dated November 7th 2017, claims a welding diagnostic device for identifying MTMs during welding with GMAW and a method to identify MTMs, basically short circuit, globular and spray transfer [9]. There are no reports of a short circuit frequency map constructed for the widely-used combination of ER70S-6 filler metal and 75%Ar-25%CO_2, which is one of the most preferred gas for GMAW-S because CO_2 added to Argon improves wettability [1] and reduces the amount of spatter compared to 100% CO_2 [10]. This work presents a particular MTM map and short circuit frequency map as tools to define boundaries of transfer modes around short circuit and process stability for ER70S-6 wire and 75%Ar-25%CO_2 shielding gas mixture. The methodology for the construction of these maps is also discussed.



(A)



(B)

Figure 1. (A) Welding equipment and devices used during the study. (B) Dimensions in mm of the welding test coupon used for the construction of frequency and MTM maps.
Source: Authors' own work.

Table 1.
Welding parameters fixed during the experiment.

Fixed Parameter	Value
Base material	ASTM A36
Plate thickness	4.8 mm (3/16")
Filler metal classification	ER70S-6
Filler metal diameter	1.14 mm (0.045")
Shielding gas	75% Ar-25% CO_2
Gas flow rate	30 SFCH (14 LPM)
Inductance (%)	75
Contact tip to work-piece distance	16 mm (5/8")
Welding speed	4.2 mm/s (10 ipm)
Electrode position angle	0°
Work angle (°)	90°
Nozzle diameter	16 mm (5/8")
Polarity	DCEP
Maximum inter-pass temperature	100˚C

Source: Authors' own work.

2. Experimental method

A Miller Invision 456MP welding power source and a Miller 70 Series wire feeder Miller 70 Series were used to run the testing welds. The welding gun was fixed and the base metal was held on a sliding or movable table, as shown in the photograph in Fig. 1(A). Bead on plate (BOP) welds, 70 mm long, were deposited on 4.8mm (3/16") thickness ASTM A36 steel plates, as shown in Fig. 1(B).

The fixed variables used in the experiment are shown in Table 1 and constitute typical parameter values for GMAW applications [1]. The independent variables were wire feed speed (WFS) and voltage setting in the power source. WFS, according to recommendations given by the electrode manufacturer, was varied between 100 in/min and 600 in/min with increments of 50 in/min, and voltage was varied from 12 to 34 volts with increments of 1 volt. Two hundred and twenty (220) welding beads were applied and replicated in order to develop both frequency and MTM maps.

Current and voltage signals were recorded using a data acquisition system with a Hall Effect Current Sensor and a voltage divisor. The sampling rate was 5000 samples per minute for every signal. Signals were captured for 10 seconds during each weld deposition and stored for subsequent analysis. A moving average with a window of three data was used to smooth signals and reduce noise. The beads were visually inspected to correlate weld quality to signals, transfer modes and instability boundaries. Some typical signals and bead photos are shown in Section 3.

The first step in signal analysis was metal transfer mode identification. This step was completed through visual observation of droplet detachment during welding and the analysis of the recorded signals based on the shape of each signal and some of their statistical parameters. For short circuit and globular-short circuit transfer modes, a frequency boundary of 20Hz was established based on values given by Scotti et al [11], the US Patent 9,808,879 B2 [9] and annex C-3 of AWS D1.1 [2]. Several data and some statistical parameters were obtained and analyzed, including average arc time, average short circuit frequency, short circuit period, short circuit time, and standard deviation of short circuit frequency and period for each weld. RMS values of welding voltage and current were calculated from the recorded data. The maps were plotted with RMS current and RMS voltage because they are obtained with the usual welding meters when signals are not lineal (like current clamps specified as "True RMS", and ammeters and voltmeters of the welding power sources). Furthermore, with direct current, RMS and average values are relatively similar and provide suitable computation values of arc power in order to make correct estimates of heat input in welds [12,13].

3. Results and discussion

3.1. Typical signals for several MTMs

Before the construction of the short frequency map, it is necessary to see the big picture of different metal transfer modes; therefore, the first step was to construct the MTM map by analyzing the characteristics of each signal obtained with different sets of welding parameters. Some typical signals registered in this study for each MTM are shown and analyzed in this section in order to describe the general method to of construction of the MTM map.

Fig. 2 shows an illustration of the detachment of one molten metal droplet in GMAW-S (short circuit MTM) and the behavior over time of the current and voltage signals during this metal transfer. The time span during which the voltage is near zero is referred to as short circuit time (instants 1 through 3). During this time, the electric arc is extinguished and the current rises towards a maximum level that depends on system conditions (wire diameter, wire material, inductance, stability and electric characteristics of the power source). As the welding current increases, so does the electromagnetic force pinching the molten metal which, along with surface tension, drives the metal drop into the weld pool [11]. The form of the current signal during up and down periods (called "Inductive effect") maintains an almost equal slope disregard the voltage used. This is in line with the work by Scotti et al. [14], who observed that the change in voltage values does not have an influence on the up and down current rate for the same inductance setting in the welding equipment. During the short circuit time, the arc does not burn and the heat input is low due to the low voltage in this period, as shown in the instant power plot on top of Fig. 2, therefore the weld pool freezes and short circuits [4].

At instant 4 in Fig. 2, the arc is reignited and maintained until instant 6. Over this time span, called arc time, the voltage tends to be constant and near a maximum level; besides, the current begins to fall towards a constant arc current at a speed inverse to the inductance level of the power source [1,11]. During this period, the electric arc starts to form and grow a new metal drop on the electrode tip and heats the weld pool. At the end of the arc period, after instant 6, the drop touches the weld pool and a new short circuit time starts.

Other different kinds of metal transfer signals in GMAW, or mixed modes composed of two or more MTMs, were acquired during the present study. They are shown in Fig. 3 and explained below.

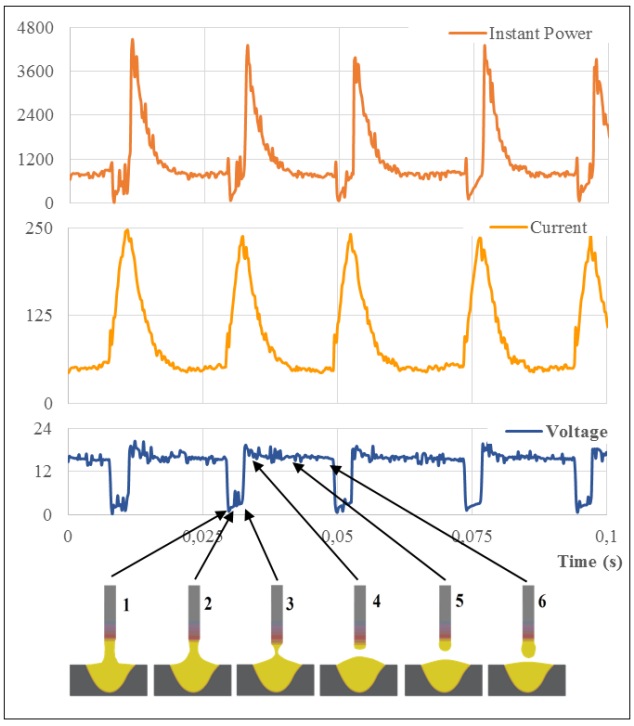


Figure 2. Schematic of the metal transfer between electrode and weld pool in the short circuit transfer mode in relation to current, voltage and instant power signals.
Source: Authors' own work.

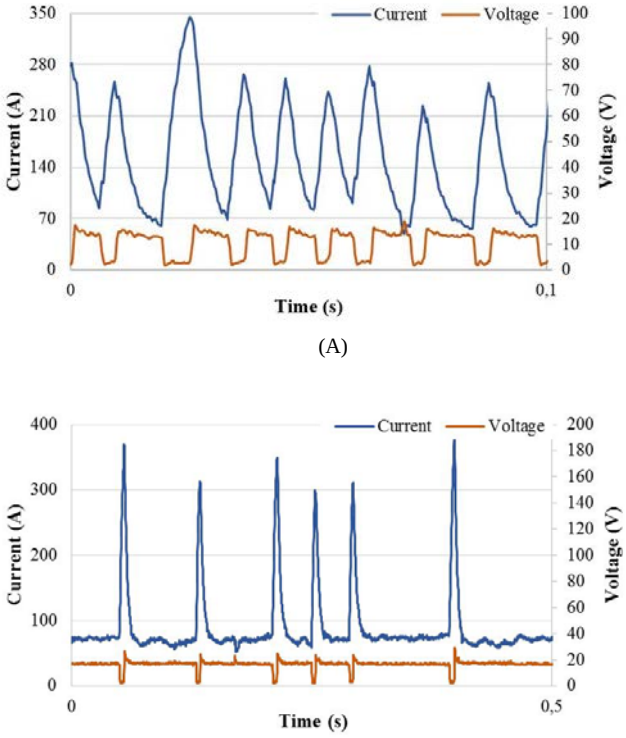


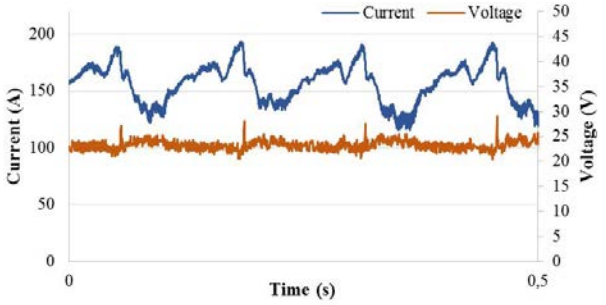
Figure 3. Signal forms acquired from several metal transfer modes: (A) Short circuit, (B) Short circuit-Globular, (C) Globular, (D) Spray, (E) Short circuit-Spray and (F) Momentary arc interruption.
Source: Authors' own work.

Fig. 3(A) shows a typical signal for GMAW-S, included for comparison purposes. A mixed Short circuit-Globular metal transfer (Fig. 3(B)), as described by Scotti [16], occurs at relatively high voltages and low wire feed speeds. The droplet grows in a globular like shape before touching the molten weld pool and detaching. In this case, the signals are similar to those of a short circuit transfer mode (Fig. 3(A)), but with longer arc times and lower frequencies, as shown in Fig. 3(B). It could be considered to be just short circuit transfer mode, but the fact that gravitational force becomes significant for molten metal detachment enables to consider it a particular case. Welding in vertical, horizontal or over-head positions becomes difficult due to the effect of gravity on the droplet. In order to have a practical classification, a droplet is assumed to detached in Short circuit-Globular transfer mode when the short circuit frequency is lower than or equal to 20 Hz.

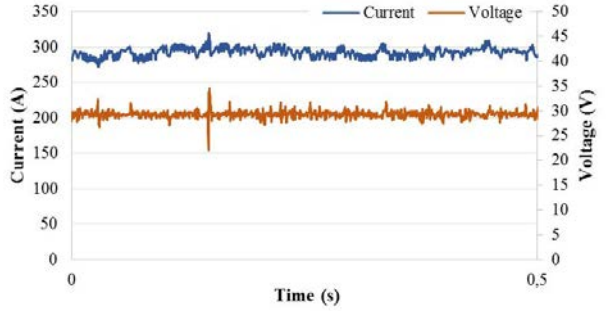
Globular transfer is characterized by the formation of large droplets, 1.5–3 times the wire diameter. It is a free flight MTM and the main driving force allowing metal detachment is due to gravity, with values around 0.2-1.5g-f, calculated from the formula provided by Pires et al. [15]. This mode of transfer occurs at voltages higher than required for Short circuit-Globular. Within the scope of this paper, globular transfer may refer to axial globular or repelled globular transfer modes alike. The current signal of globular MTM, Fig. 3(C), oscillates due to the change in arc length while the droplet grows with the corresponding response of the constant voltage characteristic of the power source. As shown in Fig. 3(C), voltage remains almost constant during the weld, while current varies.

Spray transfer mode is characterized by small droplets detached from the electrode tip smaller than the electrode size. It occurs at relatively high voltages and currents. The current must be above the transition current level and, because of its high value, droplet detachment is promoted by an electromagnetic pinch force [11, 15]. This MTM is common when high penetration and deposition rates are required in flat position or in out-of-position with pulsed applications. Further classification of this MTM is possible by differentiating projected spray and streaming spray, but it is necessary to use high speed filmography. Note in Fig. 3(D) that voltage and current are constant over time.

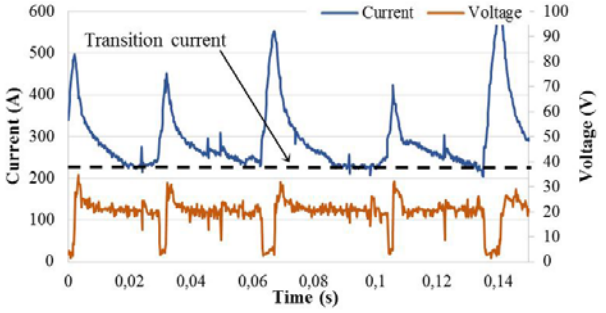
Short circuit-Spray transfer, see Fig. 3(E), is an interchangeable metal transfer mode in which current values are high enough to allow droplet detachment by an electromagnetic pinch force, but the voltage (hence, the arc length) is not enough to maintain a stable free flight transfer mode. Then, a short circuit occurs (voltage drops to zero) detaching material or even pieces of electrode and droplets detach as in spray transfer when the arc is reestablished. When the arc is momentarily extinguished at the lowest voltages (Fig. 3(F)), the current drops to zero and the voltage reaches the OCV value of the power source; this cycle may be repeated several times per second. This kind of metal transfer mode is not commonly used because it results in high spatter formation and increased weld pool size.



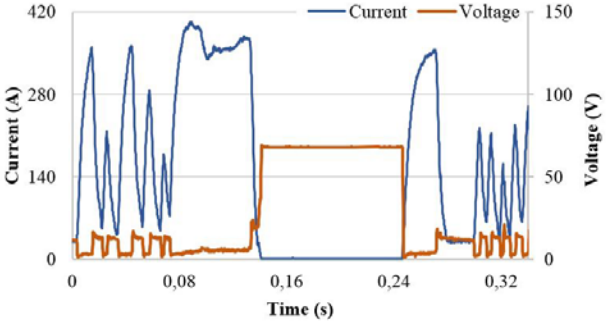
(C)



(D)



(E)



(F)

Figure 3 (Cont.). Signal forms acquired from several metal transfer modes: (A) Short circuit, (B) Short circuit-Globular, (C) Globular, (D) Spray, (E) Short circuit-Spray and (F) Momentary arc interruption.
Source: Authors' own work.

3.2. Metal transfer modes map and weld's appearance

Fig. 4 shows the MTM map constructed in this study, which is the big picture of metal transfer modes for this particular gas-filler metal combination. Each point in the MTM map is determined by the analysis of the voltage and amperage signals acquired during the application of each weld, as was shown in Fig. 3. Eight different areas can be observed: short circuit (SC), globular (G), spray (S), short circuit-globular (SC/G), short circuiting/spray (SC/S), short circuit/Globular/Spray and arc interruption (AI) where stubbing begins. This map shows the short circuit metal transfer region and its boundaries in terms of RMS and equipment setting values for voltage and current. Additionally, the relationship of RMS current vs wire feed speed is shown in Fig. 5 for two groups of MTM: free flight transfer (Globular and Spray transfer modes) and contact transfer (short circuit, Short circuit-Globular and Short circuit-Spray transfer modes). The WFS vs RMS Current plot is particularly useful when the current value is known and it needs to be correlated with the WFS in order to set-up the GMAW equipment. Welds with arc interruptions were not included in some plots due to the increase in RMS Voltage as consequence of an open arc voltage (OCV), as shown in the signal of a stubbing included in Fig. 3(F).

In each MTM area, the weld bead appearance was observed and recorded with the corresponding pictures. Photographs of typical weld beads obtained with different parameters and MTMs are shown in Fig. 6. All BOP welds in globular or mixed with globular (A, B and C in Fig. 6) exhibit spatter. Welds in unstable areas, like E and I, are not uniform in appearance, just like their arc signals, because of considerable fluctuations in voltage and amperage. Short circuiting and spray welds are smoother and present lower spatter levels as well. Interestingly, the welds in the short circuiting-spray area (a very wide zone in the MTM map, Fig. 4) are free of spatter and have a good appearance (Fig. 6(H)); this aspect, combined with relatively high arc powers (between 5 and 7 kW), opens a window to explore possibilities for use this MTM to weld higher thicknesses than allowed for GMAW-S (up to 6-10 mm).

3.3. Frequency map construction

The frequency of short circuit was determined from the voltage signal. Data were analyzed so that that every time the voltage dropped below a low threshold near zero, a short circuit was recorded and accounted for. Fig. 7 shows the distribution of short circuiting frequencies for each weld according to its welding parameters (RMS Voltage and RMS current). The frequencies reported in the graph are ±5Hz; as a result, some welds with approximately the same frequency are grouped within the same marker.

The frequency map in Fig. 7 has a similar distribution to those developed by Liu and Siewert [3] for an ER70S-6 wire with 100% CO_2 and 98% Ar +2%O_2 gas mixtures. However, in contrast with their findings, in this study stubbing and arc interruptions were found to take place with lower voltages at a given current value. Stubbing is an instant of welding instability that occurs when the electrode fusion rate is lower than the wire feed speed, therefore, there is contact between the solid electrode tip and the weld pool without proper material detachment and subsequent arc re-ignition [4]. This situation makes the welder feel that the weld gun is being pushed backwards and it increases the risk of lack of fusion due to an increase in weld pool freezing.

Average short circuiting period versus voltage for some of the wire feed speeds and standard deviation of single short

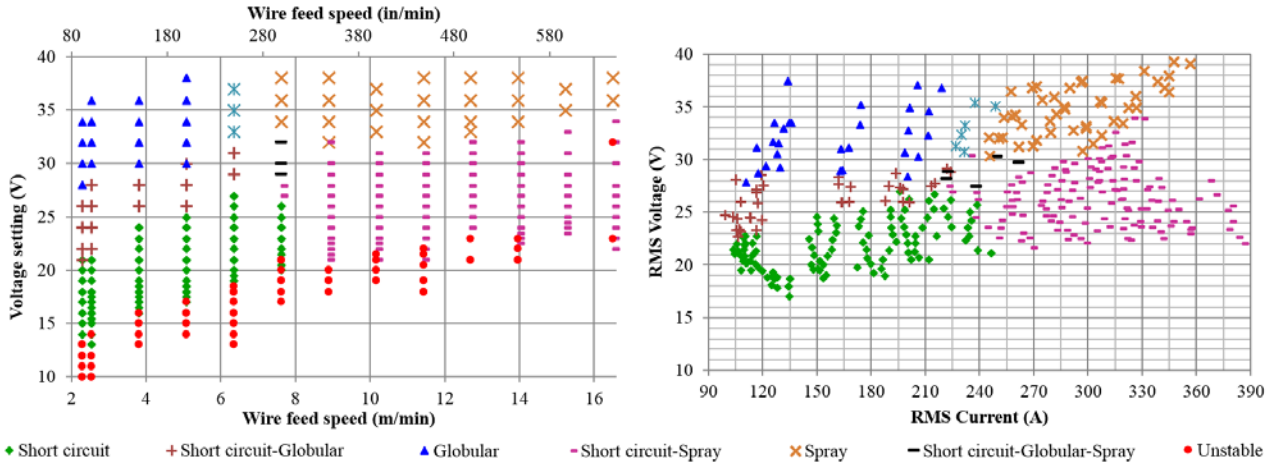


Figure 4. MTM map as a function of the voltage setting in the power source vs WFS (left) and actual RMS Voltage vs RMS current (right).
Source: Authors' own work.

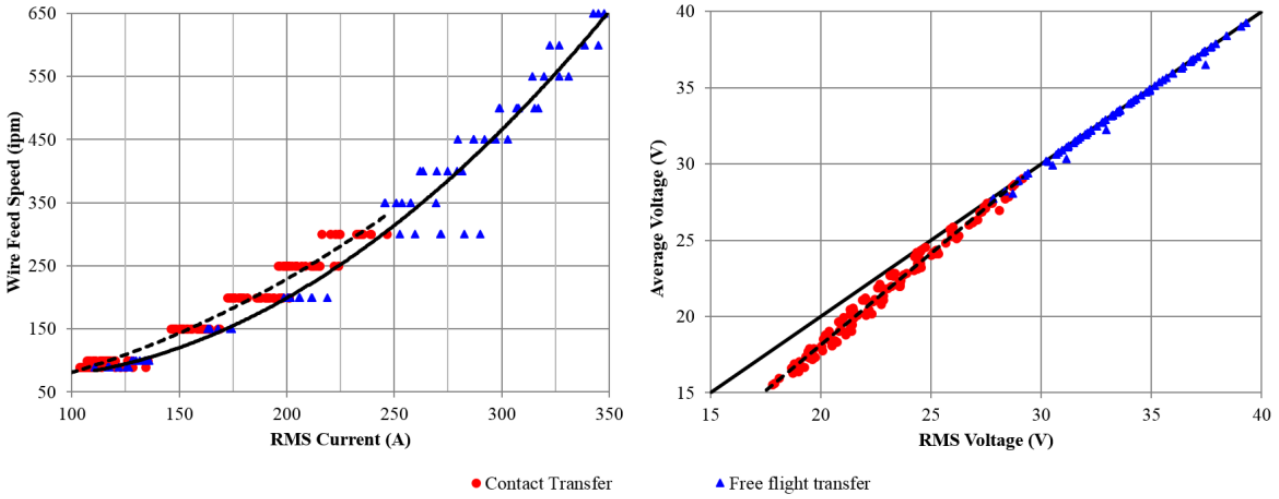


Figure 5. RMS current vs wire feed speed (left) and Average Voltage vs RMS Voltage (Right).
Source: Authors' own work.

circuit periods against voltage are shown in Fig. 8. These graphs are similar to those developed by Liu and Siewert with 98%Ar+2%O_2, but constructed here for 75%Ar+25%CO_2 shielding gas. In these curves, the minimum average periods and the minimum standard deviation of periods are obtained with the same voltage values for 2.28 and 2.54 m/min (90 and 100 ipm). At such voltage values, the arc is more stable, metal deposition is more uniform and better weld quality can be achieved. As a result of a decrease in just one volt, the mean period and its standard deviation increase, arc stability becomes poor due to electrode stubbing and the weld quality is affected because the electrode tip approaches to the weld pool and hits it repeatedly; the welder can feel the impacts in the welding gun. Decreasing the voltage even more produces arc interruptions and the weld cannot be deposited.

For higher WFS, the voltage value required to obtain the maximum frequency is near the area of arc interruptions and no stubbing area is present. Therefore, when the arc re-ignition problem arises, a slight increase in voltage should produce a favorable solution.

Fig. 8(B) shows drop Detachment Frequency Vs. RMS Voltage. Typical bell shaped curves, as those presented by Houldcroft [17], were only achieved with low wire feed speeds (2.28, 2.54, and 3.81 m/min, i.e. 90, 100 and 150 ipm-). At these wire feed rates, maximum stability (maximum drop detachment frequency) was found around 20 volts. Nevertheless, for higher rates, maximum stability is achieved by reducing voltage, but not as much as to cause stubbing.

A simplified short circuiting frequencies map is shown in Fig. 9. It is formed by isopleths drawn on a Voltage vs. Current coordinate system. It was constructed by tracing lines through points of equal frequency and defining areas where a given detachment frequency can be located. Boundaries between the short circuit transfer mode and other modes were also traced. A black solid line indicates electrode stubbing and the arc interruption limit, beyond which arc cannot be established due to excessively low voltage.



A. Globular. B. Short circuiting –Globular. C. Short circuiting –Globular.

D. Short circuiting (90Hz). E. Unstable ("Stubbing"). F. Short circuiting.

G. Spray. H. Short circuiting-Spray (3) I. Unstable SC-Spray.

Figure 6. Weld bead's appearance obtained with several metal transfer modes.
Source: Authors' own work.

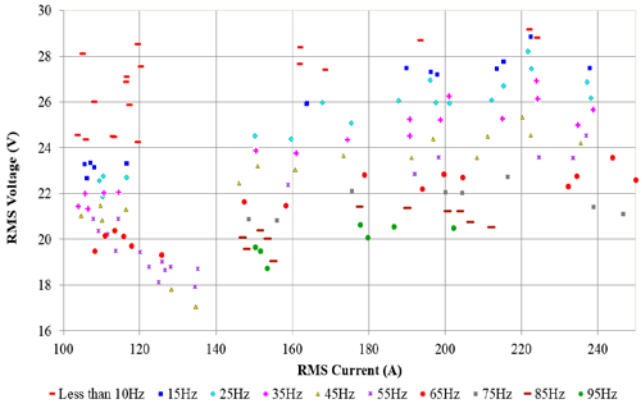


Figure 7. Short circuit frequency map for ER70S-6 electrode and 75%Ar + 25%CO2 shielding gas.
Source: Authors' own work.

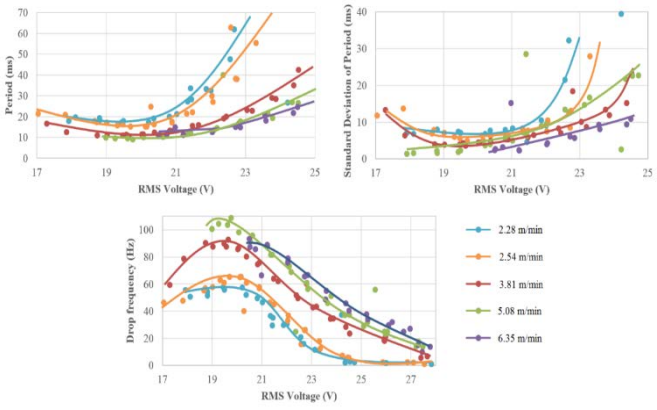


Figure 8. Average short-circuiting period (A), standard deviation of period (B) and drop frequency (C) for some WFS Vs RMS Voltage settings.
Source: Authors' own work.

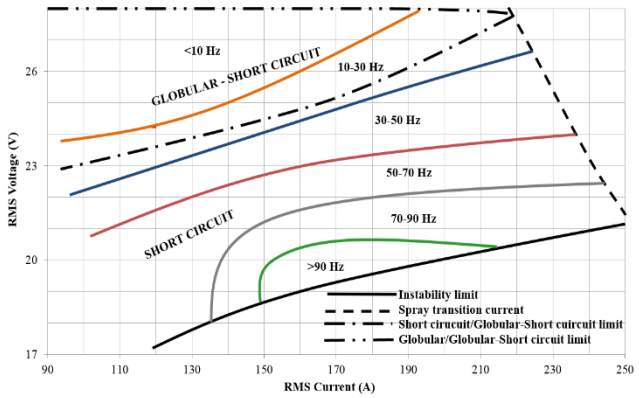


Figure 9. Simplified short circuiting frequencies map.
Source: Authors' own work.

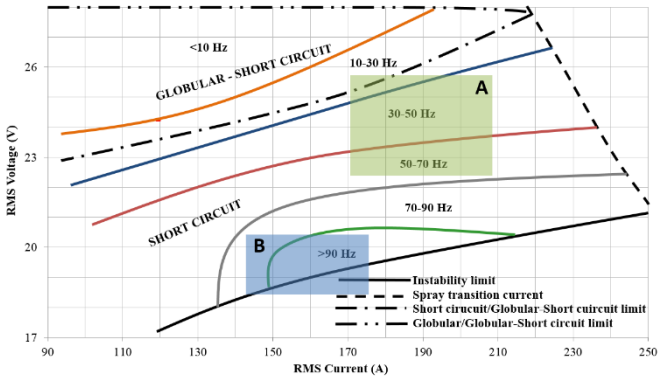


Figure 10. Location of qualification ranges for the given example.
Source: Authors' own work.

4. Applications of the short circuit frequency map

In the industry, it is very common to use the two following sets of parameters to qualify welding procedures for GMAW-S with ER70S-6 of Ø0.045" and 75%Ar-25% CO_2 shielding gas: (1) 190 amperes and 24 volts and (2) 170 amperes and 19 volts. These two sets are taken as examples to explain the way in which the short circuit frequency map can be used in connection with the requirements of AWS D1.1:2015 to define limits for welding procedures specifications (WPSs). Points A and B in Fig. 10 represent 190 amperes and 24 volts and 170 amperes and 19 volts, respectively. Shaded squares were drawn to represent the current and voltage variation ranges where depositing of production welds are allowed with the same procedure qualification record (PQR), in accordance with the limitations stated in AWS D1.1:2015 Structural Welding Code–Steel [2]. These limitations are established for GMAW and are also applicable to welding in short circuit transfer mode (GMAW-S). In this particular case, the current and voltage can change ±10% and ±7%, respectively, from the values recorded during welding the qualification coupon. For example, for the procedure qualification record corresponding to the case A, the code would allow to make welds between 171 and 209 A and between 22.3 and 25.7 V (shaded in green); for point B, the code would allow to make welds between 144 and 176 A and between 18.4 and 20.3V (shaded in blue).

However, in the case of point A, the square includes several metal transfer modes (Short circuit and SC/Globular) and this would be a change in an essential variable for the GMAW process according to Table 4.5 of the code (Variable 14). For point B, the window includes the interruption arc area where the quality of the beads is not consistent and it is possible to find stubbing, lack of fusion and arc interruptions, which make the process difficult to operate by welders. Suitable operation parameters may be found for the definitive WPS drawing the windows allowed by the welding code in the short circuit frequency map and taking in consideration the boundaries where a change in the MTM may occur or where a poor arc stability compromise the quality of the production welds. Engineers or inspectors should consider them so that suitable parameters are achieved during the development of their WPSs, which must meet both the Code and the technical feasibility to produce good welds.

5. Conclusions

- A short circuit frequency map for ER70S-6 steel wire of Ø1.14 mm using 75%Ar-25% CO_2 shielding gas was constructed based on voltage and current signals. Said map proved to be a tool that offers a graphic representation to identify the stability areas for the GMAW-S process and boundaries with different transfer modes.
- High short circuit frequencies (>50Hz) are recommended during welding when high quality is required. A broad range of parameters in the short circuit frequency map can be used to achieve these frequencies.
- With low WFS (2.28 and 2.54 m/min), the highest recorded short circuiting frequencies were 58 and 65.5 Hz at 120A/19.4V and 118A/19.7V, respectively. These parameters also exhibit the minimum standard deviation of the short-circuiting period for each WFS, which is consistent with the studied literature.
- With higher WFS (3.81–6.35 in/min), the maximum short circuit frequency is located near the instability limit. Therefore, a little voltage reduction may cause instability during the weld and, as a result, care should be taken when such parameters are being used.
- Weld beads with good surface appearance were obtained with short circuit and spray MTM, even with short circuit-spray. Globular welds exhibit spatter. Welds in unstable areas with low voltages are very poor in quality and surface appearance.

Aknowledgements

The authors wish to thank the National University of Colombia in Medellín (Universidad Nacional de Colombia, Sede Medellín) and, especially, the Welding Group & Welding Laboratory in said campus for their support, financing, and infrastructure, which enabled to develop this project.

References

[1] American Welding Society. AWS Welding Handbook, Welding processes, Part 1. Ninth Edition, 2, AWS, Miami, FL. 2004.
[2] American Welding Society. AWS D1.1/D1.1M:2015 Structural welding code - steel, 23ª Edition, AWS, Miami, FL, 2015.

[3] Liu, S. and Siewert, T.A., Metal transfer in gas metal arc welding: droplet transfer, Welding Journal, [Online]. 2, pp. 52s-58s, 1989. [Date of reference May 20th of 2018]. Available at: http://files.aws.org/wj/supplement/WJ_1989_02_s52.pdf

[4] Hermans, M.J.M. and Den Ouden, G., Process behavior and stability in short circuit gas metal arc welding, Welding Journal, [Online]. 78(4), pp. 137s-141s. 1999. [Date of reference May 20th of 2018]. Available at: http://files.aws.org/wj/supplement/Hermans/ARTICLE4.pdf

[5] Sorensen, C.D. and Eagar, T.W., Modeling of oscillations in partially penetrated weld pools, Journal of. Dynamic Systems, Measurement and Control. ASME, 112(3), pp. 469-474, 1990. DOI: 10.1115/1.2896166

[6] American Society of Mechanical Engineers. Boiler and pressure vessel Code, Section IX. USA, ASME, 2015.

[7] Zhao, Y. and Chung, H., Numerical simulation of the transition of metal transfer from globular to spray mode in gas metal arc welding using phase field method. Journal of Materials Processing Technology, 251, pp. 251-261, 2018. DOI: 10.1016/j.jmatprotec.2017.08.036

[8] Rudas, J.S., Restrepo, J.S. and Gómez, L.M., Prediction of metal transfer modes in the GMAW process. Proceedings of the Institute of Electrical and Electronics Engineers, IEEE, Automatic Control (CCAC), IEEE 2nd Colombian Conference on Manizales: October 2015. [ONLINE]. [Date of reference May 20th of 2018]. Available at: https://www.researchgate.net/publication/304628756_Prediction_of_metal_transfer_modes_in_the_GMAW_process?ev=publicSearchHeader&_sg=bKM4KdUAO4w0Q_pyPx7Gjdprcy8JCy1QFncwCK4WxM06TkEdFjhgBSvQDGC-6Y0b3UkLho6DY4WZLWI. DOI: 10.1109/CCAC.2015.7345190

[9] Adonyi, Y., Russell, J., Hoyt, D.S. and Berthiaume, N., United States Patent No 9,808,879 B2. Welding diagnostic device for identifying metal transfer modes during a welding process and a method of identifying metal transfer modes of a welding process. [Online]. 2017. [Date of reference May 20th of 2018]. Available at: https://patents.google.com/patent/US9808879

[10] Stenback, N. and Persson, K.A., Shielding gases for gas metal arc welding. Welding Journal, 68(11), pp. 41-47. AWS, 1989.

[11] Scotti, A,V., Ponomarev, V. and Lucas, W., A scientific application oriented classification for metal transfer modes in GMA welding, Journal of Materials and Processing Technology, 212(6), pp. 1406-1413, 2012. DOI: 10.1016/j.jmatprotec.2012.01.021

[12] Bosworth, M.R., Effective heat input in pulsed current gas metal arc welding with solid wire electrodes, Welding Journal, [Online].70(5), pP. 111s-117s, 1991. [Date of reference May 20th of 2018]. Available at: https://app.aws.org/wj/supplement/WJ_1991_05_s111.pdf

[13] Joseph, A.P., Assessing the effects of GMAW-pulsed parameters on arc power and weld heat input. MSc. Thesis, Welding Engineering, The Ohio State University, USA, 2001.

[14] Scotti, A., Olivera, L., Castanheira, V., Keocheguerians, F., Lemos, M. and Souza, D., The influence of the welding voltage and of the shielding gas on the correlation between inductance and metal transfer regularity in Short-Circuiting MIG/MAG Welding. Soldagem & Inspecao, 16(2), pp. 111-122, 2011. DOI: 10.1590/S0104-92242011000200004

[15] Pires, I., Quintino, L. and Miranda, R.M., Analisys of the influence of shielding gas mixtures on the gas metal arc welding metal transfer modes and fume formation rates. Materials & Design, 28(5), pp. 1623-1631, 2007. DOI: 10.1016/j.matdes.2006.02.012

[16] Scotti, A., Mapping transfer modes for stainless steel gas metal arc welding, Science and Technology of Welding and Joining, 5(4), pp. 227-234, 2000. DOI: 10.1179/136217100101538254

[17] Houldcroft, P.T., Welding process technology. Cambridge Engineering. Cambridge University Press, 1977.

D.B. Hoyos-Agudelo, received his BSc. Eng in Mechanical Engineering in 2013 from the Universidad Nacional de Colombia. AWS Certified Welding Inspector (CWI) since 2017. He was a member of the Welding Group at the Universidad Nacional de Colombia and supported several projects related to research and consultancy. He has also worked part-time with several research groups from other universities in Medellín.
ORCID: 0000-0002-7813-9243

O. Mejía-López received his BSc. Eng in Mechanical Engineering in 2009 and his MSc. degree in Materials and Processing Engineering in 2014 from the Universidad Nacional de Colombia. Certified Welding Inspector since 2014. He has been an operative/technician for the Laboratory of Manufacturing Processes at the Universidad Nacional de Colombia since 2009. He was a member of the Welding Group at the same institution.
ORCID: 0000-0002-1252-2805

J.E. Giraldo-Barrada received his BSc. Eng in Mechanical Engineering in 1992, his Sp. degree in Materials Engineering in 1999 and his MSc. degree in Materials and Processing Engineering in 2005, all of them from the Universidad Nacional de Colombia, Medellin, Colombia. AWS Senior Certified Welding Inspector (SCWI) since 2012 and Certified Welding Inspector (CWI) since 1998. From 1990 to 2000, he worked as a design and supervisory engineer for a consulting company related to public hydroelectric power projects and fabrication/erection of steel structures, tanks and electro-mechanical equipment. Since 2000, he has worked as a full time professor at the Engineering of Materials Department, Faculty of Mines, Universidad Nacional de Colombia. He currently works on welding research and development and provides engineering consulting services to companies in the hydroelectric, infrastructure and massive transport sectors. His research interests, as leader of the Welding Group, include welding processes, welding metallurgy and NDT.
ORCID: 0000-0001-6614-0661



UNIVERSIDAD NACIONAL DE COLOMBIA
SEDE MEDELLÍN
FACULTAD DE MINAS

Área Curricular de Ingeniería Mecánica

Oferta de Posgrados

Maestría en Ingeniería - Ingeniería Mecánica

Mayor información:

E-mail: acmecanica_med@unal.edu.co
Teléfono: (57-4) 4259262

UNIVERSIDAD NACIONAL DE COLOMBIA
SEDE MEDELLÍN
FACULTAD DE MINAS



DYNA
http://dyna.medellin.unal.edu.co/

Analysis of the European tourist mines and caves to design a monitoring system

Lluís Sanmiquel [a], Pura Alfonso [a], Marc Bascompta [a], Carla Vintró [b], David Parcerisa [a] & Josep Oliva [a]

[a] *Department of Mining Engineering, Industrial and ICT, Polytechnic University of Catalonia (UPC), Manresa, Spain. lluis.sanmiquel@upc.edu; pura@emrn.upc.edu; marc.bascompta@upc.edu; dparcerisa@epsem.upc.edu; josep.oliva@upc.edu*
[b] *Department of Business Organization, Industrial and ICT, Polytechnic University of Catalonia (UPC), Manresa, Spain. carla.vintro@upc.edu*

Received: January 8th, 2018. Received in revised form: May 16th, 2018. Accepted: May 28th, 2018

Abstract
A database of tourist mines and caves has been created to investigate the requirements of an integrated monitoring system with the aim of ensuring the safety of visitors and preserving the environment of the activities. It contains the main features of each site, in particular the physical, geological and technical information. The results unfold the main characteristics of these sites and give an insight of the parameters to be monitored: number of visitors, temperature, noise, gas concentrations, ground movements, among other factors. All these features are crucial for the safety of tourists and guides, as well as for the preservation of biodiversity and geodiversity. This information will be used to create a system capable of controlling the entire underground activity, such as the one tested in the two case studies.

Keywords: safety; geoheritage; tourism; monitoring; European Union.

Análisis de las cuevas y minas turísticas de Europa para diseñar un sistema de monitorización

Resumen
Se ha creado una base de datos de cuevas y minas turísticas para investigar los requerimientos necesarios para implementar un sistema integrado de monitorización capaz de mantener las condiciones de seguridad de los visitantes y el ambiente adecuado de la actividad. Dicho sistema controla las principales características físicas, geológicas y de información del sitio. Los resultados detallan las principales condiciones de las cuevas y minas turísticas, mostrando los parámetros importantes a controlar: Número de visitantes, temperatura, ruido, concentraciones de gas y movimientos del terreno, entre otros. Todos estos parámetros son fundamentales para mantener la seguridad de los turistas y guías, así como para preservar la biodiversidad y formaciones geológicas particulares de cada sitio. La información incluida en este estudio se usará para obtener un producto similar al mostrado en los casos de estudio.

Palabras clave: seguridad; patrimonio geológico; turismo; monitorización Unión Europea.

1. Introduction

The exploration of natural caves and tourist mines has become increasingly popular in recent years. Around two million people visit caves at national parks in the United States each year [1] and a similar number do so in the European Union (EU). For instance, the Postojna Cave in Slovenia had nearly 500,000 visitors in 2010 [2], while caves from the Dordogne region of western France receive thousands of visitors every year, and more than 20,000 people venture annually through Ireland's Marble Arch Caves Global Geopark or approximately 800,000 tourists visit the Drach Caves in Mallorca, Spain [3].

Besides, the use of mines as a sightseeing place is increasing, especially after mine closure. This activity provides an economic alternative when the natural resource is not economically worthwhile [4]. Tourist mines can constitute a place where visitors can learn about mining and how the society was in mining settlements [4]. Mines are used as tourist places around the world, for example, Coal

How to cite: Sanmiquel, L., Alfonso, P., Bascompta, M., Vintró, C., Parcerisa, D. and Oliva, J., Analysis of the European tourist mines and caves to design a monitoring system. DYNA, 85(205), pp. 249-255, June, 2018.

© The author; licensee Universidad Nacional de Colombia.

mines from Wales [5], the Wieliczka Salt mine in Poland [6], La Union from Spain [7] or the Gambatesa Mine in Italy [8].

Visitors are usually unaware of the risks in underground environments and may behave unpredictably in critical situations [9]. Moreover, many tourist underground places are not equipped with an adequate monitoring system to guarantee visitor's safety, and several authors have reported accidents occurring in underground tourist sites [10]. Although control measures have been widely implemented to mitigate these hazards, there is still a long way to go in improving safety levels.

In addition, atmospheric parameters are very important for the conservation of speleothems and microorganisms in caves and are usually influenced by the number of visitors [7,11-13]. Body heat and lights contribute to increasing the temperature and changing the degree of humidity and evaporation rate [13]. While the air exhaled by visitors can substantially increase CO_2 levels [14], CO_2 levels above 5000 ppm (parts per million) can be dangerous to humans, whereas more than 2400 ppm can deteriorate cave formations or speleothems [15]. Radon is another gas of interest formed by natural radioactivity [16-18]. The presence of radon in confined spaces, such as caves and mines, may be harmful to the health of visitors and guides [19-21]. The control of radon is also important because it is a tracer to predict earthquakes, volcanic eruptions and air movements [22]. Therefore, it should be monitored in tourist caves to obtain correct calculations of the annual effective dose per visitor and to guide and preserve the activities [16]. Currently, European law requires regular controls in tourist mines and caves [21].

Tourist mines and caves are an important part of our heritage as a society. Mines have provided essential raw materials for industrial processes. Nowadays, some abandoned mines have been converted into tourist attractions to educate the public about the geoheritage of the area. Unfortunately, most of the research has focused on archaeological aspects and relics. As a result, castles, churches and other sites associated with important historical events have received great attention, while mining and industry have been among the least-known aspects of heritage [23]. Nevertheless, in recent decades, various authors have begun to study the geoheritage of these places [23,24].

The present study aims to contribute to the development of a technical system designed to ensure safety in underground tourist sites and preserve its optimal environmental conditions. The system consists of specialized wireless ZigBee-based with static and mobile nodes for detecting various parameters and sending corresponding signals to a central unit to process the inputs; for instance, temperature, noise, gases, ventilation, environmental conditions or slow movements (falls, movements in floors and ceilings of galleries, etc.). The system also includes the real-time positioning of visitors. There are several products available in the market that performs some of these functions [25], but they are too expensive for most tourist activities or only consider limited aspects such as monitoring the location of visitors [26,27]. For this reason, a novel product specifically tailored, easy-to-use with low-maintenance was proposed. The developed product will be tested prior to commercialization in several tourist caves and mines in the EU. A database of the safety characteristics from different tourist caves and mines has been gathered as a first step to determine the situation in such activities.

1.1. Safety legislation in the European Union

The regulatory framework applicable to tourist mines and caves is crucial in the development of a technical system designed to ensure safety in underground tourist sites. These regulations cover the planning (permits and licenses for the activity), safety, electrical and electronic devices, as well as the threshold limit values for gases. Furthermore, underground tourist sites may be affected by other laws, such as those concerning the natural environment (protection of ecosystems, animals and vegetation), water, town planning, mountains, geological heritage, etc. The regulatory framework from Germany, Austria, Spain, France, the United Kingdom, Ireland, Italy and Portugal has been analyzed, choosing these countries because they include 70% of all the tourist mines and caves in the EU. Other countries with a long mining tradition were also analyzed.

The mining legislation has not yet been harmonized within the EU. However, there is a specific law concerning health and safety: The European Framework Directive on Health and Safety at Work (Directive 89/391/EEC of 12 June 1989; OJ L 183, 29.6.1989), which has been transposed into the national law of the EU member states. The purpose of this Directive is to improve the safety and health of workers. It includes general principles concerning prevention of occupational hazard, safety and health protection, elimination of risk factors, accident information, consultation and participation of workers in accordance with the national laws, training programs for workers and their representatives and general guidelines for the application of these principles.

On the other hand, Directive 92/104/EEC of 3 December 1992 sets out the common EU regulatory framework for safety in the mining sector, including minimum requirements to improve the protection of workers' health and safety in surface and underground mining (12th individual Directive adopted under paragraph 1 of Article 16 of Directive 89/391/EEC). These basic rules have been transposed into national law by each EU member country, and some countries have even introduced more stringent and more specific regulations.

In most cases, mine safety legislation is the only specific reference for underground tourist sites in the EU. However, regulations have been enacted and guidance notes have been compiled for tourist mines and caves in other countries, such as Australia, where the Queensland Department of Mines and Energy published the Guidance Note QGN 08: Safety at Tourist Mines: Mining and Quarrying Safety and Health Act 1999, or in the United States with the Regulations of the Mine Safety and Training Program for Tourist Mines on 30 November 2002 (2 C.C.R. 407-6).

The presence and concentration of pollutants should be controlled at these sites, with each gas having its specific threshold limit value (TLV). However, there is no harmonized legislation for TLVs. Some countries have established national regulations, while countries with no

national regulations generally adopt the values indicated by the American Conference of Industrial Hygienists (ACGIH) or by the EU Directives. For example, EU Directive 96/62/EC states that EU members must adopt measures to ensure that carbon monoxide (CO) concentrations in the air do not exceed 10 mg/m^3 (average of 8 hours), and EU Directive 96/29/EURATOM states that radon levels must be monitored in natural caves and mines. The ACGIH has also established a maximum concentration of 5000 ppm of carbon dioxide (CO_2) for 8 hours. The International Commission on Radiological Protection (ICRP) (1994) recommends the annual effective dose of radon, implemented by national regulations such as the Spanish Royal Decree 783/2001.

2. Methodology

A database of underground activities has been done by means of the ArcGIS software, with 549 caves and 324 mines, containing their physical and geological characteristics (Fig. 1). Specialized sources were consulted for this purpose, and a survey was needed to obtain more specific information and design an efficient monitoring system.

The open circles stand for caves that did not respond to the survey, while the ones that answered the survey are represented with filled circles. On the other hand, the crosses are mines that did not respond to the survey and filled circles with a white cross of mines with an answer.

The questionnaire was developed in nine languages: English, Spanish, Catalan, French, Polish, Italian, Estonian, Portuguese and German. It was designed to obtain short responses with three main sections:

1. General information of the activity.
2. Seventeen items relating to physical characteristics, technical aspects, environment, safety, and tourist cave regulations in the country.
3. Nine questions to evaluate the utility of the research project.

Some questions were open-ended, while others had a multiple-choice or using a five-point Likert scale. The Cronbach's alpha coefficient was applied to validate the questionnaire [28,29], obtaining a value of $\alpha = 0.827$, indicating its internal consistency and reliability. The initial mailing to 873 facilities (549 caves and 324 mines) was answered by 51 caves and 38 mines, which represents 10.2% of the total, with a maximum sampling error of 12%.

A database of underground activities has been done by means of the ArcGIS software, with 549 caves and 324 mines, containing their physical and geological characteristics (Fig. 1). Specialized sources were consulted for this purpose, and a survey was needed to obtain more specific information and design an efficient monitoring system.

2.1. Undersafe system

Using the information gathered, a system to control tourist mines and caves was created. It consists of a basic unit controlled by a low-power ARM processor. The equipment includes:

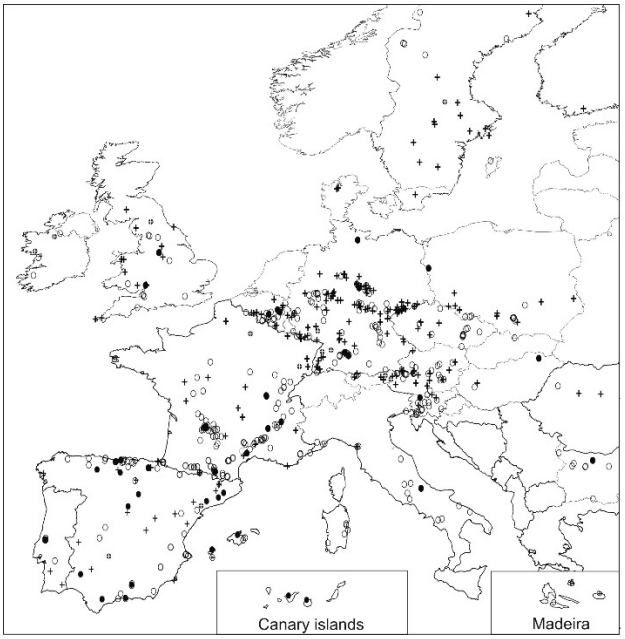


Figure 1. Location of the mines and show caves included in the database. Source: Authors.

- Long distance RFID reader module
- ZigBee communication module
- Battery backup module
- Emergency lighting
- Internal intercom speaker

Communication took place via an Ethernet cable of 1 Gb capacity. It can be done via Wi-Fi module in situations where it is not possible, which is an integral part of the device. The system is able to:

- Track personnel and visitors
- Act as a communication system
- Soil sound detection and underground vibration
- Real-time monitoring of the underground environment: CO, CO2, O2, temperature and humidity.

All this information can be monitored by mobile phone or computer. Fig. 2 displays the system exposed above.

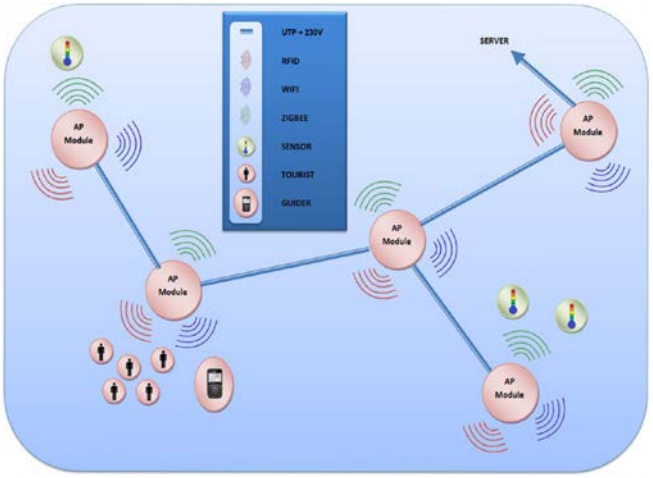


Figure 2. Undersafe system created. Source: Authors.

Table 1.
Number of surveyed mines and caves and answers per country.

Country	Mines or caves	Answers	Percentage of answers (%)
Austria	72	3	4.2
Belgium	25	4	16.0
Bulgaria	19	2	10.5
Croatia	11	3	27.3
Czech Republic	23	0	0.0
Denmark	3	0	0.0
Estonia	1	0	0.0
Finland	5	0	0.0
France	180	15	8.3
Germany	213	14	6.6
Hungary	5	1	20.0
Ireland	5	3	60.0
Italy	44	2	4.5
Luxembourg	1	0	0.0
Malta	1	0	0.0
Holland	2	0	0.0
Poland	33	2	6.1
Portugal	18	1	5.6
Rumania	18	0	0.0
Slovenia	22	2	9.1
Spain	103	32	31.1
Sweden	28	1	3.6
United Kingdom	41	5	12.2
Total	**873**	**89**	**10.2**

Source: Authors.

3 Results and discussion

The facilities analyzed constitute a representative sample of show caves and tourist mines from the EU, of which 10.2% of the answers have similar figures to those of other studies [30]. Table 1 shows the number of activities and answers for each country.

3.1. Physical characteristics of the sites

They are located in diverse geological settings, comprising different types of rocks, with carbonate rocks being the most abundant; although, there are also examples of conglomerates (Font Major Cave, Catalonia, Spain), sandstones and shales (Clearwell Caves, Gloucestershire, United Kingdom; Speedwell and Peak Caverns, Derbyshire, United Kingdom), and volcanic rocks (La Pintada and El Viento Caves, Canary Islands, Spain). In addition, the study encompassed mines containing several types of minerals, such as the salt mines of Wieliczka, Poland, the Eugènia lead mine from Catalonia, Spain, and the Almadén mercury mines from Castile-La Mancha, Spain.

Underground tourist sites vary in length from very short, less than 7 m to more than 1 km. Moreover, most routes had a depth of less than 100 m, all of them being less than 200 m.

Another characteristic that should be considered when planning the safety monitoring system is the presence of water. As a result of karstic processes, many caves contain rivers or lakes. However, these bodies of water are not used for tourist purposes in most cases.

3.2. Visitor control

When designing a monitoring system, the carrying capacity of visitors is an important parameter to consider in terms of safety and influence of visitors to the environment among other parameters [31,32]. Fig. 3 displays the number of visitors per year in the surveyed activities and the maximum capacity of visitors at the same time. The capacity of the facilities depends on the geometrical characteristics, as well as the environmental, ecological and safety issues. The number of available guides is another factor that affects the number of simultaneous visitors.

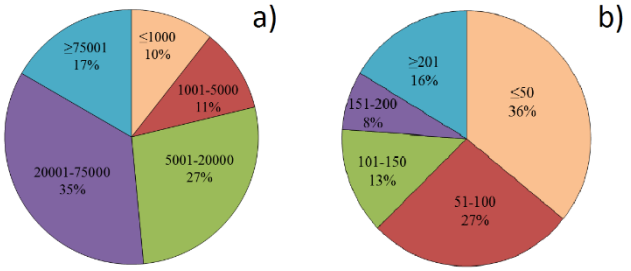


Figure 3. (a) Number of visitors per year; (b) visitors capacity of the activities.
Source: Authors.

Only 11 activities can be visited without a guide. Besides, most of them have less than 15 employees. Some managers mentioned that they would increase the maximum number of visitors if they had the right technology to do so. Most caves (85%) are accessed on foot, and only a few (15%) have other options like vehicles or lifts. The percentages reported in tourist mines were very similar, 83% access on foot and 17% by vehicles or lift.

3.3. Physico-chemical conditions

The control of environmental conditions is crucial to maintain safety levels in underground activities. Maximum and minimum mean temperatures vary between 6 and 15ºC, with some cases below 0ºC or above 20ºC. Internal combustion vehicles in underground tourist facilities can also have an influence on the environment due to the emission of various gases, including CO_2. Fortunately, its use is not common as 2% uses internal combustion vehicles according to the questionnaire.

Ventilation control is also crucial to remove the affected air and provide oxygen to humans. The ventilation system can be either natural or forced, but 14% has set up artificial ventilation.

3.4. Geotechnical control

These risks are often monitored using extensometers or other techniques [33]. Data can be recorded *in situ* or using remote servers [34], and then landslides are predicted to prevent accidents involving visitors. The developed system has been tested using the information gathered from the questionnaire.

3.5. Geoheritage

Most of the tourist sites analyzed in this study have special ecological, geological or prehistoric elements that

should be preserved (for example, karst formations or ancient paintings). A suited monitoring system is crucial to preserve these elements.

3.6. Biodiversity

Many underground sites contain characteristic fauna and flora of interest that could be affected by human impact. An important parameter in this regard is illumination [35-37]. In addition, tourist caves and mines may require physical modifications to allow easy access for visitors, which could alter ecosystems and biodiversity [13,38].

4. Cases studies

The results have been used to design the monitoring system and validate it in a two-case study.

4.1. The Minilla mine (Cardona, Spain)

The tourist mine called Minilla is located in Cardona, 100 km from Barcelona. A former potash mine was closed in 1987 with only one drift accessible to the public. It is a small activity that excavates into a diaper near the surface. It was adapted to touristic visits in 1996 with a length of approximately 500 m.

Previous studies pointed out the hazard due to the existence of dolines, collapsing 70 m eventually. Hence, a network of 8 extensometers was installed in the drift to verify the security level, four in the rock mass and other four through the main fissures (Fig. 4). Each extensometer was connected by means of wires to a junction box located at the exit of the mine, where there was a central unit to detect any movement from the face or floor.

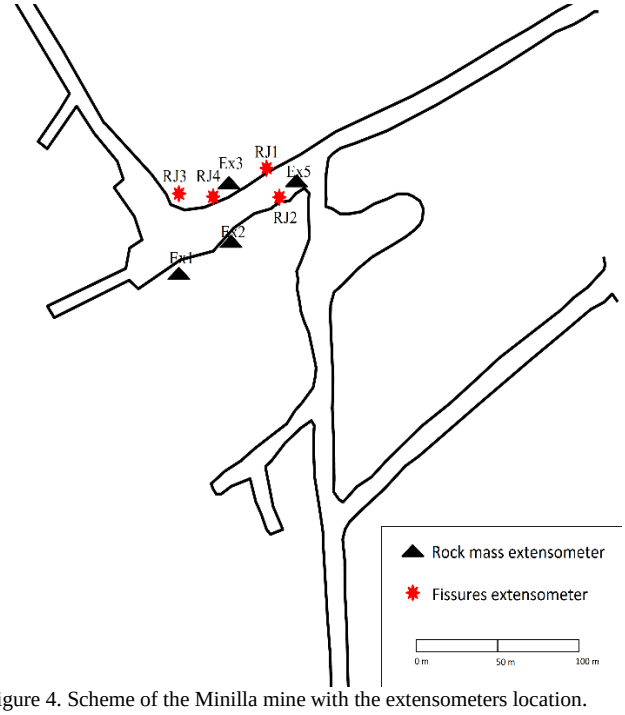


Figure 4. Scheme of the Minilla mine with the extensometers location. Source: Authors.

The use of multiple extensometers to control floor and ceiling movements in mines and caves was successful. For this reason, the system is suggested as a useful option to control geotechnical conditions instead of traditional methods that are more expensive.

4.2 Salt Mine of Wieliczka (Spain)

The Wieliczka mine is one of the most important tourist mines in the world, receiving more than one million tourists per year. In addition, several natural caves are connected to the galleries resulting from the mining activity, such as the Groty Krysztalowe [39].

Salt mines are intrinsically hazardous and are essentially related to gas emissions [40,41]. The preliminary safety system was tested at the Wieliczka mine. The entire system was set up and tested in an underground passage for two days, checking the position of the tourists, temperatures, humidity, gas levels, geophones signal (falling rocks and ground movements) and laser detectors (ceiling, ground and walls movement). These parameters were gathered and managed by the software, obtaining positive validations in all cases. This information was obtained live and was displayed on a digital map. The tests demonstrated that the system is an appropriate tool to improve safety in underground tourist activities.

5. Conclusions

The survey has given an overview of the tourist mines and caves in Europe, their main characteristics and what the system should include to control the site. The proposed system and data gathered may help to open new underground tourist sites and boost their importance as part of the geological and historical heritage. According to the managers of underground tourist sites, the most important factors to control include: number of visitors, physico-chemical and geotectonic parameters, geoheritage care and biodiversity control. Most of the tourist sites analyzed have special ecological, geological or prehistoric elements that should be preserved. However, they may require physical modifications in order to allow easy access to visitors and alter the ecosystem and biodiversity. A balanced solution must be found to promote them while conserving their natural features.

It has also been noted that each country applies different regulations for underground activities, and there is no harmonized regulatory framework. A common EU regulation integrating administrative requirements, geoheritage, ecological and environmental issues, and safety conditions in underground tourist activities would be of great interest.

In addition, the system created has been verified as a useful tool for monitoring the safety and environmental conditions of tourist underground places. The information previously collected has been crucial to know the necessities of the system, verifying its suitability in two case studies.

Acknowledgements

This study forms part of the UnderSafe project, supported by the European Economic Community as part of the 7th Framework Program. The authors would like to thank the staff who responded to the various activities of the questionnaire.

References

[1] Pereira, R., Infectious diseases associated with caves. Wilderness & Environmental Medicine, 22, pp. 115-121, 2011. DOI: 10.1016/j.wem.2011.02.012.

[2] Šebela, S., Prelovšek, M.and Turk, J., Impact of peak period visits on the Postojna Cave (Slovenia) microclimate. Theor. Appl. Climatol. 111, pp. 51-64. 2010.

[3] Ginés, J., Las cuevas turísticas de las Islas Baleares: antecedentes y estado de la cuestión. Publicaciones del Instituto Geológico y Minero de España, Serie Hidrogeología y Aguas Subterráneas, 24, pp. 17-30, 2007. ISSN 0211-2515

[4] Ruíz-Ballesteros, E. and Hernández-Ramírez, M., Identity and community reflections on the development of mining heritage tourism in Southern Spain. Tourism Management, 28, pp. 677-687, 2007. DOI: 10.1016/j.tourman.2006.03.001.

[5] Wanhill, S., Mines- a tourist atraction: coal mining in industrial South Wales. Journal of travel research, 39, pp .60-69, 2000. DOI: 10.1177/004728750003900108.

[6] Smith, M.K., Issues in cultural tourism studies. Routledge, London, UK, 272. 2009.

[7] Peñas-Castejón, J.M., Maciá-Sánchez, J.F., Jiménez-Medina, M.P. and Peñalver-Martínez, M.J., Cyclical salt efflorescence weathering: An invisible threat to the recovery of underground mine environment for tourist exploitation. Environmental Earth Science, 72, pp. 1901-1913, 2014.

[8] Garofano, M. and Govoni, D., Underground geotourism: a historic and economic overview of show caves and show mines in Italy. Geoheritage, 4, pp. 79-92, 2012. DOI: 10.1007/s12371-012-0055-3

[9] Papini, M., Longoni, L. and Dell'Orto, K., Emergency guidelines for two abandoned mines in Piani dei Resinelli area (Lecco). In: Underground spaces: design, engineering and environmental aspects. Book series: WIT Transactions on the Built Environment 102, pp. 99-108, 2008.

[10] Wharton, D.R. and Mortimer, R.B., Rhabdomyolysis after prolonged suspension in a cave. Wilderness & Environmental Medicine, 22, pp. 52-53, 2011. DOI: 10.1016/j.wem.2010.12.007.

[11] Huppert, G., Burri, E., Forti, P. and Cigna, A., Effects of tourist development on caves and karst. In: Williams, P.W. (ed.), Karst terrains: environmental changes and human impact. Catena Supplement, 25, pp. 251-268, 1993.

[12] Gillieson, D., Caves: processes, development, management. Blackwell, Oxford. 1996.

[13] Russell, M.J. and MacLean, L., Management issues in a Tasmanian tourist cave: potential microclimatic impacts of cave modifications. Journal of Environmental Management, 87, pp. 474-483, 2008. DOI: 10.1016/j.jenvman.2007.01.012.

[14] Faimon, J., Stelcl, J. and Sas, D., Anthropogenic CO2-flux into cave atmosphere and its environmental impact: a case study in the Cisařská Cave (Moravian Karst, Czech Republic). Science of the Total Environment, 369, pp. 231-245, 2006.

[15] Kermode, L.O., Cave corrosion by tourists: cave management in Australia 3. Proceedings of the 3rd Australian Conference on Cave Tourism and Management, Mt. Gambier, South Australia. Australasian Cave and Karst Management Association, Carlton South, Victoria, pp. 97-104, 1979.

[16] Lario, J., Sánchez-Moral, S., Cañaveras, J.C., Cuezva, S. and Soler, V., Radon continuous monitoring in Altamira Cave (northern Spain) to assess user's annual effective dose. Journal of Environmental Radioactivity, 80, pp. 161-174, 2005. DOI: 10.1016/j.jenvrad.2004.06.007.

[17] Bahtijari, M., Vaupotic, J., Gregoric, A., Stegnar, P. and Kobal, I., Exposure to radon in the Gadime Cave, Kosovo. Journal of Environmental Radioactivity, 99, pp. 343-348, 2008. DOI: 10.1016/j.jenvrad.2007.08.003

[18] Dumitru, O., Onac, B.P., Fornós, J.J., Cosma, C., Ginés, A., Ginés, J. and Merino, A., Radon survey in caves from Mallorca Island, Spain. Science of the Total Environment, 526, pp. 196-203, 2015 DOI: 10.1016/j.scitotenv.2015.04.076.

[19] Gillmore, G.K., Sperrin, M., Phillips, P. and Denman, A., Radon hazards, geology and exposure of cave users: a case study and some theoretical perspectives. Ecotoxicology and Environmental Safety, 46, pp. 279-288, 2000. DOI: 10.1006/eesa.2000.1922.

[20] Sperrin, M., Denman, T. and Phillips, P., Estimating the dose from radon to recreational cave users in the Mendips, UK. Journal of Environmental Radioactivity, 49, pp. 235-240, 2000. DOI: 10.1016/S0265-931X(99)00108-3.

[21] Bruzzone, D., Bussallino, M., Castello, G., Maggiolo, S. and Rossi, D., Measurement of the concentration of radon gas in the Toirano's caves (Liguria). Annali di Chimica, 96, pp. 515-524, 2006. DOI: 10.1002/adic.200690053.

[22] Tchorz-Trzeciakiewicz, D.E. and Parkitny, T., Radon as a tracer of daily, seasonal and spatial air movements in the Underground Tourist Route "Coal Mine" (SW Poland). Journal of Environmental Radioactivity, 149, pp. 90-98, 2015. DOI: 10.1016/j.jenvrad.2015.07.006.

[23] Edwards, J.A. and Llurdés, J.C., Mines and quarries: industrial heritage tourism. Annals of Tourism Research, 23, pp. 341-363, 1996. DOI: 10.1016/0160-7383(95)00067-4.

[24] Ferrero, E., Giardino, M., Lozar, F., Lozar, F., Giordano, E., Belluso, E. and Perotti, L., Geodiversity action plans for the enhancement of geoheritage in the Piemonte region (north-western Italy). Annals of Geophysics, 55, pp. 487-495, 2012.

[25] Sondag, F., van Ruymbeke, M., Soubiès, F., Santos, R., Somerhausen, A., Seidel, A. and Boggiani, P., Monitoring present day climatic conditions in tropical caves using an Environmental Data Acquisition System (EDAS). Journal of Hydrology 273, pp. 103-118, 2003. DOI: 10.1016/S0022-1694(02)00362-1.

[26] Orellana, D., Bregt, A.K., Ligtenberg, A. and Wachowicz, M., Exploring visitor movement patterns in natural recreational areas. Tourism Management, 33, pp. 672-682, 2012. DOI: 10.1016/j.tourman.2011.07.010.

[27] Versichele, M., de Groote, L., Claeys Bouuaert, M., Neutens, T., Moerman, I. and Van de Weghe, N., Pattern mining in tourist attraction visits through association rule learning on Bluetooth tracking data: a case study of Ghent, Belgium. Tourism Management, 44, pp. 67-81, 2014. DOI: 10.1016/j.tourman.2014.02.009

[28] Cronbach, L.J., Coefficient alpha and the internal structure of tests. Psychometrika, 16(3), pp. 297-334, 1951. DOI: 10.1007/BF02310555

[29] Yang, Y. and Green, S.B., Coefficient alpha: a reliability coefficient for the 21st century? Journal of Psychoeducational Assessement, 29, pp. 377-392, 2011. DOI: 10.1177/0734282911406668.

[30] Sanmiquel, L., Rossell, J.M., Vintró, C. and Freijo, M., Influence of occupational safety management on the incidence rate of occupational accidents in the Spanish industrial and ornamental stone mining. Work 49(2), pp. 307-314, 2014. DOI: 10.3233/WOR-141854

[31] Lobo, A.S.L., Trajano, E., Marinho, M. de A., Bichuette, M.E., Scaleante, J.A.B., Scaleante, O.A.F., Rocha, B.N. and Laterza, F.V., Projection of tourist scenarios onto fragility maps: framework for determination of provisional tourist carrying capacity in a Brazilian show cave. Tourism Management, 35, pp. 234-243, 2013. DOI: 10.1016/j.tourman.2012.07.008.

[32] Lobo, A.S.L., Tourist carrying capacity of Santana cave (PETAR-SP, Brazil): a new method based on a critical atmospheric parameter. Tourism Management Perspectives, 16, pp. 67-75, 2015. DOI: 10.1016/j.tmp.2015.07.001.

[33] Gosar, A., Šebela, S., Košťák, B. and Stemberk, J., On the state of the TM 71 extensometer monitoring in Slovenia: seven years of micro-tectonic displacement measurements. Acta Geodynamica et Geomaterialia, 8, pp. 389-402, 2011.

[34] Klimeš, J., Rowberry, M.D., Blahut, J., Briestenský, M., Hartvich, F., Košťák, B., Rybář, J., Stemberk, J. and Štěpančíková, P., The monitoring of slow-moving landslides and assessment of stabilization measures using an optical-mechanical crack gauge. Landslides 9, pp. 407-415, 2012. DOI: 10.1007/s10346-011-0306-4.

[35] Cardiff, S.G., Ratrimomanarivo, F.H. and Goodman, S.M., The effect of tourist visits on the behavior of Rousettus madagascariensis (Chiroptera: Pteropodidae) in the Caves of Ankarana, Northern Madagascar. Acta Chiropterologica, 14, pp. 479-490, 2012. DOI: 10.3161/150811012X661783.

[36] Merritt, D.J. and| Clarke, A.K., The impact of cave lighting on the bioluminescent display of the Tasmanian glow-worm Arachnocampa

tasmaniensis. J. Insect Conserv. 17, pp. 147-153, 2013. DOI: 10.1007/s10841-012-9493-0.
[37] Piano, E., Bona, F., Falasco, E., La Morgia, V., Badino, G. and Isaia, M., Environmental drivers of phototrophic biofilms in an Alpine show cave (SW-Italian Alps). Science of the Total Environment, 536, pp. 1007-1018, 2016. DOI: 10.1016/j.scitotenv.2015.05.089.
[38] Bourges, F., Genthon, P., Genty, D., Lorblanchet, M., Mauduit, E. and D'Hulst, D., Conservation of prehistoric caves and stability of their inner climate: Lessons from Chauvet and other French caves. Science of the Total Environment, 493, pp. 79-91, 2014. DOI: 10.1016/j.scitotenv.2014.05.137.
[39] Urban, J., Caves and karst sites of Poland as a contribution to geological heritage of Central Europe. Polish Geological Institute Special Papers, 13, pp. 89-96, 2004.
[40] Carrasco-Galán, J., Alarcón-Rojas, D., Albuerne-Pérez, J., Fernández-Bustillo, E., Fernández-Vilas, E., García-García, L. y Madera-García, J., Manual de ventilación de minas y obras subterráneas. Aitemin Centro Tecnológico, Madrid. 2011.
[41] Hedlund, F.H., The extreme carbon dioxide outburst at the Menzengraben potash mine 7 July 1953. Safety Science, 50, pp. 537-553, 2012. DOI: 10.1016/j.ssci.2011.10.004.

L. Sanmiquel, is PhD, working as a professor in the Department of Mining, Industrial and ICT, at the Polytechnic University of Catalonia, Spain.
ORCID: 0000-0001-5612-4713

P. Alfonso, is PhD, he is working as a professor in the Department of Mining, Industrial and ICT, at the Polytechnic University of Catalonia, Spain.
ORCID: 0000-0002-1515-4999

M. Bascompta, is PhD, he is working as an assistant professor in the Department of Mining, Industrial and ICT, at the Polytechnic University of Catalonia, Spain.
ORCID: 0000-0003-1519-6133

C. Vintró. is PhD, he is working as an assistant professor in the Department of Mining, Industrial and ICT, at the Polytechnic University of Catalonia, Spain.
ORCID: 0000-0003-4189-1500

D. Parcerisa, is PhD, he is working as a professor in the Department of Mining, Industrial and ICT, at the Polytechnic University of Catalonia, Spain.
ORCID: 0000-0001-8071-9936

J.Oliva, is PhD, he is working as a professor in the Department of Mining, Industrial and ICT, at the Polytechnic University of Catalonia, Spain.
ORCID: 0000-0001-6214-5713

UNIVERSIDAD NACIONAL DE COLOMBIA
SEDE MEDELLÍN
FACULTAD DE MINAS

Área Curricular de Medio Ambiente

Oferta de Posgrados

Especialización en Aprovechamiento de Recursos Hidráulicos
Especialización en Gestión Ambiental
Maestría en Ingeniería Recursos Hidráulicos
Maestría en Medio Ambiente y Desarrollo
Doctorado en Ingeniería - Recursos Hidráulicos
Doctorado Interinstitucional en Ciencias del Mar

Mayor información:

E-mail: acma_med@unal.edu.co
Teléfono: (57-4) 425 5105

UNIVERSIDAD NACIONAL DE COLOMBIA
SEDE MEDELLÍN
FACULTAD DE MINAS



DYNA
http://dyna.medellin.unal.edu.co/

Characterization of postures to analyze people's emotions using Kinect technology

Julián Alberto Monsalve-Pulido [a] & Carlos Alberto Parra-Rodríguez [b]

[a] *Universidad Santo Tomás Tunja, Colombia. julian.monsalve@usantoto.edu.co*
[b] *Pontificia Universidad Javeriana, Bogotá, Colombia. carlos.parra@javeriana.edu.co*

Received: December 15th, 2017. Received in revised form: May 10th, 2018. Accepted: May 29th, 2018

Abstract
This article synthesizes the research undertaken into the use of classification techniques that characterize people's positions, the objective being to identify emotions (astonishment, anger, happiness and sadness). We used a three-phase exploratory research methodology, which resulted in technological appropriation and a model that classified people's emotions (in standing position) using the Kinect Skeletal Tracking algorithm, which is a free software. We proposed a feature vector for pattern recognition using classification techniques such as SVM, KNN, and Bayesian Networks for 17,882 pieces of data that were obtained in a 14-person training sample. As a result, we found that that the KNN algorithm has a maximum effectiveness of 89.0466%, which surpasses the other selected algorithms.

Keywords: analysis of emotions; recognition of postures; free software; Kinect, KNN.

Caracterización de posturas para el análisis de emociones de personas, por medio de la tecnología Kinect.

Resumen

El presente artículo sintetiza la investigación realizada en el uso de técnicas de clasificación para un proceso de caracterización de posturas de personas que tiene como objetivo la identificación de emociones (Asombro, Enfado, Felicidad y Tristeza). En este proyecto de investigación fue necesario utilizar una metodología de investigación exploratoria en tres fases donde el resultado es una apropiación tecnológica y un modelo de clasificación de emociones en personas en posición de pie, usando el algoritmo de Skeletal Tracking de Kinect basado en software libre. Se propuso un vector de características para el reconocimiento de patrones usando técnicas de clasificación como SVM, KNN y Redes Bayesianas en 17.882 datos obtenidos en una muestra de entrenamiento de 14 personas. Como resultado se evidenció que el algoritmo KNN tiene una efectividad máxima del 89.0466% superando a los demás algoritmos seleccionados.

Palabras clave: análisis de emociones; reconocimiento de posturas; software libre; Kinect; KNN.

1. Introduction

Human-machine interaction has been evolving over recent years, in particular Natural User Interface (NUI), which aims to integrate the user interaction with a computer system using natural perception. NUI can be manipulated depending on user-needs through direct or intermediate devices that create a transparent and discreet perception [1,2]. This research appropriates the Kinect technology as a Natural User Interface, and the objective is to characterize people's positions to identify emotions.

The application of this research focuses on the development of a regional problem in Boyacá, Colombia. Problems have been identified in the tourism sector due to the absence of effective mechanisms to promote and market tourist destinations resulting from the poor coordination and execution of good strategies to boost the sector. To help the development of tourism in the region it is necessary to carry out an analysis of experiential tourism as this is a new form of tourism that is based on the emotions and experiences tourists experience through interacting with the

How to cite: Monsalve-Pulido, J.A. and Parra-Rodríguez, C.A., Characterization of postures to analyze people's emotions using Kinect technology. DYNA, 85(205), pp. 256-263, June, 2018.

© The author; licensee Universidad Nacional de Colombia.

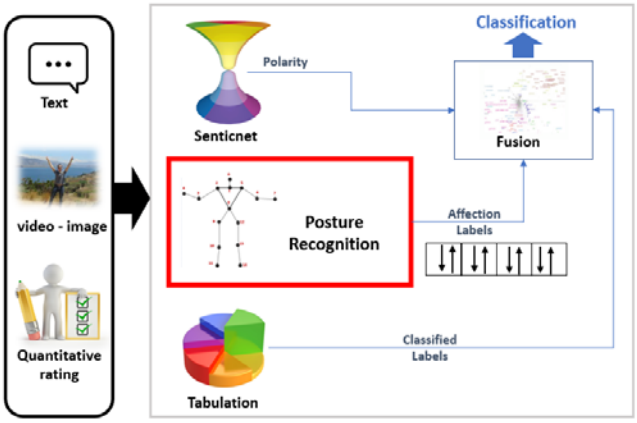


Figure 1. Integration of posture recognition to the multimodal model
Source: Authors

destination; it can be defined as an extraordinary personal experience that combines both tangible aspects that are represented in tourism products, and intangible aspects such as freedom, security, tranquility, and relaxation [3,4]. As digital media is used in all aspects of a tourist's experience, it is necessary to create automatic interpretation mechanisms that qualify emotions or feelings about a tourist product or service. These mechanisms are part of the Natural Language Processing area that can be defined as: *"Discipline focused on the design and implementation of computer applications that communicate with people through the use of natural language"* [5]. Also, when applying sentiment analysis opinions, the most complete definition is the following: It is a *"Set of computational techniques for the extraction, classification, understanding and evaluation of opinions expressed in sources published on the Internet, comments on web portals and other content generated by users"* [6].

The data to be analyzed come from various sources (social networks, travel planners, blogs, etc.) and from different types of data (text, images, sounds, videos, and numerical values) for which it is necessary to use multimodal methodologies to perform a classification and thus identify a good polarity. As a solution to the problem, we propose creating a multimodal model to generally analyze feelings or by using a fusion process that would integrate the results of text classification, postures, and quantitative qualifications of a tourist product or service. This article only documents the results of recognizing positions that, in the future will be integrated into the multimodal model by interpreting the resulting vector through a merger at the decision or identity level. In Fig. 1, the multimodal model is described.

The diversity of information and the volume of data that must be analyzed is due to the mass storage of digital media information that is generated by people and electronic devices. Digital's January 2016 report,[1] for example, mentions that 46% of the global population has Internet access (3,419 billion people), and 31% (2,307 billion people) are active users of social networks. Facebook is top on the list with 1,550 million users, Qzone has 653 million users, Tumblr has 555 million users, Instagram has 400 million, Twitter has 320 million, baidu has 300 million, sina weibo has 222 million, and YY has 122 million users. Facebook users generate more than 500 Terabytes of content each day; there are more than 2,700 million "likes" and around 300 million photographs [7]. This data source is desired by the large marketing industries whose objective is to undertake a large-scale analysis of structured and unstructured information using BigData or Data Mining techniques.

Identifying emotions is a complex process that is the result of physical and psychological reactions that develop in behavior such as thinking and creating ambiguous natural language variables that are difficult to interpret such as surprise, anxiety, fear, and irony [8,9]. Emotions influence different ways of acting depending on our thoughts. Unexpected events that affect our normal behavior can lead to changes in behavior and decision making. To develop applications, human emotions are important in terms of usability, especially in intelligent environments, where emotions influence cognition, and, therefore, intelligence. This is particularly true when social decisions [8,10] are made. Therefore, the research focuses on identifying emotions (happiness, amazement, anger, and sadness) based on supervised postures.

The article begins with an explanation of the methodology that was applied to the investigation followed by a brief description of the state of art, and then some pattern recognition techniques are considered. Finally, we present the conclusions of the results obtained.

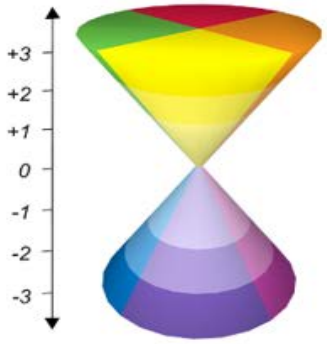
2. Related work

Non-verbal communication is the communication process in which messages are sent and received without words: through signs, and gestures [11]. This has no syntactic structure, so sequences of hierarchical constituents cannot be analyzed. The first impression a person makes occurs within seven seconds, and 93% of the information we communicate depends on our body language. A conversation is constituted by two parts: the verbal or conscious and the non-verbal or unconscious and emotional. This research only analyzes unconscious non-verbal conversation and focuses on body positions where gestures communicate feelings, emotions, intentions in a fraction of a second using Kinect technology [12].

When identifying emotions, several authors have investigated models that combine different areas such as psychology, biology, and neuroscience; their results include how emotions and intelligence are combined. One example is the Sentic Computing [8] research for which investigators have developed a 3D sandglass model that represents affective states through labels. Four independent but related affective dimensions are used that can potentially describe the full range of emotional experiences rooted in any of us.

Sentiment analysis in digital environments has changed the way of analyzing user-opinions through quantitative or qualitative indicators that qualify a product or service from which information generated by consumers is extracted in large volumes freely and spontaneously during the process of

[1] https://www.slideshare.net/wearesocialsg/digital-in-2016



	Pleasantness	Attention	Sensitivity	Aptitude
+3	ecstasy	vigilance	rage	admiration
+2	joy	anticipation	anger	trust
+1	serenity	interest	annoyance	acceptance
0	—	—	—	—
-1	pensiveness	distraction	apprehension	boredom
-2	sadness	surprise	fear	disgust
-3	grief	amazement	terror	loathing

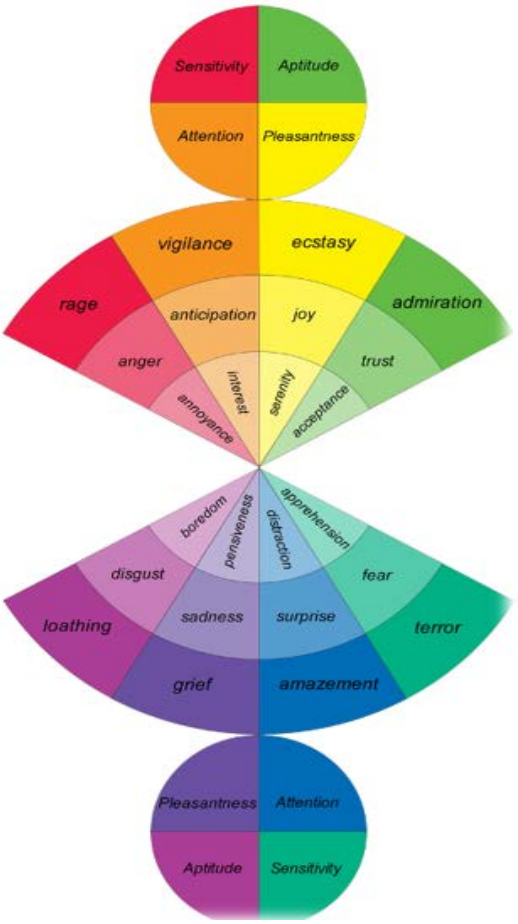


Figure 2. 3D model and emotions hourglass
Source: [8]

buying a product or service (the before, during, or at the end). In most cases, opinion-mining is applied to large volumes of information, specifically in text analysis, where approaches are used such as subjective lexicon, the use of the N-Gram model, and machine learning [13]. In sentiment analysis research, several methodologies that function as a basis for an effective process have been proposed. An example is the one proposed by [14] which includes five steps to develop an effective analysis. These steps are: lexicon generation, subjectivity detection, polarity detection, sentimental structure, and sentiment visualization.

Information that is currently stored in diverse sources is multimodal, and the combination of text, image, video, or sound generates a broader problem when analyzing feelings, and it is necessary to create and identify models or recognition techniques for a multimodal classification. The ability to perform multimodal fusion is an important prerequisite to successfully implement agent-user interaction. One of the main obstacles to multimodal fusion is the development and specification of a methodology that integrates cognitive and affective information from variant sources at diverse time scales and with different measurement values [15]. There are fusion techniques that will help with more effective interpretation. One example is

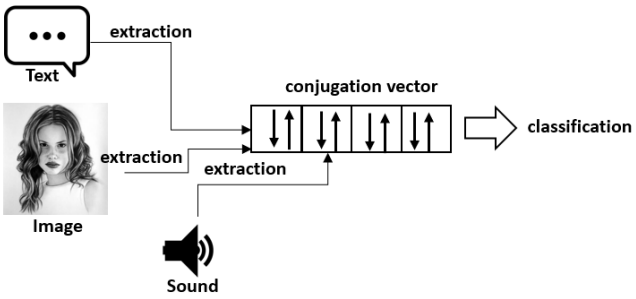


Figure 3. Fusion at the identity level
Source: Adapted from [15].

fusion on an entity level, which combines the characteristics extracted from each input channel in a vector of the conjunction before any classification operation is performed in any fusion [16]. This presents a problem that integrates highly disparate input characteristics in the synchronization of multiple inputs by unnecessary repetitions and increasing the computational resource [15].

Moreover, when considering merger at the decision level, each modality is modeled and classified independently. Unimodal results are combined at the end of the process by

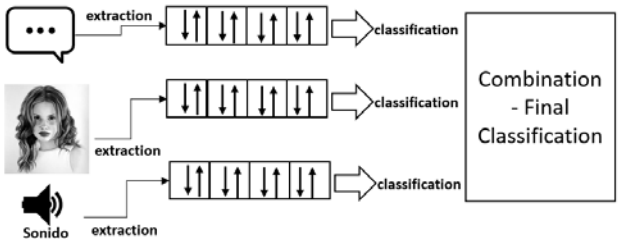


Figure 4. Fusion at the decision level
Source: Adapted from [17]

choosing suitable metrics such as expert rules and simple operators, including majority votes, sums, products, and statistical weighting. This merger has a decision-level benefit as the preferred method of data fusion since the different classifier errors tend not to be correlated, and the methodology is independent of the characteristics [17].

The investigation in [18] is an example of the above; the authors developed a new approach to recognizing bimodal emotions based on facial expression and speech and used the fusion method of range regression (SKRRR). Furthermore, in the research carried out by [19], a methodology was developed to analyze multimodal feelings, which aims to collect feelings in web videos and then demonstrate a model that integrates audio, visuals, and text by fusing characteristics and extracting affective information in multiple modalities. The results obtained are accurate by almost 80%; this figure surpasses all the vanguard systems by more than 20%.

An evolution of NUI was the creation of the Kinect sensor, for which the initial functionality evolved and improved the user experience in video games by using a natural interaction such as movement and voice. This has been used in research in various areas, and important results have been obtained in image and sound recognition [20]. The Kinect[2] sensor incorporates several detection components; and it contains a depth sensor, a color camera, and a matrix of four microphones that provide the entire body with 3D motion capture, facial recognition, and speech recognition capabilities.

Kinect technology has been used in the identification of emotions during multimodal analysis. [22], for example, recorded video and depth images of some students in a classroom with Kinect technology; the data were processed with techniques that tracked posture and face-to-face gestures. The results obtained related to the tutor´s identification of perception that was implicitly found in students´ physical demand and frustration. In addition, posture and gesture were correlated with student´s cognitive-affective states that tutors perceived through the implicit affective channel. [23] used Kinect technology to identify consumer reactions in a food testing kiosk with a multimodal system programmed to recognize affection to classify if a consumer likes or dislikes a tested product. The consumer´s facial expression, body posture, hand gestures, and voice were analyzed after testing the product. The result was that a classifier was created through an algorithm that assigned emotion templates using vector support machines.

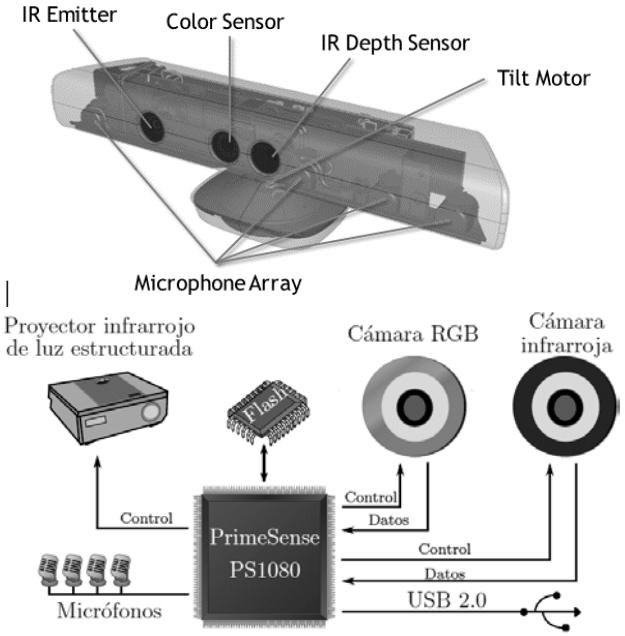


Figure 5. Physical structure of the camera
Source: [20, 21].

3. Materials and methods

To undertake this research, we proposed a three-phase methodology, and the main objective is to characterize emotions through postures. The first phase included detailing the state of the art regarding previous research in the following areas: feelings analysis using Kinect technology, feelings analysis in psychology, technical analysis of the Kinect device, and social analysis when identifying emotions and feelings. The second phase included the creation of a model to collect and interpret information postures generated by Kinect technology, and the characterization of four feelings using pattern recognition algorithms. Phase three concludes with the results obtained and with a proposal for future work.

One of the main functions of the Kinect sensor "Skeletal tracking" was used during the research. This is based on a skeleton tracking algorithm that manages to identify people´s body parts who are in the sensor´s field of vision. Using this algorithm, we can obtain points that refer to a person´s body parts and then identify gestures and / or postures. The sensor identifies twenty reference points (head, center of the shoulder, shoulder right, shoulder left, elbow right, elbow left, right wrist, left wrist, right hand, left hand, spine, center of hip, left hip, right hip, right knee, left knee, right ankle, left ankle, right foot, and left foot).

To track the Kinect skeleton, the depth images must be processed, human forms must be detected, and the body parts of the user in the image must be identified. Each body part is abstracted as a 3D coordinate called an articulation; a set of articulations forms a virtual skeleton for each of Kinect´s depth images, that is, 30 skeletons are obtained per second.

2 https://blogs.msdn.microsoft.com/esmsdn/2011/08/09/reto-sdk-de-kinect-detectar-posturas-con-skeletal-tracking/

Item	Reference Point
0	Head
1	Neck
5	Right Shoulder
6	Right Elbow
7	Right Hand
2	Left Shoulder
3	Left Elbow
4	Left Hand
8	Center of Torso
9	Left Hip
12	Right Hip
10	Left Knee
13	Right Knee
11	Left Foot
14	Right Foot

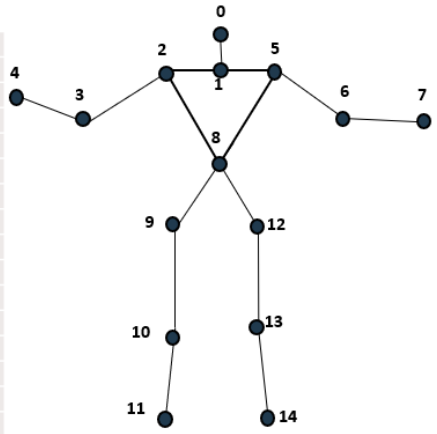


Figure 6. Kinect benchmarks in OpenNI
Source: Adapted from [20]

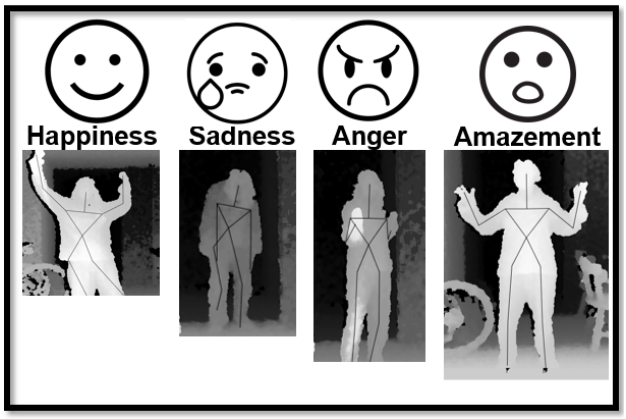


Figure 7. Emotions for classifier training.
Source: Authors

The articulations generated vary according to the Kinect library used [20]. For this research, the free distribution framework OpenNI[3] (Open Natural Interaction) was used with an open source license and multiplatform development. This supports a middleware that implements characteristics of complete analysis and skeletal follow-up and an analysis of the position and follow-up of the hands or gesture recognition. The framework incorporates the NITE module. This module integrates a library that identifies each skeleton with its 15 articulations ai = {xi, yi, zi} with zi> 0 (see Fig. 6). The coordinates of this are expressed in millimeters with respect to the position of Kinect in the scene. In the Microsoft SDK and the Xbox console, five joints are added (the ankles, the wrists, and the center of the hip). The configuration and programming of the framework used was made on a GNU / Linux platform with java programming language using a three-layer architecture to integrate the storage and query of information in a posture characteristics model. Weka libraries are integrated so we could use the recognition algorithms and a Postgres database.

This research identified four feelings (happiness, sadness, anger, and amazement), which are described in Fig. 7. Happiness is a feeling of fullness, joy, fulfillment, and enjoyment; sadness a feeling of emptiness, restlessness, decay, and demotivation; anger a feeling of annoyance and offense; and amazement a feeling of discovering something unforeseen or unexpected.

To construct of the classifier, we tested unsupervised algorithms for pattern recognition: one of the main ones evaluated was the Support Vector Machines (SVM). The main objective of this method is to find an optimal hyperplane margin using support vectors capable of forming a decision border around the learning data domain. The hyperplane is defined by:

$$F(x) = w^t.x + b = 0 \quad (1)$$

$$\text{Margin: } min\ \frac{1}{2}\ \|w\|^2 \quad (2)$$

where w is the normal weight vector of the separation hyperplane, b is the partial term, and x is the vector of n characteristics. The classification of a new individual x (i) is given by his or her position relative to that of the Hyperplane. SVM is based on the use of kernel functions that allow optimal separation data to be obtained. These are some of the kernel examples used in SVM [24]:

$$\text{Polynomial: } K(x,z) = \langle x,z\rangle^a \quad (3)$$

$$\text{Radial base functions: } K(x,z) = e^{-\|x-z\|^2/2\sigma} \quad (4)$$

$$\text{Sigmoid: } K(x,z) = \tanh(\tanh(k\langle x,z\rangle - \delta \quad (5)$$

$$\text{Reverse quadratic multi: } K(x,z) = (\|x - z\|^{\frac{1}{2}}\ 2\sigma + C^2)^{-1} \quad (6)$$

$$\text{Insertion kernel: } K(x,z) = \sum_{i=1}^{n} \min(x(i), z(i)) \quad (7)$$

Other classification methods explored are the nearest k-neighbor, the KNN target given a vector x (i), and a set N of neighbors marked with mN. The task of the classifier is to predict the class tag of x (i) based on the class labels of set N by majority vote. In KNN, the most important parameter is the number of neighbors k. The choice of k is essential to build the nearest k-neighbors model. Thus, k can strongly influence the performance of generalization. The value of k must be large enough to minimize the probability of error, but also reasonably low compared to mN or the size of the set N [25].

Furthermore, the Bayesian classifier is a supervised learning algorithm and a statistical method based on Bayes theorem. Given a sample x (i) and a set of training samples S, each with its class label Cl with l ∈ [1, L] and L being the number of classes, the classifier predicts that x (i) belongs to the class with the highest posterior probability:

[3] http://openni.ru/reference-guide/index.html?t=index.html

$$P(C_l \mid x^{(i)} = \frac{P(x^{(i)} \mid C_l)P(C_l)}{P(x^{(i)})} \quad (8)$$

4. Results

To develop the system, we used free software tools, and the objective was to integrate a scalable solution to continue with the research without any limitations regarding proprietary licenses. The following tools were used in the model: was Processing[4]; which is the core of flexible and adapted solutions to learn about visual arts in digital environments; OpenNI, as previously mentioned, stands for Open Natural Interaction, and is a tool that focuses on the certification and improvement of the interoperability of the natural user interface and the organic user interface for natural interaction devices for device applications such as the Kinect [20]. To recognize the skeleton of the 15 reference points, the Simple-Openni library was used and libraries extracted from WEKA[5] were used to apply the pattern recognition algorithms. The model´s integral solution was developed with the Eclipse development interface using the Java language and libraries.

When constructing the model, we identified the existing protocols to collect information on people´s movements using a video device; the Protocol of positioning marked Davis [26] is taken as a basis for this research since it is one of the most commonly used in biomechanics. It consists of using the anatomical points of bony eminences depending on the movement analysis that must be analyzed. The fifteen points obtained from the skeleton that are captured in the camera are stored in a "Capture" table with the structure (node, PosX, PosY, PosZ); they are then consulted during the training and classification process.

The classifier starts with a capture process using the Kinect camera for an initial calibration; it then starts the training process so that the classifier interprets the data input using the Kinect camera (see Fig. 8).

The general model begins with capturing the information through the Skeletal Tracking´s 15 points that are generated by Kinect; the information is then stored on a database created in Postgres where the classifier can consult it. For the training process, we created a file.arff with a specific structure to be verified by the Weka library (see Fig. 9).

Weka captures information and generates a classification model according to the selected algorithm (SVM, KNN, NB) and creates the final classification according to the Skeletal Tracking input information based on the proposed model (see Fig. 10).

For the model´s tests, 17,882 training data were used from fourteen randomly selected people who simulated basic emotions (astonishment, anger, happiness, and sadness). The coordinates xi, yi, and zi (0 <i <14), depend on the size and position of the person in the scene, and the following feature vector was identified:

[x0,y0,z0,x1,y1,z1,x2,y2,z2,x2,y2,z3,x3,y3,z3,x4,y4,z4,x5,y5,z5,x6,y6,z6,x7,y7,z7]

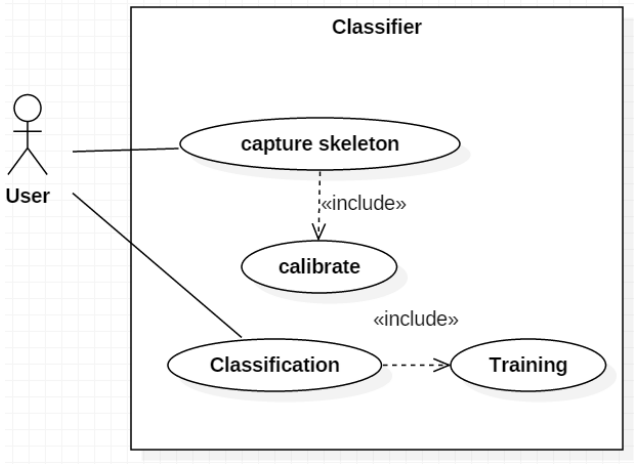


Figure 8. Use case diagram
Source: Authors

```
@RELATION gestos

@ATTRIBUTE nodo REAL
@ATTRIBUTE x    REAL
@ATTRIBUTE y    REAL
@ATTRIBUTE z    REAL
@ATTRIBUTE class    {Asombro,Enfado,Felicidad,Tristeza}

@DATA
0,325.2185,71.8983,2090.5146,Asombro
```

Figure 9. ARFF file Structure
Source: Authors

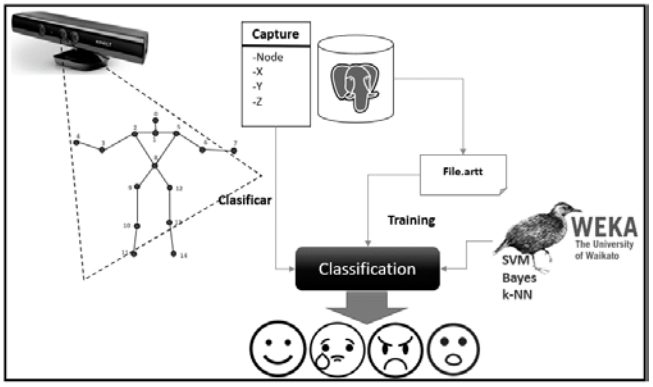


Figure 10. Posture characterization proposed model.
Source: Authors

Table 1.
Distribution of data on emotions for training purposes.

Emotion	No data
Amazement	4076
Anger	4680
Happiness	4851
Sadness	4275

Source: Authors

[4] https://processing.org

[5] https://www.cs.waikato.ac.nz/ml/weka/

Table 2.
Performance of the classifiers.

Training data	SVM RBF	KNN -	NB -
10	80.5894 %	85.807 %	81.6575 %
20%	77.5269 %	89.0466 %	78.9808 %
40%	79.6812 %	88.5357 %	80.9582 %
60%	80.7773 %	87.7254 %	81.8817 %
80%	80.8166 %	86.5213 %	82.019 %

Source: Authors

For the classifiers analysis tests, five different types of training data were used (see Table 2), The first included ten random samples and had important results with a KNN that was 86.1928% effective. The second had 20% training data, and it was shown that the KNN algorithm is 89.0466% effective, which significantly surpasses the other classifiers. In the other training tests (using 40%, 60%, and 80% of total data for training) the KNN algorithm remains above the rest of the classification algorithms.

5. Conclusions

This study showed that the KNN algorithm performs more completely than SVM and NB and has a maximum effectiveness of 89.0466% for the set of selected data. It can also be used as a foundation to develop applications that recognize basic emotions (astonishment, anger, happiness, and sadness) using Kinect technology. The algorithms based on SVM and NB have a lower percentage than the KNN, but future studies could consider their effectiveness since this can be improved with unsupervised learning.

The applied vector of characteristics can vary for classifications of more complex negative emotions, for example ((+) rage, anger, annoyance, (-) apprehension, fear, terror). This means that it would be necessary to identify additional points of the skeleton, which would increase the complexity when recognizing emotions.

The data results of this investigation will be integrated into a general multimodal sentiment analysis model that considers the tourist area in the department of Boyacá Colombia. It will be merged using a conjunction vector for a final sentiment classification that analyzes data types such as text and images.

Using free distribution tools for research processes creates a channel of collaborative help communication. This takes advantage of solutions from communities around the world to make contributions to science without the need to reinvent the wheel or have a large budget to carry out a research project. For this research, we used tools including OpenNI, NITE, Weka, Java that helped classify emotions, and the result was a technically functional and economically viable product.

Human-computer interaction (HCI) has improved over recent years; the Natural User Interfaces (NUI) have created usability solutions where valuable information is stored and can be analyzed to identify users´ emotions. Kinect is not only for use in video games; it can also be applied in various areas of knowledge due to its great potential for innovative hardware and its increasing usefulness in research.

Referencias

[1] Mann, S., Intelligent image processing. IEEE, John Wiley & Sons, Inc., 2002. DOI: /10.1002/0471221635

[2] Valli, A., Natural interaction white paper, 2007.

[3] Rivera-Mateos, M., El turismo experiencial como forma de turismo responsable e intercultural, en: García-Rodríguez, L., Roldán-Tapía, A.R., Eds., Relac. Intercult. en la Divers., 2013, pp. 199-217.

[4] Smith, W.L., Experiential tourism around the world and at home: definitions and standards, Int. J. Serv. Stand., 2(1), 1 P, 2006. DOI: 10.1504/IJSS.2006.008156

[5] Dale, R., Moisl, H. and Somers, H.L., Handbook of natural language processing, Marcel Dekker, 2000.

[6] Cambria, E. and Hussain, A., Sentic album: content-, concept-, and context-based online personal photo management system, Cognit. Comput., 4(4), pp. 477-496, 2012. DOI: 10.1007/s12559-012-9145-4ch

[7] Simon-Kemp, W.A.S., Digital in 2016, 2016.

[8] Cambria, E., Livingstone, A. and Hussain, A. The Hourglass of Emotions. In: Esposito, A., Esposito, A.M., Vinciarelli, A., Hoffmann, R. and, Müller, V.C., (eds.), Cognitive Behavioural Systems. Lecture Notes in Computer Science, vol 7403. Springer, Berlin, Heidelberg. 2012. DOI: 10.1007/978-3-642-34584-5_11

[9] Minsky, M., The emotion machine: commonsense thinking, artificial intelligence, and the future of the human mind, 2007.

[10] Vesterinen, E., Affective computing. Pattern Analysis and Applications, 1(1), pp. 71-73, 1998.

[11] Siegman, A.W. and Feldstein, S., Nonverbal behavior and communication. L. Erlbaum, 1987.

[12] Pons, C., Comunicación no verbal. Barcelona: Editorial Kairós, 2015.

[13] Kaur, A. and Gupta, V., A survey on sentiment analysis and opinion mining techniques, J. Emerg. Technol. Web Intell., 5(4), pp. 367-371, 2013. DOI: 10.4304/jetwi.5.4.367-3

[14] Gamon, M., Aue, A., Corston-Oliver, S. and Ringger, E., Pulse: mining customer opinions from free text, Springer, Berlin, Heidelberg, 2005, pp. 121-132. DOI: 10.1007/11552253_12

[15] Poria, S., Cambria, E., Hussain, A. and Bin Huang, G., Towards an intelligent framework for multimodal affective data analysis, Neural Networks, 63, pp. 104-116, 2015. DOI: 10.1016/j.neunet.2014.10.005

[16] Kapoor, A., Burleson, W. and R Picard, W., Automatic prediction of frustration, Int. J. Hum. Comput. Stud., 65(8), pp. 724-736, 2007. DOI: 10.1016/J.IJHCS.2007.02.003

[17] Lisetti, C.L., Pattern Analysis & Applic, 1, J. Wiley, 1998, 71 P. DOI: 10.1007/BF01238028

[18] Yan, J., Zheng, W., Xu, Q., Lu, G., Li, H. and Wang, B., Sparse Kernel reduced-rank regression for bimodal emotion recognition from facial expression and speech, IEEE Trans. Multimed., 18(7), pp. 1319-1329, 2016. DOI: 10.1109/TMM.2016.2557721

[19] Poria, S., Cambria, E., Howard, N., Bin Huang, G. and Hussain, A., Fusing audio, visual and textual clues for sentiment analysis from multimodal content, Neurocomputing, 174, pp. 50-59, 2016. DOI: 10.1016/j.neucom.2015.01.095

[20] Benhumea, H.S., Interfaz de lenguaje natural usando Kinect. Unidad Zacatenco, 2012.

[21] Zeev-Zalevsky, J.G., Shpunt, A. and Maizels, A., Method and system for object reconstruction [online]. [date of reference: Sept. 04th of 2016]. Available at: https://patents.google.com/patent/US20170004623

[22] Grafsgaard, J.F., Fulton, R.M., Boyer, K.E., Wiebe, E.N. and Lester, J.C., Multimodal analysis of the implicit affective channel in computer-mediated textual communication, Proc. 14th ACM Int. Conf. Multimodal Interact., pp. 145-152, 2012. DOI: 10.1145/2388676.2388708

[23] Patwardhan, A.S. and Knapp, G.M., Multimodal affect analysis for product feedback assessment, 2013, pp. 178-187.

[24] Choubik, Y. and Mahmoudi, A., Machine learning for real time poses classification using kinect skeleton data, in: 13th International Conference on Computer Graphics, Imaging and Visualization (CGiV), 2016, pp. 307-311. DOI: 10.1109/CGiV.2016.66

[25] Shum, H.P. H., Ho, E.S.L., Jiang, Y. and Takagi, S., Real-time posture reconstruction for Microsoft Kinect, IEEE Trans. Cybern., 43(5), pp. 1357-1369, 2013. DOI: 10.1109/TCYB.2013.2275945

[26] Davis, R.B., Ounpuu, S., Tyburski, D. and Gage, J.R., A gait analysis data collection and reduction technique, Hum. Mov. Sci., 10(5), pp. 575-587, 1991. DOI: 10.1016/0167-9457(91)90046-Z

J.A. Monsalve-Pulido, obtained his BSc. in Systems and Computing degree in 2005 and his MSc. degree in Free Software in 2008 from the Universidad Autónoma de Bucaramanga, Colombia and the Universitat Oberta de Catalunya, Spain respectively. Heb is currently undertaking his PhD in engineering at the Pontificia Universidad Javeriana, Colombia. Also, he works as a research professor in the Systems Engineering Faculty at St. Thomas University in Tunja, Colombia, and he is a leader of the GIDINT research group. His research has included big data, information systems, and learning networks, and his research interests include software engineering and data mining.
ORCID: 0000-0002-0706-5881

C.A. Parra-Rodríguez, is a full professor in the Department of Electronics at the Pontificia Universidad Javeriana, Colombia and the director of the School of Engineering. prof. Parra has experience in the application of data science in robotics and perception for robotics and has published over fifty publications.
ORCID: 0000-0001-7209-6150



UNIVERSIDAD NACIONAL DE COLOMBIA
SEDE MEDELLÍN
FACULTAD DE MINAS

Área Curricular de Ingeniería
de Sistemas e Informática

Oferta de Posgrados

Especialización en Sistemas
Especialización en Mercados de Energía
Maestría en Ingeniería - Ingeniería de Sistemas
Doctorado en Ingeniería- Sistemas e Informática

Mayor información:

E-mail: acsei_med@unal.edu.co
Teléfono: (57-4) 425 5365

UNIVERSIDAD NACIONAL DE COLOMBIA
SEDE MEDELLÍN
FACULTAD DE MINAS



DYNA
http://dyna.medellin.unal.edu.co/

Local polynomial approximation and intersection of confidence intervals for removing noise of lightning electric field measurements

Herbert Enrique Rojas-Cubides [a], Camilo Andrés Cortés-Guerrero [b] & María Carolina Forero-Mejía [c]

[a] *Department of Electrical Engineering, Universidad Distrital Francisco José de Caldas, Bogotá DC, Colombia. herojasc@udistrital.edu.co*
[b] *Department of Electrical and Electronic Engineering, Universidad Nacional de Colombia, Bogotá DC, Colombia. caacortesgu@unal.edu.co*
[c] *ENEL Colombia., Bogotá DC, Colombia. maria.forero@enel.com*

Received: April 20th, 2017. Received in revised form: May 3th, 2018. Accepted: May 30th, 2018.

Abstract
Lightning electric field (LEF) measurements are aperiodic signals characterized by inherent noise of different sources, i.e., it is not possible to register a noise-free signal. In the last decade, the denoising of LEF measurements has been achieved using some time-frequency representations such as short-time Fourier transform (STFT), wavelet transform (WT) and fractional Fourier transform (FRFT) without definitive results. In this paper, a denoising process applied on LEF measurements using the Local Polynomial Approximation (LPA) is proposed. The window size selection is made by combining the LPA with the intersection of confidence intervals (ICI) algorithm. Furthermore, a cross-validation criterion is used to select the optimal value of the threshold parameter in the LPA-ICI denoising method. It is shown that for different signal-to-noise ratio (SNR) values, the proposed method significantly reduces the noise present in the recorded signals. Finally, a discussion about the processed signatures in terms of some lightning electric field temporal features is performed.

Keywords: electric field; intersection of confidence intervals; lightning flash; local polynomial approximation; noise reduction.

Aproximación local polinomial e intersección de intervalos de confianza para la remoción de ruido en mediciones de campo eléctrico generado por rayos

Resumen
Las mediciones de campo eléctrico producido por rayos (LEF) son señales aperiódicas caracterizadas por ruido inherente de diferentes fuentes, es decir, no es posible registrar una señal libre de ruido. En la última década, se ha logrado filtrar mediciones de LEF utilizando algunas representaciones tiempo-frecuencia tales como la transformación de Fourier de corto tiempo (STFT), la transformación wavelet (WT) y la transformación de Fourier fraccionaria (FRFT) sin resultados definitivos. En este trabajo, se propone un proceso de eliminación de ruido aplicado a mediciones de LEF usando la aproximación polinomial local (LPA). La selección del tamaño de la ventana se realiza combinando la LPA con el algoritmo de intersección de intervalos de confianza (ICI). Además, un criterio de validación cruzada se utiliza para seleccionar el valor óptimo del umbral en el método de reducción de ruido LPA-ICI. Se muestra que para diferentes valores de relación señal-a-ruido (SNR), el método propuesto reduce significativamente el ruido presente en las señales registradas. Finalmente, se realiza una discusión sobre las señales procesadas en términos de algunas características temporales del campo eléctrico.

Palabras clave: aproximación local polinomial; campo eléctrico; intersección de intervalos de confianza; rayos; reducción de ruido.

1. Introduction

The measurement of electromagnetic fields generated by lightning has been carried out in the last four decades and consequently many features of the phenomenon have been revealed. A major part of these works was conducted using sensors to measure the radiated electric or magnetic fields generated by cloud-to-ground (CG) lightning flashes [1].

The knowledge of the electric fields produced by lightning (LEF) is important to: (a) identify some parameters

How to cite: Rojas-Cubides, H.E., Cortés-Guerrero, C.A. and Forero-Mejía, M.C., Local polynomial approximation and intersection of confidence intervals for removing noise of lightning electric field measurements, DYNA, 85(205), pp. 264-273, June, 2018.

© The author; licensee Universidad Nacional de Colombia.

of lightning flashes (multiplicity, flash duration, interstroke intervals and currents); (b) understand the discharge mechanism and physical discharge processes; (c) design lightning protection systems; (d) lightning location networks; (e) determine the electromagnetic compatibility requirements of equipment and systems [1-4].

Due its importance, lightning characterization using LEF measurements has been developed in several regions of the world. In fact, lightning location networks, detection and warning systems, lightning flash density estimations and indirect determination of lightning current amplitudes are successful applications of indirect measurements of LEF. In addition, the measurement of these fields allows establishing relationships between lightning flash events and transients that could help in the classification of electromagnetic disturbances [5].

To develop and evaluate models of the lightning return stroke and determine the lightning current features, it is necessary to determine, in a reliable way, various temporal features of the electric field waveforms such as: the peak value, rise-time, zero-crossing time, slow-front and fast-front duration, and peak value of the electric field derivative [6–8] [6–8]. However, the extraction of lightning parameters from LEF or current measurements is not a simple task due to the presence of noise in the recorded signals, mainly caused by the measuring system itself and other undesired components present in the electromagnetic environment [7-9].

In the past, noise removal from LEF signals has been achieved using low-pass filters (hardware) and digital filters based on the discrete Fourier transform (software), both methods with cut-off frequencies ranging from 200 kHz to 30 MHz [9,10]. However, these methods may affect part of the original signal, causing loss of information. To overcome this problem, some denoising techniques based on time, frequency or hybrid time–frequency domains have been proposed in the last two decades.

The conventional Fourier transform (FT) and the short-time Fourier transform (STFT) were the first approaches to reduce the noise on lightning electric field signatures [11]. Because of the limitations of FT and STFT (loss of resolution in time or frequency), new signal processing methods have been proposed. Wavelet transform (WT) has been used for different purposes in the study of lightning activity, including noise reduction and frequency anlaysis [3,8,12]. The major disadvantages of WT are the complexity of calculations, the sensitivity to some noise levels, and the dependence of its accuracy on the selected wavelet base (mother) function [8,12].

Recently, noise reduction methods on LEF signals have been extended to the application of the discrete fractional Fourier transform (DFRFT) [13,14]. However, it is not possible to have a desired signal because, by nature, the LEF have a random behavior and the waveforms change with respect to the distance from the lightning strike point. This disadvantage makes it difficult to minimize the error between the filtered and the original signal for any adaptive denoising process.

The local polynomial approximation (LPA) is a method proposed and developed in Statistics for processing scalar and multidimensional noisy data [15]. However, several applications have shown that LPA is a powerful technique to deal with linear and non-linear problems [16], reduction of leakage errors [17], nonparametric modelling [18] and filter design [19]. In this way, this paper presents a method for denoising lightning electric field measurements based on the LPA application. Furthermore, to solve the problem of window size selection, the LPA and the intersection of confidence intervals (ICI) algorithm are combined.

This work continues with the research project launched by the authors oriented to develop signal processing tools to analyze LEF signals. Considering that the essential features of lightning flashes are affected by geographical and environmental conditions, Bogotá-Colombia is an interesting place due to its tropical location, its high altitude (2550 masl), and its high lightning activity, which allows a continuous study of lightning [20].

2. Local polynomial approximation

2.1. Local approximation theory

The basic signal model considered in this paper assumes that the measured signal $z(t)$, defined in eq. (1), is composed by N observations of a noise-free signal $y(t)$ with a sampling time T_S.

$$\begin{aligned} z(t_k) &= y(t_k) + \eta(t_k) \\ t_k &= kT_S, \quad k = 1,2,\dots,N \end{aligned} \tag{1}$$

In eq. (1), $\eta(t_k)$ are independent additive noise components with $E[\eta(t_k)] = 0$, $E[\eta^2(t_k)] = \sigma^2$ and $E[\vartheta]$ is the expected value of ϑ.

From this signal model, the local approximation theory involves two general problems. The first of these arises when it is necessary to find a polynomial function that can be used to determine the approximate values of a function $y(t_k)$. The second problem is related to the use of fitting functions on a given data sequence and determine the best function to represent those data [17,21]. The first problem is associated with the parametric estimation, while the second one is linked with the non-parametric estimation.

2.3. Filtering in the LPA domain

The LPA is a locally adaptive non-parametric technique, which provides estimates of the signal $y(t) \approx y(t_k)$ defined in eq. (1) from the observations of $z(t)$ in a pointwise manner and using a polynomial fitting in a sliding window. In this estimation, the error should be as small as possible [22].

In terms of the signal processing, LPA is a flexible tool to design linear transforms with respect to polynomial components of signals. For this reason, to obtain an estimation of $y(t)$, the following criterion must be applied on the linear LPA [22,23]:

$$\begin{aligned} J_h(t_0, C) &= \sum_{k=1}^{N} \rho_h(t_k - t_0)\left(z(t_k) - C^T\phi(t_k - t_0)\right)^2 \\ \phi(x) &= [1, x, x^2/2, \dots, x^{m-1}/(m-1)!]^T \\ C &= (C_0, C_1, C_2, \dots, C_{m-1})^T \end{aligned} \tag{2}$$

where t_0 is the point of interest (center), C is a vector with the coefficients of the polynomial used during the estimation of $y(t)$ and m is the order of the LPA. The window function $\rho_h(x)$, which formalizes the location of fitting with respect to the center point x, is a finite support function and must satisfy the conventional properties of the "kernel" used in non-parametric estimation, in particular: $\rho(x) \geq 0, \rho(0) = \max_x \rho(x)$, $\rho(x) \to 0$ as $|x| \to \infty$ and $\int_{-\infty}^{\infty} \rho(u)du = 1$.

Now, if the function $J_h(t_0, C)$ (eq. (2)) is minimized with respect to C:

$$\hat{C}(t_0, h) = \arg \min_{C \in R^m} J_h(t_0, C) \tag{3}$$

the coefficient $\hat{C}_0(t_0, h) = \hat{y}(t_0, h)$ is an estimate of $y(t_0)$ with respect to a window function of bandwidth h, while $\hat{C}_l(t_0, h) = \hat{y}_l(t_0, h)$ are related with the estimates of the derivatives $y^{(l)}(t_0)$ with $l = 1,2, \dots, m-1$. In this way, the estimates $\hat{C}_l(t_0, h)$ can be represented in the form of a linear transform as follows [15,23]:

$$\hat{y}_h(t) = \sum_k g_h(t_k, t_0)\, z(t_k) \tag{4}$$

where g_h is the kernel of the estimator defined by [23]:

$$\begin{aligned} g_h(t_k, t_0) &= \rho_h(t_k - t_0)\, [\phi_h(t_k - t_0)]^T\, \Phi_h^{-1}\, \phi_h(0) \\ \Phi_h &= \sum_k \rho_h(t_k - t_0)[\phi_h(t_k - t_0)][\phi_h(t_k - t_0)]^T \end{aligned} \tag{5}$$

Here, ϕ_h is a column vector of polynomials of the LPA whose length is equal to $m + 1$, and Φ_h is a symmetric matrix. It is necessary to emphasize that, for a parametric estimation, the order of the polynomial model defines the type of estimation curve (constant, linear, quadratic, etc.) and the coefficients C are fixed. On the other hand, in the non-parametric process, the estimate of $y(t)$ is not a polynomial function and the sliding window estimation makes the coefficients $\hat{C}_l(t, h)$ different for each point of interest t_0.

2.3. Influence of the window function

Mathematically, the window function used in the LPA is expressed by a scale parameter $h > 0$ that determines the window size or bandwidth. For this reason, the window function in eq. (2) and eq. (5) must be replaced by:

$$\rho_h(x) = \rho(x/h)/h \tag{6}$$

Smaller or larger values of h narrow or widen the function $\rho_h(x)$, respectively. The scale factor $(1/h)$ in eq. (6) normalizes the window and the property $\int_{-\infty}^{\infty}[\rho(x/h)/h]dx = 1$ is satisfied. Thus, the polynomial approximation function ϕ_h also needs to be scaled by the parameter h:

$$\phi_h(x) = \phi_h(x/h) \tag{7}$$

From eq. (4) to eq. (7), it is possible to observe that the length of the window function h controls the smoothness of the estimate $\hat{y}_h(t)$ [22,23]. If h is large, the difference between parametric and non-parametric approaches disappears and the estimation function is constant, linear, quadratic, etc., depending on the polynomial degree of the LPA. In this case, the smoothing of random noise in observations is the maximum. On the other hand, when h is relatively small, the estimate $\hat{y}_h(t)$ is near (or exactly the same) to $z(t)$ and there is no smoothing of the data. For intermediate values of the windows size, the resulting curves demonstrate different levels of smoothing.

In eq. (2), if the window is a rectangular function, all observations have equal weights. Nonrectangular window functions such as Gaussian, Hamming, Welch, Hann, etc., usually provide higher weights for observations that are closer to the center point t_0. In addition, there are three types of windows (with respect to the center point) that LPA can use: central, right and left windows.

3. Window size selection and the ICI algorithm

3.1. The ICI algorithm and the bandwidth selection

The intersection of confidence intervals (ICI) is a bandwidth selection algorithm that has been proposed and substantiated in several publications [19,22,24-26]. This approach does not require the bias estimation and presents an accuracy approximation better than the quality-of-fit statistics [19]. LPA combined with the ICI algorithm improves the windows size selection process and enables the algorithm to be adaptive. The basic idea of the ICI algorithm uses a finite set of bandwidths (H) expressed by:

$$H = \{h_1 < h_2 < \cdots < h_M\} \tag{8}$$

Then, for each sample (t), the LPA-ICI algorithm introduces a sequence of M estimates accompanied with the following confidence intervals:

$$D_M(t) = [L_M(t), U_M(t)] \tag{9}$$

The lower and upper limits of $D_M(t)$ are defined as:

$$\begin{aligned} L_M(t) &= \hat{y}_{h_M}(t) - \Gamma\sigma_{h_M}(t) \\ U_M(t) &= \hat{y}_{h_M}(t) + \Gamma\sigma_{h_M}(t) \end{aligned} \tag{10}$$

where Γ is the threshold of the confidence interval and the standard deviation of the estimated signal $\hat{y}_{h_M}(t)$ is defined by [15]:

$$\begin{aligned} \sigma_{h_M}(t) &= \sigma' \sqrt{\sum_k \left[g_{h_M}(t_k, t_0)\right]^2} \\ \sigma' &= \frac{\text{median}\,|z(t_k) - z(t_k - 1)|}{\sqrt{2} \cdot 0.6745};\ k = 2, \dots, N \end{aligned} \tag{11}$$

The ICI algorithm tracks the values of the largest lower $\underline{U}_M$ and the smallest upper $\overline{L}_M$ confidence intervals limits:

$$\overline{L}_M(t) = \max_{i=1,\dots,M} L_i(t) \tag{12}$$

$$\underline{U}_M(t) = \min_{i=1,\dots,M} U_i(t)$$

The chosen filter support (bandwidth) h^+ is the largest i support for which the following condition is still satisfied:

$$\overline{L}_i(t) \leq \underline{U}_i(t) \tag{13}$$

It was shown in [15,22] that h^+ is close to the optimal support h^*, which results in the optimal trade-off between bias $\left(\omega_h(t)\right)$ and variance $\left(\sigma^2{}_{h_M}(t)\right)$. Besides, this solution minimizes the MSE [19].

The parameter Γ in eq. (10) plays an important role in the bandwidth selection. A large value of Γ gives $h^+ > h^*$, producing an over-smoothing in the signal. On the other hand, smaller values of Γ give $h^+ < h^*$, cause an under smoothing on the signal.

3.2. Threshold parameter Γ

To find the optimal value of the threshold parameter Γ from an theoretical analysis presents great difficulties [15]. For this reason, to compare the performance of the ICI algorithm with respect to Γ, a cross-validation (CV) criteria was selected to assess the statistical prediction. This validation technique has been used to compare the performance of different predictive models [27] and, from the experiments presented in [15,19,28], it can be used as a reasonable and efficient selector of Γ.

For the linear filter defined in eq. (4), the CV function with an estimator support h^+ is represented as a weighted sum of the squared residuals [15]:

$$I_{CV} = \sum_k \left(\frac{z(t_k) - \hat{y}_{h^+}(t_k)}{1 - g_{h^+}(t_k, t)} \right)^2 \tag{14}$$

It is important to mention that the process explained in this section must be repeated for every value of $\Gamma \epsilon R$, $R = \{\Gamma_1, \Gamma_2, \dots, \Gamma_R\}$. In addition, the value of the threshold parameter used in the "best" estimation is defined for the following expression:

$$\hat{\Gamma} = \arg\min_{\Gamma \epsilon R} I_{CV} \tag{15}$$

4. The LPA-ICI denoising method

The main purpose of denoising LEF signatures is to reduce the noise components present in measurements without modifying the most important signal features. Although it is possible to carry out actions to reduce the emissions produced by the measuring system itself, all recorded signals are also distorted by undesired signals from the electromagnetic environment, whose sources cannot be controlled or eliminated.

For these reasons, the method based on LPA combined with the ICI algorithm for noise reduction on LEF signals consists of the following steps:

- Set $\Gamma = \Gamma_R$, for $R = \{\Gamma_1, \Gamma_2, \dots, \Gamma_R\}$
- Determine the sampling time (T_S) from the noisy signal observations $z(t_k)$ and select a set of samples $t_k = kT_S$ with $k = 1,2,\dots,N$
- For $H = h_i$, with $i = 1,2,\dots,M$, calculate the estimates $\hat{y}_h(t)$ and the confidence intervals defined by eq. (12)
- Select the largest of those i for which $\overline{L}_M(t) \leq \underline{U}_M(t)$ gives the bandwidth $i^+ = h^+$. From this result determine the adaptive window size $h^+(t)$ and the estimate $\hat{y}_{h^+}(t)$.
- Repeat the previous step for all t_k and each Γ_R
- Find $\hat{\Gamma}$ from eq. (15) and select the final estimation of $\hat{y}_{h^+}(t_k)$ corresponding to the $\hat{\Gamma}$.

In all cases, the cross-validation presented in eq. (14) and the maximum SNR of the signal (before and after noise reduction) were selected as appropriate indicators for comparing the obtained results. In this paper, the SNR is expressed as the relation between the power of the filtered signal (P_{signal}) and the power of noise removed from the measured signal (P_{noise}), so:

$$SNR_{dB} = 10 \cdot log_{10}\left(\frac{P_{signal}}{P_{noise}}\right) \tag{16}$$

5. Instrumentation and data

5.1. Typical waveforms of LEF signals

CG lightning flashes are transient discharges of high current that can be generated in the atmosphere by clouds, storms (rain, snow or dust) and volcanic eruptions. A typical CG lightning flash is composed by more than one discharge known as return stroke. These individual discharges have a duration of tens of microseconds and they are usually separated in time from 20 ms to 100 ms [29]. The typical waveforms for the electric fields produced by the first return stroke (FRS) and the subsequent return strokes (SRS) that compose a flash are shown in Fig. 1.

The most relevant characteristics of these waveforms include: (a) an initial peak with an acute shape (due to a high rate of growth) that decreases approximately with the inverse of the distance; (b) a slow descent ramp after the initial peak that may last more than 100 μs in signals recorded in a nearby range (few tens of kilometers); (c) a zero crossing point that may be several tens of microseconds after the initial peak for the fields registered at distances greater than 50 km; and (d) an opposite-polarity overshoot typical of the electric fields recorded at distances greater than 100 km.

5.2. Measuring system

The typical system to measure LEF was proposed by Cooray and Lundquist in 1982 [30]. In this configuration, an electric field sensor is connected to an electronic circuit for the acquisition of the signal and it is used an equipment to record the data. This arrangement has been used during the last three decades in several regions (Sweden, Germany, Italy, Japan, Sri Lanka, Malaysia, Singapore, USA, Colombia and Brazil), providing valuable information about the behavior and characteristics of lightning flashes [10,31,32].

The scheme of the measuring station used in this work to record the LEF signals is shown in Fig. 2, and it is composed by the following parts:

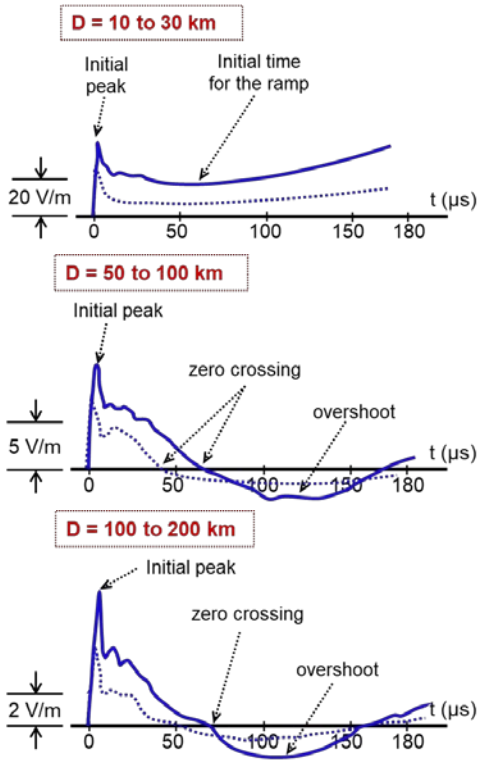


Figure 1. Typical waveforms of the electric field signals produced by CG lightnings with respect to different distance ranges. First return stroke (solid lines), subsequent return stroke (dashed lines).
Source: Adapted from [29]

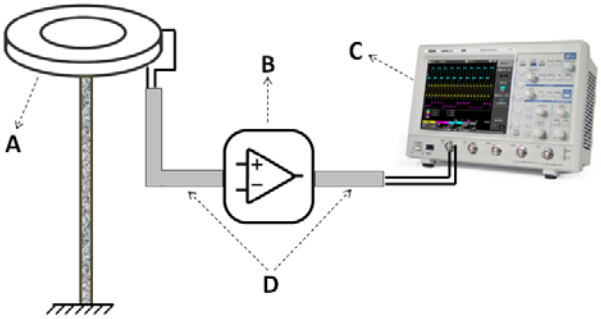


Figure 2. Lightning electric field measuring system. (A) parallel-plate antenna, (B) electronic circuit, (C) oscilloscope, (D) coaxial cables.
Source: The authors

- The electric field sensor is a 1.5 meters height parallel flat-plate antenna, which had two circular metallic plates with diameter of 0.45 m supported by insulating elements and 0.03 m air gap between them.
- The electronic circuit is based on the buffer-amplifier BUF-602 with 1000 MHz bandwidth and 8 kV/μs slew rate. The decaying time constant of the circuit is 38 ms, which is large enough to record signatures composed by electrostatic (near lightning electric fields) and radiated components (far lightning electric fields).
- Two coaxial cables were used to connect the devices. First, a 0.5 m length RG58/U cable was used to connect the antenna to the electronic circuit. Second, a 12 m length RG58/U coaxial cable was used between the electronic circuit and the acquisition equipment.
- The acquisition equipment was an 8-bits, digital oscilloscope Agilent DSO6104A with a sampling rate of 10 MSa/s (sampling time of 100 ns).

The arrangement composed by the antenna, the short coaxial cable and the electronic circuit works as a passband filter with a cut-off frequency of 11.8 MHz, which is enough to study lightnings because this range of frequencies covers the bandwidth in which most of the spectrum of the return strokes is found (some hundreds of kHz) [3,12]. A complete description of the measuring system and the electronic circuit, including its calibration process, can be reviewed in [33].

During measurements, the digital oscilloscope was adjusted using a full observation window of 500 ms. This time was selected in order to record a complete CG lightning flash signature that includes the electric field waveforms produced by the first stroke and the subsequent strokes. The vertical trigger level was set at 100 mV to reduce the interference caused by the noise inherent to the measuring system (92 mV average) and to avoid the oscilloscope drive due to pulses caused by intra-cloud lightnings. In order to acquire signals before and after the trigger transient pulse, a 75 ms horizontal pre-trigger was adjusted. In addition, to reduce additional noise that could be produced at the output of the buffer-amplifier, the bandwidth of the oscilloscope was configured in 25 MHz.

Finally, during the pre-processing stage, each return stroke signal (first and subsequents) was extracted from the complete lightning flash signature and it was adjusted for an observation window of 400 μs. Under this condition, using a sampling time of 100 ns, each return stroke signal analyzed in the following sections has 4000 samples.

5.3. Reference signatures

The measurements presented in this section were extracted from the records obtained during August-November 2016. The measuring system was installed in Bogotá, Colombia (4.641° N, 74.091° W) at an altitude of 2550 m above sea level. All the signatures analyzed belong to negative CG lightning flashes. Examples of the recorded events are shown in Fig. 3 and Fig. 4. These signals correspond to normalized signatures of two return strokes (FRS and SRS) and they agree with the waveforms shown in Fig. 1 (distance range between 50 and 200 km). The vertical axis in each plot represents the electric field magnitude in V/m whereas the horizontal axis represents the time in microseconds.

Reviewing Fig. 3 and Fig. 4 it can be seen the presence of noise components that makes it difficult to analyze and characterize the signal features. This is relevant especially in the estimation of temporal lightning parameters, such as: maximum value, signal rise-time (10–90%), zero-crossing time and the maximum electric field derivative, which is an important parameter to estimate the maximum variation of lightning current.

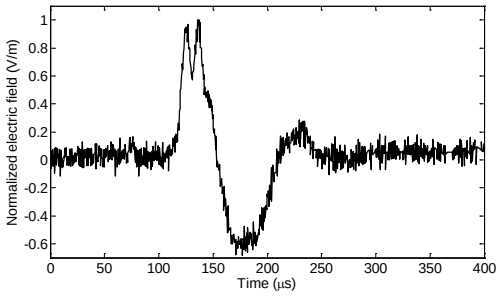


Figure 3. Electric field signature of a first return stroke (Bog3_st1)
Source: The authors

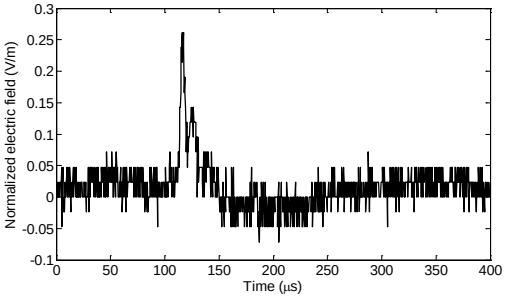


Figure 4. Electric field signature of a subsequent return stroke (Bog3_st5)
Source: The authors

6. Signal processing results

In this section, simulation results of the LPA-ICI denoising method over LEF measurements, the role of the threshold parameter in the ICI algorithm, and the performance of adaptive bandwidths are presented. In addition, the effects of different parameters of the LPA-ICI algorithm are analyzed.

6.1. Simulation parameters

To get a comparative idea about the temporal features and the magnitude of lightning electric field signatures, a set of six return stroke signatures (3 FRS and 3 SRS) were selected. These signals were extracted and normalized from different lightning flashes. In order to analyze the role of the threshold parameter, several values of $\Gamma = \{0.01{:}\,0.01{:}\,4\}$ are defined.

Simulations were performed using a symmetric Gaussian window $[\rho_L(u) = \rho_L(-u)]$. This function was selected because it is well known, from numerical analysis, that symmetric windows result in smaller approximation errors than asymmetric windows [21,34]. The adaptive bandwidths (sample size) for the window function are given by $h = \{3, 5, 6, 9, 12, 18, 25, 35, 50, 71, 100, 143, 203, 290\}$.

In order to select an adequate polynomial order for LPA, a linear algorithm was employed by increasing the order of LPA from $m = 2$ to $m = 9$. From simulations, it was observed that polynomial orders less than $m = 4$ provide results with ripples and remarkable noise components, while high polynomial orders ($m \geq 4$) present similar results but increase the computational costs. In this way, a polynomial order of $m = 5$ for the LPA-ICI algorithm was selected for all the cases. Signal processing results were obtained from routines developed in MATLAB® by the authors.

6.2. High SNR environment – first return strokes

For the example given in Fig. 5(a), the best estimate using a symmetric Gaussian window is presented in Fig. 5(b). In this case, the graphical results illustrate a substantial improvement in the signal features when $\Gamma = 1.23$. This result is reinforced by the behavior of the threshold parameter with respect to the CV criterion shown in Fig. 5(c).

In addition, the adaptive bandwidths for the adjusted Γ are shown in Fig. 5(d). It can be seen from this curve that at the peak value of $y(t)$ and at the points where the signal slope

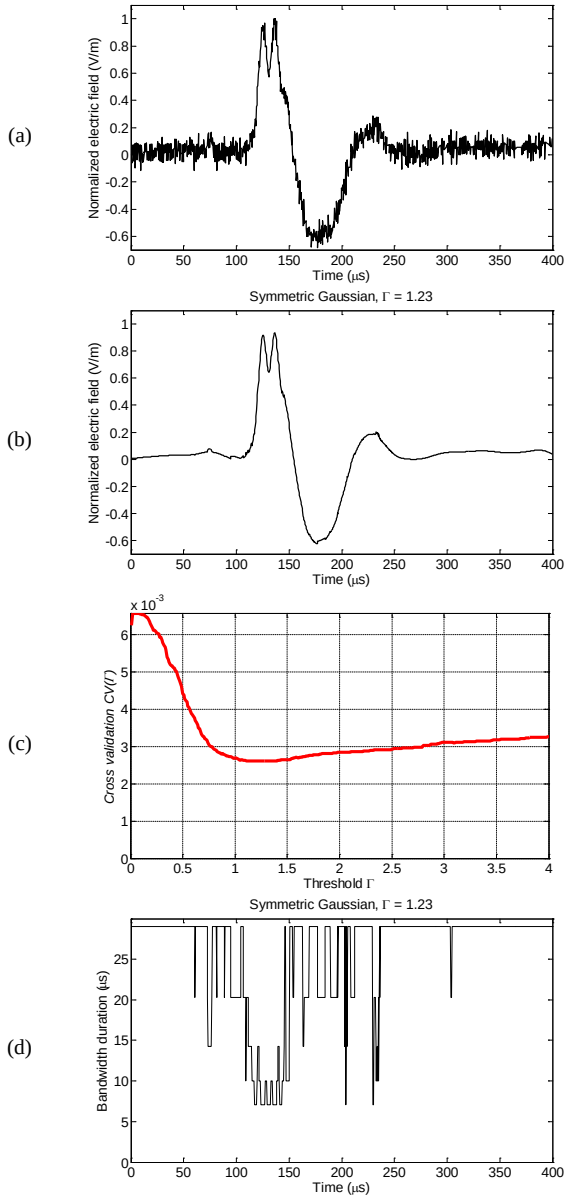


Figure 5. Results for FRS signature (Bog3_st1). (a) measured signal; (b) LPA-ICI denoising signal for symmetric Gaussian window with $\Gamma = 1.23$; (c) CV criterion for LPA-ICI with $m = 5$; (d) adaptive bandwidth variation.
Source: The authors

changes, the adaptive bandwidths decrease. This means that the LPA-ICI method is sensitive with respect to fast variations of the signal and the symmetrical window presents a good filter response.

6.3. Low SNR environment – subsequent return strokes

Fig. 6(a) and Fig. 6(b) show the measured signal and the filtered signal of a subsequent return stroke using the LPA-ICI denoising method with polynomial order $m = 5$. In this case, the denoising result is better because the subsequent stroke signal has a low SNR.

The cross-validation criterion as a function of the threshold parameter is illustrated in Fig. 6(c). For the subsequent stroke

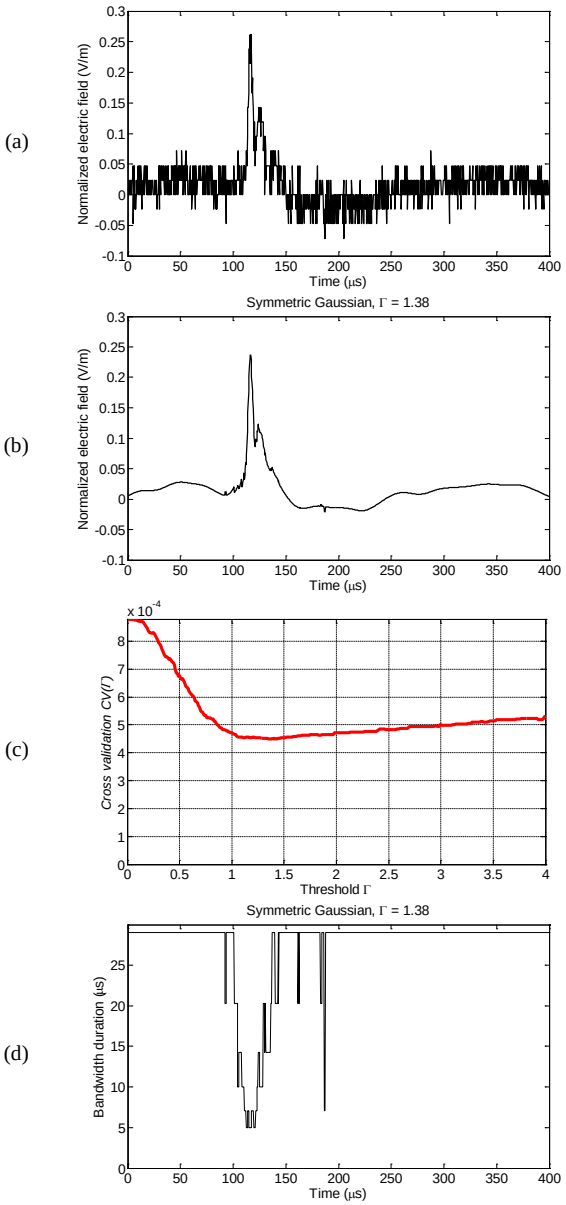


Figure 6. Results for SRS signature (Bog3_st5). (a) measured signal; (b) LPA-ICI denoising signal for symmetric Gaussian window with $\Gamma = 1.38$; (c) CV criterion for LPA-ICI with $m = 5$; (d) adaptive bandwidth variation.
Source: The authors

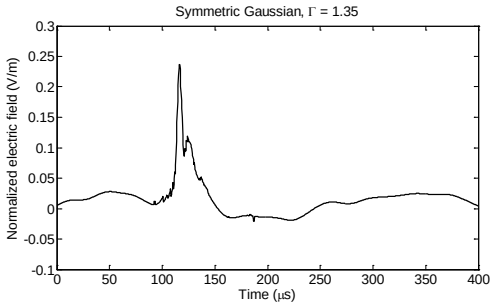


Figure 7. LPA-ICI estimates for electric field signature of a subsequent return stroke (Bog3_st5) to $\Gamma = \{0.1 : 0.25 : 4.1\}$
Source: The authors

signal, the minimal value of CV is 4.505×10^{-4} for the adjusted value $\Gamma = 1.38$. Fig. 6(d) shows the adaptive varying bandwidths for the symmetric window filter. These bandwidths present faster changes in time, which means that the LPA approximation is enough for denoising the measured signal using the size of windows that are available.

It is important to note that, in this case, the threshold parameter changed from $\Gamma = 1.23$ (FRS) to $\Gamma = 1.38$ (SRS), which demonstrates the adaptive response of the ICI algorithm. An advantage of the LPA-ICI denoising method is that the best estimate does not present high noise oscillations and ripples from the measured signal that certainly represent difficulties in the interpretation of lightning parameters.

From the best estimate obtained for the SRS signal it was noticed that the adaptive window size, especially for a small value of Γ, could be corrupted by spikes and ripples that erroneously isolate small values of the window sizes. Fig. 7 shows the estimate when the threshold parameter is adjusted from the initial conditions (see section 7.1) to $\Gamma = \{0.1 : 0.25 : 4.1\}$.

Note that when the change in the step-size of Γ is made, some ripples in the initial stage of the signal rise and the spikes on the crossing-to-zero region (between $t = 1.2 \times 10^{-4}\ s$ and $t = 3 \times 10^{-4}\ s$) are slightly reduced. In addition, the threshold parameter of the signal estimate changes from 1.38 to 1.35 with a larger step-size.

7. Discussion

In this work, the parameters selected to analyze LEF are 10–90% signal rise-time (Tr), zero crossing time (ZC) and maximum electric field (Ep). In addition, it is important to know the maximum electric field derivative ($\partial \mathrm{Ep}/\mathrm{dt}$), which is a useful parameter in the estimation of the maximum variation of lightning current. Finally, the SNR improvements after the denoising process are included.

Besides the results obtained from a visual comparison, Table 1 presents the results obtained from characterizing the parameters (Tr, ZC, Ep, $\partial \mathrm{Ep}/\mathrm{dt}$ and SNR) of the signatures before and after noise removal. In addition, the right column in Table 1 (% DIF) presents the percentage difference (for each parameter) between the measured signal and the estimation obtained with the LPA-ICI (processed signal). The maximum values of the electric field and the electric field derivative were normalized taking the maximum of the respective flash as the reference value.

Table 1.
Parameters of the LEF signatures before and after the denoising process.

Signature		Parameter	Signal		% DIF
			ME	PR	
FRS	Bog1_st1	Tr (μs)	8.4	6.4	23.8%
		ZC (μs)	78.2	78.9	0.9%
		Ep (V/m)	1	0.987	1.3%
		∂Ep/dt (V/m/μs)	1	0.66	34.0%
		SNR (dB)	17.9	30.6	70.9 % *
	Bog3_st1 (Fig. 5)	Tr (μs)	11.4	10.4	8.8%
		ZC (μs)	43.2	42.3	2.1%
		Ep (V/m)	1	0.989	1.1%
		∂Ep/dt (V/m/μs)	1	0.588	41.2 %
		SNR (dB)	15.6	33.8	116.7 % *
	Bog4_st1	Tr (μs)	12.4	13	4.8%
		ZC (μs)	65.2	66.4	1.8%
		Ep (V/m)	1	0.988	1.2%
		∂Ep/dt (V/m/μs)	1	0.635	36.5%
		SNR (dB)	20.5	31.1	51.7% *
SRS	Bog1_st4	Tr (μs)	7.8	7.6	2.6%
		ZC (μs)	47.5	51.3	8.0%
		Ep (V/m)	0.5	0.491	1.9%
		∂Ep/dt (V/m/μs)	1	0.535	46.5%
		SNR (dB)	11.7	23.3	99.1% *
	Bog2_st3	Tr (μs)	8.6	7.1	17.4%
		ZC (μs)	73.2	79.8	9.0%
		Ep (V/m)	0.375	0.341	9.1%
		∂Ep/dt (V/m/μs)	1	0.452	54.8%
		SNR (dB)	9.4	22.52	139.6% *
	Bog3_st5 (Fig. 6)	Tr (μs)	5.8	4.1	29.3%
		ZC (μs)	40.6	41.6	2.5%
		Ep (V/m)	0.262	0.236	9.9%
		∂Ep/dt (V/m/μs)	1	0.306	69.4%
		SNR (dB)	6.5	19.8	204.6% *

ME: measured signal --- PR: processed signal --- % DIF: percentage difference between measured signal (ME) and processed signal (PR)
* Improved
Source: The authors

From the results presented in Table 1, it can be observed that the rise-time presents a difference up to 23.8% and 29.3% in the FRS and SRS cases, respectively. These differences may produce inadequate interpretation of lightning parameters. For the zero-crossing time, the differences were less than 3% for high SNR environments (FRS), while for the low SNR signals (SRS) a maximum difference of about 9% was found (signature Bog2_st3).

On the other hand, the maximum normalized electric field (Ep) shows a variation up to 2% for the FRS signatures, whereas for the SRS cases the variation in this parameter reached 10%. These results indicate that the reduction in the peak value of the signatures depends on the signal noise level. However, it is important to clarify that the removal of noise is directly affected by the selected filtering method.

Regarding the maximum electric field derivative ($\partial \mathrm{Ep}/\partial \mathrm{t}$), remarkable differences were observed between the measured signatures and the filtered ones. The minimum difference was 34% for Bog1_st1 signature (FRS case) and the maximum difference was 70% for Bog3_st5 signature (SRS case). These results show that the estimation of electric field derivative from the measured signal could be erroneous due to the presence of high frequency noise.

By comparing the SNR of the measured signal with the best result obtained with the LPA-ICI method, it is possible to notice that for the signal Bog3_st1 (shown in Fig. 3 and Fig. 5) the change in SNR ranged from 15.6 dB to 33.8 dB after noise removal. For the signal Bog3_st5 (shown in Fig. 4 and Fig. 6), the SNR exhibits a change from 6.5 dB to 19.8 dB. In general terms, for the whole group of signatures, the improvement in the SNR varied from 51% up to 117% for the FRS cases, while for the SRS cases this parameter was improved between 99% and 205%.

In order to verify the usefulness of LPA-ICI denoising method, a comparison with an alternative method using adaptive filters in the discrete fractional Fourier domain (DFRFd) was conducted. This filtering process is described with detail in [14]. In this work, the adaptive filter in DFRFd is configured with the following parameters: fractional order $a = 0.25$; normalized leakage LMS adaptive (NL-LMS) algorithm; normalized step-size $\mu_{NL-LMS} = 0.95$; leakage factor $\gamma = 0.997$; stabilization factor $\beta = 2 * 10^{-14}$; number of coefficients is 6. Fig. 8 shows the comparison between the signatures filtered with the LPA-ICI method (black dotted line) and using adaptive filters in DFRFd (red continuous line).

In this case, it is possible to observed that the LPA-ICI provides similar results than those obtained with the technique based on DFRFT. However, a slight reduction is observed in the peak value of the FRS signature filtered with LPA-ICI algorithm (see Fig. 8a). In addition, adaptive filters in DFRFd introduce oscillations, especially in the SRS signature (see Fig. 8b). These oscillations are typical of Fourier rotated methods, which produce difficulties in the interpretation of some temporal parameters.

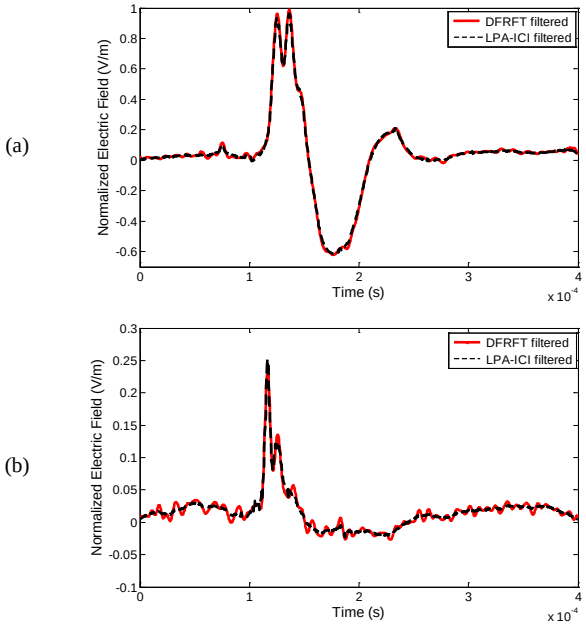


Figure 8. Comparison between LPA-ICI and adaptive filters in DFRFd. (a) FRS signature (Bog3_st1); (b) SRS signature (Bog3_st5)
Source: The authors

Table 2.
Parameters comparison of LEF signatures (Bog3_st1 and Bog3_st5) filtered with LPA-ICI method and adaptive filters in DFRFd

Signature		Tr (μs)	CZ (μs)	Ep (V/m)	∂Ep/dt (V/m/μs)	SNR (dB)
Bog3_st1 (Fig. 8a)	Measured	11.4	43.2	1	1	15.6
	LPA-ICI	10.4	42.3	0.989	0.59	33.8
	FRFT	10.3	42.1	0.991	0.60	31.4
Bog3_st5 (Fig. 8b)	Measured	5.8	40.6	0.262	1	6.5
	LPA-ICI	4.1	41.3	0.236	0.31	19.8
	FRFT	3.7	42	0.253	0.33	22.1

Source: The authors

Table 2 presents the comparison of parameters for signals presented in Fig. 8, which were obtained using both denoising methods. With respect to rise-time, the differences between denoising methods are less than 2% for the FRS signature (shown in Fig. 8a), while for the SRS signature (show in Fig. 8b) the difference reaches 10%. This result in the SRS case is also produced because of the oscillations present in the filtered signal using DFRFT, which do not allow to clearly identify the initial zero-crossing point of the processed signal.

For zero-crossing time and maximum electric field, the differences for both examples were less than 2% and 7%, respectively. The main difference (up to 9%) is presented in the estimation of the maximum value of the electric field derivative for SRS signature (Fig. 8b). This is due to the difference between the maximum value of the filtered signal using LPA-ICI and the output signal obtained with the method based on DFRFT.

8. Conclusions

In this paper, the local polynomial approximation (LPA) combined with the adaptive size window algorithm (ICI) is applied to achieve a successful noise removal process on lightning electric field (LEF) signatures. The advantage of the proposed method compared to other filter methods, as adaptive filters, is that the LPA-ICI does not require a preliminary desired signal that represents the phenomenon.

The proposed method for denoising LEF signals is simple to implement and requires only the calculation of the estimates and their standard deviations for a set of bandwidth values. It is important to note that the LPA-ICI algorithm does not require the estimation of the bias. In addition, the proposed algorithm could be considered an adaptive method because its performance depends on an adequate selection of the window size (bandwidths).

The obtained results show that the LPA-ICI method is efficient to work with non-stationary signals that have jumps, ripples and fast slope changes, such as LEF signatures. In fact, the use of adaptive bandwidths provides better estimates because the most suitable bandwidth controls the smoothness of the filtered signal. In the particular case of LEF signals, the results provided by the LPA-ICI algorithm were found using symmetric Gaussian windows. However, other kinds of symmetric window functions can be tested to analyze the response of the algorithm.

Simulation results, including the effect of window bandwidth h and threshold parameter Γ, were analyzed for both high and low SNR environments. From the tests, it was observed that the change in the step-size of Γ improved the performance of LPA-ICI algorithm. In the low SNR cases, the use of a larger Γ reduces ripples and spikes on several zones of the output signal which are presented when the step-size of Γ is small.

The performance of the proposed method was evaluated in terms of a temporal parameter comparison and the SNR improvement factor for electric field signals produced by first return strokes (FRS) and subsequent return strokes (SRS). Remarkable differences between the measured signal and the filtered signal were found in terms of the rise-time (up to 29.3%) and the maximum electric field derivative (up to 70%). The maximum improvement achieved with respect to SNR was 118% in the FRS cases and 205% in the SRS cases.

Acknowlegdements

Prof. H. E. Rojas would like to acknowledge Universidad Distrital Francisco José de Caldas for support this work through the postgraduate commission contract N° 00002-2016. Eng. Carlos Rivera M.Sc. and Eng. Johanna Chaves from the EMC-UNC Research Group are also acknowledged for their collaboration in the construction of the remote lightning measuring station (EMIR-UN).

References

[1] Sonnadara, U., Cooray, V. and Götschl, T., Characteristics of cloud-to-ground lightning flashes over Sweden. Phys. Scr., 74(5), pp. 541-548, 2006. DOI: 10.1088/0031-8949/74/5/010.

[2] Cooray, V., The mechanism of the lightning flash, in: The lightning flash, London: IEE Power Engineering Series, 2003, pp. 127-240.

[3] Sharma, S.R., Cooray, V., Fernando, M. and Miranda, F.J., Temporal features of different lightning events revealed from wavelet transform. J. Atmos. Solar-Terrestrial Phys., 73(4), pp. 507-515, 2011. DOI: 10.1016/j.jastp.2010.11.009

[4] Bennett, A.J., Identification and ranging of lightning flashes using co-located antennas of different geometry. Meas. Sci. Technol., 24(12), pp. 1-8, 2013. DOI: 10.1088/0957-0233/24/12/125801.

[5] Peretto, L., Rinaldi, P., Sasdelli, R., Tinarelli, R. and Fioravanti, A., Implementation and characterization of a system for the evaluation of the starting instant of lightning-induced transients. IEEE Trans. Instrum. Meas., 56(5), pp. 1955-1960, 2007. DOI: 10.1109/TIM.2007.895669.

[6] Hussein, A.M., Milewski, M. and Janischewskyj ,W. Correlating the characteristics of the CN Tower lightning return-stroke current with those of its generated electromagnetic pulse. IEEE Trans. Electromagn. Compat., 50(3), pp. 642-650, 2008. DOI: 10.1109/TEMC.2008.924398.

[7] Gou, X., Chen, M., Zhang, Y., Dong, W. and Qie, X., Wavelet multiresolution based multifractal analysis of electric fields by lightning return strokes. Atmos. Res., 91(2–4), pp. 410-415, 2009. DOI: 10.1016/j.atmosres.2008.04.012.

[8] Santamaria, F., Cortés, C. and Román., F., Use of the Wavelet transform in noise reduction of the electric field signals produced by lightning. Inf. Tecnológica, 23(1), pp. 65-78, 2012. DOI: 10.4067/S0718-07642012000100008.

[9] Nedjah, O., Hussein, A.M., Krishnan, S. and Sotudeh, R., Comparative study of adaptive techniques for denoising CN tower lightning current derivative signals. Digit. Signal Process, 20, pp. 607-618, 2010. DOI: 10.1016/j.dsp.2009.08.002.

[10] Sonnadara, U., Cooray, V. and Fernando, M., The lightning radiation field spectra of cloud flashes in the interval from 20 kHz to 20 MHz.

IEEE Trans. Electromagn. Compat., 48(1), pp. 234-239, 2006. DOI: 10.1109/TEMC.2006.870692.
[11] Islam M.J. and Hussein, A.M., Frequency domain approach to de-noise the CN tower lightning derivative signal and its parameters calculations. J. Comput. Electr. Eng., 1(3), pp. 328-333, 2009. DOI: 10.7763/IJCEE.2009.V1.52.
[12] Miranda, F.J., Wavelet analysis of lightning return stroke. J. Atmos. Solar-Terrestrial Phys., 70(11–12), pp. 1401-1407, 2008. DOI: 10.1016/j.jastp.2008.04.008.
[13] Escobar, O.F., Rojas, H.E., Román, F. and Cortes, C.A., Lightning magnetic field measuring system in Bogotá — Colombia: signal proccesing method, Proceedings of 2013 International Symposium on Lightning Protection (XII SIPDA), 1, 2013, pp. 162-166. DOI: 10.1109/SIPDA.2013.6729210.
[14] Rojas, H.E. and Cortés, C.A., Denoising of measured lightning electric field signals using adaptive filters in the fractional Fourier domain. Measurement, 55, pp. 616-626, 2014. DOI: 10.1016/j.measurement.2014.05.026.
[15] Katkovnik, V., Egiazarian, K. and Astola, J., Adaptive window size image de-noising based on intersection of confidence intervals (ICI) rule. J. Math. Imaging Vis., 16, pp. 223-235, 2002. DOI: 10.1023/A:1020329726980.
[16] Li, X., Bi, G., Stankovic, S. and Zoubir, A.M., Local polynomial Fourier transform: a review on recent developments and applications. Signal Processing, 91(6), pp. 1370-1393, 2011. DOI: 10.1016/j.sigpro.2010.09.003.
[17] Schoukens, J., Vandersteen, G., Pintelon, R., Emedi, Z. and Rolain, Y., Bounding the polynomial approximation errors of frequency response functions. IEEE Trans. Instrum. Meas., 62(5), pp. 1346-1353, 2013. DOI: 10.1109/TIM.2012.2232451.
[18] Agrež, D. and Lušin, T., Non-parametric estimation of the amplitude ratio of sinusoidal signals with common frequency. Measurement, 55, pp. 176-185, 2014. DOI: 10.1016/j.measurement. 2014.04.039.
[19] Lerga, J., Vrankic, M. and Sucic, V., A signal denoising method based on the improved ICI rule. IEEE Signal Process. Lett., 15(8), pp. 601-604, 2008. DOI: 10.1109/LSP.2008.2001817.
[20] Rojas, H.E., Santamaría, F., Escobar, O.F. and Román, F.J., Lightning research in Colombia: lightning parameters, protection systems, risk assessment and warning systems. Ing. y Desarro., 35(1), pp. 240-261, 2017. DOI: 10.14482/inde.35.1.8951.
[21] Richard, B. and Faires, D., Numerical Analysis, 9th Ed. Boston, USA: Cengage Learning, 2010.
[22] Katkovnik, V., A new method for varying adaptive bandwidth selection. IEEE Trans. Signal Process., 47(9), pp. 2567-2571, 1999. DOI: 10.1109/78.782208.
[23] Katkovnik, V., Egiazarian, K. and Astola, J., Local approximation techniques in signal and image processing, 1st ed. Washington, USA: SPIE Publications, 2006.
[24] Goldenshluger, A. and Nemirovski, A., On spatially adaptive estimation of nonparametric regression. Math. methods Stat., 6(2), pp. 135-170, 1997.
[25] Tomic, M., Sersic, D. and Vrankic, M., Edge-preserving adaptive wavelet denoising using ICI rule. Electron. Lett., 44(11), pp. 698-699, 2008. DOI: 10.1049/el:20080227.
[26] Song, Y., Han, Y. and Lee, S., Structure based noise reduction using LPA-ICI, Proceedings of 2012 IEEE International Conference on Consumer Electronics, 2012, pp. 498-499. DOI: 10.1109/ICCE.2012.6161992.
[27] Stone, M., Cross-validatory choice and assessment of statistical predictions. J. R. Stat. Soc. Ser. B, 36(2), pp. 111-147, 1974.
[28] Katkovnik, V., Egiazarian, K. and Astola, J., A spatially adaptive nonparametric regression image deblurring. IEEE Trans. image Process., 14(10), pp. 1469-1478, 2005. DOI: 10.1109/TIP.2005.851705
[29] Lin, Y.T., Uman, M.A., Tiller, J.A., Brantley, R.D., Beasley, W.H., Krider, E.P. and Weidman, C.D., Characterization of lightning return stroke electric and magnetic fields from simultaneous two-station measurements. J. Geophys. Res., 84(C10), p. 6307- 6314, 1979. DOI: 10.1029/JC084iC10p06307.
[30] Cooray, V. and Lundquist, S., On the characteristics of some radiation fields from lightning and their possible origin in positive ground flashes. J. Geophys. Res., 87(C13), pp. 11203-11214, 1982. DOI: 10.1029/JC087iC13p11203.
[31] Galvan, A. and Fernando, M., Operative characteristics of a parallel-plate antenna to measure vertical electric fields from lightning flashes, 1st ed. Uppsala, Sweden: Uppsala University, 2000.
[32] Salimi, B., Mehranzamir, K. and Abdul-Malek, Z., Statistical analysis of lightning electric field measured under Malaysian condition. Asia-Pacific J. Atmos. Sci., 50(2), pp. 133-137, 2014. DOI: 10.1007/s13143-014-0002-0.
[33] Rojas, H.E., Rivera, C.A., Chaves, J., Cortés, C.A., Roman, F.J. and Fernando, M., New circuit for the measurement of lightning generated electric fields, Proceedings of 2017 International Symposium on Lightning Protection (XIV SIPDA), 2017, pp. 1-7. DOI: 10.1109/SIPDA.2017.8116922.
[34] Ralston, A. and Rabinowitz, P., A first course in numerical analysis, 2nd Ed. New Jersey, USA: Dover Publications, 2003.

H.E. Rojas- Cubides, received the BSc. degree in Electrical Engineer (with honors), the MSc. degree in High Voltage and the PhD. degree from the Universidad Nacional de Colombia in 2003, 2007 and 2018, respectively. He was doctoral visiting student in 2016 at the Atmospheric and Lightning Physics Group, University of Colombo, Sri Lanka. During 2017, he was doctoral visiting student at the Institute of Energy Systems, Energy Efficiency and Energy Economics (IE3), Technical University of Dortmund, Germany. Since 2012, he has been with the Universidad Distrital Francisco José de Caldas, Bogotá, Colombia, where he is currently an Associate professor and researcher at the Electromagnetic Compatibility and Interference Group (GCEM-UD). His current research interests include signal processing, lightning measurements and characterization, high voltage techniques, grounding systems, power quality and electromagnetic compatibility.
ORCID: 0000-0003-1253-6964

C.A. Cortes- Guerrero, received the BSc. degree in Eng. from the Universidad Nacional de Colombia in 2000 and the PhD. degree (with honors) from the Universidad Nacional de San Juan, Argentina, in 2005. He was doctoral visiting student in 2002 at the FH Giessen-Friedberg and the NLÖ, Hannover, Germany. From 2005 to 2007, he was professor of the Universidad de la Salle, Bogotá, Colombia. In 2006, he was postdoctoral visiting scholar at the Katholieke Universiteit Leuven, Belgium. Between 2015 and 2016, he was a visiting researcher at the Galvin Center for Electricity Innovation, Illinois Institute of Technology, Chicago, IL, USA. He is an associate professor of the Universidad Nacional de Colombia since 2008, and a DAAD Research Ambassador since 2017.
ORCID: 0000-0002-0986-3975

M.C. Forero- Mejía, received the BSc. degree Eng. (with honors) in Universidad Distrital Francisco José de Caldas, Bogotá, Colombia in 2016. From 2012 to 2014, she was undergraduate researcher at the GCEM-UD research group. Since 2015, she is with Grupo Enel–Colombia as junior auditor. Her research interests include distribution system analysis, energy management, signal processing and power quality disturbances.
ORCID: 0000-0002-1312-6417

UNIVERSIDAD NACIONAL DE COLOMBIA
SEDE MEDELLÍN
FACULTAD DE MINAS



DYNA
http://dyna.medellin.unal.edu.co/

Methodology for determining the mean and extreme sea level regimes (astronomical and meteorological tides) considering scarce records in microtidal zones: colombian Caribbean case

Andrés Fernando Orejarena-Rondón [a], Luis Jesús Otero-Díaz [a], Juan Camilo Restrepo L[a], Isabel María Ramos De la Hoz [a] & Leonardo Marriaga-Rocha [b]

[a] *Grupo de Física Aplicada, Departamento de Física, Universidad del Norte (UNINORTE), Barranquilla, Colombia. orejarenaa@uninorte.edu.co, ljotero@uninorte.edu.co, restrepocj@uninorte.edu.co, isaramos1014@gmail.com*
[b] *Área de Oceanografía Operacional , Centro de Investigaciones Oceanográficas e Hidrográficas del Caribe (CIOH), Escuela Naval de Cadetes Almirante Padilla, Cartagena, Colombia. lmarriaga@dimar.mil.co*

Received: February 27th, 2018. Received in revised form: May 12th, 2018. Accepted: May 31th, 2018.

Abstract
Synthetic sea level (SL) records of the Cartagena Bay and the Urabá Gulf, from 1991 to 2010, were obtained through this methodology. Simulated series were adjusted against different probability functions (e.g. Log-Normal, Normal, Weibull, Gumbel). Normal and Gumbel distributions provided the best fit for mean and extreme regimes, respectively. Within the Cartagena Bay, there were no significant differences in the mean regime; whereas for the Urabá Gulf its magnitude increased as much as twice southward. Moreover, the extreme regime exhibited the largest values in the southern sector of the Urabá Gulf. This methodology might be implemented in areas where sea level records are scarce or poorly reliable. Thus, it may valuable for planning and building port and coastal infrastructure, as well as for implementing risk reduction measures.

Keywords: sea level; astronomical tide; meteorological tide; mean regime; extreme regime.

Metodología para determinar regímenes medios y extremales del nivel del mar (marea astronómica y meteorológica) cuando se cuenta con escasos registros instrumentales en áreas micromareales: caso Caribe colombiano

Resumen
Se calibraron y modelaron series sintéticas del nivel del mar (NM) con una extensión temporal de 20 años (1991-2010) en la Bahía de Cartagena y el Golfo de Urabá. Las series simuladas fueron ajustadas a diferentes funciones de probabilidad obteniendo los mejores ajustes con las funciones de distribución Normal y de Gumbel para los regímenes medios y extremos respectivamente. Dentro y fuera de la bahía de Cartagena no existen variaciones representativas en el régimen medio, mientras que en el Golfo de Urabá la magnitud aumenta al doble en la parte sur. Además, el régimen extremo presenta magnitudes superiores en la parte sur del Golfo en relación a las demás zonas estudiadas. Esta metodología podría implementarse en áreas donde los registros del nivel del mar son escasos o poco confiables. Por lo tanto, puede ser valiosa para planificar y construir infraestructuras portuarias y costeras, o implementar medidas de reducción de riesgos.

Palabras clave: Nivel del mar; marea astronómica; marea meteorológica; régimen medio; régimen extremo.

1. Introduction

Population growth in coastal areas due to multiple human activities, such as recreation, industrial expansion, and economic exploitation, exposes coastal inhabitants to the permanent threat of erosion, flooding, and natural disasters [1]. These events might be triggered by a significant rise in sea level due to strong winds (tropical storms), cold fronts

How to cite: Orejarena-Rondón, A.F., Otero-Díaz, L.J., Restrepo L., J.C., Ramos-De la Hoz, I.M. and Marriaga-Rocha, L., Methodology to determine the mean and extreme sea level regimes (astronomical and meteorological tide) considering scarce records in micro-tidal zonzones: colombian Caribbean case, DYNA 85(205), pp. 274-283, June, 2018.

© The author; licensee Universidad Nacional de Colombia.
Revista DYNA, 85(205), pp. 274-283, June, 2018, ISSN 0012-7353
DOI: https://doi.org/10.15446/dyna.v85n205.70677

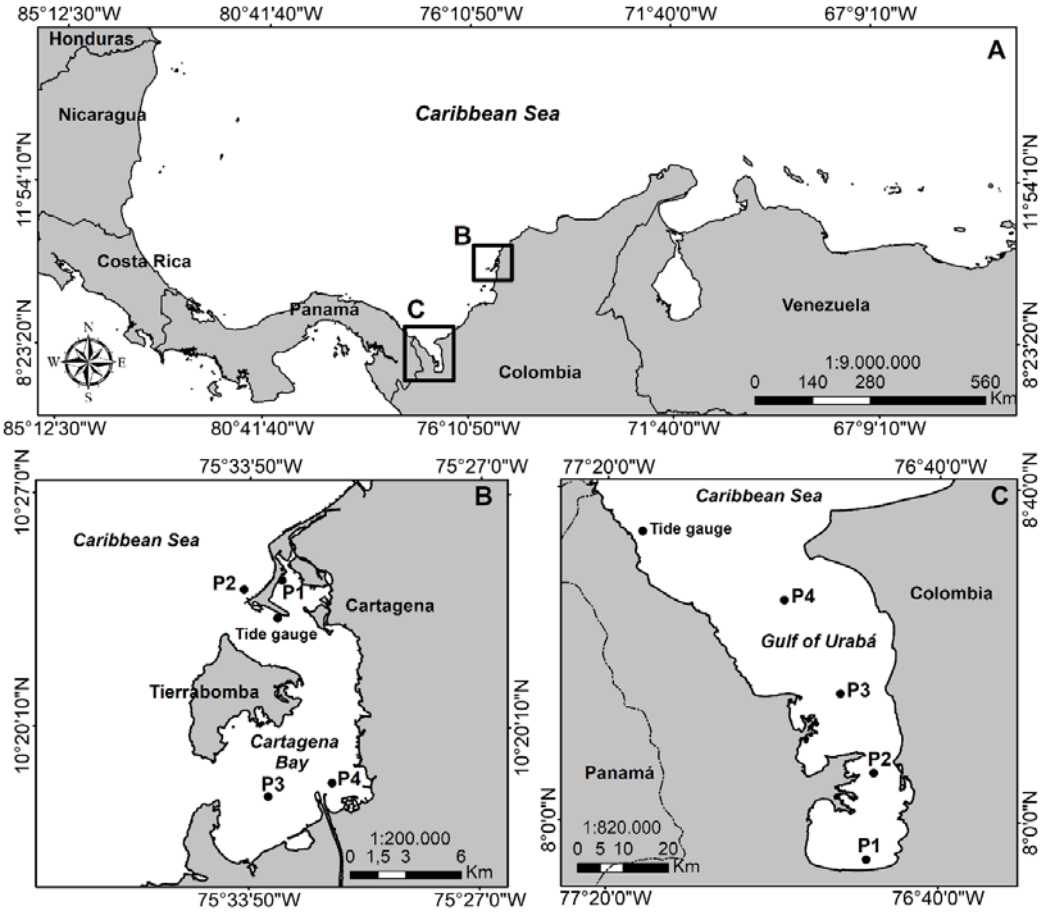


Figure 1. A. Location of Cartagena Bay and the Gulf of Urabá in the Colombian Caribbean. B. Computational domain for Cartagena Bay. C. Computational domain for the Gulf of Urabá. In A and C, the tide gauge points indicates the place where the measured data in the field were obtained for model calibration. The other points (P1, P2, P3, P4) indicate the places where the sea level simulations were performed with a temporary extension of 20 years for the study areas.
Source: The authors

and lower atmospheric pressure [2-4]. These latter phenomena have been grouped into and named as meteorological tides (MT) [5], whereas the regular oscillations of the sea level induced by the gravitational forces of the Earth-Moon-Sun system are denominated astronomical tides (AT) [6]. The sea level at a certain moment is calculated by adding the (AT) to the (MT) [6]. The sum of these components constitutes a crucial parameter for calculating the levels of hazard linked to coastal areas flooding, as well as in the estimation of wave crest heights for safety in port and maritime projects. Some studies have been carried out in the Caribbean Sea to estimate the trend and variability of sea level fluctuations, using tide-gauge historical records and satellite altimetry [7]. However, several locations along the Caribbean littoral lack reliable data or their spatial/temporal resolution is inadequate for such analysis; thus, difficulting the assessment of sea level rise triggered by extreme climatological events as well as the implementation of measures for coastal flood prevention and mitigation.

There have not been any studies focusing on determine the sea levels accurately and on a long-term perspective in the Colombian Caribbean. Particularly, in areas with scarce and disperse tide-gauge records. Most studies focused on assessing the partial contribution to sea level coming from both tide components. Some authors have estimated the height of flooding in coastal areas considering sea level as an important component within the flood systems [8-10].

These latter authors respectively used the same methods for the regions of the Pacific and Caribbean coasts in Colombia, using instrumental series and analyzing the astronomical and meteorological tides separately. The latter component was analyzed from residual meteorological data, the series that remains after deducting the level of the astronomical tide from the original instrumental series. These studies used the hypothesis that the residual meteorological data corresponds to variations in sea level due mostly to wind and atmospheric pressure.

Furthermore, these studies assumed that each instrumental sea level series is representative for a region within each area studied, which means that the methods do not consider whether the coastal area is an open area or is a semi-enclosed body of water, such as bays, gulfs, estuaries or mouths. Other studies identified and analyzed oceanographic parameters in the Mira River delta and the Bay of Tumaco on the Colombian Pacific coast [11,12]. These investigations used a

long-wave numerical model to reconstruct series of astronomical tides, as well as the residual instrumental meteorological series from Tumaco to represent the behavior of the meteorological tide due to pressure and wind. Globally, other authors take into account sea levels to determine flood levels caused by the combination of oceanographic effects [13-17].

This work aims to present an alternative method for the construction of sea levels regimes in microtidal areas with low spatial coverage of tide gauges for measuring sea level, a lack of extensive time series, or non-existent data, from the numerical reconstruction of the sea level, considering the contribution of astronomical and meteorological components at the same time, as well as local effects of variations in the bottom and contours. The validation and verification of this method was performed in two areas of the Colombian Caribbean Coast: The Bay of Cartagena and the Gulf of Urabá (Fig. 1).

Phenomena such as tsunamis, fluvial discharge of large rivers, and other anomalies generated by ocean-atmospheric phenomena or climatic effects such as the melting of the poles, which determine the flooding of low-lying coastal areas, were not considered in the methods proposed hereafter.

In its first stage, the method is based on the application of a hydrodynamic model comprising the equations of long waves to simultaneously model the astronomical and meteorological tides. The numerical results are calibrated using instrumental records (tide-gauges) from two areas of Colombia's Caribbean region, the Bay of Cartagena and the Gulf of Urabá (Fig. 1A, 1B). Once the results were validated, the numerical model was able to generate the series of data used for the construction of the mean and extreme sea level regimes

2. Methods

The first step for implementing this methodology was to set the initial conditions of the hydrodynamic model H2D [18]. A computational mesh domain was defined from bathymetric data provided by the Colombian Hydrographic Service (Servicio hidrográfico Colombiano – CIOH). Data obtained from the AG95.1 Model (Grenoble) were used for calculating the astronomical tide (AT) in the boundaries of the computational mesh. This model generates astronomical tide data worldwide [19]. Atmospheric pressure and wind data from the NOAA NARR (North American Regional Reanalysis) Database, extracted from the same computational mesh domain, were employed for estimating the meteorological tide (MT).

Synthetic sea level series were simulated using *in-situ* measurements of sea level obtained through pressure sensors deployed in the study area (Figs. 1B and 1C) and the model boundary conditions (AT + MT). The simulated series comprise the same period in which the pressure sensors were deployed in the Cartagena Bay (May 18th to June 18th of 2011) and the Urabá Gulf (February 26th to March 27th of 2010). Several combinations of roughness, friction and drag wind coefficients parameters were used for establishing the best fit between the real and simulated series.

Once model validation was completed, sea level series over 20 years were simulated in different sites within the study area. These series were fit using different probability functions (e.g. Log Normal, Normal, Weibull, Gumbel). The Normal and Gumbel distributions exhibited the best fit for the mean and extreme regimes, respectively. This approach allows determining sea level regimes in zones where records are scarce or unreliable.

2.1. Model equations

To generate the astronomical tide and the meteorological data series in the Gulf of Urabá and the Bay of Cartagena, a hydrodynamic model was used to solve the nonlinear equations of long waves, implying that $L >> h$, where L is the wavelength and h the depth at which it propagates. The long-wave condition can be considered applicable from $L > 20\ h$ [20].

Under this consideration, the flow is essentially horizontal. Thus, the horizontal velocity components (u and v) are much greater than the vertical component (w). This claim is valid, except in local areas with steep slopes (> 1/5) or where outcrops (*upwelling*), subsidences (*downwelling*) or oceanic fronts occur [21].

Horizontal flow consideration simplifies the general equations of motion also known as Navier-Stokes, allowing the elimination of the vertical component (w) and establishing a hydrostatic pressure distribution where the equation $\frac{\partial P}{\partial z} = -\rho g$ can be integrated in depths from z to η and expressed as:

$$P_{(n)} - P_{(z)} = -\rho g(\eta - z) \tag{1}$$

where $P_{(n)}$ is the atmospheric pressure, $P_{(z)}$ the hydrostatic pressure, η the free surface level, ρ the density and g gravity.

The depth-averaged equations of continuity and momentum lead to the following expressions:

$$\frac{\partial H}{\partial t} + \frac{\partial (UH)}{\partial x} + \frac{\partial (VH)}{\partial y} = 0 \tag{2}$$

$$\frac{\partial U}{\partial t} + U\frac{\partial U}{\partial x} + V\frac{\partial U}{\partial y} + g\frac{\partial \eta}{\partial x} + \frac{gH}{2\rho_0}\frac{\partial \rho_0}{\partial x} + g\frac{U\sqrt{U^2+V^2}}{C^2 H} = \frac{C_a \rho_a W^2 \cos\psi}{\rho H} + \varepsilon\left[\frac{\partial^2 U}{\partial x^2} + \frac{\partial^2 U}{\partial y^2}\right] + f_c V \tag{3}$$

$$\frac{\partial V}{\partial t} + U\frac{\partial V}{\partial x} + V\frac{\partial V}{\partial y} + g\frac{\partial \eta}{\partial y} + \frac{gH}{2\rho_0}\frac{\partial \rho_0}{\partial y} + g\frac{V\sqrt{U^2+V^2}}{C^2 H} = \frac{C_a \rho_a W^2 \sin\psi}{\rho H} + \varepsilon\left[\frac{\partial^2 V}{\partial x^2} + \frac{\partial^2 V}{\partial y^2}\right] - f_c U \tag{4}$$

where U is the fluid velocity in direction x, V is the fluid velocity in direction y, η is the free surface, $H = h + \eta$ is the mean depth, C_a is the wind drag coefficient, W is the wind speed 10 meters above the sea surface, ψ is the angle between the wind direction in y x, C is the friction coefficient of Chezy, ε is the coefficient of turbulent viscosity, g is the acceleration of gravity, x is the horizontal coordinate, y is the vertical coordinate, t is time, and f_c is the Coriolis acceleration.

Eq. (2) is the equation of the continuity of fluid. Eqs. (3), (4) are the quantity of movement of the fluid at x and y respectively. The left side represents local and advective acceleration control volume and the right side represents the forces that induce or restrict these accelerations. These gradient forces are the free surface, the surface tension due to wind, bottom friction, the effect of turbulence, and the effect of the rotation of the earth, respectively [20]. The way in which the model solves the Eqs. (2)-(4) is by using a finite difference algorithm that is implicit in the alternating direction of double scanning [22].

2.2. Viscosity coefficients of Eddy, friction and wind drag

The coefficients of friction of Chezy (*C*), eddy viscosity coefficient (ε) and wind drag coefficient (*Ca*), present in the eq. (2)-(4), were used for model calibration. These coefficients rely on a wide range of factors; such as, bathymetry, roughness, properties of the bottom sediments, flow conditions, wind speed, etc. These factors are in turn dependent on the site or location and will vary with time. The uncertainty of the behavior of two-dimensional flow is concentrate of these parameters [21].

The eddy viscosity coefficient (ε) is used to describe turbulence, including several terms ranging from numerical dispersion caused by the transformation of differential equations in finite-difference equations that correspond to the average of vertical flow equations. In this case, a constant value of the eddy viscosity is set for the two points of study, which is used throughout the entire grid domain of the model. This condition is close to real conditions when the depth is much less than the discretization used, since in such situation the friction at the bottom is more important than turbulence. According to [23] the value of the eddy viscosity depends on the dimensions of the cells and its value can be calculated by using the following formula:

$$\varepsilon = K\Delta x u \tag{5}$$

Where the surface roughness is between $0.05 - 0.15$, Δx is the cell size (m) and u is the characteristic velocity ($m\ s^{-1}$). In the case of the Bay of Cartagena study, the grid has a cell size $\Delta x = 150m$; taking the characteristic velocity as $u = 1\ ms^{-1}$, the value of ε ranges between 7.5 and 22.5 $m^2\ s^{-1}$. For this case a value of $\varepsilon = 10\ m^2 s^{-1}$ was used, which, after various tests performed in the present work, fits the results better. In the case of the Gulf of Urabá study, the grid has a cell size of $\Delta x = 200m$; thus taking the characteristic velocity as $u = 1\ ms^{-1}$, the ε value oscillates between 10 and 30 $m^2\ s^{-1}$.A value of $10\ m^2 s^{-1}$ was selected, the same as in the case of Cartagena.

The seabed friction ratio refers to the dissipation of a quantity of flow movement by friction at the contours or the seabed. The parameter used in the model to represent this effect is the Chezy coefficient which has a value between 45 and 60 $m\ s^{-1}$ in nearshore areas. The equation used by the model to define the friction coefficient based on seabed roughness is:

$$C = 18\log\left(\frac{12H}{K}\right) \tag{6}$$

where *K* is the roughness in meters that represents seabed roughness, due to the size of the sediment and the shape of the floor [24-28] and *H* is a function of depth. The *K* value taken for both case studies was 0.01 m based on several tests performed in this study, in which the value of this coefficient was determined with optimal results.

Wind friction is triggered by the shear stress exerted by the wind on the surface of the ocean. It is represented by the equation:

$$\frac{1}{\rho H}(\tau_{sx,}\tau_{sy}) = \frac{C_a\rho_a w^2\ (\cos\psi\ , sen\ \psi)}{\rho H} \tag{7}$$

In this equation, the wind drag coefficient of C_a [29] analyzes numerous measurements, concluding that in stable atmospheric conditions C_a depends linearly on wind speed. However, does not exist a universal formulation for the drag coefficient C_a, therefore it is necessary to perform adaptations whit instrumental data bases to validate a specific zone. In this case we define the drag coefficient as C_a=0.023 for both areas tested, according to the calibration results obtained.

2.3. Initial and boundary conditions

Series of astronomical tides were generated using data obtained from an interpolation method based on the AG95.1 model developed by [19], using the Grenoble database. These series were used as boundary conditions within the long-wave model, establishing periods coinciding with measurements made using tide-gauges in the Bay of Cartagena and the Gulf of Urabá. In Cartagena Bay a database was generated from the 18th of May 2011 to the 18th of June 2011 (Fig. 1B). In the Gulf of Urabá a database was generated for the period from the 27th of February 2010 until the 26th of March 2010 (Fig. 1C).

Two independent grids were generated for the application of the numerical model. In the Bay of Cartagena with a cell size of 150 m (Fig. 1B) and in the Gulf of Urabá with cell size of 200 m (Fig. 1C). These grids were generated from available nautical bathymetry charts and detailed bathymetric surveys developed by the Caribbean Center for Oceanographic and Hydrographic Research. They were complemented with global bathymetric information obtained from ETOPO 1, a NOAA (National Geophysical Data Center) database with a resolution of one minute for the Caribbean Sea area of Colombia.

The sea level variation also depends on the contribution made by meteorological tides (wind and pressure). These parameters were included as input conditions, obtaining the respective data-sets from the global database of NOAA's NARR, on the same date in which data from tide-gauge was obtained. Atmospheric pressure and wind are implicit in the long-wave equations of the H2D hydrodynamic model. In addition, the inclusion of the effect of the tidal regime was necessary to determine the coefficient of wind drag (*Ca*). Through repeated executions of the model, varying the value between 0.019 and 0.025, the coefficient of wind drag that best fitthe simulated data to real conditions was *Ca* = 0.023.

2.4. Adaptation and calibration of the hydrodynamic model

To calibrate the model, the synthetic sea level series were compared with data measured by tide-gauges in the areas of study. The wind drag coefficient (Ca), Chezy friction (C) and turbulent viscosity (ε) were configured in the model to find the best statistical fit between the two series and to later generate synthetic sea level series with an extension of 20 years at each of the points observed in Fig. 1B and 1C. The mean and extreme regimes were extracted from this data through cumulative probability distribution and Gumbel extreme value distribution respectively for the current study. The Nash-Sutcliffe efficiency test (NSE) was employed for estimating the accuracy of the calibration. NSE indicates how well the observed data versus simulated data fits a 1:1 line, and is computed as shown in Equation 8:

$$NSE = 1 - \left[\frac{\sum_{i=1}^{n}\left(Y_i^{obs} - Y_i^{sim}\right)^2}{\sum_{i=1}^{n}\left(Y_i^{obs} - Y^{mean}\right)^2}\right] \quad (8)$$

where the model simulation can be judged as satisfactory if NSE >0.5 [30]

2.5. Determination of the mean sea level regime

A hydrodynamic calibrated (astronomical tide + meteorological tide) model allows simulate periods of 20 years (1991-2010) at various points in the study areas to determine the mean sea level regime. These mean sea level regimes represent the mean sea level behavior in terms of probability. Thus, different probability functions were evaluated, including Log Normal, Normal, Weibull, and Gumbel. Finally, the Normal distribution function provided the best statistical fit to the synthetic tidal series generated in the study areas.

2.6. Determination of the extreme sea level regime

To determine the extreme sea level regime the synthetic series were fit to a probability function. In this case the function allows the calculation of return periods and probabilities of non-exceedance of a sea level height determined from a set of independent extreme values over time. Once these extreme values were determined, and they were split into annual series to subsequently fit them to a distribution function. In this case, the Gumbel maximum distribution function provides the best statistical fit.

3. Results

The following shows the comparisons between measured and simulated time series of sea level within the study areas. In the first instance the measured time series of sea level were compared with simulated series of astronomical tides. Then, the effects of wind and atmospheric pressure (meteorological tide) in the modeled data were incorporated. Through this process a best fit between the measured data and the modeled data was obtained.

3.1. Sea level calibration (AT + MT) in the bay of Cartagena and the gulf of Urabá

For both study areas, comparisons were performed between the mean sea level measured by tide-gauges (AT + MT) and the astronomical tide, considered as the only input condition for the hydrodynamic model. The modeled astronomical tide resembles the patterns exhibited by the mean sea level signal measured in both areas, the Bay of Cartagena (Fig. 2) and the Gulf of Urabá (Fig. 4).

NSE analyses were performed between the modeled and measured sea level time series to determine in greater detail the fit of the model outputs to the real conditions. NSE coefficients of 0.82 and 0.63 were obtained for the Bay of Cartagena (Fig. 3) and Urabá (Fig. 5), respectively.

After obtaining statistical significant results in modeling the astronomical tide as the only input condition of the hydrodynamic model, the variations in sea level caused by the meteorological tide (wind and pressure) was added to simulate synthetic sea level series; and thus, to improve the correlation between the measured and simulated time series.

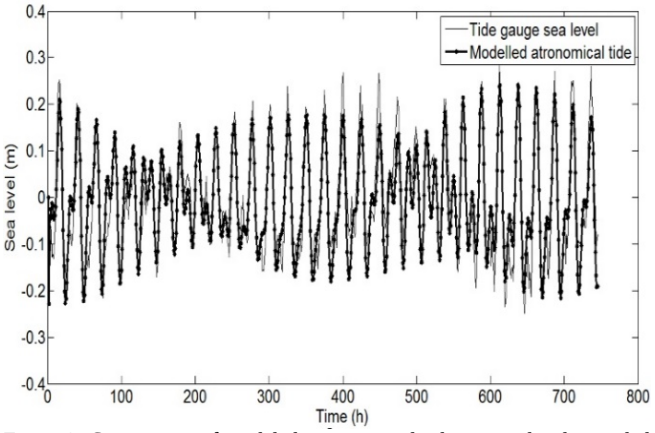


Figure 2. Comparison of modeled astronomical tide vs. sea level recorded by the tidal gauge in the Bay of Cartagena.
Source: The authors.

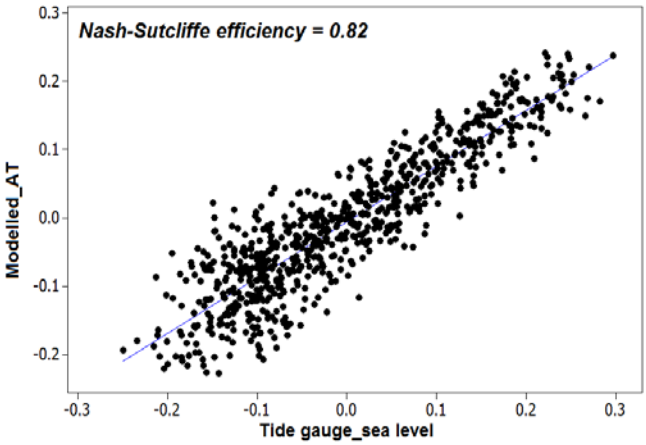


Figure 3. Linear comparison between the simulated astronomical tidal series and sea level recorded by the tide gauge in the Bay of Cartagena. The Nash-Sutcliffe efficiency test shows a good agreement between both series.
Source: The authors

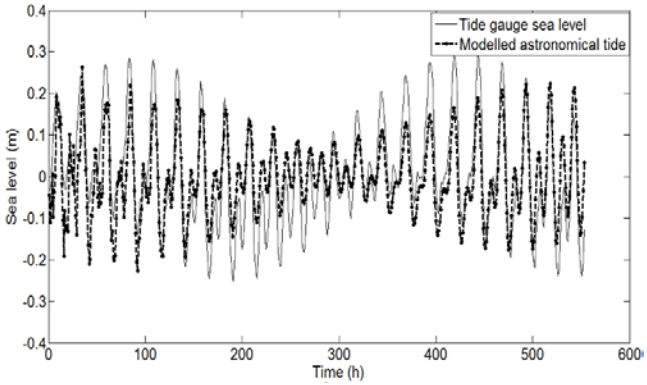


Figure 4. Comparison of modeled astronomical tide vs. sea level recorded by the tide gauge in the Gulf of Urabá.
Source: The authors

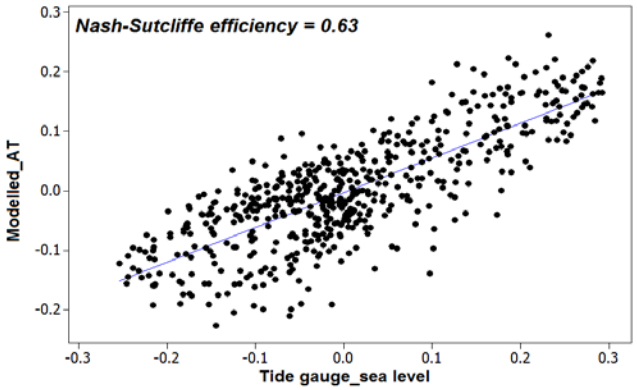


Figure 5. Linear comparison between the simulated astronomical tidal series and sea level recorded by the tide gauge in the Gulf of Urabá.
Source: The authors

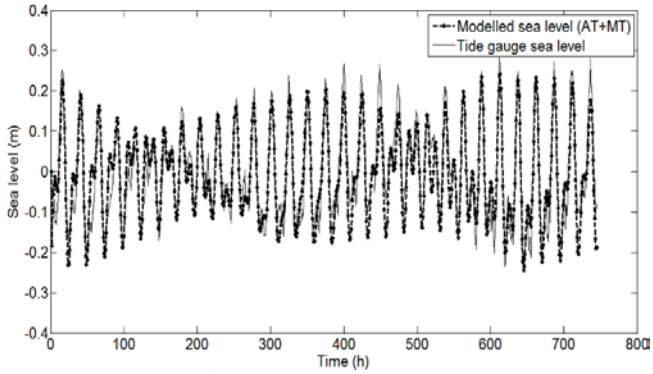


Figure 6. Comparison of modeled sea level (AT + MT) vs. signal extracted from the gauge in the Cartagena area.
Source: The authors

Similarity patterns of the measured and modeled time series were improved by almost a 3%, because this approach include the effect of atmospheric pressure and wind intensity within the modeling parameters (Figs. 6, 8). The NSE coefficient estimated for the Bay of Cartagena increased to 0.85 (Fig. 7), whereas the correlation coefficient in Urabá rose to 0.66 (Fig. 9).

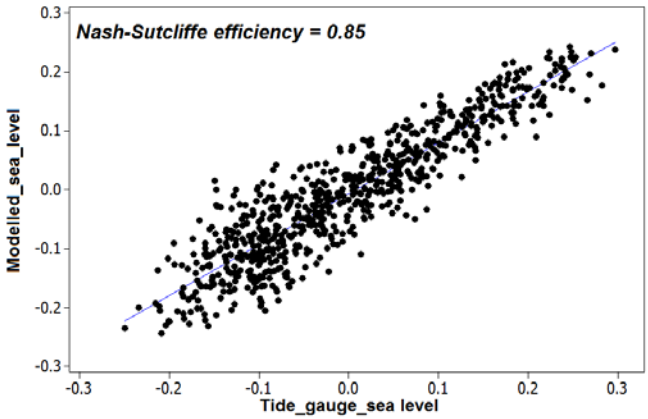


Figure 7. Linear comparison between the simulated series (AT + MT) and sea level taken from the gauge in the Cartagena area.
Source: The authors

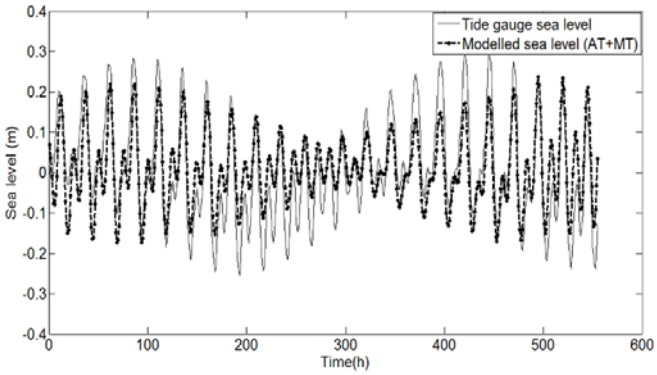


Figure 8. Comparison of modeled sea level (AT + MT) vs. signal extracted from the gauge in the region of Urabá.
Source: The authors

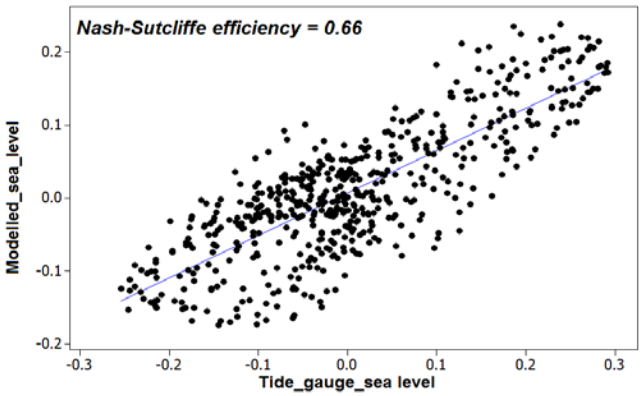


Figure 9. Linear comparison between the simulated series (AT + MT) and sea level taken from the gauge in the region of Urabá.
Source: The authors

3.2. Mean sea level regime (AT + MT) in Cartagena bay and the gulf of Urabá

The determination of the mean regime, as indicated above, is the mean behavior of sea level over a period. In this case, for a period of 20 years (1991-2010) for each of the points located

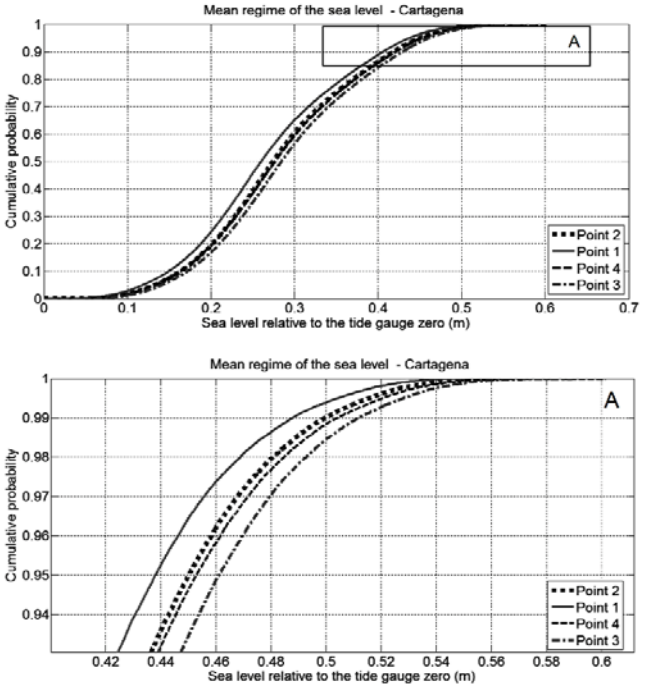


Figure 10. Mean sea level regime for the modeling point distribution in the Bay of Cartagena, zoomed at the top of the graph to see better results.
Source: The authors

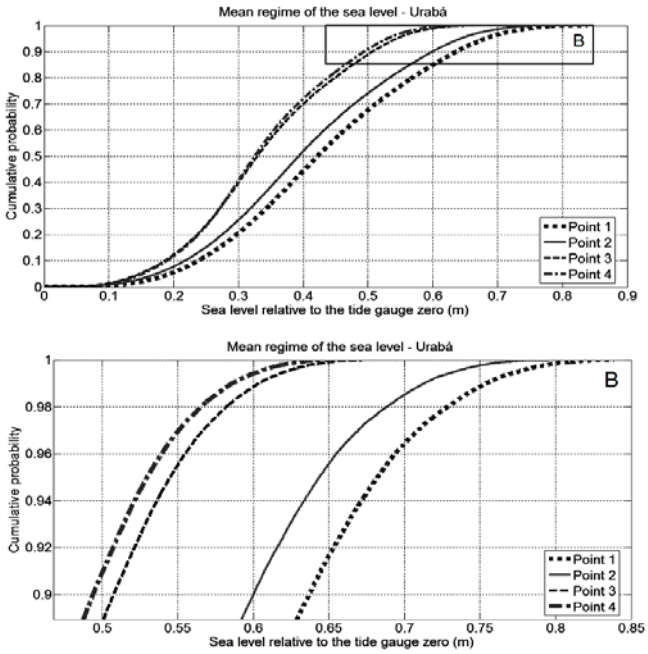


Figure 11. Mean sea level regime for the modeling point distribution in the Gulf of Urabá, zoomed at the top of the graph to see better results.
Source: The authors

Table 1.
Values of non-exceedance probability of the heights of mean sea level in meters, for 95%, 99% and 99.9% in each of points in the Bay of Cartagena.

	Non-exceedance probability for the heights of mean sea level in the Bay of Cartagena		
	95.0%	**99.0%**	**99.9%**
Point 1	0.4381m	0.4880m	0.5282m
Point 2	0.4502m	0.4998m	0.5391m
Point 3	0.4612m	0.5118m	0.5514m
Point 4	0.4529m	0.504m	0.5446m

Source: The authors

Table 2.
Values of non-exceedance probability of the heights of mean sea level in meters, for 95%, 99% and 99.9% in each of points in the Gulf of Urabá.

	Non-exceedance probability for the heights of mean sea level in the Gulf of Urabá		
	95.0%	**99.0%**	**99.9%**
Point 1	0.6823m	0.7540m	0.8071m
Point 2	0.6437m	0.7132m	0.7645m
Point 3	0.5449m	0.6034m	0.6478m
Point 4	0.5298m	0.5860m	0.6296m

Source: The authors

in the areas of study. In the Bay of Cartagena (Fig. 1B) four points were used for determining the mean sea level regime (i.e. two on the north side, P2 and P1, and two more inside the bay on the south side, P4 and P3). The results are shown in Fig. 10. For this area, the mean sea level regime amounts to 0.43 and 0.55 m for non-exceedance values between 95% and 99.9%, respectively, as shown in Table 1.

Four points were selected to estimate the mean sea level regime in the Gulf of Urabá. Two points in the south of the Gulf (P1 and P2), one in the center of the Gulf (P3), and one closer to the north of the Gulf (P4) (Fig. 1C). The mean sea level regime results in this area (Fig. 11) were 0.52 and 0.80 m for non-exceedance values between 90% and 99.9%, respectively, as shown in Table 2.

The annual maximum method was used to determine the extreme sea level regime in Cartagena Bay and the Gulf of Urabá. This method divides the time series annually by selecting the maximum values of that variable over time. Thus, obtaining a continuous series of independent extreme values through time. Once these extreme values were determined, the Gumbel distribution function was applied to determine the return periods of sea level heights in the areas mentioned above. The extreme sea level regime is presented as the result of a maximum Gumbel probability, in which sea level is shown in meters and the return period in years for both study areas (Figs. 12, 13).

3.3. Extreme sea level regime in the bay of Cartagena and the gulf of Urabá

The Bay of Cartagena (Fig. 12) exhibits levels of 0.55 m for a return period of 10 years and 0.63 m levels for a return period of 100 years as extreme behavior of sea level at the selected points, whereas, for the Gulf of Urabá area (Fig. 13), the extreme sea level is to 0.66 m for a return period of 10 years and 0.88 m for a return period of 100 years.

4. Discussion

The methodology for estimating sea level patterns did not consider the effects of rivers discharging into Cartagena Bay and Urabá Gulf, due to the lack of reliable streamflow

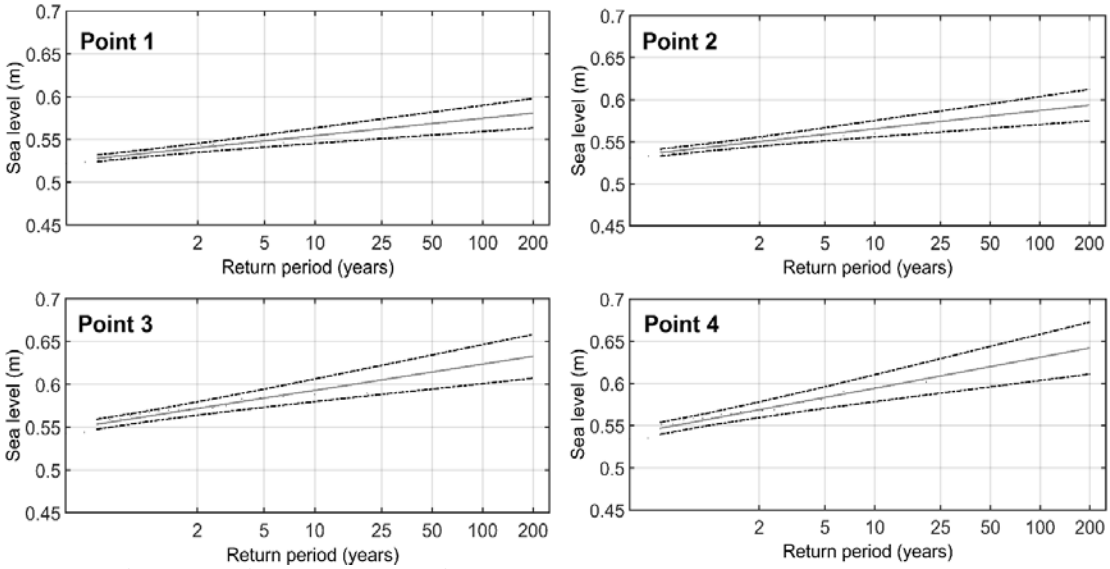


Figure 12. Return period of the heights of sea level in the Bay of Cartagena in search points P1, P2, P3 and P4.
Source: The authors

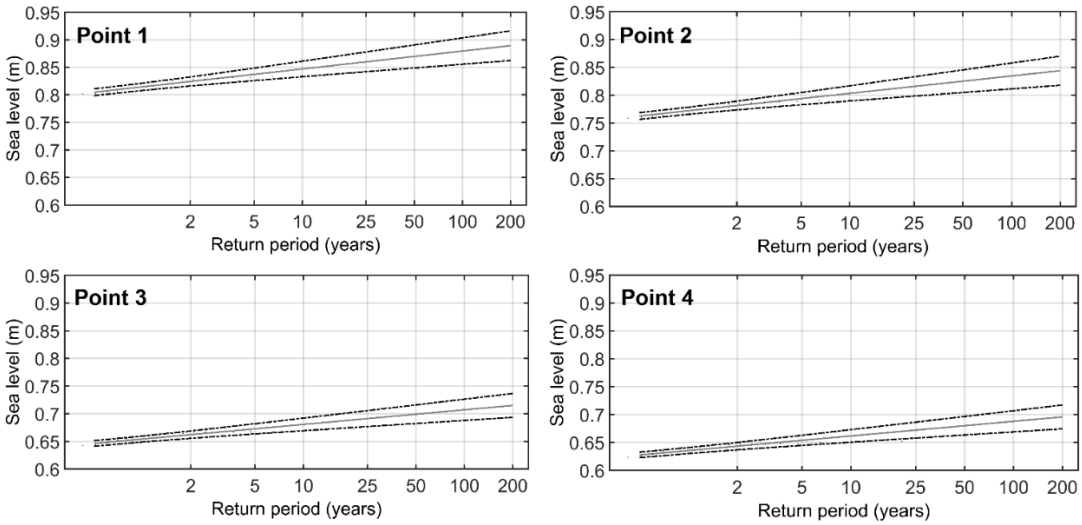


Figure 13. Return period of the heights of sea level in the Gulf of Urabá, for points P1, P2, P3 and P4.
Source: The author

data on a high resolution time-scale, mainly for the latter. Therefore, the results of this study only represent the contribution of the astronomical and meteorological tides, ignoring fluvial effects.

The sea level in the Bay of Cartagena, according to the results of this study, varies between 0.528 m and 0.551 m (values representing the 99.9% of not exceeding -Table1), consistent with [31], which asserted that the Caribbean Sea exhibits a microtidal range (astronomical tide) ranging from 0.2 to 0.4 m, depending on the geographic location. This range lie below our estimates for the Cartagena Bay (0.528 and 0.551 m). However, these estimates include the additional rise caused by wind and atmospheric pressure (meteorological tide).

The extreme regime of the Cartagena Bay exhibited a slight increase inside the Bay (P3 and P4 points), in comparison with the extreme regimes observed in P2. The internal sector (P4) exhibits values of 0.58, 062 and 0.65 m, corresponding to 10, 25 and 50-yrs return periods, respectively. Whereas the external sector (P2) show values of 0.53, 0.56 and 0.59 m, corresponding to 10, 25 and 50-yrs return periods, respectively. Tidal gauge data located in the Bay of Cartagena referred to by [32,33] were not used for this study because there is a large quantity of gaps in the seasonal sea level records. In addition, this gauge has been located in different places within the Bay of Cartagena which resulted in a change of the reference level at each point.

The mean and extreme sea level regimes in the Urabá Gulf increase southward. At P4, located in the North of the gulf, the range of the mean regime was 0.65 m; whereas at P1, located in the southernmost part, this range rises up to 0.82 m. This

pattern was also observed in the extreme regime. P4 exhibited extreme values of 0.59, 0.61 and 0.63 m for return periods of 10, 25 and 50 years, respectively; while, P1 exhibited extreme values of 0.85, 0.87 and 0.89 m for those return periods, respectively. This pattern might be linked to tide superposition, since tides can be described as overlapping waves, in which the interaction of incoming and outgoing tides increases due to reflection at the boundaries; which in turn, leads to a rise in sea level oscillations according to the gulf setting (i.e. depth and length) [34].

The improvement in the statistical adjustment caused by meteorological tide contribution is nearly 3%. Such improvement might be considered to be negligible. Nevertheless, it must be considered that in extreme conditions, atmospheric pressure and wind contributions might be significant. Therefore, this study considered both factors as key parameters when estimating sea level regimes in the Colombian Caribbean. The statistical model seems is to the underestimate the values of the sea level when comparing to instrumental records measured near Capurganá - Urabá Gulf (Fig. 1C). Such underestimation may be induced by the low spatial resolution of the bathymetric data in this zone, which impedes a proper signal representation of the tides.

In addition, the fit between the simulated and observed meteorological tide signals might be further enhanced. This is mainly because we assume a single value of wind and atmospheric pressure for each time step along the entire grid employed in the H2D model. Due to its spatial resolution (32 km) just one or two points of the NARR database of wind and atmospheric pressure coincided with the grids employed in this study. These coinciding points were used to define grids with the same spatial resolution as that of the grids employed in the Cartagena Bay and Urabá Gulf. Consequently, a larger discretization of the wind and atmospheric pressure fields, as a model input, would improve the modelling results. It was determined that at the southern end of the Gulf of Urabá, the mean sea level regime was characteristically rise relative to sea level values found in the Cartagena Bay by 67%, due to the marked effect of sea level rise produced by the configuration of the gulf. It was found that sea level values in the southern Gulf of Urabá reach 0.807 m, which differ from other known tidal ranges in Colombia's Caribbean region, as determined in previous studies.

The results of the mean and extreme regime determined by the proposed method serve as a statistical tool for defining technical control criteria, design, construction and programming of the design and use of coastal and port protection structures. Future research should include the streamflow effects (mainly in semi-enclosed areas such as bays and gulfs) when determining the sea level regime.

It is also recommended that wind and atmospheric pressure databases (from measurements or Reanalysis) with greater spatial resolution to obtain a better simulation of the meteorological tide regime in the surveyed areas (Cartagena Bay and Urabá Gulf).

5. Summary and conclusions

A method was established for reconstructing mean and extreme sea level regimes in microtidal areas where there are no historical instrumental records of sea level. This was done through the calibration and numerical simulation of sea level data sets considering the effects of astronomical tide and meteorological tide. This method was validated in two areas of Colombia's Caribbean coast. It was found that simulated sea level results fit better to the measured instrumental data when the initial conditions of the effect on tide levels from weather and wind pressure are included in the model. The mean sea level regime, both within and outside the Bay of Cartagena, did not vary significantly. In the south of the bay, slight changes in the values of extreme ranges were due to the appearance of compound tides, although in the results this effect was not very pronounced.

References

[1] Rangel-Buitrago, N.G., Anfuso, G. and Williams, A.T., Coastal erosion along the Caribbean coast of Colombia: magnitudes, causes and management. Ocean & Coastal Management 114, pp. 129-144, 2015. DOI: 10.1016/j.ocecoaman.2015.06.024.

[2] Otero, L.J., Ortiz-Royero, J.C., Ruiz-Merchan, J.K., Higgins, A.E. and Henriquez, S.A., Storms or cold fronts: what is really responsible for the extreme waves regime in the colombian Caribbean coastal region?, Nat. Hazards Earth Syst. Sci., 16, pp. 1-11, 2016. DOI: 10.5194/nhess-16-1-2016.

[3] Ortiz, J.C., Exposure of the colombian Caribbean coast, including San Andrés island, to tropical storms and hurricanes, 1900–2010, Nat. Hazard J., 61, pp. 815-827, 2012. DOI: 10.1007/s11069-011-0069-1.

[4] Ortiz, J.C., Plazas, J.M. and Lizano, O., Evaluation of extreme waves associated with cyclonic activity on San Andrés island in the Caribbean sea since 1900, J. Coast. Res., J. Coast. Res., 31, pp. 557-568, 2015. DOI: 10.2112/JCOASTRES-D-14-00072.1.

[5] GIOC (Grupo de Ingeniería Oceanográfica y de Costas). Documento temático de cota de inundación. Santander, España Universidad de Cantabria – Ministerio de Medio Ambiente. 59 P, 1998.

[6] GIOC (Grupo de Ingeniería Oceanográfica y de Costas). Documento de referencia – Dinámicas, volumen I. Santander, España Universidad de Cantabria – Ministerio de Medio Ambiente. 580 P, 2002.

[7] Torres, R.R. and Tsimplis M.N., Sea-level trends and interannual variability in the Caribbean sea. J. Geophys. Res. Oceans. 118, pp. 2934-2947, 2013. DOI: 10.1002/jgrc.20229.

[8] Agudelo, P., Gonzales, M. and Medina, R., Determinación de la cota de inundación del Pacífico colombiano. XXI Congreso latinoamericano de hidráulica,São Pedro, estado de São Paulo, Brasil) pp. 1-5, 2004.

[9] Martínez, J.C., Osorio, A.F., Bernal, G. y Agudelo, P., Una metodología para la determinación de la cota de inundación en la zona costera del Caribe Colombiano. XXVI Congreso latinoamericano de hidráulica, pp. 1-12, 2010.

[10] Peláez-Zapata, D.S., Osorio, A.F., Álvarez-Silva, O., Osorio-Cano, J. D. y Payán, L., Estimación de la cota de inundación como herramienta para la conservación de las tortugas marinas en el Pacífico colombiano. XXV Congreso Latinoamericano de Hidráulica San José, Costa Rica, 9 al 12 de Septiembre de 2012. DOI: 10.13140/2.1.5035.8402

[11] Otero, L. and Restrepo, J.C, Modelamiento numérico y dinámico en deltas: aplicación de modelos hidrodinámicos para el análisis oceanográfico del delta del río mira. en Restrepo, J.D., Deltas de Colombia: morfodinámica y vulnerabilidad ante el cambio global. Medellín, Colombia: Fondo Editorial de la Universidad EAFIT, 2008. pp. 221-235.

[12] Toro, V. and Otero L., Aplicación de un modelo hidrodinámico bidimensional para describir las corrientes y la propagación de la onda de marea en las bahías de Buenaventura y San Andrés de Tumaco. XVI Seminario Nacional de Hidráulica e Hidrología, 324 P, 2004.

[13] Castillo, M.C., Desarrollo de una metodología para la obtención de un atlas de cota de inundación en playas en el litoral español, MSc. Thesis, Universidad de Cantabria, Santander, España, 1998.

[14] Medina, R. and Méndez, F.J., Inundación costera originada por la dinámica marina. Ingeniería y Territorio. [Online] 74, 68-75, 2006. Available at: http://www.ciccp.es/revistaIT/portada/img_portada/issue_306/pdf/IT-74.pdf
[15] Pugh, D.T. and Vassie, J., Extreme sea level from tide and surge probability. Proceedings. 16th Coastal Engineering Conference, pp. 911-930, 1978. DOI: 10.1061/9780872621909.054
[16] Fleming, R.J.V., Luettich, R. and Fleming, J.G. Comparative hydrodynamics during events along a barrier island: explanation for overwash. Estuar. Coasts 36(2), pp. 334-346, 2013. DOI: 10.1007/s12237-012-9578-8
[17] Dietrich, J., Tanaka, S., Westerink, J., Dawson, C., Luettich Jr., R.A., Zijlema, M., Holthuijsen, L., Smith, J., Westerink, L. and Westerink, H., Performance of the unstructured mesh, SWAN+ADCIRC model in computing hurricane waves and surge. J. Sci. Comput. 52(2), pp. 468-497, 2011. DOI: 10.1007/s10915-011-9555-6.
[18] GIOC (Grupo de Ingeniería Oceanográfica y de Costas). Manual de referencia modelo numérico H2DII. Ministerio de Medio Ambiente y Universidad de Cantabria. Santander, España, 2001.
[19] Andersen, O.B., Woodworth, P. and Flather, R., Intercomparison of recent ocean tide models. Journal of Geophysical Research, 100(C12), pp. 25261- 25282, 1995. DOI: 10.1029/95JC02642
[20] Pedlosky, J., Geophysical fluid dynamics. New York: Springe Verla, 710 P, 1987. DOI: 10.1007/978-1-4612-4650-3.
[21] Dean, R.G. and Dalrymple, R.A., Water wave mechanics for engineers and scientists. Singapore: World Scientific, 371 P, 1991.
[22] Leendertse, J.J., A water quality simulation model for well mixed estuaries and coastal seas: vol. 1, Principles of computation. Santa Monica, California: The Rand Corporation, 77 P, 1970.
[23] Madsen, P.A., Rugbjerg, M. and Warren, I.R., Subgrid modelling in depth integrated flows. Proceedings of 21-First Conference on Coastal Engineering, pp. 505-511, 1988. DOI: 10.1061/9780872626874.036
[24] Van Rijn, L.C., Principles of sediment transport in rivers, estuaries and coastal seas. Netherlands: Aqua Publications, 690 P, 1993.
[25] Van Rijn, L.C., Unified view of sediment transport by currents and waves I: initiation of motion, bed roughness and bed-load transport. Journal of Hydraulic Engineering 133(6), pp. 649-667, 2007. DOI: 10.1061/(ASCE)0733-9429(2007)133:6(649)
[26] Van Rijn, L.C., Unified view of sediment transport by currents and waves II: Suspended transport. Journal of Hydraulic Engineering, 133(6), pp. 668-689, 2007. DOI: 10.1061/(ASCE)0733-9429(2007)133:6(668)
[27] Yalin, M.S., Mechanics of sediment transport. Braunschweig: Pergamon Press, 314 P, 1972.
[28] Yalin, M.S., River mechanics. Oxford: Pergamon Press, 219 P, 1992.
[29] Garratt, J.R., Review of drag coefficients over oceans and continents. Monthly Weather Review, 105(7), pp. 915-929, 1977. DOI: 10.1175/1520-0493(1977)105<0915:RODCOO>2.0.CO;2
[30] Moriasi, D.N., Arnold, J.G., Van Liew M.W., Bingner, R.L., Harmel, R.D. and Veith, T.L., Model evaluation guidelines for systematic quantification of accuracy in watershed simulations. American Society of Agricultural and Biological Engineers. [online]. 50(3), pp. 885-900, 2007. Available at: http://citeseerx.ist.psu.edu/viewdoc/download?doi=10.1.1.532.2506&rep=rep1&type=pdf
[31] Kjerfve, B., Tides of the Caribbean sea. Journal of Geophysical Research, 86(C5), pp. 4243-4247, 1981. DOI: 10.1029/JC086iC05p04243
[32] Torres R.R., Otero L.J., Franco F.A. y Rocha L.M., Comportamiento del nivel del mar en el litoral Caribe colombiano. Boletín Científico Centro de Investigaciones Oceanográficas e Hidrográficas, [online]. 26(0120-0542), pp. 8-21, 2008. Available at: https://www.researchgate.net/profile/Rafael_Torres31/publication/318725814_Comportamiento_del_nivel_del_mar_en_el_litoral_Caribe_colombiano/links/597a17a2aca272e8cc0d38aa/Comportamiento-del-nivel-del-mar-en-el-litoral-Caribe-colombiano.pdf
[33] Torres, R.R. and Tsimplis, M.N., Tides and long-term modulations in the Caribbean sea. Journal of Geophysical Research: Oceans 116(C10022), pp. 1-18, 2011. DOI: 10.1029/2011JC006973
[34] Hicks, S.D., Understanding tide. U.S Department of Commerce. National Oceanic and Atmospheric Administration, National Ocean Service, [online]. 83 P, 2006. Available at: https://tidesandcurrents.noaa.gov/publications/Understanding_Tides_by_Steacy_finalFINAL11_30.pdf

A.F. Orejarena-Rondón, received his BSc. Eng in Civil Engineering in 2009, from the Universidad Industrial de Santander, Colombia, MSc. degree in Oceanography from the Escuela Naval de Cadetes Almirante Padilla, Colombia, in 2014 and currently is PhD candidate in Marine Sciences from Universidad del Norte, Colombia. He has worked as researcher at the Centro de Investigaciones Oceanograficas e Hidrográficas del Caribe and Universidad del Norte, Colombia. His research interest include numerical modeling of hydrodynamic and morphodynamic in beaches, storm surge, extreme waves and wave runup.
ORCID: 0000-0001-6355-6282

L.J. Otero-Díaz, is assistant professor at Universidad del Norte, Colombia, and BSc. in Physical Oceanographer with a MSc. degree and PhD degree in Marine and Technologies Sciences. His main research fields are in numerical modeling of ocean waves (tides, tsunami, gravity and infragravity waves), geohazard assessment (tsunami, storm surge, extreme waves, wave runup) and other marine phenomenons that impact severely in the coastal zones. Also he has worked in several projects related to coastal processes and morphodynamics changes in the Colombian coasts, estuarine dynamics processes. He worked for the Colombian navy at the National Maritime Authority (DIMAR) in activities of Coastal Managements (public goods like beaches). He has experience through developing several researches and consulting projects in Hydrodynamics in the surf zone of macrotidal beaches, coastal erosion in colombian coasts and islands, coastal oceanography and morphodynamic of several rivers like Patia, Mira and Magdalena in a context of global changes and anthropogenic impact.
ORCID: 0000-0002-1322-253X

J.C. Restrepo-L., is PhD in Marine Sciences from the Interinstitutional Doctoral Programme in Marine Sciences; MSc. of Earth Sciences from Universidad Eafit, Colombia and BSc. in Environmental Engineer from Escuela de Ingeniería de Antioquia, Colombia. Its research focus on the analyses of fluvial and coastal processes in tropical environments with emphasis in sedimentary processes, the assessment of relationships between coastal hydrodynamic, sediment transport and coastal geomorphology, and the estimation of anthropogenic impacts on fluvial and coastal systems. Currently appointed as a professor and researcher in the Physics and Geosciences Department at Universidad del Norte, Colombia. Former researcher of Centro de Investigaciones Oceanográficas e Hidrográficas and Centro de Control de Contaminación del Pacífico.
ORCID: 0000-0001-5696-8625

I.R. Ramos-De la Hoz graduated the BSc. in Biology, from Universidad del Atlántico, with a and a MSc. degree in Oceanography from the Escuela Naval de Cadetes Almirante Padilla, Colombia. She has worked as researcher at the Centro de Investigaciones Oceanográficas e Hidrográficas del Caribe and Universidad del Norte, Colombia. Her research interest include coastal hydrodynamic and morphodynamic processes and GIS for coastal zone management. She is currently worked in the Marine, Environmental and Coastal Research Group of the Escuela Naval de Suboficiales, Colombia.
ORCID: 0000-0002-5853-5046

L.M. Marriaga-Rocha, is BSc. in Physical Oceanographer with a MSc. degree in Oceanography and PhD candidate in Marine Sciences, working with the colombian maritime authority. His main research fields are in numerical modeling of ocean processes (waves, currents), morphodynamics and coastal erosion assessment. He has worked as responsible of coastal management and operational oceanography in the Caribbean Oceanographic and Hydrographic Research Centre, and as director of Pacific Oceanographic and Hydrographic Research Centre.
ORCID: 0000-0001-5413-6163

UNIVERSIDAD NACIONAL DE COLOMBIA
SEDE MEDELLÍN
FACULTAD DE MINAS



DYNA
http://dyna.medellin.unal.edu.co/

Development of an information system for teleoperated physical rehab care service via Internet. Pilot case: patients with mild knee injury who live in geographically vulnerable zones

José Rafael Tovar-Cuevas[a], Juan David Díaz Mutis[a], Getssy Elizabeth Quiñones Mora[a], Anabella Pabón Romero[b] & José Isidro García-Melo[c]

[a] *Escuela de Estadística, Facultad de Ingeniería, Universidad del Valle, Cali, Colombia. Jose.r.tovar@correounivalle.edu.co, Juan.diaz@correounivalle.edu.co, gettsyelizabeth@gmail.com*
[b] *Escuela de Ingeniería Industrial, Facultad de Ingeniería, Universidad del Valle, Cali, Colombia. anabella.pabon@correounivalle.edu.co,*
[c] *Escuela de Ingeniería Mecánica, Facultad de Ingeniería, Universidad del Valle, Cali, Colombia. Jose.i.garcia@correounivalle.edu.co*

Received: September 26th, 2017. Received in revised form: January 16th, 2018. Accepted: February 16th, 2018

Abstract
In recent years, new technologies have been implemented for treating and rehabilitating of diseases, such as distance medicine, known as telemedicine. With the participation of an interdisciplinary group of researchers from Universidad del Valle and health professionals, a pilot project was established to test a teleoperated care system with a prototype designed for the rehabilitation of patients with mild knee injury in the of public health network ESE Ladera in Cali, Colombia, to provide physical rehabilitation services from the urban health center to patients living in rural areas of Cali. In order to comprehensively evaluate the functioning of this teleoperated physical rehabilitation system comprenhensively, an information system (IS) was designed that includes a set of indicators that assess the health care system from a mechanical, economic, clinical and social points of view.

Keywords: telemedicine; teleoperated rehabilitation; information system

Desarrollo de un sistema de información para el servicio de atención teleoperado de rehabilitación física, vía Internet. Caso piloto: pacientes con lesiones leves de rodilla que viven en zonas de vulnerabilidad geográfica

Resumen
En los últimos años, se han implementado nuevas tecnologías para el tratamiento y la rehabilitación de enfermedades, como la medicina a distancia, conocida como telemedicina. Con la participación de un grupo interdisciplinario de investigadores de la Universidad del Valle y profesionales de la salud, se estableció un proyecto piloto para probar un sistema de atención teleoperado con un prototipo diseñado para la rehabilitación de pacientes con lesión leve de rodilla, en la red de salud pública ESE Ladera en Cali, Colombia, para proporcionar servicios de rehabilitación física desde el centro de salud urbano a pacientes que viven en áreas rurales de Cali. Con el fin de evaluar de manera integral el funcionamiento de este sistema de rehabilitación física teleoperado, se diseñó un sistema de información (SI) que incluye un conjunto de indicadores que evalúa el sistema de atención de la salud desde un punto de vista mecánico, económico, clínico y social.

Palabras clave: telemedicina; rehabilitación teleoperada; sistema de información.

1. Background

Breakthroughs in telecommunication technologies have allowed the creation of new services, such as telemedicine [1]. Telemedicine is a health service in which information is remotely exchanged between a medical specialist and a

How to cite: Tovar-Cuevas, J.R., Díaz-Mutis, J.D., Quiñones-Mora, G.E., Pabón-Romero, A. and García-Melo, J.I., Development of an information system for teleoperated physical rehab care service via internet. Pilot case: patients with mild knee injury who live in geogr

© The author; licensee Universidad Nacional de Colombia.

patient for the awareness, prevention, diagnosis, and treatment of and rehabilitation from diseases using information and communication technologies that promote access to and opportunity to receive services by populations facing limited supply of and/or access to such services in their geographical area (i.e., the geographically vulnerable population) [2,3]. Remote clinical care has been performed in both teleassisted [4-7] and teleoperated manners [8-11]. The term "teleassisted" refers to a visual or over-the-phone telemonitoring system by which the therapy processes are specified and that works as a guide for treating of the patient [12]. The term "teleoperated" describes a system that allows long-distance human-device interaction to be controlled and operated remotely through a master device [13,14].

Due to the novelty of the telemedicine processes, information systems (ISs) are typically implemented to guarantee the efficiency of the remotely generated information flows during the patient care process. In the health sector, an IS consists of a set of elements that interact with one another to collect, store, manage and transfer a large amount of information obtained from the clinical processes performed in a health center [15]. These systems are a key factor for improving the efficacy of care processes because they provide fast and complete access to information [16].

Different authors have developed ISs for different clinical domains. Teixeira et al. [17] developed a web-based IS for the comprehensive care of hemophilic patients via user-centered engineering processes. Eguskiza A. et al. [18] created a generic methodology for developing ISs for the patient screening process for diabetic retinopathy in the Health Service of Navarro – Osasunbidea Service in Spain. Regarding previous ISs implemented in teleassisted or teleoperated processes, only a few studies are available. Castellano N. et al. [1] designed an IS for telemonitoring patients during transportation in an ambulance, which was coordinated though a portable system implemented by reference hospitals in Spain.

The limited number of studies on ISs implemented for telemedicine processes could be due to the fact that this technology was developed only a few years ago but has become very important in countries with insufficient health coverage for their populations.

Given the benefits of telemedicine for patient health and the importance of well-structured telemedicine systems, this study presents the development of an IS for the web-based teleoperated care of patients with mild knee injuries in geographically vulnerable zones. The aim of this work was to facilitate the construction of a set of technical, clinical, economic and social indicators for the evaluation and follow-up of the teleoperated rehabilitation system.

This report is organized as follows: The materials and methods considered for the development of the IS are described in Section 2. The results of the IS development process are presented in section 3. The methodology and results are discussed in section 4, and finally, conclusions are drawn in section 5.

2. Materials and methods

2.1. Study context

The prototype was developed by an interdisciplinary group formed by two physiotherapists, one industrial designer, one electronics engineer, one systems engineer, one industrial engineer and one statistician. The prototype's mechanical structure and the requirements related to the functionality of the machine to meet the needs of the population with physical disability and poor access to the health system, were defined by the multidisciplinary group as a whole. Then the design methodology was defined focusing on the development of a modular device and an architecture that integrated the required computer, electronic and mechanical.

First of all, the by physiotherapists defined the functional parameters according to the protocols of active and passive therapy in the knee joint. Subsequently, the industrial designer created the interaction with the user, through the hardware-software interfaces, the mechanical engineers participated in the verification and validation of the mechanical structure of the rehabilitation devices and the electronic engineer installed the control structure in the electronic components and conditioned the power system according to the requirements of the hardware components. The systems engineer managed the database, software interfaces; and the computational applications of the distributed system.

The IS was developed to evaluate the process of teleoperated rehabilitation care for patients with mild knee injuries in the physiotherapy sector of the ESE Ladera Health Network in Cali, Colombia. This network consists of ten and six centers distributed in rural and urban zones, respectively [19]. The care process is directed to patients with minor knee injuries because the people living in the rural areas of Cali are frequently affected because of the geographical conditions in these areas and their daily activities.

At ESE Ladera, the rehabilitation process is performed with a teleoperated assistive functional prototype for the knee joint (Fig.1), which is controlled by a computer that adjusts the therapy protocols relating to the speed, strength and position at which the prototype performs the therapeutic routines in two types of movements: passive and active. Because the prototype is multifunctional, the developed IS is applicable to all joints treated by the device (i.e., shoulders, hips, knees and elbows). The prototype addressed in this work is located in a rural center, where the facilities have been adapted to receive patients and perform the therapy with the help of an assistant. In the urban zone, a specialist is in charge of determining the therapy routine for the patient and performing the rehabilitation process. The guidelines to follow in each therapy are defined by the specialist, meeting the requirements of the conventional physical therapy protocols.

2.2. Development of the IS

In developing the IS, the care processes implemented before and during the patient rehabilitation therapy were considered. Flowcharts for the prototype, assistant and specialist roles were used, in addition to the flow chart of the care process previously established by ESE Ladera. The data inputs of the system; the required materials; human and technological capital; technical, mechanical and economic data; and the data outputs of clinical and social information were also determined. These aspects are presented in this section.

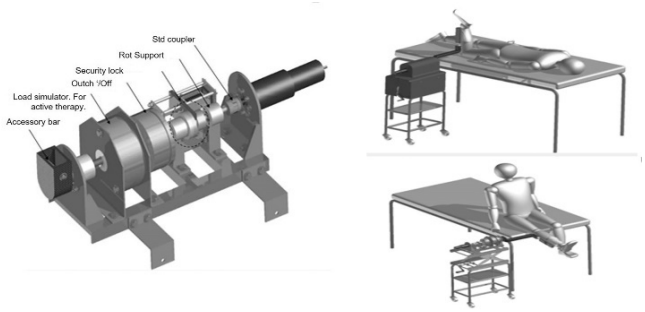


Figure 1. Functional prototype teleoperated assistive device that can be connected to a health care system and its implementation in a pilot case (knee joint rehabilitation).
Source: The authors

2.2.1. Identification of the needs for teleoperated therapy

The design of the IS focused primarily on characterizing the data flowcharts of the processes and roles of the patient, assistant, specialist and assistive device in the care process. Furthermore, because part of the rehabilitation process for each patient is performed with the device, the development of the IS focused on ensuring the safety of the patient during the care process and constantly verifying that the elements involved in the process were working properly. The IS was intended to generate physical and virtual records of possible incidents that could affect the correct operation of the teleoperated process and to report the respective corrections and data associated with the evaluation of the various components of the teleoperated system. The elements, records and components considered in the development of the IS are presented below.

2.2.2. Elements involved in the teleoperated therapy process

The tangible and intangible elements involved in the teleoperated rehabilitation process were as follows:

- Teleoperated assistive device: This prototype was designed by a group of engineers with differente specialties for knee rehabilitation. A computer establishes the duration of the therapy (from 1- 240 min), the speed (from 30 to 150 °/min), maximum extension/maximum flexion (from -10 to 140°) and the duration of the movement change delay (from 0 to 30 s).
- Program or interface: To allow the specialist to follow the rehabilitation protocol, two programs or interfaces were developed: one for the medical specialist and the other for the assistant.
  The assistant interface allows searching the clinical history (patient identification number); reviewing the number of therapy sessions performed by the patient, the type of injury and the affected joint; determining whether the machine and the patient are in optimal condition to start the therapy session; and, in the case of an incident, reporting to the specialist and stopping the operation of the device.
  The specialist interface is a computational medium that allows visualizing the clinical history of the patient who will start the therapy session, entering the physical parameters of the therapy protocol to be performed; and initializing and ending of the therapy in its geographical location (i.e., stopping the assistive device).
  Usability and interoperability were used with the user in order to achieve an intuitive interaction between the user and the system, minimizing the risks due to poor operation of the teleoperation system. This interface has a visual output that records observations made by the assistant about the patient, indicates whether the assistant wishes to accept the therapy protocol and provides information about its development. At the end of this process, the specialist saves the information about the therapy protocol performed, and the patient's clinical history is automatically updated.
  The specialist can make decisions regarding the patient's treatment with the help of the patient information recorded and transferred through the teleoperated equipment and the direct observation of the patient through the video camera. Moreover, there is a permanent communication between the specialist and the assistant. In the same way, the system keeps the information of each care, so it is possible to make a better to keep track of to the patient.
  The two interfaces were created in the web service programming environment of the Microsoft Visual Studio free edition, and the clinical history of the patient was structured in a SQL database. The interface and the web service are located on a remote server.
- Internet: The communication between the two centers occurs through an interface via the internet, which requires a connection of at least 2 MB and a standard computer in each center.

2.2.3. Physical and virtual records

To verify the correct functioning of the elements involved in the teleoperated system, a technical mechanical checklist and an incident recording form were created. A patient satisfaction survey about the teleoperated system was also developed. The relevant variables involved in the assessment of the teleoperated system were identified in a literature review and based on the knowledge of a team of mechanical engineering, industrial design and industrial engineering and statistics experts from Univalle as well as physical therapists from the ESE Ladera. The development and application of these forms are detailed below:

- Technical mechanical operation checklist: This checklist is a tool that functions as a guide for checking the correct operation of each part of the teleoperated device, interfaces and internet. In the rural centers, the assistant should go over the checklist before and during the performance of the therapy. This checklist identified the possible failures of the elements in the teleoperated system.
- Incident recording form: This form is completed by the assistant to notify the specialist about the occurrence of any technical mechanical failure or failure attributed to the patient before and during the performance of the therapy. This form also includes the record of the corrective action performed to resolve the incident, the result obtained after the application of the corrective action and the possibility of continuing the therapy.

- Satisfaction survey: This survey is administered by the assistant to the patient once all therapy sessions are completed. It is intended to determine the acceptance level of the new technology and the level of satisfaction with the teleoperated rehabilitation service received.
- Therapeutic compliance form: This form is filled in by the assistant monitoring the patients and is used to record all patients who have completed the therapy satisfactorily, those who completed it with little improvement and those who did not complete all the assigned therapy sessions.

2.3. Components of the IS

The development of the IS involved the desing of a management indicator system for the comprehensive evaluation of the care system in terms of four components: technical mechanical, clinical, economic and social.

2.3.1. Technical mechanical component

This component includes all aspects related to mechanical, electronic and systems engineering and the industrial design characteristics of the teleoperated system. The information about this component should be used to evaluate the operational characteristics of the teleoperated system from the technical perspective, to monitor the system and to make decisions regarding preventive maintenance. The information for the evaluation of this component is sourced from the technical mechanical operation checklist and the incident recording form.

2.3.2. Clinical or rehabilitation component

This component has two subcomponents:

- Efficacy of intervention. The aim of this evaluation is to compare the initial clinical parameters upon the patient's arrival to the values after performing all therapy sessions assigned in the therapeutic rehabilitation process. The initial physical parameters are used to configure the assistive device, specify the initial therapy, angles of movement and speed levels initially tolerated by the patient and compare them with those achieved by the patient once the teleoperated rehabilitation process is completed.
- Evaluation of patient compliance with the rehabilitation process. To evaluate the therapeutic compliance, the patient care records for the assigned therapy sessions and their level of improvement are used. These forms are filled by the nurse assistant and reflect the numbers of patients who have satisfactorily completed the therapy sessions, those who completed them with little improvement and those who failed to complete all the assigned therapy sessions.

2.3.3. Economic component

To analyze this component, a bibliography search was done to explore costing studies applied to health care systems. Based on the project requirements, the absorption costing system was considered. To this end, the cost of the physical therapy service using the new (teleoperated) system was estimated according to the cost structure of the ESE Ladera Health Network. In this model, the direct costs are related to inputs and material, labor, operations and maintenance costs. The indirect costs are associated with the service provided, which comprise payments for public services and the salaries of the administrative staff.

2.3.4. Social component

This component analyzes the tangible and intangible social benefits obtained by implementing the teleoperated rehabilitation system. This component indicates the extent to which the implementation of the teleoperated system benefits the patients in terms of facilitating access to the service and improving the opportunity for receiving care. It also reflects the level of patient satisfaction with the teleoperated physical rehabilitation process and the level of acceptance of the new technology. The information for evaluating this component is based on the results of the satisfaction survey.

3. Results

Considering the various components, elements and records listed in the methodology, the IS was based on the four primary activities: to review internet connection warnings, execute the program and the operation of the teleoperated machine; register patients in the assistant interface; log into the specialist interface; and initialize teleoperated therapy (Fig. 2).

The first activity establishes the internet communication between the two geographical locations. Then, via interface, the assistant (remotely located) registers the patient with his or her identification number, searches his or her clinical history and informs the specialist (local), about the therapy session that is about to begin. Through the interface, the specialist consults the clinical history of the patient and assigns the therapy routine. This information is updated in the assistant interface, and the assistant then informs the patient about the rehabilitation process that will be performed. Then, the patient decides whether to accept the therapy process. If accepted, the therapy session starts; otherwise, the therapy session is canceled.

In the IS, the communication is synchronous; i.e., the patient and assistant function as transmitters and the specialist as the receiver to coordinate their activities during a therapy session. The processes involved in these activities are specified below.

3.1. Information system

3.1.1. Verify internet connection warnings, program execution and rehabilitation machine operation

In this process, the internet access conditions and interfaces in both centers and the access to the machine in the rural center are verified (Fig. 3). The verification of the elements of the rehabilitation system is performed to ensure proper functioning so that when patient care is provided, all the components are in perfect condition and able to perform the therapy safely.

For this verification, a checklist is used, which asks the assistant to verify the following:

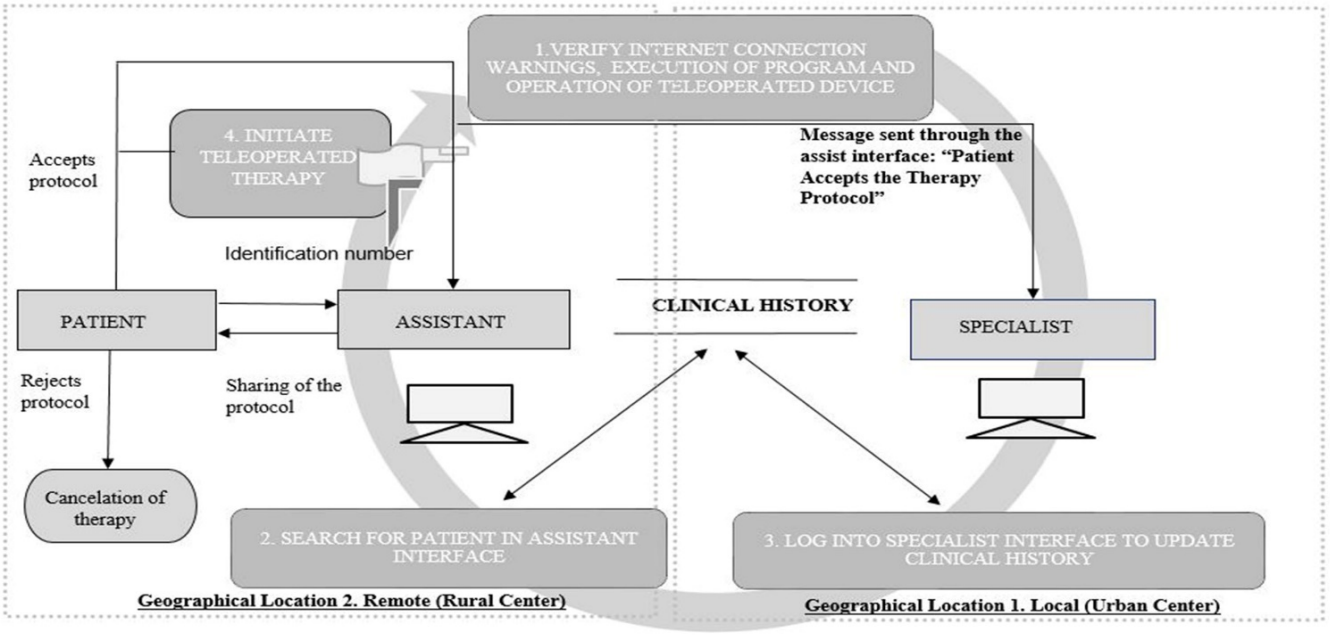


Figure 2. General description of the IS and its components.
Source: The authors

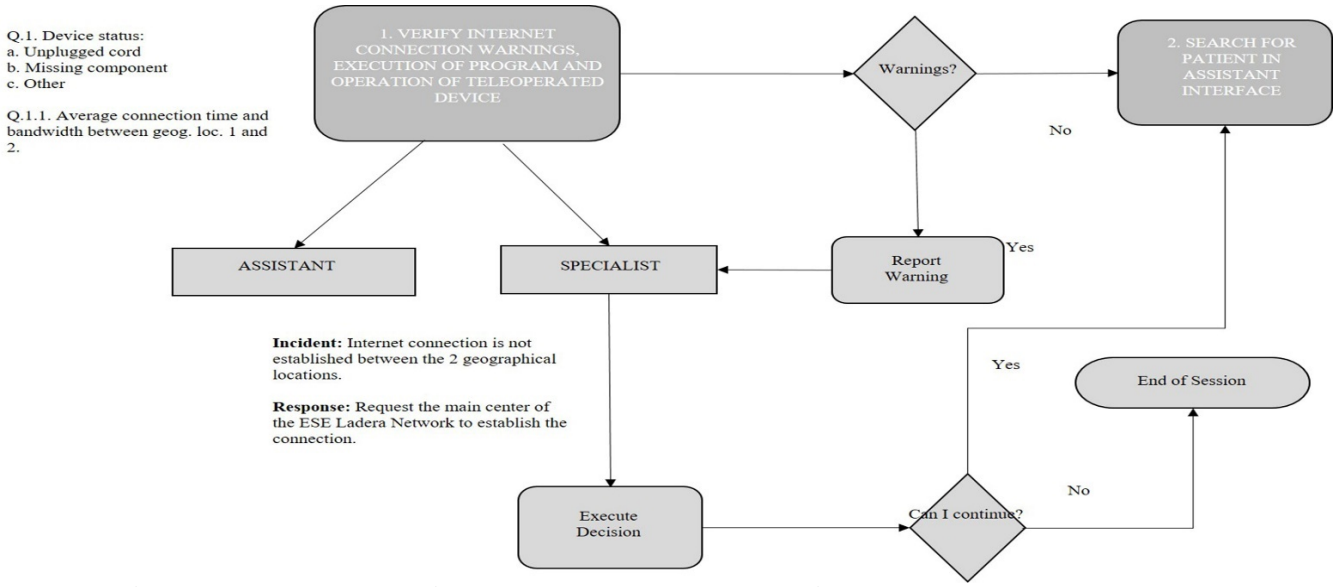


Figure 3. Data flow diagram Level 1: Revision of internet connection warnings, execution of the program and rehabilitation device operating prior to initiation of therapy
Source: The authors

- The status of the machine before starting the therapy: A record should be created reflecting whether the technical assistive device is in good condition and whether any unplugged cord, missing component or other factor could affect proper operation (Question 1); and
- The average internet connection time between the local point and the remote point (Question 1.1).

In the absence of warnings during verification, the registration of the patient is performed through the assistant interface. If warnings are found, the assistant should report them to the specialist through the Incident Reporting Form and include the following information:

- The name of the specialist to whom the incident is being reported;
- The corrective action implemented;

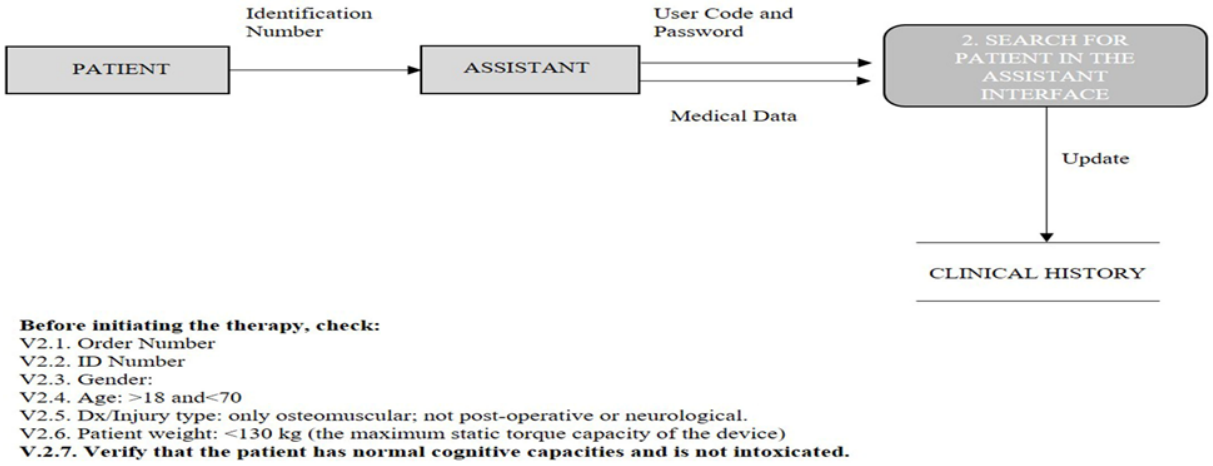


Figure 4. Data flow diagram Level 2: Review the patient record through the assistant interface and update the clinical history
Source: The authors

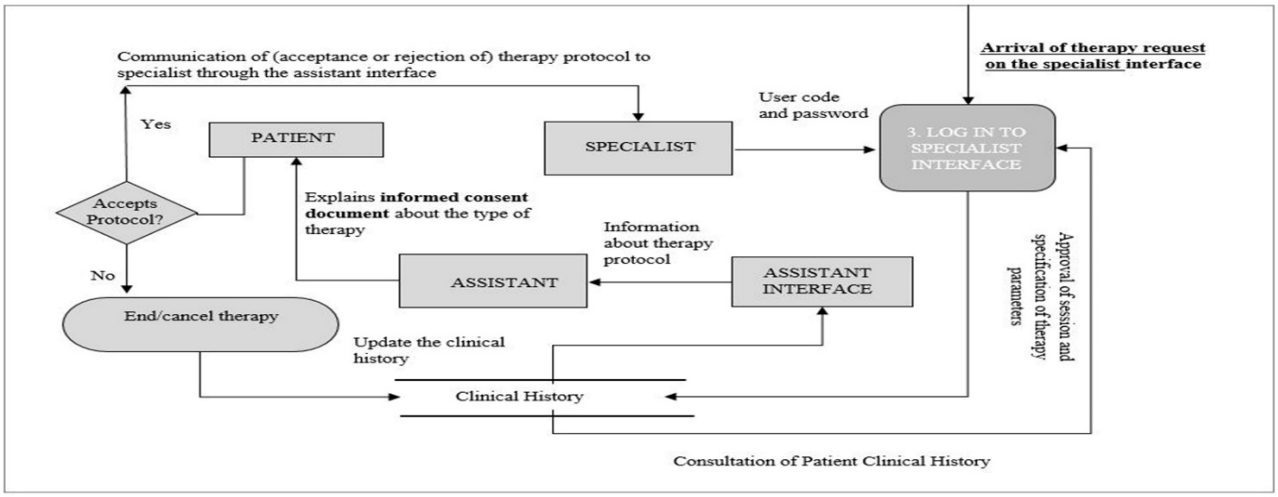


Figure 5. Data flow diagram Level 3: Arrival of therapy request at urban center. The Expert logs into the interface, approves the session and sends the clinical parameters of the therapy
Source: The authors

- Whether the incident was resolved by the corrective action implemented; and
- The possibility of starting the therapy session.

If the corrective measure resolved the problem, the patient is then registered through the assistant interface; otherwise, the session is ended, and the teleoperated therapy will not be performed until the incident is resolved.

3.1.2. Register the patient in the assistant interface

After receiving confirmation of the proper operation of the elements in the teleoperated system, the assistant in the rural center logs in to the assistant interface by entering his or her user code and password and then uses the patient identification number to search for his or her clinical history. The assistant interface displays the patient's data, including his or her name, surname, gender, age, occupation, home address, order number, injury type, and affected side. The assistant must verify the patient's weight because the maximum capacity of the device is 130 kg and evaluate the patient's cognitive state to ensure, among other things, that the patient is not intoxicated. This information is then used to update the clinical history of the patient (Fig. 4).

3.1.3. Log into the specialist interface

After identifying the patient in the rural center, the specialist located in the urban center logs into the specialist interface entering his or her user code and password. The patient's clinical data recorded in the rural center are automatically downloaded into the specialist´s interface environment. The specialist reviews the clinical history of the patient, the number of therapy sessions performed, and the treated injury or pathology. Once this review is complete, the specialist approves or rejects the therapy session, depending on the patient's injury because not all pathologies can be treated remotely. Next, the specialist updates the clinical parameters used in the current session (i.e., the movement,

speed, position, strength and number of series).

Through the interface, the assistant reviews the therapy protocol assigned by the specialist and proceeds to explain the type of therapy to be performed to the patient. If the patient is willing to accept this therapy, he or she must sign the legal informed consent document. If the patient does not accept the therapy, the therapy session is ended, the clinical history is updated, and the patient is referred for consultation regarding conventional therapy (Fig. 5).

When the patient accepts the teleoperated therapy protocol, the assistant notifies the specialist via the interface.

3.1.4. Initiate therapy with assistive device

After the teleoperated therapy is accepted by the patient, the assistant follows the machine initialization protocol (Fig. 6) and checks the operational conditions with the help of the checklist, answering the following questions:

- ¿Was the initialization protocol followed? (Question 2)
- ¿Are the sensors operative? (Question 3)
- In the case of sensor failure, ¿which sensor is inoperative? (Question 3.1)
- In the case of sensor failure, ¿is the safety system responding? (Question 4)
- ¿Are the motors working? (Question 5)
- In the case of motor failure, ¿is the safety system responding? (Question 5.1)

If problems arise with the initialization protocol or initial auto diagnostic, the assistant should check to determine whether the device stops moving and whether the safety system is activated (Question 6.2). Additionally, they should verify that the device sounds the safety alarm and that the error is reported on the screen (Question 8).

Next, the assistant should complete the incident form by recording the type of incident, the name of the specialist to whom it is being reported, the corrective action, and whether the problem was resolved.

After implementing the corrective action and following the initialization protocol, the assistant should check the following: If the initialization protocol was followed, did the device return to its neutral position? (Question 6).

Through the interface, the specialist sends the therapy protocol, and the assistant, through the respective interface, then verifies and transfers the clinical parameters to the device. Finally, the assistant should confirm the following: Was communication established between the device and the computer? (Question 7) That is, are the therapy parameters shown on the machine's screen and are they correct? (Question 10).

One last activity that should be performed by the assistant before starting the therapy session is to verify the functioning of the therapy mode depending on the protocol established by the specialist. Additionally, regarding the activation of the passive therapy mode, the following questions should be answered: Is the motor engaged and the load simulator disengaged? (Question 11) Upon activating the active therapy mode, is the motor disengaged and the load simulator engaged? (Question 11.1)(Fig.7).

At this point, the assistive device is ready and in optimal condition to start operating. The patient has accepted the therapy protocol, and the assistant is ready to start the therapy session once the initialization order issued by the specialist arrives (Question 11.2). The assistive device performs the initial specification or evaluation to establish the range of motion, speed and force tolerated by the patient, and the rehabilitation process begins. These specifications are recorded in the patient's clinical history.

During the execution of the active or passive phase, any of the following incidents may occur (Fig. 8):

- Prolonged internet outage;
- Power outage;
- Patient sickness;
- Sensor failure;
- Actuator failure;
- Device–computer communication failure; or
- Motor failure.

In any of these cases, the assistant should report the incident to the specialist and verify whether the machine returns to its neutral position (Question 20).

With the information obtained from each of the activity flowcharts in the IS, a set of indicators for with the comprehensive evaluation of the teleoperated rehabilitation system could be developed.

3.2. Indicators

According to the information from the checklist, incident form and various clinical records, a set of indicators showed in the Table 1, was identified to evaluate the components of the teleoperated system (see Table 1).

4. Discussion

Given the increasing use of modern technologies, such as telemedicine, in various clinical processes, the implementation of ISs has become necessary to generate, store and transfer the large amounts of information generated during these processes. Thus, it is important for these ISs to be properly designed and modeled. An IS for care processes should feature user-centered design to improve the effectiveness of the processes and provide quality health care services while ensuring the safety of the user.

Proper IS design is relevant because it facilitates better control and execution of the clinical care process, helps to identify human or technical error and the excessive use of resources, and contributes to improving the follow-up of patients' therapeutic processes. In this study, an IS was designed in cooperation with a multidisciplinary team of experts to evaluate the viability of implementing a small-scale teleoperated care system to benefit users in need of physical rehabilitation care who live in zones where accessing health services is difficult.

It is important to emphasize that the IS can be used as input for the evaluation of the clinical processes. Another advantage is that the developed IS is applicable to all joints treated by the device (i.e., shoulders, hips, knees and elbows). Therefore, for subsequent studies during the implementation phase of the teleoperated device in its various modes, the IS could be used with few changes. One of the limiting factors for the efficient use of the developed IS may be the level of compatibility of the assistant and specialist with both the teleoperated assistive device and the interface; however, clear instructions have been developed for the users of this system.

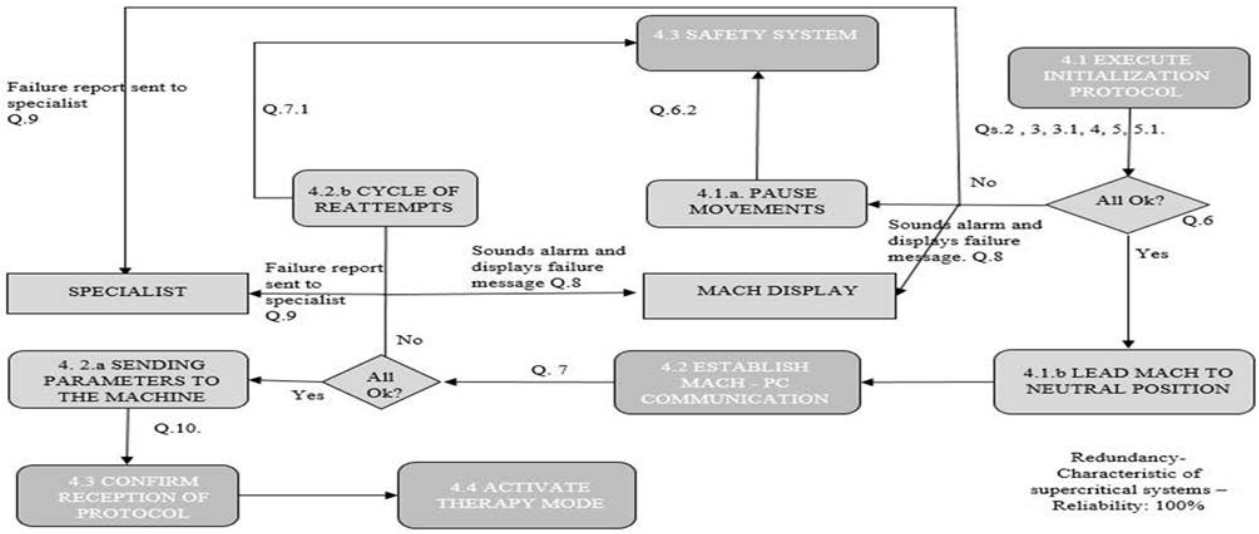


Figure 6. Data flow diagram Level 4A: Execution of initialization protocol of assist device (MACH), transmission clinical parameters and receipt of protocol.
Source: The authors

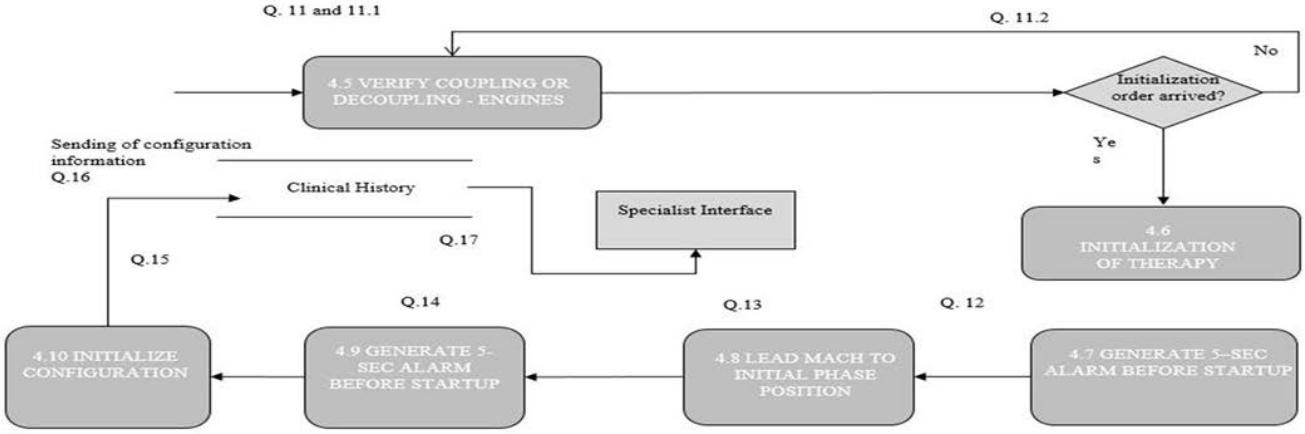


Figure 7. Data flow diagram Level 4B: Initialization of teleoperated therapy and execution of configuration (initial physical parameters tolerated by the patient).
Source: The authors

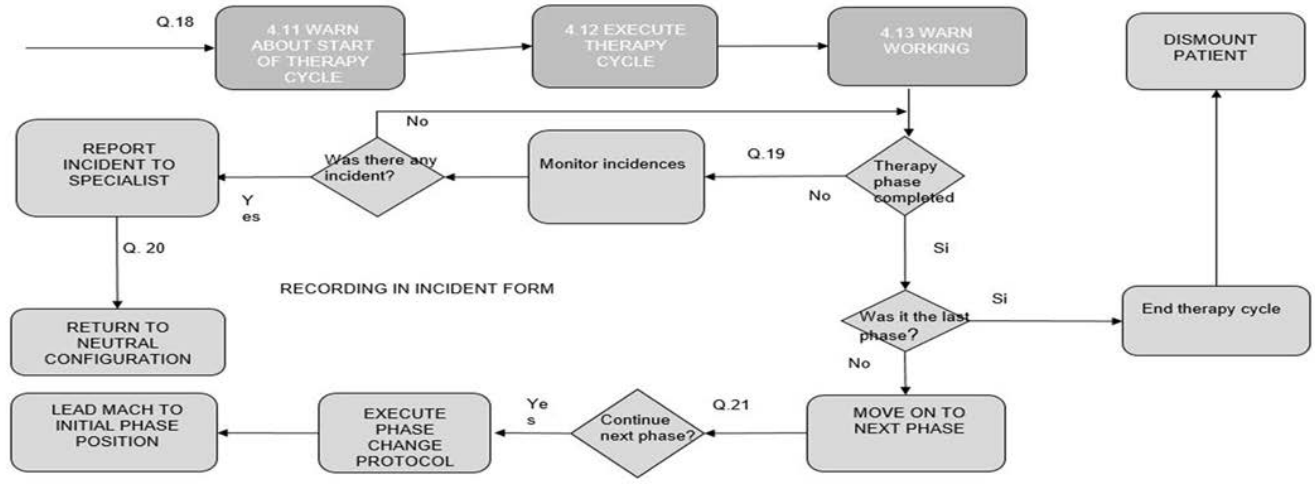


Figure 8. Data flow diagram Level 4C: Execution of first therapy cycle (active or passive) and monitoring of incidents during therapy session.
Source: The authors

Table 1.
Management indicators of the teleoperated physical rehabilitation care system.

Technical mechanical indicators	Economic indicators	Clinical indicators	Social indicators
Number of times when the initialization protocol is followed successfully	Operational cost of the machine for each therapy session	Opportunity for the assignment of teleoperated therapy	Improved access to physical therapy services by users
Rates of cancellation of therapy sessions due to technical mechanical failures (e.g., internet outage)	Direct labor costs	Number of teleoperated physical therapy sessions performed	Opportunity to provide the service
Number of times that the safety system responds to startup or communication failure	Cost of materials and inputs	Rate of cancellation of physical therapy sessions attributed to the patient (e.g., patient gets sick)	Patients satisfied with the local conditions of the service
Number of times when the protocol is successfully read by the device	Cost of equipment for each physical therapy session	Improvement in clinical parameters of functionality/efficacy indicators (i.e., muscle strength, and flexibility)	Patients satisfied with the information provided before the start of the therapy
Number of times that active therapy is correctly activated	Cost of equipment maintenance for each physical therapy session	Compliance with the therapy process and improvement	Patients satisfied with the attentiveness
Number of times that passive therapy is correctly activated	Operational cost of the network data usage for therapy session		Patients satisfied with the treatment
Number of times when the device returns to its neutral position in the case of an incident	Administrative expenses for each physical therapy session		Acceptance level of the new physical rehabilitation technology
Management and solution rate of technical mechanical incidents			Overall satisfaction with the teleoperated physical rehabilitation service
Hours of device use in the month			

Source: The authors

The results of this evaluation can serve as the basis for implementing this system in other contexts in Colombia where geographical vulnerability and economic conditions also pose obstacles to accessing physical rehabilitation services. These contexts require examination of the setup conditions of the assistive device and the conditions of the internet connection and the interface. If acceptable working conditions can be achieved, variations would not substantially affect the model of clinical processes considered for the design of the IS or the capacity and efficiency of information management.

5. Conclusions

A web-based IS was developed to model the care processes of patients with mild knee injuries provided through a teleoperated system and to generate information for the comprehensive evaluation of this system. The designed IS allows the assistant and specialist to perform the patient care process more efficiently while evaluating the operation of the elements involved in the teleoperated system and managing the information in a controlled manner for each therapy session. Because the two centers communicate through the interface and internet, ESE Ladera can take advantage of time and cost savings and provide benefits for patients who live in areas in which accessing physical rehabilitation processes is difficult. The information provided by the IS through the forms implemented in the data flow was used to create indicators for the evaluation of the technical mechanical, clinical and social components of the teleoperated system. Based on this study, it can be concluded that the initial design of ISs for implementation in the health sector is very complex, but when ISs are developed with the appropriate focus, they can improve the quality of the processes and, thereby, increase their extension and usability in other clinical scenarios.

References

[1] Castellano, N., Gazquez, J., García, R., Gracia, A., Fernandez, M. and Manzano, F., Design of a real-time emergency telemedicine system for remote medical diagnosis. Biosystems engineering, 38, pp. 23-32, 2015. DOI: 10.1016/j.biosystemseng.2015.03.017

[2] World Health Organization., Telemedicine: opportunities and developments in Member States: report on the second global survey on eHealth, Switzerland, 2010, 94 P.

[3] Brooks, N., Telemedicine is here. World Neurosurgery, 95, pp. 603-604, 2016. DOI: 10.1016/j.wneu.2016.02.113

[4] Masiero, S., Celia, A., Rosati, G. and Armani, M., Robotic-assisted rehabilitation of the upper limb after acute stroke. Archives of Physical Medicine and Rehabilitation, 88(2), pp. 142-149, 2016. DOI: 10.1016/j.apmr.2006.10.032

[5] Ueki, S., Kawasaki, H., Ito, S., Nishimoto, Y., Abe, M., Aoki, T., Ishigure, Y., Ojika, T. and Mouri, T. Development of a Hand-Assist Robot with Multi-Degrees-of-Freedom for Rehabilitation Therapy. IEEE/ASME Transactions on Mechatronics, 17(1), pp. 136-146, 2012. DOI: 10.1109/TMECH.2010.2090353

[6] Lanini, J., Tsuji, T., Wolf, P., Riener, R. and Novak D. Teleoperation of two six-degree-of-freedom arm rehabilitation exoskeletons, IEEE International Conference on Rehabilitation Robotics, pp. 514-519, 2015. DOI: 10.1109/ICORR.2015.7281251

[7] Carpinella, I., Cattaneo, D., Abuarqub, S. and Ferrarin, M. Robot-based rehabilitation of the upper limbs in multiple sclerosis: Feasibility and preliminary results, Journal of Rehabilitation Medicine, 41(12), pp. 966-970, 2009. DOI: 10.2340/16501977-0401.

[8] Jackson, J., Ely, E., Morey, M., Anderson, V., Denne, L., Clune, J., Siebert, C., Archer, K., Torres, R., Janz, D., Schiro, E., Jones, J., Shintani, A., Levine, B., Pun, B., Thompson, J., Brummel, N. and Hoenig H. Cognitive and Physical Rehabilitation of intensive care unit Survivors: Results of the RETURN randomized, controlled pilot investigation, Critical Care Medicine 40(4), pp. 1088-1097, 2012. DOI: 10.1097/CCM.0b013e3182373115.

[9] Odole, A. and Ojo, O. Is Telephysiotherapy an Option for Improved Quality of Life in Patients with Osteoarthritis of the Knee? International Journal of Telemedicine and Applications, vol. 2014, pp. 1-9, 2014. DOI: 10.1155/2014/903816

[10] Russell, T., Blumke, R., Richardson, B. and Truter, P., Telerehabilitation mediated physiotherapy assessment of ankle disorders, physiotherapy. Research International, 15(3), pp.167-175, 2010. DOI: 10.1002/pri.471.

[11] Moffet, H., Tousignant, M., Nadeau, S., Mérette, C., Boissy, P., Corriveau, H., Marquis, F., Cabana, F., Ranger, P., Belzile, E. and Dimentberg, R., In-home telerehabilitation compared with face-to-face rehabilitation after total knee arthroplasty: A non inferiority randomized controlled trial, The Journal of Bone & Joint Surgery 97(14), pp.1129-1141, 2015. DOI: 10.2106/JBJS.N.01066.

[12] Zampolini, M., Todeschini, E., Bernabeu, M., Hermens, H., Ilsbroukx, S., Macellari, V., Magni, R., Rogante, M., Scattareggia, S., Vollenbroek, M. and Giacomozzi, C., Tele-rehabilitation: present and future, Ann Ist Super Sanità [online]. 44(2), pp.125-134, 2008. [date of reference July 27th of 2017]. Available at: http://www.iss.it/publ/anna/2008/2/442125.pdf

[13] Farkhatdinov, L. and Ryu, J., Teleoperation of multi-robot and multi-property systems, The IEEE International Conference on Industrial informatics, pp. 1453-1458, 2008. DOI: 10.1109/INDIN.2008.4618333

[14] Kifle, M., Mbarika, V. and Datta, P., Telemedicine in sub-Saharan Africa: the case of teleophthalmology and eye care in Ethiopia, Journal of the American Society for Information Science and Technology 57(10), pp. 1383-1393, 2006. DOI: 10.1002/asi.20448

[15] Sirintrapun, S. and Artz, D., Health Information Systems, Clinics in Laboratory Medicine, 36(1), pp. 133-152, 2016. DOI: 10.1016/j.cll.2015.09.012.

[16] Lenz, R. and Kuhn, K., Toward a continuous evolution and adaptation of information systems in healthcare, International Journal Medical Informatics, 73(1), pp. 75-89, 2004. DOI: 10.1016/j.ijmedinf.2003.09.003

[17] Teixeira, L., Ferreira, C. and Sousa, B., User-centered requirements engineering in health information systems: A study in the hemophilia field, Computer Methods and Programs in Biomedicine, 106(3), pp.160-174, 2012. DOI: 10.1016/j.cmpb.2010.10.007

[18] Eguzkiza, A., Trigo, J., Martínez, M., Serrano, L. and Andonegui, J., Formalize clinical processes into electronic health information systems: Modelling a screening service for diabetic retinopathy, Journal of Biomedical Informatics, 56, pp.112-126, 2015. DOI: 10.1016/j.jbi.2015.05.017

[19] Red de Salud de Ladera. Area of influence [Online], [consulted, February 07th of 2005]. Available at: http://www.saludladera.gov.co/nosotros/area-de-influencia

J.R. Tovar-Cuevas, is PhD degree in Statistic in 2011 from the Universidade Estadual De Campinas, Campinas, Brazil. He worked as a statistician for CIDEIM research center and worked in teaching activities at universities such as Pontificia Universidad Javeriana, (Colombia), Universidad Católica de Chile (Chile), Universidade Estadual De Campinas (Brazil) and since 2014 for the Universidad Del Valle (Cali, Colombia). Currently, he is a full time professor in the Statistic School of the Universidad del Valle, Colombia. His research interests include: Bayesian Statistics, rehabilitation sciences, psychometric measurement and statistics applied to the health sciences.
ORCID: 0000-0003-0432-4144

J.D. Diaz-Mutis, received the BSc. in Statistic in 2017 from the Universidad Del Valle, Cali, Colombia. He is currently a statistical consultant and works with researchers from the Pontificia Universidad Javeriana Cali and the Universidad del Valle, Cali, Colombia.
ORCID: 0000-0002-3977-4092

G.E. Quiñones-Mora, received the BSc. in Statistic in 2008 from the Universidad del Valle, Cali, Colombia. She worked as research assistant in the project that allows obtain the data to develop the information system.
ORCID: 0000-0001-6780-8416

A. Pabón-Romero, is MSc. degree in Engineering in 2007, from the Universidad del Valle de Colombia. Cali, Colombia. She works as financial consultant and currently, she is a full professor in the Industrial Engineering School, Universidad del Valle. Her research interests include: financial risk analysis, cost analysis, real options valuations, technology valuations.
ORCID: 0000-0001-8212-4645

J.I. García Melo, is PhD degree in Mechanical Engineering in 2011 from the Universidade De São Paulo, São Paulo, Brazil. From 1999 to 2017, he worked in teaching, administrator and researcher activities in the Universidad del Valle, Cali, Colombia. Currently, he is a full professor in the Mechanical School of the Universidad Del Valle. His research interests include: Bioengineering, modeling and analysis of products and systems, system integration and design of biomechanical devices.
ORCID: 0000-0003-1672-7768



UNIVERSIDAD NACIONAL DE COLOMBIA

SEDE MEDELLÍN

FACULTAD DE MINAS

Área Curricular de Ingeniería Mecánica

Oferta de Posgrados

Maestría en Ingeniería - Ingeniería Mecánica

Mayor información:

E-mail: acmecanica_med@unal.edu.co
Teléfono: (57-4) 4259262

UNIVERSIDAD NACIONAL DE COLOMBIA
SEDE MEDELLÍN
FACULTAD DE MINAS



DYNA
http://dyna.medellin.unal.edu.co/

Design and implementation of a photolithography system to fabricate microdevices from thin films

Jhon Jairo Realpe [a], Gilberto Bolaños-Pantoja [a] & Juan Fernando Florez [b]

[a] *Facultad de Ciencias Naturales Exactas y de la Educación, Universidad del Cauca, Popayán, Colombia. jhrealpe@unicauca.edu.co, gbolanos@unicauca.edu.co*
[b] *Facultad de Ingeniería Electrónica y Telecomunicaciones, Universidad del Cauca, Popayán, Colombia. jflorez@unicauca.edu.co*

Received: November 14th, 2017. Received in revised form: February 12th, 2018. Accepted: March 15th, 2018.

Abstract
This article presents the design and implementation of a photolithography system to manufacture microdevices based on thin films. The system works with ultraviolet (UV) source of 380nm and allows to obtain 10-200 µm microstructures. The implementation was made with the product design and development process, where the technical specifications, generation, selection and proof of concepts of the system equipment modules were determined. A spincoater with an operating range of 500-6000 rpm and UV radiation source, based on LEDs, with ranges in power of 1-20mW/cm^2 and time of exposure 1-60s, were implemented. With optical microscopy and digital image processing, it was determined that the percentage relative error in their areas is less than 4% and the variability in their widths is less than two times the standard deviation.

Keywords: product design; photolithography; microdevice; thin films.

Diseño e implementación de un sistema de fotolitografía para fabricar microdispositivos a partir de películas delgadas

Resumen
Este artículo presenta el diseño e implementación de un sistema de fotolitografía para fabricar microdispositivos basados en películas delgadas. El sistema trabaja con una fuente ultravioleta (UV) de 380nm y permite obtener microestructuras de 10-200 µm. La implementación se hizo con el proceso de diseño y desarrollo de productos, donde se determinó las especificaciones técnicas, generación, selección y prueba de conceptos de los módulos de equipo del sistema. Se implementó un spincoater con rango de operación de 500-6000 rpm y una fuente de radiación UV basada en LEDs UV, con potencia de radiación de 1-20mW/cm^2 y tiempo de exposición de 1-60s. Se obtuvo micropuentes (mPs) de 30-105µm sobre películas delgadas de cobre. Con microscopía óptica y procesamiento digital de imágenes, se determinó que el error relativo porcentual en sus áreas es menor al 4% y la variabilidad en sus anchos es menor a dos veces la desviación estándar.

Palabras clave: diseño de productos; fotolitografía; microdispositivo; películas delgadas.

1. Introducción

La técnica de fotolitografía ha contribuido al desarrollo de dispositivos con base en los semiconductores, en las últimas cuatro décadas han alcanzado un alto nivel de sofisticación, permitiendo el desarrollo de la micro/nano electrónica, MEMs (Sistemas microelectromecánicos) NEMs (Sistemas nanoelectromecánicos), microfluídica, entre otros [1-3].

Las primeras técnicas de fabricación de circuitos integrados por la baja complejidad y costo son por contacto y proximidad con radiación UV, obteniéndose resoluciones de 1-10 µm. Pero se reemplazarían debido a las exigencias en la industria de los semiconductores [4]. Luego surge la técnica por proyección mejorando la resolución de los patrones impresos hasta el orden de los nanómetros, calidad de los micro/nano dispositivos y alta tasa de producción.

Mejoras en las fuentes de radiación, sistemas de lentes y

How to cite: Realpe, J.J., Bolaños-Pantoja, G. and Florez, J.F., Diseño e implementación de un sistema de fotolitografía para fabricar microdispositivos a partir de películas delgadas. DYNA, 85(205), pp. 294-301, June, 2018.

© The author; licensee Universidad Nacional de Colombia.

resinas fotosensibles, se han dado por el esfuerzo de la industria, centros de investigación y la academia, con el fin de seguir lo planteado por la ley de Moore, donde el número de transistores en un circuito integrado se duplicará cada dos años [2].

Reducción en el tamaño de unidades lógicas (transistor) en un circuito integrado ha representado desafíos tecnológicos y económicos [4-7]. A cada reducción se le ha denominado "nodo" y está relacionado con la dimensión crítica (CD), parámetro que mide la calidad de las estructuras fabricadas a partir de su grosor, rugosidad y altura y determina el límite en la resolución de los sistemas de fotolitografía [5,6]. En los últimos 10 años se han desarrollado nodos que van desde los 45-10nm y se prevé que en el 2020 se alcanzará el nodo de 5nm [6]. De ahí la importancia de controlar todos estos parámetros que son operacionalmente imprescindibles. Por lo tanto, la producción de un nuevo nodo, implica cambios en instrumentación, materiales e infraestructura ocasionando un aumento en los costos de producción [6,8].

La instrumentación de mayor costo en los sistemas de fotolitografía son las fuentes de radiación, sofisticados arreglos de lentes, sistema electromecánicos para alinear la fotomáscara, equipos de esparcimiento de fotoresina de alta precisión, sistemas de metrología para inspeccionar las etapas de producción y la infraestructura donde se controla la temperatura, humedad, flujo y cantidad de partículas en el aire [3].

Por tal razón, el acceso a sistemas de fotolitografía e infraestructura a pequeños y medianos laboratorios de investigación es limitado debido a su elevado costo, imposibilitando la investigación en las disciplinas de micro/nano fabricación y otras áreas de ingeniería [9]. Para abordar este problema se ha desarrollado instrumentación adaptable a los recursos económicos e infraestructura como son fuentes de radiación basadas en LEDs UV [9,10] y equipos de esparcimiento de fotoresina [11,12]. Sin embargo, a la fecha no se han reportado sistemas de fotolitografía que integren esta instrumentación y dado que la industria de los semiconductores y centros de investigación continúan desarrollando nuevas técnicas de fotolitografía, es necesario acceder a instrumentación especializada y así contribuir al avance de la próxima generación de micro/nano dispositivos.

En este artículo se presenta el diseño e implementación de un sistema de fotolitografía, siguiendo el proceso de diseño y desarrollo de productos donde se identifica materia prima y módulos de equipo que conforman el sistema, se determina las condiciones óptimas de fabricación de microdispositivos, se realiza caracterización con microscopía óptica para determinar la calidad de los microdispositivos, se muestran los resultados, discusión y conclusiones.

2. Técnica de fotolitografía

Consiste en transferir un patrón a la superficie de un sustrato o película delgada, a través del proceso: 1) limpieza del sustrato para eliminar compuestos orgánicos y partículas de polvo. 2) Esparcimiento de fotoresina sensible a la radiación UV en la superficie del sustrato. 3) Calentamiento suave, para mejorar la adhesión de la fotoresina en la superficie del sustrato. 4) Irradiar con UV la superficie de la capa de fotoresina sobre el sustrato a través

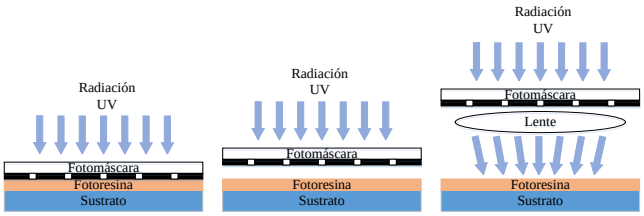


Figura 1. Técnicas de exposición UV. a) Contacto. b) proximidad. c) proyección.
Fuente: Modificado de [4].

de una fotomáscara con los patrones a imprimir mediante las técnicas: por contacto, donde la fotomáscara se presiona sobre sustrato, proximidad donde la fotomáscara está separada del sustrato o proyección donde se usa un sistema de lentes (Fig. 1). 5) Revelado donde se elimina las regiones que fueron irradiadas con UV. 6) Grabado de la superficie del sustrato en las regiones donde el material fotorresistente fue removido con el proceso de revelado, por medio de técnicas húmedas (solución ácida) o secas (plasma). 7) Remoción de fotoresina residual de la superficie del sustrato por técnicas húmedas o secas. 8) Inspección de la calidad de los patrones grabados con alguna técnica de microscopia [4,13].

3. Diseño e implementación del sistema de fotolitografía

Para diseñar e implementar el sistema de fotolitografía se sigue el proceso diseño y desarrollo de productos, ampliamente usado en el sector industrial para la fabricación de nuevos productos, que ha implementado distintas herramientas que dan seguimiento continuo a las actividades que realiza una empresa en el proceso de creación o mejora de un producto [14], a través de tres funciones: mercadotecnia, diseño y manufactura, integradas a la cadena de producción, que van desde la planeación del producto hasta su fabricación e inclusión en el mercado [14].

Se resalta la etapa diseño, ya que demanda más coordinación entre funciones y actividades, donde se usan recursos cognitivos como la solución de problemas, toma de decisiones, creatividad, máxima optimización de materia prima y tiempo [15]. Permitiendo desarrollar un artefacto, sistema o servicio, con características técnicas, funcionales y estéticas, que cumplen las necesidades planteadas por el cliente. Los recursos se organizan en actividades que facilitan acciones a ejecutar por el diseñador (Fig. 2).

Las actividades de desarrollo de concepto usadas para la implementación del sistema de fotolitografía son:

3.1. Identificar necesidades

El objetivo de esta fase es recopilar y determinar cuáles son las necesidades del cliente respecto al sistema de fotolitografía (Tabla 1).

3.2. Establecer especificaciones objetivo

Las necesidades identificadas se transforman en enunciados con un valor y métrica (valor numérico y

unidades respectivas) [16], para identificar las especificaciones técnicas (Tabla 2). La importancia relativa se define en función de las necesidades recogidas en la generación de la idea (donde 1 es el valor de mayor relevancia y 5 el de menor).

Es fundamental analizar el error en las dimensiones de las microdispositivos, es decir, cuanto pueden variar propiedades como la rugosidad y homogeneidad, sin que afecten sus propiedades eléctricas y mecánicas. Por lo que se adoptó el criterio sugerido por la ITRS (International Technology Roadmap Semiconductor) para controlar la calidad de los circuitos integrados y la repetibilidad del proceso de fabricación [4,17,18].

3.3. Selección del microdispositivo caso de estudio

Se seleccionó como dispositivo caso de estudio un mP, usado en el estudio de propiedades de transporte eléctrico (Fig. 3) [19,20].

3.4. Generación de conceptos

Se utilizó el diagrama de caja negra (Fig. 4) [14], que opera con flujos de material, energía y señales, para identificar problemas y subproblemas (Fig. 5). Las líneas finas y continuas denotan la transferencia y conversión de energía, las gruesas y continúas el flujo y transformación del material y la línea discontinua denota las señales de control y realimentación. Se enfocó en los subproblemas de esparcir fotoresina e irradiar con UV por su complejidad.

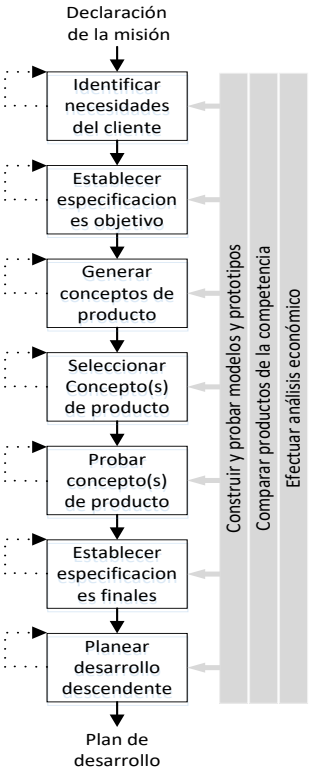


Figura. 2. Actividades del desarrollo de concepto.
Fuente: Modificado de [14].

Tabla 1.
Necesidades que debe satisfacer el sistema de fotolitografía.

Núm.	Producto	Necesidad	Importancia relativa
1	Sistema de fotolitografía	Repetibilidad	1
2	Sistema de fotolitografía	A partir de películas delgadas	1
3	Sistema de fotolitografía	Microdispositivos a escala micrométrica	1
4	Sistema de fotolitografía	Con base en la técnica de fotolitografía.	1

Fuente: Los autores.

Tabla 2.
Métricas para el sistema de fotolitografía.

Núm. Métrica	Núm. de necesidad	Métrica	Importancia relativa	Unidades
1	1	Error en las dimensiones de las microestructuras de los microdispositivos $< 2\sigma$	1	µm
2	2	Espesor de películas delgadas	1	nm
3	3	Rango dimensión de las microestructuras 10-200	1	µm
4	3, 4	Fotolitografía con fuente de radiación UV con longitud de onda en el rango 365-436	1	nm

Fuente: Los autores.

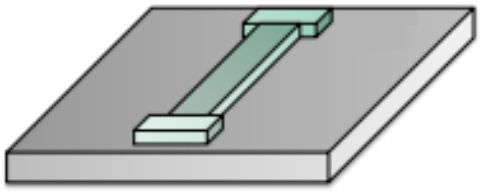


Figura 3. Microdispositivo caso de estudio.
Fuente: Los autores.

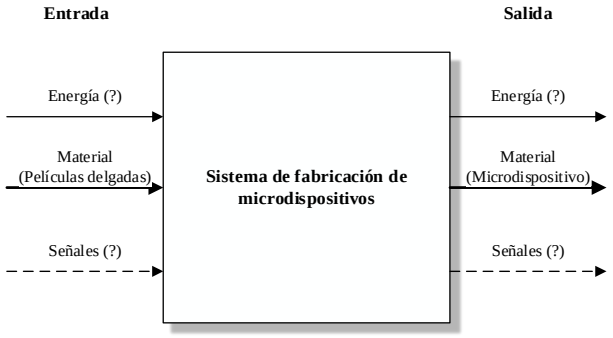


Figura 4. Diagrama de caja negra del sistema de fotolitografía.
Fuente: Los autores.

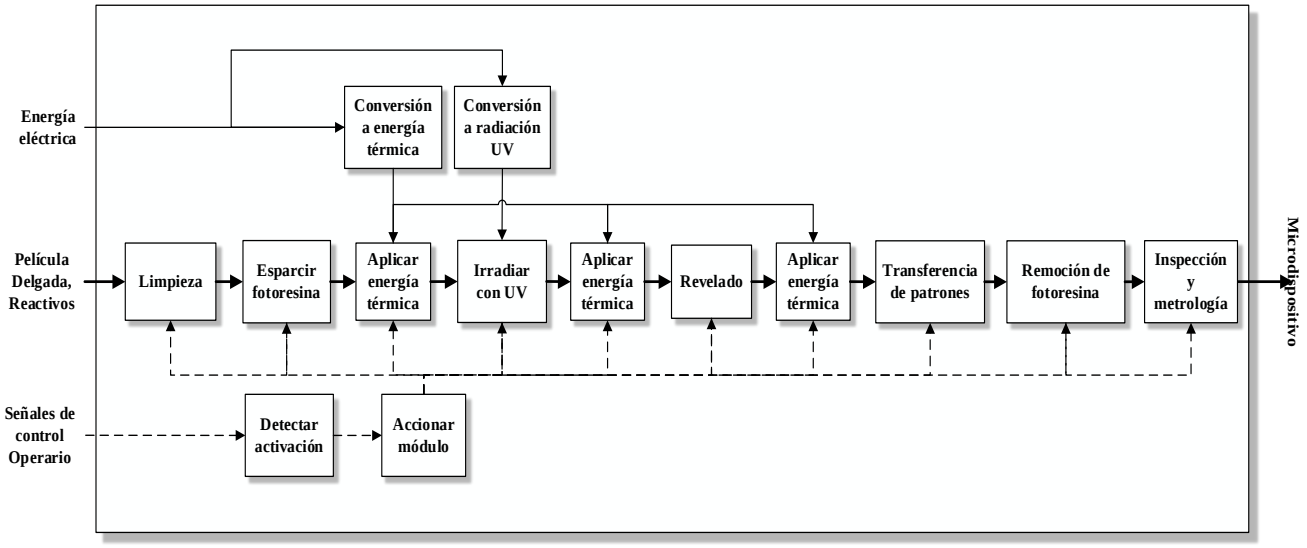


Figura 5. Subproblemas del sistema de fotolitografía.
Fuente: Los autores.

3.5. Selección de conceptos

Para dar la solución más óptima a los subproblemas, se hizo la búsqueda y selección de conceptos mediante la revisión en la literatura, búsqueda y comparación de instrumentación existente en el mercado.

Para el subproblema esparcir fotoresina se plantearon dos conceptos: un spray para depositar la fotoresina en la superficie de la película delgada, este proceso es sencillo de implementar pero el espesor de la capa de fotoresina depositada es variable y no homogéneo [21], afectando la repetibilidad en la fabricación de los microdispositivos.

Otro concepto es el spincoater donde se deposita la fotoresina sobre la película delgada, se hace rotar en el rango 1500-6000 rpm y por fuerza centrífuga esparcirla hasta el borde de la película delgada creando una capa fina y uniforme [2,3]. La fotoresina tiene características definidas, obteniéndose precisión en el espesor en la capa de fotoresina en función de la velocidad de rotación. Así el concepto más apropiado para el subproblema esparcimiento de fotoresina es el spincoater.

Para el subproblema irradiar con UV se plantea tres conceptos: la técnica de radiación por proyección, constituida por un arreglo de lentes, fuente de radiación UV y alineador de fotomáscaras. Actualmente es el sistema más utilizado para la fabricación de micro/nano dispositivos por su versatilidad, rendimiento en la producción y resolución de los patrones impresos [2,3]. Sin embargo los costos de implementación son elevados. La técnica de radiación por proximidad, consiste de una fuente de radiación UV y una fotomáscara separada de la película delgada con la fotoresina, no obstante la calidad y resolución en las microestructuras disminuye por efectos de difracción [2,3]. La técnica de radiación por contacto consiste en una fuente de radiación UV y una fotomáscara en contacto con la fotoresina sobre la película delgada. Se obtiene buena calidad en las microestructuras de los dispositivos ya que los efectos de la difracción son mínimos, la instrumentación no es compleja y los costos de implementación son bajos respecto a las técnicas anteriores [3,4]. Por lo tanto el concepto más apropiado para el subproblema irradiar con UV es la técnica por contacto.

3.6. Prueba e implementación de prototipos

Para el spincoater se diseñó e implementó un control de velocidad PID de un motor DC marca Pololu [22], en el rango de 500-6000 rpm, con error menor al 5% en el control y medición de velocidad y un módulo de potencia para su alimentación. Para el concepto de radiación con UV por contacto (Fuente de radiación UV) se usaron LEDs UV de 380nm con una potencia de radiación de 20mW/cm^2 de la empresa superbrightleds [23]. Se implementó una matriz de 10x10 LEDs y el control de potencia y tiempo de exposición. Cada concepto posee una interfaz de usuario constituido por teclado y pantalla LCD para programar y visualizar los parámetros de operación. El diseño electrónico se realizó en el entorno de desarrollo KiCad, la implementación sobre la plataforma de desarrollo electrónico arduino uno, fabricándose PCBs (Printed Circuit Board) para disponer los componentes electrónicos. Las especificaciones técnicas de los dos equipos se muestran en la Tabla 3. El diseño mecánico de los prototipos se desarrolló en el entorno Solid Edge versión estudiantil y se fabricaron prototipos en lámina y acrílico (Fig. 6).

3.7. Selección de fotoresina y película delgada

Se adquirió un kit de fotolitografía de la empresa Transene, está compuesto por fotoresina positiva (PC800), revelador (PC1800), rinse (PC2800), stripper (PC3800) y tiner (PC4800) [24].

Se utilizaron películas delgadas de cobre crecidas sobre sustrato de silicio por la técnica de sputtering DC [25].

Tabla 3.
Especificaciones técnicas de los módulos de equipo.

Spincoater	Equipo de Radiación UV
Rango de velocidades: 500-6000 rpm	Longitud de onda: 380nm
Error en la medida y control de velocidad menor al 5%.	Rango de potencia de radiación: 1-20mW/cm^2
Rata rampa: 100-1000 rpm/s	Tiempo de exposición: 1-60s

Fuente: Los autores.



(a) (b)

Figura 6. Prototipos finales (a) Spincoater. (b) Fuente de radiación UV.
Fuente: Los autores.

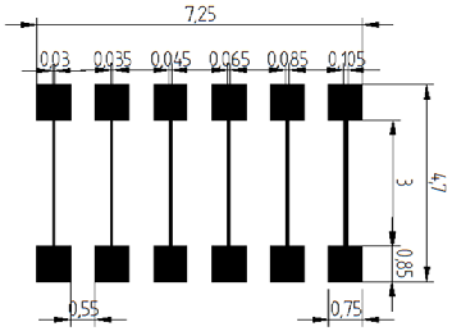


Figura 7. Diseño de la fotomáscara (unidades en mm).
Fuente: Los autores.

3.8. Fabricación de la fotomáscara

Para fabricar la fotomáscara se considera las condiciones: 1) Patrón geométrico un mP en campo claro (el patrón es negro con fondo claro) puesto que la fotoresina es positiva. 2) Que los mPs en la fotomáscara no excedan el área de 10x10 mm^2 ya que las películas delgadas crecidas sobre sustratos de silicio son menores a 10 mm de lado. 3) mPs con distintos anchos. Así se planteó el diseño de una fotomáscara con 6 mPs de 0.30-0.105 mm de ancho, 3 mm de longitud y nodos de 0.75 mm de ancho por 0.85 mm de alto, como contactos eléctricos (Fig. 7). El diseño se realizó con el software L-Edit versión estudiantil y se imprimió sobre acetato con impresión láser de alta resolución (25400dpi), en la empresa CAD/Art Services Inc [26].

3.9. Integración de equipos

El spincoater y la fuente de radiación UV se integraron al sistema de fotolitografía, que se ha denominado SysMicFUV-FB (Fig. 8) y está constituido por: (1) Soplador de aire, (2) Limpiador de ultrasonido, (3) Spincoater, (4) Plancha de calentamiento, (5) Medidor de temperatura, (6) Fuente de radiación UV, (7) Cuatro beaker, (8) Dos tarros de enjuague, (9) Mortero de ágata, (10) Pinzas, (11) Lámpara. Estos se organizan en 7 sistemas: limpieza, esparcimiento de fotoresina, calentamiento, radiación UV, revelado, transferencia de patrones y remoción de fotoresina.

4. Resultados y discusión

Para verificar la repetibilidad en la fabricación de microdispositivos con el sistema SysMicFUV-FB y dar cumplimiento a las especificaciones de diseño, se obtuvieron las condiciones de producción (Tabla 4) a partir de los parámetros sugeridos por el fabricante de la fotoresina [24], lo reportado en la literatura [27,28] y pruebas experimentales. Con lo cual se fabricó cuatro lotes de seis mPs cada uno sobre películas delgadas de cobre usando la fotomáscara de la Fig. 7.

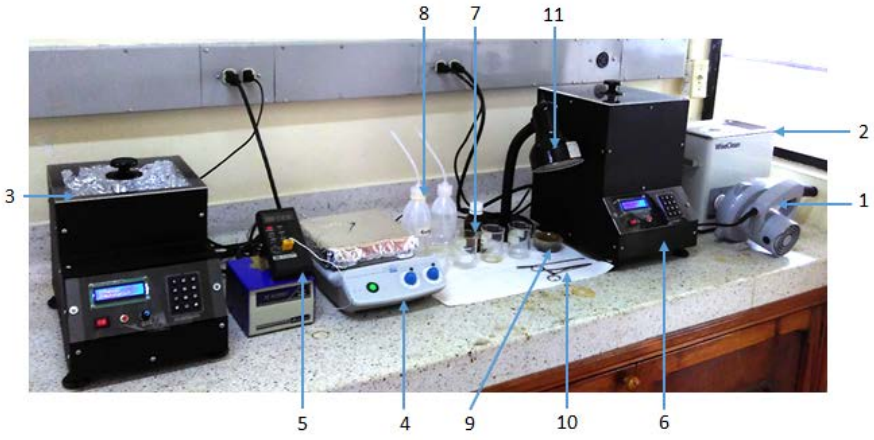


Figura 8. Descripción modular del sistema SysMicFUV-FB.
Fuente: Los autores.

Tabla 4.
Etapas del proceso de fabricación de mPs.

Etapa	Parámetros
Limpieza de película delgada de cobre	Limpiar la película delgada con acetona en ultrasonido por tres minutos a 40°C. Secar humedad con aire comprimido por 20s.
Esparcimiento de la fotoresina	Depositar de 3-5 gotas de fotoresina (PC800) en la película delgada de cobre sujetada al portasustrato del spincoater y programar una rampa de velocidad con: velocidad inicial: 400 rpm, velocidad estabilización: 3000 rpm, tiempo de estabilización: 40s, rampa de subida: 100 rpm/s, rampa de bajada: 100 rpm/s, velocidad final: 0 rpm/s
Calentamiento suave	Poner la película delgada de cobre en plancha de calentamiento a 80 °C por tres minutos. Retirar y dejar enfriar por dos minutos.
Radiación UV	Alinear película delgada sobre la fotomáscara en el sistema de radiación UV e irradiar con una potencia de 20mW/cm^2 y tiempo de exposición de 60s.
Revelado	Colocar la película delgada en el revelador (PC1800) agitando continuamente por 40s. Retirar y enjuagar en rinse (PC2800) por 10s. Lavar con agua destilada por 10s.
Inspección post revelado	Inspeccionar la calidad de los patrones impresos sobre la fotoresina con un microscopio óptico.
Transferencia de patrones	Colocar la película delgada en una solución de percloruro férrico al 0.1gr/mL agitando continuamente por 20s. Retirar y enjuagar con agua destilada por 20s.
Remoción de fotoresina	Colocar la película delgada en acetona agitando continuamente por 30s. Enjuagar con agua destilada por 20s.
Inspección post grabado	Inspeccionar la calidad de las microestructuras con un microscopio óptico.

Fuente: Los autores.

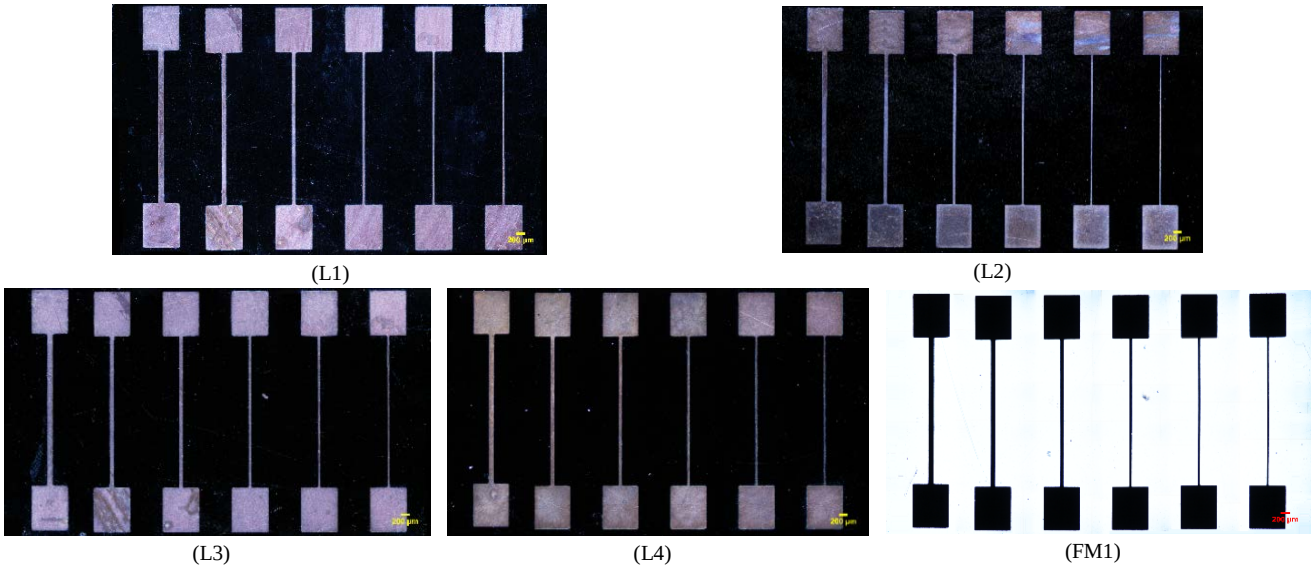


Figura 9. Micrografías de los lotes de mPs y la fotomáscara.
Fuente: Los autores.

4.1. Caracterización de los microdispositivos

La caracterización de los mPs se realizó con un sistema de microscopia óptica constituido por: microscopio óptico marca NIKON 80i, cámara digital marca DS-MV-U2, computador marca Dell, fuente variable de iluminación y el software NIS-Elements F, para configurar los parámetros de la cámara, captura y almacenamiento de las imágenes.

Con el software ImageJ [27] se realizó el procesamiento digital de imágenes determinando el área de las mPs y el ancho siguiendo los pasos:

Paso 1: Reconstrucción digital de la imagen. Se ha etiquetado a los lotes con L1-L4 y a la fotomáscara con FM1 (Fig. 9). Paso 2: Establecimiento de escala.
Paso 3: Conversión a escala de grises.
Paso 4: Segmentación.
Paso 5: Identificación del área de interés (ROI).
Paso 6. Medición del área de las mPs.
Paso 7. Medición del ancho de los mPs.

Se obtuvo el área de los mPs y la fotomáscara (Tabla 5), donde cada fila se ha etiquetado desde mP1-mP6 asociado a cada micropuente y las columnas hacen referencia a las medidas del ancho de cada mP en los 4 lotes fabricados.

Se calculó la repetibilidad del proceso de fabricación con el error relativo porcentual, planteando como medida patrón (valor teórico) el área de los mPs impresos en la fotomáscara (Tabla 6).

Tabla 5.
Medida del área en los mPs para los 4 lotes de microdispositivos y la fotomáscara.

	FM1	L1	L2	L3	L4
mP1(μm^2)x10^6	1.37	1.40	1.37	1.42	1.41
mP2(μm^2)x10^6	1.38	1.42	1.38	1.43	1.43
mP3(μm^2)x10^6	1.40	1.42	1.42	1.46	1.46
mP4(μm^2)x10^6	1.46	1.46	1.45	1.49	1.49
mP5(μm^2)x10^6	1.52	1.52	1.49	1.55	1.55
mP6(μm^2)x10^6	1.58	1.59	1.54	1.59	1.62

Fuente: Los autores.

Tabla 6.
Porcentaje de error en los mPs de cada microdispositivo.

	L1	L2	L3	L4
mP1 (%)	2.8	0.5	3.3	4.1
mP2 (%)	2.9	0.2	3.6	3.7
mP3 (%)	1.8	1.6	4.4	3.9
mP4 (%)	0.3	0.8	2.0	2.2
mP5 (%)	0.2	2.2	1.9	1.9
mP6 (%)	1.0	2.3	2.6	1.0

Fuente: Los autores.

Tabla 7.
Cálculo de promedio, desviación estándar y los valores más bajos y altos medidos en la agrupación de mPs.

	$\bar{x}$ (µm)	2σ (µm)	Diferencia entre $\bar{x}$ y el valor más bajo medido (µm)	Diferencia entre $\bar{x}$ y el valor más alto medido (µm)
mP1	29.9	2.50	2.4	2.5
mP2	34.7	2.75	2.1	2.5
mP3	44.8	2.79	2.4	2.6
mP4	64.8	2.25	1.8	2.0
mP5	85.0	2.42	2.0	1.9
mP6	105.1	2.62	2.3	2.1

Fuente: Los autores.

Se evidencia errores por encima del 3% en el área de los mPs P1, P2, P3 de MD1 y P1, P3 de MD3. También se determina que los errores son mayores para los mPs de áreas menores (P1-P3). Este comportamiento se debe a que la transferencia de patrones sobre la superficie de la película delgada de cobre se hace en un medio ácido, presentándose regiones donde el ataque químico es más selectivo. Además factores como la temperatura, agitación y procesos de interacción acido-superficie afectan las condiciones de grabado [4], [28-30]. Otra causa del error se atribuye a la oxidación de la superficie de los mPs por el contacto con el medio y por otro lado a la presencia de pequeños residuos de fotoresina en los bordes, lo que aumentaría el área de los micropuentes.

Se agruparon las mediciones de ancho en los mPs que comparten las mismas características, calculándose el valor promedio, desviación estándar, doble de la desviación estándar y lo diferencia entre los valores más bajos y altos medidos respecto al valor promedio (Tabla 7).

La diferencia entre el valor promedio y los valores máximos y mínimos en las mediciones de los mPs, así como la desviación estándar es mayor para mP1, mP2 y mP6. No obstante, la variabilidad en la anchura de los 6 mPs para los 4 lotes es menor al criterio de dos veces la desviación estándar. Con base en lo anterior se verifica que el sistema SysMicFUV-FB permite fabricar microestructuras con alto grado de repetibilidad y por tanto satisfacen las necesidades planteadas.

5. Conclusiones

En este trabajo se diseñó e implementó un sistema de fotolitografía por contacto aplicando el diseño y desarrollo de productos, lo que permitió la identificación de los módulos de equipo, especificaciones de diseño, generación, selección y prueba de conceptos y fabricación de dos prototipos: un spincoater basado en el control de velocidad de un motor DC y una fuente de radiación UV con base en un arreglo de LEDs UV con longitud de onda de 380nm. Se fabricaron cuatro lotes con 6 mPs cada uno, a partir de películas delgadas de cobre crecidas sobre sustrato de silicio, con la técnica de sputtering DC. La repetibilidad del proceso de fabricación se determinó a partir de la medición del área y el ancho de los micropuentes usando la técnica de microscopía óptica y procesamiento digital de imágenes. Donde se obtuvo que el error relativo porcentual en el área de los micropuentes es de 1-4%. Además, se determinó que la variabilidad de las microestructuras en los micropuentes es menor a 2σ. Los resultados sugieren que el sistema de fotolitografía desarrollado, permite la obtención de micropuentes y microcircuitos con alta tasa de producción, repetibilidad y calidad óptima y por lo tanto da cumplimiento a las especificaciones de diseño.

Referencias

[1] Zheng, Y., You, Z. and Shriram, R., Studies on room-temperature electric-field effect in ionic-liquid gated VO_2 three-terminal devices, J. Appl. Phys., 111(1), 014506, 2012. DOI: 10.1063/1.3665399.

[2] Pimpin, A. and Srituravanich, W., Review on micro and nanolithography techniques and their applications, Eng. J., 16(1), 19 P, 2011. DOI: 10.4186/ej.2012.16.1.37.

[3] Krishna, P.K., Srimanth, M.A. and Reddy, P.S., A review on contemporary practices in lithography, IOSR J. Appl. Chem., 7(4), pp. 27-31, 2014. DOI: 10.9790/5736-07422731.

[4] Madou, M.J., Manufacturing techniques for microfabrication and nanotechnology - Vol 2, 3ra ed., CRC Press, 2011.

[5] Neisser, M. and Wurm, S., ITRS lithography roadmap: 2015 challenges, Adv. Opt. Technol., 4(4), Jan. 2015. DOI: 10.1515/aot-2015-0036.

[6] Rothschild, M., A roadmap for optical lithography, Opt. Photonics News, 21(6), 26 P, Jun. 2010. DOI: 10.1364/OPN.21.6.000026.

[7] Rice, B., NIST TIP white paper: TIP critical national needs ideas: next generation lithography, as we push down to 11 nm lines and spaces, 2011. [online]. [accessed: 02-Feb-2018]. Available at:

https://www.nist.gov/sites/default/files/documents/2017/04/28/272_next_generation_lithography.pdf.
[8] Morris, M.A., Directed self-assembly of block copolymers for nanocircuitry fabrication, Microelectron. Eng., 132, pp. 207-217, 2015. DOI: 10.1016/j.mee.2014.08.009.
[9] Yapici, M.K. and Farhat, I., UV-LED exposure system for low-cost photolithography, en SPIE, 2014, vol. 9052, 90521T P. DOI: 10.1117/12.2046123.
[10] Kim, J., Paik, S., Herrault, F. and Allen, M., UV-LED lithography for 3-D high aspect ratio microstructure patterning, Solid-State Sensors, Actuators Microsystems Work., 2012, pp. 481-484.
[11] Gómez, R. and Ortiz, J., Low cost instrumentation for spin-coating deposition of thin films in an undergraduate laboratory, Latin-American J. Phys. Educ., 5(2), pp. 368-373, 2011. [date of reference: June 11th of 2011]. Available at: http://www.lajpe.org/june11/8_LAJPE_525_Ramon_Gomez_Preprint_corr_f.pdf
[12] Meftahul, M., Rashid, M. and Ataur, M., Design and fabrication of a simple cost effective spin coater for deposition of thin film, Adv. Environ. Biol., 8(3), pp. 729-733, 2014.
[13] Lin, B.J., Optical lithography. Bellingham, Washington USA: SPIE Publications, 2010.
[14] Ulrich, K. and Eppinger, S., Diseño y desarrollo de productos, 5ta ed. Mexico: Mc Graw Hill, 2013.
[15] Charry, G., Diseño en ingeniería, Aug-2016. [En linea]. [Accedido: 16-Aug-2016]. Disponible en: http://blog.utp.edu.co/giovannitorres/lecturasx/.
[16] Olsina, L., Métricas e indicadores: dos conceptos claves para medición y evaluación, 2003. [En linea]. [Accedido: 16-Aug-2016]. Disponible en: http://www.ciw.cl/recursos/Charla_Metricas_Indicadores.pdf
[17] Landis, S., Nano-lithography, 1ra ed. Great Britain: Wiley-ISTE, 2011.
[18] Ikegami, T., Yamaguchi, A. and Tanaka, M., Evolution y future of critical dimension measurement system for semiconductor processes, Hitachi High Technologies Inc, 2011. [online]. [accessed: February 02nd of 2018]. Available at: http://www.hitachi.com/rev/pdf/2011/r2011_05_104.pdf.
[19] Aurelian, C., Marc, F., Julie, C. and Maggy, C., Electric field-assisted metal insulator transition in vanadium dioxide (VO_2) thin films: optical switching behavior y anomalous far-infrared emissivity variation, Proc. SPIE, no. 9364, pp. 93640J1-J11, 2015. DOI: 10.1117/12.2076260.
[20] Malatto, L., Giménez, G. and Mangano, E., Thin-film VO_2 and NiCr resistors: a MEMS application. 7th Ibero-American Congress on Sensors (IBERSENSOR), Lisboa, PORTUGAL., 2010.
[21] Gonsalve, S., Tecnología y procesos de fabricación de microsistemas, Tesis de grado, Universidad de Sevilla, Sevilla, España, 2005.
[22] Pololu Robotics & Electroics, Motor with 64 CPR Encoder for 37D mm Metal Gearmotors (No Gearbox), 2016. [online]. [accessed: August 14th of 2016]. Available at: https://www.pololu.com/product/2821.
[23] https://www.superbrightleds.com/. [online]. [accessed: April 12th of 2017]. Available at: https://www.superbrightleds.com/moreinfo/component-leds/5mm-uv-led-15-degree-viewing-angle-380-nm-30mw/632/.
[24] Transist Photoresist Products, Aug-2016. [online]. [accessed: August 16th of 2016]. Available at: http://transene.com/transist/.
[25] Guerrero, A.M., Crecimiento de películas delgadas multicapa DE NiFe-Co con capas intermedias de Cu por la técnica de sputtering, Universidad del Cauca, Popayán, Colombia, 2016.
[26] CAD/Art Services, Inc. [online]. [accessed: April 15th of 2017]. Available at: http://www.outputcity.com.
[27] SU-8 2000 Permanent Epoxy Negative Photoresist. [online]. [accessed: July 25th of 2017]. Available at: http://microchem.com/pdf/SU-82000DataSheet2025thru2075Ver4.pdf.
[28] Pinto, V., Sousa, P., Cardoso, V. and Minas, G., Optimized SU-8 processing for low-cost microstructures fabrication without cleanroom facilities, Micromachines, 5(4), pp. 738-755, Sep. 2014. DOI: 10.3390/mi5030738.
[29] Broeke, J. and Mateos J.M., Image processing with ImageJ, 2da ed. Packt Publishing, 2015.
[30] Mack, C.A., Fundamental principles of optical lithography, 1ra ed. John Wiley & sons, Ltd., 2008.
[31] Levinson, H.J., Principles of lithography, Third Edition (SPIE Press Monograph, Vol. PM198), 3ra ed. SPIE Press, 2011.
[32] Franssila, S., Introduction to microfabrication, 2da ed. United Kindom: John Wiley & sons, Ltd., 2010.

J. Realpe, es Ing. Físico en 2011, MSc. en Ingeniería Física en 2017 de la Universidad del Cauca, Colombia. Se desempeña como investigador del grupo de Física de Bajas Temperaturas FISBATEM, de la Universidad del Cauca, Colombia. Sus áreas de interés son: instrumentación electrónica, programación de sistemas embebidos, diseño CAD, biosensores y microcircuitos y síntesis y caracterización de materiales en película delgada y en bloque.
ORCID: 0000-0001-7918-011X

G. Bolaños, es Lic. en Matemática y Física en 1985 de la Universidad de Nariño, Colombia. MSc. en Ciencias Físicas en 1992, PhD en Ciencias Físicas en 2000 de la Universidad del Valle, Colombia. Se desempeña como docente de planta, coordinador de la maestría en Ingeniería Física e investigador en la Universidad del Cauca, Colombia. Sus áreas de interés son: física del estado sólido, películas delgadas, materiales con propiedades magnéticas, semiconductoras y multiferróicas.
ORCID: 0000-0002-3080-9236

J. Florez, es Ing. en Electrónica y Telecomunicaciones en 1997, Esp. en Informática Industrial en 1999, Esp. en Redes y Servicios Telemáticos en 1999 y MSc. en Ingeniería, énfasis en Electrónica y Telecomunicaciones en 2010 de la Universidad del Cauca, Colombia. Se desempeña como docente de Planta e investigador en la Universidad del Cauca, Colombia. Sus áreas de interés son: robótica, control, robótica móvil, lógica difusa, redes neuronales, instrumentación industrial, control automático de procesos e integración empresarial.
ORCID: 0000-0003-1646-4419



UNIVERSIDAD NACIONAL DE COLOMBIA
SEDE MEDELLÍN
FACULTAD DE MINAS

Área Curricular de Ingeniería
Eléctrica e Ingeniería de Control

Oferta de Posgrados

Maestría en Ingeniería - Ingeniería Eléctrica

Mayor información:

E-mail: ingelcontro_med@unal.edu.co
Teléfono: (57-4) 425 52 64

UNIVERSIDAD NACIONAL DE COLOMBIA
SEDE MEDELLÍN
FACULTAD DE MINAS



DYNA
http://dyna.medellin.unal.edu.co/

Mitigation potential of active transport projects: trip attraction and CO_2 avoidance indicators in colombian cities

Mónica Espinosa [a], José Pacheco [b] & Juan Felipe Franco [a]

[a] *Facultad de Ingeniería, Universidad de los Andes, Bogotá, Colombia. m.espinosa28@uniandes.edu.co, jffranco@uniandes.edu.co*
[b] *Hill Consulting S.A.S, Bogotá, Colombia. jpacheco@hillconsulting.co*

Received: October 17th, 2017. Received in revised form: March 13th, 2018. Accepted: April 2nd, 2018.

Abstract
The global context on climate change and Colombia's recent international commitments to reduce greenhouse gas emissions, are an opportunity to encourage projects in sustainable mobility. In this study, indicators associated to trips attraction and carbon dioxide (CO_2) avoidance were estimated for measures related to bicycle use. Such indicators were then applied in different scenarios for two Colombian cities. For the assessed measures, the construction of dedicated bike-paths is the one with a greater trip-attraction indicator (455 trips / km of infrastructure-day). The CO_2 emissions reduction potential significantly changes among the studied measures and with the size of the city, the results for this indicator ranged between 92 gCO_2/trip up to 810 gCO_2/trip. These indicators represent a simple and flexible tool to have a first approximation to the mitigation potential of active transport projects in the context of Latin America cities. For instance, when an ex-ante evaluation is needed as an initial requirement for access to climate change finance funds.

Keywords: non-motorized transport; urban sustainability; climate change; emissions; greenhouse gases.

Potencial de mitigación de proyectos de transporte activo: indicadores de atracción de viajes y emisiones CO_2 en ciudades colombianas

Resumen
El contexto global de cambio climático y los recientes compromisos internacionales del país en reducción de emisiones de gases efecto invernadero, son una oportunidad para incentivar proyectos en movilidad sostenible. En este estudio se estimaron indicadores de atracción de viajes y emisiones de dióxido de carbono (CO_2) evitadas para medidas relacionadas con la promoción del uso de la bicicleta a nivel urbano. Los indicadores obtenidos se aplicaron en distintos escenarios para dos ciudades colombianas. De las medidas evaluadas, la construcción de ciclorrutas y bicicarriles es la que mayor atracción de viajes genera con 455 viajes/km de infraestructura–día. El potencial de reducción de emisiones de CO_2 cambia significativamente entre las medidas estudiadas y con el tamaño de la ciudad, los resultados para este indicador estuvieron entre los 92 gCO_2/viaje hasta 810 gCO_2/viaje. Estos indicadores representan una herramienta simple y flexible para contar con una aproximación al potencial de mitigación del cambio climático de proyectos en transporte activo en el contexto de ciudades de América Latina. En particular cuando se requiera una evaluación ex-ante como requisito inicial para acceder a fondos de financiación.

Palabras clave: transporte no motorizado; sostenibilidad urbana; cambio climático; emisiones; gases efecto invernadero.

1. Introducción

De acuerdo con el Inventario de Emisiones de Gases Efecto Invernadero (GEI) en 2012 el sector transporte en Colombia emitió 30 millones de toneladas de dióxido de carbono (CO_2), equivalentes al 12% del total de emisiones nacionales [1]. Al igual que otros países de economías en desarrollo, en Colombia se espera que las emisiones de GEI provenientes del transporte continúen creciendo a un ritmo acelerado durante las próximas décadas. Se estima que la contribución del transporte a las

How to cite: Espinosa, M., Pacheco, J. and Franco, J.F., Potencial de mitigación de proyectos de transporte activo: indicadores de atracción de viajes y emisiones CO2 en ciudades colombianas. DYNA, 85(205), pp. 302-309, June, 2018.

© The author; licensee Universidad Nacional de Colombia.

emisiones globales totales de GEI aumentará hasta un 15% en los próximos 20 años, y la mitad de esas emisiones provendrán del transporte urbano [2]. Este escenario representa un reto importante en términos de definición de políticas dirigidas a desvincular el desarrollo económico del crecimiento de las emisiones de GEI.

Desde el gobierno colombiano se vienen impulsando lineamientos para consolidar programas de movilidad urbana sostenible, incluidos el fortalecimiento de sistemas integrados de transporte público y la promoción de modos activos (bicicleta y caminata). En el actual Plan Nacional de Desarrollo se definió como meta aumentar la participación de los viajes urbanos realizados en modos de transporte sostenible (v.g., sistemas integrados de transporte público y masivo, y modos activos) del 27% en 2014 al 40% en 2018 [3].

Para alcanzar este objetivo, las autoridades de planificación y transporte a nivel nacional están diseñando iniciativas y proyectos específicos orientados a fomentar el uso de la bicicleta en las ciudades. Por otra parte, en línea con el compromiso nacional de reducción de emisiones de CO_2 en un 20% al año 2030 [4], el sector transporte en su Plan de Acción Sectorial [5] incluye la promoción del transporte no motorizado, como una opción que contribuye a los objetivos propios del sector, y que adicionalmente conlleva beneficios en la reducción de emisiones de GEI.

Además de los recursos propios para la financiación de este tipo de estrategias, los territorios y las autoridades a nivel nacional cuentan con distintas oportunidades de financiamiento climático internacional. Estas oportunidades están enmarcadas a través de mecanismos financieros tales como: Global Environmental Facility, Least Developed Countries Fund, Special Climate Change Fund y el Green Climate Fund. La fase inicial en los procesos de aplicación a estas fuentes de financiamiento incluye una estimación ex-ante del potencial beneficio que los proyectos podrían generar en cuanto a la reducción de emisiones de GEI. Esta tarea no es obvia ni simple, cuando la falta de datos locales de movilidad es una condición común en el contexto de las ciudades de colombianas y de otros países de economías en desarrollo [6].

En Colombia el Departamento Nacional de Planeación (DNP) desarrolló unas primeras guías de apoyo a proyectos urbanos para facilitar su formulación técnica y financiera [7]. El trabajo que aquí se presenta, va en este mismo sentido e intenta cerrar la brecha en información disponible, definiendo indicadores en términos de viajes atraídos y emisiones de CO_2 que permitan la estimación del potencial de mitigación del cambio climático de proyectos de transporte activo a nivel urbano. Este resultado constituye una herramienta simple para que las autoridades locales, estimen en una etapa de prefactibilidad los beneficios ambientales de este tipo de proyectos. Cumpliendo de esta forma con uno de los requisitos para acceder a financiación de los mencionados fondos internacionales.

2. Metodología

Este estudio se desarrolló en tres etapas. Primero se identificaron diferentes tipos de acciones con las que es posible promover el uso de la bicicleta como modo de transporte urbano. Después, para el conjunto de medidas escogidas, se evaluó su potencial en atracción de viajes y se estimó la reducción de emisiones de CO_2 asociada a cada opción. A partir de dicha información, se construyeron dos tipos de indicadores que son de utilidad para que ciudades en el contexto colombiano y latinoamericano utilicen en las primeras etapas de diseño de los proyectos de movilidad activa para evaluar su potencial de reducción de emisiones de CO_2. El primero de estos indicadores hace referencia a la atracción de viajes, y el segundo tiene que ver con las emisiones evitadas. La etapa final del análisis, consistió en la aplicación de los indicadores en dos casos de estudio de ciudades colombianas.

2.1. Selección de las medidas

Diferentes ciudades en Colombia cuentan con estrategias para incentivar el uso de la bicicleta. Dentro de los ejemplos exitosos cabe mencionar la infraestructura de ciclovías en Bogotá y el sistema público de bicicletas en Medellín. Otras iniciativas, asociadas con sistemas de transporte masivo en mayor medida, son los sistemas públicos de bicicletas en las estaciones de buses y el uso de bicitaxis como modo de alimentación a los sistemas. Adicionalmente, están la oferta de parqueaderos privados y la delimitación de zonas en donde se restringe el uso de automotores. Estas medidas en las diferentes configuraciones posibles, hacen parte de las principales opciones que sugiere la literatura para promover la participación de modos activos dentro del transporte urbano [8,9].

El Gobierno Colombiano está en el proceso de formulación de una Acción Nacionalmente Apropiada de Mitigación (NAMA) en transporte activo y gestión de la demanda, para lo cual realizó diferentes ejercicios de priorización de medidas para promover el uso de la bicicleta [10]. Dichos resultados, así como los lineamientos establecidos en el actual Plan Nacional de Desarrollo [3], fueron la base para seleccionar las medidas a incluir en este estudio.

2.2. Construcción de indicadores

Para cada medida se proponen dos indicadores. El primero, es un indicador de atracción de viajes y está definido como$\frac{v_m}{l_m}$:. El numerador es el número de viajes atraídos hacia la bicicleta con una acción m, y el denominador es una unidad que representa el grado de implementación del proyecto de interés (v.g., km de ciclovía, número de parqueaderos). Los potenciales de atracción de viajes para cada una de las medidas se estimaron usando información sobre el desempeño de proyectos a nivel nacional.

El segundo indicador corresponde a la de reducción de emisiones de CO_2 $(e_{CO_2,m})$ por cada viaje sustituido (v_m), definido como: $\frac{e_{CO_2,m}}{v_m}$ (ver Ecuación 1). Las emisiones de CO_2 evitadas son función de la proporción (p_i) de viajes de diferentes modos (i) reemplazados, de la intensidad de carbono de dichos viajes que ahora son atraídos hacia la bicicleta $\left(\frac{CO_2}{pax-km}\right)_i$, y de la distancia de los viajes sustituidos (d_i):

$$e_{CO_{2,m}} = v_m \cdot \Sigma_i p_i \cdot \left(\frac{CO_2}{pax-km}\right)_i \cdot d_i \quad (1)$$

La información acerca de la proporción de viajes de otros modos que son sustituidos por el uso de la bicicleta, no hace parte de las variables típicas recolectadas para la caracterización de los sistemas de transporte urbano. Dado que son variables no observables, se requiere de otros instrumentos para obtenerlos, como por ejemplo de encuestas de preferencias declaradas o de modelos del comportamiento de los usuarios de bicicletas, aunque estos últimos no permiten hacer una diferenciación por cada tipo de medida [6]. En este estudio, los valores utilizados acerca de la proporción de los viajes que se atrae de cada modo con la implementación de las medidas evaluadas son representativos de proyectos previos en Bogotá y Río de Janeiro [11].

La intensidad de carbono para los diferentes modos de transporte es representativa de la flota vehicular colombiana. Por categoría vehicular ésta se presenta clasificada en dos grupos de ciudades, según su tamaño. De acuerdo a la población se definió ciudad grande como aquella con más de un millón de habitantes e intermedia como aquella ciudad con tamaño de población entre 300 mil habitantes y un millón. Los valores de intensidad de carbono se obtuvieron de los registros de proyectos que hacen parte del Mecanismo de Desarrollo Limpio (MDL) y por lo tanto ya han sido sometidos a procesos de validación y verificación [12-16]. Finalmente, los supuestos sobre la longitud de los viajes reemplazados por viajes en bicicleta se obtuvieron de estudios locales.

Para cada medida de promoción del uso de la bicicleta, las emisiones evitadas de CO_2 en un periodo (t) se estiman haciendo uso de los dos indicadores según la Ecuación 2:

$$E_{CO_{2,i,t}} = \Sigma_m \left(i_m \cdot \frac{v_m}{i_m} \cdot \frac{e_{CO_{2,m}}}{v_m}\right) \quad (2)$$

En donde $E_{CO_{2,i,t}}$ representa las emisiones evitadas debido a los viajes atraídos por cada tipo de medida. Éstas se calculan según el nivel de implementación (i_m) de la medida (v.g., km de ciclovía, número de biciparqueaderos), el indicador de viajes atraídos hacia el uso de la bicicleta y las emisiones de CO_2 evitadas por cada viaje sustituido según el tipo de medida.

2.3. Casos de estudio

Se seleccionaron las ciudades de Villavicencio (ciudad intermedia) y Cali (ciudad grande) para estimar la reducción de emisiones de CO_2 derivadas de proyectos de transporte en bicicleta. El impacto en disminución de emisiones se evaluó comparando dos escenarios. Un escenario de línea base, el cual representa las emisiones de CO_2 si la distribución modal continuara con la tendencia observada en los últimos años. Es decir, si continuara incrementándose la participación del transporte privado y se redujera la del transporte público. El escenario con proyectos, supone que se logra la meta de 10% de participación de la bicicleta en los viajes diarios en 2030.

Tabla 1.
Supuestos sobre distribución modal en el escenario de línea base.

Modo	Supuesto
Transporte privado: motocicletas y vehículos particulares	La participación de estos modos al 2030 crece a la misma tasa anual equivalente con la cual éstos crecieron en el periodo 2005-2014, según el consolidado nacional del observatorio Ciudades Cómo Vamos [21].
Transporte público	Su participación decrece a la misma tasa anual equivalente reportada para el transporte público durante el periodo 2005-2014, según el consolidado nacional del observatorio Ciudades Cómo Vamos [21].
Taxis y otros	Se supuso constante su participación en la distribución modal durante todo el periodo de análisis.
Modos no motorizados: bicicleta y caminata	La participación de los modos no motorizados decrece para compensar el aumento de los viajes en modos privados, y la reducción de los que se hacen en transporte público.

Fuente: los autores.

La construcción de los escenarios parte de la proyección de viajes al año 2030 según el crecimiento de la población en cada ciudad. La información sobre partición modal se tomó de la Encuesta de Movilidad de 2015 para Cali [17] y del Plan de Movilidad de Villavicencio [18]. Las proyecciones de población son las del Departamento Administrativo Nacional de Estadística en Colombia (DANE) [19], y las tasas de movilidad son de la Encuesta de Movilidad de Cali [17] y estimaciones locales para Villavicencio [20]. De este último estudio también se obtuvo la proyección de las tasas de movilidad para cada ciudad [20]. Los supuestos utilizados para estimar la distribución modal al año 2030 se presentan en la Tabla 1.

Tabla 2.
Proyectos evaluados por ciudad y definición de metas al 2030.

	Medida	Unidad	Capacidad adicional 2030	
			Ciudad Intermedia	Ciudad Grande
1.	Sistemas públicos de bicicletas	Número de bicicletas	500	8,000
2.	Construcción de cicloinfraestructura (ciclorrutas y biciclarriles)	Km de ciclorrutas	200	450
3.	Construcción de biciparqueaderos privados	Cupos de biciparqueaderos	500	7,000
4.	Construcción de biciparqueaderos en estaciones de transporte público	Cupos de cicloestacionamientos	200	12,000
5.	Formalización y promoción de bicitaxis	Bicitaxis	0	5,000
6.	Delimitación de áreas calmadas	Km^2 con tráfico pacificado	0.3	1.5

Fuente: los autores.

Tabla 3.
Indicadores de atracción de viajes hacia la bicicleta por tipo de medida.

	Medida	Valor	Unidades
1.	Sistemas públicos de bicicletas	10	viajes/bicicleta - día
2.	Construcción de cicloinfraestructura (ciclorrutas y bicicarriles)	455	viajes/km de infraestructura - día
3.	Construcción de biciparqueaderos privados	2	viajes/por espacio - día
4.	Construcción de biciparqueaderos en estaciones de transporte público	2	viajes/por espacio - día
5.	Formalización y promoción de bicitaxis	40	viajes/por bicitaxi - día
6.	Delimitación de áreas calmadas	10%	porcentaje: incremento en viajes

Fuente: los autores a partir de: Medida 1 según [22]; Medida 2 según [24]; Medidas 3 y 4, supuestos realizados en este estudio; Medida 5 según [25]; Medida 6 según [26].

El escenario con 10% de participación de la bicicleta en los viajes urbanos, se construyó considerando la viabilidad de aplicar las medidas, tomando como referencia los planes locales de las ciudades. A partir de documentos de planeación de cada una se identificaron iniciativas específicas en transporte activo para los próximos años y se incorporaron al escenario. Así mismo se incluyeron otro tipo de iniciativas o acciones que ya se vienen implementando a nivel urbano en Colombia. A partir de estos proyectos y considerando la meta al 2030 en viajes en bicicleta, se dimensionaron las medidas según como se presenta en la Tabla 2.

Finalmente, se estimó el potencial anual de atracción de viajes y la reducción de emisiones de CO_2 para el portafolio de medidas seleccionado para cada ciudad, haciendo uso de los indicadores propuestos.

3. Resultados y discusión

3.1. Indicadores

Los indicadores de atracción de viajes corresponden a los presentados en la Tabla 3. Todos son representativos de proyectos locales, excepto para la medida de delimitación de áreas calmadas (Medida 6 en la Tabla 1) para la cual no se contaba con ejemplos a nivel nacional.

Las medidas implementadas en Colombia tienen indicadores de desempeño diferentes a los de medidas similares en otros países. Por ejemplo, para la Medida 1 sobre sistemas públicos de bicicletas, se utilizaron registros del Programa Encicla en Medellín [22]. Estos muestran que en promedio cada bicicleta del sistema es usada 10 veces por día. La tasa de uso en Medellín se ubica en el límite superior de tasas de uso registradas para sistemas norteamericanos y europeos. De acuerdo con los resultados de sistemas públicos de bicicletas en diferentes ciudades de países desarrollados, sistemas con un nivel de cobertura como el de Medellín, se caracterizan por una tasa de uso inferior a tres viajes por bicicleta al día [23].

Para caracterizar el potencial de atracción de viajes de la Medida 2, sobre construcción de ciclorrutas y bicicarriles, se utilizó información de Bogotá [24]. Según el estudio mencionado, una proporción de los viajes totales que se hacen en bicicleta se hacen por infraestructura diseñada para este fin, mientras que otra proporción se hace por carriles mixtos, por lo que no todos los viajes en bicicleta pueden atribuirse a la construcción de infraestructura. Del estudio de uso de infraestructura para uso de bicicletas en Bogotá se obtuvo que en promedio se puede atribuir 455 viajes por cada kilómetro de ciclorruta construido. Metodologías de referencia para estimar el beneficio de construcción de ciclovías [11] podrían estar sobrevalorando su efecto, pues sugieren utilizar por defecto un indicador de 2,000 viajes atraídos por cada kilómetro de ciclorruta construido.

El éxito de una medida en la cantidad de nuevos viajes que atrae hacia el uso de la bicicleta depende de múltiples factores inherentes al contexto de cada ciudad (v.g., topográficos, tamaño, clima, cultura), al diseño y nivel de implementación de cada una, más a que su tipología. Es por esta razón que se considera más apropiado usar datos de ciudades colombianas siempre que exista información, respecto a usar datos de atracción de viajes de la literatura internacional, que en su mayoría corresponden a indicadores derivados de contextos de ciudades europeas o norteamericanas.

Los resultados sobre los modos de los cuales se atraen los viajes con las diferentes medidas para promover el uso de bicicleta se muestran en la Tabla 4.

Vale la pena resaltar que las medidas para promover transporte no motorizado pueden diseñarse para diferentes tipos de usuarios. Según los valores consignados en la Tabla 2, una medida como la de instalar parqueaderos de bicicletas privados (Medida 3) atrae una alta proporción de usuarios que en ausencia de la medida usarían transporte privado, mientras que los viajes que atrae una medida como la de proveer parqueaderos de bicicletas en estaciones de transporte público, principalmente está sustituyendo viajes que se harían en transporte público, como puede ser el caso de uso de la bicicleta para sustituir viajes que se hacen en buses alimentadores de sistemas de transporte masivo. En términos de reducción de emisiones de CO_2, es muy diferente sustituir por modos no motorizados un viaje que se realice en un automóvil cuya ocupación promedio es cercana a un usuario, que sustituir un viaje que se realice en un bus, con ocupación cercana al 100%.

Tabla 4.
Proporción de los viajes que se atraen de cada modo por medida.

Modos de donde provienen los viajes sustituidos	Medidas 1,2,4,6	Medida 3	Medida 5
Vehículos particulares	12%	41%	
Motocicleta	6%		
Taxis	6%	11%	10%
Bus público	48%	48%	40%
Bicicleta (nuevos viajes)	6%		
Caminando	24%		50%

Medida 1: sistemas públicos de bicicletas; Medida 2: construcción de cicloinfraestructura (ciclorrutas y biciclarriles); Medida 3: construcción de biciparqueaderos privados; Medida 4: construcción de biciparqueaderos en estaciones de transporte público; Medida 5: formalización y promoción de bicitaxis; Medida 6: delimitación de áreas calmadas.
Fuente: los autores a partir de: Medidas 1,2,4,6: modificado de [11]; Medida 3: [27]; Medida 5: supuesto de este estudio.

Tabla 5.
Intensidad de carbono por modo y tipo de ciudad.

Modo	g CO_2/pax-km	
	Ciudad intermedia[1]	Ciudad grande[2]
Vehículos particulares	145	168 ± 31
Motocicleta	83	57 ± 16
Taxis	206	238 ± 115
Bus público	105	93 ± 40

[1]Los valores corresponden a Pereira; [2] La muestra incluye: Medellín, Cali, Bogotá, Barranquilla.
Fuentes: [12-16].

Tabla 6.
Longitud promedio de los viajes que se sustituyen.

	Medida	Longitud promedio (km/viaje)	
		Ciudad intermedia	Ciudad grande
1.	Sistemas públicos de bicicletas	4	4
2.	Construcción de cicloinfraestructura (ciclorrutas y biciclarriles)	1.6	5.5
3.	Construcción de biciparqueaderos privados	1.7	5.8
4.	Construcción de biciparqueaderos en estaciones de transporte público	0.7	2.5
5.	Formalización y promoción de bicitaxis	1.5	1.5
6.	Delimitación de áreas calmadas	1.5	1.5

Fuente: los autores a partir de: Medida 1 según [29]; Medida 2 de [27] modificado con la relación del área urbana de las ciudades; Medida 4 de [30]; Medidas 5 y 6 según [25].

Estudios sobre atracción de viajes por la implementación de sistemas públicos de bicicletas en ciudades europeas muestran un amplio rango en cuanto a la proporción de viajes que se atraen desde otros modos. La tasa de sustitución de viajes de modos motorizados privados varía entre 4% (Berlín, Alemania) hasta 77% (Senigallia, Italia). Por su parte la proporción de viajes que se sustituye de transporte público está entre 8% (Barcelona, España) y 58% (Estocolmo, Suecia) [28]. El amplio rango en los valores se explica por características propias de cada ciudad, como por ejemplo la existencia y cobertura de los sistemas de transporte público, la densidad de estaciones de los sistemas públicos de bicicletas, el nivel de congestión y el tamaño de las ciudades [28].

En la Tabla 5 se muestra la intensidad de carbono para los diferentes modos de transporte. La intensidad de carbono depende por una parte de las características tecnológicas de la flota, como por ejemplo edad media de los vehículos, tipo de combustible que se utilice y si la flota cuenta con algún sistema de control de emisiones. Adicionalmente, la ocupación media de los vehículos también influye en los valores, dado que las emisiones se estiman para cada modo por pasajero. Son estas características, de flota y ocupación, las que generan diferencias en los valores reportados para cada tipo de ciudad.

La longitud de los viajes reemplazados por viajes en bicicleta se presenta en la Tabla 6. Los indicadores de reducción de CO_2 por tipo de ciudad y para cada medida se muestran en la Tabla 7. Los indicadores de CO_2 incorporan diferencias entre los dos tipos de ciudades, específicamente reflejan la longitud de los viajes y las características ambientales de la flota. Los resultados en emisiones evitadas se basan en el desempeño que han tenido proyectos similares en el país, sin embargo, el potencial de mitigación total más allá de responder a la tipología de la medida, será el resultado del diseño y proceso de implementación. Por ejemplo, un proyecto de ciclo-infraestructura puede ser exitoso o no, dependiendo de cómo se construya, en dónde y a qué tipo de usuarios esté dirigido.

De los resultados que se presentan en la Tabla 7 se observa que el potencial de reducción de emisiones por la implementación de ciertas medidas es similar entre ambos tipos de ciudades, como es el caso de la construcción de sistemas públicos de bicicletas, el uso de bicitaxis y la delimitación de áreas calmadas. En el caso de medidas como la construcción de cicloinfraestructura y biciparqueaderos (públicos y privados), las diferencias en el potencial de reducción de CO_2 según el tipo de ciudad, se explica principalmente por las distancias promedio de los viajes, y en menor medida por el desempeño ambiental de la flota de los viajes sustituidos en cada caso.

En este estudio no se exploró la complementariedad entre medidas, ni entre políticas blandas y duras. Diferentes casos reportados en la literatura [11,31,32] muestran que el efecto de acciones coordinadas en transporte no motorizado con otros modos es de mayor beneficio que la implementación aislada.

3.2. Casos de estudio

Escenario de línea base: en el año base el 54% de los viajes en Cali se hicieron en modos de trasporte sostenible (transporte público, caminata y bicicleta), mientras que en Villavicencio dichos modos representan el 62% del total. Para ambas ciudades, el escenario de línea base muestra que, si no se intensifican las políticas actuales de promoción del uso de modos sostenibles de transporte, en las próximas décadas serán los modos privados (vehículo particular y motocicleta) los que dominarán en los viajes urbanos (Fig. 1). Específicamente, se estima que la participación de la bicicleta en los viajes diarios en Cali pasa de 5.4% en 2015 a 1.1% en 2030. En Villavicencio los viajes en bicicleta pasan de representar 5.3% en el año 2012 a 2.3% en el año 2030.

Tabla 7.
Indicadores de reducción de emisiones de CO_2 por tipo de medida.

	Medida	Emisiones evitadas (g CO_2/pax-día)	
		Ciudad intermedia	Ciudad grande
1.	Sistemas públicos de bicicletas	333	323
2.	Construcción de cicloinfraestructura (ciclorrutas y biciclarriles)	134	445
3.	Construcción de biciparqueaderos privados	225	810
4.	Construcción de biciparqueaderos en estaciones de transporte público	61	202
5.	Formalización y promoción de bicitaxis	94	92
6.	Delimitación de áreas calmadas	409	450

Fuente: los autores.

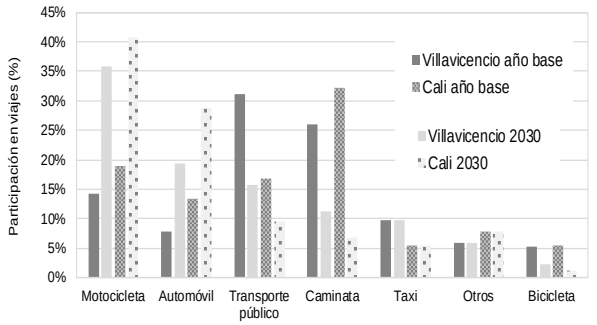


Figura 1. Participación modal para escenario de año base y año 2030.
Fuente: los autores.

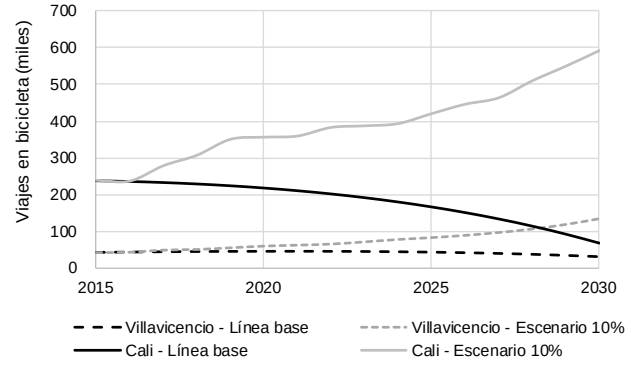


Figura 2. Número de viajes en bicicleta para escenario de año base y año 2030.
Fuente: los autores.

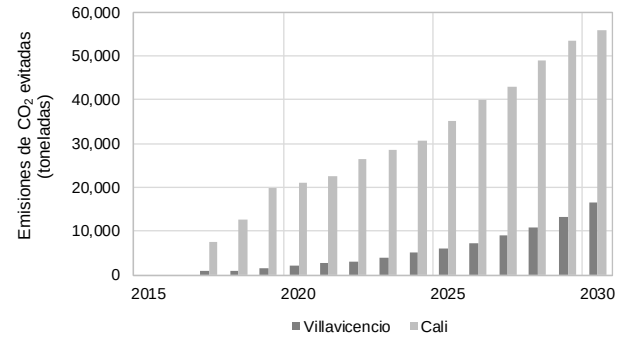


Figura 3. Emisiones anuales de CO_2 evitadas.
Fuente: los autores.

Escenario con 10% participación modal de la bicicleta en 2030: para Villavicencio se estimaron 104,205 viajes diarios adicionales en bicicleta en el año 2030, respecto al escenario base para el mismo año (ver Fig. 2). Para Cali se calculó un incremento en 526,871 viajes al día en bicicleta para cumplir la meta del 10% de participación modal. Para poner en contexto las cifras se cita el caso de Bogotá, en donde hoy en día se hacen alrededor de 450,000 viajes en bicicleta [33].

En términos de mitigación de emisiones con el incremento de viajes en bicicleta en una ciudad como Villavicencio se evitaría la emisión de 83,245 toneladas de CO_2 acumuladas entre 2015 y 2030, mientras que para una ciudad como Cali el potencial de reducción estimado es del orden 445,976 toneladas de CO_2 (ver Fig. 3). Esto es equivalente a reducir 2% de las emisiones acumuladas en el escenario de línea base entre 2015 y 2030. Entendiendo además que una meta de partición modal del 10% como la planteada para este ejercicio es ambiciosa para el contexto de ciudades colombianas.

4. Conclusiones

Se generaron indicadores para estimar la reducción de emisiones de CO_2 asociada a proyectos locales de promoción del uso de la bicicleta como modo de transporte urbano. Los indicadores se estimaron considerando las principales características demográficas y en movilidad de ciudades en Colombia. Los resultados muestran que el potencial de reducción de emisiones varía entre 92 gCO_2/viaje hasta 810 gCO_2/viaje, para las medidas evaluadas. La metodología propuesta es simple y flexible en cuanto a la facilidad de incorporación de nuevos y mejores datos en la medida en que las ciudades vayan contando con éstos. Los indicadores pueden ser utilizados para estimar potenciales beneficios en mitigación del cambio climático de estrategias en transporte no motorizado el contexto urbano de América Latina, en particular cuando es común que la información relacionada con la movilidad y su impacto ambiental, sea escasa, no estandarizada, y no sea recolectada de manera frecuente. Los indicadores aquí presentados ayudan a superar las barreras de información a las que se enfrentan los proyectos en su etapa inicial para acceder a mecanismos de financiación de cambio climático. Adicionalmente, éstos son consistentes con los objetivos de los sistemas de monitoreo, reporte y verificación en mitigación de emisiones GEI.

Se evaluó además el potencial de mitigación de emisiones de CO_2 asociado con una mayor participación de viajes en bicicleta en dos ciudades colombianas, una intermedia y una grande. Para estas ciudades incrementar de la partición modal de la bicicleta al 10% en el año 2030 conlleva una reducción del 2% de las emisiones respecto a la línea base. Si bien el potencial de mitigación de emisiones GEI es modesto, la versatilidad de las estrategias orientadas al transporte en bicicleta y su posibilidad de atracción de usuarios de diferentes grupos de la población y con diferentes patrones de movilidad, hace que este tipo de medidas tengan un gran potencial en el diseño de estrategias integrales de bajo carbono. El diseño de iniciativas en transporte activo, requiere del conocimiento de las prioridades y necesidades inherentes al contexto de cada área urbana, y sobre todo requiere que se diseñen como parte de estrategias completas en movilidad, y no como medidas aisladas.

Agradecimientos

La metodología presentada en este estudio fue desarrollada por los autores para apoyar la formulación de la NAMA TAnDem que lidera el gobierno colombiano con el

apoyo financiero de Programa Transfer de la Agencia de Cooperación Alemana (GIZ).

Las opiniones y conclusiones presentadas en este artículo son las de los autores y no representan necesariamente las de las entidades oficiales, ni financiadoras.

Referencias

[1] Primer informe bienal de actualización de Colombia ante la convención marco de las Naciones Unidas sobre el Cambio Climático, Colombia, Instituto de Hidrología, Meteorología y Estudios Ambientales – IDEAM, 2015.

[2] Cadena, A., Bocarejo, J., Rodríguez, M., Rosales, R., Delgado, R., Flórez, E., Espinosa, M., Lombo, C., López, H., Londoño, M., Palma, M. and Rodríguez, J., Upstream analytical work to support development of policy options for mid- and long-term mitigation objectives in Colombia, Bogotá, Colombia, Universidad de los Andes, 2016.

[3] Plan Nacional de Desarrollo 2014-2018. Todos por un nuevo país [en línea], Bogotá, Colombia, 2015 [Fecha de consulta 10 de febrero de 2017]. Disponible en: https://www.dnp.gov.co/Plan-Nacional-de-Desarrollo/Paginas/Que-es-el-Plan-Nacional-de-Desarrollo.aspx.

[4] Colombia's INDC [en línea], United Nations Framework Convention on Climate Change - UNFCCC, Colombia, 2015 [Fecha de consulta 10 de febrero de 2017]. Disponible en: http://www4.unfccc.int/submissions/INDC/Submission%20Pages/submissions.aspx.

[5] Plan de Acción Sectorial del Sector Transporte [en línea], Bogotá, Colombia, Ministerio de Transporte de Colombia, 2014 [Fecha de consulta 9 de febrero de 2017]. Disponible en: http://www.minambiente.gov.co/index.php/component/content/article?id=470:plantilla-cambio-climatico-26#planes-sectoriales-de - mitigación.

[6] Massink, R., Zuidgeest, M., Rijnsburger, J., Sarmiento, O.L. and van Maarseveen, M., The climate value of cycling. Natural Resources Forum, 35, pp 100-111, 2011. DOI: 10.1111/j.1477-8947.2011.01345.x

[7] Proyectos TIPO por sector. [en línea], Bogotá, Colombia, Departamento Nacional de Planeación – DNP, 2016 [Fecha de consulta 15 de febrero de 2017]. Disponible en: https://proyectostipo.dnp.gov.co.

[8] Hoogzaad, J., Lee, A. and Greiner, S., MRV of cycling: measuring the carbon impact of bicycle policy and infrastructure [online] 2013. [date of reference: February 12th of 2017]. Available at: http://www.climatefocus.com/publications/mrv-cycling-measuring-carbon-impact-bicycle-policy-and-infrastructure.

[9] Ríos, R.A., Taddia, A.P., Pardo, C. y Lleras, N. Ciclo inclusión en América Latina y el Caribe: guía para impulsar el uso de la bicicleta, Washington D.C, US, Banco Interamericano de Desarrollo, 2015.

[10] Estimación ex-ante del potencial de mitigación de emisiones GEI y apoyo en el diseño del sistema de monitoreo, reporte y verificación de las medidas de mitigación de la NAMA de Transporte Activo en Bicicleta y Gestión de la Demanda (NAMA TAnDem), Bogotá, Colombia, GIZ-Tranfer Program & Hill Consulting, 2016.

[11] Hook, W., Reploge, M. and Hughes, C.K., Manual for calculating greenhouse gas benefits of global environment facility transportation projects, New York, US, Scientific and Technical Advisory Panel of the Global Environment Facility, 2015.

[12] Clean Development Mechanism Project Design Document Form (Cdm-Pdd), BRT Transmetro, Versión 1.8 [online], Barranquilla, Colombia, United Nations Framework Convention for Climate Change - UNFCCC, 2011. [Date of reference: February 10th of 2017]. Available at: https://cdm.unfccc.int.

[13] Clean development mechanism project design document form (Cdm-Pdd), BRT Metroplús, Versión 1.3 [online], Medellín, Colombia, United Nations Framework Convention for Climate Change - UNFCCC, 2011. [Date of reference: February 10 th of 2017]. Available at: https://cdm.unfccc.int.

[14] Clean development mechanism project design document form (Cdm-Pdd), TRANSMILENIO Phase II to IV, Version 6.2 [online], Bogotá, Colombia, United Nations Framework Convention for Climate Change - UNFCCC, 2012. [Date of reference: February 10th of 2017]. Available at: https://cdm.unfccc.int.

[15] Clean development mechanism project design document form (Cdm-Pdd), BRT MIO, Versión 2.0 [online], Cali, Colombia, United Nations Framework Convention for Climate Change - UNFCCC, 2012. [Date of reference: February 10th of 2017]. Available at: https://cdm.unfccc.int.

[16] Clean development mechanism project design document form (Cdm-Pdd), BRT Megabús, Versión 2.7 [online], Pereira, Colombia, United Nations Framework Convention for Climate Change - UNFCCC, 2012. [Date of reference: February 10th of 2017]. Available at: https://cdm.unfccc.int.

[17] Encuesta de movilidad Cali [en línea], Cali, Colombia, Alcaldía de Cali, Metrocali, Tranvias SAS, Steer Davies Gleave & Centro Nacional de Consultoría, 2015. [Fecha de consulta 10 de febrero de 2017]. Disponible en: http:// http://www.metrocali.gov.co.

[18] Formulación del plan de movilidad para el municipio de Villavicencio, Villavicencio, Colombia, Alcaldía de Villavicencio & Universidad Nacional, 2013.

[19] Proyecciones de población 2005-2020 [en línea], Bogotá, Colombia, Departamento Administrativo Nacional de Estadística – DANE, 2016. [Fecha de consulta 10 de febrero de 2017]. Disponible en: http://www.dane.gov.co.

[20] Acevedo, J., Bocarejo, J.P., Lleras, G., Echeverry, J.C., Ospina, G. y Rodriguez, A., El transporte como soporte al desarrollo de Colombia, una visión al 2040. Bogotá, Colombia, Universidad de los Andes, 2009.

[21] Informe de calidad de vida comprado en 14 ciudades de Colombia, Bogotá, Colombia, Red de Ciudades Cómo Vamos, 2015, Boletín Número 6, ISSN: 1909-8545.

[22] Movilidad y espacio público en Medellín [en línea], Medellín, Colombia, Medellín Cómo Vamos, 2014. [Fecha de consulta 8 de febrero de 2017]. Disponible en: http://www.medellincomovamos.org/movilidad-y-espacio-p-blico/.

[23] The bike-share planning guide [online], New York, Institute for Transportation and Development Policy, 2018. [Date of reference: February 10th of 2017]. Available at: https://www.itdp.org/wp-content/uploads/2014/07/ITDP_Bike_Share_Planning_Guide.pdf

[24] Fernández, L.A., La bicicleta, opción real de movilidad en Bogotá [en línea], Bogotá, Colombia, UN Periódico, 2009. [Fecha de consulta 10 de febrero de 2017]. Disponible en: http://www.unperiodico.unal.edu.co/dper/article/la-bicicleta-opcion-real-de-movilidad-en-bogota

[25] Gómez, J., Los bicitaxistas se tomaron las calles de Bogotá: hay más de 5 mil [en línea], Bogotá, Colombia, Diario El Tiempo, 2010. [Fecha de consulta 10 de octubre de 2017]. Disponible en: http://www.eltiempo.com/archivo/documento/CMS-8298040.

[26] Littman, T., Traffic calming benefits, costs and equity impacts, [online], Victoria, Canada, Victoria Transport Policy Institute, 1999. [Date of reference: February 10th of 2017]. Available at: http://www.vtpi.org/calming.pdf

[27] Pardo, C.F. Caviedes, A. y Calderón, P., Estacionamiento para bicicletas: guía de elección, servicio, integración y reducción de emisiones, Bogotá, Colombia, Despacio, Institute for Transportation and Development Policy, 2013.

[28] Cycle more often 2 cool down the planet. Quantifying CO2 savings of cycling [online], Brussells, Belgium, European Cyclist´s Federation, 2011. [Date of reference: February 10th of 2017]. Available at: https://ecf.com/sites/ecf.com/files/ECF_CO2_WEB.pdf

[29] Ospina J.P., Definición de una metodología para el estudio de la accesibilidad bajo una estrategia de integración modal bicicleta y transporte público, Medellín, Colombia, Universidad Nacional de Colombia, Grupo de Investigación Vías y Transporte VITRA, 2015.

[30] Elsner, L., Estudio exploratorio sobre el uso y calificación de usuarios de cicloparqueaderos en transmilenio, Bogotá, Colombia, Despacio, 2016.

[31] Gerlach, J., Quantifying and monitoring GHG and CO-benefits of NMT and GDM measures (input document), Dresden, Germany, Deutsche Gesellschaft für Internationale Zusammenarbeit GIZ, 2015.

[32] Scheepers, C.E., Wendel-Vos, G.C., den Broeder, J.M., van Kempen, E.M., van Wesemael, P.J.V. and Schuit, J.A., Shifting from car to active transport: a systematic review of the effectiveness of

interventions, Transportation Research Part A, (70), pp. 264-80, 2014. DOI: 10.1016/j.tra.2014.10.015
[33] Observatorio de movilidad - Reporte anual de movilidad 2015, Cámara de Comercio de Bogotá y Universidad de los Andes, Bogotá, Colombia, No. 9, 2015.

M. Espinosa, es Ing. Ambiental de la Universidad de los Andes, Colombia, actualmente estudiante de doctorado de la Facultad de Ingeniería de la misma Universidad. Tiene experiencia en modelación de emisiones de gases efecto invernadero en diferentes sectores, diseño de acciones de reducción de emisiones y análisis de costos marginales de mitigación. Sus intereses en investigación incluyen también temas relacionados con calidad del aire, exposición personal a contaminación atmosférica y externalidades ambientales generadas por el transporte.
ORCID: 0000-0001-7437-162X

J. Pacheco, es Ing. Ambiental de la Universidad de los Andes, Colombia, MSc. en Ingeniería Ambiental de la misma universidad. Ha trabajado como consultor en transporte sostenible desde agencias de cooperación internacional y entidades del gobierno como el Ministerio de Transporte de Colombia. Actualmente se desempeña como asociado en la firma consultora Hill Consulting S.A.S donde lidera los temas de cambio climático y transporte. Sus intereses de investigación comprenden la calidad del aire, la contaminación auditiva, la movilidad activa y los inventarios de emisiones de Gases de Efecto Invernadero.
ORCID: 0000-0002-0668-5288

J.F. Franco, es Ing. Químico de la Universidad Nacional de Colombia, con MSc. en Ingeniería de la Universidad de los Andes, Colombia, donde además cursa el programa de doctorado en ingeniería. Cuenta con experiencia como profesor, investigador y consultor en control de la contaminación atmosférica, mitigación de gases de efecto invernadero (GEI) y gestión de la sostenibilidad urbana. Sus intereses incluyen la participación en proyectos de investigación transversales orientados a generar soluciones sostenibles a través de proyectos de alto impacto en la comunidad y la formulación de políticas públicas.
ORCID: 0000-0002-7260-8221

UNIVERSIDAD NACIONAL DE COLOMBIA
SEDE MEDELLÍN
FACULTAD DE MINAS

Área Curricular de Medio Ambiente

Oferta de Posgrados

Especialización en Aprovechamiento de Recursos Hidráulicos
Especialización en Gestión Ambiental
Maestría en Ingeniería Recursos Hidráulicos
Maestría en Medio Ambiente y Desarrollo
Doctorado en Ingeniería - Recursos Hidráulicos
Doctorado Interinstitucional en Ciencias del Mar

Mayor información:

E-mail: acma_med@unal.edu.co
Teléfono: (57-4) 425 5105

UNIVERSIDAD NACIONAL DE COLOMBIA
SEDE MEDELLÍN
FACULTAD DE MINAS



DYNA
http://dyna.medellin.unal.edu.co/

Shear modulus of mining tailings from resonant column tests

Eliana Martínez-Rojas [a], Fausto Molina-Gómez [b] & Juan Carlos Ruge [b]

[a] *Programa de Ingeniería Civil, Universidad Piloto de Colombia, Colombia. eliana-martinez@unipiloto.edu.co*
[b] *Facultad de Ingeniería, Universidad Militar Nueva Granada, Colombia. fausto.molina@unimilitar.edu.co, juan.ruge@unimilitar.edu.co*

Received: November 8th, 2017. Received in revised form: March 16th, 2018. Accepted: April 4rd, 2018.

Abstract
This article presents the results of seventy-two resonant column tests performed in two types of materials from the waste deposits of the Riotinto mines (Huelva – Spain). Methodology test included different conditions of effective consolidation pressure and torsional excitation level. The equipment used was a fixed-free resonant-column system. The effective consolidation pressures were established within a range between 50 - 300 kPa and the torsional excitations were equal to 0.025, 0.05, 0.1, 0.2, 0.4 and 0.8 V. It was found that such test combinations lead to angular deformations between 0.003% and 0.148%. The results indicate that it is possible to establish simple empirical functions of the stiffness module as a function of the angular deformation and the effective consolidation pressure.

Keywords: resonant frequency; shear modulus; effective consolidation pressure; angular deformation.

Módulo de corte de relaves mineros a partir de ensayos de columna resonante

Resumen
En este artículo se presentan los resultados de setenta y dos ensayos de columna resonante desarrollados en dos tipos de materiales provenientes de los depósitos de estériles de las minas de Riotinto (Huelva-España). La metodología de ensayo incorporó diferentes condiciones de presión efectiva de consolidación y nivel de excitación torsional. El equipo utilizado para la ejecución de las pruebas fue una columna resonante de base fija y extremo superior libre. Las presiones efectivas de consolidación se establecieron dentro de un rango variable entre 50 - 300 kPa y las excitaciones torsionales fueron iguales a 0.025, 0.05, 0.1, 0.2, 0.4 y 0.8 V. Se encontró que dichas combinaciones de ensayo conducen a deformaciones angulares que varían entre 0.003% y 0.148%. Los resultados indican que es posible establecer funciones empíricas sencillas del módulo de rigidez como una función de la deformación angular y de la presión efectiva de consolidación.

Palabras clave: frecuencia de resonancia; módulo de corte; presión efectiva de consolidación; deformación angular.

1. Introducción

No cabe duda de que, a nivel mundial, la industria que más volumen de residuos produce es la minera. Por lo tanto, esta ha dado origen a un número no determinado de presas construidas por métodos hidráulicos y sin ningún tipo de compactación (presas de relaves), lo cual las hace susceptibles a presentar algún tipo de falla. Entre los factores detonantes de las fallas ocurridas en las presas de relaves se encuentran el grado de saturación de los residuos, el deslizamiento de los taludes, las solicitaciones dinámicas, la tubificación y la capacidad de carga del material de la cimentación [1].

Azam y Li [2] reportaron 198 casos de rotura de presas de relaves hasta el año 2000 y otros 20 de los años 2000 al 2010. De acuerdo con estos resultados estadísticos, se estima que la tasa de falla de las presas de relaves es del 1.2%, mientras que la tasa de falla de las presas de retención de agua convencionales es del 0.01% aproximadamente; es decir, más de dos órdenes de magnitud por debajo de la primera [1,2]. Esta situación ha dado lugar a la toma de conciencia de la necesidad de mejorar la seguridad en el diseño y operación de las presas de relaves, lo cual depende profundamente de las características de los materiales en condiciones estáticas

How to cite: Martínez-Rojas, E., Molina-Gómez, F. and Ruge, J.C., Módulo de corte de relaves mineros a partir de ensayos de columna resonante. DYNA, 85(205), pp. 310-318, June, 2018.

© The author; licensee Universidad Nacional de Colombia.

y cíclicas, así como de las condiciones geológicas e hidrogeológicas del sitio de disposición [3].

Las propiedades del suelo que influyen en los fenómenos de pequeñas deformaciones incluyen la rigidez, el amortiguamiento, la relación de Poisson y la densidad. Sin embargo, las características más importantes de los suelos cargados cíclicamente son: el módulo dinámico de rigidez al cortante (G), el módulo dinámico de elasticidad (E), y la razón de amortiguamiento (ζ) [4]. La evaluación de las propiedades dinámicas es posible mediante una serie de técnicas de laboratorio y ensayos de campo, que se ajustan a rangos de deformación específicos, frecuencias de operación y velocidades de deformación tangencial.

En general, el ensayo de columna resonante es la técnica comúnmente más utilizada en el laboratorio para medir las propiedades dinámicas de los suelos a un nivel bajo de deformación [5]. Los diferentes diseños desarrollados someten a las probetas cilíndricas macizas o huecas a cargas armónicas axiales o torsionales, mediante sistemas electromagnéticos capaces de controlar con precisión la frecuencia y la amplitud de los diferentes tipos de onda que pueden generar.

La columna resonante (CR) fue utilizada por primera vez por Ishimato e Iida [6] y Iida [7,8] para ensayar suelos de Japón y casi dos décadas después por Bisshopp [9]. A partir de la década de los 60, la técnica se ha utilizado ampliamente en muchos países y ha sido sometida a numerosas modificaciones en lo que se refiere a las condiciones de restricción de la muestra. Wilson y Dietrich [10] utilizaron en su época uno de los equipos de columna resonante más novedosos en los Estados Unidos, con el que ensayaron muestras de arcilla. Hall y Richart [11] diseñaron y desarrollaron un equipo de columna resonante en el que las condiciones de restricción fueron "fixed – free"; es decir, fija en la base y libre en el extremo superior, el cual permitía inducir en las muestras de suelo vibraciones de tipo torsional y longitudinal. Drnevich et al. [12,13] desarrollaron un equipo en el que se utilizaban muestras cilíndricas huecas de suelo para determinar el módulo de corte y la relación de amortiguamiento a grandes deformaciones. La razón por la que utilizaron probetas huecas está relacionada con la dificultad de obtener un valor representativo de la deformación angular en las probetas macizas. Además, sustentaron la teoría en la que se basa la interpretación de los resultados obtenidos mediante la prueba de columna resonante. El principio de funcionamiento de un equipo de CR, las recomendaciones de calibración, el procesamiento de la información y la interpretación de resultados fueron descritos claramente por Drnevich, V. P. et al. [14].

En lo que respecta a la rigidez de los suelos granulares, investigaciones relevantes publicadas en la literatura destacan que el módulo de corte está influenciado fundamentalmente por la amplitud de la deformación cíclica, la presión de confinamiento, el índice de poros o relación de vacíos (e), el número de ciclos de carga, el grado de saturación, la frecuencia de la vibración, el índice de plasticidad, la historia de tensiones, la relación de tensión cíclica, la distribución granulométrica y la estructura del suelo [15-18]. Como producto de estas y muchas otras más investigaciones experimentales, en la literatura se reportan una serie de correlaciones empíricas para la evaluación del módulo de rigidez al cortante. No obstante, es importante resaltar que la validez de cualquiera de las relaciones propuestas está limitada a las condiciones bajo las que fueron desarrolladas (tipo de suelo, estado de tensiones, nivel de deformación, características de la vibración, entre otras). Sin embargo, para otros parámetros o condiciones este tipo de formulaciones pueden ser válidas o no.

Teniendo en cuenta los antecedentes citados anteriormente, el objetivo de esta investigación es evaluar, mediante la ejecución de ensayos de columna resonante, la influencia de la presión efectiva de consolidación y la magnitud de la excitación torsional, en la determinación del módulo de rigidez al cortante de dos tipos de materiales provenientes de los depósitos de estériles de las minas de Riotinto (Huelva - España). Además, se estudia la posibilidad de proponer funciones empíricas sencillas que correlacionen estos parámetros entre sí. La estructura del artículo incluye la descripción del equipo utilizado, la descripción de los materiales estudiados, el programa experimental ejecutado, el proceso de fabricación y montaje de las probetas en el equipo de columna resonante, el análisis de resultados y, finalmente, las conclusiones.

2. Descripción del equipo utilizado

El equipo de columna resonante empleado durante la fase experimental de esta investigación fue fabricado por la compañía Wykeham Farrance, de Inglaterra. Se trata de un equipo instrumentado y automatizado que ofrece un conjunto de ventajas, dentro de las que destacan: (*i*) es un dispositivo combinado de columna resonante y corte torsional simple; (*ii*) calcula de manera automática la frecuencia de resonancia, la velocidad de propagación de las ondas de corte, el módulo de rigidez, la deformación angular y la razón de amortiguamiento; este último parámetro evaluado mediante la curva de decadencia de vibración libre, la cual daría una medida del amortiguamiento viscoso, o a partir del método de la media potencia (vibración forzada), cuyo resultado correspondería a un amortiguamiento histerético; (*iii*) no requiere del uso externo de osciloscopio, ni de generador de funciones; (*iv*) el sistema de excitación de estructura flotante interna permite realizar ensayos en los que las muestras pueden experimentar grandes deformaciones axiales durante la consolidación; y (*v*) permite visualizar, en tiempo real, la respuesta de los sensores durante la ejecución del ensayo. En la Fig. 1 se presenta un esquema ilustrativo del equipo.

Desde un punto de vista mecánico, el equipo de columna resonante se asemeja a un sistema de oscilación forzada con un grado de libertad, en el cual se hace vibrar una muestra de suelo dentro de un rango de frecuencias en el que se encuentra su primer modo natural. Una vez alcanzada la frecuencia de resonancia del material, y a partir de la teoría de propagación de ondas en medios elásticos continuos, es posible la evaluación de la velocidad de propagación de las ondas de corte (V_s) o compresión (V_p), según el tipo de excitación inducida (cargas armónicas torsionales o longitudinales), el módulo de rigidez al cortante (G), la razón de amortiguamiento (D), el módulo de Young (E), entre otros.

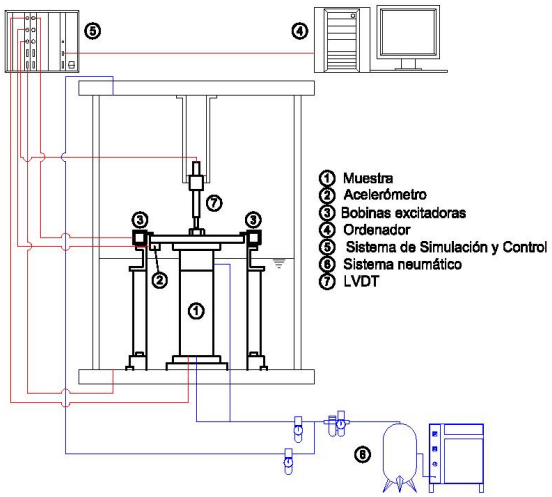


Figura 1. Esquema ilustrativo del equipo de columna resonante utilizado.
Fuente: Elaboración propia.

En este caso en particular, las condiciones de restricción de la muestra fueron "fixed-free", es decir, que la probeta se mantenía fija en la base y libre en el extremo superior, y la vibración fue de tipo torsional.

El equipo consta básicamente de los elementos y sensores que se mencionan a continuación. 1) Dos células cilíndricas huecas de policarbonato que permiten, mediante la célula interior, aplicar la presión de consolidación a las probetas a través de un fluido, sin que los componentes electrónicos queden sumergidos, y, mediante la célula exterior, aplicar al fluido confinante la presión suministrada por un sistema de acción neumática. 2) Una base inferior a través de la cual se aplica la presión de cola o contrapresión y se permite el drenaje de las probetas durante la fase de consolidación. 3) una cabeza corrugada, sin posibilidad de drenaje, encargada de transmitir las acciones torsionales. 4) Un mecanismo impulsor compuesto por ocho bobinas y cuatro imanes encargados de aplicar la tensión torsional a la muestra. 5) Un acelerómetro adosado al mecanismo destinado a generar la acción torsional; el cual suministra la información necesaria para calcular la velocidad de propagación de las ondas de corte (Vs). 6) Un LVDT que permite medir las deformaciones axiales. 7) Dos transductores de proximidad que permiten medir las deformaciones angulares, en el caso de que no se utilice la información del acelerómetro para calcularlas. 8) tres transductores de presión destinados a medir la presión de Cámara (σ_c), y la presión de cola o contrapresión (Pc) y las presiones intersticiales (u). 9) Un transductor para registrar los cambios volumétricos durante la fase de consolidación. 10) Una unidad compacta dotada con una fuente de poder, un regulador de presión manual, dos electro-reguladores de presión, 8 componentes electrónicos de acondicionamiento de señal y un módulo de control y adquisición de datos. 11) Un computador que controla el equipo y adquiere los datos.

3. Descripción de los materiales

Los materiales utilizados en esta investigación fueron extraídos mediante la exploración superficial de los depósitos de estériles de las minas de Riotinto, las cuales se localizan en la zona centro oriental de la Provincia de Huelva (España).

Tabla 1
Propiedades índice de los materiales ensayos.

Material	w_n %	$w_{lab.}$ %	Finos <80 µ	IP %	G_s	Densidad seca γ_d (g/cm^3)
ACS	8.1	8.1	32.7	N.P	3.02	1.60
LAD	14.3	7.8	48.5	N.P	2.99	1.65

Fuente: Elaboración propia.

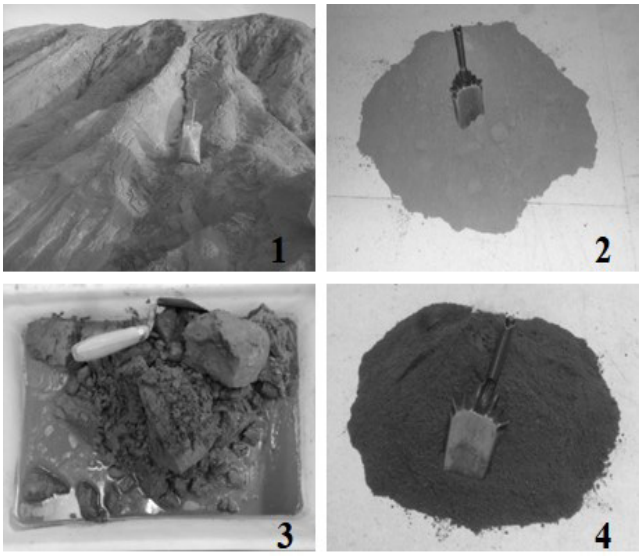


Figura 2. Aspecto de los materiales provenientes de las minas de Riotinto. 1) detalle del sitio donde se tomó la muestra de arena ACS, 2) aspecto de las arenas ACS en estado natural, 3) aspecto de los LAD en estado natural, 4) aspecto de los LAD una vez homogenizados en laboratorio.
Fuente: Elaboración propia.

En el sitio de la mina los materiales objeto de estudio se conocen bajo los nombres: Arena Cerro Salomón (ACS) y Lodos de alta densidad (LAD). De acuerdo con la identificación visual de las muestras representativas de ambos materiales, estos corresponden a una arena limosa gris de grano fino, en el caso de las ACS, y a una arena limosa gris verdoso de grano fino, en el caso de los LAD. La información relacionada con las propiedades índice de los materiales ensayados, se incluye en la Tabla 1.

En la Fig. 2 se puede observar el aspecto de los materiales en estado natural y una vez homogeneizada su humedad al ambiente de laboratorio.

En la Tabla 1 se puede evidenciar que, debido a la composición mineralógica de los materiales ACS y LAD, los valores de gravedad específica obtenidos resultaron ser elevados comparados con los valores típicos reportados en la literatura para las arenas limosas. De acuerdo con Djoenaidi [19] y Bardet [20], la gravedad específica de sólidos de las arenas limosas puede ser del orden de 2.65.

Por otra parte, cabe anotar que los materiales investigados contienen elementos químicos tóxicos y nocivos para la salud; un ejemplo de ello es el Arsénico, que es fácilmente identificable por el fuerte olor a acido que expele durante el proceso de secado en estufa y, además, es el responsable de la coloración que toma el agua y los elementos que entran en contacto con el material. Otros datos de interés de los materiales investigados se pueden consultar en Martínez [21].

Tabla 2.
Condiciones generales de las pruebas de Columna Resonante.

Material	γ_d (g/cm^3)	σ'_c (kPa)	Excitación torsional (Voltios - V)
ACS	1.60	50	0.025 - 0.05 - 0.1 - 0.2 - 0.4 y 0.8
		100	0.025 - 0.05 - 0.1 - 0.2 - 0.4 y 0.8
		150	0.025 - 0.05 - 0.1 - 0.2 - 0.4 y 0.8
		200	0.025 - 0.05 - 0.1 - 0.2 - 0.4 y 0.8
		250	0.025 - 0.05 - 0.1 - 0.2 - 0.4 y 0.8
		300	0.025 - 0.05 - 0.1 - 0.2 - 0.4 y 0.8
LAD	1.65	50	0.025 - 0.05 - 0.1 - 0.2 - 0.4 y 0.8
		100	0.025 - 0.05 - 0.1 - 0.2 - 0.4 y 0.8
		150	0.025 - 0.05 - 0.1 - 0.2 - 0.4 y 0.8
		200	0.025 - 0.05 - 0.1 - 0.2 - 0.4 y 0.8
		250	0.025 - 0.05 - 0.1 - 0.2 - 0.4 y 0.8
		300	0.025 - 0.05 - 0.1 - 0.2 - 0.4 y 0.8

Fuente: Elaboración propia.

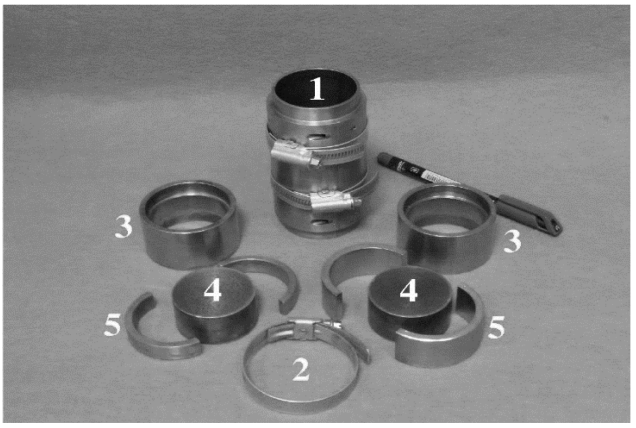


Figura 3. Elementos necesarios para la fabricación de probetas: 1) molde tripartido; 2) abrazaderas; 3) guías cilíndricas, collarines o extensores de molde; 4) cilindros metálicos o pistones; 5) cilindro hueco bipartido
Fuente: Elaboración propia.

4. Programa experimental

Con las muestras de los materiales ACS y LAD se realizaron los ensayos de columna resonante por barrido continuo, conducentes a la determinación de la frecuencia de resonancia (Fr) y el módulo de rigidez al cortante (G), de acuerdo a las condiciones generales que se incluyen en la Tabla 2.

Como se puede observar en la Tabla 2, dada una densidad seca predefinida, se programó la ejecución de las pruebas variando la amplitud de la señal de estimulación desde 0.025 Voltios hasta 0.8 Voltios, para cada uno de los estados de confinamiento indicados.

Las presiones "efectivas" de consolidación se establecieron dentro de un rango variable entre 50 kPa y 300 kPa, debido a que la capacidad máxima estable del compresor utilizado es de 750 kPa. La presión de cola o contrapresión aplicada en todas las pruebas fue igual a 400 kPa. Las dimensiones de los especímenes fueron H = 100.8 mm y D = 49.7 mm, cumpliendo así con una relación altura/diámetro igual a 2.03 y eliminando, por lo tanto, la incertidumbre relacionada con la esbeltez de las probetas. En total se realizaron 72 pruebas de columna resonante, debido a las combinaciones de los parámetros de ensayo (σ'_c y V) para caracterizar dinámicamente los dos tipos de materiales.

5. Fabricación y montaje de probetas

Dada la necesidad de reproducir un buen número de probetas con densidades secas (γ_d) y humedades (w) iguales, se emplearon los accesorios incluidos en la Fig. 3, los cuales garantizan la homogeneidad entre ellas. Asimismo, debido al grado de dificultad que supone la fabricación de probetas con materiales arenosos, fue necesario recurrir al diseño y fabricación de accesorios, no tradicionales, que garantizan la verticalidad de la cabeza excitadora y el paralelismo de los extremos de las probetas. Dichos elementos pueden ser observados en las Figs. 4-8

Los materiales que llegaron al laboratorio se secaron al aire y se mezclaron hasta lograr una humedad uniforme al ambiente del laboratorio. Después, fueron conservados en una cámara húmeda con los contenidos de agua mencionados en la tercera columna de la Tabla 1.

El procedimiento para la fabricación de las probetas, de los materiales ACS y LAD, se indica a continuación. 1) Cálculo de la densidad húmeda (γ_h), a partir de la densidad seca (γ_d) y conocida la humedad de homogeneización (w_{lab}). 2) Preparación de la probeta con material homogeneizado, cuya cantidad es estimada con base en la densidad húmeda y el volumen del molde. 3) Colocación del molde tripartido abrazando la base inferior del equipo de CR y apoyado sobre un cilindro hueco bipartido (elevador de molde); el molde tripartido contiene en su interior una membrana de látex que se adhiere a este mediante la aplicación de vacío a través de un conducto lateral. 4) Colocación del material en el interior del molde, mediante compactación dinámica, en cinco capas de igual peso e igual altura. Para la compactación de la última capa se coloca un extensor de molde o collarín sobre el extremo superior del molde tripartido, para evitar la pérdida de material durante la compactación del suelo (Ver Fig. 4). 5) Colocación de un cilindro metálico, de igual altura a la del extensor de molde, sobre la última capa de material en estado suelto. 6) Compactación dinámica de la última capa hasta lograr que el cilindro metálico quede a ras con el collarín; de este modo se garantiza la densidad especificada. 7) Remoción del cilindro y el collarín que se utilizaron durante la compactación de la última capa (Ver Figs. 5 - 8) Colocación de la estructura porta cabeza excitadora, con el fin de asegurar la verticalidad de la cabeza excitadora durante el montaje de las probetas. 9) Colocación de la cabeza excitadora apoyada sobre la muestra y firmemente asegurada a la estructura portadora. 10) Remoción del vacío aplicado entre la membrana de látex y el molde tripartido e inundación de la probeta. Debido a que, en general, los equipos convencionales de columna resonante adolecen de drenaje superior a través de la cabeza excitadora, lo cual dificulta la saturación de las probetas por la imposibilidad de remover el aire atrapado tanto en el sistema como en el interior de la muestra, en esta investigación se le dio solución a este problema mediante el flujo lento ascendente, originado por acción de la gravedad. El flujo lento se mantiene hasta el momento en que empieza el goteo a través de la interface formada por la muestra y la cabeza excitadora (Ver Figs. 6. 11) Remoción del elevador de molde y sujeción de la membrana de látex tanto a la cabeza excitadora como

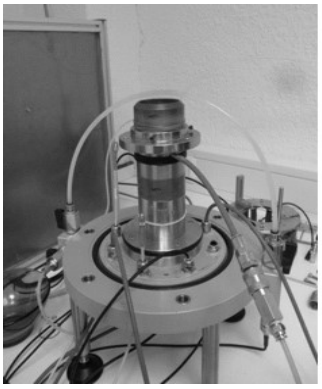
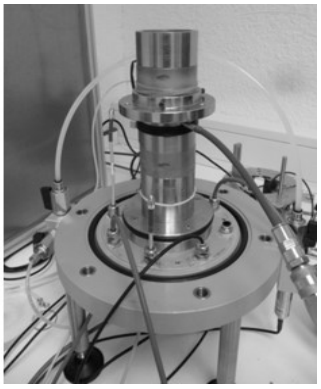



Figura 4. Fabricación de muestras cilíndricas de arena mediante molde tripartido y compactación dinámica (pasos 1-4).
Fuente: Elaboración propia.

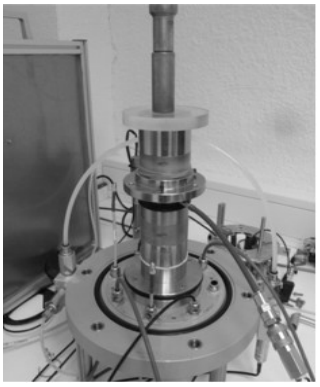
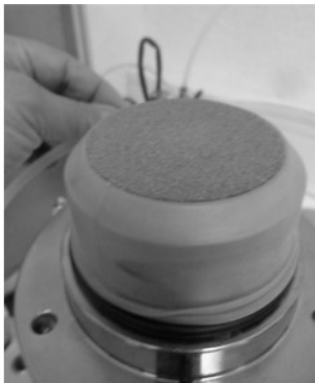



Figura 5. Compactación de la última capa de material para garantizar la densidad predefinida (pasos 5-7).
Fuente: Elaboración propia.

a la base inferior del equipo de CR, mediante un par de sellos "O'-Rings". 12) Aplicación de vacío al interior de la probeta. El objetivo de aplicar vacío, a través del drenaje inferior, es garantizar la estabilidad de la probeta mientras se completa el proceso de montaje del equipo. 13) Remoción de todos los accesorios utilizados para la fabricación de las probetas (Ver Figs. 7. 14) Colocación de la célula triaxial interior que sirve de soporte al sistema excitador. 15) Instalación del sistema excitador. 16) Instalación de los transductores de proximidad y del LVDT destinado a medir las deformaciones axiales. 17) Conexionado de los transductores de presión y cambio volumétrico. 18) Finalmente, montaje de la célula triaxial exterior (Ver Fig. 8).

6. Resultados y análisis

Los resultados de las 72 pruebas de columna resonante se incluyen en la Tabla 3. La información contenida en la Tabla 3 permite evaluar, para cada uno de los materiales estudiados (ACS y LAD), la influencia de factores como la presión efectiva de consolidación (σ'_c) y la deformación angular unitaria (γ) en la determinación del módulo de rigidez al cortante (G).

Además de presentar un análisis cualitativo de los resultados, el análisis está orientado hacia la obtención de funciones empíricas que permitan reproducir los resultados

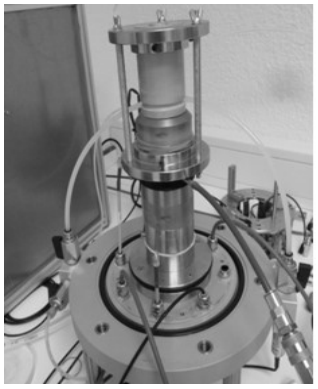



Figura 6. Montaje de la cabeza excitadora sobre la muestra de suelo e inundación de la misma (pasos 8-10).
Fuente: Elaboración propia.

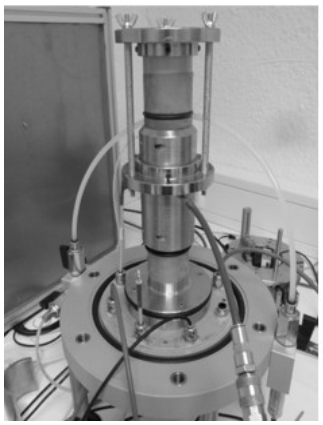
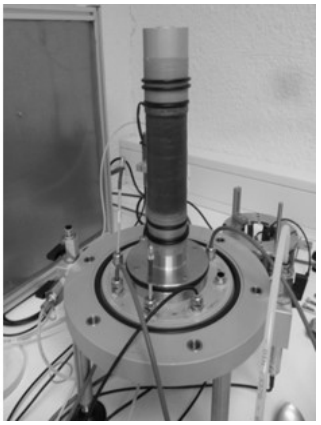



Figura 7. Sujeción de la membrana de látex a la base inferior del equipo y a la cabeza excitadora mediante "o-rings" y remoción de todos los accesorios utilizados (pasos 11-13).
Fuente: Elaboración propia.




Figura 8. Montaje de la célula triaxial interior y del sistema excitador. Instalación y conexionado de todos los transductores y montaje de la célula triaxial exterior (pasos 14-18).
Fuente: Elaboración propia.

experimentales obtenidos a través de las pruebas de columna resonante. No obstante, conviene resaltar que estos resultados son válidos fundamentalmente dentro de los rangos de deformación angular experimentados por cada uno de los

Tabla 3.
Resultados de los ensayos de CR en los materiales ACS y LAD.

σ'_c	E_t	ACS			LAD		
		Fr	G	γ	Fr	G	γ
kPa	Voltios	Hz	MPa	%	Hz	MPa	%
50	0.025	87.2	66.6	0.004	50	22.4	0.004
	0.05	84.9	63.2	0.006	50	22.4	0.008
	0.1	81	57.5	0.009	47	19.8	0.017
	0.2	77.5	52.7	0.014	43.3	16.9	0.033
	0.4	69.3	42.2	0.023	38.3	13.2	0.065
	0.8	56.7	28.3	0.048	27.2	6.65	0.148
100	0.025	91.4	75.3	0.003	64.5	38.1	0.003
	0.05	91	74.7	0.005	61.2	34.3	0.006
	0.1	88.1	70	0.009	58.7	31.5	0.011
	0.2	83.5	62.8	0.014	52.7	25.4	0.024
	0.4	77.3	53.9	0.022	47.7	20.9	0.048
	0.8	67.5	41.2	0.039	41.1	15.5	0.096
150	0.025	99.9	91.8	0.003	71.9	47.8	0.004
	0.05	97.8	87.9	0.005	69.7	45.1	0.008
	0.1	96.5	85.6	0.008	67.3	41.9	0.013
	0.2	92.2	78.2	0.013	63.9	37.8	0.022
	0.4	85.9	67.8	0.021	59.5	32.8	0.038
	0.8	77.6	55.4	0.035	52	25	0.064
200	0.025	108	109	0.003	76.8	55	0.004
	0.05	106	105	0.005	76.9	55.1	0.008
	0.1	105	102	0.008	74.7	52.1	0.013
	0.2	100	94	0.013	71.6	47.8	0.022
	0.4	94.2	82.7	0.020	67.2	42.1	0.037
	0.8	85.9	68.9	0.033	61.8	35.7	0.062
250	0.025	113	120	0.003	84.1	66.4	0.004
	0.05	112	119	0.005	82.3	63.5	0.007
	0.1	110	114	0.008	81.2	61.8	0.013
	0.2	106	106	0.012	78.3	57.5	0.022
	0.4	100	94.1	0.019	74.5	52	0.036
	0.8	92.2	79.9	0.031	69	44.6	0.058
300	0.025	118	132	0.003	88.4	73.5	0.004
	0.05	117	128	0.005	89.6	75.5	0.007
	0.1	115	125	0.007	87.5	72	0.012
	0.2	112	117	0.011	86	69.6	0.021
	0.4	106	106	0.018	82	63.2	0.034
	0.8	98.3	91	0.028	76.1	54.4	0.050

Fuente: Elaboración propia.

materiales (de 0.003 a 0.048% en el caso de las ACS y de 0.003 a 0.148% en el caso de los LAD). Por lo tanto, si se quiere estimar el comportamiento dinámico de los materiales ACS y LAD bajo condiciones de ensayo que están fuera de los rangos de deformación mencionados previamente, es necesario calibrar nuevamente las funciones empíricas en un plan de ensayos complementario al de esta investigación.

6.1. Módulo de corte vs deformación angular

Como se ilustra en la Fig. 9 la deformación angular experimentada por los materiales ACS y LAD se incrementa en la medida en que aumenta el nivel de excitación torsional [22]. Los resultados siguen una trayectoria de tipo potencial con un coeficiente de correlación cercano a uno ($R^2 \approx 1$). Asimismo, puede observarse que independientemente del valor de la excitación torsional, la deformación angular disminuye en la media en que aumenta la presión efectiva de consolidación.

Los valores de deformación angular representados en la Fig. 10 corresponden a la deformación angular media (γ_m) evaluada como $2\gamma_{máx}/3$; donde $\gamma_{máx}$ es la deformación angular máxima medida por el acelerómetro.

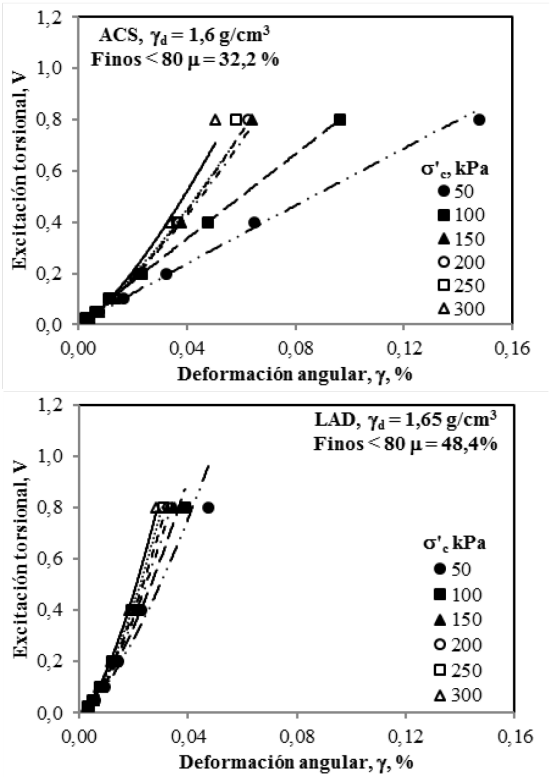


Figura 9. Tendencias de variación de γ en función del nivel de excitación torsional. para diferentes valores de σ'_c y tipos de material.
Fuente: Elaboración propia.

La Fig. 10 ilustra, para cada uno de los materiales, las tendencias de variación del módulo de rigidez al cortante (G) en función de la deformación angular (γ) bajo diferentes presiones efectivas de consolidación (σ'_c). De la Fig. 10 se deduce que independientemente del tipo de material estudiado y de la magnitud σ'_c el valor G tiende a disminuir con el incremento de γ. Por ejemplo, para un valor de σ'_c = 100 kPa, la degradación de G en los materiales ACS y LAD es del orden del 28% y 48%, respectivamente, cuando γ se incrementa del 0.003% al 0.04%. En el material ACS, la influencia del nivel de deformación en la degradación de G, disminuye con la reducción de la presión efectiva de consolidación.

Por otra parte, teniendo en cuenta que el material ACS es el constitutivo del material LAD y que ambos materiales fueron ensayados bajo iguales condiciones de excitación torsional (nivel de deformación) y de presión efectiva de consolidación, se encontró que el incremento del contenido de finos y de la densidad seca influyen significativamente en la evaluación de G; puesto que a iguales valores de γ y σ'_c, el valor de G en el material LAD resulta ser casi el doble del correspondiente al material ACS. No obstante, la tasa de degradación de G es mucho más alta en los LAD.

Independientemente del material estudiado y de la presión efectiva de consolidación, la degradación de G en función de γ sigue aproximadamente una tendencia de tipo exponencial con muy baja dispersión. Lo anterior pone en evidencia la no linealidad del comportamiento tensión – deformación dentro del rango de deformaciones angulares experimentado por cada

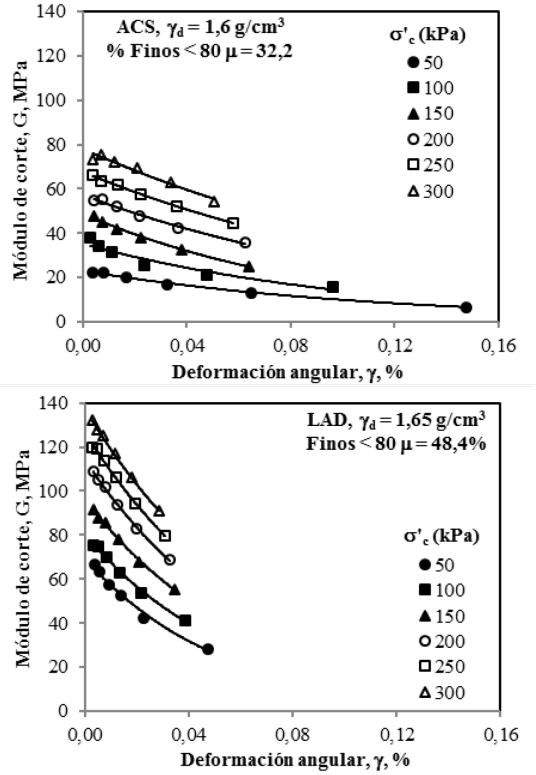


Figura 10. Tendencias de variación de G en función de γ para diferentes presiones efectivas de consolidación y tipos de material.
Fuente: Elaboración propia.

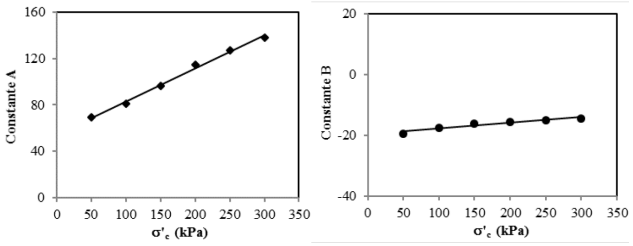


Figura 11. Variación de las constantes empíricas A y B en función de la presión efectiva de consolidación para el material LAD.
Fuente: Elaboración propia.

uno de los materiales. Con base en la deducción anterior, para cada valor de σ'$_c$, es posible establecer una relación exponencial entre el módulo de corte y la deformación angular (γ) de la forma:

$$G = Ae^{B\gamma} \quad (1)$$

Donde G es el módulo de corte en MPa, γ es el nivel de deformación en porcentaje y A y B son constantes empíricas que dependen de σ'$_c$. Debido a que las tendencias de variación de las constantes A y B en función de σ'$_c$ son similares en ambos materiales, en la Fig. 11 se muestran únicamente las tendencias correspondientes al material LAD. De esta manera, de la Fig. 11 se deduce que la variación de las constantes A y B en función de σ'$_c$ siguen aproximadamente tendencias lineales que se pueden expresar como:

Tabla 4.
Constantes empíricas que correlacionan G y γ para diferentes presiones efectivas de consolidación

Material	C	D	E	F
ACS	0.22	13.6	0.01	-10.07
LAD	0.28	55.0	0.02	-20.0

Fuente: Elaboración propia.

$$A = C\sigma'_c + D \quad (2)$$

$$B = E\sigma'_c + F \quad (3)$$

Al reemplazar las eq. (2)-(3) en la eq. (1) se tiene:

$$G = (C\sigma'_c + D)e^{(E\sigma'_c + F)\gamma} \quad (4)$$

Donde σ'$_c$ está en kPa; γ en porcentaje y C, D, E y F son las constantes que resultan de las regresiones lineales. En la Tabla 4 se incluyen los valores de las constantes para los diferentes materiales.

6.2. Influencia de σ'$_c$ en el módulo de corte

Con el fin de evaluar la variación del módulo de corte en función de la presión efectiva de consolidación, para diferentes niveles de deformación angular, se procedió a calcular G a partir de la eq. (1) mediante la sustitución de las constantes A y B por los valores correspondientes a cada estado de confinamiento y tipo de material. La Fig. 12 representa los valores obtenidos de G en función de σ'$_c$, para diferentes niveles de deformación angular.

De la Fig. 12 se deduce que independientemente del tipo de material ensayado y del nivel de deformación angular G resulta severamente afectado por la reducción de σ'$_c$. La influencia del incremento de γ en la degradación de G, tiende a ser más importante para valores altos de la presión efectiva de consolidación.

Independientemente del tipo de material y del nivel de deformación angular la variación de G en función de σ'$_c$ sigue aproximadamente una tendencia de tipo lineal con muy baja dispersión. Lo anterior se puede expresar como:

$$G = K\sigma'_c + L \quad (5)$$

Donde G es el módulo de corte en MPa; σ'$_c$ la presión efectiva de consolidación en kPa; K y L son constantes empíricas que dependen de la deformación angular. Debido a que las tendencias de variación de las constantes K y L en función de γ son similares en los dos materiales estudiados, en la Fig. 13 se incluyen únicamente las tendencias correspondientes al material LAD.

De la Fig. 13 se deduce que la variación de las constantes K y L en función de γ sigue aproximadamente tendencias lineales [23] y se pueden expresar como:

$$K = M\gamma + N \quad (6)$$

$$L = O\gamma + P \quad (7)$$

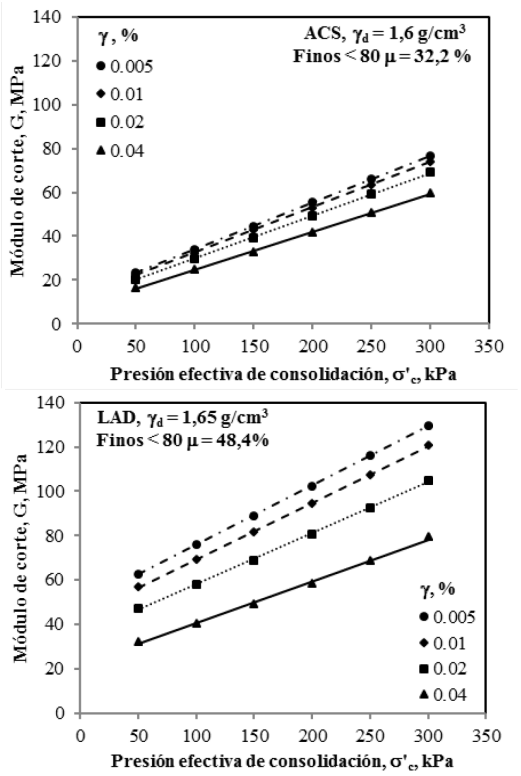


Figura 12. Tendencias de variación de G en función de σ'$_c$ para diferentes niveles de deformación angular y tipos de material.
Fuente: Elaboración propia.

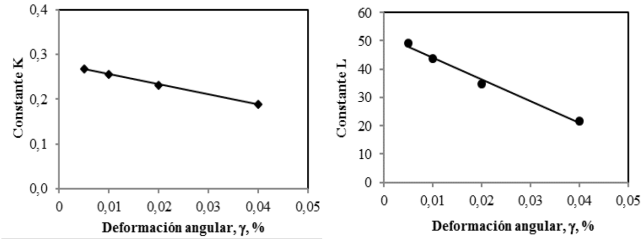


Figura 13. Variación de las constantes empíricas K y L en función de la presión efectiva de consolidación para el material LAD.
Fuente: Elaboración propia.

Al sustituir las eq. (6)-(7) en la eq (5) se tiene:

$$G = (M\gamma + N)\sigma'_c + O\gamma + P \quad (8)$$

Donde γ está en %; G en MPa; σ'$_c$ en kPa; M, N, O y P son las constantes que resultan de las regresiones lineales. En la Tabla 5 se incluyen los valores de las constantes obtenidas para los diferentes materiales.

7. Conclusiones

Las conclusiones derivadas de este estudio son producto de un amplio programa experimental realizado con materiales provenientes de los depósitos de estériles de las minas de Riotinto, ubicadas en la Provincia de Huelva – España. Se realizaron 72 ensayos de columna resonante sobre muestras reconstituidas de los materiales ACS y LAD, con el fin de estudiar la influencia de parámetros como la presión efectiva de consolidación (σ'$_c$) y el nivel de deformación angular (γ) en el módulo de rigidez al cortante (G) bajo deformaciones angulares que varían entre 0.003 y 0.148% y presiones efectivas de consolidación 50, 100, 150, 200, 250 y 300 kPa. Las conclusiones derivadas de la investigación son las siguientes:

1. A pesar que los materiales estudiados tienen un contenido de finos (< 80μ) alto, variable entre el 32% y el 48%, las arenas Cerro Salomón (ACS) y los lodos de alta densidad (LAD) se clasifican como una arena de grano muy fino a medio. Lo anterior en razón que los finos menores de 400μ no son plásticos; seguramente debido a que estos son generados durante el proceso de explotación de las minas y no como consecuencia de la alteración o la meteorización de la roca madre. Los materiales investigados se caracterizan por tener una gravedad específica alta y variable entre 2.99 y 3.02, lo cual puede deberse a la presencia dominante de elementos pesados como hierro, silicio y azufre.
2. Se evidenció que, sin importar el tipo de material y el valor de la presión efectiva de consolidación, la frecuencia de resonancia y el módulo de rigidez al cortante tienden a disminuir en la medida que se incrementa el nivel de excitación torsional (nivel de deformación).
3. Se encontró que para los dos tipos de materiales y las diferentes presiones efectivas de consolidación, la variación de la frecuencia de resonancia y del módulo de rigidez en función de la deformación angular describen una tendencia de variación de tipo exponencial con coeficiente de correlación (R^2) prácticamente igual a la unidad.
4. Independientemente del tipo de material estudiado y del nivel de deformación angular, la variación de G en función de σ'$_c$, sigue aproximadamente una tendencia de tipo lineal con muy baja dispersión.
5. Mediante la combinación de regresiones matemáticas es posible proponer funciones empíricas para el módulo de corte en función de la presión efectiva de consolidación y la deformación angular.

Tabla 5.
Constantes empíricas que correlacionan G y σ'$_c$ para diferentes niveles de deformación angular

Material	M	N	O	P
ACS	-1.16	0.22	-144.43	13.29
LAD	-2.25	0.28	-770.76	51.88

Fuente: Elaboración propia.

Agradecimientos

Los autores expresan sus agradecimientos a la Fundación José Entrecanales Ibarra y a EPTISA Servicios de Ingeniería por subvencionar la investigación.

Referencias

[1] ICOLD. Tailing dams - Risk of dangerous occurrences: lessons learnt from practical experiences. Bulletin 121. Paris. 2001.
[2] Azam, S. and Li, Q.R., Tailings dam failures: a review of the last one hundred years. Geotechnical News. 28(4), pp. 50-53, 2010.

[3] Hu, L., Wu. H., Zhang, L., Zhang, P. and Wen, Q., Geotechnical properties of mine tailings. Journal of Materials in Civil Engineering. 29(2), 2017. DOI: 10.1061/(ASCE)MT.1943-5533.0001736
[4] Kramer, S., Geotechnical earthquake engineering. New Jersey. Prentice-Hall Inc, 653 P., 1996.
[5] Camacho-Tauta, J., Molina-Gómez, F.A. y Reyes-Ortiz, Ó.J., Ensayo combinado columna resonante - bender elements para evaluar la rigidez del suelo. En XIV Congreso Colombiano de Geotecnia (8 P). Bogotá: SCG, 2014.
[6] Ishimato, M. and Iida, K., Determination of elastic constants of soils by means of vibration methods. Bulletin of the Earthquake Research Institute. Tokyo Imperial University, 15, 67 P, 1937.
[7] Iida, K., The velocity of elastic waves in sand. Bulletin of the Earthquake Research Institute. Tokyo Imperial University, 16, pp. 131-144, 1938.
[8] Iida, K., On the elastic properties of soil particularly in relation to its water contents. Bulletin of the Earthquake Research Institute. Tokyo Imperial University, 18, pp. 675-690, 1940.
[9] Bisshopp, K.E., Forced torsional vibration of system with distributed mass and internal and external damping. Transactions of the ASME, 8-12, 1959.
[10] Wilson, S.D. and Dietrich, R.J., Effect of consolidation pressure on elastic and strength properties of clay. Proceedings of the Research Conference on Shear Strength of Cohesive Soils. ASCE, 1960, pp. 419-435.
[11] Hall, J.R. and Richard, F.E., Discussion of elastic wave energy in granular soils. Journal of the Soil Mechanics and Foundations Division. ASCE, 89(SM6), pp. 27-56, 1963.
[12] Drnevich, V.P., Hall, J.R. and Richart, F.E., Large amplitude vibration effects on the shear modulus of sand. University of Michigan, Report to Waterways Experiment Station. Corps of Engineers. U.S. Army Contact DA-22-079-Eng-340, 1966.
[13] Drnevich, V.P., Hall, J.R. and Richart, F.E., Effect of amplitude of vibration on the shear modulus of sand. Proceeding of the International Symposium on Wave Propagation and Dynamic Properties of Earth Materials. Albuquerque. USA, 1967, pp 189-199.
[14] Drnevich, V.P., Hardin, B.O. and Shippy, D.J., Modulus and damping of soils by the resonant-column method. Dynamic Geotechnical Testing. ASTM STP 654, pp. 91-125, 1978. DOI: 10.1520/STP35673S
[15] Hardin, B.O. and Drnevich, V.P., Shear modulus and damping in soils: measurement and parameter effects. Journal of the Soil Mechanics and Foundation. ASCE, 98(SM6). pp. 603-624, 1972a.
[16] Hardin, B.O. and Drnevich, V.P., Shear modulus and damping in soils: design equation and curves. Journal of the Soil Mechanics and Foundation. ASCE, 98(SM7), pp. 667-692, 1972b.
[17] Krizek, R.J., Maclean, F.G. and Giger, M.W., Effect of particle characteristics on wave velocity. Journal of the Soil Mechanics and Foundations Division. ASCE, 100(1), pp 89-94, 1974.
[18] Kuribayashi, E., Iwasaki, T. and Tatsuoka, F., Effects of stress conditions on dynamic properties of sand. Bulletin Intl. of Seismology and Earthquake Engineering, 12, pp. 117-130, 1974.
[19] Djoenaidi, W.J., A compendium of soil properties and correlations. University of Sydney, Autralian, 1985.
[20] Bardet, J.P., Experimental soil mechanics. Prentice Hall. 1997.
[21] Martínez, E., Propiedades geotécnicas de los estériles mineros de las minas de Riotinto. Huelva – España. PhD. Tesis, Escuela Técnica Superior de Ingenieros de Caminos, Canales y Puertos, Universidad Politécnica de Madrid, España, 2017.
[22] Camacho-Tauta, J., Ali, H., Cascante, G. and Viana da Fonseca, A., Experimental and numerical observations of the frequency-domain method in bender-element testing. Journal of Geotechnical and Geoenvironmental Engineering, 143(2), pp. 4016096, 2017. DOI:10.1061/(ASCE)GT.1943-5606.0001603
[23] Patiño, H., Martínez, E., González, J. and Soriano, A., Shear modulus of a saturated granular soil derived from resonant column tests. Acta Geotechnica Slovenica, [online]. 33(2), pp. 33-45, 2017. Available at: http://fgserver3.fg.um.si/journal-ags/pdfs/AGS_2017-2_article_3.pdf

E. Martínez-Rojas, recibió el título de Ing, Civil en 2008 en la Universidad Católica de Colombia, el título de MSc. en Ingeniería Geológica y Geotecnia en 2013 en la Universidad Complutense de Madrid, España, y el título de Dra. por la Universidad Politécnica de Madrid, España, en 2017 dentro del Programa Oficial de Doctorado en Ingeniería de Estructuras, Cimentaciones y Materiales. Actualmente, es docente investigador de la Universidad Piloto de Colombia.
ORCID: 0000-0002-5092-5920

F.A. Molina-Gómez, recibió el título de Ing. Civil en 2014 en la Universidad Militar Nueva Granada, Colombia, el título de Esp. en Estadística Aplicada en 2017 en la Fundación Universitaria Los Libertadores, Colombia y el título MSc. en Ingeniería Civil con énfasis en Geotecnia en 2016 en la Universidad de los Andes, Colombia. Trabajó como joven investigador y director académico de los programas de postgrado en la facultad de ingeniería de la Universidad Militar Nueva Granada.
ORCID: 0000-0002-8831-0315

J.C. Ruge, recibió el título de Ing. Civil en 2002 de la Universidad Francisco de Paula Santander (UFPS), Colombia, el título de MSc. en Ingeniería Civil con énfasis en Geotecnia en 2005 de la Universidad de los Andes, Colombia, y el título de Dr. en Geotecnia en 2014 de la Universidad de Brasilia (UnB), Brasil. Anteriormente, fue investigador postdoctoral en el Departamento Civil y Agrícola de la Universidad Nacional de Colombia. Actualmente, es profesor asistente de la Universidad Militar Nueva Granada, Bogotá D.C., Colombia.
ORCID: 0000-0002-9100-6058

UNIVERSIDAD NACIONAL DE COLOMBIA
SEDE MEDELLÍN
FACULTAD DE MINAS

Área Curricular de Ingeniería Civil

Oferta de Posgrados

Especialización en Vías y Transportes
Especialización en Estructuras
Maestría en Ingeniería - Infraestructura y Sistemas de Transporte
Maestría en Ingeniería – Geotecnia
Doctorado en Ingeniería - Ingeniería Civil

Mayor información:

E-mail: asisacic_med@unal.edu.co
Teléfono: (57-4) 425 5172

UNIVERSIDAD NACIONAL DE COLOMBIA
SEDE MEDELLÍN
FACULTAD DE MINAS



DYNA
http://dyna.medellin.unal.edu.co/

Assessment strategies for the integral management of waste electrical and electronic equipment-WEEE

Johan Manuel Redondo [a], Danny Ibarra-Vega [b], Liliana Monroy [c] & Jorge Bermúdez [c]

[a] *Facultad de Ciencias Económicas y Administrativas, Universidad Católica de Colombia, Bogotá, Colombia jmredondo@ucatolica.edu.co*
[b.] *Universidad Nacional de Colombia, sede Manizales, Colombia. ingdanny09@hotmail.com*
[c] *Escuela de Posgrados, Universidad Sergio Arboleda, Bogotá, Colombia. lilikmon10@hotmail.com, jorgebermudez77@hotmail.com*

Received: February 13th, 2017. Received in revised form: December 13th, 2017. Accepted: February 25th, 2018

Abstract
This paper presents a model for the evaluation of strategies in the management of Waste Electrical and Electronic Equipment (WEEE). Waste represents a risk to public health and the environment, the dangerous type compounds that constitute them and the increase of their generation. In Colombia, there is a law of 1672 guidelines for the adoption of a policy that improves the management of WEEE.
This Law proposes public management objectives, of which in this article three of them were evaluated (Reduction in generation, incentive to use, promote integrated participation). For this evaluation, a model was built using the Dynamics of Systems methodology, which allowed the establishment of the socio-environmental system structure for the generation and management of WEEE. Likewise, the evaluation scenarios were defined, the first is the initial or natural state that corresponds to the system without any strategy and the second is the system with the implementation of the strategies, which were divided into two groups. One is Economic Circular Strategies, Environmental Education and Job Promotion, and the other group contains the producer's extended liability strategies, citizenship incentives and the collection rate. Model simulations and scenario comparisons showed that the first group of strategies decreased in the generation rate of WEEE. Likewise, they allowed a second group of strategies on disposition rate. Likewise, the proposed model for the management of Waste Electrical and Electronic Equipment is useful for the evaluation of waste management strategies in different scenarios.

Keywords: waste; modeling; system dynamics; public management.

Evaluación de estrategias para la gestión integral de residuos de aparatos eléctricos y electrónicos

Resumen
Este artículo presenta un modelo para la evaluación de estrategias en la gestión de Residuos de Aparatos Eléctricos y Electrónicos (RAEE). Estos residuos representan un riesgo para la salud pública y para el medio ambiente, por los compuestos de tipo peligroso que los constituyen y el aumento de su generación. En Colombia existe desde 2013 la ley 1672 lineamientos para la adopción de una política que mejore la gestión de los RAEE. Esta Ley propone objetivos gestión pública, de los cuales en este artículo se evaluaron tres de ellos (Reducción en la generación, incentivo al aprovechamiento, promover la participación integrada). Para esta evaluación, se construyó un modelo utilizando la metodología de Dinámica de Sistemas, la cual permitió establecer la estructura del sistema socio-ambiental de generación y manejo de los RAEE. Así mismo, fueron definidos dos escenarios de evaluación, el primero es el estado inicial o natural que corresponde al sistema sin ninguna estrategia y el segundo es el sistema con la implementación de las estrategias, las cuales se dividieron en dos grupos. Uno es Estrategias de economía circular, educación ambiental y fomento de empleo, y el otro grupo contiene las estrategias de responsabilidad extendida del productor, estímulos de la ciudadanía y tarifa de recolección. Las simulaciones del modelo y comparaciones los escenarios, mostraron que el primer grupo de estrategias disminuyeron la tasa de generación de RAEE. De igual manera, permitieron evaluar segundo grupo de estrategias sobre la tasa de disposición. De igual manera El modelo propuesto para la gestión de Residuos de Aparatos Eléctricos y Electrónicos es útil, para la evaluación de estrategias de gestión de residuos en distintos escenarios.

Palabras clave: residuos; modelamiento; dinámica de sistemas; gestión pública.

How to cite: Redondo, J.M., Ibarra-Vega, D., Monroy, L. and Bermúdez, J., Evaluación de estrategias para la gestión integral de residuos de aparatos eléctricos y electrónicos. DYNA, 85(205), pp. 319-327, June, 2018.

© The author; licensee Universidad Nacional de Colombia.

1. Introducción

Uno de los problemas creados por el incremento poblacional y por las distintas actividades antrópicas impulsadas por el desarrollo económico, es la generación de residuos, de tipo sólidos, [1]. Actualmente en Colombia, en los países en desarrollo y en el mundo en general emergen nuevos residuos tales como, los Residuos de Aparatos Eléctricos y Electrónicos – RAEE. Estos son uno de los residuos que más ha amentado su tasa de generación [2, 5]. Debido al crecimiento tecnológico de la humanidad, el aumento de ingreso per cápita y las necesidades creadas de comunicaciones y dispositivos tecnológicos a precios competitivos. Cabe resaltar que el actual ciclo de vida de un teléfono celular, un computador portátil, televisores y otros productos similares, tiene un rango de entre 2 y 6 años [3]. Después de su uso estos aparatos son descartados y por lo tanto no tienen algún valor para el usuario [4]. Al ser descartado, ya es considerado un residuo sólido. Estos residuos al ser catalogados como residuos peligrosos, demandan un manejo especial, ya que pueden afectar la salud humana y el medio ambiente. Para disminuir los riesgos generados por los RAEE, los países han desarrollado políticas públicas, las cuales en su estructura proponen modelos de gestión eficiente, definen responsabilidades y obligaciones, promueven mecanismos de información, definen las fuentes de financiación y ordenan el seguimiento y la evaluación (MADS, 2013). Sin embargo la evaluación de las estrategias propuestas en las políticas representa una preocupación especial, porque a través de estas se valora la efectividad que tiene la gestión integral propuesta para RAEE [4].

En Colombia, existe una Ley (1672 de 2013) que establece los lineamientos para la adopción de una política pública de gestión integral de residuos de aparatos eléctricos y electrónicos (RAEE) generados en el territorio nacional. Sin embargo, no se cuenta con un mecanismo que permita, realizar una evaluación de la implementación de las estrategias de la política, de manera que se pueda estimar si éstas son apropiadas para la tarea que se le ha impuesto. De esta forma en este artículo se construyó un modelo que permite realizar la evaluación de estrategias de manejo en distintos escenarios, para la adopción de una política pública nacional orientada a la gestión integral de residuos de aparatos eléctricos y electrónicos.

2. Metodología

La metodología para el desarrollo del presente trabajo se dividió en cinco fases: interpretación de los tres objetivos de la política nacional de residuos de aparatos eléctricos y electrónicos RAEE. La definición de criterios a modelar, el proceso de modelado del sistema socio-natural, la definición de escenarios tendenciales y por último la definición de estrategias para la calificación del programa. Como muestra la Fig. 1.

2.1. Modelado con dinámica de sistemas

La Dinámica de Sistemas es una metodología para el análisis y resolución de problemas, desarrollada en el MIT y con amplio marco referencial [6,7,19]. En Dinámica de Sistemas, se concibe

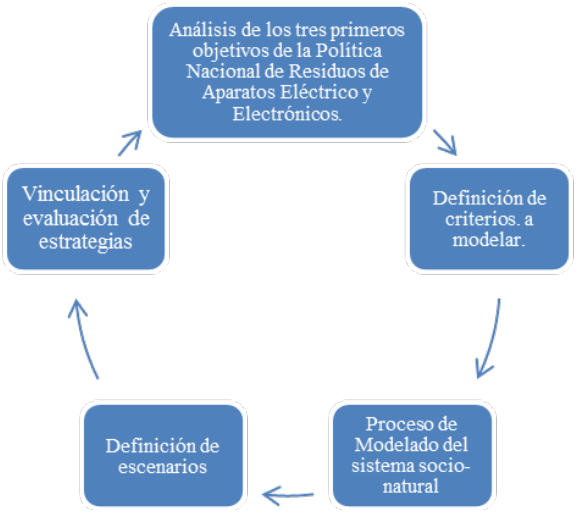


Figura 1. Metodología General.
Fuente: Los autores.

cualquier aspecto del mundo como la interacción causal entre atributos que lo describen. De esta forma, se construyen representaciones sistémicas con flechas y puntos, denominadas diagramas causales, que capturan todas las hipótesis propuestas por el modelador, desde las que se puede aprender del sistema para intervenir sobre él en el ejercicio de decisión [8,20]. El modelamiento con Dinámica de sistemas para la gestión de residuos incluyendo los RAEE, recientemente ha sido utilizado en investigaciones similares [5,9-12]. Esta consiste en 3 etapas, conceptualización del problema, Formulación del modelo y evaluación [13].

2.2. Conceptualización del problema

Para construir el modelo y basándose en la interpretación de los tres primeros objetivos propuestos en la Política Nacional de Residuos de Aparatos Eléctricos y Electrónicos (RAEE) se partió con la construcción de las hipótesis (H) dinámicas que corresponde a cada uno de los objetivos:

H1: Si aumenta el ciclo de vida de los aparatos eléctricos y electrónicos – AEE y si además cambian los hábitos de consumo, entonces disminuirá la producción de RAEE.

H2: Los riegos sobre la salud humana y el medio ambiente disminuyen cuando aumenta la integración de los diferentes actores en la gestión de RAEE.

H3: Si aumenta el aprovechamiento de los distintos materiales que contiene los RAEE (reciclaje), se generan nuevos puestos de trabajo, aumentando el Producto Interno Bruto. Así mismo, disminuye la extracción de materia primas vírgenes. De esta forma se conceptualizó el problema se obtuvo el siguiente diagrama causal como base.

2.3. Definición de criterios, escenarios, estrategias y modelado del sistema socio-natural de RAEE

Con base en la revisión bibliográfica caracterizamos y determinamos la estructura del sistema socio-natural para los residuos de aparatos eléctricos y electrónicos (RAEE). Consecutivamente y a partir del entendimiento de dicha

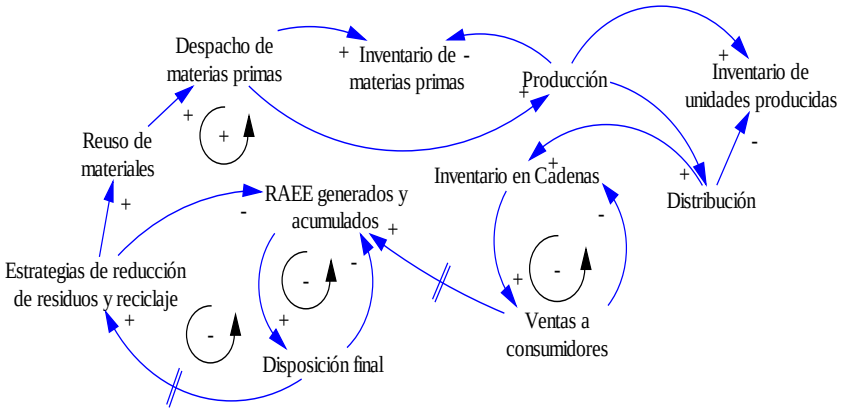


Figura 2. Diagrama Causal general.
Fuente: Los autores.

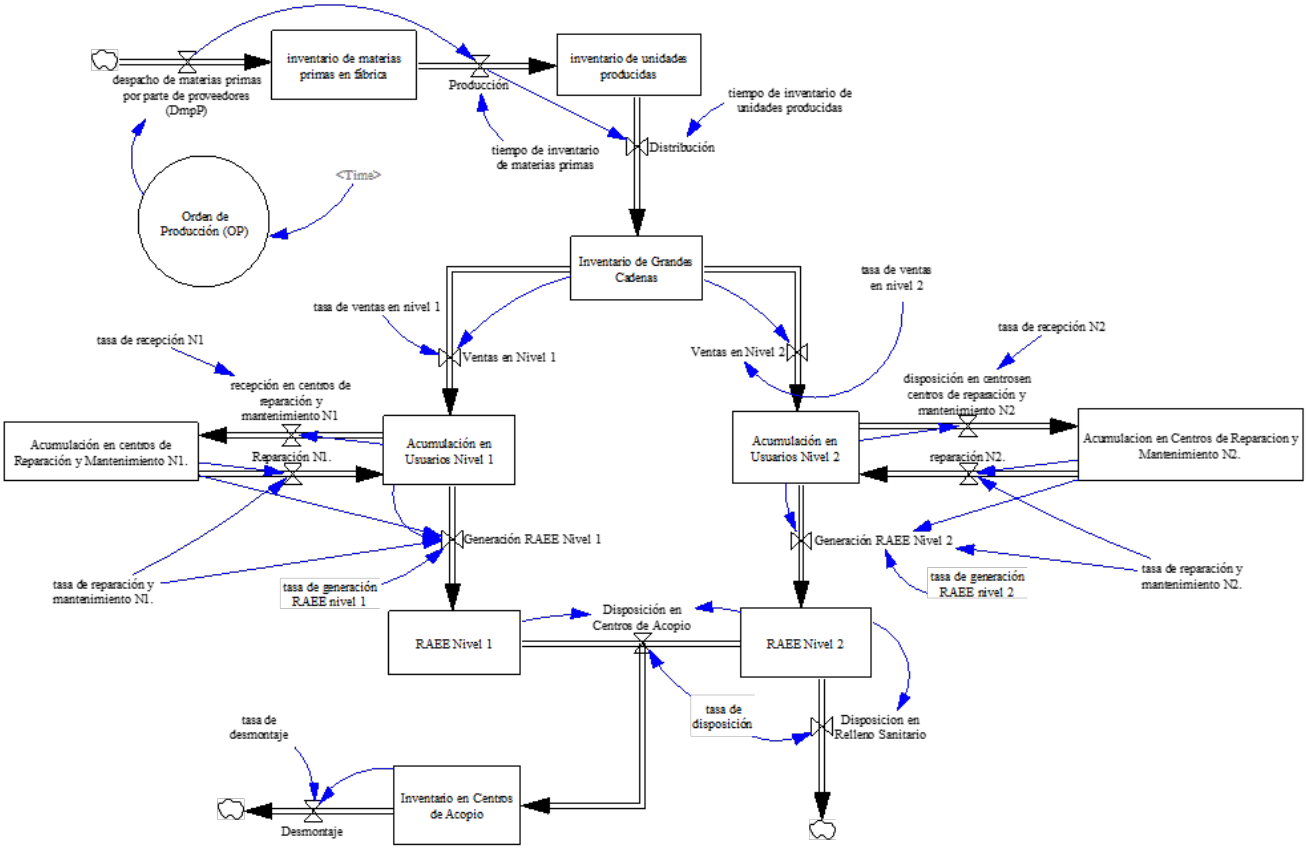


Figura 3. Diagrama de Niveles y Flujos del Modelo propuesto.
Fuente: Los autores.

Para la simulación del modelo desarrollado, utilizamos el software libre Vensim Ple. El período de simulación del modelo fue de 30 días, teniendo en cuenta que la producción de RAEE es diaria. El método de integración numérica utilizado para la generación de las trayectorias del sistema fue el método Runge-Kutta 4 automático.

Previo a la simulación definimos dos escenarios, los cuales siempre utilizamos en todas las simulaciones y que permitieron comparar el comportamiento del sistema socio-ambiental para RAEE. El primero, corresponde a un escenario en el que el factor o factores que determinan las diferentes estrategias tienen un valor igual a cero, es decir, representa el comportamiento inicial o actual del sistema socio-ambiental de RAEE y el segundo corresponde a escenarios futuros en los cuales los factores tienen valores mayores a cero y cercanos a 1 (como valor máximo).

Tabla 1.
Ecuaciones del modelo.

Ecuaciones del Modelo			
Ecuaciones de Nivel			
Variables	**Sigla**	**Unidad**	**Ecuación**
Inventario de materias primas en fabrica	$IMPF$	Ton	$IMPF = DmpP - P$
Inventario de unidades producidas	IUP	Ton	$IUP = P - D$
Inventario de grandes cadenas	IGC	Ton	$IGC = D - Vn1 - Vn2$
Acumulación en usuarios nivel 1	$AUn1$	Ton	$AUn1 = Vn1 - GRn1$
Acumulación en centros de Reparación y Mantenimiento Nivel 1	$(AcrmN1)$	Ton	$AcrmN1 = RcrmN1 - RpN1$
Acumulación en usuarios nivel 2	$AUn2$	Ton	$AUn2 = Vn2 - GRn2$
Acumulación en centros de Reparación y Mantenimiento Nivel 2	$AcrmN2$	Ton	$AcrmN2 = RcrmN2 - RpN2$
RAEE nivel 1	$Rn1$	Ton	$Rn1 = GRn1 - DisCA$
RAEE nivel 2	$Rn2$	Ton	$Rn2 = GRn2 - DisRS - DisCA$
Inventario en centros de acopio	ICA	Ton	$ICA = DisCA - Des$
Despacho de materias primas por parte de proveedores	$DmpP$	Ton/mes	$DmpP = OP$
Producción	P	Ton/mes	$P = DELAYFIXED(DmpP, tIMP)$
Distribución	D	Ton/mes	$D = DELAYFIXED(P, tIUP)$
Ventas Nivel 1	$Vn1$	Ton/mes	$Vn1 = TVn1 * IGC$
Ventas Nivel 2	$Vn2$	Ton/mes	$Vn2 = TVn2 * IGC$
Recepción en Centros de Reparación y Mantenimiento Nivel 1	$RcrmN1$	Ton/mes	$RcrmN1 = TrcN1 * Aun1$
Reparación Nivel 1	$RpN1$	Ton/mes	$RpN1 = TrmN1 * AcrmN1$
Recepción en Centros de Reparación y Mantenimiento Nivel 2	$RcrmN2$	Ton/mes	$RcrmN2 = TrcN2 * Aun2$
Reparación Nivel 2	$RpN2$	Ton/mes	$RpN2 = TrmN2 * AcrmN2$
Generación RAEE Nivel 1	$GRn1$	Ton/mes	$GRn1 = TGRn1 * AUn1$
Generación RAEE Nivel 2	$GRn2$	Ton/mes	$GRn2 = TGRn2 \cdot AUn2$
Disposición en centro de acopio	$DisCA$	Ton/mes	$DisCA = Rn1 + (1 - TDis) * Rn2$
Disposición en relleno sanitario	$DisRS$	Ton/mes	$DisRS = TDis * Rn2$
Desmontaje	Des	Ton/mes	$Des = TDes * ICA$
Variables Auxiliares			
Orden de Producción	OP	Ton/mes	$Tiempo$
Tasa de disposición:	(TD)	Ton/mes	TD=

Fuente: Los autores.

Tabla 2.
Parámetros del modelo.

Parámetros	Sigla	Unidad	Condición
Tiempo de inventario de materias primas	$tIMP$	$meses^{-1}$	0,5
Tiempo de inventario de unidades producidas	$tIUP$	$meses^{-1}$	0,5
Tasa de ventas de nivel 1	$TVn1$	$meses^{-1}$	0,85
Tasa de ventas de nivel 2	$TVn2$	$meses^{-1}$	0,99
Tasa de recepción nivel 1	$TrcN1$	$meses^{-1}$	0,005
Tasa de reparación y mantenimiento nivel 1	$TrmN1$	$meses^{-1}$	0,05
Tasa de recepción nivel 2	$TrcN2$	$meses^{-1}$	0,005
Tasa de reparación y mantenimiento nivel 2	$TrmN2$	$meses^{-1}$	0,5
Tasa de disposición	$TDis$	$meses^{-1}$	0,15
Tasa de Generación de RAEE nivel 1	$TGRn1$	Ton/mes	0,00834
Tasa de Generación de RAEE nivel 2	$TGRn2$	Ton/mes	0,0167
Tasa de desmontaje	$TDes$	Ton/mes	0,02

Fuente: Los autores.

3. Resultados y discusiones de la evaluación de estrategias

Se definieron seis estrategias las cuales fueron seleccionadas, basadas en elementos teóricos encontrados en la revisión bibliográfica, y divididas en dos grupos. El primero, denominadas no implementadas son estrategias propuestas por nosotros y cuya aplicación en trabajos de dinámica de sistemas relacionados con nuestro objetivo de investigación no ha sido efectuada. Este grupo de estrategias las direccionamos para que disminuyera la tasa de generación lo que nos permitió evaluar el primer objetivo de la política.

La primera estrategia denominada economía circular, muy similar a la Logística Inversa presentada en [19]. Esta estrategia tiene en cuenta un sistema de reciclaje y recolección adecuada, en el cual, se aprovechan todos los componentes de los RAEE, con el fin de incorporarlos de nuevo a la cadena productiva, contribuyendo a una gestión adecuada.

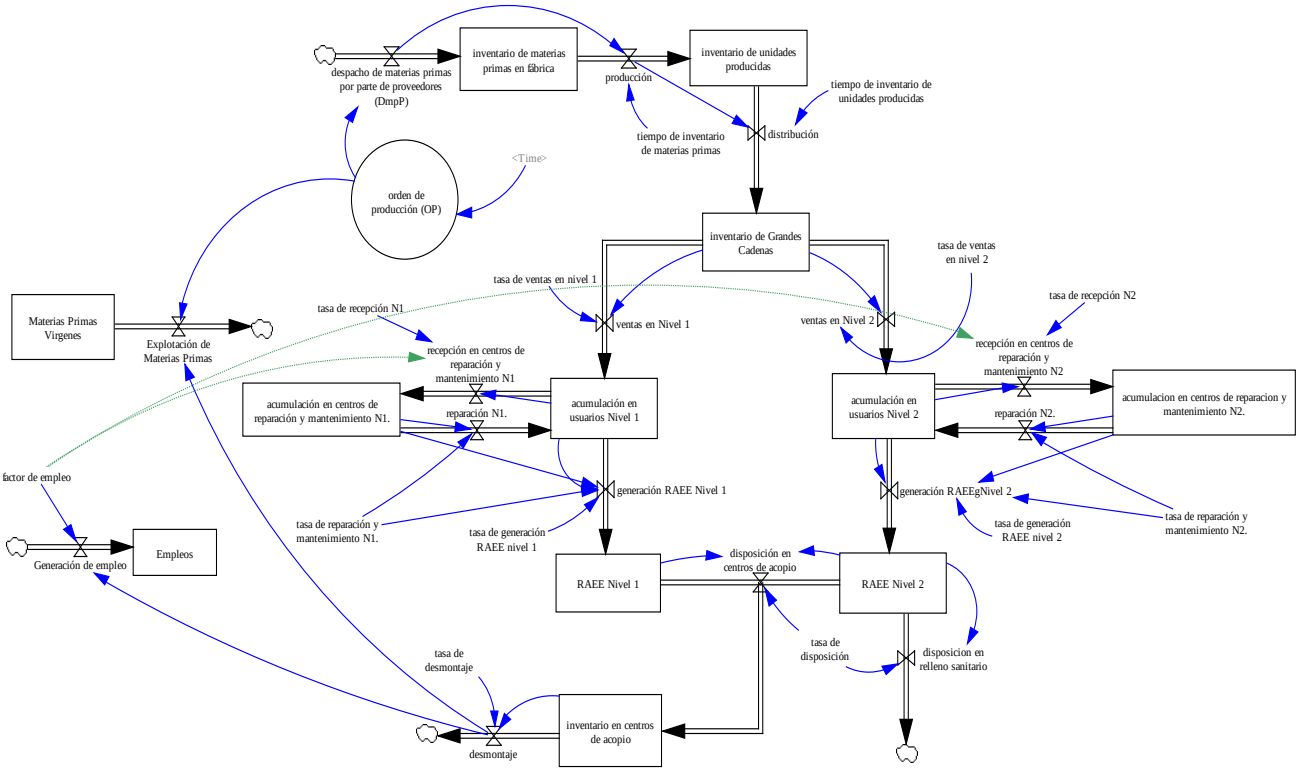


Figura 4. Diagrama de niveles y flujos del modelo propuesto con la estrategia de economía circular.
Fuente: Los autores.

Para el desarrollo de esta estrategia implementamos en el modelo, la variable de estado denominada materias primas vírgenes y su explotación para la elaboración de los Aparatos Eléctricos y Electrónicos (Fig. 4).

Después se realizaron movimientos de la tasa de desmontaje, la tasa de disposición y la tasa de generación de RAEE del sistema, hasta sus valores más altos, esperando que la curva de explotación de las materias primas vírgenes comenzara a tener pendiente negativa lo cual significaría que las materias primas vírgenes no serían explotadas lo cual solo sucedió con la tasa de desmontaje. Sin embargo, lo que encontramos fue un comportamiento contra intuitivo en el que claramente, si las ordenes de producción no cambiaban, entonces debía llevarse hasta los valores limites las tasas de generación, las tasas de desmontaje y disposición para que de esta manera se pudiera suplir la necesidad de materias primas desde lo que se había tomado de los RAEE y no de las materias primas vírgenes (vea Figs. 5 y 6).

La segunda estrategia denominada educación ambiental, (Fig. 7), consiste en una serie de campañas de concienciación que buscan cambiar hábitos poco sostenibles de la comunidad en general.

Además pretende gestionar los RAEE de una manera responsable teniendo en cuenta las consecuencias al medio ambiente, la salud pública y la calidad de vida de la población. Esta estrategia está determinada por tres factores (de educación para el consumo, de educación para aumentar la disposición y de educación para disminuir la generación de RAEE)

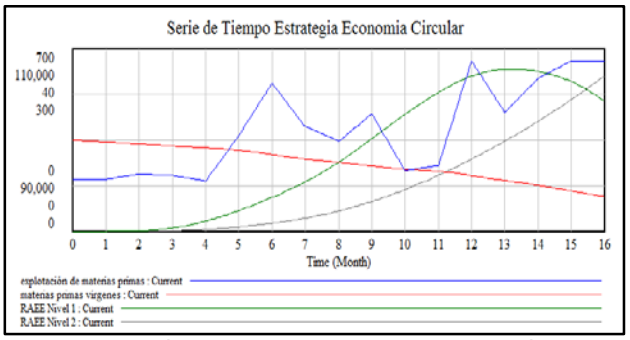


Figura 5. Simulación del modelo con la estrategia de economía circular con los valores de las tasas = 0.
Fuente: Los autores.

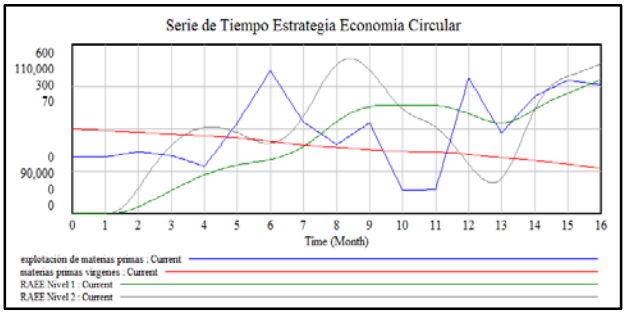


Figura 6. Simulación del modelo con la estrategia de economía circular con los valores de las tasas = 1.
Fuente: Los autores.

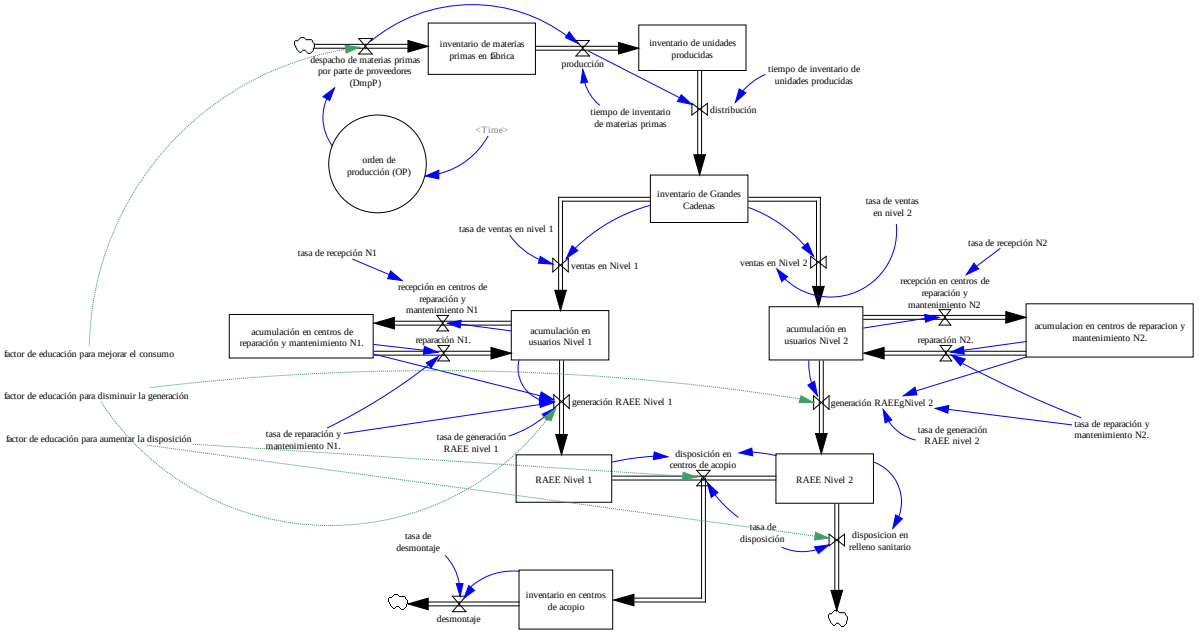


Figura 7. Diagrama de niveles y flujos del modelo propuesto con la estrategia de educación ambiental.
Fuente: Los autores.

Después de realizar la modelación y de manera general podemos determinar que a medida que aumentan los valores de los factores (hasta llegar a 1) disminuye la cantidad de RAEE generados tanto a nivel empresarial e institucional (Nivel 1) como en los hogares y usuarios (Nivel 2). También se reduce la cantidad de materias primas y por ende la cantidad de RAEE que llegan a los rellenos sanitarios (Figs. 8 y 9).

Esta estrategia claramente reduce los riesgos a la salud pública y al medio ambiente al reducir la generación de RAEE y al incrementar la correcta disposición de RAEE, pero al mismo tiempo la economía del sector industrial referente a la producción de aparatos eléctricos y electrónicos-AEE se ve afectada, al cambar los hábitos de consumos de los usuarios. Consecuencia de ese cambio podría generarse una disminución de empleos en el sector. Entonces podemos inferir que la estrategia no logra un equilibrio entre la protección ambiental, la economía y el sector social.

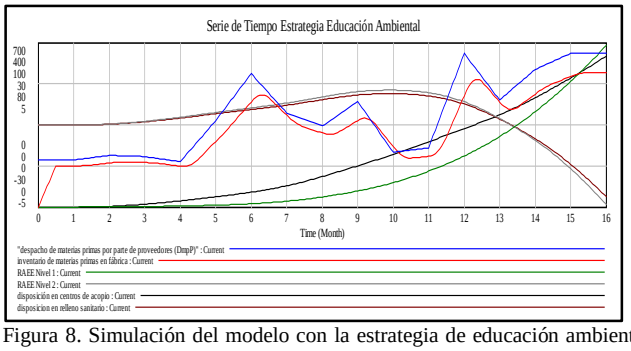


Figura 8. Simulación del modelo con la estrategia de educación ambiental con los factores de educación con valores = 0.
Fuente: Los autores.

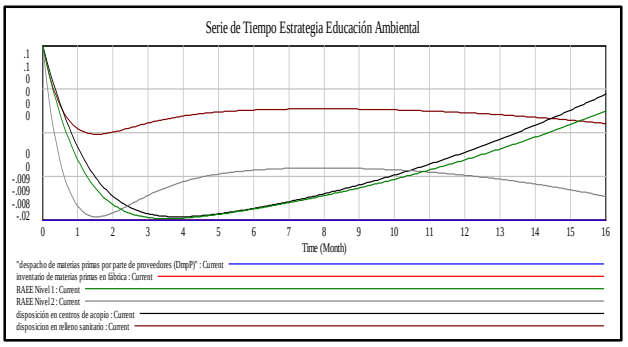


Figura 9. Simulación del modelo con la estrategia de educación ambiental, los tres factores con valores de =1.
Fuente: Los autores.

Por último, la tercera estrategia llamada fomento de empleo busca aumentar el número de empleos a partir de la prevención, reutilización, valorización y desmontaje manual, para una mejor recuperación de los componentes de RAEE. Dicha estrategia está conformada por las siguientes variables de la estructura del sistema: las ordenes de producción, producción de RAEE, generación de RAEE, desmontaje de RAEE y adicionalmente se agregó una variable denominada empleos. En este caso, no realizamos la simulación sino que el resultado de la implementación de la estrategia fue descrito a través de un bucle de realimentación (Fig. 10). El bucle obtenido fue de realimentación positiva, el cual nos mostró la influencia de una variable sobre otra y a su vez su refuerzo de forma indefinida. Específicamente, a medida que aumenta el desmontaje, este determina un aumento del empleo, que a

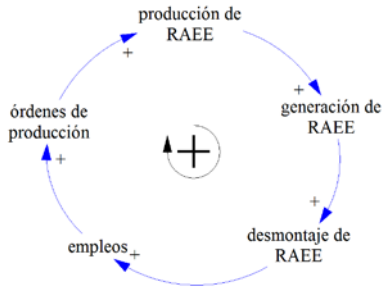


Figura 10. Bucle de realimentación positiva, simulación estrategia de empleo.
Fuente: Los autores.

su vez aumenta las órdenes de producción y al aumentar esta, crece la cantidad de AEE lo cual genera más RAEE y por último determina un aumento en el desmontaje, reiniciando el proceso y creando así un círculo vicioso. Este bucle muestra que el sistema no es estable porque aumenta las salidas o actividades del sistema, es decir los lleva a un límite en el que uno depende del otro para funcionar.

Teniendo en cuenta las simulaciones realizadas con las estrategias economía circular y educación ambiental y la creación del bucle de realimentación positiva con la estrategia de fomento de empleo podemos decir que la hipótesis planteada para el objetivo número 1 es verdadera. Con la implementación de la estrategia uno y la estrategia dos el modelo mostró que al aumentar el ciclo de vida de los AEE y al cambiar los hábitos de consumo disminuyó la tasa de generación de RAEE. Al mismo tiempo y resultado de los efectos anteriormente descritos, la producción de AEE se redujo drásticamente y por lo tanto la extracción de materias primas. Es decir, que se lograría minimizar la producción de RAEE, afectando el desarrollo económico del sector, lo que no sería viable.

Por último y reforzando lo anterior la estrategia tres demuestra un sistema económico y social de crecimiento acelerado y por ende inestable, este tipo de sistemas no se produce en la naturaleza o en los sistemas sociales porque todo proceso de crecimiento en algún momento encuentra sus límites.

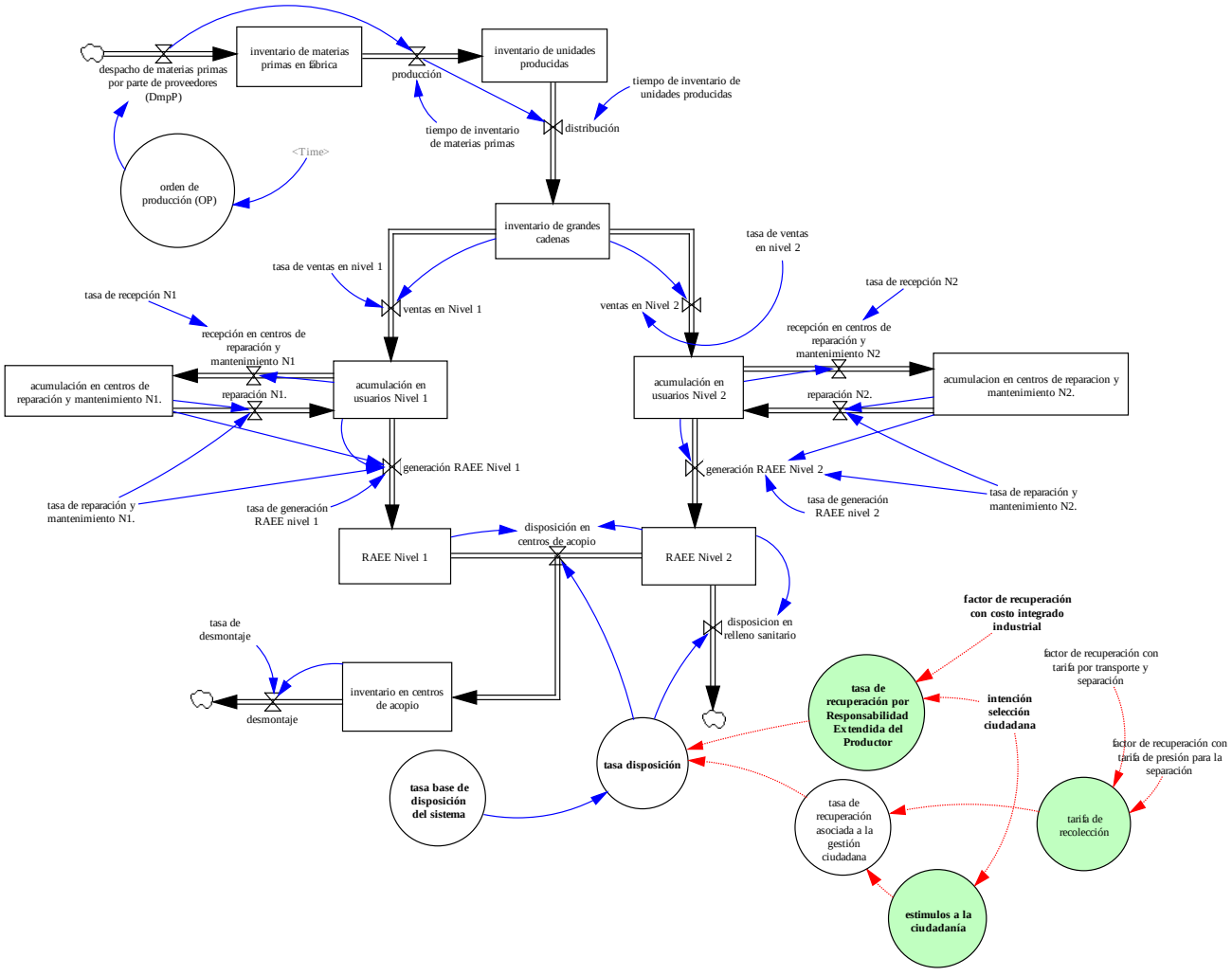


Figura 11. Diagrama de niveles y flujos con estrategias.
Fuente: Los autores.

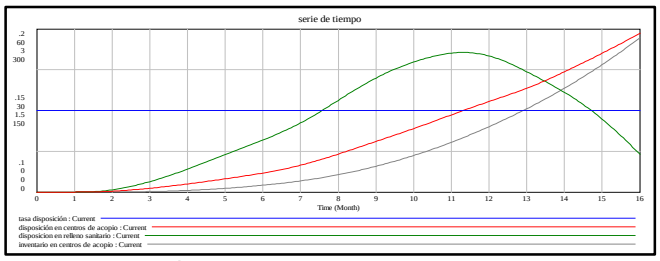


Figura 12. Simulación del sistema socio-ambiental de RAEE.
Fuente: Los autores.

El segundo grupo de estrategias designadas como estrategias implementadas, son: responsabilidad extendida del productor [14], estímulos a la ciudadanía [15,16] y tarifa de recolección de residuos [17]. Estas estrategias han sido utilizadas en trabajos con dinámica de sistemas que tienen cierta relación con nuestra investigación y que fueron direccionadas a influenciar la tasa de disposición lo que nos permitió evaluar los objetivos dos y tres de la política. En la Fig. 11 se observa la forma cómo fueron implementadas en el Modelo, en el diagrama de niveles y flujos. Para observar el comportamiento inicial o natural del sistema socio-ambiental de RAEE, las estrategias las cuales influyen en la tasa de disposición, presentaron valores igual a cero (Fig. 12). Luego de la simulación podemos deducir como la disposición en centros de acopio y el inventario de material en centros de acopio se incrementó a medida que con el tiempo.

De la misma manera identificamos como la disposición en el relleno sanitario tuvo una tendencia inicial al aumento.

Ahora bien, cuando implementamos cada una de las estrategias de forma independiente y cada una con un incremento del 50% y cuando el incremento de las estrategias no fue el mismo (tasa de recuperación por responsabilidad extendida del productor = 60%, tarifa de recolección = 80% y estímulo a la ciudadanía = 90%), se observó de forma generalizada en todos los escenarios realizados un incremento en la tasa de disposición. Además evidenciamos como las estrategias cuando tenían diferentes valores no cambiaron de forma abrupta el comportamiento natural del sistema (Figs. 13 a 17). A la vez generaron un incremento en el inventario en centros de acopio y una reducción de RAEE que llegan al relleno sanitario. Entre las estrategias y cuando todas presentaron el mismo incremento (50%) la tasa de recuperación por responsabilidad extendida del productor fue la estrategia que más incremento la tasa de disposición (Fig. 13), posiblemente no solo porque demanda un costo pagado por la industria si no porque incluye parte de la estrategia denominada estímulos a los ciudadanos.

Estos resultados indican como las estrategias incrementan la correcta disposición de RAEE provenientes de usuarios y hogares. Al mismo tiempo disminuye la mala disposición y la cantidad de residuos que llegan al relleno sanitario. Así mismo con el incremento de unidades de RAEE en centros de acopio hay más material que necesita ser tratado lo que representa nuevos empleos para el desmontaje, separación y reciclado de los distintos componentes que hacen parte de estos residuos. También y de forma intuitiva, resultado de todo el tratamiento realizado a los RAEE en los centros de acopio se podrán extraer más componentes que pueden ser utilizados como materia prima para la elaboración de nuevos AEE y cuya existencia permite disminuir la explotación de materias vírgenes. Al mismo tiempo la disponibilidad de materiales provenientes del tratamiento de RAEE permitirá abrir un nuevo mercado, el cual fomenta el desarrollo social y económico del sector relacionado con la gestión de RAEE.

Podemos determinar que las hipótesis dinámicas propuestas para los objetivos dos y tres son verdaderas por ende los objetivos son viables. Primero porque el comportamiento inicial o natural del sistema (sin ninguna implementación de estrategias o escenario inicial) permite disminuir los riesgos a la salud humana y al medio ambiente cuando los RAEE provenientes de hogares y usuarios son correctamente dispuestos en centros de acopio, determinado por estímulos a la ciudanía y una responsabilidad extendida del productor, reflejando una integración de actores en la gestión de RAEE. Adicionalmente, y como resultado de ese incremento de RAEE en centros de acopio consecuencia de una mayor integración de los productores y usuarios, existe más materiales para ser aprovechados lo que crearía nuevos puesto de trabajo favoreciendo el sector económico del país y por ende el producto interno bruto. Y segundo porque el comportamiento del sistema socio-ambiental reflejado con la implementación de las estrategias aumenta a un más los efectos ya descritos.

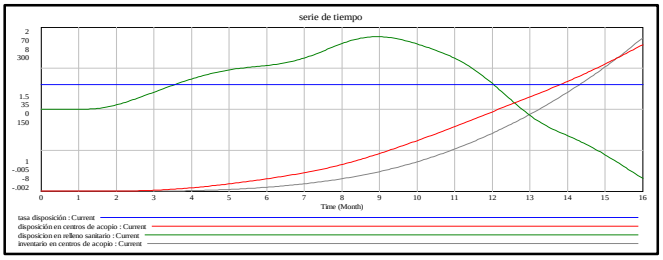


Figura 13. Simulación del sistema con la estrategia tasa de recuperación por responsabilidad extendida del productor = al 50%
Fuente: Los autores.

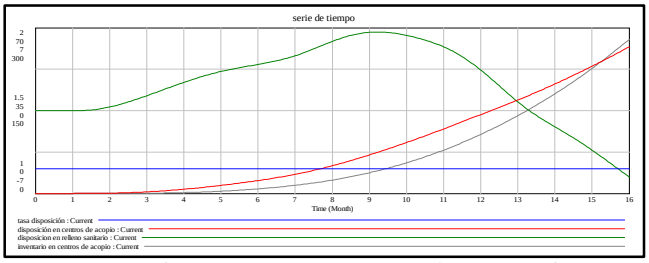


Figura 14. Simulación del sistema con la estrategia tarifa de recolección = al 50%.
Fuente: Los autores.

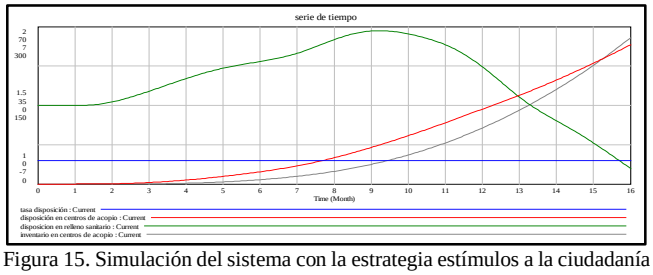


Figura 15. Simulación del sistema con la estrategia estímulos a la ciudadanía = al 50%.
Fuente: Los autores.

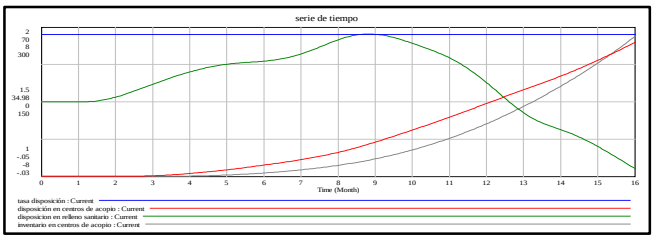


Figura 16. Simulación del sistema con la estrategia tasa de recuperación por responsabilidad extendida del productor = al 60%.
Fuente: Los autores.

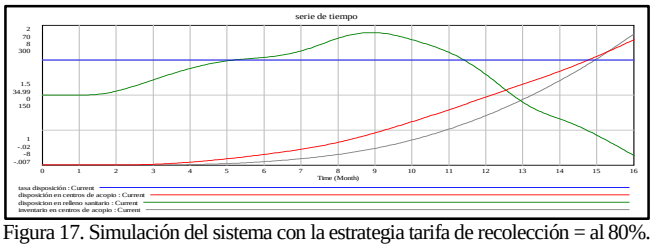


Figura 17. Simulación del sistema con la estrategia tarifa de recolección = al 80%.
Fuente: Los autores.

4. Conclusiones

El sistema socio-ambiental para la gestión integral de residuos de aparatos eléctricos y electrónicos (RAEE) descrito con base a los elementos teóricos presentes en la ley 1672 de 2013 y en el marco referencial, muestra, como en su estado inicial o natural se genera una disminución de RAEE que llegan al relleno sanitario y un aumento en la correcta disposición de los mismos.

Las estrategias economía circular y educación ambiental disminuyen la generación de RAEE cuando aumenta el ciclo de vida de los AEE y cuando cambian los hábitos de consumo, pero al mismo tiempo el sector industrial relacionado con la producción de AEE se ve afectado drásticamente. Por esto la hipótesis dinámica planteada para el primer objetivo es verdadera lo que permite establecer que dicho objetivo cumplen con la finalidad con la que fue creado. La estrategia fomento de empleo mostro un sistema en crecimiento continuo que con el tiempo se hace inestable.

Las estrategias tasa de recuperación por responsabilidad extendida del productor, estímulos a la ciudadanía y tarifa de recolección de residuos incrementaron aún más la tasa de disposición, lo que genero un mayor incremento en la correcta disposición y disminución de RAEE que llegan al relleno sanitario. Además como existen más RAEE en los centros de acopio entonces hay más material para ser aprovechado lo que representa nuevos puestos de trabajo. El efecto de las estrategias sobre el sistema permitió aceptar las hipótesis dinámicas planteadas para los objetivos dos y tres como verdaderas y por lo tanto pudimos determinar que dichos objetivos cumplen con la finalidad con la que fueron establecidos.

Finalmente se evidenció lo complejo que es disminuir la tasa de generación, las estrategias direccionadas a hacerlo lo logran, pero inmediatamente el sector económico cae rápidamente.

Referencias

[1] Acurio, G., Rossin, A., Teixeira, P. y Zepeda, F., Diagnóstico de la situación del manejo de residuos sólidos municipales en América Latina y el Caribe. Inter-American Development Bank, 1997, 165 P.

[2] Krol, A., Nowakowski, P. and Mrowczynska, B., How to improve WEEE management? Novel approach in mobile collection with application of artificial intelligence. Waste Management. 50, pp. 222-233, 2016. DOI: 10.1016/j.wasman.2016.02.033

[3] Islam, T., Abdullah, A., Shahir, S., Kalam, M., Masjuki, H., Shumon, R. and Rashid, H., A public survey on knowledge, awareness, attitude and willingness to pay for WEEE management: Case study in Bangladesh. Journal of Cleaner Production.137(20), pp 728-740, 2016 DOI: 10.1016/j.jclepro.2016.07.111

[4] Ott, D., Gestión de residuos electrónicos en Colombia: diagnóstico de computadores y teléfonos celulares. Federal Institute for Material Science and Research (Empa). 2008, 146 P.

[5] Ardi, R. and Leisten, R., Assessing the role of informal sector in WEEE management systems: a system dynamics approach. Waste Management 57, pp 3-16, 2016. DOI: 10.1016/j.wasman.2015.11.038

[6] Forrester, J., Industrial Dynamics. Pegasus communications. 482 P. Inc. Waltham, 1999. ISBN 978-1614275336.

[7] Forrester, J., Urban Dynamics. Pegasus communications. Inc. Waltham, 1969, 286 P.

[8] Ibarra, D. y Redondo, J., Dinámica de sistemas, una herramienta para la educación ambiental en ingeniería. Revista Luna Azul, 41, pp 152-16, 2015.

[9] Sukholthaman, P. and Sharp, A., A system dynamics model to evaluate effects of source separation of municipal solid waste management: a case of Bangkok, Thailand. Waste Management, 52, pp 50-61, 2016. DOI: 10.1016/j.wasman.2016.03.026

[10] Ibarra-Vega, D., Modeling waste management in a bioethanol supply chain: a system dynamics approach. DYNA 83(195), pp. 99-104. 2016. DOI: 10.15446/dyna.v83n195.47514

[11] Ding, Z., Yi, G., Tam, V. and Huang, T., A system dynamics-based environmental performance simulation of construction waste reduction management in China. Waste Manag., 51, pp 130-141, 2016. DOI: 10.1016/j.wasman.2016.03.001

[12] Ghisolfi, V., Diniz-Chaves, G., Ribeiro, R. and Xavier, L., System dynamics applied to closed loop supply chains of desktops and laptops in Brazil: a perspective for social inclusion of waste pickers, Waste Management 60, pp 14-31, 2016. DOI: 10.1016/j.wasman.2016.12.018

[13] Aracil, J. y Gordillo, F., Dinámica de sistemas. Madrid. Alianza Editorial S.A., 1997, 189 P.

[14] OECD (The Organization for Economic Cooperation and Development), Extended producer responsibility: a guidance manual for governments, OECD, 2001.

[15] Forero, J., La psicología del consumidor. Revista Latinoamericana de Psicología, 10(1), pp. 83-92, 1978.

[16] Neef, M.M., Desarrollo a escala humana. Barcelona: Nordan Comunidad, 1993, 93 P.

[17] Gilpin, A., Economía ambiental: un análisis crítico. Alfaomega, 2003, 352 P.

[18] Sterman, J., Business dynamics: systems thinking and modeling for a complex world, Irwin/McGraw-Hill, 2000, 982 P.

[19] Monterrey, M., Priore, P.y Quesada, I., Definición de un modelo de desarrollo y gestión de un parque empresarial de logística inversa en España. DYNA, 80(179), pp. 14-22, 2013.

[20] Redondo, J., Olivar, G., Ibarra-Vega, D. and Dyner, I., Modeling for the regional integration of electricity markets. 43, pp 100-113, 2018. DOI: 10.1016/j.esd.2017.12.003

J. Redondo, es Dr. en Ingeniería, MSc. en Gestión Ambiental, MSc. en Docencia e investigación, Sp. en matemática aplicada e Ing. Ambiental.
ORCID: 0000-0002-9427-1324

D. Ibarra-Vega, es Dr. en Ingeniería, MSc. en Gestión Ambiental, Sp. en Gerencia del Medio Ambiente e Ing. Biotecnológico.
ORCID: 0000-0002-3339-6430

L. Monroy, es MSc. en Gestión y Evaluación Ambiental, Sp. en Gerencia del Medio Ambiente e Ing.Ambiental.
ORCID: 0000-0002-9960-0086

J. Bermúdez, es MSc. en Gestión y Evaluación Ambiental, Sp. en Gerencia del Medio Ambiente e Ing. Ambiental.
ORCID: 0000-0002-7309-9270

UNIVERSIDAD NACIONAL DE COLOMBIA
SEDE MEDELLÍN
FACULTAD DE MINAS



DYNA
http://dyna.medellin.unal.edu.co/

Bioactivity analysis of the AZ31 Mg alloy coated by PEO (Plasma Electrolytic oxidation)

Kevin Dorado-Bustamante [a], Benjamín Zuluaga-Díaz [b] & Hugo Estupiñán-Duran [b]

a Departamento de Física Nuclear, Instituto Balseiro, Bariloche, Argentina. kadorado@gmail.com
b Grupo de Tribología y Superficies, Facultad de Minas, Universidad Nacional de Colombia, Medellín, Colombia. bzuluagad@unal.edu.co, haestupinand@unal.edu.co

Received: December 26th, 2017. Received in revised form: March 11th, 2018. Accepted: April 13th, 2018.

Abstract
Magnesium is a material that presents favorable properties for its selection as biomaterial; however, its application is restricted by the rapid corrosion. In this research was evaluated the surface modification of magnesium AZ31 by PEO and its effect on the protective and bioactive properties. The microstructure, phase composition and distribution of elements in the coating were characterized by SEM, XRD and EDX. Chemical stability, corrosion resistance, the bioactivity and electronic properties were evaluated using EIS and Mott-Schottky in simulated body fluid. The analysis of XRD and EDX indicated the presence of MgO, $MgSiO_4$ in the coatings. The cross section analysis present a compact layer close to the substrate followed by an outer porous layer. EIS analysis showed that treatment increased the substrate protection in a simulated physiological medium.

Keywords: anodized; coating; corrosion; biocompatibility; biomaterial.

Análisis de la bioactividad de Mg AZ31 recubierta por PEO (Plasma Electrolytic Oxidation)

Resumen
El Magnesio es un material que presenta propiedades favorables para su selección como biomaterial; sin embargo, su aplicación se ve restringida por la rápida corrosión. En esta investigación se evaluó la modificación superficial de magnesio AZ31 mediante PEO y su efecto sobre las propiedades protectoras y bioactivas. La microestructura, composición de la fase y la distribución de los elementos en el recubrimiento fue caracterizada mediante MEB, DRX y EDX. La estabilidad química, la resistencia a la corrosión, la bioactividad y las propiedades electrónicas se evaluaron usando EIE y Mott-Schottky en solución de fluido corporal simulado. El análisis de DRX y EDX índico la presencia de MgO, $MgSiO_4$ en los recubrimientos. Un análisis de la sección transversal presento un recubrimiento compacto cerca al sustrato seguido por un estrato poroso en la superficie. Del análisis de EIE se mostró que el tratamiento incrementa la protección del sustrato en un medio fisiológico simulado.

Palabras clave: anodizado; recubrimiento; corrosión; biocompatibilidad; biomaterial.

1. Introducción

Actualmente para la sustitución y reparación de tejido óseo dañado existe una amplia gama de materiales que cumplen con las características suficientes para remplazar las funciones mecánicas del hueso [1]. Sin embargo, según sea el estado y el tipo de tejido puede requerirse diferentes velocidades de degradación [2]. En algunos casos se requieren materiales bio-inertes y en algunos otros materiales biodegradables [3].

Los materiales bio-inertes han tenido mayor desarrollo histórico en las aplicaciones biomédicas, por lo que han sido más utilizados. Aunque los implantes bio-inertes han demostrado un éxito indudable en aplicaciones como fijaciones internas de los huesos, también han presentado algunos problemas inevitables [4]. Por ejemplo, los

How to cite: Dorado-Bustamante, K., Zuluaga-Díaz, B. and Estupiñán-Duran, H., Análisis de la bioactividad de Mg AZ31 recubierta por PEO (Plasma Electrolytic Oxidation). DYNA, 85(205), pp. 328-337, June, 2018.

© The author; licensee Universidad Nacional de Colombia.

implantes inertes permanecen en el cuerpo humano por periodos de tiempo largos inclusive después de haber cumplido su función de reparación [5], por lo que eventualmente requieren una cirugía de revisión o extracción del implante [6]. Debido al uso de intervenciones quirúrgicas adicionales, se han presentado efectos adversos sobre pacientes, debido al aumento en las probabilidades de infección [7,8]. Por otro lado, se encuentran los implantes biodegradables, que brindan la posibilidad de interactuar con el tejido dañado mediante la estimulación celular, con respuestas favorables de cicatrización [9]. Esto no solo favorece el proceso de mineralización del tejido óseo, también favorece el proceso de degradación del material hasta su total desaparición en el organismo, por lo que no se requiere, su remoción posterior [10-12]. Así los implantes biodegradables se presentan como una alternativa de solución a las intervenciones quirúrgicas necesarias para los implante bio-inertes. Logrando así, que los implantes permanezcan en el cuerpo humano por un periodo de tiempo controlado, en el cual el implante soporte el proceso de sanación del tejido afectado y a su vez, sea absorbido, consumido y excretado sin causar ningún efecto desfavorable al cuerpo humano [13].

Los metales y las aleaciones han sido ampliamente utilizados en la fabricación de dispositivos biomédicos debido su resistencia mecánica, la cual es necesaria para dar soporte estructural al tejido óseo afectado [14]. Sin embargo, características como la resistencia a la tracción, módulo de Young y la resistencia a la fractura, no han sido tenidas en cuenta al momento de sustituir un tejido o parte de él por una prótesis de naturaleza metálica, porque puede ocasionar problemas con el tejido huésped, como fractura, desgaste o mineralización excesiva [15,16]. Para evitar tales inconvenientes, es necesario que estos materiales tengan propiedades mecánicas similares a las del hueso humano, garantizando un buen acople con el tejido huésped y el establecimiento de sus funciones [17]. Entre Los metales más empleados están, cobalto (Co), Titanio (Ti) y sus aleaciones, Magnesio (Mg) y sus aleaciones [18].

Por el lado de los biomateriales degradables, surgen requerimientos adicionales, tales como su cinética de degradación en el entorno fisiológico del cuerpo humano durante el periodo de cicatrización y que los productos generados no ocasionen efectos adversos a la salud del paciente [19]. Para tal fin, los materiales deben presentar resistencia a la corrosión en el fluido corporal en la etapa inicial de la implantación; pero que con el paso del tiempo, el implante se degrade a una velocidad específica, de tal manera que el cuerpo humano sea capaz de absorber dentro del desarrollo de sus funciones biológicas ordinarias, los productos formados [20]. Hasta el momento, la dificultad de lograr un control sobre la tasa de degradación sigue siendo un problema en el desarrollo de implantes. En este sentido, se hace necesario profundizar en el estudio de la descomposición de los implantes biodegradables y su absorción por parte del cuerpo humano [21].

El grupo de aleaciones de magnesio dentro de las aleaciones metálicas, han sido ampliamente estudiadas en la selección de materiales para implantes biodegradables [22], debido a que sus propiedades mecánicas son muy similares a las del hueso, combinadas con su capacidad de degradación y su excelente biocompatibilidad, haciendo de este material, un candidato apropiado para este tipo de aplicaciones [23]. Las aleaciones de magnesio comerciales tienen un contenido de aluminio (3%-12%), manganeso (0.1%-0.4%), zinc (0.5%-3%) [24]. la aleación AZ31 tiene un contenido alto de magnesio el cual es considerado un metal ligero por su densidad (1.74- 2g/cm^3) [24], en comparación con otras aleaciones como las de titanio que tienen una densidad mayor (4.4-4.5g/cm^3). También es importante resaltar la similitud que hay entre la densidad del magnesio y la densidad del hueso (1.8-2.1g/cm^3) [25]. La tenacidad a la fractura del magnesio es mayor en comparación con los biomateriales cerámicos, tales como hidroxiapatita (Ca_{10} $(PO_4)_6(OH)_2$), mientras que el módulo de elasticidad y resistencia a la deformación son más próximas a las del hueso natural que otros implantes metálicos utilizados [26]. Sin embargo, la aplicación de las aleaciones de magnesio se ve restringida por su baja resistencia a la corrosión [27-29]. La rápida corrosión del magnesio favorece la evolución de hidrogeno sobre la superficie del implante [8,30], siendo esto un inconveniente porque puede modificar su pH superficial hacia valores de mayor acidez, disminuyendo así la interacción del implante con el tejido circundante, lo cual lleva a retrasar el proceso de curación, que a su vez ponen en riesgo la vida del paciente, ya que entre otros efectos, la absorción de hidrogeno se da de manera lenta [30,31]. En este orden de ideas, se han desarrollado técnicas químicas y físicas de modificación superficial con el objetivo de mejorar la resistencia a la corrosión de este material [32].

La Oxidación Electrolítica por Plasma (PEO), es una técnica de modificación superficial que mejora la resistencia a la corrosión del magnesio y sus aleaciones [33]. En este proceso, el campo eléctrico se mantiene a través de la creciente película anódica, superando un voltaje crítico llamado tensión de ruptura dieléctrica, que normalmente es notado por la descarga de chispas, el desprendimiento de gas y los cambios en la pendiente de la curva de voltaje-tiempo [34]. El rol de los electrolitos es tan importante como el tipo de la fuente de alimentación para controlar el proceso de PEO [35]. El origen de las fases cristalinas y amorfas de naturaleza cerámica formada sobre la superficie del metal, procede tanto del sustrato como del electrolito utilizado. Dentro los compuestos más utilizados en la técnica PEO se destacan: hidróxido de sodio y de potasio (NaOH, KOH) [36], silicato de sodio (Na_2SiO_3) [37], fosfato de sodio (Na_3PO_4) y los electrolitos de aluminato de sodio ($Na_2Al_2O_4$) [38]. Siendo entonces la composición y concentración del electrolito variables fundamentales para la obtención de recubrimientos bioactivos que controlen los procesos de degradación del implante [6].

En este trabajo se evaluó la estabilidad química, la resistencia a la corrosión, la composición química, estructura, propiedades semiconductoras y la bioactividad de recubrimientos obtenidos por PEO sobre la aleación de magnesio AZ31, con el fin de identificar si el material sintetizado cumple con los requisitos suficientes para ser biodegradable. Con esto, se busca controlar la rápida degradación de la aleación de magnesio AZ31 mediante el crecimiento de un recubrimiento de Mg_2SiO_4, tipo barrera, de naturaleza cerámica, con propiedades de estabilidad química

superficial, interacción con iones de la solución corporal que promuevan la bioactividad, regulación de la actividad del hidrógeno por la facilidad de este compuesto de formar grupos hidroxilos en la superficie [39], propiedades que definirán la capacidad de ser usado en implantes de sustitución y reparación ósea biodegradables.

2. Materiales y métodos

2.1. Materiales

Magnesio AZ31 fue utilizado como sustrato en este estudio, la composición química en porcentaje en peso fue de 2.65 % Al, 1.03 % Zn, 0.31 % Mn, 0.15 % Si, 0.003 % Fe, 0.002 % Sn, 0.0002 % Ni y completa el balance el Mg. Antes del proceso de anodizado la muestras fueron cortadas en dimensiones de 10 mm x 10mm x 0.1mm. Las superficies de estas muestras fueron pulidas utilizando papel de lija de carburo de silicio (SiC) gradualmente desde 400 hasta 1200 de tamaño de grano, de acuerdo a la norma ASTM E3-01. Finalmente, los sustratos fueron limpiados en baño con ultrasonido en solución de acetona por 5 minutos, enjuagados con agua destilada y etanol y posteriormente, secados antes de ser sometidos al proceso electroquímico de plasma.

2.2. Obtención de la película anódica

El anodizado fue llevado a cabo con una fuente de alimentación de corriente directa *Kikusui (PAS-500-1.8)* de una potencia de 1.5kW. La muestra de Mg AZ31 es conectada al terminal positivo de la fuente como ánodo y a una placa de acero inoxidable por el terminal negativo como cátodo. Tanto el sustrato como la placa de acero inoxidable fueron sumergidas en diferentes soluciones electrolíticas de KOH (1.5 g/L) y Na2SiO3 (0, 2, 4 y 6 g/L). La distancia entre placas, la densidad de corriente aplicada y el tiempo de tratamiento se mantuvieron constantes en 1cm, 125mA/cm^2 y 5 minutos respectivamente, como condiciones de operación.

2.3. Caracterización química e identificación de estructuras cristalinas por difracción de rayos X

La identificación química y las fases cristalinas de los compuestos formados sobre la aleación AZ31 durante el tratamiento con PEO, fueron obtenidas mediante Difracción de Rayos X en un equipo *PANalytical X´PERT PRO MPD* con una radiación Kα de cobre, usando un voltaje de aceleración de 45 kV y una corriente sobre el filamento de 40 mA. La adquisición de los espectros se realizó por escaneo en 2θ entre 20° y 80° con un paso de 0.001° y una velocidad de barrido 1°/min. El análisis de las bandas de difracción para determinar las fases presentes en el espectro se realizó con ayuda del software *H'XPert HighScore* versión 2.1b.

2.4. Caracterización química y morfológica por Espectroscopia de Energía Dispersa (EDS) y Microscopia Electrónica de Barrido (MEB)

Un análisis químico y morfológico de los recubrimientos obtenidos por PEO sobre la aleación de Mg AZ31 fue realizado sobre una sección trasversal de cada recubrimiento correspondiente a cada concentración de Na_2SiO_3 propuesta. Para esto se empleó una cortadora de precisión *ISOMET 1000*, a una velocidad de 100RPM, con un refrigerante soluble en agua. Posteriormente, los cortes transversales fueron montados sobre resina acrílica autopolimerizable utilizando una prensa de montaje automático *simplimet 1000* y subsecuentemente pulidas hasta suspensión de diamante de 3 micras. La caracterización morfológica fue realizada en un microscopio electrónico de barrido de emisión termoiónica *Carl Zeiss EVO MA10*, por medio de la imagen obtenida por electrones secundarios. Adicionalmente, se obtuvieron imágenes por la técnica de electrones retro proyectados para reconocer variaciones en la composición del sustrato y del recubrimiento de la muestra, ya que el número de electrones retro proyectados varía según la densidad electrónica de cada átomo [40]. La identificación de los elementos y su distribución en la imagen, fue realizada por espectroscopia de energía dispersa *EDS* con un detector *Oxford X-act* acoplado al MEB. Una distancia de trabajo de 8.5mm y un voltaje de aceleración de 20kV fueron empleados como condiciones de operación para este análisis.

Tabla 1.
Parámetros de la prueba de EIE y M-S.

Espectroscopia de Impedancia Electroquímica	Frecuencia inicial: 10000 Hz Frecuencia final: 0,01 Hz Amplitud: 20mV
Mott-Schottky	voltaje inicial: -0.5V voltaje final: 1V Amplitud: 20mV Frecuencia: 100Hz

Fuente: Los autores

2.5. Espectroscopia de impedancia electroquímica (EIE) y mott-schottky (M-S)

Los ensayos de espectroscopia de impedancia electroquímica y Mott Schottky se llevaron a cabo en un Potenciostato/Galvanostato del tipo *Gamry instruments interface 1000* empleando una celda plana electroquímica vertical de tres electrodos en medio fisiológico simulado como electrolito, para simular condiciones fisiológicas corporales a una temperatura de 37 °C, la cual fue mantenida constante por medio de una baño termostático *LAUDA E 100* conectado a la celda [41]. Durante los ensayos se empleó como electrodo de referencia, un electrodo de Ag/AgCl, como contra electrodo una barra de grafito y como electrodo de trabajo la aleación de Mg AZ31 recubierta por PEO. En la Tabla 1 se presentan los parámetros utilizados para estos ensayos.

Los espectros obtenidos de impedancia fueron ajustados a modelos propuestos de circuitos equivalentes mediante un software de análisis espectral hasta un ajuste de chi-cuadrado de 10^{-4}.

3. Resultados y discusión

3.1. Difracción de rayos X (DRX)

El análisis por difracción de rayos X para la aleación AZ31 tratada por PEO se muestra en la Fig. 1. Este difractograma

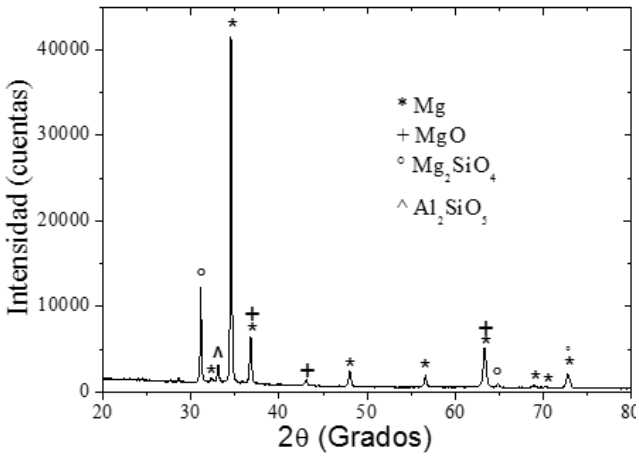


Figura 1. Difractograma para una aleación de magnesio AZ31 recubierta con PEO.
Fuente: Los autores

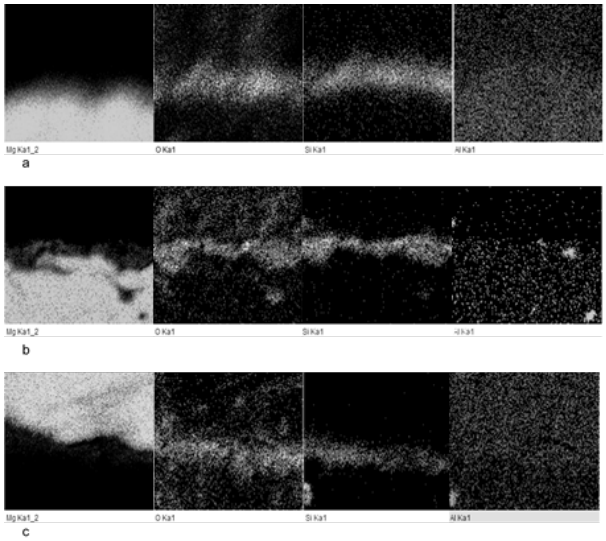


Figura 2. Mapa de elementos del corte transversal de Mg AZ31 recubierto por PEO a) 6 g/L, b) 4 g/L y c) 2 g/L de Na_2SiO_3.
Fuente: Los autores

fue similar para todas las condiciones evaluadas. En este análisis, se identificaron las bandas correspondientes al sustrato, principalmente el magnesio y adicionalmente, las bandas de los compuestos que se formaron durante el proceso PEO, que corresponden a las fases cristalinas de la forsterita (Mg_2SiO_4), la periclasa (MgO) y aluminosilicatos (Al_2SiO_5), que son productos de la oxidación del magnesio y aluminio como elementos de la aleación AZ31.

La identificación de compuestos de Mg_2SiO_4 confirma la difusión de iones desde la solución electrolítica hacia la superficie del recubrimiento, el cual por la energía disponible que se genera durante el proceso de plasma, permite la formación de óxidos cerámicos con naturaleza química diferente a la generada espontáneamente por el material y según lo reportado por otros investigadores, la presencia de este tipo de compuesto en el recubrimiento le confiere propiedades protectoras al sustrato [42].

3.2. Espectroscopia de energía dispersa (EDS) y microscopia electrónica de barrido (MEB)

En la Fig. 2.a,b, y c, se muestra la distribución de los elementos en un mapa obtenido sobre una sección transversal de las muestras recubiertas por PEO para la condiciones de 2, 4 y 6g/L de Na_2SiO_3 respectivamente. Tanto en las imágenes de electrones retrodispersos como secundarios, el elemento magnesio se presenta con un mayor contraste (blanco) en la parte inferior de la imagen, lo cual corresponde al elemento del sustrato. Igualmente, el contraste (blanco) de la imagen en la Fig. 2a, 2b y 2c, corresponde a los elementos de oxígeno y silicio asociados a la presencia de estos elementos en el recubrimiento. Adicionalmente en el mapa del aluminio, la variación del contraste no fue tan significativa como para los otros elementos mencionados. Es importante notar que en la interface sustrato/recubrimiento se presentó una difusión de iones de magnesio desde la aleación hacia el recubrimiento evidenciándose en la Fig. 3 como un cambio en el contraste de dicha localidad.

Las imágenes del corte transversal de los recubrimientos obtenidas por MEB se muestran en la Fig. 3. En estas imágenes se observa un recubrimiento con un estrato interno compacto adyacente al sustrato de Mg AZ31 y un estrato externo con micro fisuras y micro canales interconectados, los cuales son formados generalmente por las descargas o chispas características del PEO [43]. Estos dos estratos, coinciden con la estructura típica reportada para los recubrimientos de óxido de magnesio obtenidos por PEO [44]. Los espesores obtenidos se dieron entre 10.05-20.91 µm, 7.351 -11.54 µm, 1.87-2.95 µm para la muestras de 2g/L, 4g/L, 6g/L de Na_2SiO_3, respectivamente. Los elementos presentes en los recubrimientos y sus porcentajes en peso se muestran en la Tabla 2.

Tabla 2.
Composición elemental de los recubrimientos.

Muestra	Composición % peso									
	O	Na	Mg	Al	Si	Cl	K	Ca	Zn	C
2g/L	38.7	0.23	19.9	0.57	8	0.2	0.19	0.13	0.26	32.5
4g/L	40.1	1.39	42.4	2.01	11.02	1.72	0.78	0.15	0.45	0
6g/L	47.1	0.88	35.96	1.46	12.08	1.03	0.51	0.44	0.52	0

Fuente: Los autores

De acuerdo a estos resultados se puede identificar la formación de un recubrimiento homogéneo constituida principalmente de los elementos Si, Al, O y Mg, concordando con los resultados obtenidos por DRX asociados a los óxidos de magnesio, oxido de aluminio y a la presencia de cerámicos como la forsterita (Mg_2SiO_4) y los aluminosilicatos (Al_2SiO_5) [45].

De los resultados presentados en la Tabla 2, se observa un alto contenido de oxígeno en cada una de las muestras, seguido por el contenido de magnesio y silicio respectivamente, que corresponde a la formación preferencial de óxidos de magnesio y silicatos de magnesio en los recubrimientos. La presencia de un 32.5% de carbono en la muestra de 2 g/L, se puede atribuir a que dado el tamaño pequeño de la muestra, la medición por rayos X (diámetro de interacción con la muestra de 3 a 5 µm) pudo ser afectada por

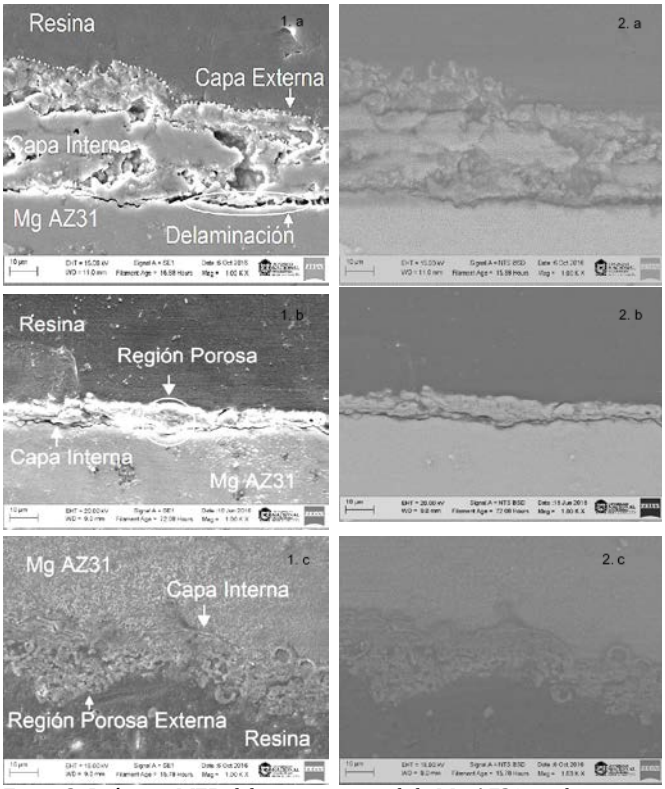


Figura 3. Imágenes MEB del corte transversal de Mg AZ31 recubierto por PEO a) 6 g/L, b) 4 g/L y c) 2 g/L de Na2SiO3 en 1) electrones secundarios y 2) retro dispersados.
Fuente: Los autores

los componentes de la resina, la cual está constituida principalmente de carbono, a pesar de haber tomado varias mediciones.

Los porcentajes de Si fueron mayores en el recubrimiento que en la aleación de magnesio AZ31, cuya presencia se puede atribuir a la co-deposición elemental, desde el electrolito hacia el recubrimiento en el proceso de plasma electrolítico. El porcentaje de silicio en el recubrimiento aumentó con el incremento en la concentración de Na_2SiO_3 disuelto en el electrolito.

La morfología superficial de las muestras tratadas con PEO obtenida por las imágenes de electrones secundarios, se muestra en la Fig. 4. De allí se distingue la formación de estructuras porosas, común de los recubrimientos obtenidos por PEO, como consecuencia de la cavitación generada por las burbujas de gas cuando se alcanza el potencial de ruptura [39,40]. También se observa que al aumentar la concentración del compuesto que contiene Silicio (Si) en el electrolito, se incrementa las fisuras micrométricas sobre la superficie y a su vez, estas se hacen más grandes. Estas características son posibles relacionarlas con las depresiones de los arcos obtenidos en los espectros de Nyquist a partir del análisis por espectroscopia de impedancia electroquímica mostrado más adelante, específicamente, en el valor de la fase de la capacitancia, asumiendo elementos de fase constante, para representar la capacitancia no ideal entre dos interfaces paralelas, compuestas por irregularidades morfológicas que generan inhomogeneidades a la transferencia de carga.

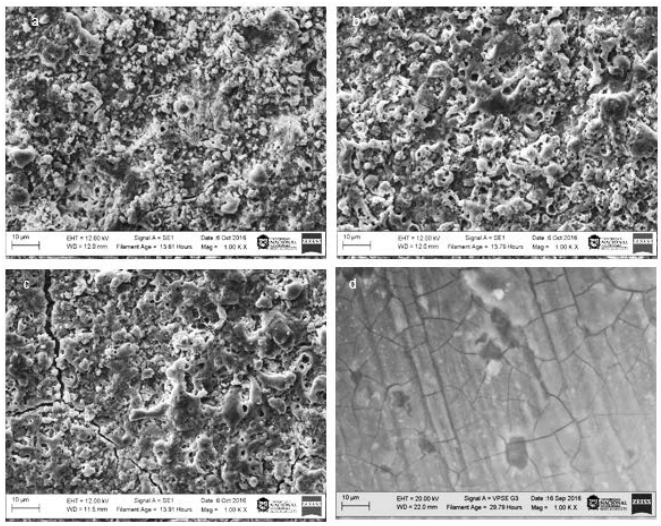


Figura 4. Morfología de los recubrimientos a) 2g/L, b) 4g/L, c) 6g/L de Na_2SiO_3 y d) 1.5g/L KOH sin Na_2SiO_3.
Fuente: Los autores

3.3. Comportamiento electroquímico de los recubrimientos

Los resultados de espectroscopia de impedancia electroquímica EIE, proveen información detallada de los procesos electroquímicos que ocurren en la interface electrolito/recubrimiento y recubrimiento/electrodo [48]. La cual está relacionada con la rugosidad de la superficie, espesor del recubrimiento y composición química. Los espectros de Nyquist y de Bode obtenidos, son mostrados en la Fig. 5 para las cuatro condiciones evaluadas. De la gráfica del Módulo de impedancia en función de la frecuencia (Fig. 5a), se observa, para las muestras recubiertas con Na_2SiO_3, un incremento entre 1.5 y 2 órdenes de magnitud en los valores de impedancia comparados con la muestra recubierta solo con KOH. Los valores más altos de impedancia en todo el rango de frecuencia evaluado, fueron obtenidos en las muestras recubiertas con los electrolitos de 4g/L y 6g/L de Na_2SiO_3.

De acuerdo al espectro de bode, se identifican 3 relajaciones a la transferencia de carga, en tres regiones bien definidas en intervalo de frecuencias, altas, medias y bajas. De estas tres, la primera se presenta a altas frecuencias 1.000-10.000 Hz, correspondiendo al comportamiento resistivo del electrodo, presentando una baja variación del logaritmo de la impedancia con respecto al logaritmo de la frecuencia. Este comportamiento se corrobora en la Fig. 5b, donde se presenta un ángulo de fase menor a 40° a excepción de la muestra recubierta con 6g/L Na_2SiO_3, la cual llega a valores cercanos de 50° en ángulo de fase. A medias frecuencias, entre 100-1.000 Hz corresponde a cambios capacitivos del electrodo y el recubrimiento, siendo este comportamiento propio de un recubrimiento semiprotector, el cual muestra un ángulo de fase cercano a 60°. La muestra de Mg AZ1 recubierta con solo 1.5g/L de KOH, presento un comportamiento capacitivo a altas frecuencias y un semi-bucle inductivo a bajas frecuencias, lo cual es similar a lo hallado por otros investigadores [49]. El comportamiento inductivo está relacionado con la reacción de reducción de magnesio que produce hidrogeno [50]. A más bajas frecuencias, se presentan las relajaciones relacionadas por los procesos de transferencia de masa del electrodo.

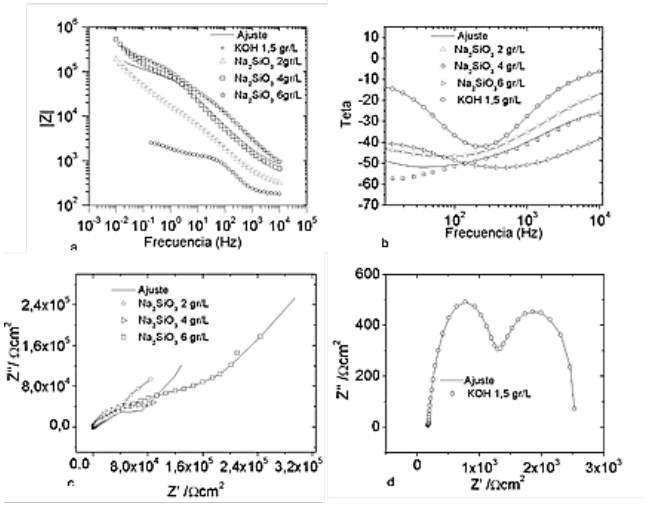


Figura 5. Graficas de EIE de Mg AZ31 sin y con recubrimientos obtenidos por PEO a diferentes concentraciones de Na_2SiO_3.
Fuente: Los autores

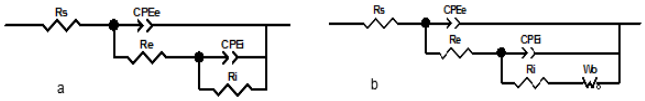


Figura 6. Circuitos equivalentes usados para ajuste de datos de EIE en fluido fisiológico simulado. a) 1.5gr/L KOH, 2g/L de Na_2SiO_3 b) 4g/L y 6g/L de Na_2SiO_3.
Fuente: Los autores

Tabla 3.
Composición elemental de los recubrimientos.

	Contenido de Na_2SiO_3			
	0g/L	**2g/L**	**4g/L**	**6g/L**
Rs(Ωcm²)	176.2	240	609.5	349.2
Re(Ωcm²)	1231	22478	1.2192E^{5}	76320
CPEe-T(F/cm^2)	4.5053E^{-6}	1.0635E^{-5}	2.6294E^{-6}	1.3229E^{-6}
CPEe-P	0.85611	0.60927	0.63704	0.63143
Ri (Ωcm²)	1060	1E20	213.3	34020
CPEi-T(F/cm^2)	1.7479E^{-4}	2.0321E^{-5}	4.6091E^{-5}	4.8654E^{-7}
CPEi-P	0.9191	0.5909	0.8789	0.9999
Wo1-R (Ωcm²)	-	-	1565	2.8216E^{-5}
Wo1-T	-	-	0.12565	9.95
Wo1-P	-	-	1.174	0.34592
Chi-cuadrado	0.001796	0.000935	0.001475	0.000483

Fuente: Los autores

En los diagramas de Nyquist de la Fig. 5c, se presentaron dos semicírculos superpuestos y deprimidos, en la región de altas y medianas frecuencias. Este comportamiento visto en los espectros de Bode en la gráfica de módulo de impedancia contra frecuencia, se muestra como un cambio de alta a baja pendiente en el rango de mayor a menor frecuencia y se relaciona con los cambios capacitivos desde el electrodo de AZ31 al recubrimiento obtenido por PEO a medias-altas frecuencias. La superposición de estas relajaciones se fundamenta en la naturaleza del ion metálico de magnesio común entre el sustrato y el recubrimiento.

Basado en las gráficas de EIE se propuso dos circuitos eléctricos equivalentes para el ajuste de los datos obtenidos de los espectros de impedancia, es así como para la muestra tratada solo con KOH y la muestra de 2g/L, el circuito que los representa se muestra en la Fig. 6a. Para el caso de las muestras tratadas con 4 y 6g/L se ajustan a otro tipo de circuito equivalente, el cual se muestra en la Fig. 6b. Todas las capacitancias puras del circuito fueron reemplazadas por elementos de fase constante para compensar las inhomogeneidades dadas por las rugosidades, grietas o porosidades del recubrimiento.

En estos circuitos equivalentes, la resistencia del fluido fisiológico simulado, Rs, están en serie con los elementos de fase constante y resistencia, correspondientes al recubrimiento de óxido en contacto con el electrolito. Re, representa la resistencia del recubrimiento poroso exterior que está en paralelo con CPEe como elemento de fase constante. Los elementos CPEi y Ri, representan las propiedades de la interfase metal/recubrimiento, los cuales se muestran en paralelo con los anteriores elementos del circuito descritos, por la superposición de los semicírculos capacitivo-resistivo en los espectros de impedancia. Basado en el ajuste a estos circuitos equivalentes, las curvas se muestran en la Fig. 5, representadas por una línea oscura continua, junto con las curvas obtenidas de los espectros experimentales. Los parámetros obtenidos se muestran en la Tabla 3.

La diferencia entre los dos modelos propuestos, se basa específicamente en la presencia de una impedancia de Warburg para las muestras de 4g/L y 6 g/L de Na_2SiO_3, que representa la difusión de oxígeno cuya contribución se puede reflejar en la formación de hidróxidos sobre el recubrimiento, donde los defectos de la película se convierten en espacios de posible formación de silanoles (Si $(OH)_2$).

Los valores de capacitancia CPEe-T disminuyeron con el incremento de la concentración de Si en el electrolito, lo cual indica que a mayor adición de Silicio (Si) en los recubrimientos obtenidos por PEO, aumenta la estabilidad de los recubrimientos, aumentando la protección y disminuyendo la tendencia a la corrosión de la aleación de magnesio [46].

A partir de la relación que existe entre la capacitancia, carga superficial y el potencial en la superficie que se muestra en la ec. (1), se puede encontrar una relación con la energía libre de Gibbs de la ec. (2) por medio del potencial en la superficie. Por ende, al disminuir la capacitancia, la energía libre de Gibbs disminuye, indicando una menor actividad química de los óxidos formados que componen el recubrimiento. Luego, la muestra con menor actividad

química se presentó para la condición con 6g/L de Na_2SiO_3. En el mismo orden le siguen la muestra con 4 g/L de Na_2SiO_3, seguido por la recubierta solo con KOH y por último la de 2g/L de Na_2SiO_3. Es posible interpretar estos resultados basados en incrementos de bioactividad sin sacrificar propiedades protectoras. De acuerdo a los resultados obtenidos, electrolitos con baja concentración de silicio son suficientes para aumentar la bioactividad y proteger la integridad del sustrato y del recubrimiento [51,52].

$$C = \frac{\sigma^2}{E} \tag{1}$$

$$\Delta G = -nFE \tag{2}$$

Donde n es el número de electrones transferidos y F es la constante de Faraday.

Para determinar las propiedades semiconductoras: densidad de donadores Nd y potencial de banda plana E_{fb} de los recubrimientos se utilizó la técnica Mott-Schottky [44,45]. Esta técnica tiene como modelo, el mostrado en las ec. (3) y (4).

$$\frac{1}{C_{sc}^2} = \frac{2N_A}{N_d F \varepsilon_r \epsilon_0}\left((E - E_{Fb}) - \frac{RT}{F}\right) \tag{3}$$

$$\frac{1}{C_m} = \frac{1}{C_{sc}} + \frac{1}{C_H} \tag{4}$$

Donde C_{SC} es la capacitancia en la región de espacios de carga, N_A el número de Avogadro $6{,}023\times10^{23}$ 1/mol, N_d es la densidad de donadores, F es la constante de Faraday 9.65×10^4C/mol, ε_r es la constante dieléctrica relativa que para el caso del óxido de magnesio es de 9.86 [46,47], ϵ_0= 8.8542×10^{-12}F/m es la permitividad en el vacío, E es el potencial aplicado en la prueba , E_{Fb} es el potencial de banda plana , R es la constante de los gases 8.314J/mol*K y T la temperatura absoluta (301K). C_m es la capacitancia obtenida de las gráficas de Mott Schottky, la cual es la suma de la capacitancia del espacio de carga C_{SC} y la capacitancia de la doble capa electroquímica C_H asumida como un valor constante de 20µF/cm^2 [57].

Para calcular el potencial de banda plana se hace un ajuste a una línea recta de la curva obtenida mediante M-S (capacitancia vs voltaje) mostrada en la Fig. 7. De la pendiente de la línea recta obtenida se calcula la densidad de donadores como se observa en la ec. (5) y a partir del intercepto se calcula el potencial de banda plana como se muestra en la ec. (6).

$$m = \frac{2N_A}{N_d F \varepsilon_r \epsilon_0} \rightarrow N_d = \frac{2N_A}{mF\varepsilon_r\epsilon_0} \tag{5}$$

$$b = \frac{2N_A}{N_d F \varepsilon_r \epsilon_0} * E_{fb} \rightarrow E_{fb} = \frac{N_d F \varepsilon_r \epsilon_0 b}{2N_A} \tag{6}$$

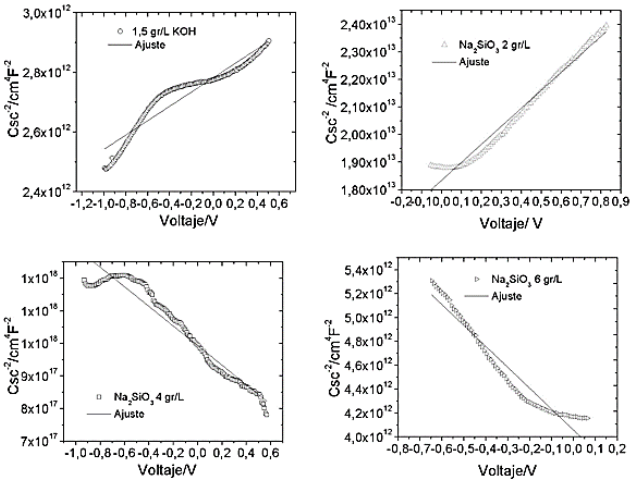


Figura 7. Gráficas Mott-Schottky para recubrimientos obtenido por PEO sobre Mg AZ31 a 2g/L, 4g/L, 6g/L de Na_2SiO_3 y 1.5g/L KOH.
Fuente: Los autores

Tabla 4.
Valores de Densidad de donadores Nd y potencial de banda EFb.

Contenido de Na_2SiO_3	**Densidad de donadores N_d (cm^{-3})**	**Potencial de banda plana E_{fb} (V)**
0g/L	$6.61\text{x}10^{17}$	11.6
2g/L	$1.16\text{x}10^{13}$	2.80
4g/L	$1.67\text{x}10^{9}$	3.30
6g/L	$2.23\text{x}10^{15}$	2.32

Fuente: Los autores

El término $\frac{RT}{F}$ de la ec. (3) se considera insignificante a temperaturas próximas a la corporal, debido a que la magnitud de la constante de Faraday en el denominador es un valor alto, los resultados se presentan en la Tabla 4.

Debido a que a los donantes de un electrodo semiconductor de tipo n son principalmente vacancias de oxigeno (V_O^{2+}) y algunos intersticiales de metal (M_i^{n+}) con cargas positivas en la interface electrodo/electrolito [58], estas vacancias hacen que el electrodo tienda a reaccionar con los aniones de la solución durante la inmersión en el fluido fisiológico simulado que contienen iones Cl^-, HCO_3^-, HPO_4^{2-}, SO_4^{2-} y por ende las películas de óxido pueden ser destruidas por la penetración de estos iones que migran o difunden a través de la películas de óxido y finalmente pueden llegar a desestabilizar el recubrimiento. En investigaciones anteriores [56-58], fue reportado que un menor potencial de banda plana y una menor densidad de donadores hacen que la reactividad de la superficie con los aniones provenientes de la solución sea menor, por tal motivo las muestras con mayor densidad de donadores y adsorción de aniones muestra mayor reactividad, especialmente las

especies de Cl^- por tener mayor movilidad. Por otro lado, la muestra con menor valor de densidad de donadores y menor adsorción de aniones durante la inmersión en solución fisiológica simulada mostró menor reactividad con los aniones [56]. De la Tabla 4 se observa que la adsorción de aniones sobre el electrodo fue disminuida para las tres condiciones de obtención del recubrimiento por PEO debido a que la densidad de donadores disminuyó con respecto a la muestra de aleación de magnesio recubierta solo con KOH. El valor más bajo de densidad de donadores lo presentó la muestra de 4g/L, lo que indica una mayor resistencia a la corrosión, coincidiendo con los resultados obtenidos por EIE. La muestra de 2g/L presento el valor más grande de densidad de donadores, lo que está en relación con los valores más pequeños de impedancia en todo el rango de frecuencia evaluado para esta muestra. Un caso aislado se dio para la muestra de 6g/L, que a pesar de tener los valores más altos de impedancia se encontró que el valor de densidad de donadores fue el más alto, lo cual puede estar relacionado con una mayor interacción del recubrimiento con los aniones de la solución, pudiéndose deber esto al exceso de oxigeno que se difunde del electrolito hasta la interface sustrato/recubrimiento. También es claro notar que el valor de impedancia warburg **Wo1-R** fue menor para la muestra obtenida con 6g/L, comparado con la muestra de 4g/L, indicando esto, que el paso de oxígeno a la interface no tuvo grandes restricciones. El mayor valor de potencial de banda plana fue para la muestra de 4g/L, siendo esto, relacionado con la alta resistencia del recubrimiento al paso de electrones, al contrario que para la muestra de 2g/L, la cual presento un menor valor de resistencia, de acuerdo a los resultados obtenidos en los ensayos de EIE.

4. Conclusiones

De acuerdo al conjunto de resultados obtenidos en esta investigación es posible reconocer que la modificación superficial de la aleación de magnesio AZ31 mediante PEO es un tratamiento que potencializa el uso de este material en aplicaciones biomédicas, ya que con el recubrimiento cerámico formado se disminuye la rápida degradación propia del magnesio y se favorece la interacción con los iones del fluido fisiológico simulado empleado. La correlación de los resultados de DRX y EDS con las pruebas electroquímicas, permitió establecer claramente el rol del Mg_2SiO_4 sobre las propiedades protectoras y bioactivas del recubrimiento, ya que a medida que aumenta la presencia de este compuesto en la muestra, la actividad química superficial disminuye. Sin embargo la disminución en la actividad química superficial puede afectar la reacción de intercambio iónico entre el implante bioactivo y el fluido corporal circundante, desfavoreciendo a su vez, la formación de precursores biológicamente activos de la fase mineral, es decir, para los resultados obtenidos, a una baja concentración de Si en el recubrimiento, se pueden generar propiedades tanto de bioactividad como de protección y en los recubrimientos con mayor cantidad de Si podría generarse una mayor protección pero una disminución en la bioactividad. Este comportamiento es explicado por la difusión de oxigeno encontrada en los ensayos de EIE para las muestras de 4 y 6g/L de Na_2SiO_3, lo cual está relacionado con la posible formación de silanoles (Si $(OH)_2$) sobre la superficie, actuando como regulador buffer del pH en la interface solución fisiológica /Recubrimiento [59], concordando con lo obtenido en los ensayos Mott-Schottky.

Las imágenes MEB obtenidas de la superficie y del corte transversal, permitieron reconocer la cantidad de poros, grietas y micro-canales que se forman durante el proceso de PEO, que corresponde a lo reportado comúnmente para tratamientos superficiales de este tipo. Igualmente se observa que para las muestras preparadas con mayor contenido de Na_2SiO_3, las microfisuras presentes, pueden ser una consecuencia de la naturaleza cerámica que adquiere este recubrimiento a medida que aumenta la formación de Mg_2SiO_4 e incrementa el voltaje hasta el límite dieléctrico.

Estos resultados brindan bases importantes para el diseño de implantes con materiales biodegradables como el magnesio y sus aleaciones, ya que debe encontrarse un equilibrio adecuado entre la protección del material y la actividad química superficial, que le permitan interactuar con los iones del fluido corporal y a su vez favorezcan el crecimiento de la fase mineral del hueso.

Agradecimientos

Los autores agradecen al Sistema General de Regalías SGR, por la financiación de esta investigación. Con código BPIN: 2012000100172 Macroproyecto de salud.

Referencias

[1] Godavitarne, C., Robertson, A., Peters, J. and Rogers, B., Biodegradable materials, Orthop. Trauma, 31, pp. 316-320, 2017. DOI: 10.1016/J.MPORTH.2017.07.011.

[2] Sol, P., Martins, A., Reis, R.L. and Neves, N.M., Advanced polymer composites and structures for bone and cartilage tissue engineering, en: Nanocomposites Musculoskelet. Tissue Regen., Elsevier, 2016: pp. 123-142. DOI: 10.1016/B978-1-78242-452-9.00005-4.

[3] Gohil, S.V., Suhail, S., Rose, J., Vella, T. and Nair, L.S., Polymers and composites for orthopedic applications, en: Mater. Bone Disord., Elsevier, 2017, pp. 349-403. DOI: 10.1016/B978-0-12-802792-9.00008-2.

[4] Wan, P., Tan, L. and Yang, K., Surface modification on biodegradable magnesium alloys as orthopedic implant materials to improve the bio-adaptability: a review, J. Mater. Sci. Technol., 32, pp. 827-834, 2016. DOI: 10.1016/J.JMST.2016.05.003.

[5] Radha, R. and Sreekanth, D., Insight of magnesium alloys and composites for orthopedic implant applications – a review, J. Magnes. Alloys, 5(3), pp. 286-312, 2017. DOI: 10.1016/J.JMA.2017.08.003.

[6] Wan, P., Tan, L. and Yang, K., Surface modification on biodegradable magnesium alloys as orthopedic implant materials to improve the bio-adaptability: a review, J. Mater. Sci. Technol. 32, pp. 827-834, 2016. DOI: 10.1016/j.jmst.2016.05.003.

[7] Dehghanian, C., Aboudzadeh, N. and Shokrgozar, M.A., Characterization of silicon- substituted nano hydroxyapatite coating on magnesium alloy for biomaterial application, Mater. Chem. Phys. 203, pp. 27-33, 2018. DOI: 10.1016/J.MATCHEMPHYS.2017.08.020.

[8] Zeng, R., Dietzel, W., Witte, F., Hort, N. and Blawert, C., Progress and challenge for magnesium alloys as biomaterials, Adv. Eng. Mater., 10(8), pp. 3-14, 2008. DOI: 10.1002/adem.200800035.

[9] M.Y. Salud, materiales metálicos biodegradables en el campo biomédico, 2011, pp. 30-34.

[10] An, J., Leeuwenburgh, S., Wolke, J. and Jansen, J., Mineralization processes in hard tissue: bone, in: Biomineralization and

Biomaterials. 2015, pp. 129-146. DOI: 10.1016/B978-1-78242-338-6.00005-3.

[11] Vieira, A.C., Marques, A.T., Guedes, R.M. and Tita, V., Material model proposal for biodegradable materials, Procedia Eng. 10, pp. 1597-1602, 2011. DOI: 10.1016/j.proeng.2011.04.267.

[12] Wu, G., Ibrahim, J.M. and Chu, P.K., Surface design of biodegradable magnesium alloys - A review, Surf. Coatings Technol. 233(1), pp. 2-12, 2013, DOI: 10.1016/j.surfcoat.2012.10.009.

[13] Guo, L., Wu, W., Zhou, Y., Zhang, F., Zeng, R. and Zeng, J., Layered double hydroxide coatings on magnesium alloys: a review, J. Mater. Sci. Technol. (2018). DOI: 10.1016/J.JMST.2018.03.003.

[14] Meischel, M., Hörmann, D., Draxler, J., Tschegg, E.K., Eichler, J., Prohaska, T. and Stanzl-Tschegg, S.E., Bone-implant degradation and mechanical response of bone surrounding Mg-alloy implants, J. Mech. Behav. Biomed. Mater. 71, pp. 307-313, 2017. DOI: 10.1016/J.JMBBM.2017.03.025.

[15] Miura, K., Yamada, N., Hanada, S., Jung, T.-K. and Itoi, E., The bone tissue compatibility of a new Ti-Nb-Sn alloy with a low Young's modulus., Acta Biomater. 7, pp. 2320-2326, 2011. DOI: 10.1016/j.actbio.2011.02.008.

[16] Guangsheng, X., Hongchao, K., Xianghong, L., Fuping, L., Jinshan, L. and Lian, Z., Microstructure and mechanical properties of porous titanium based on controlling young's modulus, Rare Met. Mater. Eng., 46(8), pp. 2041-2048, 2017. DOI: 10.1016/S1875-5372(17)30176-5.

[17] Mohammed, M.T., Development of a new metastable beta titanium alloy for biomedical applications, Karbala Int. J. Mod. Sci. 3(4), pp. 224-230, 2017. DOI: 10.1016/J.KIJOMS.2017.08.005.

[18] Elahi, N., Kamali, M. and Baghersad, M.H., Recent biomedical applications of gold nanoparticles: a review, Talanta. 184, pp. 537-556, 2018. DOI: 10.1016/J.TALANTA.2018.02.088.

[19] Md-Saad, A.P., Abdul-Rahim, R.A., Harun, M.N., Basri, H., Abdullah, J., Abdul-Kadir, M.R. and Syahrom, A., The influence of flow rates on the dynamic degradation behaviour of porous magnesium under a simulated environment of human cancellous bone, Mater. Des. 122 () pp. 268-279, 2017. DOI: 10.1016/j.matdes.2017.03.029.

[20] Wang, Y., Newman, M.R. and Benoit, D.S.W., Development of controlled drug delivery systems for bone fracture-targeted therapeutic delivery: a review, Eur. J. Pharm. Biopharm. 127, pp. 223-236, 2018. DOI: 10.1016/J.EJPB.2018.02.023.

[21] Li, Y., Liu, L., Wan, P., Zhai, Z., Mao, Z., Ouyang, Z., Yu, D., Sun, Q., Tan, L., Ren, L., Zhu, Z., Hao, Y., Qu, X., Yang, K. and Dai, K., Biodegradable Mg-Cu alloy implants with antibacterial activity for the treatment of osteomyelitis: in vitro and in vivo evaluations, Biomaterials. 106, pp. 250-263, 2016. DOI: 10.1016/j.biomaterials.2016.08.031.

[22] Goharian, A., Kadir, M.R.A., Abdullah, M.R. and Abdullah, M.R., Biodegradable metals (biodegradable magnesium alloys), in: Trauma Plat. Syst., Elsevier, 2017, pp. 143-158. DOI: 10.1016/B978-0-12-804634-0.00008-2.

[23] Niu, W., Wang, Y., Liu, Y., Zhang, B., Liu, M., Luo, Y., Zhao, P., Zhang, Y., Wu, H., Ma, L. and Li, Z., Starch-derived absorbable polysaccharide hemostat enhances bone healing via BMP-2 protein, Acta Histochem. 119(3), pp. 257-263, 2017. DOI: 10.1016/J.ACTHIS.2017.01.011.

[24] Zhang, L., Zhang, J., Chen, C.F. and Gu, Y., Advances in microarc oxidation coated AZ31 Mg alloys for biomedical applications, Corros. Sci. 91, pp. 7-28, 2014. DOI: 10.1016/j.corsci.2014.11.001.

[25] Sankara-Narayanan, T.S.N., Park, I.S. and Lee, M.H., Strategies to improve the corrosion resistance of microarc oxidation (MAO) coated magnesium alloys for degradable implants: Prospects and challenges, Prog. Mater. Sci. 60, pp. 1-71, 2014. DOI: 10.1016/j.pmatsci.2013.08.002.

[26] Wu, Y.F., Wang, Y.M., Jing, Y.B., Zhuang, J.P., Yan, J.L., Shao, Z.K., Jin, M.S., Wu, C.J. and Zhou, Y., In vivo study of microarc oxidation coated biodegradable magnesium plate to heal bone fracture defect of 3 mm width, Colloids Surfaces B Biointerfaces. 158, pp. 147-156, 2017. DOI: 10.1016/J.COLSURFB.2017.06.031.

[27] Liao, J., Hotta, M., Motoda, S. and Shinohara, T., Atmospheric corrosion of two field-exposed AZ31B magnesium alloys with different grain size, Corros. Sci. 71, pp. 53-61, 2013. DOI: 10.1016/j.corsci.2013.02.003.

[28] Hou, X., Qin, H., Gao, H., Mankoci, S., Zhang, R., Zhou, X., Ren, Z., Doll, G.L., Martini, A., Sahai, N., Dong, Y. and Ye, C., A systematic study of mechanical properties, corrosion behavior and biocompatibility of AZ31B Mg alloy after ultrasonic nanocrystal surface modification, Mater. Sci. Eng. C. 78, pp. 1061-1071, 2017. DOI: 10.1016/J.MSEC.2017.04.128.

[29] Esmaily, M., Svensson, J.E., Fajardo, S., Birbilis, N., Frankel, G.S., Virtanen, S., Arrabal, R., Thomas, S. and Johansson, L.G., Fundamentals and advances in magnesium alloy corrosion, Prog. Mater. Sci. 89, pp. 92-193, 2017. DOI: 10.1016/J.PMATSCI.2017.04.011.

[30] Xianhua, C., Yuxiao, G. and Fusheng, P., Research progress in magnesium alloys as functional materials, Rare Met. Mater. Eng., 45, pp. 2269-2274, 2016. DOI: 10.1016/S1875-5372(17)30015-2.

[31] Hornberger, H., Virtanen, S. and Boccaccini, A.R., Biomedical coatings on magnesium alloys - a review, Acta Biomater. 8, pp. 2442-55, 2012. DOI: 10.1016/j.actbio.2012.04.012.

[32] Abatti, G.P., Nunes-Pires, A.T., Spinelli, A., Scharnagl, N. and da Conceição, T.F., Conversion coating on magnesium alloy sheet (AZ31) by vanillic acid treatment: preparation, characterization and corrosion behavior, J. Alloys Compd. 738, pp. 224-232, 2018. DOI: 10.1016/J.JALLCOM.2017.12.115.

[33] Apelfeld, A., Krit, B., Ludin, V., Morozova, N., Vladimirov, B. and Wu, R.Z., The characterization of plasma electrolytic oxidation coatings on AZ41 magnesium alloy, Surf. Coatings Technol. 322, pp. 127-133, 2017. DOI: 10.1016/J.SURFCOAT.2017.05.048.

[34] Schneider, M., Liebmann, T., Langklotz, U. and Michaelis, A., Microelectrochemical investigation of anodic oxide formation on the aluminum alloy AA2024, Electrochim. Acta. 249, pp. 198-205, 2017. DOI: 10.1016/J.ELECTACTA.2017.07.160.

[35] Martin, J., Nominé, A., Brochard, F., Briançon, J.-L., Noël, C., Belmonte, T., Czerwiec, T. and Henrion, G., Delay in micro-discharges appearance during PEO of Al: Evidence of a mechanism of charge accumulation at the electrolyte/oxide interface, Appl. Surf. Sci. 410, pp. 29-41, 2017. DOI: 10.1016/J.APSUSC.2017.03.088.

[36] Stojadinović, S., Vasilić, R., Radić-Perić, J. and Perić, M., Characterization of plasma electrolytic oxidation of magnesium alloy AZ31 in alkaline solution containing fluoride, Surf. Coatings Technol. 273(273), pp. 1-11, 2015. DOI: 10.1016/j.surfcoat.2015.03.032.

[37] Chen, H., Lv, G., Zhang, G., Pang, H., Wang, X., Lee, H. and Yang, S., Corrosion performance of plasma electrolytic oxidized AZ31 magnesium alloy in silicate solutions with different additives, Surf. Coatings Technol. 205, pp. S32-S35, 2010. DOI: 10.1016/j.surfcoat.2010.03.032.

[38] Li, X., Liu, X. and Luan, B.L., Corrosion and wear properties of PEO coatings formed on AM60B alloy in NaAlO2 electrolytes, Appl. Surf. Sci. 257, pp. 9135-9141, 2011. DOI: 10.1016/j.apsusc.2011.05.115.

[39] Henke, M., Tessmar, J. and Göpferich, A., Biomimetic polymers (for biomedical applications), Polymer Science: A Comprehensive Reference, pp. 339-361, 2012. DOI: 10.1016/B978-0-444-53349-4.00222-3.

[40] Chisholm, M.F., Scanning microscopy for nanotechnology, 2006. DOI: 10.1007/978-0-387-39620-0.

[41] Kokubo, T. and Takadama, H., How useful is SBF in predicting in vivo bone bioactivity?, Biomaterials. 278159, pp. 2907-2915, 2006. DOI: 10.1016/j.biomaterials.2006.01.017.

[42] Veys-Renaux, D., Rocca, E., Martin, J. and Henrion, G., Initial stages of AZ91 Mg alloy micro-arc anodizing: growth mechanisms and effect on the corrosion resistance, Electrochim. Acta. 124, pp. 36-45, 2014. DOI: 10.1016/j.electacta.2013.08.023.

[43] Mori, Y., Koshi, A., Liao, J., Asoh, H. and Ono, S., Characteristics and corrosion resistance of plasma electrolytic oxidation coatings on AZ31B Mg alloy formed in phosphate – Silicate mixture electrolytes, Corros. Sci. 88, pp. 254-262, 2014. DOI: 10.1016/j.corsci.2014.07.038.

[44] Hwang, D.Y., Kim, Y.M. and Shin, D.H., Corrosion resistance of plasma-anodized AZ91 Mg alloy in the electrolyte with/without potassium fluoride, Mater. Trans. 50(3), pp. 671-678, 2009. DOI: 10.2320/matertrans.MER2008345.

[45] Cakmak, E., Tekin, K.C., Malayoglu, U. and Shrestha, S., The effect of substrate composition on the electrochemical and mechanical properties of PEO coatings on Mg alloys, Surf. Coatings Technol. 204(8), pp. 1305-1313, 2010. DOI: 10.1016/j.surfcoat.2009.10.012.
[46] Zhuang, J.J., Guo, Y.Q., Xiang, N., Xiong, Y., Hu, Q. and Song, R.G., A study on microstructure and corrosion resistance of ZrO2-containing PEO coatings formed on AZ31 Mg alloy in phosphate-based electrolyte, Appl. Surf. Sci. 357, pp. 1468-1471, 2015. DOI: 10.1016/j.apsusc.2015.10.025.
[47] Gupta, P., Tenhundfeld, G., Daigle, E.O. and Ryabkov, D., Electrolytic plasma technology: science and engineering - an overview, Surf. Coatings Technol. 201(21), pp. 8746-8760, 2007. DOI: 10.1016/j.surfcoat.2006.11.023.
[48] Yao, Z.P., Jiang, Z.H., Xin, S.G., Sun, X.T. and Wu, X.H., Electrochemical impedance spectroscopy of ceramic coatings on Ti-6Al-4V by micro-plasma oxidation, Electrochim. Acta. 50(16), pp. 3273-3279, 2005. DOI: 10.1016/j.electacta.2004.12.001.
[49] Lim, T.S., Ryu, H.S. and Hong, S.-H., Electrochemical corrosion properties of CeO2-containing coatings on AZ31 magnesium alloys prepared by plasma electrolytic oxidation, Corros. Sci. 62, pp. 104-111, 2012. DOI: 10.1016/j.corsci.2012.04.043.
[50] Song, G., John, D.S.T. and Nairn, J., The anodic dissolution of magnesium and sulphate solutions in chloride, Corros. Sci. 39(10-11), pp. 1981-2004, 1997. DOI: 10.1016/S0010-938X(97)00090-5.
[51] Huang, K., Cai, S., Xu, G., Ye, X., Dou, Y., Ren, M. and Wang, X., Preparation and characterization of mesoporous 45S5 bioactive glass – ceramic coatings on magnesium alloy for corrosion protection, J. Alloys Compd. 580, pp. 290-297, 2013. DOI: 10.1016/j.jallcom.2013.05.103.
[52] Liu, X., Chu, P.K. and Ding, C., Surface modification of titanium, titanium alloys, and related materials for biomedical applications, Mater. Sci. Eng. R Reports. 47(3), pp. 49-121, 2004. DOI: 10.1016/j.mser.2004.11.001.
[53] De Gryse, R., On the interpretation of mott-schottky plots determined at semiconductor/electrolyte systems, J. Electrochem. Soc. 122(5), pp. 711-712, 1975. DOI: 10.1149/1.2134298.
[54] Metikoš-Huković, M., Omanović, S. and Jukić, A., Impedance spectroscopy of semiconducting films on tin electrodes, Electrochim. Acta. 45(6), pp. 977-986, 1999. DOI: 10.1016/S0013-4686(99)00298-4.
[55] Xia, S.J., Yue, R., Rateick, R.G. and Birss, V.I., Electrochemical studies of AC/DC anodized Mg alloy in NaCl solution, J. Electrochem. Soc. 151(3), pp. B179-B187, 2004. DOI: 10.1149/1.1646139.
[56] Duan, H., Yan, C. and Wang, F., Effect of electrolyte additives on performance of plasma electrolytic oxidation films formed on magnesium alloy AZ91D, Electrochim. Acta. 52(11), pp. 3785-3793, 2007. DOI: 10.1016/j.electacta.2006.10.066.
[57] Scully, J. and Silverman, D., Electrochemical impedance: analysis and interpretation, 2013.
[58] Li, Y., Zhang, T. and Wang, F., Effect of microcrystallization on corrosion resistance of AZ91D alloy, Electrochim. Acta. 51(14), pp. 2845-2850, 2006. DOI: 10.1016/j.electacta.2005.08.023.
[59] Cipriano, A.F., Sallee, A., Tayoba, M., Cortez-Alcaraz, M.C., Lin, A., Guan, R.G., Zhao, Z.Y. and Liu, H., Cytocompatibility and early inflammatory response of human endothelial cells in direct culture with Mg-Zn-Sr alloys, Acta Biomater. 48, pp. 499-520, 2016. DOI: 10.1016/j.actbio.2016.10.020.

K, Dorado-Bustamante, received the BSc. Eng in Chemical Engineering in 2016 from the Universidad Nacional de Colombia, Medellin. He won in the same year a full scholarship from the Instituto Balseiro, Patagonia, Argentina and currently he is working in the department of nuclear physics in the Sp. degree of applications of nuclear energy (CEATEN) in Buenos Aires, Argentina. His research interest includes: electrochemical processes, smart materials, and nuclear applications for biomedical devices.
ORCID: 0000-0002-2810-1191

B. Zuluaga-Díaz, received the BSc. Eng in Chemical Engineering in 2013 from Universidad Nacional de Colombia, Medellin. During two years he worked for companies of coatings manufacturing. Actually, he works for the Universidad Nacional de Colombia, Medellin as the technician of characterization devices in the laboratory of biomaterials and he is MSc. Eng Materials and processes from Universidad Nacional de Colombia, Medellin. His research interest includes biological characterization of biomaterials, development of coatings and biomedical devices.
ORCID: 0000-0003-2412-3761

H. Estupiñán-Duran, received the BSc. Eng in Metallurgy Engineering in 2001, MSc. degree in Engineering in 2005, and the PhD. degree in Chemical Engineering in 2011, all of them from the Universidad Industrial de Santander, Santander, Colombia. He worked in corrosion and development of biomaterials. Actually, he is a full professor in the Department of Materials and Minerals, Facultad de Minas, Universidad Nacional de Colombia, Medellin. His research interest include corrosion processes, surface characterization, biosensors, biocompatible and antibacterial coatings and orthopedic materials.
ORCID: 0000-0002-9607-3364



UNIVERSIDAD NACIONAL DE COLOMBIA
SEDE MEDELLÍN
FACULTAD DE MINAS

Área Curricular de Ingeniería
Geológica e Ingeniería de Minas y Metalurgia

Oferta de Posgrados

Especialización en Materiales y Procesos
Maestría en Ingeniería - Materiales y Procesos
Maestría en Ingeniería - Recursos Minerales
Doctorado en Ingeniería - Ciencia y Tecnología de Materiales

Mayor información:

E-mail: acgeomin_med@unal.edu.co
Teléfono: (57-4) 425 53 68

UNIVERSIDAD NACIONAL DE COLOMBIA
SEDE MEDELLÍN
FACULTAD DE MINAS



DYNA
http://dyna.medellin.unal.edu.co/

Manufacture of oxy-acetylene thermally sprayed coatings on refractory substrates from unconventional feedstock material

Edwin H. Cadavid-Iglesias [a], Fabio Vargas-Galvis [a], María Esperanza López-Gómez [a], Carlos Mario Mesa [b], Fabio Alonso Vargas [b], Guillermo Latorre [c] & Gabriel Peña [d]

[a] *Grupo GIPIMME, Universidad de Antioquia, Medellín-Colombia. edwin.cadavid@udea.edu.co, fabio.vargas@udea.edu.co, esperanza.lopez@udea.edu.co*
[b] *Erecos S.A.S, Medellín-Colombia. carlos.mesa@erecos.com, fabio.vargas@erecos.com*
[c] *Instituto Colombiano del Petróleo, Ecopetrol-ICP, Piedecuesta, Santander, Colombia. guillermolatorrecortes@gmail.com*
[d] *Grupo GIFIMAC y GITEC, Universidad Francisco de Paula Santander, Cúcuta, Colombia. ggabrielp@yahoo.com*

Received: June 7th, 2017. Received in revised form: August 23th, 2017. Accepted: September 19th, 2017

Abstract
A chromite mineral and two industrial residues produced in the petrochemical and thermoelectric industries, were selected, characterized, processed and deposited on refractory bricks. By means of X-ray fluorescence and X-ray diffraction the chemical composition and crystallographic phases of raw materials were analyzed, morphology and particle size was determinate using Scanning Electron Microscopy. The materials were deposit by oxyacetylene thermal spray on silica-alumina refractory bricks and high alumina low cement concrete, commercial references ER-40 and CBC-50 from ERECOS S.A.S.. The parameters used for the coating deposition were optimized based on preliminary test and simulations using the Jets&powders software. The chromite mineral coating displayed greater structure homogeneity than the other two coatings; the last ones presented partially melted particles and high porosity. However, based on the chemical composition, the response to adhesion test and the crystallographic phases present in the coatings, all of them are potential candidates to be used as protective barriers against corrosive effects on refractories.

Keywords: thermal spray; coatings; refractory; adherence; Industrial residues; residues reuse.

Elaboración de recubrimientos cerámicos sobre sustratos refractarios utilizando proyección térmica oxiacetilénica a partir de materias primas no convencionales

Resumen
Se seleccionaron, caracterizaron, procesaron y depositaron sobre ladrillos refractarios, dos residuos industriales provenientes de procesos de la industria petroquímica y termoeléctrica, así como un mineral de cromita. La composición química y las fases cristalográficas de cada uno de estos polvos fueron determinadas mediante Fluorescencia y Difracción de Rayos X, mientras que la morfología y tamaño de partícula fueron analizados mediante Microscopía Electrónica de Barrido. Estos polvos fueron depositados mediante proyección térmica oxiacetilénica sobre ladrillos refractarios silico-aluminosos y concretos de alta alúmina de bajo cemento, cuyas referencias comerciales de la empresa Erecos S.A.S. son ER-40 y CBC-50 respectivamente. Los parámetros utilizados para la elaboración de los recubrimientos fueron optimizados a partir de recubrimientos elaborados previamente y de los resultados de simulaciones realizadas con el software Jets&poudres. De los recubrimientos obtenidos el que presentó mayor homogeneidad en su estructura fue el elaborado con el mineral de cromita, los demás evidenciaron gran cantidad de partículas sin fundir y mayor porosidad. Sin embargo, por la composición química, su buena adherencia y las fases presentes en los recubrimientos todos son potenciales candidatos para ser usados como medio protector contra el deterioro de refractarios expuestos a altas temperaturas.

Palabras clave: proyección térmica; recubrimientos; refractarios; adherencia; residuos industriales; reutilización de residuos.

How to cite: Cadavid-Iglesias, E.H., Vargas-Galvis, F., López-Gómez, M.E., Mesa, C.M., Vargas, F.A., Latorre, G. and Peña G., Elaboración de recubrimientos cerámicos sobre sustratos refractarios utilizando proyección térmica oxiacetilénica a partir de materias primas no convencionales. DYNA 85(205), pp. 338-347, June, 2018.

© The author; licensee Universidad Nacional de Colombia.
Revista DYNA, 85(205), pp. 338-347, June, 2018, ISSN 0012-7353
DOI: https://doi.org/10.15446/dyna.v85n205.65539

1. Introducción

Los recubrimientos cerámicos depositados mediante proyección térmica son ampliamente utilizados para proteger estructuras, equipos y componentes de equipos expuestos a condiciones tribológicas altamente agresivas, así como a ambientes corrosivos y a altas temperaturas[1-5].

En el ámbito industrial este tipo de recubrimientos son depositados principalmente sobre sustratos metálicos, sin embargo, algunos trabajos realizados por otros investigadores han demostrado su potencial para proteger materiales refractarios [6-8].

Bolelli y sus colaboradores [6] han recubierto mediante proyección térmica por plasma a partir de polvos comerciales, ladrillos refractarios convencionales (prensados y sinterizados) de Alúmina-Mullita usados en hornos para la producción de vidrio. De acuerdo con pruebas de resistencia química y abrasiva realizadas a los refractarios recubiertos, concluyeron que su desempeño es similar al de refractarios de Al_2O_3-ZrO_2-SiO_2 electro-fundidos cuyo valor comercial es entre 15 y 20 veces superior al de un ladrillo convencional recubierto [6].

A pesar de los excelentes resultados reportados por Bolelli y sus colaboradores [6] respecto al mejoramiento del desempeño de refractarios convencionales, su uso en el ámbito industrial ha sido limitado, debido principalmente a que el mercado objetivo no ha asumido el aumento en el costo que implica la aplicación del recubrimiento.

Teniendo en cuenta que uno de los factores que más influye en el costo de los recubrimientos cerámicos depositados mediante proyección térmica son los polvos de partida, (cuyos precios han incrementado debido a la disminución de las reservas minerales de las cuales provienen) [9], el uso de materias primas no convencionales podría reducir significativamente el costo de los recubrimientos depositados sobre refractarios, dando mayores posibilidades para su utilización industrial.

De acuerdo con lo anterior, en este trabajo se pretende elaborar recubrimientos con la técnica de proyección térmica por combustión a partir de materias primas no convencionales sobre elementos refractarios con la intención de mejorar su resistencia superficial en ambientes corrosivos de altas temperaturas.

2. Metodología experimental

2.1. Tratamiento, caracterización y análisis de materias primas

Debido a su naturaleza refractaria, se seleccionaron dos residuos provenientes de procesos de la industria petroquímica y termoeléctrica nombrados catalizador de reforma y cenizas volantes, así como un mineral de cromita, como posibles candidatos para ser usados como materias primas en recubrimientos aplicados por proyección térmica.

Con el fin de adecuar cada una de las materias primas a los requerimientos de tamaño que tiene el proceso de proyección térmica, las partículas del catalizador de reforma y las del mineral de cromita fueron molturadas en un molino de bolas. Los polvos obtenidos, junto con las cenizas volantes fueron clasificados por tamizado a la fracción -270 + 325 de la serie Tyler.

Su composición química y fases cristalográficas fueron determinadas mediante fluorescencia de rayos X y difracción de rayos X respectivamente empleando un espectrómetro ARL OPTIMIX™ y un difractómetro Panalytical-Empyream con ánodo de cobre de radiación Kα λ=1.540598Å con una velocidad de escaneo de 0.026º/minuto, los espectros de difracción obtenidos fueron analizados mediante el método de Rietveld haciendo uso del software PANalytical HighscorePlus con el fin de cuantificar las fases cristalinas detectadas en cada muestra. Por su parte, la morfología de las partículas, después de la molienda y del tamizado, fueron analizadas por medio de un ensayo de microscopia de barrido electrónico en un equipo de marca Jeol™ JSM-6490LV.

2.2. Caracterización de sustratos

La rugosidad en la superficie del sustrato influye directamente en la adherencia del recubrimiento, razón por la cual generalmente se realiza una preparación superficial al material sobre el cual será depositado el recubrimiento, con el fin de proporcionarle suficiente àrea de anclaje a las partículas que serán depositadas sobre él. Normalmente la rugosidad se mide a través de instrumentos de contacto como perfilómetros y rugosímetros, no obstante, en el caso de los ladrillos refractarios utilizados en este trabajo, la superficie posee cambios topográficos excesivos que superan la capacidad de medida de los instrumentos de contacto, razón por la cual fue necesario utilizar una técnica de no contacto que permite correlacionar la rugosidad de la superficie del sustrato con su porosidad superficial.

De acuerdo con lo anterior, se evaluó la porosidad superficial de los ladrillos refractarios de referencia ER-40 y de concreto refractario de referencia CBC-50, ambos fabricados por la empresa ERECOS S.A.S., los cuales fueron utilizados como sustrato; para la determinación de la porosidad superficial se utilizó el método de análisis de imágenes a partir de fotografías tomadas a la superficie de cada uno de los ladrillos, utilizando un microscopio estereográfico y el software ImageJ. Los valores de porosidad reportados son el promedio de las medidas obtenidas a partir de 5 imágenes, las cuales fueron seleccionadas tratando de cubrir un área representativa de la superficie de la muestra y teniendo en cuenta el tamaño de los poros.

2.3. Elaboración de recubrimientos

Para establecer las condiciones adecuadas para la elaboración de los recubrimientos mediante proyección térmica, se llevó a cabo la elaboración de recubrimientos preliminares complementados con simulaciones numéricas realizadas con el software Jets&Poudres [10] desarrollado por la Universidad de Limoges, el cual permite determinar el perfil de temperaturas de llamas oxiacetilénicas a partir del flujo del gas combustible y comburente, así como el número de Sommerfeld (K), que indica si una partícula proyectada sobre un sustrato tendrá alta posibilidad de adherirse a él [4].

Los flujos de gas utilizados para la simulación de los perfiles de temperatura de la llama son mostrados en la Tabla 1. Por su parte, las características físicas, así como las propiedades térmicas teóricas de las partículas a las cuales se les determinó el número de Sommerfeld, calculadas con base en el porcentaje de fases cristalográficas presentes en las materias primas, son mostradas en la Tabla 2.

Tabla 1.
Relaciones volumétricas usadas en la simulación.

C2H2 [L/min]	O2 [L/min]	Relación volumétrica
	31	1:1,4
	37	1:1,7
22	55	1:2,5
	70	1:3,2
	88	1:4,0

Fuente: Cadavid, E.

Tabla 2.
Propiedades térmicas teóricas de las partículas.

	Mineral de Cromita	Catalizador de reforma	Cenizas volantes
Densidad [Kg/m3]	4129.9	3860	1888
Calor específico [J/KgK]	812.5	1276.9	2161.6
Conductividad térmica [J/msK]	7.2	29.1	4.4
Temperatura de fusión [K]	2126.5	2332.9	2065.6
Calor latente de fusión [J/Kg]	2526392.5	1180819.2	964769.8
Masa molar [g/mol]	170.5	103.9	235.4

Fuente: Cadavid, E.

Tabla 3.
Parámetros usados para la elaboración de los recubrimientos.

	Mineral de cromita	Catalizador de reforma	Cenizas volantes
Distancia de proyección [cm]	9	9	8
Flujo de materia prima [g/min]	13.6	12.6	6
Pases de precalentamiento	5	5	7
Pases de proyección	18	10	12
Flujo de Oxígeno [L/min]	55	92	88
Flujo de Acetileno [L/min]	22	22.5	22
Flujo de Nitrógeno [L/min]	17	17	17

Fuente: Cadavid, E.

Los recubrimientos fueron elaborados en la cámara de proyección térmica ARESTE I de la Universidad de Antioquia, la cual está equipada con una antorcha Eutectic Castolin Terodyn^{TM} 2000 modificada y posee dispositivos electromecánicos para controlar los principales parámetros de la proyección, así como un pirómetro óptico para medir la temperatura de precalentamiento del sustrato. En la elaboración de los recubrimientos se utilizó el Roto Jet RPA3 para guiar y acelerar las partículas dentro de la llama. La velocidad lineal de desplazamiento de la antorcha frente a los sustratos fue de 0,59 cm/s y la velocidad de rotación del porta-muestras fue de 92,2 RPM. Los demás parámetros usados para elaborar los recubrimientos son presentados en la Tabla 3.

2.4. Caracterización de los recubrimientos

La caracterización estructural de los recubrimientos se realizó mediante microscopia de barrido electrónico utilizando un equipo de marca Jeol^{TM} JSM-6490LV, mientras que sus fases cristalinas se identificaron por medio de Difracción de Rayos X utilizando un equipo PANalytical Empyream con los mismos parámetros de la sección 2.1. Las pruebas de adhesión se realizaron mediante pull off de acuerdo con la norma ASTM D4541[11].

Tabla 4.
Resultados de la prueba de Fluorescencia de Rayos X de las materias primas.

Elemento	Mineral de cromita [% peso]	Catalizador Reforma [% peso]	Cenizas volantes [% peso]
Fe	40.53	0.84	37.89
Cr	36.61	---	0.13
Mg	8.66	---	0.04
Al	6.61	69.58	21.26
Ti	5.39	---	0.76
Si	2.17	1.87	34.34
Ni	---	24.06	0.23
Na	---	2.81	---
S	---	0.81	0.62
P	---	---	0.11
K	---	---	2.57
Ca	---	---	1.99

Fuente: Cadavid, E.

3. Resultados y discusión

3.1. Caracterización de materias primas

De acuerdo a los resultados del análisis químico, consignados en la Tabla 4, se pudo establecer que el mineral de cromita está constituido principalmente por hierro, cromo, aluminio, magnesio y titanio; por su parte, en el catalizador de reforma los principales constituyentes son aluminio y níquel, acompañados de silicio, sodio y azufre. Así mismo se evidenció que las cenizas volantes contienen principalmente silicio, aluminio y hierro. Los elementos anteriores pueden estar en forma de óxido o mezclados entre sí formando compuestos.

3.1.1. Fases cristalográficas

Los materiales refractarios deben ser resistentes al calor, a esfuerzos mecánicos de compresión y tensión, a esfuerzos térmicos, a la corrosión/erosión y a la abrasión mecánica, por ende, se debe prestar especial atención a su composición química y en particular a la presencia de fases que les puedan conferir dichas propiedades.

Con base en las pruebas de difracción de rayos X realizadas a los materiales estudiados, se evidenció que las fases cristalinas de mayor proporción en el mineral de cromita son el aluminato de magnesio $MgAl_2O_4$, la magnesioferrita $Mg_8Al_{6.32}Fe_{9.68}O_{32}$ y el silicato de hierro Fe_2SiO_4. Por su parte, la fase predominante en el catalizador de reforma es el corindón o alúmina α, seguida por óxido de níquel. En lo que respecta a las cenizas volantes, sus fases predominantes son la mullita y el cuarzo.

En la Fig. 1. y en la Tabla 5 se presentan los espectros de difracción y los porcentajes de fases determinadas por medio de refinamiento Rietveld en las materias primas utilizadas para la elaboración de los recubrimientos.

Mineral de cromita

En lo que respecta a las principales fases que constituyen el mineral de cromita, se ha encontrado que las espinelas son de gran importancia para el buen desempeño de los materiales expuestos a altas temperaturas [12]; por otro lado el aluminato de magnesio ($MgAl_2O_4$), es usado en revestimientos de cucharas de acero y en otras aplicaciones

Tabla 5.
Porcentajes de fases determinadas en las materias primas.

Fase cristalina	Mineral de cromita [% en peso]	Catalizador de reforma [% en peso]	Cenizas Volantes [% en peso]
Aluminato de magnesio ($MgAl_2O_4$)	29.1	--	--
Magnesioferrita	21.7	--	--
Silicato de hierro	19.6	--	--
Magnesiocromita	7.7	--	--
Periclasa	9.3	--	--
Cromita	0.5	--	--
Magnetita	3	--	--
Greenalita	0.4	--	--
Ilmenita	4.6	--	--
Óxido de titanio	4.1	--	--
Corindón	--	79.7	--
Óxido de Níquel	--	12.5	--
Aluminato de Níquel	--	6.3	--
Níquel	--	1.5	--
Mullita	--	--	45
Cuarzo	--	--	40
Hematita	--	--	10
Óxido de magnesio	--	--	5

Fuente: Cadavid, E.

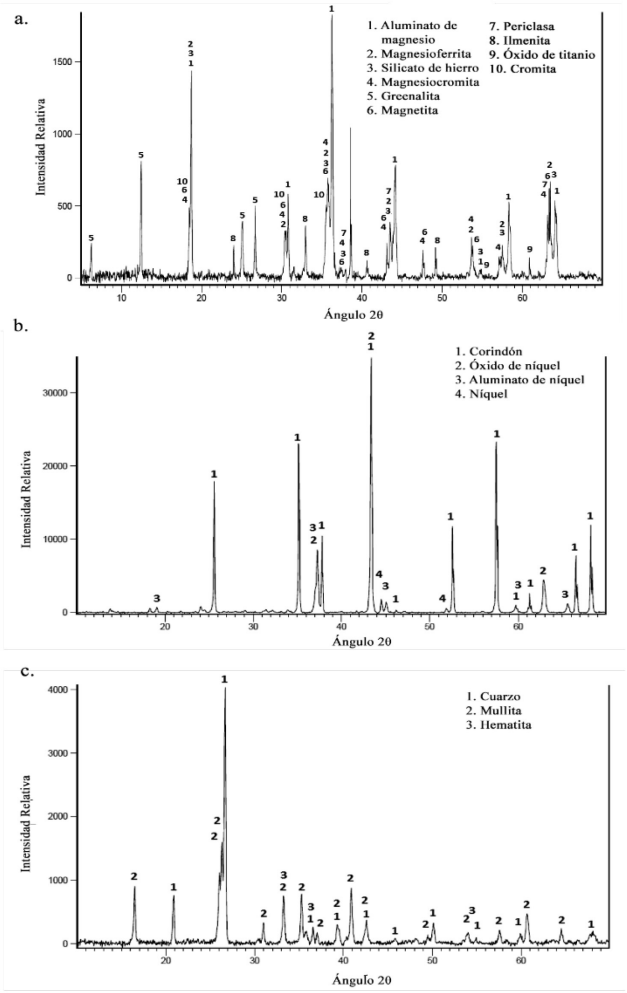


Figura 1. Difractogramas de las materias primas, a. Mineral de cromita, b. Catalizador de Reforma y c. Cenizas volantes.
Fuente: Cadavid, E.

refractarias debido a sus propiedades termo-mecánicas y resistencia a la corrosión a altas temperaturas con presencia de escorias acidas/básicas [13-16].

Por su parte, la fayalita (silicato de hierro), es utilizada para la producción de fosterita, la cual es de gran utilidad en la elaboración de ladrillos refractarios. Así mismo la magnesiocromita presenta alta resistencia química contra ortosilicatos de Mg, Sr, Ba y Ca [17-20].

Se ha reportado también la adición de minerales tales como periclasa, forsterita, caolinita y serpentina, en refractarios de magnesia (MgO) [21,22] con el fin de reducir su costo de producción.

Igualmente, la adición de ciertos dopantes, entre ellos la hematita (Fe_2O_3), el óxido de titanio (TiO_2) y la ilmenita ($FeTiO_3$), tienden a mejorar ciertas propiedades de refractarios fabricados con base en el sistema MgO - CaO, entre ellas el control de tamaño de grano, lo que conlleva una diminución en la infiltración de escoria [23-25].

Por otro lado la magnesioferrita contribuye como unos de los principales agentes ligantes en los materiales refractarios de magnesia [26,27].

- *Catalizador de reforma*

Respecto a las principales fases presentes en el catalizador de reforma, se ha reportado que el aluminato de níquel $NiAl_2O_4$ ha sido propuesto para aplicaciones como material magnético, pigmentos, catalizadores y en materiales refractarios gracias a su estructura tipo espinela [28].

Por otro lado, estudios han demostrado que la adición de NiO en refractarios básicos elaborados con base en $MgAl_2O_4$, disminuye su reactividad respecto a mezclas de gases que contienen O_2 gas / SO_2 / SO_3 los cuales corroen los refractarios provocando pérdida de masa en el material, y aunque sus propiedades físicas tienden a disminuir con la adición de NiO, es posible obtener refractarios con propiedades similares a las de aquellos sin la adición del NiO [29].

Por su parte, la alúmina tiene gran resistencia a la corrosión en medio acido a altas temperaturas, por ende, es ampliamente usada como materia prima para la elaboración de refractarios; generalmente estos materiales se definen dependiendo del contenido de alúmina en su composición y otros agregados como el Fe_2O_3. Entre los principales están las arcillas refractarias, bauxita y la alúmina sinterizada [30].

Cenizas Volantes

En lo concerniente a las fases presentes en las cenizas volantes, se ha reportado que la mullita no solo tiene buenas propiedades refractarias a altas temperaturas, sino también excelente capacidad de aislamiento eléctrico, baja razón de cedencia, baja expansión y conductividad térmica, buena resistencia química, térmica y física, haciéndola potencialmente útil en un gran rango de aplicaciones, desde refractarios hasta sustratos electrónicos [31,32].

Por otra parte la sílice es una materia prima altamente demandada en la industria de los refractarios, ya que gracias a sus propiedades y que en presencia de alúmina permite la formación de mullita, puede ser usada en diversas aplicaciones como en refractarios silico-aluminosos para

recubrimientos en hornos de laboratorios, soportes refractarios, aislantes térmicos, en la industria cerámica, del papel, y las relacionadas con la producción de alimentos, estos refractarios son relativamente menos costos que otros ladrillos refractarios elaborados a partir de materias primas de difícil obtención y procesamiento [33]. No obstante, en compañía de mullita, la sílice es utilizada para la fabricación de refractarios de bajo peso [34], sin embargo la presencia de altos volúmenes de fase vítrea (de 30 a 70%), asociada al cuarzo, puede resultar en una disminución de la resistencia termo-mecánica de los refractarios mulliticos [35].

Los resultados anteriores permiten establecer que aunque los materiales evaluados no son los empleados convencionalmente para elaborar recubrimientos depositados por proyección térmica, las fases que los constituyen están presentes comúnmente en materiales refractarios, y es de esperar que las transformaciones cristalográficas que se podrían dar durante la fabricación de los recubrimientos no alteren significativamente el desempeño que ellos puedan tener a las condiciones a las cuales dichos refractarios son expuestos generalmente. Las transformaciones de fase que experimentan cada uno de los polvos durante la elaboración de los recubrimientos son presentadas en la sección 3.3.

3.1.2. Morfología y fluidez de la materia prima

En la Fig. 2. Se presenta la morfología de las partículas de mineral de cromita y del catalizador de reforma luego del proceso de molienda y tamizado, así como de las cenizas volantes después de ser tamizadas y clasificadas en un rango de tamaño entre 45 y 53 μm. En el proceso de elaboración de recubrimientos por proyección térmica este rango de tamaño de partícula favorece el flujo de los polvos y la fusión de las partículas, ya que si estas son demasiado pequeñas (normalmente inferiores a 5 μm) dificultan su transporte por los conductos de la antorcha de proyección, dando como resultado recubrimientos discontinuos, mientras que partículas demasiado grandes (generalmente superiores a 60 μm) dificultan su fusión en la llama, dando como resultado recubrimientos con partículas parcialmente fundidas y por ende una mayor porosidad en el recubrimiento [36].

Las partículas del catalizador de reforma y del mineral de cromita, Fig. 2a y 2b. Respectivamente, son irregulares y con planos de fractura producto de la molienda mecánica, esto podría dificultar su fluidez si no tienen un tamaño apropiado, por otro lado, las cenizas volantes, Fig. 2c. Son en su mayoría esféricas lo cual facilita su fluidez en los conductos que las transportan a la fuente de calor en el proceso de proyección térmica.

Con el fin de establecer si las partículas de cada polvo pueden ser transportadas por los conductos de la antorcha Eutectic Castolin Terodyn^{TM} 2000 utilizada para elaborar los recubrimientos, se midió el flujo de las materias primas de acuerdo con lo establecido en la norma ASTM B213: "Standard Test Methods for Flow Rate of Metal Powders Using the Hall Flowmeter" [37]. La prueba consiste en depositar un volumen determinado de material en una copa, para determinar si fluye de manera continua por efecto de la gravedad, lo que indica que fluirá correctamente al momento de elaborar el recubrimiento, de lo contrario debería ajustarse el tamaño de partícula de los polvos. Los resultados de esta prueba se muestran en la Tabla 6.

El flujo obtenido en cada una de las materias primas utilizadas para elaborar los recubrimientos fue continuo, lo que indica que estos materiales tendrán una fluidez suficiente para ser transportados por los ductos del equipo de proyección térmica, por lo tanto, la alimentación de los polvos de partida a la llama será continua, lo que favorece la obtención de recubrimientos homogéneos.

3.2. Porosidad superficial de los sustratos

De acuerdo con el análisis de imágenes realizado a la superficie de cada uno de los sustratos, se pudo establecer que la porosidad superficial del ladrillo y del concreto refractario es de 10.5 ± 3.9% y de 4.9 ± 0.8% respectivamente, y que el tamaño de los poros del ladrillo es más pequeño que en los refractarios de concreto. Superficies con porosidades como las medidas en los refractarios que se utilizarán como sustratos, aumentarán de forma importante la adhesión del recubrimiento, ya que cada uno de estos poros constituyen puntos de anclaje para las partículas depositadas.

3.3. Caracterización de los recubrimientos obtenidos

Los resultados de las simulaciones realizadas con el fin de predecir la afectación térmica de las materias primas en vuelo durante el proceso de proyección térmica por llama oxiacetilénica, se presentan en las Fig. 3, 4 y 5. Donde se aprecia el porcentaje de fusión y el valor del K-Sommerfeld para las diferentes materias primas a lo largo de la llama, así como los perfiles de temperatura de la llama respectivamente. Estas mediciones se obtuvieron con base en las relaciones volumétricas de gases especificadas en la Tabla 1.

En las Figs. 6 y 7. Se muestran los recubrimientos obtenidos y su microestructura respectivamente.

A partir del análisis realizado a las imágenes de la Fig. 7. Se pudo establecer que el espesor de los recubrimientos elaborados con el mineral de cromita, el catalizador de reforma y las cenizas volantes son 489.79 ± 22 μm, 570.10 ± 29.8 μm y 423.06 ± 21.5 μm respectivamente. Así mismo, en los recubrimientos elaborados con catalizador de reforma, Fig. 7b. Y cenizas volantes, Fig. 7c. Se evidencia la presencia de partículas sin fundir, lo que propicia la formación de defectos en la estructura del recubrimiento; por otro lado, en el recubrimiento elaborado con mineral de cromita las partículas alcanzaron un estado de fusión adecuado para la formación de lamells con alto grado de empaquetamiento, Fig. 7a.

La falta de fusión de las partículas del residuo de catalizador de reforma y de las cenizas volantes está asociado a la alta porosidad de los polvos de partida, lo que reduce la transferencia de calor desde la superficie de la partícula hacia su interior durante el calentamiento en la llama oxiacetilénica utilizada para la proyección térmica.

Por su parte, los resultados del análisis de difracción de rayos X realizado a los recubrimientos depositados permitieron establecer que las fases cristalinas identificadas

en el recubrimiento elaborado con el mineral de cromita solo presenta una fase cristalina, aluminato de magnesio ($MgAl_2O_4$), Fig. 8a. Mientras que el recubrimiento depositado a partir del catalizador de reforma está constituido principalmente por alúmina γ, alúmina α y con una pequeña cantidad de níquel metálico, ver Fig. 8b. Por otro lado, las fases cristalinas presentes en el recubrimiento de las cenizas volantes son cuarzo, mullita y hematita, ver Fig. 8c.

Durante la elaboración de los recubrimientos, las materias primas sufren transformaciones de fase debido al tratamiento térmico al que son expuestas, este consiste en aumentos de temperatura, en muchos casos hasta su punto de fusión, y enfriamientos a tasas muy altas; por esta razón no todas las fases cristalográficas identificadas en las tres materias primas, ver Fig. 1. fueron detectadas en los recubrimientos obtenidos.

Por su parte, en la Tabla 7 se reporta el valor del esfuerzo de la falla producida durante el ensayo de adhesión mediante pull off. El análisis de la fractura producida hizo evidente que los recubrimientos elaborados con catalizador de reforma fallan de manera cohesiva entre capas del recubrimiento, lo que indica que la energía de enlace entre las partículas que lo conforman es menor a la fuerza de adhesión con el sustrato, esto se debe a que no logran un estado de fusión adecuado y por ende la estructura del recubrimiento es menos homogénea. Lo Anterior puede influir negativamente en el desempeño del recubrimiento cuando sea expuesto bajo condiciones mecánicas que puedan promover la descohesión de las capas que lo constituyen. A pesar de lo anterior, es importante tener en cuenta que el valor del esfuerzo al que se produce la falla cohesiva es lo suficientemente alto como para soportar los requerimientos mecánicos a los que normalmente son expuestos los materiales refractarios. Por otro lado, los recubrimientos elaborados con residuos de cromita y cenizas volantes presentan fallas cohesivas en el sustrato, es decir, que los enlaces entre las capas de recubrimiento y su adherencia al sustrato son más fuertes que las fuerzas cohesivas del ladrillo refractario.

4. Conclusiones

Se elaboraron recubrimientos mediante proyección térmica oxiacetilénica sobre ladrillos refractarios silico-aluminosos y concretos de alta alúmina y bajo cemento, utilizando tres materias primas no convencionales (Mineral de cromita, residuos de catalizador de reforma y cenizas volantes).

Tabla 6.
Resultados de medición de flujo de materia prima.

	Volumen [ml]	Peso [g]	Flujo [g/min]
Mineral de cromita		34	46.36
Catalizador de reforma	10	15.75	47.25
Cenizas volantes		6.96	13.92

Fuente: Cadavid, E.

Tabla 7.
Resultados de ensayo de determinación de adherencia.

	Valor [MPa]	Tipo de falla
Mineral de cromita	8.35 ± 1.7	Cohesiva Sustrato
Catalizador	3.7 ± 0.4	Cohesiva Recubrimiento
Cenizas volantes	9 ±1.1	Cohesiva del sustrato

Fuente: Cadavid, E

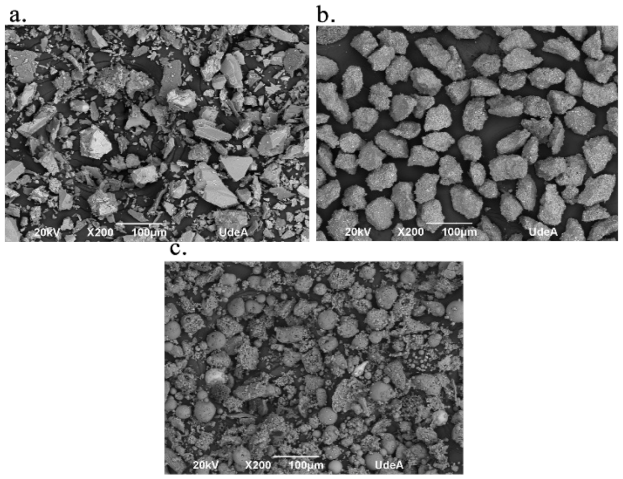
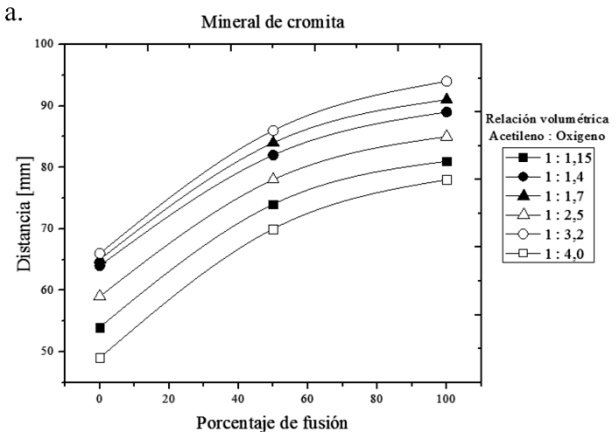
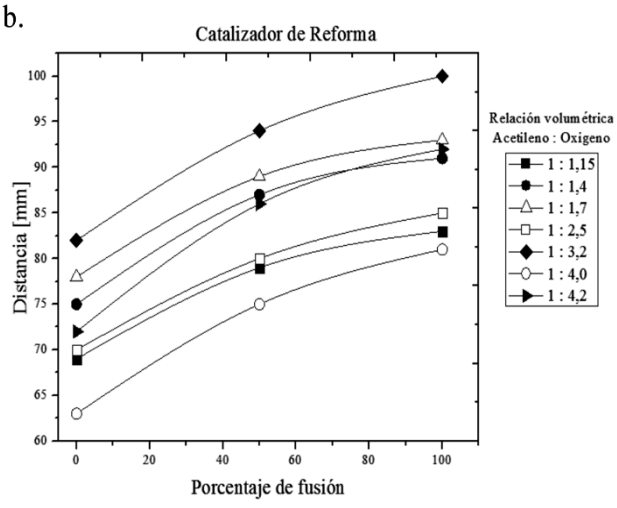


Figura 2. Morfología de las materias primas, a. Mineral de cromita, b. Catalizador de reforma y c. Cenizas volantes.
Fuente: Cadavid, E.





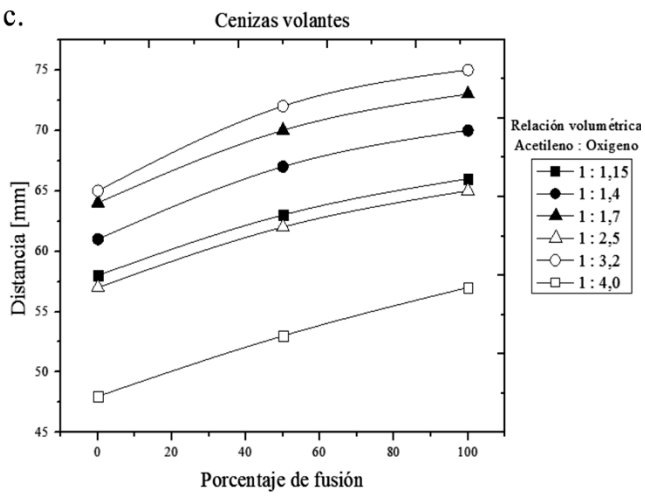
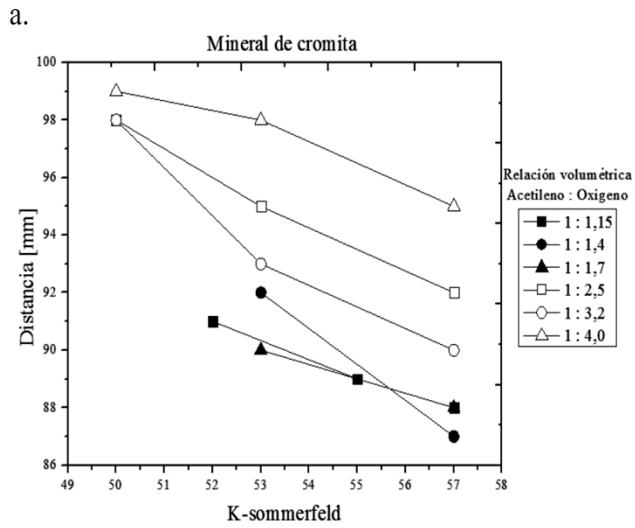
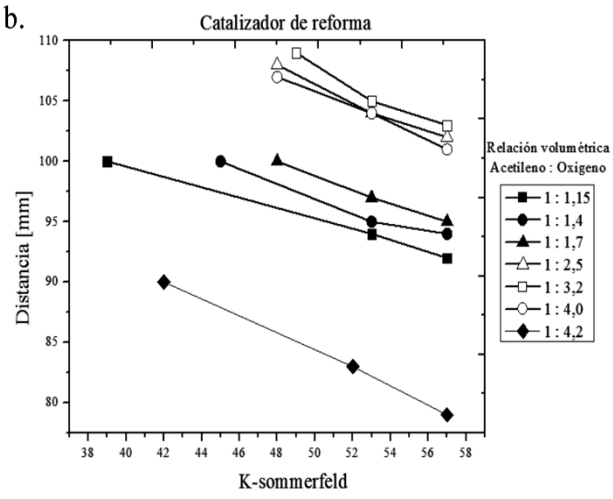


Figura 3. Porcentaje de fusión para diferentes relaciones volumétricas de a. El mineral de cromita, b. El catalizador de reforma y c. Las cenizas volantes.
Fuente: Cadavid, E.





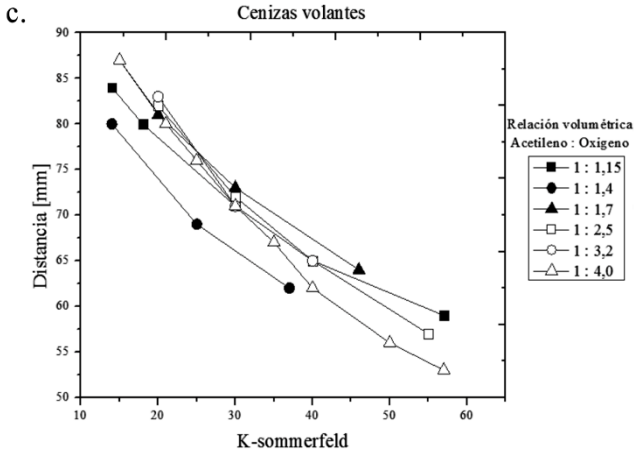


Figura 4. K- Sommerfeld para diferentes relaciones volumétricas de a. Mineral de cromita, b. Catalizador de reforma y c. Cenizas volantes.
Fuente: Cadavid, E

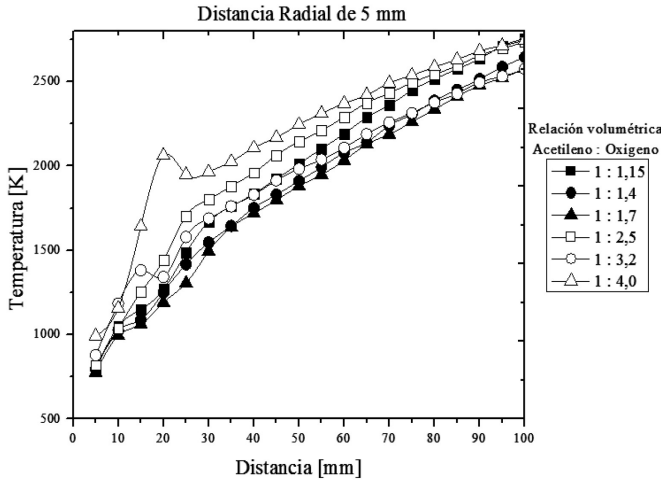


Figura 5. Perfiles de temperatura para diferentes relaciones volumétricas de oxígeno y acetileno
Fuente: Cadavid, E.

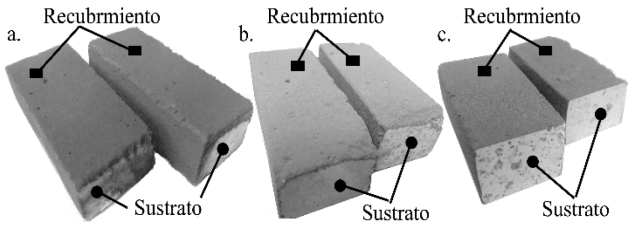


Figura 6. Recubrimientos elaborados con a). Mineral de cromita, b). Catalizador de reforma y c). Cenizas volantes.
Fuente: Cadavid, E

El recubrimiento elaborado con el mineral de cromita mostró los mejores resultados respecto a su microestructura, la presencia de lamells bien empaquetadas entre ellas indica que los parámetros utilizados para la proyección fueron propicios para la formación de un recubrimiento de baja recubrimiento

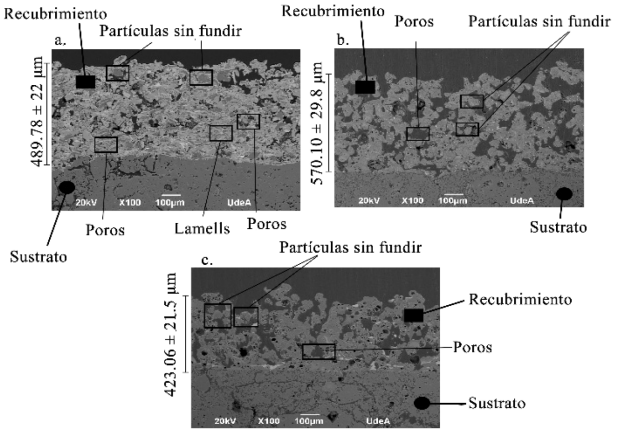


Figura 7. Microestructura de los recubrimientos elaborados con a. Mineral de cromita, b. Catalizador de reforma y c. Cenizas volantes.
Fuente: Cadavid, E

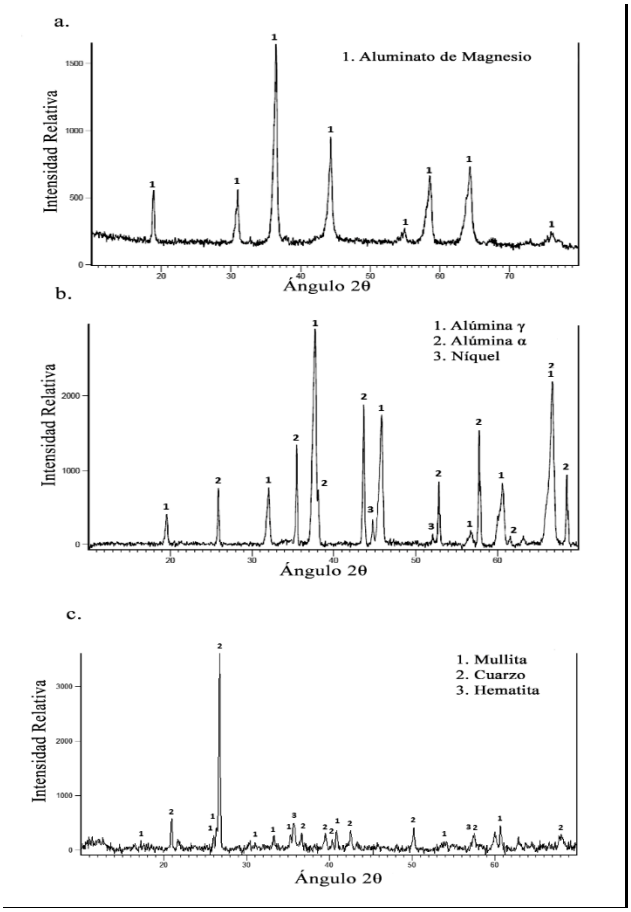


Figura 8. Difracción de rayos X para los recubrimientos elaborados con a. Mineral de cromita, b. Catalizador de reforma y c. Cenizas volantes.
Fuente: Cadavid, E

porosidad, cuya resistencia cohesiva y adhesión al sustrato es tan alta que supera la resistencia cohesiva del refractario. La única fase cristalina presente en este es el Aluminato de magnesio ($MgAl_2O_4$), que tiene buenas propiedades termo-mecánicas, alta resistencia a la corrosión en altas temperaturas, por lo que este mineral resulta potencialmente útil para mejorar el desempeño de materiales refractarios cuyo comportamiento este asociado a los fenómenos que se desarrollan en su superficie.

Por su parte, las muestras elaboradas con los residuos industriales denominados catalizador de reforma y cenizas volantes presentaron en su estructura gran cantidad de partículas sin fundir, lo que conlleva a recubrimientos de alta porosidad. No obstante, la resistencia cohesiva y la adhesión al sustrato del recubrimiento depositado a partir de las cenizas volantes es superior a la resistencia cohesiva de los refractarios sobre los cuales fue depositado, lo cual no ocurre con el catalizador de reforma, pues su resistencia cohesiva es menor a la adhesión al sustrato y a la resistencia cohesiva de los refractarios sobre los que fue depositados.

La Al_2O_3-α y Al_2O_3-γ, principales fases cristalinas detectadas por difracción de rayos X en el recubrimiento elaborado a partir del catalizador de reforma gastado, le podrían conferir buenas propiedades refractarias a dicho material, No obstante, queda pendiente por estudiar si el níquel metálico que fue la otra fase detectada en la muestra puede alterar negativamente el desempeño del recubrimiento.

El cuarzo y la mullita detectados en el recubrimiento elaborado a partir de las cenizas volantes son fases generalmente presentes en algunos refractarios ácidos con buena resistencia química, sin embargo, queda por establecer si la hematita detectada puede poner en riesgo el desempeño térmico del recubrimiento.

Agradecimientos

Al Programa de Jóvenes Investigadores Colciencias 2015 y al CODI de la Universidad de Antioquia por el apoyo al proyecto PRG 14-1-04, en el cual estuvo enmarcada esta investigación.

Referencias

[1] Herrmann, M., Toma, F.L., Berger, L.M., Kaiser, G. and Stahr, C.C., Comparative study of the corrosion resistance of thermally sprayed ceramic coatings and their bulk ceramic counterparts. J Eur Ceram Soc., 34(2), pp. 493-504, 2014. DOI: 10.1016/j.jeurceramsoc.2013.08.033.

[2] Vargas, F., Ageorges, H., Fauchais, P., López, M.E. and Calderon, J.A., Permeation of saline solution in Al2O3-13wt.% TiO2 coatings elaborated by atmospheric plasma spraying. Surf Coatings Technol., 220, pp. 85-89, 2013. DOI: 10.1016/j.surfcoat.2012.11.038.

[3] Liu, H.F., Xiong, X., Li, X.B. and Wang Y.L., Hot corrosion behavior of Sc2O3-Y2O3-ZrO2 thermal barrier coatings in presence of Na2SO4+V2O5 molten salt. Corros Sci., 85, pp. 87-93, 2014. DOI: 10.1016/j.corsci.2014.04.001.

[4] Fauchais, P.L., Heberlein, J.V.R. and Boulos, M.I., Thermal spray fundamentals from powder to part. Boston, MA: Springer US; 2014. DOI: 10.1007/978-0-387-68991-3.

[5] Secosan, I.F., Utu, D., Serban, V.A. and Brandl, W., Wear resistance of internal WC-CoCr coatings produced by high velocity oxy-fuel spraying. 4th Int Conf Adv Mater Struct AMS 2011. 188, pp.416-421, 2012. DOI: 10.4028/www.scientific.net/SSP.188.416.

[6] Bolelli, G., Cannillo, V., Lugli, C., Lusvarghi, L. and Manfredini, T., Plasma-sprayed graded ceramic coatings on refractory materials for improved chemical resistance. J Eur Ceram Soc., 26(13), pp. 2561-2579, 2006. DOI: 10.1016/j.jeurceramsoc.2005.07.066.

[7] Li, J.F., Li, L. and Stott, F.H., Multi-layered surface coatings of refractory ceramics prepared by combined laser and flame spraying.

Surf Coatings Technol., 180, pp. 500-505, 2004. DOI: 10.1016/j.surfcoat.2003.10.127.
[8] Araque-Pabón, M., Peña-Rodríguez, G. y Vargas-Galvis, F., Desempeño mecánico y tribológico de baldosas cerámicas de arcilla roja recubiertas por proyección térmica a partir de alúmina. Tecno Lógicas, 18, pp. 125-135, 2015.
[9] Pawlowski, L., Strategic oxides for thermal spraying: problems of availability and evolution of prices. Surf Coatings Technol., 220, pp. 14-19, 2013. DOI: 10.1016/j.surfcoat.2012.04.096.
[10] Pateyron, B., Jets&Poudres and T&Twinner. [online]. Available at: http://www.unilim.fr/spcts.
[11] ASTM. Standard Test Method for Pull-Off Strength of coatings using portable adhesion, 2014, pp. 1-16. DOI: 10.1520/D4541-09E01.2.
[12] Khan, N.M.T.B., High pressure and high temperature study of magnesiochromite and its geophysical implications, Thesis MSc., University of Western, Ontario, Canada, 2015.
[13] Gehre, P., Aneziris, C.G., Berek, H. and Parr, C., Reinmller M., Corrosion of magnesium aluminate spinel-rich refractories by sulphur-containing slag. J Eur Ceram Soc., 35(5), pp. 1613-1620, 2015. DOI: 10.1016/j.jeurceramsoc.2014.11.031.
[14] Moritz, K., Aneziris, C.G., Hesky, D. and Gerlach, N., Magnesium aluminate spinel ceramics containing aluminum titanate for refractory applications. J Ceram Sci Technol., 5(2), pp. 125-130, 2014. DOI: 10.4416/JCST2013-00037.
[15] Ping, L.R., Azad, A.M. and Dung, T.W., Magnesium aluminate (MgAl2O4) spinel produced via self-heat-sustained (SHS) technique. Mater Res Bull., 36(7), pp. 1417-1430, 2001. DOI: 10.1016/S0025-5408(01)00622-5.
[16] Gehre, P., Aneziris, C.G., Veres, D., Parr, C., Fryda, H. and Neuroth, M., Improved spinel-containing refractory castables for slagging gasifiers. J Eur Ceram Soc., 33(6), pp. 1077-1086, 2013. DOI: 10.1016/j.jeurceramsoc.2012.11.011.
[17] Ston. R., Thermochemistry of North Carolina olivine in the manufacture of forsterite refractories. J Am Ceram Soc., 22, pp. 342-348, 1939.
[18] Tathavakar, V.D., Antony, M.P. and Jha, A.. The physical chemistry of thermal decomposition of South African chromite minerals. Metall Mater Trans B, 36(1), pp. 75-84, 2005. DOI: 10.1007/s11663-005-0008-1.
[19] Borovkova, L., Koval'Skaya, K.V. and Poluboyarinov, D., Sintering and thermomechanical properties of magnesiochromite. Refract Ind Ceram., 7, pp. 715-720, 1966.
[20] Atkinson, A., Bastid, P. and Liu, Q., Mechanical properties of magnesia-spinel composites. J Am Ceram Soc., 90(8), pp. 2489-96. 2007. DOI: 10.1111/j.1551-2916.2007.01733.x.
[21] Sergienko, V.S. and Evtushenko, V.B., The service of reactories in the slide gates of 250-ton steel teeming ladles. Refractories, 27, pp. 705-708, 1987.
[22] Othman, A.G.M. and Khalil, N.M., Sintering of magnesia refractories through the formation of periclase-forsterite-spinel phases. Ceram Int., 31(8), pp. 1117-1121, 2005. DOI: 10.1016/j.ceramint.2004.11.011.
[23] Soltan, A.M., Wendschuh, M., Willims, H. and Serry, M., Densification and resistance to hydration and slag attack of ilmenite-doped MgO-dolomite refractories in relation to their thermal equilibrium and microfabric. J Eur Ceram Soc., 34(8), pp. 2023-2033, 2014. DOI: 10.1016/j.jeurceramsoc.2014.01.030.
[24] Chaudhuri, M. and Banerjee, G., Secondary phases in natural magnesite sintered with addition of titania, ilmenite and zirconia. J Mater Sci., 34(23), pp. 5821-5825, 1999.
[25] Lampropoulou, P.G., Katagas, C.G. and Papamantellos, D.C., Composition of periclase and calcium-silicate phases in magnesia refractories derived from natural microcrystalline magnesite. J Am Ceram Soc., 88(6), pp. 1568-1574. 2005. DOI: 10.1111/j.1551-2916.2005.00263.x.
[26] Faulkner, L.L., Refractories Handbook. Pittsburgh, Pennsylvania, U.S.A: n.d.
[27] Li, J., Wang, Q. and Shen, N.. Magnesium ferrite is a kind of main bonding phase in magnesia refractory materials. Mater Sci Technol Conf Exhib., 2009.
[28] Kim, J.W., Shin, P.W., Lee, M.J. and Lee, S.J., Effect of particle size on the strength of a porous nickel aluminate fabricated by a polymer solution route. J Ceram Process Res., 7, pp. 117-121, 2006.
[29] Podwórny, J., Wojsa, J. and Gerle, A., Nickel oxide in technology of basic refractory materials - the perspective of use. Mater Ceram., 66(3), pp. 331-335, 2014.
[30] Melvyn-Bradley, T.H., An overview of refractory raw materials - Part 1 Alumina. Refract Eng., pp. 21-22, 2011.
[31] Ebadzadeh, T. and Lee, W.E., Processing-microstructure-property in mullite-cordierite composites. J Eur Ceram Soc., 2219, pp. 837-848, 1998.
[32] Zawrah, M.F.M. and Khalil, N.M., Effect of mullite formation on properties of refractory castables. Ceram Int., 27(6), pp. 689-694, 2001. DOI: 10.1016/S0272-8842(01)00021-9.
[33] Sadik, C., El-Amrani, I-E. and Albizane, A., Recent advances in silica-alumina refractory: A review. J Asian Ceram Soc., 2, pp. 83-96, 2014. DOI: 10.1016/j.jascer.2014.03.001.
[34] Rabinovich, M., Lightweight mullite-silica refractories. Refract Ind Ceram., 17, pp. 146-147, 1976.
[35] Sardy, M., Arib, A., Abbassi, K., El-Moussa, R. and Gomina, M., Elaboration and characterization of mullite refractory products from Moroccan Andalusite. New J Glas Ceram., 2, pp. 121-125, 2012.
[36] Davis, J.R., Handbook of thermal spray technology. ASM Intern. USA, 2004.
[37] ASTM. Standard test methods for flow rate of metal powders using the hall flowmeter, pp. 213-216, 2014. DOI: 10.1520/B0213-13.2.

E. Cadavid, es Ing. de Materiales de la Universidad de Antioquia en 2015. Se desempeñó como joven investigador Colciencias de 2015-2016, inicia sus estudios para obtener el título de Doctor en Ingeniería de Materiales en la Universidad de Antioquia en 2016. Ha participado en proyectos de investigación en el área de recubrimientos cerámicos aplicados por proyección térmica. Ponente en el VIII Congreso Internacional de Materiales CIM-2015. Posee una publicación en la Revista Colombiana de Materiales. Integrante del Grupo de Investigación en Materiales y recubrimientos Cerámicos GIMACYR (categoría B en Colciencias) y del Grupo de Investigaciones Pirometalúrgicas y de Materiales GIPIMME (Categoría A1 Colciencias). Sus Campos de interés en trabajo e investigación se incluyen: Materiales cerámicos, Recubrimientos depositados mediante proyección térmica.
ORCID: 0000-0001-9452-4240.

F. Vargas Galvis, es Ing. Metalúrgico 1998 y MSc. en Ingeniería Metalúrgica en 2003 de la Universidad Industrial de Santander, Dr. en Matériaux Céramiques et Traîtements de Surface de la Université de Limoges, Francia, en 2010 y Dr. en Ingeniería de la Universidad de Antioquia en 2011. Ha sido ingeniero en misión en el Instituto Colombiano del Petróleo de Ecopetrol, en proyectos de investigación y desarrollo de nuevos materiales, y profesor catedrático adscrito a la Escuela de Ingeniería Metalúrgica de la Universidad Industrial de Santander. Desde el 2013 y hasta la fecha se ha desempeñado como profesor de planta del Departamento de Ingeniería Metalúrgica y de Materiales de la Universidad de Antioquia. Ha participado proyectos de investigación y desarrollo y publicado más de 20 artículos científicos. Es coautor de 2 secretos industriales y ha recibido varios reconocimientos profesionales. En la actualidad se encuentra clasificado por Colciencias como Investigador Senior. Sus campos de interés en trabajo e investigación incluyen: Materiales cerámicos, Recubrimientos depositados mediante proyección térmica.
ORCID: 0000-0003-4484-3950.

M.E. López Gómez, es Ing. de Minas y Metalurgia de la Universidad Nacional de Colombia (Medellín) en 1991, MSc. en Ingeniería Metalúrgica de la Universidad Industrial de Santander en 1999 y Dra. en Ciencia y Tecnología de Materiales de la Universidad de Oviedo, España en 2006. Se desempeñó como Investigadora en el CIMEX de la Universidad Nacional de Colombia. En la Universidad de Antioquia fue profesora de cátedra en el año 2000. Entre el año 2001 y la actualidad está vinculada como profesora titular de tiempo completo del programa de Ingeniería de Materiales de la Universidad de Antioquia. Ha realizado proyectos de investigación en el área de materiales cerámicos, recubrimientos cerámicos y metalurgia extractiva. Actualmente es la directora del Grupo de Investigación en Materiales y

recubrimientos Cerámicos GIMACYR (categoría B en Colciencias) e integrante del Grupo de Investigaciones Pirometalúrgicas y de Materiales GIPIMME, directora de la Revista Colombiana de Materiales. Sus campos de interés en trabajo e investigación se incluyen: materiales cerámicos, metalurgia extractiva, recubrimientos cerámicos, biocerámicos, nanomateriales.
ORCID: 0000-0002-1038-6504.

C.M. Mesa-Toro, es Ing. Químico en 2005, MSc. en Ingeniería: Materiales y Procesos en e 2011, ambos de la Universidad Nacional de Colombia Medellín (Colombia). Posee 12 años de experiencia en la industria cerámica, de los cuales más de 8 años los ha enfocado específicamente en la industria de los materiales refractarios. Actualmente Jefe de Investigación y Desarrollo de ERECOS (Empresa de refractarios colombianos S.A.S). Sus campos de interés e investigación incluyen: Materiales refractarios, cerámicos y energía.
ORCID: 0000-0001-7620-3857.

F.A. Vargas Bermúdez, es Ing. de materiales de la Universidad de Antioquia, Colombia, en 2015. Durante su pregrado se enfoca en el área de metales, propiamente en fundición de metales ferrosos y no ferrosos junto con el grupo de Investigaciones Pirometalúrgicas y de Materiales GIPIMME. Se desempeña durante 2 años como joven investigador junto con la alcaldía y el grupo de investigación de Materiales Preciosos MAPRE. Desde el 2014 hasta la actualidad hace parte del área de investigación y desarrollo de la empresa ERECOS SAS, dedicada a la producción de materiales cerámicos refractarios. Entre sus campos de interés en trabajo e investigación se incluyen: materiales cerámicos, metálicos y refractarios.
ORCID: 0000-0002-9425-0670.

G. Latorre, es Ing. Mecánico de la Universidad Nacional de Colombia en 1984 y de MSc. en Física de la Universidad Industrial de Santander en 1998. Entre 1987 y 2010 fue Ingeniero de proyectos en el Instituto Colombiano del Petróleo-Ecopetrol, realizando proyectos de investigación y desarrollo de nuevos materiales, análisis de falla, modelamiento numérico, en 2011 fue profesor asistente en la Escuela de Ingeniería y la Universidad Industrial de Santander, desde 2011 se desempeña como consultor independiente; ha publicado más de 20 artículos científicos, un capítulo en el libro de Materiales de Ingeniería. Entre sus campos de interés en trabajo e investigación se incluyen: materiales cerámicos, barreras térmicas.
ORCID: 0000-0003-0813-1921.

G. Peña, es Lic. Matemáticas y Física rn 1989 y Esp. Informática en 1996 ambos de la Universidad Francisco de Paula Santander, Msc. en Ciencias Físicas en 2001 y Dr. Ciencias en Tecnología Avanzada en 2003, ambos en el Instituto Politécnico Nacional, México, además es Dr. en Ingeniería de Materiales, MEN, Resolución 1168, de 7 abril de 2005, Colombia. Profesor titular en la Universidad Francisco de Paula Santander, adscrito al departamento de Física. Miembro del Grupo GITEC y GIFIMAC de la UFPS. Miembro del sistema de pares evaluadores de Colciencias, investigador asociado Colciencias. Sus campos de interés y áreas de trabajo incluyen: materiales cerámicos, recubrimientos cerámicos por proyección térmica, caracterización de materiales, fotoacústica, física de la materia condensada. Editor de revista científica. Experiencia docente universitaria de 22 años.
ORCID: 0000-0002-7114-9174.

UNIVERSIDAD NACIONAL DE COLOMBIA
SEDE MEDELLÍN
FACULTAD DE MINAS

Área Curricular de Ingeniería
Geológica e Ingeniería de Minas y Metalurgia

Oferta de Posgrados

Especialización en Materiales y Procesos
Maestría en Ingeniería - Materiales y Procesos
Maestría en Ingeniería - Recursos Minerales
Doctorado en Ingeniería - Ciencia y Tecnología de Materiales

Mayor información:

E-mail: acgeomin_med@unal.edu.co
Teléfono: (57-4) 425 53 68

UNIVERSIDAD NACIONAL DE COLOMBIA
SEDE MEDELLÍN
FACULTAD DE MINAS



DYNA
http://dyna.medellin.unal.edu.co/

Evaluation of the genotoxic and mutagenic effect in human lymphocytes exposed to modified carbon nanotubes

Claudia Espinosa [a], Lina Marcela Hoyos-Palacio [a], Lucelly López-López [b], Daniel Gallego-González [a], Andrés David Aranzazu-Ceballos [a], Juan Sebastián Marín-Cárdenas [a], Dayana Andrea Quintero-Moreno [a] & Isabel Cristina Ortiz-Trujillo [a]

[a] *Grupo de Investigación Biología de Sistemas, Facultad de Medicina, Universidad Pontificia Bolivariana, Medellín, Colombia. espinosa.claudia.e@gmail.com, lina.hoyos@upb.edu.co, daniel.gallegogo@upb.edu.co, andres.aranzazu@upb.edu.co, juan.marinca@upb.edu.co, dayana.quinteroq@upb.edu.co, isabel.ortiz@upb.edu.co*
[b] *Grupo de Investigación en Salud Pública, Facultad de Medicina, Universidad Pontificia Bolivariana, Medellín, Colombia. lucelly.lopez@upb.edu.co*

Received: November 8th, de 2017. Received in revised form: April 27th, 2018. Accepted: May 16th, 2018

Abstract
Objective: evaluate the genotoxic and mutagenic effect in human lymphocytes exposed to pristine and N-doped carbon nanotubes. Methods: Methods: human lymphocytes were exposed to pristine and N-doped carbon nanotubes (NTC) (0.08, 0.09, 0.1mg/mL). Sister chromatid exchange (SCE) and chromosomal alterations (CA) tests were evaluated. Results: chromatid breaks and chromosomal breaks (double strand breaks) were identified in lymphocytes exposed to 0.1 and 0.08 mg/mL of the pristine CNT. N-doped CNT, induced dicentric chromosomes and chromosomal rings. There was significant difference in the percentage of SCE of cells treated with doped NTC versus negative control and pristine NTC ($p<0.0001$). Conclusion: the highest concentration of pristine CNTs induced the most chromatid and chromosomal damage. Although the percentage was less than 10%, such degree of damage is considered harmful to cells. Lymphocytes treated with N-doped CNT presented lower percentages of CA and high percentage of SCE, which shows a greater repair of genetic material with these compounds.

Keywords: carbon nanotubes; genotoxicity; mutagenicity tests; lymphocytes.

Evaluación del efecto genotóxico y mutagénico en linfocitos humanos expuestos a nanotubos de carbono modificados

Resumen
Objetivo: evaluar efecto genotóxico y mutagénico en linfocitos humanos expuestos a nanotubos de carbono (NTC) prístinos y dopados con Nitrógeno. Métodos: linfocitos humanos fueron expuestos a NTC dopados y prístinos (0.08, 0.09, 0.1mg/mL), se evaluó alteraciones cromosómicas e intercambio de cromátidas hermanas (ICH). Resultados: se presentaron rupturas cromatídicas y cromosómicas en linfocitos expuestos a 0.1mg/mL y 0.08mg/mL de NTC prístinos. NTC dopados, indujeron cromosomas dicéntricos y anillos cromosómicos. Se presentó diferencia significativa en el porcentaje de ICH de células tratadas con NTC dopados versus control negativo y NTC prístinos ($p<0.0001$). Conclusión: la concentración más alta de NTC prístinos indujo daños cromatídicos y cromosómicos; aunque el porcentaje de la población con daño fue inferior al 10%, se consideran perjudiciales para las células. Linfocitos tratados con NTC dopados presentaron menores porcentajes de AC y altos valores en ICH, lo que muestra mayor reparación de material genético con estos compuestos.

Palabras clave: nanotubos de carbono; genotoxicidad, pruebas de mutagenicidad; linfocitos.

1. Introducción

Los nanotubos de carbono (NTC) son estructuras polares, hidrófobas e insolubles, miden entre 1 y 100 nm, fueron sintetizados originalmente por Sumio Lijima en 1919 como cilindros de grafeno relacionados con el fullereno y consisten

How to cite: Espinosa, C., Hoyos-Palacio, L.M., López-López, L., Gallego-González, A.D., Aranzazu-Ceballos, D., Marín-Cárdenas, J.S., Quintero-Moreno, D.A. and Ortiz-Trujillo, I.C.. Evaluación del efecto genotóxico y mutagénico en linfocitos humanos expuestos a nanotu. DYNA 85(205, pp. 348-354, June, 2018.

© The author; licensee Universidad Nacional de Colombia.

en una matriz hexagonal de átomos de carbono que son enrollados por capas; dependiendo del número de éstas, pueden ser nanotubos de carbono de pared simple (NTCPS), si sólo tienen una capa, y nanotubos de carbono de pared múltiple (NTCPM), si tienen más de dos capas[1-6]. En su estado puro o prístino, los NTC son químicamente inertes e incompatibles con la mayoría de solventes orgánicos, por lo que suelen ser funcionalizados de forma covalente a través del tratamiento con ácidos, o de forma no covalente por medio de la interacción con ciertas proteínas, ácido desoxirribonucleico (ADN), surfactante u otros polímeros [7-10].

Su modificación permite aprovechar al máximo todas sus propiedades. La funcionalización es un conjunto de reacciones químicas mediante las cuales los grupos funcionales se unen covalentemente a la pared del tubo. Los grupos funcionales hacen que los CNT sean biocompatibles a diferencia de los nanotubos no modificados (prístinos) [11]. Otro método alternativo para cambiar la estructura del nanotubo se realiza mediante reacciones de sustitución, también conocidas como dopaje, donde otros átomos de diferentes electrones de valencia (nitrógeno o boro) reemplazan los átomos de carbono en el nanotubo. Estas sustituciones generalmente cambian el estado de equilibrio de los nanotubos de carbono y la morfología y reactividad química cuando se usa nitrógeno como agente dopante. Los nanotubos dopados con nitrógeno son extremadamente fuertes [12,13].

La funcionalización y el dopaje de los NTC pristinos, aumentan su solubilidad y abren un conjunto de nuevas propiedades que permiten usarlos en medicina en diagnósticos, agentes de administración de fármacos y dispositivos implantables, entre otros [1-5,7,8,14,16].

Múltiples estudios a nivel mundial han reportado el daño genotóxico y mutagénico en diferentes líneas celulares por exposición a NTC y en individuos por exposición accidental [3,7,10,17-19]. Incluso algunos de ellos han catalogado los NTC como posibles agentes carcinógenos [5,18,20-22]. Sin embargo, los resultados siguen siendo contradictorios, pues otras investigaciones no han encontrado que se produzca un daño significativo sobre el material genético expuesto a los NTC [3-5]. Dentro de las razones para justificar los diferentes hallazgos se encuentra el tipo de ensayo empleado para evaluar la genotoxicidad, la longitud y diámetro de las fibras de carbono utilizadas, propiedades y reacciones causadas sobre su superficie, tendencia a aglomerarse, dispersabilidad en el medio, funcionalización, mayor proporción de grupos ácidos que básicos y presencia de impurezas, entre otras [1,7,10,16,19,23].

Por su fácil obtención, la sangre venosa se ha convertido en uno de los tejidos más utilizados para los estudios de alteraciones cromosómicas, siendo los leucocitos y en especial los linfocitos T, las células a partir de las cuales es posible realizar la obtención cromosómica y aplicación de ensayos de citotoxicidad y genotoxicidad inducida por diferentes compuestos [18,19,20]. El objetivo del presente artículo es describir la evaluación del efecto genotóxico y mutagénico en linfocitos humanos expuestos a NTC prístinos y dopados con nitrógeno (NTC-N), mediante los ensayos de aberraciones cromosómicas (AC) e intercambio de cromátidas hermanas (ICH) con el fin de comparar el efecto inducido por ambos tipos de NTCs.

2. Materiales y métodos

2.1. Nanotubos de Carbono

Para el desarrollo de este estudio fueron utilizados NTC, elaborados por deposición química de vapor en el laboratorio de síntesis y procesos especiales de la Universidad Pontificia Bolivariana. Todos los NTC fueron catalizados con cobalto, algunos fueron dopados con nitrógeno y otros permanecieron sin ser modificados (prístinos). Además, fueron purificados por microfiltración con 10% de ácido fluorhídrico y 1M de ácido clorhídrico. La caracterización se realizó mediante espectroscopia Raman, por resonancia magnética y microscopía electrónica de transmisión. A partir de 1mg/mL de NTC se realizaron diez diluciones seriadas con un rango de 0,01mg/mL, utilizando medio de cultivo RPMI-1640; este procedimiento se realizó con ambos tipos de nanotubos [24].

2.2. Valoración de viabilidad

Se realizó un análisis de viabilidad con concentraciones de NTC desde 0,1 mg/mL hasta 0,01 mg/mL con el fin de seleccionar concentraciones subletales para llevar a cabo los demás ensayos. La viabilidad celular se evaluó con azul de tripano y se corroboró por citometría de flujo. Los análisis de genotoxicidad y mutagenicidad se realizaron utilizando las tres concentraciones subletales 0,08, 0,09, 0,1 mg/mL de cada uno de los NTC (dopados y prístinos). Con el fin de evaluar la reproducibilidad de los resultados, se realizaron tres experimentos independientes de cada tratamiento [25].

2.3. Cultivo y tratamiento de linfocitos humanos

El cultivo se realizó a partir de 1mL de sangre heparinizada de un adulto sano, no fumador sin ningún tipo de tratamiento clínico, no deportista de alto rendimiento, quien firmó el consentimiento informado, aprobado por el Comité de Ética de la Escuela de Ciencias de la Salud (UPB). Los cultivos se mantuvieron en medio RPMI-1640 suplementado con 10% de suero bovino fetal (SBF), antibiótico (penicilina 1000U/mL - estreptomicina 100µg/mL) y fitohemaglutinina (PHA, 0,2g/mL), a 37°C y en una atmósfera de 5% CO_2 por 56 horas [23, 31]. Posteriormente, los cultivos celulares fueron tratados con cada una de las concentraciones de ambos tipos de NTC (0,08, 0,09, 0,1 mg/mL) durante 24 horas. Como control negativo se utilizó medio de cultivo RPMI-1640 y como control positivo se usó Mitomicina C (MMC, 10µg/mL).

2.4. Obtención de extendidos cromosómicos

Al finalizar el tiempo de tratamiento, se obtuvieron los extendidos cromosómicos según el protocolo de Speit et al. [24], 1985 y Mamur et al., 2012[26]. En resumen, dos horas antes de la obtención de los extendidos cromosómicos, se agregó el antimitótico Colcemid (10µg/mL). Posteriormente, las

muestras se homogenizaron y centrifugaron a 1200 rpm por 7 minutos, luego se hizo tratamiento hipotónico con KCl (0,075M). Las células se fijaron con Carnoy (Metanol – Ácido Acético, 3:1) por 15 minutos a temperatura ambiente. Luego de lavar las muestras con fijador, se obtuvieron los extendidos cromosómicos para la coloración diferencial de cromátidas hermanas con un pretratamiento con solución Hoechst 33258 (0,05mg/mL) durante 10 minutos, para luego iluminarlas con luz directa a una temperatura de 65°C durante 20 minutos y finalmente, hacer la tinción con Giemsa (4%). De cada tratamiento se obtuvieron cuatro placas, dos para el análisis de AC y las otras dos para el conteo de ICH. Las lecturas fueron realizadas por una persona capacitada y entrenada durante un año y constantemente, el experto revisaba el trabajo.

2.5. Valoración de aberraciones cromosómicas (AC)

El análisis de AC fue realizado utilizando un microscopio de luz con un aumento 100X. Para cada muestra de NTC, dopados y prístinos, se obtuvo el índice mitótico realizando un conteo total de 500 células por placa, equivalente a 2000 células por muestra, pues por cada muestra se prepararon 4 placas. La evaluación de las aberraciones cromosómicas se realizó mediante el conteo de 100 células en metafase 1 (M1) en cada una de las placas, haciendo especial énfasis en la presencia de alteraciones estructurales en los cromosomas (quiebres cromatídicos (B), quiebres cromosómicos (BB), cromosomas dicéntricos (DC), cromosoma en anillo (R) y figuras multirradiales (MR). El daño basal en un individuo sano ha sido reportado entre 2 y 5% [26].

2.6. Valoración de intercambio de cromátidas hermanas

El análisis de ICH se hizo mediante el conteo de 50 células en metafase 2 (M2) por tratamiento. Para cada una de ellas se contó el número total de ICHs presentes en células mitóticas. La frecuencia de ICH en un individuo sano ha sido previamente establecida entre 5 y 7 intercambios en un total de 30 células [27]. En la Fig. 1 se ilustra el intercambio entre las cromátidas hermanas.

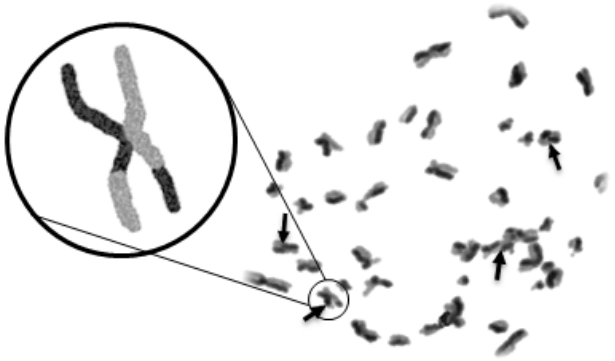


Figura 1. Intercambio de cromátidas hermanas en linfocitos humanos expuestos a NTC. Como control negativo se usó medio RPMI-1640, cada una de las flechas señala un intercambio de cromátidas hermanas.
Fuente: los autores.

2.7. Análisis estadístico

El análisis estadístico fue realizado utilizando el paquete estadístico IBM SPSS versión 23. Se realizaron las pruebas de normalidad de Kolmogorov-Smirnov, D'Agostino y Pearson Omnibus o Shapiro Wilk, para determinar el tipo de análisis estadístico a utilizar. Los resultados obtenidos de las pruebas de AC e ICH fueron analizados con la prueba no paramétrica Chi-cuadrado (X2), debido a la poca cantidad de daño encontrado en el ADN evaluado, se analizó esta variable de forma cualitativa, estimando frecuencias relativas.

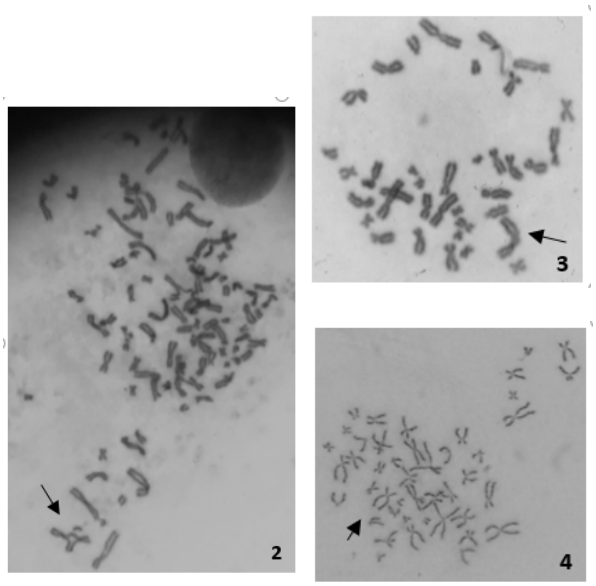
3. Resultados

3.1. Aberraciones cromosómicas

En las Figs. 2-4 se muestran las aberraciones cromosómicas encontradas en linfocitos humanos tratados con concentraciones subletales de NTC-N y prístinos [0,08, 0,09 y 0.1mg/mL] durante 24 horas. Los NTC prístinos presentaron 13 (6,5%) quiebres cromatídicos y 11 (5,5%) quiebres cromosómicos, a la concentración de 0,1 mg/mL; evidenciándose una diferencia estadísticamente significativa, cuando fueron comparados con el control negativo, con un valor p de 0,011 y 0,001, respectivamente.

El porcentaje de quiebres cromatídicos y cromosómicos expuestos a bajas concentraciones de NTC prístinos [0,08 y 0,09 mg/mL] fue también significativo cuando se comparó con el control negativo.

Con respecto a los NTC dopados con nitrógeno no se encontró una diferencia estadísticamente significativa para ningún tipo de daño, cuando se comparó con el control negativo y las concentraciones subletales.



Figuras 2, 3 y 4. Aberraciones cromosómicas observadas en cromosomas obtenidos a partir de linfocitos humanos expuestos a NTC (Figura 2: figura multirradial, Figura 3: cromosoma dicéntrico, Figura 4: quiebre cromatídico).
Fuente: los autores.

Tabla 1.
Aberraciones cromosómicas identificadas en linfocitos humanos expuestos durante 24h a NTC dopados con nitrógeno y pristinos. ctb: quiebre cromatídico, csb: quiebre cromosómico, dic: cromosoma dicéntrico, r: anillo y mr: figura multiradial (por sus siglas en ingles). Como control negativo se utilizó RPMI-1640, el control positivo correspondio a mitomicina-c (10µM) y las concentraciones de los NTC fueron 0,08, 0,09 y 0,1mg/mL.

Concentración (mg/mL)		Ctb				Csb				dic/r				mr			
		No daño		Daño		No daño		Daño		No daño		Daño		No daño		Daño	
		N	%	N	%	N	%	N	%	N	%	N	%	N	%	n	%
Control	0,00	200	100,0	0	0,00	199	99,5	1	0,50	197	98,5	3	1,50	199	99,5	1	0,50
NTC Prístinos	0,08	163	95,9	7	4,12	162	95,3	8	4,71	169	99,4	1	0,59	170	100,0	0	0,00
	0,09	198	99,0	2	1,00	200	100,0	0	0,00	194	97,0	6	3,00	199	99,5	1	0,50
	0,1	187	93,5	**13**	**6,50**	189	94,5	**11**	**5,50**	196	98,0	4	2,00	198	99,0	2	1,00
X^2			0,011				0,001				0,272				0,779		
NTC-N	0,08	200	100,0	0	0,00	200	100,0	0	0,00	196	98,0	4	2,00	199	99,5	1	0,50
	0,09	185	98,9	2	1,07	185	98,9	2	1,07	178	95,2	9	4,81	185	98,9	2	1,07
	0,1	198	99,0	2	1,00	199	99,5	1	0,50	198	99,0	2	1,00	198	99,0	2	1,00
X^2			0,473				0,318				0,064				0,870		

Fuente: los autores.

Tabla 2
Intercambio de cromátidas hermanas en linfocitos humanos expuestos a NTC prístinos y NTC-N durante 24h. (Min: valor mínimo, Max: valor máximo, $\bar{X}$: media, DE: desviación estándar, M: mediana). Como control negativo se usó RPMI-1640 y como control positivo Mitomicina-C (10µM). Valor $p < 0,0001$ para ambos tipos de NTC.

Compuesto	Concentración (mg/mL)	Min	Max	$\bar{X}$	DE	M	P25	P75
NTC Prístinos	Control	0,0	1,0	0,2	0,4	0,0	0,0	0,0
	0,08	0,0	7,0	0,5	1,3	0,0	0,0	0,0
	0,09	0,0	6,0	**1,6**	**1,7**	1,0	0,0	3,0
	0,1	0,0	6,0	0,7	1,3	0,0	0,0	1,0
NTC – N	Control	0,0	1,0	0,2	0,4	0,0	0,0	0,0
	0.08	0,0	10,0	**2,8**	**3,1**	2.0	0,0	5,0
	0.09	0,0	7,0	**2,1**	**1,9**	2,0	0,0	3,0
	0,1	0,0	8,0	**2,3**	**2,1**	2,0	0,0	4,0

Fuente: los autores.

3.2. Intercambio de cromátidas hermanas

Los NTC dopados con N indujeron una cantidad estadísticamente significativa de ICH (Fig. 5) con las tres concentraciones utilizadas, en comparación con el control negativo, mientras que las células expuestas a NTC prístinos presentaron un aumento significativo en el número de ICH para la concentración 0.09mg/mL ($p = 0,0001$) (Tabla 2 y Fig. 6).

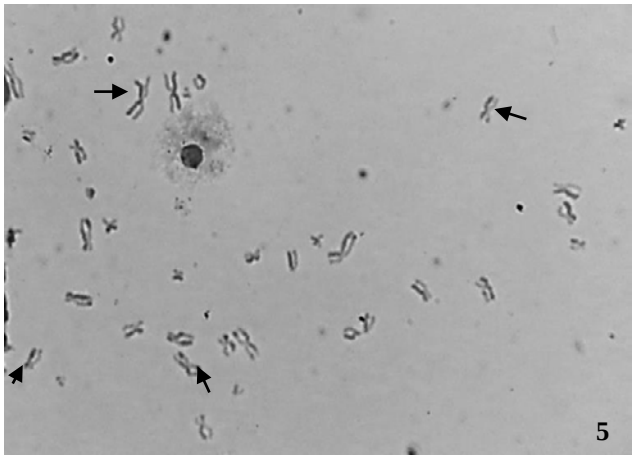


Figura 5. Intercambio de cromátidas hermanas en linfocitos humanos expuestos a NTC.
Fuente: los autores.

4. Discusión

El conocimiento de la toxicidad inducida por los NTC al material genético es de suma importancia, pues el advenimiento de la nueva tecnología y de los nanomateriales a la industria biomédica y su utilización genera preguntas sobre el daño celular que estos pueden inducir. En la literatura biomédica se encuentra mucha controversia por los múltiples y diferentes resultados obtenidos en las investigaciones en el campo de la genotoxicidad y mutagenicidad, sin llegar a una conclusión clara y concisa relacionada con el daño en el material genético [22, 28], por lo que nuevos resultados relacionados con el tema ayudan a esclarecer los efectos propiamente dichos de estos compuestos.

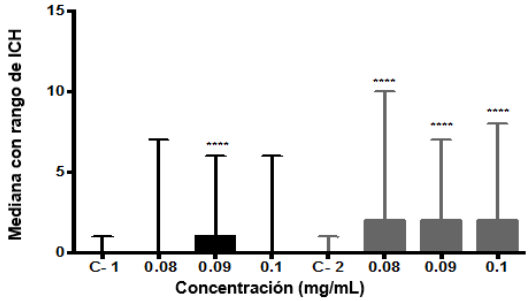


Figura 6. ICH en linfocitos humanos expuestos a NTC prístinos (barras negras) $p<0,0001$ y NTC-N (barras grises) $p<0,0001$. C-1 y C-2 corresponden al control negativo RPMI-1640.
Fuente: los autores.

En este estudio se evidenció daño cromatídico, cromosómico e ICH, posiblemente causados por la producción de especies reactivas de oxígeno (ERO) inducidas por el tratamiento con los NTC. Las principales especies reactivas de oxigeno inducidas por los NTC son radicales hidroxilo y anión superóxido, las cuales dañan el ADN [28, 29]. Trazas de los catalizadores hierro y cobalto usados en la síntesis de los NTC también pueden inducir la producción de radicales libres, generando daño indirecto sobre el ADN vía la reacción de Fenton [30]. Finalmente, la respuesta innata de la célula al tratamiento con los NTC, podría aumentar la producción de ERO con el efecto que estos causan sobre el ADN previamente mencionado.

La prueba de aberraciones cromosómicas realizada en linfocitos humanos expuestos a tres concentraciones subletales de NTC prístinos reveló que hubo una diferencia significativa ($p = 0,001$ y $p = 0,011$) correspondiente a rupturas cromosómicas y cromatídicas, respectivamente. La mayor concentración utilizada de NTC prístinos en este estudio, indujo daño a cromatídico y cromosómico, y aunque, el porcentaje de daño cromosómico se mantuvo por debajo del 10%, estos daños siguen siendo perjudiciales para la célula, debido a que ésta tiene una mayor capacidad de reparación de rupturas de una sola cadena, mientras que las roturas de doble cadena son más difíciles de reparar [2]. Estos daños provocados por los NTC prístinos podrían convertirse en mutaciones dado que las células afectadas no disminuyen su viabilidad, sino que, continúan el ciclo celular perpetuando el daño en el material genético.

El ensayo de intercambio de cromátidas hermanas (ICH) proporciona información sobre la reparación celular después de sufrir daño y refleja una lesión existente en el ADN. Los resultados de ICH obtenidos para las células tratadas con todas las concentraciones ensayadas de NTC dopados con nitrógeno (NTC N-dopados) mostraron una diferencia significativa en el porcentaje de ICH en comparación con el control negativo $p < 0,0001$. Las células tratadas con NTC prístinos sólo mostraron una diferencia significativa cuando se empleó una concentración de 0,09 mg/mL en comparación con el control negativo con un valor $p < 0,001$. Una posible causa en el aumento de ICH en linfocitos humanos expuestos a NTC N-dopados se podría explicar por la interacción que se presenta ente los NTC con el ADN mediante la formación de aductos estructurales [7].

Los aductos podrían formarse en toda la extensión de los NTC o en regiones estructurales defectuosas de los NTC que interactúan con el ADN [29]. Cabe señalar que los NTC N-dopados no indujeron ningún tipo de alteración cromosómica a las concentraciones evaluadas respecto al control negativo ($p > 0,05$). Con el fin de probar esta hipótesis, sería necesario realizar otra prueba para identificar el aducto de NTC que se une al ADN. Por otro lado, los NTC prístinos a una concentración 0,09 mg/mL causaron un aumento en el porcentaje de ICH en linfocitos humanos, esta misma concentración no induce rupturas cromosómicas y sólo induce un 1% de rupturas cromatídicas. Los NTC prístinos indujeron ICH de manera menos frecuente en comparación con los NCT N-dopados, posiblemente por el mismo mecanismo (formación de aductos). Sin embargo, estos hallazgos no son despreciables, pues según Orecchioni M et al. [30], hasta las más bajas concentraciones de NTC prístinos pueden generar activación en el sistema inmune del ratón provocando un proceso inflamatorio donde la única salida de las células dañadas por los NTC es la apoptosis [30]. Por otra parte, los NCT N-dopados tienen mayor interacción con el ADN debido a que la incorporación de nitrógeno aumenta su afinidad por el mismo [31], por lo tanto, es posible que los NTC N-dopados aumenten la formación de aductos con el ADN, reflejándose en el aumento de ICH.

La presencia de daño cromatídico en linfocitos humanos expuestos a NTC pristinos a una concentración de 0,09 mg/mL podría reflejarse en la frecuencia ICH para linfocitos humanos expuestos a esta misma concentración ya que como se indicó anteriormente el ICH refleja la presencia de una lesión del ADN [29]. El daño del ADN podría dar resultados variables dependiendo del tipo de célula utilizada, por ejemplo, K Szendi et al. (2008) [32], y Van Berlo et al. (2012) [2], no encontraron ICH con NTC en otras líneas celulares (CHO A88 y A549 células) diferente a los linfocitos humanos, lo que demuestra que cada línea celular tiene una susceptibilidad al daño en el material genético provocado por los NTC. Es así como Vales G et al. (2016) [5], lograron identificar que las células epiteliales pulmonares (BEAS-2B) eran más susceptibles al daño genético frente a otros tipos celulares, cuando eran expuestas de forma crónica a concentraciones de 0,02 mg/mL de NTC de pared múltiple; este estudio concluyó que la exposición crónica por más de 4 semanas a estas concentraciones inducen daños en el material genético que terminan en la expresión de protooncogenes involucrados en el cáncer de origen broncogénico, esto llama la atención, pues si los NTC logran generar estos fenómenos en las células pulmonares, también podrían generarlo en otras líneas celulares [5].

Los NTC pueden actuar como un agente de doble filo, por un lado, pueden disminuir la cantidad de agentes antioxidantes presentes en la célula y de esta manera generar daño en el ADN, pero también, por los defectos estructurales de los NTC pueden atrapar los ERO producidos por la célula, disminuyendo de esta manera el daño en el ADN [19, 33].

En conclusión, se evidenció daño en el ADN (quiebres en una o ambas cromátidas) y como la viabilidad celular no se vio alterada, estos daños pueden pasar a otras generaciones con la posibilidad de fijar mutaciones que pueden llevar a desarrollo de cáncer. Además, el ICH evidencia que los NTC N-dopados pueden tener mayor afinidad por el ADN debido a su modificación química, ya que éstos tienen átomos de nitrógeno incrustados en su red. Por consiguiente, existe la posibilidad de generar mutaciones que pasarían a generaciones futuras. Sin embargo, el estudio y conocimiento de los daños al material genético causado por los NTC da nuevas herramientas y conocimiento para la utilización de los nanomateriales, generando expectativas relacionadas con su uso y aprovechamiento en la industria biomédica.

A nivel mundial se han publicado múltiples estudios que reportan el daño genotóxico y mutagénico ocasionado por la exposición de diferentes líneas celulares a estos nanomateriales, por lo que es fundamental la realización de estudios que garanticen la seguridad de los mismos y los diferentes impactos sobre la salud de los individuos expuestos a ellos. De igual forma, al presentarse tanta

controversia sobre la toxicidad de estos compuestos y sus diferentes modificaciones [18], no se puede excluir estos materiales como fuente de futuros tratamientos, instrumentos y posibles ayudas en el área de la bioingeniería y su aplicación a la medicina.

5. Conclusión

La concentración más alta de NTC prístinos indujo la mayor parte de daños cromatídicos y cromosómicos; aunque el porcentaje fue inferior al 10%, se consideran perjudiciales para las células. Los linfocitos tratados con NTC dopados presentaron menores porcentajes de AC y altos valores en el ICH, lo que muestra una mayor reparación de material genético con estos compuestos.

Agradecimiento

Los autores agradecen a la Universidad Pontifica Bolivariana por su apoyo en el desarrollo de esta investigación.
Los autores declaran no tener conflictos de interés.

Referencias

[1] Chatterjee, N., Yang, J., Kim, S., Woo, S. and Choi, J., Diameter size and aspect ratio as critical determinants of uptake, stress response, global metabolomics and epigenetic alterations in multi-wall carbon nanotubes. Carbon, 108, pp. 529-540, 2016. DOI: 10.1016/j.carbon.2016.07.031

[2] Van Berlo, D., Clift, M.J., Albrecht, C. and Schins, R.P., Carbon nanotubes: an insight into the mechanisms of their potential genotoxicity. Swiss Med Wkly, 142, pp. 136-198, 2012. DOI: 10.4414/smw.2012.13698

[3] Thurnherr, T., Brandenberger, C., Fischer, K., Diener, L., Manser, P., Maeder-Althaus, X., et al., A comparison of acute and long-term effects of industrial multiwalled carbon nanotubes on human lung and immune cells in vitro. Toxicol Lett [online]. 200(3), 2011. DOI: 10.1016/j.toxlet.2010.11.012. [Date of reference: June 07th of 2017]. Available at: http://www.sciencedirect.com/science/article/pii/S0378427410017728?via%3Dihub

[4] Al Moustafa, A.E., Mfoumou, E., Roman, D.E., Nerguizian, V., Alazzam, A., Stiharu, I., et al., Impact of single-walled carbon nanotubes on the embryo: a brief review. Int J Nanomedicine, 11, pp. 11, pp. 349-355, 2016. DOI: 10.2147/IJN.S96361

[5] Vales, G., Rubio, L. and Marcos, R., Genotoxic and cell-transformation effects of multi-walled carbon nanotubes (MWCNT) following in vitro sub-chronic exposures. J Hazard Mater [online]. 306, 2016. DOI: 10.1016/j.jhazmat.2015.12.021. [Date of reference: June 07th of 2017]. Available at: http://europepmc.org/abstract/med/26736170

[6] Lijima, S., Helical microtubules of graphitic carbon. Nature, 354, pp. 56-58, 1991. DOI: 10.1038 / 354056a0

[7] Ursini, C.L., Cavallo, D., Fresegna, A.M., Ciervo, A., Maiello, R., Buresti, G., et al., Comparative cyto-genotoxicity assessment of functionalized and pristine multiwalled carbon nanotubes on human lung epithelial cells. Toxicol in Vitro, 26(6), pp. 831-840, 2012. DOI: 10.1016/j.tiv.2012.05.001

[8] Lanone, S., Andujar, P., Kermanizadeh, A. and Boczkowski, J., Determinants of carbon nanotube toxicity, Adv Drug Deliv Rev [online]. 65(15), 2013. DOI: 10.1016/j.toxrep.2016.01.011. [Date of reference: June 07th of 2017]. Available at: http://www.sciencedirect.com/science/article/pii/S0169409X13001737?via%3Dihub

[9] Nagaraju, K., Reddy, R. and Reddy, N., A review on protein functionalized carbon nanotubes. J Appl Biomater Funct Mater [online]. 13(4), 2015. DOI: 10.5301/jabfm.5000231. [Date of reference: June 07th of 2017]. Available at: http://www.jab-fm.com/article/a-review-on-protein-functionalized-carbon-nanotubes

[10] Vitkina, T.I., Yankova, V.I., Gvozdenko, T.A., Kuznetsov, V.L., Krasnikov, D.V., Nazarenko, A.V., et al., The impact of multi-walled carbon nanotubes with different amount of metallic impurities on immunometabolic parameters in healthy volunteers. Food Chem Toxicol, 87, pp. 138-147, 2016. DOI: 10.1016/j.fct.2015.11.023.

[11] Ghosh, M., Chakraborty, A. and Mukherjee, A., Cytotoxic, genotoxic and the hemolytic effect of titanium dioxide (TiO2) nanoparticles on human erythrocyte and lymphocyte cells in vitro. J Appl Toxicol, 33(10), pp. 1097-1110, 2013. DOI: 10.1002/jat.2863.

[12] Kuzmany H., Kukovecz A., Simon F., Holzweber M., Kramberger C. and Pichler T., Functionalization of carbon nanotubes, Synth. Met., 141(1), pp. 113-122, 2004.

[13] Glerup M., Krstić V., Ewels C., Holzinger M. and Van Lier 6, Doping of Carbon Nanotubes, in: Doped nanomaterials and nanodevices, 2007, pp. 1-66.

[14] Koós A.A., Dillon F., Obraztsova E. A., Crossley A. and Grobert N., Comparison of structural changes in nitrogen and boron-doped multi-walled carbon nanotubes, Carbon N. Y., 48(11), pp. 3033-3041, Sep. 2010.

[15] Wong B.S., Yoong S.L., Jagusiak A., Panczyk T., Ho H.K., Ang W.H. and Pastorin G., Carbon nanotubes for delivery of small molecule drugs., Adv. Drug Deliv. Rev., 65(15), pp. 1964-2015, 2013.

[16] Werengowska-Ciećwierz, K., Wiśniewski, M., Terzyk, A.P., Roszek, K., Czarnecka, J., Bolibok, P., et al., Conscious changes of carbon nanotubes cytotoxicity by manipulation with selected nanofactors. Appl Biochem Biotechnol, 176(3), pp. 730-741, 2015. DOI: 10.1007/s12010-015-1607-1.

[17] Nakanishi, J., Morimoto, Y., Ogura, I., Kobayashi, N., Naya, M., Ema, M., et al., Risk assessment of the carbon nanotube group. Risk Anal [online]. 35(10), 2015. DOI: 10.1111/risa.12394. [Date of reference: June 07th of 2017]. Available at: https://www.ncbi.nlm.nih.gov/pmc/articles/PMC4736668/

[18] Louro, H., Pinhão, M., Santos, J., Tavares, A., Vital, N. and Silva, M.J., Evaluation of the cytotoxic and genotoxic effects of benchmark multi-walled carbon nanotubes in relation to their physicochemical properties. Toxicol Lett, 262, pp.123-134, 2016. DOI: 10.1016/j.toxlet.2016.09.016.

[19] Dong, J. and Ma, Q., Advances in mechanisms and signaling pathways of carbon nanotube toxicity. Nanotoxicology [online]. 9(5), 2015. DOI: 10.3109/17435390.2015.1009187. [Date of reference: June 07th of 2017]. Available at: http://onlinelibrary.wiley.com/doi/10.1111/risa.12394/full

[20] Takagi, A., Hirose, A., Futakuchi, M., Tsuda, H. and Kanno, J., Dose-dependent mesothelioma induction by intraperitoneal administration of multi-wall carbon nanotubes in p53 heterozygous mice. Cancer Sci, 103(8), pp. 1440-1444, 2012. DOI: 10.1111/j.1349-7006.2012.02318.x

[21] Grosse, Y., Loomis, D., Guyton, K.Z., Lauby-Secretan, B., El Ghissassi, F., Bouvard, V., et al., International agency for research on cancer monograph working group. Carcinogenicity of fluoro-edenite, silicon carbide fibres and whiskers, and carbon nanotubes. Lancet Oncol, 15(13), pp. 1427-1428, 2014. DOI: 10.1016/S1470-2045(14)71109-X.

[22] Møller P. and Jacobsen N.R., Weight of evidence analysis for assessing the genotoxic potential of carbon nanotubes. Critical Reviews in Toxicology 47(10), pp 871-888, 2017. DOI: 10.1080/10408444.2017.1367755.

[23] Khalili Fard, J., Jafari, S. and Eghbal, M.A., A review of molecular mechanisms involved in toxicity of nanoparticles. Adv Pharm Bull, 5(4), pp.447-454, 2015. DOI: 10.15171/apb.2015.061.

[24] Hoyos-Palacio, L.M., Efecto de los catalizadores hierro, cobalto, níquel, molibdeno, y mezclas soportadas sobre sílice sol gel, para la síntesis de nanotubos de carbono mediante deposición química de vapor, Tesis de Doctorado en Ingeniería. Universidad Pontificia Bolivariana, Medellín, Colombia 2010, 204 P.

[25] Uhl, M., Christoph, H. and Siegfried, K., Single-cell gel electrophoresis assays with human-derived hepatoma (Hep G2) cells. Mutat Res [online]. 441(2), 1999. [Date of reference: June 07th of 2017]. Available at: http://citeseerx.ist.psu.edu/viewdoc/download?doi=10.1.1.21.9716&rep=rep1&type=pdf

[26] Yüzbaşıoğlu, D., Ünal, F., Koç, F., Öztemel, S., Aksoy, H., Mamur, S., et al., Genotoxicity assessment of vaccine adjuvant squalene. Food Chem Toxicol, 56, pp. 240-246, 2013. DOI: 10.1016/j.fct.2013.02.034.
[27] Mamur, S., Yüzbaşıoğlu, D., Unal, F. and Aksoy, H., Genotoxicity of food preservative sodium sorbate in human lymphocytes in vitro. Cytotechnology [online]. 64(5), 2012. DOI: 10.1007/s10616-012-9434-5. [Date of reference: June 07th of 2017]. Available at: https://www.ncbi.nlm.nih.gov/pmc/articles/PMC3432536/
[28] Tavares, A.M., Louro, H., Antunes, S., Quarré, S., Simar, S., De Temmerman, P.J., et al., Genotoxicity evaluation of nanosized titanium dioxide, synthetic amorphous silica and multi-walled carbon nanotubes in human lymphocytes. Toxicol In Vitro, 28(1), pp.60-69, 2014. DOI: 10.1016/j.tiv.2013.06.009.
[29] Cruz-Vallejo, V.L., Reparabilidad durante G1 de las lesiones inductoras de intercambios entre cromatidas hermanas producidas por mitomicina C en células de la glándula salival de raton in vivo. México DF: Universidad Nacional Autónoma de México [en línea] 1991. [Fecha de consulta: 7 de junio de 2017]. Disponible en: https://inis.iaea.org/search/search.aspx?orig_q=RN:24063560
[30] Orecchioni, M., Bedognetti, D., Sgarrella, F., Marincola, F., Bianco, A. and Delogu, L., Impact of carbon nanotubes and graphene on immune cells. J Transl Med [online] 12(1), 2014. DOI: 10.1186/1479-5876-12-138. [Date of reference: June 07th of 2017]. Available at: https://translational-medicine.biomedcentral.com/articles/10.1186/1479-5876-12-138
[31] Zhao, M.L., Li, D.J., Yuan, L., Yue, Y.C., Liu, H. and Sun, X., Differences in cytocompatibility and hemocompatibility between carbon nanotubes and nitrogen-doped carbon nanotubes. Carbon, 49(9), pp. 3125-3133, 2011. DOI: 10.1016/j.carbon.2011.03.037.
[32] Szendi, K. and Varga, C., Lack of genotoxicity of carbon nanotubes in a pilot study. Anticancer Res [online]. 28(1A), 2008. [Fecha de consulta 7 de junio de 2017]. Disponible en: http://ar.iiarjournals.org/content/28/1A/349.long
[33] Shvedova, A.A., Yanamala, N., Kisin, E.R., Tkach, A.V., Murray, A.R., Hubbs, A., Castranova, V., et al., Long-term effects of carbon containing engineered nanomaterials and asbestos in the lung: one year postexposure comparisons. Am J Physiol Lung Cell Mol Physiol. 306(2), pp. L170-L182, 2014. DOI: 10.1152/ajplung.00167.2013

L. López-López, es Gerente en Sistemas de Información en salud en 2001 de la Universidad de Antioquia, Esp. en Estadística en 2008 de la Universidad Nacional de Colombia, sede Medellín, PhD (c) en Gestión de la Tecnología y la Innovación de la UPB, entre 2008 y 2015 trabajó como profesora de estadística y diseño de experimentos en la Universidad de Antioquia, desde 2015 trabaja en la UPB como profesora del área de investigación y como asesora metodológica en proyectos de investigación. Interés en investigación son epidemiología de la tuberculosis, modelado con enfoque de dinámica de sistemas, modelos estadísticos lineales generalizado y modelado con redes neuronales**.**
ORCID: 0000-0002-1534-520X

L.M. Hoyos-Palacio, es Ingeniera Química de la Universidad Nacional de Colombia en Medellín, 2005. En 2006, inició su doctorado y se convirtió en investigador del Grupo de Investigación de Nuevos Materiales en la Universidad Pontificia Bolivariana, Medellín Colombia. En 2011 culminó su Dr. en Ingeniería, Energía y Termodinámica. Es coordinadora de la línea de investigación de Nanosistemas del grupo de investigación Biología de Sistemas de la Universidad Pontificia Bolivariana. Ha publicado varios artículos en revistas indexadas y ha participado en simposios internacionales. Participa como evaluador de proyectos para Colciencias y como revisor de artículos.
ORCID: 0000-0003-2430-8504

C. Espinosa, recibió un BSc en Biología de la Universidad Estatal de Nueva York en Oswego, EE.UU. Miembro del Grupo de Investigación Biología de Sistemas de la Universidad Pontificia Bolivariana, Medellín Colombia. Completó su MSc. en Ingeniería Biomédica en la misma Institución. Actualmente, trabaja como voluntaria de Peace Corp en el sector de la salud en Paraguay.
ORCID: 0000-0003-1085-0992

D Gallego-González, es estudiante de medicina de la Universidad Pontificia Bolivariana. Integrante activo del grupo de investigación Biología de Sistemas, línea mutagenesis y epigenética ambiental desde el año 2013. Ha sido monitor de Fisiología de la misma Universidad. Interesado en biología aplicada y estudios de salud pública.
ORCID: 0000-0001-5049-7877

D.A. Quintero-Moreno, es estudiante de medicina de la Facultad de Medicina de la Universidad Pontificia Bolivariana, miembro del grupo de investigación Biología de Sistemas, desde 2015 y de la línea de hematología del grupo de investigación de Medicina Interna desde 2017. Interés en estudios de biología aplicada, mutagenicidad y hematología clínica.
ORCID: 0000-0001-5004-3162

I.C. Ortiz-Trujillo, es Bióloga, MSc y PhD en Biología de la Universidad de Antioquia, Colombia. Coordinadora del grupo de investigación Biología de Sistemas y docente de la Facultad de Medicina de la Universidad Pontificia Bolivariana, Colombia. Ha publicado varios artículos originales en el área de genotoxicidad, mutagénesis y epigenética. Participa como par evaluador de proyectos para Colciencias y como revisora de artículos originales.
ORCID: 0000-0002-1620-2809.

A.D. Aranzazu-Ceballos, es estudiante de medicina de último semestre de la Universidad Pontificia Bolivariana (UPB), con un diplomado en epidemiología clínica y práctica basada en la evidencia de la UPB. Ha sido monitor de biología celular durante 2014-2016. Con interés en la investigación se basa en áreas de medicina, específicamente biología, bioquímica, medicina interna y pediatría.
ORCID: 0000-0002-0867-4793

J Marin, es estudiante de último año de medicina de la Universidad Pontificia Bolivariana. Integrante del grupo de investigación Biología de Sistemas de la misma Universidad. Tiene un diplomado en Medicina basada en la evidencia y educación a estudiantes de medicina. Ha sido monitor de biología molecular y anatomía de la Facultad de Medicina de la misma Universidad. Sus intereses son medicina interna y medicina basada en la evidencia.
ORCID: 0000-0001-6386-391X

UNIVERSIDAD NACIONAL DE COLOMBIA
SEDE MEDELLÍN
FACULTAD DE MINAS



DYNA
http://dyna.medellin.unal.edu.co/

Freight vehicle condition monitoring through the availability

Laksmi Penabad-Sanz, Pedro Antonio Rodríguez-Ramos & Arsenio Miguel Iznaga-Benítez

Centro de Estudios de Ingeniería en Mantenimiento, Facultad de Ingeniería Mecánica, Universidad Tecnológica de La Habana "José Antonio Echeverría", La Habana, Cuba. laksmi@mecanica.cujae.edu.cu, parr@ceim.cujae.edu.cu, iznaga@mecanica.cujae.edu.cu

Received: October 27th, 2017. Received in revised form: April 12th, 2018. Accepted: May 2nd, 2018

Abstract
The application of decision making approaches based on systems degradation monitoring in real situations are difficult. Among those difficulties are methods complexity and data, technology and capable personnel availability. In this paper, a way for monitoring freight vehicle condition through availability assessment is proposed. In order to do that, the rational use limit condition of freight vehicles is proposed and a mathematical model of the availability threshold linked with operation economic results is presented. The latest makes possible to value the vehicle operation convenience. The application of the proposal to a fleet shows its possibilities in real conditions. An "Almost perfect" agreement degree between the availability assessment results and the economic result of the vehicle operation was obtained.

Keywords: availability; availability threshold; rational use; transport fleet; decision making.

Monitoreo de la degradación de los vehículos de transporte de cargas a través de la disponibilidad

Resumen
La aplicación de enfoques de toma de decisión basados en el monitoreo de la degradación de los sistemas a situaciones reales presenta un grupo de barreras tales como la complejidad de los métodos, la disponibilidad de datos, tecnología y personal capacitado. En este trabajo se propone una vía para el monitoreo del estado del vehículo de transporte de cargas a través de la disponibilidad. Para ello se introduce la condición límite de uso racional de los vehículos y se presenta la expresión de la disponibilidad límite vinculada a los resultados económicos de la operación del vehículo, lo que posibilita valorar la conveniencia de la operación del mismo. La aplicación de la propuesta a una flota ilustra sus posibilidades en condiciones reales, obteniéndose un grado de acuerdo "Casi perfecto" entre los resultados del análisis de la disponibilidad y el resultado económico de la operación del vehículo.

Palabras clave: disponibilidad; disponibilidad límite; uso racional; flotas de transporte; toma de decisiones.

1. Introducción

Las empresas operadoras de flotas de transporte automotor tienen como principal objetivo la generación de utilidades. Para ello requieren disponer de vehículos en un estado técnico tal que les permita ejecutar la transportación de forma rápida y segura. Sobre el estado técnico de un vehículo influyen sus cualidades inherentes, la logística y el mantenimiento [1], que se manifiesta en la velocidad con la que se desarrollan procesos como el desgaste, la corrosión o la fatiga, entre otros. La influencia de los factores sobre la velocidad con las que se desarrolla el proceso de degradación es atenuable pero no evitable.

El deterioro del estado técnico limita la capacidad del vehículo de generar utilidades. Por ello, conocer hasta qué punto el deterioro del estado del vehículo es permisible para la empresa resulta importante, ya que le permitiría determinar el momento a partir del cual la continuidad en operación del vehículo debe ser cuestionada. O sea, que se encuentra ante una situación de toma de decisión como el reemplazo, mantenimiento proactivo, la programación de la operación, entre otras.

El estudio de la vinculación de los procesos de degradación de los sistemas a través de indicadores del estado

How to cite: Penabad-Sanz, L., Rodríguez-Ramos, P.A. and Iznaga-Benítez, A.M., Monitoreo de la degradación de los vehículos de transporte de cargas a través de la disponibilidad. DYNA, 85(205), pp. 355-362, June, 2018.

© The author; licensee Universidad Nacional de Colombia.

del sistema con las situaciones de toma de decisión se realiza desde varias perspectivas: el mantenimiento basado en el estado (CBM, por sus siglas en inglés); la gestión de activos (GA); y más recientemente, la gestión y pronóstico de la salud de los sistemas (PHM, por sus siglas en inglés). En ellas, un pilar importante es el monitoreo del estado de los activos, de forma continua o a intervalos, a través de indicadores (que Knezevic denomina estimador adecuado de la condición, EAC [1]), lo que muestra la capacidad funcional de los activos y posibilita la toma de decisiones como el diseño del programa de mantenimiento [2], la reparación o el reemplazo [3] o la fiabilidad [4-5], desde el CBM; como la planificación estratégica de las operaciones, mantenimiento e inversiones desde la GA [6]; o para determinar la necesidad de acciones preventivas y correctivas de mantenimiento, optimizar la programación del mantenimiento y de los niveles de repuestos almacenados desde el PHM [7].

Los EAC más empleados suelen ser aquellos que son medidos directamente del sistema como las vibraciones, temperatura, análisis de aceite, entre otros. También se han utilizado EAC indirectos como los parámetros de proceso vinculados con la calidad de los procesos, empleándose las técnicas propias del control estadístico de procesos para establecer los límites de los parámetros y su monitoreo, tanto para parámetros cuantitativos [8-9] como cualitativos [10]. Específicamente en el caso de los vehículos, trabajos como los realizados por Jiang y Shi [11-13] en flotas de transporte muestran la posibilidad de utilizar indicadores de desempeño como EAC.

Lo anterior indica que es posible emplear tanto estimadores directos como indirectos de la condición de un sistema, para los cuales la recolección de los datos se realice a intervalos. El seguimiento del comportamiento de los EAC que se analicen permite, al comparar respecto a un valor límite, evaluar la capacidad del mismo de cumplir con su función y con ello la presencia de una situación de toma de decisión, que están relacionadas con la gestión del mantenimiento del transporte de acuerdo a la definición dada por Nowakowski [14].

El empleo de enfoques de toma de decisión basados en la degradación de los sistemas presenta un conjunto de barreras. Autores como Dekker [15], Van Horenbeek [16], Van de Kerkhof [17] y Tsui [18] en sus revisiones, coinciden en la existencia de una brecha entre la teoría y la práctica, dada por la diferencia entre la gran cantidad de contribuciones realizadas en el nivel teórico y la relativamente poca presencia de aplicaciones en condiciones reales relacionadas con estos temas. Destacan la importancia de acercar las investigaciones en el campo del mantenimiento a las situaciones reales de las organizaciones, teniendo en cuenta los objetivos de los negocios. Según estos autores, la complejidad de los modelos propuestos en las investigaciones limitan las posibilidades de ser comprendidos por aquellos que deben implementarlos en las organizaciones, así como los requerimientos de abundantes datos de calidad. Por tanto, una propuesta aplicable debe ser lo suficientemente sencilla como para emplearse por los operadores de flotas de transporte.

El presente trabajo se centra en proponer una vía para el monitoreo del estado del vehículo, vinculado con los resultados económicos de la operación del mismo. La propuesta debe ser aplicable en condiciones reales, particularmente en entornos de fuertes restricciones económicas, con bajo nivel tecnológico de la flota y de disponibilidad de datos, como contribución a la reducción de la brecha existente en este sentido.

2. Parámetros para el monitoreo del estado del vehículo

2.1. Selección del EAC

El monitoreo de la degradación de los sistemas requiere de tres definiciones iniciales: los EAC que serán monitoreados, la frecuencia de inspección y los valores límites de los EAC a partir de los cuales la operación de los activos no es permisible [19].

Los EAC directos más conocidos son los análisis de aceite, temperatura, ruido y análisis de los gases de escape. Otros parámetros relacionados con los avances en la electrónica de los vehículos también pueden emplearse. La introducción de la medición de parámetros directos, aunque es más efectiva en la detección, diagnóstico y pronóstico de los estados que suponen una operación no permisible, suele ser costosa y requerir un nivel alto de especialización para el empleo exitoso de éstas tecnologías [20-21]. Ello constituye una barrera para la implementación del monitoreo de la degradación de los vehículos y no facilita su introducción en condiciones económicas más restrictivas.

El indicador disponibilidad, junto con el costo y la fiabilidad, es uno de los indicadores más empleados en estudios relacionados con la degradación de los sistemas [2]. Fundamentalmente como criterio de optimización [5,22] y límite de control [22]. No así como EAC, a diferencia de la tasa de fallos [23] o de la fiabilidad [4-5] que sí se han considerado como EAC. No obstante, considerando que el indicador disponibilidad mide la cualidad de los equipos que se relaciona con la funcionalidad [24], es ampliamente utilizado y disminuye en la medida que se incrementa el deterioro del activo, se propone como el EAC a emplear.

Con relación a la frecuencia de inspección se hace referencia en la literatura a tres formas fundamentales: continua, con intervalos fijos y con intervalo variable [2]. Los criterios económicos son los que prevalecen a la hora de seleccionar la frecuencia de inspección [2]. La evaluación de la disponibilidad de los vehículos suele realizarse diariamente con el objetivo de asignar el trabajo, también se realiza de forma mensual y anual, en el nivel jerárquico flota, con vistas a la planificación de la operación. La evaluación a intervalo fijo no introduce cambios en los procedimientos para la recolección de los datos lo que no dificulta la introducción de la propuesta ni encarece el procedimiento.

Solo resta la determinación de un límite de referencia que posibilite diferenciar el estado de operación permisible del que no lo es. La disminución de la disponibilidad a valores inferiores al límite, indicaría que la operación del activo no es permisible y de esa forma la presencia de una situación de toma de decisión. A continuación se introduce el límite de uso racional de un vehículo y luego, la obtención de la expresión matemática para la cuantificación de los valores límites de la disponibilidad.

2.2. Límite de uso racional

Las vías para la determinación de los valores límites de los EAC son tres: la experiencia, la modelación matemática por la vía analítica y la modelación matemática por la vía empírica [25]. En el presente trabajo se opta por la vía analítica. La misma precisa de la definición de los criterios con respecto a los cuáles se obtendrán los valores.

La mayor parte de los estudios que se realizan considerando el estado de los vehículos se centran en minimizar los costos de adquisición, operación y mantenimiento basado en la concepción de que el comportamiento del costo es creciente con respecto al uso [26], siendo las medidas del uso más empleadas la edad y el kilometraje acumulado, aunque diversos estudios han demostrado el comportamiento decreciente del costo total con respecto a la edad del vehículo o su kilometraje. Ello se debe a los patrones de preferencia de los usuarios de la flota bajo los cuales vehículos más nuevos o con menor kilometraje son preferentemente empleados [26].

La utilidad o beneficio es sensible a la influencia del deterioro del estado y del patrón de preferencia del usuario, además puede ser directamente asociado a cada vehículo de la flota. A juicio de los autores, es posible considerar la utilidad como un mejor criterio que el costo, con lo que se podría contribuir además, a establecer un vínculo entre la degradación del vehículo y el primer objetivo de todo negocio. En esta dirección, Kochnov y Basté [27] relacionan la disponibilidad de los vehículo con el resultado económico de su operación en la obtención de un valor límite de la disponibilidad con el objetivo de estimar la distancia media que puede recorrer un vehículo entre dos reparaciones generales consecutivas. En esta relación no se consideran las pérdidas que se producen por acciones periódicas de mantenimiento, el tiempo empleado en cuestiones logísticas y administrativas (tiempo en actividades de apoyo al mantenimiento), así como el tiempo inactivo que influyen en el resultado económico de la operación. Tampoco se proveen todas las relaciones matemáticas necesarias para el cálculo de los parámetros económicos. El alcance del índice es limitado no obstante constituye un antecedente importante.

Los sistemas pueden encontrarse en dos estados según la capacidad de cumplir con su función con los parámetros requeridos: estado de funcionamiento y estado de fallo [1]. El estado de funcionamiento se conoce como disponible y el de fallo como fuera de servicio.

En el caso de las flotas de transporte, la asignación de los trabajos de transportación está dada por la conjugación de diversos factores: la irregularidad de la demanda que se manifiesta no solo en fluctuaciones a largo plazo (debido a la tendencia o los cambios estacionales) sino en el corto plazo con diferencias mensuales y diarias [28-29]; la planificación de la operación [30-31]; el tiempo de descanso de los choferes para recuperarse de la fatiga durante la conducción [32]; y las dimensiones de la flota y su composición [29]. Eso significa que un vehículo disponible puede encontrarse en dos estados: trabajando o inactivo. Se entiende por vehículo trabajando al estado en el cual el vehículo se encuentra en alguna de las actividades relacionadas con el proceso de producción. Estas actividades son: en movimiento (posicionamiento para la carga, el traslado de la carga y regreso a la base), en las paradas relacionadas con el descanso obligatorio de los choferes, durante la carga/descarga y otros procedimientos (maniobras, documentación, pesaje y expedición) [33-34].Un vehículo está inactivo cuando estando disponible no se encuentra en alguna de las tareas relacionadas con el proceso de producción.



Figura 1. Relación entre el estado del vehículo y el resultado económico de la operación.
Fuente: Los autores.

Desde el punto de vista de económico, con la tenencia de un vehículo se incurren en un grupo de gastos que son fijos, por lo que están presentes en cualquiera de los estados en que este se encuentre.

Un vehículo trabajando genera ingresos que están dados por el valor de servicio realizado. Para la ejecución del servicio consume recursos como el combustible, que dependen del nivel de actividad. Ello conduce a un resultado económico en forma de utilidad o pérdida, según sea el balance entre los ingresos y gastos. Por otro lado, un vehículo que no produce (lo que ocurre en los estados inactivo y fuera de servicio) no genera el beneficio que pudiera esperarse si estuviese trabajando. Este constituye un costo de oportunidad, que conduce a una afectación económica. La Fig. 1 muestra la relación entre los elementos resultantes de este análisis.

De acuerdo a lo mostrado en la Fig. 1, el tiempo trabajado por un vehículo genera beneficios económicos, mientras que el tiempo sin trabajar influye negativamente, provocando una afectación económica. El beneficio económico (BE) por el tiempo trabajado (T_t) de un vehículo se puede expresar según ec. (1), mientras que la afectación económica (AE) por el tiempo no trabajado (T_{nt}) según ec. (2).

$$BE = aT_t \quad (1)$$

$$AE = bT_{nt} \quad (2)$$

Donde a es el beneficio generado por el trabajo del vehículo en la unidad de tiempo, b la afectación económica por no trabajar en la unidad de tiempo y T_{nt} la suma del tiempo inactivo y el tiempo fuera de servicio.

La relación entre estos tiempos se puede expresar teniendo en cuenta un período de estudio o análisis determinado como puede verse en la ec. (3). En un determinado T_p el incremento del tiempo trabajado provoca la disminución del tiempo sin trabajar ya que:

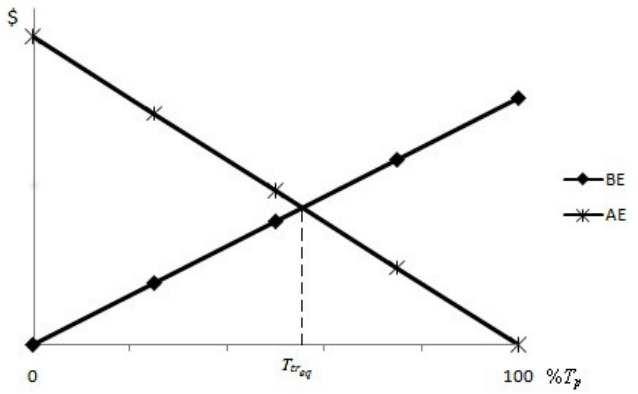


Figura 1. Comportamiento de los beneficios y las afectaciones económicas en función del tiempo trabajado, expresado como porciento del tiempo del periodo.
Fuente: Los autores.

$$T_p = T_t + T_{nt} \quad (3)$$

El parámetro *a* está asociado al beneficio por el trabajo y *b* se relaciona con el costo de oportunidad por no trabajar y los gastos fijos (de acuerdo a la Fig. 1); considerando el día como unidad de tiempo entonces se obtiene que:

$$a = I_d - v \cdot l_{t_d} - F_d \quad (4)$$

$$b = I_d - v \cdot l_{t_d} + F_d \quad (5)$$

Donde:

I_d: Ingreso medio diario del vehículo, $/d.

v: Costo variable unitario de la operación del vehículo, $/km.

l_{t_d}: Distancia media diaria recorrida por el vehículo, km/d.

F_d: Gastos fijos diarios del vehículo, $/d.

La forma específica en la que se calculan los ingresos y los gastos para la determinación de los parámetros a y b dependen del tipo de medio de transporte de la flota y del servicio al que esté destinada. Por ejemplo flotas de transporte de carga, flotas de arrendamiento, flotas de transporte de pasajeros por ómnibus, etc.

La relación entre el beneficio y la afectación económica en un periodo determinado se muestra en la Figura 1. Al expresar AE en función de T_t se puede constatar que a medida que aumenta el porciento del tiempo trabajado en el periodo, BE aumenta mientras que AE disminuye. Por tanto, existe un punto de equilibro en el cual BE = AE.

Al despejar T_t en la relación de equilibrio anterior y dividiendo por T_p se obtiene:

$$\alpha_{a_{LIM}} = \frac{b}{a+b} \quad (6)$$

Donde $\alpha_{a_{LIM}}$ es el coeficiente de aprovechamiento del vehículo correspondiente al punto de equilibrio. Si $\alpha_a \geq \alpha_{a_{LIM}}$ entonces BE ≥ AE (ver Figura 1, en el caso contrario ($\alpha_a \geq \alpha_{a_{LIM}}$) BE < AE. A este valor ($\alpha_{a_{LIM}}$), que representa el nivel de utilización del vehículo a partir del cual el beneficio económico de su operación es mayor que la afectación por la permanencia del vehículo sin trabajar se le denominará **límite de uso racional.**

2.3. Expresión de la disponibilidad límite

El indicador α_a depende de dos factores: relacionado con la operación de la flota, caracterizada por el coeficiente de salida (α_s) y por su estado técnico, expresado a través de la disponibilidad (α_t), como muestra la siguiente expresión [35].

$$\alpha_a = \alpha_s \cdot \alpha_t \quad (7)$$

El coeficiente de salida es un indicador que muestra el grado de aprovechamiento de los vehículos técnicamente aptos para trabajar [35], caracteriza la Función Operación y se calcula como muestra la ec. (8), mientras que la disponibilidad según (9).

$$\alpha_s = \frac{T_t}{T_p - T_{fs}} \quad (8)$$

$$\alpha_t = \frac{T_p - T_{fs}}{T_p} \quad (9)$$

Donde T_{fs} representa el tiempo fuera de servicio del vehículo

Sustituyendo la ec. (7) en (6) y despejando α_t se obtiene:

$$\alpha_{t_{LIM}} = \frac{b}{\alpha_s(a+b)} \qquad \forall\, \alpha_S \in \left[\frac{b}{a+b}, 1\right] \quad (10)$$

Donde $\alpha_{t_{LIM}}$ es la disponibilidad límite. Representa límite de uso racional, o sea, el equilibrio entre BE y AE.

El modelo de la ec. (10) muestra una hipérbola con parámetros *a* y *b* y α_s como variable independiente. Tanto α_s como α_t tienen significado físico en el intervalo [0;1] (ver ec. (8) y (9)) lo cual restringe el intervalo de valores de α_s.

Un vehículo se encuentra en situación de toma de decisión cuando su uso no es racional. El uso no es racional cuando se cumple que $\alpha_t < \alpha_{t_{LIM}}(\alpha_s)$.

3. Aplicación de la propuesta a una situación real.

3.1. Procedimiento

Los parámetros I_d, v, l_{t_d}, F_d, que intervienen en el cálculo de *a* y *b* para la obtención de la constante de la función $\alpha_{t_{LIM}}$ dependen de características de los vehículos (como el régimen de mantenimiento o los precios de los insumos) y del contexto operacional (distancias entre los orígenes y destinos de la carga o las características de la misma). Por lo que se

Tabla 1.
Niveles para cada tratamiento a contrastar.

Tratamiento	Niveles	Condición
Evaluación de la disponibilidad	Racional	$\alpha_{t_{ij}} \geq \alpha_{t_{eq}}(\alpha_{s_{ij}})_i$
	Irracional	$\alpha_{t_{ij}} < \alpha_{t_{eq}}(\alpha_{s_{ij}})_i$
Evaluación de la condición de equilibrio	Racional	$BE_{R_{ij}} \geq AE_{R_{ij}}$
	Irracional	$BE_{R_{ij}} < AE_{R_{ij}}$

Fuente: Los autores.

puede asumir en el cálculo de $\alpha_{t_{LIM}}$ que vehículos con características similares en condiciones de operación similares tienen el mismo valor de los parámetros de I_d, v, l_{t_d}, F_d y por consiguiente la misma función límite $\alpha_{t_{LIM}}$. Lo que significa que los vehículos pueden ser agrupados. Por otro lado, si se desea monitorear el indicador disponibilidad debe disponerse del comportamiento límite (función $\alpha_{t_{LIM}}$) con anterioridad al análisis de la disponibilidad por lo que el momento para el cálculo es el de la planificación del periodo a monitorear.

Atendiendo a estas dos suposiciones, unidas al hecho de que a través de la vía propuesta se realizan inferencias sobre el resultado económico de la operación de los vehículos a partir del comportamiento de la disponibilidad (los cuales se miden en las escalas diferentes: tiempo en el caso del análisis de la disponibilidad y unidades monetarias en el caso del resultado económico), se consideró pertinente realizar una verificación de la correspondencia entre los resultados del análisis de la disponibilidad y el resultado económico de la operación del vehículo paralelamente a la aplicación. Para ello se empleó el análisis de concordancia que permite cuantificar la medida en la que dos factores coinciden en sus clasificaciones (ver Tabla 1). El primer factor es la evaluación de la disponibilidad con respecto al equilibrio calculado según el modelo propuesto en la ec. (10). El segundo, es la evaluación de la condición de equilibrio con respecto a los beneficios reales (BE_R) aportados por cada vehículo según la ec. (11) y las afectaciones generadas por el tiempo real sin trabajar (AE_R) dado por la ec. (12).

$$BE_{R_{ij}} = I_{ij} - G_{ij} \tag{11}$$

$$AE_{R_{ij}} = b_i + \left(T_{i_{ij}} + T_{fs_{ij}}\right) \tag{12}$$

Donde:

i: Representa el i-ésimo bloque.

j: representa la j-ésima unidad (vehículo).

I_{ij}: Ingresos reales obtenidos por la operación de la unidad j en el periodo correspondiente al bloque i, $.

G_{ij}: Gastos directos asociados a la operación de la unidad j en el periodo correspondiente al bloque i, $.

El procedimiento seguido fue el siguiente:

1) Segmentar la flota en bloques homogéneos atendiendo a las características de los vehículos y del contexto operacional.
2) Calcular los parámetros del modelo para cada bloque a partir de los datos de la planificación realizada para el periodo, con lo que se obtiene la función $\alpha_{t_{LIM}}$. Clasificar los vehículos, según el valor de disponibilidad de cada uno, en el nivel correspondiente (Tabla 1).
3) Calcular los beneficios reales por el trabajo y la afectación real por el tiempo sin trabajar de cada vehículo a partir de los datos primarios (registros de operación y mantenimiento), con lo que se evalúa la condición de equilibrio y se clasifican los vehículos según el nivel correspondiente en la Tabla 1.
4) Cuantificar, para cada bloque, las coincidencias y discrepancias en las clasificaciones de los vehículos por ambos métodos y resumir en la tabla de contingencia (Tabla 2).

Donde:

n_{ij}: cantidad de unidades que se clasifican en el nivel *i* según la evaluación del tiempo de trabajo y el nivel *j* según evaluación de la condición de equilibrio.

$n_{i\bullet}$, $n_{\bullet j}$: distribuciones marginales

N: total de unidades experimentales.

Evaluar el grado de acuerdo entre los factores: se calcula a través de la medida kappa (κ) [36] según la ec. (13).

$$\kappa = \frac{N\sum_i^I n_{ii} - \sum_i^I n_{i\bullet} n_{\bullet i}}{N^2 - \sum_i^I n_{i\bullet} n_{\bullet i}} \tag{13}$$

La interpretación del resultado de κ se muestra en la Tabla 3.

Esta clasificación se reconoce como arbitraria [37] pero es ampliamente aceptada [36, 38]. No se encontraron estudios que definieran el límite de la fuerza del acuerdo para aceptar los métodos contrastados. Para los efectos de este trabajo se considerará que se acepta método propuesto si $\kappa \geq 0{,}61$, lo cual significaría que el grado de acuerdo es considerablemente superior respecto al que podría esperarse debido al azar.

3.2. Datos

La flota estudiada cuenta con 37 camiones con los atributos que muestra la Tabla 4. La misma pertenece a una

Tabla 2.
Tabla de contingencia para la evaluación del acuerdo entre los factores.

Evaluación de la disponibilidad	Evaluación de la condición de equilibrio		Total
	Racional	Irracional	
Racional	n_{11}	n_{12}	$n_{1\bullet}$
Irracional	n_{21}	n_{22}	$n_{2\bullet}$
Total	$n_{\bullet 1}$	$n_{\bullet 2}$	*N*

Fuente: Los autores.

Tabla 3.
Reglas para evaluar el grado de acuerdo.

κ	Dimensión del acuerdo
0	Pobre
0.00-0.20	Pequeño
0.21-0.40	Mediano
0.41-0.60	Moderado
0.61-0.80	Considerable
0.81-1.00	Casi perfecto

Fuente: [36]

Tabla 4.
Composición de la flota.

Bloque	Capacidad de carga (t)	Peso bruto(t)	Nivel de actividad planificado (km)	Tiempo en Operación (años)	Cantidad
A	30	16	135000	8	25
B	30	25	105000	6	12
				Total	37

Fuente: Los autores.

Tabla 5.
Valores de los parámetros de la disponibilidad límite.

Bloque	I_d	l_{t_d}	v	F_d	*a*	*b*	$\frac{b}{a+b}$
A	1012.36	473.68	0.44962	43.97	763.61	849.82	0.5267
B	935.03	437.50	0.51267	71.00	649.18	789.45	0.5488

Fuente: Los autores.

empresa que realiza transportaciones a carga completa, que ha sido seleccionada aleatoriamente. El régimen de trabajo es continuo (24 h los 7 días de la semana) en dos turnos de trabajo y un chofer por turno por vehículo.

El plan de transportación y planificación económica junto con la información recogida en los registros de operación y mantenimiento (cartas porte, órdenes de trabajo de mantenimiento y los reportes económicos), en un año de trabajo se emplearon para el cálculo de los parámetros de $\alpha_{t_{LIM}}$.

4. Resultados y discusión

Aplicando el primer paso del procedimiento, se obtuvo la tecnología como criterio relevante para la agrupación de los vehículos, ya que la flota cuenta con vehículos de dos modelos (A y B) que difieren entre sí, por sus características técnicas. El nivel de actividad planificado y el tiempo en operación es igual para cada modelo por lo que no se subdivide. El resto de los factores inciden indistintamente sobre los vehículos por lo que se consideraron aleatorios. Por ende, se segmentó la flota en dos bloques homogéneos (A y B) correspondientes a cada modelo de vehículo.

Los valores calculados de: I_d, v, l_{t_d}, F_d, así como de *a* y *b*, correspondientes a cada bloque se muestran en la Tabla 5. La clasificación obtenida al evaluar la disponibilidad, así como al evaluar la condición de equilibrio se muestra en las Tabla 6 y 7.

En la Tabla 6 se puede observar que la disponibilidad de los vehículos 7, 12, 17 y 22 del bloque A es menor que el límite de uso racional, lo que representa un 16% del bloque. Lo mismo sucede con los vehículos 7, 8, 9, 10 y 12 del bloque B (Tabla 7), representando un 41,66%. Del mismo modo, se puede observar que existe correspondencia con los resultados obtenidos a través de la evaluación de la condición de equilibrio (Tablas 8 y 9). Finalmente, el valor de κ obtenido a través del análisis estadístico para ambos bloques se muestra en la Tabla 10.

Tabla 6.
Clasificación de acuerdo a los tratamientos contrastados del bloque A.

Vehículos	Evaluación de la Disponibilidad				Evaluación de la condición de equilibrio		
	α_t	α_s	α_{tlim}	Nivel	BE	AE	Nivel
1	0.93	0.83	0.63	R	229701.60	76170.78	R
2	0.87	0.90	0.58	R	219455.68	72543.60	R
3	0.94	0.91	0.58	R	251495.98	46246.55	R
4	0.93	0.87	0.61	R	246706.42	64382.45	R
5	0.91	0.96	0.55	R	273313.73	40805.78	R
6	0.95	0.89	0.59	R	267010.40	49873.73	R
7	0.37	0.92	0.57	I	63839.82	219444.39	I
8	0.90	0.94	0.56	R	197254.14	51687.32	R
9	0.77	0.93	0.57	R	199895.44	93399.89	R
10	0.96	0.98	0.54	R	267568.80	19949.49	R
11	0.97	0.94	0.56	R	289803.59	28110.65	R
12	0.59	0.80	0.66	I	143487.40	175011.44	I
13	0.83	0.96	0.55	R	252028.96	68009.63	R
14	0.95	0.92	0.57	R	262885.02	41712.57	R
15	0.79	0.93	0.57	R	200583.76	87959.12	R
16	0.94	0.93	0.57	R	234321.25	41712.57	R
17	0.04	0.63	0.84	I	-8991.14	321912.23	I
18	0.93	0.91	0.59	R	251962.11	50780.52	R
19	0.80	0.88	0.60	R	197658.58	98840.66	R
20	0.95	0.95	0.55	R	236274.97	34458.21	R
21	0.97	0.95	0.55	R	282185.13	25390.26	R
22	0.00	0.00	1	I	-15733.40	330980.18	I
23	0.77	0.92	0.57	R	216988.59	97027.07	R
24	0.95	0.99	0.53	R	254769.97	18135.90	R
25	0.82	0.91	0.59	R	239305.72	85238.73	R

R- racional, I- irracional
Fuente: Los autores.

En la Tabla 10, se puede observar el nivel de acuerdo es casi perfecto para ambos bloques por lo que se puede aceptar que no hay diferencias significativas entre los resultados aportados por ambos métodos. Por tanto, la vía propuesta permite realizar inferencias sobre el resultado económico del uso de los vehículos a partir de un indicador relacionado con el estado técnico de los mismos. Se puede afirmar además que la segmentación en bloques y el uso de datos provenientes de la planificación del período no introdujeron errores significativos en la evaluación de los vehículos.

Los resultados muestran que no solo es posible identificar aquellos vehículos que se encuentran en situación de toma de decisión, sino la presencia de situaciones en el nivel jerárquico de flota, como es el caso de la comparación con respecto a los criterios de segmentación. Obsérvese que casi la mitad de los vehículos del bloque B están clasificados en el nivel irracional, lo que sugiere situaciones relacionadas con la tecnología, ya que este grupo tiene menos tiempo en operación y menos nivel de actividad planificado. Este mismo hecho relacionado con el tiempo en operación y el nivel de actividad planificado sugiere además, la presencia de otros patrones de preferencia además del reportado [26].

Tabla 7.
Clasificación de acuerdo a los tratamientos contrastados del bloque B.

Vehículos	Evaluación de la disponibilidad				Evaluación de la condición de equilibrio		
	α_t	α_s	α_{tlim}	Nivel	BE	AE	Nivel
1	0.94	0.90	0.60	R	265061.28	52191.21	R
2	0.92	0.93	0.58	R	216514.24	46599.30	R
3	0.92	0.93	0.58	R	212278.68	50327.24	R
4	0.89	0.91	0.60	R	223030.12	66171.00	R
5	0.98	0.95	0.57	R	288874.72	22367.66	R
6	0.97	0.99	0.55	R	191662.83	13979.79	R
7	0.00	0.00	1.00	I	-14475.90	340174.88	I
8	0.00	0.00	1.00	I	-14475.90	340174.88	I
9	0.00	0.00	1.00	I	-14475.90	340174.88	I
10	0.37	0.76	0.71	I	37942.62	244180.33	I
11	0.70	0.92	0.59	R	143738.84	120226.19	R
12	0.25	0.81	0.66	I	30691.00	271207.92	I

R- racional, I- irracional
Fuente: Los autores.

Tabla 8.
Tabla de contingencia para el contraste de los factores del bloque A.

Evaluación de la disponibilidad	Evaluación de la condición de equilibrio		Total
	Racional	Irracional	
Racional	21	0	21
Irracional	0	4	4
Total	21	4	25

Fuente: Los autores.

Tabla 9.
Tabla de contingencia para el contraste de los factores del bloque B.

Evaluación de la disponibilidad	Evaluación de la condición de equilibrio		Total
	Racional	Irracional	
Racional	7	0	7
Irracional	0	5	5
Total	7	5	12

Fuente: Los autores.

Tabla 10.
Resultados del cálculo estadístico.

Bloque	κ	Grado de acuerdo
A	1	Casi perfecto
B	1	Casi perfecto

Fuente: Los autores.

El modelo obtenido (ec. 10) para el cálculo del límite de la disponibilidad se diferencia del mostrado por Kochnov y Basté [27], en el alcance de las pérdidas que considera, dado por la introducción de la variable α_s. Junto con las ec. (4) y (5) constituyen un sistema de ecuaciones algebraicas, la más sencilla de las formulaciones, por lo que no se requieren habilidades especiales en el uso de las matemáticas ni sistemas complejos de procesamiento de datos. Ello unido a que el indicador disponibilidad es uno de los indicadores más utilizados para el control de la actividad de mantenimiento de las flotas, no se requiere instrumentación adicional, y los datos requeridos son básicos en cualquier entorno, hace que sea posible su aplicación en condiciones reales con presencia de restricciones económicas y bajo nivel tecnológico de la flota.

Los parámetros y variables empleados son comunes no solo para flotas de transporte de carga tanto TL como LTL, sino a otras flotas de vehículos automotores como las de alquiler o de transporte de pasajeros, por lo que la aplicación de este modelo es posible que pueda extenderse a estos casos, aunque la dependencia en el cálculo del límite de los ingresos limita el alcance de la aplicación a flotas que pertenecen a empresas proveedoras de servicios de transporte.

Se introduce el término límite de uso racional para referirse al valor del aprovechamiento del vehículo para el cual los beneficios económicos generados por el trabajo de mismo y las afectaciones que se producen por no trabajar se encuentran en equilibrio.

El empleo del día como unidad de tiempo responde a la forma en la que se registra y procesa la información en las bases de transporte disponibles. A criterio de los autores, la hora es una mejor alternativa.

5. Conclusiones

La propuesta de monitorear la degradación de los vehículos de transporte de cargas a través del análisis de la disponibilidad es factible y permite realizar inferencias sobre la permisibilidad de la operación del vehículo con relación a su resultado económico, primer objetivo de todo negocio. Es una propuesta sencilla y su empleo debe contribuir a estrechar la brecha entre teoría y práctica planteada por diversos autores, con relación a los enfoques de toma de decisión basados en la degradación de los sistemas.

La aplicación del método propuesto está limitada a flotas de transporte de cargas que generen ingresos, aunque puede ser extendido a otros tipos de flotas al ser los parámetros y variables empleados, de uso común entre los operadores de flotas.

Bibliografía

[1] Knesevic, J., Mantenimiento. Madrid, Isdefe, 1996.

[2] Alaswad, S. and Xiang, Y.-A., Review on condition-based maintenance optimization models for stochastically deteriorating system. Reliability Engineering and System Safety. 157, pp. 54-63, 2017. DOI: 10.1016/j.ress.2016.08.009

[3] Ahmad, R. y Kamaruddin, S.-A review of condition-based maintenance decision-making. European Journal of Industrial Engineering, 6(5), pp. 519-541, 2012. DOI: 10.1504/EJIE.2012.048854.

[4] Zhou, X., Xi, L. y Lee J., Reliability-centered predictive maintenance scheduling for a continuously monitored system subject to degradation. Reliability Engineering & System Safety, 92, pp. 530-534, 2007.DOI: 10.1016/j.ress.2006.01.006.

[5] Li, L., You, M. and Ni, J., Reliability-based dynamic maintenance threshold for failure prevention of continuously monitored degrading systems. Journal of Manufacturing Science and Engineering, Transactions of the ASME, 131, pp. 031010-1-031010-9, 2009. DOI: 10.1115/1.3123340.

[6] Tywoniak, S., Rosqvist, T., Mardiasmo, D. and Kivits, R.-A., Towards an integrated perspective on fleet asset management: engineering and governance considerations. Proceedings of 3rd World Congress on Engineering Asset Management and Intelligent Maintenance Systems Conference (WCEAM-IMS 2008): Engineering Asset Management - A Foundation for Sustainable Development, 2008, pp. 1553-1567.

[7] Collins, D.-H., Anderson-Cook, C.-M. and Huzurbazar, A.-V., System Health Assessment. Quality Engineering, 23(2), pp. 142-151, 2011. DOI: 10.1080/08982112.2010.529484.

[8] Panagiotidou, S. and Tagaras, G. Statistical process control and condition-based maintenance, a meaningful relationship through data sharing. Production and Operations Management, 19(2), pp. 156-171,

2010. DOI: 10.3401/poms.1080.01073.
[9] Xiang, Y., Joint optimization of X control chart and preventive maintenance policies: a discrete-time Markov chain approach. European Journal of Operational Research, 229(2013), pp. 382-390, 2013. DOI: 10.1016/j.ejor.2013.02.041.
[10] Zhong, J., Ma, Y. and Tu, Y.-L. Integration of SPC and performance maintenance for supply chain system. International Journal of Production Research, 54(19), pp. 5932-5945, 2016. DOI: 10.1080/00207543.2016.1189104.
[11] Jiang, R. and Shi, G., Condition-based vehicle fleet retirement decision, a case study. International Journal of Performability Engineering, 6(4), pp. 355-362, 2010.
[12] Jiang, R. and Shi, G., Development and application of vehicle health index. Advanced Materials Research, (118-120), pp. 459-463, 2010. DOI: 10.4028/www.scientific.net/AMR.118-120.459.
[13] Jiang, R., An overall performance measure for vehicle retirement decision. Chemical Engineering Transactions, 33, pp. 775-780, 2013. DOI: 10.3303/CET1333130.
[14] Nowakowski, T., Tubis A., and Werbińska-Wojciechowska, S., Maintenance decision making process - a case study of passenger transportation company, en W. Zamojski, et al. Theory and engineering of complex systems and dependability, Springer, Brunów. pp. 305-318, 2015. DOI: 10.1007/978-3-319-19216-1_29.
[15] Dekker, R., Applications of maintenance optimization models: a review and analysis. Reliability Engineering & System Safety, 51(3), pp. 229-240, 1996.
[16] Van Horenbeek, A., Pintelon, L. and Muchiri, P., Maintenance optimization models and criteria. International Journal of System Assurance Engineering and Management, 1(3), pp. 189-200, 2010. DOI: 10.1007/s13198-011-0045-x.
[17] van de Kerkhof, R.-M., Akkermans, H.-A. and Noorderhaven, N.-G., Knowledge lost in data: organizational impediments to condition-based maintenance in the process industry, in Logistics and Supply Chain Innovation, Lecture Notes en H. Zijm et. al. Logistics, , Springer International Publishing: Switzerland, 2016.
[18] Tsui, K.-L., Chen, N., Zhou, Q., Hai Y. and Wang, W., Prognostics and health management: a review on data driven approaches. Mathematical Problems in Engineering, 2015, 17 P, 2015. DOI: 10.1155/2015/793161.
[19] Shin, J.-H. and Jun, H.-B., On condition based maintenance policy. Journal of Computational Design and Engineering, 2(2015), pp. 119-127, 2015. DOI: 10.1016/j.jcde.2014.12.006.
[20] Bivona, E. and Montemaggiorea, G.-B., Understanding short- and long-term implications of "myopic" fleet maintenance policies: a system dynamics application to a city bus company. System Dynamics Review, 26(3), pp. 195-215, 2010. DOI: 10.1002/sdr.450.
[21] Stecki, J.-S., Rudov-Clark, S. and Stecki, C., The rise and fall of CBM (Condition based Maintenance). Key Engineering Materials. 588(2014), pp. 290-301. 2014. DOI: 10.4028/www.scientific.net/KEM.588.290.
[22] Liao, H., Elsayed, E.-A. and Chan, L.-Y., Maintenance of continuously monitored degrading systems. European Journal of Operational Research, 175(2006), pp. 821-835, 2006. DOI: 10.1016/j.ejor.2005.05.017.
[23] Yeh, R.-H. and Chang, W.-L., Optimal threshold value of failure-rate for leased products with preventive maintenance actions. Mathematical and Computer Modelling, 46(2007), pp. 730-737, 2007. DOI: 10.1016/j.mcm.2006.12.001.
[24] Penabad-Sanz, L., Iznaga-Benítez, A.M. y Rodríguez-Ramos, P.A., Disposición y disponibilidad como indicadores para el transporte. Revista Ciencias Técnicas Agropecuarias, 25(4), pp. 64-73, 2016.
[25] Gerdes, M., Scholz, D. and Galar, D., Effects of condition-based maintenance on costs caused by unscheduled maintenance of aircraft. Journal of Quality in Maintenance Engineering, 22(4), pp. 394-417, 2016. DOI: 10.1108/JQME-12-2015-0062.
[26] Parthanadee, P., Buddhakulsomsiri, J. and Charnsethikul, P., A study of replacement rules for a parallel fleet replacement problem based on user preference utilization pattern and alternative fuel considerations. Computers & Industrial Engineering, 63(2012), pp. 46-57, 2012. DOI: 10.1016/j.cie.2012.01.011.
[27] Kochnov, N. y Basté, J., Reparación de los automóviles. Vol. 1, La Habana, Cuba: EMPSES, 1986.
[28] Trompet, M., Anderson, R.J. and Graham, D.J., Variability in comparable performance of urban bus operations. Transportation Research Record, December, pp. 177-184, 2009. DOI: 10.3141/2111-20.
[29] Redmer, A., Strategic vehicle fleet management - the composition problem. LogForum, 11(1), pp. 119-126, 2015. DOI: 10.17270/J.LOG.2015.1.11.
[30] Buchanan, J. and Scott, J. Vehicle utilization at bay of plenty electricity. Interfaces, 22(2), pp. 28-35, 1992.
[31] Lopes-da-Costa-Filho, J.L. and de Athayde-Prata, B., Programação de caminhões de múltiplos tipos no transporte de derivados de petróleo para a construção de rodovias. Journal of Transport Literature, 9(2), 2015. DOI: 10.1590/2238-1031.jtl.v9n2a11.
[32] Goel, A., A mixed integer programming formulation and effective cuts for minimising schedule durations of Australian truck drivers. Journal of Scheduling, 15(6), pp. 733-741, 2012. DOI: 10.1007/s10951-012-0282-0.
[33] McKinnon, A., Synchronised auditing of truck utilisation and energy efficiency: a review of the British Government's transport KPI programme, en World Conference on Transport Research. University of California, Berkeley, 2007.
[34] Alves, R.T., Fiedler, N.C, da Silva, E.N., da Silva-Lopes, E. and do Carmo, F.C.d.A., Análise técnica e de custos do transporte de madeira com diferentes composições veículares. Revista Árvore, 37, pp. 897-904, 2013.
[35] Afanasiev, L.L., et al, Sistema único de transportación y transportaciones por vehículos automotores. Moscú: Transport. 1984.
[36] Everitt, B.S., The analysis of contingency tables. CRC Press.1992
[37] Landis, J. and Koch, G., The measurement of observer agreement for categorical data. Biometrics, 33, pp. 159-74, 1977.
[38] López-de-Ullibarri-Galparsoro, I. y Pita-Fernández, S., Medidas de concordancia: el coeficiente kappa. Cad aten primaria, 6, pp. 169-171, 1999.

L. Penabad-Sanz, es graduada de Ing. Mecánica en 1999, Ing. Industrial en 2009 y MSC. en Gestión Integral del Transporte, Mención Automotor en 2011, todos en la Universidad Tecnológica de La Habana "José Antonio Echeverría", Cuba, es profesora auxiliar en el Centro de Estudios de Ingeniería en Mantenimiento (CEIM) de la Facultad de Ingeniería Mecánica, Universidad Tecnológica de La Habana "José Antonio Echeverría", Cuba. Dirige e investiga en proyectos relacionados con la operación y mantenimiento de flotas de transporte, particularmente, gestión del mantenimiento, evaluación tecnológica de los vehículos y del mantenimiento automotor.
ORCID: 0000-0001-9106-2087

P.A. Rodríguez-Ramos, es graduado de Ing. del Transporte Marítimo en 1977, de MSc. en Explotación de la Flota en 1977 y de Dr. en Ciencias en Gestión del Transporte Marítimo in 1986, todos en la Universidad Marítima de Odesa. Ucrania. Desde 1977 a 2017, trabaja en la Universidad Tecnológica de La Habana, Cuba. Actualmente, es profesor titular, tiempo completo, en el Centro de Estudios de Ingeniería en Mantenimiento (CEIM) de la Facultad de Ingeniería Mecánica. Las líneas investigativas de interés incluyen: análisis de ciclo de vida, gestión del mantenimiento, gestión medioambiental, gestión de la calidad, análisis de factibilidad económica. Actualmente trabaja en varios programas y proyectos vinculados a estas líneas.
ORCID: 0000-0003-2862-0984

A.M. Iznaga-Benítez, es graduado de Ing. Mecánico en 1984, Universidad Politécnica de la Habana José A. Echeverría (Cujae), Cuba, MSc. en Ciencias de la Ingeniería Agrícola en 1997 en la Universidad Estatal de Campinas, São Paulo, Brasil y Dr. en Ciencias Técnicas en 2001, Cujae, Cuba. Más de veinticinco años de experiencia profesional ejerciendo cátedra universitaria y participando en la solución de problemas de investigación y desarrollo en las ramas del azúcar, el petróleo, la salud y la sideromecánica entre otras, incluyendo la formación de personal técnico especializado. Investiga en temas relacionados con la gestión del mantenimiento, la gestión de activos e ingeniería biomédica.
ORCID: 0000-0001-6409-9044

UNIVERSIDAD NACIONAL DE COLOMBIA
SEDE MEDELLÍN
FACULTAD DE MINAS



DYNA
http://dyna.medellin.unal.edu.co/

Integration of tools for decision making in vehicular congestion

Nelson Iván-Herrera-Herrera[a], Sergio Luján-Mora[b] & Estevan Ricardo Gómez-Torres [a]

[a] *Facultad de Ciencias de la Ingeniería e Industrias, Universidad Tecnológica Equinoccial, Quito, Ecuador. nelson.herrera@ute.edu.ec, etevan.gomez@ute.edu.ec*
[b] *Departamento de Lenguajes y Sistemas Informáticos, Universidad de Alicante, Alicante, España. sergio.lujan@ua.es*

Received: September 15th, 2017. Received in revised form: March 15th, 2018. Accepted: March 21th, 2018.

Abstract
The purpose of this study is to present an analysis of the use and integration of technological tools that help decision making in situations of vehicular congestion. The city of Quito-Ecuador is considered as a case study for the done work. The research is presented according to the development of an application, using Big Data tools (Apache Flume, Apache Hadoop, Apache Pig), favoring the processing of a lot of information that is required to collect, store and process. One of the innovative aspects of the application is the use of Twitter social network as source of origin. For this, it used its application programming interface (API), which allows to take data from this social network and identify probable points of congestion. This study presents results of tests carried out with the application, in a period of 9 months.

Keywords: congestion; traffic; Twitter; big data; application; Quito.

Integración de herramientas para la toma de decisiones en la congestión vehicular

Resumen
Este estudio tiene como finalidad presentar un análisis de la utilización e integración de herramientas tecnológicas que ayudan a tomar decisiones en situaciones de congestión vehicular. La ciudad de Quito-Ecuador es considerada como un caso de estudio para el trabajo realizado. La investigación se presenta en función del desarrollo de una aplicación, haciendo uso de herramientas *Big Data* (Apache Flume, Apache Hadoop, Apache Pig), que permiten el procesamiento de gran cantidad de información que se requiere recolectar, almacenar y procesar. Uno de los aspectos innovadores de la aplicación es el uso de la red social Twitter como fuente de origen de datos. Para esto se utilizó su interfaz de programación de aplicaciones (*Application Programming Interface*, API), la cual permite tomar datos de esta red social en tiempo real e identificar puntos probables de congestión. Este estudio presenta resultados de pruebas realizadas con la aplicación, durante un período de 9 meses.

Palabras clave: congestión; tráfico; Twitter; big data; aplicación; Quito.

1. Introducción

La dinámica de las grandes ciudades genera situaciones complejas y difíciles de abordar. Entre estas situaciones se tiene la alta densidad poblacional en espacios geográficos muy estrechos y sin posibilidades de crecimiento urbano.

La ciudad de Quito es la capital del Ecuador, siendo esta el centro económico del país, donde se desarrollan actividades comerciales, administrativas y turísticas. Debido a su gran expansión poblacional, la ciudad ha experimentado grandes cambios, que ha tenido como consecuencia del problema de congestión vehicular [1].

Entre las principales causas de la congestión vehicular [1] están las características topográficas de la ciudad, ya que cuenta con grandes montañas al lado occidental y desniveles y valles al lado oriental. Esta situación ha generado, que la ciudad se expanda en dirección norte – sur, es decir de forma alargada y con muy poca organización y planificación [2], sumadas a un explosivo crecimiento del parque automotor, han agudizado aún más el problema [2].

How to cite: Herrera-Herrera, N.I., Luján-Mora, S. and Gómez-Torres, E.R., Integración de herramientas para la toma de decisiones en la congestión vehicular DYNA, 85(205), pp. 363-370, June, 2018.
[1] Relación entre la capacidad de la Infraestructura Vial (Oferta) y el tráfico que circula por ella (Demanda).

© The author; licensee Universidad Nacional de Colombia.

A través del tiempo han existido importantes iniciativas de movilidad en la ciudad, incluyéndose sistemas de control de tránsito, monitoreo, construcción de vías perimetrales, e inclusive la medida "pico y placa" para restringir el uso vehicular en horas pico, de acuerdo a la placa del vehículo [3]. Cabe mencionar que esta alternativa ha sido una iniciativa que se ha adoptado en varios países de América Latina. Sin embargo, todas estas iniciativas no han sido suficientes y la congestión aumenta cada vez más, generando malestar en la ciudadanía.

Con base a esta problemática, se necesita una aplicación que permita: recolectar, almacenar, procesar y visualizar información no estructurada en tiempo real; lo cual sirve de soporte a la toma de decisiones, en situaciones de congestión vehicular, tanto a nivel de entidades oficiales como de personas.

Esta aplicación hace uso de dos grupos principales de datos, los datos sensoriales y sociales. Para el primer tipo de datos, se considera los recopilados a través de sensores, que miden el flujo vehicular en sectores estratégicos, colocados a lo largo de la ciudad. Para lo cual un agente de tránsito por experiencia, determina que puntos son propensos a generar congestión y por lo tanto donde se los deben colocar. El otro grupo de datos hace uso de información pública, existente a través de las redes sociales, en este caso, Twitter.

La información disponible de sensores del volumen de tráfico, así como de las redes sociales, se procesará mediante una aplicación creada para ello. Posteriormente se presentarán los resultados de este análisis, que servirá de apoyo a la toma de decisiones, en situaciones de congestión vehicular.

En un trabajo previo [4], se realizó un análisis de los factores que influyen en la congestión vehicular en Quito; además del estudio de la cuestión acerca de herramientas tecnológicas, que han ido utilizadas alrededor del mundo, como una alternativa de solución a este problema.

El presente artículo está orientado a la presentación técnica de la aplicación y sus componentes; sin embargo el estudio realizo incluye todos los elementos formales de una investigación. En este sentido, partiendo desde el planteamiento del problema, hasta las conclusiones y recomendaciones, se efectuó la fundamentación teórica respaldada en el análisis del uso de técnicas y estrategias utilizadas mundialmente relacionadas el tráfico vehicular.

Los aspectos metodológicos del presente trabajo se orientaron a una investigación de campo para conocer, a través de la aplicación de instrumentos, la percepción de la población sobre la congestión y el uso de redes sociales.

Los hallazgos de la investigación de campo proporcionaron información mediante la cual se logró fundamentar de mejor manera la presente propuesta que a continuación se detalla.

El presente trabajo tiene el contexto de una investigación Big Data [5], pues los elementos de esta tecnología se conjugan perfectamente:

Volumen: miles de datos serán generados mediante la red social Twitter y la proporcionada por los sensores instalados en la ciudad.

Variedad: datos generados por sensores y la red social Twitter.

Velocidad: diariamente se generarán datos mediante la red social Twitter a una importante velocidad. Esto requiere que su procesamiento y posterior análisis, normalmente, ha de hacerse en tiempo real, para mejorar la toma de decisiones [6].

Veracidad: la información de la red social Twitter, debe ser filtrada para seleccionar, únicamente, la que sirva para el estudio.

2. Trabajos relacionados

Se han realizado varias investigaciones relacionadas con herramientas tecnológicas utilizadas en situaciones de congestión vehicular.

- Utilización de modelos macroscópicos [7], equipando a los vehículos con dispositivos de detección cada vez más sofisticados, como cámaras. Las personas y los vehículos están compartiendo datos de detección para mejorar la experiencia de conducción [8].
- Sistemas que monitorean, procesan y almacenan grandes cantidades de datos, lo que permite detectar la congestión del tráfico de manera precisa. Para esto se utiliza una serie de algoritmos que reducen la emisión localizada de vehículos, mediante el re-encaminamiento de los automóviles [9].
- Utilización de sistemas de detección participativa, como Foursquare e Instagram, que se están volviendo muy populares. Los datos compartidos en estos sistemas tienen la participación activa de los usuarios mediante la utilización de dispositivos portátiles. Estos sistemas pueden ser vistos como una especie de sensores que, junto a información de condiciones de tráfico, constituyen en eficientes predictores de congestión vehicular [10].

En este ámbito, otra de las redes sociales potentes que permiten realizar análisis en tiempo real, de los mensajes permitidos y poder determinar puntos de congestión vehicular, es la red social Twitter [11]. Otro insumo importante al momento de analizar y detectar situaciones de tráfico es la utilización de sensores inalámbricos. Estos dispositivos están ganado más atención en la detección de tráfico [12], por lo cual, adicional a Twitter, se utilizará también información de sensores de conteo vehicular. Esto permitirá tener dos criterios previos que, finalmente mediante contraste, ayudará a entregar información más precisa de puntos de congestión vehicular en la ciudad de Quito.

3. Herramientas utilizadas

3.1. Información de sensores

Para lograr la medición del tráfico en la ciudad, el Municipio de Quito, a través de la Secretaría de Movilidad, dispone de sensores a lo largo de la localidad.

La Fig. 1 muestra un ejemplo de sensores de tráfico que están ubicados en lugares estratégicos donde existe más afluencia vehicular, de acuerdo a los criterios del Municipio de Quito. Estos sensores recolectan información de la cantidad de vehículos que circulan por cada punto.



Figura 1. Sensores en la ciudad.
Fuente: Tomado de [2].

Adicionalmente, el Municipio de Quito dispone de parámetros que corresponden a valores preestablecidos de acuerdo al sector, donde se establece una cantidad límite máxima. Si el número de vehículos sobrepasa este valor**,** esto implica que el lugar se encuentra congestionado.

La aplicación que se ha desarrollado y se presenta, genera información útil que establece posibles puntos de congestión vehicular; mediante el análisis de datos generados por sensores y; la correlación con la información presentada en base a tuits recolectados en un determinado momento. La información se presenta en un mapa elaborado para la investigación, que utiliza el API de Google Maps; los puntos de congestión que puedan ser analizados, con lo cual se establecen sectores de mayor tráfico y, a su vez, horas pico. Finalmente, mediante estos resultados se pueda tomar decisiones de cambio de ruta y comunicarlas a la ciudadanía, a efectos de aliviar la congestión vehicular existente.

3.2. Datos de Twitter

La segunda fuente de datos considerada para el análisis corresponde a los datos que proporcionan las personas al hacer uso de la red social Twitter. Se requiere tener una cuenta en Twitter, además de ser necesaria la activación del servicio de GPS en el teléfono inteligente o tableta. Esta red social genera información variada y, por tanto, es utilizada con diversos propósitos, uno de ellos es estimar el tráfico existente en la ciudad. Por lo que los tuits que se generan a todas horas tienen una geolocalización, que permite identificar el origen del mismo. Para lo cual se hace uso del API de Twitter que se detalla a continuación.

3.3. Uso del API de Twitter

Para poder utilizar el API de Twitter es necesario tener una cuenta en esta red social y crear otra adicional de desarrollador, la versión utilizada es la 1.0 [13]. La aplicación

"geo"; "coordinates" y
"place"; "name";"full_name";"country_code";"country"

Figura 2. Campos de geolocalización de un Tuit
Fuente. Los autores

se ha habilitado para la lectura de tuits; sin embargo, la misma permite la publicación de los mismos en caso de ser requerido, para lo cual se habilita la escritura en las opciones de la misma.

Se debe considerar que Twitter debe estar configurado en el teléfono inteligente o tableta, además del GPS. El cual en la mayor parte de casos está habilitado, por defecto.

3.4. Creación del hashtag

Con la finalidad de recolectar y filtrar información relacionada a la congestión generada por el tráfico vehicular en el Distrito Metropolitano de Quito, se creó la etiqueta[2] #TraficoUIO. La utilización de esta etiqueta fue socializada a toda la comunidad de la Universidad Tecnológica Equinoccial (UTE). Inicialmente se recolectaron todos los


```
"geo": {  "type": "Point",
          "coordinates": [38.9069,
                  -6.33876]
          },
          "coordinates": {
                "type": "Point",
                "coordinates":[-6.33876,
                    38.9069]
          },
          "place": {
               "id": "6d564e12cf533f7a",
                    "url":
"https:\/\/api.twitter.com\/1.1\/geo\/id\/6d564e12cf533f7
a.json",
          "place_type": "city",
          "name": "Quito",
          "full_name":"Quito, Pichincha",
          "country_code": "EC",
          "country": "Ecuador",
          "contained_within": [],
          "bounding_box": {
              "type": "Polygon",
               "coordinates": [[[-6.6568728,
                38.7268887],
             [-6.1404139,
    38.7268887],
    [-6.1404139,
    39.1814719],
    [-6.6568728,
    39.1814719]]]
    }
```


Figura 3. Valores asociados a un tuit
Fuente. Los autores

[2] La etiqueta o hashtag tiene como objetivo agrupar tuits que hablen de un mismo tema y facilitar la búsqueda de información

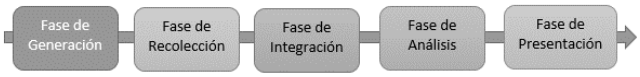


Figura 4. Flujo de información del sistema.
Fuente: Los autores.

tuits asociados al hashtag antes mencionado. La Fig. 2 muestra los campos que permiten a la aplicación acceder a los datos de geolocalización del tuit.

La configuración del tuit considera la ubicación desde la que se genera el mismo, con lo cual es posible obtener la localización del tráfico para los tuits que denuncien esta situación.

La Fig. 3 detalla algunos valores asociados a un tuit, que permiten acceder a datos que muestran, por ejemplo: la ciudad, provincia, país, desde donde se generó el tuit.

La sección "coordinates" indica la geolocalización del tuit, que sirve para filtrar los tuits generados considerando solamente los originados en las vías, donde se ha identificado existe mayor congestión vehicular. La sección "place type" indica el tipo de lugar en el cual se están generando los tuits; el tipo indicado es una ciudad. Otra sección importante, que ayuda a delimitar los tuits generados es "country", que indica la ciudad en la que se generan los tuits; para el presente estudio la ciudad descrita es Quito. Finalmente, la sección "name" permite identificar el lugar desde el cual se genera el tuit; el sitio de interés en el presente caso es la ciudad de Quito.

4. Metodología

La revisión documental de casos de ciudades con la misma problemática permitió analizar y evaluar las aplicaciones utilizadas a nivel mundial en relación a la movilidad inteligente.

En este contexto, los casos de estudio analizados y detallados en este estudio sirvieron para respaldar tanto en contenido o fundamento teórico como metodológico la presente propuesta.

En la Fig. 4, se muestra la arquitectura e integración de las fases que utilizará la aplicación de apoyo a la toma de decisiones en la congestión vehicular.

4.1. Fase de generación

Esta fase es contemplada como una entrada externa importante para la aplicación, pues aquí se generan los datos que posteriormente servirán de entrada, que alimentarán el proceso principal de la aplicación. Las fuentes generadoras de información son: red social Twitter y sensores de volumen de tráfico ubicados en ciertas intersecciones consideradas conflictivas para la congestión vehicular. La información generada por los sensores corresponde a la cantidad autos que están circulando a una distancia de tres metros a partir de la ubicación del sensor instalado, hacia adelante. La distancia establecida, obedece a la longitud promedio de un auto, que es la requerida, para que el sensor pueda detectar el movimiento vehicular.

4.2. Fase de recolección

En esta fase existen dos mecanismos de recolección de datos que serán utilizados por la aplicación propuesta, los cuales constituyen una importante fuente de datos primarios:

- *API Twitter*, mediante el cual se obtienen mensajes que reflejan la opinión de la población, en relación a situaciones de congestión vehicular detectadas.
- *Sensores de volumen de tráfico*, el segundo componente importante está relacionado con la información recolectada por los sensores que alimentan el Sistema de Registro Vehicular, que es manejado por el Centro de Gestión de la Movilidad (CGM) de la ciudad de Quito; en el mismo se registra la carga vehicular existente en determinadas intersecciones de la ciudad.

Para obtener la información relacionada con este componente, se realizaron varias entrevistas con autoridades del CGM de Quito, obteniéndose dos elementos importantes: conteos vehiculares y la georreferenciación de los sensores.

4.3. Fase de integración

Con la finalidad de agrupar los tuits generados, junto con los sensores distribuidos en la ciudad, se utilizó el método de agrupación K-means [14], concentrando los tuits en varios grupos dependiendo de la ubicación de los sensores.

Posteriormente, se filtró el grupo de tuits generados, mediante un análisis semántico y de sentimientos [15], recogiendo los tuits en los que se denota malestar y cuyo texto final mencione temas de congestión vehicular.

Finalmente, el grupo de tuits fue integrado con la información generada por el conteo de los sensores, para su posterior análisis y contraste de la información.

4.4. Fase de análisis

Con la información recolectada mediante redes sociales y sensores de congestión vehicular se obtuvieron índices de congestión. Los mismos fueron generados para cada uno de los sectores en los cuales están ubicados los sensores y alrededor de los cuales existen tuits reportando situaciones de congestión. Los índices son:

- RVD (retraso viaje días).
- FRv (nivel de congestión del tráfico).
- Índice de tiempo de viaje (TTI).

Posteriormente, se determinó la correlación de Pearson [16] entre los tres índices generados. En la Tabla 1 se puede determinar si existe tráfico en cada uno de los sectores de la ciudad, mediante la aplicación de reglas de decisión.

El nivel de correlación Alta, es la que se considera en la investigación, para mostrar gráficamente posibles puntos de congestión vehicular.

Tabla 1.
Reglas de correlación y resultados

Regla	Correlación	Resultado
$R=0$	Nula	Tráfico nulo
$0<R\leq0.4$	Débil	Tráfico leve
$0.4<R\leq0.7$	Media	Tráfico medio
$0.7<R\leq1$	Alta	Congestión

Fuente. Los autores

4.5. Fase de presentación

Finalmente, con los datos almacenados y el procesamiento de los mismos, se ha creado una aplicación desarrollada en JSP para el *backend*, JQuery (Biblioteca de Java) y bootstrap para el *frontend*. Se utilizó Mysql como motor de base de datos y como servidor web Apache Tomcat. El entorno de desarrollo Netbean IDE. El sistema desarrollado es multinavegador y multiplataforma.

El software creado permite incluir la base de datos tanto de los lugares donde existe un sensor en Quito, como de la base de datos de tuits que indican la existencia de tráfico en la ciudad. Esta herramienta web permite apreciar cartográficamente los resultados del análisis y poder determinar posibles zonas de congestión vehicular.

El desarrollo del software contempló tres partes centrales que son:

1. Presentación de lugares de mayor tráfico en la ciudad, considerando los datos de los sensores que dispone el Municipio de Quito.
2. Presentación en tiempo real de los tuits generados en la ciudad, mediante de la red social Twitter, considerando para ello el parámetro ubicación del tuit. Sin embargo, la principal función es presentar en tiempo real el tráfico en la ciudad.
3. Análisis de resultados mediante reportes tanto gráficos como analíticos de los diferentes ámbitos de análisis de tráfico en la ciudad a partir de los tuits cargados en la base de datos.

5. Elección de las herramientas a utilizar

Para determinar la plataforma a usar en la propuesta de desarrollo, en la Tabla 2 se muestra el análisis de las distintas opciones existentes.

Apache Hadoop[3] es actualmente la herramienta libre más utilizada para el análisis de Big Data. Hadoop proporciona dos elementos principales: un *framework MapReduce* y un sistema de archivos (*Hadoop Distributed File Systems*, HDFS). Por un lado, el HDFS provee una base de datos tolerante a fallos con una alta disponibilidad. Por otra parte, el paradigma de programación MapReduce, permite dividir y paralelizar los cálculos entre un número indefinido de ordenadores de bajo coste. En el uso de un clúster de computadores convencionales para el análisis de datos radica una de las mayores ventajas de Apache Hadoop [17].

Tabla 2.
Indicadores de plataformas usadas para *Big Data.*

Plataforma	**A**	**B**	**C**	**D**
Apache Hadoop	No	Alta	Alta	Sí
Disco project	No	Alta	Baja	Sí
Apache Storm	No	Alta	Baja	Sí

A: Limitación de entrada de datos.
B: Adaptabilidad con otros lenguajes.
C: Facilidad de uso y soporte.
D: Uso en temas relacionados.

Fuente. Los autores

Por tanto, Hadoop proporciona una doble funcionalidad que en algunos casos las plataformas alternativas no van a poder ofrecer. Es decir, algunas de las herramientas cumplen únicamente una de las funcionalidades de Hadoop, aunque de un modo muy eficiente [17].

La arquitectura de Hadoop permite asegurar la entrega de mecanismos de conmutación por error y recuperación; está basada en flujos de contenidos multimedia en la Web. La red social Twitter genera información que se puede recolectar mediante Apache Flume; una herramienta que toma esta información en línea y la envía a un almacén centralizado como HDFS o HBase [18].

5.1. Herramientas para la obtención de datos

Existe gran variedad de bibliotecas para las API de Twitter en diferentes lenguajes. Recientemente, Twitter dispone de una librería hbc; un cliente Java HTTP para consumir de Streaming API, la cual tiene como requisito introducir las respuestas en formato JSON que devuelve Streaming API dentro de Hadoop Distributed File System. Para elegir la opción más adecuada se puede realizar una comparación entre los componentes de software más comunes para este propósito, Apache: Sqoop, Kafka, Scribe y Flume [19].

- **Sqoop**. Biblioteca que permite importar datos desde una base de datos estructurada, organizada en entidades que tienen un formato definido, hacia Hadoop. Permitiendo además exportar datos en sentido contrario. No se va a utilizar en el proyecto ya que no se desea importar datos desde una base de datos relacional.
- **Kafka.** Su principal caso de uso es un sistema distribuido de paso de mensajes publicación-suscripción. Adecuado para sistemas altamente confiables y escalables de mensajería empresarial en los que se deben conectar múltiples sistemas, incluyendo Hadoop. Tampoco haremos uso de este software que no se necesita un sistema de paso de mensajes con varios tipos de sistemas informáticos.
- **Scribe**. Está diseñado para escalar a un número muy grande de nodos y resistir a fallos en la red y en el nodo. El soporte que recibe cada vez es menor.
- **Flume**. Servicio distribuido, seguro y con alta disponibilidad para una eficiente recolección, unión y movimiento de grandes cantidades no solo de log data, sino también de cantidades masivas de eventos de datos. Incluye tráfico de datos de red y datos generados por "social media" procedentes de fuentes de datos no relacionales.

Luego de este análisis se seleccionó Apache Flume ya que maneja datos semiestructurados como son los tuits en JSON. Una de las ventajas de esta herramienta es su estructura: simple, robusta y flexible, orientada a *"Streams"*; los flujos de datos se componen de agentes que pueden agregar o transformar los eventos.

La misma que es una solución Java que permite recolectar y mover grandes cantidades de datos, desde algunas fuentes, principalmente servidores de aplicaciones HDSF con mayor

[3] El tipo de instalación realizada es Single Node

TwitterAgent.sources.Twitter.keywords= atasco, embotellamiento, transito, circulación, congestión, atascamiento, trafico, #tráficoUIO, #MOVILIDADuio, #viasAlternasUIO, #RadaresUIO

TwitterAgent.sources.Twitter.locations=--92.68,-S.01,-75.19.-2.34

TwitterAgent.sinks.HDFS.hdfs.path=hdfs://localhost: 54310/user/hduser/flume/tweets

Figura 5. Configuración Apache Flume
Fuentes. Los autores.

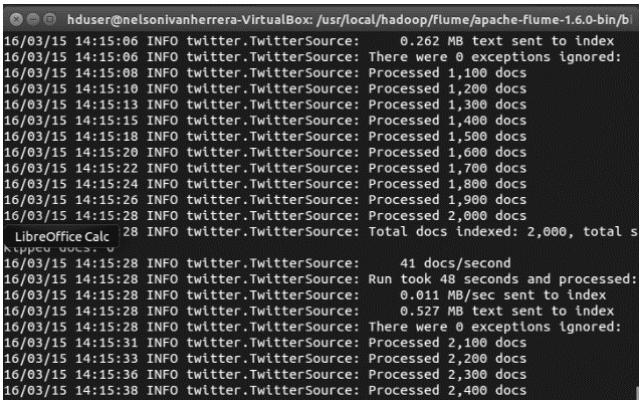


Figura 6. Pantalla de ejecución del agente Flume
Fuente. Los autores

velocidad a un espacio de almacenamiento de datos, permitiendo subir datos de Hadoop [20].

La instalación fue realizada en el sistema operativo Ubuntu 14.04, la Fig. 5 muestra los parámetros de configuración del agente Apache Flume[4].

Los campos utilizados para la configuración son:

TwitterAgent.sources.Twitter.keywords: esta configuración está dividida en dos grupos que son: keywords y hashtag. Los hashtags son los utilizados por el centro de gestión de la movilidad, por ello se los consideró.

TwitterAgent.sources.Twitter.locations: en esta configuración se colocó los puntos cardinales de la ciudad de Quito.

TwitterAgent.sinks.hdfs.pathTwitter.locations: dentro de esta configuración se colocó la ruta en donde se almacenarán los tuits recolectados.

En la Fig. 6, se muestra la ejecución del agente Flume, que tomará la información de tuits relacionados con situaciones de congestión vehicular, reportados por los ciudadanos.

5.2. Herramientas para el almacenamiento de datos

Para el almacenamiento de los datos y acorde con el análisis anterior, se ha seleccionado Apache Hadoop. Éste es un *framework* de software, que permite a las aplicaciones trabajar con miles de nodos. También es de licencia libre y se instaló la versión 2.6.0.

La Fig. 7 muestra la información de tuits almacenados en el sistema de archivos de Haddop, se puede apreciar los permisos, el grupo, el tamaño y el nombre de cada uno de ellos.

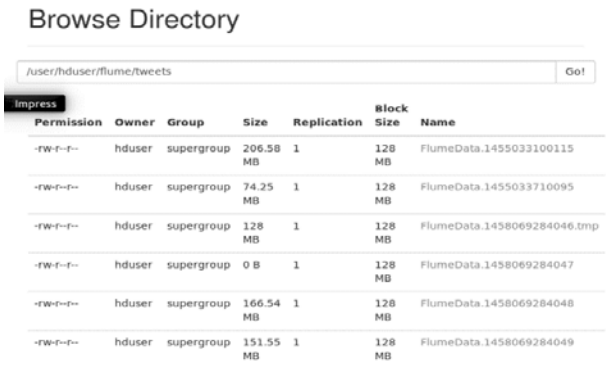


Figura 7. Recolección de tweets almacenados en Hadoop
Fuente. Los autores

5.3. Herramientas para el procesamiento de datos

A continuación, se realizará una comparación entre los componentes de software más comunes para analizar el conjunto de datos JSON almacenados en bruto, que contiene HDFS. Las herramientas son: Hive (Apache Hive), Cascading (Cascading.) y Pig (Apache Pig). Para investigación sobre datos en bruto son mejores los lenguajes procedimentales [19].

- **Cascading**. Framework de procesamiento de datos procedimental que permite a los usuarios construir flujos de datos en Java sobre Hadoop. Usa MapReduce para ejecutar todo su procesamiento de datos. Proporciona una librería de operadores, aunque también se pueden construir unos propios [19].
- **Pig**. Motor para ejecutar flujos de datos en paralelo sobre Hadoop. Usa MapReduce para ejecutar todo su procesamiento de datos. Para expresar estos flujos de datos utiliza el lenguaje procedimental Pig Latin. El cual incluye operadores tradicionales como join, sort, filter, etc. así como la posibilidad para los programadores de desarrollar sus propias funciones de lectura, procesamiento y escritura de datos [19].

Tanto Cascading como Pig son adecuados para Twitter Data Collection pero, finalmente, se ha escogido Pig ya que tiene más compatibilidades con todo el entorno Hadoop.

Pig Latin es un lenguaje de flujo de datos. Permite a los usuarios escribir cómo los datos de una o más entradas deben ser leídos, procesados y almacenados en una o más salidas en paralelo. Pig al igual que MapReduce, está orientado al procesamiento por lotes de grandes porciones del conjunto total de datos. Lee todos los registros de un archivo y escribe todas sus salidas secuencialmente. [19]

Se ha considerado el uso de Apache Pig para el procesamiento de datos, debido a que esta aplicación es un lenguaje de procedimientos que permite la consulta de grandes conjuntos de datos semiestructurados haciendo uso de Hadoop. La versión que se utilizó de Apache Pig es pig-0.16.0

6. Resultados

6.1. Información presentada por los sensores en Quito

Con el análisis de los valores presentados por los sensores y la relación con el parámetro de tráfico establecido por el

[4] La versión de utilizada es apache-flume-1.6.0



Figura 8. Mapa de tráfico de la ciudad de Quito (sensores)
Fuente. Los autores

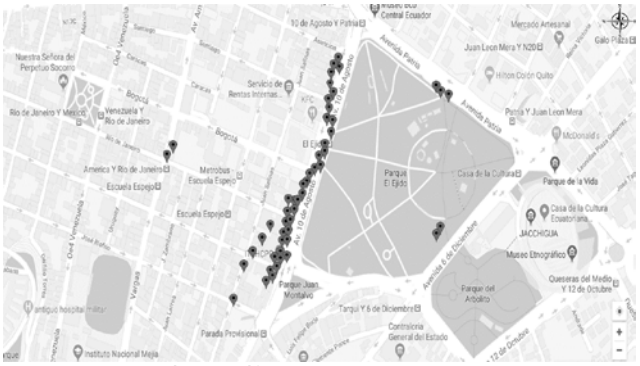


Figura 9. Localización geográfica de los tuits recopilados sobre un mapa de Quito
Fuente. Los autores

CGM, la Fig. 8 presenta cartográficamente posibles puntos de congestión vehicular en la ciudad de Quito, que corresponden al tráfico existente en el sector norte de la ciudad en el horario de 6:00 am a 7:00 am.

Como se puede observar, existen dos arterias principales donde existe tráfico vehicular que son la Av. Prensa – Diego de Vásquez y la 10 de agosto. Además, se observa tráfico en la Panamericana Norte y en la Av. Eloy Alfaro, con ello es claramente identificable los tramos donde existe congestión vehicular. El gráfico presentado corresponde a solamente un segmento de la ciudad; sin embargo, se puede observar que existe una simetría en los datos. Esto se debe a que los sensores no se encuentran a lo largo de toda la ciudad; solamente se encuentran en vías específicas que han sido consideradas más transitadas. Pueden existir muchos lugares con tráfico y que no son detectados, pues la cobertura de los sensores, no abarca todos los posibles lugares de congestión vehicular.

Uno de los puntos centrales de la aplicación en la cual se utilizarán las herramientas estudiadas, es el poder presentar en tiempo real el tráfico en la ciudad. Para esto es necesario captar los tuits indicativos de tráfico, la recopilación en una base de datos y la presentación gráfica de los puntos donde existe congestión.

De la información obtenida por la municipalidad de Quito, actualmente los sensores generan información, que es utilizada bajo demanda para analizar situaciones de congestión vehicular. Hoy en día esta entidad no dispone de una aplicación que le permita observar en tiempo real el tráfico en la ciudad, además que la misma solo hace referencia a los sectores en los cuales están instalados los sensores, lo cual no permite analizar todos los sectores que registran tráfico vehicular, en la localidad.

6.2. Información recolectada de la red social Twitter

La aplicación creada permite, a través de los tuits; disponer de información inmediata del tráfico, presentando los lugares donde al momento las personas indica que existe tráfico vehicular, con una actualización cada 5 minutos. Sin embargo, la alerta de tráfico se mantiene por un período de 30 minutos, lo cual permite observar de mejor manera el tráfico en la ciudad.

Para observar y verificar los resultados, se realizó un estudio inicial por un período de 3 meses, incluyendo los meses de mayo, abril y junio en los que se obtuvo información que sirve para validar la investigación realizada, contrastándola con la generada por los sensores existentes en la urbe.

En la figura presentada por el sistema puede observarse parte de la ciudad de Quito, donde se ha generado congestión vehicular. Se puede evidenciar también la existencia de lugares donde existe tráfico vehicular, de acuerdo a lo indicado por la población.

Comparando esta información con la presentada por los puntos informados a través de los sensores, se verifica por una parte la eficacia del sistema y por otra la falta de eficacia para determinar todos los puntos de tráfico con los sensores del municipio.

Al observar los datos generales de tráfico en la ciudad de Quito, señalados en la Fig. 9, establecidos a través de tuits, se puede observar que en la parte urbana existe a lo largo del día acumulación en diversos puntos, existiendo mayormente a nivel de sector centro norte puntos de congestión vehicular.

Con esta información se puede observar puntos de congestión, tanto con la información de los sensores, como de los tuits, mediante la interfaz gráfica de la aplicación. Para esto se utilizó la API de Google Mapas.

7. Conclusiones y trabajos futuros

La investigación ha permitido determinar, por una parte, la necesidad de la ciudad de Quito por contar con herramientas que permitan la toma de decisiones para mejorar la congestión vehicular.

Las herramientas de sustento y recopilación de la información analizada y considerada, han permitido la creación de una aplicación que permite medir la congestión vehicular. Para lo cual, se hace uso de los sensores existentes en la ciudad, pero principalmente mediante la data proporcionada por la red social Twitter, misma que ha sido recopilada para su procesamiento.

Los datos proporcionados por los tuits mostraron, en la mayoría de casos, mayor cobertura que los que presentan los sensores colocados a lo largo de la ciudad.

Se debe considerar como una opción viable y de menor costo el uso de la aplicación desarrollada, que toma los datos obtenidos de los tuits, para la toma de decisiones sobre congestión vehicular.

Se verifica la importancia y potencialidad de la aplicación, para que la misma sea utilizada como: ente emisor de alertas a los conductores, en la eficiencia y control del transporte público, entre otras, en beneficio de la ciudad de Quito.

Existe un sesgo en la investigación realizada, pues la misma se centra solamente en ciertos lugares de la ciudad en donde existen sensores, lo cual genera resultados parciales. Frente a esto, se recomienda considerar la implementación de sistemas de bajo costo (Arduino) [21], mediante la instalación de una constelación de sensores, en el resto de lugares de la ciudad.

La investigación realizada tiene una limitante importante, que está relacionada con la necesidad de que las cuentas de Twitter utilizadas deben tener activada la opción de geolocalización.

Una importante utilidad, que no forma parte del alcance de la presente investigación, hace referencia a poder retuitar los mensajes, informando rutas alternativas en caso de que las principales estén congestionadas.

Se limita la utilización del hashtag #TraficoUIO con la comunidad universitaria UTE.

Como trabajo futuro, se debe considerar mostrar gráficamente el tráfico desde el nivel Débil hasta el nivel Medio, y poder ejecutar acciones que prevengan situaciones de congestión vehicular.

Para comprobar que el sistema de sistema de información propuesto posibilita detectar situaciones de congestión vehicular en la ciudad de Quito. Se utiliza para el análisis estadístico el coeficiente de Pearson; que correlaciona el indicador de congestión vehicular de los sensores y el detectado por los mensajes de la red social Twitter.

Referencias

[1] INEC, Proyecciones de la población Ecuatoriana según Cantón, Cifras y estadisticas. [En línea]. [Consultado: 01-01-2015]. Disponible en: http://www.ecuadorencifras.gob.ec/documentos/web-inec/Poblacion_y_Demografia/Proyecciones_Poblacionales/proyeccion_cantonal_total_2010-2020.xlsx. [Último acceso: 10 12 2017].

[2] Alcaldía de Quito, Noticias, Distritro Metropolitano de Quito. [En línea]. [Consultado: 01-01-2011]. Disponible en: http://www.diariocritico.com/noticia/155769/noticias/la-congestion-vehicular-sigue-sin-solucion-en-quito.html.. [Último acceso: 15 10 2015].

[3] Pinto, G., Hacia una movilidad inteligente en la ciudad de Quito, pp. 20-25, 2013.

[4] Herrera, N.H. and Santamaria, H.S., Analysis of the factors generating vehicular traffic, de ICEDEG Conference on eDemocracy & eGovernment, Quito, 2016.

[5] Zikopoulos, C.E.P., Understanding Big Data: analytics for enterprise class hadoop and streaming data, Chicago: McGraw-Hill Osborne Media, 2011.

[6] Aguilar, L.J., Big Data análisis de grandes volúmenes de datos en organizaciones, México: Alfaomega Grupo Editor, S.A, 2013.

[7] Delgado, P.S.M.V.J., CBI Ciencias básicas e ingeniería,. [En línea]. [Consultado: 7-12-2011]. Disponible en: http://sgpwe.izt.uam.mx/pages/cbi/psb/vfinal.pdf. [Último acceso: 08 03 2018].

[8] Kwak, D., Liu, R., Kim, D., Nath, B. and Iftode, L., Seeing is believing: sharing real-time visual traffic information via vehicular clouds, IEEE Access, 4(12), pp. 3617-3631, 2016. DOI: 10.1109/ACCESS.2016.2569585

[9] Cárdenas-Benítez, N., Aquino-Santos, R., Magaña-Espinoza, P., Aguilar-Velazco, J., Edwards-Block, A. and Medina-Cass, A., Traffic congestion detection system through connected vehicles and Big Data, Sensors, 16(5), p. 599, 2016. DOI: 10.3390/s16050599

[10] Tostes-Ribeiro, A., Henrique-Silva, T., Duarte-Figueiredo F. and Loureiro, A.A.F., Studying traffic conditions by analyzing foursquare and instagram data, in: Symposium on performance evaluation of wireless ad hoc, sensor, & ubiquitous networks, Canada, 2014.

[11] P.D.B.L. Eleonora D' Andrea, Real-Time Detection of Traffic From Twitter Stream Analysis, IEEE Transactions on Intelligent Transportation Systems, 16(4), pp. 2269-2283, 2015. DOI: 10.1109/TITS.2015.2404431

[12] Nellore, K. and Hancke, G.P., A survey on urban traffic management system using wireless sensor networks, Sensors, 16(2), p. 157, 2016. DOI: 10.3390/s16020157

[13] García, F.C., Umap, inteligencia colectiva extraída de las redes sociales, Profit, Barcelona-España, 2010.

[14] Reyes-Zambrano, G. and Hidalgo-Veliz, R.N., Vehicular swept path analysis using K-means algorithm, International Journal of Applied Engineering Research, 11(18), pp. 9536-9538, 2016.

[15] Villena-Román, J., Luna-Cobos, A. y González-Cristóbal, J.C., Análisis semántico de la opinión de los ciudadanos, SEPLEN, 53, pp. 59-162, 2014.

[16] Universidad Distrital Francisco José de Caldas, [En línea]. [Consultado: 08-03-2018]. Disponible en: http://repository.udistrital.edu.co/bitstream/11349/3815/3/ParraRinconDanielaAlejandraAnexo-3.pdf.

[17] Herramientas para Big Data: Entorno Hadoop., 2014.

[18] Time Outsourcing Center, Introducción a Hadoop y su ecosistema, 2015. [En línea]. Disponible en: http://www.ticout.com/blog/2013/04/02/introduccion-a-hadoop-y-su-ecosistema/.

[19] Pérez, B.G., TDC (Twitter Data Collection): creación de una gran base de datos de Tweets., Universidad Autónoma de Madrid, Madrid, España, 2014.

[20] Schmarzo, B., Big data, el poder de los datos, Estados Unidos: Anaya Multimedia-Anaya Interactiva, 2014.

[21] Faludi, R., Building Wireless sensor networks, United States of America: O' Reilly Media, 2011.

N.I. Herrera-Herrera, es profesor auxiliar de la Facultad de Ciencias de la Ingeniería e Industrias de la Universidad Tecnológica Equinoccial, Quito Ecuador. Obtuvo su grado de MSc. en Gerencia de Sistemas en la Universidad de las Fuerzas Armadas "ESPE", Quito-Ecuador. En la actualidad está finalizando su grado doctoral en la Universidad de Extremadura, España. Profesionalmente ha colaborado con importantes instituciones financieras en el manejo de proyectos tecnológicos. Su especialidad de investigación está centrada en ciudades inteligentes con Big Data. Desarrolla e implementa sistemas informáticos para Pymes.
ORCID: 0000-0002-5781-6444

S. Lujan-Mora, es profesor titular de Departamento de Lenguajes y Sistemas Informáticos de la Universidad de Alicante. Obtuvo su grado de Doctor Ingeniero en Informática en la Universidad de Alicante, España en el año 2005 con una tesis sobre el modelado de almacenes de datos con UML. Ha realizado estancias posdoctorales en Estados Unidos y Ecuador. Desarrolla e implementa aplicaciones web desde 1997 y enseña a hacerlo en la universidad desde 1999. Sus temas principales de investigación incluyen el desarrollo de aplicaciones web, la usabilidad y la accesibilidad web, el e-learning, los cursos en línea abiertos y masivos (Massive Open Online Courses, MOOC) y los recursos educativos abiertos (REA).
ORCID: 0000-0001-5000-864X

E.R. Gómez-Torres, se graduó de Ing en Sistemas en 1998, es MSc. en Gerencia de Sistemas en el 2001, todos ellos de la Universidad de las Fuerzas Armadas "ESPE" en Quito-Ecuador. Desde 2000 hasta la presente fecha labora como profesor en la ESPE, trabajando también como consultor en diferentes empresas del sector privado y público en el Ecuador y otros países; posteriormente se unió trabajar en la Universidad Tecnológica Equinoccial, Quito, Ecuador, a partir del 2013 hasta la presente fecha. Su campo de investigación incluyen líneas como: desarrollo de aplicaciones móviles en contextos, Big data, inteligencia de negocios, analítica de datos, machine learning, IoT, modelos predictivos y minería de texto y datos.
ORCID: 0000-0002-1171-7256

Entregando
lo mejor de los
colombianos

Línea de atención al Cliente Nacional: **01 8000 111 210**
Línea de atención al Cliente Bogotá: **(57-1) 472 2000**
www.4-72.com.co

DYNA
85 (205), June, 2018
is an edition consisting of 150 printed issues
which was finished printing in the month of June of 2018
in Todograficas Ltda. Medellín - Colombia

The cover was printed on Propalcote C1S 250 g,
the interior pages on Propal Beige 90 g.
The fonts used are Times New Roman, Imprint MT Shadow

- Discrimination between the lognormal and Weibull distributions by using multiple linear regression
- Study of agglomeration and magnetic sedimentation of Glutathione@Fe3O4 nanoparticles in water medium
- Ab-initio analysis of magnetic, structural, electronic and thermodynamic properties of the Ba2TiMnO6 manganite
- A geometrical robust design using the Taguchi method: application to a fatigue analysis of a right angle bracket
- Normalized difference vegetation index for rice management in El Espinal, Colombia
- Effects of cutting parameters on surface roughness and hardness in milling of AISI 304 steel
- Verification of the vibrational theoretical assignment of the DADP using isotopic labelling
- Effect of the tryptone concentration on the calcium carbonate biomineralization mediated by Bacillus cereus
- Development of a high performance batteries charger with low THD, high power factor, and high efficiency
- Elastic behavior of stiffened curved plates subjected to transverse loading
- Incorporation of aluminum oxide in the formulation of pastes for building materials
- Risk analysis using meteorological weather factors in solar energy conversion systems
- Obtaining the electrical impedance phase using Wavelet transform and Fourier transform from transient signals. Part 2: practical assessment and validation
- Streptomyces clavuligerus strain selection for clavulanic acid biosynthesis: a study based on culture composition effects and statistical analysis
- Hydraulic conductivity in layered saturated soils assessed through a novel physical model
- Impact of changing location and power of a PV system in electrical distribution networks, integrating MATLAB and OpenDSS
- Crack filling in concrete by addition of Bacillus subtilis spores – Preliminary study
- Thermal conductivities estimation in orthotropic materials making use of global optimization algorithms
- Obtention and characterization of lithium superionic conductors using the glass-ceramic method
- Hydrogen production in a novel configuration of UASB reactor under different hydraulic retention time
- Flash flotation of free coarse gold using dithiophosphate and dithiocarbamate as a replacement for traditional amalgamation
- Model of nonlinear behavior applied to prediction of settlement in deep foundations
- Evaluation of the lubricating power of sweet almond oil without additives
- Application of double filtration with granular activated carbon for Atrazine reduction on water treatment processes
- Experimental characterization, modeling and compensation of hysteresis in force sensing resistors
- Comparison of three IRP-based models to reduce logistics costs and greenhouse gas emissions
- Highway designs: effects of heavy vehicles stability
- An analysis of the socioenvironmental problems created by the construction of road tunnels in Colombia: case study
- Microalgae biorefineries: applications and emerging technologies
- Evaluation of turbidity and dissolved organic matter removal through double filtration technology with activated carbon
- Construction of a short circuit frequency map to define GMAW-S parameters during WPSs development
- Analysis of the European tourist mines and caves to design a monitoring system
- Characterization of postures to analyze people's emotions using Kinect technology
- Local polynomial approximation and intersection of confidence intervals for removing noise of lightning electric field measurements
- Methodology to determine the mean and extreme sea level regimes (astronomical and meteorological tide) considering scarce records in microtidal zones: colombian Caribbean case
- Development of an information system for teleoperated physical rehab care service via Internet. Pilot case: patients with mild knee injury who live in geographically vulnerable zones
- Design and implementation of a photolithography system to fabricate microdevices from thin films
- Mitigation potential of active transport projects: trip attraction and CO2 avoidance indicators in colombian cities
- Shear modulus of mining tailings from resonant column tests
- Assessment strategies for the integral management of waste electrical and electronic equipment-WEEE
- Bioactivity analysis of the AZ31 Mg alloy coated by PEO (Plasma Electrolytic oxidation)
- Manufacture of oxy-acetylene thermally sprayed coatings on refractory substrates from unconventional feedstock material
- Risk assessment in treatment processes for the development of a Water Safety Plan – WSP
- Freight vehicle condition monitoring through the availability
- Integration of tools for decision making in vehicular congestion

- Discriminación entre la distribución lognormal y la distribución Weibull utilizando regresión lineal múltiple
- Estudio de aglomeración y sedimentación magnética de nanopartículas de Glutatión@Fe3O4 en medio acuoso
- Análisis ab-initio de las propiedades magnéticas, estructurales, electrónicas y termodinámicas de la manganita Ba2TiMnO6
- Un diseño geométrico robusto empleando el Método de Taguchi: aplicación a un análisis de fatiga de una escuadra
- Índice de vegetación de diferencia normalizada para el manejo del arroz en El Espinal, Colombia
- Efectos de los parámetros de corte en la rugosidad superficial y la dureza en el fresado del acero AISI 304
- Verificación de la asignación vibracional teórica de DADP usando marcaje isotópico
- Efecto de la concentración de triptona en la biomineralización de carbonato de calcio mediada por Bacillus cereus
- Desarrollo de un cargador de baterías de alto desempeño con bajo THD, alto factor de potencia y alta eficiencia
- Comportamiento elástico de placas curvas rigidizadas sometidas a cargas transversales
- Incorporación de óxido de aluminio en la formulación de pastas para materiales de construcción
- Análisis de riesgo usando factores meteorológicos en sistemas de conversión de energía de solar
- Obtención de la fase de la impedancia eléctrica usando transformada Wavelet y transformada de Fourier de señales transitorias. Parte 2: evaluación práctica y validación"
- Selección de una cepa de Streptomyces clavuligerus para la biosíntesis de ácido clavulánico: un estudio basado en los efectos de la composición del medio de cultivo y análisis estadístico
- Estimación de la conductividad hidráulica en suelos saturados estratificados mediante un nuevo modelo físico
- Impacto del cambio de la ubicación y la potencia de un sistema FV en redes de distribución eléctrica, integrando MATLAB y OpenDSS
- Relleno de fisuras en concreto por la adición de esporas de Bacilos subtilis - Estudio preliminar
- Estimación de conductividades térmicas en materiales ortotrópicos mediante algoritmos de optimización global
- Obtención y caracterización de conductores superiónicos de litio utilizando la ruta vitrocerámica
- Producción de hidrogeno utilizando una nueva configuración de reactor anaerobio UASB bajo diferentes tiempos de retención hidráulica
- Flotación flash de oro nativo grueso usando ditiofosfato y ditiocarbamato como remplazo de la amalgamación tradicional
- Modelo de comportamiento no lineal aplicado a la predicción de asentamiento en fundaciones profundas
- Evaluación del poder lubricante de aceite de almendras dulces sin aditivos
- Aplicación de la doble filtración con carbón activado granular para la reducción de Atrazina en procesos de tratamiento de agua potable
- Caracterización experimental, modelado y compensación de la histéresis en sensores de fuerza resistivos
- Comparación de tres modelos basados en el IRP para reducir costos logísticos y emisiones de gases efecto invernadero
- Diseño de autopistas: efectos de la estabilidad de vehículos pesados
- Análisis de la problemática socioambiental generada por la construcción de túneles viales en Colombia: caso de estudio
- Biorefinerías de microalgas: aplicaciones actuales y nuevas tecnologías en desarrollo
- Evaluación de la remoción de turbiedad y materia orgánica disuelta mediante la tecnología de doble filtración con carbón activado
- Construcción de un mapa de frecuencias de corto-circuito para definir parámetros de GMAW-S durante el desarrollo de WPSs
- Análisis de las cuevas y minas turísticas de Europa para diseñar un sistema de monitorización
- Caracterización de posturas para el análisis de emociones de personas, por medio de la tecnología Kinect.
- Aproximación local polinomial e intersección de intervalos de confianza para la remoción de ruido en mediciones de campo eléctrico generado por rayos
- Metodología para determinar regímenes medios y extremales del nivel del mar (marea astronómica y meteorológica) cuando se cuenta con escasos registros instrumentales en áreas micromareales: caso Caribe colombiano
- Desarrollo de un sistema de información para el servicio de atención tele-operado de rehabilitación física, vía Internet. Caso piloto: pacientes con lesiones leves de rodilla que viven en zonas de vulnerabilidad geográfica
- Diseño e implementación de un sistema de fotolitografía para fabricar microdispositivos a partir de películas delgadas
- Potencial de mitigación de proyectos de transporte activo: indicadores de atracción de viajes y emisiones CO2 en ciudades colombianas
- Módulo de corte de relaves mineros a partir de ensayos de columna resonante
- Evaluación de estrategias para la gestión integral de residuos de aparatos eléctricos y electrónicos
- Análisis de la bioactividad de Mg AZ31 recubierta por PEO (Plasma Electrolytic Oxidation)
- Elaboración de recubrimientos cerámicos sobre sustratos refractarios utilizando proyección térmica oxiacetilénica a partir de materias primas no convencionales
- Evaluación del riesgo en procesos de tratamiento para el desarrollo de un Plan de Seguridad del Agua – PSA
- Monitoreo de la degradación de los vehículos de transporte de cargas a través de la disponibilidad
- Integración de herramientas para la toma de decisiones en la congestión vehicular

DYNA
Publication admitted to the
Sistema Nacional de Indexación y Homologación de
Revistas Especializadas CT+I - PUBLINDEX, Category A2

Red Colombiana de Revistas de Ingeniería

UNIVERSIDAD NACIONAL DE COLOMBIA
SEDE MEDELLÍN
FACULTAD DE MINAS